NIST Special Publication 1239-1

NIST Conference Papers
Fiscal Year 2017
Volume 1: Engineering Laboratory

Compiled and edited by:
Andrea Medina-Smith
Kathryn Miller
Karen Wick

This publication is available free of charge from:
https://doi.org/10.6028/NIST.SP.1239-1

National Institute of
Standards and Technology
U.S. Department of Commerce

NIST Special Publication 1239-1

NIST Conference Papers Fiscal Year 2017

Volume 1: Engineering Laboratory

Compiled and edited by:
Andrea Medina-Smith
Kathryn Miller
Karen Wick
Information Services Office

This publication is available free of charge from:
https://doi.org/10.6028/NIST.SP.1239-1

August 2019

U.S. Department of Commerce
Wilbur L. Ross, Jr., Secretary

National Institute of Standards and Technology
Walter Copan, NIST Director and Undersecretary of Commerce for Standards and Technology

National Institute of Standards and Technology Special Publication 1239-1
Natl. Inst. Stand. Technol. Spec. Publ. 1239-1, 720 pages (August 2019)
CODEN: NSPUE2

This publication is available free of charge from: https://doi.org/10.6028/NIST.SP.1239-1

Foreword

NIST is committed to the idea that results of federally funded research are a valuable national resource and a strategic asset. To the extent feasible and consistent with law, agency mission, resource constraints, and U.S. national, homeland, and economic security, NIST will promote the deposit of scientific data arising from unclassified research and programs, funded wholly or in part by NIST, except for Standard Reference Data, free of charge in publicly accessible databases. Subject to the same conditions and constraints listed above, NIST also intends to make freely available to the public, in publicly accessible repositories, all peer-reviewed scholarly publications arising from unclassified research and programs funded wholly or in part by NIST.

This Special Publication represents the work of Engineering Laboratory researchers at professional conferences, as reported in Fiscal Year 2017.

More information on public access to NIST research is available at https://www.nist.gov/open**.**

Table of Contents

Commissioning High-Performance Residential Buildings: Lessons from the NIST Net-Zero Energy Residential Test Facility

Natascha Milesi Ferretti
National Institute of Standards and Technology

Synopsis

This paper provides an overview of important considerations for commissioning (Cx) high-performance residential buildings, including recommendations based on lessons learned from designing, constructing, and operating the Net-Zero Energy Residential Test Facility (NZERTF). Common quality assurance practices in residential construction are reviewed, and the benefits of applying commissioning processes from commercial buildings to ensure proper system performance in high-performance residential buildings are described. Although the National Institute of Standards and Technology (NIST) NZERTF was only partially commissioned in a formal sense, a review of the processes employed is conducted, including initial commissioning considerations for each of the major NZERTF building systems: thermal envelope, heating ventilating and air-conditioning (HVAC), water heating, solar photovoltaic, and lighting. Specific recommendations are made for key performance assurance measures to form the basis of an ongoing commissioning plan for the NZERTF.

About the Author

Natascha Milesi Ferretti is a Mechanical Engineer at the National Institute of Standards and Technology. Her current research is focused on building commissioning for improved energy performance. She has worked on several projects in the areas of commissioning and fault detection and diagnostics, including two International Energy Agency research projects on building commissioning (Annex 40 and Annex 47).

Milesi-Ferretti, Natascha.
"Commissioning High-Performance Residential Buildings: Lessons from the NIST Net-Zero Energy Residential Test Facility."
Paper presented at National Conference on Building Commissioning, Indian Wells, CA. May 15, 2017 - May 17, 2017.

Overview of Residential Commissioning

The residential construction industry already voluntarily performs a variety of quality control measures, such as visual inspections and functional performance checks of mechanical equipment. However, many factors that influence installation quality cannot be controlled under field-construction conditions and can result in deficiencies. For example, in a review of 17 houses with an average fan flow of 1495 m^3/h (880 cfm) built by the same design and construction crews in the same subdivision, Walker et al (1998) found variations in duct leakage on the order of 170 m^3/h (100 cfm) for supply ducts and 85 m^3/h (50 cfm) for return ducts and concluded that the specific installation, rather than system design, was the determining factor for duct leakage. Matson et al. (2002) studied the potential benefits of commissioning homes in California and estimated the resulting savings of HVAC-related energy to be 15 % to 30 % in existing houses, 10 % to 20 % in new conventional houses, and up to 8 % in advanced energy efficient houses.

The use of a formal Cx procedure to identify and correct deficiencies can improve building performance, but is rare in residential construction. This is in part due to the inherent difficulty in quantifying avoided costs, and the belief that quality assurance is already part of the construction contract. Assumptions are often made that new construction means excellent energy performance, and that any potential problems would be visible to and resolved by the builder. However, since performance cannot be tested over the full range of operating conditions, the identification of issues often falls to the individual owner or occupant; without the owner calling for the builder to address a warranty, maintenance, or service issue, the deficiencies will not be addressed. The problem with this situation is that homeowners do not generally have the expertise to identify performance issues associated with the building envelope (including the roof, exterior walls, windows, doors, and foundation), ventilation system and ductwork, controls, and appliances (including furnaces, air-conditioners and water heaters). It is often only during the purchase of an existing home that buyers will contract a licensed home inspector to conduct a detailed home inspection to identify problems, including issues that could have been corrected during the construction process but these inspectors focus on functionality and safely, rather than efficiency. There is a benefit in reviewing the design as part of the commissioning as it is most cost-effective to correct potential issues on paper than during construction or after completion.

Within residential construction, there are niche applications, such as high-performance buildings, where system complexity and risk of not achieving the full potential of the design more clearly justify the investment in a formal commissioning process for quality assurance. Lukachko et al. (2011) presented Building America Program case studies showing how systems engineering of residential buildings, including applying specific construction requirements and performance metrics, reduced 50 % of heating-related energy and 30 % of cooling-related energy consumption relative to code-compliant construction. An advanced building design, such as the NZERTF, employs strategies to improve system and equipment efficiency on a component-by-component basis and its success is dependent on ensuring that the home is designed, built and operated properly. Pettit et al. (2015) present ten design principles for net-zero energy homes, which includes coordinating and commissioning systems as part of the project plan. Integrated commissioning for residential construction considers the house as a system of interacting

subsystems, auditing and testing components and systems, and implementing improvements to energy efficiency and occupant comfort.

For commercial buildings, ASHRAE Guideline 0-2013 (ASHRAE 2013) presents the commissioning process to verify that the systems meet the owner's project requirements. Commissioning extends into the operations phase in order to verify performance under a full range of operating conditions and seasonal differences, to ensure that the performance of both the heating and cooling systems are verified. The main activities are to: identify the Cx team, identify the performance requirements, update the Cx plan, verify achievement of current facility requirements, investigate unacceptable performance or outcomes, implement corrective actions, update systems manual and facility personnel training, write/deliver a Cx report, and obtain owners acceptance. For residential buildings, the process is simpler because houses have less complex control systems, fewer elements, and no formal operations and maintenence personnel. Wray et al. (2004) present three phases for residential commissioning as follows:

- Survey the house performance using audit and diagnostic techniques
- Perform 'on the spot' tuning and tweaking to improve system performance
- Identify opportunities for potential repair or retrofit

In the case of high-performance residential buildings, the increased complexity and risk warrants a hybrid approach. Lukachko et al. (2008) present a quality assurance roadmap for the construction of high performance buildings which includes seven steps:

1. Review of past construction and risk assessment
2. Setting performance goals
3. Changes to drawings, specifications, contracts and trades scopes-of-work
4. Training for site supervision and trades
5. On-site inspections, verification, and trouble-shooting
6. [1]Commissioning (testing the mechanical systems and other equipment)
7. Post construction evaluation

Although it has become more commonplace to have service contracts for home HVAC systems, the same type of tune-up and assessment is needed for a broad variety of systems to ensure persistence of good operation and performance.

The NZERTF was commissioned during the design phase as part of the requirements of the Leadership in Energy & Environmental Design (LEED) certification process, but was not fully

[1] The ASHRAE definition of commissioning process is broader, encompassing the tasks associated with these seven steps listed here and defines the tasks described in Step 6 as Functional Performance Testing:

commissioned using the recommended hybrid approach. The objective of this paper is to take a retrospective look at what was done to commission the NZERTF, and consider what could have been done differently to improve the process. The recommendations for initial commissioning presented in the next section are based on industry best practices as well as the experience gained from the design, construction and two years of operating the NZERTF. The subsequent section presents a plan for the ongoing commissioning of the NZERTF. It is anticipated that the recommendations and ongoing Cx plan can be more broadly applied to other high-performance residential buildings projects.

Initial Commissioning Considerations for the NIST Net Zero Energy Residential Test Facility

The Net Zero Energy Residential Test Facility (NZERTF) shown in Figure 1 is a LEED Platinum-designed facility with state-of-the-art building components including thermal envelope, solid state lighting, high-efficiency space conditioning equipment, solar water heating, and solar photovoltaics (NIST and BSC 2011).

Figure 1: NIST NZERTF (Photo Credit: B. Young)

Fanney et al. (2015) describe the design and performance of the NZERTF, a 252 m^2 (2700 ft^2), two-story residential building with a basement, attic, and rooms typical of what is found in a house in the state of Maryland, plus a detached 65 m^2 (700 ft^2) garage. The entire house, including the unfinished 135 m^2 (1450 ft^2) basement and the attic, is conditioned. The unconditioned garage serves as the facility control room, housing the extensive instrumentation that is used to monitor the performance of the building and its various components/systems. The facility also emulates the energy and hot water consumption of a "simulated family of four," using programmed occupancy and energy use profiles. The sensible and latent heat loads of the simulated occupants, lights turning on and off, showers starting and stopping, and cooking and other systems are all controlled from the garage (Omar and Bushby 2013).

NIST envisions using this facility for many years to address the measurement science challenges associated with a range of building systems as well as the whole building system performance as buildings approach net-zero operation (Davis et al. 2014). The project successfully demonstrated net-zero operation of the NZERTF over the course of one year with simulated occupancyand currently serves as a research and development test facility where additional mechanical and design features are being evaluated. The NZERTF was initially commissioned in 2012 by Thierren Waddell, which provided points to qualify for the LEED Platinum rating. The scope of the commissioning effort was limited to design and construction phase. Only the photovoltaic system was commissioned separately by the supplier, which also included basic operator training. Third-party testing was limited to evaluating airtightness and did not address functional performance testing of all systems. Instead, a team of NIST researchers carried out the work of monitoring the system, once the building was put into operation. Their expertise, combined with the tremendous monitoring capabilities of the facility instrumentation, enabled very effective surveillance of system performance that would likely only have been found through active testing as a part of commissioning building operations. As a result, some of issues that negatively impacted the energy efficiency performance were identified during the net-zero demonstration period, (Kneifel et al. 2015).

The following subsections give a high-level overview of the various systems in the NZERTF, along with specific commissioning tasks and lessons learned. In each subsection, a table lists the recommended commissioning activites. Shaded items were not originally part of the NZERTF commissioning activities but would add value to the process. These form the basis for the key recommendations for the ongoing commissioning plan found in the last section of this paper.

Thermal Envelope

The building envelope consists of the major systems intended to separate the indoor spaces from outdoors in terms of heat transfer and airflow, including the roof, exterior walls, foundation, windows, and doors. In residential buildings, the building envelope is the primary system responsible for heating and cooling loads, with internal loads being secondary. In a high performance building, the building envelope must include a continuous air barrier to minimize infiltration of unconditioned air, and a continous insulation system to minimize conductive losses. These goals include minimizing mechanical penetrations through the envelope that can compromise its thermal integrity. The building envelope must be properly designed to achieve high levels of airtightness, insulation, moisture control and glazing performance, and subsequently verified. Improper design, material selection, or faulty installation can result in poor performance in any or all of these respects. Table 1 presents the plan for commissioning the thermal envelope of the NZERTF.

At design, a simple way to confirm continuity of the building envelope is to perform a ‘pen-test’, tracing the water barrier, thermal barrier, air barrier, and vapor barrier from roof to slab. At no point should there be a break in the continuity of these barriers. these barriers must also be inspected at the time of installation, focusing on envelope subsystem interfaces (e.g., wall-window, wall-wall), insulation type, placement of the air barrier and vapor barrier, any damage during construction, and other potential issues (e.g., blocked ventilation pathways).

Visual inspections must be carried out to inspect the envelope for wetness, microbial growth, color or texture changes, decay, or structural dislocation, paying special attention to plumbing system leaks. This inspection extends to construction materials before they are installed. Pressurization testing to determine air leakage rates, also known as blower-door testing, can identify the existence of construction deficiencies but does not pinpoint the air leakage locations.

Table 1: Recommendations for commissioning the NZERTF thermal envelope *

Element	Test Description
Envelope Design	1-1. **Perform a 'pen-test', tracing the water barrier, thermal barrier, air barrier, and vapor barrier from roof to slab. At no point should there be a break in the continuity of these barriers.**
Insulation Quality	1-2. **Visual inspection- framing, insulation type, installation, placement of air and vapor barrier, barrier damage, blocked ventilation pathways etc.** a. **3rd-party testing, check for gaps and voids pre-insulation and post insulation per specifications, tested thickness/density pre-drywall.**
	1-3. Thermographic survey/Infrared inspection- a. **Check for thermal bridging, air leakage, air intrusion, missing, displaced, or improper insulation.** b. **Check under pressurized and depressurized conditions**
Windows	1-4. **Visual Inspection -framing, glazing type, installation**
	1-5. **Handheld Spectrometer to determine window emittance class**
	1-6. **ANSI 1105 test method for air/water leakage**
Airtightness	1-7. **Pressurization testing to determine air leakage per ASTM E779.** a. **test after the moisture barrier without any penetrations is installed and repeat when windows/doors are installed** b. **perform air leakage test on windows, doors and other moisture barrier penetrations**
Envelope Moisture	1-8. **Visual inspection for wetness, microbial growth, color or texture changes, decay, or structural dislocation. Special attention to plumbing system leaks.**
	1-9. **Electrical inspection (for detection or diagnosis of any moisture problem)** a. **surface scanning dielectric meters emit low frequency electromagnetic waves and detect their disturbance to determine average moisture content** b. **determine moisture content for building framing.**

*Shaded items were not part of the original NZERTF commissioning activities.

Airtightness testing is recommended at various stages in the construction process: 1) after air barriers are in place, but before any penetrations are made, 2) once windows and doors are installed, but before drywall is installed, 3) at substantial completion, and 4) at final completion. For the NZERTF, a total of four separate blower door tests were performed as quality control during construction and to confirm that the thermal envelope airtightness met the design targets. The early tests provided valuable information on the construction of the NZERTF at times when corrective measures such as improving building seals, or reducing air leakage could be taken with minimal impact on costs. For troubleshooting, a thermographic survey or infrared inspection carried out under pressurized and depressurized conditions can help identify thermal bridging, air leakage, and missing, displaced or improper insulation, but such an evaluation of the envelope was not conducted in the NZERTF. Thermographic surveys were carried out later during operation to identify potential issues with the photovoltaic system.

In the case of the NZERTF, the blower-door testing conducted at final completion with the kitchen vent and clothes dryer vents sealed and all the results showed high levels of building airtightness. Nevertheless, visual inspections for wetness led to the discovery of improperly manufactured window seals that failed to maintain the moisture barrier and were replaced under warranty by the manufacturer. A pressurized water spray test, such as ASTM E1105 (2015) water penetration test would have identified this deficiency earlier in construction, but are not typically carried out in residential construction.

Heating Ventilating and Air-Conditioning (HVAC) Systems

The NZERTF was designed as a laboratory, with the ability to use one of four different HVAC configurations: 1) a centrally-ducted system with a dehumidifying, air-to-air heat pump or gas furnace/AC; 2) a small-duct, high-velocity heat pump system; 3) two, smaller, multi-split heat pump units with minimal ducting; or 4) a ground-source heat pump using one of three, independent in-ground heat exchangers (vertical, straight line horizontal, and a horizontal slinky coil) and the traditional air ducts. Additionally, a heat recovery ventilator (HRV) was selected and installed to provide constant-volume airflow with air-to-air heat recovery to minimize energy losses associated with ventilation, while ensuring that the space provides the ventilation rate required to meet ASHRAE Standard 62.2-2010 (ASHRAE 2010) requirements.

For the first two years of operation, HVAC Configuration 1, with a dedicated, dehumidifying, air-to-air heat pump was installed as shown in Figure 2. The dehumidification function is provided by control algorithms and a hot gas bypass arrangement, with an additional reheat heat exchanger placed within the indoor air handler. Studies during the third year of operation are comparing a modified Configuration 1 (without dehumidification) to Configuration 2 (small duct, high velocity system). The additional ducts and ground-source loops for Configurations 3 and 4 were constructed for use in future experiments and have not yet been commissioned. This section will address commissioning of the vapor compression equipment, air distribution ducts, heat pump and HRV, as well as the future commissioning of the geothermal systems. Table 2 presents the plan for commissioning the NZERTF HVAC systems.

Figure 2. Air-source heat pump installed at NZERTF

Key factors for meeting capacity and efficiency targets for vapor compression equipment include refrigerant charge levels, airflow across coils, and proper control. Domanski et al. (2015) found that duct leakage, refrigerant undercharge, oversized heat pumps, low indoor airflow due to undersized ductwork and refrigerant overcharge had the greatest potential for causing significant performance degradation and increased energy consumption. For duct leakage, the impact on air distribution systems can be particularly significant if leakage is into unconditioned space. Jump et al. (1996) found that duct losses on the order of 35 % are common for residential construction, and measured an average 18 % decrease in HVAC energy use after sealing and insulating ducts. Testing and balancing is important to ensure that the designed air flows actually are provided at each vent is key. Otherwise it leads to over/under heating/cooling of some areas, which leads to inefficiency and thermal discomfort. Other ventilation systems, such as those installed in bathrooms, kitchens and attics can increase heat loads, can increase the likelihood of moisture problems, and degrade indoor environmental quality if not properly commissioned. For ground-source heat pumps, the system loop integrity, control of the loop flow rate and to loop thermal response characteristics are critical.

In terms of commissioning activities for ducts, Walker and Sherman (2002) indicate that total duct leakage should be measured by one of two means:

1. Duct pressurization test: this can be done in unfinished or finished houses using a small fan-assisted flow meter, and in some cases a blower-door as well, to determine duct leakage by pressurizing the duct system to 25 Pa with the supply and return grilles sealed, or

2. Delta Q duct leakage test: changing airflows through the distribution system by turning the air handler on and off while pressurizing and then depressurizing the building envelope to various pressure differentials using a blower-door.

Walker and Sherman propose that testing must show that the duct leakage is less than 5 % of the rated flow for the total air handling system. Two compliance mechanisms are acceptable: one can test total duct leakage to the exterior at finish stage, or test total duct leakage at duct rough-in stage. When more than one air handler exists, each air-handling system must individually meet the requirement. If zoning is used, all zone dampers must be open and any motorized outside air ventilation dampers must be closed. The system must also be properly balanced, with the forced-air system providing balanced distribution of airflow to all conditioned spaces and zones of the house.

In the NZERTF, duct pressurization tests were done by the design-build firm, together with NIST. Each duct run was individually tested in the rough-in stage. In addition, special care was taken in design of the NZERTF to minimize the impacts of duct leakage, to run ducts in conditioned space, and to implement good construction practices. These efforts included ensuring the following: duct work is covered and dry before installation; filters are in place during construction and then changed before occupancy; the house is kept clean to minimize contaminants; the house is sealed

before bringing in the drywall to reduce the likelihood of moisture problems, and testing and balancing is conducted for each room with return air vents.

Following industry best practices, heat pumps should be commissioned, including conducting a full inspection to confirm proper installation, verifying that the flow measurements are complete and accurate, and performing functional performance tests with controls calibration, as well as basic heating and cooling performance tests. There are several publicly-available industry references that provide useful guidance and templates for heat pump comissioning (Seattle City Light 1999, PTSC 2013). In the case of the NZERTF, this process was not applied. Instead, a control issue that could have been identified in functional performance testing was discovered during system monitoring in the first-year demonstration period. The design was for a single-zone system with a thermostat located at the first floor, while the heat pump was located in the basement. In heating mode or defrost mode, the indoor unit controller can energize up to 10 kW of electrical resistance heat. During operations, it was seen that the heat pump ran on low speed for 40 min, and if the temperature setpoint was not met, the heat pump shifted to high-speed operation. If the setpoint was still not met after another 40 min, the electrical resistance heat was activated. It was determined that the non-adjustable thermostat time periods of 40 min were such that the system was frequently using this electrical resistance heat, having a significant impact on the energy use of the house (Kneifel et al. 2015). In the NZERTF, this was detected by the engineer monitoring the system within 12 d but was not changed until after the demonstration period. Because comfort conditions are maintained and without a baseline to indicate the inefficiency, a typical homeowner would not be aware of the increased energy use, or the benefit to replacing the thermostat. NIST researchers replaced the thermostat in the second year of operation and saw that use of the electric resistance heat was reduced, producing a 27 % reduction in degree-day normalized energy use from 1555 Wh $°C^{-1}$ day to 1136 Wh $°C^{-1}$ day.

To commission the HRV, NIST engineers began with a review of the equipment selection. The HRV had been selected to ventilate the house with a nominal airflow rate of of 256 m^3/h. However, in design review, the minimum outdoor air requirement to meet ASHRAE Standard 62.2-2010 (ASHRAE 2010) was calculated to be 137 m^3/h. The standard allows for reducing that requirment if infiltration is found to exceed 0.01 m^3/s per 100 m^2, however, this was not applicable in the NZERTF due to the tight construction. When the installed system was brought into operation, NIST engineers used a hot wire anemometer traverse to measure the actual outdoor air flow rate provided by the HRV. It was evident that the HRV could not meet the minimum ventilation requirements with the lowest fan setting due to pressure drops in the ducts associated with the geometries of the final installation. Therefore, to meet the ventilation requirements, the system was operated using a constant speed fan that was measured to provide 171 m^3/h (the airflow rate coresponding to the next highest fan setting). This higher rate provides greater ventilation for the occupants, but at a greater energy cost.

Finally, we consider the future commissioning needs for the geothermal heat pump, as this system was not operated during the first two years of testing of the NZERTF. An important commissioning test for the geothermal installation is to measure the change in temperature across the ground loop and ensure that there is a 2.7 ºC to 5.6 ºC (5 ºF to 10 ºF) drop in cooling season, or rise in heating season. The supply air temperature during cooling season should also be in the range of 10 ºC to 12.8 ºC (50 ºF to 55 ºF) to ensure sufficient latent cooling to maintain comfort. In general, the

most effective data point to measure or trend is the temperature of the water or heat transfer fluid entering the heat exhanger in the house, which should usually be below 35 ºC (95 ºF) in summer and above -6.7 ºC (20 ºF) in winter. This measurement sensor is a cost-effective investment as it will enable the identification of faults that would negatively impact energy efficiency, and that would likely go undetected since comfort conditions are not significantly degraded.

Table 2. Recommendations for commissioning the NZERTF HVAC systems

Element	Test Description
Duct Leakage	2-1. **Test for duct leakage using Duct Pressurization or Test Delta Q duct leakage test (Wray and Sherman 2002). Total space conditioning system duct leakage must be less than five percent of the total air handling system rated air flow at high speed determined by pressurization testing at 25 Pa (0.1 WIC). Two compliance mechanisms are acceptable: (1) test total duct leakage to the exterior at finish stage, or (2) test total duct leakage at duct rough-in stage. When more than one air handler exists, each air handling system must individually meet the requirement. If zoning is used, all zone dampers must be open. Motorized outside air ventilation dampers must be closed.**
Mechanical Ventilation Airflows	2-2. Mechanical ventilation airflows: local and whole house mechanical ventilation system airflows must be tested during commissioning of the building. *Determine airflow as a function of the fan's external static pressure and speed setting 2-3. Balanced airflow: check that inter-zonal air pressure differences, when doors are closed, must be less than 3 Pa using passive transfer grilles or jump ducts, or active return ducts. 2-4. External Static Pressure: Air handler external static pressure must be within manufacturer specifications (125 Pa (0.5 WIC) maximum typically).
Heat Pump Diagnostics	2-5. **Heat pump inspection** a. **Test and balance report reviewed for completion of flow measurements** b. **No unusual noise or vibration identified** c. **Adequate access for service & filter change verified** d. **Room thermostats/sensors confirmed to be in appropriate locations** e. **Electrical connections confirmed to be tight** f. **Piping configuration match design** g. **Condensate drains are unobstructed, properly sloped, & trapped** h. **No visible water leaks present** i. **Filter is clean and tight-fitting** j. **Ductwork appears tight, with no obvious leaks** k. **Duct insulation appears in good condition where visible** l. **O&M manuals are on site** m. **Refrigerant properly charged** 2-6. **Functional performance tests (e.g., Seattle City Light 1999)** a. **Controls calibration tests** b. **Basic heating and cooling performance tests**
Ground-source loops	2-7. **Manufacturer testing requirements: Sustained Pressure Hoop Stress test (ASTM D-1598)** 2-8. **Pressurization test- Testing shall be by water pressure at 100 psi for a minimum of 30 minutes.** 2-9. **Flush the loops and filter particulates.**
Indoor Air Quality	2-10. **Investigate generation, transport, and removal of pollutants** a. **Volatile organic compound testing of samples conducted periodically** b. **Radon**
Make-up air	2-11. **Check barometric activation of motorized damper to kitchen exhaust and dryer exhaust**

*Shaded items were not part of the original NZERTF commissioning activities.

Water Heating Systems

The hot water system consists of two solar-thermal preheat loops that used an active, indirect forced circulation system that is suitable for cool climates. Each preheat loop uses two solar thermal flat-plate collectors installed on the porch roof facing true south. A pump is energized to circulate loop fluid when sensor temperatures exceed a 10 ºC differential and turned off when the differential temperature is below 3 ºC. A 302 L (80 gal) tank provides storage for the water heating system. The solar collectors, heat exchangers, circulators and controls are identical for the second solar thermal system, though the storage tank is 454 L (120 gal) and is intended for future use with the basement radiant floor heating system and ground source heat pump system. Davis et al. (2014) describe the two-collector circulation loop, hot water storage, and heat pump water heater that was used in year two. The heat pump water heater downstream of the solar water heating system provides hot water in the event that demand exceeds the capacity of the solar water heating system. The heat pump water heater is a 189 L(50 gal) tank having electric auxiliary heating and multiple operating modes: heat pump, hybrid and standard electric. Energy data is stored in the control unit which has a Wi-Fi hub for communication, including to report errors.

Table 3 presents the commissioning plan for the water heating systems in the NZERTF. It includes steps to verify clean piping; visual, pH, and performance checks of the solar thermal system; and visual, mechanical, and performance checks of the heat pump water heater. During the first-year of operation, a loose control wire at the solar loop pump resulted in control failure that effectively put the solar thermal system out of service, leading to a greater demand on the heat pump water heater and auxiliary water heating components. This was a result of NIST's intervention to obtain the control signal for monitoring purposes. The fault was detected by the engineer monitoring the system and resolved within 10 d; a typical homeowner would only be aware of the error (and the increased energy use) by connecting to the Wi-Fi interface to review error messages. An installation error from the manufacturer led to another fault, i.e., loose controller wiring that led to the inoperability of the heat pump compressor. For 10 d, this fault increased the demand on the auxiliary water heating element. Furthermore, a review of the piping installation for the solar thermal loop led engineers to shorten the length of the pipe connecting the solar loop tank to the heat pump water heater and to improve insulation in that section. The issue of unnecessary or inefficient piping layout is important as it leads to greater heat losses than more direct piping and is best been carried out prior to operations, as it is unlikely that a homeowner would make these changes post-occupancy due to cost.

Table 3. Recommendations for commissioning the NZERTF water heating systems

Element	Commissioning Activity
Piping	3-1. **Verify clean piping.** a. For the NZERTF this included flushing the system, then chlorinating to sanitize the system, then re-flushing the system, pressurizing the system, connecting appliances and finally adding a filter to the open loop and a screen in the closed loop. b. Perform annual checks for particles on closed loop.

Solar thermal	3-2. **Visual Inspection of collector installation** a. Verify equipment selection b. Check the mechanical integrity of components, proper fastening to support collector weight and wind/snow loads c. Check that the system has been wired correctly d. Check waterproofing and air sealing of all pipe penetrations 3-3. **Inspection of plumbing connections in solar loop** a. Verify equipment selection and installation (e.g., expansion and pressure relief valves are properly sized, check valves are in place to prevent reverse circulation b. Ensure there are no leaks in the circulation loop through which the heat transfer fluid is pumped by pressurizing the system with all valves closed. See if gauge pressure reading drops. c. Verify that the external piping is properly insulated and that connections are secure d. Determine system operating pressure, recording the gauge reading at the initial commissioning stage and monitor any large system pressure drops (e.g., 50 kPa) as system runs. 3-4. Perform pH testing as a part of yearly maintenance as high operating temperatures can lower the pH of the heat transfer fluid. 3-5. Check the functional performance of the system. 3-6. **Determine troubleshooting procedures after system installation and operation.**
Heat pump water heater	3-7. **Visual inspection of equipment selection** a. Check for mechanical integrity of all system components. b. Check all plumbing connections 3-8. Ensure unit is installed on flat surface and close to drain. Provide connection between condensate port on water heater to drain. 3-9. Ensure fan vents are unobstructed and filter is checked and changed periodically. 3-10. **Functional performance tests**

*Shaded items were not part of the original NZERTF commissioning activities.

Solar Photovoltaics

The NZERTF has 32 solar photovoltaic (PV) panels installed on the south half of the main roof. The PV modules are installed in the same plane as the roof, in four horizontal strings of eight panels each. Two strings or sixteen panels are then connected to one of two DC-to-AC inverters located in the main attic area, and the thermal energy released by the inverter enters the attic space. There is no battery storage. In total, the peak capacity of the **solar photovoltaic array is 10.2 kW. It is designed to** provide 15 % more electricity than is required over the course of an average year.

In the case of the photovoltaic system, the system installers carried out most commissioning activities, including training system operators. The Florida Solar Energy Center provides a valuable reference for the industry on installing photovoltaic systems (FSEC 1999.) It documents in detail the process for carrying out design review, performance verification, key metrics to evaluate the system visual inspections of the installation, and operation and maintenance procedures. Table 4 presents the high-level commissioning plan for the NZERTF photovoltaic systems and provides greater detail for checks that the system operators should do on an ongoing basis. Due to the distinctive nature of the design, having two identical collector strings operating in parallel, operators are able to make performance comparisons as a means to identify gross deviations from normal operation. During the first test year, one combiner box was determined to have a defective connection and was repaired. In the NZERTF, this fault was found by the engineer monitoring the system and resolved under a service contract with the installation company. A

typical homeowner may not be aware of the performance degradation without a benchmark for normal operation such as a normal energy bill for the season.

Table 4. Recommendations for commissioning the NZERTF Photovoltaic systems

Element	Commissioning Activity
Solar photovoltaics	4-1. **Visual Inspection of equipment selection and installation** 4-2. Verify installation is as per contract documents, manufacturer's instructions, and local code and document with photographs the condition of the PV array and the balance-of-system components. 4-3. Verify system is safe and is performing as designed. a. Measure the open circuit voltage of each series string of PV modules under relatively constant irradiance conditions and verify consistency. b. Prior to inverter start-up, measure the following voltages at the AC disconnect: line-to-line, line-to-neutral, neutral-to-ground and line (hot)-to-ground (expected values are 240 V, 120 V, 0 V and 120V, respectively). c. Start-up the inverter and confirm normal operation d. At each inverter, use a DC clamp-on meter to measure the current in the ungrounded conductor of each series string of PV modules. Make these measurements while the irradiance on the array is relatively steady. Verify that all four strings are producing the same maximum power point current levels. e. Verify that the measured AC voltage output from the inverter equal the inverter's indicated value. f. Measure the instantaneous AC power, module temperature, and instantaneous plane-of-array irradiance at nearly the same time and/or when the irradiance is changing very slowly (e.g., clear day near solar noon) and repeat to create multiple (e.g., 10 to 15) datasets. 4-4. Develop and implement operation and maintenance procedures. a. Take detailed IR scan of PV array and inverters to identify normal operating temperatures and profiles, avoiding reflection from solar-thermal panels. b. Take periodic scans of the PV array and inverters to identify potential issues c. Perform occasional (e.g., biannual) cleaning of panels 4-5. Train the system owners on the basic system operation. a. Conduct "walkthrough" noting disconnect locations and procedures. b. Review inverter operations, including display screens and status lights.

*Shaded items were not part of the original NZERTF commissioning activities.

Lighting

Adequate and appropriate lighting (whether daylighting, artificial lighting, or a combination) should be provided so that people are able to perform visual tasks efficiently and accurately. General illumination is provided for visual comfort and for safety. Commissioning tasks verify whether the design specifications and performance criteria have been met. The lighting system must be checked to verify that the proper lighting fixtures have been installed appropriately and in the correct locations. Furthermore, measurements of actual light levels are needed to confirm that the performance criteria have been met. In the NZERTF, lights are remotely controlled to simulate occupancy. A photosensor is installed that can be used in Year 3. Illuminance testing can determine the number or combination of lights that are required to meet the needs of the user. Table 5

presents the commissioning plan for the lighting systems, which is applicable to lighting projects in general.

Table 5. Recommendations for commissioning the NZERTF lighting systems

Element	Test Description
Solid state lighting	5-1. **Visual inspection of equipment selection** 5-2. **Wiring review to check switches control lights according to the design** 5-3. **Illuminance testing to confirm requirements have been met.**

*Shaded items were not part of the original NZERTF commissioning activities.

Plan for ongoing commissioning of the NZERTF

This section presents the plan for ongoing commissioning of the NZERTF. It is based on industry guidelines for commissioning existing buildings (ASHRAE 2015) and presents a summary of the people, activities and reporting that will be important in ensuring proper system performance. The first subsection identifies the Cx team and their responsibilities. The second subsection lists the Cx activities. The third section outlines the process to review performance under current facility requirements, investigate issues, and document findings and recommendations.

Identify the Commissioning Team and Project Goals

The NZERTF is a federal facility and as such, the development process, including design and construction requirements, is uncommon for a net-zero energy home, as is the availability of an operations and maintenance staff. The Cx team listed in Table 6 includes the NIST scientists and engineers who helped design the systems, and they also have an extensive network of sensors to monitor the performance of each building subsystem and the environmental conditions (Davis et al. 2014).

Table 6. Roles and responsibilities for the NZERTF commissioning team

Roles	Responsibilities
Owner	NIST is the owner of the building and controls its use and pays for its operations and maintenance.
Owners representative	The NIST Principal Investigator for the project has knowledge of the research needs and serves as the Owner's representative. The Owners representative is responsible for providing information required for updating the current facility requirements, establishing the Cx project goals and priorities, and monitors the process and provide resources to support the Cx team.
Operations Staff	Because of the unique nature of the facility, both NIST Facilities personnel and research staff that operate the systems must work together to monitor and report systems performance, identify and implement recommendations, and help ensure the persistence of benefits. This includes NIST Plant and Research Staff

Commissioning Authority (CxA)	The CxA is responsible for the management of the Cx Plan and for updating the Cx priorities. The CxA can be a third-party, or the role may be assigned by the Principal Investigator if all activities are kept in-house.
Cx team (All)	The Cx team will design the testing procedures and plan data collection/analysis. They will report on the year-long evaluation of the NZERTF's energy-consuming systems to identify energy reduction recommendations. They will help to direct the implementation of energy reduction recommendations. The Cx team will work with the CxA to update the documentation in the event that any components are introduced or changed and will also develop relevant training to help increase the persistence of benefits. The Cx team includes: the CxA, operation staff, maintenance staff, representative from researchers, service contractors

Maintaining or continually improving energy efficiency, indoor environmental quality, and system control are the three project goals to be addressed by the on-going commissioning efforts. The Cx team will review current building operation, confirm the previously implemented initial commissioning recommendations are still in place, using both passive monitoring and active functional testing, and adjust these recommendations to meet the Cx goals. Testing will be similar to what would normally be carried out in the inital Cx, with sensor data and trending capabilities leveraged to verify performance.

Review current facility requirements and update the commissioning plan

In the case of the NZERTF, facility requirements are expected to change from year to year as the building systems are used in different ways to address a wide range of research issues. The commissioning plan specifies which tests are to be conducted along with the testing interval. One major consideration is the need for data. In the NZERTF, there are over 200 sensors, generating thousands of points daily and analyzed weekly. For ongoing commissioning of other projects, it is recommended that data for normal operation and functional performance testing be analyzed for a minimum of two weeks in heating season, cooling season, and swing season. This frequency would be adequate to establish a benchmark for proper operation. Stand alone measurements with trends can be used when such detailed sensing is not available.

For the NZERTF, several Cx steps are combined because the project is smaller than typical commercial applications and because in many cases the same individual is responsible for carrying

out the performance review, investigating any potential issues, and implementing improvements. Much like any other construction project, there was time pressure to get the construction completed and the occupancy period initiated. Although it was noted that design and construction phase commissioning activities were carried out by the commissioning authority to meet the LEED certification requirements, not all systems were fully commissioned. Instead, functional performance testing was carried out at the discretion of installers and NIST researchers.

The experiences of the occupants and building staff are valuable inputs into the comfort and performance of the house for the ongoing commissioning process. However, in the NZERTF, the occupants are simulated with latent and sensible loads and sensors located throughout the house provide a record of comfort conditions. The NIST team that monitored data over the one-year demonstration period has a wealth of knowledge regarding system design and performance issues. Their experience will be leveraged to carry out commissioning activities for the various subsystems and the whole building system. These include the inspections, trend reviews and utility statement reviews from the real world operation of the systems under the normal range of operating conditions and exercised in a way that is impossible during initial commissioning. A retrospective comparison was made of the NZERTF initial commissioning activities and the recommendations presented in the last section to determine the gaps and ensure that any remaining tasks become part of the ongoing commissioning plan. The NZERTF Cx activites listed in Table 7 are identified as important, based on the operating experience, and demonstrate how the Cx plan must be tailored to meet the needs of the individual application. The activities are organized by system and when appropriate, recommendations for testing frequency are listed. Activities denoted with an asterisk were not originally part of the NZERTF commissioning plan, but would add value to the process.

Table 7. Ongoing commissioning plan for the NZERTF

System/Subsystem	Commissioning Activity	Frequency
Monitoring System	7-1. Check sensor placement and reading accuracy and frequency, calibrate key sensors.	Annually
Insulation and Glazing Systems	7-2. Visually inspect building envelope for wetness, microbial growth, color or texture changes, decay, or structural dislocation. Pay special attention to plumbing system leaks 7-3. Perform air leakage testing and compare to initial commissioning results. (ASTM 2010) 7-4. *Perform a thermographic survey/Infrared inspection- Check for thermal bridging, air leakage, air intrusion, displaced insulation. Check under pressurized and depressurized conditions	Seasonally Initially
HVAC System	7-5. Perform duct pressurization test and compare to initial commissioning results 7-6. Perform functional performance test for heat pump 7-7. *Check barometric activation at 10 pa of motorized damper to kitchen exhaust and dryer exhaust	Initially Initially Initially

	7-8. Perform a functional performance test of the heat recovery ventilation system. 7-9. *Perform a functional performance test of a high-velocity air distribution system before the system is used in research studies. 7-10. *Perform a functional performance test of the ground source loops before the system is used in research studies.	Initially
Water Heating System	7-11. Visually inspect collector installation, check for damage/debris, waterproofing of penetrations 7-12. Review functional performance and compare to initial commissioning results. 7-13. Perform checks for particles on closed loop. 7-14. Perform pH testing. 7-15. Perform check for refrigerant leaks in heat pump using a soap solution or other leak detection method 7-16. Conduct a functional performance test of the solar pumps to verify proper control.	Seasonally Annually Annually Initially
Photovoltaic Systems	7-17. Visually inspect collector installation, check for damage/debris, waterproofing of penetrations 7-18. Review energy monitoring and trending compare to initial commissioning results 7-19. Review functional performance. 7-20. Inspect the inverter using an infrared camera to identify hot spots or other changes that may occur over time. 7-21. Make performance comparisons of the two identical collector strings operating in parallel as a means to identify gross deviations from normal operation.	Seasonally
Lighting System	7-22. *Conduct illuminance testing (Table 3, Item 3-3) 7-23. Evaluate the lighting layout based on the results of illuminance testing.	Initially, following changes.

Review Performance, Investigate Issues and Documenting Findings in OCx Report

Throughout the commissioning process, findings will be documented and information will be presented in Commissioning Reports, including the findings, a listing of recommendations that were implemented, a plan to implement additional corrective actions, updates to the systems manuals, including new/revised maintenance actions that are needed, and the results of any additional functional performance tests. Many of the low-cost and no-cost recommendations such as tuning the sytem or tweaking parameters can be carried out on the spot. These changes must be documented along with any additional recommendations for additional repairs or retrofits. In the event that any systems are added or modified, as is likely the case for the research facility, the systems manual must be updated and the staff working with the system should be informed and trained. Any tasks to be added as preventative maintenance should be added along with the corresponding frequency.

Although as-built documentation for residential applications is rare, such records provide important data for operation and maintenance (O&M) efforts as well as for future renovations, upgrades or repairs. Technical reports and other commissioning documents serve as benchmarks for future system testing, re-commissioning and maintenance or renovation activities. Systematic development of commissioning documentation facilitates knowledge transfer from one phase of delivery to the next, and from the delivery process to the ensuing ongoing operation of the facility.

Summary

This report discusses the practice of residential commissioning and investigates the motivation for commissioning the NIST Net-Zero Energy Residential Test Facility (NZERTF), a high-performance residential house/test facility located in Gaithersburg, MD. The NZERTF was partly commissioned in 2012 by a registered commissioning authority, with activities focused on design and construction. A review of best practices led to the conclusion that this level of commissioning was not sufficient. The unique nature of the facility, a complex and high-risk residential application, led to a hybrid adaptation of existing commissioning approaches. Guidelines for both commercial and residential building commissioning processes were reviewed and used to form the basis of the commissioning plan for the NZERTF.

A review of the subsystems was carried out in consultation with NIST experts to form recommendations for commissioning the various subsystems, and tables are presented that document these activities for each subsystem. A commissioning plan was developed and presents each of the major elements, established the roles and responsibilities for the Cx team members, defined the goals for the process, outlined the measurement and verification plan, and the use of functional testing to verify proper system performance. This collectively provided guidance as to what should be done for this type of facility to help ensure that the specifications of the design intent are met, and that the testing and inspection of the systems identify issues so that corrective measures can be undertaken before developing into serious operational flaws that impact comfort, efficiency or equipment life. The testing activities, which extend into the operation phase, verify performance under a full range of operating conditions.

Acknowledgements

The author acknowledges the contributions of the NZERTF design team from Building Science Corporation, and Therrien Waddell, Inc., the general contractor, as well as system experts from NIST involved in the design and monitoring of the NZERTF: Mark Davis, Vance Payne, Brian Dougherty, Hunter Fanney, Tania Ullah, Farhad Omar, and Robert Zarr. Delmar Ferguson of Therrien Waddell, Inc. provided insight into the commissioning activities carried out and best practices. Mark Davis, Jerry Therrien, LEED AP, W. Vance Payne and Joshua Kneifel served as reviewers for this report. This work was funded, in part, by the Department of Energy, Office of Energy Efficiency and Renewable Energy (Interagency Agreement #DE-EE0002058).

References

ASHRAE. 2010. "Standard 62.2-2010: Ventilation and Acceptable Indoor Air Quality in Low-Rise Residential Buildings**"**. Atlanta, GA; ASHRAE, Inc.

ASHRAE. 2013. "ASHRAE Guideline 0-2013 **The Commissioning Process"**. Atlanta, GA; ASHRAE, Inc.

ASHRAE. 2015. ASHRAE Guideline 0.2 "**The Commissioning Process for Existing Systems and Assemblies".** Atlanta, GA; ASHRAE, Inc.

ASTM Standard E779-10, 2010, " Standard Test Method for Determining Air Leakage Rate by Fan Pressurization" ASTM International, West Conshohocken, PA, 2010, DOI: 10.1520/E0779-10, www.astm.org.

ASTM Standard E1105, 2015, " Standard Test Method for Field Determination of Water Penetration of Installed Exterior Windows, Skylights, Doors, and Curtain Walls, by Uniform or Cyclic Static Air Pressure Difference" ASTM International, West Conshohocken, PA, 2010, DOI: 10.1520/E1105-15, www.astm.org.

Domanski, P.A., H. Henderson, and W.V. Payne. 2015. Effect of Heat Pump Commissioning Faults on Energy Use in a Slab-on-Grade Residential House. Applied Thermal Engineering

Davis, M., W. Healy, M. Boyd, L. Ng, W.V. Payne, H. Skye, and T. Ullah. 2014. Monitoring Techniques for the Net-Zero Energy Residential Test Facility. National Institute of Standards and Technology's Technical Note 1854. http://dx.doi.org/10.6028/NIST.TN.1854 December 2014.

Fanney, A.H., W.V. Payne, T.Ullah, L.C. NG, M.T. Boyd, F. Omar; M.W. Davis, H.M. Skye, B.P. Dougherty, B.J. Polidoro, W.M. Healy, J.D. Kneifel, and B. Pettit. 2015. Net-Zero and Beyond! Design and Performance of NIST's Net-Zero Energy Residential Test Facility. Energy and Buildings 101 (2015) 95–109.

Florida Solar Energy Center (FSEC). 1999. Installing Photovoltaic Systems. http://www.fsec.ucf.edu/en/research/photovoltaics/vieo/resources/documents/PVPrimer.pdf

Jump, D. A., I.S. Walker, M.P. Modera. 1996 "Field Measurements of Efficiency and Duct Retrofit Effectiveness in Residential Forced Air Distribution Systems" In Proceedings of the ACEEE 1996 Summer Study on Energy Efficiency in Buildings, 1.147-1.155. Washington, D.C.: American Council for an Energy Efficient Economy.

Kneifel, J.D., W.V. Payne, T. Ullah, and L.C. Ng. 2015. Simulated versus Measured Energy Performance of the NIST Net Zero Energy Residential Test Facility Design. NIST Special Publication (NIST SP) – 1182. http://dx.doi.org/10.6028/NIST.SP.1182

Lukachko, A. 2008. Quality Assurance Roadmap for High Performance Residential Buildings. Building Science Corporation

Lukachko, A., C. Gates, and J. Straub. 2011. Strategy Guideline: Advanced Construction Documentation Recommendations for High Performance Homes. Building Science Corporation

Matson, N., C. Wray, I. Walker, and M. Sherman. 2002. Potential Benefits of Commissioning California Homes," Lawrence Berkeley Laboratory Report LBNL-48258, 2002.

NIST and Building Science Corporation(BSC), 2011. NIST NZERTF-Fire, Plumbing, Electrical, and Mechanical Plans. Retrieved March 23, 2014, from http://www.nist.gov/el/nzertf/upload/NZERTF-FirePlumbElecMech-Plans-June2011.pdf

Omar, F. and S.T. Bushby. 2013 Simulating Occupancy in the NIST Net-Zero Energy Residential Test Facility, NIST Technical Note 1817.

Pettit, B., C. Gates, A.H. Fanney, W.M. Healy. 2015. Design Challenges of the NIST Net Zero Energy Residential Test Facility, NIST Technical Note 1817.

Performance Tested Comfort Systems (PTSC). 2013. Air Source Heat Pump Installation Specification. https://www.bpa.gov/EE/Policy/IManual/Documents/ASHP_Specifications_2013.pdf

Seattle City Light. 1999. "Standard Commissioning Procedure for Water Loop Heat Pump Systems" http://www.seattle.gov/light/conserve/business/bdgcoma/bca7.pdf

Walker, I.S., M.H. Sherman, M. Modera, and J. Siegel. 1998. "Leakage Diagnostics, Sealant Longevity, Sizing and Technology Transfer in Residential Thermal Distribution Systems", Phase V Report to CIEE, Lawrence Berkeley Laboratory, Report No. LBL-41118.

Walker, I.S., and M.H. Sherman, 2002 "An Easier Way to Measure Duct Leaks", Home Energy, 19(5); pp. 34-38, Sept/Oct 2002. [LBNL-49749]

Wray, C.P., I. Walker and M.H. Sherman. 2004. "Guidelines for Residential Commissioning" www.energy.ca.gov/reports/500-04-012/2004-04-

Confidence Estimation in Stem Cell Classification

Zahra Rajabi, Jana Kosecka
Dept. of Computer Science
George Mason University
Fairfax, USA
zrajabi, kosecka @gmu.edu

Peter Bajcsy
National Institute of Standard and Technology
Information Technology Laboratory
peter.bajcsy@nist.gov

***Abstract* - We study the problem of supervised classification of stem cell colonies and confidence estimation of the attained classification labels. The problem is investigated in the application context of heterogeneity labels of stem cell colonies observed by using fluorescent microscopy imaging. Given the features of colonies using numerous image statistics, we report the classification results using adaptive *k*-Nearest Neighbor (NN) algorithm. This algorithm minimizes typical *k*-NN classification bias by giving more weight to more informative features in predicting class posterior probabilities. We then estimate the confidence of each prediction for unlabeled data using transductive p-value and strangeness metrics. We show that such an introspection can gradually increase the accuracy of learned model, quantify false positives, and guide the resource-limited manual colony annotation process to provide training labels for the less confident unlabeled samples.**

***Index Terms*— k-Nearest Neighbor, Confidence Estimation**

I. INTRODUCTION

Recent advances in automated microscopy imaging techniques enables scientists to capture large amount of imagery to classify cell colony heterogeneity and monitor the heterogeneity changes over time. Providing biologists with automated classification capabilities is central to gaining further insights into human diseases, drug discovery, and stem cell treatments. The terabyte-sized image representations in stem cell biology necessitate establishment of not only an automated qualitative and quantitative characterization of cell colony heterogeneity under various biological conditions but also the confidence estimation of those automated analyses. In this context, automated classification analyses must be robust and have an introspection capability of quantifying uncertainty for the predicted class labels. In this paper, we use an adaptive *k-Nearest Neighbor (*NN) classification of heterogeneity of stem cell colonies, and describe a confidence metric to predict the uncertainty of classification.

II. RELATED WORK

One area of research in computational cell biology is automated characterization of stem cells in stem cell therapies. The characteristics include, for instance, colony growth rate and function (i.e., pluripotency). The function of a colony can be measured via heterogeneity of cells forming the colony and their protein expression. This colony heterogeneity is perceived as a textured image region that can be labeled manually by experts. A common approach to classification in cell microscopy images is to use some manually labeled colony instances in a supervised setting to generate models. The models can be used for future classifications/predictions and ideally have good generalization capability. In [7], a supervised segmentation technique based on Gaussian Mixture Model (GMM) Bayes classifier assigns pixels in sub-cellular images into biologically meaningful regions. The biases from such model assumptions using GMM are analyzed in [5]. The work refutes the conditional independence of cellular visual features (intensity, texture, shape). Similarly, the k-Nearest Neighbor (NN) classifiers can also suffer from a bias due to the assumption of locally constant class conditional probabilities. To address this bias one can use an adaptive k-NN algorithm proposed in [1]. The adaptive k-NN method considers feature relevance while identifying neighbors.

In addition to the classification bias, we address the confidence estimation of obtained classification results which requires some knowledge of ground truth labels. It is shown in [5] that classification accuracy can be estimated as a function of GMM components. However, we need to provide a confidence measure based on the uncertainty of a classifier. The confidence measure assigns a probability that unlabeled test data is misclassified.

Another restricting issue with classical supervised learning methods is the limited number of labeled instances. An insufficient number of training samples (labeled instances) often prevents us from learning a classification model with good generalization capacity. Furthermore, obtaining annotations for training samples, specifically in highly specialized areas such as cell biology, requires exact expertise and is a time consuming effort. Thus, new paradigms for collecting training samples have been proposed to reduce human supervision with the goal of increasing learned model performance. Many research teams look at using typically abundant unlabeled data. For example, active learning methods start with a small amount of labeled data and identify the most informative unlabeled instances to be labeled by a human expert iteratively. In the active learning frameworks, the capability of assessing the uncertainty of current classifier's label is essential. A commonly used measure is classification entropy [8]. However, entropy is often unreliable due to unimportant classes being included in the estimation of label likelihood. To address the confidence estimation and incorporate the concepts from active learning, we estimate the confidence of a classification label using strangeness [3] in the context of transductive learning. Transductive learning estimates the properties of unlabeled (test) instances directly from specific labeled (training) instances.

Bajcsy, Peter; Kosecka, Jana; Rajabi, Zahra.
"Confidence Estimation in Stem Cell Classification."
Paper presented at BioImage Informatics Conference 2015, Gaithersburg, MD. October 14, 2015 - October 16, 2015.

III. Proposed Approach

In order to understand heterogeneity of cell colonies from microscopy images, we explore characterization of stem cell colonies represented by groups of image features related to textural appearance, shape signatures, and intensity. Using such image features, we classify segmented colonies into three classes of {*homogeneous, heterogeneous and dark*}. Next, we evaluate the discriminative power of different features to predict class labels. This is achieved by adaptively emphasizing more relevant features and by applying the weighted *k*-NN algorithm as explored in [4] in order to improve classification accuracy.

To compute the confidence of each classification label, we use the strangeness measure to associate a confidence value with the output of our weighted k-NN non-parametric approach. This confidence value can be used for future solicitation of new annotations to improve current performance and also as an introspective tool to identify incorrectly classified samples. We show that p-value confidence estimates can be used for assessing which test data instances may have been classified incorrectly.

Dataset: In our experiments, we consider the annotated experimental dataset of stem cell colonies accessible from the NIST web interface at https://isg.nist.gov/deepzoomweb/. The test data consist of three replicas of stem cell colonies growing in a 10 cm dish over a period of five days. The stem cell colonies are imaged by using phase contrast and green fluorescent protein (GFP) modalities with Oct4 stain used as a GFP marker. A total of 396 (18x22) or 320 (16x20) fields of view were stitched together to form a large composite image (i.e., a mosaic) consisting of hundreds of colonies at each time point. Each composite image consists of about 22,912 x 20,775 pixels with 16 bits per pixel (bpp). The images are segmented, and colonies are tracked over time. The example images of the colonies are shown in Fig. 1. Each colony represents a classification example $\boldsymbol{x}$ that is characterized by 74 dimensional feature vector extracted from each imaging modality. We analyze the colony examples formed from the GFP imaging modality and characterized by intensity, shape and texture statistics. The set of manually annotated colonies includes 68 homogeneous, 47 heterogeneous and 24 dark samples. Thus, each colony example $\boldsymbol{x}$ is associated with its label y in a training data set.

IV. K-NN

K-Nearest Neighbors algorithm (*k*-NN) is a non-parametric method used for supervised classification. An unlabeled sample is classified by assigning the label which is the most frequent among the k training examples nearest to the unlabeled sample based on a chosen distance function. The class label of a query example is assigned to be the majority class label among the retrieved test examples. In the case of a tie, the class label with the smallest distance is taken.

We first normalize all features to have a zero mean and unit variance. This is achieved by subtracting mean from each sample and normalizing it by the variance. After normalization, k-NN and adaptive k-NN classification algorithms are applied to the normalized feature dataset. The classification model is built by a percentage split of the normalized data into training and test subsets.

We performed the *k*-NN classification with all combinations of the following training percentages {50%, 60%, 70%, 80%} and k values {1, 3, 5, 7, 9}. In our baseline experiments we used the *k*-NN classifier with Euclidean distance metric. Average accuracies of the *k*-NN classification using different k values and split percentages are shown in Table 1.

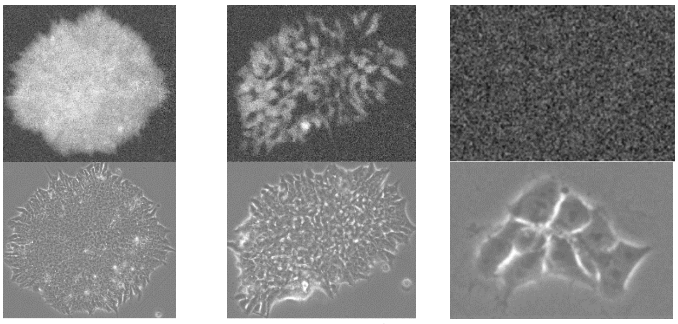

Figure 1) Top: Corrected GFP images of homogeneous, heterogeneous and dark colonies. Bottom: The corresponding phase contrast images of the colonies in the top row.

TABLE I. Accuracy of *k*-NN classifier metric for a range of k's and percentage splits of training data

Split	k=1	k=3	k=5	k=7	k=9
50%	82	77	81	76	79
60%	80	80	82	83	84
70%	81	90	87	89	89
80%	86	92	92	92	92

V. Adaptive *k*-NN

A k-NN classification algorithm assumes a locally constant class posterior probability and uses the Euclidean distance to compute the nearest neighbors around a query sample. However, this assumption is prone to a bias especially around a class boundary. Therefore, we examined a locally adaptive metric for nearest neighbor classification proposed in [1] in which posterior probabilities are adaptive to query locations. In this approach, the goal is to estimate the relevance of a feature group (or channel) i by computing its ability to predict the class posterior probabilities locally at the query sample. To do so, let us consider a query sample with the feature vector $\boldsymbol{x_0}$, and $\boldsymbol{x}$ be the nearest neighbor of $\boldsymbol{x_0}$ computed according to the Euclidean distance. After splitting the input feature vector into intensity, shape and texture groups/channels, we compute the total weighted distance between the query sample during the test phase and training sample according to [2] as follows:

$$d_w^2 = w_1 d_I^2 + w_2 d_T^2 + w_3 d_S^2 \qquad (1)$$

where $[d_I^2, d_T^2, d_S^2]^t$ are the three squared Euclidean distances between the intensity, texture and shape channels of feature vectors computed at every query sample $\boldsymbol{x_0}$ with respect to training data $\boldsymbol{x}$, and $\boldsymbol{W} = [w_1, w_2, w_3]^t \in \Re^3$ defines the weights for the distances of the three feature channels. To compute weights $\boldsymbol{W}$, first we compute the class conditional expectation of posterior $P(j|\boldsymbol{x})$ denoted by $\bar{P}(j|x_i = z_i)$, for

each class label $j = \{1,2,3\}$ corresponding to homogeneous, heterogeneous and dark class labels, given that x_i represents the i^{th} channel of $\boldsymbol{x}$ and assumes value z_i. The ability of i-th feature channel to predict $P(j|\boldsymbol{z})$ is defined as follows:

$$r_i(\boldsymbol{z}) = \sum_{j=1}^{L} \frac{(P(j|\boldsymbol{z}) - \bar{P}(j|x_i = z_i))^2}{\bar{P}(j|x_i = z_i)} \qquad (2)$$

where L is the number of classes. The smaller the difference of these two probabilities, $P(j|\boldsymbol{z})$ and $\bar{P}(j|x_i = z_i)$, the more information feature channel i carries in predicting the posterior probability $P(j|\boldsymbol{z})$ locally at $\boldsymbol{z}$. The details of estimation of $P(j|\boldsymbol{z})$ using local neighbourhood of $\boldsymbol{z}$ can be found in [1]. Given the summation over all class labels for such r_i's at the query point and averaging over all such summations in the neighborhood of the query sample, we can compute the feature relevance factor $\bar{r}_i$. The relevance factor measures how well on average the class posterior probability is approximated by a channel i in the vicinity of the query point $\boldsymbol{x_0}$

$$\bar{r}_i(\boldsymbol{x}_0) = \frac{1}{k} \sum_{z \in N_k(x_0)} r_i(\boldsymbol{z}) \qquad (3)$$

where $N_k(\boldsymbol{x_0})$ is the neighborhood of point $\boldsymbol{x_0}$. The weight calculation is repeated iteratively according to the equation below

$$w_i(\boldsymbol{x}_0) = \frac{\exp(c\, R_i(x_0))}{\sum_{l=1}^{q} \exp(c\, R_l(x_0))} \qquad (4)$$

where $R_i(\boldsymbol{x}_0) = \max_{j=1,2,3} \bar{r}_j(\boldsymbol{x}_0) - \bar{r}_i(\boldsymbol{x}_0)$ is the relevance of i-th feature channel (i.e. subset of features) with maximal relevance, $q=3$ is the number of features channels, and here $c=5$ is a parameter that can be chosen to affect the influence of $\bar{r}_i(x_0)$ on w_i . The number of all iterations is set to 5. More details about the weight computation can be found in [1]. Once the weights are computed, the nearest neighbors are retrieved using the weighted distance $\boldsymbol{d}_w$ in Eq. (1). In our case, the weights are computed for two different percentage splits of 70% and 80% of training data. The weight distributions across colonies of each feature channels, intensity, shape, and texture, for the test data are plotted in Fig. 2. We can see that the weights are smaller for the shape feature channel (around *0.2)* which implies less capacity of the feature channel to predict class probability. The texture channel has the largest weights between 0.4 and 0.6. The results of adaptive k-NN can be found on Table II for all feature channels. While the weight computation correctly corroborates our intuition about relevance of different feature channels, the absolute values of classification accuracy are comparable with Table I.

VI. Confidence Estimation using Strangeness

In this section, the goal is to quantify the confidence of the prediction using a *strangeness* measure. This measure characterizes the uncertainty of a sample (instance) with respect to its own label and provides the k-NN classifier with an introspection ability. For each example $\boldsymbol{x}_i$ in this dataset, a strangeness α_i^y with respect to a class y is computed as:

$$\alpha_i^y = \frac{\sum_{r=1}^{k} d_{ir}^{y}}{\sum_{r=1}^{k} d_{ir}^{\bar{y}}} \qquad (5)$$

where y is the predicted class label y_i for instance $\boldsymbol{x}_i$, d_{ir}^{y} is the r-th shortest distance between a point i and another point with class label y, $d_{ir}^{\bar{y}}$ is the r-th shortest distance between point i and another point with the class label other than class y, and k is the number of nearest neighbors considered. The strangeness measure is a ratio of the sum of k nearest distances from the same class to the sum of the k nearest distances from all other classes. It measures how "strange" an instance in question is with respect to its semantic category. An example closer to other class instances in comparison to its own class instances has higher strangeness and vice versa.

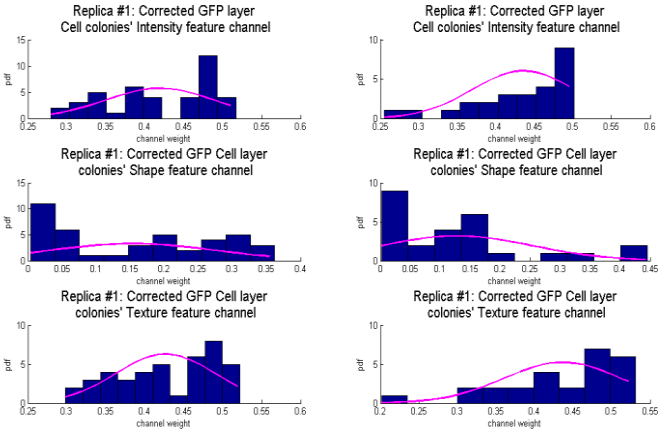

Figure 2) Distribution of learned weights that reflect the relevance of the individual feature channels of intensity (top row), shape (middle row), and texture (bottom row) for predicting class labels using weighted k-nearest neighbor algorithm trained on 70% (left) and 80% (right) of the training samples.

After computing the strangeness, we compute transductive **p-value** statistics according to [3]. The p-value is a measure of the probability of obtaining a result equal to or more extreme than what was actually observed under the null hypothesis (i.e., class label assignment). The p-value quantifies how well the data supports our classification hypothesis. The smaller the p-value the greater the evidence against the hypothesis (a sample does not belong to a class) and vice versa. Therefore, by using the strangeness values obtained for test data, we can compute a p-value measure t_r^y for all test samples r with respect to each y-labeled class as *homogeneous*, *heterogeneous* or *dark* colony according to the equation below:

$$t_r^y = \sum_{\substack{i=1 \\ y_i = y_r = y}}^{n} 1\{\alpha_{iy_i} > \alpha_{ry_r}\}/n \qquad (6)$$

where n is the number of instances in the entire training set with the label y and $1\{.\}$ is the indicator function, which is 1 when the i-th example from the training set of the same class has strangeness value greater than the one of the test point denoted by r. The p-value t_r^y can be viewed as a measure of the probability of having instances in the class with strangeness greater than or equal to that of test point r. Using Eq. 5 and Eq. 6, the strangeness and p-values are computed for all test points.

TABLE II. Average accuracies of adaptive k-NN classifier for a range of Ks and percentage splits of training data.

Split	K=1	K=3	K=5	K=7	K=9
50%	83	80	82	74	78
60%	81	79	81	82	83
70%	79	90	90	87	87
80%	86	90	96	92	92

To estimate the confidence in a label from the adaptive *k*-NN classification, we consider a split of the data into 80% training and 20% testing samples and use adaptive k-NN described in previous section, with *k* is set to 5. We compute p-values for all 26 examples in the test set with respect to *homogeneous*, *heterogeneous* and *dark* classes (20% rounded down of 68 homogeneous, 47 heterogeneous and 24 dark). We visualize colonies with high p-values which are labeled correctly. Visualization of the p-values for different examples and with respect to *homogeneous* and *heterogeneous* classes can be seen in Fig. 3. Note that in all the test examples True Positives have a transductive p-value greater than 0.5. This indicates that the p-value can be effectively used for quantifying which examples are true positives. The color coding shows that examples with high p-values are often true positives (TP), while examples with low p-values with respect to the class are mostly true negatives (TN) and a few are false positives (FP) and false negatives (FN). The colonies with p-values less than 0.2 were misclassified by adaptive *k*-NN classifier for k=5 and split 80%. Their images are shown in Fig. 4. The vertical lines in Fig. 3 separate indices of homogenous, heterogeneous and dark test examples. By association of p-value estimates with classification output, we can estimate which test samples might have been classified incorrectly.

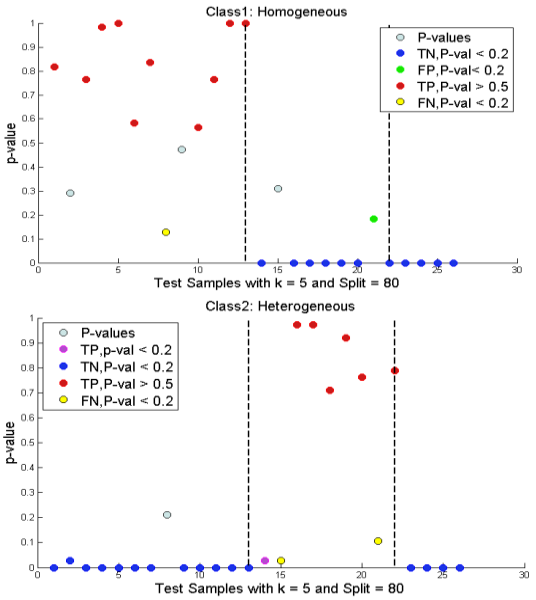

Figure 3) P-values for the subset of samples (replica #1) in the test dataset with respect to homogeneous (top) and heterogeneous (bottom) computed for k = 5 and split 80%. The color schema in the legend corresponds to combinations of p-value ranges and classification evaluations (TP=true positive, TN=true negative, FP=false positives, and FN=false negatives).

VII. Conclusion

We have demonstrated the effectiveness of k-NN and adaptive k-NN classifiers together with their per sample confidence estimates. Observing the p-value confidence estimates enabled us to assess which examples may have been classified incorrectly. Fig. 4 illustrates examples of the incorrect classification of a homogenous colony due to the inappropriate choice of the parameter *k* for the k-NN classifier. Using *k=5 f*or these examples the three most distant neighbors were from incorrect classes, while with *k=2* the examples were correctly classified. This suggests that choosing the parameter *k* adaptively per example may be more appropriate.

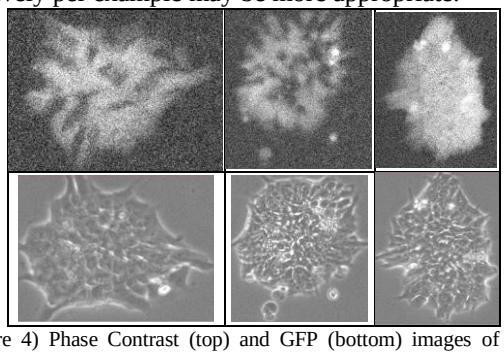

Figure 4) Phase Contrast (top) and GFP (bottom) images of three test colonies which have lower p-values than 0.2 within classes and are misclassified. Left: Colony index 15 in heterogeneous p-value plot is misclassified to homogeneous (FN with p-value < 0.2). Middle: Colony index 21 is a heterogeneous colony that is misclassified to homogeneous (FP with p-value < 0.2). Right: Colony index 8 in the homogeneous p-value plot is misclassified to heterogeneous (FN for homogenous class).

VIII. Disclaimer

Commercial products are identified in this document in order to specify the experimental procedure adequately. Such identification is not intended to imply recommendation or endorsement by the National Institute of Standards and Technology, nor is it intended to imply that the products identified are necessarily the best available for the purpose.

References

[1] C. Domeniconi, J. Peng, and D. Gunopulos. Locally adaptive metric nearest-neighbor classification. IEEE Transactions on Pattern Analysis and Machine Intelligence, 24(9):1281-1285, 2002.

[2] G. Singh and J. Kosecka, “Nonparametric Scene Parsing with Adaptive Feature Relevance and Semantic Context”, Proceedings of CVPR, 3151-3157, 2013.

[3] K. Proedrou, I. Nouretdinov, V. Vovk, and A. Gammerman. “Transductive Confidence machines for pattern recognition”. In ECML, pages 381-390, 2002.

[4] G. Singh and J. Kosecka, “Introspective Semantic Segmentation”, 2014 IEEE Winter Conference on Applications of Computer Vision (WACV), 714-720.

[5] A. Cardone, J. Amelot, Y. -Shian Li-Baboud, M. Brady and P. Bajcsy, “Biases from model assumptions in texture sub-cellular image segmentation”, SPIE Newsroom, 13 November, 2012.

[6] M. Halter, Y.-S. Li-Baboud, A. Peskin, P. Bajcsy, D. Hoeppner, and A. L. Plant, "Addressing Uncertainty in the Automated Evaluation of Stem Cell Colony Quality," in CYTO 2013 May 19-22, 2013, San Diego, CA..

[7] J. Gu, J. Chen, Q. Zhou, H. Zhang, Gaussian mixture model of texture for extracting residential area from high-resolution remotely sensed imagery. Updating Geo-spatial Databases Imagery/5th ISPRS Workshop. DMGISs, p. 157-162, 2004.

[8] A. Holub, P. Perona, and M. Burl. Entropy-based active learning for object recognition. In CVPR Workshop, pages 1-8, 2008.

A better-than-3n lower bound for the circuit complexity of an explicit function*

Magnus Gausdal Find[1], Alexander Golovnev[2], Edward A. Hirsch[3], and Alexander S. Kulikov[3]

[1]National Institute of Standards and Technology, magnus.find@nist.gov
[2]New York University, alexgolovnev@gmail.com
[3]Steklov Institute of Mathematics at St. Petersburg, Russian Academy of Sciences, {hirsch,kulikov}@pdmi.ras.ru

October 31, 2015

Abstract

We consider Boolean circuits over the full binary basis. We prove a $(3+\frac{1}{86})n - o(n)$ lower bound on the size of such a circuit for an explicitly defined predicate, namely an affine disperser for sublinear dimension. This improves the $3n - o(n)$ bound of Norbert Blum (1984). The proof is based on the gate elimination technique extended with the following three ideas. We generalize the computational model by allowing circuits to contain cycles, this in turn allows us to perform affine substitutions. We use a carefully chosen circuit complexity measure to track the progress of the gate elimination process. Finally, we use quadratic substitutions that may be viewed as delayed affine substitutions.

*Research is partially supported by NSF (grant 1319051) and the Government of the Russian Federation (grant 14.Z50.31.0030). A full version of this text is available as ECCC Technical Report 15-166 and attached to this extended abstract.

Find, Magnus; Golovnev, Alexander; Hirsch, Edward; Kulikov, Alexander.
"A better-than-3n lower bound for the circuit complexity of an explicit function."
Paper presented at 57th Annual IEEE Symposium on Foundations of Computer Science (FOCS 2016),
New Brunswick, NJ. October 9, 2016 - October 11, 2016.

1 Introduction

In this paper we consider Boolean circuits over the full binary basis. A simple counting argument [Sha49] shows that most Boolean functions require circuits of exponential size. However, showing superpolynomial lower bounds for explicitly defined functions (for example, for functions from **NP**) remains a hopelessly difficult task. (In particular, such lower bounds would imply **P**$\neq$ **NP**.) Moreover, even superlinear bounds are unknown for functions in $\mathbf{E}^{\mathbf{NP}}$. Superpolynomial bounds are known for **MAEXP** (exponential-time Merlin-Arthur games) [BFT98], and arbitrary polynomial lower bounds are known for $\mathbf{O_2}$ (the oblivious symmetric second level of the polynomial hierarchy) [CR06].

People started to tackle the problem in the 60s. Kloss and Malyshev [KM65] proved a lower bound of $2n - O(1)$. Schnorr [Sch74] proved a $2n - O(1)$ lower bound for a class of functions with certain structure. Stockmeyer [Sto77] proved a $2.5n - O(1)$ bound for certain symmetric functions. Paul [Pau77] proved a $2.5n - o(n)$ lower bound for a variant of the storage access functions. Eventually, Blum [Blu84] extended Paul's argument and proved a $3n - o(n)$ bound.

Mysteriously, Blum's bound remained unbeaten for more than thirty years. Recently, Demenkov and Kulikov [DK11] showed a similar bound for affine dispersers. Their proof is much simpler (if one assumes the existence of explicitly defined dispersers for granted), but that does not improve the bound (actually, the $o(n)$ term in [DK11] is worse than that in [Blu84]). In this paper we eventually improve the bound for affine dispersers to $(3 + \frac{1}{86})n - o(n)$, which is stronger than Blum's bound.

Other models. The exact complexity of computational problems is different in different models of computation: for example, switching from multitape to single-tape Turing machines squares the time complexity; random access machines are even more efficient. Boolean circuits over the full binary basis make a very robust computational model. Using a different constant-arity basis only changes the constants in the complexity. A fixed set of gates of arbitrary arity (for example, ANDs, ORs and XORs) still preserves the complexity in terms of the number of wires. After all, finding a function hard for Boolean circuits can be viewed as a combinatorial problem, in a contrast to lower bounds for uniform models. Therefore, breaking the linear barrier for Boolean circuits can be viewed as an important milestone on the way to stronger complexity lower bounds.

For the basis U_2 consisting of all binary Boolean functions except for parity (xor) and its complement, Schnorr [Sch76] proved that the circuit complexity of the parity function is $3n - 3$. Zwick [Zwi91] gave a $4n - O(1)$ lower bound for certain symmetric functions, Lachish and Raz [LR01] showed a $4.5n - o(n)$ lower bound for a strongly two-dependent function (a function that has exactly four subfunctions with respect to any two variables and remains so after sufficiently many substitutions). Iwama and Morizumi [IM02] improved this bound to $5n - o(n)$. Demenkov et al. [DKMM15] gave a simpler proof of a $5n - o(n)$ lower bound for a function with $o(n)$ outputs as well as presented a $7n - o(n)$ lower bound for a function with n outputs.

While we do not have nonlinear bounds for constant-arity Boolean circuits, stronger bounds are known for weaker models, including monotone circuits (Razborov [Raz85]), circuits of constant depth with no XOR (Yao and Håstad [Yao85, Hås86]), circuits of polylogarithmic depth over infinite fields (Shoup and Smolensky [SS91]), formulas (Subbotovskaya [Sub61], Khrapchenko [Khr71], [Nec66], Andreev [And87], Impagliazzo and Nisan [IN93], Paterson and Zwick [PZ93], Håstad [Hås98] and Tal [Tal14]). These bounds, however, do not translate to superlinear lower bounds for general constant-arity Boolean circuits.

Connections to CircuitSAT algorithms. A recent promising direction initiated by Williams [Wil13] connects the complexity of circuits

the problem of checking whether a given circuit has a satisfying assignment, that is, a substitution of inputs by constants that forces the circuit to output one). Namely, the existence of better-than-2^n algorithms for CircuitSAT for a particular circuit model implies exponential lower bounds for these circuits for functions in large classes like **NEXP**. This way unconditional exponential lower bounds have been proved for ACC_0 circuits (constant-depth circuits with unbounded-arity OR, AND, NOT, and arbitrary modular gates) [Wil14]. Ben-Sasson and Viola [BV14] have demonstrated that in order to prove a specific linear lower bound for a function in $\mathbf{E}^{\mathbf{NP}}$ it suffices to lower the base of the exponent in the 3-SAT complexity down to an appropriate constant. It should be noted, however, that currently available algorithms for the satisfiability problem for general circuit classes are not sufficient for proving new lower bounds.

Also techniques similar to the ones used in proving circuit lower bounds algorithms are employed in a number of algorithms for CircuitSAT and FormulaSAT, see e.g. [Nur09, Sav14, San10, ST13, KRT13, CKK$^+$15, CK15].

Our methods. Almost all previous lower bounds have been proved using a simple gate elimination technique: one gradually simplifies the function (for example, by substituting variables one by one) showing that every simplification step eliminates a certain number of gates. A crucial idea [Sch74] is to keep the function in the same class. Following [DK11], we prove lower bounds for affine dispersers, that is, functions that are non-constant on affine subspaces of certain dimensions: Ben-Sasson and Kopparty [BK12] gave an explicit construction of affine dispersers for sublinear dimensions.

Feeding an appropriate constant to a non-linear gate (for example, AND) makes this gate constant and therefore eliminates subsequent gates, which helps to eliminate more gates than in the case of a linear gate (for example, XOR). On the other hand, linear gates, when stacked together, sometimes allow to reorganize the circuit. Then affine restrictions can kill such gates while keeping the properties of an affine disperser. This idea has been used in [Pau77, Sto77, Blu84, ST13, DK11].

Thus, it is natural to consider a circuit as composed of linear circuits connected by non-linear gates. In our case analysis we make affine substitutions but not restrictions. That is, instead of just saying that $x_1 \oplus x_2 \oplus x_3 \oplus x_9 = 0$ and removing all gates that become constant, we make sure to replace all occurrences of x_1 by $x_2 \oplus x_3 \oplus x_9$. Since a gate computing such a sum might be unavailable and we do not want to increase the number of gates, we "rewire" some parts of the circuit, which, however, may potentially introduce cycles. This is the first ingredient of our proof: *cyclic circuits*. That is, the linear components of our "circuits" may now have directed cycles; however, we require that the values computed in the gates are still uniquely determined. Cyclic circuits have already been considered in [Riv77, DC89, NTW04, RB12] (the last reference contains an overview of previous work on cyclic circuits).

Thus we are able to make affine substitutions. We try to make such a substitution in order to make the topmost (i.e., closest to the inputs) non-linear gate constant. This, however, does not seem to be enough. The second ingredient in our proof is a *complexity measure* that manages difficult situations (bottlenecks) by allowing to perform an amortized analysis: we count not just the number of gates, we compute a linear combination of the number of gates and the number of bottlenecks. Such measures were previously considered by several authors. For example, Zwick [Zwi91] counted the number of (internal) gates minus the number of inputs of outdegree 1. The same measure was later used by Lachish and Raz [LR01] and by Iwama and Morizumi [IM02]. Kojevnikov and Kulikov [KK10] used a measure assigning different weights to linear and non-linear gates to show that Schnorr's $2n - O(1)$ lower bound [Sch76] can be strengthened to $7n/3 - O(1)$. Carefully chosen complexity measures are also used to estimate the progress of splitting algorithms for **NP**-hard problems [Kul99, KK06, FGK09].

Our main bottleneck (called "troubled gate") is shown in Figure 1 on page 15. (All gates have outdegrees exactly as shown on the picture, i.e., two inputs of degree 2 feed a gate of outdegree 1 that computes $(x \oplus a)(y \oplus b) \oplus c$ where $a, b, c \in \{0, 1\}$ are constants.)

Sometimes in order to fight a troubled gate, we have to make a *quadratic substitution*, which is the third ingredient of our proof. This happens if the gate below G is a linear gate fed by a variable z; in the simplest case a substitution $z = xy$ kills G, the linear gate, and the gate below (actually, we show it kills much more). However, quadratic substitutions may make affine dispersers constant, so we consider a special type of quadratic substitutions. Namely, we consider quadratic substitutions as a form of delayed affine substitutions (in the example above, if we promise to substitute later a constant either to x or to y, the substitution can be considered affine). In order to maintain this, instead of affine subspaces (where affine dispersers are non-constant by definition) we consider so-called read-once depth-2 quadratic sources (essentially, this means that all variables in the right-hand sides of the quadratic substitutions that we make are pairwise distinct free variables). We show that an affine disperser for a sublinear dimension remains non-constant for read-once depth-2 quadratic sources of a sublinear dimension.

2 Definitions

Gates and notation. A circuit is an acyclic directed graph in which incoming edges are numbered for every node. The nodes are called *gates*. A gate may have either indegree zero (in which case it is called an *input* gate, or a *variable*) or indegree two (in which case it is called an *internal* gate). Every internal gate is labelled by a Boolean function $g\colon \{0,1\} \times \{0,1\} \to \{0,1\}$, and the set of all the sixteen such functions is denoted by B_2. We call these binary functions *operations* in order to distinguish them from functions of n variables computed in the gates. The size of a circuit is the number of internal gates.

We say that an operation is of *and-type* if it computes $g(x, y) = (c_1 \oplus x)(c_2 \oplus y) \oplus c_3$ for some constants $c_1, c_2, c_3 \in \{0, 1\}$, and of *xor-type* if it computes $g(x, y) = x \oplus y \oplus c_1$ for some constant $c_1 \in \{0, 1\}$. Similarly, we call gates and-type and xor-type. If a gate computes an operation depending on precisely one of its inputs, we call it *passing*.

If an (internal) gate computes a constant operation, we call it *trivial* (note that it still has two incoming edges). If a substitution forces some gate G to compute a constant, we say that it *trivializes* G. (For example, for a gate computing the operation $g(x, y) = x \wedge y$, the substitution $x = 0$ trivializes it.)

We denote by $out(G)$ the outdegree of the gate G. If $out(G) = k$, we call G a k-gate. If $out(G) \geq k$, we call it a k^+-gate. We adopt the same terminology for variables (so we have 0-variables, 1-variables, 2^+-variables, etc.).

One gate of outdegree zero is designated as the output.

A toy example of a circuit is shown in Figure 2 on page 15. For input gates, the corresponding variables are shown inside. For an internal gate, we show its operation inside and its label near the gate. As figure shows, a circuit corresponds to a simple program for computing a Boolean function: each instruction of the program is a binary Boolean operation whose inputs are input variables or the results of the previous instructions.

An *affine disperser* for dimension $d(n)$ is a family of functions $f_n\colon \mathbb{F}_2^n \to \mathbb{F}_2$ such that for all sufficiently large n, f_n is non-constant on any affine subspace of dimension at least $d(n)$. There exist polynomial-time computable affine dispersers for sublinear dimensions $d(n) = o(n)$ [BK12, Yeh11, Li11, Sha11, Li15].

2.1 Generalizations of circuits

Cyclic circuits. In this paper we use generalizations of circuits that simplify circuit transformations. These generalized circuits may contain cycles; however, the underlying graphs are still not arbitrary labelled directed graphs.

A *cyclic circuit* is a directed (not necessarily acyclic) graph where all vertices have indegree either 0 or 2. We adopt the same terminology for its nodes (input and internal gates) and its size as for ordinary circuits. We restrict our attention to *cyclic xor-circuits*, where all gates compute affine operations. While the most interesting internal gates compute either $\oplus$ or $\equiv$, for technical reasons we also allow passing gates and trivial gates. We will be interested in multioutput cyclic circuits, so, in contrast to our definition of ordinary circuits, several gates may be designated as outputs, and they may have nonzero outdegree.

A circuit, and even a cyclic circuit, naturally corresponds to a system of equations over $\mathbb{F}_2$, where internal gates correspond to variables of the system and variables of the (cyclic) circuit are counted in the constants of the system (that is, we formally have a separate system for every assignment to the input gates, but all these systems share the same matrix). For a gate G fed by gates F and H and computing some operation $\odot$, we write the equation $G \oplus (F \odot H) = 0$. A more specific clarifying example would be a gate G computing $F \oplus x \oplus 1$, where x is an input gate; then the line in the system would be $G \oplus F = x \oplus 1$, where G and F contribute two 1's to the matrix, and $x \oplus 1$ contributes to the constant vector.

For a cyclic xor-circuit, this is a linear system with a square matrix. We call a cyclic xor-circuit *fair* if this matrix has full rank. It follows that for every assignment of the inputs, there exist *unique* values for the gates such that these values are consistent with the circuit (that is, for each gate its value is correctly computed from the values in its inputs). Thus, similarly to an ordinary circuit, every gate in a fair circuit computes a function of the values fed into its input gates (clearly, it is an affine function). A simple example of a fair cyclic xor-circuit is shown in Figure 3 on page 15. Note that if we additionally impose the requirement that the graph is acyclic, we arrive at ordinary linear circuits (that is, circuits consisting of xor-type gates, passing gates, and constant gates).

Semicircuits. We introduce the following notion, called *semicircuits*, a generalization of both Boolean circuits and cyclic xor-circuits.

A semicircuit is a composition of a cyclic xor-circuit and an (ordinary) circuit. Namely, its nodes are split into two sets, X and C. The nodes in the set X form a cyclic xor-circuit. The nodes in the set C form an ordinary circuit (if wires going from X to C are replaced by variables). There are no wires going back from C to X. A semicircuit is called fair if X is fair. ***In what follows we abuse the notation by using the word "circuit" to mean a fair semicircuit.***

3 Lower bound

3.1 Overview

In this section we prove the main theorem. The proof goes by induction. We start with an affine disperser and a circuit computing it on $\{0,1\}^n$. Then we gradually shrink the space where it is computed by adding equations ("substitutions") for variables. This allows us to simplify the circuit by reducing the number of gates (and other parameters counted in the complexity measure) and eliminating the variable we have just substituted.

In Section 3.2 we show how to make substitutions in fair semicircuits, and how to simplify them afterwards. We also introduce "troubled" gates, special "unwanted" fragments of circuits that we

count in the complexity measure. We check that the simplification methods we use do not increase the number of these gates too much.

In order to eliminate troubled gates, sometimes we use quadratic substitutions. In Section 3.3 we describe formally subsets of points of $\{0,1\}^n$ resulting from all kinds of the substitutions we make and show that affine dispersers are non-constant on such subsets. In Section 3.4 we define the circuit complexity measure and formulate the main result: we can always reduce the measure by an appropriate amount by shrinking the space; the lower bound follows.

Finally, Section 3.5 proves the main result by going through a number of cases.

3.2 Cyclic circuit transformations

In this section we consider several types of substitutions. It is straightforward how to substitute a constant to an input:

Proposition 1. *Let C be a circuit with input gates $x_1, \dots, x_n$, and let $c \in \{0,1\}$ be a constant. For every gate G fed by x_1 replace the operation $g(x_1, t)$ computed by G with the operation $g'(x_1, t) = g(c, t)$ (thus the result becomes independent of x_1). This transforms C into another circuit C' (in particular, it is still a fair semicircuit) such that it has the same number of gates, the same topology, and for every gate H that computes a function $h(x_1, \dots, x_n)$ in C, the corresponding gate in the new circuit C' computes the function $h(c, x_2, \dots, x_n)$.*

We call this transformation a *substitution by a constant*.

A more complicated type of a substitution is when we replace an input x with a function computed in a different gate G. In this case in each gate fed by x, we replace wires going from x by wires going from G. We call this transformation a *substitution by a function*.

Proposition 2. *Let C be a circuit with input gates $x_1, \dots, x_n$, and let $g(x_2, \dots, x_n)$ be a function computed in a gate G. Consider the construction C' obtained by substituting a function g to x_1 (it has the same number of gates as C). Then if G is not reachable from x_1 by a directed path in C, then C' is a fair semicircuit, and for every gate H that computes a function $h(x_1, \dots, x_n)$ in C, except for x_1, the corresponding gate in the new circuit C' computes the function $h(g(x_2, \dots, x_n), x_2, \dots, x_n)$.*

In what follows, however, we will also use substitutions that do not satisfy the hypothesis of this proposition: substitutions that create cycles. We defer this construction to Section 3.2.2.

3.2.1 Normalization and troubled gates

In order to work with a circuit, we are going to assume that it does not contain obvious inefficiencies (such as trivial gates, etc.), in particular, those created by substitutions. We describe certain normalization rules below; however, while normalizing we need to make sure the circuit remains within certain limits: in particular, it must remain fair and compute the same function. We need to check also that we do not "spoil" a circuit by introducing "bottleneck" cases. Namely, we are going to prove an upper bound on the number of newly introduced unwanted fragments called "troubled" gates.

We say that an internal gate G is *troubled* if it satisfies the following three criteria: G is an and-type gate of fanout 1, the gates feeding G are input gates, and both input gates feeding G have fanout 2. See also Figure 1 on page 15. *From now on, we denote all and-type gates by $\wedge$, and all xor-type gates by $\oplus$.*

We always make substitutions consciously and thus can count the number of troubled gates that can possible emerge. However, what if a gate is killed because of simplifications? We limit the

process of removing gates to normalization rules, and make sure that we never get more than four new troubled gates per killed gate. We say that a circuit is *normalized* if none of the following rules is applicable to it. Each rule eliminates a gate G whose inputs are gates I_1 and I_2. (Note that I_1 and I_2 can be inputs or internal nodes, and, in rare cases, they can coincide with G itself). Figure 4 on page 16 illustrates the rules.

Rule 1: If G has no outgoing edges and is not marked as an output, then remove it. Note also that it could not happen that the only outgoing edge of G feeds itself, because this would make a trivial equation and violate the circuit fairness.

Rule 2: If G is trivial, i.e., it computes a constant operation c, remove G and "embed" this constant to the next gates. That is, for every gate H fed by G, replace the operation $h(g,t)$ computed in this gate (where g is the input from G and t is the other input) by the operation $h'(g,t) = h(c,t)$. (Clearly, h' depends on at most one argument, which is not optimal, and in this case after removing G one typically applies Rule 3 or Rule 2 to its successors.)

Rule 3: If G is passing, i.e., it computes an operation depending only on one of its inputs, remove G by reattaching its outgoing wires to that input. This may also require changing the operations computed at its successors (the corresponding input may be negated; note that an and-type gate (xor-type gate) remains an and-type gate (xor-type gate)).

If G feeds itself and depends on another input, then the self-loop wire (which would now go nowhere) is dropped. (Note that if G feeds itself it cannot depend on the self-loop input.)

If G has no outgoing edges it must be an output gate (otherwise it would be removed by Rule 0). In this special case, we remove G and mark the corresponding input of G (or its negation) as the output gate.

Rule 4: If G is a 1-gate that feeds a single gate Q, Q is distinct from G itself, and Q is also fed by one of G's inputs, then replace in Q the incoming wire going from G by a wire going from the other input of G (this might also require changing the operation at Q); then remove G. We call such a gate G *useless*.

Rule 5: If the inputs of G coincide (I_1 and I_2 refer to the same node) then we replace the binary operation $g(x,y)$ computed in G with the operation $g'(x,y) = g(x,x)$. Then perform the same operation on G as described in Rule 3 or 2.

Proposition 3. *Each of the Rules 1–5 removes one internal gate, introduces at most four new troubled gates. None of the rules change the functions of n input variables computed in the gates that are not removed. A fair semicircuit remains a fair semicircuit.*

3.2.2 Affine substitutions

In this subsection, we show how to make substitutions that do create cycles. This will be needed in order to make affine substitutions. Namely, we take a gate computing an affine function $x_1 \oplus \bigoplus_{i\in I} x_i \oplus c$ (where $c \in \{0,1\}$ is a constant) and "rewire" a circuit so that this gate is replaced by a trivial gate computing a constant $b \in \{0,1\}$, while x_1 is replaced by an internal gate. The resu lting circuit over $x_2, \ldots, x_n$ may be viewed as the initial circuit under the substitution $x_1 \leftarrow \bigoplus_{i\in I} x_i \oplus c \oplus b$. The "rewiring" is formally explained below; however, before that we need to prove a structural lemma (which is trivial for acyclic circuits) that guarantees its success.

For an xor-circuit, we say that a gate G depends on a variable x if G computes an affine function in which x is a term. Note that in a circuit without cycles this means that precisely one of the inputs of G depends on x, and one could trace this dependency all the way to x, therefore there always exists a path from x to G. The following lemma states that it is always possible to find such a path in a fair cyclic circuit too. However, it may be possible that some nodes on this path do not

depend on x. Note that dependencies in cyclic circuits are sometimes counterintuitive. For example, in Figure 3 on page 15, gate G_2 is fed by x_4 but does not depend on it.

Lemma 1. *Let C be a fair cyclic xor-circuit, and let the gate G depend on the variable x. Then there is a path from x to G.*

We now come to rewiring. The sketch in Figure 5 on page 16 shows the main idea.

Lemma 2. *Let C be a fair semicircuit with input gates $x_1, \dots, x_n$ and internal gates $G_1, \dots, G_m$. Let G be a gate not reachable by a directed path from any and-type gate. Assume that G computes the function $x_1 \oplus \bigoplus_{i\in I} x_i \oplus c$, where $I \subseteq \{2, \dots, n\}$. Let $b \in \{0, 1\}$ be a constant. Then one can transform C into a new circuit C' with the following properties: 1) graph-theoretically, C' has the same gates as C, plus a new internal gate Z; some edges are changed, in particular, x_1 is disconnected from the circuit; 2) the operation in G is replaced by the constant operation b; 3) $\mathrm{in}_{C'}(Z) = 2$, $\mathrm{out}_{C'}(G) = \mathrm{out}_C(G) + 1$, $\mathrm{out}_{C'}(x_1) = 0$. $\mathrm{out}_{C'}(Z) = \mathrm{out}_C(x_1) - 1$. 4) The indegrees and outdegrees of all other gates are the same in C and C'. 5) C' is fair. 6) all gates common for C' and C compute the same functions on the affine subspace defined by $x_1 \oplus \bigoplus_{i\in I} x_i \oplus c \oplus b = 0$, that is, if $f(x_1, \dots, x_n)$ is the function computed by an internal gate in C and $f'(x_2, \dots, x_n)$ is the function computed by its counterpart in C', then $f(\bigoplus_{i\in I} x_i \oplus c \oplus b, x_2, \dots, x_n) = f'(x_2, \dots, x_n)$. The gate Z computes the function $\bigoplus_{i\in I} x_i \oplus c \oplus b$ (which on the affine subspace equals x_1).*

This transformation does not introduce new troubled gates.

After we apply the transformation, we apply Rule 2 to G. Since the only troubled gates introduced by this rule are the inputs of the removed gate, no troubled gates are introduced (and one gate, G itself, is eliminated, thus the combination of Lemma 2 and Rule 2 does not increase the number of gates).

3.3 Read-once depth-2 quadratic sources

We generalize affine sources as follows.

Definition 1. *Let the set of variables $\{x_1, \dots, x_n\}$ be partitioned into three disjoint sets $F, L, Q \subseteq \{1, \dots, n\}$ (for* free*,* linear*, and* quadratic*). Consider a system of equalities that contains for each variable x_j with $j \in Q$, a quadratic equality of the form $x_j = (x_i \oplus c_i)(x_k \oplus c_k) \oplus c_j$, where $i, k \in F$ and c_i, c_k, c_j are constants; the variables from the right-hand side of all the quadratic substitutions are pairwise disjoint. For each variable x_j with $j \in L$, an affine equality of the form $x_j = \bigoplus_{i\in F_j\subseteq F} x_i \oplus \bigoplus_{i\in Q_j\subseteq Q} x_i \oplus c_j$ for some constant c_j. A subset R of $\{(x_1, x_2, \dots, x_n) \in \mathbb{F}_2^n\}$ that satisfies these equalities is called a* read-once depth-2 quadratic source *(or* rdq-source*) of dimension $d = |F|$.*

An example of such a system is shown in Figure 6 on page 16. The variables from the right-hand side of quadratic substitutions are called *protected*. Other free variables are called *unprotected*.

For this, we will gradually build a straight-line program (that is, a sequence of lines of the form $x = f(\dots)$, where f is a function depending on the program inputs (free variables) and the values computed in the previous lines) that produces an rdq-source. We build it bottom-up. Namely, we take an unprotected free variable x_j and extend our current program with either a quadratic substitution $x_j = (x_i \oplus c_i)(x_k \oplus c_k) \oplus c_j$ depending on free unprotected variables x_i, x_k or a linear substitution $x_j = \bigoplus_{i\in J} x_i \oplus c_j$ depending on any variables. It is clear that such a program can be rewritten into a system satisfying Definition 1. In general, we cannot use protected free variables without breaking the rdq-property. However, there are two special cases where this is possible: (1)

we can substitute a constant to a protected variable (and update the quadratic line accordingly: for example, $z = xy$ and $x = 1$ yield $z = y$ and $x = 1$); (2) we can substitute one protected variable for another variable (or its negation) from the same quadratic equation (for example, $z = xy$ and $x = y$ yield $z = y$ and $x = y$).

In what follows we abuse the notation by denoting by the same letter R the source, the straight-line program defining it, and the mapping $R\colon \mathbb{F}_2^d \to \mathbb{F}_2^n$ computed by this program that takes the d free variables and evaluates all other variables.

Let $R \subseteq \mathbb{F}_2^n$ be an rdq-source of dimension d, let the free variables be $x_1, x_2, \ldots, x_d$, and let $f\colon \mathbb{F}_2^n \to \mathbb{F}_2$ be a function. Then f restricted to R, denoted $f|_R$, is a function $f|_R\colon \mathbb{F}_2^d \to \mathbb{F}_2$, defined by $f|_R(x_1, \ldots, x_d) = f(R(x_1, \ldots, x_d))$. Note that affine sources are precisely rdq-sources with $Q = \emptyset$. We define dispersers for rdq-sources similarly to dispersers for affine sources: A family of functions $f_n\colon \mathbb{F}_2^n \to \mathbb{F}_2$ is an *rdq-disperser* for dimension $d(n)$ if for all sufficiently large n, for every rdq-source R of dimension at least $d(n)$, $f_n|_R$ is non-constant. The following proposition shows that affine dispersers are also rdq-dispersers for related parameters. By setting one protected variable to 0 for each quadratic restriction, we get that if R is an rdq-source of $\mathbb{F}_2^n$ of dimension d, Then R contains an affine subspace of dimension at least $d/2$.[1] In particular we have the following.

Corollary 1. *An affine disperser for sublinear dimension is also an rdq-disperser for sublinear dimension.*

3.4 Circuit complexity measure

For a circuit C and a straight-line program R defining an rdq-source, we define the following circuit complexity measure:

$$\mu(C, R) = g + \alpha_Q \cdot q + \alpha_T \cdot t + \alpha_I \cdot i\,,$$

where g is the number of internal gates in C, q is the number of quadratic substitutions in R, t is the number of troubled gates in C, and i is the number of *influential* input gates in C. We say that an input is influential if it feeds at least one gate or is protected (recall that a variable is protected if it occurs in the right-hand side of a quadratic substitution in R). The constants $\alpha_Q, \alpha_T, \alpha_I > 0$ will be chosen later.

Proposition 3 implies that when a gate is removed from a circuit by applying a normalization rule the measure μ is reduced by at least $\beta = 1 - 4\alpha_T$. The constant α_T will be chosen to be very close to 0 (certainly less than 1/4), so $\beta > 0$.

In order to estimate the initial value of our measure, we need the following lemma.

Lemma 3. *Let C be a circuit computing an affine disperser $f\colon \mathbb{F}_2^n \to \mathbb{F}_2$ for dimension d, then the number of troubled gates in C is less than $\frac{n}{2} + \frac{5d}{2}$.*

We are now ready to formulate our main result.

Theorem 1. *Let $f\colon \mathbb{F}_2^n \to \mathbb{F}_2$ be an rdq-disperser for dimension d and C be a fair semicircuit computing f. Let $\alpha_Q, \alpha_T, \alpha_I \geq 0$ be some constants, and $\alpha_T \leq 1/4$. Then $\mu(C, \emptyset) \geq \delta(n - d - 2)$ where*

$\delta := \alpha_I + \min\ \frac{\alpha_I}{2}, 4\beta, 3 + \alpha_T, 2\beta + \alpha_Q, 5\beta - \alpha_Q, 2.5\beta + \frac{\alpha_Q}{2}$ *, and $\beta = 1 - 4\alpha_T$.*

We defer the proof of this theorem to the next section. This theorem, together with Corollary 1, implies a lower bound on the circuit complexity of affine dispersers.

[1] This is obviously false for quadratic *varieties*: no Boolean function can be non-constant on all sets of common roots of $n - o(n)$ quadratic polynomials. For example, the system of $n/2$ quadratic equations $x_1x_2 = x_3x_4 = \ldots = x_{n-1}x_n = 1$ defines a single point, so any function is constant on this set.

Corollary 2. *Let $\delta, \beta, \alpha_Q, \alpha_T, \alpha_I$ be constants as above, then the circuit size of an affine disperser for sublinear dimension is at least $\left(\delta - \frac{\alpha_T}{2} - \alpha_I\right) n - o(n)$.*

The maximal value of $\delta - \frac{\alpha_T}{2} - \alpha_I$ satisfying the condition from Corollary 2 is achieved when $\alpha_T = \frac{1}{43}$, $\alpha_Q = \frac{65}{43}$, $\alpha_I = 6 + \frac{2}{43}$, $\beta = \frac{39}{43}$, $\delta = 9 + \frac{3}{43}$. This gives a $(3 + \frac{1}{86})n - o(n)$ lower bound for an affine disperser for sublinear dimension.

3.5 Gate elimination

In order to prove Theorem 1 we first show that it is always possible to make a substitution and decrease the measure by δ. The main theorem then follows by a simple induction proof.

Theorem 2. *Let $f\colon \mathbb{F}_2^n \to \mathbb{F}_2$ be an rdq-disperser for dimension d, let R be an rdq-source of dimension $s \geq d + 2$, and let C be an optimal (i.e., C with the smallest $\mu(C, R)$) fair semicircuit computing the function $f|_R$. Then there exist an rdq-source R' of dimension $s' < s$ and a fair semicircuit C' computing the function $f|_{R'}$ such that $\mu(C', R') \leq \mu(C, R) - \delta(s - s')$.*

The proof of Theorem 2 is based on a careful consideration of a number of cases. Due to the page limit restrictions, here we show a high-level picture of the case analysis only.

We fix the values of constants $\alpha_T, \alpha_Q, \alpha_I, \beta, \delta$ to the optimal values: $\alpha_T = \frac{1}{43}, \alpha_Q = \frac{65}{43}, \alpha_I = 6\frac{2}{43}, \beta = \frac{39}{43}, \delta = 9\frac{3}{43}$. Now it suffices to show that we can always make one substitution and decrease the measure by at least $\delta = 9\frac{3}{43}$. First we normalize the circuit. By Proposition 3, during normalization if we eliminate a gate then we introduce at most four new troubled gates, this means that we decrease the measure by at least $1 - 4\alpha_T = \frac{39}{43}$. Therefore, normalization never increases the measure.

We always make constant, linear or simple quadratic *substitution* to a variable. Then we remove the substituted variable from the circuit, so that for each assignment to the remaining variables the function is defined. It is easy to make a constant substitution $x = c$ for $c \in \{0, 1\}$. We propagate the value c to the inputs fed by x and remove x from the circuit, since it does not feed any other gates. An affine substitution $x = \bigoplus_{i \in I} x_i \oplus c$ is harder to make, because a straightforward way to eliminate x would be to compute $\left(\bigoplus_{i \in I} x_i \oplus c\right)$ elsewhere. Fortunately, Lemma 2 shows how to compute it on the affine subspace defined by the substitution without using x and without increasing the number of gates (after an extra gate introduced by this lemma is removed by normalization).

Thus, in this sketch we will be making arbitrary affine substitutions for sums that are computed in gates without saying that we need to run the reconstruction procedure first. Also, we will make a simple quadratic substitution $z = (x \oplus c_1)(y \oplus c_2) \oplus c_3$ only if the gates fed by z are cancelled out after the substitution, so that we do not need to propagate this quadratic value to other gates. We want to stay in the class of rdq-sources, therefore we cannot make an affine substitution to a variable x if it already has been used in the right-hand side of some quadratic restriction $z = (x \oplus c_1)(y \oplus c_2) \oplus c_3$ (that is, x is protected), also we cannot make quadratic substitutions that overlap in the variables. In this proof sketch we ignore these two issues, but they are addressed in the full version of the paper.

Let A be a topologically minimal and-type gate (i.e., an and-type gate that is not reachable from any and-type gate), let I_1 and I_2 be the inputs of A (I_1 and I_2 can be variables or internal gates). Now we consider the following cases (see Figure 7 on page 17).

1. At least one of I_1, I_2 (say, I_1) is an internal gate of outdegree greater than one. There is a constant c such that if we assign $I_1 = c$, then A becomes constant. (For example, if A is an and, then $c = 0$, if A is an or, then $c = 1$ etc.) When A becomes constant it eliminates all the gates it feeds. Therefore, if we assign the appropriate constant to I_1, we eliminate I_1, two of

the gates it feeds (including A), and also a successor of A, four gates total, and we decrease the measure by at least $\alpha_I + 4\beta = 9\frac{29}{43} > \delta$.

2. At least one of I_1, I_2 (say, I_1) is a variable of outdegree one. We assign the appropriate constant to I_2. This eliminates I_2, A, a successor of A, and I_1. This assignment eliminates at least two gates and two variables, so the measure decrease is at least $2\alpha_I + 2\beta = 13\frac{39}{43} > \delta$.

3. I_1 and I_2 are internal gates of outdegree one. Then if we assign the appropriate constant to I_1, we eliminate I_1, A, a successor of A, and I_2 (since I_2 does not feed any gates). We decrease measure by at least $\alpha_I + 4\beta > \delta$.

4. I_1 is an internal gate of outdegree one, I_2 is a variable of outdegree greater than one. Then we assign the appropriate constant to I_2. This assignment eliminates I_2, at least two of its successors (including A), a successor of A, and I_1 (since it does not feed any gates). Again, we decrease the measure by at least $\alpha_I + 4\beta > \delta$.

5. I_1 and I_2 are variables of outdegree greater than one.

   (a) I_1 or I_2 (say, I_1) has outdegree at least three. By assigning the appropriate constant to I_1 we eliminate at least three of the gates it feeds and a successor of A, four gates total.

   (b) I_1 and I_2 are variables of degree two. If A is a 2^+-gate we eliminate at least four gates by assigning I_1 so in what follows we assume that A is a 1-gate. In this case A is a troubled gate. We want to make the appropriate substitution and eliminate I_1 (or I_2), its successor, A, and A's successor.

      i. If this substitution does not introduce new troubled gates, then we eliminate a variable, three gates and decrease the number of troubled gates by one. Thus, we decrease the measure by $\alpha_I + 3 + \alpha_T = 9\frac{3}{43} = \delta$.

      ii. If the substitution introduces troubled gates, then we consider which normalization rule introduces troubled gates. The full case analysis is presented in the full paper, here we demonstrate just one case of the analysis. Let us consider the case when a new troubled gate is introduced when we eliminate the gate fed by A (see Figure 7 on page 17, the variable z will feed a new troubled gate after assignments $x = 0$ or $y = 0$). In such a case we make a different substitution: $z = (x \oplus c_1)(y \oplus c_2) \oplus c_3$. This substitution eliminates gates A, D, E, F and a gate fed by F. Thus, we eliminate one variable, five gates, but we introduce a new quadratic substitution, and decrease the measure by at least $\alpha_I + 5\beta - \alpha_Q = 9\frac{3}{43} = \delta$.

It is conceivable that when we count several eliminated gates, some of them coincide, so that we actually eliminate fewer gates. Usually in such cases we can prove that some other gates become trivial. This and other degenerate cases are handled in the full version of the paper.

References

[And87] Alexander E. Andreev. On a method for obtaining more than quadratic effective lower bounds for the complexity of π-schemes. *Moscow Univ. Math. Bull.*, 42(1):63–66, 1987.

[BFT98] Harry Buhrman, Lance Fortnow, and Thomas Thierauf. Nonrelativizing separations. In *CCC-98*, 1998.

[BK12] Eli Ben-Sasson and Swastik Kopparty. Affine dispersers from subspace polynomials. *SIAM J. Comput.*, 41(4):880–914, 2012.

[Blu84] Norbert Blum. A Boolean function requiring $3n$ network size. *Theor. Comput. Sci.*, 28:337–345, 1984.

[BV14] Eli Ben-Sasson and Emanuele Viola. Short PCPs with projection queries. In Javier Esparza, Pierre Fraigniaud, Thore Husfeldt, and Elias Koutsoupias, editors, *Automata, Languages, and Programming - 41st International Colloquium, ICALP 2014, Copenhagen, Denmark, July 8-11, 2014, Proceedings, Part I*, volume 8572 of *Lecture Notes in Computer Science*, pages 163–173. Springer, 2014.

[CK15] Ruiwen Chen and Valentine Kabanets. Correlation bounds and #sat algorithms for small linear-size circuits. In Dachuan Xu, Donglei Du, and Dingzhu Du, editors, *Computing and Combinatorics - 21st International Conference, COCOON 2015, Beijing, China, August 4-6, 2015, Proceedings*, volume 9198 of *Lecture Notes in Computer Science*, pages 211–222. Springer, 2015.

[CKK+15] Ruiwen Chen, Valentine Kabanets, Antonina Kolokolova, Ronen Shaltiel, and David Zuckerman. Mining circuit lower bound proofs for meta-algorithms. *Computational Complexity*, 24(2):333–392, 2015.

[CR06] Venkatesan T. Chakaravarthy and Sambuddha Roy. Oblivious symmetric alternation. In Bruno Durand and Wolfgang Thomas, editors, *STACS 2006, 23rd Annual Symposium on Theoretical Aspects of Computer Science, Marseille, France, February 23-25, 2006, Proceedings*, volume 3884 of *Lecture Notes in Computer Science*, pages 230–241. Springer, 2006.

[DC89] Patrick W. Dymond and Stephen A. Cook. Complexity theory of parallel time and hardware. *Inf. Comput.*, 80(3):205–226, 1989.

[DK11] Evgeny Demenkov and Alexander S. Kulikov. An elementary proof of a $3n - o(n)$ lower bound on the circuit complexity of affine dispersers. In Filip Murlak and Piotr Sankowski, editors, *Mathematical Foundations of Computer Science 2011 - 36th International Symposium, MFCS 2011, Warsaw, Poland, August 22-26, 2011. Proceedings*, volume 6907 of *Lecture Notes in Computer Science*, pages 256–265. Springer, 2011.

[DKMM15] Evgeny Demenkov, Alexander S. Kulikov, Olga Melanich, and Ivan Mihajlin. New lower bounds on circuit size of multi-output functions. *Theory Comput. Syst.*, 56(4):630–642, 2015.

[FGK09] Fedor V. Fomin, Fabrizio Grandoni, and Dieter Kratsch. A measure & conquer approach for the analysis of exact algorithms. *J. ACM*, 56(5), 2009.

[Hås86] Johan Håstad. Almost optimal lower bounds for small depth circuits. In Juris Hartmanis, editor, *Proceedings of the 18th Annual ACM Symposium on Theory of Computing, May 28-30, 1986, Berkeley, California, USA*, pages 6–20. ACM, 1986.

[Hås98] Johan Håstad. The shrinkage exponent of de Morgan formulas is 2. *SIAM J. Comput.*, 27(1):48–64, 1998.

[IM02] Kazuo Iwama and Hiroki Morizumi. An explicit lower bound of $5n - o(n)$ for Boolean circuits. In Krzysztof Diks and Wojciech Rytter, editors, *Mathematical Foundations of Computer Science 2002, 27th International Symposium, MFCS 2002, Warsaw, Poland, August 26-30, 2002, Proceedings*, volume 2420 of *Lecture Notes in Computer Science*, pages 353–364. Springer, 2002.

[IN93] Russell Impagliazzo and Noam Nisan. The effect of random restrictions on formula size. *Random Struct. Algorithms*, 4(2):121–134, 1993.

[Khr71] Valeriy M. Khrapchenko. A method of determining lower bounds for the complexity of π-schemes. *Math. Notes of the Acad. of Sci. of the USSR*, 10(1):474–479, 1971.

[KK06] Arist Kojevnikov and Alexander S. Kulikov. A new approach to proving upper bounds for MAX-2-SAT. In *Proceedings of the Seventeenth Annual ACM-SIAM Symposium on Discrete Algorithms, SODA 2006, Miami, Florida, USA, January 22-26, 2006*, pages 11–17. ACM Press, 2006.

[KK10] Arist Kojevnikov and Alexander S. Kulikov. Circuit complexity and multiplicative complexity of Boolean functions. In Fernando Ferreira, Benedikt Löwe, Elvira Mayordomo, and Luís Mendes Gomes, editors, *Programs, Proofs, Processes, 6th Conference on Computability in Europe, CiE 2010*, volume 6158 of *Lecture Notes in Computer Science*, pages 239–245. Springer, 2010.

[KM65] Boris M. Kloss and Vadim A. Malyshev. Estimates of the complexity of certain classes of functions. *Vestn.Moskov.Univ.Ser.1*, 4:44–51, 1965. In Russian.

[KRT13] Ilan Komargodski, Ran Raz, and Avishay Tal. Improved average-case lower bounds for demorgan formula size. In *54th Annual IEEE Symposium on Foundations of Computer Science, FOCS 2013, 26-29 October, 2013, Berkeley, CA, USA*, pages 588–597. IEEE Computer Society, 2013.

[Kul99] Oliver Kullmann. New methods for 3-SAT decision and worst-case analysis. *Theor. Comput. Sci.*, 223(1-2):1–72, 1999.

[Li11] Xin Li. A new approach to affine extractors and dispersers. In *Proceedings of the 26th Annual IEEE Conference on Computational Complexity, CCC 2011, San Jose, California, June 8-10, 2011*, pages 137–147. IEEE Computer Society, 2011.

[Li15] Xin Li. Extractors for affine sources with polylogarithmic entropy. *Electronic Colloquium on Computational Complexity (ECCC)*, 22:121, 2015.

[LR01] Oded Lachish and Ran Raz. Explicit lower bound of $4.5n - o(n)$ for Boolean circuits. In Jeffrey Scott Vitter, Paul G. Spirakis, and Mihalis Yannakakis, editors, *Proceedings on 33rd Annual ACM Symposium on Theory of Computing, July 6-8, 2001, Heraklion, Crete, Greece*, pages 399–408. ACM, 2001.

[Nec66] Edward I. Nechiporuk. On a Boolean function. *Doklady Akademii Nauk. SSSR*, 169(4):765–766, 1966.

[NTW04] Arfst Nickelsen, Till Tantau, and Lorenz Weizsäcker. Aggregates with component size one characterize polynomial space. *Electronic Colloquium on Computational Complexity (ECCC)*, 028, 2004.

[Nur09] Sergey Nurk. An $2^{0.4058m}$ upper bound for Circuit SAT. Technical Report 10, Steklov Institute of Mathematics at St.Petersburg, 2009. PDMI Preprint.

[Pau77] Wolfgang J. Paul. A $2.5n$-lower bound on the combinational complexity of Boolean functions. *SIAM J. Comput.*, 6(3):427–443, 1977.

[PZ93] Mike Paterson and Uri Zwick. Shrinkage of de Morgan formulae under restriction. *Random Struct. Algorithms*, 4(2):135–150, 1993.

[Raz85] Alexander A. Razborov. Lower bound on monotone complexity of some Boolean functions. *Doklady Akademii Nauk. SSSR*, 281(4):798–801, 1985.

[RB12] Marc D. Riedel and Jehoshua Bruck. Cyclic boolean circuits. *Discrete Applied Mathematics*, 160(13-14):1877–1900, 2012.

[Riv77] Ronald L. Rivest. The necessity of feedback in minimal monotone combinational circuits. *IEEE Trans. Computers*, 26(6):606–607, 1977.

[San10] Rahul Santhanam. Fighting perebor: New and improved algorithms for formula and QBF satisfiability. In *51th Annual IEEE Symposium on Foundations of Computer Science, FOCS 2010, October 23-26, 2010, Las Vegas, Nevada, USA*, pages 183–192. IEEE Computer Society, 2010.

[Sav14] Sergey Savinov. Upper bounds for the Boolean circuit satisfiability problem. Master Thesis defended at St.Peterburg Academic University of Russian Academy of Sciences, 2014. In Russian.

[Sch74] Claus-Peter Schnorr. Zwei lineare untere Schranken für die Komplexität Boolescher Funktionen. *Computing*, 13(2):155–171, 1974.

[Sch76] Claus-Peter Schnorr. The combinational complexity of equivalence. *Theor. Comput. Sci.*, 1(4):289–295, 1976.

[Sha49] Claude E. Shannon. The synthesis of two-terminal switching circuits. *Bell Systems Technical Journal*, 28:59–98, 1949.

[Sha11] Ronen Shaltiel. Dispersers for affine sources with sub-polynomial entropy. In Rafail Ostrovsky, editor, *IEEE 52nd Annual Symposium on Foundations of Computer Science, FOCS 2011, Palm Springs, CA, USA, October 22-25, 2011*, pages 247–256. IEEE Computer Society, 2011.

[SS91] Victor Shoup and Roman Smolensky. Lower bounds for polynomial evaluation and interpolation problems. In *32nd Annual Symposium on Foundations of Computer Science, San Juan, Puerto Rico, 1-4 October 1991*, pages 378–383. IEEE Computer Society, 1991.

[ST13] Kazuhisa Seto and Suguru Tamaki. A satisfiability algorithm and average-case hardness for formulas over the full binary basis. *Computational Complexity*, 22(2):245–274, 2013.

[Sto77] Larry J. Stockmeyer. On the combinational complexity of certain symmetric Boolean functions. *Mathematical Systems Theory*, 10:323–336, 1977.

[Sub61] Bella A. Subbotovskaya. Realizations of linear functions by formulas using $+, \cdot, -$. *Doklady Akademii Nauk. SSSR*, 136(3):553–555, 1961.

[Tal14] Avishay Tal. Shrinkage of de Morgan formulae by spectral techniques. In *Foundations of Computer Science (FOCS), 2014 IEEE 55th Annual Symposium on*, pages 551–560. IEEE, 2014.

[Wil13] Ryan Williams. Improving exhaustive search implies superpolynomial lower bounds. *SIAM J. Comput.*, 42(3):1218–1244, 2013. Extended abstract appeared in Proc. STOC-2010.

[Wil14] Ryan Williams. Nonuniform ACC circuit lower bounds. *JACM*, 61(1), 2014. Extended abstract appears in Proc. CCC-2011.

[Yao85] Andrew C. Yao. Separating the polynomial-time hierarchy by oracles (preliminary version). In *FOCS*, pages 1–10. IEEE Computer Society, 1985.

[Yeh11] Amir Yehudayoff. Affine extractors over prime fields. *Combinatorica*, 31(2):245–256, 2011.

[Zwi91] Uri Zwick. A $4n$ lower bound on the combinational complexity of certain symmetric Boolean functions over the basis of unate dyadic Boolean functions. *SIAM J. Comput.*, 20(3):499–505, 1991.

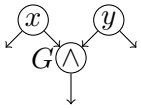

Figure 1: "Troubled gate"

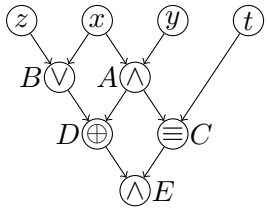

$$
\begin{aligned}
B &= (z \vee x)\\
A &= (x \wedge y)\\
D &= (B \oplus A)\\
C &= (A \equiv t)\\
E &= (D \wedge C)
\end{aligned}
$$

Figure 2: An example of a circuit and the program it computes.

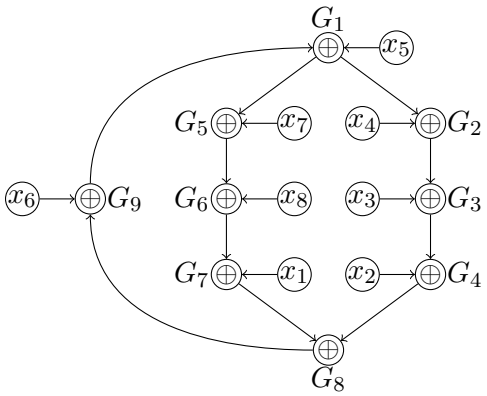

$$
\begin{aligned}
G_1 &= x_1 \oplus x_2 \oplus x_3 \oplus x_4 \oplus x_5 \oplus x_6 \oplus x_7 \oplus x_8\\
G_2 &= x_1 \oplus x_2 \oplus x_3 \oplus x_5 \oplus x_6 \oplus x_7 \oplus x_8\\
G_3 &= x_1 \oplus x_2 \oplus x_5 \oplus x_6 \oplus x_7 \oplus x_8\\
G_4 &= x_1 \oplus x_5 \oplus x_6 \oplus x_7 \oplus x_8\\
G_5 &= x_1 \oplus x_2 \oplus x_3 \oplus x_4 \oplus x_5 \oplus x_6 \oplus x_8\\
G_6 &= x_1 \oplus x_2 \oplus x_3 \oplus x_4 \oplus x_5 \oplus x_6\\
G_7 &= x_2 \oplus x_3 \oplus x_4 \oplus x_5 \oplus x_6\\
G_8 &= x_1 \oplus x_2 \oplus x_3 \oplus x_4 \oplus x_7 \oplus x_8\\
G_9 &= x_1 \oplus x_2 \oplus x_3 \oplus x_4 \oplus x_6 \oplus x_7 \oplus x_8
\end{aligned}
$$

$$
\begin{aligned}
G_1 &= G_9 \oplus x_5\\
G_2 &= G_1 \oplus x_4\\
G_3 &= G_2 \oplus x_3\\
G_4 &= G_3 \oplus x_2\\
G_5 &= G_1 \oplus x_7\\
G_6 &= G_5 \oplus x_8\\
G_7 &= G_6 \oplus x_1\\
G_8 &= G_4 \oplus G_7\\
G_9 &= G_8 \oplus x_6
\end{aligned}
\qquad
\begin{bmatrix}
1 & 0 & 0 & 0 & 0 & 0 & 0 & 0 & 1\\
1 & 1 & 0 & 0 & 0 & 0 & 0 & 0 & 0\\
0 & 1 & 1 & 0 & 0 & 0 & 0 & 0 & 0\\
0 & 0 & 1 & 1 & 0 & 0 & 0 & 0 & 0\\
1 & 0 & 0 & 0 & 1 & 0 & 0 & 0 & 0\\
0 & 0 & 0 & 0 & 1 & 1 & 0 & 0 & 0\\
0 & 0 & 0 & 0 & 0 & 1 & 1 & 0 & 0\\
0 & 0 & 0 & 1 & 0 & 0 & 1 & 1 & 0\\
0 & 0 & 0 & 0 & 0 & 0 & 0 & 1 & 1
\end{bmatrix}
\times
\begin{bmatrix} G_1\\ G_2\\ G_3\\ G_4\\ G_5\\ G_6\\ G_7\\ G_8\\ G_9 \end{bmatrix}
=
\begin{bmatrix} x_5\\ x_4\\ x_3\\ x_2\\ x_7\\ x_8\\ x_1\\ 0\\ x_6 \end{bmatrix}
$$

Figure 3: A simple example of a cyclic xor-circuit. In this case all the gates are labeled with $\oplus$. The affine functions computed by the gates are shown to the right of the circuit. The bottom row shows the program computed by the circuit as well as the corresponding linear system.

Find, Magnus; Golovnev, Alexander; Hirsch, Edward; Kulikov, Alexander.
"A better-than-3n lower bound for the circuit complexity of an explicit function."
Paper presented at 57th Annual IEEE Symposium on Foundations of Computer Science (FOCS 2016),
New Brunswick, NJ. October 9, 2016 - October 11, 2016.

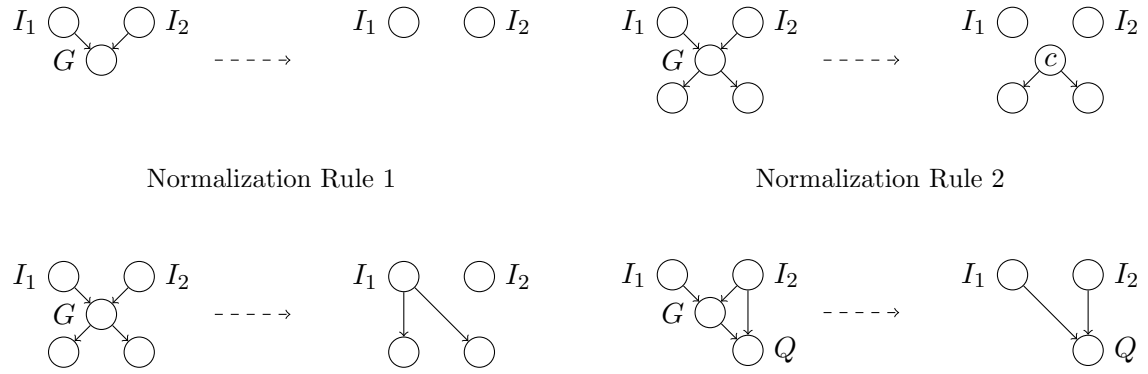

Figure 4: Illustration of the normalization rules

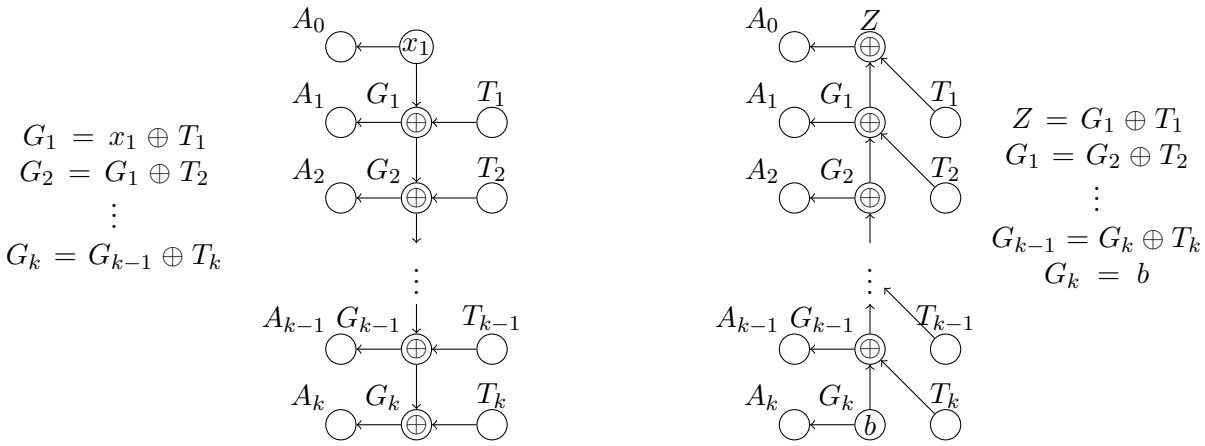

Figure 5: This figure illustrates the transformation from Lemma 2. We use $\oplus$ as a generic label for xor-type gates. That is, in the picture, gates labelled $\oplus$ may compute the function $\equiv$.

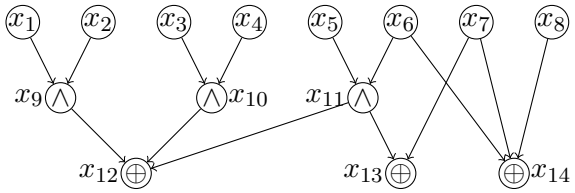

Figure 6: An example of an rdq-source. Note that a variable can be read just once by an and-type gate while it can be read many times by xor-gates.

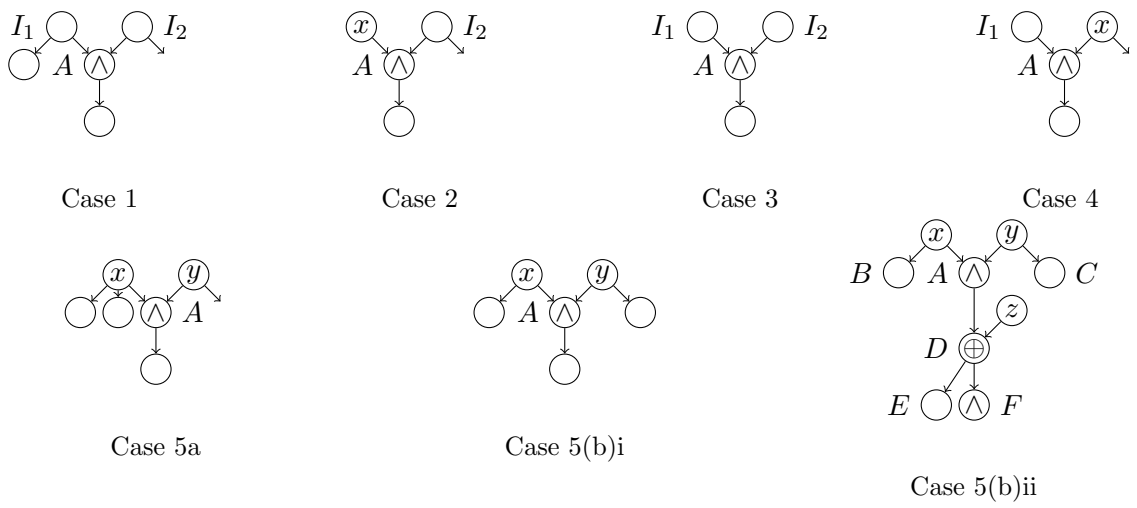

Figure 7: Gate elimination process in Theorem 2.

A better-than-3n lower bound for the circuit complexity of an explicit function

Magnus Gausdal Find[1], Alexander Golovnev[2], Edward A. Hirsch[3], and Alexander S. Kulikov[3]

[1]National Institute of Standards and Technology
[2]New York University
[3]Steklov Institute of Mathematics at St. Petersburg, Russian Academy of Sciences

October 31, 2015

Abstract

We consider Boolean circuits over the full binary basis. We prove a $(3+\frac{1}{86})n - o(n)$ lower bound on the size of such a circuit for an explicitly defined predicate, namely an affine disperser for sublinear dimension. This improves the $3n - o(n)$ bound of Norbert Blum (1984). The proof is based on the gate elimination technique extended with the following three ideas. We generalize the computational model by allowing circuits to contain cycles, this in turn allows us to perform affine substitutions. We use a carefully chosen circuit complexity measure to track the progress of the gate elimination process. Finally, we use quadratic substitutions that may be viewed as delayed affine substitutions.

Find, Magnus; Golovnev, Alexander; Hirsch, Edward; Kulikov, Alexander.
"A better-than-3n lower bound for the circuit complexity of an explicit function."
Paper presented at 57th Annual IEEE Symposium on Foundations of Computer Science (FOCS 2016),
New Brunswick, NJ. October 9, 2016 - October 11, 2016.

Contents

1 Introduction

In this paper we consider Boolean circuits over the full binary basis, that is, directed acyclic graphs where each internal node computes a binary Boolean operation $\{0,1\}\times\{0,1\}\to\{0,1\}$, inputs are fed into nodes of indegree zero, and one node (or the negation of a node) is designated as the output. The *size* of a circuit is the number of its internal nodes. A simple counting argument [Sha49] shows that most Boolean functions require circuits of exponential size. However, showing superpolynomial lower bounds for explicitly defined functions (for example, for functions from **NP**) remains a hopelessly difficult task. (In particular, such lower bounds would imply $\mathbf{P}\neq\mathbf{NP}$.) Moreover, even superlinear bounds are unknown for functions in $\mathbf{E}^{\mathbf{NP}}$. The smallest uniform complexity class for which superpolynomial bounds are known is **MAEXP** (exponential-time Merlin-Arthur games) [BFT98], and the smallest such class with arbitrary polynomial lower bounds is $\mathbf{O_2}$ (the oblivious symmetric second level of the polynomial hierarchy) [CR06].

People started to tackle the problem in the 60s. Kloss and Malyshev [KM65] proved a $2n-O(1)$ lower bound for the function $\bigoplus_{1\le i<j\le n} x_ix_j$. Schnorr [Sch74] proved a $2n-O(1)$ lower bound for functions that for any pair of variables x,y, have at least three different subfunctions among the four functions obtained after substituting constants to x and y. Stockmeyer [Sto77] proved a $2.5n-O(1)$ bound for certain symmetric functions. Paul [Pau77] proved a $2n-o(n)$ lower bound for the storage access function and a $2.5n-o(n)$ lower bound for a function combining several storage access functions using simple operations. Eventually, Blum [Blu84] extended Paul's argument and proved a $3n-o(n)$ bound.

Mysteriously, Blum's bound remained unbeaten for more than thirty years. Recently, Demenkov and Kulikov [DK11] showed a similar bound for affine dispersers. Their proof

Find, Magnus; Golovnev, Alexander; Hirsch, Edward; Kulikov, Alexander.
"A better-than-3n lower bound for the circuit complexity of an explicit function."
Paper presented at 57th Annual IEEE Symposium on Foundations of Computer Science (FOCS 2016),
New Brunswick, NJ. October 9, 2016 - October 11, 2016.

is much simpler (if one assumes the existence of explicitly defined dispersers for granted), but that does not improve the bound (actually, the $o(n)$ term in [DK11] is worse than that in [Blu84]). In this paper we eventually improve the bound for affine dispersers to $(3 + \frac{1}{86})n - o(n)$, which is stronger than Blum's bound.

Other models. The exact complexity of computational problems is different in different models of computation: for example, switching from multitape to single-tape Turing machines squares the time complexity; random access machines are even more efficient. For example, the quadratic lower bound for recognizing palindromes by a single-tape Turing machine [HU69] is worthless for stronger computational models. Boolean circuits over the full binary basis make a very robust computational model. Using a different constant-arity basis only changes the constants in the complexity. A fixed set of gates of arbitrary arity (for example, ANDs, ORs and XORs) still preserves the complexity in terms of the number of wires. After all, finding a function hard for Boolean circuits can be viewed as a combinatorial problem, in a contrast to lower bounds for uniform models. Therefore, breaking the linear barrier for Boolean circuits can be viewed as an important milestone on the way to stronger complexity lower bounds.

In this paper we consider single-output circuits (that is, circuits computing predicates). It would be natural if allowing many outputs would lead us to non-linear bounds. However, the only tool we have to transfer bounds from one output to several outputs is Lamagna and Savage [LS73] argument showing that in order to compute simultaneously m different functions requiring c gates each, one needs at least $m + c - 1$ gates. That is, we do not have superlinear bounds for multioutput functions either.

For the basis U_2 consisting of all binary Boolean functions except for parity (xor) and its complement, Schnorr [Sch76] proved that the circuit complexity of the parity function is $3n - 3$. Zwick [Zwi91] gave a $4n - O(1)$ lower bound for certain symmetric functions, Lachish and Raz [LR01] showed a $4.5n - o(n)$ lower bound for a strongly two-dependent function (a function that has exactly four subfunctions with respect to any two variables and remains so after sufficiently many substitutions). Iwama and Morizumi [IM02] improved this bound to $5n - o(n)$. Demenkov et al. [DKMM15] gave a simpler proof of a $5n - o(n)$ lower bound for a function with $o(n)$ outputs as well as presented a $7n - o(n)$ lower bound for a function with n outputs.

While we do not have nonlinear bounds for constant-arity Boolean circuits, exponential bounds are known for weaker models: one thread was initiated by Razborov [Raz85] for monotone circuits, another one was started by Yao and Håstad for constant-depth circuits without XORs [Yao85, Hås86]. Shoup and Smolensky [SS91] proved a superlinear lower bound $\Omega(n \log n / \log \log n)$ for linear circuits of polylogarithmic depth over infinite fields. Also, superlinear bounds for formulas are known for half a century. For de Morgan formulas (i.e., formulas over AND, OR, NOT) Subbotovskaya [Sub61] proved an $\Omega(n^{1.5})$ lower bound for the parity function using the random restrictions method. Khrapchenko [Khr71] showed an $\Omega(n^2)$ lower bound for parity. Applying Subbotovskaya's random restrictions method to the universal function by Nechiporuk [Nec66], Andreev [And87] proved an $\Omega(n^{2.5-o(1)})$ lower bound. By analyzing how de Morgan formulas shrink under random restrictions, Andreev's lower

Find, Magnus; Golovnev, Alexander; Hirsch, Edward; Kulikov, Alexander.
"A better-than-3n lower bound for the circuit complexity of an explicit function."
Paper presented at 57th Annual IEEE Symposium on Foundations of Computer Science (FOCS 2016),
New Brunswick, NJ. October 9, 2016 - October 11, 2016.

bound was improved to $\Omega(n^{2.55-o(1)})$ by Impagliazzo and Nisan [IN93], then to $\Omega(n^{2.63-o(1)})$ by Paterson and Zwick [PZ93], and eventually to $\Omega(n^{3-o(1)})$ by Håstad [Hås98] and Tal [Tal14]. For formulas over the full binary basis, Nechiporuk [Nec66] proved an $\Omega(n^{2-o(1)})$ lower bound for the universal function and for the element distinctness function. These bounds, however, do not translate to superlinear lower bounds for general constant-arity Boolean circuits.

Connections to CircuitSAT algorithms. A recent promising direction initiated by Williams [Wil13] connects the complexity of circuits to the complexity of algorithms for CircuitSAT (this is the problem of checking whether a given circuit has a satisfying assignment, that is, a substitution of inputs by constants that forces the circuit to output one). Namely, the existence of better-than-2^n algorithms for CircuitSAT for a particular circuit model implies exponential lower bounds for these circuits for functions in large classes like **NEXP**. This way unconditional exponential lower bounds have been proved for ACC_0 circuits (constant-depth circuits with unbounded-arity OR, AND, NOT, and arbitrary modular gates) [Wil14]. Ben-Sasson and Viola [BV14] have demonstrated that in order to prove a specific linear lower bound for a function in $\mathbf{E}^{\mathbf{NP}}$ it suffices to lower the base of the exponent in the 3-SAT complexity down to an appropriate constant.

It should be noted, however, that currently available algorithms for the satisfiability problem for general circuit classes are not sufficient for proving new lower bounds. Current techniques require upper bounds of the form $O(2^n/n^a)$ for circuits with n inputs and size n^k, while for most classes only c^g-time algorithms are available, where g is the number of the gates and $c > 1$ is a constant.

On the other hand, the techniques used in the c^g-time algorithms for CircuitSAT are somewhat similar to the techniques used for proving linear lower bounds for (general) Boolean circuits over the full binary basis. In particular, an $O(2^{0.4058g})$-time algorithm by Nurk [Nur09] (and subsequently an $O(2^{0.389667g})$-time algorithm by Savinov [Sav14]) use reconstruction of the linear part of a circuit similar to the one suggested by Paul [Pau77]. These algorithms and proofs use similar tricks in order to simplify circuits; however, at present no rigorous statement is known that would connect these two complexities. The only cases where certain types of algorithms for general complexity classes yield linear lower bounds for them are average-case results for formulas [San10, ST13, KRT13, CKK+15] and circuits [CK15], which are somewhat weaker than the current worst-case bounds.

Our methods. Almost all previous lower bounds have been proved using a simple gate elimination technique: one gradually simplifies the function (for example, by substituting variables one by one) showing that every simplification step eliminates a certain number of gates. A crucial idea [Sch74] is to keep the function in the same class. Following [DK11], we prove lower bounds for affine dispersers, that is, functions that are non-constant on affine subspaces of certain dimensions: Ben-Sasson and Kopparty [BK12] gave an explicit construction of affine dispersers for sublinear dimensions.

Feeding an appropriate constant to a non-linear gate (for example, AND) makes this gate constant and therefore eliminates subsequent gates, which helps to eliminate more gates than

Find, Magnus; Golovnev, Alexander; Hirsch, Edward; Kulikov, Alexander.
"A better-than-3n lower bound for the circuit complexity of an explicit function."
Paper presented at 57th Annual IEEE Symposium on Foundations of Computer Science (FOCS 2016),
New Brunswick, NJ. October 9, 2016 - October 11, 2016.

in the case of a linear gate (for example, XOR). On the other hand, linear gates, when stacked together, sometimes allow to reorganize the circuit. Then affine restrictions can kill such gates while keeping the properties of an affine disperser. Such linear reconstructions were used for proving circuit lower bounds by Paul [Pau77], Stockmeyer [Sto77], and Blum [Blu84]. Seto and Tamaki [ST13] used it to prove upper bounds for satisfiability of formulas over the full binary basis. Demenkov and Kulikov [DK11] used affine substitutions to prove a circuit lower bound for affine dispersers.

Thus, it is natural to consider a circuit as composed of linear circuits connected by non-linear gates. In our case analysis it is important that we make affine substitutions but not restrictions. That is, instead of just saying that $x_1 \oplus x_2 \oplus x_3 \oplus x_9 = 0$ and removing all gates that become constant, we make sure to replace all occurrences of x_1 by $x_2 \oplus x_3 \oplus x_9$. Since a gate computing such a sum might be unavailable and we do not want to increase the number of gates, we "rewire" some parts of the circuit, which, however, may potentially introduce cycles. This leads us to the first ingredient of our proof: *cyclic circuits*. That is, the linear components of our "circuits" may now have directed cycles; however, we require that the values computed in the gates are still uniquely determined (which is actually a requirement on the rank of the corresponding linear system). Cyclic circuits were studied, e.g., by Rivest [Riv77], Dymond and Cook [DC89], Nickelsen, Tantau, and Weizsäcker [NTW04], Riedel and Bruck [RB12] (the last reference also contains an overview of previous work on cyclic circuits).

Thus we are able to make affine substitutions. We try to make such a substitution in order to make the topmost (i.e., closest to the inputs) non-linear gate constant. This, however, does not seem to be enough. The second ingredient in our proof is a *complexity measure* that manages difficult situations (bottlenecks) by allowing to perform an amortized analysis: we count not just the number of gates, we compute a linear combination of the number of gates and the number of bottlenecks. Such measures were previously considered by several authors. For example, Zwick [Zwi91] counted the number of (internal) gates minus the number of inputs of outdegree 1. The same measure was later used by Lachish and Raz [LR01] and by Iwama and Morizumi [IM02]. Kojevnikov and Kulikov [KK10] used a measure assigning different weights to linear and non-linear gates to show that Schnorr's $2n - O(1)$ lower bound [Sch76] can be strengthened to $7n/3 - O(1)$. Carefully chosen complexity measures are also used to estimate the progress of splitting algorithms for **NP**-hard problems [Kul99, KK06, FGK09].

Our main bottleneck (called "troubled gate") is as follows:

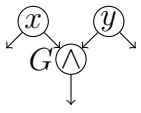

(All gates have outdegrees exactly as shown on the picture, i.e., two inputs of degree 2 feed a gate of outdegree 1 that computes $(x \oplus a)(y \oplus b) \oplus c$ where $a, b, c \in \{0, 1\}$ are constants.)

Sometimes in order to fight a troubled gate, we have to make a *quadratic substitution*, which is the third ingredient of our proof. This happens if the gate below G is a linear gate fed by a variable z; in the simplest case a substitution $z = xy$ kills G, the linear gate, and

Find, Magnus; Golovnev, Alexander; Hirsch, Edward; Kulikov, Alexander.
"A better-than-3n lower bound for the circuit complexity of an explicit function."
Paper presented at 57th Annual IEEE Symposium on Foundations of Computer Science (FOCS 2016),
New Brunswick, NJ. October 9, 2016 - October 11, 2016.

the gate below (actually, we show it kills much more). However, quadratic substitutions may make affine dispersers constant, so we consider a special type of quadratic substitutions. Namely, we consider quadratic substitutions as a form of delayed affine substitutions (in the example above, if we promise to substitute later a constant either to x or y, the substitution can be considered affine). In order to maintain this, instead of affine subspaces (where affine dispersers are non-constant by definition) we consider so-called read-once depth-2 quadratic sources (essentially, this means that all variables in the right-hand sides of the quadratic substitutions that we make are pairwise distinct free variables). We show that an affine disperser for a sublinear dimension remains non-constant for read-once depth-2 quadratic sources of a sublinear dimension.

Open questions. An affine disperser for dimension d may be viewed as a function that is not constant on any affine subspace of *size* at least 2^d. A natural extension is to allow similarly sized varieties defined by quadratic polynomials. As shown by Golovnev and Kulikov [GK16], such dispersers with appropriate parameters must have circuit size at least $3.1n$. However, explicit constructions of such dispersers are currently unknown. There are known constructions of dispersers for algebraic varieties for large finite fields [Dvi12], and known constructions of such dispersers for $\mathbb{F}_2$ [CT15, Sha11] but with weaker parameters than needed for the lower bound to work.

2 Definitions

Gates and notation. A circuit is an acyclic directed graph in which incoming edges are numbered for every node. The nodes are called *gates*. A gate may have either indegree zero (in which case it is called an *input* gate, or a *variable*) or indegree two (in which case it is called an *internal* gate). Every internal gate is labelled by a Boolean function $g\colon \{0,1\} \times \{0,1\} \to \{0,1\}$, and the set of all the sixteen such functions is denoted by B_2. We call these binary functions *operations* in order to distinguish them from functions of n variables computed in the gates. The size of a circuit is the number of internal gates.

We say that an operation is of *and-type* if it computes $g(x,y) = (c_1 \oplus x)(c_2 \oplus y) \oplus c_3$ for some constants $c_1, c_2, c_3 \in \{0,1\}$, and of *xor-type* if it computes $g(x,y) = x \oplus y \oplus c_1$ for some constant $c_1 \in \{0,1\}$. Similarly, we call gates and-type and xor-type. If a gate computes an operation depending on precisely one of its inputs, we call it *passing*.

If an (internal) gate computes a constant operation, we call it *trivial* (note that it still has two incoming edges). If a substitution forces some gate G to compute a constant, we say that it *trivializes* G. (For example, for a gate computing the operation $g(x,y) = x \wedge y$, the substitution $x = 0$ trivializes it.)

We denote by $out(G)$ the outdegree of the gate G. If $out(G) = k$, we call G a k-gate. If $out(G) \geq k$, we call it a k^+-gate. We adopt the same terminology for variables (so we have 0-variables, 1-variables, 2^+-variables, etc.).

One gate of outdegree zero is designated as the output.

Find, Magnus; Golovnev, Alexander; Hirsch, Edward; Kulikov, Alexander.
"A better-than-3n lower bound for the circuit complexity of an explicit function."
Paper presented at 57th Annual IEEE Symposium on Foundations of Computer Science (FOCS 2016),
New Brunswick, NJ. October 9, 2016 - October 11, 2016.

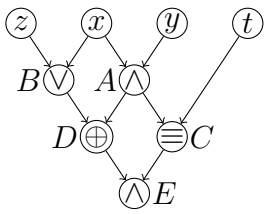

$B = (z \vee x)$
$A = (x \wedge y)$
$D = (B \oplus A)$
$C = (A \equiv t)$
$E = (D \wedge C)$

Figure 1: An example of a circuit and the program it computes.

A toy example of a circuit is shown in Figure 1. For input gates, the corresponding variables are shown inside. For an internal gate, we show its operation inside and its label near the gate. As figure shows, a circuit corresponds to a simple program for computing a Boolean function: each instruction of the program is a binary Boolean operation whose inputs are input variables or the results of the previous instructions.

Affine dispersers. An *affine disperser* for dimension $d(n)$ is a family of functions $f_n \colon \mathbb{F}_2^n \to \mathbb{F}_2$ such that for all sufficiently large n, f_n is non-constant on any affine subspace of dimension at least $d(n)$. Explicit constructions of affine dispersers have drawn a lot of attention recently. First, polynomial-time computable affine dispersers for any linear dimension were constructed [BKS$^+$10, Bou07], and then it was shown that there are polynomial-time computable affine dispersers for sublinear dimensions $d(n) = o(n)$ [BK12, Yeh11, Li11, Sha11, Li15].

2.1 Generalizations of circuits

Cyclic circuits. In this paper we use generalizations of circuits that simplify circuit transformations. These generalized circuits may contain cycles; however, the underlying graphs are still not arbitrary labelled directed graphs.

A *cyclic circuit* is a directed (not necessarily acyclic) graph where all vertices have indegree either 0 or 2. We adopt the same terminology for its nodes (input and internal gates) and its size as for ordinary circuits. We restrict our attention to *cyclic xor-circuits*, where all gates compute affine operations. While the most interesting internal gates compute either $\oplus$ or $\equiv$, for technical reasons we also allow passing gates and trivial gates. We will be interested in multioutput cyclic circuits, so, in contrast to our definition of ordinary circuits, several gates may be designated as outputs, and they may have nonzero outdegree.

A circuit, and even a cyclic circuit, naturally corresponds to a system of equations over $\mathbb{F}_2$, where internal gates correspond to variables of the system and variables of the (cyclic) circuit are counted in the constants of the system (that is, we formally have a separate system for every assignment to the input gates, but all these systems share the same matrix). For a gate G fed by gates F and H and computing some operation $\odot$, we write the equation $G \oplus (F \odot H) = 0$. A more specific clarifying example would be a gate G computing $F \oplus x \oplus 1$, where x is an input gate; then the line in the system would be $G \oplus F = x \oplus 1$, where G and

Find, Magnus; Golovnev, Alexander; Hirsch, Edward; Kulikov, Alexander.
"A better-than-3n lower bound for the circuit complexity of an explicit function."
Paper presented at 57th Annual IEEE Symposium on Foundations of Computer Science (FOCS 2016),
New Brunswick, NJ. October 9, 2016 - October 11, 2016.

F contribute two 1's to the matrix, and $x \oplus 1$ contributes to the constant vector.

For a cyclic xor-circuit, this is a linear system with a square matrix. We call a cyclic xor-circuit *fair* if this matrix has full rank. It follows that for every assignment of the inputs, there exist *unique* values for the gates such that these values are consistent with the circuit (that is, for each gate its value is correctly computed from the values in its inputs). Thus, similarly to an ordinary circuit, every gate in a fair circuit computes a function of the values fed into its input gates (clearly, it is an affine function). A simple example of a fair cyclic xor-circuit is shown in Figure 2. Note that if we additionally impose the requirement that the graph is acyclic, we arrive at ordinary linear circuits (that is, circuits consisting of xor-type gates, passing gates, and constant gates).

Relationship between cyclic and acyclic xor-circuits. It is not difficult to show that for multiple outputs, fair cyclic xor-circuits form a stronger model than acyclic xor-circuits. For example, the 9 functions computed simultaneously by the cyclic xor-circuit shown in Figure 2 cannot be computed by an acyclic xor-circuit with 9 gates. To see this, assume for the sake of contradiction, that an acyclic xor-circuit with 9 gates computes the same functions. Since the circuit has 9 gates all gates must compute outputs. Consider a topologically minimal gate G. Such a gate exists since the circuit is acyclic. Since G is topologically minimal it computes the sum of two input gates, therefore it cannot compute an output.

On the other hand, a minimal xor-circuit of k variables computing a single output has exactly $k - 1$ internal gates and is acyclic.

Semicircuits. We introduce the following notion, called *semicircuits*, a generalization of both Boolean circuits and cyclic xor-circuits.

A semicircuit is a composition of a cyclic xor-circuit and an (ordinary) circuit. Namely, its nodes are split into two sets, X and C. The nodes in the set X form a cyclic xor-circuit. The nodes in the set C form an ordinary circuit (if wires going from X to C are replaced by variables). There are no wires going back from C to X. A semicircuit is called fair if X is fair. ***In what follows we abuse the notation by using the word "circuit" to mean a fair semicircuit.***

3 Lower bound

3.1 Overview

In this section we prove the main theorem.

The proof goes by induction. We start with an affine disperser and a circuit computing it on $\{0,1\}^n$. Then we gradually shrink the space where it is computed by adding equations ("substitutions") for variables. This allows us to simplify the circuit by reducing the number of gates (and other parameters counted in the complexity measure) and eliminating the variable we have just substituted.

Find, Magnus; Golovnev, Alexander; Hirsch, Edward; Kulikov, Alexander.
"A better-than-3n lower bound for the circuit complexity of an explicit function."
Paper presented at 57th Annual IEEE Symposium on Foundations of Computer Science (FOCS 2016),
New Brunswick, NJ. October 9, 2016 - October 11, 2016.

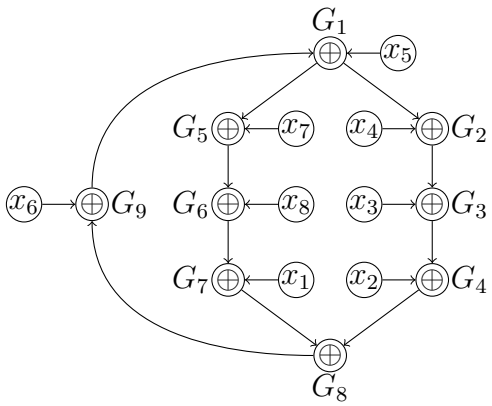

$$
\begin{aligned}
G_1 &= x_1 \oplus x_2 \oplus x_3 \oplus x_4 \oplus x_5 \oplus x_6 \oplus x_7 \oplus x_8 \\
G_2 &= x_1 \oplus x_2 \oplus x_3 \oplus x_5 \oplus x_6 \oplus x_7 \oplus x_8 \\
G_3 &= x_1 \oplus x_2 \oplus x_5 \oplus x_6 \oplus x_7 \oplus x_8 \\
G_4 &= x_1 \oplus x_5 \oplus x_6 \oplus x_7 \oplus x_8 \\
G_5 &= x_1 \oplus x_2 \oplus x_3 \oplus x_4 \oplus x_5 \oplus x_6 \oplus x_8 \\
G_6 &= x_1 \oplus x_2 \oplus x_3 \oplus x_4 \oplus x_5 \oplus x_6 \\
G_7 &= x_2 \oplus x_3 \oplus x_4 \oplus x_5 \oplus x_6 \\
G_8 &= x_1 \oplus x_2 \oplus x_3 \oplus x_4 \oplus x_7 \oplus x_8 \\
G_9 &= x_1 \oplus x_2 \oplus x_3 \oplus x_4 \oplus x_6 \oplus x_7 \oplus x_8
\end{aligned}
$$

$$
\begin{aligned}
G_1 &= G_9 \oplus x_5 \\
G_2 &= G_1 \oplus x_4 \\
G_3 &= G_2 \oplus x_3 \\
G_4 &= G_3 \oplus x_2 \\
G_5 &= G_1 \oplus x_7 \\
G_6 &= G_5 \oplus x_8 \\
G_7 &= G_6 \oplus x_1 \\
G_8 &= G_4 \oplus G_7 \\
G_9 &= G_8 \oplus x_6
\end{aligned}
\qquad
\begin{bmatrix}
1 & 0 & 0 & 0 & 0 & 0 & 0 & 0 & 1 \\
1 & 1 & 0 & 0 & 0 & 0 & 0 & 0 & 0 \\
0 & 1 & 1 & 0 & 0 & 0 & 0 & 0 & 0 \\
0 & 0 & 1 & 1 & 0 & 0 & 0 & 0 & 0 \\
1 & 0 & 0 & 0 & 1 & 0 & 0 & 0 & 0 \\
0 & 0 & 0 & 0 & 1 & 1 & 0 & 0 & 0 \\
0 & 0 & 0 & 0 & 0 & 1 & 1 & 0 & 0 \\
0 & 0 & 0 & 1 & 0 & 0 & 1 & 1 & 0 \\
0 & 0 & 0 & 0 & 0 & 0 & 0 & 1 & 1
\end{bmatrix}
\times
\begin{bmatrix} G_1 \\ G_2 \\ G_3 \\ G_4 \\ G_5 \\ G_6 \\ G_7 \\ G_8 \\ G_9 \end{bmatrix}
=
\begin{bmatrix} x_5 \\ x_4 \\ x_3 \\ x_2 \\ x_7 \\ x_8 \\ x_1 \\ 0 \\ x_6 \end{bmatrix}
$$

Figure 2: A simple example of a cyclic xor-circuit. In this case all the gates are labeled with $\oplus$. The affine functions computed by the gates are shown to the right of the circuit. The bottom row shows the program computed by the circuit as well as the corresponding linear system.

Find, Magnus; Golovnev, Alexander; Hirsch, Edward; Kulikov, Alexander.
"A better-than-3n lower bound for the circuit complexity of an explicit function."
Paper presented at 57th Annual IEEE Symposium on Foundations of Computer Science (FOCS 2016),
New Brunswick, NJ. October 9, 2016 - October 11, 2016.

In Subsection 3.2 we show how to make substitutions in fair semicircuits, and how to simplify them afterwards. We also introduce "troubled" gates, special "unwanted" fragments of circuits that we count in the complexity measure. We check that the simplification methods we use do not increase the number of these gates too much.

In order to eliminate troubled gates, sometimes we use quadratic substitutions. In Subsection 3.3 we describe formally subsets of points of $\{0,1\}^n$ resulting from all kinds of the substitutions we make and show that affine dispersers are non-constant on such subsets. In Subsection 3.4 we define the circuit complexity measure and formulate the main result: we can always reduce the measure by an appropriate amount by shrinking the space; the lower bound follows.

Finally, Subsection 3.5 proves the main result by going through a number of cases.

3.2 Cyclic circuit transformations

3.2.1 Basic substitutions

In this section we consider several types of substitutions. It is straightforward how to substitute a constant to an input:

Proposition 1. *Let C be a circuit with input gates $x_1,\dots,x_n$, and let $c\in\{0,1\}$ be a constant. For every gate G fed by x_1 replace the operation $g(x_1,t)$ computed by G with the operation $g'(x_1,t)=g(c,t)$ (thus the result becomes independent of x_1). This transforms C into another circuit C' (in particular, it is still a fair semicircuit) such that it has the same number of gates, the same topology, and for every gate H that computes a function $h(x_1,\dots,x_n)$ in C, the corresponding gate in the new circuit C' computes the function $h(c,x_2,\dots,x_n)$.*

We call this transformation a *substitution by a constant*.

A more complicated type of a substitution is when we replace an input x with a function computed in a different gate G. In this case in each gate fed by x, we replace wires going from x by wires going from G.

We call this transformation a *substitution by a function*.

Proposition 2. *Let C be a circuit with input gates $x_1,\dots,x_n$, and let $g(x_2,\dots,x_n)$ be a function computed in a gate G. Consider the construction C' obtained by substituting a function g to x_1 (it has the same number of gates as C). Then if G is not reachable from x_1 by a directed path in C, then C' is a fair semicircuit, and for every gate H that computes a function $h(x_1,\dots,x_n)$ in C, except for x_1, the corresponding gate in the new circuit C' computes the function $h(g(x_2,\dots,x_n),x_2,\dots,x_n)$.*

Proof. Note that we require that G is not reachable from x_1 (thus we do not introduce new cycles), and also that g does not depend on x_1. Functions computed in the gates are the solution of the system corresponding to the circuit (see Section 2.1). The transformation simply replaces every equation of the form $H=F\odot x_1$ with the equation $H=F\odot G$ (and equation of the form $H'=x_1\odot x_1$ with the equation $H'=G\odot G$). Consider specific values for $x_2,\dots,x_n$. Assume that the solution for the old system does not satisfy the new equation.

Find, Magnus; Golovnev, Alexander; Hirsch, Edward; Kulikov, Alexander.
"A better-than-3n lower bound for the circuit complexity of an explicit function."
Paper presented at 57th Annual IEEE Symposium on Foundations of Computer Science (FOCS 2016),
New Brunswick, NJ. October 9, 2016 - October 11, 2016.

Then take $x_1 = g(x_2, \ldots, x_n)$, it violates the corresponding equation in the old system, a contradiction. Vice versa, consider a different solution for the new system. It must satisfy the old system (where $x_1 = g(x_2, \ldots, x_n)$), but the old system has a unique solution. □

In what follows, however, we will also use substitutions that do not satisfy the hypothesis of this proposition: substitutions that create cycles. We defer this construction to Section 3.2.3.

3.2.2 Normalization and troubled gates

In order to work with a circuit, we are going to assume that it is "normalized", that is, it does not contain obvious inefficiencies (such as trivial gates, etc.), in particular, those created by substitutions. We describe certain normalization rules below; however, while normalizing we need to make sure the circuit remains within certain limits: in particular, it must remain fair and compute the same function. We need to check also that we do not "spoil" a circuit by introducing "bottleneck" cases. Namely, we are going to prove an upper bound on the number of newly introduced unwanted fragments called "troubled" gates.

We say that an internal gate G is *troubled* if it satisfies the following three criteria:

- G is an and-type gate of fanout 1,
- the gates feeding G are input gates,
- both input gates feeding G have fanout 2.

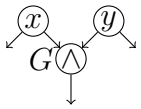

From now on, we denote all and-type gates by $\wedge$, and all xor-type gates by $\oplus$.

We always make substitutions consciously and thus can count the number of troubled gates that can possible emerge. However, what if a gate is killed because of simplifications? We limit the process of removing gates to normalization rules, and make sure that we never get more than four new troubled gates per killed gate.

We say that a circuit is *normalized* if none of the following rules is applicable to it. Each rule eliminates a gate G whose inputs are gates I_1 and I_2. (Note that I_1 and I_2 can be inputs or internal nodes, and, in rare cases, they can coincide with G itself.)

Rule 1: If G has no outgoing edges and is not marked as an output, then remove it.

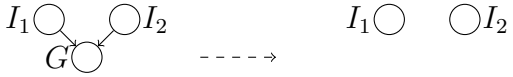

Note also that it could not happen that the only outgoing edge of G feeds itself, because this would make a trivial equation and violate the circuit fairness.

Find, Magnus; Golovnev, Alexander; Hirsch, Edward; Kulikov, Alexander.
"A better-than-3n lower bound for the circuit complexity of an explicit function."
Paper presented at 57th Annual IEEE Symposium on Foundations of Computer Science (FOCS 2016),
New Brunswick, NJ. October 9, 2016 - October 11, 2016.

Rule 2: If G is trivial, i.e., it computes a constant operation c, remove G and "embed" this constant to the next gates. That is, for every gate H fed by G, replace the operation $h(g,t)$ computed in this gate (where g is the input from G and t is the other input) by the operation $h'(g,t) = h(c,t)$. (Clearly, h' depends on at most one argument, which is not optimal, and in this case after removing G one typically applies Rule 3 or Rule 2 to its successors.)

Rule 3: If G is passing, i.e., it computes an operation depending only on one of its inputs, remove G by reattaching its outgoing wires to that input. This may also require changing the operations computed at its successors (the corresponding input may be negated; note that an and-type gate (xor-type gate) remains an and-type gate (xor-type gate)).

If G feeds itself and depends on another input, then the self-loop wire (which would now go nowhere) is dropped. (Note that if G feeds itself it cannot depend on the self-loop input.)

If G has no outgoing edges it must be an output gate (otherwise it would be removed by Rule 0). In this special case, we remove G and mark the corresponding input of G (or its negation) as the output gate.

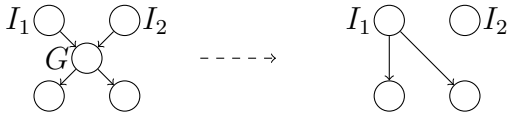

Rule 4: If G is a 1-gate that feeds a single gate Q, Q is distinct from G itself, and Q is also fed by one of G's inputs, then replace in Q the incoming wire going from G by a wire going from the other input of G (this might also require changing the operation at Q); then remove G. We call such a gate G *useless*.

Rule 5: If the inputs of G coincide (I_1 and I_2 refer to the same node) then we replace the binary operation $g(x,y)$ computed in G with the operation $g'(x,y) = g(x,x)$. Then perform the same operation on G as described in Rule 3 or 2.

Proposition 3. *Each of the Rules 1–5 removes one internal gate, introduces at most four new troubled gates. None of the rules change the functions of n input variables computed in the gates that are not removed. A fair semicircuit remains a fair semicircuit.*

Proof. Fairness. The circuit remains fair since no rule changes the set of solutions of the system.

New troubled gates. For all the rules, the only gates that may become troubled are I_1, I_2 (if they are and-type gates), and the gates they feed after the transformation (if I_1 or I_2 is a variable). Each of I_1, I_2 may create at most two new troubled gates. Hence each rule, when applied, introduces at most four new troubled gates. □

Find, Magnus; Golovnev, Alexander; Hirsch, Edward; Kulikov, Alexander.
"A better-than-3n lower bound for the circuit complexity of an explicit function."
Paper presented at 57th Annual IEEE Symposium on Foundations of Computer Science (FOCS 2016),
New Brunswick, NJ. October 9, 2016 - October 11, 2016.

3.2.3 Affine substitutions

In this subsection, we show how to make substitutions that do create cycles. This will be needed in order to make affine substitutions. Namely, we take a gate computing an affine function $x_1 \oplus \bigoplus_{i \in I} x_i \oplus c$ (where $c \in \{0,1\}$ is a constant) and "rewire" a circuit so that this gate is replaced by a trivial gate computing a constant $b \in \{0,1\}$, while x_1 is replaced by an internal gate. The resulting circuit over $x_2, \ldots, x_n$ may be viewed as the initial circuit under the substitution $x_1 \leftarrow \bigoplus_{i \in I} x_i \oplus c \oplus b$. The "rewiring" is formally explained below; however, before that we need to prove a structural lemma (which is trivial for acyclic circuits) that guarantees its success.

For an xor-circuit, we say that a gate G depends on a variable x if G computes an affine function in which x is a term. Note that in a circuit without cycles this means that precisely one of the inputs of G depends on x, and one could trace this dependency all the way to x, therefore there always exists a path from x to G. In the following lemma we show that it is always possible to find such a path in a fair cyclic circuit too. However, it may be possible that some nodes on this path do not depend on x. Note that dependencies in cyclic circuits are sometimes counterintuitive. For example, in Figure 2, gate G_4 is fed by x_2 but does not depend on it.

Lemma 1. *Let C be a fair cyclic xor-circuit, and let the gate G depend on the variable x. Then there is a path from x to G.*

Proof. Let us substitute all variables in C except for x to 0. Since G depends on x, it can only compute x or its negation.

Let $\mathcal{R}$ be the set of internal gates that are reachable from x, and $\mathcal{U}$ be the set of internal gates that are not reachable from x. Let us enumerate the gates in such a way that gates from $\mathcal{U}$ have smaller indices than gates from $\mathcal{R}$. Then the circuit C corresponds to the system

$$\begin{bmatrix} U & 0 \\ R_1 & R_2 \end{bmatrix} \times \mathcal{G} = \begin{bmatrix} L_U \\ L_R \end{bmatrix},$$

where $\mathcal{G} = (g_1, \ldots, g_{|C|})^T$ is a vector of unknowns (the gates' values), U is the principal submatrix corresponding to $\mathcal{U}$ (a square submatrix whose rows and columns correspond to the gates from $\mathcal{U}$). Note that

- the upper right part of the matrix is 0, because there are no wires going from $\mathcal{R}$ to $\mathcal{U}$, and thus unknowns corresponding to gates from $\mathcal{R}$ do not appear in the equations corresponding to gates from $\mathcal{U}$,
- L_U is a vector of constants, it cannot contain x since $\mathcal{U}$ is not reachable from x,
- L_R is a vector of affine functions of x, since all other inputs are substituted by zeros.

If U is singular, then the whole matrix is singular, which contradicts the fairness of C. Therefore, U is nonsingular, i.e., the values $\mathcal{G}' = (g_1, \ldots, g_{|\mathcal{U}|})^T$ are uniquely determined by

Find, Magnus; Golovnev, Alexander; Hirsch, Edward; Kulikov, Alexander.
"A better-than-3n lower bound for the circuit complexity of an explicit function."
Paper presented at 57th Annual IEEE Symposium on Foundations of Computer Science (FOCS 2016),
New Brunswick, NJ. October 9, 2016 - October 11, 2016.

$U \times \mathcal{G}' = L_U$, and they are constant (independent of x). This means that G cannot belong to $\mathcal{U}$.

□

We now come to rewiring.

Lemma 2. *Let C be a fair semicircuit with input gates $x_1, \dots, x_n$ and internal gates $G_1, \dots, G_m$. Let G be a gate not reachable by a directed path from any and-type gate. Assume that G computes the function $x_1 \oplus \bigoplus_{i \in I} x_i \oplus c$, where $I \subseteq \{2, \dots, n\}$. Let $b \in \{0, 1\}$ be a constant. Then one can transform C into a new circuit C' with the following properties:*

1. *graph-theoretically, C' has the same gates as C, plus a new internal gate Z; some edges are changed, in particular, x_1 is disconnected from the circuit;*
2. *the operation in G is replaced by the constant operation b;*
3. *$\mathrm{in}_{C'}(Z) = 2$, $\mathrm{out}_{C'}(G) = \mathrm{out}_C(G) + 1$, $\mathrm{out}_{C'}(x_1) = 0$. $\mathrm{out}_{C'}(Z) = \mathrm{out}_C(x_1) - 1$.*
4. *The indegrees and outdegrees of all other gates are the same in C and C'.*
5. *C' is fair.*
6. *all gates common for C' and C compute the same functions on the affine subspace defined by $x_1 \oplus \bigoplus_{i \in I} x_i \oplus c \oplus b = 0$, that is, if $f(x_1, \dots, x_n)$ is the function computed by an internal gate in C and $f'(x_2, \dots, x_n)$ is the function computed by its counterpart in C', then $f(\bigoplus_{i \in I} x_i \oplus c \oplus b, x_2, \dots, x_n) = f'(x_2, \dots, x_n)$. The gate Z computes the function $\bigoplus_{i \in I} x_i \oplus c \oplus b$ (which on the affine subspace equals x_1).*

Proof. Consider a path from x_1 to G that is guaranteed to exist by Lemma 1. Denote the internal gates on this path by $G_1, \dots, G_k = G$. Denote by $T_1, \dots, T_k$ the other inputs of these gates. Note that we assume that $G_1, \dots, G_k$ are pairwise different gates while some of the gates $T_1, \dots, T_k$ may coincide with each other and with some of $G_1, \dots, G_k$ (it might even be the case that $T_i = G_i$).

The transformation is as shown in Figure 3. The gates $A_0, \dots, A_k$ are shown on the picture just for convenience: any of $x_1, Z, G_1, \dots, G_k$ may feed any number of gates, not just one A_i.

To show the fairness of C', assume the contrary, that is, the sum of a subset of rows of the new matrix is zero. The row corresponding to $G_k = b$ must belong to the sum (otherwise we would have only rows of the matrix for C, plus an extra column). However, this would mean that if we sum up the corresponding lines of the system (not just the matrix) for C, we get $G_k = \mathrm{const} \oplus \bigoplus_{j \in J} x_j$ where $J \not\ni 1$ (note that x_1 was replaced by Z in the new system, and cancelled out by our assumption). This contradicts the assumption of the Lemma that G_k computes the function $x_1 \oplus \bigoplus_{i \in I} x_i \oplus c$. Therefore, the matrix for C' has full rank.

The programs shown next to the circuits explain that for $x_1 = \bigoplus_{i \in I} x_i \oplus c \oplus b$, the gates $G_1, \dots, G_k$ compute the same values in C' and C; the value of Z is also clearly correct. □

Find, Magnus; Golovnev, Alexander; Hirsch, Edward; Kulikov, Alexander.
"A better-than-3n lower bound for the circuit complexity of an explicit function."
Paper presented at 57th Annual IEEE Symposium on Foundations of Computer Science (FOCS 2016),
New Brunswick, NJ. October 9, 2016 - October 11, 2016.

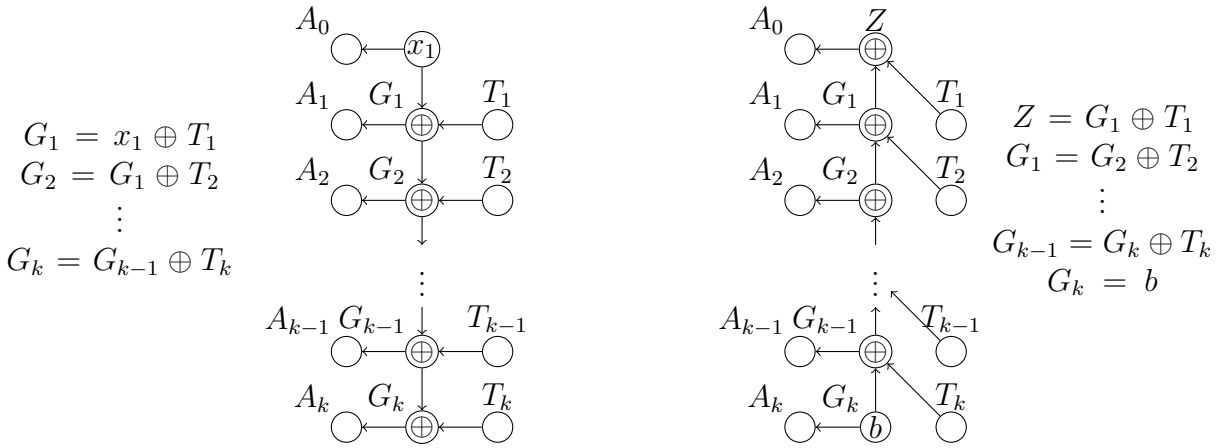

Figure 3: This figure illustrates the transformation from Lemma 2. We use $\oplus$ as a generic label for xor-type gates. That is, in the picture, gates labelled $\oplus$ may compute the function $\equiv$.

Corollary 1. *This transformation does not introduce new troubled gates.*

Proof. Indeed, the gates being fed by $G_1, \ldots, G_{k-1}, G_k, Z$ are not fed by variables; these gates themselves are not and-type gates; other gates do not change their degrees or types of input gates. □

After we apply the transformation, we apply Rule 2 to G. Since the only troubled gates introduced by this rule are the inputs of the removed gate, no troubled gates are introduced (and one gate, G itself, is eliminated, thus the combination of Lemma 2 and Rule 2 does not increase the number of gates).

3.3 Read-once depth-2 quadratic sources

We generalize affine sources as follows.

Definition 1. *Let the set of variables $\{x_1, \ldots, x_n\}$ be partitioned into three disjoint sets $F, L, Q \subseteq \{1, \ldots, n\}$ (for* free*,* linear*, and* quadratic*). Consider a system of equalities that contains*

- *for each variable x_j with $j \in Q$, a quadratic equality of the form*

$$x_j = (x_i \oplus c_i)(x_k \oplus c_k) \oplus c_j \,,$$

where $i, k \in F$ and c_i, c_k, c_j are constants; the variables from the right-hand side of all the quadratic substitutions are pairwise disjoint;

Find, Magnus; Golovnev, Alexander; Hirsch, Edward; Kulikov, Alexander.
"A better-than-3n lower bound for the circuit complexity of an explicit function."
Paper presented at 57th Annual IEEE Symposium on Foundations of Computer Science (FOCS 2016),
New Brunswick, NJ. October 9, 2016 - October 11, 2016.

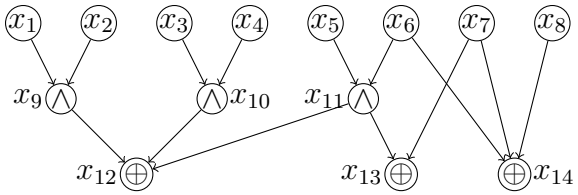

Figure 4: An example of an rdq-source. Note that a variable can be read just once by an and-type gate while it can be read many times by xor-type gates.

- *for each variable x_j with $j \in L$, an affine equality of the form*

$$x_j = \bigoplus_{i \in F_j \subseteq F} x_i \oplus \bigoplus_{i \in Q_j \subseteq Q} x_i \oplus c_j$$

  for a constant c_j.

A subset R of $\{(x_1, x_2, \ldots, x_n) \in \mathbb{F}_2^n\}$ that satisfies these equalities is called a read-once depth-2 quadratic source *(or* rdq-source*) of dimension $d = |F|$.*

An example of such a system is shown in Figure 4.

The variables from the right-hand side of quadratic substitutions are called *protected*. Other free variables are called *unprotected*.

For this, we will gradually build a straight-line program (that is, a sequence of lines of the form $x = f(\ldots)$, where f is a function depending on the program inputs (free variables) and the values computed in the previous lines) that produces an rdq-source. We build it bottom-up. Namely, we take an unprotected free variable x_j and extend our current program with either a quadratic substitution

$$x_j = (x_i \oplus c_i)(x_k \oplus c_k) \oplus c_j$$

depending on free unprotected variables x_i, x_k or a linear substitution

$$x_j = \bigoplus_{i \in J} x_i \oplus c_j$$

depending on any variables. It is clear that such a program can be rewritten into a system satisfying Definition 1. In general, we cannot use protected free variables without breaking the rdq-property. However, there are two special cases where this is possible: (1) we can substitute a constant to a protected variable (and update the quadratic line accordingly: for example, $z = xy$ and $x = 1$ yield $z = y$ and $x = 1$); (2) we can substitute one protected variable for another variable (or its negation) from the same quadratic equation (for example, $z = xy$ and $x = y$ yield $z = y$ and $x = y$).

In what follows we abuse the notation by denoting by the same letter R the source, the straight-line program defining it, and the mapping $R\colon \mathbb{F}_2^d \to \mathbb{F}_2^n$ computed by this program that takes the d free variables and evaluates all other variables.

Find, Magnus; Golovnev, Alexander; Hirsch, Edward; Kulikov, Alexander.
"A better-than-3n lower bound for the circuit complexity of an explicit function."
Paper presented at 57th Annual IEEE Symposium on Foundations of Computer Science (FOCS 2016),
New Brunswick, NJ. October 9, 2016 - October 11, 2016.

Definition 2. *Let $R \subseteq \mathbb{F}_2^n$ be an rdq-source of dimension d, let the free variables be $x_1, x_2, \ldots, x_d$, and let $f\colon \mathbb{F}_2^n \to \mathbb{F}_2$ be a function. Then f restricted to R, denoted $f|_R$, is a function $f|_R\colon \mathbb{F}_2^d \to \mathbb{F}_2$, defined by $f|_R(x_1, \ldots, x_d) = f(R(x_1, \ldots, x_d))$.*

Note that affine sources are precisely rdq-sources with $Q = \emptyset$. We define dispersers for rdq-sources similarly to dispersers for affine sources.

Definition 3. *An* rdq-disperser *for dimension $d(n)$ is a family of functions $f_n\colon \mathbb{F}_2^n \to \mathbb{F}_2$ such that for all sufficiently large n, for every rdq-source R of dimension at least $d(n)$, $f_n|_R$ is non-constant.*

The following proposition shows that affine dispersers are also rdq-dispersers for related parameters.

Proposition 4. *Let R be an rdq-source of $\mathbb{F}_2^n$ of dimension d. Then R contains an affine subspace of dimension at least $d/2$.*

Proof. For each quadratic substitution $x_j = (x_i \oplus c_i)(x_k \oplus c_k) \oplus c_j$, further restrict R by setting $x_i = 0$. This replaces a quadratic substitution by two affine substitutions $x_i = 0$ and $x_j = c_i(x_k \oplus c_k) \oplus c_j$; the number of free variables is decreased by one. Also, since the free variables do not occur on the left-hand side, the newly introduced affine substitution is consistent with the previous affine substitutions.

Since the variables occurring on the right-hand side of our quadratic substitutions are disjoint we have initially that $2|Q| \leq |F| = d$, so the number of newly introduced affine substitutions is at most $d/2$. □

Note that it is important in the proof that protected variables do not appear on the left-hand sides. The proposition above is obviously false for quadratic *varieties*: no Boolean function can be non-constant on all sets of common roots of $n - o(n)$ quadratic polynomials. For example, the system of $n/2$ quadratic equations $x_1x_2 = x_3x_4 = \ldots = x_{n-1}x_n = 1$ defines a single point, so any function is constant on this set.

Corollary 2. *An affine disperser for sublinear dimension is also an rdq-disperser for sublinear dimension.*

3.4 Circuit complexity measure

For a circuit C and a straight-line program R defining an rdq-source, we define the following circuit complexity measure:

$$\mu(C, R) = g + \alpha_Q \cdot q + \alpha_T \cdot t + \alpha_I \cdot i\,,$$

where g is the number of internal gates in C, q is the number of quadratic substitutions in R, t is the number of troubled gates in C, and i is the number of *influential* input gates in C. We say that an input is influential if it feeds at least one gate or is protected (recall that a

Find, Magnus; Golovnev, Alexander; Hirsch, Edward; Kulikov, Alexander.
"A better-than-3n lower bound for the circuit complexity of an explicit function."
Paper presented at 57th Annual IEEE Symposium on Foundations of Computer Science (FOCS 2016),
New Brunswick, NJ. October 9, 2016 - October 11, 2016.

variable is protected if it occurs in the right-hand side of a quadratic substitution in R). The constants $\alpha_Q, \alpha_T, \alpha_I > 0$ will be chosen later.

Proposition 3 implies that when a gate is removed from a circuit by applying a normalization rule the measure μ is reduced by at least $\beta = 1 - 4\alpha_T$. The constant α_T will be chosen to be very close to 0 (certainly less than 1/4), so $\beta > 0$.

In order to estimate the initial value of our measure, we need the following lemma.

Lemma 3. *Let C be a circuit computing an affine disperser $f\colon \mathbb{F}_2^n \to \mathbb{F}_2$ for dimension d, then the number of troubled gates in C is less than $\frac{n}{2} + \frac{5d}{2}$.*

Proof. Let V be the set of the inputs, $|V| = n$. In what follows we let $\sqcup$ denote the disjoint set union. Let us call two inputs x and y neighbors if they feed the same troubled gate. Assume to the contrary that $t \geq \frac{n}{2} + \frac{5d}{2}$. Let v_i be the number of variables feeding exactly i troubled gates. Since a variable feeding a troubled gate must have outdegree 2, $v_i = 0$ for $i > 2$. By double counting the number of wires from inputs to troubled gates, $2t = v_1 + 2v_2$. Since $v_1 + v_2 \leq n$,

$$n + 5d \leq 2t = v_1 + 2v_2 \leq n + v_2.$$

Let T be the set of inputs that feed two troubled gates, $|T| = v_2 \geq 5d$. We now construct two disjoint subsets $X \subset T$ and $Y \subset V$ such that

- $|X| = d$,
- there are $|Y|$ consistent linear equations that make the circuit C independent of variables from $X \sqcup Y$.

When the sets X and Y are constructed the theorem statement follows immediately. Indeed, we first take $|Y|$ equations that make C independent of $X \sqcup Y$, then we set all the remaining variables $V \setminus (X \sqcup Y)$ to arbitrary constants. After this, the circuit C evaluates a constant (since it does not depend on variables from $X \sqcup Y$ and all other variables are set to constants). We have $|Y| + |V \setminus (X \sqcup Y)| = |V \setminus X| = n - d$ linear equations which contradicts the assumption that f is an affine disperser for dimension d.

Now we turn to constructing X and Y. For this we will repeat the following routine d times. First we pick any variable $x \in T$, it feeds two troubled gates, let y_1 and y_2 be neighbors of x (y_1 may coincide with y_2). We add x to X, also we add y_1, y_2 to Y. Note that it is possible to assign constants to y_1 and y_2 to make C independent of x. (See the figure below. If y_1 differs from y_2, then we substitute constants to them so that they eliminate troubled gates fed by x and leave C independent of x. If y_1 coincides with y_2, then either $x = c$, or $y_1 = c$, or $y_1 = x \oplus c$ eliminates both troubled gates for some constant c; if we make an $x = c$ substitution, then formally we have to interchange x and y, that is, add y rather than x to X.) Each of y_1, y_2 has at most one neighbor different from x. We remove x, y_1, y_2, neighbors of y_1 and y_2 (at most five vertices total) from the set T, if they belong to it. Since at each step we remove at most five vertices from T, we can repeat this routine d times. Since we remove the neighbors of y_1 and y_2 from T, we guarantee that in all future steps when we pick an input, its neighbors do not belong to Y, so we can make arbitrary substitutions to them and leave the system consistent.

Find, Magnus; Golovnev, Alexander; Hirsch, Edward; Kulikov, Alexander.
"A better-than-3n lower bound for the circuit complexity of an explicit function."
Paper presented at 57th Annual IEEE Symposium on Foundations of Computer Science (FOCS 2016),
New Brunswick, NJ. October 9, 2016 - October 11, 2016.

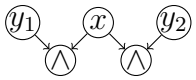

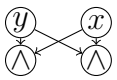

□

We are now ready to formulate our main result.

Theorem 1. *Let $f\colon \mathbb{F}_2^n \to \mathbb{F}_2$ be an rdq-disperser for dimension d and C be a fair semicircuit computing f. Let $\alpha_Q, \alpha_T, \alpha_I \geq 0$ be some constants, and $\alpha_T \leq 1/4$. Then $\mu(C, \emptyset) \geq \delta(n-d-2)$ where*

$$\delta := \alpha_I + \min\left\{\frac{\alpha_I}{2}, 4\beta, 3+\alpha_T, 2\beta+\alpha_Q, 5\beta-\alpha_Q, 2.5\beta+\frac{\alpha_Q}{2}\right\}, \tag{1}$$

and $\beta = 1 - 4\alpha_T$.

We defer the proof of this theorem to the next section. This theorem, together with Corollary 2, implies a lower bound on the circuit complexity of affine dispersers.

Corollary 3. *Let $\delta, \beta, \alpha_Q, \alpha_T, \alpha_I$ be constants as above, then the circuit size of an affine disperser for sublinear dimension is at least*

$$\delta - \frac{\alpha_T}{2} - \alpha_I \quad n - o(n)\,.$$

Proof. Note that $q = 0$, $i \leq n$, $t < \frac{n}{2} + \frac{5d}{2}$ (see Lemma 3). Thus, the circuit size is

$$\begin{aligned} g &= \mu - \alpha_Q \cdot q - \alpha_T \cdot t - \alpha_I \cdot i > \delta(n-d-2) - \alpha_T \cdot \left(\frac{n}{2} + \frac{5d}{2}\right) - \alpha_I \cdot n \\ &= \left(\delta - \frac{\alpha_T}{2} - \alpha_I\right) n - \left(\delta + \frac{5\alpha_T}{2}\right) d - 2\delta = \left(\delta - \frac{\alpha_T}{2} - \alpha_I\right) n - o(n)\,. \end{aligned}$$

□

The maximal value of $\delta - \frac{\alpha_T}{2} - \alpha_I$ satisfying the condition from Corollary 3 is given by the following linear program: maximize $\delta - \frac{\alpha_T}{2} - \alpha_I$ subject to

$$\begin{aligned} \beta + 4\alpha_T &= 1 \\ \alpha_T, \alpha_Q, \alpha_I, \beta &\geq 0 \\ \delta &\leq \alpha_I + \min\left\{\frac{\alpha_I}{2}, 4\beta, 3+\alpha_T, 2\beta+\alpha_Q, 5\beta-\alpha_Q, 2.5\beta+\frac{\alpha_Q}{2}\right\}. \end{aligned}$$

Find, Magnus; Golovnev, Alexander; Hirsch, Edward; Kulikov, Alexander.
"A better-than-3n lower bound for the circuit complexity of an explicit function."
Paper presented at 57th Annual IEEE Symposium on Foundations of Computer Science (FOCS 2016),
New Brunswick, NJ. October 9, 2016 - October 11, 2016.

The optimal values for this linear program are

$$\begin{aligned}
\alpha_T &= \frac{1}{43}, \\
\alpha_Q &= 1 + 22\alpha_T = \frac{65}{43}, \\
\alpha_I &= 6 + 2\alpha_T = 6 + \frac{2}{43}, \\
\beta &= 1 - 4\alpha_T = \frac{39}{43}, \\
\delta &= 9 + 3\alpha_T = 9 + \frac{3}{43}.
\end{aligned}$$

This gives a $(3 + \frac{1}{86})n - o(n)$ lower bound for an affine disperser for sublinear dimension.

3.5 Gate elimination

In order to prove Theorem 1 we first show that it is always possible to make a substitution and decrease the measure by δ.

Theorem 2. *Let $f\colon \mathbb{F}_2^n \to \mathbb{F}_2$ be an rdq-disperser for dimension d, let R be an rdq-source of dimension $s \geq d + 2$, and let C be an optimal (i.e., C with the smallest $\mu(C, R)$) fair semicircuit computing the function $f|_R$. Then there exist an rdq-source R' of dimension $s' < s$ and a fair semicircuit C' computing the function $f|_R$ such that*

$$\mu(C', R') \leq \mu(C, R) - \delta(s - s').$$

Before we proceed to the proof, we show how to infer the main theorem from this claim:

Proof of Theorem 1. We prove that for optimal C computing $f|_R$, $\mu(C, R) \geq \delta(s - d - 2)$. We do it by induction on s, the dimension of R. Note that the statement is vacuously true for $s \leq d + 2$, since μ is nonnegative. Now suppose the statement is true for all rdq-sources of dimension strictly less than s for some $s > d + 2$, and let R be an rdq-source of dimension s. Let C be a fair semicircuit computing $f|_R$. Let R' be the rdq-source of dimension s' guaranteed to exist by Theorem 2, and let C' be a fair semicircuit computing $f|_R$. We have that

$$\mu(C, R) \geq \mu(C', R') + \delta(s - s') \geq \delta(s - d - 2),$$

where the second inequality comes from the induction hypothesis. □

3.5.1 Proof sketch

The proof of Theorem 2 is based on a careful consideration of a number of cases. Before considering all of them formally, we show a high-level picture of the case analysis.

We fix the values of constants $\alpha_T, \alpha_Q, \alpha_I, \beta, \delta$ to the optimal values: $\alpha_T = \frac{1}{43}, \alpha_Q = \frac{65}{43}, \alpha_I = 6\frac{2}{43}, \beta = \frac{39}{43}, \delta = 9\frac{3}{43}$. Now it suffices to show that we can always make one

Find, Magnus; Golovnev, Alexander; Hirsch, Edward; Kulikov, Alexander.
"A better-than-3n lower bound for the circuit complexity of an explicit function."
Paper presented at 57th Annual IEEE Symposium on Foundations of Computer Science (FOCS 2016),
New Brunswick, NJ. October 9, 2016 - October 11, 2016.

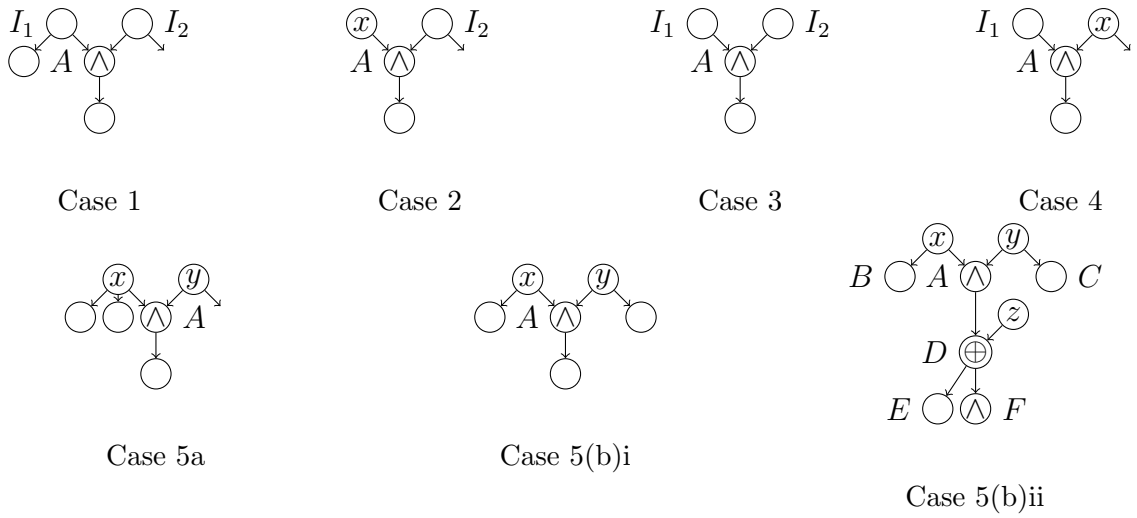

Figure 5: Gate elimination process in Theorem 2.

substitution and decrease the measure by at least $\delta = 9\frac{3}{43}$. First we normalize the circuit. By Proposition 3, during normalization if we eliminate a gate then we introduce at most four new troubled gates, this means that we decrease the measure by at least $1 - 4\alpha_T = \frac{39}{43}$. Therefore, normalization never increases the measure.

We always make constant, linear or simple quadratic *substitution* to a variable. Then we remove the substituted variable from the circuit, so that for each assignment to the remaining variables the function is defined. It is easy to make a constant substitution $x = c$ for $c \in \{0, 1\}$. We propagate the value c to the inputs fed by x and remove x from the circuit, since it does not feed any other gates. An affine substitution $x = \bigoplus_{i \in I} x_i \oplus c$ is harder to make, because a straightforward way to eliminate x would be to compute $\left(\bigoplus_{i \in I} x_i \oplus c\right)$ elsewhere. Fortunately, Lemma 2 shows how to compute it on the affine subspace defined by the substitution without using x and without increasing the number of gates (after an extra gate introduced by this lemma is removed by normalization).

Thus, in this sketch we will be making arbitrary affine substitutions for sums that are computed in gates without saying that we need to run the reconstruction procedure first. Also, we will make a simple quadratic substitution $z = (x \oplus c_1)(y \oplus c_2) \oplus c_3$ only if the gates fed by z are canceled out after the substitution, so that we do not need to propagate this quadratic value to other gates. We want to stay in the class of rdq-sources, therefore we cannot make an affine substitution to a variable x if it already has been used in the right-hand side of some quadratic restriction $z = (x \oplus c_1)(y \oplus c_2) \oplus c_3$, also we cannot make quadratic substitutions that overlap in the variables. In this proof sketch we ignore these two issues, but they are addressed in the full proof in the next subsection.

Let A be a topologically minimal and-type gate (i.e., an and-type gate that is not reachable from any and-type gate), let I_1 and I_2 be the inputs of A (I_1 and I_2 can be variables or internal gates). Now we consider the following cases (see Figure 5).

1. At least one of I_1, I_2 (say, I_1) is an internal gate of outdegree greater than one. There

Find, Magnus; Golovnev, Alexander; Hirsch, Edward; Kulikov, Alexander.
"A better-than-3n lower bound for the circuit complexity of an explicit function."
Paper presented at 57th Annual IEEE Symposium on Foundations of Computer Science (FOCS 2016),
New Brunswick, NJ. October 9, 2016 - October 11, 2016.

is a constant c such that if we assign $I_1 = c$, then A becomes constant. (For example, if A is an and, then $c = 0$, if A is an or, then $c = 1$ etc.) When A becomes constant it eliminates all the gates it feeds. Therefore, if we assign the appropriate constant to I_1, we eliminate I_1, two of the gates it feeds (including A), and also a successor of A, four gates total, and we decrease the measure by at least $\alpha_I + 4\beta = 9\frac{29}{43} > \delta$.

2. At least one of I_1, I_2 (say, I_1) is a variable of outdegree one. We assign the appropriate constant to I_2. This eliminates I_2, A, a successor of A, and I_1. This assignment eliminates at least two gates and two variables, so the measure decrease is at least $2\alpha_I + 2\beta = 13\frac{39}{43} > \delta$.

3. I_1 and I_2 are internal gates of outdegree one. Then if we assign the appropriate constant to I_1, we eliminate I_1, A, a successor of A, and I_2 (since I_2 does not feed any gates). We decrease measure by at least $\alpha_I + 4\beta > \delta$.

4. I_1 is an internal gate of outdegree one, I_2 is a variable of outdegree greater than one. Then we assign the appropriate constant to I_2. This assignment eliminates I_2, at least two of its successors (including A), a successor of A, and I_1 (since it does not feed any gates). Again, we decrease the measure by at least $\alpha_I + 4\beta > \delta$.

5. I_1 and I_2 are variables of outdegree greater than one.

   (a) I_1 or I_2 (say, I_1) has outdegree at least three. By assigning the appropriate constant to I_1 we eliminate at least three of the gates it feeds and a successor of A, four gates total.

   (b) I_1 and I_2 are variables of degree two. If A is a 2^+-gate we eliminate at least four gates by assigning I_1 so in what follows we assume that A is a 1-gate. In this case A is a troubled gate. We want to make the appropriate substitution and eliminate I_1 (or I_2), its successor, A, and A's successor.

      i. If this substitution does not introduce new troubled gates, then we eliminate a variable, three gates and decrease the number of troubled gates by one. Thus, we decrease the measure by $\alpha_I + 3 + \alpha_T = 9\frac{3}{43} = \delta$.

      ii. If the substitution introduces troubled gates, then we consider which normalization rule introduces troubled gates. The full case analysis is presented in the next subsection, here we demonstrate just one case of the analysis. Let us consider the case when a new troubled gate is introduced when we eliminate the gate fed by A (see Figure 5, the variable z will feed a new troubled gate after assignments $x = 0$ or $y = 0$). In such a case we make a different substitution: $z = (x \oplus c_1)(y \oplus c_2) \oplus c_3$. This substitution eliminates gates A, D, E, F and a gate fed by F. Thus, we eliminate one variable, five gates, but we introduce a new quadratic substitution, and decrease the measure by at least $\alpha_I + 5\beta - \alpha_Q = 9\frac{3}{43} = \delta$.

Find, Magnus; Golovnev, Alexander; Hirsch, Edward; Kulikov, Alexander.
"A better-than-3n lower bound for the circuit complexity of an explicit function."
Paper presented at 57th Annual IEEE Symposium on Foundations of Computer Science (FOCS 2016),
New Brunswick, NJ. October 9, 2016 - October 11, 2016.

It is conceivable that when we count several eliminated gates, some of them coincide, so that we actually eliminate fewer gates. Usually in such cases we can prove that some other gates become trivial. This and other degenerate cases are handled in the full proof in the next subsection.

3.5.2 Full proof

Proof of Theorem 2. Since normalization does not increase the measure and does not change R, we may assume that C is normalized.

In what follows we will further restrict R by decreasing the number of free variables either by one or by two, then we will implement these substitutions in C and normalize C afterwards. Formally, we do it as follows:

- We add an equation or two to R.
- Since we now compute the disperser on a smaller set, we simplify C (in particular, we disconnect the substituted variables from the rest of the circuit). For this, we
  - change the operations in the gates fed by the substituted variables or restructure the xor part of the circuit according to Lemma 2,
  - apply some normalization rules to remove some gates (and disconnect substituted variables).
- We count the decrease of μ.
- We further normalize the circuit (without increase of μ) to bring it to the normalized state required for the next induction step.

Since $s \geq d + 2$, even if we add two more lines to R, the disperser will not become a constant. This, in particular, implies that if a gate becomes constant then it is not an output gate and hence feeds at least one other gate. By going through the possible cases we will show that it is always possible to perform one or two consecutive substitutions matching at least one of the following types (by $\Delta\mu$ we denote the decrease of the measure after subsequent normalization).

1. Perform two consecutive affine substitutions to reduce the number of influential inputs by at least three. Per one substitution, this gives $\Delta\mu \geq 1.5\alpha_I$.
2. Perform one affine substitution to reduce the number of influential inputs by at least 2: $\Delta\mu \geq 2\alpha_I$ (numerically, this case is subsumed by the previous one).
3. Perform one affine substitution to kill four internal gates: $\Delta\mu \geq 4\beta + \alpha_I$.
4. Perform one constant substitution to eliminate three internal gates including at least one troubled gate so that no new troubled gate is introduced: $\Delta\mu \geq \alpha_I + 3 + \alpha_T$.

Find, Magnus; Golovnev, Alexander; Hirsch, Edward; Kulikov, Alexander.
"A better-than-3n lower bound for the circuit complexity of an explicit function."
Paper presented at 57th Annual IEEE Symposium on Foundations of Computer Science (FOCS 2016),
New Brunswick, NJ. October 9, 2016 - October 11, 2016.

5. Perform one *quadratic* substitution to kill five internal gates: $\Delta\mu \geq 5\beta - \alpha_Q + \alpha_I$.

6. Perform two affine substitutions to kill at least five internal gates and replace a quadratic substitution by an affine one, reducing the measure by at least $5\beta + \alpha_Q + 2\alpha_I$. Per substitution this is $\Delta\mu \geq 2.5\beta + \frac{\alpha_Q}{2} + \alpha_I$.

7. Perform one affine substitution to kill two internal gates and replace one quadratic substitution by an affine one: $\Delta\mu \geq 2\beta + \alpha_Q + \alpha_I$.

All substitutions that we perform are of the form such that adding them to an rdq-source results in a new rdq-source.

We check all possible cases of (C, R). In every case we assume that the conditions of the previous cases are not satisfied. We also rely on the specified order of applications of the normalization rules where applicable.

Note that the measure can accidentally drop less than we expect if new troubled gates emerge. We take care of this when counting the number of internal gates that disappear, recall Proposition 3 that guarantees the decrease of β per one eliminated gate. If some additional gate accidentally disappears, it may introduces new troubled gates but does not increase the measure, because $\beta \geq 0$.

Cases:

1. The circuit contains a protected variable q that either feeds an and-type gate or feeds at least two internal gates. Then there is a type 7 substitution of q by a constant.

2. The circuit contains a protected 0-variable q occurring in the right-hand side of a quadratic substitution together with some variable q'. We substitute a constant to q'. After this neither q nor q' are influential, so we have a type 2 substitution.

   Note that after this case all protected variables are 1-variables feeding xor gates.

3. The circuit contains a variable x feeding an and-type gate T, and $out(x) + out(T) \geq 4$. Then if x gets the value that trivializes T, we remove four gates: T by Rule 2, and descendants of x and T by Rule 3. If some of these descendants coincide, this gate becomes trivial (instead of passing) and is removed by Rule 2 (instead of Rule 3), and an additional gate (a descendant of this descendant) is removed by Rule 3. This makes a type 3 substitution.

   Note that after this case all variables feeding and-gates have outdegree one or two.

4. There is an and-type gate T fed by two input gates x and y, one of which (say, x) has outdegree 1. Adopt the notation from the following picture. In this and all the subsequent pictures we show the outdegrees near the gates that are important for the case analysis.

Find, Magnus; Golovnev, Alexander; Hirsch, Edward; Kulikov, Alexander.
"A better-than-3n lower bound for the circuit complexity of an explicit function."
Paper presented at 57th Annual IEEE Symposium on Foundations of Computer Science (FOCS 2016),
New Brunswick, NJ. October 9, 2016 - October 11, 2016.

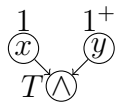

We substitute y by a constant trivializing T. This removes the dependence on x and y (which are both influential and unprotected), a type 2 substitution.

5. There is an and-type gate T fed by two input gates x and y, and at this point (due to the cases 3 and 4) we inevitably have $out(T) = 1$ and $out(x) = out(y) = 2$, that is, T is "troubled". Adopt calling conventions from the following picture:

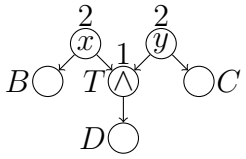

Since the circuit is normalized, $B = D$ and $C = D$ (Rule 4). One can now remove three gates by substituting a constant to x that trivializes T. If in addition to the three gates one more gate can be killed, we are done (substitution of type 3). Otherwise, we have just three gates, but the troubled gate T is removed. If this does not introduce a new troubled gate, it makes a substitution of type 4. Likewise, if this is the case for a substitution to y, we are done.

So in the remaining subcases of Case 5 we will be fighting the situation where only three gates are eliminated while one or more troubled gates are introduced.

How can it happen that a new troubled gate is introduced? This means that something has happened around some and-type gate E. Whatever has happened, it is due to two gates, B and D, that became passing (if some of them became trivial, then one more gate would be removed). The options are:

- *E gets as input a variable* instead of an internal gate (because some gate in between became passing).
- A variable *increases its outdegree* from 1 to 2 (because a gate of degree at least two became passing), and this variable starts to feed E (note that it could not feed it before, because after the increase it would feed it twice).
- A variable *decreases its outdegree* to 2. This variable could not feed E before this happens, because this would be Case 3. It takes at least one passing gate, X, to pass a new variable to E, thus the decrease of the outdegree has happened because of a single passing gate Y. In order to decrease the outdegree of the variable this gate must have outdegree 1, thus it would be removed by Rule 4 as useless.
- *E decreases its outdegree* to 1.

Find, Magnus; Golovnev, Alexander; Hirsch, Edward; Kulikov, Alexander.
"A better-than-3n lower bound for the circuit complexity of an explicit function."
Paper presented at 57th Annual IEEE Symposium on Foundations of Computer Science (FOCS 2016),
New Brunswick, NJ. October 9, 2016 - October 11, 2016.

– This could happen if two gates, B and D, became passing, and they fed a single gate. However, in this case E should already have 2-variables as its inputs, Case 3.
– This could also happen if E feeds B and some gate X, and B becomes passing to X. However, in this case B is useless (Rule 4). (Note that $out(B) = 1$, because otherwise E would not decrease its outdegree to 1.)

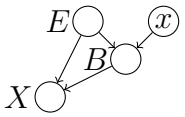

– Similarly, if E feeds D and some gate X, and D becomes passing to X.

Summarizing, only the two first possibilities could happen, and both pass some variable to E through either B or D (or both).

The plan for the following cases it to exploit the local topology, that is, possible connections between B, D, and C. First we consider "degenerate" cases where these gates are locally connected beyond what is shown in the figure in case 5. After this, we continue to the more general case.

6. If $B = C$, then one can trivialize both T and B either by substituting a constant to x or y or by one affine substitution $y = x \oplus c$ (using Proposition 2) for the appropriate constant c (this can be easily seen by examining the possible operations in the two gates). Since x and y are unprotected, the number of influential variables is decreased by 2, making a substitution of type 2.

7. Assume that D feeds both B and C. In this case, a new troubled gate may emerge only because D is fed by a variable u, and it is passed to some and-type gate E. Note that $out(D) \leq 2$, because otherwise u would become a 3-variable and E would not become troubled. Therefore, u cannot be passed by D to E directly, it is passed via B.

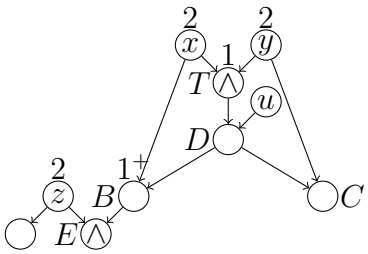

If $out(B) \geq 2$, then even if $out(u) = 1$, it must be that $C = E$ or that B feeds C, because otherwise u would become a 3-variable after substituting x. Neither are possible: $C = E$ would imply $B = D$ and $y = z$, contradicting the assumption that $D = B$ (from 5); if B feeds C, that means that $B = D$, which is impossible. Therefore, we conclude that $out(B) = 1$. So we can substitute constants for z, to make B a 0-gate, and for y,

Find, Magnus; Golovnev, Alexander; Hirsch, Edward; Kulikov, Alexander.
"A better-than-3n lower bound for the circuit complexity of an explicit function."
Paper presented at 57th Annual IEEE Symposium on Foundations of Computer Science (FOCS 2016),
New Brunswick, NJ. October 9, 2016 - October 11, 2016.

to trivialize T. This way x ceases to be influential, and we have $\Delta\mu \geq 3\alpha_I$ for two substitutions (type 1).

Note that after this case we can assume that D does not feed B. If it does, we switch the roles of the variables x and y.

8. Assume now that B feeds D, and D feeds C. (Or, symmetrically, C feeds D, and D feeds B.) Then substituting y to trivialize T removes T, D, and C, and introduces *no new troubled gates*, because C and D are passing the internal gate B. We assumed it is not the case.

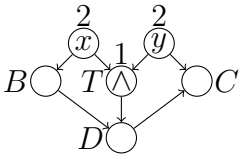

9. We can now assume that B and D are not connected (in any direction).

   Indeed, if B feeds D, we can switch the roles of x and y unless C feeds D (impossible, because then D has three inputs: T, B, and C) or unless we switched x and y before (that is, D feeds C, Case 8).

   (a) Assume that D feeds a new troubled gate under the substitution of x. The troubled gate E gets some variable z from D (directly, as D and B are not connected).

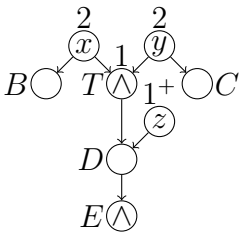

   - If $out(z) \geq 2$, then $out(D) = 1$ and E is fed by another variable t either directly or via B. In the former case, we can substitute t to trivialize E, this kills E and the gate it feeds, and also makes D and then T 0-gates; a type 3 substitution. In the latter case:

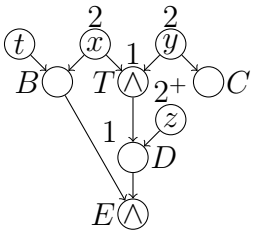

Find, Magnus; Golovnev, Alexander; Hirsch, Edward; Kulikov, Alexander.
"A better-than-3n lower bound for the circuit complexity of an explicit function."
Paper presented at 57th Annual IEEE Symposium on Foundations of Computer Science (FOCS 2016),
New Brunswick, NJ. October 9, 2016 - October 11, 2016.

  - if $out(B) \geq 2$, then B is a xor-type gate (see Case 5a), and by substituting $x = t \oplus c$ for the appropriate constant c, we can make B a constant trivializing E and remove two more descendants of B and E, a type 3 substitution;
  - if $out(B) = 1$, then we can set z and y to constants trivializing T and E, respectively. Then B becomes a 0-gate and is eliminated, which means that x becomes a 0-variable. We then get a substitution of type 1.

  We can now assume that $out(z) = 1$ and thus $out(D) \geq 2$, because z must get outdegree two in order to feed the new troubled gate.

- If D is an and-type gate, substituting z by the appropriate constant trivializes D and kills both gates that it feeds; also T becomes a 0-gate, a type 3 substitution.
- If z is protected, we set x and z to constants trivializing T, D, and E. This additionally removes B and the gates that E feeds, at least five gates in total. Since we also kill a quadratic substitution, this makes a type 6 substitution.
- Since we can now assume that z is unprotected and D is an xor-type gate, we can make a substitution $z = (x \oplus c_1)(y \oplus c_2) \oplus c_3$ for appropriate constants c_1, c_2, c_3 to assign D a value that trivializes E. This makes T a 0-gate and removes also D, E, another gate that D feeds, and the gate(s) that E feeds. As usual, if some passing gates coincide, another gate is removed. Taking into account the penalty for introducing a quadratic substitution, we get a substitution of type 5.

(b) Since D does not feed a new troubled gate, B does, and B is fed directly by a variable t (since B and D are not connected). The new troubled gate E must be also fed directly by a variable z (because D does not feed it).

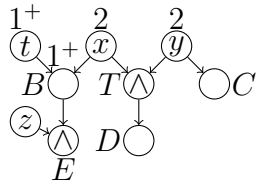

- If $out(B) \geq 2$ (which means B is a xor-type gate, see Case 5a), then by substituting $x = t \oplus c$ (using Proposition 2) for the appropriate constant c, we can make B a constant trivializing E and remove two more descendants of B and E, a type 3 substitution.
- If $out(B) = 1$, then we can set z and y to constants trivializing T and E, respectively. Then B becomes a 0-gate and is eliminated, which means that x becomes a 0-variable. We then get a substitution of type 1.

Find, Magnus; Golovnev, Alexander; Hirsch, Edward; Kulikov, Alexander.
"A better-than-3n lower bound for the circuit complexity of an explicit function."
Paper presented at 57th Annual IEEE Symposium on Foundations of Computer Science (FOCS 2016),
New Brunswick, NJ. October 9, 2016 - October 11, 2016.

Starting from the next case we will consider a topologically minimal and-type gate and call it A for the remaining part of the proof. Here A is topologically minimal if it cannot be reached from another and-type gate via a directed path.

Note that the circuit C must contain at least one and-type gate (otherwise it computes an affine function, and a single affine substitution makes it constant). The minimality implies that both inputs of A are computed by fair cyclic xor-circuits (note that a subcircuit of a fair circuit is fair, because it corresponds to a submatrix of a full-rank matrix); in particular, they can be input gates.

10. One input of A is an input gate x of outdegree 2 while the other one is an internal gate Q of outdegree 1.

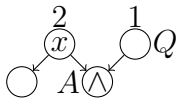

Recall that x is unprotected due to Case 1, and x cannot feed Q because of Rule 4. Substituting x by the constant trivializing A eliminates the two successors of x, all the successors of A, and makes Q a 0-gate which is then eliminated by Rule 1. A type 3 substitution. (As usual, if the only successor of A coincides with the other successor of x then this gate becomes constant so its successors are also eliminated. That is, in any case at least four gates are eliminated.)

11. One input to A is an internal gate Q. Denote the other input by P. If P is also an internal gate and has outdegree larger than Q we switch the roles of P and Q.

    In this case we will try to substitute a value to Q in order to trivialize A. Q is a gate computed by a fair xor-circuit, so it computes an affine function $c \oplus \bigoplus_{i \in I} x_i$. For this, we use the xor-reconstruction procedure described in Lemma 2. In order to perform it, we need at least one unprotected variable x_i with $i \in I$.

    (a) Such a variable x_1 exists.

    We then add the substitution $x_1 = b \oplus c \oplus \bigoplus_{i \in I \setminus \{1\}} x_i$ to the rdq-source R for the appropriate constant b (so that Q on the updated R computes the constant trivializing A). We could now simply replace the operation in Q by this constant (since the just updated circuit computes correctly the disperser on the just updated R). However, we need to eliminate the just substituted variable x_1 from the circuit. To do this, we perform the reconstruction described in Lemma 2. Note that it only changes the in- and outdegrees of x_1 (replacing it by a new internal gate Z) and Q. No new troubled gates are introduced, and the subsequent application of Rule 2 to Q removes Q without introducing new troubled gates as well.

    Moreover, normalizations remove all descendants of Q, all descendants of A, and, in the case $out(P) = 1$, Rule 1 removes P if it is an internal gate, or P becomes a 0-variable, if it was a variable. It remains to count the decrease of the measure.

Find, Magnus; Golovnev, Alexander; Hirsch, Edward; Kulikov, Alexander.
"A better-than-3n lower bound for the circuit complexity of an explicit function."
Paper presented at 57th Annual IEEE Symposium on Foundations of Computer Science (FOCS 2016),
New Brunswick, NJ. October 9, 2016 - October 11, 2016.

Below we go through several subcases depending on the type of the gate P.

i. Q is a 2^+-gate. We recall the general picture of xor-reconstruction.

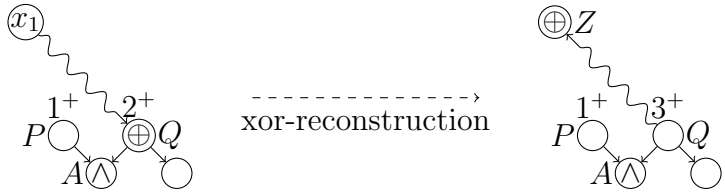

After the reconstruction, there are at least three descendants of Q and at least one descendant of A, a type 3 substitution.

ii. Q is an internal 1-gate and P is an input gate. Then P has outdegree 1 and is unprotected (see Cases 10, 1).

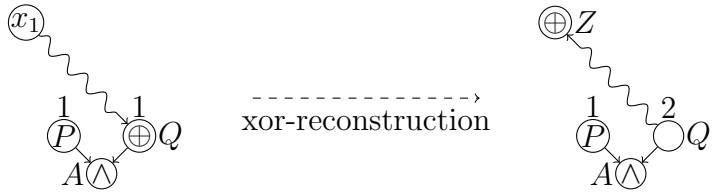

Note that $P = x_1$ since the only outgoing edge of P goes to an and-type gate. This means that P is left untouched by the xor-reconstruction. After trivializing A the circuit becomes independent of both x_1 and P giving a type 2 substitution.

iii. Q is an internal 1-gate and P is an internal gate. Then P is a 1-gate (if the outdegree of P were larger we would switch the roles of P and Q).

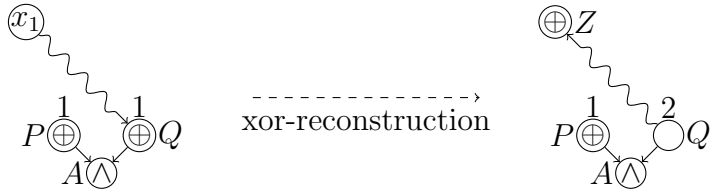

Again, P is left untouched by the xor-reconstruction since it only has one successor and it is of and-type while the xor-reconstruction is performed in the linear part of the circuit. After the substitution, we remove two successors of Q, at least one successor of A, and make P a 0-gate. A type 3 substitution. Note that P cannot be a successor of Q because of Rule 4.

(b) All variables in the affine function computed by Q are protected.

i. Both inputs to Q, say x_j and x_k, are variables, and they occur in the same quadratic substitution $w = (x_j \oplus c)(x_k \oplus c') \oplus c''$. Then perform a substitution $x_j = x_k \oplus c'''$ (using Proposition 2) in order to trivialize the gate A. It kills the quadratic substitution (and does not harm other quadratic substitutions, because x_j and x_k could not occur in them), Q, A, its descendant (and more, but we do not need it), which makes $\Delta\mu \geq 3\beta + \alpha_Q + \alpha_I$, a type 7 substitution.

Find, Magnus; Golovnev, Alexander; Hirsch, Edward; Kulikov, Alexander.
"A better-than-3n lower bound for the circuit complexity of an explicit function."
Paper presented at 57th Annual IEEE Symposium on Foundations of Computer Science (FOCS 2016),
New Brunswick, NJ. October 9, 2016 - October 11, 2016.

ii. Q is a 2^+-gate. Take any $j \in I$. Assume that x_j occurs in a quadratic substitution $x_p = (x_j \oplus a)(x_k \oplus b) \oplus c$. Recall that at this point all protected variables are 1-variables feeding xor-gates (see Cases 1 and 2). We substitute x_k by a constant d and normalize the circuit. This eliminates the successor of x_k, kills the quadratic substitution, and makes x_j unprotected. If at least two gates are removed during normalization then we get $\Delta\mu \geq 2\beta + \alpha_Q + \alpha_I$, a type 7 substitution. In what follows we assume that the only gate removed during normalization after the substitution $x_k \leftarrow d$ is the successor of x_k.
If the gate Q is not fed by x_k then it has outdegree at least 2 after the substitution $x_k \leftarrow d$ and normalizing the descendants of x_k. If the gate Q is fed by x_k then its second input must be an internal xor-gate Q' (if it were an input gate it would be a variable x_j but then we would fall into Case 11(b)i). Then after substituting $x_k \leftarrow d$ and normalizing Q the gate Q' feeds A and has outdegree at least 2. We denote Q' by Q in this case.
Hence in any case, in the circuit normalized after the substitution $x_k \leftarrow d$, the gate A is fed by the 2^+-gate Q that computes an affine function of variables containing an unprotected variable x_j. We then make Q constant trivializing A by the appropriate affine substitution to x_j. This kills four gates. Together with the substitution $x_k \leftarrow d$, it gives $\Delta\mu \geq 5\beta + \alpha_Q + 2\alpha_I$, a type 6 substitution.

Hence in what follows we assume that $out(Q) = 1$. *Therefore* P *is either a variable or an internal xor-type* 1*-gate.*

iii. P is an input gate. Then it has the following properties as in Case 11(a)ii. Take any $j \in I$ and assume that x_j appears with x_k in a quadratic substitution. We first substitute $x_k \leftarrow d$ and normalize the circuit. After this the second input of A still computes a linear function that depends on x_j which is now unprotected. We make an affine substitution to x_j trivializing A. This makes P a 0-variable, a type 1 substitution.

iv. P is an internal xor-type 1-gate. If P computes an affine function of variables at least one of which is unprotected, we are in Case 11(a)iii with P and Q exchanged. So, in what follows we assume that both P and Q compute affine functions of protected variables.

A. Both inputs to P or Q (say, P) are variables x_p and x_q. Let x_j be a variable from the affine function computed at Q and let x_k be its couple. Note that $x_j = x_p, x_q$ while it might be the case that $x_k = x_p$ or $x_k = x_q$. We substitute x_k by a constant to make x_j unprotected. We then trivialize A by an affine substitution to x_j. This way, we kill the dependence on three variables by two substitutions. A type 1 substitution.
Thus in what follows we can assume that both P *and* Q *have at least one internal xor-gate as an input.*

B. One of P and Q (say, Q) computes an affine function of variables one of

Find, Magnus; Golovnev, Alexander; Hirsch, Edward; Kulikov, Alexander.
"A better-than-3n lower bound for the circuit complexity of an explicit function."
Paper presented at 57th Annual IEEE Symposium on Foundations of Computer Science (FOCS 2016),
New Brunswick, NJ. October 9, 2016 - October 11, 2016.

which (call it x_j) have a couple x_k that does not feed P. We substitute x_k by a constant and normalize the descendant of x_k. It only kills one xor-gate fed by x_k and makes x_j unprotected. Note that at this point P is still a 1-xor. We then trivialize A by substituting x_j by an affine function. Similarly to Case 11(a)iii, this kills four gates and gives, for two substitutions, $\Delta\mu \geq 5\beta + \alpha_Q + 2\alpha_I$. A type 6 substitution.

C. The only case when the condition of the previous case does not apply is the following: P computes an affine function on a single variable x_i, Q computes an affine function on a single variable x_j, the variables x_i and x_j appear together in a quadratic substitution, and moreover x_i feeds Q while x_j feeds P. But this is just impossible. Indeed, since x_i is a protected variable it only feeds Q. As Q computes an affine function on x_i, Lemma 1 guarantees that there is a path from x_i to Q. But this path must go through P and A leading to a cycle that goes through an and-type gate A.

□

Acknowledgements

Research is partially supported by NSF (grant 1319051) and the Government of the Russian Federation (grant 14.Z50.31.0030). We also would like to thank Dmitry Itsykson and Alexander Knop who survived a six-hour seminar on the proof and made valueable comments.

References

[And87] Alexander E. Andreev. On a method for obtaining more than quadratic effective lower bounds for the complexity of π-schemes. *Moscow Univ. Math. Bull.*, 42(1):63–66, 1987.

[BFT98] Harry Buhrman, Lance Fortnow, and Thomas Thierauf. Nonrelativizing separations. In *CCC-98*, 1998.

[BK12] Eli Ben-Sasson and Swastik Kopparty. Affine dispersers from subspace polynomials. *SIAM J. Comput.*, 41(4):880–914, 2012.

[BKS+10] Boaz Barak, Guy Kindler, Ronen Shaltiel, Benny Sudakov, and Avi Wigderson. Simulating independence: New constructions of condensers, Ramsey graphs, dispersers, and extractors. *J. ACM*, 57(4), 2010.

[Blu84] Norbert Blum. A Boolean function requiring $3n$ network size. *Theor. Comput. Sci.*, 28:337–345, 1984.

Find, Magnus; Golovnev, Alexander; Hirsch, Edward; Kulikov, Alexander.
"A better-than-3n lower bound for the circuit complexity of an explicit function."
Paper presented at 57th Annual IEEE Symposium on Foundations of Computer Science (FOCS 2016),
New Brunswick, NJ. October 9, 2016 - October 11, 2016.

[Bou07] Jean Bourgain. On the construction of affine extractors. *GAFA Geometric And Functional Analysis*, 17(1):33–57, 2007.

[BV14] Eli Ben-Sasson and Emanuele Viola. Short PCPs with projection queries. In Javier Esparza, Pierre Fraigniaud, Thore Husfeldt, and Elias Koutsoupias, editors, *Automata, Languages, and Programming - 41st International Colloquium, ICALP 2014, Copenhagen, Denmark, July 8-11, 2014, Proceedings, Part I*, volume 8572 of *Lecture Notes in Computer Science*, pages 163–173. Springer, 2014.

[CK15] Ruiwen Chen and Valentine Kabanets. Correlation bounds and #sat algorithms for small linear-size circuits. In Dachuan Xu, Donglei Du, and Dingzhu Du, editors, *Computing and Combinatorics - 21st International Conference, COCOON 2015, Beijing, China, August 4-6, 2015, Proceedings*, volume 9198 of *Lecture Notes in Computer Science*, pages 211–222. Springer, 2015.

[CKK+15] Ruiwen Chen, Valentine Kabanets, Antonina Kolokolova, Ronen Shaltiel, and David Zuckerman. Mining circuit lower bound proofs for meta-algorithms. *Computational Complexity*, 24(2):333–392, 2015.

[CR06] Venkatesan T. Chakaravarthy and Sambuddha Roy. Oblivious symmetric alternation. In Bruno Durand and Wolfgang Thomas, editors, *STACS 2006, 23rd Annual Symposium on Theoretical Aspects of Computer Science, Marseille, France, February 23-25, 2006, Proceedings*, volume 3884 of *Lecture Notes in Computer Science*, pages 230–241. Springer, 2006.

[CT15] Gil Cohen and Avishay Tal. Two structural results for low degree polynomials and applications. In Naveen Garg, Klaus Jansen, Anup Rao, and José D. P. Rolim, editors, *Approximation, Randomization, and Combinatorial Optimization. Algorithms and Techniques, APPROX/RANDOM 2015, August 24-26, 2015, Princeton, NJ, USA*, volume 40 of *LIPIcs*, pages 680–709. Schloss Dagstuhl - Leibniz-Zentrum fuer Informatik, 2015.

[DC89] Patrick W. Dymond and Stephen A. Cook. Complexity theory of parallel time and hardware. *Inf. Comput.*, 80(3):205–226, 1989.

[DK11] Evgeny Demenkov and Alexander S. Kulikov. An elementary proof of a $3n - o(n)$ lower bound on the circuit complexity of affine dispersers. In Filip Murlak and Piotr Sankowski, editors, *Mathematical Foundations of Computer Science 2011 - 36th International Symposium, MFCS 2011, Warsaw, Poland, August 22-26, 2011. Proceedings*, volume 6907 of *Lecture Notes in Computer Science*, pages 256–265. Springer, 2011.

[DKMM15] Evgeny Demenkov, Alexander S. Kulikov, Olga Melanich, and Ivan Mihajlin. New lower bounds on circuit size of multi-output functions. *Theory Comput. Syst.*, 56(4):630–642, 2015.

Find, Magnus; Golovnev, Alexander; Hirsch, Edward; Kulikov, Alexander.
"A better-than-3n lower bound for the circuit complexity of an explicit function."
Paper presented at 57th Annual IEEE Symposium on Foundations of Computer Science (FOCS 2016),
New Brunswick, NJ. October 9, 2016 - October 11, 2016.

[Dvi12] Zeev Dvir. Extractors for varieties. *Computational Complexity*, 21(4):515–572, 2012.

[FGK09] Fedor V. Fomin, Fabrizio Grandoni, and Dieter Kratsch. A measure & conquer approach for the analysis of exact algorithms. *J. ACM*, 56(5), 2009.

[GK16] Alexander Golovnev and Alexander S. Kulikov. Weighted gate elimination: Boolean dispersers for quadratic varieties imply improved circuit lower bounds. In *Proceedings of the 7th Innovations in Theoretical Computer Science (ITCS)*, 2016. To appear.

[Hås86] Johan Håstad. Almost optimal lower bounds for small depth circuits. In Juris Hartmanis, editor, *Proceedings of the 18th Annual ACM Symposium on Theory of Computing, May 28-30, 1986, Berkeley, California, USA*, pages 6–20. ACM, 1986.

[Hås98] Johan Håstad. The shrinkage exponent of de Morgan formulas is 2. *SIAM J. Comput.*, 27(1):48–64, 1998.

[HU69] John E. Hopcroft and Jeffrey D. Ullman. *Formal Languages and Their Relation to Automata*. Addison-Wesley Longman Publishing Co., Inc., Boston, MA, USA, 1969.

[IM02] Kazuo Iwama and Hiroki Morizumi. An explicit lower bound of $5n - o(n)$ for Boolean circuits. In Krzysztof Diks and Wojciech Rytter, editors, *Mathematical Foundations of Computer Science 2002, 27th International Symposium, MFCS 2002, Warsaw, Poland, August 26-30, 2002, Proceedings*, volume 2420 of *Lecture Notes in Computer Science*, pages 353–364. Springer, 2002.

[IN93] Russell Impagliazzo and Noam Nisan. The effect of random restrictions on formula size. *Random Struct. Algorithms*, 4(2):121–134, 1993.

[Khr71] Valeriy M. Khrapchenko. A method of determining lower bounds for the complexity of π-schemes. *Math. Notes of the Acad. of Sci. of the USSR*, 10(1):474–479, 1971.

[KK06] Arist Kojevnikov and Alexander S. Kulikov. A new approach to proving upper bounds for MAX-2-SAT. In *Proceedings of the Seventeenth Annual ACM-SIAM Symposium on Discrete Algorithms, SODA 2006, Miami, Florida, USA, January 22-26, 2006*, pages 11–17. ACM Press, 2006.

[KK10] Arist Kojevnikov and Alexander S. Kulikov. Circuit complexity and multiplicative complexity of Boolean functions. In Fernando Ferreira, Benedikt Löwe, Elvira Mayordomo, and Luís Mendes Gomes, editors, *Programs, Proofs, Processes, 6th Conference on Computability in Europe, CiE 2010*, volume 6158 of *Lecture Notes in Computer Science*, pages 239–245. Springer, 2010.

Find, Magnus; Golovnev, Alexander; Hirsch, Edward; Kulikov, Alexander.
"A better-than-3n lower bound for the circuit complexity of an explicit function."
Paper presented at 57th Annual IEEE Symposium on Foundations of Computer Science (FOCS 2016),
New Brunswick, NJ. October 9, 2016 - October 11, 2016.

[KM65] Boris M. Kloss and Vadim A. Malyshev. Estimates of the complexity of certain classes of functions. *Vestn.Moskov.Univ.Ser.1*, 4:44–51, 1965. In Russian.

[KRT13] Ilan Komargodski, Ran Raz, and Avishay Tal. Improved average-case lower bounds for demorgan formula size. In *54th Annual IEEE Symposium on Foundations of Computer Science, FOCS 2013, 26-29 October, 2013, Berkeley, CA, USA*, pages 588–597. IEEE Computer Society, 2013.

[Kul99] Oliver Kullmann. New methods for 3-SAT decision and worst-case analysis. *Theor. Comput. Sci.*, 223(1-2):1–72, 1999.

[Li11] Xin Li. A new approach to affine extractors and dispersers. In *Proceedings of the 26th Annual IEEE Conference on Computational Complexity, CCC 2011, San Jose, California, June 8-10, 2011*, pages 137–147. IEEE Computer Society, 2011.

[Li15] Xin Li. Extractors for affine sources with polylogarithmic entropy. *Electronic Colloquium on Computational Complexity (ECCC)*, 22:121, 2015.

[LR01] Oded Lachish and Ran Raz. Explicit lower bound of $4.5n - o(n)$ for Boolean circuits. In Jeffrey Scott Vitter, Paul G. Spirakis, and Mihalis Yannakakis, editors, *Proceedings on 33rd Annual ACM Symposium on Theory of Computing, July 6-8, 2001, Heraklion, Crete, Greece*, pages 399–408. ACM, 2001.

[LS73] Edward A. Lamagna and John E. Savage. On the logical complexity of symmetric switching functions in monotone and complete bases. Technical report, Brown University, 1973.

[Nec66] Edward I. Nechiporuk. On a Boolean function. *Doklady Akademii Nauk. SSSR*, 169(4):765–766, 1966.

[NTW04] Arfst Nickelsen, Till Tantau, and Lorenz Weizsäcker. Aggregates with component size one characterize polynomial space. *Electronic Colloquium on Computational Complexity (ECCC)*, 028, 2004.

[Nur09] Sergey Nurk. An $2^{0.4058m}$ upper bound for Circuit SAT. Technical Report 10, Steklov Institute of Mathematics at St.Petersburg, 2009. PDMI Preprint.

[Pau77] Wolfgang J. Paul. A $2.5n$-lower bound on the combinational complexity of Boolean functions. *SIAM J. Comput.*, 6(3):427–443, 1977.

[PZ93] Mike Paterson and Uri Zwick. Shrinkage of de Morgan formulae under restriction. *Random Struct. Algorithms*, 4(2):135–150, 1993.

[Raz85] Alexander A. Razborov. Lower bound on monotone complexity of some Boolean functions. *Doklady Akademii Nauk. SSSR*, 281(4):798–801, 1985.

Find, Magnus; Golovnev, Alexander; Hirsch, Edward; Kulikov, Alexander.
"A better-than-3n lower bound for the circuit complexity of an explicit function."
Paper presented at 57th Annual IEEE Symposium on Foundations of Computer Science (FOCS 2016),
New Brunswick, NJ. October 9, 2016 - October 11, 2016.

[RB12] Marc D. Riedel and Jehoshua Bruck. Cyclic boolean circuits. *Discrete Applied Mathematics*, 160(13-14):1877–1900, 2012.

[Riv77] Ronald L. Rivest. The necessity of feedback in minimal monotone combinational circuits. *IEEE Trans. Computers*, 26(6):606–607, 1977.

[San10] Rahul Santhanam. Fighting perebor: New and improved algorithms for formula and QBF satisfiability. In *51th Annual IEEE Symposium on Foundations of Computer Science, FOCS 2010, October 23-26, 2010, Las Vegas, Nevada, USA*, pages 183–192. IEEE Computer Society, 2010.

[Sav14] Sergey Savinov. Upper bounds for the Boolean circuit satisfiability problem. Master Thesis defended at St.Peterburg Academic University of Russian Academy of Sciences, 2014. In Russian.

[Sch74] Claus-Peter Schnorr. Zwei lineare untere Schranken für die Komplexität Boolescher Funktionen. *Computing*, 13(2):155–171, 1974.

[Sch76] Claus-Peter Schnorr. The combinational complexity of equivalence. *Theor. Comput. Sci.*, 1(4):289–295, 1976.

[Sha49] Claude E. Shannon. The synthesis of two-terminal switching circuits. *Bell Systems Technical Journal*, 28:59–98, 1949.

[Sha11] Ronen Shaltiel. Dispersers for affine sources with sub-polynomial entropy. In Rafail Ostrovsky, editor, *IEEE 52nd Annual Symposium on Foundations of Computer Science, FOCS 2011, Palm Springs, CA, USA, October 22-25, 2011*, pages 247–256. IEEE Computer Society, 2011.

[SS91] Victor Shoup and Roman Smolensky. Lower bounds for polynomial evaluation and interpolation problems. In *32nd Annual Symposium on Foundations of Computer Science, San Juan, Puerto Rico, 1-4 October 1991*, pages 378–383. IEEE Computer Society, 1991.

[ST13] Kazuhisa Seto and Suguru Tamaki. A satisfiability algorithm and average-case hardness for formulas over the full binary basis. *Computational Complexity*, 22(2):245–274, 2013.

[Sto77] Larry J. Stockmeyer. On the combinational complexity of certain symmetric Boolean functions. *Mathematical Systems Theory*, 10:323–336, 1977.

[Sub61] Bella A. Subbotovskaya. Realizations of linear functions by formulas using $+, \cdot, -$. *Doklady Akademii Nauk. SSSR*, 136(3):553–555, 1961.

[Tal14] Avishay Tal. Shrinkage of de Morgan formulae by spectral techniques. In *Foundations of Computer Science (FOCS), 2014 IEEE 55th Annual Symposium on*, pages 551–560. IEEE, 2014.

Find, Magnus; Golovnev, Alexander; Hirsch, Edward; Kulikov, Alexander.
"A better-than-3n lower bound for the circuit complexity of an explicit function."
Paper presented at 57th Annual IEEE Symposium on Foundations of Computer Science (FOCS 2016),
New Brunswick, NJ. October 9, 2016 - October 11, 2016.

[Wil13] Ryan Williams. Improving exhaustive search implies superpolynomial lower bounds. *SIAM J. Comput.*, 42(3):1218–1244, 2013. Extended abstract appeared in Proc. STOC-2010.

[Wil14] Ryan Williams. Nonuniform ACC circuit lower bounds. *JACM*, 61(1), 2014. Extended abstract appears in Proc. CCC-2011.

[Yao85] Andrew C. Yao. Separating the polynomial-time hierarchy by oracles (preliminary version). In *FOCS*, pages 1–10. IEEE Computer Society, 1985.

[Yeh11] Amir Yehudayoff. Affine extractors over prime fields. *Combinatorica*, 31(2):245–256, 2011.

[Zwi91] Uri Zwick. A $4n$ lower bound on the combinational complexity of certain symmetric Boolean functions over the basis of unate dyadic Boolean functions. *SIAM J. Comput.*, 20(3):499–505, 1991.

Find, Magnus; Golovnev, Alexander; Hirsch, Edward; Kulikov, Alexander.
"A better-than-3n lower bound for the circuit complexity of an explicit function."
Paper presented at 57th Annual IEEE Symposium on Foundations of Computer Science (FOCS 2016),
New Brunswick, NJ. October 9, 2016 - October 11, 2016.

Cross-Industry Standard Test Method Developments – from Manufacturing to Wearable Robots*

Roger BOSTELMAN[†‡1,2], Elena MESSINA[1], Sebti FOUFOU[3]

([1] *National Institute of Standards and Technology, Gaithersburg, MD 20899, USA*)

([2] IEM, Le2i, Université de Bourgogne, BP 47870, 21078 Dijon, France)

([3] CSE Dept., College of Engineering, PO. Box 2713, Qatar University, Doha, Qatar)

[†]E-mail: roger.bostelman@nist.gov

Abstract: Manufacturing robotics are moving towards human-robot collaboration with light duty robots being used side-by-side with workers. Similarly, exoskeletons that are both passive (spring and counterbalance forces) and active (motor forces) are worn by humans and move body parts. Exoskeletons are also called wearable robots when they are actively controlled using a computer and integrated sensing. Safety standards now allow, through risk assessment, both manufacturing and wearable robots to be used. However, performance standards for both systems are still lacking. Ongoing research to develop standard test methods to assess performance of manufacturing robots and emergency response robots can inspire similar test methods for exoskeletons. This paper describes recent research on performance standards for manufacturing robots, as well as search and rescue robots. It also provides a discussion on how performance of wearable robots can benefit from using the same test methods.

Key words: wearable robot, exoskeleton, cross-industry, artifact, standards, grasping

1 Introduction

Wearable robots, such as exoskeletons, are a broad category that includes systems that guide humans to assist them in moving their bodies as well as human-guided systems that augment body motions and forces for added speed or strength. Wearable robots can be partial- or full-body systems and are currently being developed throughout many countries around the world [1]

Wearable robots have current or potential applications in rehabilitation [2], elderly care [3, 4], military operations [5], and manufacturing [6]. The International Organization of Standardization (ISO) 13482 personal care robot safety standard was developed to provide safeguards for elderly or other persons using wearable robots, such as exoskeletons, and provide some cross-industry [7] consideration to manufacturing, the military, or other industries. Although ISO 13482 has been published, it includes no normative references to directly assess risks or hazards, design, verification, installation, and validation. Additionally, [8] suggests that there are some types of exoskeletons that haven't been developed to demonstrate, for example, "significant decrease in the

Bostelman, Roger; Foufou, Sebti; Messina, Elena.
"Cross-Industry Standard Test Method Developments – from Manufacturing to Wearable Robots."
Paper presented at ICWSR 2015: International Conference on Wearable Sensor and Robot Workshop,
Hangzhou, China. October 16, 2015 - October 18, 2015.

metabolic demands of walking or running" where some measures for the standard may be required.

Cross-industry exoskeleton technology and collaborative industrial robots require both safe human-robot performance and capabilities. However, unlike for collaborative industrial robots, there are currently no standard test methods for measuring the safety and performance of wearable robots. Non-wearable (collaborative) robots, such as industrial robots, mobile robots, and mobile manipulators, have been technologically improving, many of which allow robots and humans to work side-by-side or robots to work with other robots [9]. Collaborative robot safety standards have been developed and continue to evolve. [Ref: R15.06-2012, ISO 10218 and TS 15066]

Safety and performance test methods are being developed so that manufacturers and users can evaluate and compare capabilities of emergency response robots [10] and industrial robots against the requirements of their applications and particular tasks. Test methods for these industries can provide valuable insights for the subject wearable robot standards, including what metrics should be considered, what safety and/or performance test methods should be developed, and how generic test methods demonstrate a measure of safety and/or performance.

This paper will begin by identifying the types of wearable robots used in the manufacturing industry that require safety and performance testing and will consider metrics for testing these systems. Standard test methods that have been, or are currently being, developed for emergency response robots and for industrial collaborative robots will be discussed. This will be followed by a brief discussion on the process considered for test method development. Lessons learned and basic concepts from response and industrial robot areas will then be considered towards the development of test methods for wearable robots.

‡ Corresponding author
ORCID: Roger BOSTELMAN, http://orcid.org/ 0000-0002-8605-7758
National Institute of Standards and Technology
A preliminary version was presented at ICWSR 2015: International Conference on Wearable Sensor and Robot Workshop, October 16-18, 2015, Zhejiang University, Hangzhou, China

2 Types of wearables to be tested

Both passively- and actively- controlled exoskeletons can provide useful capabilities for the manufacturing industry. Passive exoskeletons, such as Fortis shown in Figure 1 (a), are not robots although they possess capabilities that extend the worker's capabilities for longer periods of time. Passive systems can be adapted to the wearer and to the task with mechanical adjustments to the system. Similarly, actively controlled exoskeletons, considered wearable robots, provide capabilities that can potentially be programmed to adapt to the

wearer and to the task. An example of an actively-controlled exoskeleton is shown in Figure 1 (b) where a worker demonstrates his increased lifting capability at a shipyard. Actively-controlled exoskeletons use electronics, motors, computers, and intelligent software control to provide adaptability to the wearer and task.

a

b

Figure 1 – Examples of: (a) passive (courtesy of Lockheed Martin via Wired [5]*) and (b) active exoskeletons (courtesy of Daewoo Shipbuilding and Marine Engineering via Discovery News [11]).

Recent research by Herr and others described in [6] have suggested that there can be metabolic energy cost reduction when wearing some types of "parallel-limb exoskeletons" and other shoes. This is one measure of safety and performance that can be used to define exoskeleton usefulness. However, other metrics that are not currently in the literature go beyond metabolic cost/increase. In [6], there are also some surveyed exoskeletons that can provide increased lift capacity, although there is, little supporting information available on these systems being used on a variety of people (i.e., various sizes, shapes, genders, ages, etc.).

Metrics for both passive and active exoskeletons, each considered a generic system-under-test (SUT), are similar, including:

- Duration: maximum time that a task can be performed with the SUT as compared to performing the task without the SUT
- Speed: velocities that can be achieved and sustained with the SUT as compared to performing the task without the SUT
- Pose: uncertainty - accuracy/resolution (e.g., precision to move to a commanded location) and repeatability (e.g., move to the same commanded location more than once) for the SUT to position and orient the operator's arm or leg as commanded. Positioning error of a tool or device when held by the controlled arm or leg is the measured component.
- Back-drivability or Control Force: force required to resist component reaction or move any or all

* Disclaimer: NIST does not endorse products discussed within this paper nor manufacturers of these products. Products mentioned are for information purposes only and are not expressed as an endorsement for them or their manufacturer.

components of the SUT when they are both driven or not driven.

- Put-on/Take-off Complexity: difficulty in putting on or removing the SUT
- Ease of use: simplicity of initial training and ease of control of the SUT as it allows or improves task completion performance
- Vertical Maneuvering: capability, speed to traverse inclines, steps, undulating terrain
- Horizontal Maneuvering: capability, speed to traverse forward, back, side-to-side

Other metrics are listed in [1] for exoskeletons being considered or used for rehabilitation, including: comfort, cost, portability, battery life, range of use, and several others related to maneuvering the body.

3 Test methods from non-wearable robots

The market for non-wearable or collaborative robots has been recently increasing, perhaps in part due to ISO 10218-2 and ISO/TS 15066 [14] approvals, as well as research activities. The United States National Institute of Standards and Technology (NIST) has been performing research on collaborative robots within its Performance of Collaborative Robot Systems Project [12] as part of the Robotics for Smart Manufacturing Program.

Robots for flexible factory environments are limited by the robots' inability to coordinate, communicate, and understand their actions, roles, and task statuses to effectively and efficiently collaborate with others. Limitations are driven by both the absence of tools and protocols needed for describing collaborative functions, and the complete lack of metrics for assessing how well robots can work together and with humans. The project is in the process of providing the methods, protocols, and metrics necessary to evaluate the collaborative capabilities of robot systems.

Similarly, emergency response robotics is being researched at NIST within the Robotics Test Facility [13], which is a laboratory for developing standard methods of measuring robot performance. The facility houses artifacts and equipment for measuring how well robots perform under a variety of tasks that abstract real-world challenges. The application domains supported by this facility include urban search and rescue, bomb-disposal, military ground operations, disaster response, and manufacturing. Artifacts are designed to be abstract representations of the environment and task challenges that a particular requirement addresses. Experiments are conducted by running a wide variety of robots through the prototype test methods to understand how to best capture data and to refine the physical artifacts and methodology.

The wearable robots community can leverage experience gained from the performance test method development and applications from both manufacturing collaborative robotics and search and rescue robotics research. The following sections describe industrial and response robots standards and test methods that may have

aspects that could be considered for the development of wearable robot standards.

3.1 Industrial robot standards and test methods

Current standards and working documents forming the foundation for eventual standards for industrial robots, service robots, mobile robots, mobile manipulators, and robotic hands that may be of interest to the wearable robots community are listed here.

Standards

Industrial Robots:

- International Organization of Standards (ISO) [14] 10218 -1,2: Robots and robotic devices — Safety requirements for industrial robots – Parts 1 and 2
- ISO/Technical Specification (TS) ISO/TS 15066 Robots and robotic devices - Safety requirements for industrial robots - Collaborative operation
- Robot Industry Association (RIA) [15] 15.06-2012 - American National Standard for Industrial Robots and Robot Systems-Safety Requirements.

Service Robots:

- ISO/DIS 18646-1 Robots and robotic devices -- Performance criteria and related test methods for service robot -- Part 1: Locomotion for wheeled robots

Mobile Robots:

- American National Standards Institute/Industrial Truck Standards Development Foundation (ANSI/ITSDF) [16] B56.5-2012, Safety Standard for Driverless, Automatic Guided Industrial Vehicles and Automated Functions of Manned Industrial Vehicles
- ASTM [16] F45.02 Navigation (Performance) for Driverless Automatic Guided Industrial Vehicles (Working Document WK48955)

Mobile Manipulators:

- ASTM F45.02 Docking (Performance) for Driverless Automatic Guided Industrial Vehicles (Working Document WK50379)
- RIA 15.08: Working Group on Mobile Industrial Robots Safety

More detail is provided for some draft standard test methods that could have greater relevance to the exoskeleton community.

Navigation

Recent research on industrial robots in the area of navigation, docking, and ground truth system measurement systems provides an order of magnitude improved measurement basis for test method development [18]. Figure 2 shows an example navigation concept currently being considered for the ASTM F45.02 navigation standard.

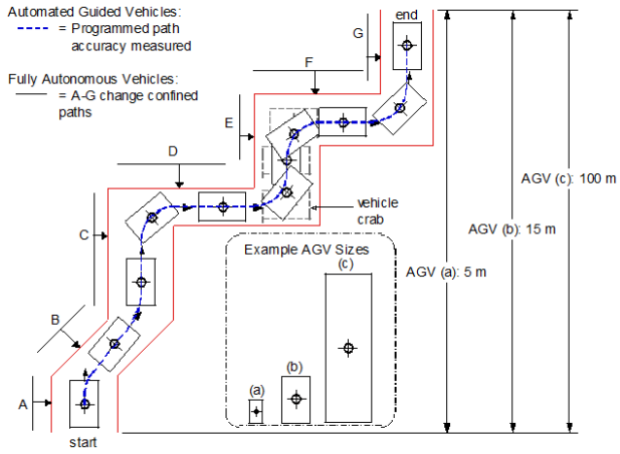

Figure 2. Example reconfigurable apparatus for navigation tests for various AGV sizes.

The moveable barriers increase the path confinement per trial. An automatic guided vehicle (AGV) or mobile robot is to traverse the reconfigurable path without contacting the barriers. The vehicle performance is measured by how well it follows the path without detecting the barriers as their width decreases.

Docking

Positioning, or "docking", of the vehicle and onboard equipment after navigating allows the vehicle to access a pallet, tray-station, or a table of parts for assembly. Measurements of how well the vehicle docking performs is therefore critical for users to understand vehicle integration for assembly, material handling, etc. Docking is also being studied using collaborative robots and artifacts through use of a mobile manipulator which includes a robot arm onboard an AGV. Figure 3 shows the evaluation of mobile manipulator performance using a reconfigurable mobile manipulator artifact (RMMA).

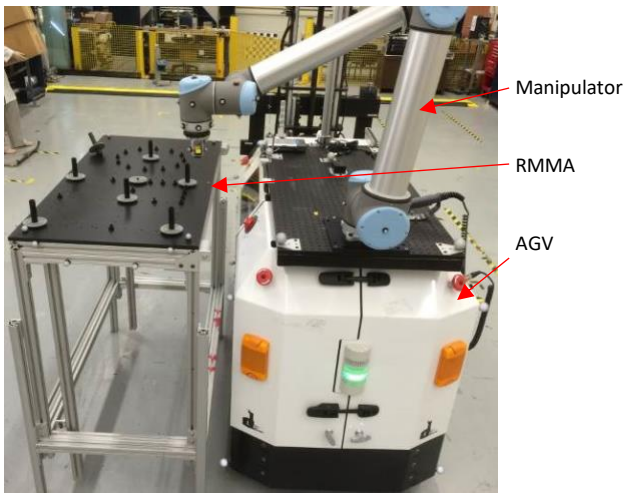

Figure 3. Docking performance measurement of a mobile manipulator with a reconfigurable mobile manipulator artifact (RMMA). Small spheres mounted on both the mobile manipulator and RMMA are used as fiducials for an optical ground truth system to measure mobile manipulator motion relative to the RMMA during test method development.

The RMMA can be reconfigured to be horizontal as shown in the figure or vertical, as well as positioned below or above the mobile manipulator. The RMMA allows for a non-contacting manipulator pose to align a laser retroreflector with reflector fiducials on the artifact to within a few millimeters, dependent upon required uncertainty measurement. Static base, indexed base (i.e., stop and measure the RMMA followed by moving to a new position, stopping and measuring at the second position), and dynamic base positioning can be tested using the RMMA.

Another test used in evaluating performance of AGVs, mobile robots, and mobile manipulators is obstacle detection and avoidance. Reference [18] also describes this test method.

Grasping

Current industrial grippers are typically two-fingered, pinch-type. Three or more-fingered, industrial grippers are being developed for more dexterous manufacturing applications, such as assembly [19]. Some advanced grippers resemble human hands, although most don't have five digits. Figure 4 shows an example of an advanced, highly dexterous robotic hand being developed and example prehension of typical objects [20] [21].

Grasping is another area in which performance test methods can be considered. A proposed roadmap for dexterous manipulation [22] includes impact areas focused on several aspects of dexterous arm and hand performance, including sensing, motion, control, and applications.

Test methods are expected to address at least some level of the following capabilities:

- Hand Mechanics
  - Position control
  - Torque control of fingers/digits
  - Grasp capacity (e.g., graspable object size and mass)
  - Grasp types supported
  - Accuracy
  - Repeatability

Figure 4. Example advanced highly dexterous robotic hand being developed [21]

- Tactile Sensing:
  - Normal forces and pressure
  - Force and impact sensitivity
  - Location of touch
- Functional Tasks
  - Quasi-static and dynamic effects on grasp stability
  - In-hand manipulation of objects
  - Touch sensitivity (e.g., using touch to control finger position/force)

Draft test methods are being developed for robotic hands and advanced grippers under a metrics working group for an Institute of Electrical and Electronic Engineers Technical Committee on Robotic Hand Grasping and Manipulation. [23] [24]

Hand exoskeletons that can benefit from industrial gripper test methods are being embedded in an astronaut's glove [25] and as hand exercise devices [26].

The aforementioned roadmap [22] also includes dexterous robot arms, proposing less complex performance metrics than for dexterous grippers, such as:

- Reachable volume (i.e., the positions and orientations that an *arm* can achieve within the workspace)
- Operational space (i.e., the positions and orientations in which the arm and/or hand can effectively perform the required operation.
- Confined space access
- Grasping objects while in motion

3.2 Response robot test methods

Several performance standards have been created through the ASTM International standards development organization under the E54 Committee for Homeland Security Applications. [17]

Specifically, the E54.08 Subcommittee-developed Standard Test Method Suite for Evaluating Emergency Response Robot Capabilities focuses on measuring capabilities of robots with respect to mobility, energy/power, radio communication, durability, logistics, safety, human-system interaction (HSI), sensors, and autonomy, although most response robots are teleoperated. This suite of standards can provide cross-industry test methods that may apply to wearable robots and passive systems. Below are the potentially relevant standards (noted by "ASTM"), working documents under development (i.e., indicated by 'WK' prior to a number), and planned standards for future development:

Mobility, Confined Area Terrains and Obstacles:

- Gaps (ASTM E2801),
- Hurdles (ASTM E2802),
- Inclined Planes (ASTM E2803),
- Stair/Landings (ASTM E2804),
- Gravel (WK35213),
- Sand (WK35214)
- Continuous Pitch/Roll Ramps (ASTM E2826)
- Crossing Pitch/Roll Ramps (ASTM E2827)
- Symmetric Stepfields (ASTM E2828),

Human-Systems Interaction:

- Maneuvering, Sustained Speed (ASTM E2829)[†]
- Maneuvering Tasks, Towing Grasped/Hitched Sleds (ASTM E2830)
- Maneuvering Tasks, Post/Hole Slaloms
- Search Tasks, Random Mazes with Complex Terrain (ASTM E2853),
- Navigation Tasks: Hallway Labyrinths with Complex Terrain (WK33260)
- Confined Space Voids with Complex Terrain (WK34434)

Sensors:

- Image Acuity (WK42363)
- Ranging: Spatial Resolution (planned)
- Localization and Mapping: Hallway Labyrinths with Complex Terrain, (planned)
- Localization and Mapping: Wall Mazes with Complex Terrain, Sparse Feature Environments (planned)

[†] Maneuvering Tasks are under the Human-System Interaction category because they are performed at a standoff distance by the operator, requiring high levels of situational awareness to perform successfully.

Manipulation:

- Door Opening and Traversal Tasks (WK27852)
- Heavy Lifting: Surrounding Area (WK44323)
- Dexterous Inspection (planned)
- Dexterous Retrieval (planned)

Examples of some of the above standard performance test method artifacts are shown in Figures 5 [13].

Current response robot test methods have been, or are being, developed to make it simple to measure, for example, how well a robot navigates around an obstacle on a level floor. Incrementally more challenging conditions can also be tested, for example to measure how well a robot navigates inclined planes, steps, undulating floors or complex terrains, and around obstacles as illustrated in Figure 5. Additionally, the navigation and obstacle avoidance tests can be combined with vision tests since most response robots are teleoperated. This combination also provides a human-in-the-loop test where a robot's pitch and roll can skew the operator's reference frame for the images provided by the onboard camera(s),

a

b

c

d

Figure 5. Examples of (a) inclined planes, (b) stairs, and (c) varying terrain test apparatus and actual varying terrain (above the apparatus). (d) Example artifacts of increasingly complex terrains.

thus can hinder robot control. Each test generically simulates a particular capability which response robots must possess to be useful in critical situations. For example, undulating floors or complex terrains may appear in collapsed buildings where search and rescue robot missions are required.

4 Test Method Development

Industrial robot and search and rescue robot test methods have been, or are being, developed in a similar manner. In the case of ASTM F45 performance standards development, the mobile robot and AGV industries were surveyed to establish their current and potential system capabilities to meet specific user application requirements.

In the case of ASTM E54.08.01 response robot standards development, the process began with in-depth workshops with emergency responders to identify key performance metrics and deployment scenarios, particularly focusing on urban search and rescue operations. Over 100 requirements were initially identified over the course of three workshops and were used to guide the test method development process. [27] Over time, additional requirements are added from new constituencies, such as bomb squads (e.g., for counter-vehicle-borne improvised explosive devices).

Test method development begins with establishing metrics and as with any experiment, isolation of variables and hypothesized results follow. Test methods that allow simple, isolated measurements of capabilities, for example navigation, can be then broken down into simple-through-complex tests. For example, open-area navigation of a straight line, followed by the addition of a curve, and then added obstacles in the path, and lastly, increasingly narrower path confinement is one simple test method. In the response robots test suite, the configuration of a robot under test is to remain unchanged through all the test methods. In other words, if a heavier battery is used to extend the robot's endurance in the power/energy tests, it must be in place during mobility tests, such as stair climbing or inclines, where a changed center of gravity may impact the performance. This provides realistic information about configuration tradeoffs.

Ideally, the method does not require expensive, resource-intensive measurement systems and procedures, and thus minimalist test method apparatus design and use must be considered. Apparatus materials should resemble the actual robot application environment and be readily available, relatively inexpensive, and simple to construct as in the apparatuses shown in Figures 2 and 5 for industrial and response robot test methods, respectively. Alternatively, the need for high precision measurement may require a different approach. The RMMA shown in Figure 3 was designed and machined to be relatively precise as compared to positioning capability of a mobile manipulator. Even in this case, it is expected that the components can be fabricated through additive manufacturing (three-dimensional printing) to save cost and avoid machining while still maintaining required precision.

The test method administration, procedures, and reporting methods are established. Periodic reviews of draft test methods with potential end users and robot developers, resulting in iterative improvement of the test method design and procedures are also desirable for ensuring that the resulting standards are useful and usable.

5 Cross-Industry test methods

This section discusses how industrial and response robot navigation, docking,

combined navigation and docking, and grasping test methods could be applied to wearable robots. Methods developed for industrial and response robot performance tests can help minimize the development process or guide designs for wearable robots. For example, one type of navigation surface may be applicable to one manufacturer's exoskeleton and may not be applicable to another. Increasing complex terrain navigation may also show limitations throughout the robot development process. Similarly, exoskeleton motor, spring, and/or counterbalance may be tuned for lifting or manipulating heavy loads and may not be tuned for threading a needle. More specific applications of previously discussed concepts follow.

Navigation

Wearable robots for lower body movement can perform tests similar to manufacturing mobile robots and AGVs demonstrating navigation through confined areas. For example, barriers or a series of objects can be placed along a path that the human must follow while wearing the robot. The walls can be moved closer to the path and if the human collides with the barriers or objects, the metrics of stability, maneuverability, and velocity can be measured. An additional test could be to test avoidance or maneuverability when obstacles suddenly appear in the human's path.

Similarly, wearable robot navigation tests can also be performed using response robot artifacts and methods. For example, inclined planes, undulating floors, stairs, and various complex terrains such as sand, gravel, or wet floors can be navigated while avoiding obstacles in the path.

Docking

Wearable robots or passive exoskeletons that allow human arms to move and hold tools for longer periods of time at intended locations could be measured using the RMMA. The human can instead carry a laser retroreflector or insert pegs in holes on such an artifact using a variety of geometric patterns and RMMA configurations. Also, similar to the mobile manipulator, as shown in Figure 3, fiducials detectable by an optical tracking system can measure the wearable robot motion if higher precision measurement data is required. This fine motion detection data can be used to further refine wearable robot motor tuning.

Figure 6 depicts the same RMMA, previously described for measuring performance of industrial robot arms and mobile manipulators, being used to measure the performance of an exoskeleton. The figure shows a human wearing arm exoskeletons and aligning a laser retroreflector to reflectors. The same RMMA could instead include holes in which the human could insert pegs or screws as potentially required for precision assembly applications. The RMMA is shown in (a) horizontal, (b) vertical-low, (c) vertical-high, and (d) over-head-angled configurations.

Both navigation and docking can be combined for full-body exoskeleton (i.e., legs

and arms) access and dexterity tests. For example, the human in exoskeleton would repeatedly move from a different location to the RMMA, similar to tests for the mobile manipulator. Once at the RMMA, the same docking test would be administered. The results of this test could show the time for a human, wearing leg and arm exoskeletons, to repeatedly move to and be positioned to reach the RMMA (using leg exoskeletons) followed by the time to transition from full-body motion to arm-only motion (using arm exoskeletons) when controlled by the exoskeleton.

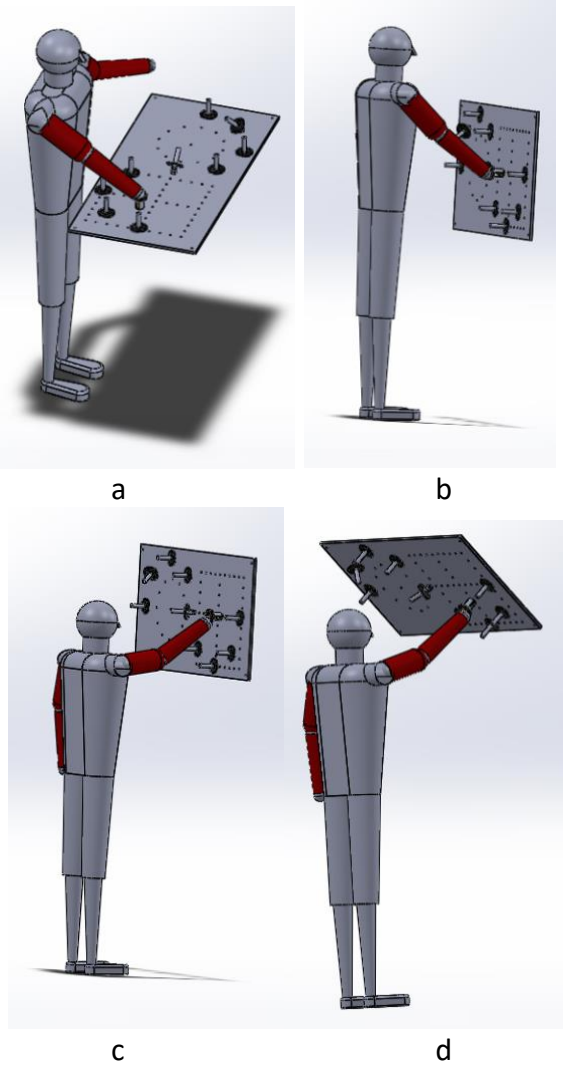

Figure 6. Graphics of a human wearing arm exoskeletons (red) testing its performance using the RMMA for precision assembly applications when the RMMA is in (a) horizontal, (b) vertical-low, (c) vertical-high, and (d) overhead-angled configurations.

Dynamic tests can also be administered with the RMMA moving relative to the human and the same alignment task performed as previously described. Additionally, both the human with exoskeleton and RMMA can be moving while alignment or peg insertion tasks are performed.

Grasping

Grasping tests for hand exoskeletons are very similar to advanced robot gripper tests where various objects are picked up and manipulated (e.g., rolled, yawed, pitched) in the hand using fingertips and/or the palm and placed (e.g., set on a surface, inserted into a mating hole). Four grasp tests described in [25] and performed on the exoskeletons shown in Figure 7 are: 1) power grip, 2) two finger pinch, 3) three finger pinch, and 4) lateral pinch. The following are examples of more specific hand exoskeleton tests:

- a key could be picked up, inserted into a keyhole, and rotated,
- a ball is picked up, grasped using the fingers and palm, moved using only the fingers to the finger tips, and then rolled using only the fingertips,
- varying diameter bars each attached to a spring, or thin to thick ropes each attached to a weight, is grasped and pulled and force is measured,

- a doorknob is grasped with the hand and rotated using the wrist and/or a hand-wheel is grasped with the hand and rotated using the wrist and arms,
- a needle is threaded or a wrist watch-size gear is placed on a post and meshed with other similar-sized gears,
- repeated exercise of fingers followed by performing the above tests.

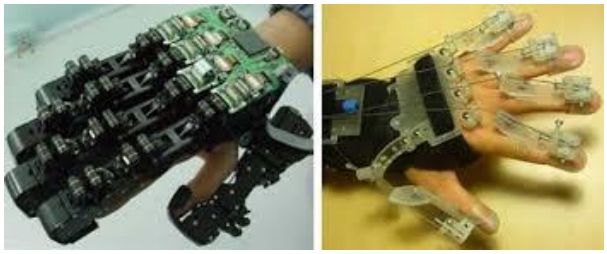

Figure 7. Example hand exoskeletons (courtesy Politecnico di Torino) [24].

6 Conclusions

Much experience in the development of metrics and test methods for the manufacturing and response applications can be applied to wearable robots. Manufacturing robotics are moving towards human-robot collaboration and response robotics is moving towards robot deployment instead of people. Test methods for both robot types are being developed to measure their performance and match it to the task at hand. Similarly, active exoskeletons are worn by humans to move body parts and passive exoskeletons are already being used to allow humans to extend their productivity and endurance. Safety standards now allow both manufacturing and wearable robots to be used. However, performance standards for both systems are still lacking. Test methods that are being or that have been developed for manufacturing and response robots can be directly applied to wearable robots as described in this paper. Nearly direct cross-over between these industries appears feasible and associated performance standards can also be developed for wearable robots. Future research should include demonstration and testing of wearable robots using similar test methods as that of manufacturing and response robots.

References

[1] Wolff, J., Parker, C., Borisoff, J., Mortenson, W. B., & Mattie, J. (2014). A survey of stakeholder perspectives on exoskeleton technology. Journal of NeuroEngineering and Rehabilitation, 11, 169. http://www.ncbi.nlm.nih.gov/pmc/articles/PMC3304563/.
[2] Upper body exo: David Szondy, “Harmony rehab robot guides recovery”, http://www.gizmag.com/harmony-rehab -robot/37293/ , May 4, 2015.
[3] Jessica Leber, “A Wearable Robot Suit That Will Add Power To Your Step”, http://www.fastcoexist.com/3035535/a-wearable-robot-suit-that-will-add-power-to-your-step, September 11, 2014.
[4] Brady Dale, “A new industry flexes its servos”, http://fortune.com/2014/08/27/exoskeletons-wearable-robotics/, August 27, 2014.
[5] Patrick Tucker, “The Very Real Future of Iron Man Suits for the Navy”, http://www.defenseone.com/technology/2015/01/very-real-future-iron-man-suits-navy/102630/, January 12, 2015.
[6] Liz Stinson, “Navy’s Exoskeleton Could Make Workers 20 Times More Productive”, http://www.wired.com/2014/09/navys-exoskeleton-could-make-workers-20-times-more-productive/, September 10, 2014.
[7] Roger Bostelman, “International Standards Efforts Towards Safe Accessibility Technology for Persons with Disabilities: Cross-Industry Activities”, Standards Engineering Society Journal, August 24, 2010.
[8] Hugh Herr, “Exoskeletons and orthoses: classification, design challenges and future directions”, Journal of NeuroEngineering and Rehabilitation, 6:21 doi:10.1186/1743-0003-6-21, 18 June 2009
[9] Fryman, Jeff, and Björn Matthias. "Safety of industrial robots: From conventional to collaborative applications." In Robotics; Proceedings of ROBOTIK 2012; 7th German Conference on, pp. 1-5. VDE, 2012.
[10] Jacoff, Adam and Elena Messina, “Experiences in deploying test arenas for autonomous mobile robots”, Performance Measurement for Intelligent Measurement

Systems (PerMIS), National Institute of Standards and Technology Special Publication 982, Gaithersburg, MD, USA, September 2001
[11] Glenn McDonald, "'Aliens'-Style Exoskeleton Gives Shipbuilders a Boost," http://mashable.com/2014/08/05/daewoo-exoskeleton/, Discovery News, Aug 05, 2014.
[12] Performance of Collaborative Robot Systems Project, http://www.nist.gov/el/isd/ms/pcrs.cfm, 2015.
[13] Robotics Test Facility, http://www.nist.gov/el/isd/ms/roboticsbldg.cfm, 2014.
[14] International Organization of Standards (ISO), www.iso.org, 2015.
[15] Robot Industry Association (RIA), www.robotics.org, 2015
[16] American National Standards Institute/Industrial Truck Standards Development Foundation (ANSI/ITSDF), www.itsdf.org, 2015.
[17] ASTM International Committee E54, http://www.astm.org/COMMITTEE/E54.htm, 2015.
[18] Roger B. Bostelman, Tsai H. Hong, and Elena Messina, "Intelligence Level Performance Standards Research for Autonomous Vehicles", International Robot Systems (IROS) 2015, Hamburg, Germany, September 2015.
[19] Roger Bostelman, Joe Falco, "Survey of Industrial Manipulation Technologies for Autonomous Assembly Applications", NIST Internal Report 7844, March 16, 2012.
[20] Roger Bostelman, "International Standards Efforts Towards Safe Accessibility Technology for Persons with Disabilities: Cross-Industry Activities", Journal of the Standards Engineering Society, August 24, 2010
[21] Johns Hopkins University Applied Physics Laboratory, http://www.jhuapl.edu/newscenter/pressreleases/2007/070426.asp , 2010.
[22] Joe Falco, Jeremy Marvel, Elena Messina, "A Roadmap to Progress Measurement Science in Robot Dexterity and Manipulation", NIST Internal Report, 7993, March 2014.
[23] J. Falco, K. Van Wyk, S. Liu, S. Carpin, "Robotic Grasping: Facilitating Replicable Performance Measures via Benchmarking and Standardized Methodologies", IEEE Robotics and Automation Magazine, December 2015.
[24] Performance Metrics and Benchmarks to Advance the State of Robotic Grasping, http://www.nist.gov/el/isd/grasp.cfm, September 2015.
[25] Alain Favetto, Elisa Paola Ambrosio, Silvia Appendino , Alessandro Battezzato , Fai Chen Chen , Diego Manfredi, Mehdi Mousavi, Francesco Pescarmona, "Embedding an Exoskeleton Hand in the Astronaut's EVA Glove: Feasibility and Ideas", International Journal of Aerospace Sciences, Vol. 1 No. 4, 2012, pp. 68-76. doi: 10.5923/j.aerospace.20120104.03.
[26] Sarakoglou, Ioannis, Darwin G. Caldwell, Nikolaos G. Tsagarakis, and Sophia Kousidou. "Exoskeleton-based exercisers for the disabilities of the upper arm and hand". INTECH Open Access Publisher, 2007.
[27] Messina, E. et al., "Statement of requirements for urban search and rescue robot performance standards," http://www.nist.gov/el/isd/ms/upload/Prelim_Requirements_Report.pdf, 2005.

Roger Bostelman is an Advanced Mobility Engineer at the National Institute of Standards and Technology, Gaithersburg, MD, USA. He was Engineering Project Manager for 25 of his 38 years at NIST, the Intelligent Control of Mobility Systems Program, and many NIST and military technology research and development projects. Roger has designed, built and tested mechanical systems and their interface electronics on robot cranes, robot arms, and autonomous vehicles including the RoboCrane, HLPR (Home Lift, Position, and Rehabilitation) Chair, and several other technologies. He is Chairman of ASTM Committee F45 and serves as experts on ANSI/ITSDF B56.5, ISO 13482, and ASTM E57 and ASTM AC220. He holds a B.S. in Electrical Engineering from the George Washington Univ., an M.S. degree in Tech. Management from the Univ. of Maryland Univ. College, and is seeking a PhD in Computer Science at the University of Bourgogne, France. He has over 100 publications in books, journals, and conference proceedings and he holds 7 patents.

Elena Messina manages the Robotic Systems for Smart Manufacturing Program at the National Institute of Standards and Technology, where she also leads the Manipulation and Mobility Systems Group within the Intelligent Systems Division. She is internationally recognized for her work in the development of performance metrics and evaluation methodologies for robotic and autonomous systems. Ms. Messina founded key efforts to develop test methodologies for measuring performance of robots, which range from long-term use of robotic competitions to drive innovation to consensus standards for evaluating robotic components and systems. For the Robotic

Systems for Smart Manufacturing Program, Ms. Messina directs a portfolio of five projects focused on advancing the capabilities of collaborative robots in smart manufacturing through the definition of performance requirements, metrics, test methods, tools, and testbeds. Ms. Messina's other roles at NIST have included supporting the NIST Director with Programmatic, Policy, and Budget Analysis, Acting Chief of the Intelligent Systems Division, and Leader of the Knowledge Systems Group. Prior to joining NIST, Ms. Messina worked in private industry on computer-aided design software and industrial robots.

Sebti Foufou obtained a Ph.D. in computer science in 1997 from the University of Claude Bernard Lyon I, France, for a dissertation on parametric surfaces intersections. He worked with the computer science department at the University of Burgundy, France from 1998 to 2009 as faculty member, then as adjunct professor since Sept. 2009. He also worked in 2005 and 2006, as a temporary guest researcher, at the National Institute of Standards and Technology, Gaithersburg, MD, USA. He is with the Department of Computer Science & Engineering at Qatar University since Sept. 2009. His research interests include geometric modeling and geometric constraint solving for curves and surfaces representations, and image processing for face recognition. He is also interested in data models for product lifecycle management and smart machining systems. He is currently with the Department of Computer Science and Engineering, Qatar University, Doha, Qatar.

Performance Evaluation of Secure Industrial Control System Design: A Railway Control System Case Study

Xenofon Koutsoukos, Himanshu Neema,
Goncalo Martins, Sajal Bhatia, Janos Sztipanovits
Institute for Software Integrated Systems
Vanderbilt University Nashville, TN, USA

Keith Stouffer, Chee Yee Tang, Richard Candell
National Institute of Standards and Technology
Gaithersburg, MD, USA

***Abstract*—Industrial control systems (ICS) are composed of sensors, actuators, control processing units, and communication devices all interconnected to provide monitoring and control capabilities. Due to the integral role of the networking infrastructure, such systems are vulnerable to cyber attacks. In-depth consideration of security and resilience and their effects to system performance are very important. This paper focuses on railway control systems (RCS), an important and potentially vulnerable class of ICS, and presents a simulation integration platform that enables (1) Modeling and simulation including realistic models of cyber and physical components and their interactions, as well as operational scenarios that can be used for evaluations of cybersecurity risks and mitigation measures and (2) Evaluation of performance impact and security assessment of mitigation mechanisms focusing on authentication mechanisms and firewalls. The approach is demonstrated using simulation results from a realistic RCS case study.**

I. Introduction

The exponential growth of information and communication technologies over the last decade has given rise to their expansion in real-world computing applications involving physical processes. This expansion has led to the emergence of closed-loop systems involving strong integration and coordination of physical and cyber components, often referred to as cyber-physical systems (CPS). These systems are rapidly finding their way into various sectors of the economy, such as industrial control systems, transportation, healthcare, and critical infrastructure. Increasing dependence on CPS renders them critical, and in-turn demands them to be secure, robust, reliable, and trustworthy, but it also makes them very attractive targets for cyber attacks.

Because of these disruptive changes, physical systems can now be attacked through cyberspace and cyberspace can be attacked through physical means. While CPS research addresses the tight interaction between the physical and cyber parts from the performance point of view, in-depth consideration of security and resilience in an integrated manner is still in early stages. The complex nature of CPS, mainly due to tight coupling of cyber and physical phenomena, makes securing such systems a challenging problem. A multi-vector attack exploiting a combined set of vulnerabilities from individual components, none of which might pose a serious threat to the stand-alone component, can have damaging effects in the overall system.

Industrial control systems (ICS) are a specific class of CPS in the juncture of control systems and cyber systems. ICS are composed of sensors, actuators, control processing units, and communication devices all interconnected to provide monitoring and control capabilities. In contrast to traditional computing systems, ICS must perform their critical functions without interruption. This paper focuses on railway control systems (RCS), an important and potentially vulnerable class of ICS and CPS. Cybersecurity is vital for ensuring that these systems can provide their critical services without disruptions that may result in catastrophic damages.

The objectives of this work are to analyze the cybersecurity risks of RCS, propose mitigation mechanisms, and evaluate their effectiveness as well as their performance impact on system operations. We propose to achieve these goals by developing a simulation integration platform that enables (1) Modeling and simulation of RCS including realistic models of cyber and physical components and their interactions, as well as operational scenarios that can be used for evaluations of cybersecurity risks and mitigation measures and (2) Evaluation of performance impact and security assessment of mitigation mechanisms. The main innovation of our approach is that research processes and results are documented as executable software models, simulations, and generated data that support cybersecurity analysis and design in a quantifiable manner. It should be noted that RCS are treated as any other network critical infrastructure and hence the proposed approach can be directly applied to other classes of ICS.

The paper presents a simulation-based integration platform

The work at Vanderbilt is supported by NIST (70NANB13H169).

Bhatia, Sajal; Koutsoukos, Xenofon; Neema, Himanshu; Stouffer, Keith; Sztipanovits, Janos; Tang, CheeYee.
"Performance Evaluation of Secure Industrial Control System Design: A Railway Control System Case Study."
Paper presented at the 11th Annual Cyber and Information Security Research (CISR) Conference, Oak Ridge, TN. April 6, 2016 - April 7, 2016.

for RCS in order to perform experiments and acquire measurements to characterize performance and impact of secure control system design. The developed simulation integration platform uses a modular approach to integrate two open-source simulators: OMNeT++ [1] and Train Director [2]. The integration is based on a software tool infrastructure developed at the Institute for Software Integrated Systems at Vanderbilt University called Command and Control Wind Tunnel (C2WT) [3] which enables large scale heterogeneous simulations.

The platform enables the evaluation of the performance impact of implementing security solutions, complying with the ICS cybersecurity standards. The communication model used is based on the Advanced Train Control System (ATCS) [4] and the implemented security solutions comply with ICS cybersecurity guidelines [5]. In addition, the platform allows the evaluation of the performance of these applied security solutions against cyber-attacks. Specifically, this paper focuses on the evaluation of authentication mechanisms and firewalls. Authentication mechanisms in RCS incur both computational and communication overhead. Although the computational overhead is typically very small in modern microprocessor architectures, the communication overhead can result in time delays that need to be taken into consideration in the system design. Firewalls can serve a central role in securing RCS against a variety of external attacks and depending on the implementation, they can incur negligible performance impact.

The rest of the paper is organized as follows. Section 2 presents the simulation integration platform, Section 3 describes RCS focusing on the ATCS standard, Section 4 describes the simulation of RCS, Section 5 presents the evaluation results for the performance impact of authentication mechanisms and firewalls, and Section 6 concludes the paper.

II. Command and Control Wind Tunnel

A common problem with developing large-scale heterogeneous simulations is the complexity and effort required to integrate domain-specific simulation tools. Development challenges include how to integrate multiple simulation engines with varying semantics and how to integrate simulation models and manage the complex interactions between them. The High Level Architecture (HLA) provides the structural basis for simulation interoperability, distributed simulation, and is the standard technical architecture for heterogeneous simulations [6]. HLA provides application programming interfaces (APIs) that have helped to reduce the complexity of integrating multiple different simulation engines, but many challenges remain in such environments. As an example, HLA does not specify any tools to design or deploy a federation. It primarily standardizes runtime support for various tasks, such as coordinated time evolution, message passing, and shared object management. As a result, the HLA framework requires a significant amount of tedious and error-prone hand development integration code [3].

C2WT was developed to address the challenges present in the HLA framework [3]. C2WTis a graphical environment for designing and deploying heterogeneous simulation federations. Its primary contribution is to facilitate the rapid development of integration models, and to utilize these models throughout the lifecycle of the simulated environment. An integration model defines all the interactions between federated models and captures other design intent, such as simulation engine-specific parameters and deployment information. SIM uses the Generic Modeling Environment [7] and a custom Domain-Specific Modeling Language (DSML) for the definition of integration models. This language facilitates the easy capture of all of the design details for the simulation environment.

C2WT integration models follow the conceptual architecture depicted in Figure 1. A simulation environment is composed of multiple 'federates', each of which includes a simulation model, the engine upon which it executes, and some amount of specialized glue code to integrate the engine with the simulation bus. Both the engine configuration and the integration (or 'glue') code needed for each federate is highly dependent upon the role the federate plays in the environment, as well as the type of simulation engine being utilized. The main differences from HLA are the automatic generation of engine configurations, glue code to integrate the engine with the simulation bus, as well as scripts that allow the automation simulation execution and data collection. This integration enables a robust environment for users to rapidly define complex heterogeneous simulations.

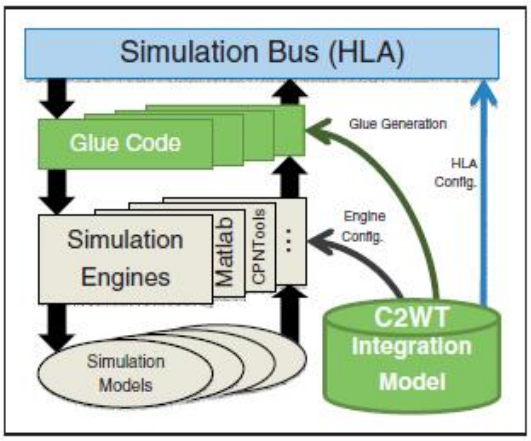

Fig. 1. C2WT Architecture

III. Railway Control Systems

The C2WT integration platform is used for simulation of RCS. The railroad network control infrastructure consists of the following main components:

Dispatch Center. The dispatch center (also known as Central Control Center) is a centralized control center for train management. It usually has a high bandwidth connection with the carrier network (e.g., MPLS/IP), but it could have any IP services.

Wayside Equipment. This is equipment located at the side of the track, such as signal controllers, switch circuit controllers,

interlocking controllers, and various sensors for sending information back to dispatch center. Depending on the overall infrastructure, a variety of communication networks are used, such as cellular (e.g., GPRS), 900 MHz ATCS data network, and wired connection.

Locomotive Equipment. The locomotive equipment comprises of onboard equipment using a communication gateway to communicate to the base station. There may be different wireless networks such as 802.11 WiFi, cellular, 900 MHz ATCS data radio, and 160 MHz voice analog radio (individual locomotives may have a different mix).

Communication System. 900 MHz ATCS and 160 MHz voice radio are two commonly used wireless communication systems. These are legacy systems that have been used in the railroad infrastructure. WiFi and other cellular communication systems are IP based. Positive Train Control (PTC) is a more recent communication system in the US railroad infrastructure network, especially for the Class I railroads. This is a 220 MHz IP based communication network currently undergoing a large scale deployment. PTC would be used both for the onboard and wayside equipment communication, with WiFi (802.11x) reserved for terminals, yards, and other railroad facilities.

A. Advanced Train Control System (ATCS)

The Advanced Train Control System (ATCS) is an open standard that provides safe, cost efficient, and modular systems for wireless communication in railroads [8], [4]. ATCS is primarily used for monitoring and controlling signals and switches to manage the movement of trains [9]. ATCS provides compatibility of systems across railroads, modular growth path, vendor interoperability, and the ability to selectively choose capabilities and features based on specific needs.

ATCS comprises of five main systems as shown in Figure 2. Four of these systems are information gathering and processing systems – central dispatch system, on-board locomotive system, on-board work vehicle system, and field system – with the fifth system being the data communication system responsible for seamlessly interconnecting all the other systems.

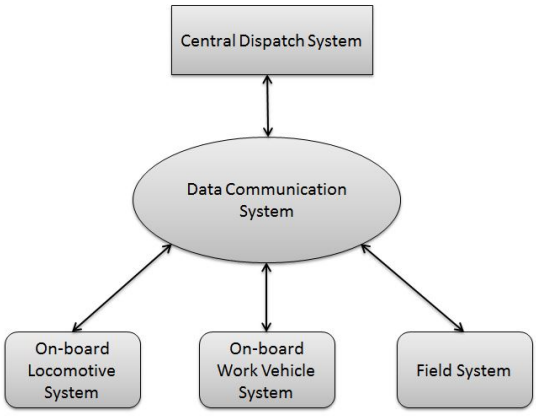

Fig. 2. ATCS Architecture Overview [4]

The Central Dispatch System is primarily responsible for managing the movement of trains throughout the railroad network with the aim to ensure safe operations without incurring delays. The On-board Locomotive System is responsible for providing automatic tracking and reporting of the vehicle as well as automated transmission of switch monitoring and control information via the Data Communication System. The On-board Work Vehicle System is responsible for providing the capability for track maintenance foremen to communicate with the Central Dispatch System via the Data Communication System. The Field System is used for monitoring and controlling wayside equipment such as switch and signal controllers, interlocking controllers, and various sensors.

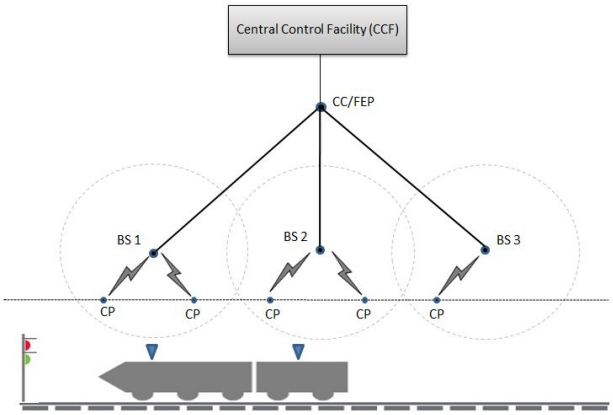

Fig. 3. Typical ATCS Network Architecture

A typical ATCS network architecture configuration consists of the main device types managed and controlled by the Central Control Facility (CCF) as shown in Figure 3. The Cluster Controller or Front End Processor (CC/FEP) coordinates all the ATCS traffic and is directly controlled by the CCF. Each CC/FEP is capable of handling multiple Base Stations (BSs) (also referred to as the Base Communication Packages BCPs). The communication link between CC/FEPs and the BSs is usually via high-speed wired lines. A key component of the ATCS architecture is the Control Point (CP), also referred to as the Mobile Communication Package (MCP), which is an interface for the on-board and wayside equipment (such as traffic lights and signals) to communicate to the CCF via BSs. Each BS serves a number of CPs. Communication between CPs and BSs usually employs full duplex wireless channels operating at different uplink and down frequencies. The communication from BSs to CPs usually operates at 935 MHz whereas the wireless channel uses 897 MHz to communicate from CPs to BSs. Typically, each CP is served by at least two BSs in order to ensure redundant communication paths in case of BS failure. Multiple BSs can receive data from a single CP which is then relayed to the CC and onto the CCF, while during the reverse path, the CC/FEP selects a BS to send the control or monitoring signal to the CP.

IV. RCS Simulation

For the assessment of security mechanisms in RCS, the SIM integrates two simulation tools: The network simulator OMNET++ [1] and the centralized traffic control simulator Train Director [2]. The integration allows the simulation of realistic scenarios in RCS that include cyber and physical phenomena as well as their interactions. Figure 5 depicts the infrastructure of an integrated simulation scenario. The railway layout used for the results in this paper is a modified version of the Oulu (OL) railway station in Finland available at [2].

A. Computer Network Simulation

OMNeT++ is a discrete event simulator that is widely used as a standard tool for studying protocols (for both wired and wireless networks), and modeling communication networks and distributed systems [1]. The simulation model is specified using an architecture description language called NED (Network Description). The language implements the desired communication model in terms of simple modules, compound modules, and a set of gates for handling the communication between these modules. The communication is governed by a set of customizable channel models and messages. The tool also provides a number of data gathering methods, including packet captures, for post-simulation analysis.

The ATCS network architecture described in Section III is mapped to a communication model shown in Figure 4. In the CCF, the controllers and servers (web and database) are connected to a Layer 2 (L2) network switch, which, in turn, is connected to the edge or gateway router. This router is connected to the gateway router of the Railroad Infrastructure Network via the Internet. Within this network, the first level L2 switch, representing the CC/FEP is connected to three BSs connected among themselves via L2 switches. The BSs are further connected wirelessly to the CPs that are responsible for controlling and monitoring the on-board and wayside equipment.

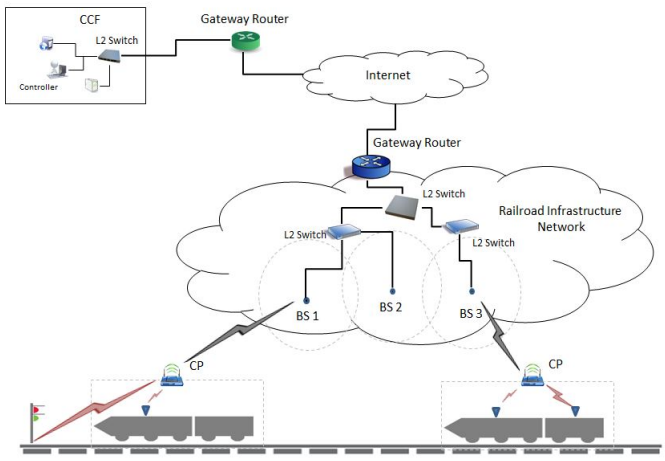

Fig. 4. Preliminary Communication Model

This model is developed in OMNeT++ and includes one instance of each of the three key devices in the ATCS architecture discussed above (Figure 5). The TDoperator node represents the CCF connected to the edge router (ccfGwRouter) via an L2 switch (ccfSwitch) using standard Ethernet (ethline) as the communication link. The gateway router of the CCF is further connected to the railway infrastructure network via the rwnGwRouter. The railway infrastructure network is connected to a single BS (baseStation) via high speed fiber optic links (fiberline). The base station connects to the CP (controlPoint) via the ATCS link operating at 900 MHz monitoring and controlling the wayside equipment (traffic lights and switches) via standard WiFi links operating at 2.4 GHz. In this initial model, the Internet link connecting the CCF network to the railway infrastructure network is omitted, however, it can be included in a large scale railway infrastructure model.

B. Railway Simulation

Train Director is a clone of Train Dispatcher, a software simulating a traffic controller for railroads [2]. Train Director simulates the work of a real-life dispatcher working as a Centralized Traffic Control (CTC) and controlling the movement of a number of trains. The key task in Train Director is to direct trains to their final destination by controlling switches and signals. Penalties are imposed for incorrect or inefficient operations such as incorrect destination and late arrivals respectively.

Train Director comprises of four key elements: tracks, signals, trains, and itineraries. Each of these elements has certain associated parameters and functions associated with them. The parameters are user defined and given at design time. Functions associated with the elements are performed based on the occurrence of specific events during the simulation. The Train Director simulator can function as a server, allowing other software to communicate externally with the simulator. In this mode, a socket connection is used to receive commands from external programs and is used for the simulation of the RCS case study.

V. Evaluation of Secure RCS Design

Our objective is to evaluate the performance impact of security mechanisms that comply with the ICS cybersecurity standards. ISA/IEC-62443 is a series of standards and technical reports that define procedures for securing IACS (Industrial Automation and Control Systems) against cyber-attacks [10]. In addition, NIST Special Publication 800-82 – Guide to ICS Security is used to identify security mechanisms for RCS [5]. This paper focuses on ISA-TR62443-3-1 which reports suitable security technologies for IACS security [10]. In particular the paper considers authentication mechanisms to secure the communication links and firewalls to filter external unauthorized messages.

A. Hash-Based Message Authentication

Authentication can be used to protect messages in the networking infrastructure against integrity attacks. However, the

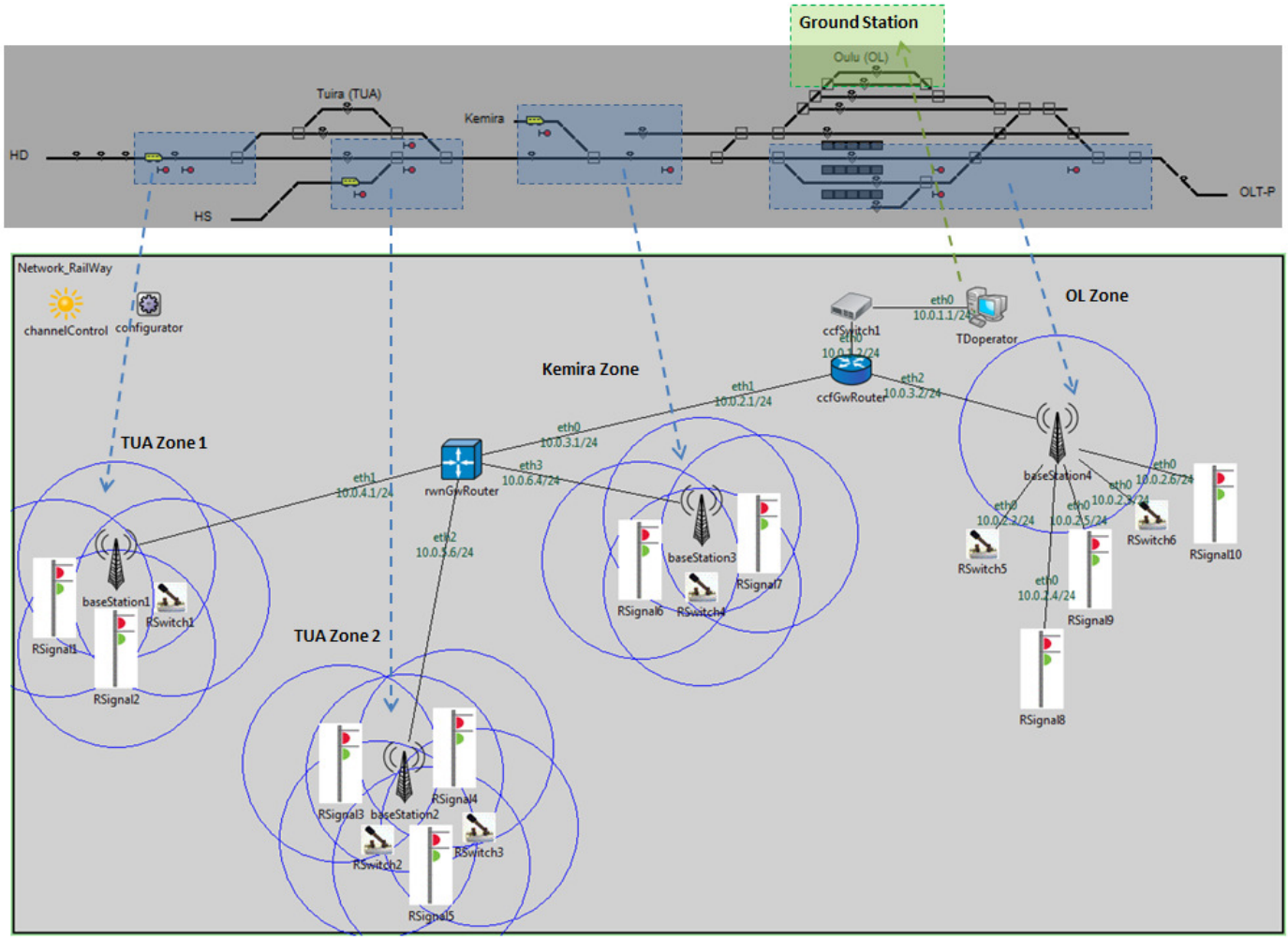

Fig. 5. Simulation Scenario

computational and communication overhead of authentication mechanisms may impact the performance of RCS. The objective is to perform a comprehensive evaluation of the computation and communication overhead of the implementation of authentication mechanisms based on the simulation integration platform. We consider a keyed-Hashed Message Authentication Code (HMAC) [11] to protect the integrity of a message. The first goal is to measure the computational overhead on the sender and receiver nodes (e.g., TDoperator and RSignal1) due to implementation of the authentication mechanism. HMAC generates additional information that needs to be attached to the original message (tag). The second goal is to measure the communication overhead on the network as a result of adding information on the message desired to transmit.

HMAC generates a tag by combining a cryptographic hash function with a secret cryptographic key. The tag is appended and transmitted with the original message (Figure 6). The cryptographic hash-functions should be one-way and collision resistant. It is computationally infeasible to find a message which corresponds to a given message digest, or to find two different messages which produce the same message digest. Any change to a message in transit will, with very high probability, result in a different message digest, and the signature will fail to verify. The strength of the HMAC depends upon the cryptographic strength of the underlying hash function, the size of its hash output, and on the size and quality of the key [11]. In this paper, three cryptographic hash functions are implemented and evaluated: ***SHA-1*** (a 160-bit hash function), ***SHA-2*** (SHA-256 hash function with 32-bit words, and ***SHA-3*** (Keccak hash function that supports the same hash lengths as SHA-2, but its internal structure is significantly different from the rest of the SHA family [12].) For all the hash functions, a secret cryptographic key with 64 bytes is used. The unique tag message authentication code generated by the hash-algorithms simultaneously verify the data integrity and the authentication of a message. Sender and receiver share the same key. The extra message tag overhead in bytes introduced is dependent on the message tag generated by the cryptographic hash-function used in HMAC. For SHA-1 the message tag is 20 bytes and for SHA-2 and SHA-3 the message tag is 32 bytes.

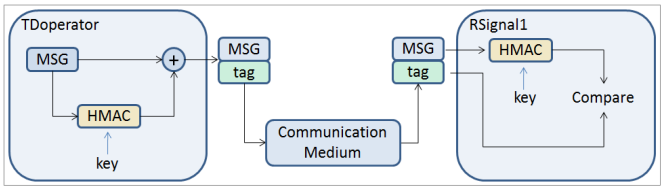

Fig. 6. Message Authentication Scheme

1) Computational Overhead: The simulation integration platform is not able to provide measurements for estimation of the computation overhead since its purpose is not to simulate hardware or microprocessor performance. However, if empirical measurements of the execution times are available, they can be incorporated in the simulation to evaluate the overall system performance. In order to acquire the empirical measurements, we implement and test HMAC in two platforms that represent possible hardware or microprocessor configurations in RCS.

- **Platform A:** Self-contained unit (IBX-530W) that includes a processor (1.6 GHz Intel Atom processor) with 1GB of memory and 512 MB of cache, and a real time operating system based on RTLinux and Ubuntu (Linux kernel 2.6.24-24-rt);
- **Platform B:** Single board unit (Trimslice2) with a CPU based on the NVIDIA Tegra2 SoC - a dual core 1 GHz ARM Cortex-A9 CPU with 1 GB of RAM, and an operating system based on Ubuntu 12.04 (Linux kernel 3.1.10-l4t.r16.02).

The platforms provide sufficient hardware and software resources for empirical evaluation of the computational overhead. All the software is running at the kernel space managed by a RTLinux scheduler, guaranteeing real time execution. RTLinux provides a crypto library that allows implementation of HMAC in a simple manner. Although these platforms may provide more resources than typical devices already deployed in RCS, they are representative of microcontrollers that are currently available for railway systems.

In order to evaluate the computational overhead, the HMAC execution time is used as the evaluation metric. The minimum, maximum, and average execution time for each hash function (SHA-1, SHA-2 and SHA-3) for a packet size of 60 bytes plus the respective message tag was measured. Figure 7 summarizes the measurements for Platform A. The execution times in Platform B are similar but SHA-3 is not implemented due to kernel incompatibilities. From the experiments, the maximum HMAC execution time is 25 μs for Platform A and can be incorporated in the simulation integration platform.

2) Communication Overhead: Our objective is to measure the communication overhead due to the the authentication hash tag. We first analyze theoretically the expected delay, and then we compare with the simulation results. Computer networks introduce delays between hosts. There are various types of delays in networks that occur due to various factors shown in Figure 8:

- **Processing Delay** (t_{proc}) is the time taken by the hardware or microprocessor to access information in a packet. This time can include for example, overhead in accessing packet header information, bit error calculation, and/or compute encryption or decryption algorithms;
- **Access Time** (t_{acc}) is the time that a packet has to wait before it can be transmitted over the link. Normally, this delay is related with the Medium Access Control (MAC) protocol used to access the transmission medium;
- **Transmission Delay** (t_{trans}) is usually caused by the data rate of the link. It is the time taken to push all the packet bits on to the link. For example, if the data rate of the link is 100 Mbps (12.5 MBytes) and the packet size is 100 Bytes, then $t_{trans} = 100/(12500000) = 8\mu s$
- **Propagation Delay** (t_{prog}) is the time taken by the first bit of the packet to reach the receiver. It can be calculated by dividing the distance between two nodes and the speed of the propagation of the link.

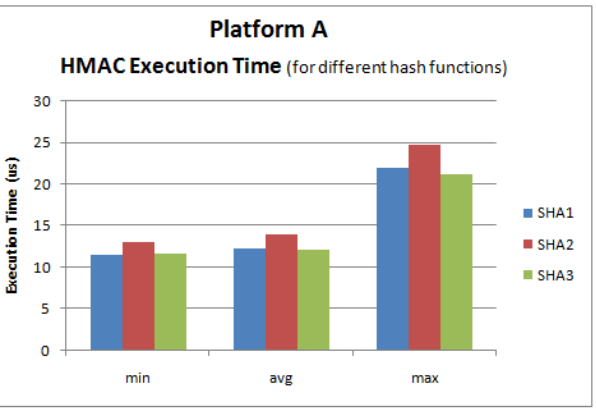

Fig. 7. HMAC Kernel Execution Time for Different Hash Functions

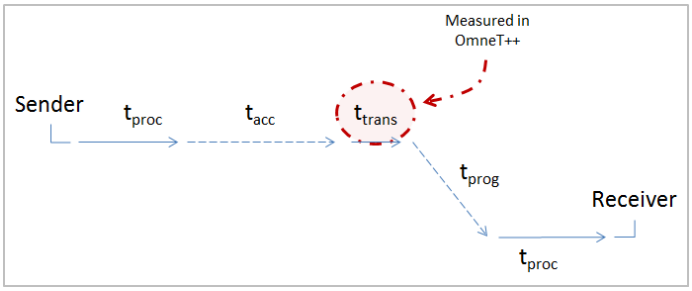

Fig. 8. Network Delays

We consider a 100 Mbits/s communication channel for wired environments and a 54 Mbits/s for wireless networks. The overhead on the frame size due to the generated hash tag is 20 or 32 bytes (depending on the hash function used). For the results in this section, we consider a tag size of 20 bytes (e.g., SHA-1). Table I shows the theoretical estimate for t_{trans} for one communication link, wired and wireless, and for frame sizes of 100 and 120 bytes.

OMNeT++ simulations can optionally create an event log file, which records simulation events such as: message cre-

TABLE I
THEORETICAL t_{trans} FOR ONE COMMUNICATION LINK

	t_{trans}	
	Wired	**Wireless**
100 Bytes	8 μs	14.8 μs
120 Bytes	9.6 μs	17.8 μs
Overhead	**1.6 μs**	**3.0 μs**

ations and deletions, event scheduling and cancellations, message sends and packet transmissions, and other information. For simplicity and to better illustrate how the communication overhead is estimated, we consider the communication between TDoperator and RSignal1 and RSignal10 (Figure 5) and we calculate the transmission delay (t_{trans}). The results are summarized in Table II. The table also summarizes the differences between the theoretical and the simulated transmission delay (t_{trans}). Despite the effort in running the experiments in a deterministic way, there is a slight difference between the theoretical and the simulated results. The simulated results present a small increase on the t_{trans} which is due to two facts: the sockets' header overhead is not considered in the theoretical calculations, nor is the access time delay (t_{acc}) from the wireless links.

TABLE II
THEORETICAL AND SIMULATED t_{trans} RESULTS

	t_{trans}			
	RSignal 10		**RSignal 1**	
	Theor.	**Meas.**	**Theor.**	**Meas.**
100 Bytes	32 μs	37 μs	46.8 μs	65 μs
120 Bytes	38 μs	41 μs	56.2 μs	70 μs
Overhead	**6.4 μs**	**4 μs**	**9.4 μs**	**5 μs**

In conclusion, both the communication and computational overhead are in the order of 10 μs for the example considered in this paper. This additional delay is relatively small and does not affect the physical components of the RCS.

B. Firewalls

Firewalls are an integral part of the defense mechanism for protecting RCS systems from a wide variety of external attacks. In order to simulate firewalls in the proposed simulation integration platform, a network filtering module is implemented at the edge router. The network topology is shown in Figure 9. The firewall module performs packet filtering based on a combination of source and destination IP addresses. The simulations include two types of attacks: internal and external. In the case of internal attacks, a denial-of-service (DoS) attack is simulated on the TDOperator node. In the case of external attacks, a rogue operator node (MaliciousTDOperator) is integrated into the network topology for sending various malign signals to disrupt the normal operation of the RCS.

Disabled Firewall and External Attack: The first simulation is performed without any firewalls, i.e., without "enabling" the filtering module in the edge router. Since no network packet filtering is implemented, the malicious packets from the MaliciousTDOperator node are able to penetrate into the network and disrupt the system operation. The results from this simulation are visualized with trains deviating from their schedules and arriving late at their desired destinations as seen in the scheduler part of Figure 10.

Enabled Firewall and External Attack: In this simulation, the packet filtering module is enabled in the edge router. As a result, the MaliciousTDOperator packets are filtered and prevented from entering the control systems' network. The simulation results confirm that all trains arrive on time at their respective destinations (figures are omitted due to length limitations).

Enabled Firewall Enable and Internal/External Attacks: The aim of this simulation is to demonstrate that although firewalls are the first line of defense and can protect a control system network from external attacks, they are not sufficient dealing with other cyber attacks such as those originating from inside or trusted sources. A DoS attack affects the TDOperator node and the simulation includes the effect of the DoS attack, which means that the TDOperator node does not respond to external attacks. The effect of the attack is that trains are forced to wait at non-scheduled stations (figures are omitted due to length limitations).

VI. CONCLUSIONS

The objective of this work is to evaluate the performance impact of implementing security mechanisms in RCS using a simulation integration platform. The platform is comprised by two open-source simulators (OMNeT++ and Train Director) and an infrastructure (C2WT) for deploying heterogeneous simulators.

A comprehensive evaluation of the computation and communication overhead of the implementation of an authentication mechanism is presented and simulated. To obtain realistic measurements for the computational overhead, the authentication mechanisms selected (HMAC SHA-1, SHA-2, and SHA-3) were tested in two different platforms. These platforms were selected to represent possible hardware or microprocessor configurations. The algorithms are implemented at the kernel space managed by a RTLinux scheduler, guaranteeing real time execution. The execution times are negligible and do not affect the overall system performance. For the communication overhead, we estimated analytically and we empirically measured the additional delay due to the adding authentication tags. The communication overhead is also negligible and does not affect the overall system behavior.

In addition, we simulated the effect of firewalls. A network filtering module was included in the simulated network system. The firewall simulations include two types of attacks, internal and external attacks. The aim is to demonstrate that even though firewalls are the first line of defense and can protect a control system network from external attacks, they are not sufficient for dealing with other cyber attacks such as those originating from internal or trusted sources.

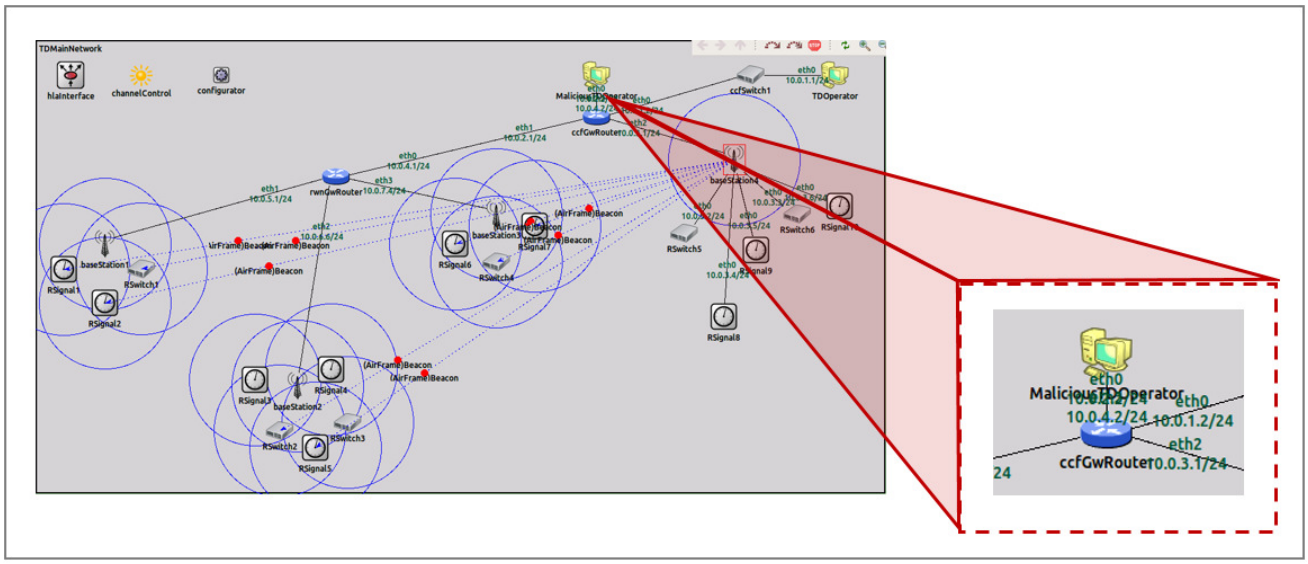

Fig. 9. Firewall and Malicious Node Network Placement

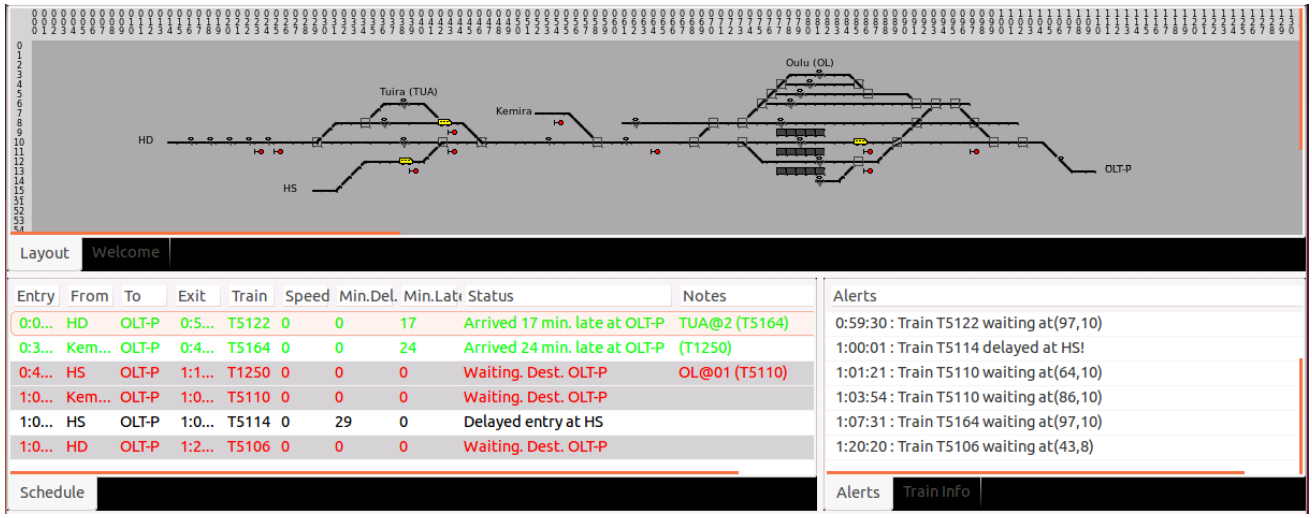

Fig. 10. Disabled Firewall and MaliciousTDOperator Attack

REFERENCES

[1] A. Varga and R. Hornig, "An overview of the omnet++ simulation environment," in *Proceedings of the 1st international conference on Simulation tools and techniques for communications, networks and systems & workshops*. ICST (Institute for Computer Sciences, Social-Informatics and Telecommunications Engineering), 2008, p. 60.

[2] BackerStreet. Train director. http://www.backerstreet.com/traindir/en/trdireng.php. [Online]. Available: http://www.backerstreet.com/traindir/en/trdireng.php

[3] G. Hemingway, H. Neema, H. Nine, J. Sztipanovits, and G. Karsai, "Rapid synthesis of high-level architecture-based heterogeneous simulation: a model-based integration approach," *Simulation: Transactions of the Society for Modeling and Simulation International, pp. 16, March*, 2011.

[4] *System Architecture: ATCS Specification 100 (Revision 4.0 – http://www.atcsmon.com/)*, Association of American Railroads, 1995.

[5] K. Stouffer, J. Falco, and K. Scarfone, "Guide to industrial control systems (ICS) security," NIST Special Publication, Rev. 2, 800-82, 2015.

[6] D. J. S. Dahmann and M. K. L. Morse, "High level architecture for simulation: An update," *IEEE Proceedings on the 2nd International Workshop on Distributed Interactive Simulation and Real-Time Applications*, 1998.

[7] A. Ledeczi, M. Maroti, A. Bakay, G. Karsai, J. Garrett, C. Thomason, G. Nordstrom, J. Sprinkle, and P. Volgyesi, "The generic modeling environment," in *Workshop on Intelligent Signal Processing, Budapest, Hungary*, vol. 17, 2001, p. 1.

[8] P. V. Craven, "A brief look at railroad communication vulnerabilities," in *Intelligent Transportation Systems, 2004. Proceedings. The 7th International IEEE Conference on*. IEEE, 2004, pp. 245–249.

[9] D. Williams, B. Metzger, and G. Richardson, "Spec 200 radio code line ducting–Cause and effect," in *Proceedings of the American Railway Engineering and Maintenance-of-Way Association Conference*, 2001.

[10] *ISA/IEC-62443 – Security of Industrial Automation and Control Systems*, International Electrotechnical Commission (IEC), 2013.

[11] W. Stallings, *Cryptography and Network Security: Principles and Practices*. 5th Edition, Prentice-Hall Press, 2010.

[12] H. Gilbert and H. Handschuh, "Security analysis of SHA-256 and sisters," 2004.

Proceedings of the ASME 2016 Manufacturing Science and Engineering Conference
ASME MSEC 2016
June 27-July 1, 2016, Blacksburg, Virginia, USA

MSEC2016-8692

IDENTIFYING UNCERTAINTY IN LASER POWDER BED FUSION MODELS

Felipe Lopez
Department of Mechanical Engineering
University of Texas at Austin
Austin, TX 78712
Email: felipelopez@utexas.edu

Paul Witherell, Brandon Lane
Engineering Laboratory
National Institute of Standards and Technology
Gaithersburg, MD 20899
Email: [paul.witherell, brandon.lane]@nist.gov

ABSTRACT

A limitation frequently encountered in additive manufacturing (AM) models is a lack of indication about their precision and accuracy. Often overlooked, information on model uncertainty is required for validation of AM models, qualification of AM-produced parts, and uncertainty management. This paper presents a discussion on the origin and propagation of uncertainty in Laser Powder Bed Fusion (L-PBF) models. Four sources of uncertainty are identified: modeling assumptions, unknown simulation parameters, numerical approximations, and measurement error in calibration data. Techniques to quantify uncertainty in each source are presented briefly, along with estimation algorithms to diminish prediction uncertainty with the incorporation of online measurements. The methods are illustrated with a case study based on a transient, stochastic thermal model designed for melt pool width predictions. Model uncertainty is quantified for single track experiments and the effect of online estimation in overhanging structures is studied via simulation. The application of these concepts to estimation and control of the L-PBF process is suggested.

Keywords: additive manufacturing, uncertainty quantification, melt pool width.

INTRODUCTION

Some have referred to additive manufacturing (AM) as the third industrial revolution [1]. AM is the use of layer-based processes for producing parts directly from computer (CAD) models, without part-specific tooling [2]. Since its introduction in the mid-1980s [3, 4], AM has become popular because of its ability to produce parts that were impossible with traditional manufacturing techniques. After decades of being limited to polymer prototypes, these technologies are now employed in the production of functional parts made of polymers, ceramics, and metals [5–7].

AM technologies still present some unresolved challenges that hinder their widespread adoption. Among these challenges are process variability, unsatisfactory part quality, and lack of process standards; all of which originate from the limited knowledge of this relatively new set of processes. Numerous models have been developed to improve the understanding of these processes and to predict the quality of AM-produced components. Although most models published in the literature have been compared with experimental measurements, they often lack measures of the precision and accuracy of their predictions.

Knowledge of uncertainty in AM models is required for applications such as:

(a) Model validation, which may use comparisons between simulation results and experimental data, accounting for uncertainty in both sources. Comparison of simulation results obtained with different models is expected to require information on their uncertainty as well.
(b) Decision making, where model predictions and their prob-

Lane, Brandon; Lopez, Felipe; Witherell, Paul.
"Identifying uncertainty in Laser Powder Bed Fusion models."
Paper presented at The ASME 2016 Manufacturing Science and Engineering Conference (MSEC2016), Blacksburg, VA. June 27, 2016 - July 1, 2016.

abilities may be used to make informed decisions. In the case of AM, for example, one would expect to use models to certify AM-produced parts. Model-enabled certification will depend on the probability of predicted key performance indicators being within admissible bounds.

(c) Uncertainty management, to identify the sources with the largest relative contributions to overall prediction error, and determine effective strategies to more accurate predictions.

This paper presents a general discussion on uncertainty in computational models of metal-based AM, and in particular, of Laser Powder Bed Fusion (L-PBF). The discussion begins with how key performance indicators (KPIs) drive the development of models, seeking simulation as a method to be used for qualification of L-PBF produced parts. We present a general description of the modeling process, and the generation and propagation of errors. We then conduct a deep dive into how errors are commonly introduced into AM models, and the contribution of each individual error source in such predictions. Uncertainty quantification (UQ) methods suitable for the L-PBF process are discussed, and Bayesian estimation is presented as a method to extend UQ by including online measurements to reduce overall prediction uncertainty. These concepts are illustrated on a low-order stochastic model.

The contribution in this paper is three-fold. It provides: 1) A discussion on methods for uncertainty quantification in L-PBF models; 2) An example of uncertainty quantification for computational models in which all sources of error are considered; and 3) A method for quantifying unmodeled process perturbations with potential applications in detection of anomalies and feedback control.

BACKGROUND

In the AM community, computational models are sought after as means to predict the outcome of physical processes. The choice of KPIs to be predicted depends on the application that is intended for the model. A common aim among modelers is model-based qualification, which will require control of several qualities: identification and reduction of defects, dimensional accuracy and surface finish, microstructure and mechanical properties, and reduction of residual stresses. In this article, it is suggested that melt pool dimensions be chosen as KPIs due to their direct relationship with the thermal processes that define these qualities[1]. Among the set of melt pool dimensions, width is chosen as the primary KPI in this first study because it can be traced both during and after the build.

Several other heat transfer models have been published in the literature with similar goals [12–19]. Though different in their formulation, as AM models, and even more specific, as L-PBF models, it is expected that at the highest levels of abstraction, sources of information and sources of error share common characteristics. A study of common uncertainty sources in L-PBF models has not been reported yet.

Until recently, the issues of model validation and verification (V&V) and uncertainty quantification (UQ) had for the most part eluded the AM community. Some of the few examples of UQ in AM models can be found in the papers by Moser [20] and Ma [21], both of which studied the sensitivity of their models to uncertainty in input parameters; and King [22], who discussed uncertainty quantification methods for surrogate models.

In engineering, computational models are designed as approximations of physical reality and, as such, are subjected to a cascade of errors and uncertainties. Figure 1 illustrates recognized sources of modeling errors [23], that we have adapted for an additive manufacturing application. Introduction of errors begin as early as the selection of the physical process to model (e.g. heat diffusion, melting/solidification, free-surface flows, etc.), which is approximated with an imperfect model of reality given by constitutive equations. All physical information that cannot be represented by the adopted mathematical model is considered to be modeling error. The mathematical model is calibrated with incomplete information of model parameters, based on incomplete calibration data gathered with imperfect sensors. Error in the determination of simulation parameters is propagated through the simulation. The mathematical model, often unsolvable with analytical methods, is approximated with a numerical method to result in a solvable form for simulation. Such approximations inject numerical errors that undermine the accuracy of the numerical predictions of the quantity of interest. Additionally, in the case of model validation, measurement error must be kept in mind for comparisons between simulation results and test data.

[1] Common L-PBF defects can be classified in two broad types: under-melting and over-melting defects. The former are generated by incomplete melting or improper fusion between successive tracks or layers [8], while the latter are caused by entrapment of gases or improper closure of a keyhole [9]. Both types have a strong influence on tensile, fatigue and hardness properties. Dimensional accuracy of the produced part is dependent on the degree of under- and over-melting too, especially in external tracks. Both for defect prevention and dimensional accuracy, the shape of the melt pool has traditionally been used as an indicator of under- and over-melting.

Grain size and morphology (key microstructural parameters that define yield strength and other mechanical properties) are dependent on the thermal history during solidification. In the case of Ti-6Al-4V, for example, grain size is known to be dependent on cooling rates, which are in turn functions of the cross-sectional area of the melt pool. Grain morphology, on the other hand, depends on the melt pool length-to-depth ratio [10].

Residual stresses, known to have a strong bearing on the fatigue crack growth, are linked to thermal cycles in the part. Large thermal gradients near the laser spot, rapid cooling, and repetition of this process produce localized compression and tension [11]. Some techniques used to mitigate residual stresses are the choice of appropriate scanning patterns, *in situ* heating, and *ex situ* heat treatment.

Even in the case of an optimal scanning pattern, the quality of an L-PBF-produced part can still be improved with accurate and responsive thermal control of melt pool dimensions.

Lane, Brandon; Lopez, Felipe; Witherell, Paul.
"Identifying uncertainty in Laser Powder Bed Fusion models."
Paper presented at The ASME 2016 Manufacturing Science and Engineering Conference (MSEC2016), Blacksburg, VA. June 27, 2016 - July 1, 2016.

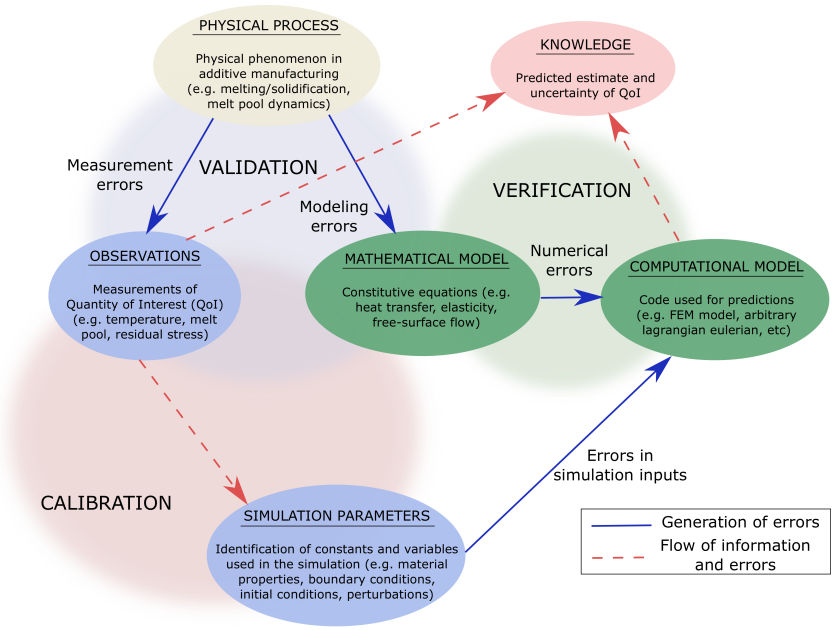

FIGURE 1: Cascade of sources of error in computer models of additive manufacturing.

IDENTIFYING UNCERTAINTY IN L-PBF MODELS

All the aforementioned sources of error are present in L-PBF process models. L-PBF involves multiple physical phenomena occurring at different length scales. The process is controlled by thermal, free-surface flow, structural and microstructural processes, which are closely coupled. Due to the complexity of the process, most computational models limit their scope to a subset of physical phenomena at a given scale, neglecting dynamics not captured by them. Modeling assumptions that neglect certain dynamics are the origin of modeling uncertainty[2]. It should be noted that only relationships of the causal type contribute to modeling uncertainty. For instance, if temperature distribution or a similar variable is chosen as the KPI, the lack of a structural model would not result in a relevant contribution to modeling uncertainty because the systems are only weakly coupled and the effect of stresses on the thermal history is insignificant.

Some common examples of modeling uncertainty in L-PBF can be found in surface tension and particle-level dynamics neglected in continuum models[3], the choice of inaccurate distributions for laser power acting on the powder bed, or an inappropriate choice of boundary conditions that neglects track-to-track and layer-to-layer interactions[4].

Input uncertainty is the result of inaccurate simulation parameters, adopted in lieu of more precise knowledge or as result of uncertainty in the training data. In the case of L-PBF models, common sources can be found in: a) absorption coefficient, which quantifies the amount of irradiated laser power that heats up the powder bed; b) thermal conductivity in loose powder, which depends on the distribution of powder particles; c) thermo-physical parameters at high temperatures; d) convection and radiation coefficients; and e) enhancing coefficients occasionally used to account for the effect of advection in the liquid phase. It is difficult to determine the precise values of these parameters for use in L-PBF models, and it is common to observe them used only as adjusting coefficients.

Various numerical methods have been used to solve the chosen mathematical models. Even when commercial packages based on finite element methods are common in academia and industry, other methods (e.g. discrete element methods, arbitrary Lagrangian Eulerian, lattice Boltzmann methods) are rapidly capturing the attention of the AM community. The choice of the numerical method depends on the physical processes included in the mathematical model (some methods are tailored for free-surface and particle-to-particle interactions), and their suitability for parallelization and implementation in high performance computing (HPC) systems. In any case, a choice of numerical method will result in an approximation error that depends on the granularity of the chosen grid. Commercial packages used for L-PBF models include convergence studies to ensure that the error

[2]The approach followed in this article makes no distinction between aleatory variability and epistemic uncertainty, and accounts only for their joint effect, as suggested in [24].

[3]Particles in the powder bed, randomly packed and a source of aleatory variability, heat up and melt creating stochastic variations in melt pool morphology.

[4]During the build, variations in thermal diffusivity in material surrounding the melt pool can have differences of up to two orders of magnitude between fully-dense material and loose powder. This effect has been observed experimentally when melting overhanging structures, where larger (almost three times) than usual melt pool areas have been observed [25].

Lane, Brandon; Lopez, Felipe; Witherell, Paul.
"Identifying uncertainty in Laser Powder Bed Fusion models."
Paper presented at The ASME 2016 Manufacturing Science and Engineering Conference (MSEC2016), Blacksburg, VA. June 27, 2016 - July 1, 2016.

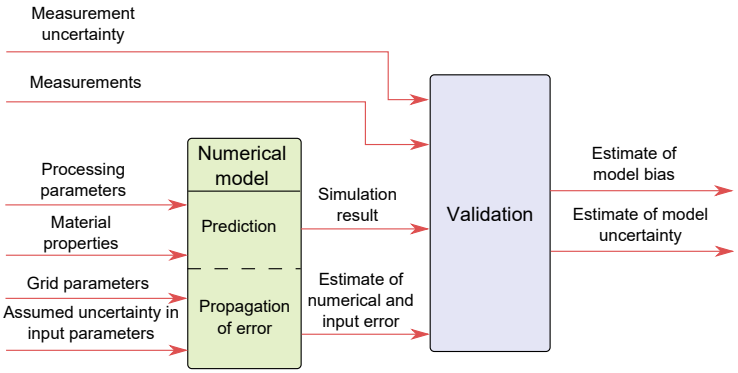

FIGURE 2: V&V and UQ in computational models as suggested in ASME V&V 20.

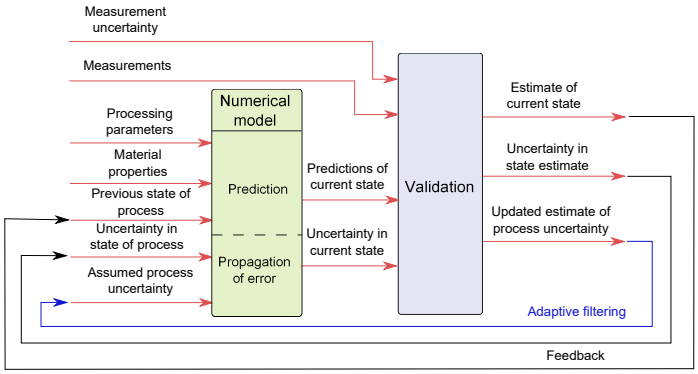

FIGURE 3: Online estimation in predictive models.

is small, but its magnitude is seldom reported.

Measurement uncertainty is independent of the choice of numerical model, and depends solely on the methods and instruments used to gather test data. The choice of appropriate measurement techniques for L-PBF is an unsolved issue, and it depends on the KPI of interest [26]. In the case of thermal variables, non-intrusive thermographic techniques hold the promise of providing online temperature measurements in the powder bed, but difficulties determining the correct emissivity of the material makes these predictions partially unreliable.

It is apparent that the different sources of uncertainty can only be conceptualized but not completely defined until the mathematical model and measurement system are selected. This discussion will be expanded in the section dedicated to our case study, where each source will be identified and quantified.

UNCERTAINTY QUANTIFICATION

Quantification of uncertainty in computational models is based on the comparison of simulation solutions with experimental data, to identify and track every source of error [23]. A comprehensive discussion on uncertainty sources in heat transfer and fluid mechanics models can be found in the standard ASME V&V 20, along with methods to quantify them [27]. The fact that AM involves thermally-activated consolidation processes makes this standard suitable for this application. Figure 2 illustrates the process of prediction and validation followed in UQ with ASME V&V 20.

In this example, a known set of processing parameters and material properties are fed to the model to obtain a simulation result S. Information about the grid is used to estimate the numerical error δ_{num} that results from the numerical method using methods based on Richardson's extrapolation or Roache's grid convergence index (GCI). Meanwhile, an assumed probability distribution in simulation parameters is propagated through the model into the predicted quantity of interest, resulting in an estimate of the error due to inaccurate inputs δ_{input}. Finally, simulation results S are confronted with measurements D and measurement error δ_D. The difference between model prediction and measurement determines the bias E, which acts as an estimate of modeling error δ_{model}. All sources of error are merged in the calculation of prediction uncertainty, which is reported along the bias as described in the first section of ASME V&V 20.

It is a well-known fact that the L-PBF process is highly variable. Heat transfer fluctuates throughout the entire build as a result of variations in processing conditions (laser power, scan speed, layer thickness, etc.), thermal diffusivity surrounding the melt pool, and random packing in the powder bed. Failure to include these sources of variability will result in unreliable melt pool width predictions.

Process variability is accounted for as uncertainty due to unknown inputs, if it can be traced back to simulation parameters, or as modeling uncertainty otherwise. Herein, we describe an application of Bayesian estimation to reduce modeling error by mapping sources of variability to random simulation parameters that are identified in real time and used in the calculation of more meaningful predictions. In the case of L-PBF, the set of identified parameters may include random variables that attempt to model the variable thermal characteristics of the material that surrounds the melt pool. Following this strategy, measurements can be used to detect these perturbations and sequentially readjust simulation parameters.

The process for online estimation is illustrated in Figure 3. In this case, a simulation is performed for a given set of simulation parameters and an initial state with its associated uncertainty, which originate from a previous step of the simulation (feedback). Uncertainty in the initial state is propagated in time using the model and process uncertainty, which is expected to capture the effect of modeling error, numerical error δ_{num} and error due to unknown inputs δ_{input}. The propagated state and uncertainty are then compared with the measurement and its error δ_D to result in estimates of the state at the next time step, its uncertainty, and an updated estimate of process uncertainty in the case of adaptive filtering.

Lane, Brandon; Lopez, Felipe; Witherell, Paul.
"Identifying uncertainty in Laser Powder Bed Fusion models."
Paper presented at The ASME 2016 Manufacturing Science and Engineering Conference (MSEC2016), Blacksburg, VA. June 27, 2016 - July 1, 2016.
SP-106

$$\frac{dy_1}{dt} = -\frac{2\mu\alpha_1}{y_1}\left(\frac{y_2}{y_2-y_1}\right) - \frac{A\times P}{\pi\rho C_p \Delta T y_1^2}\left(1+\frac{v}{2\mu\alpha_1}y_1\right)\exp\left(-\frac{v}{2\mu\alpha_1}y_1\right) + \frac{v^2}{4\mu\alpha_1}\frac{T_1-A_l}{\Delta T}(y_2-y_1) \quad (1)$$

$$\frac{dy_i}{dt} = -\frac{\mu\alpha_i}{y_i}\left(\frac{y_{i+1}}{y_{i+1}-y_i} - \frac{y_{i-1}}{y_i-y_{i-1}}\right) + \frac{v^2}{8\mu\alpha_i}\frac{T_i-A_l}{\Delta T}(y_{i+1}-y_{i-1}), \quad \text{for } i=2,3,\ldots,m-1 \quad (2)$$

$$\frac{dy_m}{dt} = -\frac{\mu\alpha_m}{(1+Ste^{-1})y_m}\left(\frac{y_{m+1}}{y_{m+1}-y_m} - \frac{y_{m-1}}{y_m-y_{m-1}}\right) - \frac{v^2}{4\mu\alpha_m(1+Ste^{-1})}\frac{A_l-2T_m+T_0}{\Delta T}\left(\frac{1}{y_{m+1}-y_m} + \frac{1}{y_m-y_{m-1}}\right)^{-1}\left\{1+2Ste^{-1}\left[1+\left(\frac{A_l-2T_m+T_0}{\Delta T}\frac{v}{2\mu\alpha_m}\right)^2\left(\frac{1}{y_{m+1}-y_m}+\frac{1}{y_m-y_{m-1}}\right)^{-2}\right]^{-1}\right\} \quad (3)$$

$$\frac{dy_i}{dt} = -\frac{\mu\alpha_i}{y_i}\left(\frac{y_{i+1}}{y_{i+1}-y_i} - \frac{y_{i-1}}{y_i-y_{i-1}}\right) + \frac{v^2}{8\mu\alpha_i}\frac{T_i-T_0}{\Delta T}(y_{i+1}-y_{i-1}), \quad \text{for } i=m+1,\ldots,N-1 \quad (4)$$

$$\frac{dy_N}{dt} = -\frac{\mu\alpha_N}{y_N}\left(\frac{y_N-2y_{N-1}}{y_N-y_{N-1}}\right) - \frac{v^2}{4\mu\alpha_N}(y_N-y_{N-1}). \quad (5)$$

It can be seen that both approaches have the same sources of uncertainty, the only difference being that some sources of process variability that are included either as modeling error or error due to unknown inputs in offline models are mapped to a random initial state.

CASE STUDY: UNCERTAINTY IN A STOCHASTIC MODEL FOR L-PBF

In this case study, an Isotherm Migration Method (IMM) model, developed for laser cladding [28], is adjusted for use in L-PBF. The model provides a set of ordinary differential equations (ODEs) that describe the motion of isotherms on the surface of the powder bed. If one of these isotherms is assigned to the melting temperature (T_m), the model can be used to dynamically track the location of the solidification front and predict melt pool width. The method is similar to Rosenthal's solution for temperature distribution due to a moving point source [29], but it allows the use of temperature-dependent material properties. Also, instead of solving for the distribution of temperature $T(x,y,z,t)$, the system is solved for the half-widths $y(T,t)$ of isotherms on the bed surface[5]. The array of half-widths corresponds to a user-defined, uniformly-spaced temperature grid $T = [T_1 \quad T_2 \quad \ldots \quad T_m \quad \ldots \quad T_N]$, for $\Delta T < 0$.

The computational model shown in equations (1) to (5) describes the evolution of the half-widths $y = [y_1 \quad y_2 \quad \ldots \quad y_m \quad \ldots \quad y_N]$, where each half-width y_i corresponds to a temperature T_i[6]. The set of ODEs can be expressed in compact form as $\dot{x} = f(x,u)$, where $x = [y \quad \mu]$ denotes the vector of state variables and $u = [P \quad v]$ the vector of control inputs. In this case, μ is the diffusion efficiency, a random variable used to correct for variable sideways thermal diffusion due to unmodeled process perturbations (modeling error is mapped to a simulation variable). Its value is set to 1 in nominal cases, when the melt pool is surrounded by fully-dense material. In the case of of overhanging structures, for example, a decrease of thermal diffusivity toward the bottom improves heat transfer to the sides, increasing the value of μ.

The system of equations is stable for positive thermal diffusivity α, and can be simulated until convergence to a steady-state melt pool width $w_{max} = w_{max}(P,v,A,h_l,T_m,\alpha(T))$. The same model can be assembled in the form of an equation that maps the present state vector $x_n = x(t_n)$ to a future instant $t_{n+1} = t_n + \Delta t$, using a forward Euler scheme of the form $x_{n+1} = x_n + f(x_n,u_n)\times\Delta t$, for example.

Uncertainty quantification

Uncertainty is quantified by comparing simulation results for fully-dense material with melt pool width measurements gathered using an EOSINT M270 system on an IN625 plate, as described by Montgomery [30]. Single bead tests were performed using different combinations of laser power and scan speed, both on a bare plate (no added powder) and one with a 20

[5]The width of an isotherm under the heat source is twice y, because y is measured from the heat source location to the isotherm. Maximum melt pool width is calculated assuming an ellipse for the isotherms [28].

[6]In these equations, α_i denotes the thermal diffusivity evaluated at temperature T_i, A is the absorption coefficient, P is laser power, ρ is density, C_p is specific heat, v is scan speed, $A_l = T_0 - h_l/(C_p + 2\mu\alpha_i C_p/v/y_m + 2\mu^2\alpha_i^2 C_p/y_m^2/v^2)$ is the apparent ambient temperature for the liquid phase, and $Ste = -C_p\Delta T/h_l$ is the Stefan number.

Lane, Brandon; Lopez, Felipe; Witherell, Paul.
"Identifying uncertainty in Laser Powder Bed Fusion models."
Paper presented at The ASME 2016 Manufacturing Science and Engineering Conference (MSEC2016), Blacksburg, VA. June 27, 2016 - July 1, 2016.

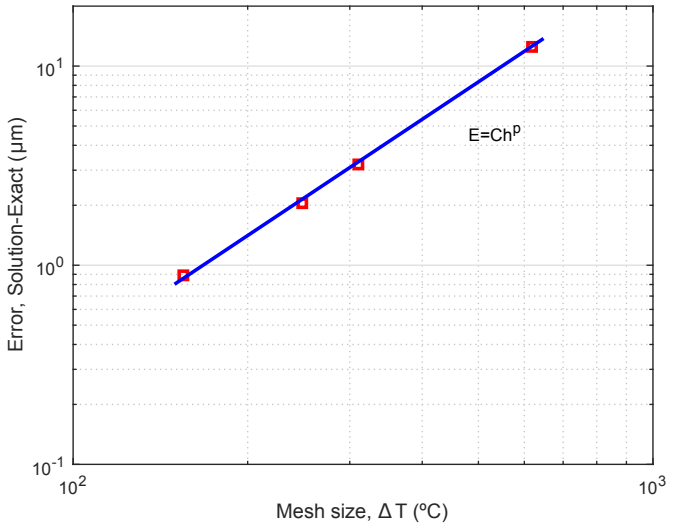

FIGURE 4: Numerical error as a function of mesh size.

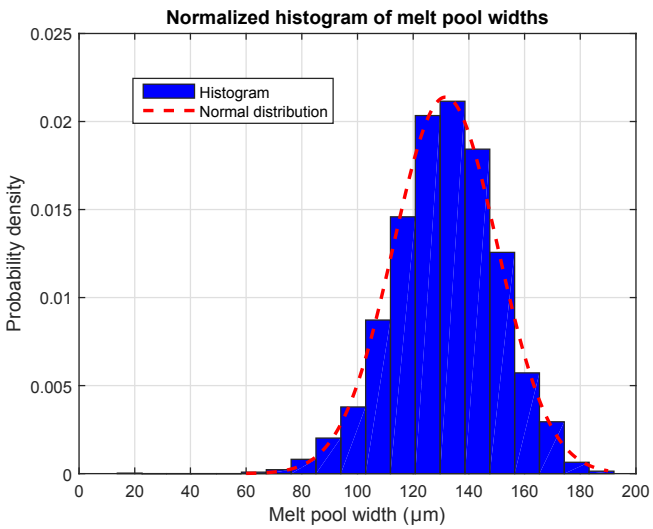

FIGURE 5: Normalized histogram of predicted melt pool widths.

μm layer of powder added. To ensure that diffusion efficiency does not introduce extra uncertainty, only scans on bare plate are compared with model predictions.

Error is approximated within the interval $\delta_{model} \in [E-u_{val}, E+u_{val}]$ centered around $E = S-D$, the bias between the simulation result S and experimental measurements D. Validation uncertainty u_{val}, which accounts for uncertainty from all sources, can be computed following $u_{val} = \sqrt{u_{num}^2 + u_{input}^2 + u_D^2}$ under the assumption that all error sources are independent.

The first steps toward quantification of modeling error are code and solution verification; in other words, assessing that the code is correct (free of bugs) and estimating the error in the numerical approximation. Code was verified with a manufactured solution and it was observed that the method converges to the analytical solution given by Rosenthal for constant material properties as $\Delta T \to 0$ and $T_{max} \to \infty$. Similar convergence studies were performed for predictions of melt pool width w (in μm) using temperature-dependent material properties. Results are presented in Figure 4, where successive grid refinement was used to identify an order of accuracy of $p = 1.9$[7].

Numerical uncertainty was quantified using Roache's Grid Convergence Index (GCI) [27] for the prediction obtained with $T_1 = 2560\ ^\circ C$ and $\Delta T = -248\ ^\circ C$, corresponding to a grid of 10 isotherms[8]. The GCI is an estimated 95 % uncertainty (a common uncertainty target) obtained by multiplying the absolute value of a Richardson extrapolation error by an empirically determined factor of safety. In this case, the numerical prediction for melt pool width for L-PBF of Inconel 625 with 195 W and 800 mm/s is $(127.3 \pm 2.7)\ \mu m$ (± 2.12 %).

The second source of uncertainty comes from imperfect knowledge of input parameters, and the effect they may have on predictions. Six factors were selected for a Monte Carlo study to determine the propagation of uncertainty in inputs: laser power (P), scan speed (v), absorption coefficient (A), latent heat (h_l), melting temperature (T_m), and thermal diffusivity ($\alpha_i(T_i)$)[9]. Normal distributions are assumed for the input parameters following:

Input	Nominal	Std. dev. (% nominal)
P	195 W	2.5%
v	0.800 m/s	1.5%
A	0.6	25%
h_l	2.97×10^5 J/kg	5.0%
T_m	1320 °C	5.0%
α_i	$\alpha_i(T_i)$	10.0%

A Monte Carlo approximation of the probability distribution of melt pool width is obtained following $p(w) \propto \sum_{n=1}^{N} \delta_{w_{max}(P^n, v^n, A^n, h_l^n, T_m^n, \alpha^n(T))}$, where δ denotes the Dirac delta and the superscript n indicates the n-th sample of the input parameters. The resulting distribution of predicted melt pool widths (for 4000 samples) resembles a normal distribution, as illustrated in Figure 5, where the 95 % confidence interval is found in $(131.6 \pm 37.3)\ \mu m$.

The last source of uncertainty comes from the experiments used for validation. This study uses measurements that were taken in the middle of the long edge of the single bead track,

[7]The formal order of accuracy of the method was found at $p = 3$, but nonlinearities in the temperature-dependent properties insert iteration error reducing the effective value of p.

[8]The reason to choose a relatively coarse grid is the desire to accelerate the computation by keeping the dimensionality of the IMM model low. This is going to be more important in the case of online predictions, to be described in the next section.

[9]Temperature dependent material properties were obtained with the TCN16 thermodynamic database within the Thermo-Calc software [31].

Lane, Brandon; Lopez, Felipe; Witherell, Paul.
"Identifying uncertainty in Laser Powder Bed Fusion models."
Paper presented at The ASME 2016 Manufacturing Science and Engineering Conference (MSEC2016), Blacksburg, VA. June 27, 2016 - July 1, 2016.
SP-108

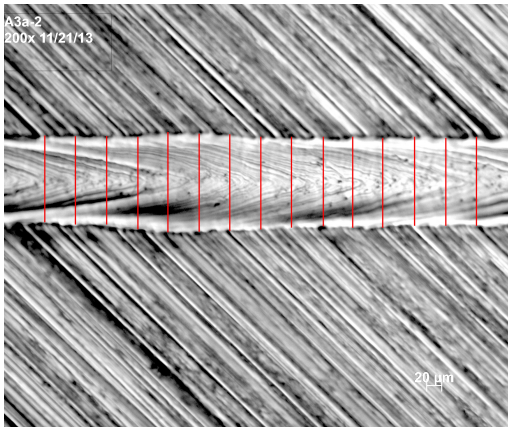

FIGURE 6: Sample image with measurement points marked (No powder added, 125 W and 600 mm/s) [30].

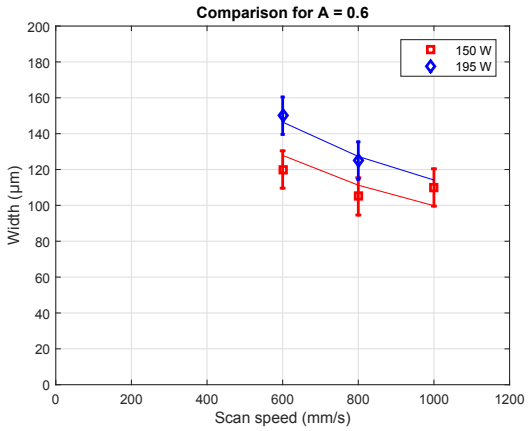

FIGURE 7: Comparison of model predictions with experiments.

which was imaged using a Zeiss AxioVision AX10 optical microscope. The image was then measured 15 times along the width at approximately equal spacing, as shown in Figure 6. These 15 measurements were then averaged for each melt pool. In this study, measurements in the steady-state region have standard deviations of close to 5.2 μm, suggesting a ± 10.4 μm confidence interval.

Measured melt pool widths are shown in Figure 7 and compared to predictions obtained from the IMM model, only for data points close to nominal operating conditions (195 W and 800 mm/s). The region of calibration for this model was delimited between 150 W and 195 W, and 600 mm/s and 1000 mm/s[10]. Assuming that all error sources are independent, validation uncertainty is estimated at (127.3 ± 38.8) μm (± 30.5 %) for nominal conditions. Some observations can be made from these results:

(a) Modeling uncertainty is relatively large, as expected due to the simplification of the thermal problem by assuming a point source instead of a distributed one. The absence of other physical phenomena considered important for melt pool dynamics, such as surface tension, only increases modeling error.

(b) Numerical uncertainty is negligible compared to uncertainty due to unknown input parameters or to experimental error, even for highly-coarse grids.

(c) Error due to uncertainty in input parameters, the error source most widely studied, has a very significant contribution to model uncertainty (± 29.3 %). This is partly due to the large uncertainty assumed for the absorption coefficient A, which was used as a tuning coefficient in this example.

(d) Uncertainty due to unknown inputs depends on the confidence in the chosen set of input parameters. Different users may choose different input uncertainties, resulting in different prediction uncertainties.

(e) It is currently not possible to assess how this model compares to the predictions obtained with other L-PBF models as their uncertainty has not been reported.

(f) The relatively large prediction uncertainty (± 30.5 %) is compensated by the speed of the model. The model returns a melt pool width prediction in 0.1 s when implemented in MATLAB R2014b running on an Intel Core i7-3770 CPU.

(g) Extrapolation of the modeling error to the other points in the region of calibration matches the obtained measurements, as observed in Figure 8, where power and scan speed were kept constant. It is important not to extrapolate predictions outside the region of calibration of each predictive model, which is often not reported.

(h) Model was validated by comparison with scans on bulk material, ignoring the addition of a powder layer. Montgomery reported that the effect of adding a layer of powder does not have a significant effect on melt pool width [30], but its effect was not quantified in this study.

Bayesian estimation

Diffusion efficiency may be allowed to vary in time to account for unmodeled track-to-track and layer-to-layer interactions, which were ignored in the previous example. In this section, we present an example that illustrates how online thermographic monitoring can be used to identify unmodeled dynamics (modeling error) and decrease uncertainty in melt pool width predictions.

The presented case, illustrated in Figure 9, is designed to represent a horizontal overhanging plane which is scanned in a direction perpendicular to the solid-to-powder transitions. This case study, designed and published by Kruth *et al.* [25], showed that melt pool area increases threefold when going through this kind of overhangs. Synthetic data was generated to mimic this

[10]The choice of the region of calibration was arbitrary, and it was chosen as an area around the nominal point where the same absorptivity is able to replicate observed melt pool widths.

Lane, Brandon; Lopez, Felipe; Witherell, Paul.
"Identifying uncertainty in Laser Powder Bed Fusion models."
Paper presented at The ASME 2016 Manufacturing Science and Engineering Conference (MSEC2016), Blacksburg, VA. June 27, 2016 - July 1, 2016.

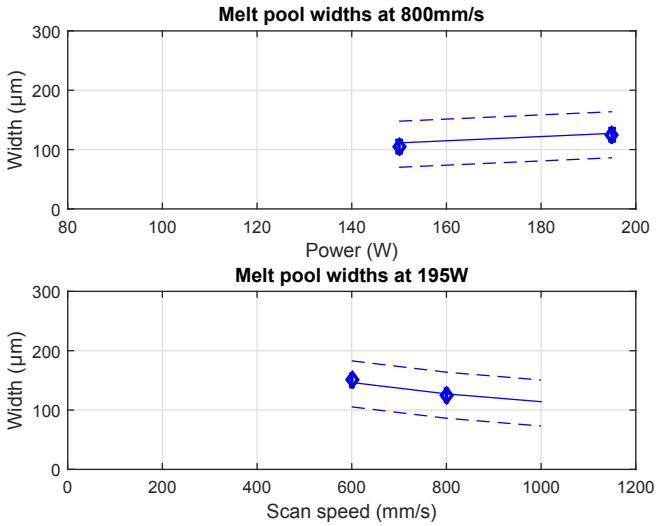

FIGURE 8: Melt pool width predictions for DMLS of Inconel 625.

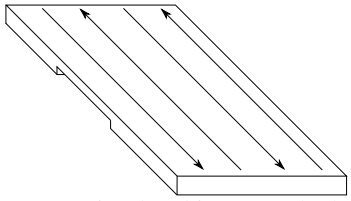

FIGURE 9: Case simulated in "perturbed" scenario.

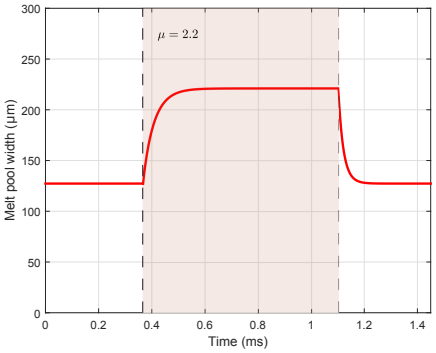

FIGURE 10: Simulation of melt pool width through overhang assuming $\mu = 2.2$.

event by artificially perturbing μ and assuming that it varies instantaneously from 1 to 2.2[11] when melting on top of loose powder.

In this study, it has been assumed that the isotherms corresponding to $T_i = \{576, 824, 1072\}^\circ C$ can be detected with thermographic sensors. To simulate measurement uncertainty, noise was added to the measured isotherm widths following a standard deviation of 26 μm[12].

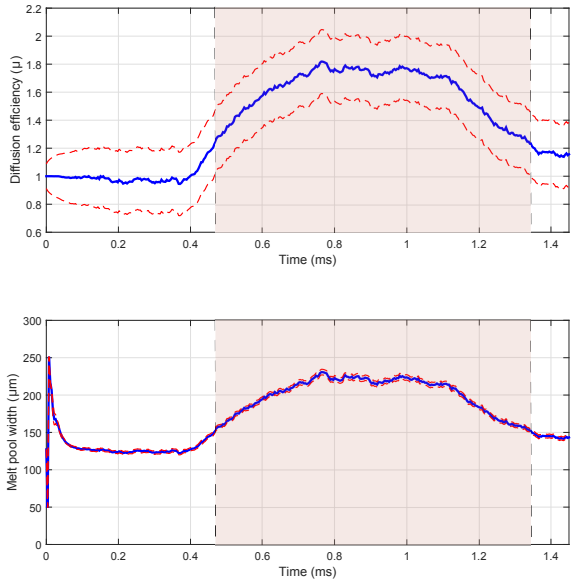

FIGURE 11: Estimated diffusion efficiency and melt pool width. Predictions are shown in blue and 95 % confidence intervals are in dashed red lines.

Process estimation, using a linear stochastic version of the IMM model and a Kalman filter [32], results in the estimates shown in Figure 11, where the null hypothesis of normal operation (no overhang, $H_0 : \mu = 1$) is rejected in favor of the alternative hypothesis of an anomaly ($H_A : \mu \neq 1$) in the shaded region. The perturbation in heat diffusion is detected between 0.47 ms and 1.35 ms, lagging from the 0.37 ms and 1.10 ms in which they occur in the simulation.

Response speed, and accuracy and uncertainty in the estimates are expected to be dependent on the process and measurement uncertainty used for estimation, which were assumed in this example and will have to be adjusted in an experimental study to close the loop shown in Figure 3.

An important point to be observed is the low uncertainty in the melt pool width prediction even in the region of anomalous operation. Without online measurements, models would have to account for the potential variation in diffusion efficiency using large uncertainties for μ, increasing uncertainty in melt pool width predictions. For example, if the study to determine sensitivity to input parameters is repeated letting μ vary following $\mu \sim \text{Unif}[1.0, 2.5]$, the obtained prediction is $(193.6 \pm 106.6)\ \mu m$ (± 55.1 %), which is much larger than the confidence intervals reported in Figure 11 ($\pm 4.0\ \mu m$).

[11] The value of the assumed perturbed diffusion efficiency was chosen to increase steady-state melt pool width approximately by $\sqrt{3}$, assuming that melt pool length changes by the same ratio and the overall melt pool area increases threefold.

[12] The assumed measurement noise used for the synthetic data corresponds to a standard deviation of half the pixel width in similar thermographic settings.

Lane, Brandon; Lopez, Felipe; Witherell, Paul.
"Identifying uncertainty in Laser Powder Bed Fusion models."
Paper presented at The ASME 2016 Manufacturing Science and Engineering Conference (MSEC2016), Blacksburg, VA. June 27, 2016 - July 1, 2016.

FUTURE WORK

The identification and quantification of the uncertainty sources in the proposed stochastic AM model is not complete until the process uncertainty assumed for diffusion efficiency is validated. Validation of model variability will only be possible in a sequential manner, by comparing model predictions with measurements. Melt pool width measurements need to be taken faster than the characteristic response time of the process, which the model identified in the order of hundredths of milliseconds for L-PBF of Inconel 625 with nominal conditions. At such high data acquisition rates, both gathering and processing the data will be challenging.

This study is scheduled to be performed in the powder bed fusion test bed that NIST is developing for studies of advanced metrology, estimation and control [33]. Once the test bed and the data acquisition system for melt pool widths are ready, the stochastic model presented in this article can be used in the design of an online monitoring system. NIST is currently working on the development of such a system to:

(a) Detect and quantify thermal perturbations and their uncertainties in the L-PBF process, which will allow engineers to locate the regions of the produced part that are most likely to have manufacturing defects.
(b) Design of a feedback process controller, which will use information of the current state of the process.

CONCLUSIONS

As metal-based AM gains popularity, closer attention has been paid to the computational models developed to predict quality in manufactured components. One aspect that has been traditionally ignored in these models is that, if they are to be used in model validation or for certification of parts, one must know how accurate and precise these models are. Uncertainty quantification presents a set of challenges that have often been ignored both by manufacturing and modeling engineers.

The series of steps that go from a physical process to a numerical representation involve successive assumptions in the mathematical models, model parameters, numerical scheme, and calibration data. It is important to quantify the relative effect of each error source to identify the ones that will result in the most significant reductions in prediction uncertainty.

A method to decrease modeling error, by mapping it to random simulation inputs that are identified in real time, is illustrated. Inclusion of random inputs requires that the assumed randomness is validated (and adjusted, if necessary). Adaptive filtering techniques are being evaluated for implementation in a future online monitoring study.

Even though the case study presented in this paper is based on a low-order model, the same ideas can be extended to high-order models. The algorithms used for uncertainty quantification, however, are different. For instance, the high computational cost of Monte Carlo methods prevents their application in the propagation of uncertainty in input parameters. Methods based on the Karhunen-Loève expansion (e.g. polynomial chaos [34]) are often preferred in such scenarios.

ACKNOWLEDGMENT

The authors gratefully acknowledge the comments and suggestions provided by Wim Devesse, developer of the laser cladding model adapted for this study; Colt Montgomery, provider of melt pool width measurements; and Jason Fox, for his comments on the physics of the process.

REFERENCES

[1] The Economist, 2012. A third industrial revolution, April 21st.
[2] Bourell, D., Beaman, J., Marcus, H., and Barlow, J., 1990. "Solid freeform fabrication: An advanced manufacturing approach". In Proceedings of the International Solid Freeform Fabrication Symposium, pp. 1–7.
[3] Hull, C. W., 1986. Apparatus for production of three-dimensional objects by stereolithography, US Patent.
[4] Beaman, J., and Deckard, C., 1989. Selective laser sintering with assisted powder handling, US Patent.
[5] Foust, M. J., Thomsen, D., Stickles, R., Cooper, C., and Dodds, W., 2012. "Development of the GE aviation low emissions TAPS combustor for next generation aircraft engines". In 50th AIAA Aerospace Sciences Meeting including the new Horizons Forum and Aerospace Exposition, Vol. 936.
[6] Holshouser, C., Newell, C., Palas, S., Duty, C., Love, L., Kunc, V., Lind, R., Lloyd, P., Rowe, J., Dehoff, R., Peter, W., and Blue, C., 2013. "Out of bounds additive manufacturing". *Advanced Materials & Processes,* ***171***(3), pp. 15–17.
[7] Sundseth, J., and Berg-Johnsen, J., 2013. "Prefabricated patient-matched cranial implants for reconstruction of large skull defects". *Journal of central nervous system disease,* ***5***, pp. 19–24.
[8] Bauereiß, A., Scharowsky, T., and Körner, C., 2014. "Defect generation and propagation mechanism during additive manufacturing by selective beam melting". *Journal of Materials Processing Technology,* ***214***(11), pp. 2522–2528.
[9] King, W. E., Barth, H. D., Castillo, V. M., Gallegos, G. F., Gibbs, J. W., Hahn, D. E., Kamath, C., and Rubenchik, A. M., 2014. "Observation of keyhole-mode laser melting in laser powder-bed fusion additive manufacturing". *Journal of Materials Processing Technology,* ***214***(12), pp. 2915–2925.
[10] Gockel, J., Beuth, J., and Taminger, K., 2014. "Integrated

Lane, Brandon; Lopez, Felipe; Witherell, Paul.
"Identifying uncertainty in Laser Powder Bed Fusion models."
Paper presented at The ASME 2016 Manufacturing Science and Engineering Conference (MSEC2016), Blacksburg, VA. June 27, 2016 - July 1, 2016.

control of solidification microstructure and melt pool dimensions in electron beam wire feed additive manufacturing of Ti-6Al-4V". *Additive Manufacturing,* ***1***, pp. 119–126.

[11] Wu, A., Brown, D., Kumar, M., Gallegos, G., and King, W., 2014. "An experimental investigation into additive manufacturing-induced residual stresses in 316L stainless steel". *Metallurgical and Materials Transactions A,* ***45A***(13), pp. 6260–6270.

[12] Roberts, I. A., Wang, C. J., Esterlein, R., Stanford, M., and Mynors, D. J., 2009. "A three-dimensional finite element analysis of the temperature field during laser melting of metal powders in additive layer manufacturing". *International Journal of Machine Tools and Manufacture,* ***49***(12-13), pp. 916–923.

[13] Matsumoto, M., Shiomi, M., Osakada, K., and Abe, F., 2002. "Finite element analysis of single layer forming on metallic powder bed in rapid prototyping by selective laser processing". *International Journal of Machine Tools and Manufacture,* ***42***(1), pp. 61–67.

[14] Zeng, K., Pal, D., and Stucker, B. E., 2012. "A Review of Thermal Analysis Methods in Laser Sintering and Selective Laser Melting". In Proceedings of the Solid Freeform Fabrication Symposium, pp. 796–814.

[15] Jiang, W., and Dalgarno, K., 2002. "Finite Element Analysis of Residual Stresses and Deformations in Direct Metal SLS Process". In Solid Freeform Fabrication, pp. 340–348.

[16] Hussein, A., Hao, L., Yan, C., and Everson, R., 2013. "Finite element simulation of the temperature and stress fields in single layers built without-support in selective laser melting". *Materials & Design,* ***52***, pp. 638–647.

[17] Hodge, N., Ferencz, R., and Solberg, J., 2014. "Implementation of a thermomechanical model for the simulation of selective laser melting". *Computational Mechanics,* ***54***(1), pp. 33–51.

[18] Körner, C., Bauereiß, A., and Attar, E., 2013. "Fundamental consolidation mechanisms during selective beam melting of powders". *Modelling and Simulation in Materials Science and Engineering,* ***21***(8), p. 085011.

[19] Cheng, B., Price, S., Lydon, J., Cooper, K., and Chou, K., 2014. "On process temperature in powder-bed electron beam additive manufacturing: Model development and validation". *Journal of Manufacturing Science and Engineering,* ***136***(6), p. 061018.

[20] Moser, D., Beaman, J., Fish, S., and Murthy, J., 2014. "Multi-layer computational modeling of selective laser sintering processes". In International Mechanical Engineering Congress and Exposition.

[21] Ma, L., Fong, J., Lane, B., Moylan, S., Filliben, J., Heckert, A., and Levine, L., 2015. "Using design of experiments in finite element modeling to identify critical variables for laser powder bed fusion". In Proceedings of the International Solid Freeform Fabrication Symposium, pp. 219–228.

[22] King, W. E., Anderson, A. T., Ferencz, R. M., Hodge, N. E., Kamath, C., Khairallah, S. A., and Rubenchik, A. M., 2015. "Laser powder bed fusion additive manufacturing of metals; physics, computational, and materials challenges". *Applied Physics Reviews,* ***2***(4).

[23] Oden, T., Moser, R., and Ghattas, O., 2010. "Computer predictions with quantified uncertainty, Part I". *SIAM News,* ***43***(9), November, pp. 1–3.

[24] Roache, P., 2002. "Code verification by the method of manufactured solutions". *ASME Journal of Fluids Engineering,* ***114***(1), pp. 4–10.

[25] Kruth, J.-P., Mercelis, P., Van Vaerenbergh, J., and Craeghs, T., 2007. "Feedback control of selective laser melting". In Proceedings of the 3rd International Conference on Advanced Research in Virtual and Rapid Prototyping, Leiria, Portugal, Sept, Citeseer, pp. 24–29.

[26] Mani, M., Lane, B., Donmez, A., Feng, S., Moylan, S., and Fesperman, R., 2015. Measurement science needs for real-time control of additive manufacturing powder bed fusion processes. NISTIR 8036, National Institute of Standards and Technology.

[27] ASME V&V 20-2009, 2009. "Standard for verification and validation in computational fluid dynamics and heat transfer". *American Society of Mechanical Engineers*.

[28] Devesse, W., De Baere, D., and Guillaume, P., 2014. "The isotherm migration method in spherical coordinates with a moving heat source". *International Journal of Heat and Mass Transfer,* ***75***, pp. 726–735.

[29] Rosenthal, D., 1946. "The theory of moving sources of heat and its application to metal treatments". *Transactions of the ASME,* ***68***, pp. 849–866.

[30] Montgomery, C., Beuth, J., Sheridan, L., and Klingbeil, N., 2015. "Process mapping of inconel 625 in laser powder bed additive manufacturing". In Proceedings of the Solid Freeform Fabrication Symposium, pp. 1195–1204.

[31] Thermo-Calc, 2014. Thermo-Calc software AB version 3.1. Tech. rep.

[32] Kalman, R. E., 1960. "A new approach to linear filtering and prediction problems". *Journal of Basic Engineering - Transactions of the ASME,* ***82***(1), pp. 35–45.

[33] Vlasea, M., Lane, B., Lopez, F., Mekhontsev, S., and Donmez, A., 2015. "Development of powder bed fusion additive manufacturing test bed for enhanced real-time process control". In Proceedings of the International Solid Freeform Fabrication Symposium, pp. 527–539.

[34] Xiu, D., and Karniadakis, G. E., 2003. "Modeling uncertainty in flow simulations via generalized polynomial chaos". *Journal of computational physics,* ***187***(1), pp. 137–167.

Lane, Brandon; Lopez, Felipe; Witherell, Paul.
"Identifying uncertainty in Laser Powder Bed Fusion models."
Paper presented at The ASME 2016 Manufacturing Science and Engineering Conference (MSEC2016), Blacksburg, VA. June 27, 2016 - July 1, 2016.

Modeling of Suspension Flow in Pipes and Rheometers

Nicos S. Martys[1], Chiara F. Ferraris[1], and William L. George[1]

[1]National Institute of Standards and Technology

Abstract Measurement and prediction of the flow of suspensions like fresh concrete represents a significant challenge for both the experimentalist and modeler. In this paper, results of a computational study of suspension flow in a pipe and a rheometer design using a four blade vane as an impellor are given. The computational method is based on the Smooth Particle Hydrodynamics approach. Flow fields and the spatial distribution of solid spherical inclusions for the case of pipe flow will be shown as a function of the matrix fluid properties, (including Newtonian, shear thinning and shear thickening), driving force, and volume fraction of particles. A strong effective slip phenomenon is shown for the case of a suspension with a shear thinning fluid matrix. Results will be compared to experiments. Aspects of shear induced migration in a vane rheometer and its effects on rheological measurements will be briefly discussed.

Keywords: Rheology, Concrete, Non-Newtonian, Smoothed Particle Hydrodynamics

Introduction

The flow of suspensions is of fundamental interest and plays an important role in a wide variety of technical applications including paints, cement based materials, slurries, and drilling fluids [1]. A suspension can be described as a collection of solid inclusions embedded in a fluid matrix. Measuring and predicting the flow of suspensions remains a great scientific challenge. Suspensions can be quite complex as the inclusions may have a wide range of shapes and a broad size distribution. Further complicating matters is that different matrix fluids may have quite disparate flow behaviour. While the simplest type of matrix fluid is Newtonian, where the local stress is proportional to the shear rate, the matrix fluid can exhibit quite complex behaviour including shear thinning (viscosity decreases with shear rate), shear thickening (viscosity increases with shear rate), viscoelastic, or even have a time dependence. In this paper, results will be presented from numerical simulation of the flow of suspensions in a pipe geometry where the matrix fluid is either Newtonian, shear thinning, or shear thickening. Flow fields and the spatial

distribution of neutrally buoyant solid spherical inclusions for the case of pipe flow will be shown as a function of the matrix fluid properties. In addition, a brief discussion of suspension flow in a vane rheometer, illustrating shear induced migration will also be given.

Computational Model

The computational approach utilized in this work, for modeling suspension flow, is based on the Smoothed Particle Hydrodynamics (SPH) method [2]. A full description of SPH is beyond the scope of this paper. A detailed description of this model is given in Martys et al. [3]. For this paper let it suffice to say SPH is a Lagrangian formulation of the Cauchy momentum equation that has been adapted to model generalized Newtonian fluids (where the viscosity is shear-rate dependent) and the motion of rigid bodies. In addition, this approach has been extended to include lubrication forces in order to properly model interactions between solid spherical inclusions when they are in very close proximity. The simulation code utilized for this work has been validated for a variety of flow scenarios (Fig.1) where excellent agreement with analytic solutions is found of flow fields for non-Newtonian continuum fluids in channel and tube geometries and flow of suspensions with power law matrix fluids in a Couette geometry [3].

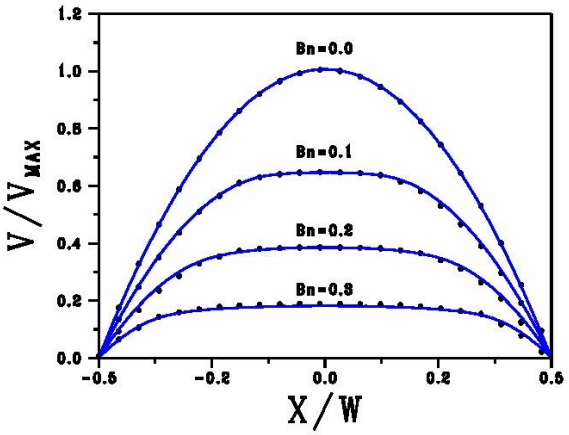

Figure 1. Velocity profiles for flow of non-Newtonian fluid in a 2D channel of width, W, driven by a body force. The fluid properties are based on an approximation of the Bingham model of Papanastasiou [3,4]. For Bingham number Bn =0, the fluid is Newtonian. As Bingham number is increased the fluid more closely approximates a Bingham fluid. The solid lines are from solution of the generalized Navier-Stokes equations using this model and the points are from the simulation.

Pipe Flow: Model

Several assumptions were made to model suspension flow in a pipe. For simplicity, a gravity driven flow is assumed. Periodic boundary conditions at the inlet and outlet are observed (Fig.2). When modelling lubrication forces between a sphere and a pipe wall, the pipe wall is assumed to be a plane locally. As long as the radius of the sphere is much smaller than the pipe radius this approximation should hold. For our simulations, the radius of the sphere is less than a factor 1/32 of the pipe radius. In addition, this relative size is not too far off from what would be associated with a sand particle in a one inch (0.0254 m) pipe which is commonly used for pumping grouts.

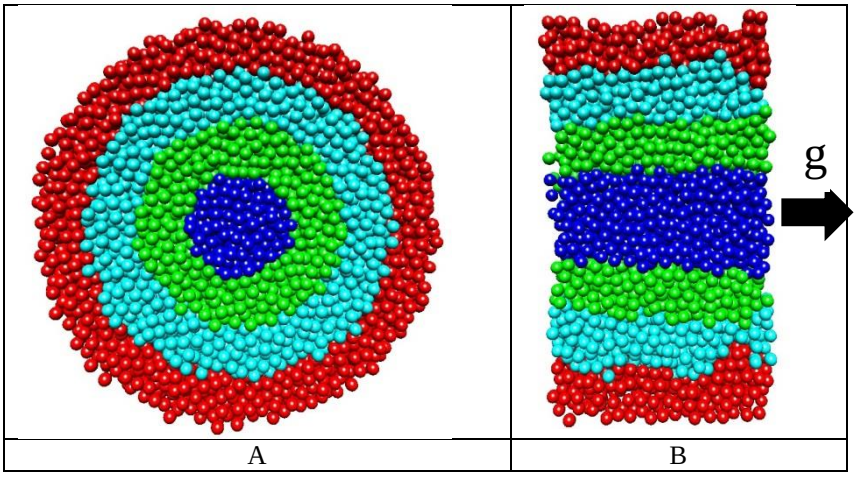

Figure 2. Cross sections of suspension in pipe flow. The solid volume fraction is 40 %. The colors correspond to the initial radial position of the spheres.

In this paper, three types of matrix fluids will be considered: shear thinning, shear thickening and Newtonian (Fig.3). For the model fluids used in this paper, all three behave as a Newtonian fluid in the low shear rate regime. However, at high shear rates the shear thinning and shear thickening fluids behave as power-law fluids with the viscosity scaling as $\dot{\gamma}^{-0.5}$ and $\dot{\gamma}^{0.5}$ respectively, where $\dot{\gamma}$ is the shear rate. A no slip boundary condition is assumed throughout all the simulations (i.e., the fluid velocity is zero at the pipe wall).

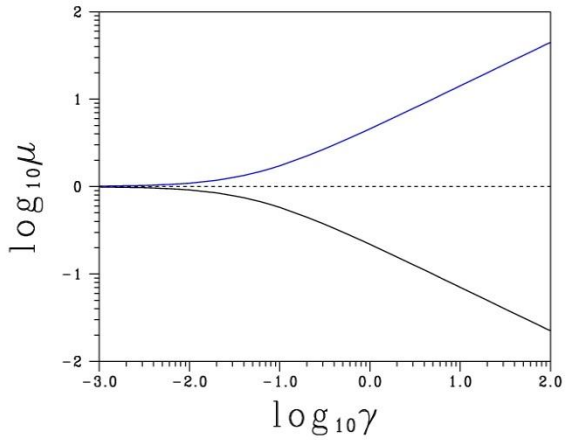

Figure 3. Viscosity vs. shear rate for matrix fluids studied. The Newtonian fluid is the dashed line. The shear thinning ($\mu \sim \dot{\gamma}^{-0.5}$ at high shear-rates) and shear thickening thinning ($\mu \sim \dot{\gamma}^{0.5}$ at high shear-rates) fluids are shown as the solid black and blue lines respectively.

Simulations Results: Pipe Flow

Consider the case of a pipe flow of a suspension in a Newtonian fluid matrix. Fig. 4A shows the velocity profiles for suspensions with volume fraction 20 % and 50 %. Also, for comparison, the flow field for the case of volume fraction 0 % is included. For each volume fraction, the velocity is scaled by the maximum velocity reached in the simulation. It is observed that as volume fraction is increased the velocity profile becomes flatter in the centre of the pipe. This is due to an increase (Fig. 4B) in the density of spheres in the centre of the pipe due to a shear induced migration. Such migration has been observed experimentally [5, 6, 7] and in quasi 2D flow simulations of channel flow using Stokesian Dynamics [8]. Although not clearly seen in the Stokesian dynamics simulations, it was found that, at high volume fractions there is a tendency for structure to develop at fairly large length scales. This is partly due to a local crystallization effect that is known for the case of monosize hard spheres where the volume fraction is approximately 49 % or higher. This phenomenon was observed in experimental data [5] as well.

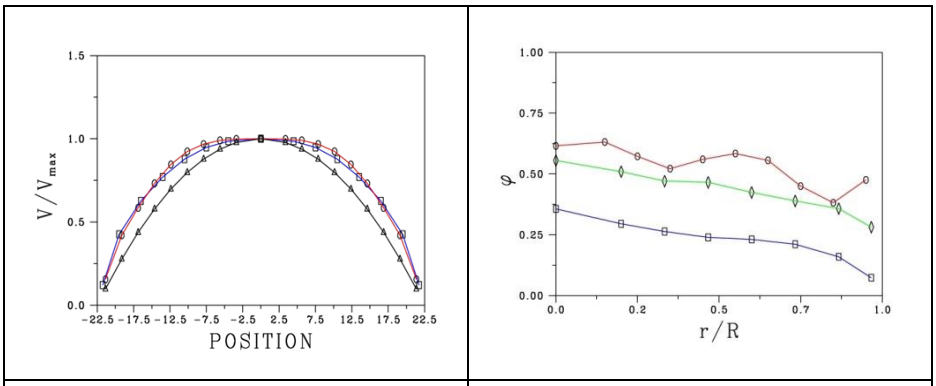

A B

Figure 4. A) Rescaled velocity profiles for pipe flow of suspension with Newtonian fluid matrix in pipe for particles volume fractions 0 % (triangles), 20 % (squares), and 53 % (circles). As particles volume fraction increases the flow profiles flatten, deviating from parabolic, as found for pipe flow of a Newtonian fluid. B) Radial dependence of the local volume fraction for suspensions with volume fraction 20 % (squares), 40 % (diamonds) and 53 % (circles). At low volume fraction the local volume fraction decreases from the centre of the pipe. At high volume fractions there is still a radially decreasing trend in density, however, there are indications of a long range order in the density profile.

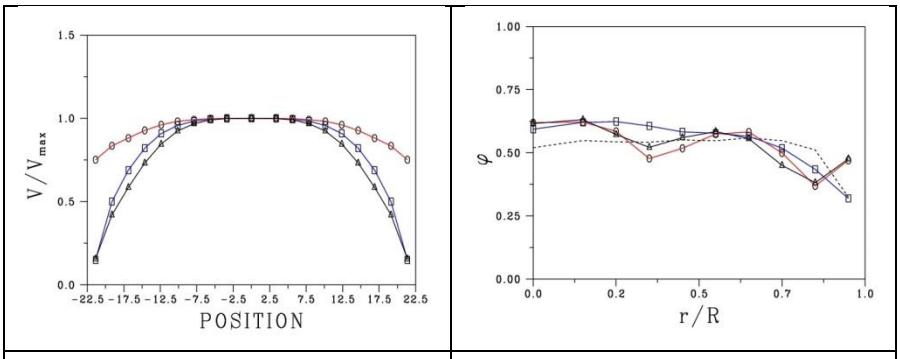

A **B**

Figure 5. A) Comparison of rescaled velocity profiles for Newtonian (triangles), shear thickening (squares), and shear thinning (circles) fluids. Volume fraction of spherical inclusion is 53 %. A strong effective slip near the pipe surface is observed for the suspension with shear thinning fluid matrix. B) Comparison of the radial dependence of the local volume fraction for suspensions with volume fraction 53 % and different fluid matrices, Newtonian (triangles), shear thickening (squares), and shear thinning (circles). The dashed line indicates the initial radial dependence for all three simulations.

Suspensions flow with a shear thinning, shear thickening, and Newtonian fluid matrices was examined. Figure 5A shows the scaled velocity profile for each type of matrix fluid. Clearly, the velocity profiles are quite different depending on the fluid matrix. Both the shear thinning and shear thickening cases appear to have a more flattened velocity profile than with a Newtonian matrix. Most interesting is the appearance of a strong effective slip for the case of the shear thinning matrix. In the simulation code, there is an enforcement of no slip boundary condition at the pipe wall. However, for spheres near the pipe wall there is a very high shear rate leading to a very low viscosity. Hence, the spheres can move quite easily near the pipe wall giving an appearance of a slip effect. Figure 5B shows the density profile for the three matrix fluids. Both the Newtonian and shear thinning fluids show the development of a long range order as seen in the oscillation of the density. However, the shear thickening fluid did not exhibit this behaviour. This may be a consequence of the system having not evolved for a long enough period of time for this structure to develop. Indeed, any lateral motion for the shear thickening matrix fluid appeared to be significantly suppressed due to the shear thickening behaviour of the matrix fluid.

All simulations in the low Reynolds number (Re) regime exhibited evidence of shear induced migration [9] towards the central axis of the pipe. Such phenomena are described by the suspension balance and related continuum models [8, 9, 10, and 11]. Reasonable estimates of the radial dependence of the density may be obtained for low to moderate volume fractions, although the exact structure observed in experiment and our simulations at high volume fractions would be difficult to recover by these approaches without further modification. For the case of a shear thinning fluid matrix, single phase continuum models may under predict the total mass flow because the effective slip, as seen in Fig. 6, may not be properly accounted for. Also, for the case of shear thickening fluid matrix, a single phase continuum prediction of flow would be higher in comparison to this simulation because any additional increase of local shear rates due to the proximity of spheres at the wall surface make the viscosity higher and hence restrict flow.

Simulations Results: High Reynolds Number Flow

As Re is increased, inertial forces are expected to play a more important role. To illustrate this, consider the case where Re is approximately 3000 for a dilute suspension with volume fraction 5 %. Figure 7A shows a succession of velocity profiles for this system. Note the slight inflection of the velocity profile not far from the pipe wall. This is an artefact of inertial forces playing a role, overcoming the shear induced forces, such that the spheres begin to form a ring near the pipe wall (Figure 7B). Such behavior has been observed in high Re flow in pipe systems [7]. It should be pointed out that the final velocity profile, shown is not an equilibrium profile as this simulation had not progressed long enough to reach that stage. However, it had reached a sufficient state as to illustrate the effect of high Re flow.

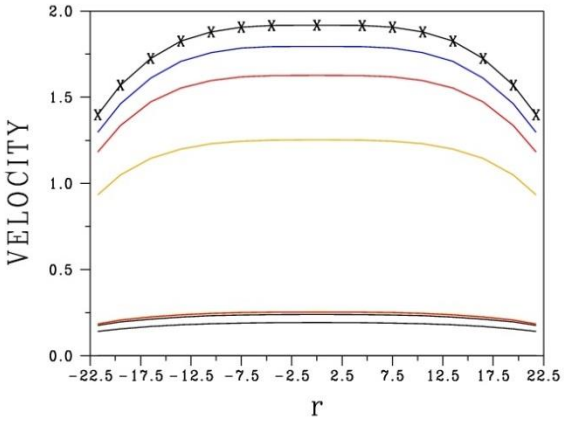

Figure 6. Snap shots of the time evolution of velocity profiles for two body forces g (lower set of curves) and 3g (upper set of curves) for the case of a suspension with volume fraction 53 % and shear thinning matrix. The effective slip is enhanced with increasing body force and roughly scales as g squared for this shear thinning fluid.

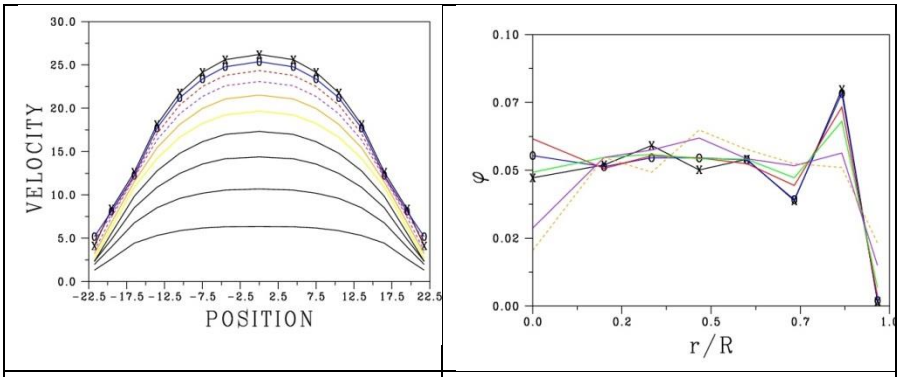

A B

Figure 7. A) Snapshots of the time evolution of velocity profiles for suspension with volume fraction 5 %, Newtonian fluid matrix and Re increasing to approximately 3000. Note the velocity profiles deviate from parabola as Re increases during the evolution of flow. B) Time evolution of the radial dependence of the local volume fraction for suspensions with volume fraction 5 %, Newtonian fluid matrix. The dashed line indicates the initial local volume fraction. The curves marked with the circle and X correspond to the velocity profiles shown in Fig. 7B. Note the density increase near the pipe wall and a secondary ring of spheres developing near r/R=.3.

Simulations Results: Vane Rheometer

Here, the effect of shear induced migration in a vane rheometer is examined. The vane rheometer is commonly used for determining the viscosity of fluids (Fig.8A)

such as concrete. Often one approximates the vane as a cylinder and assumes a coaxial geometry to estimate the viscosity of the fluid. Making this assumption will result in underestimating the value of viscosity, depending on the number of blades in the vane. However, there are analytically determined corrections, based on a continuum fluid approximation (i.e. no solid inclusions) that can help compensate for this assumption. Unfortunately, when the fluid is a suspension, other factors contribute to an even lower viscosity measurement. In our simulations, this behaviour can be attributed to the migration of particles from the blade and towards the wall as shown in Fig. 8C. Such migration outward movement can lead to considerably lower estimates of the of the suspension viscosity due to the decreased coupling of the rotator and the suspension. It was found that estimates of viscosity based on the vane simulations were a factor of two lower than that obtained from simulations using a Couette geometry. It should be pointed out that the migration observed here may be mitigated depending on the nature of the matrix fluid, volume fraction of solids, particle size distribution, vane design and applied torque.

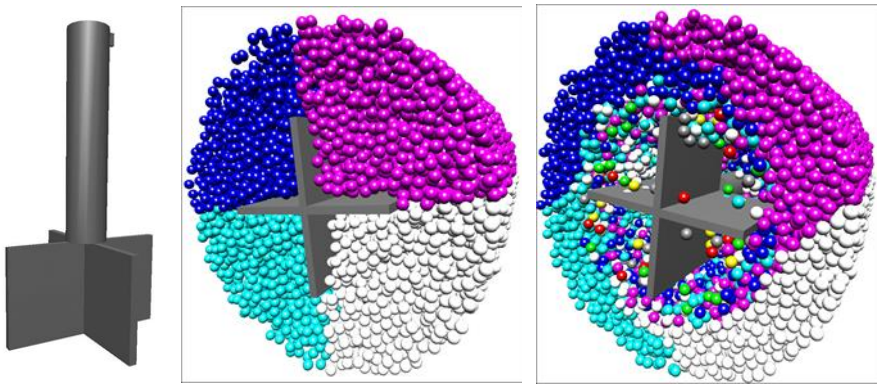

A B C

Figure 8: A) Four blade rheometer vane. B) and C) show the cross section of the vane in a suspension: B) initial (B) and C) late stage (over 20 full rotations of the vane). Note that many of the spheres have been driven outside the inner region of the blade. Sphere volume fraction is 40 %.

Conclusions

In this paper, the utility of modelling suspension flow in a variety of geometries was demonstrated. Specifically, computational modelling can help develop fundamental insights into physical mechanisms, such as the role of shear induced migration and inertial forces that influence flow and effect the interpretations of measurements in these flow geometries. Further, such knowledge can help provide insight about how to tailor mix designs for optimal flow properties in order to reduce cost in placement of concrete and to improve its performance.

Acknowledgements

The authors would like to gratefully acknowledge support from the Sustainable Materials Program at NIST. An award of computer time was provided by the Innovative and Novel Computational Impact on Theory and Experiment (INCITE) program. This research used resources of the Argonne Leadership Computing Facility, which is a DOE Office of Science User Facility supported under Contract DE-AC02-06CH11357.

References

[1] Larson, R.G., *The structure and rheology of complex fluids*, (Oxford University Press, New York, 1999).
[2] Monaghan, J. J., (2005), *Rep. Prog. Phys.*, vol. 68, p. 1703.
[3] Martys, N. S., George, W. L., Chun, B. W., Lootens, D., (2010), *Rheol. Acta*, vol. 49, p. 1059.
[4] Papanastasiou, T.C., (1987*), J. Rheol*., vol. 31, p.385.
[5] Hampron, R. E. and Mammoli, A. A. , (1997), *J. Rheol*, vol. 41, p. 621.
[6] Lyon, M. K.. and Leal L.G., (1998), *J. Fluid Mech.*, vol, 363, p. 25.
[7] Matas, J.P., Morris, J.F., and Guazzelli, *Oil and Gas Science Technology. – Rev. IFP*., (2004), vol 59 No.1. p.59.
[8] Nott, P.R., and Brady, J.F., (1994), *J. Fluid Mech*., vol. 275, p. 157.
[9] Morris, J.F. and Boulay, F., ((1999), *J. Rheol*., vol. 43, p. 1213.
[10] Leighton, D. and Acrivos A., (1987), *J. Fluid Mech.*, vol, 181, p. 415.
[11] Zarraga, I.E., Hill, D.A., and Leighton, D.T. (2000), *J. Rheol*., vol. 44, p.185.

2016 EWRI-ASCE World Environmental & Water Resources Congress

West Palm Beach, Florida, May 22-26, 2016

Proposed session:

Topic/Track: Symposium Water Distribution System

Session Title: Water Distribution System Analysis Symposium

Title: Response of water systems under extreme events: a comprehensive approach to modeling water system resilience

Authors: Hana Chmielewski[1,2], Roberto Guidotti[2,3], Therese McAllister[1,2] and Paolo Gardoni[2,3]

ABSTRACT:

Water systems (e.g. potable water, wastewater, and storm water systems) are regarded as "lifeline" infrastructure. They play a key role in supporting the everyday activities of communities. Their disruption can cause cascading effects, influencing the economy of an entire region and the general well-being of communities. In addition, past hazard events show that water availability is crucial for minimizing the societal impact of such events and for recovery processes. Water systems are typically distributed over a large area and, because of the variety of components, are vulnerable in different ways to multiple hazards. To date, research in water system reliability has focused on either probabilistic scenarios of physical damage to system components, disruption to hydraulic performance after an event, or simulation of component and system recovery. Indeed, stochastic simulations of hazards events, and their direct and indirect physical damage to water system components, are typically not coupled with hydraulic simulations of functionality loss and restoration, including water quality, pressure, and flow throughout the network. This work presents a comprehensive approach to the modeling of water system resilience subject to a seismic event; however, the procedure is general and can be applied to other network systems and hazards. The model performs: i) a baseline deterministic hydraulic analysis on an undamaged water system, focusing on meaningful functionality metrics, (i.e. water pressure, quantity, and quality); ii) a probabilistic analysis of the damaged system considering the damage state and the performance level of each component; iii) a probabilistic analysis of the water system functionality, considering the physical damage analysis and the recovery time of each component.

[1] National Institute of Standard and Technology (NIST)
[2] NIST Center of Excellence for Risk-Based Community Resilience Planning
[3] Department of Civil and Environmental Engineering, MAE Center, University of Illinois at Urbana-Champaign (UIUC)

1. INTRODUCTION

This work presents a comprehensive approach to the modeling of water system resilience for seismic events; however, the procedure is general and can be applied to other systems and hazards. Resilience is the ability to prepare for and adapt to changing conditions and withstand and rapidly recover from disruptions. Water system resilience refers to the ability of the system to meet its intended performance and functions in the community through prevention (mitigation), design, and recovery plans and actions.

Water systems (e.g., potable water, wastewater, and storm water systems) are regarded as "lifeline" infrastructure. They support residential, commercial, industrial functions and other uses by providing water through five key subsystems: supply (ground and surface), transmission, treatment, pumping, and storage of water. Disruptions to any of these subsystems can disrupt community functions and cause cascading effects influencing the economy and general well-being of communities. In past hazard events, water availability was crucial for minimizing the societal impact of such events and for recovery processes. When water service outage is widespread, it can be just as disruptive to economic recovery as electricity loss, and the restoration of water service can be the tipping point for the recovery of business operations [1], [2]. To address this issue, a growing body of research in the last decade has begun to focus on the performance of water systems under hazard events, using modeling to predict, simulate, measure or improve levels of damage and rates of recovery in water systems [3], [4]. However, no known water system model includes probabilistic scenarios of the damage state of the entire system and discrete simulation of component recovery using hydraulic analysis and performance metrics. Throughout this paper, "damage model" refers to the simulation of physical damage to system components, while "functionality model" refers to the hydraulic analysis performed to assess system functions, such as water delivery, pressure, and quality.

The next Section presents an assessment of current models of water system damage and recovery (damage models); Section 3 presents current models of hydraulic flow and water quality (functionality models); Section 4 describes the analysis workflow for the water system reliability and resilience assessment; and Section 5 shows the results from an example water system assessment.

2. WATER SYSTEM DAMAGE MODELS

Most water system damage models consider routine damage to system components (e.g., long-term environmental effects, aging materials, or periodic mechanical failures), as opposed to disruptive hazard events. As a result, a large body of research focuses primarily on isolated failures such as pipe breaks and in some cases, pump failures (e.g., [5], [6], [7], [8]). While these allow us to quantify the hydraulic importance of single elements in an otherwise functional system, the resulting information does not include hydraulic interdependencies, nor cascading failures, which are relevant for understanding the system state during hazard events.

A model of widespread damage of a water system depends on the hazard considered and on the specific vulnerability of the elements that constitute the system. The diverse components of water and wastewater systems are typically dispersed over large areas. Water system elements include linear components such as pipelines, tunnels, canals and flumes, and nodal components like tanks and reservoirs, treatment plants, pumping stations and wells. Because of the variety of components, water systems are vulnerable to a number of natural hazards and, in general, different elements are vulnerable to different hazards. For example, earthquakes may cause damage to pipes that might result in breakage or leakage and pressure

losses, and wind may damage above ground facilities like tanks, affecting system functionality. Fragility curves can represent damage to linear and nodal elements using the conditional probability of exceeding a prescribed performance level for a given hazard intensity measure (e.g., [9], [10]). Likewise, repair rate curves may provide the mean rate of repair for an element for a given hazard intensity measure (e.g., [11], [12], [13]).

A review of literature pertaining to disaster recovery in water systems shows that there are far more studies of disaster mitigation and response than of recovery. As water system component recovery is extremely challenging to model for hazard events, a large portion of the knowledge base on the effects of disasters on water systems comprises white papers, compilations of workshops proceedings and industry interviews (e.g., [3] [4]). Tierney [1] [2] surveyed businesses to estimate the economic impact of water system recovery time in North American earthquake and flood events. There is also a body of research that uses modeling to statistically predict (e.g., [14]), simulate (e.g., [15], [16]), measure, or improve disaster recovery in water systems (e.g., [17], [18]), sometimes comparing model results with recovery times from a real world event (e.g., [15]). Triangular functionality curves, which assume linear recovery for each damaged component, are commonly used to represent the rate of recovery in water system damage models [19]. Probabilistic restoration curves may be used, giving to each element a smooth recovery curve with a mean, standard deviation, and labor requirement for each damage level.

Since 1997, the HAZUS-MH software [20] developed for the Federal Emergency Management Agency (FEMA) has provided engineers and decision makers a valuable tool to help estimate losses from seismic hazards and, in its most recent versions, from flood and hurricane hazards. For a water system, HAZUS-MH includes the damage fragility and repair rate curves based on the American Lifelines Alliance guidelines [13]. The curves in the guidelines were mainly based on available empirical data and expert judgement. Some recent models for simulating infrastructure damage and recovery cite the component fragility curves and accompanying recovery times used within HAZUS-MH software as their underlying assumptions. An example is GIRAFFE (Graphical Iterative Response Analysis for Flow Following Earthquake), a program for damaged water system flow analysis that iteratively performs the hydraulic analysis of the system to assess its seismic performance [16] as restoration steps are added.

Implementing restoration curves for each damaged element independently, as in HAZUS-MH, necessarily neglects the inter- and intra-system dependencies that determine the system's actual recovery process. Conditional fragility and recovery curves can be applied to propagate damage and determine the possibility of component recovery, based on supporting components within and outside the water system. Recovery modeling of dependent systems can be performed with binary dependencies and deterministic recovery times (e.g., [21] use mathematical programming to optimize component recovery scheduling), or with discrete simulations. For example, graph-based dependency models of component recovery may use Petri nets (e.g., [22]) or repair scheduling with stochastic recovery times (e.g., [15]).

The Center for Risk-Based Community Resilience Planning (Center) led by Colorado State University, in collaboration with the National Institute of Standard and Technology (NIST), is currently conducting research on infrastructure system hazard damage and post-event recovery (http://resilience.colostate.edu/). The Center is fostering the development of a computational environment (NIST-CORE) for the modeling of community resilience planning and post-event recovery strategies using physics-based models of

dependent physical systems combined with social and economic systems. The current study represents a part of this larger effort, and is structured to incorporate external as well as internal dependencies in each recovery time step.

3. FUNCTIONALITY MODELS

To evaluate the water system functionality during the recovery process, the recovery simulation must incorporate a hydraulic model of the damaged water system. The availability of software such as HAZUS-MH has provided a platform for detailed modeling of physical damage, but without an underlying hydraulic model, performance and recovery will not take into account system pressure. Water system performance after hazard events depends upon the effects of damage on the water system, including maintaining adequate pressure to deliver water for potable usage and fire protection, and to prevent contaminant intrusion. Hydraulic simulation of flow, pressure, and water quality of a damaged system at each demand node can contribute separately, or in combination with each other, to inform system performance metrics (e.g., volume of demand satisfied, quality of delivered water, pressure thresholds and, when no separate water system distribution system exists, pressure sufficiency for fire protection).

EPANET [23], a freely available software package from the U.S. Environmental Protection Agency (EPA), is a widely-accepted tool for water distribution system hydraulic simulation. The software performs extended period steady-state simulation of hydraulic behavior and water quality. Demand-driven hydraulic models such as EPANET are not suitable to modeling low-pressure situations, such as in damaged systems. In demand-driven hydraulic models, the normal demand is assumed to always be satisfied. If the pressure at a node is insufficient to satisfy a given demand, the solution engine raises negative pressure errors, and the analysis cannot be completed. There are different strategies for amending demands in demand-driven analysis to be more realistically tied to pressure. Some demand-driven hydraulic models prevent negative pressures by removing nodes whose demand cannot be satisfied from the hydraulic model [16], [24]. Another approach, used in EPANET-EMITTER [7], functions as additional code around the EPANET solver (or wrapper) that iteratively resets emitter coefficients (a pressure-dependent demand component in EPANET) and reruns the model until the emitter coefficients and demands converge. The current study relies on the EPANET-EMITTER software to estimate pressure-driven consumption, and adapts and adds to the methodologies utilized in GIRAFFE to estimate leakage flows.

Though the possibility of cross-contamination resulting from pipe breaks, leaks, and low pressures in the network is a water quality concern that is significant in post-hazard event recovery, there has been limited research in addressing water quality in hazard event recovery models of damaged water systems. Quality concerns in damaged water distribution systems are both challenging to model, and difficult to translate into a course of action for recovery in practice. Water quality in distribution systems can be estimated with different indicators. Water quality indicators such as total coliform or E. Coli tests can signal the possible presence of harmful bacteria, but there may be a lag time of hours or days before bacteria are detected. As residual chlorine can slow the growth of bacteria, modeled or sampled chlorine levels may indicate areas of the network with low or elevated risk of contamination. Most State regulations simply require water quality testing anywhere that pressure falls below 15-20 psi (130-138 kpa) [25], [26]. The issuance or lifting of boil water notices may take days, requiring repeated testing until potentially harmful compounds are no longer detectable.

Though water quality analysis in post-hazard recovery simulation is rare, there is a broad literature covering contaminant transport and water quality sensor placement for drinking water contamination events (e.g., [17], [18], [27], [28], [29]). While these studies do not include physical system damage, many use EPANET to track contaminant transport and decay, or the extension package, EPANET-MSX to model multiple contaminant species and their interactions with each other and with chlorine residuals. These analyses can be used to improve recovery operations (such as valve closures and hydrant flushing) to limit the spread of contaminants (e.g., [17], [18]). The current study defers operational changes during recovery to future work. Interaction with residual chlorine, too, is an important aspect of water quality analysis; however, the current study instead models non-decaying, non-interacting chemicals. This is both a simplifying assumption common in many water distribution system models with contaminant transport (e.g., [27], [17], [18]), and an accurate reflection of the stringent regulations and timeframe of water quality testing and boil water advisories. Without the potential for decay, the non-decaying assumption corresponds to a worst-case contaminant propagation scenario (where contaminated water can only exit the system through demand nodes or flushing), and a conservative approach for protecting customers from potential contamination exposure.

4. WATER SYSTEM RELIABILITY AND RESILIENCE ANALYSIS

Analysis of system reliability and resilience merges the damage model and functionality model concepts described in the previous two sections. It is summarized in the following procedure. The first step inputs the hazard to the model, with spatial variations in intensity for various linear and nodal elements as appropriate. In the case of an earthquake, for example, ground motion prediction equations provide the values of intensity measures as a function of the earthquake characteristics. The second step assesses physical damage to the system's elements, according to models and methods presented in Section 2. In addition, information on physical damage to supporting systems, e.g., loss of power, can be input to more fully define the functionality of each element. Finally, the functionality analysis tracks metrics of interest, using the models and methods described in Section 3. In the case of a water system, for example, a hydraulic analysis with EPANET and EPANET-EMITTER is conducted to obtain the water pressure, flow and quality for the analysis of physical damage impacts, and compared to functional values in the undamaged baseline analysis. Figure 1 illustrates the reliability procedure, with reference to a water system.

The work presented thus far considers the aftermath of the damaging event; the reliability analysis requires an assessment of the recovery time of the different elements and of the entire system. Therefore, for each time step and for each considered element, the model updates the recovery and damage status based on the initial damage status and its recovery functions. At each step, the system status is updated with remaining system damage, and operational values are retrieved from the previous time-step. A functionality analysis performed at each step tracks the value of the functionality metrics of interest. The process is iterated until a desired level of

functionality is met, typically considering a tolerance range from the baseline scenario.

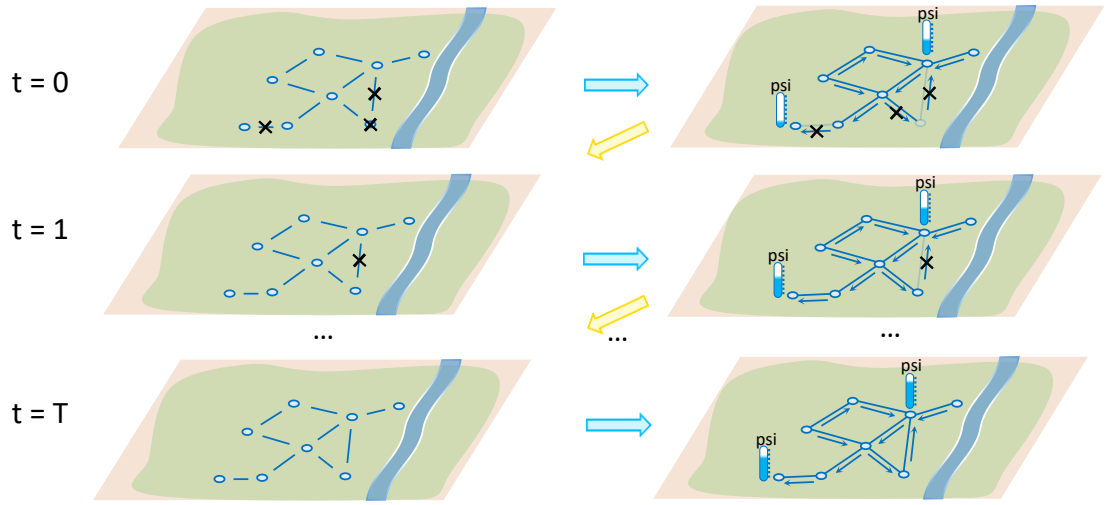

Figure *2* shows the resilience analysis with reference to a water system, with the iterations between physical damage assessment and functionality analysis.

5. ANALYSIS OF AN EXAMPLE WATER SYSTEM

The following example applies the proposed formulation to a water system subject to a seismic event, but the procedure is general and can model other systems or hazards. Consider the water system shown in Figure 3, composed of nine junctions and twelve pipelines with the characteristics listed in Table 1. A reservoir and treatment plant at node 9 provides water to the network, through a pumping station. A tank above node 12 completes the model. The functionality model first performs a hydraulic simulation using EPANET. The nodal values of pressure, water flow and quality will serve as a baseline for comparison to evaluate the functionality of the system in a post-hazard event scenario.

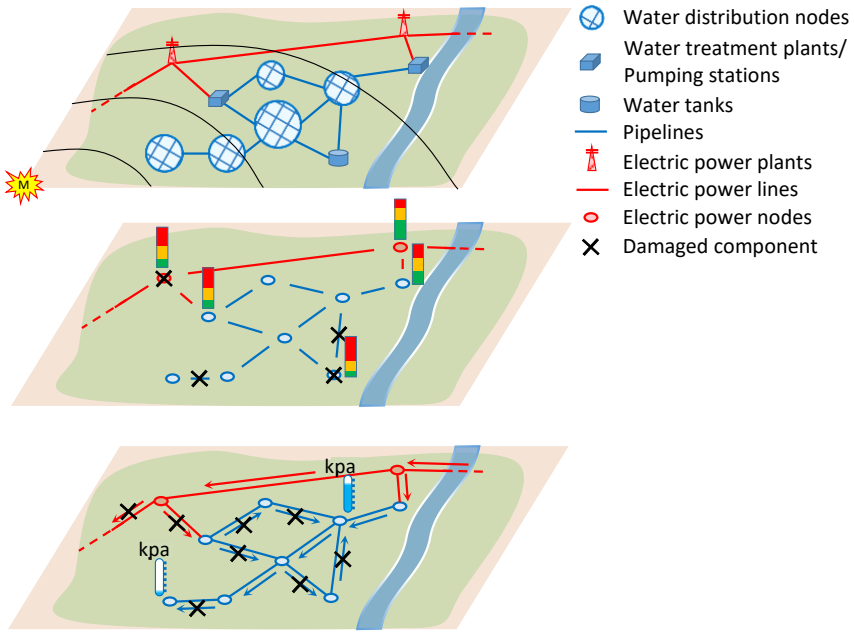

Figure 1: The simulation allows physical damage levels of the infrastructure system components to be included in the functional

model.

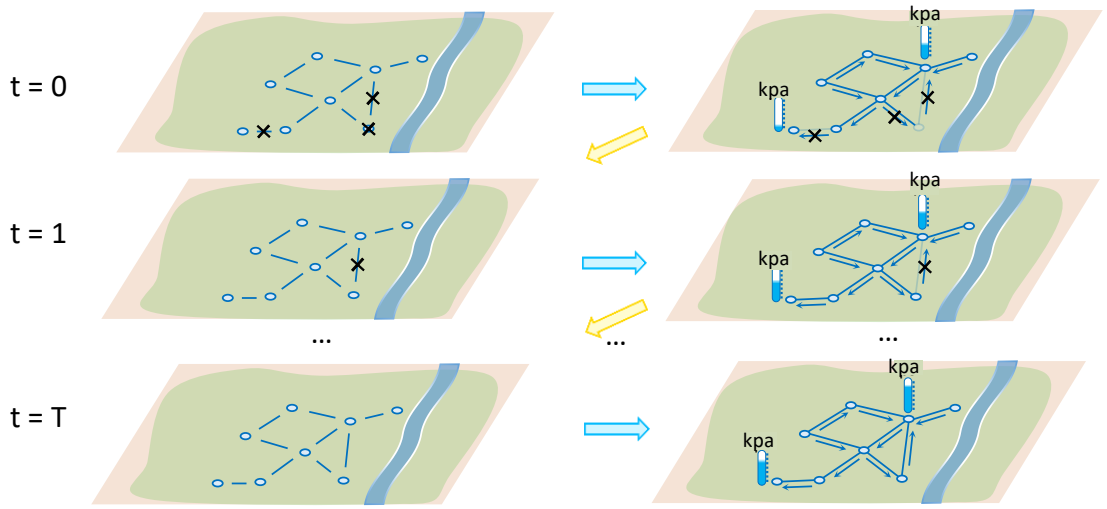

Figure 2: Conceptual scheme of a water network resilience analysis. Iterative process of damage and recovery status simulation (left hand side column) and functionality assessment (right hand side column).

The damage model assessment uses the ground motion prediction equations in Fernandez and Rix [30]. Different attenuation equations or physics-based models of seismic propagation may be adopted. In the current analysis, those equations provide the intensity measure of interests, given meaningful earthquake and site characteristics, such as magnitude, distance from the epicenter, soil conditions, faulting system, etc. With reference to an earthquake of magnitude 7.5 located approximately 10 km from the water network, **Error! Reference source not found.** maps three intensity measures of interest, respectively, the peak ground displacement (PGD), peak ground velocity (PGV) and peak ground acceleration (PGA).

Table 1: Water system characteristics: linear and nodal elements.

Pipe	Length [ft (m)]	Diameter [in (cm)]	Roughness [-]
10	10530 (3210)	18 (45.7)	145
11	5280 (1600)	14 (35.6)	135
12	5280 (1600)	10 (25.4)	135
21	5280 (1600)	10 (25.4)	135
22	5280 (1600)	12 (30.5)	135
31	5280 (1600)	6 (15.2)	135
110	200 (60.0)	18 (45.7)	125
111	5280 (1600)	10 (25.4)	120
112	5280 (1600)	12 (30.5)	120
113	5280 (1600)	8 (20.3)	120
121	5280 (1600)	8 (20.3)	120
122	5280 (1600)	6 (15.2)	120

Junction	Elevation [ft (m)]	Demand [gpm (lps)]
10	710 (216)	0.00
11	710 (216)	150 (9.46)
12	700 (213)	150 (9.46)
13	695 (212)	100 (6.31)
21	700 (213)	150 (9.46)
22	695 (212)	200 (12.6)
23	690 (210)	150 (9.46)
31	700 (213)	100 (6.31)
32	710 (216)	100 (6.31)

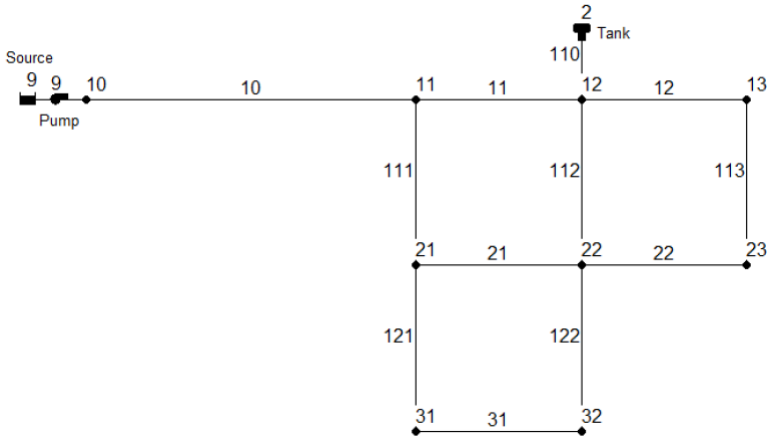

Figure 3: Water system map, as coded in EPANET software.

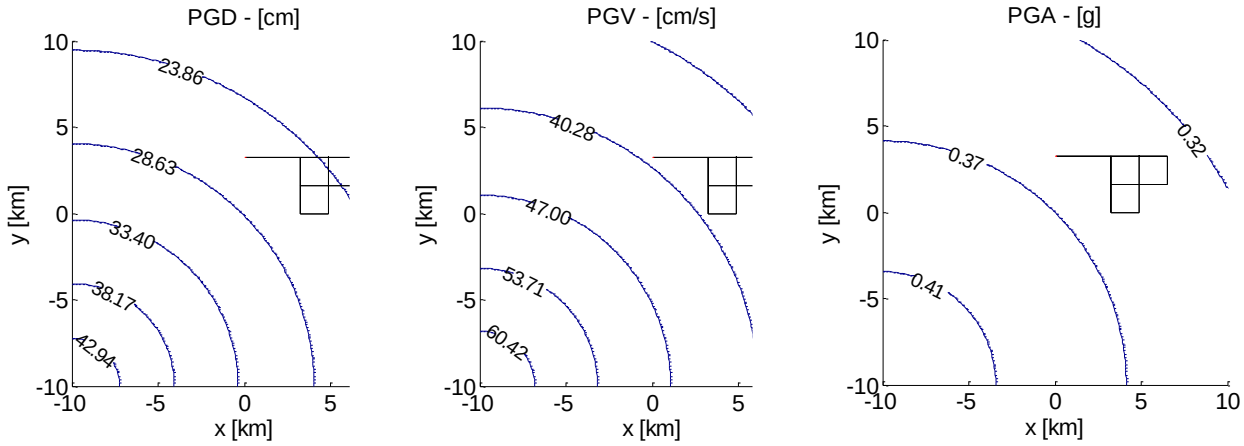

Figure 4: Intensity measures (PGD, PGV and PGA, from left to right) obtained through ground motion prediction equations [23]

Once the intensity measures of the considered hazard are known at each location, the damage to the elements of the system is evaluated. For nodal elements, such as pumping stations, tanks and treatment plants, the damage model uses fragility functions depending on PGA, while for pipelines, repair rate curves based on PGD and PGV are used. As described in Section 2, fragility curves provide the probability of attaining or exceeding a determined performance level. Four performance level curves delineate five damage states, varying from no damage (level 1) to collapse (level 5). A damage state is therefore associated with each element in the system. The HAZUS indicator for "extensive damage" (level 4) is used as the functionality threshold for tanks and pumps. Pumps with a damage level of four or greater are removed from the model and replaced with a pipe to allow water to be conveyed, but with no addition of head above static; tanks with a damage level of four or greater and their connecting pipes are removed from the hydraulic model and are no longer a water source for the system. Some of the junctions in the network model are demand nodes: they represent the small diameter distribution lines, which receive water from trunk lines and distribute it to customers. To take into account the water lost via leakage in the distribution system whose pipes are of too small a diameter to be included in the skeletonized system model, the demand at such nodes is temporarily increased in the immediate aftermath of the earthquake, as in GIRAFFE.

Damage in pipes are categorized as either leaks or breaks (generally referred to as "ruptures" in this paper). These two kinds of ruptures have different repair rate curves, depending on both PGD and PGV. The repair rate is modeled as a Poisson process to determine number and location of breaks and leaks along the pipe. Since pipelines are linear elements and repair rates are based on site-specific values of PGD and PGV, the simulation divides the pipeline into a number of segments, evaluates the intensity measures at the two ends of each segment, and sets the repair rate to their average value. Performing these calculations for a fixed number of segments may lead to an increase in the computational burden of the analysis. A more efficient approach could vary the length of the segments, depending on a percent variation of the considered intensity measure. Following the approach in GIRAFFE, a pipe leak is simulated as a fictitious pipe of cross-sectional area equal to the orifice area, with one end connected to the leaking pipe and the other end open to the atmosphere, simulated as an empty reservoir. For leaks, water loss is calculated based on orifice flow:

$$Q = A\sqrt{2gp/\gamma_w}$$

where A is the orifice area, g is gravitational acceleration, p is internal pipe pressure, and γ_w is the unit weight of water. A check valve prevents backflow from the artificial reservoir. A pipe break is modeled similarly, but with a complete breach in the original pipe, replacing it with two pipes connecting to artificial reservoirs with check valves. The artificial reservoirs with backflow prevention are a useful way to simulate water loss due to pipe damage, though this strategy does not account for the possibility of cross-contamination due to pipe ruptures.

After the damage analysis is completed for the immediate post-event damage at time zero, and for each subsequent recovery time-step, the output from the damage model is conveyed to the functionality model. A Python script reads the component identifier, damage level, and location (for pipe damage), and modifies the EPANET input file to reflect the damage. At each step, the EPANET input file is updated with remaining system damage, and operational values are retrieved from the previous time-step report file (i.e., tank levels, nodal quality measurements). Nodal demand is elevated only in the immediate aftermath of the event. The current model does not attempt to model the return of the elevated demands after time zero because of its uncertain interaction with the human behaviors of post-event demand changes, evacuation, and the decision to relocate. The process is iterated over a number of recovery time steps, until a user-defined desired level of functionality is met (in this study, we have used a desired level of 90 %).

Three indicators of water system functionality are considered: the quantity of demand satisfied, the ability to maintain system pressures, and the provision of safe, potable water quality. For each demand node in the system, these three functionality metrics are calculated for each recovery time-step, and compared to the baseline measurements at that node. Plots for each metric versus hour of recovery timeframe are provided for a representative demand node in the top three plots of **Error! Reference source not found.**. Because of changes in operating conditions during damaged operations and the recovery process, sometimes the recovered operations do not align with the unperturbed baseline cycle. In these cases, a range of baseline measurements may indicate whether operations can be considered normal. An alternate indication of recovery level is the return of the measurements to an acceptable operational threshold (e.g., a minimum pressure threshold of 15.0 psi or 103 kpa). Meeting acceptable operational thresholds is a less stringent measure of recovery than returning to baseline patterns. This is a measure of return to pre-event

conditions, which may only be possible through operational interventions beyond the current scope of this model (such as valve closures, altered pump operating schedules, etc.).

As shown in the bottom right plot in **Error! Reference source not found.**, these functionality metrics can be used to quantify system resilience. The functional recovery of the entire water system can be quantified in many ways. One way is with the percent of total system demand that is delivered. For recovery of pressure and quality, the sum of total nodal pressures and qualities conveys arguably less information than total system demand. For these indicators, it may be more useful to track the percentage of demand nodes that have satisfied the individual recovery metrics described above (return to the desired percent of baseline ranges or meeting an acceptable operational threshold). For pressure and quality recovery, the results are given in terms of the percentage of demand nodes that meet recovery thresholds. For water quality, the nodes without potential contaminant intrusion from cross-connections (whose quality measurements have returned to undetectable levels) are counted. For pressure, two different recovery indices may be used: return to at least 90 % of minimum baseline pressure for that node, or satisfaction of pressure levels above 15.0 psi (103 kpa). An alternate measure of demand recovery could be the percentage of demand nodes whose requested demand is being satisfied at each time-step. For demand recovery, the simpler indicator described is used (percentage of total system demand satisfied for each time-step).

While restoration of hydraulic functionality after physical damage is a primary consideration, another common issue for water utilities is ensuring safe water quality after a hazard event. Water quality testing, flushing and disinfection of new and repaired water mains, and the issuance and lifting of boil water advisories, are all immediate concerns during the recovery process. This analysis builds upon the water component damage representation described above by including the potential for cross-contamination and running a chemical transport analysis at each recovery time-step. Chemical transport is modeled in EPANET by introducing a setpoint booster with source quality of 1.0 to the endpoints of damaged pipes, as well as to each junction in the network where pressure has fallen below 15 psi (103 kpa). State-imposed thresholds are typically 15-20 psi (103-138 kpa) for water testing or automatic boil water notices, [25], [26]. The simulated contaminant is assumed to be conservative (non-decaying) and nonreactive. Without the potential for decay, the simulation will allow contaminant transport to any hydraulically feasible location, and only allow its removal through flushing or consumption at demand nodes. Although in reality, not every potential source for cross-contamination will necessarily become a location of chemical intrusion, this analysis uses a deterministic treatment of potential water quality threats. These assumptions correspond to a worst-case intrusion scenario, and reflect the conservative approach for issuing and lifting boil water advisories.

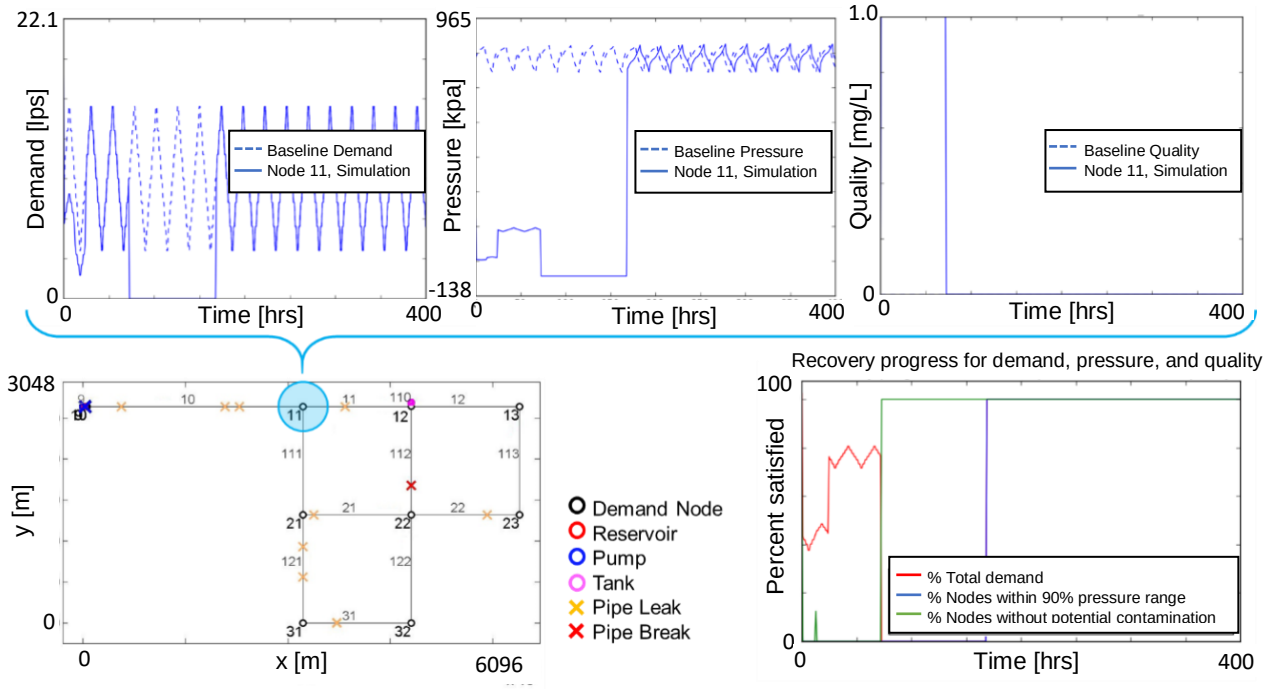

Figure 5: Top row: Variation of functionality metrics at Junction 11 (Water demand, pressure and quality from left to right). Bottom row: Water system in the damage scenario and functional recovery of the entire system.

CONCLUDING REMARKS

This paper presents a comprehensive approach to modeling water system resilience, which combines state-of-the-art methods to model both physical damage and functionality of water systems. The formulation has been demonstrated with reference to a water system, but it is general and applicable to different systems and hazards. The procedure described provides an estimate of key functionality metrics for water systems: water flow, pressure and quality. In future work, the formulation can be implemented in a Monte Carlo based simulation in order to quantify uncertainties in those estimates. Other future developments that may be achieved based on the presented formulation are: i) update current fragility curves, repair rate curves, and recovery functions considering a larger dataset of available data; ii) model the variation in demand during the recovery process; and: iii) model the cross-contamination considering operational changes (such as valve closures), in a less conservative way.

REFERENCES

[1] K. J. Tierney, "Business Impacts of the Northridge Earthquake," *Journal of Contingencies and Crisis Management*, vol. 5, no. 2, pp. 87-97, 1997.

[2] K. J. Tierney, "Impacts of Recent US Disasters on Businesses: The 1993 Midwest Floods and the 1994 Northridge Earthquake," in *Economic Consequences of Earthquakes: Preparing for the Unexpected*, 1995, pp. 189-222.

[3] N. S. Grigg, "Surviving Disasters: Learning from Experience," AWWA Research Foundation and American Water Works Association, 2002.

[4] N. S. Grigg, "Water Utility Security: Multiple Hazards and Multiple Barriers," *Journal of Infrastructure Systems*, vol. 9, no. 2, pp. 81-88, 2003.

[5] J. M. Wagner, U. Shamir and D. H. Marks, "Water distribution reliability: Simulation Methods.," *Journal of Water Resources Planning and Management*, vol. 114, no. 3, pp. 276-293, 1988.

[6] S. S. Ozger and L. W. Mays, "A semi-pressure-driven approach to reliability assessment of water distribution networks," in *Proceedings of the 30th IAHR Congress*, Thessaloniki, Greece, 2003.

[7] A. Pathirana, "EPANET2 Desktop Application for Pressure Driven Demand Modeling," in *Proceedings of the 12th Annual Conference of Water Distribution Systems Analysis 2010 WDSA2010*, Tucson, AZ, 2010.

[8] J. Muranho, A. Ferreira, J. Sousa, A. Gomes and A. Sa Marques, "Pressure-Dependent Demand and Leakage Modeling with an EPANET Extension - WaterNetGen," in *Proceedings of the 16th Conference on Water Distribution Systems Analysis - WDSA2014*, 2014.

[9] O. Ditlevsen and H. O. Madsen, Structure reliability methods, New York: Wiley, 1996.

[10] P. Gardoni, A. Der Kiureghian and K. M. Mosalam, "Probabilistic capacity models and fragility estimates for reinforced concrete columns based on experimental observations," *Journal of Engineering Mechanics*, vol. 128, pp. 1024-38, 2002.

[11] M. O'Rourke and G. Ayala, "Pipeline damage due to wave propagation," *Journal of Geotechnical Engineering*, vol. 119, pp. 1490-8, 1993.

[12] M. O'Rourke and E. Deyoe, "Seismic damage to segmented buried pipe," *Earthquake Spectra*, vol. 20, pp. 1167-83, 2004.

[13] A. L. A. (ALA), "Seismic Fragility Formulations for Water Systems: Part 1 - Guideline," 2001.

[14] C. Zorn and A. Shamseldin, "Post-disaster infrastructure restoration: A comparison of events for future planning," *International Journal of Disaster Risk Reduction*, vol. 13, no. 0, pp. 158-166, 2015.

[15] T. Tabucchi, B. Davidson and S. Brink, "Simulation of Post-earthquake Water Supply System Restoration," *Civil Engineering and Environmental Systems*, vol. 27, no. 4, pp. 263-279, 2010.

[16] A. L. Bonneau and T. D. O'Rourke, "Water supply performance during earthquakes and extreme events," MCEER: 234, 2009.

[17] M. Guidorzi, M. Franchini and S. Alvisi, "A multi-objective approach for detecting and responding to accidental and intentional contamination events in wtaer distribution systems," *Urban Water Journal*, vol. 6, no. 2, pp. 115-135, 2009.

[18] L. Alfonso, A. Jonoski and D. Solomatine, "Multiobjective optimization of operational responses for contaminant flushing in water distribution networks," *Journal of Water Resources Planning and Management*, vol. 136, no. 1, pp. 48-58, 2010.

[19] L. F. Gay Alanis, "Development of a Resilience Assessment Methodology for Networked Infrastructure Systems using Stochastic Simulation, with application to Water Distribution Systems," Virginia Tech Electronic Theses and Dissertations, 2013.

[20] Federal Emergency Management Agency, "HAZUS-MH 2.1 Technical Manual: Multi-Hazard Loss Estimation Methodology Earthquake Model," 2004.

[21] B. Cavdaroglu, E. Hammel, J. E. Mitchell, T. C. Sharkey and W. Wallace, "Integrating restoration and scheduling decisions for disrupted interdependent infrastructure systems," *Annals of Operations Research,* vol. 203, no. 1, pp. 279-294, 2013.

[22] R. Luna, N. Balakrishnan and C. Dagli, "Postearthquake Recovery of a Water Distribution System: Discrete Event Simulation Using Colored Petri Nets," *Journal of Infrastructure Systems,* vol. 17, no. 1, pp. 25-34, 2011.

[23] L. A. Rossman, "EPANET User's Manual," U.S.EPA, Cincinnati, OH, USA, 1994.

[24] N. Romero, T. D. O'Rourke, L. K. Nozick and C. A. Davis, "Seismic Hazards and Water Suppoy Performance," *Journal of Earthquake Engineering,* vol. 14, pp. 1022-1043, 2010.

[25] USEPA, "New or Repaired Water Mains," Washington, DC, USA, 2002.

[26] New Jersey Department of Environmental Protection Division of Water Supply & Geoscience, "Water Main Break Guidance Manual," Trenton, NJ, USA, 2014.

[27] J. Kumar, E. D. Brill, G. Mahinthakumar and S. R. Ranjithan, "Contaminant source characterization in wtaer distribution systems using binary signals," *Journal of Hydroinformatics,* vol. 14, no. 3, pp. 585-602, 2012.

[28] M. Propato, O. Piller and J. Uber, "A sensor location model to detect contaminants in water distribution networks," in *Proceedings of the World Water and Environmental Resources Congress 2005, May 15-19, 2005*, Anchorage, AK, USA, 2005.

[29] J. Kumar, E. D. Brill, G. Mahinthakumar and R. Ranjithan, "Identification of reactive contaminant sources in a water distribution system under the conditions of data uncertainties," in *Proceedings of the World Environmental and Water Resources Congress 2010, May 16-20*, Providence, RI, USA, 2010.

[30] J. A. Fernandez and G. J. Rix, "Soil attenuation relationships and seismic hazard analyses in the Upper Mississippi Embayment," in *Proceedings of the 8th US National Conference on Earthquake Engineering, 18-22 April 2006*, San Francisco, CA, USA, 2006.

2016 IEEE International Symposium on
Assembly and Manufacturing (ISAM)
Fort Worth, TX, USA, August 21-24, 2016

Simplified Framework for Robot Coordinate Registration for Manufacturing Applications

Jeremy A. Marvel Karl Van Wyk

Abstract— **A simplified framework is introduced for automatically and quickly registering the Cartesian coordinate systems of industrial robots to any other arbitrary coordinate system. This framework includes both explicit and implicit (sensor-based) registration techniques using as few as three reference poses per robot, and presents different methods for measuring registration uncertainty. Driven by the guiding principles of simplifying the registration process to enable rapid installation by non-expert users, a mathematical basis for fast system registration is presented. We also present methods for quickly and inexpensively approximating the registration errors, and outline mechanisms for improving registration performance. Several case study examples are provided in which the registration performance is captured across four different registration methods, and two different robots. A reference motion capture system is used to capture post-registration positioning accuracy of the robots, a sampling-based registration estimation technique is assessed, and results are systematically quantified.**

Keywords: robot registration, robot performance, multi-robot coordination

I. Introduction

Flexible robot automation encapsulates the idea that a single robot can be quickly and repeatedly reconfigured and retasked to accommodate multiple applications. With the current trends in lightweight and mobile robotic systems, the versatility of such robotic platforms is increased further with their ability to be rapidly relocated to new workstations for new applications. Moreover, with the advent of collaborative robot technologies, the historical need for hard mounts and safeguards is relaxed. However, such flexibility introduces new performance challenges for manufacturing applications.

Relocating or re-tasking robots requires the reprogramming of hard-coded, application-dependent robot positions in their respective coordinate systems. This brittle programming approach impacts the productivity of the manufacturing line by undermining software reusability. This inflexibility makes robot adoption by small- and medium-sized enterprises (SMEs) both needlessly complicated and prohibitively expensive. Two different schools of thought seek to minimize this impact. The first seeks to reduce the barrier to programming, effectively making the robots easier to program for targeted applications (e.g., [1]). The second removes the need to re-program robot positions by programming robot positions in the workspace or world coordinate frame (to which the robot registers itself), e.g., [2]. The first method pushes the process intelligence onto the robot's controller, and limits the functionality of robots to specific applications for which software has already been written. The second method requires quality registration to the world coordinate frame, which can be a burdensome process to ensure the minimization of registration errors.

The registration process and associated errors have been identified as one particular pain point for SMEs [3]. Coordinate system registration refers to the mapping of measurements in one system's frame of reference to the frame of reference of another. This process corrects for differences in coordinate system placement and orientation. In this paper, a framework is presented that reduces this burden by providing a mechanism for easy and automatic coordinate system registration with an equally easy method for estimating registration uncertainty. This framework automatically computes the homogeneous transformation from one coordinate system of any robot to any other arbitrary coordinate system and then measures the registration uncertainty using simple math and fast pose sampling. This work is inspired by the desire to make robotic solutions for smart manufacturing more accessible. It aims to do so by enabling multiple robots to be more flexible and adaptive, such that robot systems can be installed, configured, and programmed to operate quickly and with minimal negative impact on productivity. Further, this work provides a necessary precursor to enabling heterogeneous configurations of multiple robots (i.e., robots from different manufacturers with incompatible controllers) to work collaboratively on a single task.

This paper is split into the following sections: Section II provides a brief account of existing, commercial solutions for robot coordinate frame registration; Section III gives an outline of the registration process; Section IV enumerates various methods for acquiring the necessary input data for coordinate frame registration; Section V presents experimental results of four different registration methods across two different robotic platforms that demonstrate functionality, feasibility, and validity of the framework; and Section VI gives a discussion of results and future work.

II. Robot Coordinate Systems and Registration

In robotic applications, registration transforms poses from one coordinate system to poses in the robot's coordinate system. This transformation facilitates the hand-off of parts from one robot to another, and converts measurements from external camera systems to guide path planning for part acquisition and collision avoidance. For many industrial

Jeremy A. Marvel is with the National Institute of Standards and Technology, Gaithersburg, MD, USA (e-mail: jeremy.marvel@nist.gov).
Karl Van Wyk is with the National Institute of Standards and Technology, Gaithersburg, MD, USA (e-mail: karl.vanwyk@nist.gov).

Marvel, Jeremy; Van Wyk, Karl.
"Simplified Framework for Robot Coordinate Registration for Manufacturing Applications."
Paper presented at 2016 IEEE International Symposium on Assembly and Manufacturing (ISAM), Fort Worth, TX. August 21, 2016 - August 24, 2016.

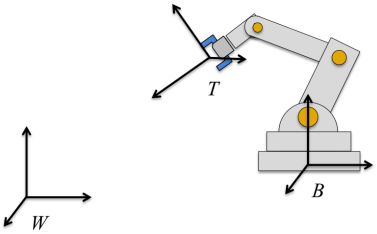

Fig. 1: Typical coordinate systems for industrial robots include the base (*B*) and tool (*T*) frames, and may also include external definitions (*W*) for world or workpiece frames.

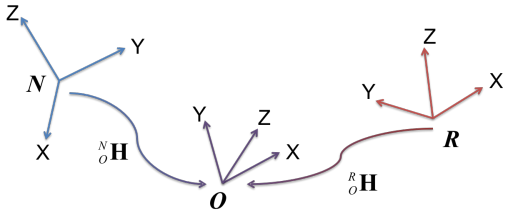

Fig. 2: The transformation from one arbitrary coordinate system, *R*, to another, *N*, relies on defining an intermediate coordinate system, *O*, with a known transformation to and from *R* and *N*.

robot systems, 6 degree-of-freedom (6DoF) poses (translations and rotations in Cartesian space) are typically defined in either the base frame or the tool frame (Fig. 1). The base frame, *B*, is usually located with its origin inside the base at or near the mounting flange. The tool frame, *T*, is located with its origin at the tool center point (TCP). Some robot vendors provide mechanisms for defining additional coordinate systems to enable a unifying world frame, *W*, for multiple robots or sensors. Furthermore, functionality may allow for the creation of a work frame (a task-relevant coordinate system) to which the robot is registered such that a robot or workpiece may be moved without requiring retraining of all hard-coded robot positions. Unfortunately, these capabilities are not universally available.

The process of registering between sensor systems is required for measuring more complex information about the world than is possible with a single sensor (e.g., measuring 3D point clouds using multiple 2D cameras [4]). The registration between a sensor system and a robot similarly enables more complex control capabilities. Depending on the level of integration, registering sensors to a robot coordinate system requires significant effort on the part of the system programmer. Sensor systems specifically designed for use with automation may provide the capability to define their own coordinate systems relative to the robot to minimize the effort needed for registration (e.g., [5]). Additionally, there exist some approaches in the literature to automatically register robot systems with external and robot-mounted (e.g., [6]) camera systems, though their use in general manufacturing applications is limited.

Registering multiple robots to accept command coordinates in a common coordinate system requires either a central point of control (e.g., [7]) or the provision of external world or work frames (e.g., [8]). Some multi-robot systems in the literature build internal representations of maps, and registration takes the form of aligning these maps using techniques common to machine vision [9]–[11].

III. 3-Point Registration Process

At the heart of our registration framework is a basic procedure for calculating a homogeneous transformation from one coordinate system (*N*) to another (*R*) by means of a third, intermediate coordinate system (*O*, Fig. 2). Such transformations may be used to register one robot's coordinate system to the coordinate system of another, or to register both robots' coordinate systems to a third coordinate system. This process consists of capturing 3D coincidental Cartesian points (*X*, *Y*, and *Z* coordinates) in both the *N* and *R* coordinate systems, and then constructing an arbitrary coordinate system, *O*, such that known homogeneous transformations exists from *O* to *N*, and from *O* to *R*. To accomplish this, the following assumptions must be satisfied:

- *N* and *R* are static (or have known transformations to static reference frames) for the collection of the registration data,
- The systems operating within *N* and *R* are calibrated to be within the users specifications for accuracy and repeatability, and
- All systems follow a right-handed orientation.

The process begins with the selection of at least three non-collinear points, $\mathbf{p}_1$, $\mathbf{p}_2$, $\mathbf{p}_3$, that can be measured in both the robot and world coordinate systems (Fig. 3a). Specifically, for each $\mathbf{p}_i = [p_{i,x}, p_{i,y}, p_{i,z}]^{\mathrm{T}}$, $1 \leq i \leq 3$, in the *R* coordinate system, there is a corresponding, co-located $\mathbf{p}_i$ in the *N* coordinate system. From these two sets of points, corresponding vectors, $\mathbf{v}_1$ and $\mathbf{v}_2$, linking $\mathbf{p}_1$ to $\mathbf{p}_2$ and $\mathbf{p}_1$ to $\mathbf{p}_3$ (Fig. 3b), respectively, are defined in both coordinate systems by:

$$\mathbf{v}_1 = \mathbf{p}_2 - \mathbf{p}_1, \tag{1}$$

$$\mathbf{v}_2 = \mathbf{p}_3 - \mathbf{p}_1, \tag{2}$$

Definitions for $\mathbf{v}_1$ and $\mathbf{v}_2$ are given in terms of the both the *R* and *N* coordinate systems (i.e., ${}^{R}\mathbf{v}_1$ and ${}^{N}\mathbf{v}_1$). These two vectors provide the bases for defining the intermediate right-hand coordinate system, *O*. The unit vector $\hat{\mathbf{x}}$ defines the *X* axis of *O*, and is aligned with v_1 in both *N* and *R* (Fig. 3c).

$$\hat{\mathbf{x}} = \frac{\mathbf{v}_1}{\|\mathbf{v}_1\|} \rightarrow {}^{N}\hat{\mathbf{x}}, {}^{R}\hat{\mathbf{x}} \tag{3}$$

The unit vector $\hat{\mathbf{y}}$ defines the Y axis of *O*, and is orthogonal to both v_2 and $\hat{\mathbf{x}}$ (Fig 3d).

$$\hat{\mathbf{y}} = \frac{\hat{\mathbf{x}} \times \mathbf{v}_2}{\|\hat{\mathbf{x}} \times \mathbf{v}_2\|} \rightarrow {}^{N}\hat{\mathbf{y}}, {}^{R}\hat{\mathbf{y}} \tag{4}$$

And the unit vector $\hat{\mathbf{z}}$ defines the Z axis of *O*, and is orthogonal to both $\hat{\mathbf{x}}$ and $\hat{\mathbf{y}}$ (Fig 3e).

$$\hat{\mathbf{z}} = \hat{\mathbf{x}} \times \hat{\mathbf{y}} \rightarrow {}^{N}\hat{\mathbf{z}}, {}^{R}\hat{\mathbf{z}} \tag{5}$$

Marvel, Jeremy; Van Wyk, Karl.
"Simplified Framework for Robot Coordinate Registration for Manufacturing Applications."
Paper presented at 2016 IEEE International Symposium on Assembly and Manufacturing (ISAM), Fort Worth, TX. August 21, 2016 - August 24, 2016.

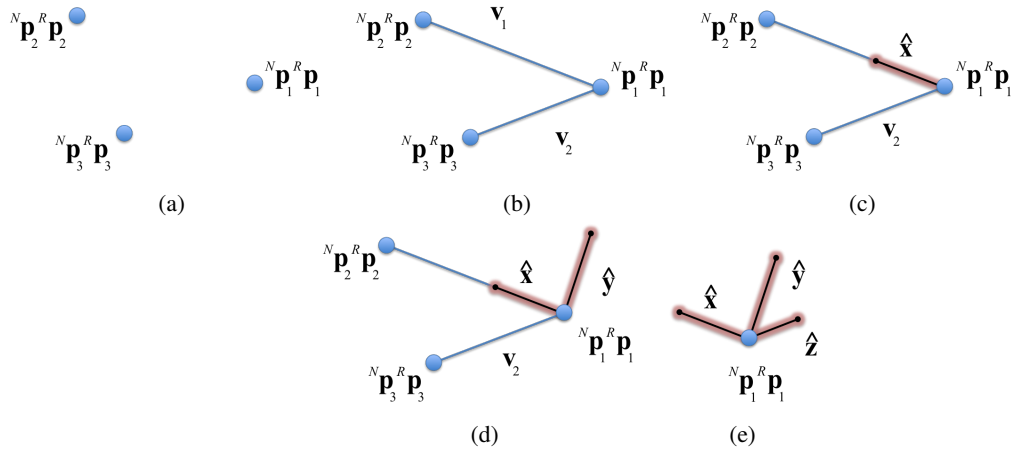

Fig. 3: The registration process is centered around the establishment of an intermediate coordinate system, *O*, using three, non-collinear sets of points (a). These three point clusters, and the vectors defining the edges connecting them (b), are then used to generate unit vectors (c-e) that establish the coordinate system *O*.

Given that $\hat{\mathbf{x}}$, $\hat{\mathbf{y}}$, and $\hat{\mathbf{z}}$ are orthonormal, they define the orientation of *O* in both *N* and *R*:

$$ {}^{N}_{O}\mathbf{R} = \begin{bmatrix} {}^{N}\hat{\mathbf{x}} & {}^{N}\hat{\mathbf{y}} & {}^{N}\hat{\mathbf{z}} \end{bmatrix} = \begin{bmatrix} {}^{N}\hat{\mathbf{x}}_x & {}^{N}\hat{\mathbf{y}}_x & {}^{N}\hat{\mathbf{z}}_x \\ {}^{N}\hat{\mathbf{x}}_y & {}^{N}\hat{\mathbf{y}}_y & {}^{N}\hat{\mathbf{z}}_y \\ {}^{N}\hat{\mathbf{x}}_z & {}^{N}\hat{\mathbf{y}}_z & {}^{N}\hat{\mathbf{z}}_z \end{bmatrix}, \tag{6} $$

$$ {}^{R}_{O}\mathbf{R} = \begin{bmatrix} {}^{R}\hat{\mathbf{x}} & {}^{R}\hat{\mathbf{y}} & {}^{R}\hat{\mathbf{z}} \end{bmatrix} = \begin{bmatrix} {}^{R}\hat{\mathbf{x}}_x & {}^{R}\hat{\mathbf{y}}_x & {}^{R}\hat{\mathbf{z}}_x \\ {}^{R}\hat{\mathbf{x}}_y & {}^{R}\hat{\mathbf{y}}_y & {}^{R}\hat{\mathbf{z}}_y \\ {}^{R}\hat{\mathbf{x}}_z & {}^{R}\hat{\mathbf{y}}_z & {}^{R}\hat{\mathbf{z}}_z \end{bmatrix}. \tag{7} $$

And because the origin of *O* is centered on $\mathbf{p}_1$, the homogeneous transformations from the origins of *O* to the origins of *N* and *R*, respectively, are defined as

$$ {}^{N}_{O}\mathbf{H} = \begin{bmatrix} & {}^{N}_{O}\mathbf{R} & & {}^{N}\mathbf{p}_1 \\ 0 & 0 & 0 & 1 \end{bmatrix}, \tag{8} $$

$$ {}^{R}_{O}\mathbf{H} = \begin{bmatrix} & {}^{R}_{O}\mathbf{R} & & {}^{R}\mathbf{p}_1 \\ 0 & 0 & 0 & 1 \end{bmatrix}, \tag{9} $$

Conversely, the homogeneous transformation from *R* to *O* is defined simply as the inverse of Eq. 9:

$$ {}^{O}_{R}\mathbf{H} = \left({}^{R}_{O}\mathbf{H}\right)^{-1} \tag{10} $$

The homogeneous transformation matrix, ${}^{N}_{R}\mathbf{H}$, takes a Cartesian point in the *R* coordinate system and transforms it into the *N* coordinate system, effectively registering the two coordinate systems together.

$$ {}^{N}_{R}\mathbf{H} = {}^{N}_{O}\mathbf{H}\,{}^{O}_{R}\mathbf{H} \tag{11} $$

Any arbitrary 6DoF pose, expressed as a homogeneous matrix, ${}^{R}\mathbf{H}_j$, in *R* is thus transformed to *N* by multiplying it by ${}^{N}_{R}\mathbf{H}$:

$$ {}^{N}\mathbf{H}_j = {}^{N}_{R}\mathbf{H}\,{}^{R}\mathbf{H}_j \tag{12} $$

Similarly, any arbitrary 6D pose in *N* can be transformed back to *R* by multiplying it by the inverse:

$$ {}^{R}\mathbf{H}_j = \left({}^{N}_{R}\mathbf{H}\right)^{-1}\,{}^{N}\mathbf{H}_j \tag{13} $$

IV. Pose Measurements

All registration information is derived from the ability to measure poses in Cartesian space. A software package can be written to take only the initial set of pose data, $P = \left\{{}^{R}\mathbf{p}_1, {}^{N}\mathbf{p}_1, {}^{R}\mathbf{p}_2, {}^{N}\mathbf{p}_2, {}^{R}\mathbf{p}_3, {}^{N}\mathbf{p}_3\right\}$, and automatically output ${}^{N}_{R}\mathbf{H}$ or provide a mechanism to convert any arbitrary pose in *N* or *R* to its respective counterpart. The requirements of the user are thus reduced to simply generating the pose data. In this section, a number of mechanisms for retrieving this data are outlined briefly, and many sources of measurement uncertainty associated with each mechanism are enumerated.

A. Manual Entry

The most direct (and potentially the least accurate and precise) mechanism for providing pose information is manually entering *X*, *Y*, and *Z* values. These measurements may be directly measured using external tools such as 1) digital or analog distance and angle indicators (e.g., measuring tape, calipers, and protractors), 2) manual transference of information acquired directly from the systems (e.g., transcribing pose measurements as displayed on a teach pendant or other human-computer interface (HCI) devices), or 3) through the design of the working environment (e.g., placing fiducials at positions known *a priori*, or using design features of environment components as measurement cues).

As the robot is moved throughout the work volume, the TCP poses are manually recorded. This process may be overly tedious and time consuming, particularly if multiple coordinate systems must be registered together. Moreover, manually measuring positions is prone to precision and measurement errors, which impacts the performance of the registration as a whole. Similarly, maneuvering through the design of the working environment may result in unexpected registration errors due to the unverified assumptions of product quality control. Specifically, extrusions, cuts, and connections may not be perfect, thus the assumptions of flatness, orientation, position, and distribution of components

need to be independently measured to compensate for small construction defects. Accuracy and precision may be improved by means of precision metrology equipment, but at the expense of increased cost and complexity.

B. Direct Kinematic Interfacing

Many robot systems allow for direct feedback access via remote connection to pose and state information. This information may be provided with higher precision than the readouts on HCI devices, and enables near instantaneous information regarding the robot's Cartesian pose, joint configuration, and input/output states. For multi-robot configurations in which the robots must register themselves automatically to one another, such functionality is required such that the robots can convey pose information directly.

It has been empirically observed with some robot systems that the robot state reported via the remote interfaces is not necessarily identical to the information displayed on the HCI. In some cases it was observed that this discrepancy was due to approximation errors of the HCI. In other instances, however, it was discovered that the errors originated from the discrepancies in reporting mechanisms. In general, measurement errors arise if the remotely accessed robot state is not provided in real time, if the information reported is stale, or if the pose data is not reported at a reliable frequency. Moreover, there may exist errors in the robot's kinematic model, which directly impacts positioning accuracy. Some compensation for such errors may be provided through externally tracking the robot, or correcting for uncertainty using noise models.

C. Force-based Center of Pressure (CoP)

Perhaps a more flexible method for collecting points required for spatial registration is through the use of a 6DoF force/torque transducer (load cell). When interacting with a load cell at a single point of application, the center of pressure may be estimated using the load cell's sensory data. For a rigid body, the well-known relationship between an extrinsically acting force $\mathbf{F} = [F_x, F_y, F_z]^T$, at a single point $\mathbf{p} = [p_x, p_y, p_z]^T$, and the induced moment $\mathbf{M} = [M_x, M_y, M_z]^T$ is defined as,

$$\mathbf{M} = \mathbf{p} \times \mathbf{F}. \tag{14}$$

Performing the cross product, a system of three scalar equations is established in matrix form,

$$\begin{bmatrix} M_x \\ M_y \\ M_z \end{bmatrix} = \begin{bmatrix} 0 & -F_z & F_y \\ F_z & 0 & -F_x \\ -F_y & F_x & 0 \end{bmatrix} \begin{bmatrix} P_x \\ P_y \\ P_z \end{bmatrix}, \tag{15}$$

where $\mathbf{M}$ and $\mathbf{F}$ are known via the load cell. This system of linear equations has infinitely many solutions since the matrix of forces is rank deficient. Therefore, at least one element of $\mathbf{p}$ must be known or one element can be expressed in terms of the remaining two elements using geometric information of the rigid body attached to the load cell. In the simplest case, a rigid plate of known, uniform thickness can be attached to the load cell to render one of the elements of $\mathbf{p}$ as known. Consequently, only two of the previous equations need to be solved to obtain the remaining elements of $\mathbf{p}$. A robot needs to interact with the load cell to yield at least three, noncollinear points, which is the minimum number necessary for spatial registration.

Given that there is more freedom in readily generating points for registration, one should avoid the following pitfalls: 1) do not generate all the contact points in a line, and 2) do not cluster contact points extremely close to one another as that makes the registration process more susceptible to sensory noise in the load cell. Ultimately, the accuracy of center of pressure estimation is dictated by the load cell's calibration, resolution, and noise level.

D. Camera-Based Localization

Camera-based observer systems are common within manufacturing for localizing parts and workpieces for processing. In some cases, similar systems can be used for monitoring the positions of robot systems for performance validation, collision avoidance, and coordinate system registration. In both instances, the camera systems and robots must be registered such that one can operate within the coordinate system of the other. In this subsection, a number of camera-based solutions for measuring the 6DoF pose of robot systems are described.

1) Fiducial-Based Localization: Rather than directly measuring the 6DoF pose of a robot, its pose may be inferred by measuring the locations of multiple target fiducials affixed to the robot, the robot's tooling, or a held workpiece. Such fiducials include 2D barcodes [12], passive retroreflective or active infrared emitter markers for motion capture systems, or artifacts that look different based on viewing angle [13].

Such mechanisms and artifacts are widely available and have documented performance benefits and limitations. For instance, 2D barcodes are cheaper and easier to distinguish than retroreflective markers due to their unique designs, but are subject to lighting and perspective issues. Similarly, commercial off-the-shelf motion capture systems are inherently easier to configure, calibrate, and integrate, but are negatively impacted by sources of light interference and marker size (smaller markers are harder to see, but the available density of larger markers within a given region is reduced). In all cases, the performance of the fiducial-based tracking system is subject to errors in the intrinsic and extrinsic camera calibrations, visual occlusions in the sensing volume, and decreased accuracy and precision as a function of fiducial size and distance from the cameras.

2) Shape-Based Localization: Markerless robot tracking methods include fitting robot models to 3D point cloud data [14], [15], evaluation of depth-space data to measure distance [16], and shape-based estimation of robot pose [17]. Some low-cost sensor solutions intended as input devices for HCI have been used as measurement systems (e.g., [18]), but are not intended for the context of robot registration. Subsequently, they are subject to errors from manufacturing quality, low sensor resolution, and shortcuts made both to

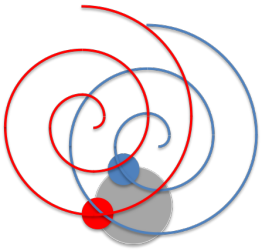

Fig. 4: Some search-based localization routines may halt as soon as a target is "found," which may occur at the periphery of the target. Initiating the search at different initial poses may have different localization results.

approximate measurements in the absence of full data and to keep costs low. In some cases, even when used for their intended purposes, such systems may still perform worse than more readily available and cheaper alternatives (e.g., using a computer mouse for system inputs [19]).

E. Laser-Based Localization

Similar to camera-based metrology solutions, laser-based systems may be used to localize the position of the robot by tracking fiducials located on or around the robot. Laser-based systems are generally more accurate than camera-based systems, but, whereas camera-based solutions can track multiple fiducials simultaneously, a given laser system is typically limited to tracking a solitary marker.

The use of extrinsic laser metrology systems (i.e., a laser tracking a fiducial mounted on the robot) is common, and is frequently used to track the tool flange of robot systems for basic robot performance evaluations (e.g., [20]). A single laser tracker will provide the 3D translation from the tracker's base to the retroreflective target. For full 6DoF solutions, however, an active target must be affixed to the robot's tool flange.

A different approach uses an intrinsic laser configuration in which the robot itself becomes the laser base. A laser emitter/detector is attached to the tool flange, and the robot servos either to maintain its bearing on a retroreflective target, or to find a target at some nominally defined location relative to the robot base. In cases where direct dynamic control of the robot is not possible, the latter of these two options would be used to register a robot to the world based on assumptions of the location of the retroreflective target plus an initial, rough approximation of the robot's base. The robot searches for the target based on where it expects to find it, and moves in a regular pattern until the target is located. Such searches are ultimately subject to the resolution of the search parameters, the size of target, and the initial search location. Simple implementations may stop the robot's search as soon as the laser detects the target (e.g., when performing a spiral search, Fig. 4), which is most likely to be on the target's periphery.

V. Registration Performance

As described in Section IV, there are a myriad of sources of measurement error. Depending on where the registration points are taken and the nature of the working environment, the errors may grow as a function of distance from the initial registration region. As such, it is important to understand how the selection of training points impacts registration performance. Here, the performance of the 3-point registration process using different pose measurement techniques on different robot platforms is evaluated and the results summarized.

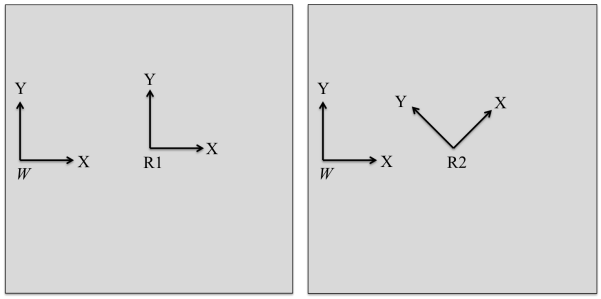

(a) (b)

Fig. 5: The locations and orientations of robots R1 and R2 relative to the world center, *W*. R1 has a lateral shift on both the *X* and *Y* axes, but its orientation is aligned with *W* (a). R2 has the same lateral shifts, but is rotated 45^o on the Z axis (b).

A. Test methodology

The registration methodology was validated in a heterogeneous robot configuration featuring two different robots with different capabilities, kinematics, and controllers. The first robot, R1, was a 7DoF, collaborative open-chain manipulator with sub-millimeter repeatability. It was rigidly mounted in an upright configuration, with its base frame oriented inline relative to the world center (Fig. 5a). The second robot, R2, was a 6DoF, collaborative open-chain manipulator with sub-millimeter repeatability. It was also rigidly mounted, but had its base frame oriented at a 45^o angle relative to the world origin (Fig. 5b). The motions of both robots were commanded via Ethernet from a central computer, but the robots and their controllers were kept in their stock configurations to handle kinematics and dynamics.

Performance testing started with randomly selecting 32 unique Cartesian poses expressed in the world coordinate system that were reachable by both robotic arms. Each of these poses were between 264 mm and 1223 mm (median 774 mm) from the world origin. These poses served as measurement sites for quantifying the error in TCP commands expressed in the world coordinate system (registration error) for either robot.

Three-point registration was performed for four different test cases in this paper. The first test case ("Short Hand") used a hand-guiding methodology in which the robot's TCP was physically moved to poses predefined in the world frame. These poses were defined by rigidly-mounted, 3D printed seats, distributed in an isosceles right triangle pattern with 150 mm leg lengths, with which the robots' tools docked

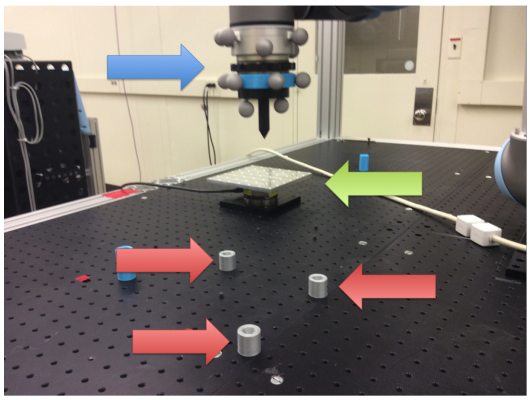

Fig. 6: Hand-guiding target seats (lower three red arrows) were rigidly mounted to the workspace, and had known translations to the world origin. A 6-axis load cell with an attached strike plate (center green arrow) was used for measuring the CoP, while tool-mounted retroreflective markers (top blue arrow) enabled a motion capture system to track the robot's TCP.

(Fig. 6). Hand-guiding the end effector enabled the robot to be coupled with the seats faster than if the robots had been jogged using the teach pendant. The second test case ("Long Hand") used the same hand-guiding methodology as the first, but with a larger registration pattern (300 mm leg lengths). The third test case ("CoP") used the CoP methodology described in Section IV-C. The fourth test case ("Average") used an element-wise average of the prior three homogeneous transformation matrices obtained from their respective registration methods.

Both R1 and R2 were used to evaluate the performance of each test case. For each method, the positions of the robots' TCPs were self-reported as described in Section IV-B, but were externally verified using an 8-camera motion capture system monitoring the $2\text{m} \times 2\text{m} \times 2\text{m}$ work volume. The motion capture system was calibrated such that the tracking of rigid objects (defined by a series of retroreflective targets mounted to the tool flange, Fig. 6) was accurate and repeatable to within 0.5 mm and 0.5°. The origin of the motion capture system was set to coincide with the origin of the world coordinate system.

B. Experimental Results

The results of the four previously mentioned test cases are presented in Table I. There are four key performance metrics for all test cases. These metrics capture the differences between the desired and actual poses of the robot in the world coordinate system, as measured by the reference system. At each of the 32 measurement sites, the L_2 norm was calculated between the desired and measured translations of the robot end-effector as expressed in the world coordinate system. Separately, the L_2 norm was calculated between the desired and measured rotations of the robot end-effector as expressed in the world coordinate system. Next, the mean and standard deviation were calculated across the 32 trials for the translations and rotations, separately.

TABLE I: Translation and orientation errors of the four test cases: Short hand-guiding pattern ("Short Hand"), long hand-guiding pattern ("Long Hand"), center-of-pressure ("CoP"), and averaging the registrations of Short Hand, Long Hand, and CoP ("Average").

Test Case	**Translation Error** *(Avg., Stdv.), mm*	**Orientation Error** *(Avg., Stdv.), deg*
$ShortHand(R1)$	(8.824, 4.851)	(1.566, 0.797)
$ShortHand(R2)$	(4.639, 1.226)	(0.893, 0.585)
$LongHand(R1)$	(11.478, 6.242)	(1.684, 0.992)
$LongHand(R2)$	(2.711, 0.943)	(0.744, 0.443)
$CoP(R1)$	(9.771, 5.274)	(1.568, 0.878)
$CoP(R2)$	(3.011, 1.105)	(0.773, 0.448)
$Average(R1)$	(10.000, 4.822)	(1.515, 0.895)
$Average(R2)$	(3.198, 1.064)	(0.786, 0.492)

A statistical analysis was performed on the experimental data to determine any significant differences in the results. In particular, the data sets were passed through the two sample Kolmogorov-Smirnov test at a confidence level of $\alpha = 0.05$. At this confidence level, there existed no statistical difference between any of the test cases for R1. Specifically, the average performances for each of the evaluated registration methods for R1 are subsumed by the standard deviations of performance. However, there does exist a statistical difference between all of the test cases for R2, except when comparing the CoP and Average registrations. This result suggests that the Long Hand registration yielded the smallest registration errors (of statistical significance) followed by the CoP and Short Hand registration methods. These results imply that larger spreads of registration points yield more accurate and more precise performance across the work volume of the robot.

Another perspective of the data is presented in Fig. 7 and Fig. 8. In these figures, the robot TCP translation and rotation errors are plotted against the translation and rotation distances (L_2 norm) from the world coordinate system. This depiction of the data was used to unveil any trends in world-based positioning errors. When looking at Fig. 7, R1 experienced a positive correlation between translation error and translation distance for all test cases. In contrast, this positive trend does not appear to exist for R2. However, there does exist an increasing disparity between test cases for either robot with increasing translation distances from the world coordinate system. When looking at Fig. 8, trends do not appear as clearly. The only perceptible trend is that there is a slight positive correlation between rotation error and rotation distance for R1.

C. Alternative Verification Methodology

Recognizing that specialized tracking and metrology sensor systems are atypical for most SME environments, an alternative, low-cost methodology for registration verification was also evaluated. This methodology focuses on placing single collared seats throughout the work volume to test and correct minor translation errors. Moving under force control, the robot inserts the tool tip into the seats. The seat collars force translation and rotation adjustments of the TCP. The

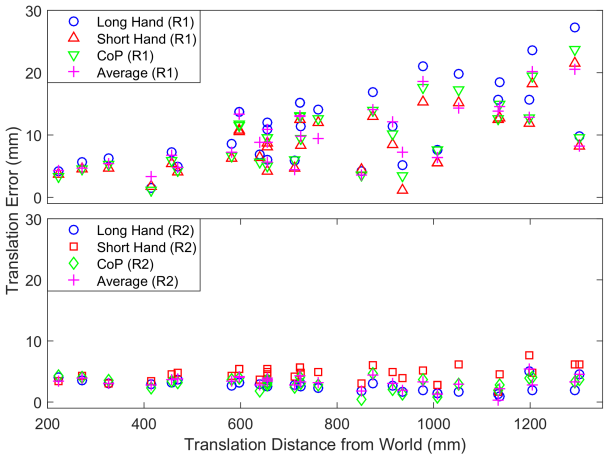

Fig. 7: Translation error as a function of the L_2 norm of translation from World.

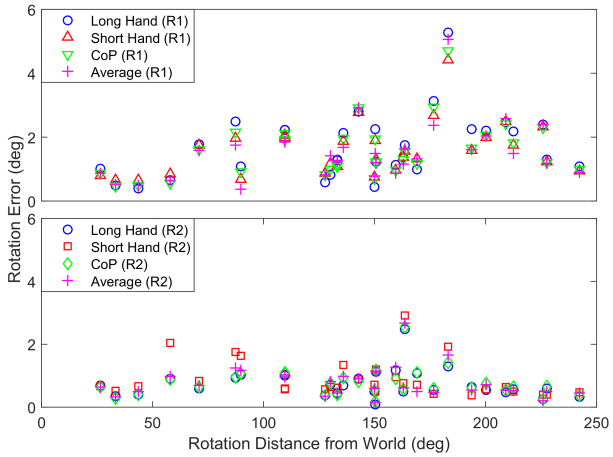

Fig. 8: Rotation error as a function of the L_2 norm of rotation from World.

nominal pose at the final insertion depth is known *a priori*, and provides a localized correction for the registration errors at that location. Six such seats were placed throughout the work volume, and the results of R1 and R2 docking with them using the Long Hand registration are reported in Table II and Table III, respectively.

The translation and rotation errors ("Trans. Error" and "Rot. Error," respectively) are reported as the L_2 norm separating the self-reported, seated poses of the robots and the nominal poses of the seats. As was observed using the motion capture reference system, the distance from world ("World Dist.") and the magnitudes of translation and rotation error are positively correlated. Moreover, the results of this self-reporting of errors are roughly equivalent with the results described in Section V-B. The difference between the self-reported and measured translations and rotations ("Trans. Delta." and "Rot. Delta." respectively) are proportional to

TABLE II: Reduced point-based verification results for R1 using the Long Hand registration based on a series of known poses throughout the work volume.

Nominal Seat Pose	World Dist. (mm)	Trans. Error (mm)	Rot. Error (deg)	Trans. Delta (mm)	Rot. Delta (deg)
(50, -400, 10, 180, 0, 0)	403.24	2.27	0.82	1.01	0.64
(575, -525, 10, 180, 0, 0)	778.68	4.56	0.86	1.48	0.65
(1175, -400, 10, 180, 0, 0)	1241.26	15.89	0.61	14.57	0.46
(1175, 425, 10, 180, 0, 0)	1249.54	24.11	0.39	17.46	0.93
(575, 550, 10, 180, 0, 0)	795.75	16.30	0.55	10.50	1.64
(50, 425, 10, 180, 0, 0)	428.05	9.09	0.87	5.25	1.27

TABLE III: Reduced point-based verification results for R2 using the Long Hand registration based on a series of known poses throughout the work volume.

Nominal Seat Pose	World Dist. (mm)	Trans. Error (mm)	Rot. Error (deg)	Trans. Delta (mm)	Rot. Delta (deg)
(50, -400, 10, 180, 0, 0)	403.24	0.57	0.25	0.24	0.25
(575, -525, 10, 180, 0, 0)	778.68	1.40	0.97	0.74	1.72
(1175, -400, 10, 180, 0, 0)	1241.26	3.13	0.48	1.28	1.03
(1175, 425, 10, 180, 0, 0)	1249.54	2.83	0.37	0.10	0.47
(575, 550, 10, 180, 0, 0)	795.75	1.40	0.90	0.89	0.08
(50, 425, 10, 180, 0, 0)	428.05	1.03	0.91	0.90	0.50

the registration errors as a function of distance. This method may thus be used to quickly and inexpensively self-report rough approximations of registration errors without requiring external measurement systems for verification.

This process has the added benefit of producing even more input data that may be subsequently and automatically used to improve overall registration performance. A new coordinate system origin may be placed at any of these verification sample locations when combined with the original registration data set. Registration performance may thus be improved by utilizing multiple associated coordinate systems, where the coordinate system origin is chosen as that which has the shortest distance to the target robot pose.

VI. Discussion

In this paper, a simplified framework was presented that registers robots to any arbitrary coordinate systems. The performances of several registration mechanisms were compared through a systematic evaluation test method that measured translation and rotation error. In general, the performance of these different registration mechanisms was found to be largely comparable, though a clear indicator of registration performance is the spread magnitude of the sampling pattern P. Moreover, several sources of registration uncertainty were

identified, including measurement error, robot kinematic uncertainty, and manufacturing irregularities.

Furthermore, the performance metrics described in this paper provide a clear, general indication of position errors associated with spatial registration. Since robot system integration will likely require a specific positioning tolerance to yield successful applications, the described test method and performance metrics can be used to quantify post-registration position performance. The test method may also be used for benchmarking registration techniques.

A. Planned Improvements to the System

From the results discussed earlier, it is clear that the accumulation of errors in the system impairs the performance of a global registration as a function of translation and orientation magnitude. If one were to notice a trend of worsening performance as a function of distance, as was seen in Section V-B, one may resort to providing multiple local (e.g., quadrant-based) registrations to "re-center" the robot depending on where it is operating (e.g., the alternative verification seats used in Section V-C).

Likewise, it is believed that both the precision and accuracy can be improved by applying machine learning to automatically correct for registration errors. For example, statistical analysis (e.g., k-means clustering [21]) and data mining (e.g., bagging [22]) may be used to automatically generate multiple local registrations throughout the work volume. Alternatively, neural networks may be used to approximate and correct for the nonlinear shifts in registration performance throughout the work volume.

B. Ongoing Work

Based on the experience gained from this exercise, ongoing efforts are focused on further developing and simplifying the interface to improve the user experience. For example, based on the system inputs described in Section IV, a simplified interface with more functionality is being developed. Planned improvements include the ability to dynamically switch between registrations, and the development of a more robust mechanism for combining multiple registrations than the simple averaging described in V-B.

Similarly, an automatic registration correction mechanism is being developed that automatically "re-centers" the global registration for localized regions. This process moves the robot to *a priori* defined test poses, measuring the pose error, and creating homogeneous transformations that correct for the error.

Finally, a more comprehensive suite of registration evaluation test methods is being developed that uses both systematic and application-based performance metrics. This test suite will include specifications for inexpensive verification and validation mechanisms (e.g., on-arm sensing such as cameras for fine-tuning registration performance at a local level). In contrast, the methodology used during the initial registration evaluations was dependent on an expensive motion capture system, the calibration of which required an extensive front-loaded effort.

DISCLAIMER

Certain commercial equipment, instruments, or materials are identified in this paper to foster understanding. Such identification does not imply recommendation or endorsement by the National Institute of Standards and Technology, nor does it imply that the materials or equipment identified are necessarily the best available for the purpose.

REFERENCES

[1] C. Fitzgerald, "Developing baxter: A new industrial robot with common sense for u.s. manufacturing," *Proc. Technol. Pract. Rob. Applic.*, pp. 1–6, 2013.

[2] H. Akeel and A. Watnabe, *Design of robot controllers*. John Wiley and Sons, Inc., 1999, ch. 12, pp. 213–244.

[3] J. Marvel, E. Messina, B. Antonishek, L. Fronczek, and K. V. Wyk, "NISTIR 8093: Tools for collaborative robots within SME workcells," National Institute of Standards and Technology, Tech. Rep., 2015.

[4] D. A. Forsyth and J. Ponce, *Computer Vision: A Modern Approach*. Upper Saddle River, New Jersey, USA: Prentice Hall, 2003.

[5] N. B. Figueroa, F. Schmidt, H. Ali, and N. Mavridis, "Joint origin identification of articulated robots with marker-based multi-camera optical tracking systems," *Rob. Auton. Syst.*, vol. 61, no. 6, pp. 580–592, 2013.

[6] K. Danilidis, "Hand-eye calibration using dual quaternions," *Int. J. Rob. Res.*, vol. 18, pp. 286–298, 1998.

[7] Y. Gan, X. Dai, and D. Li, "Off-line programming techniques for multirobot cooperation system," *Int. J. Adv. Rob. Syst.*, vol. 10, 2013.

[8] T. Tarn, A. Bejczy, and X. Yun, "Design of dynamic control of two cooperating robot arms: Closed chain formulation," *Proc. IEEE Int. Conf. Rob. Autom.*, pp. 7–13, 1987.

[9] R. Rocha, J. Dias, and A. Carvalho, "Cooperative multi-robot systems: A study of vision-based 3-d mapping using information theory," *Rob. Auton. Syst.*, vol. 53, pp. 282–311, 2005.

[10] S. Carpin, "Fast and accurate map merging for multi-robot systems," *Auton. Rob.*, vol. 25, pp. 305–316, 2008.

[11] P. Koch, S. May, M. Schmidpeter, M. Kuehn, and C. Pfitzner, "Multi-robot localization and mapping based on signed distance functions," *Proc. IEEE Int. Conf. Auton. Rob. Syst. Compet.*, pp. 77–82, 2015.

[12] M. Fiala, "Artag, a fiducial marker system using digital techniques," *Proc. IEEE Comput. Soc. Conf. Comput. Vision Pattern Recognit.*

[13] C. English, G. Okouneva, and A. Choudhuri, "Shape-based pose estimation evaluation using expectivity index artifacts," *Proc. Perf. Metrics Intell. Syst Work.*, pp. 64–68, 2012.

[14] A. Broun, C. Beck, T. Pipe, M. Mirmehdi, and C. Melhuish, "Building a kinematic model of a robot's arm with a depth camera," *Adv. Auton. Rob.*, pp. 105–116, 2012.

[15] M. Klingensmith, T. Galluzzo, C. Dellin, J. Bagnell, and N. Pollard, "Closed-loop servoing using real-time markerless arm tracking," *Proc. IEEE Int. Conf. Rob. Autom. Hum. Works.*, 2013.

[16] F. Flacco, T. Kroger, A. Luca, and O. Khatib, "A depth space approach to human-robot collision avoidance," *Proc. IEEE Int. Conf. Rob. Autom.*, pp. 338–345, 2012.

[17] P. Hebert, N. Hudson, J. Ma, T. Howard, T. Fuchs, M. Bajracharya, and J. Burdick, "Combined shape, appearance and silhouette for simultaneous manipulator and object tracking," *Proc. IEEE Int. Conf. Rob. Autom.*, pp. 2405–2412, 2012.

[18] J. A. Marvel, M. Franaszek, J. L. Wilson, and T. Hong, "Performance evaluation of consumer-grade 3d sensors for static 6dof pose estimation systems," *Proc. SPIE 8499, Appl. Digital Image Process. XXXV*, pp. 849 905 1–11, 2012.

[19] A. Pino, E. Tzemis, N. Ioannou, and G. Kouroupetroglou, "Using kinect for 2d and 3d pointing tasks: Performance evaluation," *Human-Computer Interaction. Interaction Modalities and Techniques*, pp. 358–367, 2013.

[20] T. Chang, T. Hong, M. Shneier, G. Holguin, J. Park, and R. Eastman, "Dynamic 6dof metrology for evaluating a visual servoing system," *Proc. Perf. Metrics. Intel. Syst. Work.*, pp. 173–180, 2008.

[21] J. A. Hartigan, *Clustering Algorithms*. John Wiley and Sons, Inc, 1975.

[22] L. Breiman, "Bagging predictors," *Mach. Learn.*, vol. 24, pp. 123–140, 1996.

MODELING OF DOUBLE-ANGLE CONNECTIONS FOR ROBUSTNESS EVALUATION OF STEEL GRAVITY FRAMES

Jonathan M. Weigand
National Institute of Standards and Technology, Gaithersburg, MD 20899 USA
jonathan.weigand@nist.gov

Judy Liu
Oregon State University, Corvallis, OR 97330 USA
judy.liu@oregonstate.edu

Joseph A. Main
National Institute of Standards and Technology, Gaithersburg, MD 20899 USA
joseph.main@nist.gov

ABSTRACT

Component-based models of bolted double-angle beam-to-column connections have been developed for evaluating the structural robustness of steel gravity frames. The component-based models were developed based on results from high-fidelity finite-element models, which used solid elements to model the bolts, angles, and wide-flange sections, with explicit modeling of contact and friction. Fracture was modeled using element erosion with a plastic-strain-based failure criterion and reduced ductility at the “k-area” of the angle. The high-fidelity analyses were used to investigate the influence of span length on connection failure, including angle deformations at fracture. The component-based approach modeled each bolt row using a nonlinear load-displacement relationship that captured the effects of plastic hinge formation, straightening of the angle legs, and tearing of the angle near the heel. The component-based analysis results were compared with experimental data for double-angle connections subjected to combined rotation and axial extension representative of column loss scenarios.

INTRODUCTION

Bolted double-angle beam-to-column connections are common in steel gravity framing systems and have demonstrated substantial deformation capacity in simulated column loss scenarios (Liu et al. 2012). Component-based connection models provide an efficient framework for modeling the behavior of connections under extreme loads by providing

automatic coupling between the in-plane flexural and axial connection behaviors, a feature that is essential for modeling connections under column removal. The computational efficiency of the component-based modeling approach makes it well suited for evaluating the robustness of entire buildings. This paper presents a component-based model for steel bolted-angle connections that was developed based on insights obtained from high-fidelity finite element analysis. Results from the high-fidelity analyses are first presented, including the influence of span length and observations on angle deformations at failure. The component-based modeling approach is then presented, and predictions of the model are compared to experimental data for bolted angle connections tested under a simulated column loss scenario.

HIGH-FIDELITY FINITE-ELEMENT MODELING

Modeling Approach

The behavior of the bolted double-angle connections was first investigated using high-fidelity finite-element models, as illustrated in Figure 1, which were previously validated through comparisons with experimental data under axial loading and under a column removal scenario (Liu et al. 2012). The models were developed using the LS-DYNA finite-element software package (Hallquist 2007). The double angles, bolts, and wide-flange sections were modeled using 8-node solid elements with selective-reduced integration. The typical element size was about 2.6 mm (0.10 in) in the beam and column near the connecting elements and about 1.3 mm (0.05 in) in the bolts. The element size for the angles was on the order of 1.3 mm (0.05 in) to best capture plastic hinging mechanisms and fracture. The radius of the fillet at the heel of the angle was explicitly modeled. All components were initially in contact; static and dynamic friction coefficients of 0.3 were used.

Piecewise linear plasticity material models, calibrated to match data from tensile coupon tests, were used to model the steel. Finite element models of tensile coupons with appropriate gage length and element size were used to ensure that calculated engineering stress-strain curves corresponded to the test data. The plastic strain limit for each material (e.g., A36, A992) was calibrated to match the elongation at fracture from the tensile coupon tests. Element erosion, or removal of elements upon reaching an effective plastic strain limit, simulated fracture of the steel (Liu et al. 2012).

As proposed by Liu et al. (2012), the fracture strain in the heel of the angle was reduced to 60 % of the measured percent elongation for tensile coupons taken from the angle legs. This reduced the ductility at the critical location in the k-area, the region in the angle leg just past the fillet. The reduction in ductility at the k-area proposed by Liu et al. (2012) was based on comparisons to data from monotonic and cyclic tests of double-angle connections in tension (Garlock et al. 2003, Shen and Astaneh-Asl 1999). Reduced ductility in the k-area of an angle was also supported by coupon test data from Yang and Tan (2012). For W-shapes, Tide (2000) showed that percent elongation values at fracture were significantly smaller for coupons taken from the k-area than for coupons taken from

the web and flanges, because the k-area properties were affected by the rotary straightening process conducted in the mill. It has been acknowledged (Rees-Evans 2011) that rotary straightening and cold-working of steel angles could similarly result in reduced ductility in the k-area of the angles.

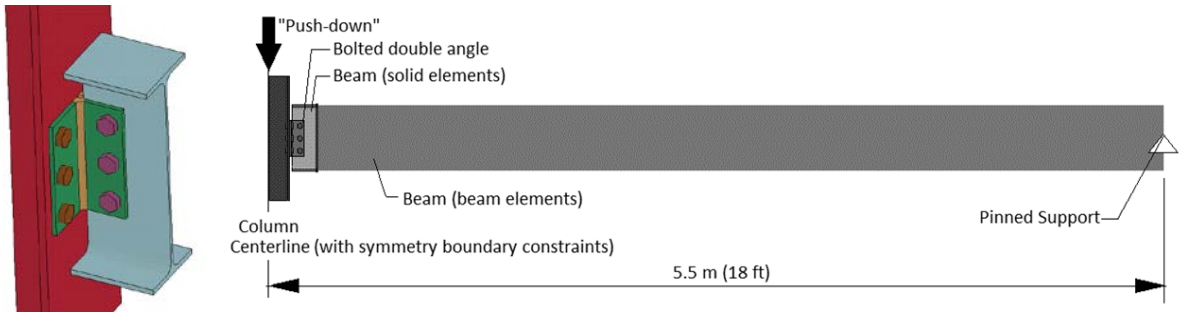

Figure 1: Two-span beam specimen modeled using symmetry boundary constraints

Influence of Span Length on Connection Failure

The influence of span length on failure of double-angle connections was investigated for a two-span beam assembly with exterior pin supports subjected to displacement-controlled vertical loading of the unsupported center column. This configuration corresponds to a full-scale test series conducted by the Defense Threat Reduction Agency and the General Services Administration (Stevens et al. 2011). Only a single span of the assembly was modeled, with symmetry boundary conditions at the column centerline (Figure 1). The beams and column were A992 W16×26 and W10×49 shapes, respectively. The A572 Grade 50, 216 mm (8.5 in) deep angles were L4×3.5×5/16. Three rows of 19 mm (0.75 in) ASTM F1852N tension control (TC) bolts were placed in standard holes at a column-leg gage of 76 mm (3 in) and a beam-leg gage of 64 mm (2.5 in). The bolts had a beam web edge distance of 51 mm (2 in) and the top bolt was located 130 mm (5 in) from the top of beam. As illustrated in Figure 1, high-fidelity modeling was used for the connection, while most of the beam span was modeled with beam elements, using constraints to enforce continuity of displacement and rotation at the interface. Additional details of the model can be found in Liu et al. (2012).

The influence of beam span was investigated by comparing results for the original 5.5 m (18 ft) beam span with results for models with span lengths of 2.7 m (9 ft) and 9.1 m (30 ft), using the same beam cross section and connection in all cases. Plots of computed horizontal reactions versus chord rotations (Figure 2(a)) show that fracture of the double-angle connection occurred at lower chord rotations for longer spans. Due to kinematics of the subassembly, a longer beam span results in greater elongation at the connection for the same beam chord rotation.

Compared to the variation in the chord rotation at failure shown in Figure 2(a), Figure 2(b) shows that the horizontal deformation of the angle at first fracture was only slightly affected by the span length. First fracture occurred at the bottom of the angle at the k-area of the column leg and propagated upward through the angle under continued

loading. While the angle's horizontal deformation at complete fracture increased somewhat with decreasing span, the angle's deformation at first fracture was nearly constant, with values of 37 mm (1.5 in), 34 mm (1.3 in), and 35 mm (1.4 in) for span lengths of 2.7 m (9 ft), 5.5 m (18 ft), and 9.1 m (30 ft), respectively. This consistency in the angle's deformation at fracture supported the use of a component-based modeling approach with a consistent value of angle deformation at failure, regardless of the span length. In the component-based approach, complete fracture of the connection is represented by successive fracture of each component in the connection, which allows the chord rotation at complete fracture to vary with span length as shown in Figure 2(b).

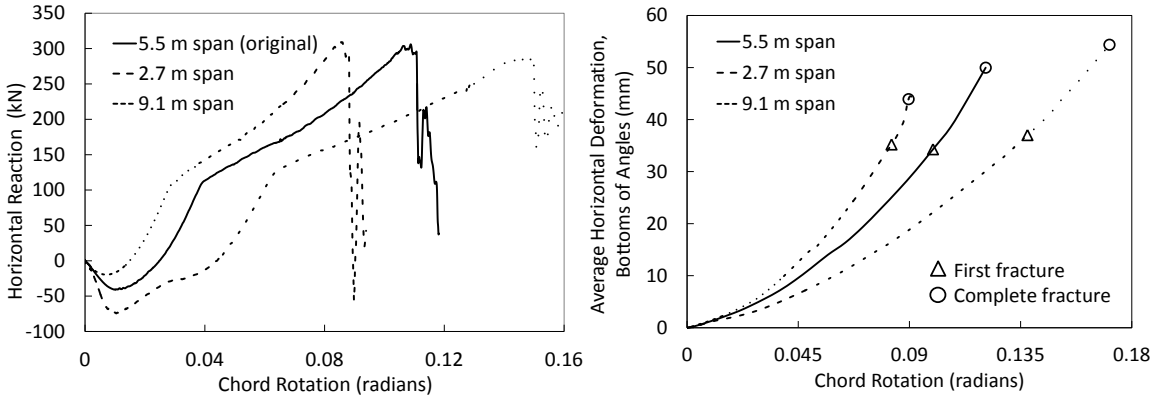

Figure 2: (a) Horizontal reactions versus chord rotation for different beam spans; (b) average horizontal deformation of angle versus chord rotation

Geometry of Deformed Angle

Figure 3 shows the geometry of a single angle in plan view, obtained from a high-fidelity finite element model in which the column leg and the beam leg of the angle were truncated at the centerlines of the column-leg bolts and the beam-leg bolts, respectively, and the angle was idealized as fully fixed at these cross sections. Figure 3(a) shows the initial, undeformed geometry of the angle, where k is the distance between the angle heel and the toe of the angle radius, g_c is the column gage length of the angle (i.e., distance between the angle heel and the centerline of the column-leg bolt), g_b is the beam gage length of the angle (i.e., distance between the angle heel and the centerline of the beam-leg bolt), and t is the angle thickness. Figure 3(b) shows the deformed geometry of the angle, in which the angle deformation along the beam axis, δ, is measured from the column face to the deformed position of the angle heel. The angle lengthens and straightens as it deforms, with two plastic hinges forming in the column leg, as indicated in Figure 3(b). This results in lateral deformation of the beam leg, δ', and curvatures γ and γ' at the ends of the k-area in the column and beam legs, respectively. As is discussed subsequently, results of the high-fidelity analyses allowed relationships to be established between the curvatures and strains at the k-area, enabling the development of the component-based model.

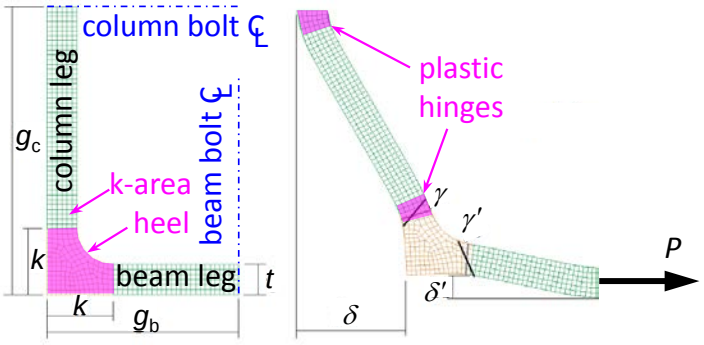

Figure 3: Angle geometry: (a) initial; (b) deformed.

COMPONENT-BASED CONNECTION MODEL

Component-based connection models provide a versatile analytical framework that can be used to model the responses of connections under extreme loads, such as column removal. In the component-based model described in this paper, the connection is discretized into multilinear component springs that are assembled into a configuration representing the geometry of the connection (Figure 4), where each component spring embodies an isolated characteristic-width segment of the two angles.

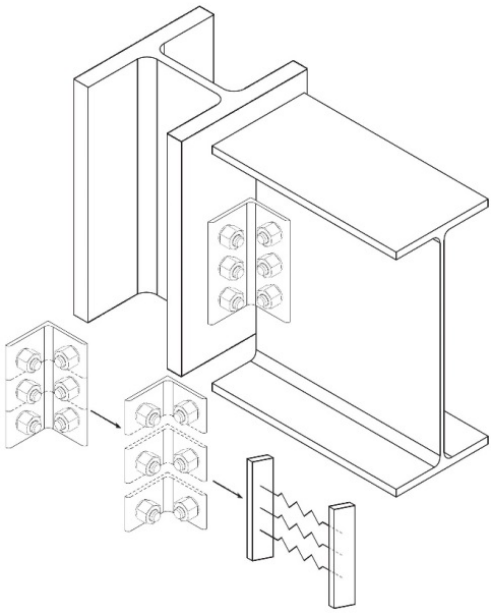

Figure 4: Discretization of bolted angle into characteristic-width angle-segments

Load-Deformation Relationship

As illustrated in Figure 5, the nonlinear behavior of the angle segment is represented through a piecewise-linear relationship between the axial load *P* and the angle deformation δ (see Figure 3). A single angle is considered with a component width *b* obtained by dividing the total depth of the angle by the number of bolts. The load

corresponding to one bolt row of a double-angle connection is obtained by doubling P. The yield capacity P_y corresponds to formation of plastic hinges in the column leg of the angle, and the ultimate capacity P_u is associated with fracture of the angle at the k-area.

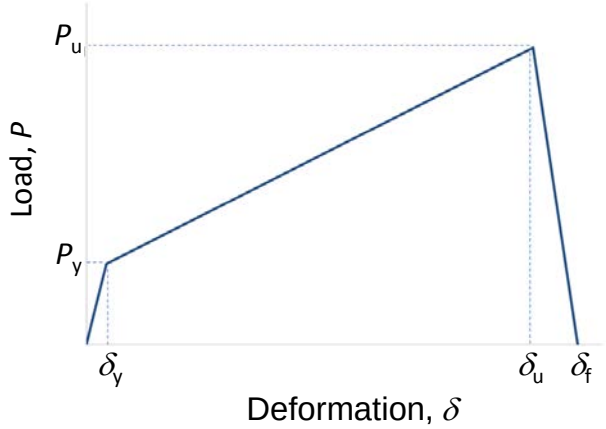

Figure 5: Load-deformation relationship for angle

Plastic Hinge Formation at Yield Load

The yield load, corresponding to the formation of two plastic hinges in the column leg of the angle (Figure 3(b)) is given by

$$P_y = \frac{2M_p}{g_{eff}}, \quad (1)$$

where $M_p = (bt^2/4)F_y$ is the plastic moment capacity of the component-width angle segment, F_y is the yield strength of the angle, $g_{eff} = g_c - k - d_h/2$ is the effective gage length of the angle's column leg after formation of the plastic hinges (i.e., the distance between the plastic hinges), and d_h is the diameter of the column-leg bolt holes. The angle deformation at the formation of the plastic hinges, δ_y, can be calculated as

$$\delta_y = \frac{P_y}{K_i}, \quad (2)$$

where K_i is the initial stiffness of the angle segment. The initial stiffness is calculated from the following expression, which was derived by Shen and Astaneh-Asl (2000) based on the geometry of the section of angle between the beam-leg bolt and the column-leg bolt, assuming elastic bending of the angle's column leg:

$$K_i = \frac{12EI}{g_c^3}\left[1 - \frac{3g_b}{4(g_c + g_b)}\right], \quad (3)$$

where E is the modulus of elasticity of steel and $I = bt^3/12$ is the moment of inertia of the angle.

Angle Fracture at Ultimate Load

Expressions for the ultimate load P_u (i.e., the load corresponding to initial tearing in the angles) and the corresponding angle deformation δ_u are derived based on the simplified geometry shown in Figure 6, in which the angle's column leg is modeled as a straight-line segment with concentrated plastic hinges at its ends, subjected to axial tension T_u, shear force V_u, and bending moment M_u. The plastic hinge lengths are assumed equal to the angle thickness t.

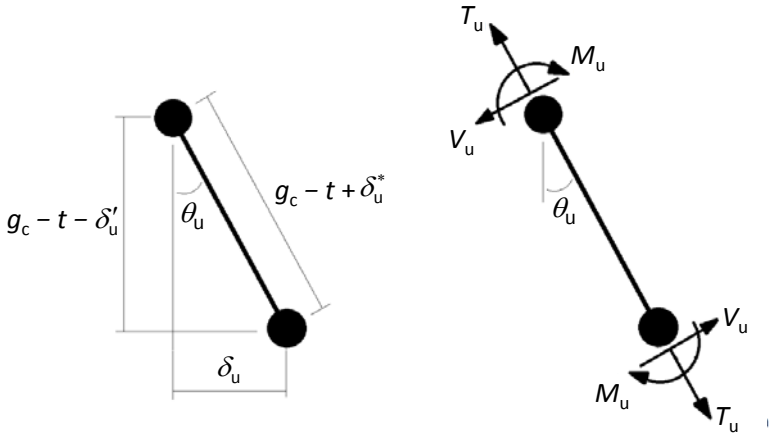

(a) (b)

Figure 6: Two-hinge idealization of the angle's column leg at the ultimate load: (a) geometry and (b) free-body diagram.

Equilibrium of forces along the beam axis yields the following expression for P_u:

$$P_u = V_u \cos\theta_u + T_u \sin\theta_u \ , \tag{4}$$

in which the chord rotation of the angle's column leg, θ_u, can be calculated as

$$\theta_u = \cos^{-1}\left(\frac{g_c - t - \delta'_u}{g_c - t + \delta^*_u}\right) , \tag{5}$$

where δ^*_u is the elongation of the column leg at the ultimate load. The shear and axial tension in the angle's column leg are calculated as

$$V_u = \alpha P_y \quad \text{and} \quad T_u = \alpha b t F_y / 3 \ , \tag{6a,b}$$

in which α = 1.2 is a strain-hardening coefficient. The expression for T_u in Eq. (6b) assumes that the cross-section is fully yielded with a linear strain profile based on observations from high-fidelity models, in which the tensile and compressive strains at the faces of the angle's column leg at fracture (at the toe of the angle radius) were found to be ε_{uk} and $\frac{1}{2}\varepsilon_{uk}$, respectively, where ε_{uk} is the elongation at fracture at the k-area. This observed strain profile can be decomposed into a bending strain of $\frac{3}{4}\varepsilon_{uk}$ and an axial strain of $\frac{1}{4}\varepsilon_{uk}$, from which the column-leg elongation can be calculated as $\delta^*_u = \frac{1}{2} t \varepsilon_{uk}$,

assuming that axial elongation occurs only at the plastic hinges, with plastic hinge lengths of *t*. As proposed by Liu et al. (2012), in the absence of test data for the k-area, 60 % of the reported elongation from certified mill test reports or tests of coupons from the leg of the angle is recommended for ε_{uk}.

The lateral deformation of the beam leg, δ'_u in Eq. (5), is calculated from the geometry:

$$\delta'_u = (g_b - t)\sin(\gamma'_u(k-t)/2) \approx \gamma'_u(g_b - t)(k-t)/2 . \quad (7)$$

Based on the observed strain profile at the ultimate load, noted above, the curvature of the angle's column leg at the end of k-area can be calculated as

$$\gamma_u = \frac{3\varepsilon_{uk}}{2t} . \quad (8)$$

The curvature of the angle's beam leg at the end of the k-area, γ'_u in Eq. (7), can be related to the curvature of the angle's column leg, γ_u in Eq. (8), through the following empirical equation, based on the results of high-fidelity finite-element analyses (to be published):

$$\gamma_u / \gamma'_u = r + \left(r^3 - 1\right)\left(t - \tfrac{5}{16}\right) + (r^5 - 1)(t - \tfrac{5}{16})^2 , \quad (9)$$

where $r = g_c / g_b$ is the ratio of the angle's gage lengths. Eq. (9) is considered to be applicable for thickness, *t*, from 6.4 mm (0.25 in) to 15.9 mm (0.63 in), and gages, g_b and g_c, from 51 mm (2.0 in) to 76 mm (3.0 in). Also, g_c should be greater than or equal to g_b. The ultimate deformation of the angle can be calculated from the geometry as

$$\delta_u = \left(g_c - t - \delta_b\right)\tan\theta_u . \quad (10)$$

The failure deformation, at which the load *P* drops to zero, is taken as $\delta_f = 1.1\delta_u$.

Comparisons with Experimental Data

Results of the component-based connection model were compared with experimental measurements from bolted-angle connection tests reported by Weigand and Berman (2015). In that study, the connections were tested under combined rotation and axial deformation demands representative of a column loss scenario, corresponding to displacement-controlled vertical loading of an unsupported center column in a two-span beam assembly. The double-angle connections at both ends of each beam span were assumed to be identical, and the end columns were assumed to be fixed, so that all deformations occurred in the connections and beams. In the component-based modeling, a single beam span was considered, assuming symmetry of the response about the unsupported center column. The load-deformation relationship for single-plate shear connections from Main and Sadek (2014) was used for the compressive response of the connections, with yield and ultimate capacities corresponding to the combined bearing strength at the bolt holes of the two angles' beam legs.

Figure 7 shows a comparison of measured and computed values of the vertical load applied to the unsupported center column and the horizontal reaction at the end column for a double-angle connection with three bolt rows (Weigand and Berman 2015, specimen ba3b|34|14). For that connection test, the thickness of the angles was t = 6.4 mm (0.25 in) and the gages of the column leg and the beam leg were g_c = 76 mm (3.0 in) and g_b = 70 mm (2.8 in), respectively. The measured yield strength of the angle steel was F_y = 382 MPa (55.4 ksi). Initial differences between the measured and computed values, for displacements less than about 300 mm (11.8 in), resulted from frictional resistance of the connection due to pre-tensioning of the bolts, which was not considered in the model. The subsequent response, after frictional slippage and loss of pre-tension, is captured fairly well by the component-based model. The peak vertical load and the peak horizontal reaction from the model exceed the measured values by 9 % and by 0.7 %, respectively. The model prediction for the center column displacement at the ultimate vertical load was 7 % less than the experimental value.

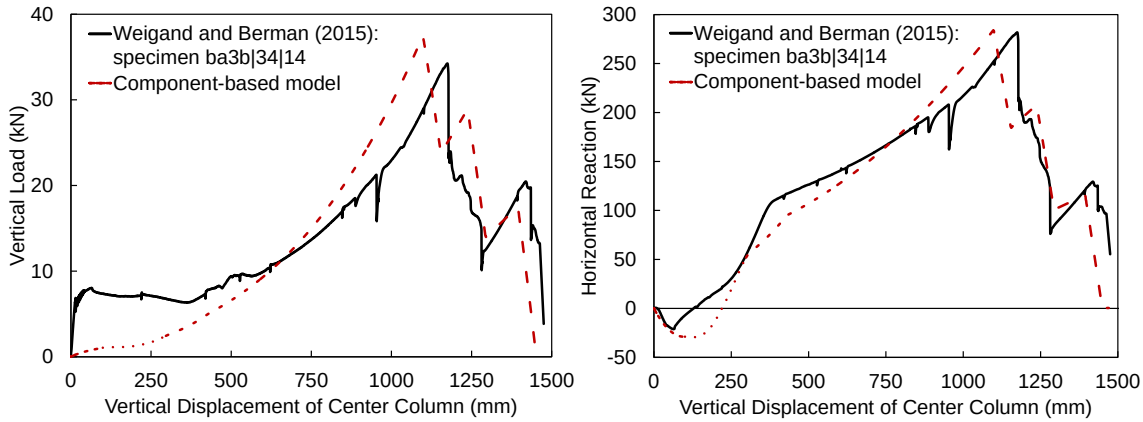

Figure 7: Comparisons of component-based model with experimental measurements for a double-angle connection with three bolt rows (estimated uncertainty in experimental data is less than ±0.5 %, based on repeated calibrations of instruments)

CONCLUSIONS

Building on insights obtained from high-fidelity finite element analyses of bolted double-angle connections, a component-based model was developed to capture the response of the connections under the combined axial and flexural loading that occurs in column removal scenarios. The high-fidelity modeling provided key insights on the initiation of angle fracture at a consistent level of deformation and the relationship between strains and curvatures in the angle at the point of fracture. By considering the mechanics of angle deformation associated with the formation of two plastic hinges in the column leg of the angle, equations were developed for the yield capacity and the ultimate capacity of the angle, along with the corresponding deformations. Using these equations, a nonlinear load-displacement relationship was defined to represent the axial response for each bolt row of the angle. Predictions of the component-based model were compared with experimental results for a bolted double-angle connection under a column removal scenario, showing that the model captured the key features of the measured response.

ACKNOWLEDGMENTS

This study was partially supported by the NIST/ UMD-ARRA Fellowship. The authors would like to thank Fahim Sadek of NIST for valuable comments and input on this work.

DISCLAIMER

Certain commercial software or materials are identified to describe a procedure or concept adequately. Such identification is not intended to imply recommendation, endorsement, or implication by NIST that the software or materials are necessarily the best available for the purpose.

REFERENCES

Garlock, M.M., Ricles, J.M., and Sause, R. (2003). “Cyclic Load Tests and Analysis of Bolted Top-and-Seat Angle Connections,” *J. Struct. Eng.,* Vol. 129, Issue 12, pp. 1615-1625.

Hallquist, J. (2007). *LS-DYNA Keyword User’s Manual, Version 971,* Livermore Software Technology Corporation, Livermore, CA.

Liu, J., Main, J. and Sadek, F. (2012) “Modeling of Double-Angle Shear Connections for Evaluation of Structural Robustness,” *Proc., 6th Congress on Forensic Engineering*, San Francisco, CA, October 31 – November 3, 2012, pp. 1081 – 1090.

Main, J.A. and Sadek, F. (2014). “Modeling and Analysis of Single-Plate Shear Connections under Column Loss,” *J. Struct. Eng*, 04013070, pp. 1-12.

Rees-Evans, D. (2011). “Re: Steel Angle Question,” message to J. Liu, 27 Sept. 2011, e-mail.

Shen, J. and Astaneh-Asl, A. (1999) “Hysteretic Behavior of Bolted-Angle Connections,” *J. Constructional Steel Research*, Vol. 51, pp. 201–218.

Stevens, D., Crowder, B., Sunshine, D., Marchand, K., Smilowitz, R., Williamson, E., and Waggoner, M. (2011). “DoD Research and Criteria for the Design of Buildings to Resist Progressive Collapse,” *J. Struct. Eng.*, Vol. 137, Issue 9, pp. 870-880.

Tide, R.H.R. (2000) “Evaluation of Steel Properties and Cracking in ‘k’-area of W Shapes,” *Engineering Structures*, Vol. 22, Issue 2, pp. 128-134.

Weigand, J. M. and Berman, J. W. (2015) “Integrity of Bolted Angle Connections Subjected to Simulated Column Removal,” *J. Struct. Eng.*, 04015165, pp. 1-13.

Yang, B. and Tan, K.H. (2012) “Numerical Analyses of Steel Beam-Column Joints Subjected to Catenary Action,” *J. Constructional Steel Research*, Vol. 70, pp. 1–11.

The Influence of Chamber Size on Chemical Emissions from Closed Cell Spray Polyurethane Foam

Dustin Poppendieck[1*], Mengyan Gong[1]

[1]Indoor Air Quality and Ventilation Group, National Institute of Standards and Technology, 100 Bureau Drive, Mail Stop 8633, Gaithersburg, MD 20899-8633, USA

[*]*Corresponding email: dustin.poppendieck@nist.gov*

SUMMARY
Spray polyurethane foam (SPF) insulation is widely used to improve building energy efficiency. Efforts are underway within ASTM subcommittee D22.05 to develop a standard method to characterize vapor phase emissions from SPF using micro-chamber systems. This study aims to examine whether chemical emission rates from SPF using two different size micro-chamber systems are comparable. Chemical concentrations in the chamber exhaust air were measured six times over a one-week period. The results indicated that emission rates of 1,4 dioxane from closed cell SPF in two different size micro-chamber systems were statistically different, while the emission rates of 1,2 dichloropropane were not statistically different, under the conditions of the proposed method.

PRACTICAL IMPLICATIONS
Reported chemical emission rates from SPF using micro-chambers should describe the chamber size along with emission rates.

KEYWORDS
Spray Polyurethane Foam (SPF), Indoor air quality, Micro-chambers, Emission rate

1 INTRODUCTION
Spray polyurethane foam (SPF) insulation improves building energy efficiency by reducing both conductive and convective heat losses through the building envelope. SPF is produced at the construction site by mixing two sets of chemicals, including methylene diphenyl diisocyanate, flame retardants, catalysts, blowing agents, and polyols. Different mixtures of the chemicals result in different products for different uses, for example open versus closed cell foam. Collaborative efforts are underway within ASTM subcommittee D22.05 to develop methods to characterize vapor phase emissions from SPF using micro-chamber systems (Poppendieck et al. 2016). One question in the development of this method is whether the emission rates from different size micro-chamber systems are comparable under the proposed method.

2 MATERIALS/METHODS
Emissions from both open and closed cell SPF were tested using two micro-chamber systems of different chamber size (Table 1). To ensure the chambers were operated at the same area specific flow rate, the flow rate of each chamber in the 48 mL and 116 mL system was set to 25 mL/min and 50 mL/min, respectively. For each type of SPF, five samples were tested in the 48 mL system simultaneously, while three were tested in the 116 mL system. Air samples were collected at 2 h, 24 h, 50 h, 76 h, 121 h, and 144 h, by sampling the chamber exhaust using sorbent tubes. Temperature was set to 35 ˚C for each chamber system and monitored by inserting a NIST traceable thermocouple into an unused chamber filled with water during the experiment period. Flow rates were measured using a NIST traceable bubble flow meter.

Concentrations of tris(1-chloro-2-propyl) phosphate (TCPP), bis (2-dimethylaminoethyl) ether (BDMAEE), 1,4 dioxane, and 1,2 dichloropropane were quantified using a thermal desorption/gas chromatogram-mass spectrometer (TD/GC-MS). The average emission specific rates (air concentration times volume of sampled air/sampling time/emission area) were calculated based on the measured concentrations.

Table 1. Experimental Conditions Tested. Surface areas are the projected areas. Data after ± represent the standard deviation.

Foam Type	Chamber Size	Chamber Volume (mL)	Foam Surface Area (cm^2)	Temperature (˚C)	Flow Rate (mL/min)
Open	Small	48	16	34.5 ± 0.2	24 ± 0.7
Open	Large	116	33	31.3 ± 0.05	48 ± 1.3
Closed	Small	48	16	34.5 ± 0.2	24 ± 0.8
Closed	Large	116	33	35.4 ± 0.3	46 ± 2.6

3 RESULTS AND DISCUSSION

Data for open cell foam were not used as the large chamber did not meet the temperature requirements (35 ˚C ± 1 ˚C) of the proposed method (Table 1). TCPP data from the closed cell foam were also not used, as they did not meet quality assurance criteria. For closed cell SPF, the impact of the chamber size was chemical dependent (Figure 1). For 1,2-dichloropropane, the average emission rates were not statistically different, while the average emission rates of 1,4 dioxane were statistically different at all sampling times (MANOVA, $p<0.05$). The higher boiling point of 1,4 dioxane (117 ˚C) relative to 1,2 dichloropropane (83 ˚C) may explain the differing results. For 1,4 dioxane, the difference between the average emission rates from the two chambers was larger for the first sampling period than for the later period, which may reflect that the mass transfer coefficient over the foam surface influenced the emission rate more at the early stage of the emission period more than the later stage.

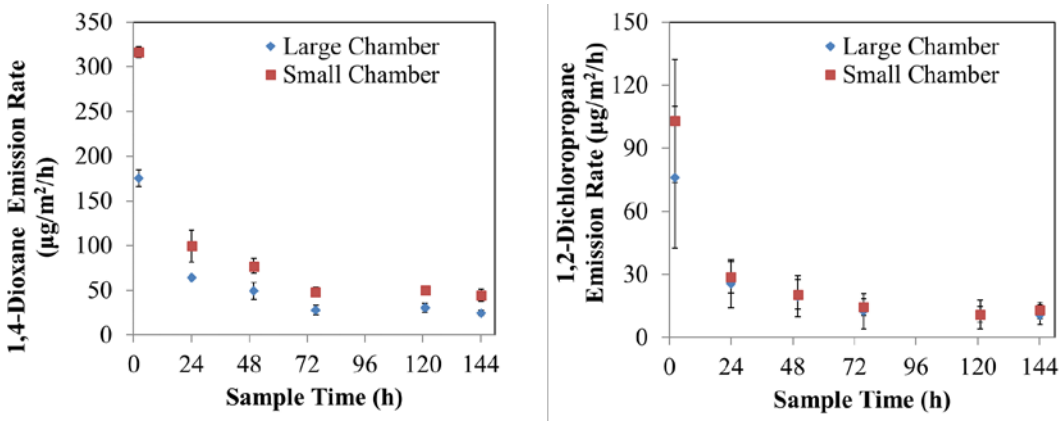

Figure 1. Emission rates from 1,4 dioxane and 1,2 dichloropropane from closed cell foam.

5 CONCLUSIONS

This study indicates that comparison of chemical emission rates from SPF using micro-chamber with different sizes should be done with caution and that the chamber size should be reported along with emission rates.

6 REFERENCES

Poppendieck, D.; M. Schlegel; A. Connor; A. Blickley. “Flame Retardant Emissions from Spray Polyurethane Foam Insulation.” Accepted for publication. ASTM Selected Technical Papers. 2016.

Online Airtightness Savings Calculator for Commercial Buildings in the United States, Canada, and China

Som Shrestha, PhD, BEMP
Member ASHRAE

Diana Hun, PhD

Lisa Ng, PhD
Member ASHRAE

Andre Desjarlais

Steven Emmerich
Fellow ASHRAE

Laverne Dalgleish
Associate Member ASHRAE

ABSTRACT

The relative contribution of air leakage to heating and cooling loads has been increasing as the thermal resistance of commercial building envelopes continues to improve. Easy-to-access data are needed to convince building owners and contractors that enhancing the airtightness of new and existing buildings is the next logical step to achieve a high-performance building envelope. To this end, Oak Ridge National Laboratory, the National Institute of Standards and Technology, the Air Barrier Association of America, and the U.S.-China Clean Energy Research Center for Building Energy Efficiency partnered to develop an online calculator that estimates the potential energy and cost savings in major U.S., Canadian, and Chinese cities from improvements in airtightness. This tool will have a user-friendly graphical interface that accesses a database of CONTAM and EnergyPlus prerun simulation results and will be available to the public at no cost. Baseline leakage rates are either user specified or selected by the user from a list of supplied leakage rates. Users will then enter the expected airtightness after the installation of an air barrier system. Energy costs are estimated based on the building location and other user inputs. This paper provides an overview of the methodology implemented in this calculator as well as example results. The deployment of this calculator could influence construction practices, contributing to significant reductions in energy use and greenhouse gas emissions from the United States, Canada, and China.

INTRODUCTION

The U.S. Department of Energy's (DOE) *Windows and Building Envelope Research and Development: Roadmap for Emerging Technologies* (DOE 2014) indicates that improving airtightness is among the most cost-effective strategies to decrease energy loads due to the building envelope. This conclusion is based on the fact that air leakage (i.e., infiltration and exfiltration) is responsible for about 6% of total energy used by commercial buildings in the United States, or about 15% of primary energy consumption in commercial buildings that is attributable to fenestration and building envelope components in 2010 was due to air leakage (DOE 2014). Nevertheless, improving airtightness is not always recognized by owners of commercial buildings, as they have been slow in acknowledging and diminishing the detrimental effects of air leakage on energy use and other aspects of building performance. The construction industry needs a credible, easy-to-use tool that estimates potential energy and financial savings in a standardized manner so designers and contractors can give building owners compelling reasons to invest in reducing air leakage.

Although air leakage has long been recognized as a key contributor to heating and cooling loads, methods that estimate its effects on energy consumption vary due to the complexity of this task (Crawley et al. 2008; Goel et al. 2014; Gowri et al. 2009; Ng et al. 2012). Comprehensive building design and energy simulations should take into account the fact that air leakage rates vary due to the operation of heating, ventilation, and air-conditioning (HVAC) systems, occupancy, and weather (i.e., indoor-to-outdoor temperature and wind). However, typical energy simulations tend to take shortcuts to expedite the analysis, such as assuming constant leak-

Som Shrestha and **Diana Hun** are research and development staff members and **Andre Desjarlais** is the program manager of the Building Envelope Systems Research Group at Oak Ridge National Laboratory, Oak Ridge, TN. **Lisa Ng** is a mechanical engineer and **Steven Emmerich** is the group leader of the Indoor Air Quality and Ventilation Group at the National Institute of Standards and Technology, Gaithersburg, MD. **Laverne Dalgleish** is the executive director of the Air Barrier Association of America, Walpole, MA.

Dalgleish, Laverne; Emmerich, Steven; Hun, Diana; Ng, Lisa; Shrestha, Som.
"Online Airtightness Calculator for the US, Canada and China."
Paper presented at Buildings XIII conference, Clearwater, FL. December 4, 2016 - December 8, 2016.

age rates and/or using simplified algorithms, which can lead to under- or over-estimated energy usage. Also, use of macro climate data versus micro climate data may impact the pressure distribution on buildings, and hence the infiltration rate. However, quantifying the impact of using macro climate data is beyond the scope of this paper.

Oak Ridge National Laboratory (ORNL), the National Institute of Standards and Technology (NIST), the Air Barrier Association of America (ABAA), and the U.S.-China Clean Energy Research Center for Building Energy Efficiency (CERC BEE) are collaborating to develop an online calculator that will be free to the public, user friendly, and powerful enough to address the previously mentioned variables when estimating energy savings due to improvements in airtightness. Figure 1 describes the general steps to achieve this goal. The tool will use a database of EnergyPlus pre-run simulation results for DOE commercial prototype buildings. The main difference between the online calculator and the procedure followed in the DOE prototypes is that the calculator utilizes CONTAM-calculated air changes per hour (ACH) or air leakage rates as inputs, whereas the prototypes make simplified assumptions that are described in the following sections of this paper. CONTAM (Dols and Polidoro 2015) is a multizone airflow and contaminant transport analysis software developed at NIST and validated by multiple studies, such as Haghighat and Megri (1996), Chung (1996), Emmerich (2001), and Emmerich et al. (2004). This software takes into account multiple variables, such as weather conditions, envelope airtightness, and HVAC system operation, to calculate air leakage rates through the building enclosure. The CONTAM-calculated hourly air leakage rates are imported into DOE's whole-building energy simulation software EnergyPlus (DOE 2016a) with the CONTAM Results Export Tool (Polidoro et al. 2016). EnergyPlus is then used to calculate the effect of air leakage on energy consumption.

In addition to CONTAM, the Airflow Network module in EnergyPlus could have been used to calculate the air leakage rates through the building envelope. However, comparing results from CONTAM and the Airflow Network were beyond the scope of this project. Future efforts may cover this assessment.

The ultimate objective of the tool is for users to be able to estimate expected energy and financial savings for different airtightness levels in commercial buildings that are located in the United States, Canada, and China. This paper presents an overview of this calculator and results for a stand-alone retail building prototype in Chicago, Winnipeg, and Shanghai.

BUILDING MODELS

In order to cover a large percentage of the common building types in the United States, the calculator uses DOE

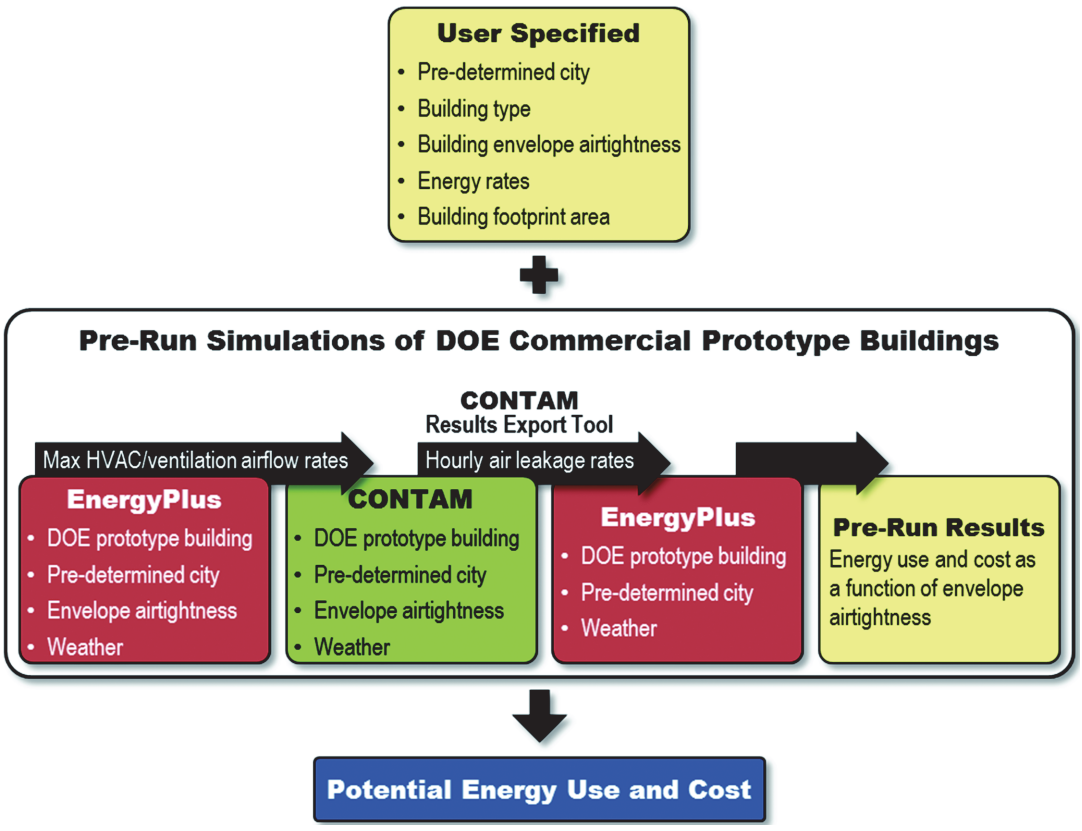

Figure 1 *General procedure to estimate potential energy costs for different levels of envelope airtightness in DOE commercial prototype buildings.*

Dalgleish, Laverne; Emmerich, Steven; Hun, Diana; Ng, Lisa; Shrestha, Som.
"Online Airtightness Calculator for the US, Canada and China."
Paper presented at Buildings XIII conference, Clearwater, FL. December 4, 2016 - December 8, 2016.

commercial prototype building models (DOE 2016b). These prototypes were derived from DOE commercial reference building models (DOE 2016c) and represent about 80% of new construction. Moreover, these prototypes cover 16 commercial building types, including mid- to high-rise residential buildings in 17 climate locations defined in ASHRAE/IES Standard 90.1-2013 (ASHRAE 2013b). The variables that are prescribed in these models include building envelope components, HVAC equipment types and efficiency, and occupancy schedules. As Standard 90.1 evolves, Pacific Northwest National Laboratory (PNNL) modifies these models with input from ASHRAE Standing Standard Project Committee 90.1 members and building industry experts. Features of the building models and a detailed description of their development are provided by Goel et al. (2014) and the Building Energy Codes Program website (DOE 2016b).

The first phase in the development of the calculator will cover three prototype building models (stand-alone retail, medium office, and mid-rise apartment) in 45 cities in the United States, 5 cities in Canada, and 5 cities in China. Models that represent typical commercial buildings in Canada and China are not available in the public domain; therefore, the DOE prototypes will also be used in these two countries.

EXAMPLE CALCULATIONS

The example in this paper uses the DOE prototype building model for a stand-alone retail building (Figure 2). The main characteristics of this prototype are based on ASHRAE/IES Standard 90.1-2013 and listed in Table 1. Note that Table 1 describes the simplified method used with prototype buildings to take into account the effects of HVAC operation on air leakage rates. This method assumes that the air leakage rate is 1 L/s·m^2 at 75 Pa when the HVAC is off and that the leakage rate decreases by 75% when the HVAC is on (Gowri et al. 2009). This approach is followed because EnergyPlus does not consider the effects of HVAC operation and wind direction on air leakage unless the Airflow Network module is used, which is not typically done because it is not a trivial task. In contrast, the online calculator utilizes CONTAM to estimate air leakage rates. A complete description of the prototype building is provided by DOE (DOE 2016d).

Ng et al. (2012) developed CONTAM models using EnergyPlus models of the ASHRAE/IESNA Standard 90.1-2004 prototype buildings as a baseline, and they were updated for this effort based on the ASHRAE/IES Standard 90.1-2013 models. The EnergyPlus and CONTAM models shared the same building geometry, occupancy, heating and cooling set points, and outdoor air ventilation requirements. However, the building zoning was modified in the CONTAM models in instances where additional zones were needed to support realistic airflow analyses (e.g., elevator shafts and restrooms). Modeling these additional zones is important to properly capture pressure relationships and airflow patterns in buildings. The present work utilizes the CONTAM model generated for the stand-alone retail building that includes a restroom that is not present in the prototype building model.

In order to determine the HVAC supply flow rates that would be used in CONTAM, a preliminary comparison was made of the maximum values that are calculated by EnergyPlus for the prototype stand-alone retail building in different cities by Ng et al. (2012). EnergyPlus results varied by less than 10% on average among the evaluated cities. Since the HVAC system modeled in CONTAM would retain approximately 10% more supply air than return air, the differences found in the maximum supply rates did not warrant changing their values in the CONTAM models for each city. Thus, the supply flow rates that were obtained for Chicago were applied to Winnipeg and Shanghai.

The stand-alone retail building has five thermal zones as shown in Figure 2. All zones, except the front entry, are conditioned in the summer and winter according to the set points listed in Table 1. These temperatures were scheduled in CONTAM because CONTAM does not perform thermal calculations. In the prototype building models, the front entry had a cooling set point of 38°C in the summer. However, it was assumed in the CONTAM model that the temperature in this

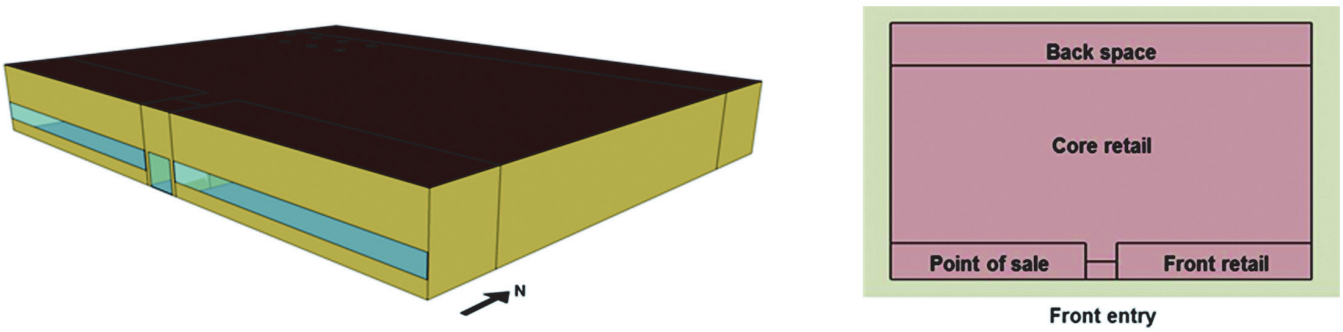

Figure 2 *Stand-alone retail building prototype: (a) building shape and orientation and (b) layout of five thermal zones (DOE 2016d).*

Table 1. Modeling Specifications of Stand-Alone Retail Building Prototype (DOE 2016d)

Characteristic	Description
Floor area, m^2	2300 (length 54.3 m × width 42.4 m)
Number of floors	1
Floor to ceiling height, m	6.1
Window-to-wall ratio, % Windows on south-facing façade	25.4
Building Envelope	
Walls	20.3 cm concrete masonry block + insulation per ASHRAE/IES Standard 90.1-2013 + 1.3 cm drywall
Roof	Roof membrane + insulation per ASHRAE/IES Standard 90.1-2013 + metal decking
Window U-factor and solar heat gain coefficient (SHGC)	Per ASHRAE/IES Standard 90.1-2013
Foundation	15.2 cm concrete slab-on-grade + insulation per ASHRAE/IES Standard 90.1-2013
Air leakage rates for prototype buildings (not used in the present study)	HVAC off = 1 L/s·m^2 at 75 Pa HVAC on = 25% of HVAC off rate = 0.25 L/s·m^2 at 75 Pa
HVAC	
Heating type	Gas furnace inside the packaged air-conditioning unit
Cooling type	Packaged air-conditioning unit
Size	Autosized to design day
Efficiency	Based on climate location and design cooling/heating capacity and ASHRAE/IES Standard 90.1-2013 requirements
Thermostat set point, °C	23.9 cooling/21.1 heating
Thermostat setback, °C	29.4 cooling/15.6 heating
Ventilation	Per ASHRAE Standard 62.1-2013 (ASHRAE 2013a)

zone was equal to the outdoor temperature in the cooling months. Also, in the EnergyPlus model the front entry had scheduled air leakage with a maximum flow rate of 0.94 m^3/s that varied between 0% and 100%, corresponding to unoccupied and occupied periods, respectively. This large air leakage was not modeled in CONTAM because its high flow rates would artificially increase the leakage of the entire building envelope in the whole-building air leakage rate data that would be exported to EnergyPlus. The outdoor air economizers and night cooling options in the EnergyPlus models were not implemented in the CONTAM models because CONTAM does not perform thermal calculations and would not be able to predict when economizers or night cooling options would be activated. Indoor temperatures in the CONTAM model were scheduled according to the set points in the EnergyPlus model.

Table 2 lists the four levels of airtightness that were assumed in the simulations. These include the slab and below-grade envelope area in the normalization of the air leakage rate, which is why they are referred to as *six-sided envelopes*, as well as the assumption that the air leakage is equally distributed over all exterior surfaces. The six-sided value is used in many building codes and standards; however, the CONTAM and EnergyPlus models assume no air leakage through the exterior envelope that is not exposed to ambient air. The baseline value in Table 2 was calculated using the average leakage rate for commercial buildings reported by Emmerich et al. (2005) of 9 L/s·m^2 at 75 Pa for a five-sided envelope. The baseline of 5.4 L/s·m^2 at 75 Pa was obtained by multiplying the average leakage rate by the five-sided to six-sided envelope area ratio of the stand-alone retail building prototype. Table 2 also lists three target levels for improved airtightness at 75 Pa: 2 L/s·m^2 is the most stringent of three options in the *2015 International Energy Conservation Code* (ICC 2015) because it involves a blower door test, whereas the other two options are based on laboratory tests per ASTM E2357 (ASTM 2011) and ASTM E2178 (ASTM 2013); 1.25 L/s·m^2 is the airtightness required by the U.S. Army Corps of Engineers (USACE

2012); and 0.25 L/s·m^2 is the leakage rate targeted by the DOE buildings envelope roadmap (DOE 2014). Emmerich and Persily (2014) analyzed the NIST U.S. commercial building air leakage database and found that the 79 buildings categorized as having an air barrier had an average six-sided leakage of 1.39 L/s·m^2 at 75 Pa, which was 70% below the average leakage of the 290 buildings without an air barrier (i.e., 4.33 L/s·m^2 at 75 Pa) and is similar to the second target level above. Zhivov et al. (2014) reported the average six-sided leakage for a set of 285 new and retrofitted military buildings constructed to the USACE specifications to be 0.9 L/s·m^2.

The three cities that were evaluated are Chicago, IL, USA; Winnipeg, Canada; and Shanghai, China. Table 3 shows their DOE climate zones and the locations of the corresponding prototype building models that were used in the simulations. CONTAM was used to calculate the hourly air leakage rates for the prototype building for each of these cities. Table 4 lists the ACH results for when the HVAC system is on ($ACH_{HVAC\ on}$), when the HVAC system is off ($ACH_{HVAC\ off}$), and the annual average (ACH_{avg}). Results indicate that ACH_{avg} for Winnipeg is the highest, followed by Chicago and Shanghai. This is mainly due to differences in weather among the cities; for example, the annual average wind speed for these cities is 4.78, 4.56, and 3.25 m/s, respectively. Results suggest that reducing the air leakage rate from 5.4 to 2 L/s•m^2 at 75 Pa led to a decrease in ACH_{avg} of about 75% across the three locations. By further lowering the leakage rate to 1.25 and 0.25 L/s•m^2 at 75 Pa, ACH_{avg} was reduced by about 86% and 98%, respectively, compared to the baseline.

Table 2. Assumed Building Envelope Airtightness Levels for a Six-Sided Envelope

Case	Air Leakage Rate at 75 Pa, L/s·m^2	Source
Baseline	5.4	Emmerich et al. (2005)
1	2.0	ICC (2015)
2	1.25	USACE (2012)
3	0.25	DOE (2014)

Table 3. Evaluated Cities

City	Climate Zone	Prototype Building Model Used in Calculator
Shanghai, China	3A (warm, humid)	Memphis, TN, USA
Chicago, IL, USA	5A (cold, humid)	Chicago, IL, USA
Winnipeg, Canada	7 (very cold)	Duluth, MN, USA

Table 4. Predicted Air Changes per Hour

Leakage Rate at 75 Pa, L/s·m^2	Air Changes per Hour, 1/h			$\frac{ACH_{HVAC\ on}}{ACH_{HVAC\ off}}$, %	Decrease in ACH_{avg} from Baseline ACH, %
	HVAC On	HVAC Off	Annual Average		
Chicago					
5.4	0.2077	0.2861	0.2389	73	
2.0	0.0366	0.1061	0.0642	35	73
1.25	0.0117	0.0664	0.0334	18	86
0.25	0.0009	0.0134	0.0059	7	98
Winnipeg					
5.4	0.2804	0.3684	0.3154	76	
2.0	0.0571	0.1366	0.0887	42	72
1.25	0.0201	0.0855	0.0461	23	85
0.25	0.0012	0.0172	0.0076	7	98
Shanghai					
5.4	0.1021	0.1823	0.1340	56	
2.0	0.0118	0.0675	0.0340	18	78
1.25	0.0037	0.0422	0.0190	9	88
0.25	0.0006	0.0085	0.0037	7	98

As previously stated, in order to estimate the hourly $ACH_{HVAC\ on}$, the DOE commercial prototype building models assume that this number is 25% of $ACH_{HVAC\ off}$. However, Table 4 shows that using multizone airflow simulations, this percentage is closely linked to the airtightness of the envelope. For example, when the building enclosure leakage rate was 5.4 L/s•m^2 at 75 Pa, $ACH_{HVAC\ on}$ was 56% to 76% of $ACH_{HVAC\ off}$. In contrast, this ratio decreased to 7% when the envelope airtightness was 0.25 L/s•m^2 at 75 Pa. This implies that the approach followed by users of prototype building models significantly underestimates the contribution of air leakage to energy consumption when the HVAC system is on in buildings with leaky enclosures, while the opposite occurs in buildings with very tight envelopes.

Figure 3 illustrates the HVAC energy use as a function of the building envelope airtightness level in Winnipeg. Results indicate that improving airtightness from 5.4 to 2 L/s•m^2 at 75 Pa led to an 18% and 55% decrease in electricity and natural gas use, respectively.

Energy costs were calculated using the annual energy outputs from EnergyPlus and the annual average prices of

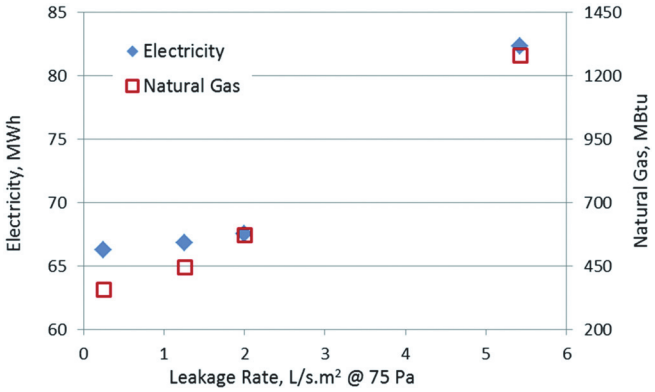

Figure 3 *Annual HVAC energy use for a prototype standalone retail building in Winnipeg based on the CONTAM+EnergyPlus approach.*

Table 5. Energy Prices

Location	Electricity Price	Natural Gas Price
Chicago	$0.0933/kWh [a]	$8.86/1000 ft^3 [b]
Winnipeg	C$0.14/kWh [c] (≈$0.10/kWh)	C$0.1605 m^3 [d] (≈$3.4/1000 ft^3)
Shanghai	¥0.781/kWh [e] (≈$0.12/kWh)	¥3.65/m^3 [f] (≈$15.9/1000 ft^3)

[a] http://www.eia.gov/electricity/sales_revenue_price/
[b] http://www.eia.gov/dnav/ng/ng_sum_lsum_a_EPG0_PCS_DMcf_a.htm
[c] https://www.ovoenergy.com/guides/energy-guides/average-electricity-prices-kwh.html
[d] http://www.economicdevelopmentwinnipeg.com/uploads/document_file/natural_gas_rates.pdf?t=1433529826
[e] http://news.asean168.com/a/20150413/5318.html
[f] http://gas.gold600.com/

electricity and natural gas listed in Table 5. Figures 4, 5, and 6 show the annual HVAC energy cost in Chicago, Winnipeg, and Shanghai, respectively, as a function of building envelope leakage rate. The figures also present quadratic regression equations. The high coefficients of determination (i.e., $R^2 >$ 0.995) suggest that the calculator may be able to use quadratic equations to estimate energy costs for any given airtightness level. Similar equations could be derived for the heating and cooling costs, as well as for energy usage.

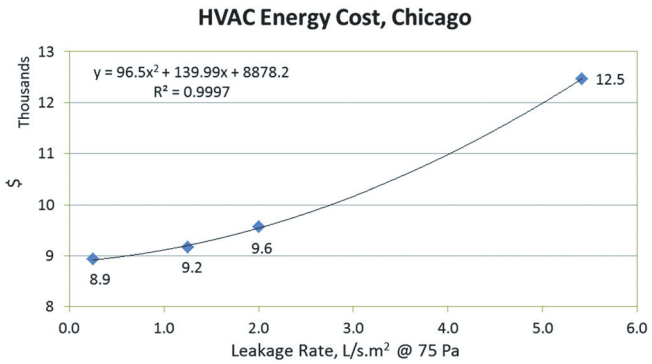

Figure 4 *Annual HVAC energy cost for a prototype standalone retail building in Chicago based on the CONTAM+EnergyPlus approach.*

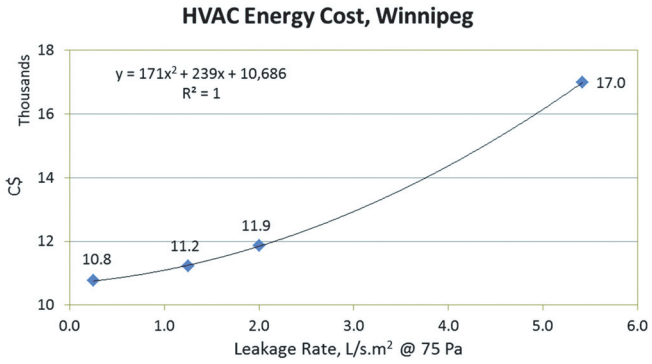

Figure 5 *Annual HVAC energy cost for a prototype standalone retail building in Winnipeg based on the CONTAM+EnergyPlus approach.*

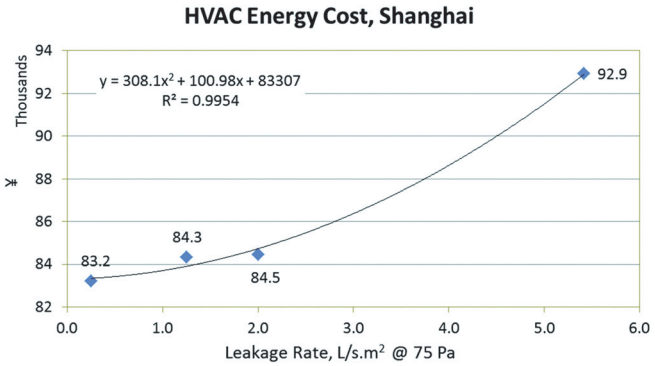

Figure 6 *Annual HVAC energy cost for a prototype standalone retail building in Shanghai based on the CONTAM+EnergyPlus approach.*

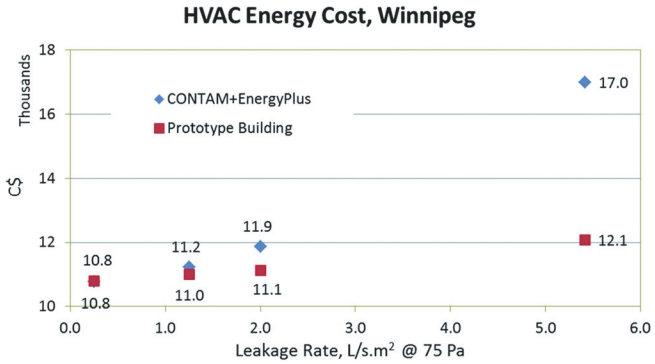

Figure 7 *Annual HVAC energy costs in Winnipeg from the CONTAM+EnergyPlus and the prototype building models.*

Further evaluations were performed to get a better understanding of the improvements that the CONTAM+EnergyPlus approach offers. To serve as a reference, simulations were conducted for Winnipeg using only EnergyPlus; that is, hourly air leakage rates from CONTAM were not imported into EnergyPlus and the prototype building assumption that $ACH_{HVAC\,on}$ equals 25% of $ACH_{HVAC\,off}$ was made Table 6 shows the results from these simulations, and Table 7 compares the ACH values that were obtained through these two approaches. These data illustrate how the simplified method used in the prototype building models underestimates the ACH and its corresponding impact on energy use. The effects are more noteworthy in leaky buildings, where the two approaches had ACH differences of 70% when the HVAC system is on and an annual average discrepancy in ACH of 49%. These differences decrease as the envelope becomes tighter, although they remained significant even when the leakage rate of the enclosure was 2 L/s·m^2 at 75 Pa.

Figure 7 compares the annual HVAC energy costs in Winnipeg that were calculated with the CONTAM+EnergyPlus and the prototype building methods. As previously stated, differences are greater in buildings with leakier envelopes: the discrepancy in buildings with a leakage rate of 5.4 L/s·m^2 at 75 Pa amounted to nearly $5000 per year. Ongoing projects at ORNL will help validate these estimated energy savings.

CONCLUSION

ORNL and NIST combined their expertise to develop a procedure that will be used in an online airtightness calculator. This procedure is different from other common methods used in energy analysis in that it uses hourly air leakage rates that are estimated by taking into account key variables such as building leakage rate, weather conditions, and HVAC operation. The calculator will provide energy cost estimates as a

Table 6. Predicted Air Changes per Hour in Winnipeg Using the Prototype Building Leakage Rate Reduction Method

Leakage Rate at 75 Pa, L/s·m^2	Air Changes per Hour, 1/h			$\frac{ACH_{HVAC\ on}}{ACH_{HVAC\ off}}$, %	Decrease from Baseline Annual Average ACH, %
	HVAC On	HVAC Off	Annual Average		
5.4	0.0841	0.2765	0.1605	30	
2.0	0.0310	0.1024	0.0594	30	63%
1.25	0.0194	0.0641	0.0372	30	77%
0.25	0.0039	0.0128	0.0074	30	95%

Table 7. Comparison of Air Changes per Hour from CONTAM+EnergyPlus and the Prototype Building Simulation Approaches

Leakage Rate at 75 Pa, L/s·m^2	Difference Between CONTAM+EnergyPlus and the Prototype Building Simulation ACH values, %		
	HVAC On	HVAC Off	Annual Average
5.4	70	25	49
2.0	46	25	33
1.25	3	25	19
0.25	-225	26	3

function of building envelope airtightness for DOE commercial prototype buildings in cities in the United States, Canada, and China. To demonstrate the CONTAM+EnergyPlus procedure, the paper presents an example where a prototype stand-alone retail building is simulated in Chicago, Winnipeg, and Shanghai. Results demonstrate that methods using simplified assumptions, such as $ACH_{HVAC\ on}$ equals 25% of $ACH_{HVAC\ off}$, underestimate the air leakage rates and the effects of building envelope airtightness on energy use. In the stand-alone retail building prototype example in Winnipeg, this discrepancy amounted to nearly $5000 per year for a building with a leakage rate of 5.4 L/s·m^2 at 75 Pa; ongoing projects at ORNL will help validate these estimated energy savings. The calculator that is under development will be a powerful, credible, and easy-to-use tool that designers and contractors can utilize to estimate the energy and financial savings that building owners could achieve by reducing the air leakage.

ACKNOWLEDGMENTS

The authors would like to thank the U.S. Department of Energy, the Air Barrier Association of America, and the U.S.-China Clean Energy Research Center for Building Energy Efficiency for funding this research.

This manuscript has been authored by UT-Battelle, LLC, under Contract No. DE-AC05-00OR22725 with the U.S. Department of Energy. The United States Government retains and the publisher, by accepting the article for publication, acknowledges that the United States Government retains a non-exclusive, paid-up, irrevocable, world-wide license to publish or reproduce the published form of this manuscript, or allow others to do so, for United States Government purposes.

REFERENCES

ASHRAE. 2013a. ANSI/ASHRAE Standard 62.1-2013, *Ventilation for acceptable indoor air quality*. Atlanta: ASHRAE.

ASHRAE. 2013b. ANSI/ASHRAE/IES Standard 90.1-2013, *Energy standard for buildings except low-rise residential buildings*. Atlanta: ASHRAE.

ASTM. 2011. ASTM E2357-11, *Standard test method for determining air leakage of air barrier assemblies. West Conshohocken, PA: ASTM International.*

ASTM. 2013. ASTM E2178-13, *Standard test method for air permeance of building materials*. *West Conshohocken, PA: ASTM International.*

Chung, K.C. 1996. Development and validation of a multizone model for overall indoor air environment prediction. *HVAC&R Research* 2:376–85.

Crawley, D.B., J.W. Hand, M. Kummert, and B.T. Griffith. 2008. Contrasting the capabilities of building energy performance simulation programs. *Building and Environment* 43(4):661–73.

DOE. 2014. Windows and building envelope research and development: Roadmap for emerging technologies. Washington, DC: U.S. Department of Energy. http://energy.gov/sites/prod/files/2014/02/f8/BTO_windows_and_envelope_report_3.pdf

DOE. 2016a. *EnergyPlus*. Retrieved February 2016 from https://energyplus.net. Washington, DC: U.S. Department of Energy.

DOE. 2016b. Commercial prototype building models. Retrieved February 2016 from https://www.energycodes.gov/commercial-prototype-building-models. Washington, DC: U.S. Department of Energy.

DOE. 2016c. Commercial reference buildings. Retrieved February 2016 from http://energy.gov/eere/buildings/commercial-reference-buildings. Washington, DC: U.S. Department of Energy.

DOE. 2016d. 90.1 prototype building models sand alone retail. Retrieved February 2016 from https://www.energycodes.gov/901-prototype-building-models-stand-alone-retail. Washington, DC: U.S. Department of Energy.

Dols, W.S., and B. Polidoro. 2015. *CONTAM user guide and program documentation*. Technical Note 1887. Gaithersburg, MD: National Institute of Standards and Technology.

Emmerich, S.J. 2001. Validation of multizone IAQ modeling of residential-scale buildings: A review. *ASHRAE Transactions*, vol. 107(2).

Emmerich, S.J., S.J. Nabinger, A. Gupte, and C. Howard-Reed. 2004. Validation of multizone IAQ model predictions for tracer gas in a townhouse. *Building Services Engineering Research and Technology* 25:305–16.

Emmerich, S.J., T.P. McDowell, and W. Anis. 2005. Investigation of the impact of commercial building envelope airtightness on HVAC energy use. NISTIR 7238. Gaithersburg, MD: National Institute of Standards and Technology.

Emmerich, S.J., and A.K. Persily. 2014. Analysis of U.S commercial building envelope air leakage database to support sustainable building design. *The International Journal of Ventilation*, vol. 12.

Goel, S., R. Athalye, W. Wang, J. Zhang, M. Rosenberg, Y. Xie, R. Hart, and V. Mendon. 2014. *Enhancements to ASHRAE Standard 90.1 prototype building models*. PNNL-23269. Richland, WA: Pacific Northwest National Laboratory.

Gowri, K., D. Winiarski, and R. Jarnagin. 2009. *Infiltration modeling guidelines for commercial building energy analysis*. PNNL-18898. Richland, WA: Pacific Northwest National Laboratory.

Haghighat, F., and A.C. Megri. 1996. A comprehensive validation of two airflow models—COMIS and CONTAM. *Indoor Air* 6:278–88.

ICC. 2015. *2015 International Energy Conservation Code*. Washington, DC: International Code Council.

Ng, L.C., A. Musser, S.J. Emmerich, and A.K. Persily. 2012. *Airflow and indoor air quality models of DOE reference commercial buildings*. Technical Note 1734. Gaithersburg, MD: National Institute of Standards and Technology.

Polidoro, B., L.C. Ng, and W.S. Dols. 2016. *CONTAM results export tool.* Technical Note 1912. Gaithersburg, MD: National Institute of Standards and Technology.

USACE. 2012. *Air leakage test protocol for building envelopes*. Washington, DC: U.S. Army Corps of Engineers.

Zhivov, A., D. Herron, J.L. Durston, M. Heron, and G. Lea. 2014. Airtightness in new and retrofitted US army buildings. *International Journal of Ventilation*, vol. 12.

EVALUATION OF STRUCTURAL PERFORMANCE BASED ON AN ENERGY BALANCE APPROACH

K.K.F. Wong[(1)], S.L. McCabe[(2)]

[(1)] *Research Structural Engineer, National Institute of Standards and Technology, kevin.wong@nist.gov*
[(2)] *Group Leader, National Institute of Standards and Technology, steven.mccabe@nist.gov*

Abstract

An analytical method is developed to quantify the potential energy and other energy characteristics of the nonlinear response of framed structures subjected to earthquake ground motions. Since the potential energy relates to the stiffness of the structure, it consists of three components in a nonlinear system: (1) stored strain energy associated with the linear elastic portion of the structural response, which can be recovered after the earthquake; (2) higher-order energy associated with geometric nonlinear behavior of the structural response, which is derived from the nonlinear stiffness matrix and can also be recovered if the axial load is removed; and (3) plastic energy representing the energy dissipated by inelastic deformation of the structure, which cannot be recovered after the earthquake. The proposed analytical method uses a change in stiffness for handling the geometric nonlinearity and a change in displacement for handling material nonlinearity before solving the equations of motion, thereby separating the effects of geometric nonlinearity and material nonlinearity when computing stiffness forces. This leads directly to integral representations of each energy form. A four-story moment-resisting framed structure is used to demonstrate the feasibility of the proposed analytical method in evaluating the energy response and the transfer among different energy forms throughout the nonlinear response history analysis.

Keywords: Plastic energy, input energy, strain energy, kinetic energy, damping energy

1. Introduction

Structures responding to earthquake shaking can be viewed as an energy transfer process. Earthquake ground motions transfer part of their energy to individual structures as input energy to produce structural vibrations. This input energy induces motion in the structure and its contents, which can generally be characterized as potential energy, kinetic energy, and damping energy. All these energy forms have positive values. While potential energy is related to the structural stiffness and kinetic energy is related to the inertial components, damping energy is associated with energy loss within the structure during its motion. Thus these energy forms have traditionally been investigated as part of the structural responses due to strong ground shaking.

Research on energy dissipation began in the 1980's as an alternative approach for seismic design, when it was recognized that significant cumulative damage can occur in structures without large global displacement responses [1-3] in long-duration earthquake ground motions. However, these studies focused on evaluating the hysteretic energy by calculating the enclosed area in a force-deformation curve of single degree of freedom systems. A numerical procedure was proposed for quantifying different energy forms for low to medium rise structures in the 1990's for linear multi-degree of freedom systems [4], and later an analytical method was developed to consider energy due to inelastic deformation [5]. These studies did not consider the reduction of lateral stiffness by axial load, which can bring considerable error in the calculation of potential energy when this effect becomes prominent.

In this research, a new analytical method of using nonlinear stiffness matrices for both geometric nonlinearity and material nonlinearity is derived to investigate the energy of framed structures responding nonlinearly to earthquake ground motions. In particular, the potential energy that is directly related to the nonlinear stiffness of the structure is investigated. This potential energy consists of three components in a fully nonlinear system: (1) the stored linear elastic strain energy; (2) the energy associated with the geometric nonlinear effects – hereby called "higher-order energy"; and (3) plastic energy dissipated by material nonlinearity of the structure. A four-story moment-resisting steel frame is used to demonstrate the feasibility of the proposed analytical method in evaluating the energy response and the transfer among different energy forms throughout the nonlinear response history analysis.

2. Stiffness Matrices for Geometric Nonlinearity

Nonlinear stiffness matrices for performing energy calculations require an accurate representation of the deflected shape of the member. By subjecting the member to an axial force, the use of stability functions is most appropriate because it is derived based on directly solving for the equilibrium equation that is expressed as a fourth-order differential equation. The theory of using stability functions to analyze moment-resisting framed structures was first developed for elastic members in the 1960's [6-8], but it found limited application because of its complexity in the closed-form solution compared to other methods, such as using the P-Δ stiffness approach [9] or the geometric stiffness approach [10]. Even with the advances in computing technology, only one research publication was found in the recent literature on the analysis of framed structures using stability functions [11]. However, when higher accuracy is required, the first-order or second-order approximation of the geometric nonlinearity may not be able to capture the nonlinear behavior accurately. Therefore, stability functions are used in this study because these functions can capture the exact shapes of the displacement profile of the member. A detailed derivation of the stiffness matrices can be found in another publication [12], and it is briefly summarized here with the consideration of yielding and formation of plastic hinge.

2.1 Element Stiffness Matrix

Four degrees of freedom (DOFs) are typically used to describe the lateral displacement (v) and rotation (v') at the two ends of a member in a moment-resisting frame. In addition, two plastic hinge locations (PHLs) for bending at the two ends of the member are used to capture the material nonlinear flexural behavior of the plastic hinges (θ''). This altogether gives 6 movements that are needed to describe the deformation of the member. To

compute the element stiffness matrix $\bar{\mathbf{k}}_i$, each of these 6 movements is displaced independently by one unit as shown in Fig. 1 while subjected to an axial compressive load P. Here, V_{1r}, M_{2r}, V_{3r}, M_{4r}, M_{5r}, and M_{6r} represent the required shear forces and moments at the two ends of the member and the corresponding plastic hinge moments to cause the lateral displacements and rotations in the prescribed pattern, and $r = 1,...,6$ represents the six cases of unit displacement patterns of the member's deflection.

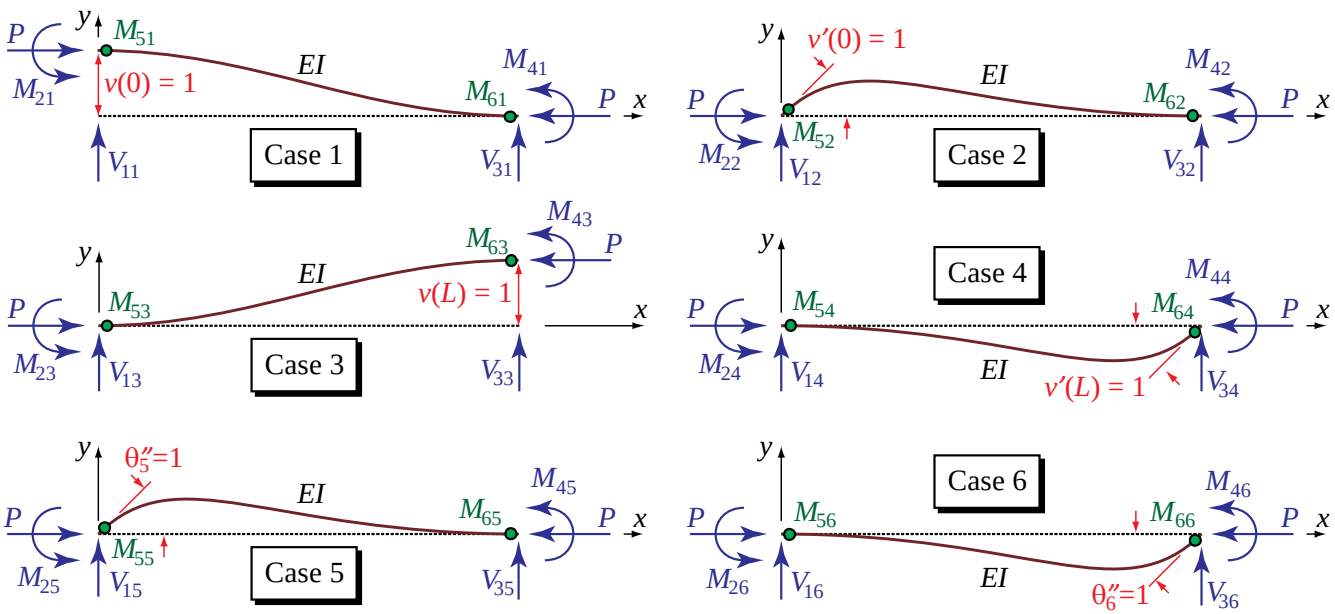

Fig. 1 – Six cases of displacement and plastic rotation patterns and the corresponding fixed-end forces

Using the classical Bernoulli-Euler beam theory with homogeneous and isotropic material properties where the moment is proportional to the curvature and plane sections are assumed to remain plane, the governing equilibrium equation describing the deflected shape of the member can be written as

$$(EIv'')'' + Pv'' = 0 \tag{1}$$

where E is the elastic modulus, I is the moment of inertia, v is the lateral deflection, and each prime represents taking derivatives of the corresponding variable with respect to the x-direction of the member. By assuming EI is constant along the member, the fourth-order ordinary differential equation in Eq. (1) can be solved. Then imposing the boundary conditions as shown in Fig. 1 for each of the four cases, the 6×6 element stiffness matrix $\bar{\mathbf{k}}_i$ can be obtained.

Case 1:

For Case 1 as shown in Fig. 1 (i.e., $r = 1$), imposing the boundary conditions $v(0) = 1$, $v'(0) = 0$, $v(L) = 0$, $v'(L) = 0$, $\theta_5'' = 0$, and $\theta_6'' = 0$, where L is the length of the member, the shears (V) and moments (M) at the two ends based on solving the differential equation in Eq. (1) are calculated as:

$$V_{11} = EIv'''(0) + Pv'(0) = s'EI/L^3 \quad , \quad M_{21} = -EIv''(0) = \bar{s}EI/L^2 \tag{2a}$$

$$V_{31} = -EIv'''(L) - Pv'(L) = -s'EI/L^3 \quad , \quad M_{41} = EIv''(L) = \bar{s}EI/L^2 \tag{2b}$$

$$M_{51} = M_{21} = \bar{s}EI/L^2 \quad , \quad M_{61} = M_{41} = \bar{s}EI/L^2 \tag{2c}$$

where

$$\bar{s} = \frac{\lambda^2(1-\cos\lambda)}{2-2\cos\lambda-\lambda\sin\lambda} \quad , \quad s' = \frac{\lambda^3\sin\lambda}{2-2\cos\lambda-\lambda\sin\lambda} \tag{3}$$

and $\lambda = L \times \sqrt{P/EI}$.

Case 2:

For Case 2 as shown in Fig. 1 (i.e., $r = 2$), imposing the boundary conditions $v(0) = 0$, $v'(0) = 1$, $v(L) = 0$, $v'(L) = 0$, $\theta_5'' = 0$, and $\theta_6'' = 0$, the shears and moments at the two ends based on solving the differential equation in Eq. (1) are calculated as:

$$V_{12} = EIv'''(0) + Pv'(0) = \bar{s}EI/L^2 \quad , \quad M_{22} = -EIv''(0) = \hat{s}EI/L \tag{4a}$$

$$V_{32} = -EIv'''(L) - Pv'(L) = -\bar{s}EI/L^2 \quad , \quad M_{42} = EIv''(L) = \hat{s}\hat{c}EI/L \tag{4b}$$

$$M_{52} = M_{22} = \hat{s}EI/L \quad , \quad M_{62} = M_{42} = \hat{s}\hat{c}EI/L \tag{4c}$$

where

$$\hat{s} = \frac{\lambda(\sin\lambda - \lambda\cos\lambda)}{2 - 2\cos\lambda - \lambda\sin\lambda} \quad , \quad \hat{c} = \frac{\lambda - \sin\lambda}{\sin\lambda - \lambda\cos\lambda} \tag{5}$$

Case 3:

For Case 3 as shown in Fig. 1 (i.e., $r = 3$), imposing the boundary conditions $v(0) = 0$, $v'(0) = 0$, $v(L) = 1$, $v'(L) = 0$, $\theta_5'' = 0$, and $\theta_6'' = 0$, the shears and moments at the two ends based on solving the differential equation in Eq. (1) are calculated as:

$$V_{13} = EIv'''(0) + Pv'(0) = -s'EI/L^3 \quad , \quad M_{23} = -EIv''(0) = -\bar{s}EI/L^2 \tag{6a}$$

$$V_{33} = -EIv'''(L) - Pv'(L) = s'EI/L^3 \quad , \quad M_{43} = EIv''(L) = -\bar{s}EI/L^2 \tag{6b}$$

$$M_{53} = M_{23} = -\bar{s}EI/L^2 \quad , \quad M_{63} = M_{43} = -\bar{s}EI/L^2 \tag{6c}$$

Case 4:

For Case 4 as shown in Fig. 1 (i.e., $r = 4$), imposing the boundary conditions $v(0) = 0$, $v'(0) = 0$, $v(L) = 0$, $v'(L) = 1$, $\theta_5'' = 0$, and $\theta_6'' = 0$, the shears and moments at the two ends based on solving the differential equation in Eq. (1) are calculated as:

$$V_{14} = EIv'''(0) + Pv'(0) = \bar{s}EI/L^2 \quad , \quad M_{24} = -EIv''(0) = \hat{s}\hat{c}EI/L \tag{7a}$$

$$V_{34} = -EIv'''(L) - Pv'(L) = -\bar{s}EI/L^2 \quad , \quad M_{44} = EIv''(L) = \hat{s}EI/L \tag{7b}$$

$$M_{54} = M_{24} = \hat{s}\hat{c}EI/L \quad , \quad M_{64} = M_{44} = \hat{s}EI/L \tag{7c}$$

Case 5:

For Case 5 as shown in Fig. 1 (i.e., $r = 5$), imposing the boundary conditions $v(0) = 0$, $v'(0) = 0$, $v(L) = 0$, $v'(L) = 0$, $\theta_5'' = 1$, and $\theta_6'' = 0$, the shears and moments at the two ends based on solving the differential equation in Eq. (1) are calculated as:

$$V_{15} = EIv'''(0) + Pv'(0) = \bar{s}EI/L^2 \quad , \quad M_{25} = -EIv''(0) = \hat{s}EI/L \tag{8a}$$

$$V_{35} = -EIv'''(L) - Pv'(L) = -\bar{s}EI/L^2 \quad , \quad M_{45} = EIv''(L) = \hat{s}\hat{c}EI/L \tag{8b}$$

$$M_{55} = M_{25} = \hat{s}EI/L \quad , \quad M_{65} = M_{45} = \hat{s}\hat{c}EI/L \tag{8c}$$

Case 6:

Finally, for Case 6 as shown in Fig. 1 (i.e., $r = 6$), imposing the boundary conditions $v(0) = 0$, $v'(0) = 0$, $v(L) = 0$, $v'(L) = 0$, $\theta_5'' = 0$, and $\theta_6'' = 1$, the shears and moments at the two ends based on solving the differential equation in Eq. (1) are calculated as:

$$V_{16} = EIv'''(0) + Pv'(0) = \bar{s}EI/L^2 \quad , \quad M_{26} = -EIv''(0) = \hat{s}\hat{c}EI/L \tag{9a}$$

$$V_{36} = -EIv'''(L) - Pv'(L) = -\bar{s}EI/L^2 \quad , \quad M_{46} = EIv''(L) = \hat{s}EI/L \tag{9b}$$

$$M_{56} = M_{26} = \hat{s}\hat{c}EI/L \quad , \quad M_{66} = M_{46} = \hat{s}EI/L \tag{9c}$$

In summary, based on Eqs. (2), (4), (6), (7), (8), and (9) for the above six cases, the element stiffness matrix of the i^{th} member $\bar{\mathbf{k}}_i$ for bending after incorporating two plastic hinges and axial compressive force using stability functions becomes:

$$\bar{\mathbf{k}}_i = \left[\begin{array}{cccc:cc} V_{11} & V_{12} & V_{13} & V_{14} & V_{15} & V_{16} \\ M_{21} & M_{22} & M_{23} & M_{24} & M_{25} & M_{26} \\ V_{31} & V_{32} & V_{33} & V_{34} & V_{35} & V_{36} \\ M_{41} & M_{42} & M_{43} & M_{44} & M_{45} & M_{46} \\ \hdashline M_{51} & M_{52} & M_{53} & M_{54} & M_{55} & M_{56} \\ M_{61} & M_{62} & M_{63} & M_{64} & M_{65} & M_{66} \end{array}\right] = \frac{EI}{L^3}\left[\begin{array}{cccc:cc} s' & \bar{s}L & -s' & \bar{s}L & \bar{s}L & \bar{s}L \\ \bar{s}L & \hat{s}L^2 & -\bar{s}L & \hat{s}\hat{c}L^2 & \hat{s}L^2 & \hat{s}\hat{c}L^2 \\ -s' & -\bar{s}L & s' & -\bar{s}L & -\bar{s}L & -\bar{s}L \\ \bar{s}L & \hat{s}\hat{c}L^2 & -\bar{s}L & \hat{s}L^2 & \hat{s}\hat{c}L^2 & \hat{s}L^2 \\ \hdashline \bar{s}L & \hat{s}L^2 & -\bar{s}L & \hat{s}\hat{c}L^2 & \hat{s}L^2 & \hat{s}\hat{c}L^2 \\ \bar{s}L & \hat{s}\hat{c}L^2 & -\bar{s}L & \hat{s}L^2 & \hat{s}\hat{c}L^2 & \hat{s}L^2 \end{array}\right] \begin{array}{l} \leftarrow v(0) \\ \leftarrow v'(0) \\ \leftarrow v(L) \\ \leftarrow v'(L) \\ \leftarrow -\theta_5'' \\ \leftarrow -\theta_6'' \end{array} \tag{10}$$

2.2 Global Stiffness Matrices

The element stiffness matrix presented in Eq. (10) needs to be assembled into the global stiffness matrix. This assembly procedure can be simplified by partitioning the element stiffness matrix in Eq. (10) as follows.

$$\bar{\mathbf{k}}_i = \left[\begin{array}{c:c} \mathbf{k}_i & \mathbf{k}_i' \\ \hdashline \mathbf{k}_i'^T & \mathbf{k}_i'' \end{array}\right] \tag{11}$$

where

$$\mathbf{k}_i = \frac{EI}{L^3}\begin{bmatrix} s' & \bar{s}L & -s' & \bar{s}L \\ \bar{s}L & \hat{s}L^2 & -\bar{s}L & \hat{s}\hat{c}L^2 \\ -s' & -\bar{s}L & s' & -\bar{s}L \\ \bar{s}L & \hat{s}\hat{c}L^2 & -\bar{s}L & \hat{s}L^2 \end{bmatrix} \quad , \quad \mathbf{k}_i' = \frac{EI}{L^2}\begin{bmatrix} \bar{s} & \bar{s} \\ \hat{s}L & \hat{s}\hat{c}L \\ -\bar{s} & -\bar{s} \\ \hat{s}\hat{c}L & \hat{s}L \end{bmatrix} \quad , \quad \mathbf{k}_i'' = \frac{EI}{L}\begin{bmatrix} \hat{s} & \hat{s}\hat{c} \\ \hat{s}\hat{c} & \hat{s} \end{bmatrix} \tag{12}$$

From the sub-matrices partitioned according in Eq. (12), the assembly into the global stiffness matrices $\mathbf{K}(t)$, $\mathbf{K}'(t)$, and $\mathbf{K}''(t)$ follows a straightforward procedure. Here, the global stiffness matrices are functions of time, since the axial compressive load P is a function of time in a dynamic analysis. A number of textbooks have discussed this procedure in great detail [13]. Consider a framed structure having a total of n DOFs and m PHLs, the global stiffness matrices can be obtained by this assembly procedure and are often written in the form:

$$\mathbf{K}(t) = \Big[\ \textit{Assembly of } \mathbf{k}_i\ \Big]_{n\times n} \quad , \quad \mathbf{K}'(t) = \Big[\ \textit{Assembly of } \mathbf{k}_i'\ \Big]_{n\times m} \quad , \quad \mathbf{K}''(t) = \Big[\ \textit{Assembly of } \mathbf{k}_i''\ \Big]_{m\times m} \tag{13}$$

3. Inelastic Displacement for Material Nonlinearity

The detailed derivation on the use of inelastic displacement for analyzing structures with material nonlinearity has been published [14] and it is briefly summarized here. Consider a moment-resisting framed structure having

a total of n DOFs and m PHLs. Let the $n\times1$ total displacement $\mathbf{x}(t)$ at each DOF be represented as the summation of the $n\times1$ elastic displacement $\mathbf{x}'(t)$ and the $n\times1$ inelastic displacement $\mathbf{x}''(t)$:

$$\mathbf{x}(t)=\mathbf{x}'(t)+\mathbf{x}''(t) \tag{14}$$

Similarly, let the $m\times1$ total moment $\mathbf{m}(t)$ at the PHLs of a moment-resisting frame be separated into the $m\times1$ elastic moment $\mathbf{m}'(t)$ and the $m\times1$ inelastic moment $\mathbf{m}''(t)$:

$$\mathbf{m}(t)=\mathbf{m}'(t)+\mathbf{m}''(t) \tag{15}$$

The displacements in Eq. (14) and the moments in Eq. (15) are related by the equations:

$$\mathbf{m}'(t)=\mathbf{K}'(t)^T\mathbf{x}'(t) \quad , \quad \mathbf{m}''(t)=-\left[\mathbf{K}''(t)-\mathbf{K}'(t)^T\mathbf{K}(t)^{-1}\mathbf{K}'(t)\right]\boldsymbol{\Theta}''(t) \tag{16}$$

where $\boldsymbol{\Theta}''(t)$ is the $m\times1$ plastic rotation at each PHL, and $\mathbf{K}(t)$, $\mathbf{K}'(t)$, and $\mathbf{K}''(t)$ are calculated in Eq. (13). The relationship between the plastic rotation $\boldsymbol{\Theta}''(t)$ and inelastic displacement $\mathbf{x}''(t)$ is:

$$\mathbf{x}''(t)=\mathbf{K}(t)^{-1}\mathbf{K}'(t)\boldsymbol{\Theta}''(t) \tag{17}$$

Substituting both equations in Eq. (16) into Eq. (15) and making use of Eqs. (14) and (17), then rearranging the terms gives the governing equation for calculating the plastic hinge responses for any given total displacement pattern:

$$\mathbf{m}(t)+\mathbf{K}''\boldsymbol{\Theta}''(t)=\mathbf{K}'^T\mathbf{x}(t) \tag{18}$$

4. Dynamic Equilibrium Equation of Motion

For a moment-resisting framed structure modeled as an n DOF system and subjected to earthquake ground motions, the dynamic equilibrium equation of motion can be written as

$$\mathbf{M}\ddot{\mathbf{x}}(t)+\mathbf{C}\dot{\mathbf{x}}(t)+\mathbf{K}(t)\mathbf{x}'(t)=-\mathbf{M}\ddot{\mathbf{g}}(t)-\mathbf{F}_a(t) \tag{19}$$

where $\mathbf{M}$ is the $n\times n$ mass matrix, $\mathbf{C}$ is the $n\times n$ damping matrix, $\dot{\mathbf{x}}(t)$ is the $n\times1$ velocity vector, $\ddot{\mathbf{x}}(t)$ is the $n\times1$ acceleration vector, $\mathbf{K}(t)$ is the time-varying $n\times n$ stiffness matrix derived in Eq. (13) while subjected to time-varying column axial compressive load $P(t)$, $\ddot{\mathbf{g}}(t)$ is the $n\times1$ earthquake ground acceleration vector corresponding to the effect of ground motion at each DOF, and $\mathbf{F}_a(t)$ is the $n\times1$ vector of additional forces imposed on the structure due to geometric nonlinearity accounting for all the gravity columns in the structure (mainly the *P*-Δ effect). This geometric nonlinearity can often be modeled using a leaning column (or sometimes called a *P*-Δ column) in a two-dimensional analysis but may require more detailed modeling of all gravity columns in a three-dimensional analysis to capture the response due to torsional irregularity of the structure. In a two-dimensional analysis, the relationship between this lateral force $\mathbf{F}_a(t)$ and the lateral displacement can be written as follows:

$$\mathbf{F}_a(t)=\mathbf{K}_a\mathbf{x}(t) \tag{20}$$

where $\mathbf{K}_a$ is an $n\times n$ stiffness matrix that is a function of the gravity loads on the leaning column and the corresponding story height, but it is not a function of time. For two-dimensional frames with horizontal DOFs only, this $\mathbf{K}_a$ matrix often takes the form:

$$\mathbf{K}_a=\begin{bmatrix} -Q_1/h_1-Q_2/h_2 & Q_2/h_2 & 0 & \cdots & 0 \\ Q_2/h_2 & -Q_2/h_2-Q_3/h_3 & \ddots & \ddots & \vdots \\ 0 & \ddots & \ddots & Q_{n-1}/h_{n-1} & 0 \\ \vdots & \ddots & Q_{n-1}/h_{n-1} & -Q_{n-1}/h_{n-1}-Q_n/h_n & Q_n/h_n \\ 0 & \cdots & 0 & Q_n/h_n & -Q_n/h_n \end{bmatrix} \tag{21}$$

where Q_i is the total axial force due to gravity loads acting on the leaning column of the i^{th} floor, and h_i is the story height of the i^{th} floor. Now substituting Eq. (20) into Eq. (19) and rearranging terms gives

$$\mathbf{M}\ddot{\mathbf{x}}(t) + \mathbf{C}\dot{\mathbf{x}}(t) + \mathbf{K}(t)\mathbf{x}'(t) + \mathbf{K}_a\mathbf{x}(t) = -\mathbf{M}\ddot{\mathbf{g}}(t) \tag{22}$$

Since $\ddot{\mathbf{y}}(t) = \ddot{\mathbf{x}}(t) + \ddot{\mathbf{g}}(t)$ where $\ddot{\mathbf{y}}(t)$ is the $n \times 1$ absolute acceleration vector, substituting this equation into Eq. (22) gives the governing equation of motion for energy balance:

$$\mathbf{M}\ddot{\mathbf{y}}(t) + \mathbf{C}\dot{\mathbf{x}}(t) + \mathbf{K}(t)\mathbf{x}'(t) + \mathbf{K}_a\mathbf{x}(t) = \mathbf{0} \tag{23}$$

While the lateral force $\mathbf{F}_a(t) = \mathbf{K}_a\mathbf{x}(t)$ in Eq. (23) takes care of the nonlinear geometric effects from all the gravity columns in the structure, the stiffness matrix $\mathbf{K}(t)$ in Eq. (23) considers both large *P*-Δ and small *P*-δ effects of geometric nonlinearity on the moment-resisting frame itself. Let this time-dependent global stiffness matrix $\mathbf{K}(t)$ be represented in the form:

$$\mathbf{K}(t) = \mathbf{K}_L + \mathbf{K}_G(t) \tag{24}$$

where $\mathbf{K}_L$ denotes the linearized elastic stiffness of the frame due to the gravity loads on the frame only, and $\mathbf{K}_G(t)$ denotes the change in the geometric stiffness due to the change in axial load on the frame during the dynamic loading. Since the $\mathbf{K}_L$ matrix is computed by using the gravity loads on the columns of the frame (which means $\mathbf{K}_L = \mathbf{K}(t_0) = \mathbf{K}(0)$, i.e., the stiffness matrix computed at time step 0) only, it is not a function of time and therefore remains as a constant throughout the dynamic analysis.

5. Energy Balance

Seismic energy evaluation begins with Eq. (23). Integrating this equation over the path of displacement response gives

$$\int_0^t \ddot{\mathbf{y}}(t)^T \mathbf{M} d\mathbf{x} + \int_0^t \dot{\mathbf{x}}(t)^T \mathbf{C} d\mathbf{x} + \int_0^t \mathbf{x}'(t)^T \mathbf{K}(t) d\mathbf{x} + \int_0^t \mathbf{x}(t)^T \mathbf{K}_a d\mathbf{x} = 0 \tag{25}$$

Note that $d\mathbf{x}(t) = d\mathbf{y}(t) - d\mathbf{g}(t)$, where $\mathbf{y}(t)$ is the $n \times 1$ absolute displacement vector and $\mathbf{g}(t)$ is the $n \times 1$ earthquake ground displacement vector. Now substituting this equation into the first integral of Eq. (25) gives

$$\int_0^t \ddot{\mathbf{y}}(t)^T \mathbf{M} d\mathbf{y} + \int_0^t \dot{\mathbf{x}}(t)^T \mathbf{C} d\mathbf{x} + \int_0^t \mathbf{x}'(t)^T \mathbf{K}(t) d\mathbf{x} + \int_0^t \mathbf{x}(t)^T \mathbf{K}_a d\mathbf{x} = \int_0^t \ddot{\mathbf{y}}(t)^T \mathbf{M} d\mathbf{g} \tag{26}$$

In addition, Eq. (14) can be expressed in incremental form as $d\mathbf{x}(t) = d\mathbf{x}'(t) + d\mathbf{x}''(t)$. Substituting this equation into the third integral of Eq. (26) gives

$$\int_0^t \ddot{\mathbf{y}}(t)^T \mathbf{M} d\mathbf{y} + \int_0^t \dot{\mathbf{x}}(t)^T \mathbf{C} d\mathbf{x} + \int_0^t \mathbf{x}'(t)^T \mathbf{K}(t) d\mathbf{x}' + \int_0^t \mathbf{x}(t)^T \mathbf{K}_a d\mathbf{x} + \int_0^t \mathbf{x}'(t)^T \mathbf{K}(t) d\mathbf{x}'' = \int_0^t \ddot{\mathbf{y}}(t)^T \mathbf{M} d\mathbf{g} \tag{27}$$

Each integral in Eq. (27) is considered separately in the following sub-sections.

5.1 Kinetic Energy (*KE*)

The first integral on the left hand side of Eq. (27) represents the absolute kinetic energy (*KE*) and can be evaluated using absolute velocity of the structure as:

$$KE(t_k) = \int_0^{t_k} \ddot{\mathbf{y}}(t)^T \mathbf{M} d\mathbf{y} = \frac{1}{2}\dot{\mathbf{y}}(t_k)^T \mathbf{M}\dot{\mathbf{y}}(t_k) - \frac{1}{2}\dot{\mathbf{y}}(0)^T \mathbf{M}\dot{\mathbf{y}}(0) = \frac{1}{2}\dot{\mathbf{y}}_k^T \mathbf{M}\dot{\mathbf{y}}_k \tag{28}$$

where $\dot{\mathbf{y}}(t)$ is the $n \times 1$ absolute velocity vector, $\dot{\mathbf{y}}_k$ represents the discretized form of $\dot{\mathbf{y}}(t_k)$, and t_k represents the k^{th} time step at which the energy value is calculated. The structure is assumed to be at rest when the earthquake begins, and therefore $\dot{\mathbf{y}}(0) = \mathbf{0}$. Due to the squaring of the absolute velocity vector in Eq. (28) and a positive definite **M** matrix, the kinetic energy is always positive.

5.2 Damping Energy (*DE*)

The second integral on the left hand side of Eq. (27) represents the damping energy (*DE*), which is the energy dissipated via viscous damping mechanism within the structure. The integrand is always positive, and therefore damping energy always accumulates over time. In terms of numerical simulation, the integral can be numerically approximated by evaluating the area underneath the curve using the trapezoidal rule:

$$DE(t_k) = \int_0^{t_k} \dot{\mathbf{x}}(t)^T \mathbf{C} d\mathbf{x} = \sum_{k=1}^{t_k} \frac{1}{2}\left(\dot{\mathbf{x}}_{k-1}^T + \dot{\mathbf{x}}_k^T\right)\mathbf{C}\left(\mathbf{x}_k - \mathbf{x}_{k-1}\right) \tag{29}$$

where $\mathbf{x}_k$ and $\dot{\mathbf{x}}_k$ represent the discretized forms of $\mathbf{x}(t_k)$ and $\dot{\mathbf{x}}(t_k)$, respectively.

5.3 Strain Energy (*SE*)

The third integral on the left hand side of Eq. (27) represents strain energy (*SE*) of the moment-resisting frame. Since the stiffness matrix $\mathbf{K}(t)$ is time-varying, obtaining a closed form solution to the integral is not possible. However, an assumption can be made by setting the $\mathbf{K}_G(t)$ matrix in Eq. (24) to zero, indicating that the overall gravity loads on the frame as a whole remains constant even though the axial forces in individual columns may vary. Based on this assumption, Eq. (24) becomes $\mathbf{K}(t) = \mathbf{K}_L$, and the strain energy of the moment-resisting frame is calculated as

$$SE(t_k) = \int_0^{t_k} \mathbf{x}'(t)^T \mathbf{K}(t) d\mathbf{x}' = \int_0^{t_k} \mathbf{x}'(t)^T \mathbf{K}_L d\mathbf{x}' = \frac{1}{2}\mathbf{x}'(t_k)^T \mathbf{K}_L \mathbf{x}'(t_k) - \frac{1}{2}\mathbf{x}'(0)^T \mathbf{K}_L \mathbf{x}'(0) = \frac{1}{2}\mathbf{x}_k'^T \mathbf{K}_L \mathbf{x}_k' \tag{30}$$

where $\mathbf{x}_k'$ represents the discretized form of $\mathbf{x}'(t_k)$. The structure is again assumed to be at rest when the earthquake begins, and therefore $\mathbf{x}'(0) = \mathbf{0}$. Due to the squaring of the elastic displacement vector in Eq. (30) and a positive definite $\mathbf{K}_L$ matrix, the strain energy is always positive.

5.4 Higher-order Energy (*HE*)

The fourth integral on the left hand side of Eq. (27) represents higher-order energy (*HE*) due to gravity loads on the structure itself. It is of higher-order because the energy comes from the large *P*-Δ effect on the gravity columns and is calculated as follows:

$$HE(t_k) = \int_0^{t_k} \mathbf{x}(t)^T \mathbf{K}_a d\mathbf{x} = \frac{1}{2}\mathbf{x}(t_k)^T \mathbf{K}_a \mathbf{x}(t_k) - \frac{1}{2}\mathbf{x}(0)^T \mathbf{K}_a \mathbf{x}(0) = \frac{1}{2}\mathbf{x}_k^T \mathbf{K}_a \mathbf{x}_k \tag{31}$$

where the structure is again assumed to be at rest when the earthquake begins, and therefore $\mathbf{x}(0) = \mathbf{0}$. Due to the squaring of the total displacement vector in Eq. (31) and a negative definite $\mathbf{K}_a$ matrix as shown in Eq. (21), the higher-order energy is always negative and varies with time.

5.5 Plastic Energy (*PE*)

The fifth integral on the left hand side of Eq. (27), which is associated with inelastic displacements, represents the plastic energy (*PE*) dissipated by the permanent deformations of the structure. Rewriting Eqs. (16) and (17) in the forms:

$$\mathbf{K}(t) d\mathbf{x}'' = \mathbf{K}'(t) d\boldsymbol{\Theta}'' \quad , \quad \mathbf{x}'(t)^T \mathbf{K}'(t) = \mathbf{m}'(t)^T \tag{32}$$

Then substituting Eq. (32) into the fifth integral of Eq. (27) gives

$$PE(t_k) = \int_0^{t_k} \mathbf{x}'(t)^T \mathbf{K}(t) d\mathbf{x}'' = \int_0^{t_k} \mathbf{x}'(t)^T \mathbf{K}'(t) d\boldsymbol{\Theta}'' = \int_0^{t_k} \mathbf{m}'(t)^T d\boldsymbol{\Theta}'' = \sum_{i=1}^{m} \int_0^{t_k} m_i'(t) d\theta_i'' = \sum_{i=1}^{m} PE_i(t_k) \tag{33}$$

where PE_i represents the plastic energy dissipation at the i^{th} plastic hinge, $i = 1,...,m$. Through this analytical derivation, it is shown in Eq. (33) that the overall plastic energy dissipation is exactly equal to the sum of plastic energy dissipation in all the plastic hinges.

The term PE_i in Eq. (33) can be numerically approximated by evaluating the area underneath the curve using the trapezoidal rule:

$$PE_i = \int_0^{t_k} m_i'(t)\,d\theta_i'' = \sum_{k=1}^{t_k} \frac{1}{2}\left(m_{i,k-1}' + m_{i,k}'\right)\left(\theta_{i,k}'' - \theta_{i,k-1}''\right) \tag{34}$$

where $m_{i,k}'$ and $\theta_{i,k}''$ represent the discretized forms of $m_i'(t_k)$ and $\theta_i''(t_k)$, respectively.

Note that PE_i is computed by integrating the product of elastic moment m_i' and the change in plastic rotation $d\theta_i''$. A positive change in plastic rotation is always caused by a positive moment, and a negative change in plastic rotation is always caused by a negative moment. Therefore, PE_i is always positive and accumulates over time.

5.6 Input Energy (*IE*)

Finally, the integral on the right side of Eq. (27) represents the absolute input energy (*IE*) due to the earthquake ground motion, and this integral can be numerically approximated by evaluating the area underneath the curve using the trapezoidal rule:

$$IE(t_k) = \int_0^{t_k} \ddot{\mathbf{y}}(t)^T \mathbf{M}\,d\mathbf{g} = \sum_{k=1}^{t_k} \frac{1}{2}\left(\ddot{\mathbf{y}}_{k-1}^T + \ddot{\mathbf{y}}_k^T\right)\mathbf{M}\left(\mathbf{g}_k - \mathbf{g}_{k-1}\right) \tag{35}$$

where $\ddot{\mathbf{y}}_k$ and $\mathbf{g}_k$ represent the discretized forms of $\ddot{\mathbf{y}}(t_k)$ and $\mathbf{g}(t_k)$, respectively.

In summary, substituting Eqs. (28), (29), (30), (31), (33), and (35) into Eq. (27), the energy balance equation becomes

$$KE + DE + SE + HE + PE = IE \tag{36}$$

6. Numerical Simulation of a 4-story Moment-Resisting Frame

To illustrate the use of Eq. (36) in calculating the energy dissipation of moment-resisting frames, consider the four-story frame shown in Fig. 2(a). This frame contains 36 DOFs (i.e., $n = 36$). and 56 PHLs (i.e., $m = 56$). Assume a mass of 72,670 kg is used on each floor, and a gravity load of 431 kN is applied on each exterior column member and 632 kN is applied on each interior column member as shown in Fig. 2(b). In addition, a leaning column is used in the model to account for all of the gravity loads from other parts of the structure as shown in Fig. 2(b). The gravity loads on the leaning column is assumed to be 2,018 kN per floor. A 2% damping is assumed in all four modes of vibration.

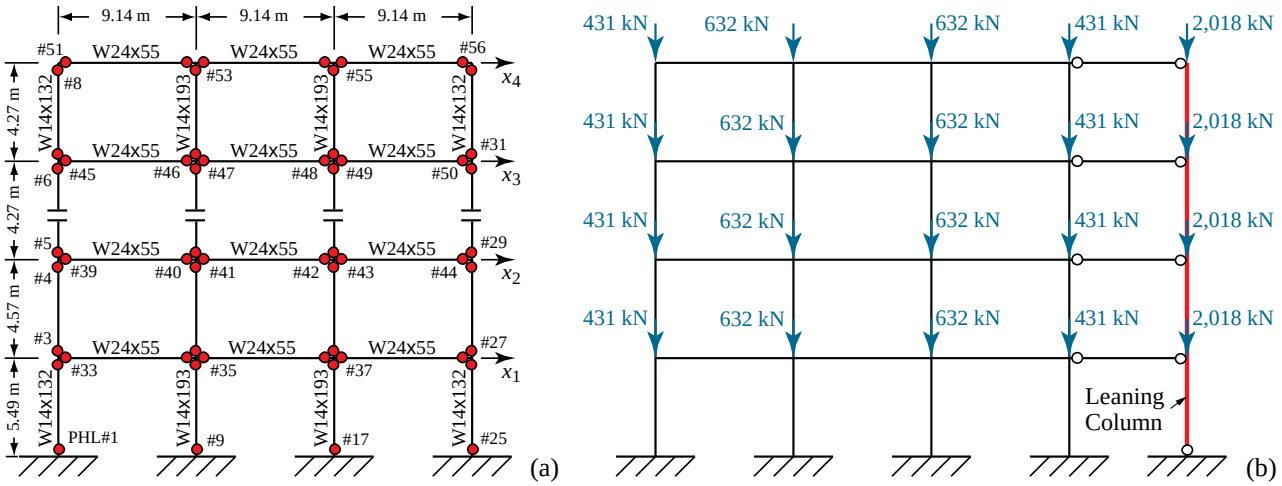

Fig. 2 – Four-story moment-resisting steel frame and corresponding gravity loads

Assume the yield stress of the member is 345 MPa and all 56 plastic hinges exhibit elastic-plastic behavior. By subjecting the steel frame to the 1995 Kobe earthquake ground acceleration shown in Fig. 3, the energy responses are summarized in Fig. 4, where the case "without axial force" represents the approach used in previous research [5] and the case "with axial force" represents the present approach with geometric nonlinearity due to axial force considered in the stiffness formulation. The results confirm that *KE* and *SE* are always positive, *DE* and *PE* are accumulative and never decreasing, and *HE* is always negative. The magnitude of *HE* is smaller than that of *DE* and *PE*, and therefore *IE* tends to follow an increasing trend. One interesting point to note is that *HE* has a larger magnitude than *SE* after 10 s, indicating that higher-order energy builds up quickly when permanent deformation occurs in the structure due to yielding.

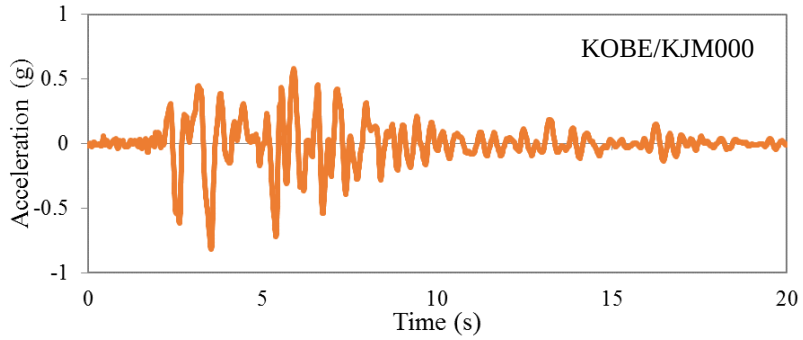

Fig. 3 – Recorded 1995 Kobe earthquake ground motion at Kajima station Component 000

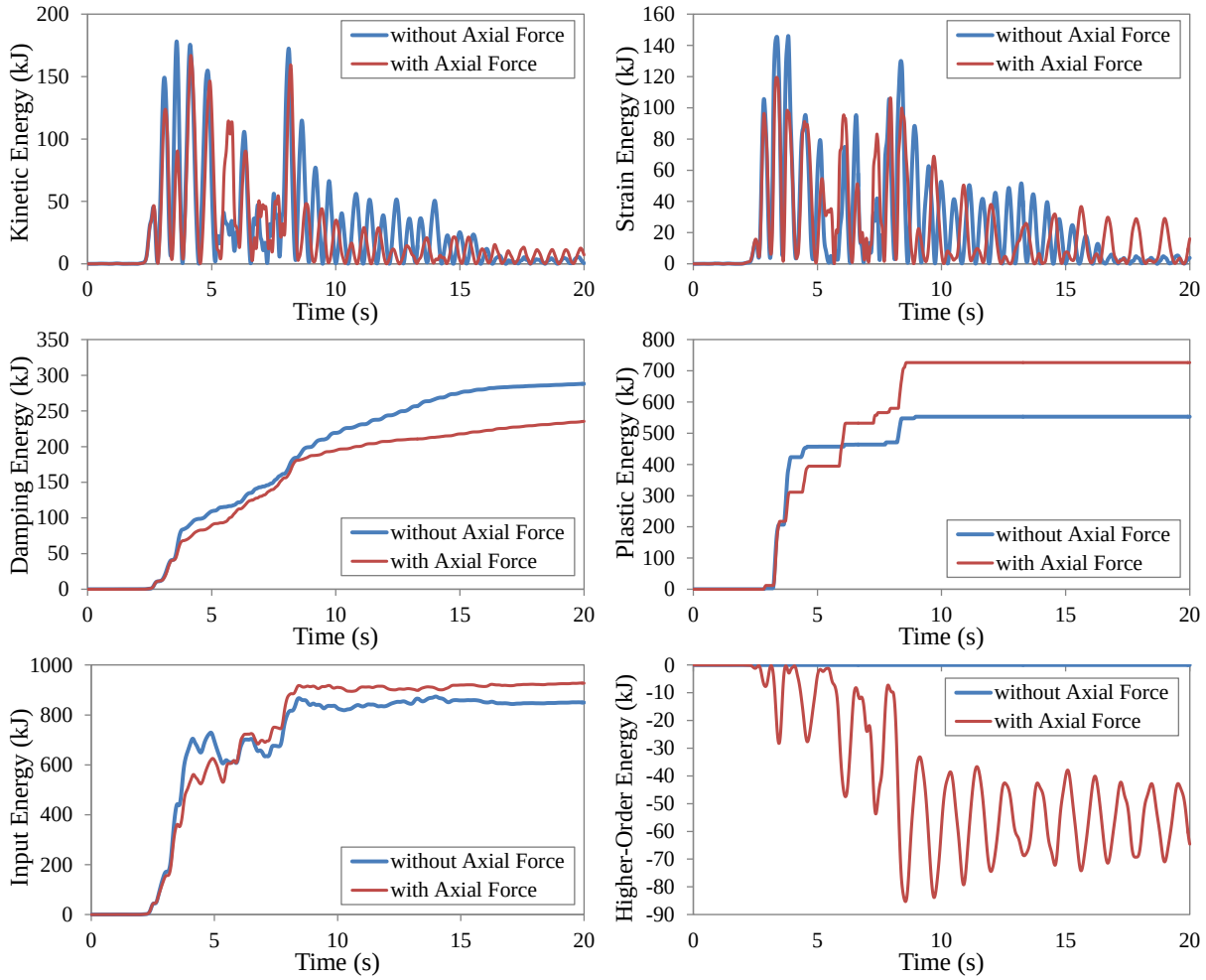

Fig. 4 – Energy response of the 4-story framed structure with geometric nonlinearity due to Kobe earthquake

In terms of energy dissipation, it can be seen from Fig. 4 that both *KE* and *SE* diminish slowly as the earthquake subsides, and the energy components responsible for dissipating the *IE* due to the earthquake are *DE* and *PE*. As shown in Fig. 4, the input energy to the frame is approximately the same for the cases with and without axial force modeled for geometric nonlinearity. However, when geometric nonlinearity is considered, larger *PE* dissipation is needed with smaller *DE* dissipation, verifying that geometric nonlinearity causes more damage to the structure.

In terms of plastic energy dissipation at individual plastic hinges, Fig. 5(a) shows the maximum plastic energy at each plastic hinge, i.e., PE_i . Since plastic energy accumulates over time, the maximum plastic energy always occurs at the end of the earthquake duration. In addition, summing the plastic energy values at all the plastic hinges in Fig. 5(a) gives the total plastic energy dissipation *PE* in Fig. 4, confirming Eq. (33) is correct. Finally, Fig. 5(b) shows the relative proportion of each energy component of those shown in Fig.5(a) for the frame with geometric nonlinearity that makes up the input energy. It can be seen from this figure that *PE* is at least three times larger than *DE*, illustrating that damage to the plastic hinges is the major source of energy dissipation for the four-story frame due to the Kobe earthquake ground motion.

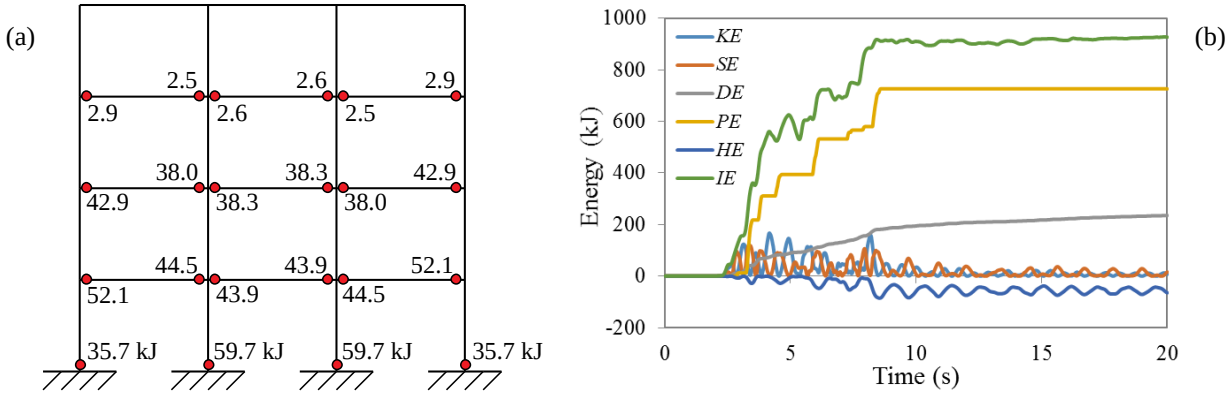

Fig. 5 – Energy response of structure with geometric nonlinearity: (a) Plastic energy dissipation at individual plastic hinges and (b) portions of individual energies making up the input energy

By including the axial force in the formulation, different forms of potential energy can now be captured and balanced. More importantly, based on the above analytical derivation and numerical example, a computational tool based on small displacement approach is now available to capture the dissipated plastic energy in the inelastic components of the structure that considers both geometric and material nonlinearities. In addition, the analytical derivation proves that the sum of dissipation plastic energy at each inelastic component equals the overall plastic energy dissipation, which is an energy form of the energy balance equation. Because of the accumulative nature of plastic energy, it can be used in a wide range of applications. These potential applications include:

- Assessment of structural damage via the comparison of plastic energy demand with the corresponding plastic energy capacity of members.
- Evaluation of residual capacity of the structure after suffering damage during an earthquake event.
- Development of assessment metrics for structural performance.

7. Conclusion

An analytical theory and the corresponding computational method for evaluating the seismic energy in structures are presented based on the use of stability functions in the formulation of the stiffness matrix. The proposed method successfully separates the coupling effect of material nonlinearity and geometric nonlinearity by using inelastic displacement. By expressing the input energy as the sum of kinetic energy, damping energy, strain

energy, higher-order energy, and plastic energy, as summarized by Eq. (36), the energy representation of the structural response due to earthquake ground motion is complete. For potential energy in particular,

- Strain energy (*SE*) represents the linear elastic portion of the structural response that is recoverable;
- Higher-order energy (*HE*) represents the addition or subtraction of energy from the overall structural response due to geometric nonlinear effects; and
- Plastic energy (*PE*) represents the dissipation of energy and reduction of structural response due to material nonlinearity.

Careful attention should be paid to the difference between *HE* and *PE*, even though both represent the nonlinear energy response of the structure. While *PE* represents damage in the structure resulting from inelastic deformation, *HE* represents the stored energy due the higher-order effect of gravity loads acting on the gravity columns, which contains both elastic displacement response and inelastic displacement response due to yielding of the structure. Therefore, the coupling effect between geometric nonlinearity and material nonlinearity, which is often found in the calculation of structural displacement responses, occurs in the energy calculation also.

8. Disclaimer

No formal investigation to evaluate potential sources of uncertainty or error, or whether multiple sources of error are correlated, was included in this study. The question of uncertainties in the analytical models, solution algorithms, material properties and as-built final dimensions and positions of members versus design configurations employed in analysis are beyond the scope of the work reported here.

9. References

[1] Tembulkar J, Nau JM (1987): Inelastic modeling and seismic energy dissipation. *Journal of Structural Engineering ASCE*, **113** (6), 1373-1377.

[2] Fajfar P, Vidic T, Fischinger M (1989): Seismic demand in medium-period and long-period structures. *Earthquake Engineering and Structural Dynamics*, **18** (8), 1133-1144.

[3] Fajfar P (1992): Equivalent ductility factors, taking into account low-cycle fatigue. *Earthquake Engineering and Structural Dynamics*, **21** (10), 837-848.

[4] Uang CM, Bertero VV (1990): Evaluation of seismic energy in structures. *Earthquake Engineering and Structural Dynamics*, **19** (1), 77-90.

[5] Wong KKF, Yang R (2002): Earthquake response and energy evaluation of inelastic structures. *Journal of Engineering Mechanics ASCE*, **128** (3), 308-317.

[6] Timoshenko SP, Gere JM (1961): *Theory of Elastic Stability, 2nd Edition*, McGraw Hill, NY, USA.

[7] Horne MZ, Merchant W (1965): *The Stability of Frames*, Pergamon Press, NY, USA.

[8] Bazant ZP, Cedolin L (2003): *Stability of Structures*, Dover Publication, NY, USA.

[9] Powell GH (2010): *Modeling for Structural Analysis: Behavior and Basics*, Computers and Structures Inc., CA, USA.

[10] Wilson E (2010): *Static and Dynamic Analysis of Structures: A Physical Approach with Emphasis on Earthquake Engineering, 4th Edition*, Computer and Structures Inc., CA, USA.

[11] Park JW, Kim SE (2008): Nonlinear inelastic analysis of steel-concrete composite beam-columns using the stability functions. *Structural Engineering and Mechanics*, **30** 6, 763-785.

[12] Li G, Wong KKF (2014): *Theory of Nonlinear Structural Analysis: The Force Analogy Method for Earthquake Engineering*, John Wiley and Sons, Singapore.

[13] Hibbeler RC (2012): *Structural Analysis, 8th Edition*, Prentice Hall, NJ, USA.

[14] Wong KKF, Yang R (1999): Inelastic dynamic response of structures using force analogy method. *Journal of Engineering Mechanics ASCE*, **125** (10), 1190-1199.

RELIABILITY OF PLASTIC ROTATION CALCULATIONS FOR DAMAGE ASSESSMENT OF MOMENT-RESISTING FRAMED STRUCTURES

K.K.F. Wong[(1)]

[(1)] *Research Structural Engineer, National Institute of Standards and Technology, kevin.wong@nist.gov*

Abstract

Performance-based standards use plastic rotation as an important measure to determine whether the response meets the acceptance criteria for moment-resisting frames. Since plastic rotation is the key parameter in performance-based seismic engineering, the method used to calculate this quantity must be robust and accurate. Although engineers often rely on the plastic rotation output from structural analysis software packages to determine acceptable performance, the actual calculation methods usually depend on the analytical formulations utilized in the particular software. Difficulties in verifying the accuracy of the output results exist because material nonlinearity is often coupled with geometric nonlinearity in the analysis of moment-resisting frames, yet a robust analytical framework for the verification process is currently unavailable because of the lack of analytical theory. To address this problem, an analytical method to calculate the plastic rotations of plastic hinges in moment-resisting frames is presented in this research. The element stiffness matrices are rigorously derived using a member formulation, which includes the coupling of geometric and material nonlinearity effects from the beginning of the derivation. Numerical simulation is performed to calculate the nonlinear responses of structural models subjected to static and dynamic loads. Plastic rotations and other response measures are compared with those obtained using other methods of handling geometric nonlinearity to demonstrate the feasibility of the proposed analytical method.

Keywords: Geometric nonlinearity; material nonlinearity; stability functions; geometric stiffness; structural analysis

1. Introduction

Plastic rotation is one of the most important structural performance metrics for moment-resisting framed structures. Current performance-based standards, such as ASCE/SEI 41 [1], use plastic rotation as the primary performance measure in the assessment process. Relatively large lateral displacement and plastic rotations are expected to occur due to the flexibility of these frames. Therefore, the analysis of moment-resisting framed structures should possess the capability of handling both material nonlinearity and geometric nonlinearity in order to provide the outputs necessary for gauging acceptable performance when large displacements are expected [2-5].

Geometric nonlinearity causes a reduction in stiffness due to the axial compressive force acting on the entire length in the member, while material nonlinearity causes a reduction in stiffness concentrated at the plastic hinges of the member. These two nonlinear phenomena interact with one another in moment-resisting frames, but different structural analysis software packages and algorithms use different assumptions to capture the interaction. The most efficient approach is to handle material and geometrically nonlinearity independently. It can be shown that running an algorithm considering material nonlinearity by itself will produce reasonably accurate results. Moreover, separately running an algorithm considering geometric nonlinearity also can produce reasonably accurate results. However, when material nonlinearity is combined with geometric nonlinearity in an analysis, algorithms often neglect the interactions between these nonlinearities, resulting in limited consistency, reduced accuracy, and solution instability. As a result, plastic rotation, as the end product of the analysis, can differ significantly based on the approach taken in the nonlinear algorithm.

One reason for the shortcoming in addressing the nonlinear interaction is that there is no analytical theory that can be used to measure this interaction. Therefore, a numerical solution is often employed that assumes the nonlinear interaction is automatically taken into account when both material and geometric nonlinearities are independently captured and combined. In view of this shortcoming, the present research proposes a method to accurately calculate the plastic rotation while capturing the interaction of material nonlinearity and geometric nonlinearity using an analytical theory based on fundamental principles of structural mechanics. Element stiffness matrices are first derived using a member with plastic hinges subjected to axial compression; therefore, both geometric nonlinearity and material nonlinearity along with their interactions are captured from the beginning of the formulation. The element stiffness matrices are then assembled in the global stiffness matrices to perform both nonlinear static analysis and nonlinear dynamic analysis. Numerical simulations are then performed on simple frames to calculate plastic rotations, and the results are compared with those obtained from other methods of analysis that consider different forms of geometric nonlinearity.

2. Stiffness Matrices for Geometric and Material Nonlinearities

The use of stability functions for analyzing moment-resisting framed structures is here derived to determine the element stiffness matrices of frame members with plastic hinges at both ends. The original theory was first developed for elastic members in the 1960's [6-7] without any consideration of yielding and formation of plastic hinge, but it found limited application because of its complexity in the closed-form solution as compared to those methods of using either the *P*-Δ stiffness approach [8] or the geometric stiffness approach [9]. However, when large lateral deflections in framed structures are expected, excessive geometric nonlinearity is coupled with excessive material nonlinearity, and the first-order or second-order approximation of the geometric nonlinearity may not be able to capture the nonlinear behavior accurately. Therefore, stability functions are used to investigate the differences in plastic rotation calculations as compared to other geometric nonlinearity formulations.

2.1 Element Stiffness Matrix $[\mathbf{k}_i]$

Four degrees of freedom (DOFs) are typically used to describe the lateral displacement and rotation at the two ends of a member of moment-resisting frames. To compute the element stiffness matrix $\mathbf{k}_i$, each of these 4 DOFs is displaced independently by one unit as shown in Fig. 1 while subjected to an axial compressive load *P*.

Here, V_{1s}, M_{1s}, V_{2s}, and M_{2s} represent the required shear forces and moments at the two ends of the member to cause the lateral displacements and rotations in the prescribed pattern, and $s = 1,...,4$ represents the four cases of unit displacement patterns of the member's deflection.

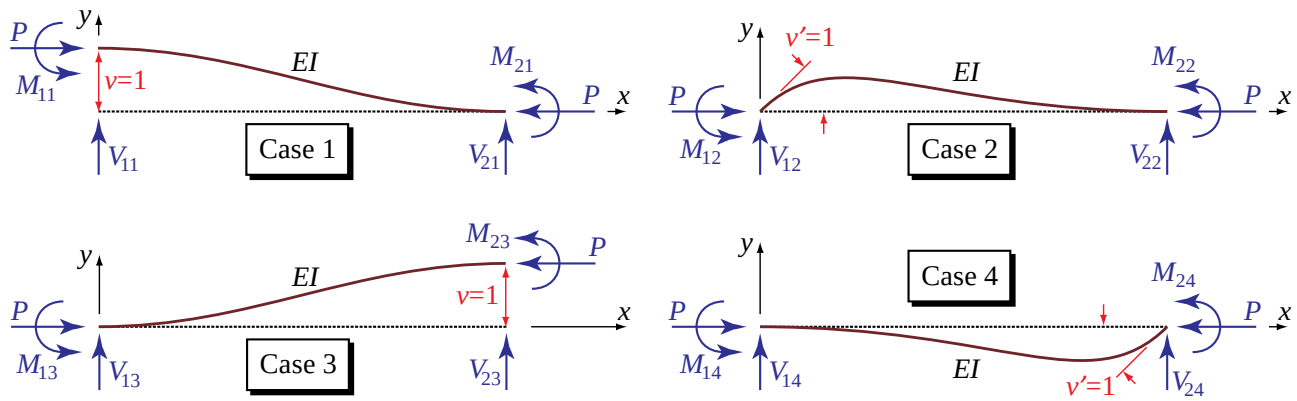

Fig. 1 – Four cases of displacement patterns and the corresponding fixed-end forces

Using the classical Bernoulli-Euler beam theory with homogeneous and isotropic material properties where the moment is proportional to the curvature and plane sections are assumed to remain plane, the governing equilibrium equation describing the deflected shape of the member can be written as

$$(EIv'')'' + Pv'' = 0 \tag{1}$$

where E is the elastic modulus, I is the moment of inertia, v is the lateral deflection, P is the axial compressive force of the member, and each prime represents taking derivatives of the corresponding variable with respect to the x-direction of the member. By assuming EI is constant along the member, the solution to the fourth-order ordinary differential equation becomes:

$$v = A\sin kx + B\cos kx + Cx + D \tag{2}$$

where $k^2 = P/EI$. Let $\lambda = kL$ to simplify the derivations, where L is the length of the member. The following four cases of boundary conditions (in reverse order) are now considered.

Case 4:

For Case 4 as shown in Fig. 1, imposing the boundary conditions $v(0) = 0$, $v'(0) = 0$, $v(L) = 0$, and $v'(L) = 1$ on Eq. (2) gives

$$v(0) = 0: \qquad B + D = 0 \tag{3a}$$

$$v'(0) = 0: \qquad kA + C = 0 \tag{3b}$$

$$v(L) = 0: \qquad A\sin\lambda + B\cos\lambda + CL + D = 0 \tag{3c}$$

$$v'(L) = 1: \qquad kA\cos\lambda - kB\sin\lambda + C = 1 \tag{3d}$$

Solving simultaneously for the constants in Eq. (3) gives

$$A = \frac{L(1-\cos\lambda)}{\lambda(\lambda\sin\lambda + 2\cos\lambda - 2)}, \quad B = \frac{L(\sin\lambda - \lambda)}{\lambda(\lambda\sin\lambda + 2\cos\lambda - 2)}, \quad C = -kA, \quad D = -B \tag{4}$$

Therefore, Eq. (2) along with the constants in Eq. (4) gives the deflected shape for Case 4. The shears (i.e., V_{14} and V_{24}) and moments (i.e., M_{14} and M_{24}) at the two ends of the member (see Fig. 1) are then evaluated using the classical Bernoulli-Euler beam theory formula:

$$M(x) = EIv'' \quad , \quad V(x) = EIv''' + Pv' \tag{5}$$

Now taking derivatives of Eq. (2) and substituting the results into Eq. (5) while using the constants calculated in Eq. (4), the shears and moments at the two ends of the member for Case 4 in Fig. 1 are calculated as:

$$M_{14} = -EIv''(0) = EIk^2 B = \hat{s}\hat{c}EI/L \tag{6a}$$

$$V_{14} = EIv'''(0) + Pv'(0) = -EIk^3 A + P \times 0 = \bar{s}EI/L^2 \tag{6b}$$

$$M_{24} = EIv''(L) = -EIk^2\left(A\sin\lambda + B\cos\lambda\right) = \hat{s}EI/L \tag{6c}$$

$$V_{24} = -EIv'''(L) - Pv'(L) = EIk^3\left(A\cos\lambda - B\sin\lambda\right) - P \times 1 = -\bar{s}EI/L^2 \tag{6d}$$

where

$$\hat{s} = \frac{\lambda\left(\sin\lambda - \lambda\cos\lambda\right)}{2 - 2\cos\lambda - \lambda\sin\lambda} \quad , \quad \hat{c} = \frac{\lambda - \sin\lambda}{\sin\lambda - \lambda\cos\lambda} \quad , \quad \bar{s} = \hat{s} + \hat{s}\hat{c} = \frac{\lambda^2\left(1 - \cos\lambda\right)}{2 - 2\cos\lambda - \lambda\sin\lambda} \tag{7}$$

The minus signs appear in front of the equations for M_{14} in Eq. (6a) and V_{24} in Eq. (6d) because there is a difference in sign convention between the classical Bernoulli-Euler beam theory and the theory for the stiffness method of structural analysis.

Case 3:

For Case 3 as shown in Fig. 1, imposing the boundary conditions $v(0) = 0$, $v'(0) = 0$, $v(L) = 1$, and $v'(L) = 0$, the constants in Eq. (2) can be solved by using a similar procedure as presented in Case 4 above. Then the shears and moments at the two ends of the member for Case 3 in Fig. 1 are calculated as:

$$M_{13} = -EIv''(0) = -\bar{s}EI/L^2 \quad , \quad V_{13} = EIv'''(0) + Pv'(0) = -s'EI/L^3 \tag{8a}$$

$$M_{23} = EIv''(L) = -\bar{s}EI/L^2 \quad , \quad V_{23} = -EIv'''(L) - Pv'(L) = s'EI/L^3 \tag{8b}$$

where

$$s' = 2\bar{s} - \lambda^2 = \frac{\lambda^3\sin\lambda}{2 - 2\cos\lambda - \lambda\sin\lambda} \tag{9}$$

Case 2:

For Case 2 as shown in Fig. 1, imposing the boundary conditions $v(0) = 0$, $v'(0) = 1$, $v(L) = 0$, and $v'(L) = 0$ on Eq. (2) and following a similar procedure as presented in Cases 3 and 4 above, the shears and moments at the two ends are calculated as:

$$M_{12} = -EIv''(0) = \hat{s}EI/L \quad , \quad V_{12} = EIv'''(0) + Pv'(0) = \bar{s}EI/L^2 \tag{10a}$$

$$M_{22} = EIv''(L) = \hat{s}\hat{c}EI/L \quad , \quad V_{22} = -EIv'''(L) - Pv'(L) = -\bar{s}EI/L^2 \tag{10b}$$

Case 1:

Finally for Case 1 as shown in Fig. 1, imposing the boundary conditions $v(0) = 1$, $v'(0) = 0$, $v(L) = 0$, and $v'(L) = 0$ on Eq. (2) and following a similar procedure as presented in Cases 3 and 4 above, the shears and moments at the two ends are calculated as:

$$M_{11} = -EIv''(0) = \bar{s}EI/L^2 \quad , \quad V_{11} = EIv'''(0) + Pv'(0) = s'EI/L^3 \tag{11a}$$

$$M_{21} = EIv''(L) = \bar{s}EI/L^2 \quad , \quad V_{21} = -EIv'''(L) - Pv'(L) = -s'EI/L^3 \tag{11b}$$

In summary, based on Eqs. (6), (8), (10), and (11) for the above four cases, the element stiffness matrix of the i^{th} member $\mathbf{k}_i$ for bending after incorporating axial compressive force using stability functions becomes:

$$\mathbf{k}_i^{SF} = \frac{EI}{L^3}\begin{bmatrix} s' & \bar{s}L & -s' & \bar{s}L \\ \bar{s}L & \hat{s}L^2 & -\bar{s}L & \hat{s}\hat{c}L^2 \\ -s' & -\bar{s}L & s' & -\bar{s}L \\ \bar{s}L & \hat{s}\hat{c}L^2 & -\bar{s}L & \hat{s}L^2 \end{bmatrix} \begin{matrix} \leftarrow v(0) \\ \leftarrow v'(0) \\ \leftarrow v(L) \\ \leftarrow v'(L) \end{matrix} \tag{12}$$

where the superscript '*SF*' is used to denote that the element stiffness matrix $\mathbf{k}_i$ is computed by using the stability functions method.

Linearization of Eq. (12) can be performed by using Taylor series expansion on each term of the element stiffness matrix and truncating higher-order terms. Doing so gives

$$\mathbf{k}_i^{GS} = \frac{EI}{L^3}\begin{bmatrix} 12 & 6L & -12 & 6L \\ 6L & 4L^2 & -6L & 2L^2 \\ -12 & -6L & 12 & -6L \\ 6L & 2L^2 & -6L & 4L^2 \end{bmatrix} - \begin{bmatrix} 6P/5L & P/10 & -6P/5L & P/10 \\ P/10 & 2PL/15 & -P/10 & -PL/30 \\ -6P/5L & -P/10 & 6P/5L & -P/10 \\ P/10 & -PL/30 & -P/10 & 2PL/15 \end{bmatrix} \begin{matrix} \leftarrow v(0) \\ \leftarrow v'(0) \\ \leftarrow v(L) \\ \leftarrow v'(L) \end{matrix} \tag{13}$$

where the first matrix in Eq. (13) represents that classic stiffness matrix without considering any geometric nonlinearity, and the second matrix represents the geometric stiffness. The superscript '*GS*' is used to denote that the element stiffness matrix $\mathbf{k}_i$ is computed by using the geometric stiffness method. Finally, the element stiffness matrix in Eq. (13) can be further simplified by retaining only the large *P*-Δ stiffness while ignoring the small *P*-δ effect. Doing so gives

$$\mathbf{k}_i^{PD} = \frac{EI}{L^3}\begin{bmatrix} 12 & 6L & -12 & 6L \\ 6L & 4L^2 & -6L & 2L^2 \\ -12 & -6L & 12 & -6L \\ 6L & 2L^2 & -6L & 4L^2 \end{bmatrix} - \begin{bmatrix} P/L & 0 & -P/L & 0 \\ 0 & 0 & 0 & 0 \\ -P/L & 0 & P/L & 0 \\ 0 & 0 & 0 & 0 \end{bmatrix} \begin{matrix} \leftarrow v(0) \\ \leftarrow v'(0) \\ \leftarrow v(L) \\ \leftarrow v'(L) \end{matrix} \tag{14}$$

where the superscript '*PD*' is used to denote that the element stiffness matrix $\mathbf{k}_i$ is computed by using the *P*-Δ stiffness method.

2.2 Element Stiffness Matrix [$\mathbf{k}'_i$]

The second element stiffness matrix, $\mathbf{k}'_i$, relates the plastic rotations at the plastic hinge locations (PHLs) of the i^{th} member with the restoring forces applied at the DOFs. Two plastic hinges typically occur at the two ends of the member, and they are labeled as '*a*' for plastic hinge at the '1' end and '*b*' for plastic hinge at the '2' end as shown in Fig. 2. The transpose of the $\mathbf{k}'_i$ matrix is here constructed. This $\mathbf{k}'^T_i$ matrix relates the lateral displacements and rotations at the two ends of the member (i.e., the four cases of unit displacements presented in Section 2.1) with the moments at the PHLs (i.e., M_{as} and M_{bs}, $s = 1,...,4$).

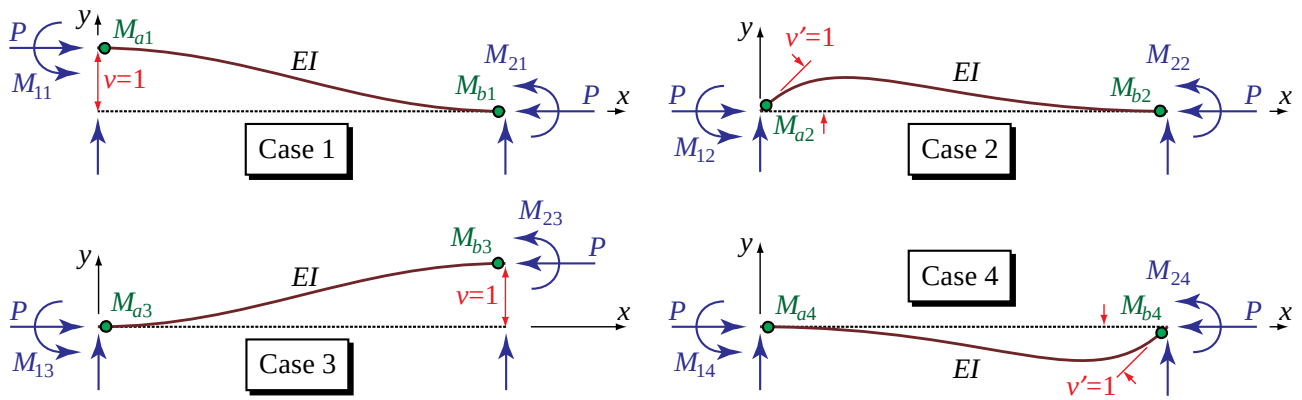

Fig. 2 – Displacement patterns for computation of moments at the PHLs

Consider each of the four cases of unit displacements for the member as shown in Fig. 2, where the moments at the plastic hinges '*a*' and '*b*' (i.e., M_{as} and M_{bs}, $s=1,...,4$) represent the desired quantities. By joint equilibrium based on Fig. 2, these moments for each of the four cases can be evaluated directly as presented in the following sub-sections.

Case 1:

For Case 1 as shown in Fig. 2, imposing the boundary conditions $v(0)=1$, $v'(0)=0$, $v(L)=0$, and $v'(L)=0$ gives the moments M_{a1} and M_{b1} (also see Eq. (11)) as:

$$M_{a1}=M_{11}=\bar{s}EI/L^2 \quad , \quad M_{b1}=M_{21}=\bar{s}EI/L^2 \tag{15}$$

Case 2:

For Case 2 as shown in Fig. 2, imposing the boundary conditions $v(0)=0$, $v'(0)=1$, $v(L)=0$, and $v'(L)=0$ gives the moments M_{a2} and M_{b2} (also see Eq. (10)) as:

$$M_{a2}=M_{12}=\hat{s}EI/L \quad , \quad M_{b2}=M_{22}=\hat{s}\hat{c}EI/L \tag{16}$$

Case 3:

For Case 3 as shown in Fig. 2, imposing the boundary conditions $v(0)=0$, $v'(0)=0$, $v(L)=1$, and $v'(L)=0$ gives the moments M_{a3} and M_{b3} (also see Eq. (8)) as

$$M_{a3}=M_{13}=-\bar{s}EI/L^2 \quad , \quad M_{b3}=M_{23}=-\bar{s}EI/L^2 \tag{17}$$

Case 4:

Finally, for Case 4 as shown in Fig. 2, imposing the boundary conditions $v(0)=0$, $v'(0)=0$, $v(L)=0$, and $v'(L)=1$ gives the moments M_{a4} and M_{b4} (also see Eq. (6)) as

$$M_{a4}=M_{14}=\hat{s}\hat{c}EI/L \quad , \quad M_{b4}=M_{24}=\hat{s}EI/L \tag{18}$$

In summary from Eqs. (15) to (18), the transpose of stiffness matrix $\mathbf{k}_i'$ for the i^{th} member becomes

$$\mathbf{k}_i'^T=\begin{bmatrix} M_{a1} & M_{a2} & M_{a3} & M_{a4} \\ M_{b1} & M_{b2} & M_{b3} & M_{b4} \end{bmatrix}=\begin{bmatrix} \bar{s}EI/L^2 & \hat{s}EI/L & -\bar{s}EI/L^2 & \hat{s}\hat{c}EI/L \\ \bar{s}EI/L^2 & \hat{s}\hat{c}EI/L & -\bar{s}EI/L^2 & \hat{s}EI/L \end{bmatrix}\begin{matrix} \leftarrow \theta_a'' \\ \leftarrow \theta_b'' \end{matrix} \tag{19}$$

Once the $\mathbf{k}_i'^T$ matrix in Eq. (19) is derived, the $\mathbf{k}_i'$ matrix can be written as:

$$\mathbf{k}_i'^{SF}=\begin{bmatrix} V_{1a} & V_{1b} \\ M_{1a} & M_{1b} \\ V_{2a} & V_{2b} \\ M_{2a} & M_{2b} \end{bmatrix}=\begin{bmatrix} M_{a1} & M_{b1} \\ M_{a2} & M_{b2} \\ M_{a3} & M_{b3} \\ M_{a4} & M_{b4} \end{bmatrix}=\begin{bmatrix} \bar{s}EI/L^2 & \bar{s}EI/L^2 \\ \hat{s}EI/L & \hat{s}\hat{c}EI/L \\ -\bar{s}EI/L^2 & -\bar{s}EI/L^2 \\ \hat{s}\hat{c}EI/L & \hat{s}EI/L \end{bmatrix}\begin{matrix} \leftarrow v(0) \\ \leftarrow v'(0) \\ \leftarrow v(L) \\ \leftarrow v'(L) \end{matrix} \tag{20}$$

where the superscript '*SF*' is used to denote that the element stiffness matrix $\mathbf{k}_i$ is computed by using the stability functions method.

2.3 Element Stiffness Matrix [$\mathbf{k}_i''$]

The third element stiffness matrix, $\mathbf{k}_i''$, relates the moments at PHLs '*a*' and '*b*' of the i^{th} member with a unit plastic rotation at each of these PHLs. To determine the $\mathbf{k}_i''$ matrix, the goal is to compute the plastic hinge moments M_{aa}, M_{ab}, M_{ba}, and M_{bb} due to a unit plastic rotation at either '*a*' or '*b*' as shown in Fig. 3. These moments for each of the two cases can be evaluated directly by using joint equilibrium as presented in the following sub-sections.

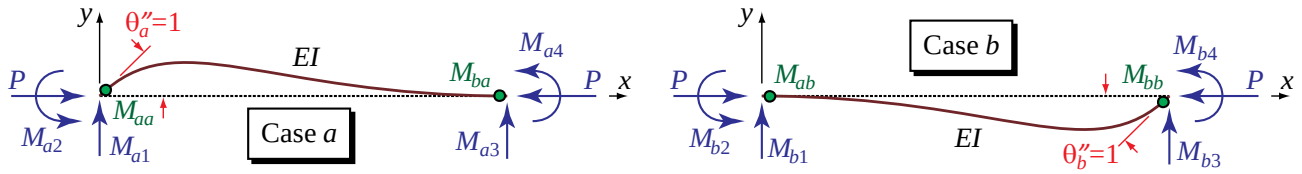

Fig. 3 – Displacement patterns for computation of moments due to unit plastic rotations

Case 'a':

For Case '*a*' of Fig. 3, imposing a unit plastic rotation $\theta''_a = 1$ and $\theta''_b = 0$ gives (see Eq. (20))

$$M_{aa} = M_{a2} = \hat{s}EI/L \quad , \quad M_{ba} = M_{a4} = \hat{s}\hat{c}EI/L \tag{21}$$

Case 'b':

For Case '*b*' of Fig. 3, imposing a unit plastic rotation $\theta''_a = 0$ and $\theta''_b = 1$ gives (see Eq. (20))

$$M_{ab} = M_{b2} = \hat{s}\hat{c}EI/L \quad , \quad M_{bb} = M_{b4} = \hat{s}EI/L \tag{22}$$

Therefore, in summary from Eqs. (21) and (22), the element stiffness matrix $\mathbf{k}''_i$ for the i^{th} member becomes

$$\mathbf{k}''^{SF}_i = \begin{bmatrix} \hat{s}EI/L & \hat{s}\hat{c}EI/L \\ \hat{s}\hat{c}EI/L & \hat{s}EI/L \end{bmatrix} \begin{matrix} \leftarrow \theta''_a \\ \leftarrow \theta''_b \end{matrix} \tag{23}$$

where the superscript '*SF*' is used to denote that the element stiffness matrix $\mathbf{k}_i$ is computed by using the stability functions method.

2.4 Global Stiffness Matrices

By using the element stiffness matrices computed in Eqs. (12), (20), and (23), the assembly of these matrices into the global stiffness matrices $\mathbf{K}$, $\mathbf{K}'$, and $\mathbf{K}''$ follows a straightforward procedure. A number of textbooks have discussed this procedure in great detail [10]. Consider a framed structure having a total of *n* DOFs and *m* PHLs, the resulting global stiffness matrices can be obtained by this assembly procedure and are often written in the form:

$$\mathbf{K} = \left[\quad \textit{Collection of } \mathbf{k}_i \quad \right]_{n\times n} , \quad \mathbf{K}' = \left[\quad \textit{Collection of } \mathbf{k}'_i \quad \right]_{n\times m} , \quad \mathbf{K}'' = \left[\quad \textit{Collection of } \mathbf{k}''_i \quad \right]_{m\times m} \tag{24}$$

The resulting stiffness equation for computing the response of the structure with both geometric and material nonlinearities can therefore be written as [11]:

$$\begin{bmatrix} F_1 \\ \vdots \\ F_n \\ \hline M_1 \\ \vdots \\ M_m \end{bmatrix} = \left[\begin{array}{c|c} \mathbf{K} & \mathbf{K}' \\ \hline \mathbf{K}'^T & \mathbf{K}'' \end{array}\right] \begin{bmatrix} x_1 \\ \vdots \\ x_n \\ \hline -\theta''_1 \\ \vdots \\ -\theta''_m \end{bmatrix} \tag{25}$$

where F_i and x_i $(i = 1,...,n)$ denote respectively the global applied forces and displacements at the DOFs, and M_i and θ''_i $(i = 1,...,m)$ denote respectively the local moments and plastic rotations at the PHLs.

3. Numerical Illustration Using Static Loading

Consider a two-dimensional frame as shown in Fig. 4(a) with one column member and one beam member, where both members have the same elastic modulus *E*, moment of inertia *I*, and length *L*. The column is subjected to a constant axial force *P*, and the frame is subjected to a lateral force F_o. Assume both members are axially rigid. The resulting structural model is a three-DOF system (labeled here as x_1, x_2, and x_3) as shown in Fig. 4(a). In addition, three PHLs are identified as shown in Fig. 4(a) with the corresponding component models for the moment vs. plastic rotation relationship as shown in Fig. 4(b). The moment vs. plastic rotation relationships exhibit strain hardening behaviors with θ_i'' denoting plastic rotation, M_i the moment, M_{Yi} the yield moment, and k_{ti} the hardening stiffness of the i^{th} plastic hinge, where $i = 1,2,3$.

Based on these labeled DOFs and PHLs, Eq. (25) becomes

$$\begin{bmatrix} F_o \\ 0 \\ 0 \\ \hline M_1 \\ M_2 \\ M_3 \end{bmatrix} = \left[\begin{array}{ccc:ccc} s'EI/L^3 & \bar{s}EI/L^2 & 0 & \bar{s}EI/L^2 & \bar{s}EI/L^2 & 0 \\ \bar{s}EI/L^2 & (\hat{s}+4)EI/L & 2EI/L & \hat{s}\hat{c}EI/L & \hat{s}EI/L & 4EI/L \\ 0 & 2EI/L & 4EI/L & 0 & 0 & 2EI/L \\ \hdashline \bar{s}EI/L^2 & \hat{s}\hat{c}EI/L & 0 & \hat{s}EI/L & \hat{s}\hat{c}EI/L & 0 \\ \bar{s}EI/L^2 & \hat{s}EI/L & 0 & \hat{s}\hat{c}EI/L & \hat{s}EI/L & 0 \\ 0 & 4EI/L & 2EI/L & 0 & 0 & 4EI/L \end{array}\right] \begin{bmatrix} x_1 \\ x_2 \\ x_3 \\ \hline -\theta_1'' \\ -\theta_2'' \\ -\theta_3'' \end{bmatrix} \tag{26}$$

where $\hat{s}$, $\hat{c}$ and $\bar{s}$ are defined in Eq. (7) and s' is defined in Eq. (9) for Member 1 as shown in Fig. 4(a).

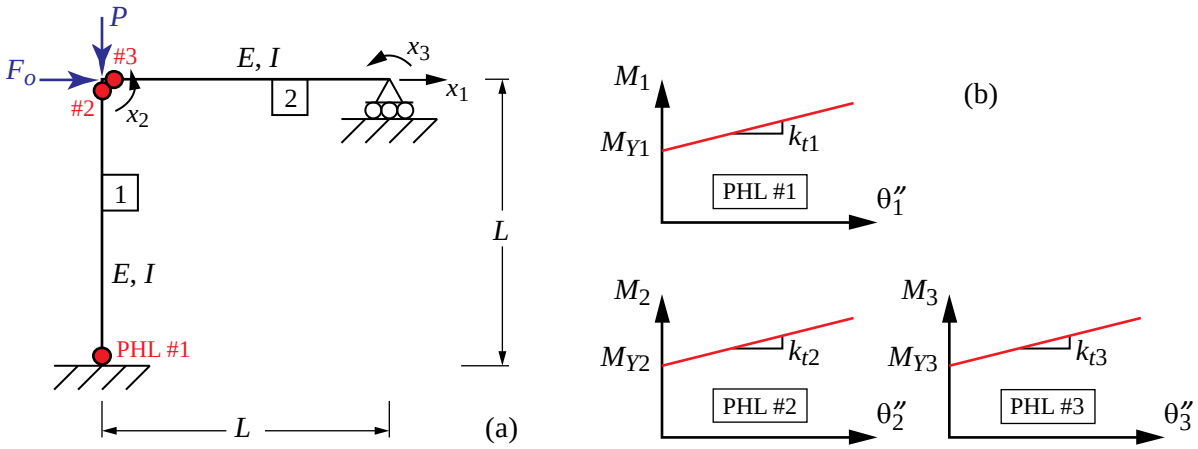

Fig. 4 – Moment frame with 3 degrees of freedom and 3 plastic hinge locations

To perform analysis on the frame with both geometric and material nonlinearities, let the applied force as shown in Fig. 5(a) be $F_o = 48F$ and $P = 0.3EI/L^2$. Assume a post-yield stiffness of $k_{t1} = k_{t2} = k_{t3} = 3EI/L$ for all three plastic hinges. Let the yield moments of the plastic hinges be $M_{Y1} = 18FL$, $M_{Y2} = 15FL$, and $M_{Y3} = 25FL$. This gives the component models of moment vs. plastic rotation relationships for the 3 PHLs as

$$\text{if } \begin{cases} |M_1| \le 18FL \\ |M_1| > 18FL \end{cases} \quad \text{then } \begin{cases} \theta_1'' = 0 \\ M_1 = 18FL + 3EI\theta_1''/L \end{cases} \tag{27a}$$

$$\text{if } \begin{cases} |M_2| \le 15FL \\ |M_2| > 15FL \end{cases} \quad \text{then } \begin{cases} \theta_2'' = 0 \\ M_2 = 15FL + 3EI\theta_2''/L \end{cases} \tag{27b}$$

$$\text{if } \begin{cases} |M_3| \le 25FL \\ |M_3| > 25FL \end{cases} \quad \text{then } \begin{cases} \theta_3'' = 0 \\ M_3 = 25FL + 3EI\theta_3''/L \end{cases} \tag{27c}$$

3.1 Step 1

Equation (26) is now used to perform structural analysis. First assume that the frame remains elastic under the applied load (i.e., $\theta_1'' = \theta_2'' = \theta_3'' = 0$). The first three equations of Eq. (26) can be used to solve for the displacements at the DOFs, and the last three equations of Eq. (26) can be used to compute the resulting moments. Doing so gives

$$\begin{Bmatrix} x_1 \\ x_2 \\ x_3 \end{Bmatrix} = \begin{Bmatrix} 7.3630FL^3/EI \\ -6.3158FL^2/EI \\ 3.1579FL^2/EI \end{Bmatrix} \quad , \quad \begin{Bmatrix} M_1 \\ M_2 \\ M_3 \end{Bmatrix} = \begin{Bmatrix} 31.2616FL \\ 18.9474FL \\ -18.9474FL \end{Bmatrix} \tag{28}$$

Since the computed moments of $M_1 = 31.2616FL$ and $M_2 = 18.9474FL$ are both larger than the corresponding yield moment, this indicates that both PHL #1 and PHL #2 have yielded.

3.2 Step 2

After determining that both PHLs #1 and #2 have yielded due to the applied force of $F_o = 48F$, this step begins by directly assuming that both PHLs #1 and #2 have yielded. The moment vs. plastic rotation relationships in Eq. (27) become

$$M_1 = 18FL + 3EI\theta_1''/L \quad , \quad M_2 = 15FL + 3EI\theta_2''/L \tag{29}$$

and $\theta_3'' = 0$ is still assumed. Then extracting the first five equations in Eq. (26) gives

$$\begin{Bmatrix} 48F \\ 0 \\ 0 \\ M_1 \\ M_2 \end{Bmatrix} = \begin{bmatrix} 11.64EI/L^3 & 5.97EI/L^2 & 0 & 5.97EI/L^2 & 2.01EI/L \\ 5.97EI/L^2 & 7.96EI/L & 2EI/L & 5.97EI/L^2 & 3.96EI/L \\ 0 & 2EI/L & 4EI/L & 0 & 0 \\ 5.97EI/L^2 & 5.97EI/L^2 & 0 & 3.96EI/L & 2.01EI/L \\ 2.01EI/L & 3.96EI/L & 0 & 2.01EI/L & 3.96EI/L \end{bmatrix} \begin{Bmatrix} x_1 \\ x_2 \\ x_3 \\ -\theta_1'' \\ -\theta_2'' \end{Bmatrix} \tag{30}$$

Now substituting Eq. (29) into Eq. (30), the stiffness equation becomes

$$\begin{Bmatrix} 48F \\ 0 \\ 0 \\ 18FL \\ 15FL \end{Bmatrix} = \begin{bmatrix} 11.64EI/L^3 & 5.97EI/L^2 & 0 & 5.97EI/L^2 & 2.01EI/L \\ 5.97EI/L^2 & 7.96EI/L & 2EI/L & 5.97EI/L^2 & 3.96EI/L \\ 0 & 2EI/L & 4EI/L & 0 & 0 \\ 5.97EI/L^2 & 5.97EI/L^2 & 0 & 6.96EI/L & 2.01EI/L \\ 2.01EI/L & 3.96EI/L & 0 & 2.01EI/L & 6.96EI/L \end{bmatrix} \begin{Bmatrix} x_1 \\ x_2 \\ x_3 \\ -\theta_1'' \\ -\theta_2'' \end{Bmatrix} \tag{31}$$

Note that by substituting M_1 and M_2 into Eq. (30), the left hand side of Eq. (31) becomes all known quantities, and the unknown quantities are the DOFs and PHLs on the right hand side of the equation.

Solving for the unknown quantities in Eq. (31) gives

$$\begin{Bmatrix} x_1 \\ x_2 \\ x_3 \\ -\theta_1'' \\ -\theta_2'' \end{Bmatrix} = \begin{Bmatrix} 10.8184FL^3/EI \\ -6.9710FL^2/EI \\ 3.4855FL^2/EI \\ -4.1108FL^2/EI \\ -1.9710FL^2/EI \end{Bmatrix} \tag{32}$$

Then the moments at each plastic hinge are calculated using the last three equations of Eq. (26), i.e.,

$$\begin{Bmatrix} M_1 \\ M_2 \\ M_3 \end{Bmatrix} = \begin{bmatrix} 5.97EI/L^2 & 2.01EI/L & 0 & 3.96EI/L & 2.01EI/L \\ 5.97EI/L^2 & 3.96EI/L & 0 & 2.01EI/L & 3.96EI/L \\ 0 & 4EI/L & 2EI/L & 0 & 0 \end{bmatrix} \begin{Bmatrix} 10.8184FL^3/EI \\ -6.9710FL^2/EI \\ 3.4855FL^2/EI \\ -4.1108FL^2/EI \\ -1.9710FL^2/EI \end{Bmatrix} = \begin{Bmatrix} 30.3325FL \\ 20.9130FL \\ -20.9130FL \end{Bmatrix} \quad (33)$$

Since the computed moments for M_1 and M_2 are both larger than the corresponding yield moment, this means the original assumption is correct. Therefore, in summary, the calculated responses are

$$\begin{Bmatrix} x_1 \\ x_2 \\ x_3 \end{Bmatrix} = \begin{Bmatrix} 10.8184FL^3/EI \\ -6.9710FL^2/EI \\ 3.4855FL^2/EI \end{Bmatrix} \quad , \quad \begin{Bmatrix} M_1 \\ M_2 \\ M_3 \end{Bmatrix} = \begin{Bmatrix} 30.3325FL \\ 20.9130FL \\ -20.9130FL \end{Bmatrix} \quad , \quad \begin{Bmatrix} \theta_1'' \\ \theta_2'' \\ \theta_3'' \end{Bmatrix} = \begin{Bmatrix} 4.1108FL^2/EI \\ 1.9710FL^2/EI \\ 0 \end{Bmatrix} \quad (34)$$

3.3 Results from Using Different Stiffness Matrices

Sections 3.1 and 3.2 demonstrated the procedure for calculating the response of the frame with both geometric and material nonlinearities. Similar procedures can be performed with a variation of stiffness matrices, such as using the geometric stiffness in Eq. (13) or the *P*-Δ stiffness in Eq. (14). By using the geometric stiffness, the responses are calculated as

$$\begin{Bmatrix} x_1 \\ x_2 \\ x_3 \end{Bmatrix} = \begin{Bmatrix} 10.8183FL^3/EI \\ -6.9709FL^2/EI \\ 3.4854FL^2/EI \end{Bmatrix} \quad , \quad \begin{Bmatrix} M_1 \\ M_2 \\ M_3 \end{Bmatrix} = \begin{Bmatrix} 30.3328FL \\ 20.9127FL \\ -20.9127FL \end{Bmatrix} \quad , \quad \begin{Bmatrix} \theta_1'' \\ \theta_2'' \\ \theta_3'' \end{Bmatrix} = \begin{Bmatrix} 4.1109FL^2/EI \\ 1.9709FL^2/EI \\ 0 \end{Bmatrix} \quad (35)$$

and by using the *P*-Δ stiffness, the responses are calculated as

$$\begin{Bmatrix} x_1 \\ x_2 \\ x_3 \end{Bmatrix} = \begin{Bmatrix} 10.7834FL^3/EI \\ -6.9493FL^2/EI \\ 3.4747FL^2/EI \end{Bmatrix} \quad , \quad \begin{Bmatrix} M_1 \\ M_2 \\ M_3 \end{Bmatrix} = \begin{Bmatrix} 30.3871FL \\ 20.8479FL \\ -20.8479FL \end{Bmatrix} \quad , \quad \begin{Bmatrix} \theta_1'' \\ \theta_2'' \\ \theta_3'' \end{Bmatrix} = \begin{Bmatrix} 4.1290FL^2/EI \\ 1.9493FL^2/EI \\ 0 \end{Bmatrix} \quad (36)$$

Comparing the results in Eq. (35) with those in Eq. (34) shows that the use of geometric stiffness approximates stability functions very well. But the comparison between Eq. (36) and Eq. (34) shows that there is a larger difference, especially in the calculation of the plastic rotations where the error is about 1% for the simple frame with statically applied load only.

4. Numerical Illustration Using Dynamic Loading

Consider the one-story one-bay moment-resisting frame as shown in Fig. 5(a) with members assumed to be axially rigid. This frame has a total of 3 DOFs (i.e., $n = 3$) and 6 PHLs (i.e., $m = 6$) as shown in the figure. Assume that the frame has a mass of $m = 318.7$ Mg and a damping of 0%. Also, let $E = 200$ GPa, $I_b = I_c = 4.995 \times 10^8$ mm^4, $L_b = 7.62$ m, $L_c = 4.57$ m, and $P = 5{,}338$ kN. Assume that the plastic hinges exhibit elastic-plastic behavior with moment capacities of $M_b = 3{,}130$ kN-m for the beam and $M_c = 3{,}909$ kN-m for the two columns. The frame is then subjected to the 1995 Kobe earthquake ground motion as shown in Fig. 5(b) but magnified with a scale factor of 1.3 to produce a larger response with more yielding at the plastic hinges, and Fig. 6 shows the horizontal displacement response of the floor using the stability functions (SF) method. In addition, results from a commercial software package developed based on the geometric stiffness (GS) method and from another commercial software package developed based on the *P*-Δ stiffness (PD) are also presented in the figure as a comparison. As shown in Fig. 6, consistency in the model among various algorithms is achieved based on the observation at the first few seconds of the response history, but the responses deviates once yielding occurs in the models.

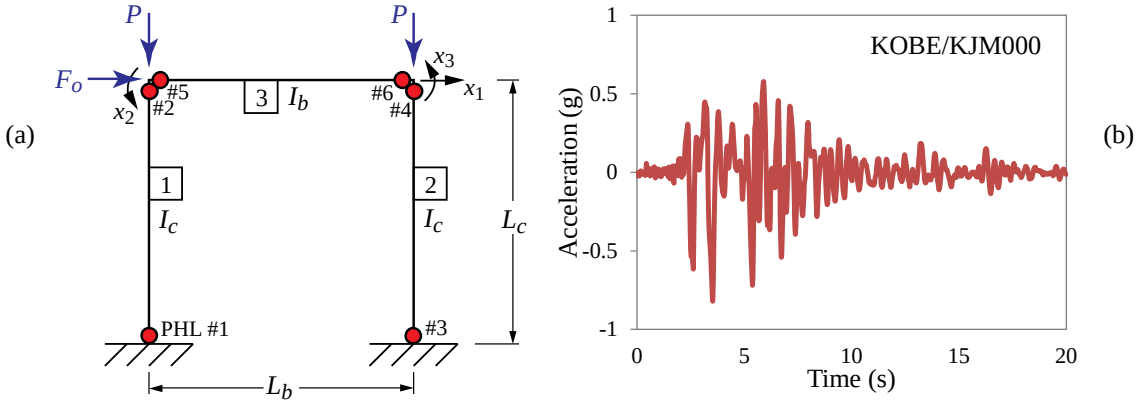

Fig. 5 – One-story one-bay moment-resisting steel frame subjected to the 1995 Kobe earthquake

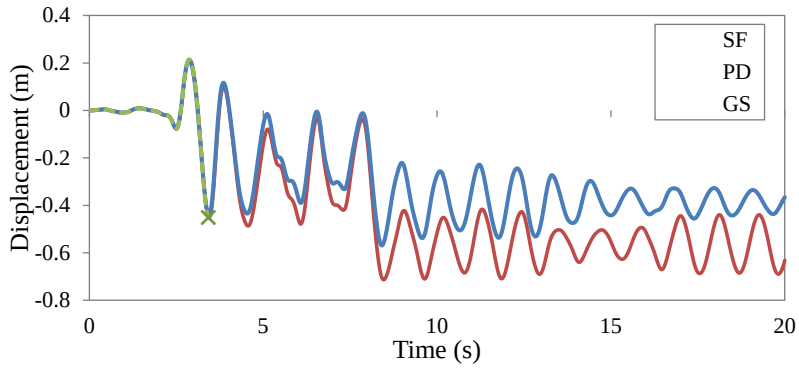

Fig. 6 – Displacement responses of the frame using various geometric nonlinearity formulations with non-convergence in the solution algorithm for GS at 3.46 seconds

The plastic rotation responses at selected plastic hinges are presented in Fig. 7. By comparing SF with PD in Fig. 7, it can be seen that even though the local plastic rotation responses change suddenly (i.e., jumps) due to yielding at the same time steps, the magnitudes of the changes are different. Given the expected accuracy of SF that it is analytically derived, this suggests that the *P*-Δ stiffness method may not be a good approximation when plastic rotation is accummulated over time, such as in the case of a dynamic analysis. At the same time, comparing SF and PD with GS in Fig. 7 shows that the non-convergence issue is only found in GS, indicating that a fundamental problem exists in either GS or the software package itself. This may be attributed to the difficulty of incorporating geometric stiffness in a dynamic analysis, where update in stiffness due to material nonlinearity causes non-convergence in the solution algorithm that can only account for geometric nonlinearity. However, further research is needed to examine why such non-convergence exists.

5. Conclusion

Plastic rotation in moment-resisting frame is an important parameter for assessing structural performance under seismic actions, and therefore it needs to be calculated correctly. In this research, fundamental principles were used to derive the stiffness matrices of a member with plastic hinges subjected to an axial load to capture the interaction between geometric nonlinearity and material nonlinearity using stability functions. This results in a rigorous method for calculating the plastic rotation demand of framed structures for both nonlinear static analysis and nonlinear dynamic analysis. Comparing the results using stability functions with other methods for handling geometric nonlinearity shows that the present approach has the advantage for being theoretically derived, and therefore it is believed to be of higher accuracy whenever there is a discrepancy of results. However, further research is necessary to explain why there is such a discrepancy, especially for the case of nonlinear dynamic analysis.

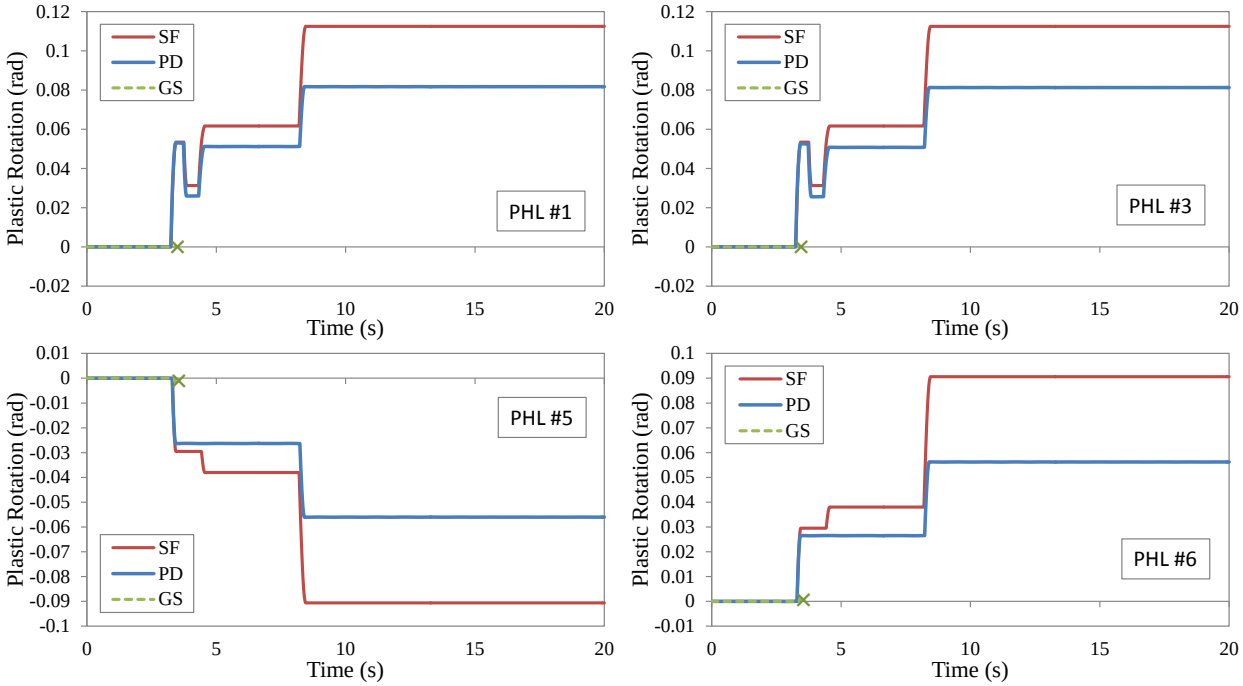

Fig. 7 – Plastic rotation responses at selected PHLs using various geometric nonlinearity formulations with non-convergence in the solution algorithm for GS at 3.46 seconds

6. Disclaimer

No formal investigation to evaluate potential sources of uncertainty or error, or whether multiple sources of error are correlated, was included in this study. The question of uncertainties in the analytical models, solution algorithms, material properties and as-built final dimensions and positions of members versus design configurations employed in analysis are beyond the scope of the work reported here.

7. References

[1] ASCE/SEI 41-13 (2013): *Seismic Evaluation and Retrofit of Existing Buildings*, American Society of Civil Engineers, Reston, VA, USA.

[2] Lignos DG, Krawinkler H, Whittaker AS (2011): Prediction and validation of sidesway collapse of two scale models of a 4-story steel moment frame. *Earthquake Engineering and Structural Dynamics*, **40** (7), 807-825.

[3] Grigorian M, Grigorian CE (2012): Lateral displacements of moment frames at incipient collapse. *Engineering Structures*, **44**, 174-185.

[4] Eads L, Miranda E, Krawinkler H, Lignos DG (2013): An efficient method for estimating the collapse risk of structures in seismic regions. *Earthquake Engineering and Structural Dynamics*, **42** (1), 25-41.

[5] Domizio M, Ambrosini D, Curadelli O (2015): Experimental and numerical analysis to collapse of a framed structure subjected to seismic loading. *Engineering Structures*, **82**, 22-32.

[6] Timoshenko SP, Gere JM (1961): *Theory of Elastic Stability, 2nd Edition*, McGraw Hill, NY, USA.

[7] Bazant ZP, Cedolin L (2003): *Stability of Structures*, Dover Publication, NY, USA.

[8] Powell GH (2010): *Modeling for Structural Analysis: Behavior and Basics*, Computers and Structures Inc., CA, USA.

[9] Wilson E (2010): *Static and Dynamic Analysis of Structures: A Physical Approach with Emphasis on Earthquake Engineering, 4th Edition*, Computer and Structures Inc., CA, USA.

[10] McGuire W, Gallagher RH, Ziemian RD (2000): *Matrix Structural Analysis*, John Wiley and Sons, NY, USA.

[11] Wong KKF, Yang R (1999): Inelastic dynamic response of structures using force analogy method. *Journal of Engineering Mechanics ASCE*, **125** (10), 1190-1199.

Proceedings of the ASME 2016 International Design Engineering Technical Conferences & Computers and Information in Engineering Conference
IDETC/CIE 2016
August 21-24, 2016, Charlotte, North Carolina, USA

DETC2016-60506

INVESTIGATING PREDICTIVE METAMODELING FOR ADDITIVE MANUFACTURING

Zhuo Yang, Douglas Eddy, Sundar Krishnamurty, Ian Grosse
University of Massachusetts Amherst
Department of Mechanical and Industrial Engineering
Amherst, MA 01003
Email: [zhuoyang, dceddy]@engin.umass.edu, [skrishna, grosse]@ecs.umass.edu

Peter Denno, Felipe Lopez
National Institute of Standards and Technology
Engineering Laboratory
Gaithersburg, MD 20899
Email: [peter.denno, felipe.lopez]@nist.gov

ABSTRACT

Additive manufacturing (AM) is a new and disruptive technology that comes with a set of unique challenges. One of them is the lack of understanding of the complex relationships between the numerous physical phenomena occurring in these processes. Metamodels can be used to provide a simplified mathematical framework for capturing the behavior of such complex systems. At the same time, they offer a reusable and composable paradigm to study, analyze, diagnose, forecast, and design AM parts and process plans. Training a metamodel requires a large number of experiments and even more so in AM due to the various process parameters involved. To address this challenge, this work analyzes and prescribes metamodeling techniques to select optimal sample points, construct and update metamodels, and test them for specific and isolated physical phenomena. A simplified case study of two different laser welding process experiments is presented to illustrate the potential use of these concepts. We conclude with a discussion on potential future directions, such as data and model integration while also accounting for sources of uncertainty.

Keywords: Metamodels, additive manufacturing, space filling sampling, DOE, model updating

1. INTRODUCTION

Additive Manufacturing (AM) processes are more complex, variable, and difficult to understand than subtractive manufacturing [1, 2]. Typical AM processes implement material patterning, energy patterning, new layer creation, and support from previous layers [3] to realize shape, material, and hierarchical complexities [4].

Material properties of AM-produced parts often depend upon the process parameters. For example, platform temperature, building direction, and post heat treatment influence the part microstructure that determines fatigue properties of selective laser melting parts [5]. Further, variations in layer thickness and hatching distance settings have affected material porosity along with hardness and density [6].

Various models have been developed in recent years to describe complex AM process-structure-property relationships. In spite of advances in model accuracy, the enormous computational cost of complex, high-fidelity physics-based simulations of AM makes these models impractical to adopt in industry [7, 8]. A more preferable strategy is to utilize surrogates, or metamodels, as they provide a "model of the model" to replace the expensive simulation model in design and optimization

Certain commercial equipment, instruments, or materials are identified in this paper are not intended to imply recommendation or endorsement by the National Institute of Standards and Technology, nor is it intended to imply that the materials or equipment are necessarily the best available for the purpose.

Denno, Peter; Eddy, Douglas; Grosse, Ian; Krishnamurty, Sundar; Lopez, Felipe; Yang, Zhuo.
"Investigating predictive metamodeling for additive manufacturing."
Paper presented at ASME 2016 International Design Engineering Technical Conferences & Computers and Information in Engineering Conference, Charlotte, NC. August 21, 2016 - August 24, 2016.

processes [9]. Metamodeling has been used successfully as an alternative to computationally expensive simulations in aerospace and other advanced manufacturing domains. [7, 10].

Currently, varieties of metamodeling techniques are applied in engineering design. Several comparative studies present the performance of these various techniques under different modeling criteria [7, 11]. Generally, different modeling methods show both advantages and disadvantages for different types of problems. These disadvantages include orders of nonlinearity and problem scales [7]. To simplify explanation in this paper, we mainly focus on the Polynomial Regression and Kriging Method for metamodel construction to illustrate selection of the most applicable metamodeling techniques for these specific cases.

In spite of the benefits envisioned through the use of such metamodeling techniques, very little research has been done in this area. Some notable exceptions include a polynomial regression model of density, hardness, and porosity of a carbon steel selective laser sintering process [6], porosity predictions in selective laser melting [12] and an energy density model of CoCrMo powder material [13]. These approaches are limited to experimental designs for a specific portion of an AM process. There is a need for a complete AM metamodeling methodology to construct and integrate local metamodels [14] for robust prediction of AM process results. Challenges for the AM situation include cost of experimentation [15], accuracy of simulation capabilities [16], and complex interactions of different physical phenomena during the AM process [17].

This study aims to investigate metamodeling as a means to generate accurate predictive models compatible with a composable multilevel structure, defined as made up of highly reusable models that can be used together and mirror the general AM process model [14]. Such a metamodeling methodology will be able to address the challenges in AM processes such as high system complexity, uncertainty, and limitations of legacy data conducted by design of experiments (DOE) that designers may need to rely on due to the expense of producing experimental sample parts [14, 15, 18].

The following section covers the necessary background to set the stage for Section 3, which introduces methodical approaches to construct and test individual metamodels. A pair of case studies in Section 4 illustrates the potential effectiveness of these approaches. Section 5 discusses this work and potential future work.

2. OVERVIEW OF METAMODELING TECHNIQUES

This section provides a brief background summary of basic metamodeling approaches. These traditional metamodeling techniques consist of several steps. First, data sets are used to construct metamodels. The composition of these data sets depend upon the experimental design used to represent and sample that design space.

Traditional sampling methods, such as full factorial, fractional factorial, and central composite, etc., have been frequently used for AM process modeling [13, 19]. Typically, variables could be either discrete or continuous [20]. Since some or most of the input variables are continuous in this case, it would be impossible to generate all possible combinations in a data set. These traditional experimental designs discretize the continuous variables to limit the number of experimental trials necessary.

The full factorial design selects all possible combinations of input variables at specific locations to maximize the amount of information and data accuracy for a prescribed sample size. Fractional factorial design symmetrically selects a fraction of full factorial samples. Central Composite Design (CCD) includes center points that can estimate curvature of the response function [21]. CCD and other classical DOE methods tend to reduce the experimental cost and cover an entire design space by placing the samples at or near the boundary of the space. However, it leaves the interior of the design space unexplored [22]. In this study the data sources used to construct the metamodels consist of DOE data sets that represent manufacturing processes empirically. The goal is to develop a method that may be universally applied to all of these main types of classical DOE sampling methods.

To capture the important characteristics of unknown systems, it is preferred to collect data that represents the entire design space to include information about the most critical regions [21, 23]. This is necessary to overcome the limitations of classical DOE approaches. Unlike the random errors in results often exhibited by physical experiments, computer experiments are often deterministic [24]. This work focuses on metamodel construction from legacy empirical data rather than computer experiments to address the issues of difficulty with obtaining accurate simulations of AM processes and the high cost of producing sample parts for new experimental designs.

Thus, any approach needs flexibility to accommodate larger DOE sample sizes and combinations of different DOE data sets, which may not conform to the classical DOE sample locations. For example, the welding test by Khan et al. was based on full factorial DOE strategy that included 18 data points [25]. A similar experiment operated by Balasubramanian et al. with the same response was based on a fractional factorial design that included 15 data points [26]. Aforementioned experiments cannot conform to one uniform DOE method due to their different design space and levels of value.

Space Filling Sampling (SFS) methods have been developed to address these various limitations of the classical DOE approaches [22]. Many SFS methods have been widely used in simulation-based metamodels, such as Grid Sampling, Lattice Design, Audze-Eglais, Orthogonal Array, and Latin Hypercube Design (LHD) [23, 27-30]. The number of sample points of LHD is the same as the number of discrete cells defined by the level, or grid spacing, of each input variable. For example, the Latin square that contains four sample points in two dimensions appears only once in each row and each column [21]. LHD fills each cell location with one sample point, but the location within each cell is randomized. LHDs are usually at least as accurate as random sampling and stratified sampling techniques [31]. Thus, Latin Hypercube can be a most suitable candidate for situations that involve nonflexible and non-uniform data locations in a design space [32].

Denno, Peter; Eddy, Douglas; Grosse, Ian; Krishnamurty, Sundar; Lopez, Felipe; Yang, Zhuo.
"Investigating predictive metamodeling for additive manufacturing."
Paper presented at ASME 2016 International Design Engineering Technical Conferences & Computers and Information in Engineering Conference, Charlotte, NC. August 21, 2016 - August 24, 2016.

2.1 Traditional Metamodel Construction Techniques

Since SFS is often not adequate to generate desired model accuracy, reliability, predictability, or robustness, Sequential Infilling Sampling (SIS) techniques are widely used. Unlike SFS methods that distribute sample points into a design space at one single stage, SIS methods assign sample points sequentially at "particular" locations [21]. SIS methods are more efficient for an unknown system [33] by providing options to a designer for determining when to stop the data collection process as sufficient information has been gathered [21]. The combination of SFS and SIS can significantly improve the results of metamodel construction [34]. The most popular construction techniques include polynomial, kriging, splines, artificial neural network, and hybrid methods [35].

Response surface modeling (RSM) techniques were originally developed to analyze the results of physical experiments and create empirical models of the observed response values [36]. The typical form of RSM is:

$$y(\tilde{x}) = f(\tilde{x}) + \varepsilon \quad (1)$$

where $y(\tilde{x})$ represents the unknown function, $f(\tilde{x})$ is a known polynomial function of $\tilde{x}$ derived statistically, and ε is random error assumed to be normally distributed. $\tilde{x}$ is the set of the system's independent input variables. A second order quadratic polynomial function would have the form of:

$$\hat{y} = \beta_0 + \sum_{i=1}^{k} \beta_i x_i + \sum_{i=1}^{k} \beta_{ii} x_i^2 + \sum_i \sum_j \beta_{ij} x_i x_j \quad (2)$$

where β_0, β_i, and β_{ij} are regression coefficients, and k is the number of design variables.

RSM provides the advantage of generating a mathematical function that can easily compute the data location predicted by that equation. However, since RSM deploys curve-fitting techniques between the data points, it can tend to smooth out such regions without data to lessen predictive accuracy for highly nonlinear responses of systems [21].

Kriging methods were initially developed for analyses of random processes and have been known to outperform RSM and other metamodel construction techniques, especially when dimensionality of a system increases [37]. The fundamental assumption of predicting in the kriging method is modeled through the variogram, or spatial correlation functions, which describes spatial correlation of observed data [38, 39]. The general form of a kriging model is:

$$\tilde{y} = f(\tilde{x}; \tilde{\beta}) + \varepsilon(\tilde{x}) \quad (3)$$

where $f(\tilde{x}; \tilde{\beta})$ is a least squares fit regression to the global trend in the observed data, $\varepsilon(\tilde{x})$ is the correlated prediction error, which is assumed to be the realization of a stochastic/Gaussian process with zero mean, non-zero variance, and covariance. Although defined as statistical error, this term represents an imposed spatial correlation in the parameter space that makes observations positively correlated when close. Kriging can potentially provide improved accuracy and reliability over other techniques available to AM metamodeling.

3 METAMODEL CONSTRUCTION METHOD

This section introduces a predictive metamodeling approach (Figure 1) to address some of the unique challenges particular to metamodel construction to represent the various sub-processes in AM. The following subsection explains the rationale of this methodical approach based on the challenges identified previously in this paper related to predictive metamodeling for AM processes.

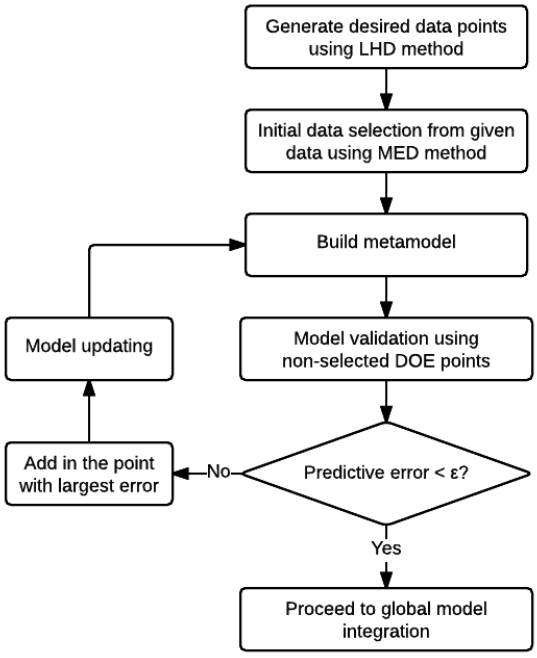

Figure 1. Maximum Predictive Error Updating (MPEU) Method

3.1 Rationale of Approach

One of the major objectives for developing a reusable metamodeling methodology is to give engineers the opportunity to use historical AM data to construct their own design, which can potentially save the cost of collecting DOE data. Thus, this work strives for compatibility with most of the AM processes and different empirical data sets. Existing data that conforms to classical DOE does not provide guidance towards selecting sample points. Further, existing data may not account for the same set of conditions (design space) provided by a metamodel. Variability of the classical DOE set-ups further complicates the quest for a method compatible with existing DOE data. The variability of different DOE methods deployed in data collection includes different numbers of levels, fractional factorials, or input variables relative to the problem non-uniformity. To overcome these disadvantages, the following subsection introduces the Minimum Euclidean Distance (MED) method for

selecting a limited number of data points for metamodel construction from nonflexible given data.

3.2 Minimum Euclidean Distance (MED) Method

The coauthors' prior work addressed a similar situation of metamodel construction in non-ideal data locations for design space filling [32][Eddy 2015]. This work identified LHD as a potential approach for the reasons given in Section 2. Given the inability to choose the points at the exact locations identified by an LHD sample set generation, this work proposed a method to find the minimum Euclidean distance between each identified data location and the data point identified in the data set [32].

The procedural steps begin with the generation of the desired amount of LHD points from a given data set. Next the Euclidean distance is calculated between each DOE data point to the generated LHD points by the Maximin method. Those points closest to the desired LHD points are selected for constructing the metamodel.

Since the selected DOE points depend upon the LHD points, selection of the initial points from these LHD results is critical to improvement of metamodel construction. Such methods as Maximin LHD [40], orthogonal array-based LHD [30], and optimal Audze-Eglais uniform LHD [41] can generate optimal LHD sampling points.

3.3 Maximum Predictive Error Updating (MPEU) Method

As mentioned in Section 2, the initial step of space filling is often not adequate to obtain the desired accuracy and predictability of a metamodel. In such cases, SIS becomes a necessary next step.

Utilizing the concepts from SIS, Shao and Krishnamurty developed a surrogate model based design optimization (SMBDO) method to sequentially update a surrogate model by capturing the critical features of an unknown system in a simulation-based experiment [42]. Similary, a comprehensive adaptive sampling methodology is presented in Sandia's Dakota framework [43] to enable selection of successive sample points based on the maximum distance from existing points or the uncertainty of model prediction. Based on these methods, the initial LHD sample points are used to construct the initial surrogate model. During each updating step, potential optimal locations predicted by the current model are then validated. Those points that exhibit high predictive error are then added into the current model iteratively until the desired model accuracy is obtained. However, the clustering based multilocation search procedure of SMBDO and the adaptive sampling method both rely upon an ample supply of data points from efficient computer simulations, which is simply not realistic in this case. Thus, there is a need to develop a model updating method for the limited data sizes inherent with using historical data for metamodel construction.

To address these challenges and limitations, we introduce the Maximum Predictive Error Updating (MPEU) method to gradually improve model accuracy. Figure 1 outlines the general framework of the MPEU method using the MED method to select the most appropriate sampling points from original DOE data. The method begins by generating LHD points using the maximin method in the design space given by the data. The kriging method with a Gaussian correlation function was employed to build the surrogate models. Then, the points are selected to construct the initial metamodel by using the MED method. A validation procedure next determines whether the current surrogate model needs further improvement. Maximum relative error magnitude (MREM) and average relative error magnitude (AREM) are calculated using the following equations to test the metamodel for predictability at each iterative stage of model updating:

$$MREM = \max\left(\frac{|y_i - \hat{y}_i|}{y_i}\right) \quad (4)$$

$$AREM = \frac{1}{m}\left(\frac{\sum_{i=1}^{m}|y_i - \hat{y}_i|}{y_i}\right) \quad (5)$$

where y_i is the observed value from given data, $\hat{y}$ is the value predicted by the metamodel of the DOE points that were not selected to construct the metamodel, and m is the number of data points.

If either error calculation exceeds a preset threshold for robustness, the point presenting the largest predictive error is added into the initial sample pool. A new model is created based on the new sample set. The model creating-validating procedure will iteratively proceed until both MREM and AREM satisfy the preset threshold value for robustness. This is the MPEU method that sequentially infills the sample set by updating the model to improve the resulting metamodel construction.

Verification and validation techniques must test the metamodel at each stage [21]. Verification tests the internal consistency of constructed metamodels and validation tests reliability with external data [44]. To validate the newly built metamodel, a model validation criterion is established based on the prediction accuracies [21] of all non-selected DOE points. If the MREM and AREM are both greater than a specified preset threshold value for robustness, the data point with the lowest prediction accuracy (or highest MREM value) would be added into the current sample pool and the metamodel is updated accordingly. Subsequently, the newly built metamodel will be validated again with the same process iteratively until convergence to within the threshold MREM and AREM values. Thus, effective model construction can be achieved efficiently by combining predictive metamodel construction simultaneously with validation to robustness requirements.

The preset threshold values of MREM and AREM are based on design requirements such as penetration depth and melt pool width. Both average and maximum error are involved in the validation process since they represent general and distinguished model performance. A designer would need to decide on what model accuracy and predictability are necessary or acceptable before model construction [32]. An unnecessarily low threshold value may significantly increase the computational cost. Conversely, an excessively high threshold value may reduce model predictability and utility. The following section

demonstrates the potential use of these proposed space filling and sequential infilling techniques in a pair of case study examples.

4 CASE STUDY: PREDICTIVE METAMODELS IN LASER WELDING PROCESSES

The laser welding process is used in the case studies reported in this section due to its similarities to directed energy deposition processes. In both applications, a heat source fuses metal as it is being deposited. The processes share similar process parameters and their quality is determined by similar metrics (dimensional accuracy, surface finish, residual stresses and mechanical properties, all of which can be traced back to the geometry of the melt pool). With that said, data is more readily available for laser welding, making the process a good candidate for demonstrating proof-of-concept.

The following two case studies illustrate the potential applicability of the proposed MPEU method for different DOE data. Both cases focus on the same response of the penetration depth (P). The cases have similar experimental methods but different DOE strategies. These two simple and somewhat similar experiments help to illustrate various results that can be expected from different data sets. This section shows the potential to deploy methods to construct and test various individual AM metamodels by use of the method introduced in the prior section.

4.1 Full Factorial DOE with Different Levels of Value for Input Variables

In the first case by Kahn, et al. [25], laser power (LP), welding speed (WS), and fiber diameter (FD) are the input variables. Among those three variables, LP and WS ranged from 800–1100 W and 4.5–7.5 m/min by three linear levels, with midpoint 950 and 6.0 respectively. The third variable of FD has only two levels at values of 300 μm and 400 μm FD [25]. The full factorial DOE consists of eighteen total data points for penetration depth, measured in micrometers after a standard washing procedure and with no special heating treatment.

The first step is generating an LHD sample set in the design space. In this case the LHD set consists of five points in order to give the initial model enough options for future updating. Fewer start points may not adequately cover the design space. Using the MED method described in the previous section, the Euclidean distance between each LHD point and DOE point are calculated. Table 1 lists the initial data points selected by the MED method. The first column represents the standard order number of each point in the original DOE. The initial metamodel would be constructed from these five points.

Table 1. Initial data points generated by MED method

	Input variables			Observed value
Data point number	LP (W)	WS (m/min)	FD (μm)	P (μm)
1	800	4.5	300	960
5	950	6	300	950
6	1100	6	300	1180
14	950	6	400	727
17	950	7.5	400	580

From the collected data, the initial metamodel is built using a standard kriging method. Kriging has built-in verification of internal consistency to prevent the error that can occur when RSM is used. The remaining thirteen data points next validate the metamodel by calculation of MREM and AREM as explained in the prior section. Model updating is next done iteratively by applying the MPEU method, as described in the prior section, to the preset thresholds for robustness of $\varepsilon_{MREM} \leq 10\%$, and $\varepsilon_{AREM} \leq 5\%$ in this case.

Table 2. MREM and AREM at each stage

Iteration	Data point number	Input variables			Observed value	Predictive value	MREM	AREM
		LP (W)	WS (m/min)	FD (μm)	P (μm)			
stage 1	3	1100	4.5	300	1610	1108	31.12%	28.37%
	7	800	7.5	300	560	891	59.18%	
	12	1100	4.5	400	1307	875	33.02%	
	13	800	6.0	400	577	818	41.86%	
	16	800	7.5	400	492	759	54.43%	
stage 2	3	1100	4.5	300	1610	1339	16.79%	11.10%
	9	1100	7.5	300	880	1019	15.76%	
	11	950	4.5	400	1043	899	13.82%	
	12	1100	4.5	400	1307	1094	16.31%	
	16	800	7.5	400	492	385	21.70%	
stage 3	2	950	4.5	300	1290	1107	14.20%	14.26%
	3	1100	4.5	300	1610	1244	22.71%	
	11	950	4.5	400	1043	845	18.93%	
	12	1100	4.5	400	1307	882	32.53%	
	15	1100	6.0	400	920	806	12.37%	

stage 4	2	950	4.5	300	1290	1241	3.81%	3.71%
	3	1100	4.5	300	1610	1472	8.57%	
	8	950	7.5	300	730	702	3.87%	
	13	800	6.0	400	577	539	6.65%	
	15	1100	6.0	400	920	963	4.62%	

Table 2 lists the results for this example of the first four iterations of the MPEU method. Note that each sequential iteration represents the validation results calculated by the current updated metamodel. Only the points showing the most significant error are included in Table 2. At each iteration, the point with the greatest MREM is marked in grey in Table 2. At stage 1, the point at standard order 7 is selected by adding it into the initial sample pool since it shows the highest MREM (59.18%). As a result, after the third iteration both the MREM and the AREM values satisfy the preset threshold value. According to the MPEU method, the updating process converged to construct the final metamodel with eight DOE data points at 8.57% MREM and 3.35% AREM. Figure 2 shows the error values at each iteration. Note that the MREM and AREM values did not always decrease monotonically prior to the final stage, as one would expect in the early stages in any numerical iterative approach, but shows monotonicity and convergence towards the end. Similar trends were observed in the application of SMBDO to several classical simulation-based model updating case studies [25].

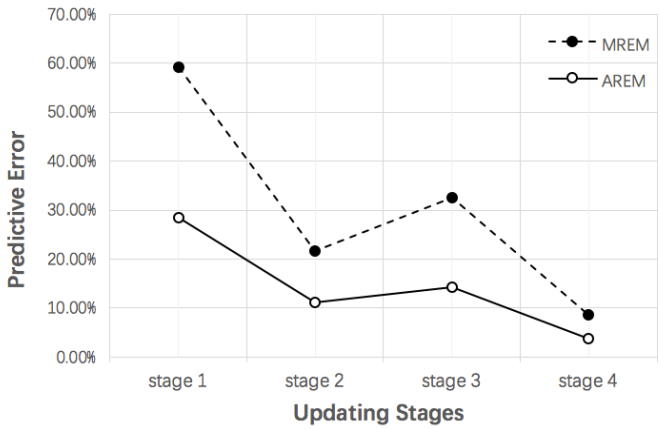

Figure 2. Error at iterations

In this first case study a two level, three factor DOE strategy becomes the only choice if one prefers to create the model by classical DOE techniques without collecting new experimental data. Beyond the proposed MPEU method and a two level DOE method, another compatible sampling method is a random search method. However, this method is not recommended here due to its uncontrolled behavior. The comparison results of AREM and MREM between random search method, two level full factorial DEO method, and MPEU method with different threshold values are listed in Table 3.

As shown in the table, both AREM and MREM of the model built by the MPEU method are significantly lower than the random search and DOE methods when the sample size is the same. When gradually reducing the threshold values of AREM and MREM, the MPEU method typically incorporates a few more points to improve the model accuracy to the new convergence requirements.

With the MPEU method, the model is iteratively improved by updating sample points. However, only the initial sample points can evenly distribute across the given design space by use of the MED method. Newly updated points are selected based on the validation results from previous iterations without considering their location in a design space. As shown in Table 4 the metamodel that is constructed by sequential infilling reduces prediction errors at comparable sample sizes. Thus, despite the possibility of the initial five data points not adequately filling the design space, the MPEU method shows potential to generate a more accurate model through the updating strategy. The following subsection examines the results of applying this same method to a situation that provides fewer data points in a data set.

Table 3. AREM and MREM results of random search method, two levels full factorial DOE method, and MPEU method

	Random	**DOE**	**MPEU**		
Sample size	n=8	n=8	n=8	n=10	n=12
AREM	22.76%	7.76%	3.35%	2.44%	1.94%
MREM	59.16%	12.99%	8.57%	4.74%	5.18%

Table 4. Comparison of different point selection strategies

	Single stage sampling	**MPEU method**	**Improvement**
Sample size	n=8	n=8	
AREM	7.60%	3.35%	55%
MREM	12.66%	8.57%	32%

4.2 Fractional Factorial DOE with Same Levels of Value

The second case study of laser welding DOE data is based on a three factor, three level Box-Behnken design with full replication [26]. “Beam angle” (BA) in this experiment replaced the input of “fiber diameter” from the first case study. The experimental design generated fifteen data points. A mean value of the data set’s three replicate points reduces the size of the data set from fifteen to thirteen.

Table 5 lists the MREM and AREM values at each stage for those points having significant predictive error. As shown, the

MREM started with five sample points from 82.00% and gradually decreased to 4.80% after five updates, or six stages. The error at the start could have a significant effect on the number of iterations required. It is notable that the error at the first stage is 39% higher than the amount shown for the first stage in Table 2 for the first case study. It is also notable that this second case study is covering more levels with less data than the first case study.

After applying the MPEU method, accuracies of the final model satisfied the threshold values ($\varepsilon_{MREM} \leq 10\%$, $\varepsilon_{AREM} \leq 5\%$). The error convergence progression is shown in Figure 3. Both MREM and AREM increased slightly during the middle stages as new points were added into the previous sample pool.

Table 5. MREM and AREM at each stage

iteration	Std. order	MREM	AREM
stage 1	3	45.89%	34.93%
	4	82.00%	
	6	52.50%	
	8	54.79%	
stage 2	1	15.46%	11.09%
	6	22.16%	
	8	21.71%	
	13	4.79%	
stage 3	1	41.51%	15.71%
	3	33.93%	
	8	0.85%	
	13	16.64%	
stage 4	3	4.48%	4.60%
	8	1.30%	
	9	2.71%	
	13	13.32%	
stage 5	3	17.07%	6.16%
	8	3.69%	
	9	3.22%	
	12	0.65%	
stage 6	9	4.80%	3.72%

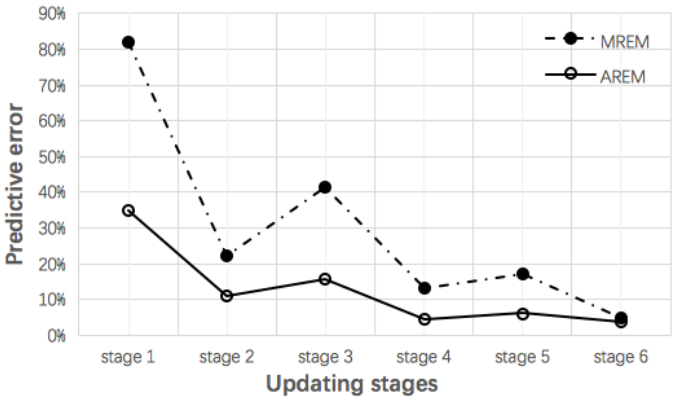

Figure 3. Error at iterations

5 DISCUSSION AND FUTURE WORK

The objective of this work was to explore a metamodeling methodology tailored for AM and adaptable to different types of empirical data. To address the challenges identified, this work introduces an MED method to select usable sample points from different types of given data and an MPEU method with an updating procedure to create predictive metamodels to predetermined robustness requirements from limited data sets. The proposed MED method can select usable initial sample points from various types of DOE data since its foundation is based on the LHD sampling method, which is adaptable for most any design space. Though the generated LHD sample locations may not be occupied by given DOE data, the MED method can improve selection of more appropriate existing points over other methods.

The MPEU method allows model developers to balance the tradeoff between model accuracy and computational cost by adjusting the threshold values of MREM and AREM to achieve specified levels of robustness. As shown in Table 3, with the same number of sample points, the MPEU method, which also utilizes the MED method, provides a more accurate model than the random search and eight DOE data points for the example that was tested. The MPEU method also provides an option if one intends to improve the model at the expense of slightly higher computational costs. In the first case study, two added new points can significantly reduce the MREM from 8.57% to 4.74%. Furthermore, the updating strategy of the proposed method can contribute more to capture the critical features of an unknown system than simply picking up points from the given data set. As shown in Table 4, MPEU method significantly reduces both MREM and AREM. In other words, the proposed method focuses more on capturing the critical system features rather than the point locations.

Despite the advantages in model construction with the MED and MPEU methods, there are some limitations. Such disadvantages can potentially limit the application of proposed methods. For example, since the MED method selects the initial points through randomly generated LHD samples, each time the MPEU method may produce different models to the same

convergence criteria. It cannot guarantee that the generated LHD sampling set is optimal in a given DOE design space. Rather, the updating procedure depends highly upon the initial MED selected points. Without a confirmed starting point, the overall performance of the MPEU method may decrease. For example, in Section 4.2, the final model required ten points for construction but left only three points for validation. Thus, another limitation relates to model validation. Unlike metamodels generated by computer simulations, historical DOE data is often not reproducible. One can only rely on the existing data since it is impossible to gather additional information. In this second case study, the start point accuracy and resulting number of points remaining to validate the model were not as acceptable as found in the first case study. This second case study also had less data than the first case study. While not conclusive, this supports the assertion that the amount of data or information can have a significant effect on the results of using metamodeling methods. Methods such as Grey System Theory that work with little data or information may be introduced along with this current proposed method [45]. Nonetheless, future work could potentially improve the MPEU method by adding a check and adjustment process based on the error at the first stage.

Two laser welding case studies in the prior section show that the proposed MPEU method is compatible with different DOE data sets in these cases. The two data sets have similar experimental conditions such as the same laser source, common input variables of laser power and welding speed, the same response of penetration depth. However, one must use these two metamodels separately due to their different ranges of data locations in the design space. To overcome such a shortcoming or data limitation, a future goal is to build towards a global metamodel by combing two local data sets. Such a development may more efficiently utilize different historical data sources to know more about a process and also raises the issue of uncertainty between data sets with different sources.

Another aspect to explore in future studies is the uncertainty in data points, which may be measurement error for experimental data or prediction uncertainty for computational predictions. Experimental variability is significant in additive manufacturing processes due to the random interactions between powder particles and melt pool, variations between different machines and models, and different manufacturing practices followed in different shops. Additive manufacturing models have a large degree of variability as well because of the different modeling assumptions that may be taken in the development of computational models. Merging of data sets of different sources requires knowledge of the amount of uncertainty in each source, to ensure that the metamodels stay closer to more accurate points and that an appropriate metric is adopted to determine the adequacy of the metamodels. The methods presented in this paper originate from the metamodeling literature, which has traditionally dealt with deterministic data. Extensions to stochastic data sets are under development.

The MPEU method lays the foundation for a predictive metamodeling methodology to use in AM. Future work could investigate development of a hybrid metamodeling method through the application of clustering techniques [34] and multi-surrogate approximation (MSA) methods [46] to build the global model by combining data sets with different input variables, process conditions, or material parameters.

ACKNOWLEDGEMENTS

This material is based upon work supported by the National Science Foundation (NSF) under Grant No. 1439683, the National Institute of Standards and Technology (NIST) under Cooperative Agreement number NIST 70NANB15H320, and industry members of the NSF Center for e-Design.

REFERENCES

[1] Gibson, I., Rosen, D.W., and Stucker, B., 2010, "Additive manufacturing technologies," Springer, .

[2] Kim, D. B., Witherell, P., Lipman, R., 2015, "Streamlining the Additive Manufacturing Digital Spectrum: A Systems Approach," Additive Manufacturing, **5**pp. 20-30.

[3] Williams, C. B., Mistree, F., and Rosen, D. W., 2011, "A Functional Classification Framework for the Conceptual Design of Additive Manufacturing Technologies," Journal of Mechanical Design, **133**(12) pp. 121002.

[4] Rosen, D.W., 2007. Design for additive manufacturing: a method to explore unexplored regions of the design space. In Eighteenth Annual Solid Freeform Fabrication Symposium pp. 402-415.

[5] Brandl, E., Heckenberger, U., Holzinger, V., 2012, "Additive Manufactured AlSi10Mg Samples using Selective Laser Melting (SLM): Microstructure, High Cycle Fatigue, and Fracture Behavior," Materials & Design, **34**pp. 159-169.

[6] Chatterjee, A., Kumar, S., Saha, P., 2003, "An Experimental Design Approach to Selective Laser Sintering of Low Carbon Steel," Journal of Materials Processing Technology, **136**(1) pp. 151-157.

[7] Jin, R., Chen, W., and Simpson, T. W., 2001, "Comparative Studies of Metamodelling Techniques Under Multiple Modelling Criteria," Structural and Multidisciplinary Optimization, **23**(1) pp. 1-13.

[8] Khairallah, S. A., Anderson, A. T., Rubenchik, A., 2016, "Laser Powder-Bed Fusion Additive Manufacturing: Physics of Complex Melt Flow and Formation Mechanisms of Pores, Spatter, and Denudation Zones," Acta Materialia, **108**pp. 36-45.

[9] Kleijnen, J.P., 1986, "Statistical tools for simulation practitioners," Marcel Dekker, Inc., .

[10] Kleijnen, J. P., and Sargent, R. G., 2000, "A Methodology for Fitting and Validating Metamodels in Simulation," European Journal of Operational Research, **120**(1) pp. 14-29.

[11] Varadarajan, S., Chen, W. and Pelka, C.J., 2000, "Robust concept exploration of propulsion systems with enhanced model approximation capabilities," Engineering Optimization A35, 32(3), pp. 309-334.

[12] Tapia, G., and Elwany, A., 2015, "Prediction of porosity in SLM parts using a MARS statistical model and Bayesian inference," Proceedings of the 2015 Annual International Solid Freeform Fabrication Symposium, pp. 1205-1219.

[13] Ciurana, J., Hernandez, L., and Delgado, J., 2013, "Energy Density Analysis on Single Tracks Formed by Selective Laser Melting with CoCrMo Powder Material," The International Journal of Advanced Manufacturing Technology, **68**(5-8) pp. 1103-1110.

[14] Witherell, P., Feng, S., Simpson, T. W., 2014, "Toward Metamodels for Composable and Reusable Additive Manufacturing Process Models," Journal of Manufacturing Science and Engineering, **136**(6) pp. 061025.

[15] Thomas, D. S., and Gilbert, S. W., 2014, "Costs and Cost Effectiveness of Additive Manufacturing," .

[16] Ding, J., Colegrove, P., Mehnen, J., 2014, "A Computationally Efficient Finite Element Model of Wire and Arc Additive Manufacture," The International Journal of Advanced Manufacturing Technology, **70**(1-4) pp. 227-236.

[17] Michopoulos, J. G., Lambrakos, S., and Iliopoulos, A., 2014, "Multiphysics challenges for controlling layered manufacturing processes targeting thermomechanical performance," ASME 2014 International Design Engineering Technical Conferences and Computers and Information in Engineering Conference, Anonymous American Society of Mechanical Engineers, pp. V01AT02A050-V01AT02A050.

[18] Van Elsen, M., Al-Bender, F., and Kruth, J., 2008, "Application of Dimensional Analysis to Selective Laser Melting," Rapid Prototyping Journal, **14**(1) pp. 15-22.

[19] Spierings, A., Levy, G., and Wegener, K., 2014, "Designing material properties locally with additive manufacturing technology SLM," ETH-Zürich, .

[20] Montgomery, D.C., 2008, "Design and analysis of experiments," John Wiley & Sons, .

[21] Shao, T., 2007, "Toward a structured approach to simulation-based engineering design under uncertainty," Ph.D. Thesis, University of Massachusetts Amherst, Amherst, MA.

[22] Giunta, A. A., Wojtkiewicz, S. F., and Eldred, M. S., 2003, "Overview of modern design of experiments methods for computational simulations," Proceedings of the 41st AIAA aerospace sciences meeting and exhibit, AIAA-2003-0649, Anonymous .

[23] Husslage, B. G., Rennen, G., van Dam, E. R., 2011, "Space-Filling Latin Hypercube Designs for Computer Experiments," Optimization and Engineering, **12**(4) pp. 611-630.

[24] Simpson, T. W., Booker, A. J., Ghosh, D., 2004, "Approximation Methods in Multidisciplinary Analysis and Optimization: A Panel Discussion," Structural and Multidisciplinary Optimization, **27**(5) pp. 302-313.

[25] Khan, M., Romoli, L., Fiaschi, M., 2010, "Experimental Investigation on Laser Beam Welding of Martensitic Stainless Steels in a Constrained Overlap Joint Configuration," Journal of Materials Processing Technology, **210**(10) pp. 1340-1353.

[26] Balasubramanian, K., Siva Shanmugam, N., Buvanashekaran, G., 2008, "Numerical and Experimental Investigation of Laser Beam Welding of AISI 304 Stainless Steel Sheet," Adv.Produc.Engineer.Manag, **3**(2) pp. 93-105.

[27] Cole, R., Healy, T., Wood, M., 2001, "Statistical Analysis of Spatial Pattern: A Comparison of Grid and Hierarchical Sampling Approaches," Environmental Monitoring and Assessment, **69**(1) pp. 85-99.

[28] Wang, Y., and Hickernell, F.J., 2002, "An historical overview of lattice point sets," Springer, .

[29] Audze, P., and Eglais, V., 1977, "New Approach for Planning Out of Experiments," Problems of Dynamics and Strengths, **35**pp. 104-107.

[30] Tang, B., 1993, "Orthogonal Array-Based Latin Hypercubes," Journal of the American Statistical Association, **88**(424) pp. 1392-1397.

[31] McKay, M. D., Beckman, R. J., and Conover, W. J., 2000, "A Comparison of Three Methods for Selecting Values of Input Variables in the Analysis of Output from a Computer Code," Technometrics, **42**(1) pp. 55-61.

[32] Eddy, D. C., Krishnamurty, S., Grosse, I. R., 2015, "A Predictive Modelling-Based Material Selection Method for

Sustainable Product Design," Journal of Engineering Design, **26**(10-12) pp. 365-390.

[33] Sacks, J., Welch, W. J., Mitchell, T. J., 1989, "Design and Analysis of Computer Experiments," Statistical Science, pp. 409-423.

[34] Shao, T., and Krishnamurty, S., 2008, "A Clustering-Based Surrogate Model Updating Approach to Simulation-Based Engineering Design," Journal of Mechanical Design, **130**(4) pp. 041101.

[35] Wang, G. G., and Shan, S., 2007, "Review of Metamodeling Techniques in Support of Engineering Design Optimization," Journal of Mechanical Design, **129**(4) pp. 370-380.

[36] Box, G.E., and Draper, N.R., 1987, "Empirical model-building and response surfaces," Wiley New York, .

[37] Simpson, T. W., 1998, "Comparison of Response Surface and Kriging Models in the Multidisciplinary Design of an Aerospike Nozzle," .

[38] Shan, S., and Wang, G. G., 2010, "Survey of Modeling and Optimization Strategies to Solve High-Dimensional Design Problems with Computationally-Expensive Black-Box Functions," Structural and Multidisciplinary Optimization, **41**(2) pp. 219-241.

[39] Cressie, N., 2015, "Statistics for spatial data," John Wiley & Sons, .

[40] Van Dam, E. R., Husslage, B., Den Hertog, D., 2007, "Maximin Latin Hypercube Designs in Two Dimensions," Operations Research, **55**(1) pp. 158-169.

[41] Bates, S. J., Sienz, J., and Langley, D. S., 2003, "Formulation of the Audze–Eglais Uniform Latin Hypercube Design of Experiments," Advances in Engineering Software, **34**(8) pp. 493-506.

[42] Shao, T., and Krishnamurty, S., 2009, "A Preference-Performance Hybrid Method for Surrogate Model Updating in Engineering Design Optimisation," International Journal of Product Development, **9**(1-3) pp. 218-264.

[43] Eldred, M.S., Giunta, A.A., van Bloemen Waanders, Bart G, 2007, "DAKOTA, a multilevel parallel object-oriented framework for design optimization, parameter estimation, uncertainty quantification, and sensitivity analysis: Version 4.1 reference manual," Citeseer, .

[44] Sargent, R. G., 2005, "Verification and validation of simulation models," Proceedings of the 37th conference on Winter simulation, Anonymous winter simulation conference, pp. 130-143.

[45] Deng, J., 1989, "Grey Information Space," The Journal of Grey System, **1**(1) pp. 103-117.

[46] Zhao, D., and Xue, D., 2011, "A Multi-Surrogate Approximation Method for Metamodeling," Engineering with Computers, **27**(2) pp. 139-153.

FIREBRAND IGNTION IN LARGE OUTDOOR FIRES: THE USE OF FULL-SCALE EXPERIMENTS TO GUIDE THE DEVELOPMENT OF LABORATORY STANDARD TEST METHODS

Samuel L. Manzello*
Fire Research Division
Engineering Laboratory (EL)
National Institute of Standards and Technology (NIST)
Gaithersburg, MD 20899-8662 USA
*Corresponding author: samuelm@nist.gov

Sayaka Suzuki
National Research Institute of Fire and Disaster (NRIFD)
4-35-3, Jindaiji Higashimachi
Chofu, Tokyo, 182-0012 Japan

ABSTRACT

Wildfires that spread into communities, referred to as Wildland-Urban Interface (WUI) fires, have destroyed communities throughout the world. Large outdoor fires in Japan mainly occur due to post-earthquake fires, which result in severe urban fires. Firebrand ignition of structures is a major factor in WUI and urban fire spread. Without standard laboratory test methods, it is impossible to evaluate and compare the performance of different building elements and/or vegetative fuels ability to resist firebrand ignition. Before such test standards are developed, detailed full-scale experiments that systematically evaluate individual building component vulnerabilities to ignition by firebrand showers are required. It is critical to understand full-scale assembly performance when exposed to firebrand showers since weak points in a given assembly can be investigated. In turn, this will lead to determining the necessary configuration of building component mock-ups that can be used in standard laboratory test methods. As wind is a critical component required to transport firebrand showers observed in large outdoor fires, and wind plays a major role in whether ignition is observed, full-scale experiments must be able to consider the influence of an applied wind field to understand such ignition vulnerabilities. The basis of this paper is to present a comparison of ignition results from full-scale roofing assembly experiments, to mockups using the recently developed experimental capability at National Research Institute of Fire and Disaster (NRIFD). The development of more ignition resistant structures in large outdoor fires, not only WUI fires, but urban fires in Japan, will greatly benefit fire services as it is envisioned that firefighting resources may be better used to battle such fires, since the number of structure ignitions may be reduced significantly.

INTRODUCTION

Wildland-Urban Interface (WUI) fires have become a problem of great concern worldwide. Japan does not have a specific problem of fires spreading from the wildlands to communities, such as the WUI fire problem [1]. After large earthquakes in Japan, many fires may simultaneously occur, leading to severe fire spread within urban areas [1]. Once a wildland fire researches a community and ignites structures, structure-structure fire spread via firebrand generation occurs in the same manner as in post-earthquake fires [1].

Post-fire studies have identified firebrands as a significant source of structure ignition in both WUI and

Manzello, Samuel; Suzuki, Sayaka.
"Firebrand Ignition in Large Outdoor Fires: The Use of Full-Scale Experiments to Guide the Development of Laboratory Standard Test Methods."
Paper presented at Interflam 2016, 14th International Conference on Fire Science and Engineering,
Windsor, England, United Kingdom. July 4, 2016 - July 6, 2016.

urban fires [2]. The dynamic process of multiple wind-driven firebrands landing and then being transported under non-combustible tiles/gaps as a function of time is not considered in current roofing assembly test standards [2]. Manzello *et al*. [3] revealed the vulnerabilities of curved ceramic tile roofing (Spanish tile roofing) assemblies to ignition under a controlled wind-driven firebrand attack using the NIST Firebrand Generator. The interested reader is referred elsewhere to a comprehensive overview of recent wind-driven firebrand research [3].

With many wildland fires propagated by wind-driven firebrands, the resistance of building elements to wind-driven firebrands has become a topic of great interest worldwide as evidenced by papers submitted on this topic from all over the world to the first ever Special Issue devoted to WUI fires in the fire safety science archival literature, as well as a recent ASTM International Workshop on this topic [4-5]. As part of an industrial collaboration with NIST and the Tile Roofing Institute (TRI) in partnership with the Roofing Tile Institute of Australia (RTAA), concrete tile roofing assemblies (flat and profiled tile) as well as terracotta tile roofing assemblies (flat and profiled tile) commonly used in the USA, Australia, and elsewhere, were exposed to wind-driven firebrand showers [6]. The results demonstrated that firebrands penetrated between the tile gaps and melted the sarking material (see [6] for details of sarking) for both types of concrete tile roofing assemblies (flat and profiled tile) and the profiled tile terracotta roofing assembly when exposed to wind-driven firebrands. These experiments used the original NIST batch feed firebrand generator, and therefore the duration of the firebrand exposure was limited to around 6 min [6]. This original batch feed device was used because: (1) industry was interested in a direct comparison to the experiment protocols used for the Spanish tile roofing assemblies, (2) the batch-feed version of the Firebrand Generator was far less expensive to operate and provided a simple cost-effective tool to determine if further work was required (*i.e.* if firebrand penetration and melting of sarking occurred).

Standard laboratory test methods are required to evaluate/compare the performance of various roofing assemblies to resist firebrand ignition. Before such test standards are developed, detailed full-scale experiments that systematically evaluate roofing assembly vulnerabilities to ignition by firebrand showers are required. It is necessary to understand full-scale assembly performance when exposed to firebrand showers since weak points in a given assembly can be investigated. In turn, this will guide the necessary configuration of roofing assembly mock-ups that can be used in standard laboratory test methods.

The objective of the present investigation was to: (1) observe the full-scale performance of tile roofing assemblies exposed to *continuous* firebrand showers for wind speeds of 6 m/s and 9 m/s, described in detail in [7], and (2) use those results to guide experiments using mock-ups of full-scale roofing assemblies using a recently developed reduced-scale experimental facility developed to study firebrand ignition. The overall goal was to determine if similar firebrand penetration vulnerabilities were observed for reduced sized experiments. A brief summary of these comparisons were presented at a Japanese conference; this paper provides a detailed summary to the international fire safety science community [8].

EXPERIMENTAL DESCRIPTION

Full-Scale Experiments at the Fire Research Wind Tunnel Facility (FRWTF)

Complete details of the full-scale roofing assembly experiments are described elsewhere [7]. However, a brief overview is provided here in order for the reader to possess the requisite understanding necessary to follow the comparison to experiments using the reduced-scale experimental facility below.

To generate firebrand showers **t**he full-scale Continuous Feed Firebrand Generator was used. The description differs from descriptions available elsewhere [9-10] since the feeding system was redesigned to be able to generate firebrand size and mass distributions using larger wood chips in an effort to produce a wider range of exposure conditions; reasons for this are provided below. The device consisted of two parts: the main body and continuous feeding component. The main body of the generator was the same as prior investigations (Dragon component); the feeding system was modified. The feeding system was connected to the main body and was equipped with two gates to prevent fire spread (described in more

detail below). A blower was connected to the main body and the purpose of the blower is described below. A major challenge when constructing this device was designing a completely contained feeding system shielded from the wind tunnel flow.

The feeding system consisted of a pneumatic cylinder coupled to a cylindrical container where wood pieces were stored (see **Figure 1**). Below the wood storage area, a plate was installed that allowed variation in the volume of wood to fall from the storage area to the first gate. This volume was set precisely to allow a specific mass of firebrands to fall into this volume. When the air pressure was applied, the sliding rod of the pneumatic cylinder moved forward and separated the wood pieces from the storage area to the first gate, where they were then dropped into the second gate that leads to the Dragon where they are ignited (see **Figure 1**). Care was taken to select the pneumatic cylinder (15 cm bore with 17.8 cm stroke; maximum pressure of 1.7 MPa and maximum load of 12 kN; this is about 4 times more force than our previous device of 3.1 kN; see [9-10]); smaller sized pneumatic cylinders were observed to be unable to cut through the wood and would jam. The gate system was required to contain the fire from spreading from the Dragon to the feed system and each gate was driven by pneumatic cylinders as well.

Figure 1 Schematic of full-scale continuous feed firebrand generator. Wood chips are shown.

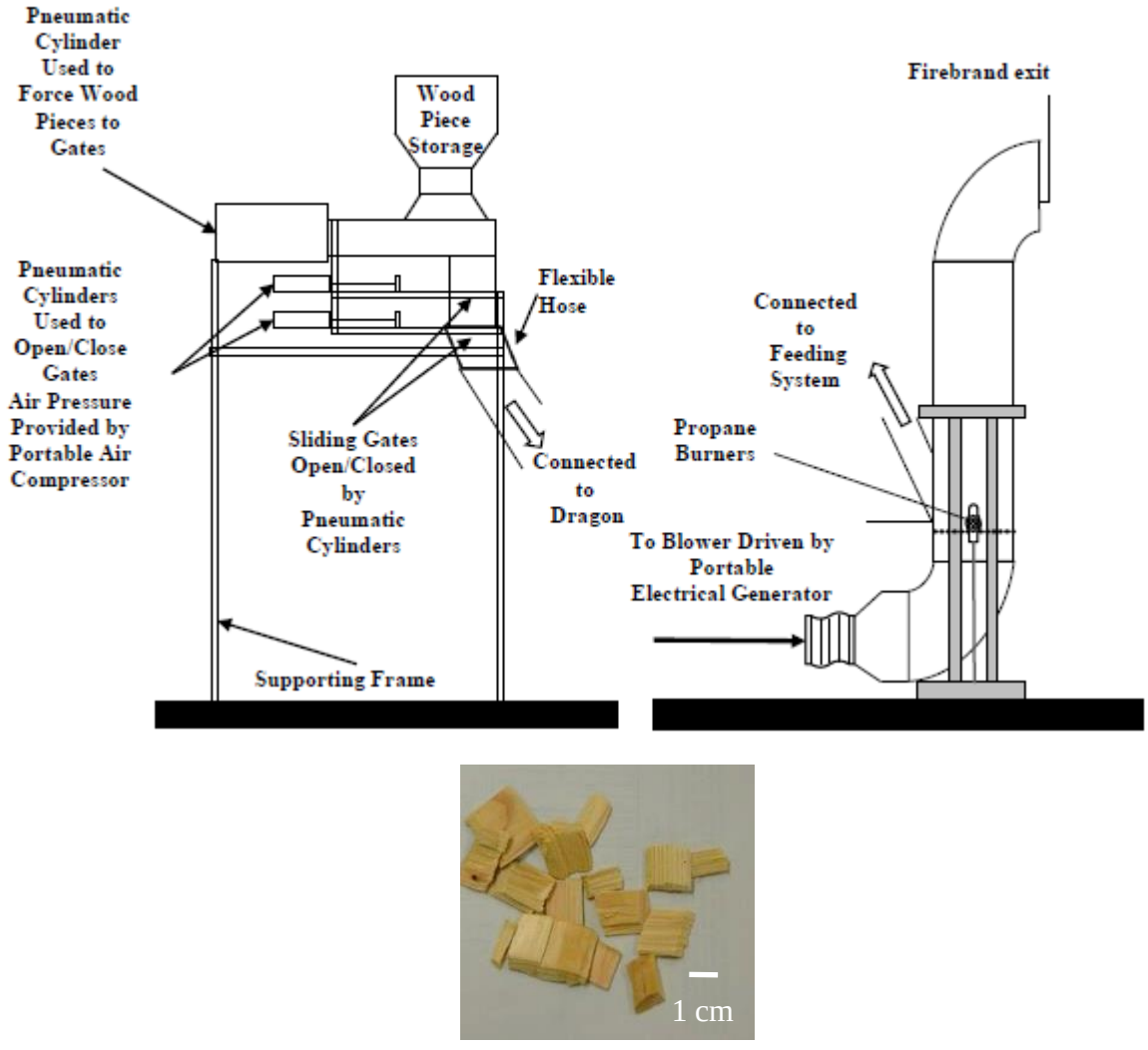

For all tests, Japanese Cypress wood chips were used to produce firebrands (see **Figure 1**). These were provided from a supplier and upon arrival, these chips were filtered using a 1 cm mesh to remove very fine wood pieces that settled during the shipping process. The chips were also oven dried, as they were shipped under wet conditions; nominal moisture content greater than 70 % on a dry basis. The size of wood pieces

were selected to produce firebrands with larger projected area at a specific mass than our prior studies using continuous firebrand generation [9-10]. An important characteristic of our prior studies was that the firebrand size and mass produced using was tailored to those measured from full-scale tree burns, and actual WUI fires [9-10]. It is clear that more data is needed for firebrand size/mass distributions from various types of vegetation, structures, and actual WUI and urban fires [9]. The authors have begun to develop a database of firebrand production from burning structures/structure components. This paper is the first attempt to generate firebrand showers with size and mass commensurate to distributions in this structure firebrand data set. Additional details are provided in the results section below.

As in prior experiments using the NIST Dragon, the new experimental device was installed inside the test section of BRI's Fire Research Wind Tunnel Facility (FRWTF). The facility was equipped with a 4 m diameter fan to produce the wind field. The cross section of the FRWTF is 5 m wide by 4 m high.

The roofing assemblies were placed at a distance of 2 m downstream of the full-scale Continuous Feed Firebrand Generator. Assemblies located at this distance are known to receive an intense flux of firebrands from the Dragon and allow for direct comparison of all prior roofing studies [6, 11]. A custom assembly was constructed to mount the roofing assemblies. In these experiments, USA construction details were followed. The Tile Roofing Institute design manual was followed for all tile roofing assemblies; counter-battens were used for all tile roofing assemblies in this study [7].

In the case of the tile roofing assemblies, the base frame was constructed of 2 x 6 boards, and was lined with oriented strand board (OSB). The OSB was not oven dried; nominally 11 % MC. Felt underlayment (No. 30 felt) was applied on top of the OSB sheathing and the wood batten spacing was adjusted depending on the type of ceramic or terracotta tile roofing assembly being tested. Three types of tile roofing assemblies were used, including two concrete tile roofing assemblies (flat and profiled tiles) as well as one terracotta tile roofing assemblies (flat tiles). A 25 degree pitch (commonly found in practice) was used for all the roofing assemblies for direction comparison to prior work [6, 11]. The overall dimensions of each roof assembly were 1.2 m by 1. 2 m.

Reduced-Scale Experimental Facility

A reduced-scale continuous-feed firebrand generator was used to generate firebrand showers. This reduced-scale continuous-feed firebrand generator consisted of two parts; the main body and continuous feeding component (see **Figure 2**). The feeding part was connected to the main body and had two gates to prevent fire spread. Each gate was opened and closed alternatively. The efficacy of a smaller sized firebrand generator to develop continuous firebrand showers has been described in detail elsewhere [12]. A conveyor was used to feed wood pieces continuously into the device. For all tests, Japanese Cypress wood chips were used to produce firebrands. These same size wood pieces were used in the full-scale roofing assembly study and have been shown to be within projected area/mass of burning structures [7]. Specifics of the wood feeding rate are provided below.

As the base of the fan used to generate the wind field is located 1.6 m from the floor, the conveyor was placed under a custom stage designed for experiments when using the National Research Institute of Fire and Disaster's (NRIFD) wind facility (see **Figure 3**). The flow field was measured to be within ± 10 % over a cross-section of 2.0 m by 2.0 m.

Experiments were conducted for two types of concrete tile roofing assemblies (flat and profiled), and one type of terracotta tile roofing assembly (flat). The dimensions of these mock-ups were half the size of the full-scale roofing assembly experiments: 0.6 m (W) and 1. 2 m (L) for the concrete roofing assemblies (flat and profiled), and 0.46 m (W) and 1.2 (L) for the terracotta tile roofing assembly (flat). For all tile roofing assemblies, the base frame was constructed of 2 x 4 boards, and was lined with oriented strand board (OSB) sheathing. The OSB was not oven dried; nominally 11 % MC. Felt underlayment (No. 30 felt) was applied on top of the OSB sheathing and the wood batten spacing was adjusted depending on the type of ceramic or terracotta tile roofing assembly being tested.

Figure 2 Schematic of reduced-scale continuous feed firebrand generator (front view).

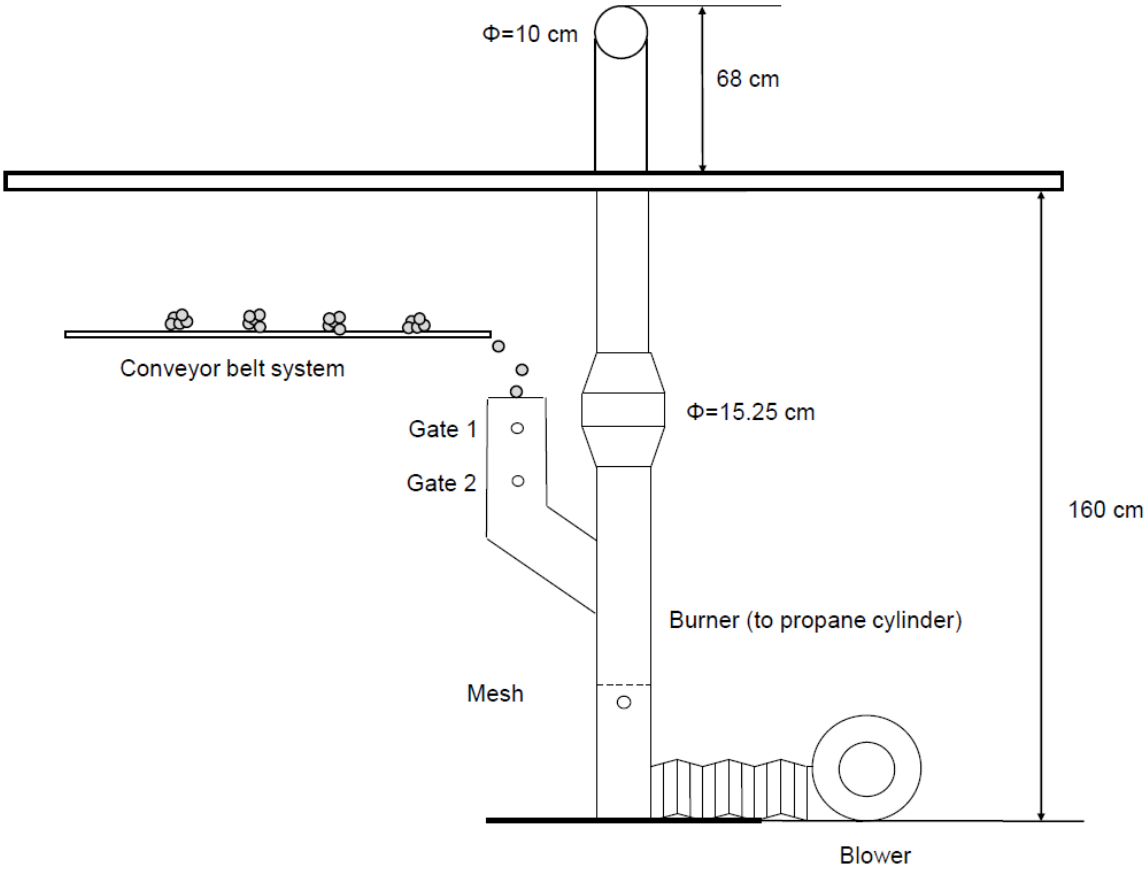

Figure 3 Picture of experimental facility (side view). The stage dimensions were 5.5 m wide, 6.4 m long, with a height of 1.6 m.

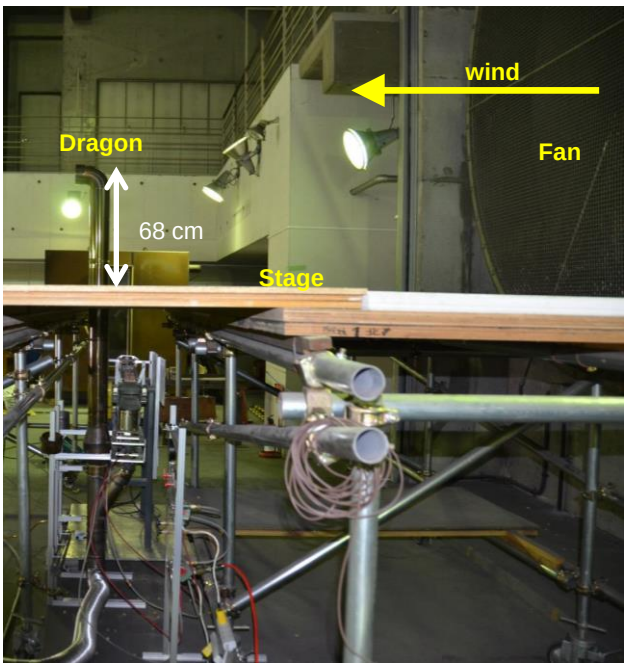

RESULTS AND DISCUSSION

Full-Scale Roofing Assemblies

The feeding rate was varied to determine the optimal conditions for continuous firebrand showers. Based on prior work, a wood mass loading 150 g to 200 g every 15 s resulted in adequate firebrand generation [9-10]. In these experiments, 170 g ± 30 g, fed into the Dragon every 15 s provided an adequate firebrand generation rate to ignite building materials. A supply of 170 g corresponded to approximately 560 wood pieces deposited every 15 s. The number flux (number of firebrands generated/m^2s), at the exit of the device, was measured at a feeding rate of 170 g every 15 s (680 g/min). To determine the number flux, the number of firebrands was counted at every frame of the video recording, and summed every second. Based on the analysis, the number flux reached a steady value of 533/m^2s 150 s after feeding began. The first firebrands began to be generated ~ 20 s after feeding was commenced [7].

Mass flux data (mass of firebrands generated/m^2s) were calculated by multiplying the number flux and the average mass of each firebrand at a feed rate of 170g every 15 s. To measure the firebrand mass, another set of experiments was conducted using a series of water pans placed downstream of the NIST full-scale Continuous Feed Firebrand Generator. Water pans were required in order to quench combustion of the firebrands. If the water pans were not used, the firebrands would continue to burn and by the time collection was completed; only ash would remain. After the experiment was finished, the pans were collected and the firebrands were filtered from the water, using a series of fine-mesh filters. Firebrands were dried in an oven, at 104 °C, for 16 h. As in previous work, the mass versus drying time was monitored to determine the duration needed to completely dry the firebrands.

Figure 4 displays the projected area of the generated firebrands at 6 m/s. Image analysis software was used to determine the projected area of a firebrand by converting the pixel area using an appropriate scale factor. It was assumed that deposited firebrands would rest flat on the ground and the projected areas with the maximum dimension and the second maximum dimension of three dimensions were measured (for cylindrical and flat shaped firebrands respectively). Images of well-defined shapes (e.g. circular objects) were used to determine the ability of the image analysis method to calculate the projected area [7]. Based on repeat measurements of different areas, the standard uncertainty in determining the projected area was ± 10 %. The mass of each firebrand was measured by a precision balance with 0.001 g resolution. Repeat measurements of known calibration masses were measured by the balance which was used for the firebrand mass analysis. The standard uncertainty in the firebrand mass was approximately ± 1 %. The mean mass and standard deviation of each firebrand were obtained and observed to be 0.03 g ± 0.02 g. Therefore, the mass flux of generated firebrands was calculated to be 16 g/m^2s [7].

It is important to note that all the generated firebrands that depart the mouth of the Dragon do not land on the surface of the roofing assemblies [6]. The average total firebrand mass flux arriving at the roofing assembly was estimated from video records to be 0.3 g/m^2s. Approximately 35 % of the firebrand mass generated from the Dragon arrived at the roofing assembly surface. It is of interest to note that that the arrival mass of flux of firebrands to the roofing assemblies was the same with prior work using the batch-feed Dragon [6]. Even though the mass flux departing the Dragon's mouth was higher than the previous batch-feed study (16 g/m^2s versus 10 g/m^2s for the batch-feed device), less firebrands arrived at the roof surface due to the overall larger projected area of the firebrands; such counter-balance produced the same arrival mass flux at the roofing assembly for both studies.

For both types of concrete tiles (flat and profiled), as well as the terracotta (flat) roofing assembly, firebrands were observed to accumulate in the gaps of the tiles. The firebrands continued to burn until they were able to penetrate the tile gaps and pass onto the underlayment/counter-batten system. In all tiles that were experimented upon, the most severe penetration occurred in the field of the roofing assembly, not at the leading edge.

Figure 4 Size and mass distribution of generated firebrands for full-scale and reduced-scale firebrand generators (comparison at 6 m/s).

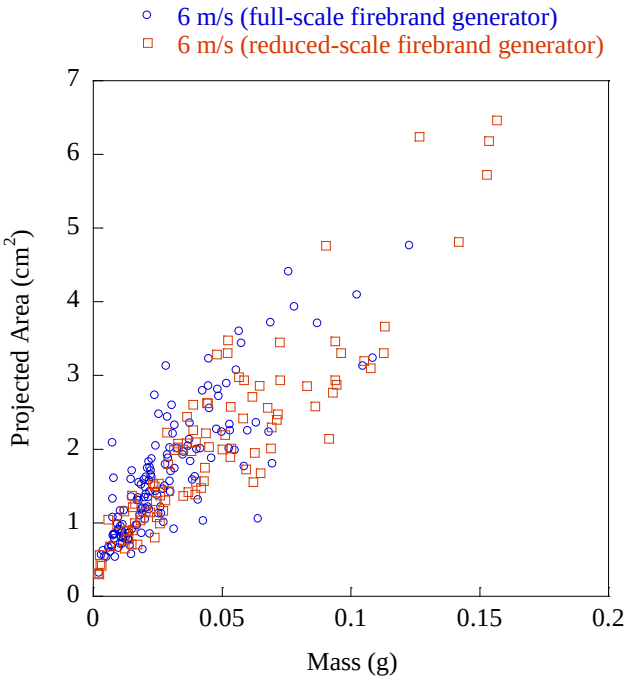

Figure 5 The number of firebrands that penetrated the tile roofing assemblies as a function of applied wind speed (20 min firebrand exposure; data from Suzuki *et al*. [7]).

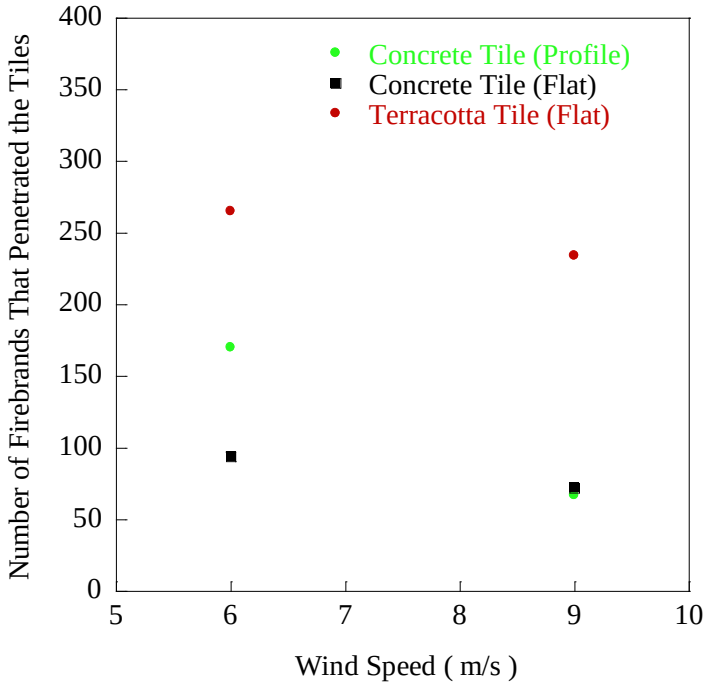

To attempt to quantify the degree of penetration, the number of firebrands that penetrated the tiles, and deposited onto the underlayment/counter-batten system was counted as function of wind speed for each tile roofing assembly. These results are shown in **Figure 5.** As can be seen, the terracotta tiles (flat), resulted in the most firebrand penetration. Firebrand penetration resulted in smoldering ignition of the counter-batten system but a transition to flaming ignition was not observed.

The concrete tiles (profiled) were the most sensitive to the amount of penetration as a function of wind speed. At the lower wind speed of 6 m/s, more firebrands were able to accumulate at the tile gaps (see **Figure 5**), which led to more firebrands being able to penetrate the tile gaps. Naturally, profiled tiles were more sensitive to this behavior, due to the raised profile.

Mock-ups of Full-Scale Roofing Assemblies

As indicated, a conveyor was used to feed wood pieces continuously into the device. The conveyor belt was operated at 1.0 cm/s, and wood pieces were put on the conveyor belt at 12.5 cm intervals. The wood feed rate was fixed at 80 g/min, near the upper limit of reduced-scale firebrand generator. These same size wood pieces were used in the full-scale roofing assembly study. **Figure 4** displays the projected area of the generated firebrands at 6 m/s using the same analysis methods described for the full-scale continuous feed firebrand generator (see above).

Figure 6 shows three different types of tile roofing assembly mock-ups experimented with, and **Figures 7-8** are typical photos of experiments. Similar to the full-scale experiments, the duration of the firebrand flux was fixed at 20 minutes and the wind speed was varied from 6 m/s to 9 m/s. For both types of concrete tiles (flat and profiled), as well as the terracotta (flat) roofing assembly, firebrands were observed to accumulate in the gaps of the tiles. The firebrands continued to burn until they were able to penetrate the tile gaps and pass onto the underlayment/counter-batten system. In all tiles that were experimented upon, the most severe penetration occurred in the field of the roofing assembly, not at the leading edge.

Figure 6 Three different types of tile roofing assembly mock-ups experimented used. In each case, these are half the size of the full-scale roofing assemblies described above.

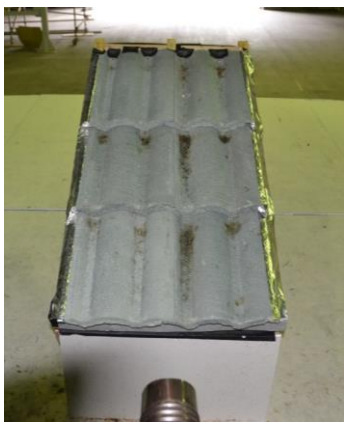

Concrete Tile (profiled)
0.6 m by 1.2 m

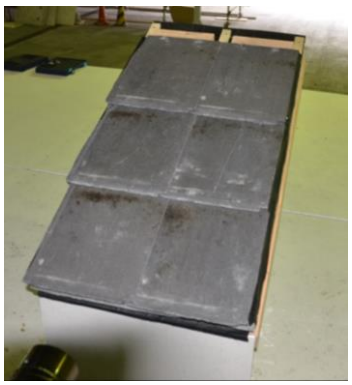

Concrete Tile (flat)
0.6 m by 1.2 m

Terracotta Tile (flat)
0.46 m by 1.2 m

To attempt to quantify the degree of penetration, the number of firebrands that penetrated the tiles, and deposited onto the underlayment/counter-batten system was counted as function of wind speed for each tile roofing assembly. These results are shown in **Figure 9**. As can be seen, the terracotta tiles (flat), resulted in the most firebrand penetration. Firebrand penetration resulted in smoldering ignition of the counter-batten system but a transition to flaming ignition was not observed in any experiments (see **Figure 10**).

Figure 7 Concrete tile (profiled) roofing assembly exposed to firebrand showers at 6 m/s. The height of the firebrand generator was 68 cm from the base of the stage. The distance from the firebrand generator to the leading edge of roofing assembly was 0.5 m. Significant firebrand arrival occurred at this generator-roof distance.

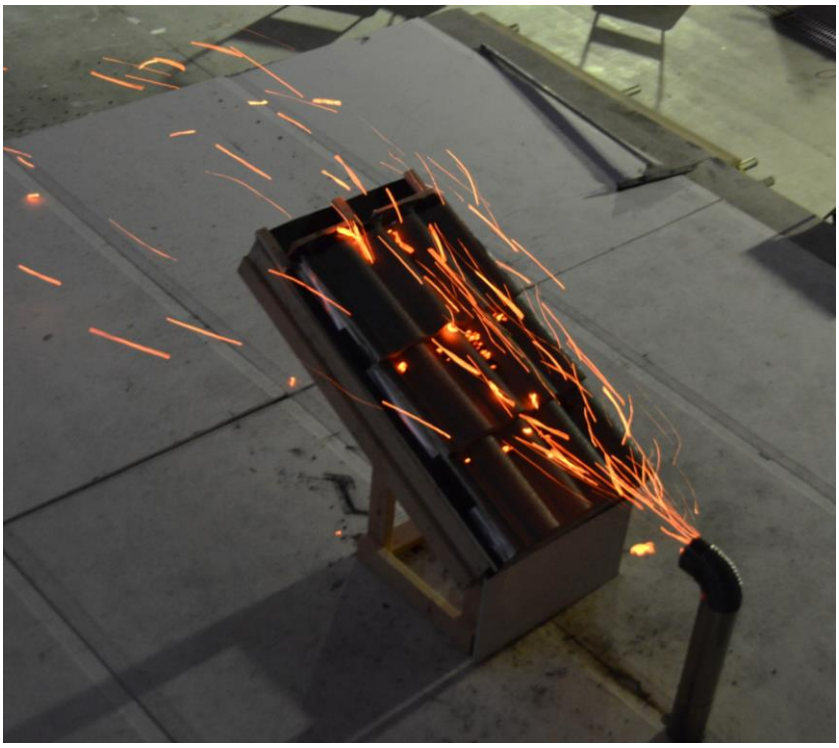

Figure 8 Concrete tile (flat) roofing assembly exposed to firebrand showers at 6 m/s. The height of the firebrand generator was 68 cm from the base of the stage. The distance from the firebrand generator to the leading edge of roofing assembly was 0.5 m. Significant firebrand arrival occurred at this generator-roof distance.

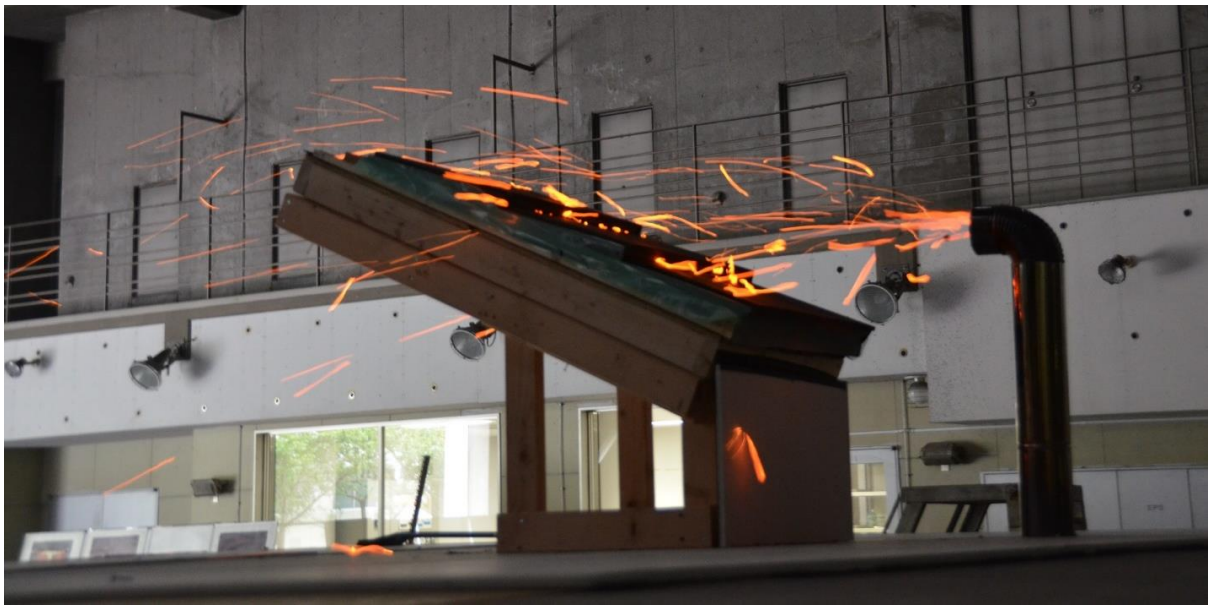

Figure 9 The number of firebrands that penetrated the tile roofing assemblies as a function of applied wind speed (20 min firebrand exposure). Firebrands were counted after the tiles were removed.

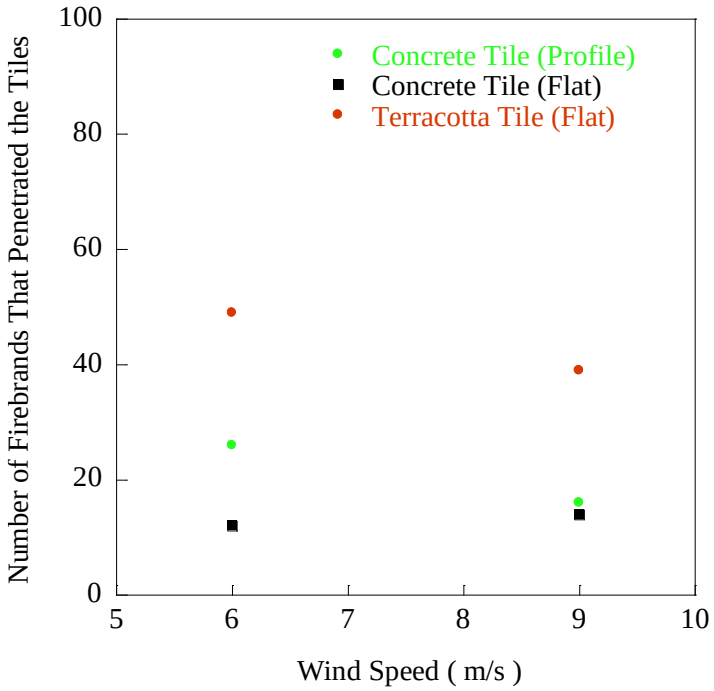

Figure 10 The Terracotta tile (flat) roofing assembly exposed to firebrand showers at 6 m/s. 20 min firebrand exposure. Smoldering ignition of battens - no transition to flaming ignition observed. The batten ignition is circled as are the firebrands that penetrated the tiles.

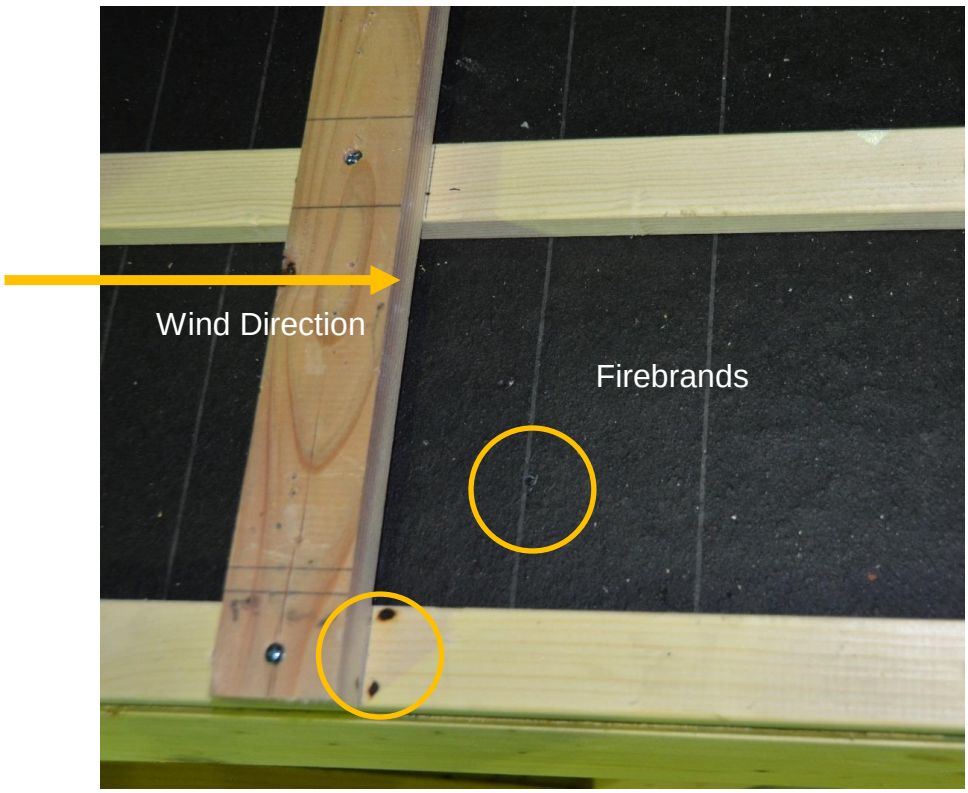

The *total number* of firebrands that penetrated the roofing section mock-ups was considerably less than the full-scale experiments. This was expected since the feeding rate of wood chips was 80 g/min, or 8.5 times less than the full-scale experiments. To further understand these differences, the arrival number flux of firebrands was compared between the full-scale experiments to the mock-up roofing assemblies. In the case of the full-scale roofing experiments, the average arrival number flux was 10 /m^{2}s as compared to 7 /m^{2}s for the mock-ups. It is natural that overall less firebrand penetration (total number) was observed for the mock-up roofing assemblies since: (1) less firebrands actually arrive, and (2) once they arrive, there are less tile gaps for the firebrands to penetrate.

SUMMARY

These experiments have demonstrated that similar firebrand penetration behavior/trends were observed for mock-ups of full-scale roofing assemblies, as compared to experiments where full-scale roofing assemblies were used, all under similar wind speeds. At the same time, the penetration data will serve as part of database of roofing assembly performance to continuous firebrand exposure.

In this work, the total exposure time of firebrand showers was selected to be 20 min, about three times longer than was possible using prior bath-feed firebrand generators. Naturally, a representative time for firebrand exposure depends on many factors in actual large outdoor fires, such as WUI and urban fires. It is believed that different durations of firebrand exposure could serve as the basis for a rating system for use in standard test methods for roofing assembly performance. In particular quantifying firebrand exposure from actual WUI and urban fires is required to determine representative firebrand exposure duration, and these will be helpful to *provide bounds of exposure severity* to wind-driven firebrand showers. This premise is analogous to what is currently done for various fire safety test methods (*i.e*. Class A assembly indicates most ignition resistant).

ACKNOWELDGEMENTS

Mr. Marco Fernandez of NIST's Engineering Laboratory (EL) is acknowledged for shipping materials for the experiments. The support of Dr. Daisaku Nii (Kyoto University, formerly of the Building Research Institute, Japan) was helpful to complete the full-scale experimental campaign in this work.

REFERENCES

[1] Manzello, S. L., *et al*., Workshop for Fire Structure Interaction and Urban and Wildland-Urban Interface (WUI) Fires – Operation Tomodachi Fire Research, *Fire Safety Journal*, 59 (2013) 122-131.

[2] Manzello, S.L., and Foote, E.I.D., Characterizing Firebrand Exposure from Wildland-Urban Interface (WUI) Fires: Results from the 2007 Angora Fire, *Fire Tech*nology, 50 (2014) 105-124.

[3] Manzello, S.L., Enabling the Investigation of Structure Vulnerabilities to Wind-Driven Firebrand Showers in Wildland Urban Interface (WUI) Fires, *Fire Safety Science* 11 (2014) 83-96.

[4] Manzello, S.L. (Invited Guest Editor), Special Issue on Wildland-Urban Interface (WUI) Fires, *Fire Tech*nology, 50 (2014) 7-8.

[5] Manzello, S. L. and Quarles, S.L., Summary of Workshop on Structure Ignition in Wildland-Urban Interface (WUI) Fires, NIST SP 1198, 2015.

[6] Manzello, S.L., The Performance of Concrete Tile and Terracotta Tile Roofing Assemblies Exposed to Wind-Driven Firebrand Showers, NIST Technical Note 1794, 2013.

[7] Suzuki, S., Manzello. S.L., and Nii, D., The Performance of Wood and Tile Roofing Assemblies

Exposed to Continuous Firebrand Assault, *Fire and Materials*, in revision, 2016.

[8] Manzello, S.L., and Suzuki, S., Proceedings of the 28th Annual JAFSE Symposium, 2 page extended abstract, in press, 2016.

[9] Suzuki, S., *et al.*, Ignition of Mulch Beds Exposed to Continuous Wind Driven Firebrand Showers, *Fire Technology*, 51:905-922, 2015.

[10] Suzuki, S., *et al*., Ignition of Wood Fencing Assemblies Exposed to Continuous-Wind Driven Firebrand Showers, published on-line, *Fire Technology*, 2016.

[11] Manzello, S.L., *et al*., Quantifying the Vulnerabilities of Ceramic Tile Roofing Assemblies to Ignition during a Firebrand Attack, *Fire Safety Journal* 45 (2010) 35-43.

[12] Suzuki, S., and Manzello, S.L., On the Development and Characterization of a Reduced-Scale Continuous Feed Firebrand Generator, *Fire Safety Science* 10 (2011) 1437-1448.

INFLUENCE OF GROUND MOTION SELECTION ON THE ASSESSMENT OF STEEL SPECIAL MOMENT FRAMES

R. Uribe[(1)], S. Sattar[(2)], M.S. Speicher[(3)], L. Ibarra[(4)]

[(1)] Graduate Student, University of Utah, raul.uribe@utah.edu
[(2)] Research Structural Engineer, National Institute of Standards and Technology, siamak.sattar@nist.gov
[(3)] Research Structural Engineer, National Institute of Standards and Technology, matthew.speicher@nist.gov
[(4)] Assistant Professor, University of Utah, luis.ibarra@utah.edu

Abstract

This paper quantifies the impact of using different ground motion selection methods to evaluate the seismic performance of steel special moment frames. Two methods are investigated: a "traditional" approach, herein referred to as the Pacific Earthquake Engineering Research (PEER) method, and a newer approach known as the conditional mean spectrum (CMS) method. Amongst other differences, the PEER method uses the risk-based maximum considered earthquake (MCE_R) as the target spectrum, while the CMS method uses the conditional mean spectrum. Two special moment frames (4- and 8-story) designed in accordance with ASCE/SEI 7-10, are used to represent archetype steel frame buildings on the West Coast of the United States. The seismic performance of these frames are assessed with the nonlinear dynamic procedure prescribed in ASCE/SEI 41-13, using ground motions selected and scaled in accordance with both methods. The performance of the buildings is evaluated at the Collapse Prevention (CP) performance level for a far-field site located in Los Angeles, CA. The two ground motion selection methods lead to different structural response predictions, where the ground motions selected and scaled using CMS can result in a smaller dispersion of the output parameters. These results provide motivation for building standards, such as ASCE/SEI 41, to advocate implementing the CMS method as an alternative ground motions selection approach. The results also shed light on the influence of the ground motion selection method in the design of new buildings using the performance-based seismic design methodology.

Keywords: ground motion selection; conditional mean spectra; steel moment frame; seismic assessment

Ibarra, Luis; Sattar, Siamak; Speicher, Matthew; Uribe, Raul.
"Influence of ground motion selection on the assessment of a steel special moment frames."
Paper presented at 16th World Conference on Earthquake Engineering, Santiago, Chile. January 9, 2017 - January 13, 2017.

1. Introduction

Nonlinear dynamic analysis has become more popular among practitioners, mainly due to advancements in simulation and computational capabilities, as well as the increasing use of performance-based seismic design approaches. One of the main steps in assessing the response of a building using nonlinear dynamic procedures is to analyze the building model using a suite of ground motions. Several ground motion selection methods have been developed that vary in terms of the selection criteria, error computation, target spectrum, etc. The premise of all ground motion selection methods is to select records that reasonably estimate ground motions for a specific building site anticipated to occur in a future earthquake. The use of different ground motion selection method leads to different nonlinear response.

In general, ground motion selection and scaling methods can be categorized as either a) amplitude scaling, or b) spectral matching (*i.e.*, modification of frequency content). This paper focuses on methods in the former category. A comprehensive list of approaches to select and scale the ground motions are reported in [1]. Typical spectra used as targets are the MCE_R spectrum, which is developed using parameters from ASCE/SEI 7-10 [2] (referred to as ASCE 7), or the Uniform Hazard Spectrum (UHS), which is constructed from hazard curves from Probabilistic Seismic Hazard Analyses. These selection methods often choose the ground motions that best match the target spectrum after they have been scaled. The basis for selecting the best match is to minimize the error between the target spectrum and the selected ground motion. However, both the error and the target spectrum can be calculated in different ways, potentially leading to significantly different results.

This study focuses on two ground motion selection methods: 1) the Pacific Earthquake Engineering Research (PEER) method, which can be considered a well-established method widely used in research and practice; and 2) the conditional mean spectrum (CMS) method, a newer method that has been employed more in research. In the PEER method, ground motions are selected to minimize the error between each ground motion spectrum and the target spectrum, MCE_R in this study, across a range of periods. The approach is referred to as the PEER method because it is implemented in the PEER online tool. In contrast, the CMS method uses the conditional mean spectrum as the target for matching ground motions and scaling them to match spectral acceleration (S_a) at a conditioning period.

To investigate the effects of these ground motion selection methods, newly designed 4- and 8-story buildings are assessed at the Collapse Prevention performance level using the nonlinear dynamic procedure outlined in ASCE/SEI 41-13 [3] (referred to as ASCE 41) for ground motions selected using the CMS and PEER methods. The predicted performance of the buildings, in terms of nonlinear hinge deformations and their corresponding dispersion, is compared for the two selection methods.

2. Background on Ground Motion Selection and Scaling Methods

2.1 Conditional Mean Spectrum

The CMS method is a site-specific ground motion selection method in which scaled ground motion records are selected based on how closely they match a conditional mean target spectrum across a range of vibrational periods [4]. The CMS was developed as an alternative to the conservative UHS. The UHS is constructed from spectral acceleration values of hazard curves developed using probabilistic seismic hazard analysis at a selected probability of exceedance (e.g., 2 % in 50 years) with every value of the UHS having the same exceedance probability. The CMS is a more realistic target for selecting and scaling ground motions, because of the UHS intrinsic conservatism due to the unlikely scenario of all the spectral accelerations occurring in a single event [4]. Instead, the CMS is conditioned, or anchored, to a single spectral acceleration at a period of significance, such as the building's fundamental period.

In this study, the risk-targeted maximum considered earthquake (MCE_R) is selected as the spectrum to anchor the CMS. Once the spectral acceleration at the conditioning period (T^*), *i.e.* the period in which the spectral acceleration of the CMS matches the MCE_R is determined, the rest of the CMS spectrum, at each given period (T_i), is computed per Equation (1) [4].

$$\mu_{lnSa(T_i)|lnSa(T^*)} = \mu_{lnSa}(M,R,T_i) + \rho(T_i,T^*)\varepsilon(T^*)\sigma_{lnSa}(M,T_i) \quad (1)$$

Where $\mu_{lnSa(T_i)|lnSa(T^*)}$ is the logarithmic mean Sa at period T_i, at a given Sa at period T^*, $\mu_{lnSa}(M,R,T_i)$ is the logarithmic mean of Sa from the GMPM [5], M and R are the earthquake mean magnitude and mean distance from deaggregation, respectively [4,6], $\rho(T_i,T^*)$ is the correlation coefficient between ε at T_i and T^*, $\varepsilon(T^*)$ represents the number of standard deviations the target spectral acceleration differs from the median ground motion at the conditioning period [4], and $\sigma_{lnSa}(M,T_i)$ is the logarithmic standard deviation of Sa from the GMPM. Additional information regarding the calculation of the CMS target spectrum is provided in [7]. The computed CMS has lower spectral accelerations than the MCE_R spectrum, with the exception of the acceleration at the conditioning period, which matches the MCE_R, as shown in Fig. 1. This implies that if a structure is subjected to ground motions matched to the CMS, better performance is expected.

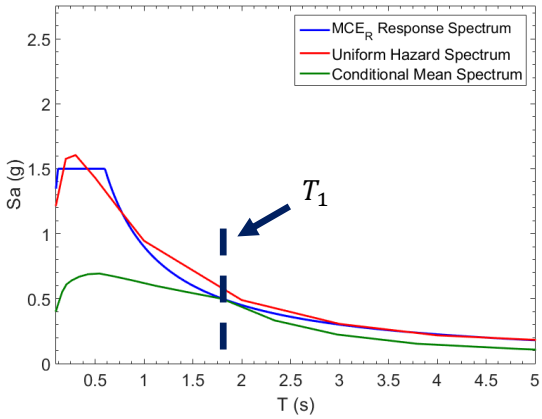

Fig. 1 – Comparison of the UHS, MCE_R spectrum, and CMS conditioned at T_1 = 1.81s for the 4-story SMF.

Once the CMS spectrum is developed, the ground motions are selected based on how similar their response spectrum is compared to the CMS. The similarity is based on the smallest sum of squared errors (SSE) as defined in Eq. (2) [4]:

$$SSE = \sum_{i=1}^{n} \left(\ln Sa(T_i) - \ln Sa^{CMS}(T_i)\right)^2 \quad (2)$$

where $\ln Sa(T_i)$ is the log spectral acceleration of individual records at period T_i, $\ln Sa^{CMS}(T_i)$ is the log CMS spectral acceleration at period T_i. The upper limit n in the summation refers to the number of partitions of the period interval of interest. Ground motions can also be selected to match the variance, σ, of the CMS spectrum computed from a ground motion prediction model, *i.e.* the conditional spectra (CS) method; but it should be noted that the CMS method does not consider minimizing the error of the variance [4]. In this method, the ground motions are scaled to match the MCE_R at the conditioning period and then selected based on least error.

2.2 PEER Method

The second approach used in this study involves scaling ground motions to minimize the error between each ground motion spectrum and the target spectrum, MCE_R, across a range of periods. The difference between the target spectrum and each individual spectrum is defined as an error, and computed using the mean squared error (MSE) as defined in Eq. (3):

$$MSE = \frac{\sum_i w(T_i)\{\ln[Sa^{target}(T_i)] - \ln[f * Sa^{record}(T_i)]\}^2}{\sum_i w(T_i)} \quad (3)$$

where $w(T_i)$ is the weight assigned to a desired period, T_i; S_a^{target} is the target spectral acceleration; S_a^{record} is the individual record spectral acceleration; and f is a scale factor. In this study, w is set to 1.0 across the period range of $0.2T_1$ and $2T_1$. The smaller the error, the better the ground motion produces a response spectrum that matches the target spectrum.

3. Archetype Building

3.1 Design and Configuration

Two archetype buildings (4- and 8-stories) are investigated in this paper. The buildings are designed in accordance with the 2012 International Building Code (IBC) [8], and its referenced standards (*i.e.*, ASCE 7 and AISC 341-10 [9]). The seismic force-resisting system (SFRS) is an exterior three-bay special moment frame (SMF) in the east-west direction and an exterior two-bay special concentrically braced frame (SCBF) in the north-south direction. This paper focuses only on the SMF performance. Fig. 2(a) and (b) show the building floor plan and SMF elevations, respectively. Reduced-beam-sections (RBSs) are used for the SMF beam-to-column connections, and columns are sized to satisfy strong-column/weak-beam requirements. Additionally, columns are upsized where necessary to avoid the use of doubler plates to strength the column webs. Detailed information regarding building properties, materials, and the design process can be found in Harris and Speicher [10].

The building is assumed to be located on a site with stiff soil (Site Class D), and is assigned to Seismic Design Category D with spectral accelerations S_S = 1.5 g at T_s = 0.2 s., and S_1 = 0.59 g at T_1 = 1.0 s. The equivalent lateral force (ELF) procedure of ASCE 7-10 is used to determine the seismic design loads. The frames are also designed to resist wind loads, in which the basic wind speeds are set to 177 km / h (110 mph) for the 700-year (strength) and 116 km / h (72 mph) for the 10-year wind (drift).

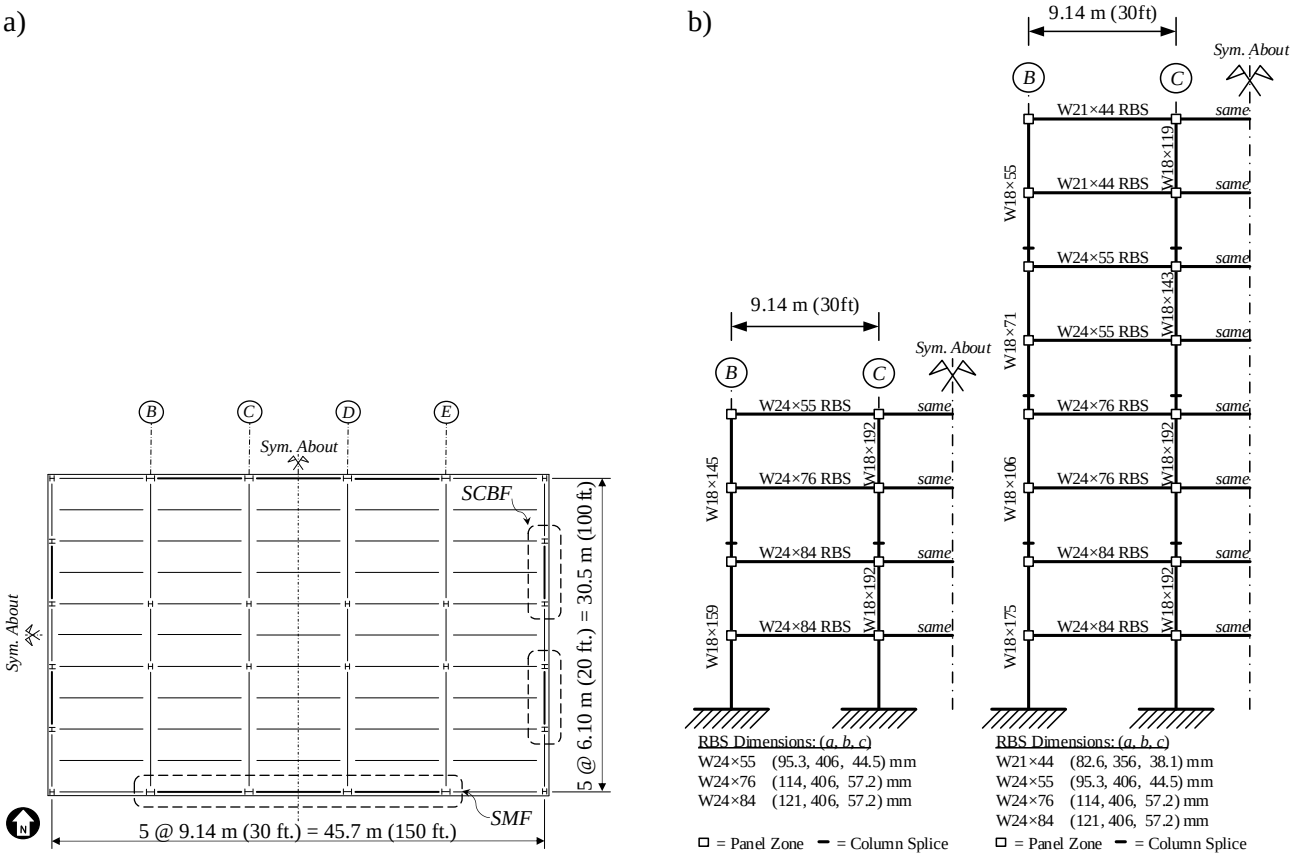

Fig. 2 – (a) Floor plan and (b) SMF elevations for the archetype buildings used in this study.

4. Site Selection

The archetype building is considered to be located in the city of Los Angeles, CA., a region with a high seismic hazard level. A far-field site within Los Angeles area is selected based on the soil classification and the mean rupture distance. The soil type was selected to match the site class for which the archetype building is designed for NEHRP soil type D with an average shear wave velocity (V_{s30}) of 180 m/s to 360 m/s [11]. The selected site has a V_{s30} value of 300 m/s to 360 m/s. The site was selected to satisfy the ASCE 7 requirements for a far-field site. According to ASCE 7 a site is considered far-field if it is located more than 15 km (9.3 miles) from a rupture plane. The information on the R_{rup} of the site was computed using the USGS's deaggregation online tool [11]. The selected far-field site (latitude/longitude = 34.197/-118.645) has a mean rupture distance of 17.2 km, according to the deaggregation computed with the USGS tool.

5. Implementation of the Ground Motion Selection

5.1 General Criteria for Ground Motion Selection

The criteria for the selection and scaling of ground motions meet or exceed ASCE 7 requirements, and include the following steps for the two methods investigated:

1. Fourteen ground motions records are selected (ASCE 7-16 requires 11 records)
2. The scale factor on individual record is no greater than 2.5 (ASCE 7-16 limits the scale factor to 4.0)
3. No more than one record is selected from a recording station
4. No more than three records are selected from the same event

A set of ground motion selection recommendations are adopted from ASCE 7-16 [12], as ASCE 7-16 is the first ASCE 7 standard that includes guidelines on the use of the CMS method. Criteria beyond the above requirements are described in the following sections specific to the two selection methods.

5.2 Implementation of Conditional Mean Spectrum Ground Motion Selection

The first step in implementing the CMS method is to choose the conditioning periods. In addition to the fundamental period of the system, T_1, multiple periods are used as conditioning periods to account for different structural performance aspects [13]. A short period is used to account for the higher mode contributions, while a long period is used to account for the effects of period elongation [7]. This study follows the suggestions of ASCE/SEI 7 that recommends using a lower limit of no more than $0.2T_1$ and an upper limit of no less than $2T_1$ for the bounds of the period range. Then, periods of $0.2T_1, T_1,$ and $2T_1$ are initially selected as the conditioning periods. A fourth conditioning period of $0.4T_1$ is added to satisfy the requirement of having the envelope of the target spectra exceed 75% of the MCE_R between $0.2T_1$ and $2T_1$.

Ground motions are selected following the procedure developed by Jayaram et al. [14]. The procedure constructs the CMS based on the structural properties and hazard deaggregation, and selects a set of ground motions from the PEER NGA-West2 ground motion database [15] with the least amount of error (SSE) with respect to the target spectrum. The scale factor for each ground motion is determined by dividing the spectral acceleration value of the CMS at the conditioning period by the acceleration value of the selected ground motion at the same period. This method of scaling ensures that every selected ground motion, for a given target spectrum, has the same S_a at the conditioning period, creating a "pinch point". Fig. 3(a) shows the 14 ground motions selected using the CMS method for the 4-story building conditioned at the fundamental period, T_1. Fig. 3(b) presents the target and the average mean spectra for the four conditioning periods used in this study (i.e, $0.2T_1, 0.4T_1, T_1,$ and $2T_1$). The 4- and 8-story frames are evaluated for four ground motion sets selected, one at each of the conditioning periods, to identify the maximum mean demand.

5.3 Implementation of PEER Ground Motion Selection

The PEER NGA-West2 database tool [15] is used to select ground motions based on minimizing the error (MSE) across a period range of $0.2T_1$ and $2T_1$. The desirable rupture distance is selected between 10 and 30 km; the shear

wave velocity (V_{s30}) is chosen between 300 m/s and 360 m/s. No restriction is employed on the fault type or shape of the ground motion. A uniform weighting of spectral acceleration (i.e., $w = 1.0$ in Eq. 3) is considered for computing the error at various periods in the range of interest. Ground motions are selected independent of component direction, and the 14 scaled records with the minimum MSE are selected with the condition that no two records are from the same station. The selected ground motions are scaled using a suite scale factor, to ensure that the arithmetic mean of the selected ground motions does not drop below the target spectrum between $0.2T_1$ and $2T_1$, as suggested by ASCE 7-16. In the PEER ground motion selection method, the maximum scale factor for *individual* ground motions is set as 2.5. However, this limit may be exceeded when the arithmetic mean spectrum of the individual records is scaled to ensure the mean spectrum is larger or equal than the target spectrum. Note that even in this case, the scale factor is still less than four, as recommended by ASCE 7-16. Fig. 3(b) shows the average of 14 ground motions selected using the PEER method for the 4-story building. The average acceleration of the PEER ground motion records is higher than that of the CMS records between $0.2T_1$ and $2T_1$. This difference implies that the PEER ground motions may lead to larger inelastic building responses than from the CMS records.

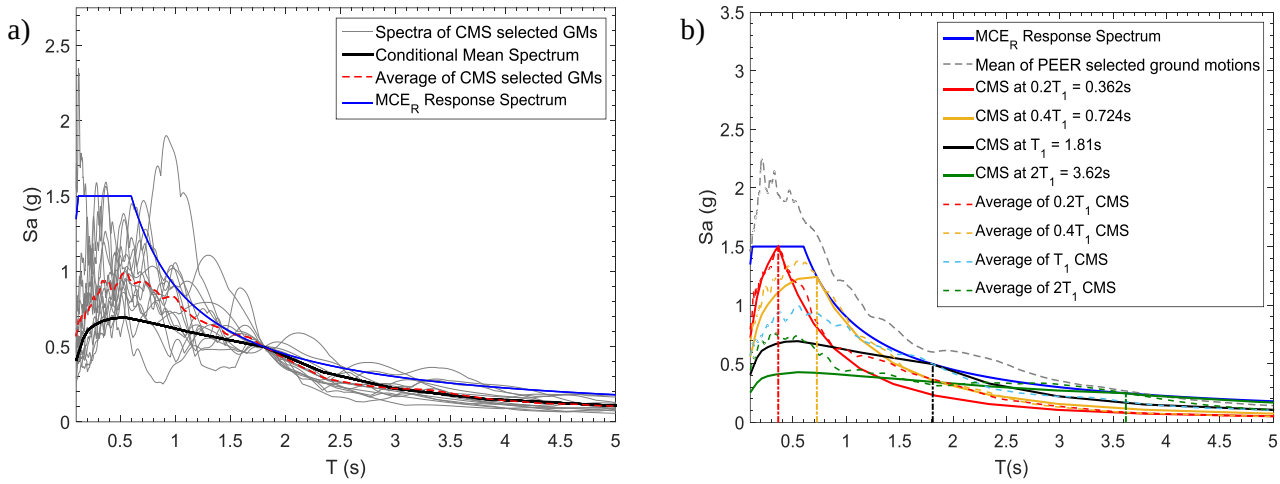

Fig. 3 – (a) Response spectra of ground motions for the 4-story building selected using the CMS method conditioned at $T_1 = 1.81$ s (b) the target and average CMS spectra for four conditioning periods in comparison with the average of the PEER spectra for the 4-story building.

6. Assessment of Moment Frames

An ASCE 41 seismic performance assessment using the nonlinear dynamic procedure is conducted in this study. The structural performance is evaluated at the Collapse Prevention level. The following sections give a brief description of the nonlinear model and then present the results. Additional details on carrying out the ASCE 41 assessment on these archetype buildings can be found in Harris and Speicher [10].

6.1 Overview of Perform 3D Model

The buildings are modeled in three dimensions using PERFORM-3D [16]. For the gravity framing system, the beams and columns are modeled with elastic elements, and the beam-to-column connections as pinned. For the SFRS, each potential nonlinear action is identified and modeled with a discrete nonlinear element. The nonlinear behavior of the beams is modeled with moment-curvature hinges that are placed at the centerline of each RBS. The reduced stiffness of the RBS is captured by using a prismatic section over the entire length of the RBS with cross-sectional properties equal to those at the ends of the center two-thirds of the RBS. The nonlinear behavior of the columns is modeled with moment-curvature hinges that vary based on axial load. These column hinges are placed at a distance of half the column depth away from the face of the beam. The column base is modeled as fixed. Lastly, the nonlinear behavior in the panel zones is modeled with PERFORM-3D'S panel zone element,

which is based on the Krawinkler model [17]. Each of these nonlinear models is initially constructed using ASCE 41 modeling parameters defined in ASCE 41 Table 9-6 and then qualitatively calibrated against experimental tests.

The nonlinear analysis is set to terminate when the solution fails to converge or when an arbitrary roof drift ratio of 20 percent is reached. Collapse modes not modeled herein (e.g., failures in the gravity framing system) would likely occur well before 20 percent is reached. The impact of the modeling uncertainty [18] is not considered in this study.6.2 Nonlinear Dynamic Procedure Results

6.2.1 Format for Results Presentation

In this paper the results are presented in terms of a *normalized* demand-capacity ratio, DCR_N (the *N* subscript is added to distinguish it from the *DCR* defined in ASCE 41 §7.3.1.1, which is the unreduced demand-capacity ratio in a linear analysis). A DCR_N value greater than unity indicates that a component does not satisfy the acceptance criteria. The DCR_N is defined as shown in Eq. (4) and Eq. (5) [10]:

$$\textit{Deformation-controlled}: \quad DCR_N = \frac{\theta_{total}}{\kappa(\theta_y+\theta_{pe}+\theta_{p,AC})} \tag{4}$$

$$\textit{Force-controlled}: \quad DCR_N = \frac{\theta_{total}}{\kappa\theta_y} \tag{5}$$

where $\theta_{plastic}$ is the plastic deformation, $\theta_{elastic}$ is the elastic deformation, θ_y is the yield deformation, θ_{pe} is the post-yield elastic deformation, θ_{total} is the total deformation, and $\theta_{p,AC}$ is the acceptance criterion based on plastic deformation defined in ASCE 41. The Collapse Prevention acceptance criterion is used for the $\theta_{p,AC}$ parameter.

ASCE 41, Chapter 9 defines which actions are force versus deformation-controlled in a SMF. In general, a component is considered deformation-controlled if inelastic action is expected and the component exhibits ductile behavior. In contrast, a component is considered force-controlled if inelastic action is not desired or if the component exhibits non-ductile behavior. Beam-to-column connections and panel zone rotations are generally considered deformation-controlled, while column rotations classification depends on the level of axial load. The axial deformations in columns are always considered force-controlled.

6.2.2 Central Measure of Dispersion using ASCE 41 Approach

In this section the DCR_N plots for nonlinear dynamic analysis of the 4- and 8-story moment frames are presented for the mean and median response of the RBS components, assuming DCR_N results can be characterized with a normal (Gaussian) distribution. In calculation of the mean and median, all analysis results including the collapsed cases identified by an upper roof drift limit of 20 % are used. Fig. 4(a) shows the DCR_N values for the RBS hinges of the 4-story building over the height using the PEER and CMS methods. The presented DCR_N values of the CMS selected ground motions are the ones obtained for the controlling period (*i.e.*, the controlling period from the analysis that produced the largest mean DCR_N). The results presented in Fig. 4(a) show that the CMS method provides lower mean and median DCR_N than those obtained from the PEER method at every floor level, with the maximum difference of about 55 % in mean and median between the two methods. Fig. 4(a) also shows that the RBS connections do not pass the ASCE 41 acceptance criteria, *i.e.* the mean DCR_N value is greater than 1.0, when PEER method ground motions are employed. Conversely, the same components show satisfactory performance when CMS method ground motions are used. Note that the mean is obtained assuming a normal (Gaussian) distribution. More important, some of the 14 realizations may collapse, and in these cases an upper roof drift limit of 20 % was used in the calculations.

The results of the 8-story building are similar to those of the 4-story building with the CMS selected ground motions providing lower DCR_N values than those from the PEER method. For the 8-story RBS components, the CMS mean is lower than the PEER mean with a maximum mean difference of 70 %, and a maximum median difference of 55 %, as shown in Fig. 4(b). A comparison of the 4- and 8-story results shows an increase in the percentage difference in the predicted mean response as the building height increases. However, the difference in the median response does not vary by the number of stories. The larger difference in the mean response of the 8-story building, in comparison to the 4-story building, occurs because more analysis cases reach the 20 % drift limit

for the PEER records. This indicates that the average response may not be the best representative of the structural response, as it will depend highly on the assumptions used in the analysis stage, such as the maximum allowable interstory drift before collapse. The median, on the other hand, is a more stable central measure of dispersion because it does not depend on the assumed probabilistic distribution function.

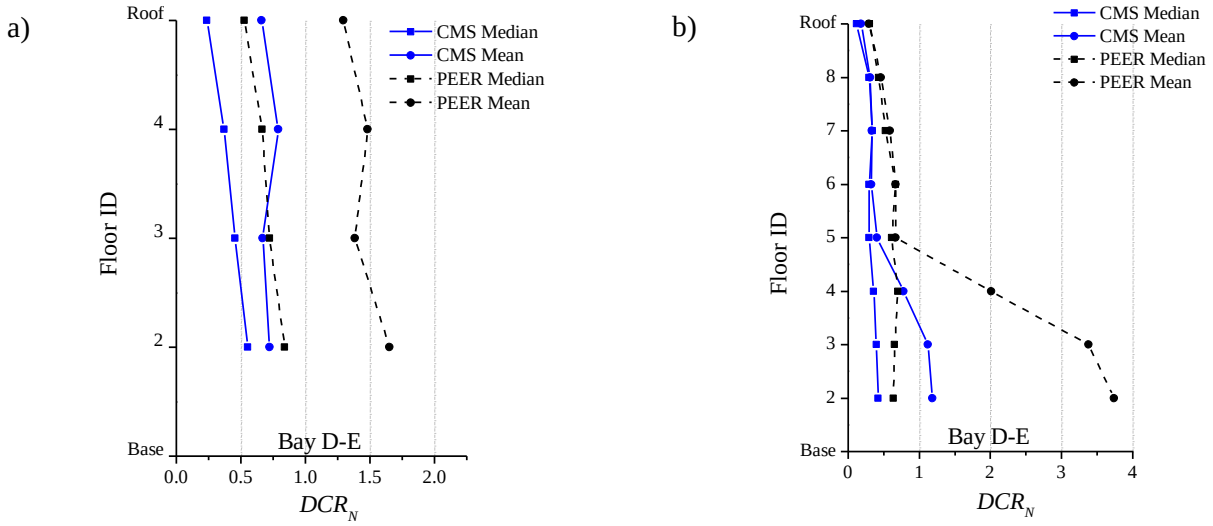

Fig. 4 – Comparison of max DCR_N values of the reduced beam section for the (a) 4-story and (b) the 8-story buildings computed for ground motions selected using the CMS and PEER methods

6.2.3 Central Measure of Dispersion using a Lognormal Distribution

A series of Kolmogorov-Smirnov tests on the DCR_N data demonstrated that the lognormal distribution fits the data more appropriately than a normal distribution. This is an expected result given that the data has only positive values, and it is skewed to the right end of the distribution [19]. Based on this outcome, the DCR_N statistical output parameters are computed in this section using a lognormal distribution. For this distribution, the mean of the data can be computed by Equation (6) [20]:

$$\mu = e^{\bar{u}_{lnx}} * e^{\frac{\sigma_{lnx}^2}{2}} = \bar{\mu} * e^{\frac{\sigma_{lnx}^2}{2}} \tag{6}$$

Where $\bar{u}_{lnx}$ is the mean of the natural logarithm of DCR_N values, $\bar{\mu}$ is the median of the data, and σ_{lnx} is the standard deviation of the natural logarithm of DCR_N values, which can be computed by Equation (7) [21]:

$$\sigma_{lnx} = \ln\left(\sqrt{\frac{84^{th}}{16^{th}}}\right) \tag{7}$$

where 84^{th} and 16^{th} represent the 84^{th} and 16^{th} percentile of the 14 DCR_N values for each element, respectively. Note that σ_{lnx} and μ are computed in such a way that collapse of a couple of realizations does not force to the use of the arbitrary roof drift limits. Fig. 5(a) and Fig. 5(b) plot the mean and median response for the beams. As observed, the median curve did not change due to the assumed probability density function, but the mean values are significantly lower. In fact, the CMS mean computed based on the lognormal distribution assumption is close to the CMS median values. The CMS lognormal mean is reduced because it was computed based on the median, $\bar{\mu}$, and standard deviation of the log of the data, σ_{lnx}, which were calculated using the 84th and 16th percentiles. As a result, extreme values that may arise due to building collapse for some realizations are not considered in the median computation. The PEER lognormal mean was also reduced because of the use of Eqns. (6) and (7). PEER median and mean values are larger than those obtained from the CMS method, but this is partly due to the fact that $S_a(T_1)$ is larger for the PEER method (Fig. 3b). Fig. 6(a) and Fig. 6(b) present similar results for 4- and 8-story building columns computed under the assumption of a lognormal distribution.

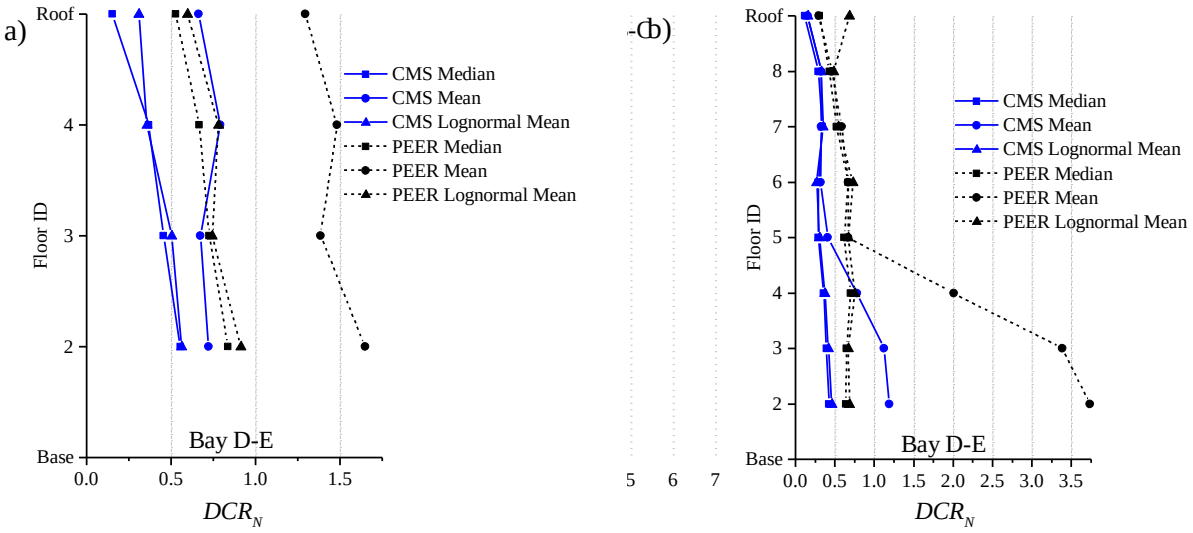

Fig. 5 – Comparison of max DCR_N values of the reduced beam sections computed for ground motions selected using the CMS and PEER ground motion selection methods for the (a) 4-story and (b) 8-story building.

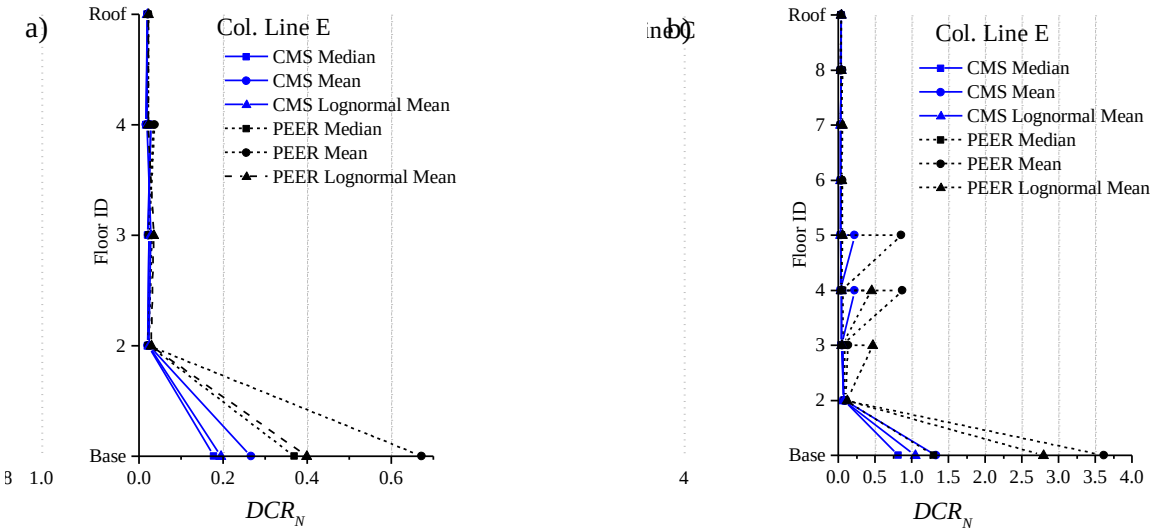

Fig. 6 – Comparison of max DCR_N values of the column hinges for (a) the 4-story and (b) the 8-story building computed for ground motions selected using the CMS and PEER methods.

6.2.4 Uncertainty in Response Prediction Using CMS and PEER

One of the primary goals of efficient ground motion selection methods is to predict structural seismic response with the smallest possible number of records. Comparison among ground motion selection approaches can be done through various metrics. Each ground motion selection method aims to select ground motions that produce a response spectrum that closely matches the prescribed target spectrum. Regardless of the importance of the target spectrum, the selection procedure that leads to a smaller variability on the structural response is considered more suitable. To determine the uncertainty associated with the results produced by each ground motion selection approach, the dispersion of the DCR_N values is computed for each element. To establish a fair comparison between the statistical results obtained from the two methods, the PEER spectrum is scaled down to match the MCE_R spectral acceleration at T_1, because the use of a larger $S_a(T_1)$ in the PEER spectrum may lead to larger nonlinear response and even more collapses, leading to a larger dispersion. Fig. 7 (a) and (b) compare the means and medians

of the beam DCR_N obtained from the CMS and the scaled down PEER ground motion for the 4- and 8-story buildings, respectively. The computed dispersion for the PEER ground motions scaled to $S_a(T_1)$ value of the conditional mean spectrum is compared to the CMS results at the controlling conditioning period. The dispersion of the RBS connections located at the bay D-E of the 4- and 8- story buildings are summarized in Fig. 8 and Fig. 9, respectively. The second column in the tables shown in Fig. 8 and Fig. 9 presents the standard deviation obtained from the CMS method, which corresponds to the conditioning period with the largest mean demand (shown in parenthesis). The third column shows the dispersion derived from the PEER method, and the fourth column is the ratio of the standard deviation between the CMS and PEER method.

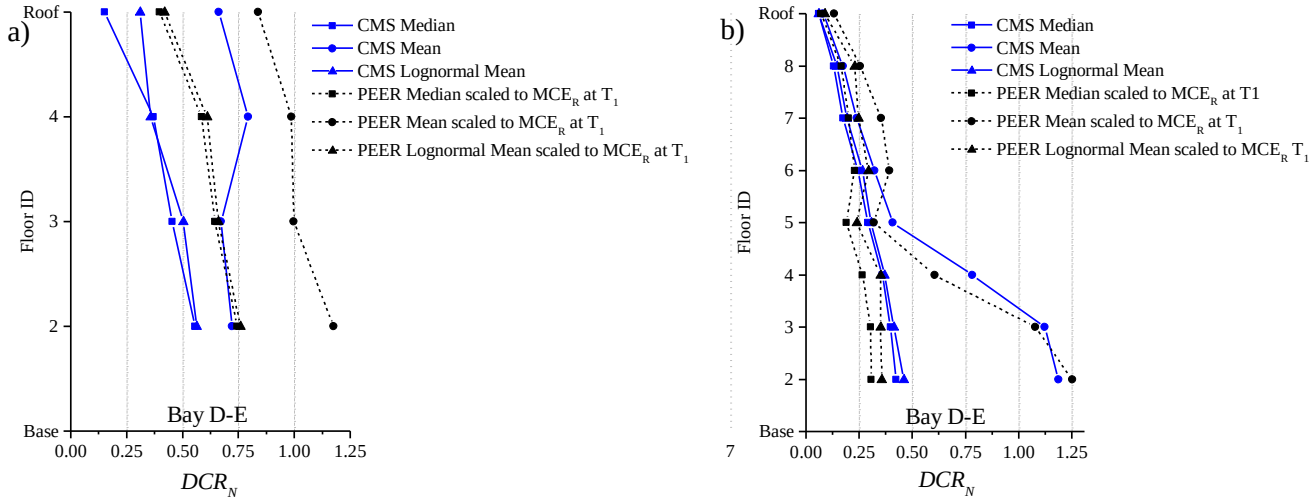

Fig. 7 – Comparison of max DCR_N values of the reduced beam sections computed for ground motions selected using the CMS and PEER ground motion selection methods scaled down to Sa(T_1) for the (a) 4-story and (b) 8-story building.

The results show that the CMS ground motions produce a higher dispersion in the predicted structural response quantified as DCR_N for the 4-story frame with the exception of the fourth story. However, in the 8-story building the dispersion trend is different, and the CMS method produces lower dispersion than that of the PEER method, with the exception of demands at the roof level. The main difference is that the larger CMS dispersion in the 4-story frame corresponds to the controlling period $0.4T_1$, whereas most floors in the 8-story building have T_1 as the controlling period. When the mean demand parameter is controlled by the conditioning period T_1, the CMS method generally leads to smaller dispersion. The reason is that the dispersion is null for the elastic period T_1, and the variability of higher modes (*i.e.*, shorter periods) and inelastic longer periods is less relevant on the overall response because the average accelerations at these other periods are smaller than those of the target spectrum, MCE_R (see Figs. 1 and 3a). However, when the mean demand is controlled by a different conditioning period, other than T_1, the dispersion of $S_a(T_1)$ is not zero, and the dispersion increases even within the elastic system performance. Moreover, the dispersion at higher modes is also different from zero, unless the controlling period coincidentally corresponds to one of these higher modes.

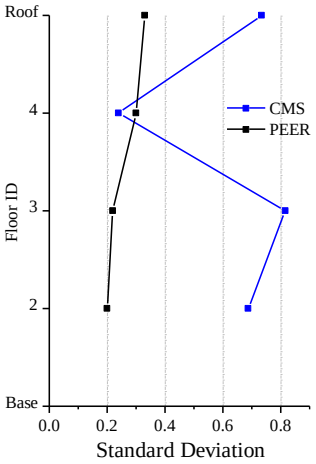

Story Number	$\sigma_{CMS}{}^{*}$	$\sigma_{PEER\ @\ T_1}$	$\frac{\sigma_{CMS}{}^{*}}{\sigma_{PEER\ @\ T_1}}$
2	0.69 ($0.4T_1$)	0.20	3.48
3	0.82 ($0.4T_1$)	0.21	3.85
4	0.24 ($0.4T_1$)	0.29	0.82
Roof	0.73 ($0.4T_1$)	0.33	2.24

* σ_{CMS} is computed for the controlling conditioning period.

Fig. 8 – Standard deviation of the DCR_N results for the RBS connections at Bay D-E of the 4-story building using CMS at the controlling period and PEER methods.

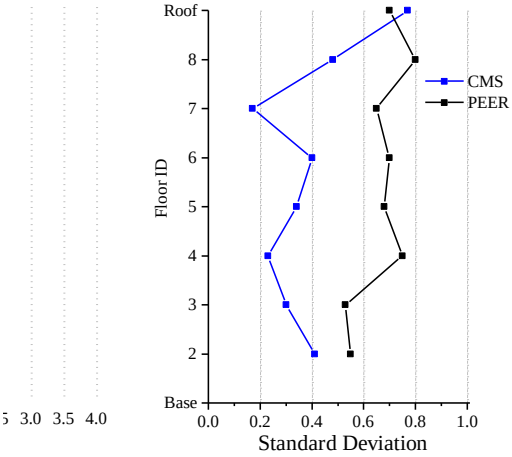

Story Number	$\sigma_{CMS}{}^{*}$	$\sigma_{PEER\ @\ T_1}$	$\frac{\sigma_{CMS}{}^{*}}{\sigma_{PEER\ @\ T_1}}$
2	0.41 (T_1)	0.55	0.74
3	0.30 (T_1)	0.53	0.56
4	0.23 (T_1)	0.75	0.31
5	0.34 (T_1)	0.68	0.50
6	0.40 (T_1)	0.70	0.57
7	0.17 ($0.4T_1$)	0.65	0.26
8	0.48 ($0.2T_1$)	0.80	0.60
Roof	0.77 ($0.2T_1$)	0.70	1.09

* σ_{CMS} is computed for the controlling conditioning period.

Fig. 9 - Standard deviation of the DCR_N results for the RBS connections at Bay D-E of the 8-story building using CMS at the controlling period and PEER methods.

7. Conclusions

Sets of 14 ground motions were selected using the CMS and PEER methods, and used as the input for nonlinear dynamic analysis of 4- and 8-story steel special moment frames. The mean and median normalized demand to capacity ratios were calculated for various components and used to determine the differences in structural response predicted using the two ground motion selection methods. The results show that the CMS method renders reduced mean and median demand-to-capacity ratios for the reduced beam section, and column hinge components, compared to the PEER method. The dispersion of the predicted structural response was calculated to determine the confidence provided by each method. The CMS method can provide lower dispersion, higher confidence, in the predicted response for buildings in which the controlling period is T_1. The results showed that the underlying distribution of the analysis results can lead to a different mean predicted response and as a result different retrofitting decision. The findings of this study showed that the ground motion selection methodology has a significant effect on the assessment outcome. Though the CMS method requires more effort in the selection and assessment process, it provides a ground motion set that, on average, leads to reduced building demands that are more realistic. This study advocates consideration of the CMS method as an alternative ground motion selection approach in evaluation standards, such as ASCE 41.

8. Disclaimer

Certain commercial software may have been used in the preparation of information contributing to this paper. Identification in this paper is not intended to imply recommendation or endorsement by NIST, nor is it intended to imply that such software is necessarily the best available for the purpose.

9. References

[1] C. B. Haselton *et al.*, "Evaluation of ground motion selection and modification methods: Predicting median interstory drift response of buildings," *PEER Rep. 2009*, vol. 1, 2009.

[2] ASCE, *Minimum Design Loads for Buildings and Other Structures*, 7th ed. Reston, VA: American Society of Civil Engineers, 2010.

[3] ASCE, *Seismic Evaluation and Retrofit of Existing Buildings*, 41st ed. Reston, VA: American Society of Civil Engineers, 2014.

[4] J. W. Baker, "Conditional Mean Spectrum: Tool for ground motion selection," *J. Struct. Eng.*, vol. 137, pp. 322–331, 2011.

[5] K. W. Campbell and Y. Bozorgnia, "NGA Ground Motion Model for the Geometric Mean Horizontal Component of PGA, PGV, PGD and 5% Damped Linear Elastic Response Spectra for Periods Ranging from 0.01 to 10 *s*," *Earthq. Spectra*, vol. 24, no. 1, pp. 139–171, Feb. 2008.

[6] P. Bazzurro and C. A. Cornell, "Disaggregation of seismic hazard," *Bull. Seismol. Soc. Am.*, vol. 89, no. 2, pp. 501–520, 1999.

[7] T. Lin, C. B. Haselton, and J. W. Baker, "Conditional spectrum-based ground motion selection. Part I: Hazard consistency for risk-based assessments," *Earthq. Eng. Struct. Dyn.*, vol. 42, no. 12, pp. 1847–1865, Oct. 2013.

[8] IBC, *2012 International Building Code*. Washington, D.C.: ICC, 2012.

[9] AISC, *Seismic Provisions for Structural Steel Buildings,(ANSI/AISC 341-10)*. American Institute of Steel Construction, Chicago, IL, 2010.

[10] J. L. Harris and M. S. Speicher, "Assessment of First Generation Performance-Based Seismic Design Methods for New Steel Buildings, Volume 1: Special Moment Frames," National Institute of Standards and Technology, NIST TN 1863-1, Feb. 2015.

[11] USGS, "CustomVs30 Mapping," 2016. [Online]. Available: http://earthquake.usgs.gov/hazards/apps/vs30/custom.php.

[12] ASCE, *Minimum Design Loads for Buildings and Other Structures (Draft)*, 7th ed. Reston, VA: American Society of Civil Engineers, 2016.

[13] NIST, "GCR 11-917-15 2011. Selecting and scaling earthquake ground motions for performing response history analyses," *Natl. Inst. Stand. Technol. US Dep. Commer.*, 2011.

[14] N. Jayaram, T. Lin, and J. W. Baker, "A Computationally Efficient Ground-Motion Selection Algorithm for Matching a Target Response Spectrum Mean and Variance," *Earthq. Spectra*, vol. 27, no. 3, pp. 797–815, Aug. 2011.

[15] PEER, "PEER Ground Motion Database - PEER Center," 2016. [Online]. Available: http://ngawest2.berkeley.edu/.

[16] CSI, *PERFORM 3D*. Berkeley, California: Computers and Structures, Inc, 2011.

[17] H. Krawinkler, "Shear in beam-column joints in seismic design of steel frames," *Eng. J.*, vol. 15, no. 3, 1978.

[18] S. Sattar, A. B. Liel, and P. Martinelli, "Quantification of Modeling Uncertainties Based on the Blind Prediction Contest Submissions," in *Structures Congress 2013: Bridging Your Passion with Your Profession*, 2013, pp. 1997–2008.

[19] N. Shome and C. A. Cornell, *Probabilistic seismic demand analysis of nonlinear structures*. 1999.

[20] J. R. Benjamin and C. A. Cornell, *Probability, Statistics, and Decision for Civil Engineers*, Reprint edition. Mineola, New York: Dover Publications, 2014.

[21] L. F. Ibarra and H. Krawinkler, *Global collapse of frame structures under seismic excitations*. Pacific Earthquake Engineering Research Center Berkeley, CA, 2005.

16th World Conference on Earthquake, 16WCEE 2017
Santiago Chile, January 9th to 13th 2017
Paper N° 2304 (Abstract ID)
Registration Code: S-M1460469417

FUTURE DEVELOPMENTS IN THE SEISMIC ANALYSIS AND DESIGN OF NONSTRUCTURAL COMPONENTS FOR BUILDINGS

M. Phipps[(1)], S. Fathali[(2)], J. Gillengerten[(3)], T. Hutchinson[(4)], R. Medina[(5)], R. Bachman[(6)] , M. Hoehler[(7)], S. Schiff[(8)], J, Heintz[(9)]

[(1)] *ATC-120 Project Technical Director, Estructure, mphipps@estruc.com*
[(2)] *ATC-120 Project Technical Committee Member, Structural Technologies, sfathali@structural.net*
[(3)] *ATC-120 Project Technical Committee Member, OSHPD (retired), johng5155@live.com*
[(4)] *ATC-120 Project Technical Committee Member, University of California San Diego, tahutchinson@ucsd.edu*
[(5)] *ATC-120 Project Technical Committee Member, University of New Hampshire, ricardo.a.medina@unh.edu*
[(6)] *ATC-120 Project Review Panel Chair, R.E. Bachman Consulting, REBachmanSE@aol.com*
[(7)] *ATC-120 Technical Point of Contact, National Institute of Standards and Technology, matthew.hoehler@nist.gov*
[(8)] *ATC-120 Associate Program Manager, Applied Technology Council, scott.schiff@atcouncil.org*
[(9)] *ATC-120 Program Manager, Applied Technology Council, jheintz@atcouncil.org*

Abstract

Damage to nonstructural components has accounted for the majority of earthquake losses in recent earthquakes, especially in the United States and Chile. This damage primarily occurred to nonstructural components located within buildings. The current procedures for seismic design of nonstructural components were first introduced in the 1994 edition of the *NEHRP Recommended Provisions for Seismic Regulations for New Buildings* with the intention of lessening this damage. The procedures were subsequently incorporated into the 1997 edition of the *Uniform Building Code* and into the 2000 edition of the *International Building Code* and provided a substantial improvement in seismic design practice. Many new concepts, new to the building codes, were introduced, including consideration of dynamic properties of the component, location of the component within the supporting structure, and explicit attention to the relative importance of the component and component ductility. The nonstructural concepts developed in the 1994 *NEHRP Recommended Provisions* have been in use for over two decades, and since 1995 have been incorporated in ASCE/SEI 7, *Minimum Design Loads for Buildings and Other Structures*. Because of the timing and epicenter locations of recent earthquakes, nonstructural components designed and installed to satisfy these current seismic design procedures have not yet been subjected to significant damaging earthquakes.

In 2013, the National Institute of Science and Technology (NIST) published GCR 13-917-23, *Development of NIST Measurement Science R&D Roadmap: Earthquake Risk Reduction in Buildings* [1]. This document identified nonstructural issues as a top-priority for studies related to earthquake engineering for new and existing buildings. New research tools and analysis results as well the availability of new international standards, makes reexamination of nonstructural design criteria possible at this time. Accordingly, NIST initiated the ATC-120 project with the Applied Technology Council (ATC) in late 2014. The goal of this project is to improve technical aspects of nonstructural system design in the areas that will have the largest impact for public safety and economic welfare with an emphasis on determining whether or not a disconnect exists between current design requirements and observed (or expected) performance of nonstructural building systems and components. Where significant gaps are identified, technical solutions are proposed. The project is being conducted in two phases. In the first phase, knowledge studies were performed looking at both the literature and the current state of practice. The goal of the first phase was to understand performance criteria objectives and measures and to prioritize potential areas for further study. In the second phase, focused studies are performed on the priority areas identified in the first phase.

Summaries of the recently completed ATC-120 project knowledge study and workshop are presented. Recommendations for improving seismic analysis and design of nonstructural components and systems (NCSs) are discussed.

Keywords: nonstructural; components; architectural; equipment, seismic; performance

1. Introduction

The goal of the ATC-120 project, *Seismic Analysis and Design of Nonstructural Components and Systems*, is to improve technical aspects of nonstructural system design in the areas that will have the largest impact for public safety and economic welfare, with an emphasis on construction subject to building codes. The improvements are intended to have practical application to the most common types of structures, and be conceived in a manner that facilitates ease of implementation throughout those areas of the country with significant seismic hazard.

The focus of the first phase of the ATC-120 project effort was to collect and summarize the body of available knowledge related to nonstructural components that can serve as the foundation for future advancements. Substantial efforts have been made over the last 50 years to study the seismic performance of nonstructural components. The intent of this first phase effort was not to summarize all past research and development, but rather to describe the context for current code requirements and highlight select areas in which code developers would benefit from additional technical information to improve nonstructural design provisions. These areas include seismic performance observations, analytical studies, testing programs and practice issues. An important task was to determine if disconnects exist between current design requirements and observed (or expected) performance of nonstructural systems and components in buildings. Additional input was solicited through a workshop that included a diverse cross-section of design practioners. Problem-focused studies are recommended in areas where significant gaps or opportunities for improvement exist.

2. Earthquake Performance of Nonstructural Components

Post-earthquake observations of damage have provided the impetus for many of the advancements in seismic-resistant design. These efforts have emphasized describing and analyzing earthquake damage to the primary seismic force-resisting systems of structures. While damage to nonstructural components has been the primary source of losses in nearly all earthquakes, nonstructural performance is rarely discussed in depth. While there are hundreds of articles and reports that cover nonstructural performance at some level of detail, the initial phase of the ATC-120 project focused on the following select samples to provide better insight on how nonstructural performance is presented in post-earthquake reports, causes of nonstructural damage, and the effectiveness of building code provisions.

2.1 1964 Great Alaska Earthquake

A study was prepared by the firm of Ayres & Hayakawa for the U.S. Army Corps of Engineers Alaska District, Anchorage Alaska, in the aftermath of the magnitude-9.2 1964 Great Alaska Earthquake at the request of the National Academy of Sciences, Committee on the Alaska Earthquake, Engineering Panel [2]. A multi-disciplinary team of mechanical and electrical engineers, with the assistance of architects and an elevator consultant, completed this study in August 1967. Subsequently, the Consulting Engineers Association of California made this study broadly available in 1971. The 460-page report includes extensive descriptions of the performance of a wide range of nonstructural components, including elevators, mechanical and electrical systems, architectural components and systems, and building contents. With the exception of fire protection sprinkler systems, none of the nonstructural components were designed considering earthquake shaking. The scope of the report was limited to damaged nonstructural components in buildings in the Anchorage area, along with a few structures in Whittier, Alaska.

Nonstructural damage was widespread, with elevators and vibration-isolated equipment found to be especially vulnerable. Piping failures were attributed to large displacements of unbraced pipe, with damage commonly occurring at threaded fittings. Failures of pipe hangers were also observed and sections of piping fell. Fire sprinkler piping, the only nonstructural system consistently braced for lateral loads, performed well. Most tanks were unanchored and many failed. Damage to architectural systems was also widespread. Unreinforced masonry partitions failed, in some cases blocking exits in the buildings. Precast concrete panels fell from a department store in Anchorage, killing two people. Suspended lath and plaster and gypsum board ceilings

suffered little damage, while suspended acoustical tile ceilings generally performed poorly. Lath and plaster partitions were badly cracked; stud and drywall partitions sustained minor damage.

The report includes a summary of the nonstructural design process in the mid-1960s. The building code requirements of the time focused on minimum standards to safeguard life. Seismic performance for most nonstructural components was considered a property damage rather than life safety issue. The design of nonstructural components was performed by subcontractors with limited review by the structural engineer or architect, a practice that persists to this day, especially in areas outside of California.

2.2 1971 San Fernando Earthquake

The 1971 San Fernando Earthquake caused significant damage to a large number of modern structures in the greater Los Angeles region, especially in the San Fernando Valley of Southern California. While the reports published following the magnitude-6.6 earthquake tended to focus on structural performance and damage, Ayres and Sun [3] documented and evaluated nonstructural damage to elevators, mechanical equipment, piping systems and light fixtures. The report did not address the performance of ceilings, partitions, electrical systems, exterior facades, and contents.

As in the 1964 Great Alaska Earthquake, damage to elevators was widespread, extending beyond the epicentral area into regions that experienced low ground shaking intensities. While the patterns of elevator damage were similar to those noted in the 1964 event, Ayres and Sun believed the increased lateral flexibility of modern buildings in the Los Angeles area contributed to the widespread damage. Except for fire sprinkler piping systems, little consideration was given to the seismic resistance of nonstructural components prior to the earthquake. While many mechanical components survived the earthquake with little damage, unanchored components shifted, rupturing pipe and duct connections. Little or no damage was observed to non-isolated components that were well anchored. Much of the damage to equipment was attributed to failures of vibration isolators.

2.3 1989 Loma Prieta Earthquake

Centered south of San Francisco in the Santa Cruz Mountains of Northern California, the magnitude-6.9 Loma Prieta Earthquake lasted less than fifteen seconds but caused more than $7 billion in damage and killed 62 people. An article covering nonstructural performance was published in an Earthquake Engineering Research Institute (EERI) special issue of Earthquake Spectra [4]. Nonstructural damage was widespread with the severity of damage strongly influenced by proximity to the epicenter and local ground conditions. The earthquake was one of the first significant tests of buildings constructed to the modern seismic codes of the time. Much of the data in the article is general in nature with limited specific descriptions of damage to individual structures. This was due in part to difficulty gaining access to the interior of building and lack of visibility from the exterior, making the actual level of damage to individual structures difficult to assess.

Some modern buildings suffered nonstructural damage severe enough to limit access. Damage to exterior glazing was observed throughout the region, and glazed storefronts in older buildings were particularly vulnerable. Damage to suspended acoustical ceiling systems was thought to result from the lack of splay-wire bracing. The article attributes great monetary losses to failure or lack of seismic restraints to utility systems. The reconnaissance observers noted failures of fire sprinkler mains and piping joints, with resulting flooding collapsing ceilings and in some cases causing the abandonment of entire floors. Patterns of damage to elevators similar to those occurring in earlier earthquakes were observed although seismic provisions for elevators had been adopted by the State of California in 1975, including requirements to upgrade existing elevators retroactively.

A study by Rihal [5] explored the nonstructural performance in detail of a thirteen-story, steel moment-resisting frame building in San Jose, California that was designed in 1972. This building was outfitted with strong motion recording instruments installed at grade level; the second, seventh, and twelfth floors; and at the roof. The recorded peak ground acceleration was about 0.10g, while the peak acceleration at the roof was 0.34g.

Because a video survey of the building was immediately conducted following the earthquake, the performance of nonstructural components was available. Rihal correlated the shaking intensity at different levels to damage, including identification of different failure modes for nonstructural components. The study illustrates what could be achieved if nonstructural performance is properly documented immediately following an earthquake. The data can be used to understand reasons for poor performance during an earthquake and justify recommendations to improve the seismic performance of nonstructural components and systems.

2.4 1994 Northridge Earthquake

On January 17, 1994, a strong earthquake struck the San Fernando Valley west-northwest of downtown Los Angeles. The magnitude-6.7 event struck the same general region as that impacted by the 1971 San Fernando Earthquake. Following the earthquake, a series of reports on nonstructural performance were produced for the California Office of Statewide Health Planning and Development (OSHPD) [6]. Three reports examined seismic design factors for nonstructural components, water damage in hospitals, and elevator performance in hospitals. The reports utilized the extensive field reports generated by the OSHPD field teams immediately following the earthquake.

The seismic design factor study utilized data from the Olive View Medical Center, which includes an instrumented six-story steel plate shear wall structure built on the site of a hospital demolished following the 1971 San Fernando Earthquake. Designed in 1976 and completed in the mid-1980s, the hospital was located ten miles from the epicenter of the Northridge Earthquake and experienced very strong shaking, with peak horizontal acceleration of 0.8g measured at the ground floor and 1.5g measured at the roof of the Main Building. The authors of the study report had access to the original drawings and calculations for the nonstructural components and systems. Hundreds of nonstructural components were examined, comparing design forces and connection capacities to the actual earthquake demands. Given the strong shaking the site experienced, there was surprisingly little damage to equipment. However damage to ceiling systems and piping was extensive and led to evacuation of approximately 300 patients.

2.5 Observations on Post-Earthquake Damage Evaluations

Fifty years after the Great Alaska Earthquake, similar patterns of nonstructural damage emerge from many earthquakes today. This similarity in damage patterns is due to the age of the building stock, but perhaps more importantly, to a persistent reluctance to deal with three critical aspects of the nonstructural problems in new construction: design responsibility, code enforcement, and construction oversight. Technical enhancements and updated codes do not always lead to substantially improved performance, as evidenced by the changes in California to the elevator design requirements following the 1971 San Fernando Earthquake. Earthquakes in California over the 20 years following implementation of the elevator seismic requirements continued to reveal vulnerabilities. Translating the knowledge accumulated by post-earthquake reconnaissance efforts and implemented in building codes and standards into finished construction is an ongoing challenge.

3. Development of Standards for Nonstructural Component Seismic Design

Provisions for seismic design of nonstructural components have been present in building codes for nearly 90 years. From 1927 to 1976, slow progress was made on seismic provisions. Towards the end of this period, the nature of building construction began to change rapidly, with the introduction of modern heating and air condition systems, complex electrical systems, and modern cladding systems. Structures also changed, as flexible, drift-controlled frame structures gained popularity. Towards the end of this same period, damaging earthquakes increased interest in improving the seismic performance of nonstructural components. During this period, lateral design forces for nonstructural components were based on simple formulas that included variables for expected shaking intensity and a factor dependent on the type of components. At the same time, few detailing requirements were incorporated. Factors to account for the importance of the structure and soil-structure resonance were added in the 1976 *Uniform Building Code* (UBC) [7].

3.1 Evolution of Modern Standards for Nonstructural Components

The late 1970s saw rapid advances in the seismic design of nonstructural components, beginning with the publication of a groundbreaking document, ATC-3-06, *Tentative Provisions for the Development of Seismic Regulations for Buildings* [8], which profoundly influenced the development of seismic design. ATC-3-06 introduced nonstructural requirements based on Performance Characteristic Levels, a function of the type of component and the seismic hazard. The lateral force calculation for mechanical and electrical components considered amplification of lateral loads due to dynamic interaction between the component and the structure, and accounted for floor acceleration increases in the upper levels of structures. ATC-3-06 triggered a period of parallel developments in nonstructural component design. The UBC developed along traditional lines, with limited, simple nonstructural design provisions, while the ATC-3-06 provisions where further developed in new series of documents, starting with FEMA 95, *NEHRP Recommended Provisions for Seismic Regulations for New Buildings* [9] published in 1985, which has been periodically updated for decades and become a key seismic design resource document for U.S. building codes and standards.

In 1997, the last edition of the UBC [10] adopted the nonstructural design approach of the 1994 *NEHRP Recommended Provisions* and in 2000 the first edition of the *International Building Code* (IBC) [11] adopted the nonstructural design approach of the 1997 *NEHRP Recommended Provisions* [12], beginning a period of convergence between the codes and the *NEHRP Recommended Provisions*. Building codes had also begun a transition from an all-inclusive document into which text from different reference standards was transcribed, to a document that adopted standards by reference. To support the transition, ASCE/SEI 7-02, *Minimum Design Loads for Buildings and Other Structures* [13], was updated from the first (1988) edition of ASCE/SEI 7 to incorporate the seismic provisions of 2000 *NEHRP Recommended Provisions* [14]. The 2003 IBC [15] adopted ASCE/SEI 7-02 by reference for seismic design. From this point forward, revisions to the design procedures for nonstructural components were made in ASCE/SEI 7 rather than in the building codes themselves.

3.2 Seismic Design Provisions for Nonstructural Components in New Structures

The seismic design provisions for nonstructural components in new structures are currently contained in Chapter 13 of ASCE/SEI 7-10 including Supplement No. 1 [16]. The next edition of the *International Building Code* in 2018 will reference ASCE/SEI 7-16, *Minimum Design Loads and Associated Criteria for Buildings and Other Structures* [17], which represents the latest iteration of the nonstructural procedures that been continuously developed since their first appearance in the 1997 UBC. The nonstructural provisions of ASCE/SEI 7-10 are organized in six sections, covering information on the applicability of the nonstructural design provisions, determination of the relative importance of the component and methods for establishing compliance with the standard, procedures for determining acceleration and displacement demands, design of attachments of components to the structure, and detailed requirements for architectural, mechanical, and electrical components. Components are classified by their importance and those identified as critical to life safety or essential to facility function are classified as “designated seismic systems” and are subject to more stringent design and quality assurance requirements. Smaller non-critical components may be completely exempt from seismic design based on their weight, size (for distribution systems), and mounting configuration. Most furniture and building contents are exempt from the seismic provisions of ASCE/SEI 7-10 and ASCE /SEI 7-16.

ASCE/SEI 7-10 provides several options for establishing compliance with the nonstructural requirements, including project-specific design and documentation, and manufacturer’s certification. Designated seismic systems may be subject to special certification requirements if they are required to remain operable following the design earthquake, or if they exceed certain amounts of hazardous substances. Special certification may require shake table testing, experience data, or more advanced analysis to establish compliance. Acceleration demands on nonstructural components may be determined using several approaches. The most commonly used formula accounts for variation of acceleration with relative height within the structure, without regard for the specific nature or dynamic properties of the building structure.

Dynamic analysis methods are available for determining building-specific values of the seismic design force if the dynamic properties of the building are known. These methods are intended for use on base-isolated

and long-period structures, where component acceleration demands are expected to be lower than those predicted using the commonly used formula. ASCE/SEI 7-16 also includes options for determining component accelerations using nonlinear response history analysis and floor response spectra methods.

3.3 Design Forces for Nonstructural Components and Attachments

The magnitude of the design forces for nonstructural components are dependent on a number of variables including the type of component, the seismic hazard level, the importance of the component, and its location in the structure. Different design standards over the years have considered some of these variables; the current standard considers them all. To illustrate the variations in component design force over time, consider a rooftop air-handling unit mounted on a structure in San Francisco, California, a region of high seismic risk. Per ASCE/SEI 7-16, the Seismic Design Category (SDC) of the structure is D, and the short-period ground spectral acceleration, S_{DS}, equals 1.0. Table 1 lists the horizontal strength-level, nonstructural component design force required by selected editions of the UBC, IBC, *NEHRP Recommended Provisions*, and ASCE/SEI 7. Note that ASCE/SEI 7 was adopted by reference in the 2003 and later editions of the IBC. It should be noted that in some cases, a small changes in a value listed in Table 1 from one edition to the update of next edition was in fact due to substantial counteracting changes in some of the paramaters used to calculated the design force. Since 2002, the design force for this example component has remained constant at around 50 percent of the weight of the component (W_p).

Table 1 – Comparison of Nonstructural Component Design Force in Various Code and Resource Documents for a Rooftop Air-Handling Unit in San Francisco

Edition	UBC/IBC	NEHRP	ASCE/SEI 7
1927-1973	--	--	--
1976	0.63 W_p	--	--
1979-1982	0.42 W_p	--	--
1985	0.42 W_p	0.80 W_p	--
1988	0.84 W_p	0.80 W_p	--
1991	0.84 W_p	0.40 W_p	--
1994	0.84 W_p	0.53 W_p	--
1997	1.46 W_p	0.48 W_p	--
2000	1.46 W_p	0.48 W_p	--
2002	--	--	0.48 W_p
2003	0.48 W_p	0.48 W_p	
2005	--	--	0.50 W_p
2006-2016	0.50 W_p	0.50 W_p	0.50 W_p

A great many nonstructural components are attached to concrete slabs and walls, or masonry walls. Post-installed anchors are often preferred for the attachment of nonstructural components, due to both the difficulty of accurately locating cast-in-place anchors, and because in many cases the exact nonstructural component has not been selected when the slabs or walls are constructed. Prior to the 1994 Northridge Earthquake, post-installed anchors were designed to withstand the calculated seismic force on the component without modification, and allowable anchor capacities were based on static tests with a factor of safety of four for anchors installed with special inspection and eight if installed without special inspection. Following reports of nonstructural component damage due to failures of anchors in the 1994 Northridge Earthquake, both the anchor capacities and the calculated seismic demands were reexamined. Over the next two decades, there were substantial changes in the design of nonstructural component anchorage, with reduction in anchor capacities under seismic loading, and increased anchor design forces. In ASCE/SEI 7-16, the design force for anchors, deemed to have nonductile behavior, depends on the values of the amplification, response and overstrength factors of the component, and can range from 50 to 100 percent higher.

4. Simulated Seismic Testing of Nonstructural Components and Systems

To complement analytical studies and field observations, experimental studies of nonstructural components and systems (NCSs) have been conducted to advance the state of understanding regarding their seismic performance. Depending on the experimental scope and objective, the simulated seismic testing of NCSs are categorized as system-level building shake table tests, component tests, and designated seismic system qualification tests.

4.1 System-Level Building Shake Table Tests

In recent years, a number of system-level shake table experimental research projects on nonstructural components and systems were completed. A representative example of one of the most recent tests was a unique research collaboration between academia, government, and industry, coined the Building Nonstructural Components and Systems (BNCS) project. The test was undertaken to contribute to understanding the earthquake resiliency of nonstructural components and systems [18]. The centerpiece of this research effort involved shake table testing of a full-scale five-story reinforced concrete building outfitted with a large variety of essential NCSs. These tests were completed in 2012, contribute a wealth of high-resolution physical data to the earthquake and fire engineering communities and will provide direct input to modeling tools, future design codes, and construction practices.

The shake-table test program was performed at the University of California, San Diego (UCSD) and involved two test phases: (1) earthquake shaking while the building was isolated at its base (BI Phase); and (2) earthquake shaking while the building was fixed at its base to the shake table (FB Phase). The test building, consisting of a cast-in-place five-story reinforced concrete structure with moment resisting frames providing lateral resistance in the direction of shaking, was outfitted with operable egress systems (elevator and steel stairs), a complete façade, a broad array of architectural layouts, and two floors of the building equipped as medical facilities.

The test building was subjected to a sequence of dynamic input motions at the base of the building, while the building was first tested in base isolated and subsequently in fixed base configurations. These excitations, 13 earthquake motion tests, 31 low amplitude white noise base excitation tests and 45 pulse-like base excitation tests, were conducted using the UCSD Large High-Performance Outdoor Shake Table. Each of the input motions was applied in the east-west direction using the single-axis shake table, whose axis coincided with the longitudinal axis of the building. The earthquake input motions selected in the test program encompassed a broad range of characteristics including different frequency contents as well as varied strong motion durations and amplitudes. The largest amplitude motion, recorded in the 2002 Denali Earthquake at TAPS Pump Station No. 9, was a spectrally matched code-shapped target response spectrum with spectral acceleration values of S_{MS} = 2.1g and S_{M1} = 1.4g.

In the BI Phase, the seismic demands were low, with peak interstory drift ratios less than 0.4% and peak floor accelerations less than 0.3g. The building sustained only minor damage to its most brittle nonstructural components such as partition walls and very little damage to its structural components. In the FB Phase, earthquake motions were applied with increasing intensity to progressively damage the structure. For the design level event, the test building achieved the design target peak interstory drift ratio of about 2.5%, while the final test represented an event well above the design event scenario with peak interstory drift ratios of 6% observed. The building sustained extensive damage during the last two FB tests from large seismic drift demands.

The observed damage of the NCSs was classified as three discrete damage states: minor, moderate, or severe. Damage sgtates were subsequently correlated with either measured peak interstory drift ratio or peak floor acceleration. Several NCSs in the test program demonstrated quite good performance, attaining design expectations and remaining functional despite the very large demands imposed upon them. These NCSs, which were limited to mostly minor damage throughout the test program, included the fire sprinkler system, seismically designed ceilings, roof-mounted equipment, and restrained contents. The precast concrete cladding panels and the passenger elevator were subjected to moderate or severe damage only during the last two earthquake motions in the FB test phase. Some NCSs installed in the test building experienced unacceptable levels of damage,

including prefabricated steel stairs, a cold-formed steel balloon framed exterior wall system overlaid with synthetic stucco, and unrestrained medical equipment.

4.2 Component Testing

Representative of component tests are a series of shake table experiments to study the seismic behavior of suspended ceiling systems conducted at the University at Buffalo–The State University of New York [19]. A total of fifteen suspended ceiling assemblies were tested, ranging in size from 400 square feet to 1,000 square feet in area. In each of the fifteen test configurations, the suspended ceiling was subjected to a series of test motions with increasing amplitude. The motions were intended to target a floor response spectrum at the roof level of the test frame, which followed the required response spectrum as defined in ICC-ES AC156 [20]. The peak vector sum of the horizontal table acceleration varied from 0.16 to 2.56g, which resulted in a maximum of 3.40g for the horizontal accelerations at the center of the roof level. The maximum vertical table acceleration was 0.68g, which resulted in a vertical acceleration of 1.54g in the mid-bay of the roof level. Damage to the suspended ceiling systems occurred in the form of panel tile damage (e.g., dislodged panels, fallen panels) and ceiling grid connection damage (e.g., seismic clip failure, grid connection failure).

4.3 Designated Seismic System Qualification Testing

Special seismic certification was introduced to provide a greater assurance that designated nonstructural components will perform as expected at design level seismic motions. Expectations for special seismic certified components is that the equipment will maintain structural integrity with minor yielding and damage allowed; however, the equipment must retain its functionality/operability following the design earthquake. Seismic qualification of equipment has been prevalent in the nuclear and defense industries since the 1970s. The requirements for special seismic certification of designated seismic systems in commercial, industrial, and institutional structures was first introduced into the building code in the 2000 IBC.

Seismic certification may be conducted using several code accepted methods. Under ASCE/SEI 7-05, seismic certifications can be conducted via analysis, testing, or experience data. Nonstructural components are grouped into two categories of either active or passive. Active components have either mechanical moving parts or energized electrical systems or a combination of both. In general, active components can be certified only by testing or experience data due to the complex nature of trying to predict operability of electrical circuits and moving parts in analysis software. Passive components can be certified by analysis, testing or experience data. The shake table testing requirements and acceptance criteria are contained in AC156.

A wide variety of mechanical, electrical and some architectural components have been tested. Testing has revealed vulnerabilities in the equipment and resulting changes have been made to improve the seismic ruggedness of nonstructural equipment. The test results have been positive for some types of robust/rugged equipment. The testing has also exposed vulnerabilities in some equipment, such as inadequate seismic load path bracing, screws used to resist out-of-plane loads in sheet metal, and anchorage which has spawned changes to the design provisions.

5. Analytical Studies on Horizontal Floor Response Spectra

Many studies have evaluated individual parameters that form part of equations to estimate the horizontal design force for nonstructural components, F_p. These studies tend to focus on a single equation, ASCE/SEI 7-16 Eq. 13.3-1, or individual variables within the equation. Estimates of peak floor accelerations represented by ASCE/SEI 7-16 Eq. 13.3-1 increase linearly with height to a maximum value of three (3) at the roof level independently of the fundamental period of the supporting structure. These estimates are subject to the minimum and maximum forces given in Eq. 13.3-2 and Eq. 13.3-3. There are numerous studies using analytical models of varying degrees of sophistication that suggest that the simplified equation will produce overly conservative results, especially when applied to tall, longer period structures. Studies also suggest that amplification of horizontal motions due to dynamic interaction of the component and the structure may be

underestimated by the simplified method. However, a comprehensive, holistic review of all factors contributing to seismic demands and observed performance of nonstructural components and systems, using the latest information from instrumented buildings, laboratory tests and analytical studies is lacking.

The effectiveness of various ASCE/SEI 7 force equations to estimate seismic force demands for nonstructural components and systems, and whether the ASCE/SEI 7 requirements provide cost-effective protection of nonstructural components and systems has been difficult to evaluate from recorded earthquake data. This evaluation has not been possible primarily because earthquakes that generated design-level or greater ground motions in populated areas have not occurred in regions with many structures designed using modern codes. Even when instrumentation is present, nonstructural components, their supports, and attachments are generally not instrumented. An evaluation of design force equations for nonstructural components and systems in the context of all the different requirements for nonstructural components is needed.

6. Practice Issues

Reducing nonstructural earthquake losses requires not only technically sound code requirements, but also effective implementation during all phases of design and construction. Many parties, including design professionals, contractors, subcontractors, manufacturers, inspectors and building officials, are responsible for implementation.

Practice issues were explored in a 2009 study undertaken by Masek and Ridge [21]. This was the first effort designed to build on anecdotal evidence and provide an understanding of the reasons for compliance and noncompliance with code requirements related to nonstructural design. The EERI study focused on identifying the primary inhibiting and enabling factors affecting nonstructural seismic design and construction practices. Factors included perceptions of current compliance with existing codes and standards, why compliance was lower than required by building codes, and who should be responsible for nonstructural seismic design and construction. There was consistent agreement that the state of practice for nonstructural seismic design and construction was not adequate, and agreement that noncompliance with current building codes occurred frequently.

As part of the first phase of the ATC-120 project, a facilitated workshop was conducted to solicit input from practicing nonstructural component designers, equipment qualification test engineers and engineers involved with the structural design of nonstructural components and systems for buildings about the challenges they face with nonstructural code provisions, design guidelines, and related implementation. The workshop was structured to obtain an independent recommendation from the attendees. Participants identified those aspects of the nonstructural component design and analysis requirements contained in ASCE/SEI 7-10 that they believe work well and those aspects that should be changed to reduce future nonstructural losses in seismic events.

Participants felt that building code requirements for life-safety are generally adequate. There was a general belief that the current code provisions are adequate to limit most serious injuries and avoid casualties. Force levels were generally judged to be reasonable and sufficient. However, enforcement of nonstructural code provisions, quality control, and protection from hazards posed by building contents and furniture all are in need of improvement, and it was believed that loads required for anchorage to concrete are too high. In addition, it was felt that differential movement and story drift requirements need improvement, and that code performance objectives are unclear. Finally, there were concerns that architects, and mechanical and electrical engineers do not generally understand the nonstructural component design provisions in ASCE/SEI 7. The standard should be more clearly written, or contain introductory language in the commentary, to help these individuals know which of the building elements under their responsibility require design and seismic restraint.

7. Conclusions

The vulnerabilities of nonstructural components in modern buildings were identified following the 1964 Great Alaska Earthquake. At that time, there was a debate regarding seismic performance objectives for nonstructural components, and whether codes and standards should provide any level of performance other than life safety in a

strong earthquake. Recommendations for changes to the building code were made, and over the next 50 years, many other changes were implemented based on observations of nonstructural performance in earthquakes. In almost every earthquake, nonstructural damage is a leading source of losses. While codes and standards evolve, the effectiveness of the new procedures for nonstructural components is difficult to gauge. In any earthquake, only a fraction of the impacted structures has been subject to modern nonstructural design standards, and an even smaller fraction of the structures actually comply with those standards especially for nonstructural components.

One of the observations made following the 1964 Great Alaska Earthquake was that the very nature of the design and construction process was a major impediment to good nonstructural performance. While the design and construction of buildings is a combined effort of a large group of skilled individuals, often only a few individuals on the project are familiar with seismic design of nonstructural components. Those most knowledgeable about seismic design may only be involved in the primary structural system, which usually represent only a fraction of the investment in the project.

There is a tendency to minimize the potential safety risks posed by nonstructural damage, based on the assumption that the vast majority of deaths and serious injuries in earthquakes will be the result of full or partial building collapses. This belief is supported by the low death tolls in earthquakes that have occurred in United States. The low casualty figures may be due in part to chance. The 1964 Great Alaska Earthquake occurred after 5:00 PM on Good Friday. Most people were either home or on their way home, few were in schools and businesses. The 1971 San Fernando and 1994 Northridge Earthquakes both occurred in the early morning hours, when schools and businesses were empty. Had any of these earthquakes occurred during the work week when schools and businesses were crowded, casualties due to nonstructural damage would have been much higher.

The first phase of the ATC-120 project identified opportunities for improvement in the nonstructural component design and construction process. If addressed, they will have a substantial impact for public safety and economic welfare. The recommendations extend beyond code development, and include implementation and practice issues believed to be essential for making measurable progress in reducing nonstructural earthquake damage. Technical subjects for research and development are specifically highlighted, as opposed to policy development, and include the suggested scope and approach for proposed problem-focused studies.

The primary objective of this research plan is to present a list of recommended studies that will lead to improved seismic performance of nonstructural components. This list is the result of a comprehensive background knowledge study that collected and summarized the body of available information on nonstructural design and performance, and identified areas of needed research. A workshop with participants representing a broad spectrum of the nonstructural design and construction industry was conducted in parallel to gather a practitioner perspective on the challenges associated with nonstructural code provisions, design guidance, and related implementation. Although there was considerable general agreement between issues identified in the background knowledge study and the workshop, workshop participants particularly emphasized concerns about the installation, attachment, and inspection of nonstructural components. Recommendations from the workshop are integrated into this research plan.

A secondary objective of this plan is to identify an approach for conducting each recommended problem-focused study to facilitate planning for future work. Each study was developed in sufficient detail to describe: (1) the importance of the proposed study; (2) a general methodology for completing each study; and (3) recommended sub-projects to facilitate planning and implementation. Although the details of each recommendation are not provided in this paper, they can be found in *Seismic Analysis, Design, and Installation of Nonstructural Components and Systems – Background and Recommendations for Future Work* [22], along with more information about the background knowledge study and the workshop.

Studies have been grouped by topic into six subject areas and placed in two priority tiers. Priority 1 studies represent efforts that are judged to be foundational for the further development of nonstructural seismic design requirements, or that will have immediate impact on the practice of design and installation of nonstructural components and systems. Priority 2 studies are important, but are not judged to have as great an impact on overall improvement of the performance of nonstructural components and systems. Each study has been broken down into smaller sub-studies. Some of these sub-studies are linked to other sub-studies and need

to be completed sequentially, while other sub-studies may be independent enough that the completion of the sub-study could lead to incremental improvement in the seismic performance of nonstructural components and systems. The breakdown of each of the six subject areas for studies into selectable sub-studies are provided in Table 2.

Table 2 – Summary of Recommended Future Studies and Sub-Studies

Priority	Study or Sub-Study No.	Description
1	1.0	Conduct Holistic Assessment of Current Code Design Approaches
	1.1	Create Archetype Building(s)
	1.2	Define Ground Motions for Study
	1.3	Conduct Building Analyses and Develop Generic Floor Spectra
	1.4	Analytically Determine Demands on Nonstructural Components
	1.5	Evaluate Code Design Force Equations
	1.6	Evaluate Anchor Design Procedures
	1.7	Propose Nonstructural Components and Systems Code Changes
1	2.0	Develop Nonstructural Component and System Performance Objectives
	2.1	Create a Framework for Nonstructural Performance Objectives
	2.2	Build Consensus for Nonstructural Performance Objectives
1	3.0	Improve Implementation and Enforcement of Code Requirements
	3.1	Hold Workshops to Identify Opportunities for Improvement
	3.2	Develop Targeted Materials and Related Training
1	4.0	Clarify Requirements for Displacement Capability Design of Nonstructural Components and Systems
	4.1	Determine Nonstructural Displacement Demands and Associated Acceptance Criteria
	4.2	Develop Enforcement and Inspection Criteria for Displacement Control
	4.3	Create Guidelines for Designers
2	5.0	Create a Plan for Post-Earthquake Reconnaissance and Data Collection
	5.1	Develop Framework for Data Collection
	5.2	Create Data Collection Protocols
2	6.0	Conduct Component Testing
	6.1	Identify Vulnerable Components for Testing
	6.2	Create Testing Protocols
	6.3	Conduct Tests

8. Acknowledgements

This work was funded by the National Institute of Standards and Technology (NIST) under Contract No. SB1341-13-CQ0009. The contents of this paper reflect the views of the authors, and do not necessarily reflect the official views or policies of NIST.

The authors of this paper would like to thank members of the ATC-120 Project Technical Committee and the ATC-120 Project Review Panel, who contributed to the research and preparation of the project report, but are not listed as authors of this paper. The report, *Seismic Analysis, Design, and Installation of Nonstructural Components and Systems – Background and Recommendations for Future Work*, provides a complete listing of all project participants.

9. References

[1] NIST (2013): Development of NIST Measurement Science R&D Roadmap: Earthquake Risk Reduction in Buildings. *GCR 13-917-23*, prepared by the Building Seismic Safety Council for National Institute of Standards and Technology, Washington, D.C., USA.

[2] Ayres JM, Sun T-Y, Brown FR (1967): *A Report on Non-Structural Damage to Buildings - Alaska Earthquake*. March 27, 1964, National Academy of Sciences, Washington, D.C., USA.

[3] Ayres JM, Sun T-Y (1973): Nonstructural Damage, *The San Fernando, California Earthquake of February 9, 1971*. National Ocean and Atmospheric Administration, Vol. 1B1(B), Washington, D.C., USA.

[4] Ding D, Arnold C, Lagorio H, Tobriner S, Rihal S, Mangum R, Hezmalhalch G, Green M, Watson A, Mah D, Metro B, Podany J, Sharpe R (1990): Architecture, Building Contents, and Building Systems. *Earthquake Spectra*, **6**:(S1), 339-377.

[5] Rihal S (1994): Correlation Between Recorded Building Data and Non-Structural Damage During the 1989 Loma Prieta Earthquake. *Data Utilization Report CSMIP/94-04*, California Strong Motion Instrumentation Program, Sacramento, California, USA.

[6] OSHPD (1996): 1994 Northridge Hospital Damage: OSHPD Studies: Water, Elevator, Nonstructural. Office of Statewide Health Planning & Development, Division of Facilities Development, Sacramento, California, USA.

[7] ICBO (1976): *Uniform Building Code*, International Conference of Building Officials, Whittier, California, USA.

[8] ATC (1978): Tentative Provisions for the Development of Seismic Regulations for Buildings. *ATC-3-06*, Applied Technology Council, Redwood City, California, USA.

[9] FEMA (1985): NEHRP Recommended Provisions for Seismic Regulations for New Buildings, Part 1: Provisions. *FEMA 95*, prepared by the Building Seismic Safety Council for the Federal Emergency Management Agency, Washington, D.C., USA.

[10] ICBO (1997): *Uniform Building Code*, International Conference of Building Officials, Whittier, California, USA.

[11] ICC (2000): *International Building Code*, International Code Council, Washington, D.C., USA.

[12] FEMA (1998): NEHRP Recommended Provisions for Seismic Regulations for New Buildings, Part 1: Provisions. *FEMA 302*, prepared by the Building Seismic Safety Council for the Federal Emergency Management Agency, Washington, D.C., USA.

[13] ASCE (2002): Minimum Design Loads for Buildings and Other Structures. *SEI/ASCE 7-02*, American Society of Civil Engineers, Reston, Virginia, USA.

[14] FEMA (2001): NEHRP Recommended Provisions for Seismic Regulations for New Buildings, Part 1: Provisions. *FEMA 368*, prepared by the Building Seismic Safety Council for the Federal Emergency Management Agency, Washington, D.C., USA.

[15] ICC (2003): *International Building Code*, International Code Council, Washington, D.C., USA.

[16] ASCE (2013): Minimum Design Loads for Buildings and Other Structures. *ASCE/SEI 7-10 including Supplement No. 1*, American Society of Civil Engineers, Reston, Virginia, USA.

[17] ASCE (2016): Minimum Design Loads and Associated Criteria for Buildings and Other Structures. *ASCE/SEI 7-16*, American Society of Civil Engineers, Reston, Virginia, USA.

[18] Hutchinson T, Restrepo J, Conte J, Pantoli E, Chen M, Wang X, Astroza R, Ebrahimian H (2014): Shake Table Testing of a Five Story Building Outfitted with NCSs (BNCS project). *Network for Earthquake Engineering Simulation* (distributor), USA.

[19] Ryu KP, Reinhorn AM, Filiatrault A (2012): Full Scale Dynamic Testing of Large Area Suspended Ceiling System. *15th World Conference on Earthquake Engineering*, Lisbon, Portugal.

[20] ICC ES (2014): Acceptance Criteria for Seismic Certification by Shake-Table Testing of Nonstructural Components. *AC156*, ICC Evaluation Service, LLC, Brea, California, USA.

[21] Masek J, Ridge R (2009): Identification of Methods to Achieve Successful Implementation of Nonstructural and Equipment Seismic Restraints. *Earthquake Engineering Research Institute*, Oakland, California, USA.

[22] NIST (2016): Seismic Analysis, Design, and Installation of Nonstructural Components and Systems – Background and Recommendations for Future Work, prepared by the Applied Technology Council for National Institute of Standards and Technology, Washington, D.C., USA (pending publication).

The Paradigm Shift in Smart Manufacturing System Architecture

Yan Lu *, Frank Riddick, and Nenad Ivezic

*Corresponding author
Systems Integration Division, NIST, Gaithersburg, USA
{ yan.lu, frank.riddick, nenad.ivezic }@nist.gov

Abstract Smart Manufacturing seeks to integrate advanced manufacturing methods, operational technologies (OT), and information and communication technologies (ICT) to drive the creation of manufacturing systems with greater capabilities in cost control and performance. A crucial differentiation of smart manufacturing systems (SMS) lies in their architectures, which are organized as networks of cooperating manufacturing components specialized for different functions as opposed to the previous organization characterized by rigid, hierarchically-integrated layers of application components. This "ecosystem" of manufacturing components enables SMS that can provide heretofore unattainable levels of performance for manufacturers with respect to agility, productivity, and quality. This paper provides a study of the architectural impact of individual ICT technologies on the emerging manufacturing ecosystem that potentially eliminates the need to design manufacturing systems based on the hierarchical levels of the legacy ISA 95 model. Additionally, we propose a service-oriented SMS architecture that leverages the benefits of ICT and the safety and security requirements from the OT domain. Key challenges of implementing such architectures are also presented.

Keywords: system architecture, smart manufacturing, cyber physical production system, service oriented architecture

1. Introduction

In the current market, customers call for products tailored to their particular needs. Manufacturers seek to meet the demand for these products, but many current manufacturing systems cannot meet the increased requirements for product customization at mass production rates that are profitable. Yet, advanced manufacturing methods, such as 3D printing and flexible production, are emerging with the promise to make highly-personalized production at scales both possible and affordable. Simultaneously, rapid advances in information and communications technologies (ICT) are being applied to manufacturing systems, driving a shift from traditional labor-intensive processes to advanced-technology-based processes [1]. This on-going integration of advanced manufacturing methods, operation technologies (OT), and the ICT technologies, is fueling the current Smart Manufacturing (SM) trend to enable systems that can

Ivezic, Nenad; Lu, Yan; Riddick, Frank.
"The Paradigm Shift in Smart Manufacturing System Architecture."
Paper presented at International Conference on Advances in Production Management Systems 2016,
Iguassu Falls, AZ. September 3, 2016 - September 7, 2016.

respond in real time to meet changing demands and conditions in the factory, in the supply network, and in customer needs [2].

Historically, manufacturing systems have been designed to follow the Purdue Reference Model for Computer Integrated Manufacturing [3], which was standardized in ISA95[4]. The ISA 95 model includes 5 levels of manufacturing functions that are often implemented as logically separated layers of applications or systems. Specifically, lower level systems (0, 1 and 2) and higher levels applications (3 and 4) are separated into the OT[1] and information technology (IT) domains. The legacy architecture has been widely adopted and implemented in last 30 years accompanied by hierarchical, diverse and domain specific communication structure [8]. However, under the legacy architecture, not only is integration between IT and OT difficult, but skip-level function integration is not supported, which makes it too rigid to adapt rapidly to evolving opportunities from ICT technology integration. For example, in the Internet of Things (IoT) world, every part of a manufacturing enterprise is designed to be connected on the internet so that communication, integration and automation can be achieved without constraints. In addition, cloud and mobile computing enable manufacturing functions once implemented at different levels of the hierarchy to now be available without even knowing where they are hosted. Smart components and smarter systems on the shop floor can run advanced analytics and simulations, and make decisions beyond the lower functions defined in ISA 95.

This suggests that a new, information-centric architecture is needed in order to realize ICT's full potential for SMS and facilitate transformation of closed or proprietary manufacturing system architectures into networks of cooperating manufacturing components so as to attain higher degrees of flexibility and integration. This paper provides a study of the architectural impact of ICT on a manufacturing ecosystem and proposes a service oriented architecture that leverages the benefits of ICT and safety and security requirements from the manufacturing OT domain.

The rest of the paper is structured as follows. Section 2 defines a manufacturing ecosystem to scope our research followed by a description of the legacy architectural model based on ISA 95. Section 3 describes the key ICT technologies identified that contribute most to the SMS architecture paradigm shift and presents their architectural impacts on SMS. In Section 4 we propose a new SMS reference architecture. Key challenges of implementing such an architecture are presented. Section 5 concludes the paper with future research direction.

2. SMS and the Legacy Architecture

Smart manufacturing encompasses a broad scope of systems in a manufacturing business including production, management, design, and engineering functions. The collection of hardware components, their related software components, and the support

[1] Operational technology (OT) is hardware and software that detects or causes a change through the direct monitoring and/or control of physical devices, processes and events in the enterprise. http://www.gartner.com/it-glossary/operational-technology-ot/

applications that make up a manufacturing enterprise are what we term the smart manufacturing ecosystem [5][6]. Figure 1 illustrates three dimensions of concern that are manifest in the smart manufacturing ecosystem. Each dimension — product, production system, and business — is shown within its own lifecycle. Each of these dimensions comes into play in the vertical integration of machines, plants, and enterprise systems in what we call the Manufacturing Pyramid.

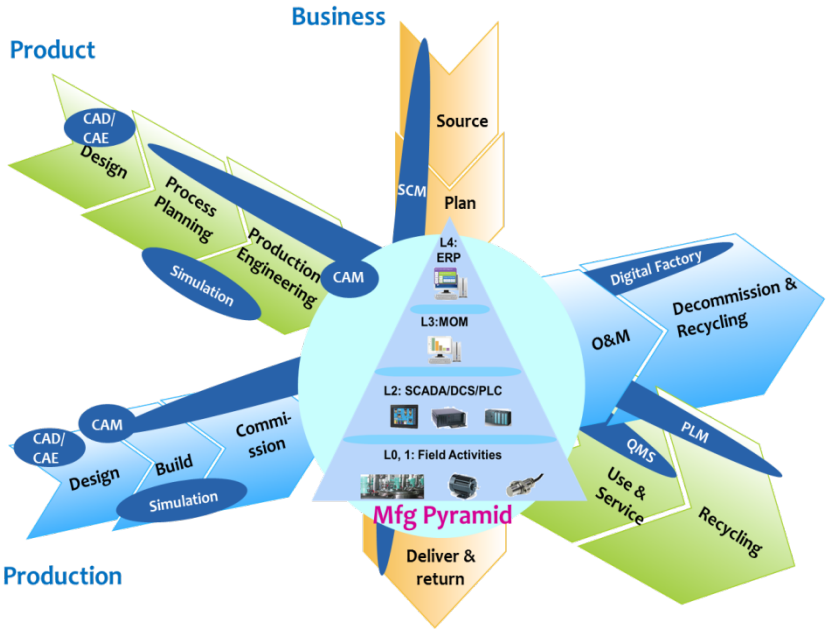

Figure 1: Manufacturing Ecosystem [2][5][6]

The Manufacturing Pyramid, in the center of Figure 1, is often referred to as the manufacturing system and implemented based on the ISA 95 model. The ISA 95 standard defines a 5-level model for activities in the manufacturing enterprise. Each level provides specialized functions and has characteristic response times [7]. Level 0 and Level 1 define field-level activities including the actual physical production process and the sensing and manipulating of the process. Level 2 defines the functions of monitoring, automated control, and supervisory control of the production process, which usually are performed by programmable logic controllers (PLC), distributed control systems (DCS) and/or supervisory control and data acquisition systems (SCADA). Level 1 and Level 2 communicate within time frames on the order of hours, minutes, seconds, and sub-seconds. Level 3 defines the Manufacturing Operation Management (MoM) activities of work flow and stepping the process through states to produce the desired end products. It deals with maintaining records and optimizing the production process. Level 3 deals with time frames of days, shifts, hours, minutes, and seconds. Level 4 defines the Enterprise Resource Planning (ERP) activities to establish the production (master) schedule (i.e., what to produce, which materials to use, where to deliver the product, and how to ship it there). It deals with determining inventory levels

and making sure that materials are delivered on time to the right place for production. Level 4 deals with time frames of months, weeks, days, and shifts.

While the ISA 95 model is used widely to support the definition of architectures for manufacturing systems, recently some drawbacks with its use have emerged [8]. These drawbacks include:

1) Integrating systems across level boundaries is difficult due in part to the use of different network technologies on different levels.
2) Integrating between Supply Chain Management (SCM), Customer Relation Management (CRM), and Product Lifecycle Management (PLM) activities on different ecosystem dimensions is not supported.

Various methods have attempted to deal with the drawbacks of systems architected based on the ISA95 model. Some software vendors and system integrators have provided solutions focused on the vertical integration of manufacturing components in the manufacturing pyramid to enable advanced controls at the shop floor and optimal decision making at the plant and enterprise. Efforts have also been observed that focus on exchanging information between manufacturing ecosystem dimensions, such as continuous process improvement (CPI) programs, flexible manufacturing systems (FMS), and design for manufacturing and assembly (DFMA) approaches. Some lean enterprise efforts connect SCM with ERP to reduce inventory and enable demand-based manufacturing [6]. However, these individual efforts fall short in providing widely applicable methods for integration within and across the three ecosystem dimensions required for SMS. The combination of these perspectives requires a new reference architecture.

3. Architectural Impacts of ICT Technologies

For our study, ICT technologies are classified in three clusters: (1) digital technology including digital thread, product/production/process modeling and simulation, knowledge management, and visualization; (2) infrastructure technology including IoT, big data and advanced computing; and (3) Smart systems technology involving Cyber Physical Production System (CPPS) and service-oriented architecture. All technology of the three clusters contribute to the paradigm shift from the legacy architectures to a new SMS architecture. Each cluster is described in the sections below.

3.1 The Impact of Digitalization

An enormous amount of information is generated and used during the product, production system and business lifecycles. This data might be used to ensure customer requirements are met, to assess product and process performance, or to meet environmental reporting requirements. Digitalization is the process through which information about the product, processes, and production chain are rendered in a digital form that can be archived, exchanged, or analyzed electronically. Digitalization capabilities help manufacturing companies create virtual representations of their products, assets and processes, exchange large amounts of data rapidly, store data efficiently, enrich processes with digital expert knowledge, generate valuable insights from analyzing “big

data", and facilitate communication and collaboration through digital channels within their value chain [9].

The pervasive adoption of digital technology will have two dominant impacts on SMS and their architecture.

1) There will be an increase in the availability of collaborative environments for product development. Their architectures will exhibit a tighter integration of PLM, ERP, MES, SCM, CRM and asset management functions. These platforms will enable customers and suppliers to directly participate in product design and manufacturing. In this way, high-quality customized products can be manufactured and increased traceability can be achieved. Direct feedback from manufacturing and product use to product development will shorten product innovation cycles.
2) Digital representations of products, physical assets, production operations, and business processes will enable the creation of a digital "twin" of the factory—a comprehensive virtual representation of a real factory and its processes that can be made to run in parallel to the real factory[20]. Models and simulations can be instantiated with product and production system data and used in the real factory decision making processes to optimize business, manufacturing, and supply chain operations and to improve product development processes. At the same time, the data coming from the real factory can be fed back to the digital factory to improve the models, knowledge bases, and simulations.

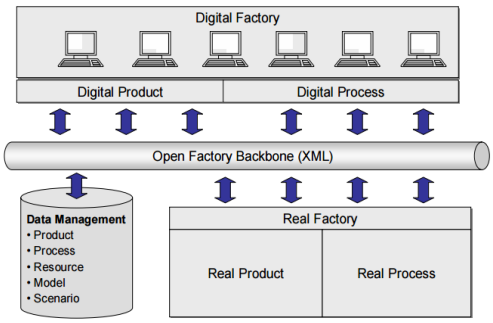

Figure 2: Digital twin for manufacturing [9]

3.2 The Impact of IoT

The development and adoption of the Internet of Things (IoT) is a critical element of Smart Manufacturing [10]. The technologies that will become pervasive because of the IoT—network-addressable physical and application components and standard communication protocols through which those components can communicate—will enable enterprise architectures, in general, and industrial system architectures, in particular, to move on from their traditional hierarchically and domain-specific network structure to a unified and IP-based structure[11], as shown in Figure 3. This shift will enable enter-

prise services, such as data analytics and edge computing services, that today are typically only available at the highest levels of an enterprise to be available to serve system components in all areas of the industrial enterprise.

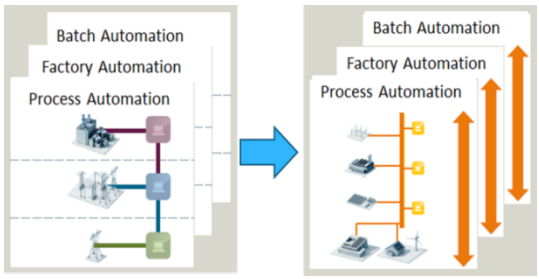

Figure 3: Ubiquitously connected manufacturing systems (adapted from [11])

The transition to more open network architectures, combined with Big Data and Cloud computing, will bring profound opportunities to SMS. At the same time, new security challenges are presented with billions of new smart devices being interconnected in the world of the IoT [12]. The biggest security concern comes from connecting IoT devices, sensors, actuators and edge-computing units, with existing controllers, automation and manufacturing information networks, and applications. Existing OT and IT security approaches and policies will need to be adapted to embrace these new IoT security challenges. Most automation and information suppliers have established industry security services to assist clients to assess security risks and harden their manufacturing plants. Reference network architectures are available from both network equipment and automation system vendors [13]. Additional challenges of integrating IOT include unreliable communications of sensors and actuators on IP networks, how to leverage IoT to boost computing power for advanced manufacturing analytics, and accessibility issues of gaining accesses to the legacy manufacturing assets.

3.3 The Impact of CPPS

While the IoT deals with unique, identifiable, and internet-connected physical objects, cyber-physical systems efforts are concerned with the nature of cyber-physical coupling and the system of systems characteristics of networked and software-controlled systems. CPPS is considered the core component for German Industrie 4.0 program, where they are also referred to as I4.0 Components[14]. SMS are essentially composed of CPPS, which can respond intelligently to changing tasks and conditions and reconfigure themselves. CPPSs partly break the traditional automation pyramid and potentially turn the manufacturing ecosystem into a service-oriented architecture (SOA) [15][16]. To leverage the safety and security requirements from the OT domain, real-time and safety critical functions in legacy automation systems will remain organized in a hierarchy, and only level 2 components will be allowed to connect as services. IoT devices connected in the IT world will naturally be part of the service-oriented architecture. Figure 4 shows how the legacy hierarchical functional architecture will be transformed to a SOA-based manufacturing system architecture.

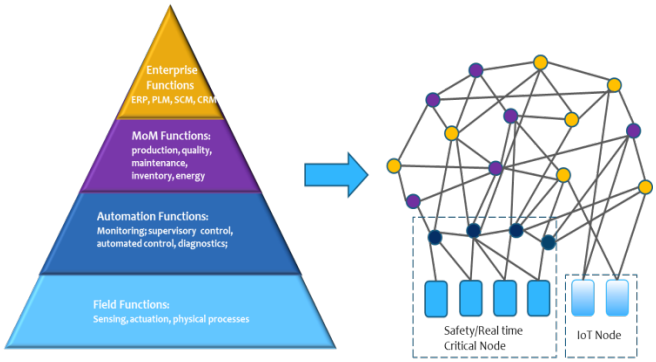

Figure 4: CPPS Impact on manufacturing system function architecture (Adopted from [19])

4. Smart Manufacturing Architecture

With the architectural impacts from ICT technologies in mind, we propose a SOA for Smart Manufacturing systems.

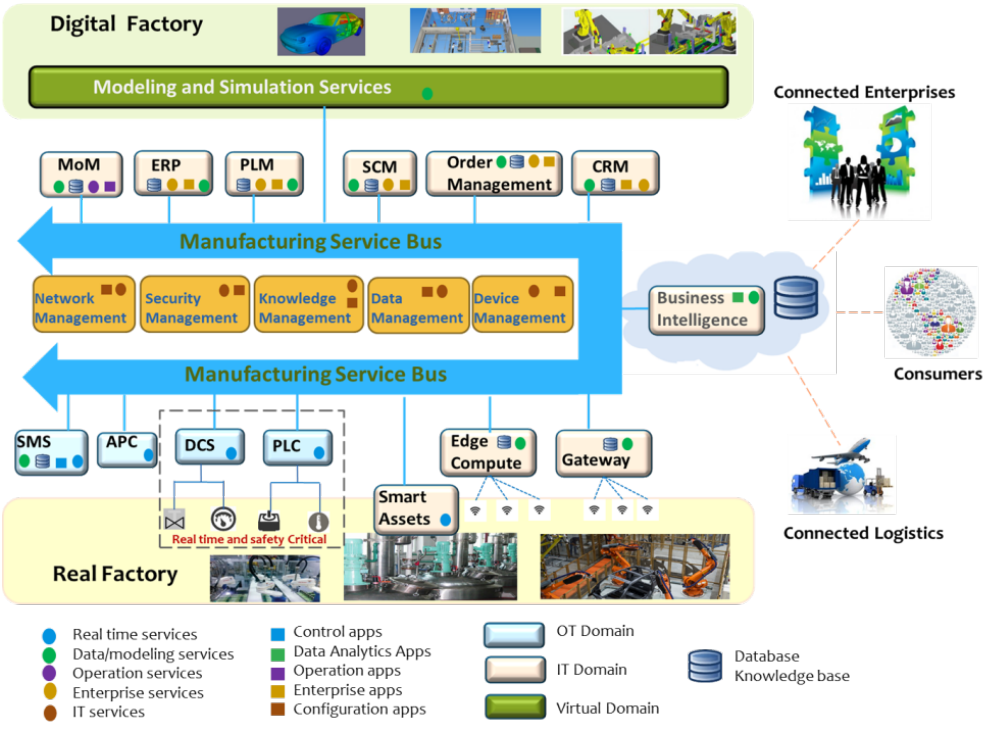

Figure 5: A Service Oriented and Model based SMS Architecture

As shown in Figure 5, the proposed architecture provides a completely integrated manufacturing ecosystem on a single manufacturing service bus, including both OT domain systems and IT domain systems and applications. Interactions with suppliers, customers, and logistics systems are enabled through a collaborative Business intelligence (BI) service.

In the new architecture, services are classified as being one of four types: IT domain services, OT domain services, virtual domain services and management/common services. IT domain services include IoT services (e.g., smart devices, edge computing, fog computing, cloud computing, etc.), MoM services, ERP services, PLM services, and other enterprise services such as Asset Management, Energy Management, SCM, Order Management and CRM. The integration approach that will be used for IT domain services is similar to today's enterprise service bus (ESB) based approach, which is built using event-driven and standards-based message-oriented middleware in combination with message queues. In the OT domain, services involve functions provided by machines, workstations, robots, production lines, complete production cells or even products themselves. The OPC Unified Architecture (OPC UA) provides interoperability at level 2 and beyond and has the potential to provide a service-oriented architecture for OT application integration[14]. Data analytics services are provided through edge computing, fog computing and cloud computing in the IoT world [18]. Virtual domain services are located in the digital factory, which stores the data models, function models, behavior models, and process models of a manufacturing enterprise and provides query and simulation functions for manufacturing applications. Management/common services sit at the core of the SOA architecture. They help manage the lifecycle of the SMS services, map client requests with service providers, and ensure quality of service levels met. Device management, network configuration, data management, knowledge management, and security management are provided by services in this cluster.

Based on the architecture described above, SMS can be developed and deployed that provide efficient and flexible solutions for the problems faced by the modern manufacturing enterprise. Supporting more streamlined processes, the SOA-based architecture enables customized production at mass production rates.

However, implementing the proposed architecture to create new SMS is neither simple, quick, nor cheap. It will take many years to fully realize the strength of the new architecture. The key implementation challenges include:

- Manufacturing Service Bus capabilities - can a single manufacturing service bus meet the needs of diverse use scenarios, supporting both real-time messaging and big volume data distribution?
- Real-time service capabilities - how should real-time services be modeled in the OT domain, how should their service interfaces be defined, and how should resource constraints be managed, i.e., when and where should resources be available to provide services?
- IT – OT integration concerns - how can security and safety issues be handled? Can high fidelity models and simulations be used in a real-time control environment without re-engineering?

- Knowledge management concerns – how can we close technology gaps in conditioning, interpreting, and contextualizing data across heterogeneous systems or situations?
- Integration standards - how can existing standards be enhanced and new standards be developed to enable more information flow among more stakeholders.

5. Conclusion

In a new era of smart manufacturing, every part of a manufacturing enterprise will be digitized and connected. With the introduction of smart devices accessible as services on a network, more embedded intelligence at every level, predictive analytics, and cloud technology, the next generation of manufacturing systems will indeed get smarter. In order to realize the vision of smart manufacturing where systems respond in real time to changing demands and conditions in the factory, in the supply network, and in customer needs, the classical manufacturing system architectural paradigm based on a hierarchical control model will no longer dominate. A new paradigm based on distributed manufacturing services is starting to be adopted.

This paper described a smart manufacturing ecosystem that enabled systems integration within and across three manufacturing lifecycle dimensions – product lifecycle, production system lifecycle, and business lifecycle. We examined how the introduction of ICT is going to impact the SMS architecture. Adoption of IoT, CPPS and cloud computing technology potentially will drive the transformation of the existing rigid hierarchical architecture style. Digital thread and digital factory technology will enable the enterprise to be fully integrated with its value chain. Based on the study of the ICT architectural impact, we propose an SOA-based and model-enabled Smart Manufacturing reference architecture. The proposed reference architecture will integrate both ICT and OT systems on a single manufacturing service bus. We discussed implementation challenges that include standards for communication protocols, data model, knowledge representation, and CPPS characterization that are necessary to facilitate the adoption of Smart Manufacturing technology and the proposed architecture.

Disclaimer

Any mention of commercial products is for information only; it does not imply recommendation or endorsement by NIST.

References

[1]. Institute for Defense Analyses, Emerging Global Trends in Advanced Manufacturing, March, 2012 https://www.wilsoncenter.org/sites/default/files/Emerging_Global_Trends_in_Advanced_Manufacturing.pdf, Accessed on March 21, 2016.
[2]. Simon Frechette, KC Morris, and Yan Lu, Smart Manufacturing Isn't So Smart Without Standards , http://blog.mesa.org/2016/03/smart-manufacturing-isnt-so-smart.html, Accessed on March 21, 2016.

[3]. Theodore J. Williams, The Purdue Enterprise Reference Architecture: A Technical Guide for CIM Planning and Implementation, Instrument Society of America, Jan 1, 1992
[4]. ANSI/ISA-95.00.01-2010 (IEC 62264-1 Mod) Enterprise-Control System Integration - Part 1: Models and Terminology, https://www.isa.org/store/products/product-detail/?productId=116636
[5]. Yan Lu; KC Morris; Simon P. Frechette, Standards Landscape and Directions for Smart Manufacturing Systems, IEEE Conference on Automation Science and Engineering 2015, Gothensburg, August 23-28, 2015
[6]. Yan Lu; KC Morris; Simon P. Frechette, Current Standards Landscape for Smart Manufacturing Systems, NISTIR 8107, 2016
[7]. Dennis Brandl, The IT Implications of ISA 95 and ISA 99, http://www.brlconsulting.com/Files/The%20IT%20Implications%20S95%20and%20S99.pdf, Accessed on march 21, 2016
[8]. LNS Research, Agile MES and IIoT: How the Traditional Hierarchies in Manufacturing Operations Management Are Being Dissolved, Webinar, Feb. 29, 2016.
[9]. Wolfgang Kühn, Digital factory-integration of simulation enhancing the product and production process towards operative control and Optimisation, International Journal of Simulation: Systems, Science and Technology 10/2006; 7(7).
[10]. Lopez Research, Building Smarter Manufacturing With The Internet of Things (IoT), https://www.iotwf.com/resources/6, Accessed on march 23, 2016
[11]. Stephan Guido, Internet of Thing and Services, Siemens Future Forum@ Hanover Messe 2014, Apr. 7-11, 2014, https://w3.siemens.com/topics/global/en/events/hannover-messe/program/Documents/pdf/Internet-of-Things-and-Services-Guido-Stephan.pdf, Accessed on March 24, 2016
[12]. Mark Davidson, IoT in Manufacturing Hurdle #2: New Security Challenges, July, 2014. http://blog.lnsresearch.com/blog/bid/199506/IoT-in-Manufacturing-Hurdle-2-New-Security-Challenges, Accessed on march 24, 2016.
[13]. GE's Intelligent Platforms business & CISCO, Architecting a Robust Manufacturing Network for the Internet of Things, August 2015, http://www.cisco.com/c/dam/en_us/solutions/industries/docs/manufacturing/architecting-robust.pdf, Accessed on March 24, 2016
[14]. VDI/VDE Society Measurement and Automatic Control (GMA), Reference Architecture Model Industrie 4.0 (RAMI4.0), July, 2015
[15]. Boyd, Alan, D. Noller, P. Peters, D. Salkeld, T. Thomasma, C. Gifford, S. Pike, and A. Smith. SOA in manufacturing—guidebook, MESA International, IBM Corporation and Capgemini Co-Branded White Paper, (2008).
[16]. IBM, SOA Approach to enterprise integration for product lifecycle management. IBM, International Technical Support Organization, 2008.
[17]. Laszlo Monostori, Cyber-physical Production Systems: Roots, Expectations and R&D Challenges, CIRP 12/2014; 17:9–13.
[18]. Maher Abdelshkour, IoT, from Cloud to Fog Computing, http://blogs.cisco.com/perspectives/iot-from-cloud-to-fog-computing, Accessed on March 24, 2016

[19]. G. Vogel-Heuser, G. Kegel, K. Bender, and K. Wucherer, Global information architecture for industrial automation. Automatisierungstechnische Praxis (atp), Oldenbourg-Verlag, Muenchen, 2009.
[20]. Michael Grieves, Digital Twin: Manufacturing Excellence through Virtual Factory Replication, 2014, http://innovate.fit.edu/plm/documents/doc_mgr/912/1411.0_Digital_Twin_White_Paper_Dr_Grieves.pdf, Accessed on May 31, 2016.

STEEL GRAVITY CONNECTIONS SUBJECTED TO LARGE ROTATIONS AND AXIAL LOADS

Jonathan M. Weigand
National Institute of Standards and Technology, Gaithersburg, MD 20899, USA
jonathan.weigand@nist.gov

Jeffrey W. Berman
University of Washington, Seattle, WA 98195, USA
jwberman@uw.edu

ABSTRACT

Steel gravity framing systems (SGFSs) rely on connections for system robustness when a column suffers damage that compromises its ability to carry gravity loads. Redistribution of gravity loads through the development of a sustained tensile configuration resulting from large vertical deflections is a key behavior in achieving robustness. Development of such an alternative load path depends on the ability of the gravity connections to remain intact after undergoing large rotation and axial extension demands. These demands are significantly larger than those considered for typical SGFS connection design. This paper presents the results of experiments on steel single-plate shear and bolted angle connections subjected to loading consistent with an interior column removal. The characteristic connection behaviors are described and the performance of multiple connection configurations are compared in terms of their peak resistances and deformation capacities.

INTRODUCTION

Steel gravity framing systems (SGFSs) are present in nearly every steel building constructed in the United States, yet they have been identified as potentially vulnerable to collapse (Foley et al., 2006; Sadek et al., 2008; Main and Sadek, 2012; Weigand, 2014). If the vertical load carrying capacity of a single column is diminished or lost, it is presently unclear if the gravity loads on the structure can be sustained. The notion of a design procedure for achieving structural robustness in SGFSs is in its infancy, and the current body of knowledge lacks experimental data on the behavior and performance of steel buildings subjected to unanticipated loads.

While it would be impractical and prohibitively expensive to directly design for unanticipated loading events (e.g., vehicular impact, blast, or accidental overload), history has shown that some inherent robustness is often present. Research on disproportionate collapse in steel framing has found that ductile connection detailing may improve system robustness under unanticipated loadings. In the event that a column in a SGFS loses the

Berman, Jeffrey; Weigand, Jonathan.
"Steel Gravity Connections Subjected to Large Rotations and Axial Loads."
Paper presented at Eighth International Workshop on Connection in Steel Structures (Connections VIII), Boston, MA. May 24, 2016 - May 26, 2016.

capacity to support its gravity loads, alternative load paths must develop in the horizontal framing members to support the gravity loads. These load paths develop from large vertical deflections that result in catenary action in the system, and that subject the connections to large rotation and axial extension demands.

The performance of steel gravity connections under seismic loading
has been studied experimentally. However, experimental investigations involving the collapse behavior of SGFSs or its components are more limited. Astaneh-Asl et al. (2001a) investigated the collapse resistance of a two-bay gravity system under column removal and showed that an improvement in capacity could be achieved (Astaneh-Asl et al., 2001c) by adding post-tensioning cables. Thompson (2009) tested specimens each consisting of a column stub with symmetrically configured single-plate shear connections tied via short stiffened pinned-end beams to a vertical perimeter frame under an interior column pulldown scenario. Using connection sub-assemblages, Guravich and Dawe (2006) conducted an investigation of four gravity connection types typical to Canadian structural engineering practice to determine if shear connections could sustain significant tensile loads in combination with their design shear capacity. Oosterhof and Driver (2012) also investigated the strength and ductility of common shear connections using sub-assemblages, under combinations of moment, shear, and tension.

To evaluate the structural robustness of SGFSs, a multi-university collaborative experimental program was established to investigate the behavior of the state of current industry practice for gravity framing and work toward developing the next-generation of SGFSs. This program was a collaborative effort which involved contributions from the University of Washington (UW), Purdue University (PU), and the University of Illinois at Urbana-Champaign (UIUC). This paper summarizes experimental results from tests on SGFS connection subassemblies conducted at the UW to evaluate their response to loading consistent with an interior column losing its vertical load carrying capacity. A broad range of single-plate shear and bolted angle connection sub-assemblage tests were conducted to characterize connection response to combined loading, and to determine controlling failure mechanisms for various connection geometries.

CONNECTION CONFIGURATIONS

The steel single-plate shear and bolted angle connection sub-assemblages tested in this study were designed to resist the shear demands resulting from a series of prototypical steel gravity framing systems, with gravity loads modeled after the SAC[1] prototype building loads. The prototype systems encompassed a broad range of configurations typical of current industry design practice, and are described in more detail in Weigand et al. (2012). The connection configurations were selected from the prototype system designs and refined to provide a wide breadth of parameter variation.

[1]SAC Joint Venture between the Structural Engineers Association of California (SEAOC), the Applied Technology Council (ATC), and the Consortium of Universities for Research in Earthquake Engineering (CUREE)

The typical connection sub-assemblage specimen consisted of a 1524 mm (60.0 in) long W12×72 column stub and a 1220 mm (48.0 in) long W21×50 beam stub, connected via a single shear plate (Fig. 1), bolted web angles, or top and seat angles; however, two specimens used W14×90 and W18×35 column and beam stub sections, respectively. The varied connection parameters for the single-plate shear connections included the number of bolts (n_b), bolt diameter (d_b), bolt grade, plate thickness (t_p), horizontal plate edge distance (L_{ehp}) relative to the minimum allowable plate edge distance (L_{emin}), hole type (standard (STD) or short-slotted (SSLT)), eccentricity with respect to the beam centerline, gap between the beam flange and the column flange, and the simulated system span. The varied connection parameters for the bolted angle specimens included the number of bolts on the angle legs bolted to the column flange (n_b), angle column-leg bolt diameter (Col. d_b), angle beam-leg bolt diameter (Bm. d_b), angle leg thickness (t_L), configuration, eccentricity with respect to the beam centerline, and gap between the beam flange and the column flange. The naming convention for the tested specimens consists of a prefix that describes the connection type (e.g., sps (Single-Plate Shear)), followed by the number of bolts (e.g., 3b), the hole type (e.g., STD), the bolt diameter fraction in inches (e.g., 34 corresponds to 3/4 in), plate thickness fraction in inches (e.g., 38 corresponds to 3/8 in), and additional descriptor (e.g., Edge) where applicable. A similar naming convention was used for the bolted angle connections using the bolt diameter fraction, angle thickness fraction, and additional descriptor, where applicable. Table 1 shows the parameter values for the single-plate shear specimens and Table 2 shows the values for the bolted angle specimens.

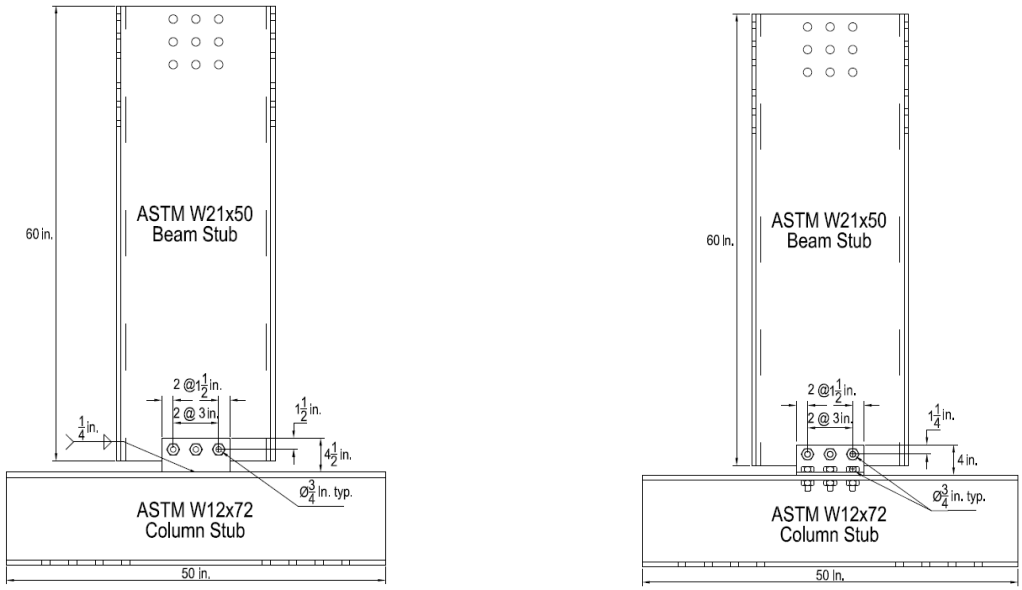

Figure 1. (a) Typical single-plate shear specimen, and (b) typical bolted angle specimen (1 in = 25.4 mm). For both: dimensions vary, see Tables 1 and 2.

Name	Connection Properties	Test Results

	Span (m)	n_b	d_b (mm)	t_p (mm)	Hole Type	L_{ehp}/L_{emin}	Δ (mm)	θ (rad)	δ (mm)	d_f (mm)	V_{max} (kN)	T_{max} (kN)	V_{max}/V_{Nom}	Failure Location
sps3b|STD|34|38|48L[1]	14.6	3	19.1	9.53	STD	1.5	1053	0.075	19.6	24.5	41.2	497	0.099	Bolt
sps4b|STD|34|38|48L[1]	14.6	4	19.1	9.53	STD	1.5	1159	0.082	23.8	32.7	55.1	647	0.093	Bolt
sps3b|STD|34|38|	9.1	3	19.1	9.53	STD	1.5	788	0.090	17.9	20.7	40.2	495	0.097	Bolt
sps3b|SSLT|34|38|	9.1	3	19.1	9.53	SSLT	1.5	890	0.092	22.7	24.5	44.1	474	0.106	Bolt
sps3b|SSLT|34|38|Edge	9.1	3	19.1	9.53	SSLT	1.0	809	0.087	18.8	22.4	32.3	384	0.067	Plate
sps4b|SSLT|34|38|	9.1	4	19.1	9.53	SSLT	1.5	863	0.093	21.4	24.2	49.6	544	0.083	Bolt
sps5b|SSLT|34|38|	9.1	5	19.1	9.53	SSLT	1.5	807	0.079	18.7	25.5	60.4	628	0.078	Bolt
sps3b|SSLT|34|38|A490	9.1	3	19.1	9.53	SSLT	1.5	943	0.099	25.5	28.7	52.4	527	0.119	Bolt
sps3b|SSLT|34|38|Offset[2]	9.1	3	19.1	9.53	SSLT	1.5	906	0.091	23.6	24.4	43.4	435	0.105	Bolt
sps4b|SSLT|78|38|	9.1	4	22.1	9.53	SSLT	1.3	795	0.081	18.2	22.7	48.7	503	0.081	Bolt
sps3b|SSLT|34|14|	9.1	3	19.1	6.35	SSLT	1.5	894	0.089	23.0	26.4	38.9	387	0.123	Plate
sps3b|SSLT|34|38|Gap[3]	9.1	3	19.1	9.53	SSLT	1.5	772	0.067	17.1	19.9	36.9	426	0.089	Bolt
sps3b|SSLT|34|14|Weak[4]	9.1	3	19.1	9.53	SSLT	1.5	972	0.110	27.1	32.6	38.5	388	0.121	Plate

Table 2. Bolted Angle Connection Test Specimens and Results

Name	Connection Properties				Test Results							
	n_b	Col d_b (mm)	Bm. d_b (mm)	t_L (mm)	Δ (mm)	θ (rad)	δ (mm)	d_f (mm)	V_{max} (kN)	T_{max} (kN)	V_{max}/V_{Nom}	Failure Location
ba3b|34|14|	3	19.1	19.1	6.35	1175	0.133	37.6	45.3	34.2	282	0.049	Angle
ba3b|34|12|	3	19.1	19.1	12.7	1168	0.132	37.2	41.6	61.1	543	0.067	Bolts
ba5b|34|14|	5	19.1	19.1	6.35	1033	0.117	29.3	46.7	46.4	373	0.041	Angle
ba5b|34|12|	5	19.1	19.1	12.7	1078	0.118	31.9	47.8	93.9	780	0.059	Bolts
ba3b|1|34|	3	25.4	25.4	19.1	1563	0.176	64.6	74.6	134.1	877	0.146	Beam Web
ba3b|34|14|Offset[1]	3	19.1	19.1	6.35	1074	0.122	31.7	41.1	33.0	258	0.047	Angle
ba3b|34|12|Offset[1]	3	19.1	19.1	12.7	1086	0.116	32.3	39.6	60.5	533	0.066	Bolts
ba3b|34|14|Gap[2]	3	19.1	19.1	6.35	1080	0.122	32.0	40.5	30.5	258	0.044	Angle
ba3b|34|12|Gap[2]	3	19.1	19.1	12.7	1150	0.122	36.1	41.2	65.2	553	0.071	Bolts
ba3b|34|14|TopSeat[3]	3	19.1	19.1	6.35	542	0.062	8.3	-	42.5	137	0.077	Angle
ba3b|34|12|TopSeat[3]	3	19.1	19.1	12.7	557	0.063	8.7	-	68.9	46	0.108	Bolts
ba3b|34|14|HConfig[4]	3	19.1	25.4	6.35	1328	0.15	47.6	52.9[8]	44.5	322	0.064	Angle
ba3b|34|12|HConfig[4]	3	19.1	25.4	12.7	1216	0.138	40.2	41.7[8]	57.8	475	0.063	Beam Web
ba3b|34|14|BlegWeld[5]	3	19.1	-	6.35	1067	0.121	31.2	-	27.2	240	0.039	Angle
ba3b|34|14|ClegWeld[6]	3	-	19.1	6.35	1125	0.127	34.6	34.1	15.8	130	0.023	Weld
ba3b|34|14|Weak[7]	3	19.1	19.1	6.35	1100	0.125	33.2	-	29.5	231	0.042	Angle
ba3b|34|14|Weak[7]	3	19.1	19.1	12.7	1373	0.155	50.6	-	79.6	591	0.087	Bolts

Note: All bolted angle specimens used a simulated span of 9.1 m (30 ft)

[1] Angles offset 76 mm (3.0 in) from beam centerline.

[2] Reduced gap of 6.4 mm (1/4 in) between beam flange and column flange.

[3] Top-and-seat angle configuration.

[4] Angles had three 19.1 mm (3/4 in) diameter bolts on column legs and two 25.4 mm (1 in) diameter bolts on beam legs.

[5] Angles bolted to column face and welded to beam web.

[6] Angles welded to column face and bolted to beam web.

[7] Weak-axis configuration that frames into column web.

[8] Value corresponds to fiber centered at beam leg bolt.

TEST SETUP AND LOADING

A self-reacting load frame (Fig. 2) was constructed in the UW Structural Research Laboratory. The reaction frame was capable of delivering combined shear, tension, and flexural loading to the gravity connection sub-assemblages. Three actuators were attached at their bases to the reaction frame and at their heads to a load beam. A single 245 kN (55 kip) actuator was mounted horizontally to the reaction column and attached to the load beam. Two 489 kN (110 kip) actuators were mounted vertically and spanned between the outriggers and the load beam. The outriggers were rigidly fixed to the foundation beams and anchored to the strong floor. Each actuator had swivels at both ends to accommodate in-plane movements while preventing flexural loading of the piston rods. Out-of-plane movements were restrained at the end of the beam stub.

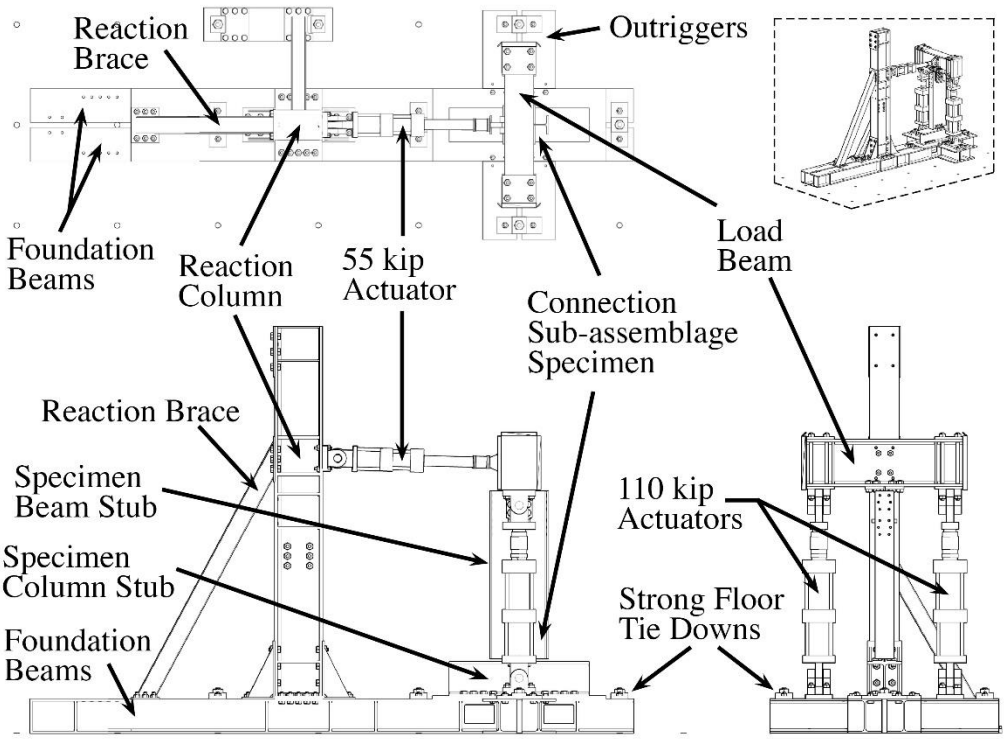

Figure 2. Connection test setup (1 kip = 4.448 kN).

Axial extension and rotation demands were applied quasi-statically to the connection sub-assemblage specimens through the load beam by the three independent actuators fixed to the reaction frame. The actuators were operated in displacement control. The displacements were computed by assuming a simple geometric relation between the extension and rotation demands at the connection and the centerline deflection of the interior column location in a simulated two-span system as shown in Fig. 3(a). The column was assumed to deflect perfectly vertically downward, and all deformations were assumed to occur at the connections about the centers of gravity of the connection bolt groups.

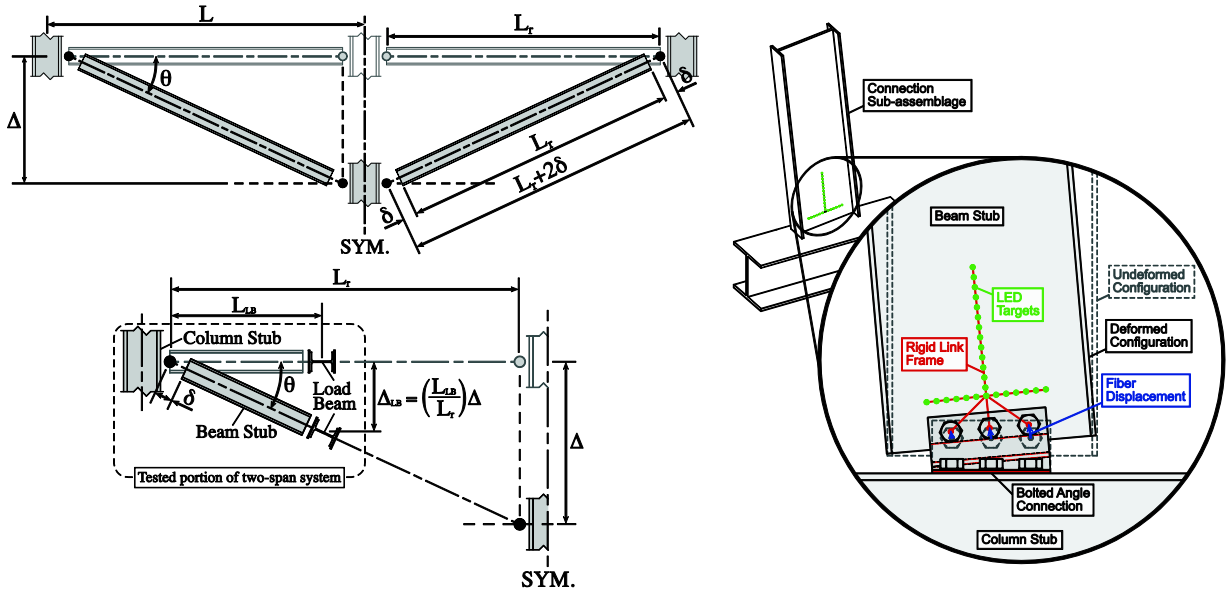

(a) (b)

Figure 3. (a) Deformed two-span system used for determining applied rotation and displacement. (b) Fiber displacements computed from light-emitting diode (LED) targets.

Considering these assumptions, the applied rotation, θ, and simultaneously applied axial extension, δ, were:

$$\theta = tan^{-1}\left(\frac{\Delta}{L_r}\right) \quad (1)$$

$$\delta = \frac{L_r}{2}\left[\sqrt{1+\left(\frac{\Delta}{L_r}\right)^2} - 1\right] \quad (2)$$

respectively, where all terms are as shown in Fig. 3. See Weigand and Berman (2014) for more details on the derivation of Eq. (1) and Eq. (2).

EXPERIMENTAL RESULTS

Experimental results are shown in Table 1 and Table 2. The estimated uncertainty in the measured data was ±1 %, based on repeated calibrations of the instruments over the course of testing. Results presented for each connection include the maximum connection rotation θ, maximum corresponding vertical displacement at the simulated damaged column, Δ, using the span lengths in Table 1 and a 9.1 m (30 ft) span for all bolted angle specimens, the maximum fiber displacement d_f, the maximum shear force at the columns face (aligned with the column), V_{max}, the maximum tension force in the connection (aligned perpendicular to the shear force), T_{max}, the maximum shear force normalized by each connection's nominal strength, $V_{max}/ V_{Nom,}$ and the failure mode. Complete discussions of the results may be found in Weigand (2014), Weigand and Berman (2015) and Weigand and Berman (2016).

To account for the combined contributions to bolt and plate deformations from the rotation and axial extension demands, the connection was discretized into individual component-width segments (fibers) each made up of a single bolt and the tributary width of beam web, and shear plate or angle. The locations of the fibers were determined prior to the application of load, with fiber-nodes centered at the light-emitting diode (LED) targets on the connection bolt-heads. One node of each fiber was assumed to be rigidly attached to the fixed specimen column stub, and the other was assumed rigidly attached to the beam web. The kinematic motions of the beam web fiber-nodes were computed by imposing a rigid-link structure onto the grid of LED targets positioned on the beam web (Fig. 3(b)). Experimental fiber displacement profiles were computed as the vectors spanning from the undeformed to the deformed locations of the fiber nodes, and decomposed into axial and shear components.

As shown in Table 1 and Table 2, different failure modes were observed depending on connection configuration and specific parameters (i.e., shear plate thickness, angle thickness, bolt diameter, etc.). Fig. 4 illustrates the progression of deformation and eventual failure for two single-plate shear specimens, one with a thinner plate (sps3b|SSLT|34|14|) that had a tearout failure and one with a thicker plate (sps3b|SSLT|34|38|) that had a bolt shear rupture failure.

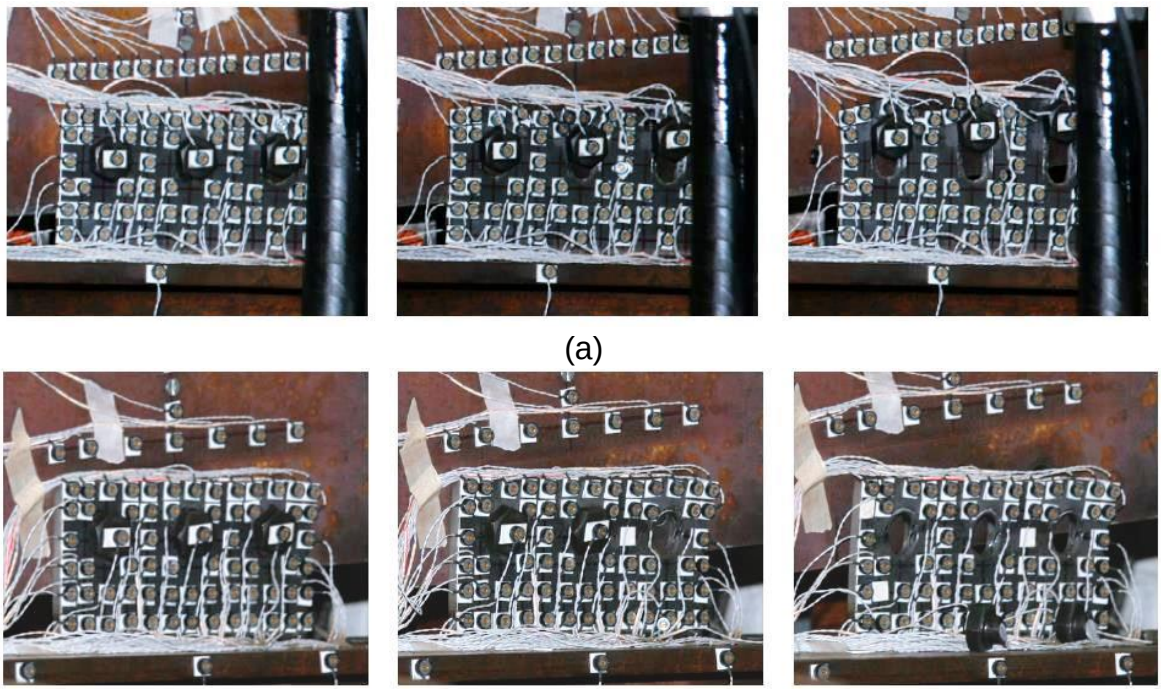

(a)

(b)

Figure 4. (a) Example of progression of plate tearout rupture in Specimen sps3b|SSLT|34|14| (b) example of bolt shear rupture in Specimen sps3b|SSLT|34|38|

The performance of connection specimens across the parameter space resulted in several key observations for gravity connections subjected to combined rotations and axial deformations. For steel single-plate shear connections:

1. The vertical shear force at the column face at connection failure is much lower than the nominal shear strength of the connection. The presence of tension in the connection greatly reduces the shear capacity. Table 1 illustrates this, as the maximum vertical shear force normalized by the nominal shear strength (V_{max}/ V_{Nom}) is typically less than 0.13.
2. Failure is generally controlled by the deformation capacity of the outer fiber. Deeper connections with more bolts have larger strength, but less deformation capacity (both rotation and tension) than shallower connections and their increase in strength is less than the increase in their nominal shear strength. This is illustrated in Fig. 5, which shows test results for three single-plate shear connections with 3 bolts, 4 bolts, and 5 bolts. The increase in vertical shear capacity (see Fig. 5(a)) is not proportional to the increase in nominal strength due to the increased number of bolts (i.e., the 4-bolt and 5-bolt connections achieved smaller percentages of their nominal strengths than the 3 bolt connection, as shown in Fig. 5(b)). Fig. 5(c) shows that the axial displacement capacity of the outer fiber of each connection was the approximately the same.
3. Connections with short slotted holes achieve larger shear forces at the column face than connections with standard holes (e.g., compare results from sps3b|STD|34|38| and sps3b|SSLT|34|38| in Table 1).
4. Binding of the beam and column flanges has a negative impact on connection performance but is unlikely to occur in typical connection configurations due to the large axial deformations at the connections (see Weigand and Berman (2014) for more details).

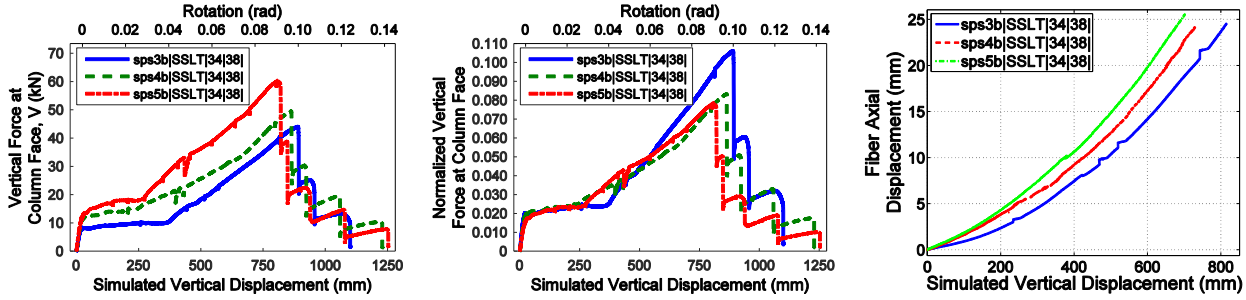

(a) (b) (c)

Figure 5. Comparison of (a) vertical force at column face normalized by connection nominal shear strength (b) horizontal force at the column face normalized by the plate tension strength, and (c) the displacement profiles in the outer fiber for 3 bolt (blue), 4 bolt (green) and 5 bolt (red) single-plate shear connections (profiles terminated at connection failure.

The key observations from the results of the tests on bolted angle specimens subjected to combined large rotations and axial deformations are:

1. For each pair of connections that differed only by angle thickness (e.g., Specimens ba3b|34|14| and ba3b|34|12|, Specimens ba5b|34|14| and ba5b|34|12|, etc.), the thicker bolted angle specimens achieve larger vertical force at the column face (Fig 6(a)).

2. Increasing the number of bolts reduces the deformation capacity of the connections and results in smaller normalized maximum vertical forces at the columns face as shown in Fig. 6(b).
3. Double angle connections with one leg welded (i.e., Specimens ba3b|34|14|BlegWeld and ba3b|34|14|ClegWeld) have reduced strength and ductility relative to bolted-bolted connections (see Table 2).
4. Double angle connections have larger deformation capacity, but lower strength than single-plate shear connections with the same nominal shear strength as shown in Fig. 7.

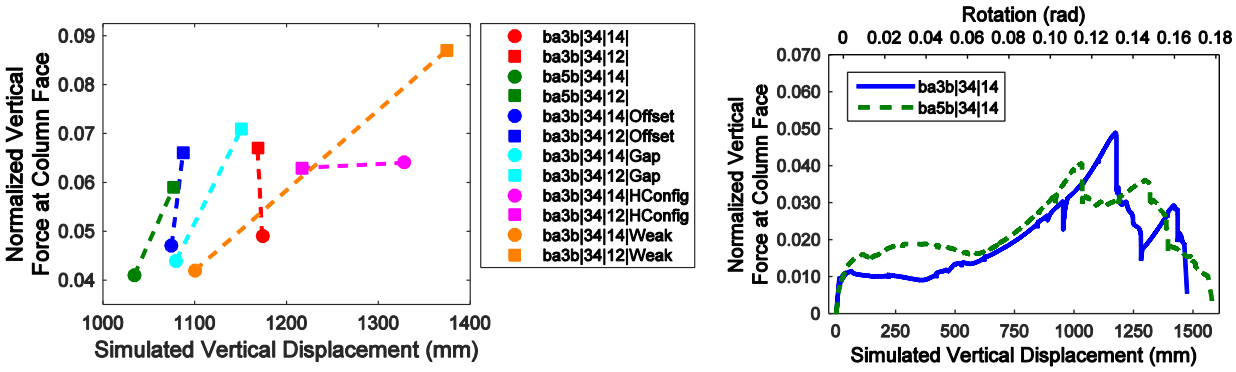

(a) (b)

Figure 6. Comparison between (a) vertical capacities of bolted web angle connections with 6.35 mm (1/4 in.) thick and 12.7 mm (1/2 in.) thick angles normalized by connection nominal shear strength (connections of the same configuration but different angle thicknesses are connected via dashed line), and (b) vertical force at column face normalized by connection nominal shear strength for 3 bolt (blue) and 5 bolt (green) double angle connections.

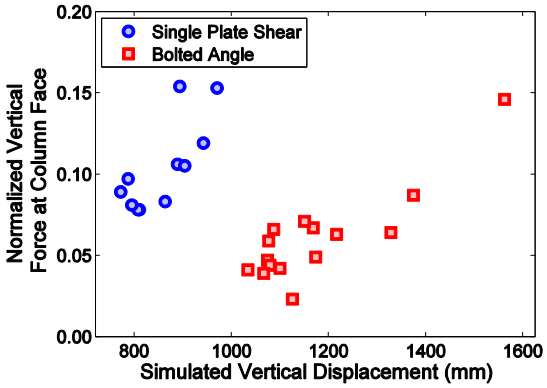

Figure 7. Maximum vertical force at column face normalized by connection nominal shear strength versus the maximum simulated vertical displacement at the removed column for all tested single-plate shear and double angle connections.

SUMMARY AND CONCLUSIONS

Tests on steel gravity framing system connections subjected to combined large rotation and tension were performed to investigate their potential contribution to structural

robustness. These tests showed that such connections are adversely affected by the large deformation demands associated with a column loss scenario and often are able to resist vertical forces at the column face of less than 15 % of their nominal shear strength. The connection strength and ductility are limited by the demands on the outer fiber (i.e., the outermost bolt and tributary plates or angles) and the limiting deformations of those outer fibers were quite consistent across connections with different depths.

ACKNOWLEDGEMENTS

This research was supported by the American Institute of Steel Construction (AISC) and the National Science Foundation under Grant No. CMMI-1000926. The steel wide flange sections used in the experiments were donated by AISC. Any opinions, findings, conclusions, and recommendations are those of the authors, and do not necessarily reflect the views of the sponsors.

REFERENCES

Astaneh-Asl, A., Jones, B., Zhao, Y., and Hwa, R. (2001). “Progressive collapse resistance of steel building floors." Report No. UCB/CEE-Steel-2001/03, University of California at Berkeley, Dept. of Civil and Environmental Engineering.

Astaneh-Asl, A., Madsen, E., Noble, C., Jung, R., McCallen, D., Hoehler, M. S., Li, W., and Hwa, R. (2001). “Use of catenary cables to prevent progressive collapse of buildings." Report No. UCB/CEE-Steel-2001/02, University of California at Berkeley, Dept. of Civil and Environmental Engineering.

Foley, C. M., Martin, K., and Schneeman, C. (2006). “Robustness in structural steel framing systems." Report No. MU-CEEN-SE-06-01, Marquette University.

Khandelwal, K., Kunnath, S., El-Tawil, S., and Lew, H. (2008). “Macromodel-based simulation of progressive collapse: Steel frame structures." Journal of Structural Engineering, 134(7), 1070-1078.

Main, J. A. and Sadek, F. (2013). \Modeling and analysis of single-plate shear connections under column loss." Manuscript Accepted to Journal of Structural Engineering.

Oosterhof, S. A. and Driver, R. G. (2012). “Performance of Steel Shear Connections under Combined Moment, Shear, and Tension." ASCE/SEI Structures Congress, Chicago, IL. 146-157.

Sadek, F., El-Tawil, S., and Lew, H. S. (2008). “Robustness of composite floor systems with shear connections: Modeling, simulation, and evaluation." Journal of Structural Engineering, 134(11), 1717-1725.

Thompson, S. L. (2009). “Axial, shear and moment interaction of single plate “shear tab" connections," PhD thesis, Milwaukee School of Engineering.

Weigand, J. M. (2014). “The Integrity of Steel Gravity Framing System Connections Subjected to Column Removal Loading." Ph.D. Dissertation in Civil Engineering, University of Washington, Seattle, WA (June).

Weigand, J. M. and Berman, J.W. (2014). “Integrity of Steel Single Plate Shear Connections Subjected to Simulated Column Removal." Journal of Structural Engineering, 140(5), 04013114.

Weigand, J. M. and Berman, J.W. (2016). “Integrity of Bolted Angle Connections Subjected to Simulated Column Removal." Journal of Structural Engineering, 142(3), 04015165.

Weigand, J. M., Meissner, J. E., Francisco, T., Berman, J. W., Fahnestock, L. A., and Liu, J. (2012). “Testing the Integrity of Steel Gravity Frames subjected to Large Vertical Deflections: Components." ASCE/SEI Structures Congress, Chicago, IL (March).

EXPERIMENTAL INVESTIGATION OF WOOD DECKING ASSEMBLIES ATTACKED BY FIREBRAND SHOWERS

Sayaka Suzuki
National Research Institute of Fire and Disaster (NRIFD), Japan
sayakas@fri.go.jp

Samuel L. Manzello
National Institute of Standards and Technology (NIST), USA
samuelm@nist.gov

ABSTRACT

Wildland-Urban Interface (WUI) fires have become a problem of great concern worldwide. Japan is located in one of the most earthquake prone areas of the world. After large earthquakes, many fires may simultaneously occur that can easily overwhelm fire-fighting resources. Since most Japanese cities are densely populated, severe fire spread occurs within these urban areas. An important mechanism of structure ignition in WUI fires and urban fires is the production of firebrands In WUI fires, decking assemblies have been observed to be an ignition vulnerability based on post-fire damage surveys conducted by NIST and elsewhere. Recently, the use of decking assemblies has also become more popular in Japan. The authors have conducted experiments and demonstrated the dangers of the dynamic process of continual, wind-driven firebrand showers landing onto decking assemblies for the first-time. In prior work, the wind speed was limited to 6 m/s (to compare to existing test methods). To this end, a series of experiments were conducted to examine possible vulnerabilities of wood decking assemblies to continuous, wind-driven firebrand showers under wind speeds of 8 m/s. Sections of wood decking assemblies (1.2 m by 1.2 m) were constructed and attached to a reentrant corner assembly lined with gypsum board in order to investigate decking assembly performance. The deck/reentrant corner assembly was then exposed to continuous, wind-driven firebrand bombardment generated by a full-scale Continuous Feed Firebrand Generator installed in the Fire Research Wind Tunnel Facility (FRWTF) at the Building Research Institute (BRI) in Japan. Finally, experiments were also conducted to determine if wall ignition was observed to occur due to the burning decking assembly. Results of these experimental investigations are provided in this paper.

INTRODUCTION

Large outdoor fires, such as Wildland-Urban Interface (WUI) fires in USA, bushfires in Australia, and urban fires that occur after earthquakes in Japan are a major concern. In particular, structure ignitions are a major problem. In urban fires or post-earthquake fires, fire spread between structures is of concern. An important factor of structure ignitions in large outdoor fires is acceleration of fire spread caused by firebrands produced from burning structures [1].

In large outdoor fires, decking assemblies have been observed to be an ignition vulnerability based on post-fire damage surveys conducted by NIST, IBHS, and CSIRO [2-4]. Recently, the use of decking assemblies has also become more popular in Japan. The Office of the State Fire Marshal (OFSM) in California adopted the test method known as State Fire Marshal (SFM) STANDARD 12-7A-4 [5]. The SFM test method is intended to determine the response of decks to firebrand exposure and is similar to ASTM E2726 [6]. Both of those test methods are extensions of ASTM E108 Roof test [7]. Namely, a firebrand is simulated by placing a burning wood crib on top of a section of a decking

Manzello, Samuel; Suzuki, Sayaka.
"Experimental Investigation of Wood Decking Assemblies Attacked by Firebrand Showers."
Paper presented at Interflam 2016, 14th International Conference on Fire Science and Engineering,
Windsor, England, United Kingdom. July 4, 2016 - July 6, 2016.

assembly under an air flow. The dynamic process of multiple firebrands bombarding decking materials as a function of time is not adequately represented or simulated in this standard. Based on firebrand attack from real WUI fires, it is expected that multiple firebrands would accumulate within gaps/crevices of decking materials. In addition to not simulating a dynamic firebrand attack, this test protocol does not fully consider possible differences between the size and mass of firebrands generated in this standard to actual firebrands produced from burning vegetation and structures.

Most recently, Hasburgh *et al.*, [8] conducted preliminary experiments to determine wall ignition vulnerabilities exposed to burning decking assemblies. In their experiments, the decking assemblies were 609 mm by 711 mm, and these were attached to a wall fitted with heat flux gages and thermocouples. Two ignition sources were considered: a below deck flame exposure using a propane burner, and an above deck test using a Class A burning brand, taken from the SFM test method above. For the Class A firebrand ignition experiments, the experimental data showed that wind speeds of 2.9 m/s (6.5 mph) and 5.4 m/s (12 mph) had the highest temperature and heat flux on the wall from the burning decking assembly. Hasburgh *et al.*, [8] desired that test methods developed in this paper and the data obtained can be used to gain insight into how a burning wood deck contributes to structural ignition. However, as pointed out by the authors, a great deal of work remains to be done, as the number of experiments were quite limited [8].

The authors have conducted experiments and demonstrated the dangers of the dynamic process of continual, wind-driven firebrand showers landing onto wood decking assemblies [9]. The accumulation of glowing firebrands resulted in flaming ignition of the deck boards. It was also observed that ignition of the deck boards produced smoldering ignition in the supporting members under the decking assembly. In that work, the wind speed was limited to 6 m/s (to compare to existing test methods).

In this present study, a series of experiments were conducted with wood decking assemblies under a wind speed of 8 m/s, higher wind speed than previous study. The reason for this is: (1) to examine possible vulnerabilities of wood decking assemblies to continuous, wind-driven firebrands under higher wind speed as firebrand accumulation patterns were expected to be influenced by wind speed, and (2) to examine the possibility of deck to wall ignition. An important aspect of the work presented here is the decking assemblies coupled to re-entrant corner assemblies are realistic scales, and the firebrand sizes were predicated on results measured from burning vegetation and actual WUI fires. Some details of these experiments were presented at recent Japanese conference but this paper presents new experimental results not covered in that two page extended abstract [10].

EXPERIMENTAL DESCRIPTION

Full-Scale Experiments at the Fire Research Wind Tunnel Facility (FRWTF)

Complete details of the full-scale decking assembly experiments conducted at 6 m/s are described elsewhere [9]. As the experimental protocols for firebrand generation were the same in the prior work when conducting experiments at 8 m/s (again done intentionally by design to compare results at various wind speeds), these details are repeated here for completeness.

The experiments made use of a full-scale Continuous Feed Firebrand Generator [9]. This version of the device is modified from the NIST Dragon and consists of two parts: the main body and continuous feeding component. The feeding system was connected to the main body and was equipped with two gates to prevent fire spread (described in more detail below). Each gate was alternatively opened and closed. A blower was connected to the main body and the purpose of the blower is also described below [9].

The feeding system consisted of a pneumatic cylinder coupled to a cylindrical container where wood pieces were stored. The pneumatic cylinder was contained inside a metal sleeve. Inside the metal sleeve, the sliding rod of the pneumatic cylinder was connected to a plate that allowed the volume of

wood contained within the sleeve to be varied. This volume was set precisely to allow a specific mass of firebrands to fall into this volume. When the air pressure was applied, the sliding rod of the pneumatic cylinder moved forward, forcing the wood pieces within the volume of the metal sleeve to the first gate, where they were then dropped into the second gate that leads to the Dragon where they were ignited. The gate system was required to contain the fire from spreading from the Dragon to the feed system and each gate was driven by pneumatic cylinders as well. For all tests, Douglas-fir wood pieces machined to dimensions of 7.9 mm (H) by 7.9 mm (W) by 12.7 mm (L) were used to produce firebrands. The same-size wood pieces were used to feed the bench-scale continuous Firebrand Generator in past studies and have been shown to be commensurate with sizes measured from full-scale burning trees, as well size distributions obtained from actual WUI fires [9].

An operational parameter that was varied was the blower speed. When the blower was set to provide an average velocity below 3.0 m/s measured at the exit of the Dragon when no wood pieces were loaded, insufficient air was supplied for combustion, and this resulted in a great deal of smoke being generated in addition to firebrands. At blower velocities above 3.0 m/s, smoke production was mitigated, but many firebrands produced were in a state of flaming combustion as opposed to glowing combustion. It is possible for firebrands to remain in a flaming state under an air flow, and it is reasonable to assume that some firebrands may still be in a state of flaming combustion upon impact. The purpose of this device is to simulate firebrand showers observed in long-range spotting and therefore glowing firebrands were desired [9].

The experimental device was installed inside the test section of BRI's FRWTF. The facility was equipped with a 4.0 m diameter fan to produce the wind field. The cross section of the FRWTF is 5.0 m wide by 4.0 m high. A parametric study was conducted to determine the influence of various conditions for the firebrands to arrive at the deck location [9]. As a result of these scoping investigations, the reentrant corner was placed at a distance of 3.25 m downstream of the full-scale Continuous Feed Firebrand Generator. The dimensions of the reentrant corner assembly were 1.2 m wide by 2.1 m high on each side. In all but one experiment, the walls of the reentrant corner were lined with gypsum board since a majority of these experiments were focused on deck assembly ignition, not the ignition of the wall assembly itself. Each of the decking assemblies was installed inside the reentrant corner assembly at the base (ground level). In all experiments, the decking assemblies were 1.2 m by 1.2 m. Three different types of wood decking boards were used: Western Red Cedar, Douglas-Fir, and Redwood. The dimensions of all decks boards were: 25.4 mm thick by 137 mm wide (Cedar), 25.4 mm thick by 139 mm wide (Douglas-Fir); 25.4 mm thick by 137 mm wide (Redwood). The spacing of the decks boards was 5 mm. The boards were installed using a wood supporting frame (boards were 38 mm thick by 140 mm height) with members spaced 16 in (406 mm) on center. **Figure 1** displays the orientation of the decking boards for all experiments.

A typical experiment was conducted in the following manner. The deck assembly was installed inside the reentrant corner. The wind tunnel speed was set to the desired level (e.g. 6 m/s or 8 m/s). Wood pieces were first loaded into the cylinder storage container and the air compressor needed to provide compressed air for the pneumatic cylinder and gate system was switched on (air compressor pressure was set to 0.7 MPa). The blower was set at 3.0 m/s, and two propane burners were ignited and inserted into the side of the device. The propane burners were operated continuously during the experiment. The pneumatic piston was then activated and the sliding rod was positioned to allow wood pieces to enter the volume in the metal sleeve. The sliding rod was moved to push the wood pieces (200 g) to the first gate. The gate was opened, closed, and the second gate was then opened, and the wood fell into the Dragon. The feeding was varied to determine the optimal conditions for continuous firebrand showers. It was observed that 200 g, fed into the Dragon every 15 s provided an adequate firebrand generation rate to ignite building materials. For completeness, 200 g corresponded to approximately 400 wood pieces deposited every 15 s [9].

The number flux (number of firebrand generated/m^2s), at the exit of the device, was measured at a feeding rate of 200 g every 15 s (800 g/min). To determine the number flux, the number of firebrands was counted at every frame of the video recording. Based on the analysis, the number flux reached a

steady value of 340.0/m^{2}s ± 10 % 300 s after feeding began. Mass flux data (mass of firebrands generated/m^{2}s) were calculated by multiplying the number flux and the average mass of each firebrand at a feed rate of 200 g every 15 s. To measure the firebrand mass, another set of experiments was conducted using a series of water pans placed downstream of the NIST full-scale Continuous Feed Firebrand Generator. Water pans were required in order to quench combustion of the firebrands. If the water pans were not used, the firebrands would continue to burn and by the time collection was completed; only ash would remain. After the experiment was finished, the pans were collected, and the firebrands were filtered from the water, using a series of fine-mesh filters. As in previous work, the mass versus drying time was monitored to determine the duration need to completely dry the firebrands. The mass was measured using a precision balance (0.001 g resolution). The mean mass and standard deviation of each firebrand were obtained and observed to be 0.05 ± 0.02 g. Therefore, the mass flux of generated firebrands was calculated to be 17 g/m^{2}s ± 10 %.

Fig. 1 Orientation of deck boards with respect to the direction of the firebrand-laden flow. Note that this drawing is for illustration purposes and is not intended to reflect the total number of deck boards used per experiment or the actual dimensions of the decking assembly itself [9].

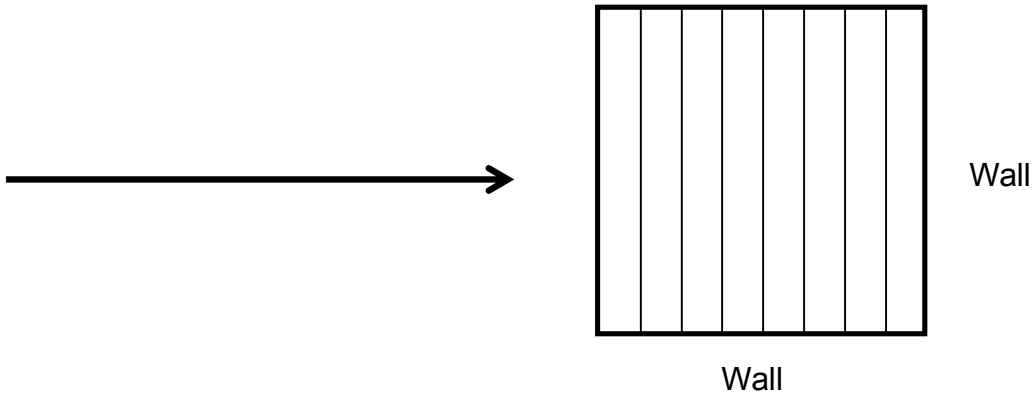

A great deal of effort has been made to link the firebrand sizes using this device with those from actual burning vegetation and actual WUI fires. Specifically, firebrand sizes produced using this device is commensurate with the characteristics of firebrand exposure at a single location during a severe WUI fire in California [9]. This is important since empirical characterization of firebrand exposure is extremely limited, especially with respect to firebrand size distributions during actual WUI fire conditions. Consistently small sizes of windblown firebrands, similar to those generated using this device, were observed by data collection adjacent to a home that survived severe interface fire exposure. This is in contrast with the size of firebrands referenced in existing test standards [5-7] and wildfire protection building construction recommendations.

The authors have also modified the firebrand feeding system described here in order to produce firebrands with size and mass distributions more similar to those measured from burning structures (nearly double the average projected area to the firebrands generated here). The interested reader is referred to the other paper presented in this conference where these distributions were directed at roofing assemblies [11].

RESULTS

Prior Work at 6 m/s

As the detailed results for experiments for 6 m/s are presented elsewhere, only a terse summary is provided here, please see [9] for significantly more details. For all three wood deck types considered, smoldering was observed to transition to flaming. **Figure 2** displays flaming ignition for Cedar, Douglas-Fir, and Redwood, respectively. These experiments clearly demonstrated that it is the

accumulation of glowing firebrands that pose an ignition danger. Specifically, glowing firebrands accumulate within the gaps of the deck boards, and when stacked together, these accumulated firebrands provide intense heat flux to the surface of the deck board, producing self-sustaining smoldering ignition of the boards that eventually transitions to flaming ignition.

It was not possible to determine the time for the exact onset of smoldering ignition. This was due the simple fact that the board gaps eventually were covered with firebrands. However, intense smoke generation, an indication of smoldering ignition, was observed. Therefore, the time to reach flaming ignition was determined for each wood type. The time was defined as the time *sustained* flaming was observed on the deck surface less the time the first firebrand landed on the deck surface. The time to reach flaming ignition was the longest, on average, for the Douglas-Fir decking assemblies. Cedar decking assemblies reached flaming ignition in the shortest time. The time to reach flaming ignition for Redwood decking assemblies occurred in between the times for other two wood types (see **Figure 3**). Firebrand generation was continued until sustained flaming ignition was observed.

Fig, 2 Flaming ignition of Cedar, Douglas-fir, and Redwood decking assemblies [9].

Finally, it is important to show that ignition of deck boards also began to produce smoldering ignition in the supporting members under the decking assembly. **Figure 4** shows the underside of the Cedar decking assembly (overall view and detail of one of the sections). Even long after the experiments were completed, sustained smoldering ignition was occurring in the supporting members. This provides direct confirmation of what has been observed in post-fire studies. Specifically, burning decking assemblies are extinguished by the fire service and these assemblies have been observed to re-ignite once again requiring additional suppression, or without suppression, resulting in the loss of the home in the WUI [4].

Fig. 3 Firebrand mass required for sustained flaming ignition as a function of wind speed. The 6 m/s data is taken from [9]. The average moisture content (MC) of all three wood decking types was 12 % (dry basis) for data at 8 m/s; the average MC was 11 % for all three wood types at 6 m/s [9].

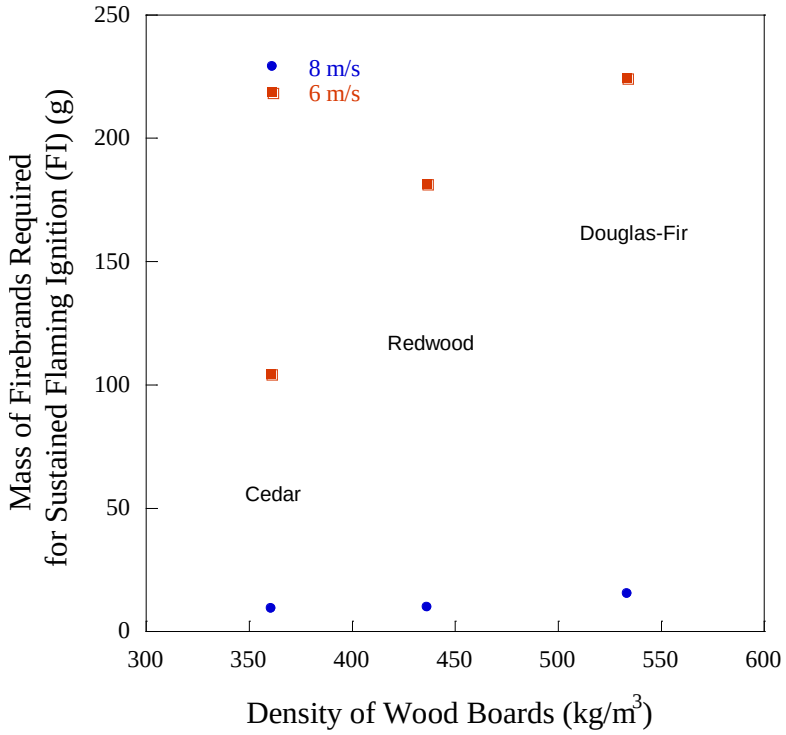

Fig. 4 (a) Picture of the underside of the decking assembly (Cedar); overall view. (b) Detail of the underside of the decking assembly (Cedar). The ignition process spread to the wood supporting members [9].

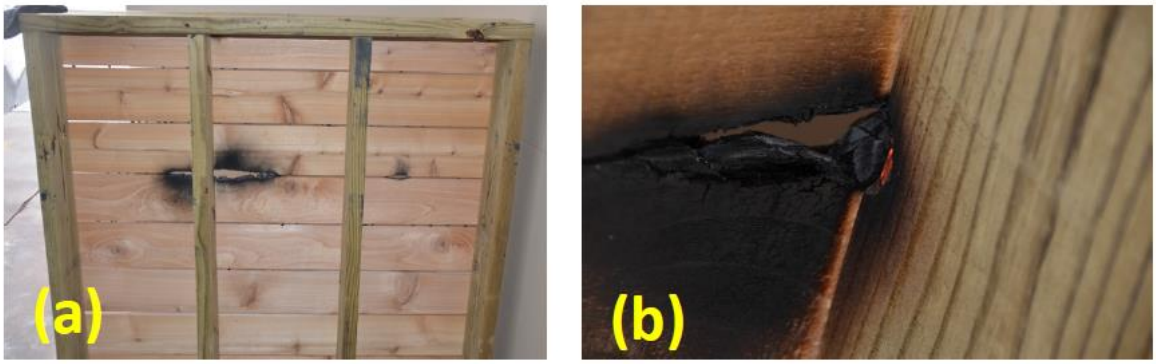

Wind Speeds of 8 m/s

Overall, it was observed that less firebrands accumulated on the surface of decking assemblies under a wind speed of 8 m/s than 6 m/s. Firebrands were observed to accumulate around the corner of deck/re-entrant corner assemblies (see **Figure 5-7**), while firebrands accumulated around the front under a wind speed of 6 m/s, and this resulted in flaming ignition (FI) of the decking boards. Ignitions occurred near the corner in 5 out of 6 experiments while in one case firebrands caused ignition near the front of the decking assembly. **Figures 5-7** shows the severity of ignition on the assemblies. Supporting members, as well as deck boards, were also found to be ignited. Firebrands that accumulated between the gaps caused ignitions.

The time to FI, which was defined as the time sustained flaming was observed on the deck surface less the time the first firebrand landed on the deck surface, was measured and the mass of firebrand required to FI was calculated as shown in **Figure 3**. Based on the calculation, approximately 7 to 25 g of firebrands were required to cause flaming ignition on deck boards under a wind speed of 8 m/s. Results were also compared with the data with 6 m/s [9]. Less than 10 % of mass of firebrands were required to cause flaming ignition of decking assemblies under a wind speed of 8 m/s than 6 m/s. The same trend (increased wood density, longer time to FI) was observed under wind speeds of 6 m/s and 8 m/s for cedar, redwood and Douglas-fir.

Fig 5 Cedar decking assembly ignition by firebrand showers at 8 m/s. Note that the circles denote the same ignition locations.

Fig 6. Redwood decking assembly ignition by firebrand showers at 8 m/s. Note that the circles denote the same ignition locations.

Fig 7. Douglas-fir decking assembly ignition by firebrand showers at 8 m/s. Note that the circles denote the same ignition locations.

Ignited Decking Assembly Resulting in Wall Ignition at 8 m/s

Two experiments were performed to examine the possibility of the deck to wall ignition. The same deck/reentrant corner assembly configuration, lined with one layer of gypsum board, was used for the first experiment. After the decking assembly was ignited by firebrand showers, combustion on the deck boards was allowed to continue. Fire spread through the assembly was observed even though the wall was protected by gypsum boards (see Figure 8). Results show that heat generated from the decking assembly's combustion was intense.

A second experiment was conducted to show the influence of bare (un-protected oriented strand board) placed adjacent to a cedar decking assembly (see **Figure 9**). Not surprisingly, the firebrands easily ignited the decking assembly as well as the OSB. The purposed of this experiment was to simply show a worst-case situation where a decking assembly is located next to unprotected wall assembly.

Fig. 8 Once ignition occurred, the cedar decking assembly was allowed to combust until flame spread was observed through the re-entrant corner. In this experiment, the wall as lined with gypsum board.

DISCUSSION

In these experiments, firebrand showers were observed to ignite the surface of the decking assemblies in the absence of other combustibles located on the surface of the deck. In this work, it was desired to determine if ignition was even possible under such conditions, so no combustible materials, such as leaf litter or lawn furniture, were placed on the decking assembly surface. In post-fire investigations, it has been suggested that if combustibles are located on the decking assembly surface, ignition by firebrand showers may be even easier [2-4].

Another interesting observation was that as the wind speed was increased, less firebrands were able to accumulate on the decking assembly surface. This was result was qualitatively similar to prior work where firebrand accumulation patterns were measured in front of walls under various wind speeds [12]. In that work, it was observed that less firebrands were able to accumulate as the wind speed was increased from 4 m/s to 10 m/s. In each of these studies, the same continuous-feed firebrand generator was used and was fed with the same wood pieces to generate similar firebrand size and mass distributions. This was done intentionally to afford a direction comparison. While firebrand accumulation patterns are dependent on several parameters in actual WUI fires, future studies should consider exposing assemblies to disparate firebrand size/mass distributions as well as higher wind speeds. Present work *suggests* it may in fact be more difficult for firebrands to accumulate on

decking assembly surface for wind speeds higher than 10 m/s.

Finally, it was observed that less than 10 % of mass of firebrands were required to cause flaming ignition of decking assemblies under a wind speed of 8 m/s than 6 m/s. The same result was found for both experiments under wind speeds of 6 m/s and 8 m/s for cedar, redwood and Douglas-fir. This result is postulated to be due to higher firebrand surface temperatures as the wind speed was increased. Manzello *et al.*, [13] quantitatively showed that glowing firebrand surface temperature increased as the wind speed was increased (see Figure 10 taken from [13]). Significant firebrand surface temperature increases are possible with attendant increases in wind speed.

Fig. 9 Once ignition occurred, the cedar decking assembly was allowed to combust until flame spread was observed through the re-entrant corner. In this experiment, the wall was not lined with gypsum board (bare OSB)

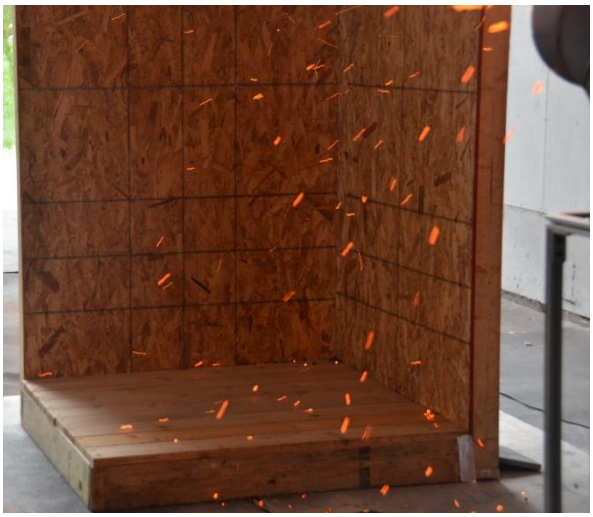

Figure 10 IR images of the glowing firebrand exposed to two different air flows [13].

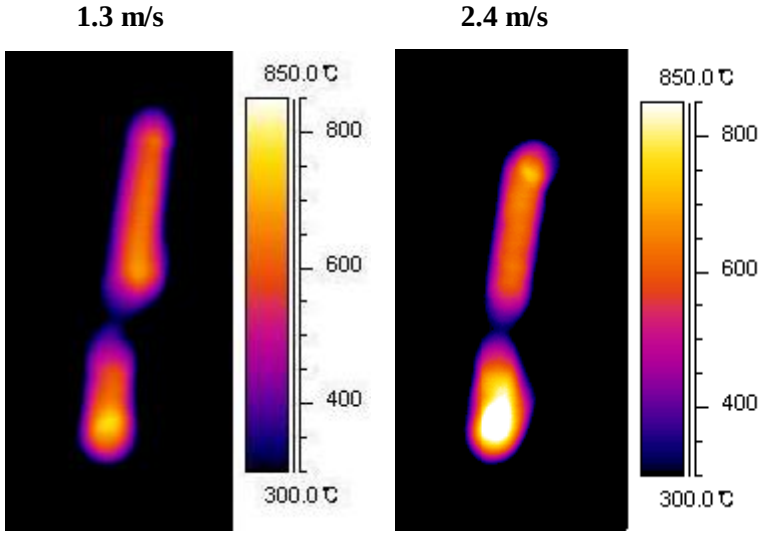

SUMMARY

A series of experiments with the decking assemblies exposed to continuous firebrand showers under a wind speed of 8 m/s were performed in order to observe the vulnerabilities to firebrands. Firebrands accumulated around the corner of the assemblies and caused flaming ignitions. The mass of firebrands required for flaming ignitions under a wind speed of 8 m/s were considerably less compared with those under a wind speed of 6 m/s. This result is postulated to be due to higher firebrand surface temperatures as the wind speed was increased.

Two experiments were performed to examine the possibility of the deck to wall ignition. The same deck/reentrant corner assembly configuration, lined with one layer of gypsum board, was used for the first experiment. After the decking assembly was ignited by firebrand showers, combustion on the deck boards was allowed to continue. Fire spread through the assembly was observed even though the wall was protected by gypsum boards. A second experiment was conducted to show the influence of bare (un-protected oriented strand board) placed adjacent to a cedar decking assembly. Not surprisingly, the firebrands easily ignited the decking assembly as well as the OSB. The purpose of this experiment was to simply show a worst-case situation where a decking assembly is located next to unprotected wall assembly.

In these experiments, firebrand showers were observed to ignite the surface of the decking assemblies in the absence of other combustibles located on the surface of the deck. In post-fire investigations, it has been suggested that if combustibles are located on the decking assembly surface, ignition by firebrand showers may be even easier.

ACKNOWLEGDEMENTS

This work was partly supported by JSPS Grant-in-Aid for Young Researchers (B) Grant Number 26750128. The help of Mr. Marco G. Fernandez of EL-NIST greatly appreciated.

REFERENCES

[1] Manzello, S.L., *et al.*, Workshop for Fire Structure Interaction and Urban and Wildland-Urban Interface (WUI) Fires – Operation Tomodachi Fire Research, *Fire Safety Journal* 59: 122-131

(2013).

[2] Maranghides, A., *et al*.., A Case Study of a Community Affected by the Waldo Fire – Event Timeline and Defensive Actions NIST TN1910, 2015.

[3] Quarles SL *et al*, Lessons learned from Waldo Canyon: Fire Adapted Communities Mitigation Assessment Team Findings. Insurance Institute for Business & Home Safety, 2013.

[4] Blanchi, R., and Leonard, J., Property Safety – Judging Structural Safety (Chapter 7), in: Community Bushfire Safety (Handmer, J., and Haynes, K., editors), CSIRO Press, 2008.

[5] California Building Standards Commission.

[6] ASTM E2726 (2012), ASTM International, West Conshohocken, PA.

[7] ASTM E108 (2003), ASTM International, West Conshohocken, PA

[8] Hasburgh *et al*., Laboratory Investigation of Fire Transfer from Exterior Wood Decks to Buildings in the Wildland–Urban Interface *Fire Techology*, published-online, 2016. DOI: 10.1007/s10694-016-0588-0.

[9] Manzello, S.L. and Suzuki, S., Exposing Decking Assemblies to Continuous Wind-Driven Firebrand Showers *Fire Safety Science* 11: 1339-1352, (2014) DOI: 10.3801/IAFSS.FSS.11-1339.

[10] Suzuki, S., *et al*., Proceedings of the 28th Annual JAFSE Symposium, in press (2016).

[11] Manzello, S.L., and Suzuki, S., Firebrand Ignition in Large Outdoor Fires: The Use of Full-Scale Experiments to Guide the Development of Laboratory Standard Test Methods, in these same INTERFLAM Proceedings, 2016.

[12] Manzello, S.L., and Suzuki, S., Firebrand Accumulation Zones in Front of Structures in Wildland-Urban Interface (WUI) Fires, Fire and Materials Conference, San Francisco, CA, 2015.

[13] Manzello, S.L., *et al*., Investigation on the Ability of Glowing Firebrands Deposited Within Crevices to Ignite Common Building Materials, *Fire Safety Journal* 44: 894-900 (2009).

ASCE/SEI 41 PREDICTED PERFORMANCE OF NEWLY DESIGNED BRBFS

M.S. Speicher[(1)], J.L. Harris[(2)]

[(1)] *Research Structural Engineer, National Institute of Standards and Technology, matthew.speicher@nist.gov*
[(2)] *Research Structural Engineer, National Institute of Standards and Technology, john.harris@nist.gov*

Abstract

Structural engineers in the United States have turned to performance-based design methodologies for design of new buildings in order to find improved design solutions as compared to those obtained using prescriptive design provisions of current model building codes or standards, such as ASCE/SEI 7. Performance-based seismic design of existing buildings has been implemented in the U.S. for seismic retrofits during the past decade (e.g., ASCE/SEI 41). Engineers are now starting to rely more heavily on the existing building procedures in ASCE/SEI 41 for the design of new buildings in order to obtain satisfactory seismic performance in the most cost effective manner. However, a translation between the two approaches is not direct and can often be a challenge due to perceived conservatism in the ASCE/SEI 41 procedures and the disjointed seismic performance expectations between ASCE/SEI 7 and ASCE/SEI 41. This paper presents the results of a performance assessment of six newly designed buckling-restrained braced frames to examine the correlation between ASCE/SEI 7 and ASCE/SEI 41. Two buildings are designed at each of the following heights: 4, 8, and 16 stories—one using the equivalent lateral force procedure and the other using the response spectrum analysis procedure. The performance of the buckling-restrained brace components is then assessed using the linear static, linear dynamic, nonlinear static, and nonlinear dynamic procedures in ASCE/SEI 41. The linear and nonlinear results generally indicate acceptable performance (except for the 8-story frames) which gives insight into how ASCE/SEI 7 and ASCE/SEI 41 compare. Additionally, the linear results are not always more conservative than the nonlinear results, which is counterintuitive and is discussed in the context of the results.

Keywords: buckling-restrained braced frames; steel structures; performance-based seismic design; seismic retrofit

1. Introduction

Prescriptive building code procedures, such as those found in the International Building Code [1] and ASCE/SEI 7 (hereafter ASCE 7) [2], may restrict design innovation, leading to potentially inefficient structural designs and higher construction costs. However, ASCE 7 allows alternative rational design methods to be used in lieu of its prescriptive provisions but provides no substantial guidance on implementing these methods. Therefore, many practitioners have turned to ASCE/SEI 41 (hereafter ASCE 41) [3], the standard for seismic assessment of existing buildings, to implement "first-generation" performance-based seismic design (PBSD) principles for the design of new buildings.

This paper presents select results from a study investigating the correlation between the intended seismic performance of an ASCE 7 code-compliant building and its performance as quantified using ASCE 41 procedures. This investigation is performed by evaluating the seismic performance of six buckling-restrained braced frame (BRBF) steel buildings designed for a region of high seismicity. The basic question is whether the standards for designing new steel buildings and assessing existing steel buildings provide consistent levels of performance. In this paper, the performance of the buckling-restrained braced (BRB) components is assessed using the linear static, linear dynamic, nonlinear static, and nonlinear dynamic procedures in ASCE 41. First, the archetype buildings will be presented. This is followed by the seismic performance assessment and associated discussions. This study is a follow-on to previous work on special concentrically braced frames [4, 5], eccentrically braced frames [6, 7], and special moment frames [8].

2. Archetype Building Design

A set of six office buildings is designed for this study. The building heights investigated are 4, 8, and 16 stories. The building framing layout is symmetric with five 9.1 m bays in the E-W direction and five 6.1 m bays in the N-S direction. The first story height is 5.5 m and the remaining story heights are 4.3 m. The seismic force-resisting system (SFRS) is composed of perimeter special moment frames (SMF) in the E-W direction and perimeter BRBFs in the N-S direction. Only the performance of the BRBFs in the N-S direction are investigated in this paper. The BRBs are placed in an inverted-V configuration in the 4-story frame and in a two-story X configuration in the 8- and 16-story frames. Additionally, the 16-story frames have the two braced bays placed adjacent to each other, as is indicated in the building plan view in Fig. 1.

The building is designed for all load effects in accordance with ASCE 7-10, AISC 360-10 [9], and AISC 341-10 [10]. Each building is assumed to be located in a region of high seismicity and is assigned to Seismic Design Category D with spectral accelerations at 0.2 s. (S_S) and 1.0 s. (S_1) of 1.5 g and 0.6 g, respectively. Two buildings are designed at each height, using seismic effects computed by either the equivalent lateral force (ELF) procedure or the response spectrum analysis (RSA) procedure. Though the ELF procedure is not allowed for the 16-story frame due to height limitations in ASCE 7, this limitation is ignored in this study. For the RSA-designed frames, the total modal base shear is scaled to 85 % of that computed using the ELF. Accidental eccentricity is included and orthogonality effects are considered. The redundancy factor, ρ, is 1.0. Effective seismic weights are set as dead load plus 20 % of the unreduced floor live load to represent partition weight (0.48 kN/m^2). For drift analysis (including period calculation) and stability verification, the story gravity load is set as dead load plus 25 % of the unreduced floor live load.

Floor and roof dead load consists of steel and slab weight (82 mm lightweight concrete (1760 kg/m^3) on 75 mm metal deck ≈ 2.2 kN/m^2). Superimposed dead load is 0.72 kN/m^2 for floors and 0.48 kN/m^2 for the roof, and includes mechanical, electrical, plumbing and other miscellaneous items. A 3.3 kN/m superimposed dead load is applied to the perimeter framing for façade weight (curtain wall). The edge of slab is 0.3 m from perimeter framing. Live load is 2.4 kN/m^2 for floors and 1.5 kN/m^2 for the roof.

The wind speed is 177 km/h and 116 km/h for the 700-year (design) and 10-year wind (drift), respectively. The structure is assigned Exposure B and not considered rigid. The gust factors (assuming 2 % damping) are 1.10 for the 700-year wind and 0.94 for the 10-year wind. Torsional wind effects are considered, and the

directionality factor, k_d, is 0.85. Wind effects do not control member sizes except for the bottom two stories of the 16-story frame.

The building is considered fixed at the seismic base. The base columns of the SFRS are embedded into a foundation wall. As such, column bases are modeled as fixed in the plane of the frame and pinned out-of-plane. Non-SFRS gravity column bases are considered pinned in both orthogonal directions. Strength and drift checks are done with a conventional second-order elastic analysis (i.e., constant stiffness matrix), and do not account for material nonlinearity or geometric imperfections (except for gravity-only load combinations). Drift limits are $h/50$ (amplified) for seismic and $h/400$ (elastic) for wind (10-year), where h is the story height. Composite action with the slab is not considered for checking seismic drifts but is included for checking wind drifts. For all the frames, the BRB, beam, and column member sizes and accompanying BRB stiffness modification factor, *KF*, are listed in Table 1. *KF* is used to adjust the axial stiffness of the steel core alone to that of the actual component.

The mathematical model is based on centerline dimensions with rigid-end offsets at the beam-to-column joints. The buildings are modeled in three dimensions in ETABS [11]. In the BRBFs, the beam ends are fixed to the columns to account for gusset plate restraint. The added stiffness caused by the gusset plate is approximated by doubling the adjacent member stiffnesses over an estimated plate length of 0.46 m (18 in.). At the end of the gusset plate, the beam is spliced with a shear tab connection, which is idealized as pinned. The brace is also assumed to be pinned at the ends, thus it only carries axial load. The brace member is assigned an area equal to the BRB steel core area and spans between work points (w.p.). Since the actual stiffness of the BRB is higher than $A_{sc} \times E / L_{w.p.}$ due to the stiffened portion outside the reduced core and the accompanying connection zone (i.e., gusset plate, member depths, etc.), a stiffness modifier, *KF*, is applied. These values are typically provided by the brace manufacturer. In this study, an average value from those received by several manufactures was used.

The floor slabs are modeled as semi-rigid membrane diaphragms with no out-of-plane bending stiffness and a 0.5 in-plane stiffness modifier to account for cracking at design loads. Gravity load-carrying framing is modeled to capture P-Δ effects. The gravity beams are assumed to be pinned at the ends to minimize their strength and stiffness contribution to the seismic performance of the BRBFs. Steel properties are those for A992 for beams and columns (F_y = 345 MPa and R_y = 1.1). The BRB core material is assumed to have an F_y = 317 MPa.

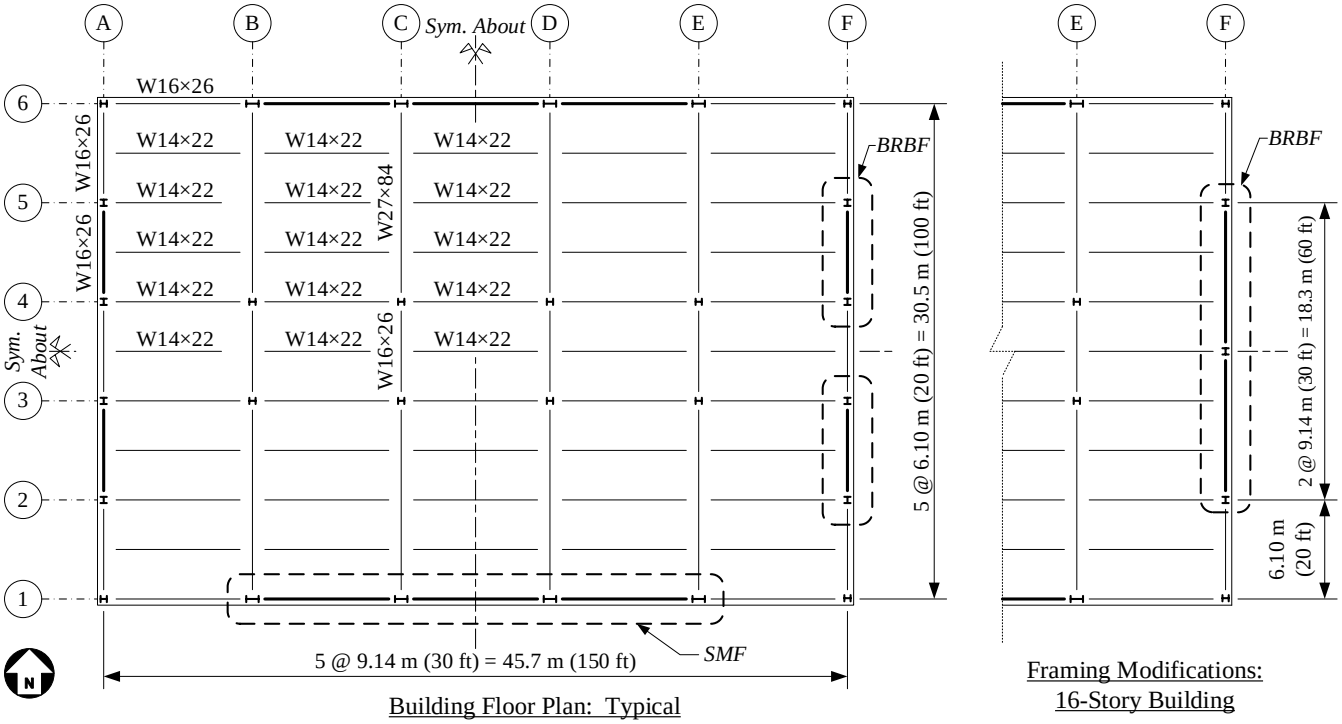

Fig. 1 – Building plan view for all designs used in this study

Table 1 – Member sizes for the BRBFs

	ELF designs						RSA designs				
	story	brace A_{sc} [1] (cm^2)	*KF*	beam	column		story	brace A_{sc} [1] (cm^2)	*KF*	beam	column
4-story	4	8.06	1.46	W16×31	W14×48	4-story	4	6.45	1.45	W16×31	W14×48
	3	12.9	1.46	W16×31	W14×48		3	11.3	1.45	W16×31	W14×48
	2	19.4	1.46	W16×31	W14×82		2	16.1	1.45	W16×31	W14×74
	1	22.6	1.46	W16×31	W14×82		1	17.7	1.45	W16×31	W14×74
8-story	8	6.45	1.50	W18×46	W14×38	8-story	8	6.5	1.48	W18×46	W14×38
	7	11.6	1.50	W16×31	W14×38		7	11.3	1.48	W16×31	W14×38
	6	16.1	1.50	W18×46	W14×68		6	11.3	1.48	W18×46	W14×68
	5	21.0	1.50	W16×31	W14×68		5	12.9	1.48	W16×31	W14×68
	4	21.0	1.50	W18×46	W14×132		4	14.5	1.48	W18×46	W14×82
	3	25.8	1.50	W16×31	W14×132		3	17.7	1.48	W16×31	W14×82
	2	25.8	1.50	W18×46	W14×145		2	19.4	1.48	W18×46	W14×132
	1	29.0	1.50	W18×60	W14×145		1	24.2	1.48	W18×60	W14×132
16-story	16	6.45	1.42	W18×55	W14×48	16-story	16	6.45	1.41	W18×55	W14×48
	15	11.3	1.42	W16×45	W14×48		15	11.3	1.41	W16×45	W14×48
	14	16.1	1.42	W18×55	W14×68		14	14.5	1.41	W18×55	W14×68
	13	21.0	1.42	W16×45	W14×68		13	16.1	1.41	W16×45	W14×68
	12	24.2	1.42	W18×55	W14×132		12	17.7	1.41	W18×55	W14×132
	11	27.4	1.42	W16×45	W14×132		11	19.4	1.41	W16×45	W14×132
	10	30.6	1.42	W18×55	W14×145		10	19.4	1.41	W18×55	W14×132
	9	33.9	1.42	W16×45	W14×145		9	24.2	1.41	W16×45	W14×132
	8	35.5	1.42	W18×55	W14×211		8	27.4	1.41	W18×55	W14×176
	7	38.7	1.42	W16×45	W14×211		7	29.0	1.41	W16×45	W14×176
	6	38.7	1.42	W18×55	W14×283		6	32.3	1.41	W18×55	W14×233
	5	40.3	1.42	W16×45	W14×283		5	33.9	1.41	W16×45	W14×233
	4	40.3	1.42	W18×55	W14×342		4	37.1	1.41	W18×55	W14×283
	3	40.3	1.42	W16×45	W14×342		3	41.9	1.41	W16×45	W14×283
	2	41.9	1.42	W18×55	W14×426		2	41.9	1.41	W18×55	W14×370
	1	45.2	1.42	W18×97	W14×426		1	46.8	1.41	W18×97	W14×370

(1) area of brace steel core

3. Seismic Performance Assessment

3.1 Modeling

For the linear analysis procedures, the buildings are modeled as described in the previous design section. For the nonlinear analysis procedures, the buildings are modeled in three dimensions using PERFORM-3D [12]. The modeling approach is similar to that used for the linear analysis procedures except that nonlinear elements are utilized. The BRBF beams and columns are modeled with nonlinear compound components to capture any nonlinear demands. Plastic hinges are placed in the beam just outside the brace-intersection and in the column above and below each beam-to-column connection. The BRBs are modeled using single compound elements connecting working points. These compound elements consist of an inelastic portion and an elastic portion. The inelastic portion is given properties consistent with the BRB steel core. The elastic portion is given an area such that the compound component achieves an overall stiffness equal to $KF \times A_{sc} \times E \; / \; L_{w.p.}$ The PERFORM-3D endzone feature for the BRB component is not used.

The BRB axial force-deformation behavior is modeled following guidelines given by Burkett and Lopez [13]. Table 2 summarizes the parameters adopted and Fig. 2(a) shows the generalized force-deformation curve that defines some of the variables. Plastic deformation parameters, (*a*, *b* and, *c* – not shown in the table or

figure), are taken directly from ASCE 41 Table 9-7, except no strength loss is captured due to the limitations in the PERFORM-3D BRB component. The nonlinear force-deformation model follows an asymmetric trilinear curve in tension and in compression. The adequacy of the model is qualitatively validated (i.e, by visual inspection) with test data as shown in Fig. 2 (b).

3.2 Hazard and Performance Level

The seismic hazard used for the performance assessment is the same as that used in the design. For the linear assessments, the forces are derived using the risk-targeted maximum considered earthquake (MCE_R) spectrum defined in ASCE 7. For the nonlinear static assessment, the MCE_R is similarly used to derive the target displacement value. For the nonlinear dynamic assessment, the MCE_R is used as the target spectrum for selecting and scaling the ground motions. The ground motions are selected from a suite of 44 records used in FEMA P695 [14]. Fourteen records with the least error (measured by computing the absolute area between the target spectrum and the individual spectrum over a structural period range of $0.2T_1$ to $1.5T_1$) are selected for the nonlinear analysis, but with no two records coming from the same station. The structural assessment is conducted using the collapse prevention (CP) performance level, which is the typical level considered when using an MCE-level hazard.

3.2 Analysis Details

The nonlinear analysis is set to terminate when the solution fails to converge or when an arbitrary roof drift ratio of 20 percent is reached. Though convergence limits and drift limits are often used as an indicator of collapse, in this study collapse is evaluated by using the assessment criteria alone (via allowable component limits in ASCE 41 Table 9-4 and Table 9-7). Collapse modes not explicitly modeled herein (e.g., failures in the gravity framing system) would likely occur well before 20 percent is reached.

Table 2 – Inelastic component properties used in PERFORM-3D model calibration

Variable	*K0*	*KF*	*FY*	*FU0*	*FUH(tension)*	*FUH(compression)*	*DU*	*DX*
Value	K_{sc}	$0.02K_{EFF}$ (1)	$0.89P_{y,sc}$ (2)	$1.05P_{y,sc}$ (3)	$1.34P_{y,sc}$	$1.51P_{y,sc}$	$0.0058L_{yz}$ (4)	$0.04L_{yz}$

(1) K_{sc} = brace core stiffness (2) K_{EFF} = brace overall elastic stiffness (3) $P_{y,sc}$ = yield strength of steel core, $A_{sc}F_y$ (4) L_{yz} = length of the yield zone

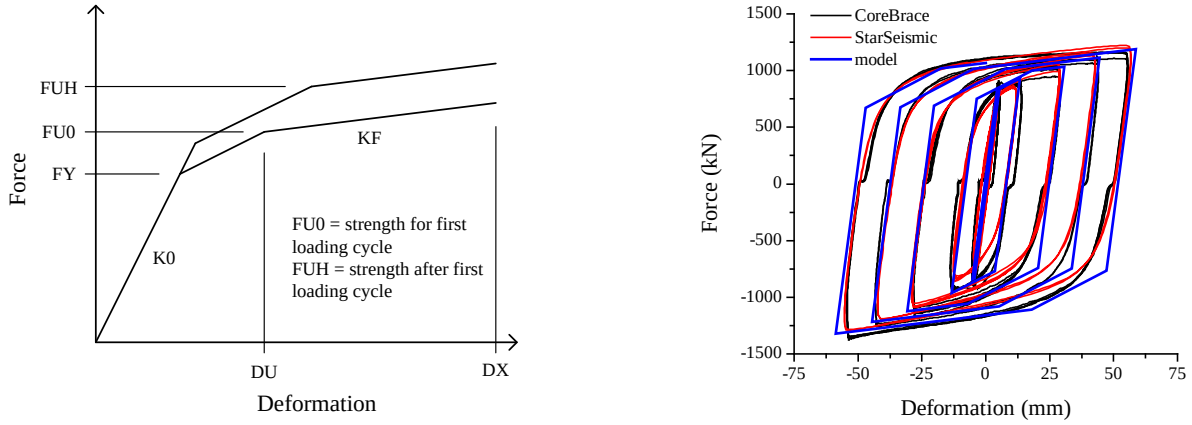

(a) (b)

Fig. 2 – (a) Generic force-deformation plot showing the BRB inelastic component model property definitions in PERFORM-3D and (b) force-deformation response of BRB inelastic portion assuming L_{yz} = 3.3 m (130 in.) and A_{sc} = 29 mm^2 (4.5 in^2). The experimental data is converted from data reported for a StarSeismic BRB in Merritt, Uang [15] and a CoreBrace BRB in Newell, Uang [16].

4. Seismic Assessment Results

4.1 Results Format

The results are presented in terms of a normalized demand-capacity ratio, DCR_N. If the value is less than unity, the component satisfies the acceptance criteria for the given hazard / performance level combination. This DCR_N is not to be confused with the *DCR* defined in ASCE 41 §7.3, which is the demand-capacity ratio considering unreduced earthquake forces. For the linear analysis, DCR_N is defined in Eq. (1) and Eq. (2):

$$\textit{Deformation-controlled}: \quad DCR_N = \frac{Q_{UD}}{m\kappa Q_{CE}} \tag{1}$$

$$\textit{Force-controlled}: \quad DCR_N = \frac{Q_{UF}}{\kappa Q_{CL}} \tag{2}$$

where Q_{UD} is the deformation-controlled demand, Q_{UF} is the force-controlled demand, Q_{CE} is the expected strength, Q_{CL} is the lower-bound strength, m is the component demand modification factor, and κ is the knowledge factor (taken as unity in this study).

For the nonlinear analysis results, DCR_N is defined in Eq. (3) and Eq. (4):

$$\textit{Deformation-controlled}: \; DCR_N = \frac{Q_{UD}}{\kappa Q_{CE}} = \begin{cases} \textit{Total} & \dfrac{\theta_{plastic} + \theta_{elastic}}{\kappa\left(\theta_y + \theta_{pe} + \theta_{p,AC}\right)} \\ \textit{Plastic} & \dfrac{\theta_{plastic}}{\kappa\theta_{p,AC}} \end{cases} \tag{3}$$

$$\textit{Force-controlled}: \; DCR_N = \frac{Q_{UF}}{\kappa Q_{CL}} \text{ and } DCR_N = \frac{\theta_{total}}{\kappa\theta_y} \tag{4}$$

where $\theta_{plastic}$ is the plastic deformation, $\theta_{elastic}$ is the elastic deformation, θ_y is the expected yield deformation, θ_{pe} is the post-yield elastic deformation, θ_{total} is the total deformation, and $\theta_{p,AC}$ is the acceptance criterion based on plastic deformation.

For steel components in ASCE 41, inelastic deformation parameters are provided in terms of plastic deformations rather than total deformations. The choice of whether to use plastic deformations or total deformations will depend on what nonlinear component model is adopted for each component action (e.g., moment-curvature hinge or moment-rotation hinge). Consequently, yield and post-yield elastic deformations may need to be added to the values given in ASCE 41 to determine the total deformation for each structural performance metric. For the axial deformation in the BRBs, PERFORM-3D outputs the results in terms of total deformations and these total deformations are used directly in the assessment.

Once the DCR_N values are obtained, they are presented together on one plot for all four analysis procedures. This is done to easily compare the results, though it should be noted that linear and nonlinear DCR_N values are arrived at in a fundamentally different way (e.g., linear is calculated based on forces vs. nonlinear is calculated based on deformations).

4.2 Results and Discussion

The brace results for the 4-, 8-, and 16-story ELF-designed frames are presented in Fig. 3, Fig. 5, and Fig. 7, respectively. The brace results for the 4-, 8-, and 16-story RSA-designed frames are presented in Fig. 4, Fig. 6, and Fig. 8, respectively. In the figures, L is for Left and R is for Right. All four analysis procedures are represented in the graphs. Three of the results (i.e., lines) are labeled as LSP for the linear static procedure, LDP for the linear dynamic procedure, and NSP for the nonlinear static procedure. The results from the nonlinear dynamic procedure (NDP) are reported using the median, mean, 84th percentile, and mean plus one standard deviation for the ground motion set.

For the 4-story frames, the results generally indicate acceptable performance of the BRBs. The linear procedures tend to be more conservative than the nonlinear procedures. The linear static procedure indicates some of the braces fail the collapse prevention criteria for the ELF-designed frame and all of the braces fail the CP criteria for the RSA-designed frame. However, the maximum DCR_N value is approximately 1.2, which may not be too concerning given the inherent uncertainty in the assessment. The nonlinear procedures indicate that the BRBs do not experience deformations greater than the allowable, with the dispersion of results (84th percentile and the mean + std.) showing a reasonably tight distribution that suggests that none of the frames lose stability.

For the 8-story frames, the results are noticeably different than those seen in the 4-story frames. The linear procedures tend to be less conservative than the nonlinear dynamic procedure, which is not expected. For the ELF-designed frame, the linear procedures show the braces passing the assessment. For the RSA-designed frame, the LDP indicates acceptable performance but the LSP indicates failure. This is not surprising given the contrast in the lateral load distributions used in the RSA design and the LSP assessment.

In contrast to the linear procedures, the nonlinear dynamic procedure suggests the worst performance. Both the ELF-designed frame and the RSA-designed frame have brace problems at the mid-height of the building. The problem is more pronounced for the RSA-designed frame, which can again be explained by the reduced member capacities resulting from the design force distribution. The mean and median values are reasonably close together, suggesting there is limited large inelastic demand excursions. The dispersion in demand is largest for the first story brace in the RSA-designed frame, suggesting that the building reaches a point of instability. This highlights how the mean value may not be a good measure of the brace performance, especially for this first story result. The inherent assumption in the mean value presented is that the DCR_N values are distributed normally. However, when a frame goes highly nonlinear and reaches large drift levels, the results may be better represented by a lognormal distribution [17]. Therefore, the median or the mean (calculated assuming a lognormal distribution) are more significant.

For the 16-story frames, the results indicate better performance than seen in the 8-story frames and are more in line with those seen in the 4-story frames. For the 16-story ELF-designed frame, the linear procedures

indicate the braces pass the assessment criteria; maximum DCR_N values are around 0.8. Though not previously discussed, the *design* demand-capacity ratios are in the 0.8-0.9 range, thus the values given by the assessment methodology are less conservative (i.e., lower) for this case. This is partly due to the difference in how ASCE 7 and ASCE 41 determine the period used in the force calculations. ASCE 7 requires the period not be greater than an upper-bound (i.e., $C_u T_a$), and ASCE 41 allows the period computed in analysis to be used directly. This can have a significant effect on the forces applied to the system.

For the 16-story RSA-designed frame, the linear static procedure pushes some of the mid-height braces beyond their allowable deformations. Given the contrast in the design and assessment force distributions for this case, failure of these mid-height braces is not surprising. Nevertheless, the maximum DCR_N values are around 1.1, which suggest little change would need to be made to the design to pass the assessment.

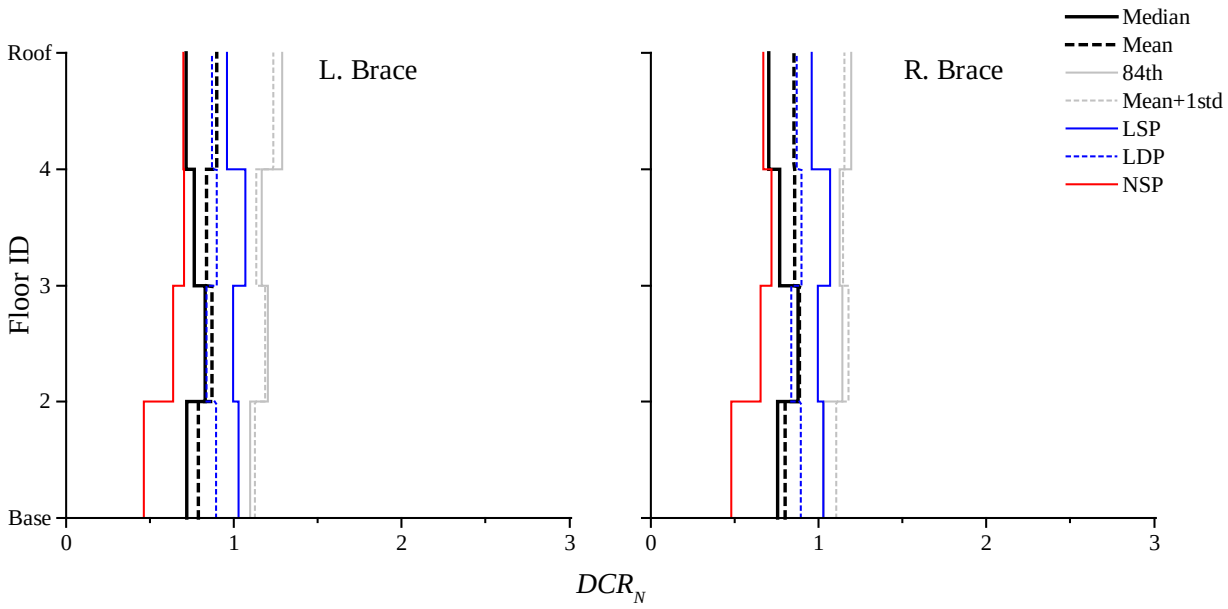

Fig. 3 – Results for the 4-story ELF-designed frame (considering CP at MCE_R)

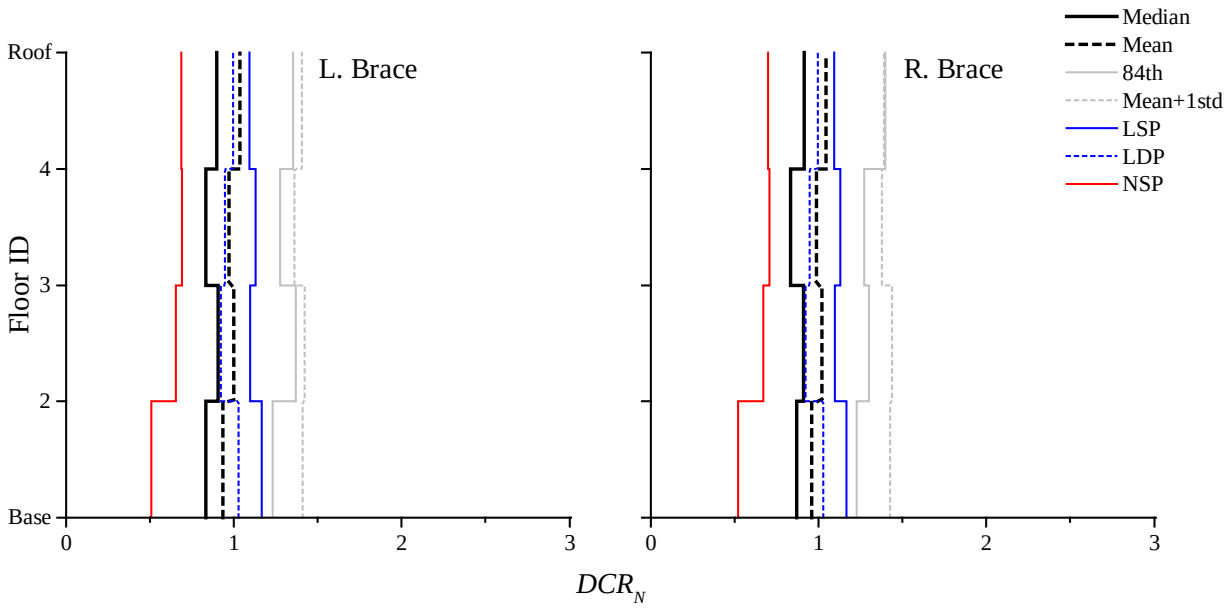

Fig. 4 – Results for the 4-story RSA-designed frame (considering CP at MCE_R)

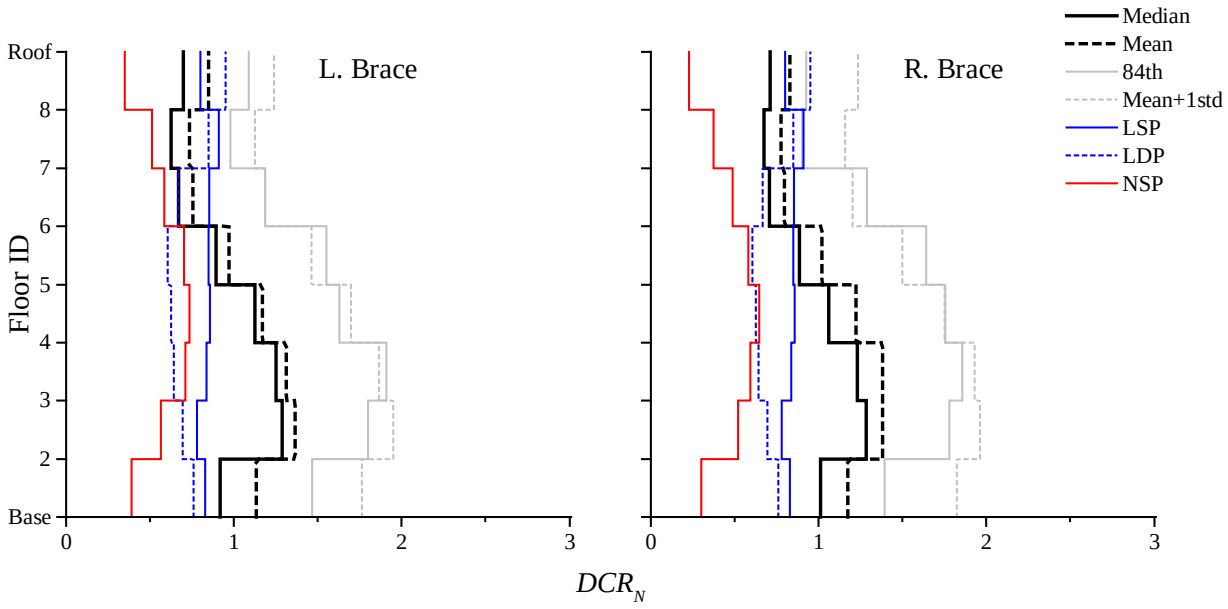

Fig. 5 – Results for the 8-story ELF-designed frame (considering CP at MCE_R)

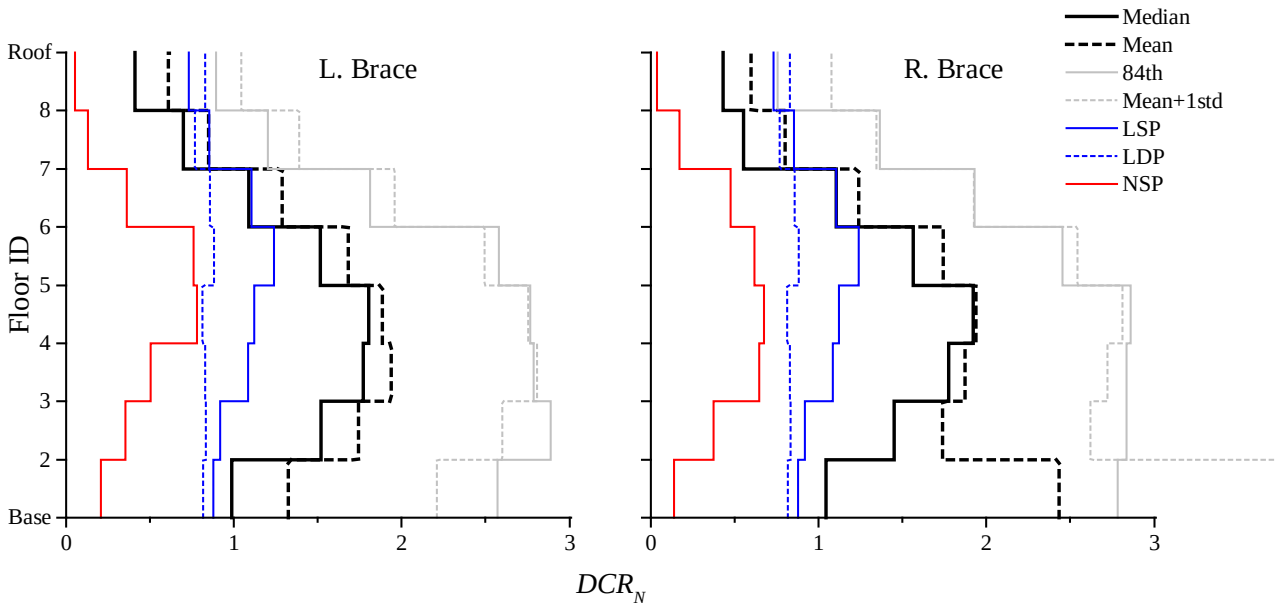

Fig. 6 – Results for the 8-story RSA-designed frame (considering CP at MCE_R)

The nonlinear dynamic results for the 16-story frames take on different deformation patterns as compared to the linear results, though the median DCR_N value stays below unity in all of the braces. In the ELF-designed frame, the highest demands are in the lower and upper stories, which highlights the influence of higher mode effects. Higher modes are not accounted for in the ELF design force distribution. However, the ELF-designed frame has sufficient capacity to pass the collapse prevention assessment criteria. It also passes the nonlinear static assessment.

In contrast to the ELF-designed frame, the RSA-designed frame has a more uniform distribution of peak demands over its height. This suggests that the RSA-designed frame's design force distribution is more in line with the nonlinear demands from the earthquake suite. The dispersion of DCR_N value is also higher for the RSA-designed frame, especially in the story range of maximum demands. This dispersion indicates that there are several ground motions records that are pushing the frame to large drift levels.

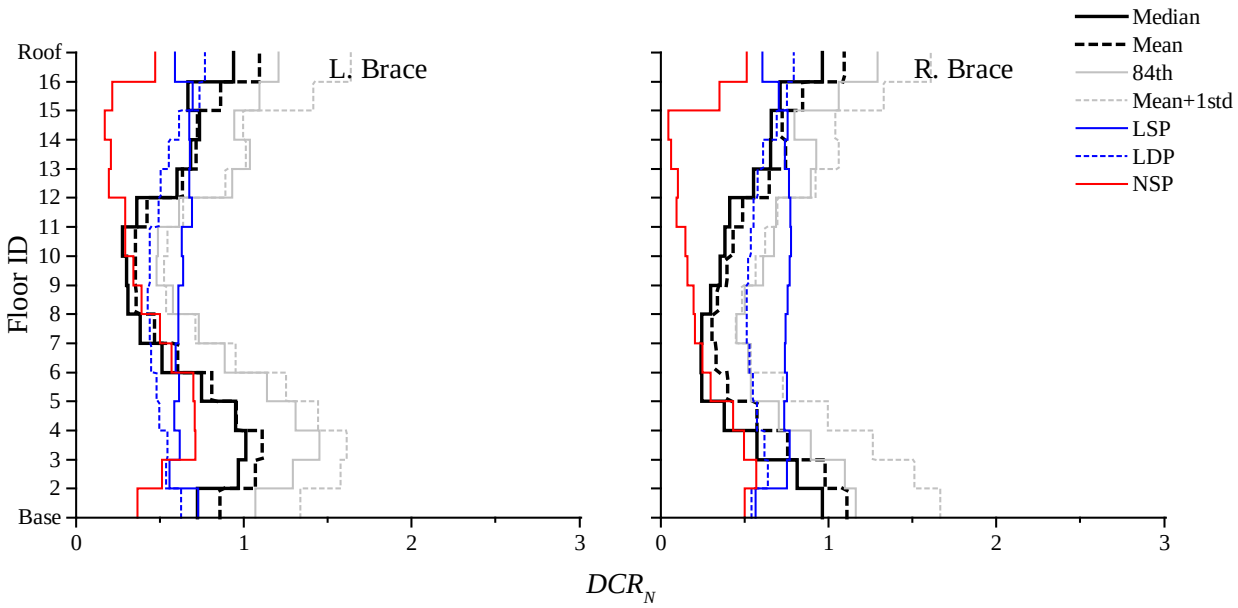

Fig. 7 – Results for the 16-story ELF-designed frame (considering CP at BSE-2)

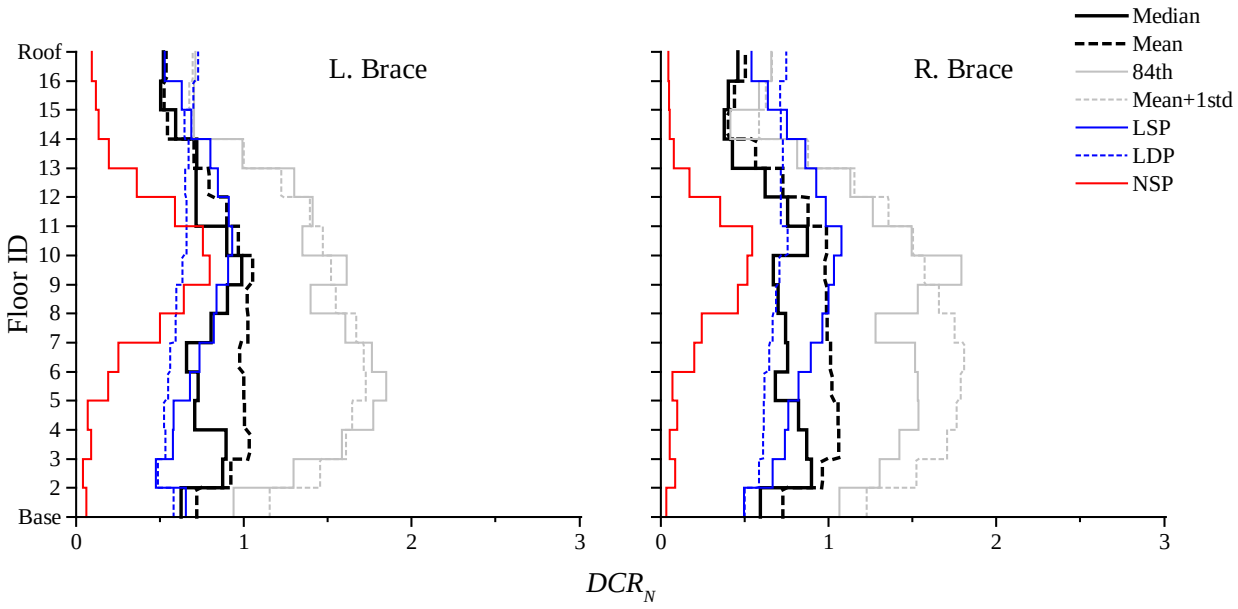

Fig. 8 – Results for the 16-story RSA-designed frame (considering CP at BSE-2)

4. Conclusions

This paper investigates the ASCE 41 predicted seismic performance of a suite of buckling-restrained braced frames designed with ASCE 7 in order to compare the consistency of the two standards. The linear and nonlinear results generally indicate acceptable performance for the buckling-restrained braces when subjected to a risk-targeted maximum considered earthquake and assessed with the collapse prevention performance level, except for the 8-story frames. The braces in the 8-story frames failed the assessment criteria for both the linear and nonlinear procedures, which highlights the challenges of capturing the nonlinear response of a building with linear design procedures. Interestingly, the ELF-designed frames generally performed better than the RSA-

designed frames. Amongst the four assessment procedures employed, a variety of performance outcomes were reached. The linear results are not always more conservative than the nonlinear results, which is counterintuitive and could discourage use of ASCE 41 in new building design or the retrofit of an existing building. Additionally, the nonlinear static procedure always indicated satisfactory performance, which is typically thought to be more conservative than the nonlinear dynamic procedure. Though all the components of the BRBF were not assessed in this paper (e.g., beams and columns), the results herein give the engineer examples of how the braces of a BRBF will perform, as indicated by an ASCE 41 assessment, for three different heights and two different design approaches. Ultimately, the results from this study would need to be compared with the results provided from analyzing the buildings in a FEMA P695 analysis. This comparison would provide the supplementary information needed to correlate the two standards. However, ASCE 41 has not yet moved to a risk-based philosophy aligned with ASCE 7.

4. Disclaimer

Certain commercial software may have been used in the preparation of information contributing to this paper. Identification in this paper is not intended to imply recommendation or endorsement by NIST, nor is it intended to imply that such software is necessarily the best available for the purpose. Mean, median, and associated variances are reported for the nonlinear dynamic results, which illustrates some of the uncertainty inherent in the selection process for input ground motions. Beyond this important issue, no formal investigation of uncertainty or error is included in this study. The question of uncertainty in the analytical models, solution algorithms, and material properties are beyond the scope of the work reported here.

5. References

[1] ICC (2012): *International Building Code (IBC)*. Washington, DC: International Code Council.

[2] ASCE (2010): *Minimum Design Loads for Buildings and Other Structures*, in *ASCE/SEI 7-10*, American Society of Civil Engineers: Reston, VA.

[3] ASCE (2013): *Seismic Evaluation and Retrofit of Existing Buildings*, in *ASCE/SEI 41-13*, American Society of Civil Engineers: Reston, VA.

[4] Harris JL, Speicher MS (2015): *Assessment of First Generation Performance-Based Seismic Design Methods for New Steel Buildings Volume 2: Special Concentrically Braced Frames*, National Institute of Standards and Technology: Gaithersburg, MD.

[5] Speicher MS, Harris III JL (2016): Collapse prevention seismic performance assessment of new special concentrically braced frames using ASCE 41. *Engineering Structures*. 126: p. 652-666.

[6] Speicher MS, Harris III JL (2016): Collapse Prevention Seismic Performance Assessment of New Eccentrically Braced Frames using ASCE 41. *Engineering Structures*. 117: p. 344-357.

[7] Harris JL, Speicher MS (2015): *Assessment of First Generation Performance-Based Seismic Design Methods for New Steel Buildings Volume 3: Eccentrically Braced Frames*, National Institute of Standards and Technology: Gaithersburg, MD.

[8] Harris JL, Speicher MS (2015): *Assessment of First Generation Performance-Based Seismic Design Methods for New Steel Buildings Volume 1: Special Moment Frames*, National Institute of Standards and Technology: Gaithersburg, MD.

[9] AISC (2010): *Specification for Structural Steel Buildings*, in *ANSI/AISC 360-10*, American Institute of Steel Construction: Chicago, IL.

[10] AISC (2010): *Seismic Provisions for Structural Steel Buildings*, in *ANSI/AISC 341-10*, American Institute of Steel Construction: Chicago, IL.

[11] CSI (2013): *Extended Three Dimensional Analysis of Building Systems*, in *ETABS*, Computers and Structures, Inc.: Berkeley, CA.

[12] CSI (2013): *Nonlinear Analysis and Performance Assessment for 3D Structures*, in *PERFORM 3D*, Computers and Structures, Inc.: Berkeley, CA.

[13] Burkett L, Lopez W (2011): *Perform Nonlinear Component Modeling of StarSeismic' Powercat™ BRBs*.

[14] FEMA (2009): *Quantification of Building Seismic Performance Factors*, in *FEMA P695*, Department of Homeland Security: Washington, D.C.

[15] Merritt S, Uang C-M, Benzoni G (2003): *Subassemblage Testing of Star Seismic Buckling-Restrained Braces*, University of California, San Diego.

[16] Newell J, Uang C-M, Benzoni G (2006): *Subassemblage Testing of CoreBrace Buckling-Restrained Braces (G Series)*, University of California, San Diego.

[17] Uribe R, Sattar S, Speicher MS, Ibarra L (2017): Influence of Ground Motion Selection on the Assessment of a Steel Special Moment Frame. in *16th World Conference on Earthquake Engineering, 16WCEE 2017*. Santiago, Chile.

A practical verification and validation approach for Computational Wind Engineering simulations using an experimental design technique

Réamonn Mac Réamoinn [a], DongHun Yeo [b]

[a] *Arup, Dublin, Ireland, r.macreamoinn@gmail.com*
[b] *National Institute of Standards and Technology, Gaithersburg, Maryland, U.S.A., donghun.yeo@nist.gov*

SUMMARY:
Understanding the sensitivity of computational wind engineering (CWE) solutions to simulation parameters facilitates the development of useful solutions. The traditional approach adopted in other fields through verification and validation (V&V) with well-defined benchmarks is not always possible in CWE. Complex flow phenomena in even simple flow conditions are not readily defined analytically or measured experimentally. This study aims to evaluate the sensitivity of CWE solutions to various simulation parameters with a view to identifying the optimal simulation configuration yielding more reliable results with the least computational effort. To this end the study uses the experimental design technique and seeks to verify the optimal size of the computational domain and level of mesh refinement.

Keywords: Computational Wind Engineering, Experimental Design Technique, Orthogonal Fractional Factorial Design, Square Cylinder Flow, Vortex Shedding

1. INTRODUCTION

In Computational Wind Engineering (CWE), a subset of computational fluid dynamics (CFD), results of simulations of the same flow condition using different model configurations can vary widely. This undermines user confidence in CWE solutions. If CWE is to be used as a tool for the design of special structures, such as tall buildings or long span bridges, in conjunction with or in place of wind tunnel testing, it is necessary to improve its credibility.

To facilitate the development of more accurate and reliable simulations it is necessary to understand the sensitivity of CWE solutions to simulation parameters. In other fields, this can be achieved through verification and validation (V&V) with well-defined benchmarks (Oberkampf & Trucano, 2008). However, in CWE complex flow phenomena can occur under relatively simple flow conditions. These phenomena, such as boundary layer separation and signature turbulence, are not readily defined analytically nor easily measured experimentally. Roache (1997) recognized that "useful *a priori* estimation is not possible for nontrivial fluid mechanics problems". Therefore, it is not always possible to adopt the same approach for CWE.

This study aims to evaluate the sensitivity of CWE solutions to various simulation parameters with a view to identifying the optimal simulation configuration yielding more reliable results with the least computational effort. In any simulation or experiment, the accuracy of the solution is improved through the reduction of error. The confidence in the reliability of the solution is

related to the quantifying the error and the identification of its sources.
The convergence of a solution is linked to the reduction of the numerical errors associated with simulation parameters. This study proposes a practical method that helps evaluate if a solution can be considered as being independent of simulation parameters. To this end it develops a V&V approach consisting of an experimental design technique for assessing the convergence of a solution. This technique makes it possible to identify the extent to which simulation results are sensitive to parameter values, evaluate the influence of single parameters and their interaction on the accuracy of the solution, and provide the optimal set of parameter values that minimize numerical errors while using typical computational resources.

As an application of the V&V approach developed in this study, the high Reynolds number flow around a square cylinder is examined. In spite of its geometric simplicity, complex flow phenomena can develop, such as vortex shedding and boundary layer separation. However, unlike in the case of a circular cylinder flow, the square cylinder flow has fixed points of separation, which implies that the flow could be assumed to be Reynold's number independent. This fundamental problem in bluff body aerodynamics has been extensively researched in both numerical simulations (Dahl, 2014, Franke et al., 1990, Lee and Bienkiewicz, 1998, Shimada and Isihara, 2002, Tamura and Yoshiyuki, 2003, Tain et al., 2012) and wind tunnel tests (Bearman and Trueman, 1972, Bearman and Obasaju, 1982, Durao et al., 1988, Lee, 1974, Lyn and Rodi, 1993, Lyn et al., 1995). Therefore, it is considered a suitable case for assessing the effectiveness of this approach.

2. EXPERIMENTAL DESIGN TECHNIQUE

Experimental design is a statistical tool that makes it possible to achieve experiment objectives by planning efficiently experimental procedures in which changes in one or more process parameters affect one or more output responses. Once the objective of a study and the process factors are determined, well-established experimental design techniques economically maximize the amount of information obtainable from a minimized amount of experimental efforts.

A traditional and common approach to experimental design involves only changing a single input parameter or factor between runs, which is known as the *one factor-at-a-time* (1FAT) *design*. As noted by Box et al. (1978), "the method provides an estimate of the effect of a single variable at selected *fixed* conditions of the other variables." It assumes the effect would be the same irrespective of the condition of the other variables and therefore, it neglects any interaction between variables. Given that 1FAT design approach ignores interactions, its estimates are biased and lack of precision if the interaction between any parameters is significant.

It is possible to design experiments to take account of interaction between parameters through orthogonality. In orthogonal designs, multiple parameters are changed between experiments. However, through controlling the adjustments to the parameters, it is possible to ensure the interaction effects between parameters balance. As a result, orthogonal design facilitates more accurate estimates of main and interaction effects of parameters when compared with more widely used approaches. When all the possible combinations of parameters are considered, it is known as a *full factorial design*. This takes account of all the interactions between parameters

while producing unbiased estimates. However, it does demand a large number of experiments be undertaken. In a *fractional factorial design*, a smaller appropriately chosen subset is adopted. It takes advantage of redundancy within the full factorial design to produce equivalent estimates while significantly reducing the number of experiments undertaken without compromising the capacity to discrimination between parameters.

In this study, it is proposed to adopt a modified orthogonal fractional factorial approach to evaluate the sensitivity of the CWE solution to a variety of parameters in minimized but well selected simulation cases. The modification involves the inclusion of an additional case, which has an intermediate value of parameters between their extreme values in the traditional factorial approach. The addition of the 'center' case makes it possible to investigate the influence of parameters on simulation results within their extreme bounds, and to assess convergence of the results as the parameter values are adjusted.

3. NUMERICAL ARRANGEMENT

This study examines 2D flow around a square cylinder. The characteristic dimension, H, of the square cylinder is taken as 0.04 m and the freestream velocity, U_∞, of the flow is taken as 8.2 m/s. The flow medium is air with a density $\rho = 1.20$ kg/m^3 and a kinematic viscosity, $\upsilon = 1.51 \times 10^{-5}$ m^2/s. The Reynolds number is therefore 20000. The turbulence effects in the flow are modelled using the Spalart-Allmaras turbulence model. A turbulence intensity I = 2 % is assumed. The simulations are carried out using the open source CFD package, OpenFOAM (The OpenFOAM Foundation, 2016). In all cases, a steady state solution was used as an initial condition. The steady state and transient simulations were solved using simpleFoam and pimpleFoam, respectively.

The initial and boundary conditions are specified on the domain boundaries. The inflow condition is prescribed as a uniform freestream velocity of 8.2 m/s normal to the incoming flow boundary surface. The turbulent viscosity, υ, is defined as 5.62×10^{-4} m^2/s on the inflow boundary. The dynamic pressure was prescribed as zero on the outlet boundary. A 'no slip' condition was applied to the square cylinder surface and wall functions were used to approximate the flow near the cylinder surfaces. A 'slip' condition was applied to the top and bottom boundaries, while the front and back boundaries were defined as 'empty' condition to maintain the 2D flow conditions.

The configuration of the mesh within the computational domain is illustrated in Figure 1 and 2. The background mesh, which has a cell size of H/8, consists of a uniform orthogonal hexagonal mesh. The mesh refinement occurs locally to the square cylinder. The mesh layers with H/8 of the cylinder surface have a cell height of H/64. The mesh transitions from H/8 to H/64 within the refinement zone. Depending on the simulation case, the cell widths along the cylinder surface range between H/16 and H/64. The transitioning in the cell widths also occurs within the refinement zone.

This study investigates the influence of four simulation parameters on CWE solutions. It is acknowledged that a wide variety of parameters could be selected including, but not limited to the time-step, mesh type, mesh expansion ratio, numerical schemes and solvers. However, this

study is most concerned with domain configuration and mesh refinement as it is considered that these parameters will have the most significant influence on the result. Therefore, the following four parameters are investigated in this study:

- x1: Upstream length;
- x2: Downstream length;
- x3: Cross-stream width;
- x4: Mesh refinement.

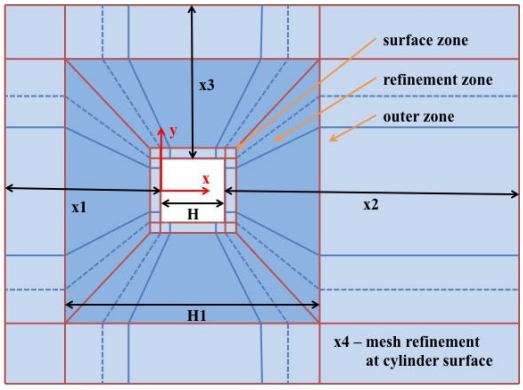

Figure 1. Extent of computational domain

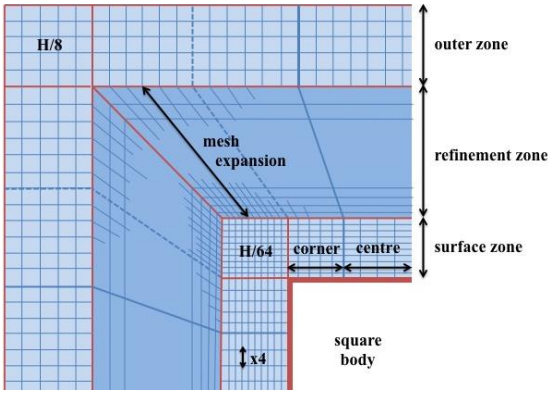

Figure 2. Mesh refinement zones within computational domain

Table 1. Simulation cases configuration based on modified half fractional factorial design approach

Parameters	Upstream	Downstream	Cross-stream	Mesh Size
-	7.5H	15H	7.5H	H/16
o	15H	30H	15H	H/32
+	22.5H	45H	22.5H	H/64
Case	x1	x2	x3	x4
s1c1	-	-	-	-
s1c2	+	-	-	+
s1c3	-	+	-	+
s1c4	+	+	-	-
s1c5	-	-	+	+
s1c6	+	-	+	-
s1c7	-	+	+	-
s1c8	+	+	+	+
s1c9	o	o	o	o

Given that the experimental design technique considers four different parameters and each parameter is assigned a lower (-) or upper (+) value (e.g., 7.5H or 22.5H for x1 parameter), at least 8 simulations are required. However, an additional simulation, or target case, is added to investigate intermediate (o) values (e.g., 15H for x1 parameter) in-between the extremes considered in the factorial design approach. The configurations of the 9 simulations, which are investigated in this study, are outlined in Table 1 below.

4. RESULTS

Visual inspection of the flow fields for each of the simulations reveal the characteristic alternating vortex shedding phenomenon originating on the upper and lower surfaces of the cylinder before progressing further downstream. The velocity and pressure fields with overlapping vorticity contours are shown in Figures 3 and 4, respectively.

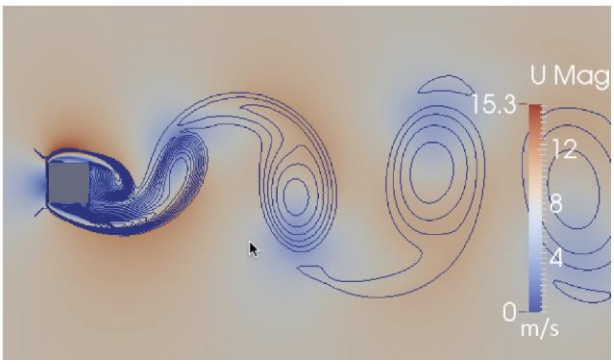

Figure 3. Instantaneous velocity field with vorticity contours (s1c9)

Figure 4. Instantaneous pressure field with vorticity contours (s1c9)

Table 2. Simulation flow parameter results for all 9 simulations

Case	Inflow velocity (P1) U_{inflow} [-]	Drag coeff. (P2) C_D [-]	Lift coeff. (P3) $C_{L,rms}$ [-]	Base press. (P5) $\lvert C_{p,base}\rvert$ [-]	Strouhal no. (P6) St [-]	Cross-stream (P7) U_{cross} [-]	Recirculation zone (P8) L_{zone} [-]	Downstream velocity (P9) U_{down} [-]
s1c1	1.004	2.110	1.460	1.396	0.145	0.249	0.506	0.983
s1c2	1.011	2.138	1.482	1.415	0.135	0.252	0.495	0.946
s1c3	1.004	2.107	1.451	1.382	0.145	0.260	0.513	0.958
s1c4	1.012	2.145	1.499	1.437	0.134	0.241	0.491	0.963
s1c5	1.000	1.999	1.388	1.260	0.146	0.264	0.527	0.953
s1c6	1.005	2.050	1.446	1.331	0.135	0.234	0.481	0.945
s1c7	1.000	2.008	1.367	1.278	0.146	0.248	0.495	0.946
s1c8	1.005	2.005	1.408	1.322	0.135	0.253	0.509	0.926
s1c9	1.006	2.066	1.434	1.337	0.135	0.248	0.500	0.943

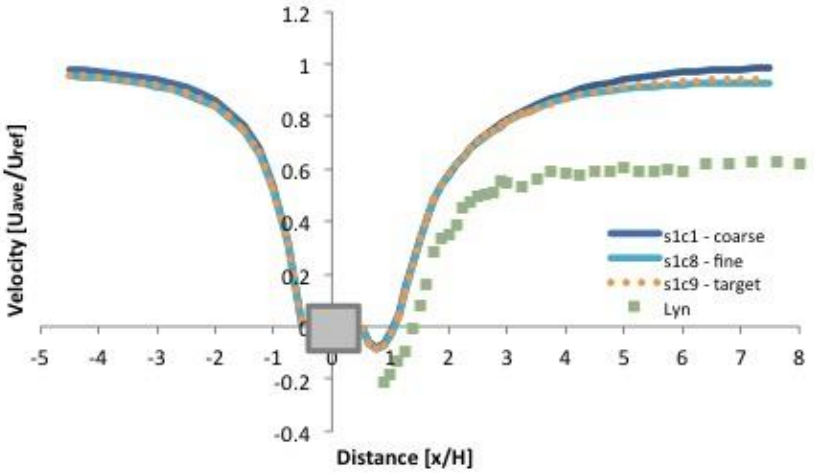

Figure 5. Time-averaged wind velocity along centerline, U_{ave}/U_{ref}

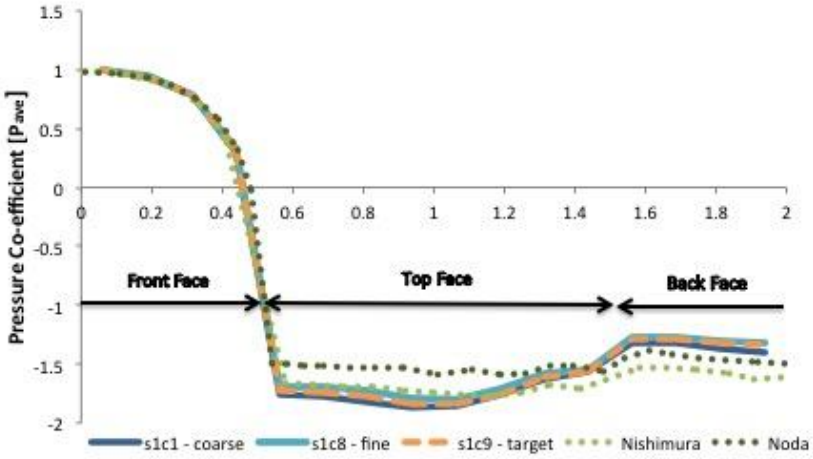

Figure 6. Time-averaged pressure coefficient, C_p, around cylinder surface

The results for a variety of flow parameters have been collected for each of the simulations. These include parameters related to the flow field such as the time-averaged inflow velocity, the time-averaged maximum cross-stream velocity, the length of the recirculation zone and the time-averaged velocity 7.5H downstream of the rear of the cylinder along the centreline of the domain. They also include parameters related to the pressure field, including the magnitude of the base pressure coefficient at the rear of the cylinder as well as the drag and lift coefficients. It should be noted that both velocity and pressure field parameters have been normalized relative to the stagnation pressure. In addition, the Strouhal number was also calculated. These results are summarized in Table 2 above.

5. DISCUSSION

5.1. Overview

Upon initial visual investigation, all simulations appear to give good results. It is apparent that

free shear layers form at the front corners of the cylinders. Due to instability within these layers, the shear layers interact and roll-up. Ultimately, this leads to the formation of vortices at the rear of the cylinder that are shed periodically downstream.

However, closer investigation does highlight a few areas of concern. For instance, the maximum magnitude of velocity, as shown in Figure 3, is significantly higher than expected. It is almost double the inflow velocity rather than between 20 % and 50 % higher. Furthermore, the velocity downstream of the cylinder along the domain makes an almost full recovery within 8H of the cylinder. Moreover, the vorticity contours follow the mesh boundaries as they extend upstream from the front face of the cylinder. It is clear that the mesh construction influences the flow field.

5.2. Experimental Design Technique

5.2.1. Velocity Field

Using the contrast of coefficients method outlined by Box et al. (1978), it is possible to identify the main and interaction effects of the different parameters. The main effects are summarized in Table 3 and illustrated in Figures 7 to 10. The interaction effects were found to be less significant and, therefore, have been omitted except for the recirculation zone length (Fig. 11).

Table 3. Main effects of simulation parameters on velocity field parameters

Parameter		Average	Main Effects			
			x1 (Upst. length)	x2 (Downst. length)	x3 (Crossst. length)	x4 (Mesh refin.)
P1	U_{inflow}	1.008	0.006 0.6 %	0.000 0.0 %	-0.005 -0.5 %	0.000 0.0 %
P7	U_{cross}	0.251	-0.010 **4.1 %**	0.001 0.3 %	-0.001 -0.3 %	0.014 **5.7 %**
P8	L_{zone}	0.501	-0.016 **-3.2 %**	0.000 -0.1 %	0.002 0.4 %	0.018 **3.5 %**
P9	U_{down}	0.962	-0.015 **-3.2 %**	-0.008 -0.9 %	-0.020 **-2.1 %**	-0.013 **-1.4 %**

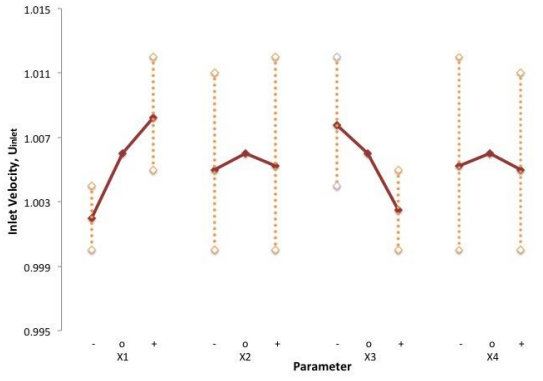

Figure 7. Inflow velocity (P1)

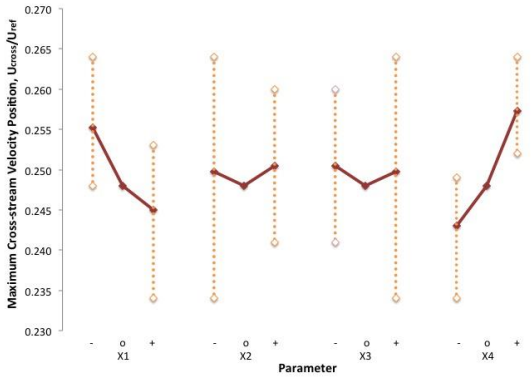

Figure 8. Cross-stream velocity (P7)

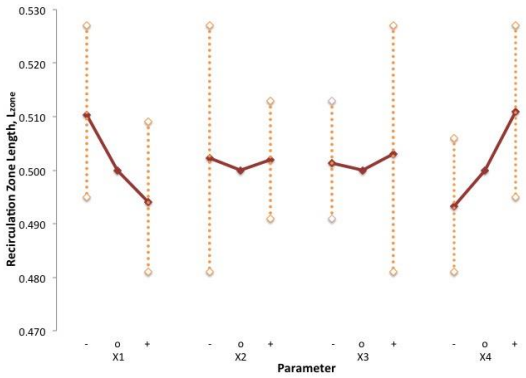

Figure 9. Recirculation zone length (P8)

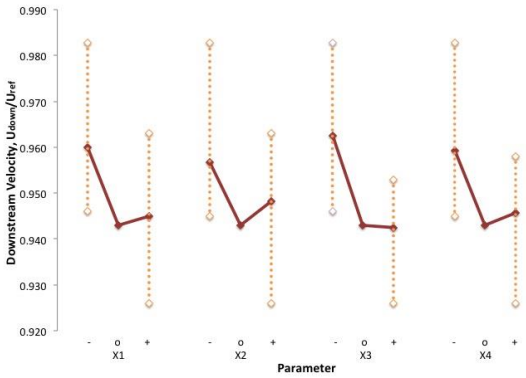

Figure 10. Downstream velocity (P9)

As shown in Fig. 7, the inflow velocity (P1) is influenced by the upstream length (X1) and the cross-stream length (X3). The short distance from the inflow boundary to the cylinder decreases the velocity at the boundary. However, the short distance from the top/bottom boundary to the cylinder increases the velocity, which is induced by funnelling effect. Note that the blockage ratios are 6.25 %, 3.2 % and 2.2 %, respectively, for the narrowest to widest domains. The upstream length and the mesh refinement are found to have a minor influence the inflow velocity.

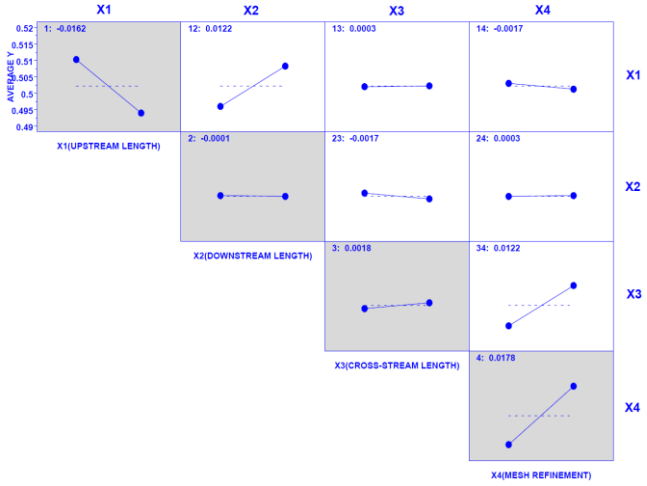

Figure 11. Interaction effects matrix: Recirculation zone length (P8)

The maximum cross-stream velocity (P7) above the middle of the cylinder's top face and recirculation zone (P8) are also influenced by upstream length and mesh refinement (Figs. 8, 9). The increase in upstream length leads to a reduction with in cross-stream velocity and recirculation zone size. While an increased mesh resolution results in an increase in cross-stream velocity and recirculation length.

Downstream velocity (P9) is dependent on all the parameters considered but, remarkably, it is least dependent on downstream length. Moreover, it is apparent from Figure 10 that an intermediate level of refinement is adequate to produce a satisfactory result.

Overall, it would appear that the velocity field is strongly influenced by the upstream width and the mesh refinement.

5.2.2. Pressure Field

The main effects are summarized in Table 4 and illustrated in Figures 12 to 14. The interaction effects were found to be less significant and therefore, have been omitted.

Table 4. Main effects of simulation parameters on pressure field parameters

Parameter		Average	Main Effects			
			x1	x2	x3	x4
P2	C_D	2.125	0.028 **1.3 %**	-0.008 -0.4 %	-0.110 **-5.2 %**	-0.016 -0.8 %
P3	$C_{L,rms}$	1.473	0.042 **2.9 %**	-0.013 -0.9 %	-0.071 **-4.8 %**	-0011 -0.7 %
P5	$\|C_{p,base}\|$	1.408	0.047 **3.4 %**	0.004 0.3 %	-0.110 **-7.8 %**	-0.016 **-1.1 %**

The cross-stream width has a strong influence over the drag and lift coefficients (P3 & P4) and the base pressure (P5). As the cross-stream width decreases, the accelerated flows above the top surface and below the bottom surface of the cylinder increase the strength of vorticity. As a result, the average drag, lift fluctuations, and pressure suction at the base increase. The upstream length has a considerable influence on those parameters. They increase with increasing upstream length.

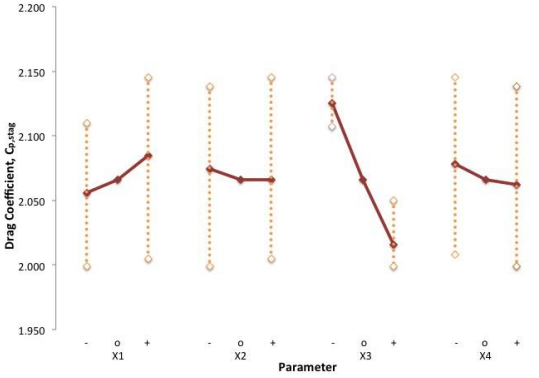

Figure 12. Time-averaged drag coefficient (P2)

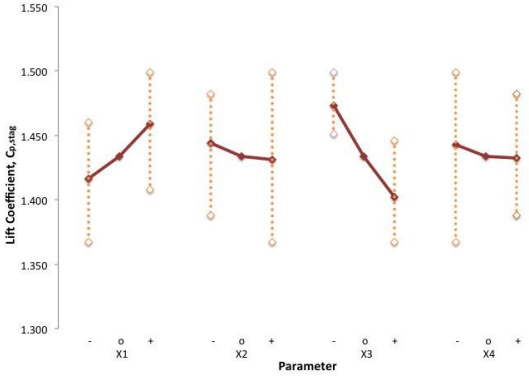

Figure 13. Root-mean-square of lift coefficient (P4)

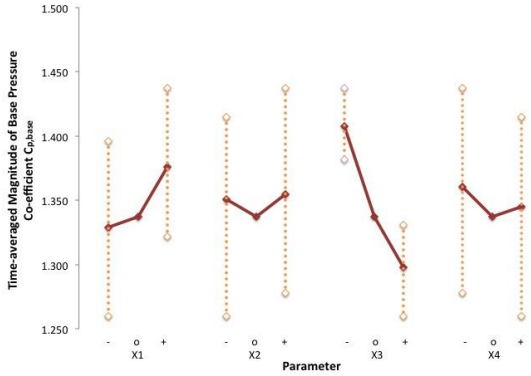

Figure 14. Time-averaged magnitude of base pressure (P5)

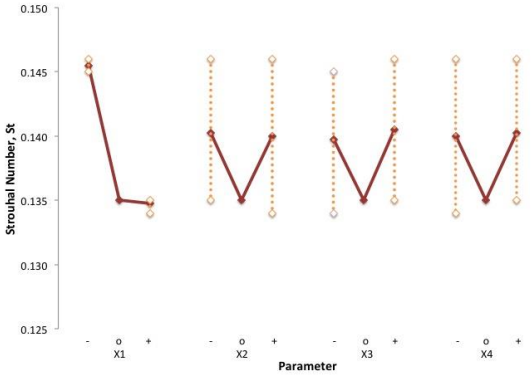

Figure 15. Strouhal number (P6)

Overall, it would appear that the pressure field is strongly influenced by the upstream length and the cross-stream width. Note that the pressure field is not sensitive to mesh refinement based on the grids employed in this study.

Table 5. Main effects of simulation parameters on Strouhal number

Parameter		Average	Main Effects			
			x1	x2	x3	x4
P6	St	0.140	-0.011 **-7.7 %**	0.000 -0.2 %	0.001 -0.5 %	0.000 -0.2 %

5.2.3. Strouhal Number

The main effects are summarized in Table 5 and illustrated in Figure 15. The Strouhal number is strongly influence by the upstream length only. As shown in Fig. 15, the intermediate upstream length (15H) is sufficient to produce a satisfactory result.

5.3. Practical Verification and Validation

The parameter values can be selected once the analysis of the sensitivity of the results pertaining to the flow or pressure field to changes in the parameter values is performed. The optimal set of parameters should be chosen to minimize the numerical errors while keeping the simulation time affordable. This is considered to be a *verification procedure* for users, though not for code developers. The simulation based on the optimal set of parameters provides the best target results in a practical manner, and can be viewed as a comparison with experimental/numerical results of the same problem. Hence, this can be considered as a *validation procedure*. Note that the verified simulation results cannot guarantee good agreement with experimental/numerical results used in the validation. The difference would not be due to numerical errors corresponding to the chosen parameters, but mainly to inappropriate modelling of the physics. If this is the case, a better model should be considered.

For this case study, to obtain reliable and efficient simulation results, the simulations for the velocity (P1, P7 - P9) and pressure/force results (P2, P3, P5) require, respectively, 15H and 15H

for the upstream length (X1), 30H and 15H for the downstream length (X2), 15H and 22.5H for cross-stream length (X3), and H/64 and H/16 for the mesh size (X4). With respect to the validation of the simulation results with experimental data, Figures 5 and 6 show a comparison of the simulated velocity along the centerline and the pressure distribution on the cylinder with experimental recorded by Lyn et al. (1995), Nishimura and Tanijke (2000), and Noda and Nakayama (2003). There are large differences between experimental results and the results with reduced numerical errors corresponding to the chosen parameters. This is mainly caused by the performance of the 2D RANS turbulence model used in this study.

6. CONCLUSIONS

This study developed a practical verification and validation (V&V) approach based on the experimental design technique for computational wind engineering applications. A modified orthogonal fractional factorial design was employed to set up simulation cases to investigate the influence of parameters (computational domain size and mesh refinement) on results of interest (flow field and pressure field). The conclusions of this case study are as follows:

- Mesh construction has undue influence on flow field;
- Upstream length and mesh refinement significant for simulating the velocity field;
- Upstream length and cross-stream width important for simulating the pressure field;
- Upstream length significant for simulating vortex shedding frequency;
- Downstream length does not appear to have a significant influence of any of the flow parameters considered except downstream velocity and base pressure. However, in both cases, its influence is relatively minor.

Once the numerical errors associated with the parameters are minimized or within acceptable level, the simulation based on the optimal set of parameters can be validated with experimental/numerical results of the same problem. Note that this sensitivity information cannot be applied to simulations that use different simulation details.

In light of these conclusions, further research is required to investigate the shortcomings of the current model configuration. It is recommended that further research be carried out to identify the appropriate turbulence model for the bluff body aerodynamics, as well as the parameters associated with the 3D simulations, such as spanwise length and spanwise grid size.

ACKNOWLEDGEMENTS

The authors would like to thank Prof. Guest and Prof. Schafer in the Civil Engineering Department of Johns Hopkins University for facilitating the running of these simulations on their high performance Linux cluster and their continued support of this research. The authors are also indebted to Dr. James J. Filliben in National Institute of Standards and Technology for his valuable advice on the experimental design technique.

REFERENCES

Bearman, P. W., Trueman, D. M., (1972). An investigation of the flow around rectangular cylinders. Aeronautical Quarterly, 23, 229-237.

Bearman, P. W., Obasaju, E. D., (1982). An experimental study of pressure fluctuations on fixed and oscillating square-section cylinders. Journal of Fluid Mechanics, 119, 297-321.

Box, G. E. P., Hunter, W. G., Hunter, J. S., (1978). Statistics for experimenters: an introduction to design, data analysis and model building. New York, NY: John Wiley & Sons.

Dahl, S. M., (2014). Unsteady RANS simulation of flow around rectangular cylinders with different aspect ratios at high Reynolds number (Master Thesis). Department of Marine Technology, Norwegian University of Science and Technology.

Durao, D. F. G., Heitor, M. V., Pereira, J. C. F., (1988). Measurements of turbulent and periodic flows around a square cross-section cylinder. Experiments in Fluids, 6, 298-304.

Franke, R., Rodi, W., and Schönung, B., (1990). Numerical calculation of laminar vortex-shedding flow past cylinders. Journal of Wind Engineering and Industrial Aerodynamics, 35, 237-257.

Lee, B. E., (1974). The effect of turbulence on the surface pressure field of a square prism. Journal of Fluid Mechanics, 69(2), 263-282.

Lee, S., Bienkiewicz, B., (1998). Finite element implementation of large eddy simulation for separated flows. Journal of Wind Engineering and Industrial Aerodynamics, 77&78, 603-617.

Lyn, D. A., Rodi, W., (1993). The flapping shear layer formed by flow separation from the forward corner of a square cylinder. Journal of Fluid Mechanics, 267, 353-376.

Lyn, D. A., Einav, S., Rodi, W., Park, J. H., (1995). A laser-Doppler velocrimetry study of ensemble-averaged characteristics of the turbulent near wake of a square cylinder. Journal of Fluid Mechanics, 304, 285-319.

Nishimura, H., Tanijke, Y., 2000. Fluctuating wind forces on a stationary two-dim square prism. 16th Wind Engineering Symposium in Japan, 255-260.

Noda, H., Nakayama, A., 2003. Free-stream turbulence effects on the instantaneous pressure and forces on cylinders of rectangular cross section. Experiments in Fluids, 34 (2003), 332-344.

The OpenFOAM Foundation, 2016. "OpenFOAM - Free, open source software from the OpenFOAM Foundation", Retreived, 7th May 2016 (http://openfoam.org).

Oberkampf, W. L., Trucano, T. G., 2008. Verification and validation benchmarks. Nuclear Engineering and Design, 238, 716-743.

Roache, P. J., 1997. Quantification of Uncertainty in Computational Fluid Dynamics. Annual Reviews Fluid Mechanics, 29:123-60.

Shimada, K., Isihara, T., (2002). Application of a modified k-ε model to the prediction of aerodynamic characteristics of rectangular cross-section cylinders. Journal of Fluids and Structures, 16(4), 465-485.

Tamura, T. Yoshiyuki, O., (2003). LES analysis on aeroelastic instability of prisms in turbulent flow. Journal of Wind Engineering and Industrial Aerodynamics, 91, 1827-1846.

Tian, X., Ong, M. C., Yang, J., Myrhaug, D., (2012). Unsteady RANS simulations of flow around rectangular cylinders with different aspect ratios. Ocean Engineering, 53, 208-216.

Networked Engineering Notebooks for Smart Manufacturing

Peter Denno,[a,1] Charles Dickerson[b], and Jennifer Harding[b]
[a] *National Institute of Standards and Technology, United States*
[b] *Loughborough University*

Abstract. A goal of the industrial internet is to make information about manufacturing processes and resources available wherever decision making may be required. Agile use of information is a cornerstone of data analytics, but analytical methods more generally, including model-based investigations of manufacturability and operations, do not so easily benefit from this data. Rather than relating anonymous patterns of data to outcomes, these latter analytical methods are distinguished as relying on conceptual or physics-based models of the real world. Such models require careful consideration of the fitness of the data to the purpose of the analysis. Verification of these analyses, then, is a significant bottleneck. A related problem, that of ascertaining reproducible results in scientific claims, is being addressed through executable notebook technology. This paper proposes to use notebook technologies to address that bottleneck. It describes how this notebook technology, linked to internet-addressable ontologies and analytical metamodels, can be used to make model-based analytical methods more verifiable, and thus more effective for manufacturers.

Keywords. Manufacturing analysis, process analysis, process optimization, analytical methods, empirical methods, industrial internet of things, metamodels

1. Introduction

Smart manufacturing [1] and similar initiatives [2], [3] are focused on improving manufacturing productivity through the use of inexpensive sensor networks, information systems, and software analytical tools. In manufacturing, a great variety of software analytical tools are being applied to an ever-expanding set of physical [4] and operational [5] problems including process optimization. However, in manufacturing, more so than engineering design, the preparation of analytical models and the interpretation of their results do not share a common methodology across the various usages. This limits the ability to develop systematic means to apply analytical techniques to decision making. The consequences of this limitation include missed opportunities to reuse knowledge, unreliable results, and high cost of analysis. A report from the NIST [6] suggests that it should be possible, near-term, to reduce the cost of system verification and validation ten-fold. But how will this reduction be achieved?

There is no silver bullet to making analytical techniques more accessible to more manufacturers, but opportunities have emerged with the development of technologies that support 1) the industrial internet of things, 2) manufacturing domain ontologies, 3) domain specific languages, 4) natural language processing, and 5) metamodeling. This paper describes how these technologies may be applied using the Python programming language and Jupyter Notebooks which are web applications for the creation and sharing of documents that embody analyses. Notebooks contain live code, equations,

[1] Corresponding Author: Peter Denno, email: peter.denno@nist.gov.

Denno, Peter.
"Networked Engineering Notebooks for Smart Manufacturing."
Paper presented at 14th International Conference on Manufacturing Research,
Loughborough, England, United Kingdom. September 6, 2016 - September 9, 2016.

visualizations and explanatory text [7]. The paper describes a notebook-based methodology, tailored for use in smart manufacturing environments, to reduce the cost of developing and validating process optimizations.

Section 2 of the paper describes the problem space. Section 3 explains how "equations as objects," formal requirements specifications, notebook annotations, and a metamodel of optimization are used in our methodology to produce analyses that are verified and integrated into manufacturing operations. Ideas are illustrated using a case study implementing a turning operation optimization described by Abdelmaguid and El-Hossany [8]. Section 4 concludes the paper with a discussion of limitations of the described process and planned future work.

2. From Analytical Problems to Systematic Solutions

Information needed to formulate manufacturing process optimizations - for example, to improve machining operations - may originate from many viewpoints. A viewpoint is a set of related concerns relevant to a particular audience [9]. Decision making in manufacturing typically relies on a composition of such viewpoints. For example, deciding what jobs to initiate in a job-shop environment might involve a composition of viewpoints concerning product demand, process plans, machine capabilities, machine instances and their availability, and inventory. The problem of composing viewpoints for decision making (i.e. of formulating the relevant analysis) is, in part, the problem of knowing what can be inferred from the union of information sources. This fundamental problem resists simple solution [10].

This paper describes a method in which it is assumed that the most creative part of the process, the problem formulation, has already been performed (perhaps guided by analyses described in the literature [8]). The practical problem that remains is that of making the analysis correct and effective for the idiosyncrasies of the given manufacturing context and the supporting information technology.

Verifying the correctness of an analysis requires knowing 1) what the analysis is to achieve (i.e. its requirements), 2) that the method (algorithm) chosen is suitable to address these requirements, and 3) that inputs to the algorithm are appropriate to it. With this knowledge, one gains confidence in the validity of the analysis, but not an understanding of the bounds on certainty, the sensitivity of parameters, nor the risk that the implied recommendations entail. Of these four qualities (validity, certainty, sensitivity and risk), validity is the most basic requirement. Though the others are important, they are not discussed in this paper.

3. Verifying Process Optimizations in Smart Manufacturing Environments

The literature contains an abundance of mathematical and physics-based models of manufacturing processes. Some of these models are "simple", since they are neither computationally demanding, nor require nuanced understanding of model parameters. Simple models can be applied more directly in daily production operations. For example, such models can be used by manufacturing engineers to adjust operating parameters in reaction to variation in raw materials.

Other models are "complex" since they require extensive setup or a geometric model (such as is the case with finite element analysis, for example). Abstractions can

sometimes be found over complex models so as to create a simple model more suitable for daily use. An example of such an abstraction is a reduced-order surrogate model based on computational experiments performed on a complex model [11]. This paper concerns simple models and the simple form of complex models.

The methodology requires three classes of information to verify the correctness of an analysis. First is information linking variables and relations to terms in an ontology defining the intended meaning, dimensionality, and sources for values (e.g. a schema providing dimensional inspection results). Second is information linking calls to specialized analytical tools (e.g. optimizers) to a conceptual model of that tool. Third is information containing formal statements of requirements describing what the analysis is to achieve. These three elements are discussed, in turn, in the following sections.

Verification is performed against analyses encoded in Jupyter notebooks using the Ipython language. Ipython is the interactive version of the Python language. Both Ipython and Python can use the many libraries developed for the language. Of particular value to manufacturing analysis are the scipy and numpy libraries for general mathematical tasks and optimization, the Pandas library for data structures and data analysis, and Statsmodels for statistics [12].

Jupyter represents user content (i.e. the analysis) as a Javascript Object Notation (JSON) data structure. The data structure (and its presentation in the browser) is divided into cells. A cell can be designated as containing (Python) code or markdown syntax annotations. Markdown cells can use LaTeX notation to represent mathematical formulas.

The design of the verification method is such that it does not interfere with the execution of the analysis. If the analysis provides markdown cells containing tables describing variables, these can be used in a separate process to annotate the analysis. If, on the other hand, such tables are not provided and sufficient information cannot be inferred through other means, verification will be incomplete.

3.1. Linking Variables to Ontology Terms and Sources

The JSON data structure can be parsed to identify variables defined in tables provided by the user; as is typical of Jupyter notebooks, these tables are in markdown syntax (See Figure 1). If the tables have the appropriate form, they will be interpreted as containing definitions of variables used in the analysis. Additionally, the process managing the validation can enable the user to associate OWL ontology terms with these variables. The ontology provides definitions and constraints on interpretation of elements important to the analysis such as symbols, variables, and their bindings to definitions. These definitions may concern manufacturing concepts.

Symbol	Variable	Meaning
$D\|$	D	Final product target diameter
$D_0\|$	d_i	depth of cut for part *i*
$\delta_i\|$	delta_i	tool wear compensation (mm) for part *i*
$V\|$	V	Cutting speed (m/min)
$f\|$	f	Feed rate (mm/rev)
$N\|$	N	Tool regrind scenario

```
| Symbol     | Variable | Meaning |
|-------------------------------------------------------------------|
| $D$        | D        | Final product target diameter|
| $D_0$      | d_i      |depth of cut for part *i* |
| $\delta_i$ | delta_i |tool wear compensation (mm) for part *i*|
| $V$        | V        |Cutting speed (m/min)|
| $f$        | f        | Feed rate (mm/rev) |
| $N$        | N        |Tool regrind scenario |
```

Figure 1. A table as it appears in the Jupyter notebook (left), and the corresponding markdown syntax provide by the user (right).

Similarly, the analysis can be annotated with knowledge of the sources of values (e.g. data conforming to XML schema or the schema translated to an OWL ontology).

Software has been written to parse the LaTeX-syntax mathematics in markdown cells to OWL statements. Because mathematical expressions can have complex syntax, a single mathematical expression can produce many interrelated OWL facts. This makes processing difficult, but not impossible. The software implements an "equations as objects" method of operation described in prior work [13]. By making mathematical relations visible outside of the tools in which they are initially developed, these relations can be reused and refined. For example, an empirically-defined, predictive model of a manufacturing process developed in one analysis (one notebook) can be referenced in an optimization or linked to additional operational data and refined in other notebooks.

3.2. Characterizing the Use of Optimizers with an Optimization Metamodel

A principal challenge in using analytical tools such as optimizers is that of knowing what pattern of tool use is appropriate to the problem at hand. There are two aspects to addressing this challenge: representing the domain problem and representing the capabilities and interface of the analytical tool. In the method, the domain problem is represented through a combination of the ontology links discussed in the previous section and the formal requirements characterization discussed in the next section. This section discusses how the user's specification of the objective function, constraints and call to the optimizer are characterized for subsequent validation.

The characteristics of optimization techniques can be modeled using a metamodel. A *metamodel,* as used here, is a model of a modeling language providing sufficient detail to serve as the storage form for instances of the model. Prior work [14] has produced a preliminary UML-based metamodel of optimization to represent optimization problems defined in the Optimization Programming Language (OPL). This metamodel is still under development and being adapted to represent the optimization techniques found in Python scipy. Depicted in Figure 2 is an optimization call such as used in the turning optimization. The vector *x* is the design vector; *x*[0] the cutting speed, and *x*[1] the feed rate. As shown, these are initialized to [60.0, 0.08] respectively. For brevity, only part of the constraint vector is shown.

```
cons =  ({'type': 'ineq',
          'fun' : lambda x: np.array([wear_limit_calc(N,x[0],x[1])
                                      - W_hat])})

def obj_func (x,sign=-1):
    return sign*(P_calc(x[0],x[1],N)/(N*t_h + T_n_calc(x[0],x[1],N)))

res = minimize(obj_func, [60.0,0.08], bounds=[(V_min, V_max), (f_min, f_max)],
               constraints=cons,
               method='SLSQP', options={'disp': True})
```

Figure 2. The call to the optimizer in the turning example.

The optimization metamodel describes a conceptualization of optimization problems. The use of the optimizer, such as in the code in Figure 2, represents a particular instance of the metamodel. This instance can be expressed as RDF and OWL triples. In creating this instance, it is essential to recognize how the information provided in the call to the optimization tool relates to the optimization metamodel. For example, in the case of the Scipy-based tool depicted in Figure 2, the parameter named *method* indicates the

algorithm applied (sequential least squares programming); *bounds* provides constants bounding the feasible region; and, *constraints* provides a vector of functions that can be called with the design vector to evaluate inequality and equality constraints. Integrating this knowledge with variable and equation definitions acquired through the markdown cells requires parsing the call to *minimize* and related constraint definitions.

3.3. Stating Requirements about Analyses

Verification is performed against requirements that originate as informal statements about what the system (in our case an analysis) is to do. Prior work [15] provides a method to construct a controlled, natural-language parser for a domain-specific language. The method involves recognizing what the sentence intends by first classifying its verb by calculating the semantic distance to it from synonyms of all "proto-verbs" of the domain-specific language. The current implementation of the method does not provide such a parser; it only provides similar resulting statements based on a pilot set of proto-verbs: "optimize" "constrain" and "find." This set is likely to grow; the prior work required 19 proto-verbs. The resulting statements are encoded in a dialect of ISO Common Logic. An example statement in the dialect – one describing the requirement that the analysis should maximize profit under constraint of acceptable surface finish and dimension tolerance – is as follows:

```
(obligation-of
   analysis-x
   (that
      (and (optimize profit)
           (under-constraint surface-finish)
           (under-constraint dimensional-tolerance))))
```

3.4. Using Links, Metamodels, and Requirements to Verify Analyses

Inconsistencies in the analysis are identified using a Bayesian approach on a graph-based structure. The process is similar to that described by Herzig [16]. In the process, a graph of binary relations is produced from the sources described in the previous three sections (ontology-annotated variables and terms, the optimization metamodel instance, and requirement statements).

As an example of how inconsistencies are recognized, consider the segment of the turning analysis depicted in Figure 2. *W_hat* in the figure is defined through links to the ontology to be the maximum acceptable tool wear. The translation of the Python constraint through the optimization metamodel indicates that the expression of the constraint on tool wear, `wear_limit_calc(N, x[0], x[1], ) - W_hat`, has its sign reversed from what is correct. (Inequality constraints provided to the python minimization function should be stated such that their values are positive inside the feasible region.) The fact that tool wear is generally not a desirable quality of machining and yet the analysis seemingly seeks a value of tool wear *above W_hat* allows Bayesian inference to identify the inconsistency against the world model reflected by the ontology.

4. Conclusion

This paper discusses a methodology for performing and verifying optimization-based analyses of manufacturing processes and operations. The method applies a "soft system perspective" [2] to facilitate the use of analytical tools in smart manufacturing environments. Elements of the method have been implemented on the turning optimization described in [8] as well as an empirical model of an additive manufacturing process [13]. Much work remains in developing the analytical metamodel for optimization and integrating system components. An analysis for job shop scheduling is being developed. As production scheduling can involve very different viewpoints from those used in unit manufacturing processes, it will be necessary to develop the ontology towards these viewpoints.[3]

References

[1] J. Davis, T. Edgar, J. Porter, J. Bernaden, and M. Sarli, "Smart Manufacturing , Manufacturing Intelligence and Demand-Dynamic Performance," in *FOCAPO2012: Foundations of Computer-Aided Process Operations*, 2012.

[2] VDE-DKE, "The German Standardization Roadmap Industrie 4.0," *Vde Assoc. Electr. Electron. Inf. Technol.*, vol. 0, pp. 1–60, 2014.

[3] Government Office for Science, "The Future of Manufacturing," London, 2013.

[4] K. Allen, Dell, Alting, Leo, and H. Todd, Robert, *Fundamental Principles of Manufacturing Processes*. Industrial Press, 2005.

[5] J. Li and S. M. Meerkov, *Production System Engineering*. Springer Science+Business Media, 2009.

[6] National Institute of Standards and Technology, "Foundations for Innovation in Cyber-Physical Systems," Gaithersburg, 2013.

[7] Project Jupyter, "Jupyter Notebooks." [Online]. Available: http://jupyter.org/. [Accessed: 28-Apr-2016].

[8] T. F. Abdelmaguid and T. M. El-hossainy, "Optimal Cutting Parameters for Turning Operations with Costs of Quality and Tool Wear Compensation," *Proc. 2012 Int. Conf. Ind. Eng. Oper. Manag. Istanbul, Turkey, July 3 – 6*, pp. 924–932, 2012.

[9] ISO, *ISO/IEC/IEEE 42010:2011 Systems and software engineering — Architecture description*. 2011.

[10] N. F. Noy, "Semantic Integration: A Survey Of Ontology-Based Approaches," *Newsl. ACM SIGMOD Rec.*, vol. 33, no. 4, pp. 65–70, 2004.

[11] A. Jeang, H. C. Li, and Y. C. Wang, "A computational simulation approach for optimising process parameters in cutting operations," *Int. J. Comput. Integr. Manuf.*, vol. 23, no. 4, pp. 325–340, 2010.

[12] W. McKinney, *Python for data analysis*. O'Reilly, 2013.

[13] P. O. Denno and D. B. Kim, "Integrating views of properties in models of unit manufacturing processes," *Int. J. Comput. Integr. Manuf.*, no. March, pp. 1–17, 2015.

[14] I. Assouroko and P. O. Denno, "A metamodel for optimization problems," Gaithersburg, 2016.

[15] P. O. Denno and C. Chang, "Validating controlled English statements of requirements using functional models," 2016, pp. 1–10.

[16] S. J. I. Herzig, "A Bayesian Learning Approach To Inconsistency Identification in Model-Based Systems Engineering," Georgia Institute of Technology, 2015.

[17] P. Checkland, "Soft Systems Methodology: A Thirty Year Retrospective," *Syst. Res. Behav. Sci. Syst. Res*, vol. 17, pp. 11–58, 2000.

[2] Checkland [17] distinguishes "hard system perspectives' from "soft systems perspectives": in the former, the world is viewed as systemic; in the later, the world is viewed as unmanageably complex, but the process of inquiry is systemic.

[3] Certain commercial software products are identified in this paper. These products were used only for demonstration purposes. This use does not imply approval or endorsement by NIST, nor does it imply these products are necessarily the best available for the purpose.

Proceedings of the 2016 Winter Simulation Conference
T. M. K. Roeder, P. I. Frazier, R. Szechtman, E. Zhou, T. Huschka, and S. E. Chick, eds.

STANDARDS BASED GENERATION OF A VIRTUAL FACTORY MODEL

Sanjay Jain

Department of Decision Sciences
School of Business
The George Washington University
2201 G Street NW, Suite #415
Washington, DC 20052, USA

David Lechevalier

Le2i – Laboratoire Electronique,
Informatique et Image
Université de Bourgogne,
allée Alain Savary
21000 Dijon, FRANCE

ABSTRACT

Developing manufacturing simulation models usually requires experts with knowledge of multiple areas including manufacturing, modeling, and simulation software. The expertise requirements increase for virtual factory models that include representations of manufacturing at multiple resolution levels. This paper reports on an effort to automatically generate virtual factory models using manufacturing configuration data in a standard format as the primary input. The execution of the virtual factory generates time series data in standard formats mimicking a real factory. Steps are described for auto-generation of model components in a software environment primarily oriented for model development via a graphic user interface. Advantages and limitations of the approach and the software environment used are discussed. The paper concludes with a discussion of challenges in verification and validation of the virtual factory prototype model with its multiple hierarchical models and future directions.

1 INTRODUCTION

A number of past and recent initiatives, such as smart manufacturing (SMLC 2012) and Industrie 4.0 (Mario, Tobias, and Boris 2015) have identified modeling and simulation as key to the advancement of manufacturing. Some have proposed the use of simulation at multiple levels within manufacturing, ranging from physics-based models of the manufacturing process at a very detailed level to high level supply chain models and everything in between.

The development of simulation models of manufacturing systems requires expertise in multiple areas including manufacturing operations, conceptual modeling of manufacturing systems at the right level of abstraction, and implementation of the conceptual model using appropriate simulation software. The expertise requirement goes up substantially if multiple levels of manufacturing are to be modeled. The expertise requirement can be a deterrence to wider use of simulation in manufacturing. It could be a roadblock for the move towards smart manufacturing and Industrie 4.0.

Past research has shown that a virtual factory model (implemented as a multi-resolution simulation model) can be used as a high fidelity representation of a corresponding real factory (Jain et al. 2015). Such a virtual factory model can provide the capabilities envisaged in smart manufacturing and Industrie 4.0.,

however at present, developing a such a model may only be an option for large corporations with substantial budgets given the high expertise requirement.

This paper proposes automatic generation of virtual factory models based on data as a way to reduce the expertise requirement and thus facilitate the increased use of simulation. This is admittedly not a new idea. There have been solutions from commercial vendors of discrete event simulation (DES) software in the past that generated factory models when provided with a data file in their proprietary data formats. This effort proposes going beyond the prior offerings in two key ways. First, the effort proposes the use of standard formats for input data describing the subject manufacturing system. Second, the generated model is proposed to be a virtual factory model as defined with multi-resolution capabilities rather than the single level models available in commercial offerings. The current implementation of the concept is a first step towards achieving the proposed capability.

The next section discusses relevant efforts reported in the literature over the last year. Section 3 discusses the proposed overall approach to achieve the vision of virtual factory and provides an overview of the approach for the current implementation. The implementation using AnyLogic, the selected software for this initial step, is then described in detail in section 4. Section 5 concludes the paper with a discussion of future work to continue implementation of the virtual factory concept.

2 LITERATURE REVIEW

Publications relevant to this effort that have appeared over the last year are briefly reviewed in this section. The relevant areas are virtual factory and the key enabling capabilities of multi-resolution modeling and hybrid simulation. Readers are referred to Jain and Shao (2014) and Jain et al. (2015) for reviews of relevant literature in the respective areas prior to last year.

2.1 Virtual Factory

Jain and Shao (2014) presented four different connotations of virtual factory in the extant literature: as a high fidelity simulation as used in this paper, as a virtual organization, as a virtual reality (VR) representation, and as an emulation facility. Over the last year, publications using the four different connotations have continued to appear, but a much higher proportion of papers use the definition of virtual factory as a high fidelity simulation, with papers using the virtual reality representation definition in second place. There are multiple papers that combine the high fidelity simulation and virtual reality representation connotation and some even extend to include the emulation aspect. A representative sample of relevant publications, that use the first definition of virtual factory are primarily reviewed here.

Terkaj, Tolio, and Urgo (2015) present an ontology-based virtual factory that is continuously updated to reflect the events of the corresponding real factory. They used ARENA as the DES software together with a 3D animation. The virtual factory is used for predictive analysis, for example evaluating management decisions on production plans and maintenance. While a capability for a multi-scale representation is mentioned, it does not appear to cover the process-machine-cell/line-factory hierarchy. Oyekan et al. (2015) utilize WITNESS simulation software connected to Visionary Renderer VR software package to create a high fidelity simulation of the factory floor. It does not appear to allow multiple resolution modeling but it does appear to have some of the core capabilities of a virtual factory as defined here.

Ayadi et al. (2015) present an information system developed using WinDev for supporting a digital factory. They place an emphasis on the product development process with the supporting information system providing access to the product and process information. The production simulation uses an unnamed software and appears to provide the capability to support multiple resolution levels including plant, line, station, and task. While the authors recognize the need for interoperability and base the concepts on standards, the data interfaces for the current system are custom developments. Constantinescu, Francalanzab, and Matarazzoc (2015) propose to develop the virtual factory using SysML and TOPCASED

open source software and emphasize the knowledge capturing and human system interface aspects to support decision makers using the results from modeling and simulation. The use of open source software may require a large effort to reach to the level of capabilities available in commercial simulation software, but it is a worthwhile effort for making the developments available to a wider community.

Some publications focus on the "digital factory" concept, suggesting the extensive use of modeling and simulation in a manufacturing context but with a product development perspective. Gregor, Hercko, and Grznar (2015) suggest that a digital factory uses data from simulation while a virtual factory uses data from a real factory, though such a distinction was not found in other publications. Matsuda and Kimura (2015) use a digital factory for evaluating the sustainability of manufacturing systems and production plans. The system is implemented using the commercial multi-agent simulator "artisoc" and provides levels of granularity for the simulation at the factory, machine, and product levels. These authors use the terms digital factory and virtual factory interchangeably.

While the efforts focusing on a virtual factory connotation other than as a high fidelity simulation are not discussed, a good source for papers identifying virtual factory as a VR representation is the review provided by Choi, Jung, and Do Noh (2015) encompassing 154 papers over last couple of decades discussing the application of VR to manufacturing.

2.2 Multi-Resolution Modeling

Schönemann et al. (2016) present a multi-level framework for manufacturing system simulation and identify the data exchanges among the disparate simulation models at different levels. The framework presented includes a few other models beyond manufacturing, such as product, building, and technical building services (TBS), to provide a holistic approach. The example is quite similar to that presented in Jain et al. (2015) including the use of AnyLogic software, Java code for the process model, agent based simulation (ABS) to model the machine level, and DES models for the cell/process chain level. They appear to use custom interfaces for data, which can lead to a large effort when using the approach for a new scenario.

Alvandi et al. (2015) use a similar approach with an example implementation of their proposed hierarchical modeling framework for the analysis of material and energy flows in manufacturing systems. They also use AnyLogic software, an ABS model for the unit process level (similar to machine level), and a DES model for the process chain level. Their factory level model includes the TBS, production planning & control, and transport modules. They access data for the models directly from ERP and SCADA, which can require a significant effort to apply the approach in scenarios with different ERP and SCADA systems.

The independent use of similar set-ups in the two efforts discussed above provides support for the approach used in Jain et al. (2015). The use of standards in such efforts will facilitate collaboration and implementation.

2.3 Hybrid Simulation

The use of hybrid simulation, that is multiple simulation paradigms in the Virtual Factory models, leads to the challenge of their effective integration. In this work, the use of AnyLogic software has enabled hybrid simulation to be used without having to use a distributed simulation mechanism such as that used by Rabelo et al. (2015) for a hierarchical model of a supply chain with the higher level modeled using system dynamics paradigm in Vensim and the functional details modeled using DES in ARENA.

Abduaziz et al. (2015) also utilize hybrid simulation for a green logistics assessment. However, in their work the supply chain system dynamics model developed in iThink doesn't run concurrently with the factory DES model in Arena. The two models are executed iteratively with information exchanges among the two models. The work supports the idea of using simulation paradigms appropriate to the level of detail.

Overall, the efforts reported in the literature over the last year support the direction of the work reported here. The use of standards based interfaces and routines for automated generation of the models is a step forward in this area.

3 APPROACH

3.1 Objectives

The objective of this part of the work is to automatically generate a virtual factory model, using data from the real factory in a standard format, with the capability of generating output data streams based on standards formats. The automatic generation of the virtual factory model is intended to go beyond previous efforts involving the automatic generation of single level factory simulations by generating a multi-resolution model and using standard formats of input files.

The target multi-resolution model currently has three levels: process, machine, and cell. The cell level can also represent the production part of a small factory. However, per the definition provided in Jain et al. (2015), the factory level model should also include functions other than production, and hence it is being referred to as the cell level. The levels, modeled phenomena, key entity, time-scales, and associated selected simulation paradigms are shown in Table 1. The target standard for reading in manufacturing configuration data is the Core Manufacturing Simulation Data (CMSD) standard from Simulation Interoperability Standards Organization. The current intent is to generate a model based on the configuration file only. The target standard for output data stream at the machine level is MTConnect.

Table 1: Resolution levels modeled and their characteristics.

Level	Modeled phenomena	Key entity	Time-scales modeled	Simulation paradigm
Cell	Production of batches of parts through a multi-step process plan	Part batch	Minutes to hours	DES
Machine	Production of parts at a single machine including batch and part setup and ejection	Part	Seconds to minutes	DES/ ABS
Process	Physics of the transformation processes such as turning and milling	Part features	Milliseconds to seconds	Continuous based on equations

3.2 Approach for Current Implementation

Automated model generation at factory level has been done in the past as mentioned earlier. Past implementations modeled each process plan step using generic representations such as serial or batch processes with defined times for set-up and operations. The generated models were generally presented as logic networks without the benefit of an animated layout based on the scenario. While such as approach can work for factory level models, the generic representation will not work at the process level given the wide variety of manufacturing processes and their unique parameters. For example, material removal operations require modeling of cutting forces based on cutting speed and feed rate, while an injection molding process may require modeling of pressure on the molten material and cooling rates. The physics at the process level is thus widely different and will require a unique meta-model or equations to represent them. One would thus need a library of machine level models with associated process level models as suggested by Matsuda

and Kimura (2015). Selected machine level models can be included in the virtual factory model as needed based on the data from the real factory to be modeled.

The automatic generation approach can broadly be described as below:

- Read the manufacturing system configuration data via an interface supporting data in a standard format
- Read in machine parameter and process level data
- Assemble the factory or cell level logic network based on the input process plans data
- Link the factory or cell level logic network to individual machine and corresponding process models using the corresponding models available in the library
- Render the layout of the facility based on the information from the configuration data with links to the logic network
- Execute the model with selected parameters such as resolution level and output formats selected by users via run-time interaction

The current approach is summarized in Figure 1. At present this approach makes a number of assumptions on the material flow control. For example, dispatching and priority rules at different cells are set by default, and a common queue is used for all machines in the cell. These will be addressed in future.

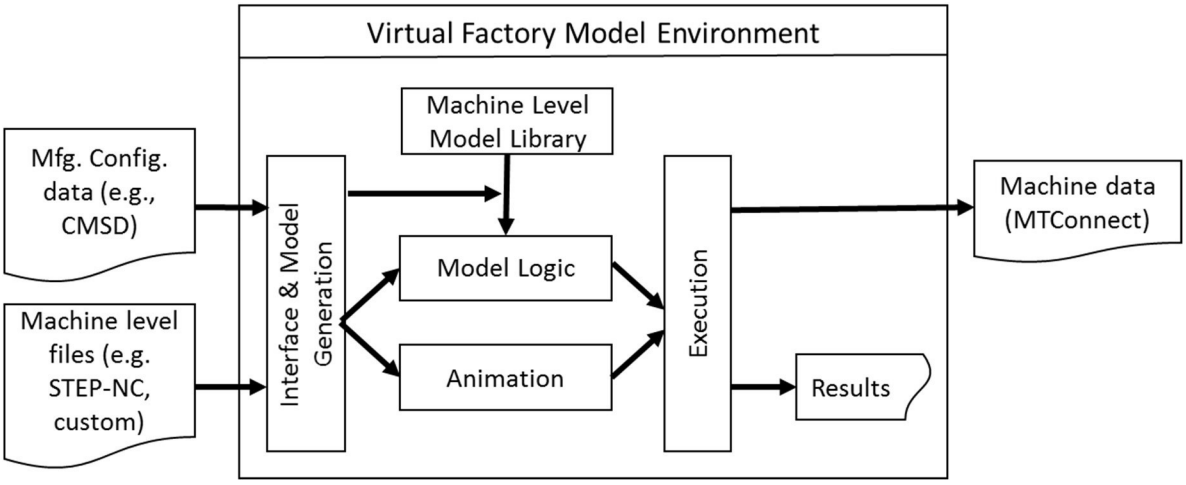

Figure 1: Current approach for automated model generation.

The targeted use of multiple paradigms to implement the multi-resolution models prompted the use of AnyLogic software to avoid the complexity of distributed simulation at this stage as was discussed in Jain et al. (2015). Like many other current commercial simulation software packages, AnyLogic appears to emphasize interactive model building via the graphical user interface (GUI). The coding of automated generation hence turned out to be challenging, and at times some aspects of automated generation appeared impossible to implement. The lessons learned from the efforts to implement automatic generation capabilities is detailed in the next section to aid other research teams who are attempting similar implementations.

4 IMPLEMENTATION

In this section, an example of a machine shop is used to illustrate the implementation process for the corresponding virtual factory. The first sub-section presents the example followed by discussion in subsequent sub-sections of an algorithm to automatically generate a virtual factory model primarily from a

CMSD file. The algorithm is capable of building models representing machine shop scenarios described via CMSD files as long as each cell is not composed of more than 5 machines.

4.1 **Model Example**

Figure 2 shows the logic network in an AnyLogic model that represents a machine shop. This machine shop is composed of a turning machine cell and a milling machine cell. The parts processed in this workshop have two operations. They are machined first in the turning cell and then in the milling cell. The parts are processed in batches of varying sizes.

The logic network representation of the workshop starts with a Source block to model arrivals of batches. Upon arrival the batches wait in the raw material storage area represented by a Delay block. This Delay is used as a queue and holds the batch until a turning machine is available. Since the turning machine cell is composed of four machines, a SelectOutput5 block (an output selector with 5 conditional outputs) is used to decide to which machine the batch should go. After the turning machine cell, the batch moves to the work in progress area represented by another Delay block, where it stays until a milling machine is available. Again, since the milling machine cell is composed of 2 machines, a SelectOutput block (an output selector with two conditional outputs) is used to select the available machine. After completion of the second operation, the batch moves to the finished goods area where batches are waiting for pick up. This area is represented with yet another Delay block. The shipping of batches from the workshop to customers is represented by batches leaving the model via a Sink block.

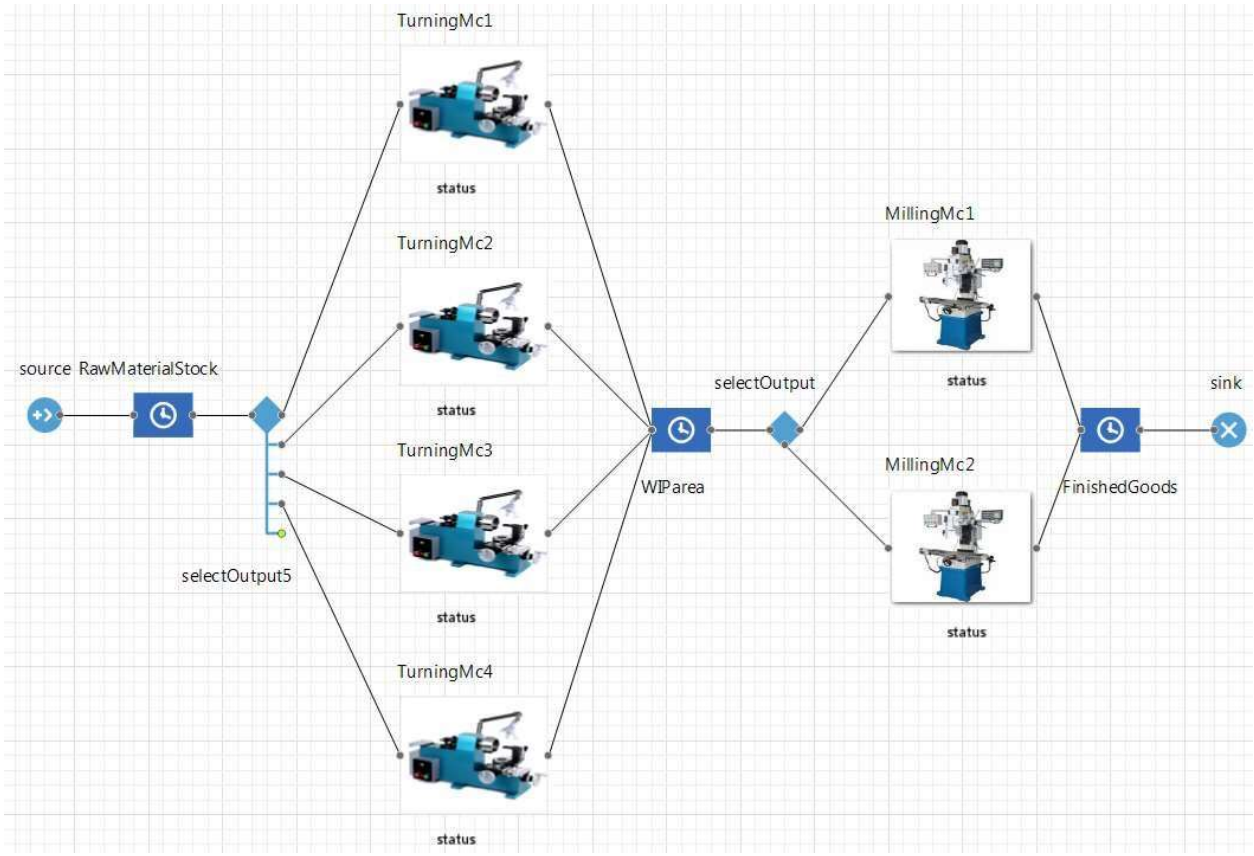

Figure 2: Example of a machine shop.

4.2 Data Input Interface

The interface has the capability to parse a CMSD file that describes the machine shop. The interface collects the required information to build the model such as the part characteristics, information on the cells, and specifications of the machines that compose each cell. Since CMSD is XML-based, parsing a CMSD file requires the ability to go through XML documents. A JAVA parser has been developed to go through a CMSD file for the machine shop and collect the information required to automatically build the corresponding virtual factory model.

4.3 Machine Level Model Library

Per the virtual factory definition used in this work the model should allow execution at the factory level as represented in Figure 2, at the individual machine level, and at the associated process level. The representation at machine level requires provision of a machine model library that allows selection and use of the machine level model corresponding to that defined in the data. At this prototype stage, only two machine level models are included in the library that represent turning machines and milling machines. These objects can be included in the logic network. Jain et al. (2015) introduced a turning machine model. Lechevalier et al. (2015) described a milling machine model that was developed following the same approach as the turning model. These two models are the first entries in the library. The machine level models follow the simple statechart represented in Figure 3.

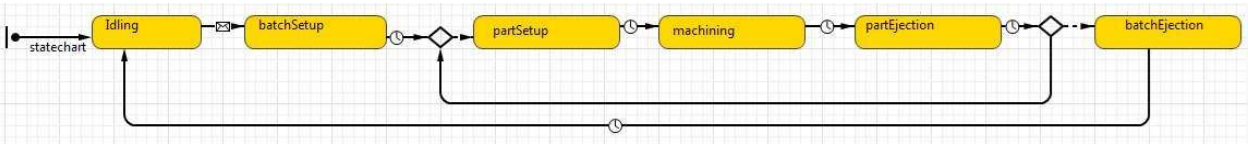

Figure 3: Statechart of the machine level models.

The transition times for batch and part setups and ejection are populated via the CMSD file. The machining time per part can be populated via the CMSD file for modeling at the machine level or generated via the associated process level model. Separate files including the STEP-NC instruction file and machine specification file with data such as feed rate, cutting speed, and depth of cut, are used by the process level model where algorithms simulate the physics of the process (turning or milling) and compute machining time and power consumption. The time generated at the process level can be used to update the part machining time at the machine level, and in turn the part times at machine level can be used to update the batch processing time at the factory level. The model library can be easily extended with additional models to include additional types of machines and associated processes.

4.4 Auto Generation of Logic Network

The logic network to represent the machine shop is automatically generated based on the data parsed from the CMSD file. First, the algorithm builds and customizes the batch Source block. Once the source is built, the algorithms build the last Delay and the Sink of the model. The last Delay represent the finished goods area where a batch is waiting for pickup. The sink represents the end of the flow in the factory level model.

After building these objects the algorithm develops representations of the cells of the machine workshop. Cells can be composed of different numbers of machines. This implementation offers the capability to build a cell having up to five machines. Depending on the number of machines, the algorithm chooses the appropriate components in the process modeling library available in AnyLogic. The cell is represented with a selected set of objects including a Delay block, an output selector (that can be SelectOutput or SelectOutput5 block), and machine level agents from the library to represent the machines

in the cell. First, the algorithm creates the appropriate number of machines using the available agent-based models. The agent based models are first created with no parameters. The parameters are populated later at the beginning of the simulation execution. This was done to work around the AnyLogic procedure that initialized all the automatically generated agents at the start of simulation execution. The procedure does not appear to affect the agents generated through the GUI in the same manner. This is another example of code manipulation required for automatic generation of the model.

Once the machines are generated, the algorithm builds associated Delay blocks. The Delay is customized to hold the batch as long as all machines of the cell are busy. As soon as one machine is available, the Delay block lets a batch go. If a cell is composed of one or two machine, the algorithm builds a SelectOutput which provides two conditional paths as outputs. The condition to decide which way the batch should go consists of checking if the first machine of the cell is available. If not, the batch goes to the second machine. If both machines are busy, the batch stays in the related Delay block. If the cell is composed of more than two machines, the algorithm builds a SelectOutput5 that provides fives conditional paths as outputs. After the objects implementation and the required customization to include the conditions, the Delay and the output selector within each cell model are connected to each other. The algorithm also connects the output selector and the machines that compose the cell.

Next, the cell models are connected as required by the part flows. The algorithm collects the parts and associated process plans from the CMSD file to determine the connections between the cells. It establishes connections between the batch Source block and the Delay block (if the cell is the first one in the flow) or the machines from the previous cell and the Delay block (if the cell is not the first one). If this cell is the last cell of the line, the output paths of the machines are connected to the last Delay block that represents the finished goods area. The approach allows for simple configuration currently. The algorithm will be enhanced iteratively in the future to support more complex logic networks.

4.5 Auto Generation of Layout

The algorithm builds a 2D representation of the machine shop using the information in the layout area of the CMSD file. The algorithm defines shapes to represent the different areas in the factory. The algorithm creates the shapes based on the location and size of the area defined in the CMSD file and adds them to the simulation animation window. To allow the real time visualization of the model execution, the algorithm associates every shape with the corresponding object defined during the automatic generation of the model. Figure 4 shows the rendered layout corresponding to the logic network shown in Figure 2.

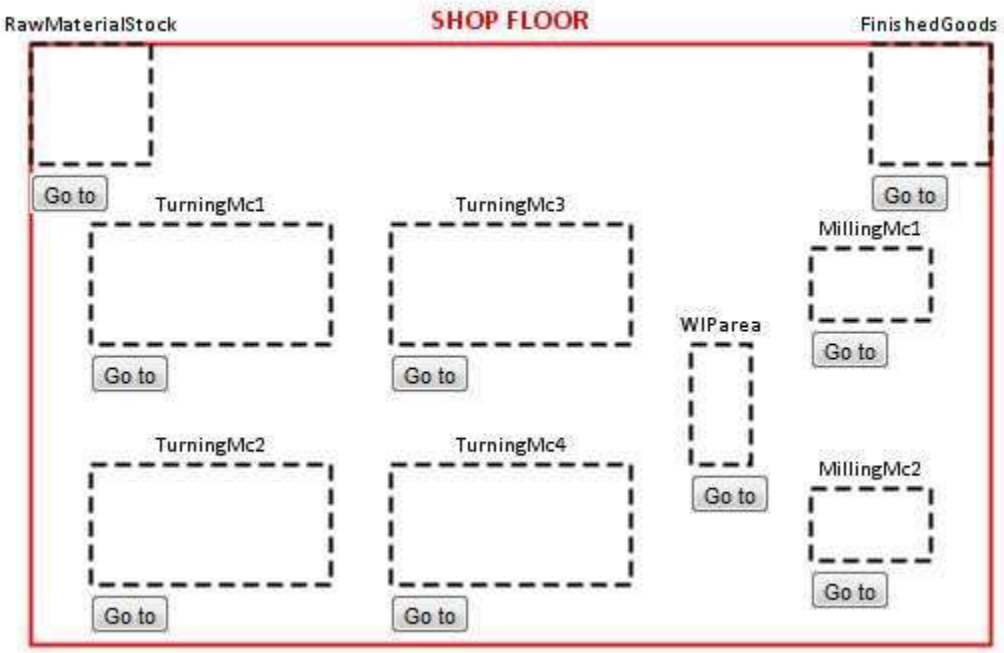

Figure 4: 2D representation of the machine shop.

The algorithm also creates buttons in the layout to allow going to the next level of resolution. The next level of resolution for the machines is the statechart of the agent based representation of the machine. The next level of resolution for storage areas is the corresponding Delay block. Using these buttons, a user can examine the animation at the next resolution level and check the current state of a machine. The addition of this capability in AnyLogic required some custom coding. AnyLogic runs an internal routine to display the blocks that have been built using the GUI. This routine cannot be overwritten to provide capabilities to display agents and blocks that have been automatically built. Since the software does allow overwriting the code of the button function, the button function code was overwritten to specify the agent that should be displayed using each button.

4.6 Data Output Interface

The execution of the machine shop model with the machine level models activated generates MTConnect data streams on demand. MTConnect is an XML-based standard to represent monitoring data collected from machines. The MTConnect files contain the tool position and the power demand values for every 100 milliseconds. Users can use a provided checkbox to generate the MTConnect files at desired times or over desired durations. An MTConnect file can be generated for each part processed in each machine.

4.7 Execution of the Algorithm

The execution of the model runs the algorithm to automatically build the logic network, the required machine level models, and the 2D representation of the scenario. Once the model and the representation of the scenario are built, the source block starts creating the batches. The generation of blocks, layout, and the animation can be watched in real time. The animation can be visualized using the layout or the logic network. Figure 5 shows a screenshot of the execution of the model using the layout. In the figure, each batch shown as a rectangle has ten parts represented by colored dots. As a part is processed it turns from red to blue. As may be noticed from the figure, a machine can have only one batch at any time while the

storage areas can have multiple batches. The checkbox for initiating generation of MTConnect data can be seen on the top left of the figure.

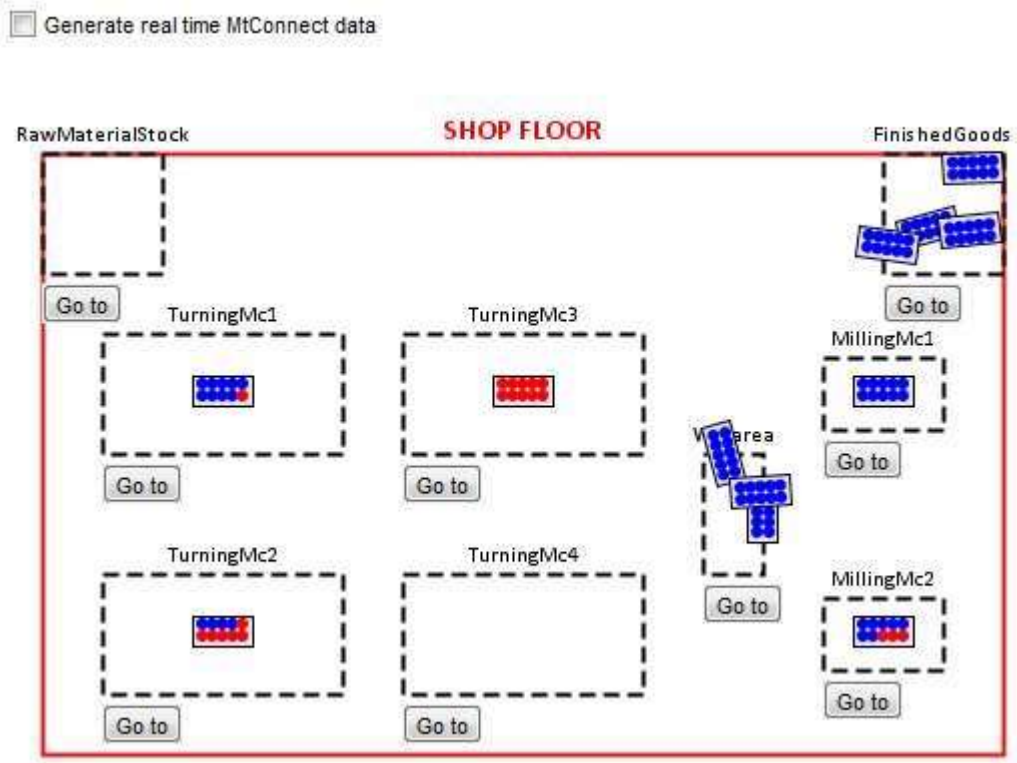

Figure 5: Animation of the model using the factory layout.

5 VALIDATION CHALLENGES

Simulation models need to be validated before their results can be used. The challenges of validation of simulation models have been discussed extensively in literature. A large part of the validation literature has focused on quantifying the intrinsic uncertainty of the model, that is, uncertainty based on the variabilities defined for the input data for modeled stochastic phenomena. Barton and Schruben (1993) pointed out the need to consider the impact of extrinsic uncertainty, introduced due to the inability to capture the input data variabilities correctly. There has been a lot of work to model input uncertainty since the 1993 paper. Barton (2012) discussed the leading methods for quantifying input uncertainty.

Each simulation model has to be validated carefully including the impact of intrinsic and extrinsic uncertainties. All the physics-based process models have to be validated against real machine processes and their ranges of applicability defined. The current two process level models for turning and milling have been validated to varying degrees as defined in Jain et al. (2015) and Lechevalier et al. (2015) respectively. Similarly, machine level and factory level models have to be validated and their ranges of applicability defined. The multi-resolution model results in stacking of uncertainties across the multiple levels of resolution. The outputs of the process level model have uncertainties. The output of the process level model becomes one of the inputs for the machine level model. The outputs of machine level model thus include uncertainties emanating from all its inputs including the machining time provided by the process level model, and the variabilities defined in the batch and part set up and ejection times. This continues further up to the outputs of the factory level model that include uncertainties due to operation times from the machine level coming as inputs. The impact of stacking of uncertainties needs to be understood and

quantified before the virtual factory and other multi-resolution models can be used to support decision making in industry.

6 CONCLUSION

The paper described the next step in a long term effort to build virtual factories corresponding to real factories. Previous reports of the work described the ad hoc implementation of multi-resolution model implementation of a virtual factory corresponding to a small machining shop. This step of the work reported on the automatic generation of the virtual factory model for the machining shop using inputs based on standards. The automated generation capability needs to be enhanced to handle larger more complex scenarios. When fully implemented the automated generation capability should help increase the use of virtual factory simulations and in turn help the move toward realization of initiatives such as smart manufacturing and Industrie 4.0.

Future work includes enhancement in the model, inputs, and outputs. The model and the interface need to be enhanced for handling more complex scenarios. The machine level model library will be grown to include more manufacturing machine and processes. The capability to read in the current status possibly based on ISA-95 standard from a warm start to the model is being contemplated. Additional capabilities for generating output data particularly at the factory level possibly based on ISA-95 standard are planned. Once the concept is well developed and issues understood in the single software environment provided by AnyLogic, integration with component models in other software via a distributed simulation mechanism may also be explored.

DISCLAIMER

No approval or endorsement of any commercial product by the National Institute of Standards and Technology (NIST) is intended or implied. Certain commercial software systems are identified in this paper to facilitate understanding. Such identification does not imply that these software systems are necessarily the best available for the purpose.

ACKNOWLEDGMENTS

Sanjay Jain's work on this effort has been sponsored under the cooperative agreement no. 70NANB13H158 between NIST and George Washington University. David Lechevalier's work on this effort was supported by National Institute of Standards and Technology's Foreign Guest Researcher Program. The work described was funded by the United States Government and is not subject to copyright.

REFERENCES

Abduaziz, O., J. K. Cheng, R. M. Tahar, and R. Varma. 2015 "A hybrid Simulation model for Green Logistics Assessment in Automotive Industry." Procedia Engineering 100: 960-969.

Alvandi, S., G. Bienert, W. Li, and S. Kara. 2015. "Hierarchical modelling of complex material and energy flow in manufacturing systems." Procedia CIRP 29: 92-97.

Ayadi, M., R. C. Affonso, V. Cheutet, and M. Haddar. 2015. "Info Sim: Prototyping an Information System for Digital Factory Management." Concurrent Engineering 23(4):355-364.

Barton, R. 2012. "Tutorial: Input Uncertainty In Output Analysis," In Proceedings of the 2012 Winter Simulation Conference, edited by C. Laroque, J. Himmelspach, R. Pasupathy, O. Rose, and A.M. Uhrmacher, 67-78. Piscataway, New Jersey: Institute of Electrical and Electronics Engineers, Inc.

Barton, R. R., and L. W. Schruben. 1993. “Uniform and Bootstrap Resampling of Empirical Distributions.” In Proceedings of the 1993 Winter Simulation Conference, edited by G. W. Evans, M. Mollaghasemi, E. C. Russell, W. E. Biles, 503-508. Piscataway, New Jersey: Institute of Electrical and Electronics Engineers, Inc.

Choi, S., K. Jung, and S. Do Noh. 2015. "Virtual reality applications in manufacturing industries: Past research, present findings, and future directions." Concurrent Engineering 23(1): 40-63.\

Constantinescu, C. L., E. Francalanzab, and D. Matarazzoc. 2015. "Towards Knowledge Capturing and Innovative Human-system Interface in an Open-source Factory Modelling and Simulation Environment." Procedia CIRP 33:23–28.

Gregor, M., J. Hercko, and P. Grznar. 2015. "The factory of the future production system research." In Proceedings of the 21st International Conference on Automation and Computing (ICAC), 1-6. IEEE.

Jain, S., and G. Shao. 2014. “Virtual Factory Revisited for Manufacturing Data Analytics.” In Proceedings of the 2014 Winter Simulation Conference, edited by A. Tolk, S. D. Diallo, I. O. Ryzhov, L. Yilmaz, S. Buckley, and J. A. Miller, 887-898. Piscataway, New Jersey: Institute of Electrical and Electronics Engineers, Inc.

Jain, S., D. Lechevalier, J. Woo, and S.-J. Shin. 2015. “Towards a Virtual Factory Prototype.” In Proceedings of the 2015 Winter Simulation Conference, edited by L. Yilmaz, W. K. V. Chan, I. Moon, T. M. K. Roeder, C. Macal, and M. D. Rossetti, 2207-2218. Piscataway, New Jersey: Institute of Electrical and Electronics Engineers, Inc.

Lechevalier, D., S.-J. Shin, J. Woo, S. Rachuri, and S. Foufou. 2015 “A virtual milling machine model to generate machine-monitoring data for predictive analytics.” At Product Lifecycle Management 2015. Doha, Qatar.

Mario, H., P. Tobias, and O. Boris. 2015. “Design Principles for Industrie 4.0 Scenarios: A Literature Review.” Working Paper No. 01 / 2015, Technische Universität Dortmund, Dortmund, Germany.

Matsuda, M., and F. Kimura. 2015. "Usage of a digital eco-factory for sustainable manufacturing." CIRP Journal of Manufacturing Science and Technology 9: 97-106.

Oyekan, J., W. Hutabarat, C. Turner, A. Tiwari, N. Prajapat, N. Ince, X.-P. Gan, and T. Waller. 2015. "A 3D immersive Discrete Event Simulator for enabling prototyping of factory layouts." Procedia CIRP 38: 63-67.

Rabelo, L., A. T. Sarmiento, M. Helal, and A. Jones. 2015. "Supply chain and hybrid simulation in the hierarchical enterprise." International Journal of Computer Integrated Manufacturing 28(5): 488-500.

Schönemann, M., C. Schmidt, C. Herrmann, and S. Thiede. 2016. "Multi-level Modeling and Simulation of Manufacturing Systems for Lightweight Automotive Components." Procedia CIRP 41: 1049-1054. SMLC 2012. SMLC Forum: Priorities, Infrastructure, and Collaboration for Implementation of Smart Manufacturing: Workshop Summary Report. Smart Manufacturing Leadership Coalition (SMLC), Washington, DC, USA. Oct. 2-3. Accessed April 6, 2014: https://smartmanufacturingcoalition.org/sites/default/files/smlc_forum_report_vf_0.pdf.

Terkaj, W., T. Tolio, and M. Urgo. 2015. "A virtual factory approach for in situ simulation to support production and maintenance planning." CIRP Annals-Manufacturing Technology 64(1): 451-454.

AUTHOR BIOGRAPHIES

SANJAY JAIN is an Associate Professor in the Department of Decision Sciences, School of Business at the George Washington University. Before moving to academia, he accumulated over a dozen years of industrial R&D and consulting experience working at Accenture in Reston, VA, USA, Singapore Institute of Manufacturing Technology, Singapore and General Motors North American Operations Technical Center in Warren, MI, USA. He served as an associate editor of the International Journal of Simulation and

Process Modelling for 2004-2014 and continues to serve as a member of the editorial board of the International Journal of Industrial Engineering. His research interests are in application of modeling and simulation of complex scenarios including smart manufacturing systems and project management. His email address is jain@email.gwu.edu.

DAVID LECHEVALIER is an international guest associate in NIST's Systems Integration Division of the Engineering Laboratory. He is a PhD student in the laboratory Le2i at the University of Burgundy. His current research topics include advanced analytics and modeling for Smart Manufacturing. He received a computer science Master's degree in Database and Artificial Intelligence from University of Burgundy in 2012. His email address is david_lechevalier@etu.u-bourgogne.fr.

Inertial Measurement Unit for On-Machine Diagnostics of Machine Tool Linear Axes

Gregory W. Vogl[1], M. Alkan Donmez[1], Andreas Archenti[2], and Brian A. Weiss[1]

[1]*National Institute of Standards and Technology (NIST), Gaithersburg, Maryland, 20899, USA*

gregory.vogl@nist.gov
alkan.donmez@nist.gov
brian.weiss@nist.gov

[2]*KTH Royal Institute of Technology, Brinellvägen 68, 10044, Stockholm, Sweden*

archenti@kth.se

ABSTRACT

Machine tools degrade during operations, yet knowledge of degradation is elusive; accurately detecting degradation of machines' components such as linear axes is typically a manual and time-consuming process. Thus, manufacturers need automated, efficient, and robust methods to diagnose the condition of their machine tool linear axes with minimal disruptions to production. Towards this end, a method was developed to use data from an inertial measurement unit (IMU) for identification of changes in the translational and angular errors due to axis degradation. The IMU-based method uses data from accelerometers and rate gyroscopes to identify changes in linear and angular errors due to axis degradation. A linear axis testbed, established for the purpose of verification and validation, revealed that the IMU-based method was capable of measuring geometric errors with acceptable test uncertainty ratios. Specifically, comparison of the IMU-based and laser-based results demonstrate that the IMU-based method is capable of detecting micrometer-level and microradian-level degradation of linear axes. Consequently, an IMU was created for application of the IMU-based method on a machine tool as a proof of concept for detection of linear axis error motions. If the data collection and analysis are integrated within a machine controller, the process may be streamlined for the optimization of maintenance activities and scheduling, supporting more intelligent decision-making by manufacturing personnel and the development of self-diagnosing smart machine tools.

1. INTRODUCTION

Machine tool linear axes move the cutting tool and workpiece to their desired positions for parts production (Altintas, Verl, Brecher, Uriarte & Pritschow, 2011). A typical machine tool has multiple linear axes, and their accuracies directly impact the quality of manufactured parts. However, over a machine tool's lifetime, various faults lead to performance degradation, lowering accuracy and repeatability (Li, Wang, Lin & Shi, 2014). Typical sources of errors within linear axes are due to pitting, wear, corrosion, and cracks of the system components such as guideways and recirculating balls (Zhou, Mei, Zhang, Jiang & Sun, 2009). As degradation increases, tool-to-workpiece errors increase that eventually may result in a failure and/or a loss of production quality (Uhlmann, Geisert & Hohwieler, 2008). Yet knowledge of degradation is illusive; proper assessment of axis degradation is often a manual, time-consuming, and potentially cost-prohibitive process.

While direct methods for machine tool performance evaluation are well-established (International Organization for Standardization, 2012) and reliable for position-dependent error quantification, such measurements typically interrupt production (Khan & Chen, 2009). An online condition monitoring system for linear axes is needed to help reduce machine downtime, increase productivity and product quality, and improve knowledge about manufacturing processes (Teti, Jemielniak, O'Donnell & Dornfeld, 2010). Efforts to monitor the condition of linear axes components have utilized various sensors, e.g., built-in rotary encoders (Verl, Heisel, Walther & Maier, 2009), current sensors (Uhlmann et al., 2008), and accelerometers (Liao & Lee, 2009; Spiewak, Zaiss & Ludwick, 2013). These attempts at condition monitoring of linear axes had limited success, partly because of the lack of robustness and defined

Archenti, Andreas; Donmez, M; Vogl, Gregory; Weiss, Brian.
"Inertial Measurement Unit for On-Machine Diagnostics of Machine Tool Linear Axes."
Paper presented at 2016 Annual Conference of the Prognostics and Health Management Society, Denver, CO. October 2, 2016 - October 8, 2016.

relationships of signals to axis degradation composed of a wide range of spatial frequencies.

Consequently, efficient quantitative measures are needed to monitor the degradation of linear axes. Recently, accelerometers have been used for dynamic metrology of machine tools (Sato, Nagaoka & Sato, 2015; Smith & Hocken, 2013) and six-degree-of-freedom motion sensors exist within integrated circuit (IC) components (InvenSense Incorporated, 2016). Thus, the use of an inertial measurement unit (IMU) is attractive for on-machine condition monitoring.

One potential solution for online monitoring of linear axis degradation is the use of an IMU (Vogl, Weiss & Donmez, 2015). As seen in the schematic of Figure 1, an IMU is mounted to a moving machine tool component. To diagnose axis degradation, the axis is moved back and forth at various speeds to capture data for different frequency bandwidths. This data is then integrated, filtered, and 'fused' to estimate the changes in the 6-degree-of-freedom (DOF) geometric errors of the axis. Because the linear axes are stacked, coordinate transformations may be used with all 6-DOF errors to estimate the errors at the functional point (International Organization for Standardization, 2012). Ideally, data would be collected periodically to track axis degradation with minimal disruptions to production. With robust diagnostics and prognostics algorithms, incipient faults may be detected and future failures may be avoided. In essence, IMU data can be used to help optimize maintenance, production planning, flexibility, and ultimately part quality.

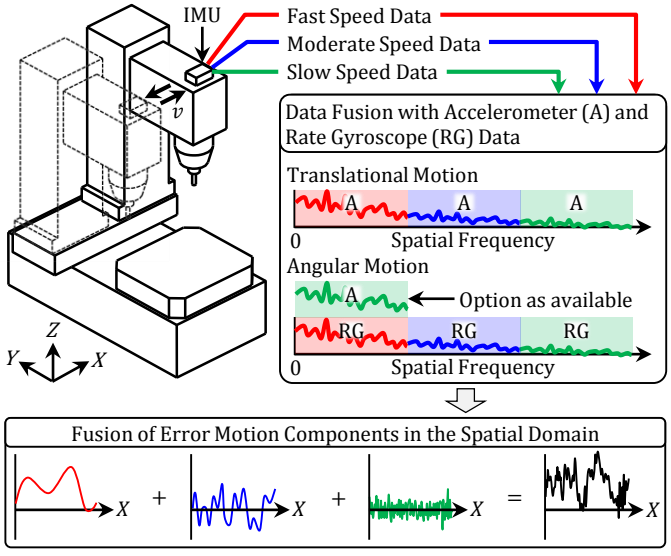

Figure 1. IMU-based method for diagnostics of machine tool performance degradation.

2. IMU AND ERROR MOTIONS FOR DIAGNOSTICS

A testbed was designed for evaluation of the IMU-based method. As seen in Figure 2(a), the testbed includes a translation stage, the IMU, a commercial laser-based system for measuring the geometric errors of the axis, and a direct current (DC) motor with encoder for motion control. While the metrology system measures the motion of the carriage with respect to the base of the linear axis, the carriage-mounted IMU measures the changes in the inertial motion of the carriage. The commercial metrology system measures straightness and angular error motions over the travel length of 0.32 m with standard uncertainties of 0.7 µm and 3.0 µrad, respectively. The laser-based system is used for verification and validation (V&V) of the IMU-based results.

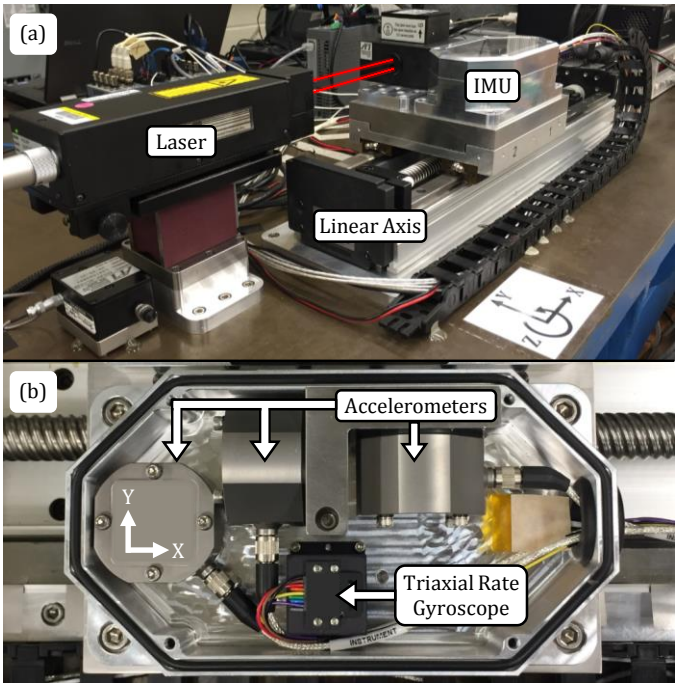

Figure 2. (a) Linear axis testbed and (b) top view of IMU without its lid.

For the detection of both translational and rotational motions, the IMU contains three accelerometers and one triaxial rate gyroscope, as seen in Figure 2(b). Table 1 outlines key specifications of the IMU sensors. Individual sensors were used to obtain sufficiently low noise, despite the larger sensor volume compared to a single 6-DOF IC sensor.

Table 1. Specified properties of sensors used in the IMU

Sensor	Bandwidth[a]	Noise
Accelerometer	0 Hz to 1800 Hz	4.0 (µm/s^2)/√Hz from 0 Hz to 100 Hz
Rate Gyroscope	0 Hz to 200 Hz	35 (µrad/s)/√Hz

[a] frequencies correspond to half-power points, also known as 3 dB points

Consequently, these sensors enable the estimation of 6-DOF motion. A typical machine tool has three linear axes, which means that a total of 18 (= 6 × 3) translational and angular motion errors exist. These errors are major contributors to the position-dependent tool-to-workpiece errors. Figure 3 shows these six errors that change with axis degradation. As the

carriage is positioned along the X axis, it experiences three translational errors from its nominal path: one linear displacement error (E_{XX}) in the X-axis direction and two straightness errors (E_{YX} and E_{ZX}) in the Y- and Z-axis directions. The carriage also experiences three angular errors (E_{AX}, E_{BX}, and E_{CX}) about the X-, Y-, and Z-axes.

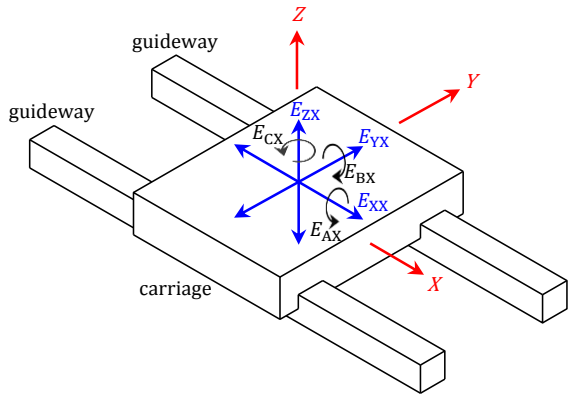

Figure 3. Translational and angular errors of a component commanded to move along a (nominal) straight-line trajectory parallel to the X-axis.

Small levels of degradation of linear axes are expected and allowed, but there are limits specified for axis errors. ISO 10791-2 (International Organization for Standardization, 2001) specifies the tolerances for linear axis errors of vertical machining centers. As shown in Table 2, the acceptable straightness error is limited to 20 µm and the acceptable angular error is limited to 60 µrad. A test uncertainty ratio (TUR) of at least 4:1 is deemed to be acceptable, which means that straightness and angular error measurement uncertainties of 5 µm and 15 µrad, respectively, are acceptable based on the tolerances outlined in Table 2.

Table 2. Tolerances for linear axis errors of vertical machining centers.

Error	Tolerance*
Straightness	20 µm
Angular (Pitch, Yaw, or Roll)	60 µrad

* for axes capable of 1 meter of travel, according to ISO 10791-2 (International Organization for Standardization, 2001)

3. IMU-Based Method and General Results

As outlined in Figure 1, the IMU-based method relies on fusion of data collected at three programmed speeds of the carriage: Fast speed ($v_1 = 0.5$ m/s), Moderate speed ($v_2 = 0.1$ m/s), and Slow speed ($v_3 = 0.02$ m/s). The different speeds allow for sensing of repeatable error motions, composed of low to high spatial frequencies, within different temporal bandwidths. Such a process takes advantage of the enhanced signal-to-noise and lower sensor drift at faster speeds, while taking advantage of the detection of higher spatial frequencies at slower speeds without violating sensor bandwidths. As seen in Figure 1, matching the spatial cutoff frequencies enables the data fusion, while filtering allows for the attenuation of significant modal excitations, especially resulting from the initial and final accelerations during the Fast speed cycle (Vogl, Donmez & Archenti, 2016).

Figure 4 shows the typical convergence of an estimated straightness error motion and an estimated angular error motion with increasing number of runs for averaging. As seen in Figure 4, 10 runs is usually sufficient for convergence within 5 µm or 15 µrad, which means the IMU-based method has the potential to estimate geometric motion errors with a test uncertainty ratio (TUR) of at least 4:1.

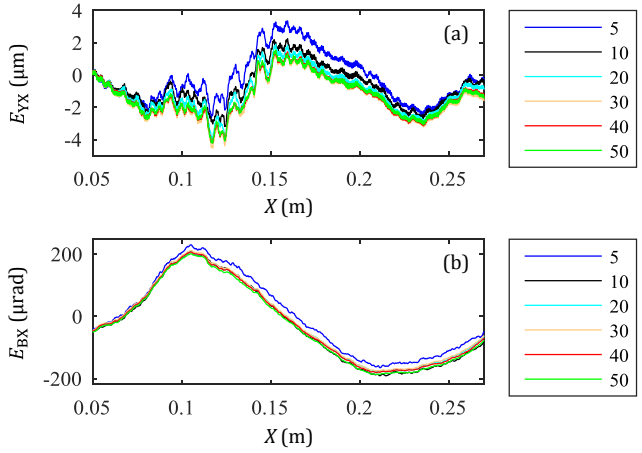

Figure 4. Typical convergence of (a) an estimated straightness error motion (via accelerometer data) and (b) an estimated angular error motion (via rate gyroscope data) with increasing number of runs for averaging (from 5 to 50).

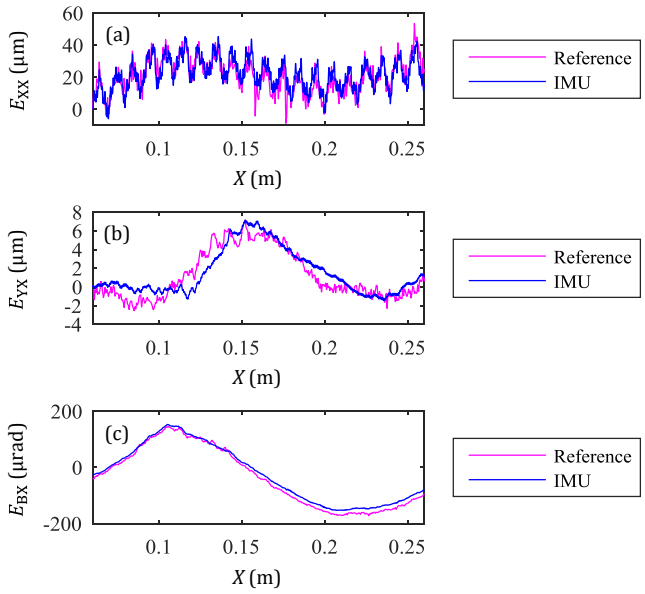

Figure 5. Example of converged (a) linear positioning error motion, (b) straightness error motion, and (c) angular error motion for various sensing methods.

Figure 5 compares the laser-based measurement and IMU-based results; the standard deviations of the differences are 11 µm, 2.3 µm, and 13 µrad for the linear positioning, straightness, and angular error motions, respectively.

4. TESTBED EXPERIMENTATION

Figure 6(a) shows how a linear axis rail was deformed with shims to simulate low spatial frequency degradations of a machine tool axis. The entire rail was raised with shims so that the center shims could be changed without loosening more than one screw (the center rail screw). Measurements for each case were taken with the reference- and IMU-based systems, resulting in the Y-axis straightness error motions seen in Figure 6(b) and Figure 6(c), respectively. The IMU-based method is able to detect the approximately 5 µm change in straightness from Case 0 to Case 4, as verified by the reference measurements.

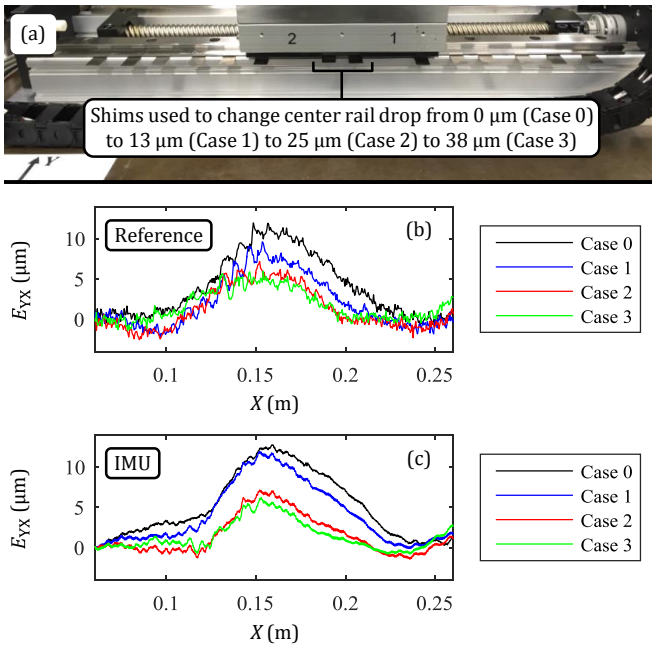

Figure 6. (a) Experimental setup to represent low-frequency degradations of a guideway rail, resulting in changes in straightness error motion (E_{YX}) observed by the (b) laser-based reference system and the (c) IMU (data averaged for 50 runs).

One approach for investigating degradation of linear axes is to use filtering to focus on certain sources of errors, such as surface pitting of the rails. Specifically, low-frequency components can be neglected through high-pass filtering. Towards this end, Figure 7(a) shows data smoothed via use of a linear Savitzky-Golay smoothing filter (The MathWorks Incorporated, 2015). The frame size for the Savitzky-Golay filter was chosen to be 2 cm, which is large compared to millimeter-sized defects. Thus, the high-pass filtered data is representative of many defects caused by wear. In Figure 7(a), the error motion ('No filter') is filtered via the Savitzky-Golay filter to produce low-pass filtered data ('Low-pass'), and the high-pass filtered data ('High-pass') is the complement of the low-pass filtered data; the low-pass and high-pass filtered data sum to yield the unfiltered error motion.

This filtering process can be applied to any linear axis error motion. Figure 7(b) shows typical high-pass filtered data for E_{CX} for various numbers of runs for averaging (from 5 to 50), where $\mathrm{hp}(E_{CX})$ is the high-pass filtered data of E_{CX}. As seen in Figure 7(b), convergence for $\mathrm{hp}(E_{CX})$ is achieved to within 5 µm (TUR = 4) in less than 10 runs for averaging. Furthermore, the high-pass filtered error motion reveals influences from the ball bearings in the trucks. Each ball has a diameter of about 4 mm, which means that each ball rolls on its rail with a ball-passing distance of 12.5 mm (the ball circumference). Figure 7(b) shows how the combined influence of these balls creates a net error motion with significant components dependent upon the ball-passing distance.

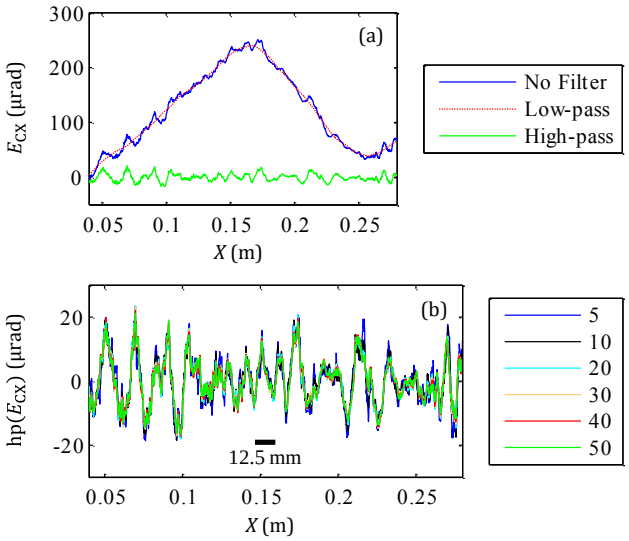

Figure 7. (a) Yaw error motion (E_{CX}) separated into low- and high-pass components, and (b) the high-pass component of E_{CX} for various number of runs for averaging (from 5 to 50).

5. IMU FOR INDUSTRIAL APPLICATION

The IMU seen in Figure 2 was created for testing of the method within the linear axis testbed. For industrial application, the IMU should be physically smaller and more economical while still satisfying the measurement needs.

Consequently, for application on machine tools, an 'industrial IMU' was created that is about 73% smaller than the 'testbed IMU'. As seen in Figure 8, the industrial IMU is about 9 cm long and contains a triaxial accelerometer and a triaxial rate gyroscope. The bandwidths and noise properties of these sensors are seen in Table 3. The rate gyroscope in the industrial IMU is identical to the one used in the testbed IMU. In contrast, the three uniaxial accelerometers seen in Figure

2(b) have been replaced with a triaxial accelerometer seen in Figure 8(b). This change had many advantages: the reduction of space required for acceleration sensors, the elimination of the L-bracket for accelerometer mounting, and a significant reduction of sensor cost. However, the change also had some disadvantages, specifically the reduction of accelerometer bandwidth from 1800 Hz to 500 Hz and the 5-fold increase of accelerometer noise from 4.0 $(\mu m/s^2)/\sqrt{Hz}$ to 20 $(\mu m/s^2)/\sqrt{Hz}$.

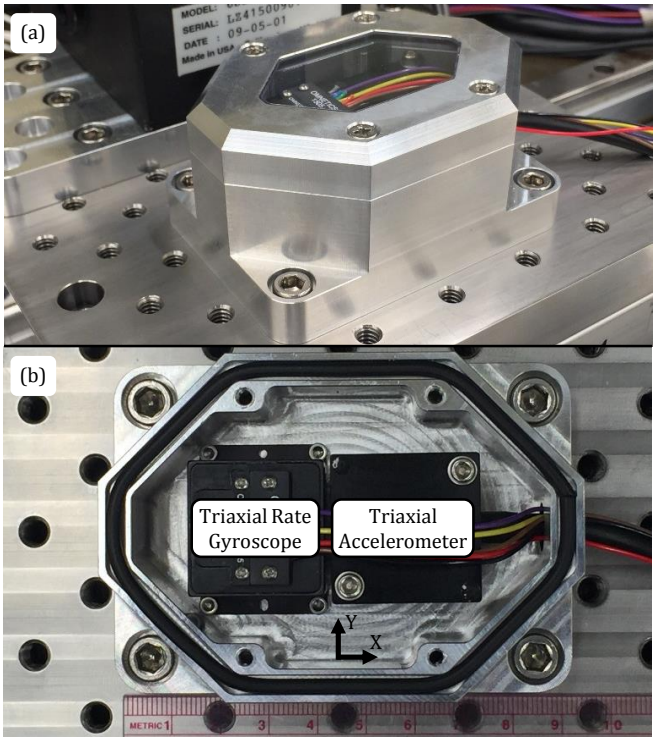

Figure 8. (a) Isometric view of industrial IMU and (b) top view of industrial IMU without its lid.

Table 3. Properties of sensors in industrial IMU

Sensor	Bandwidth[a]	Noise
Accelerometer	0 Hz to 500 Hz	20 $(\mu m/s^2)/\sqrt{Hz}$
Rate Gyroscope	0 Hz to 200 Hz	35 $(\mu rad/s)/\sqrt{Hz}$

[a] frequencies correspond to half-power points, also known as 3 dB points

According to simulations of the data fusion process, the accelerometer used in the industrial IMU will result in approximately twice as much uncertainty in straightness errors as that for the testbed IMU. As seen in Figure 9, the 5-fold increase of accelerometer noise from 4.0 $(\mu m/s^2)/\sqrt{Hz}$ (for the testbed IMU) to 20 $(\mu m/s^2)/\sqrt{Hz}$ (for the industrial IMU) should result in an approximate 2-fold increase in straightness uncertainty. Figure 9 shows that as the accelerometer noise decreases, the uncertainty decreases to a limit caused by noise of the data acquisition (DAQ) equipment. Experimental data will be collected to confirm the slower rate of convergence for the industrial IMU.

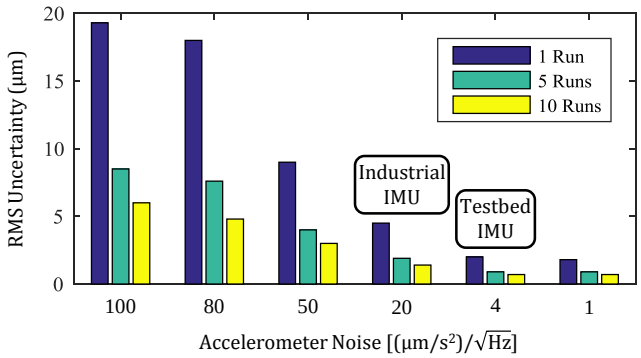

Figure 9. Simulated uncertainty for straightness error motions due to data fusion process with accelerometer noise and data acquisition noise.

6. Conclusions

Manufacturers need efficient and robust methods for diagnosis of machine tool linear axes with minimal disruptions to production. Towards this end, a new IMU-based method was developed for linear axis diagnostics. Measurements from accelerometers and rate gyroscopes are used to identify changes in translational and angular error motions due to axis degradation. Data is fused in the spatial frequency domain via filtering in order to include both low- and high-frequency error motions while excluding significant modal excitations.

A linear testbed was used to verify and validate the IMU-based method through use of a laser-based system for measurement of the geometric axis performance. The IMU-based results typically converge within 5 μm or 15 μrad when using 10 runs for averaging, needed for the estimation of changes in geometric motion errors with test uncertainty ratios of at least 4:1.

Future tests will reveal the effectiveness of the new IMU-based method for on-machine application through use of an 'industrial IMU'. The IMU and the laser-based system (for V&V) will be utilized on various machine tools within the National Institute of Standards and Technology (NIST) Fabrication Technology machine shops. Metrics will be defined based on the collected data to quantify machine tool linear axis degradation, to inform the user of the magnitude and location of wear and any violations of performance tolerances. If the data collection and analysis are integrated within a machine controller, the process may be streamlined for the optimization of maintenance, supporting the development of self-diagnosing smart machine tools. When coupled with existing data exchange and formatting standards, verified and validated data from an 'industrial IMU' could provide manufacturers and machine tool operators with near-real-time equipment health, diagnostic, and prognostic intelligence to significantly enhance asset availability and minimize unscheduled maintenance.

A by-product of this research is that IMU-related experimentation across multiple machines is likely to highlight differences in equipment health between different machine tools. This information can be coupled with equipment performance metrics and quality data (resultant from part inspection) to enable the prediction of future machine performance and part quality based upon current and projected equipment health. Ultimately, this research has the potential to have substantial impact within the manufacturing community.

ACKNOWLEDGEMENTS

The authors thank the Fabrication Technology Group (NIST) for their outstanding contributions with the experimental setup.

NIST DISCLAIMER

Certain commercial equipment, instruments, or materials are identified in this paper to foster understanding. Such identification does not imply recommendation or endorsement by the National Institute of Standards and Technology, nor does it imply that the materials or equipment identified are necessarily the best available for the purpose.

REFERENCES

Altintas, Y., Verl, A., Brecher, C., Uriarte, L., & Pritschow, G. (2011). Machine tool feed drives. *CIRP Annals - Manufacturing Technology,* vol. 60(2), pp. 779-796. doi: 10.1016/j.cirp.2011.05.010

International Organization for Standardization (2001). *ISO 10791-2 - test conditions for machining centres − part 2: Geometric tests for machines with vertical spindle or universal heads with vertical primary rotary axis (vertical z-axis)*.

International Organization for Standardization (2012). *ISO 230-1 - test code for machine tools − part 1: Geometric accuracy of machines operating under no-load or quasi-static conditions*.

InvenSense Incorporated (2016). *MPU-6050 six-axis (gyro + accelerometer) MEMS MotionTracking™ device*: https://www.invensense.com/products/motion-tracking/6-axis/mpu-6050/

Khan, A. W. & Chen, W. (2009). Calibration of CNC milling machine by direct method. *2008 International Conference on Optical Instruments and Technology: Optoelectronic Measurement Technology and Applications* (p. 716010), November 16-19, 2008, Beijing, China. doi: 10.1117/12.807066

Li, Y., Wang, X., Lin, J., & Shi, S. (2014). A wavelet bicoherence-based quadratic nonlinearity feature for translational axis condition monitoring. *Sensors,* vol. 14(2), pp. 2071-2088.

Liao, L. & Lee, J. (2009). A novel method for machine performance degradation assessment based on fixed cycle features test. *Journal of Sound and Vibration,* vol. 326(3–5), pp. 894-908. doi: 10.1016/j.jsv.2009.05.005

Sato, R., Nagaoka, K., & Sato, T., "Machine motion trajectory measuring device, numerically controlled machine tool, and machine motion trajectory measuring method," USA Patent US9144869 B2, Sep. 29, 2015.

Smith, K. S. & Hocken, R. J., "Dynamic metrology methods and systems," USA Patent US8401691 B2, Mar. 19, 2013.

Spiewak, S., Zaiss, C., & Ludwick, S. J. (2013). High accuracy, low-invasive displacement sensor (halids). *ASME 2013 International Mechanical Engineering Congress and Exposition, IMECE 2013* (p. V02AT02A077), November 15-21, 2013, San Diego, CA, United states. doi: 10.1115/IMECE2013-66767

Teti, R., Jemielniak, K., O'Donnell, G., & Dornfeld, D. (2010). Advanced monitoring of machining operations. *CIRP Annals - Manufacturing Technology,* vol. 59(2), pp. 717-739. doi: 10.1016/j.cirp.2010.05.010

The MathWorks Incorporated (2015). *Documentation: Sgolayfilt*: http://www.mathworks.com/help/signal/ref/sgolayfilt.html

Uhlmann, E., Geisert, C., & Hohwieler, E. (2008). Monitoring of slowly progressing deterioration of computer numerical control machine axes. *Proceedings of the Institution of Mechanical Engineers, Part B: Journal of Engineering Manufacture,* vol. 222(10), pp. 1213-1219.

Verl, A., Heisel, U., Walther, M., & Maier, D. (2009). Sensorless automated condition monitoring for the control of the predictive maintenance of machine tools. *CIRP Annals - Manufacturing Technology,* vol. 58(1), pp. 375-378.

Vogl, G. W., Weiss, B. A., & Donmez, M. A., "A sensor-based method for diagnostics of machine tool linear axes," presented at the Annual Conference of the Prognostics and Health Management Society 2015, Coronado, CA, 2015.

Vogl, G. W., Donmez, M. A., & Archenti, A. (2016). Diagnostics for geometric performance of machine tool linear axes. *CIRP Annals - Manufacturing Technology,*

Zhou, Y., Mei, X., Zhang, Y., Jiang, G., & Sun, N. (2009). Current-based feed axis condition monitoring and fault diagnosis. *4th IEEE Conference on Industrial Electronics and Applications, ICIEA 2009* (pp. 1191-1195), May 25-27, 2009, Xi'an, China. doi: 10.1109/ICIEA.2009.5138390

BIOGRAPHIES

Dr. Gregory W. Vogl is a Mechanical Engineer at the National Institute of Standards and Technology (NIST) located in Gaithersburg, Maryland. He received his B.S. (2000), M.S. (2003), and Ph.D. (2006) degrees in Engineering Mechanics from Virginia Tech, Virginia, USA. Currently, Greg is a member of the *Prognostics and Health Management for Smart Manufacturing Systems* (PHM4SMS) project, which seeks to develop a methodology, protocols, and reference datasets to enable robust real-time diagnostics and prognostics for smart manufacturing systems. Previously, he designed, fabricated, and experimented on microelectromechanical systems as a National Research Council Postdoctoral Researcher at NIST. He then joined the Production Systems Group, in which he worked on machine tool metrology and standards development. His interests include machine tool spindle health, diagnostic and prognostic methods, nonlinear dynamics, engineering mechanics, and metrology.

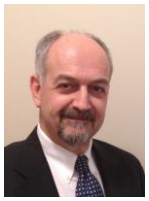

Dr. Alkan Donmez is currently the Group Leader of the Production Systems Group as well as the Program Manager for the *Measurement Science for Additive Manufacturing* program in the NIST Engineering Laboratory. He has been with NIST for more than 25 years conducting and supervising research in advanced manufacturing sciences, including machine tool performance modeling and metrology, machining process metrology, as well as the recent efforts in metal-based additive manufacturing. He has actively participated in national and international standard committees, developing machine tool performance testing standards, for more than 20 years. He has published more than 70 technical papers and reports in the area of machine tool metrology and manufacturing sciences. He has received various awards for his technical contributions, including R&D100, Applied Research Award of NIST, and Department of Commerce Silver and Bronze Medals.

Dr. Andreas Archenti is conducting research in the field of Precision Engineering and is currently the Research Leader for the Precision Manufacturing and Metrology group at KTH Royal Institute of Technology in Stockholm, Sweden. He received his M.S. (2007) in Mechanical Engineering, and Ph.D. (2011) in Production Engineering focusing on Machine and Process technology from KTH. He is also the Director of the Center for Design and Management of Manufacturing Systems (DMMS) at the KTH. As the Director of DMMS, Andreas is responsible for coordination of activities in research, education, and information dissemination between academia and manufacturing industry. His efforts have earned him the ABB Alde Nilsson Foundation award for excellence in production research (2011).

Dr. Brian A. Weiss has a B.S. in Mechanical Engineering (2000), Professional Masters in Engineering (2003), and Ph.D. in Mechanical Engineering (2012) from the University of Maryland, College Park, Maryland, USA. He is currently the Associate Program Manager of the *Smart Manufacturing Operations Planning and Control* program and the Project Leader of the *Prognostics and Health Management for Smart Manufacturing Systems* project within the NIST Engineering Laboratory. Prior to his leadership roles in the SMOPAC program and the PHM4SMS project, he spent 15 years conducting performance assessments across numerous military and first response technologies including autonomous unmanned ground vehicles; tactical applications operating on Android devices; advanced soldier sensor technologies; free-form, two-way, speech-to-speech translation devices for tactical use; urban search and rescue robots; and bomb disposal robots. His efforts have earned him numerous awards including a Department of Commerce Gold Medal (2013), Silver Medal (2011), Bronze Medals (2004 & 2008), and the Jacob Rabinow Applied Research Award (2006).

Lessons Learned from Spray Polyurethane Foam (SPF) Emission Testing using Micro-chambers

DUSTIN POPPENDIECK
National Institute of Standards and Technology
100 Bureau Drive
Gaithersburg, MD 20899-8663

MENGYAN GONG
National Institute of Standards and Technology
100 Bureau Drive
Gaithersburg, MD 20899-8663

LAUREN LAWSON
National Institute of Standards and Technology
100 Bureau Drive
Gaithersburg, MD 20899-8663

ABSTRACT

Both governmental agencies and the spray polyurethane foam (SPF) insulation industry have sought more information on potential chemical emissions from SPF to better understand worker and occupant exposures along with associated health impacts. This research was designed to contribute to the development and evaluation of voluntary standards for testing emissions from SPF to help provide answers to exposure questions. Specifically, this work was performed to support the ASTM Indoor Air (D22.05) subcommittee consensus-based efforts to develop a standard that can be used to compare emissions from SPF under uniform micro-chamber testing conditions. Although limitations in the current proposed method do not allow the generated data to be directly used in exposure modeling, it does allow conclusions to be drawn on how emissions between different types of SPF vary under the tested conditions. Micro-chamber SPF emission testing was performed at the National Institute of Standards and Technology (NIST), and it has demonstrated: 1) a wide range of chemicals can emit from SPF under the tested conditions; 2) the same chemical may emit at concentrations that are an order of magnitude different for open-cell versus closed-cell SPF, 3) the same chemical may emit at different rates from the same type of SPF (*i.e.* closed-cell SPF), 4) different chemicals may emit with different emission profiles (constant versus exponential decay) in the same foam, and 5) emission rates from SPF are highly temperature dependent. This research establishes that emissions from SPF can be highly variable. In addition, micro-chamber testing can be used to demonstrate emission differences between SPF, whether the purpose is to compare new manufacturer formulations or to compare emissions from standard spray events and misapplications.

INTRODUCTION

Spray polyurethane foam (SPF) insulation is a unique building material as it 1) reduces both conductive and convective heat loss through the building envelope and 2) is produced via a chemical reaction at the building site. The unique heat loss reducing properties of SPF and efforts towards creating more efficient buildings, such as tax incentives and programs like the U.S. Environmental Protection Agency (EPA) Energy Star[1] and Design for the Environment[2] have increased the number of SPF applications in residences.

SPF is formed onsite via an exothermic chemical reaction resulting from the mixture of A-side and B-side chemicals. The A-side typically consists of monomeric or polymeric methylene diphenyl diisocyanate. Polyols are part of the B-side chemicals, which also include amine and/or metal catalysts, blowing agents, surfactants, and flame retardants. Amine and/or metal catalysts are used to promote the reaction between polyols and A-side chemicals, which help polyurethane foam cells develop sufficient strength to maintain their structure and resist collapsing. The reactions can be designed so the resulting foam is open cell (density 6.4 kg m^{-3} to 9.6 kg m^{-3}) or closed cell (density 24 kg m^{-3} to 32 kg m^{-3}).

Gong, Mengyan; Lawson, Lauren; Poppendieck, Dustin.
"Lessons Learned from Spray Polyurethane Foam Emission Testing using Micro-chambers."
Paper presented at the 59th annual Polyurethanes Technical Conference, Baltimore, MD. September 26, 2016 - September 28, 2016.

To meet building code flame spread and smoke development performance metrics flame retardants are present in reacted polyurethane foam at up to 12 % by mass.[3] Several studies have investigated emissions of flame retardants from SPF.[4, 5] The most common identified flame retardant is tris (1-chloro-2-propyl) phosphate (TCPP). TCPP is not exclusive to SPF. It has also been used in mattresses, electronics, and upholstery.[5] TCPP has been measured in homes at airborne concentrations ranging from 2.4 ng m^{-3} to 1 260 ng m^{-3}, [5-7] and found in similar concentrations in cars, offices and furniture stores.[8] TCPP is persistent in the environment,[9] readily absorbed through skin, and breaks down rapidly into metabolites in the body.[10] Although there is limited data, TCPP is classified by the EPA Design for the Environment program as having a high hazard for reproductive and developmental effects.[10] Not all chemicals that have been detected as emitting from SPF show human health effects. However, some chemicals that have been detected as emitting from SPF show potential negative health effects. For instance, 1,4 dioxane is commonly detected as emitting from closed cell SPF and has been listed as likely to be carcinogenic to humans by the EPA Integrated Risk Information System (IRIS).[11]

The Consumer Product Safety Commission (CPSC), along with the EPA, have received a number of complaints from residents regarding health effects that are potentially associated with SPF applications.[12] The time frame of health complaints is longer than the suspected time frame for the presence of isocyanates, suggesting that the emission of other chemicals (amines, blowing agents, surfactants, flame retardants or by-products of the reactions) from the SPF may be of concern. However, no direct connection between these health symptoms and SPF emissions have yet been established. In order to scientifically investigate complaints associated with SPF applications, standardized measurement protocols to determine emission rates of chemicals from SPF and methodologies to relate those emission rates to occupant exposure are needed.

The ASTM Indoor Air Quality (D22.05) subcommittee develops standard test methods and protocols to determine emissions rates from materials. Currently a new standard for measuring chemical emissions from SPF is being developed using a micro-chamber apparatus (WK 40293: Standard Test Method for Estimating Chemical Emissions from Spray Polyurethane Foam (SPF) Insulation using Micro-Scale Environmental Test Chambers). This standard does not address emissions of isocyanates.

The objective of this paper is to summarize what has been learned about SPF emissions from conducting research to support the development of WK40293.

EXPERIMENTAL METHODS

Four SPF samples were tested in micro-chamber experiments. Many of the experiments were performed to gain insight on experimental parameter values (temperature, flow, etc.), which were conducted prior to determining consensus values for WK40293.

Foams Tested

Four different foams were tested (Table 1). Samples Open 1 and Closed 1 were provided by the American Chemistry Council's Center for the Polyurethanes Industry (CPI). These research formulations were developed in 2011 to be representative of SPF then available in the marketplace. The formulations were created for research purposes only and were not optimized to meet the specifications of commercial producers. Therefore, they may not reflect formulations currently available in the marketplace, and conclusions about how these foams would perform outside a laboratory setting are speculative. Foams Open 1 and Closed 1 were sprayed in factory settings under controlled conditions. The foams were packaged and shipped overnight to NIST in an insulated cooler in accordance with ASTM standard D7859-13e1.[13] Emission testing on Open 1 was started within 24 h of spraying. Emission testing on Closed 1 was delayed as noted in Table 1. Closed 1 was stored at room temperature (≈20 °C) in the interim.

Table 1. SPF samples tested.

Foam ID	Type	Density (Kg/m³)[1]	Spray Date	Test Date
Open 1	Open Cell	12	2/26/2014	2/27/2014
Open 2	Open Cell	7	Summer 2012	1/28/2014
Closed 1	Closed Cell	30	11/4/2014	4/13/2015
Closed 2	Closed Cell	33.0 to 49.8[1]	Summer 2015	3/14/2016

[1]Density determined by measured initial mass and volume. Density of Closed 2 depended upon the sample location.

Open 2 was a high pressure, open cell, low density SPF that was applied during the construction of the NIST Net Zero Energy Residential Test Facility (NZERTF) in the summer of 2012. The design and construction of the NZERTF are described in Pettit et al.[14] Closed 2 was closed cell, high pressure foam that was sprayed in a residential home in the winter of 2015. Residents in the home complained of health impacts after the spray installation event.[15]

Micro-chamber Experiments

A cutting tool was machined to precisely cut SPF to fit tightly within a Markes 250 or Markes 125 micro-chamber (Figure 1) according to ASTM D7859-13e1. The top film of the foam was not removed for Open 1, Open 2, and Closed 1. The top film of the foam was removed for Closed 2. For Open 1, Open 2, and Closed 1, the 114 mL micro-chambers were operated at a temperature of 40 °C with a 100 mL min^{-1} airflow of ultra-high purity air. For Closed 2, the 44 mL micro-chambers were operated at a temperature of 35 °C with a 24.1 mL min^{-1} airflow of ultra-high purity air. The proposed consensus temperature in ASTM WK 40293 (Spring 2016 Ballot) is 35 °C; 40 °C experiments were conducted prior to establishment of consensus parameters. To investigate the impact of temperature on the TCPP emission rate, samples of Open 1 were also run at 28 °C, 50 °C and 60 °C.

Figure 1. Sampling of foam Open 1 for micro-chamber analysis (left). Sample installed in micro chamber (right).

The airflow contained an absolute humidity of 8.8 g m^{-3} (equivalent to a relative humidity of 38 % at 25 °C) for the Open 1 and Open 2 samples. The airflow contained an absolute humidity of 0 g m^{-3} for the Closed 1 and Closed 2 samples. The proposed consensus humidity in ASTM WK 40293 is zero. Elevated humidity experiments were conducted prior to establishment of consensus parameters.

Each experiment lasted for at least 200 h during which there were at least seven sorbent tube sampling events. For each sampling event, Tenax TA sorbent tubes were attached to the effluent flow of each micro-chamber for 2 min to 4 h (0.2 L to 24 L of sample) depending on the concentration of TCPP. For samples longer than 2 h, a second Tenax tube was placed in series with the first tube and analyzed for breakthrough of TCPP through the first tube. The sorbent tubes also allowed analysis of amine catalysts, byproducts and other volatile organic compounds (VOC). For each foam, at least three micro-chambers were run concurrently.

Prior to sampling, the tubes were spiked with an internal standard (1.0 μL of 1.25 mg Toluene D-8 mL^{-1} of methanol) using a liquid methanol solution injected into a heatblock.

Tube Analysis

Samples were analyzed using a thermal desorption-gas chromatography/mass spectrometer system (TD-GC/MS). A non-activated guard column was used in the transfer line from the thermal desorption unit to the GC/MS. An Rtx-5 amine column (*30.0 m x 250 μm x 0.50 μm)* was used for compound separation in the GC/MS.

Instrument detection limits for TCPP were determined by multiplying three times the standard deviation of seven replicates at a concentration that was less than five times the determined method detection limit.[16] The instrument TCPP detection limit was 8.65 ng, and the method detection limit was 0.71 μg m^{-3} to 2.86 μg m^{-3} depending on the sample volume. Only values above the method detection limit for the corresponding sampling volume are shown below.

Statistical Analysis

All statistical comparisons in this document use a one-way ANOVA, Tukey-Kramer analysis with $\alpha = 0.05$.

RESULTS and DISCUSSION

Chemicals were detected as emitting to the air from each of the tested foams. The analysis of the four different SPF samples allowed conclusions to be drawn regarding the influence of the foam, the chemical, and the temperature.

Chemicals Detected

A wide range of chemicals can emit from SPF under the tested conditions. TCPP was detected as emitting from every SPF sample. Other chemicals were also present in each foam. As an example, over 80 different chemicals were identified as emitting from Closed 2. Of these chemicals, 17 were identified with the GC/MS (spectrum match with a quality score greater than 80) and had relatively large response areas (over 30 000). For each sample a GC/MS will produce a chromatogram peak that has a response area that is proportional to the mass of the compound passing the detector. Six of these chemicals (Table 2) were positively identified and quantified for Closed 2 using standards. Triethylenediamine was also identified and had the largest response area, but a standard was not available for quantification.

Table 2. Chemicals identified in preliminary sampling (ranked in order of largest GC/MS response area).

Chemical	CAS Number	Average Linear R^2
1,4-Dioxane	123-91-1	0.999
Propane, 1,2-dichloro-	78-87-5	0.992
Piperazine, 1,4-dimethyl	106-58-1	0.991
Tris-(1-chloro-2-propyl) phosphate (TCPP)	13674-84-5	0.989
Benzene, 1,2-dichloro	95-50-1	0.996
1,3-Dioxolane, 2-ethyl-4-methyl	126-39-6	0.993

Influence of Foam

The same chemicals emitted at different rates from different foams. For the tested open cell foams (Open 1 and Open 2), concentrations of the flame retardant TCPP tended to be relatively constant over time throughout the duration of the experiments (Figure 2). These two open cell foam TCPP concentrations were not statistically different (p=0.06), even though Open 1 was freshly sprayed and Open 2 was applied over 1.5 years prior to sampling. The average TCPP concentrations were 400 μg m^{-3} for Open 2 (n=98, standard error 23 μg m^{-3}) and 314 μg m^{-3} for Open 1 (n=78, standard error 23 μg m^{-3}) for more than 400 h of sampling. The

Open 2 results show that, for this foam sampled at temperature 40 °C, flame retardants are emitted at measurable concentrations longer than 24 months after application.

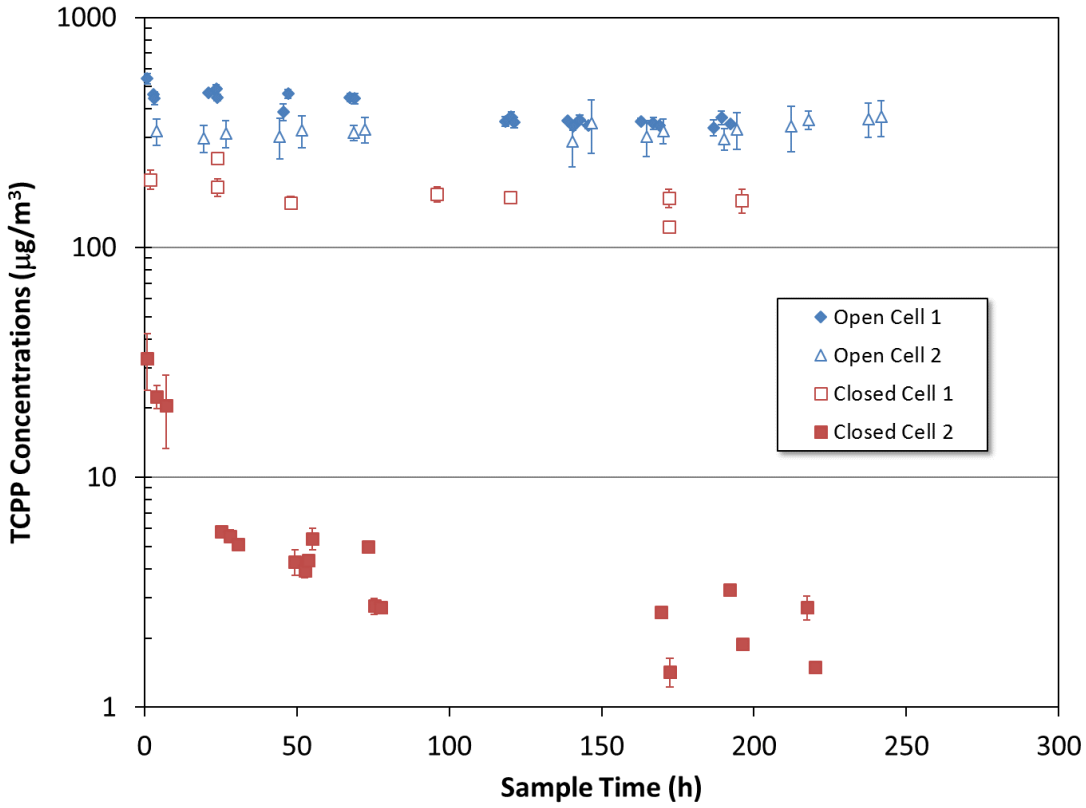

Figure 2. TCPP concentrations for different samples. Error bars show the standard error for each sampling time. Vertical axis is a logarithmic scale. Closed 1 tested at 35 °C, all other foam tested at 40 °C. Experiments on Closed 2, Open 1, and Open 2 were run for 400 h, only the first 300 h are shown.

Unlike the tested open cell foams, the TCPP concentrations from Closed 2 decreased exponentially during the first 150 h (Figure 2) and were two orders of magnitude lower than Open 1 and Open 2. In contrast, Closed 1 followed a relatively constant emission profile similar to Open 1 and Open 2. Despite the exponential decrease in TCPP concentration emitted from the Closed 2 sample, the total TCPP mass was not appreciably depleted. Over the course of the 400 h experiment, less than 8 µg of TCPP was emitted from the roughly 300 000 µg of TCPP present initially in the 3.75 g SPF sample (TCPP was roughly 8% of the mass of ingredients used to make Closed 2)[3].

One hypothesis to explain the exponential decrease in TCPP emissions for Closed 2 is that the TCPP that is initially located near the surface emits over a short time frame and that long term emission from the bulk of the foam is limited by the diffusion of TCPP to the surface. The two different emission profiles for TCPP from open and closed cell foams suggest that the limiting mass transport mechanism for TCPP is fundamentally different for the tested foams. It is possible that TCPP emissions from open cell foam is controlled by the mass transfer coefficient of the airflow above the foam surface (flow dependent), rather than diffusion of TCPP through interconnected cells. In contrast, the TCPP emissions from Closed 2 foam may be dominated by the diffusion of TCPP through the unconnected closed cells.

This data highlights the importance of determining foam-specific emission parameters (initial concentration, diffusion coefficient, partitioning coefficient and mass transfer coefficient) for each chemical prior to attempting to model TCPP emissions in full scale systems.

Influence of Chemicals

Different chemicals emit in the micro-chamber with different emission profiles (constant versus exponential decay) in the same foam. This held true for chemicals emitted from Open 1 and Closed 2. Figure 3 shows a decaying concentration for Bis (2-dimethylaminoethyl) ether (BDMAEE), and the steady emission profile for TCPP from the Open 1 sample. BDMAEE is a catalyst with an initial maximum concentration in this foam of less than 1 %, much smaller than the initial foam concentrations of TCPP.[3] Over the course of the 400 h experiment, over 5 000 µg of BDMAEE was emitted from the roughly 7,200 µg of BDMAEE present initially in the 0.8 g SPF sample (BDMAEE was roughly 0.9% of the mass of ingredients used to make Open 1)[3]. In contrast, over the course of the experiment, less than 1,400 µg of TCPP was emitted from the roughly 140 000 µg of TCPP that was present initially in the 1.2 g SPF sample (TCPP was roughly 12 % of the mass of ingredients used to make Open 1).

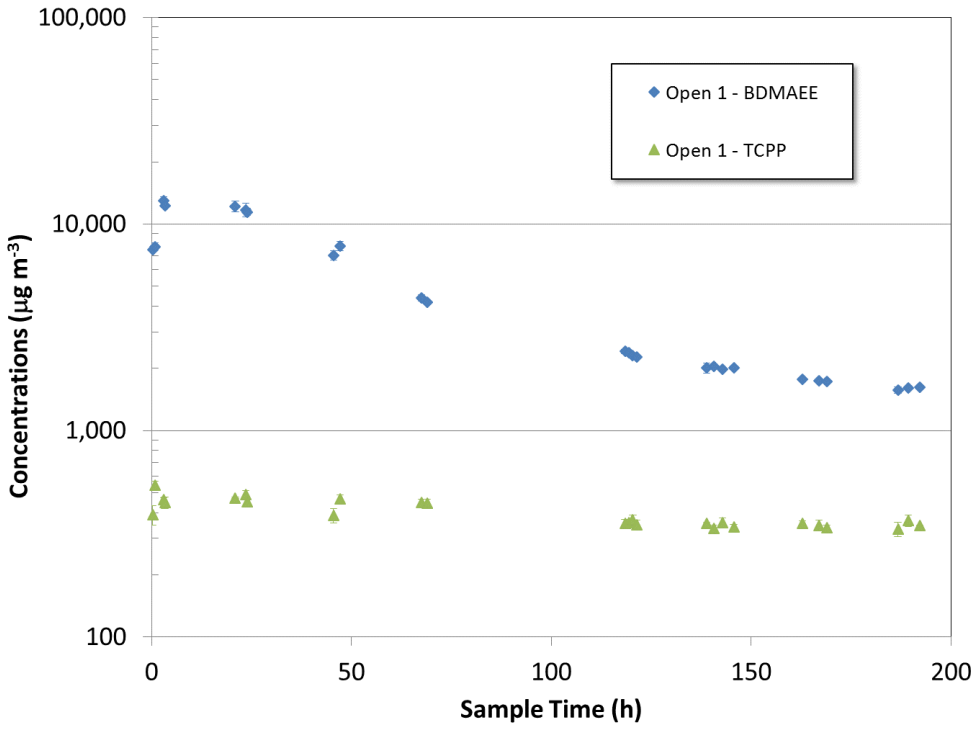

Figure 3. TCPP and BDMAEE concentrations from Open 1 tested in 40 °C micro-chambers. Error bars show standard error in triplicate data.

A similar trend was also seen for Closed 2. Figure 4 shows a steady emission profile for TCPP from the Closed 2 sample, while the concentrations for all other quantified chemicals drop exponentially. The initial concentration of these chemicals in Closed 2 is unknown.

This data highlights that emissions from SPF can be highly variable from one foam to another and within the same foam sample. This indicates that foam and chemical-specific data are needed prior to attempting to model exposure from SPF emissions.

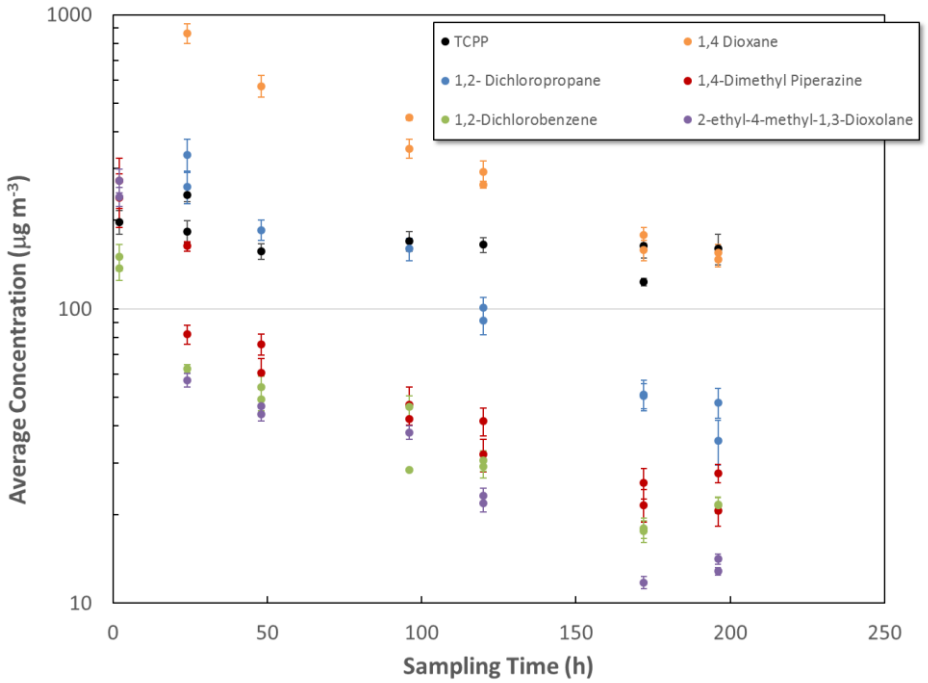

Figure 4. Concentrations of quantified chemicals emitted from Closed 2 tested in 35 °C micro-chambers. Error bars show the standard error for each sampling time. Vertical axis is a logarithmic scale.

Influence of Temperature

Emission rates from SPF are highly temperature dependent. In field applications, SPF experiences a range of temperatures. Hence, it is important to understand the temperature dependence of chemical emissions. A triplicate set of Open 1 SPF was analyzed at three temperatures (28 °C, 40 °C, and 50 °C) without removing the foam from the chambers. All samples were taken at least 24 h after the temperature change. As noted above, over 99 % of the TCPP remained at the end of the experiment. A separate test on a separate sample of Open 1 was conducted at 60 °C. Figure 5 shows the average concentrations for TCPP at the four temperatures for Open 1 foam. This data indicate that TCPP emissions are exponentially dependent upon temperature for open cell foam. Hence, a small change in building temperature may have a relatively large impact on the TCPP concentration in the building. A similar trend was seen for BDMAEE for the same Open 1.

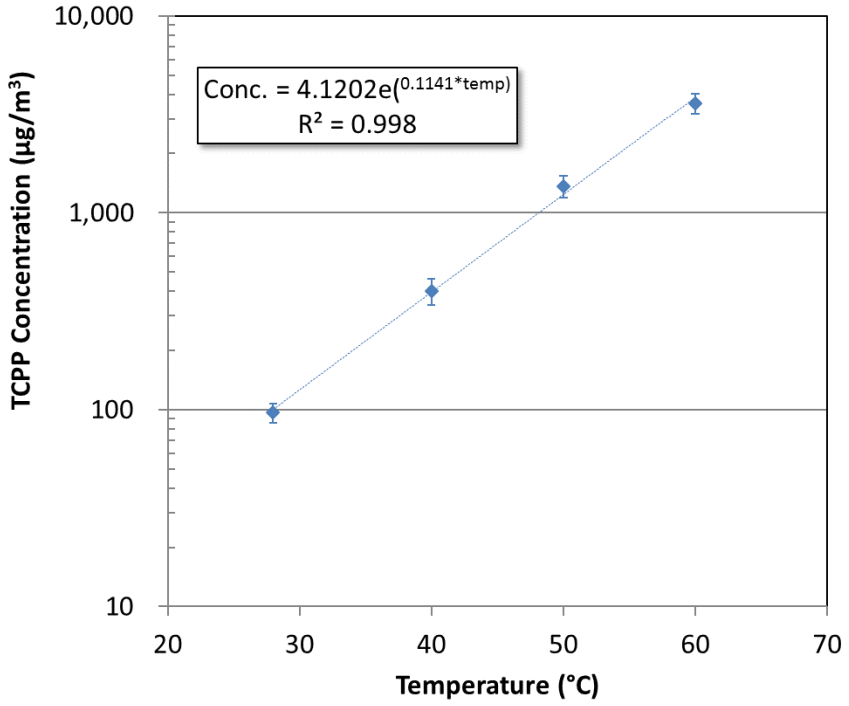

Figure 5: Average TCPP concentrations for experiments run at increasing temperate for open cell SPF. Vertical axis is logarithmic.

Use of Data

This data should not be used to directly calculate exposure in full scale scenarios. TCPP emissions highlight this issue. If TCPP emissions are controlled by internal material diffusion like VOCs are, scaling emission rates from micro-chambers to residences may be possible; however, if emissions are controlled by external mass transfer limitations, as semi-volatile organic compounds (SVOCs) are, then scaling of emission rates is unlikely to be successful. Traditionally, VOCs and SVOCs are defined based upon their vapor pressures or boiling points. TCPP has a wide range of reported values for vapor pressure and boiling point, indicating it could behave as a VOC or SVOC.[17, 18]

In general, VOC emissions from materials are controlled by the diffusion of the VOC through the material matrix and are not highly chamber dependent. This can allow the direct use of VOC chamber emission factors to predict emissions in full scale buildings. In contrast, SVOC emissions tend to be chamber dependent and controlled by the airflow above the material.[19] Since the airflow above a material can be significantly different between a chamber and a full scale building, SVOC chamber emission factors from micro-chamber studies should not be directly applied to full scale buildings. Emission parameters (mass transfer coefficient, initial concentration, partition coefficient, and diffusion coefficient) are needed to accurately predict the concentrations of SVOCs in buildings. As a result, the data in this paper should not be directly used for full scale exposure estimates.

However, the micro-chamber emission testing method described in this document and refined in WK40293 can be used to demonstrate emission differences between SPF, whether the purpose is to compare new manufacturer formulations or to compare emissions from standard spray events and possible misapplications.

CONCLUSIONS

Emissions from SPF have been quantified from four samples using micro-chamber testing. A range of chemicals being emitted from SPF can be measured as emitting from SPF under the tested conditions in timeframes relevant to

residential exposure. Emissions from SPF can vary over time and are dependent upon the foam type, chemical properties, and temperature of the SPF.

The flame retardant TCPP was emitted from all samples, even those that were sprayed over 1.5 years prior sampling. However, TCPP was emitted at concentrations that differed by over an order of magnitude, which illustrates that emissions from one foam sample should not be used to predict emissions from all foam.

The data in this paper should not be used for full scale exposure estimates. However, the micro-chamber emission testing method in WK40293 can be used to demonstrate emission differences between SPF samples to compare emissions from standard spray events and possible misapplications.

Finally, over 80 chemicals, including the amine catalyst triethylenediamine, were detected emitting from SPF that was present in a home with complaints of health effects following a SPF installation event. Hence, this method may be useful as a screening tool to detect the presence or absence of chemicals in SPF with known health effects. However, detecting chemicals with known health effects does not imply that these chemicals are responsible for the reported health effects. More research is needed on both scaling of the emission factors and exposure scenarios for any conclusions to be reached.

DISCLAIMER

Certain trade names or company products are mentioned in the text to specify adequately the experimental procedure and equipment used. In no case does such identification imply recommendation or endorsement by the National Institute of Standards and Technology, nor does it imply that the equipment is the best available for the purpose.

ACKNOWLEDGEMENTS

The authors would like to thank the review, feedback and fund support supplied by the United States Consumer Product Safety Commission (CPSC). This work was funding in part by CPSC (CPSC-I-13-0016 and CPSC-I-14-0023).

REFERENCES

1. USEPA Energy Star. https://www.energystar.gov/ (May 14, 2015),
2. USEPA Design for the Environment. http://www2.epa.gov/saferchoice/design-environment-alternatives-assessments (May 15, 2015),
3. Sebroski, J. R. *Research Report for Measuring Emissions from Spray Polyurethane Foam (SPF) Insulation*; Center for the Polyurethanes Industry (CPI): Pittsburgh, PA, September 4, 2012, 2012; p 52.
4. Kemmlein, S.; Hahn, O.; Jann, O., Emissions of organophosphate and brominated flame retardants from selected consumer products and building materials. *Atmospheric Environment* **2003,** *37*, (39-40), 5485-5493.
5. Marklund, A.; Andersson, B.; Haglund, P., Organophosphorus flame retardants and plasticizers in air from various indoor environments. *Journal of environmental monitoring : JEM* **2005,** *7*, (8), 814-9.
6. Bergh, C.; Torgrip, R.; Emenius, G.; Ostman, C., Organophosphate and phthalate esters in air and settled dust - a multi-location indoor study. *Indoor Air* **2011,** *21*, (1), 67-76.
7. Saito, I.; Onuki, A.; Seto, H., Indoor organophosphate and polybrominated flame retardants in Tokyo. *Indoor Air* **2007,** *17*, (1), 28-36.
8. Hartmann, P. C.; Burgi, D.; Giger, W., Organophosphate flame retardants and plasticizers in indoor air. *Chemosphere* **2004,** *57*, (8), 781-7.
9. Moller, A.; Sturm, R.; Xie, Z.; Cai, M.; He, J.; Ebinghaus, R., Organophosphorus flame retardants and plasticizers in airborne particles over the Northern Pacific and Indian Ocean toward the Polar Regions: evidence for global occurrence. *Environmental science & technology* **2012,** *46*, (6), 3127-34.
10. USEPA, Flame Retardants Used in Flexible Polyurethane Foam: An Alternatives Assessment Update. In Environment, D. f. t., Ed. U.S. EPA: 2014.
11. IRIS Toxicological Review of 1,4-Dioxane (with Inhalation Update). In U.S. EPA. (Interagency Science Discussion Draft). , Ed. U.S. Environmental Protection Agency,: Washington, DC, , 2013; pp EPA/635/R-11/003D.

12. CPSC http://www.saferproducts.gov/Search/Result.aspx?dm=0&q=Spray+foam+insulation&srt=0 (January 28, 2014),
13. ASTM, Standard Practice for Spraying, Sampling, Packaging, and Test Specimen Preparation of Spray Polyurethane Foam (SPF) Insulation for Testing of Emissions Using Environmental Chambers. In ASTM: West Conshohocken, PA, 2013; Vol. D7859-13e1.
14. Pettit, B.; Gates, C.; Fanney, A. H.; Healy, W. *Design Challenges of the NIST Net Zero Energy Residential Test Facility*; National Institute of Standards and Technology: Gaithersburg, MD, 2014.
15. Poppendieck, D.; Gong, M.; Lawson, L.; Emmerich, S., Characterization of Emissions from a Non-Ideal Spray Polyeurathane Foam Sample. In Technology, N. I. o. S. a., Ed. 2016.
16. CFR, Definition and procedure for the determination of the method detection limit – Revision 1.11. In 2003; Vol. CFR 40, Ch. 1, Pt. 136.
17. ATSDR, Toxicological Profile for Phosphate Ester Flame Retardants. In Registry, A. f. T. S. a. D., Ed. U.S. Department of Health and Human Service: Atlanta, Georgia, 2012; p 250.
18. Verbruggen;, E. M. J.; Rila;, J. P.; Traas;, T. P.; Posthuma-Doodeman;, C. J. A. M.; Posthumus;, R., Environmental Risk Limits for several phosphate esters, with possible application as flame retardant. In Environment, N. I. f. P. H. a. t., Ed. Bilthoven, the Netherlands., 2005.
19. Little, J. C.; Weschler, C. J.; Nazaroff, W. W.; Liu, Z.; Cohen Hubal, E. A., Rapid methods to estimate potential exposure to semivolatile organic compounds in the indoor environment. *Environmental science & technology* **2012,** *46*, (20), 11171-8.

BIOGRAPHIES

Dustin Poppendieck

Dustin earned his Ph,D. in Environmental Engineering from the University of Texas at Austin. He was an assistant professor in environmental resources engineering at Humboldt State from 2004-2010. He has been at NIST since 2012 and has worked in the indoor air quality field for the past 15 years. He has investigated the deposition of disinfection agents used in anthrax remediation, desorption of a methamphetamine surrogate from wallboard, emissions from building materials used in net zero energy houses, methods for characterizing emissions from spray polyurethane foam, and characterized particle emissions from kerosene lamps used in developing countries.

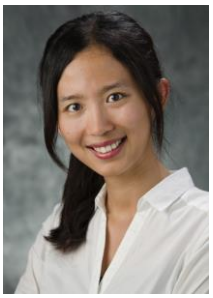

Mengyan Gong

Mengyan Gong got her Ph.D. in Civil Engineering from Tsinghua University in 2015. She assesseddermal exposure to phthalates for her Ph.D. thesis, including developing a model for predicting dermal absorption from gas phase chemicals, assessing phthalate dermal exposure by measuring its levels on different human body locations, examining the contribution of dermal absorption to total uptake, and investigating the influence of clothing on dermal exposure to phthalates. After her Ph.D., she began her work at NIST as a guest researcher. Her research topic at NIST is to characterize chemical emissions from spray polyurethane foam.

Lauren Lawson

Lauren is a student at the University of Louisville studying Chemical Engineering. She was a co-op at the National Institute of Standards and Technology in the Spring of 2016. Lauren has examined the chemical emissions of spray polyurethane foam, with a focus on volatile and semi-volatile compounds using micro-chambers.

DEFORMATION LIMITS AND ROTATIONAL CAPACITIES FOR CONNECTIONS UNDER COLUMN LOSS

Jonathan M. Weigand
National Institute of Standards and Technology, Gaithersburg, MD 20899 USA
jonathan.weigand@nist.gov

Joseph A. Main
National Institute of Standards and Technology, Gaithersburg, MD 20899 USA
joseph.main@nist.gov

ABSTRACT

For structural steel framing systems subjected to column loss, the ultimate gravity load carrying capacity of the system is often controlled by the rotation and deformation capacities of the connections within the affected bays. Within current design specifications, the potential for disproportionate collapse in structural design is evaluated by notionally removing critical load supporting elements from the structure, and designing the structure to sustain the applicable gravity loads without collapse via the alternative load path analysis method. Steel gravity framing systems subjected to column loss undergo large vertical deflections under gravity loads that induce large rotation and axial deformation demands on the connections. However, the acceptance criteria currently used to evaluate connection failure in alternative load path analysis are based on results from seismic testing that do not reflect the large axial demands imposed on the connections. Recent experimental data have shown that application of these rotation limits to column loss scenarios in steel gravity framing systems can be non-conservative. In this paper, experimental data from steel single-plate shear connections tested under column loss are compared to the rotation limits provided in existing standards, and the factors influencing the widely varying levels of conservativism for different connection geometries are explained. A new approach for calculating acceptance criteria for steel gravity connections under column loss is also introduced. The new approach provides more risk consistency and accounts for the important influence of axial deformation demands on the connections.

INTRODUCTION

Some building owners in the United States (e.g., the General Services Administration and the Department of Defense (DoD)) and certain jurisdictions (e.g., New York City) currently require buildings to be designed to resist disproportionate collapse. To evaluate the potential for disproportionate collapse in design, engineers rely on the alternative load path analysis method (see e.g. DoD (2009)), in which individual load-bearing elements

Main, Joseph; Weigand, Jonathan.
"Deformation Limits and Rotational Capacities for Connections Under Column Loss."
Paper presented at Eighth International Workshop on Connection in Steel Structures (Connections VIII), Boston, MA. May 24, 2016 - May 26, 2016.

are notionally removed from the structure, and the remaining structure is designed to support the applicable gravity load combination without collapse. For steel frames designed to support only gravity loads, the steel shear connections play a critical role in ensuring the system robustness and stability. Large-scale tests of steel gravity framing systems under column removal (Johnson et al. 2014; Johnson et al. 2015) have shown that the system robustness depends on the capacity of the connections to resist axial loads after undergoing large rotation and axial displacement demands.

Current acceptance criteria for steel connections, which are used to evaluate connection failure in alternative load path analysis, take the form of rotation limits. These rotation limits are based almost entirely on results from seismic testing. In such seismic tests, the connections are typically subjected to rotation cycles of increasing magnitude until failure. These test conditions (1) result in low-cycle fatigue of the connection components, which is not relevant to column loss, and (2) do not reflect the large axial demands placed on the connections under column loss. While the increased plastic deformations associated with low-cycle fatigue may partially compensate for the lack of axial demands, recent experimental data have shown that direct application of seismic rotation limits to column loss scenarios in steel gravity framing systems can be non-conservative. Thus a better approach for calculating rotation limits for connections under column loss is needed.

In this paper, experimental data from steel single-plate shear connections tested under column loss (Weigand and Berman 2014) are compared to the rotation limits provided in standards for seismic evaluation and retrofit of existing buildings and for alternative load path analysis. Widely varying levels of conservativism are observed for different connections, and the factors contributing to this variability are discussed. To address the issues with the existing acceptance criteria, a new approach for calculating rotation limits for steel gravity connections under column loss is introduced. The new approach accounts for the influence of axial deformation demands on the connections and provides more risk consistency in the evaluation of connection failure under column loss.

COMPARISON OF EXPERIMENTAL DATA WITH CURRENT ROTATION LIMITS

Several existing specifications incorporate rotation limits for various types of steel connections; however, the applicability of these rotation limits to connections subjected to column loss needs to be considered carefully. The American Society of Civil Engineers (ASCE/SEI) 41-13 *Seismic Evaluation and Retrofit of Existing Buildings* (ASCE 2013) provides rotation limits for different connection types derived from tests of connection subassemblies under rotation cycles of increasing magnitude without axial restraint. These rotation limits depend only on the connection type and the depth of the connection bolt group, and thus have a number of deficiencies when considering their applicability to column loss, including the following:

1. they do not account for changes in connection geometry (e.g., changes in bolt diameter, thickness of the shear plate), which strongly influences the connection rotational capacity,

2. they do not include the effects of axial demands on the connections, and
3. they do not account for the effect of span length.

The Unified Facilities Criteria (UFC) 4-023-03 *Design of Buildings to Resist Progressive Collapse* (DoD 2009), which covers buildings under the jurisdiction of the DoD, adopted life-safety rotation limits from ASCE/SEI 41-13 for most connections, but provided reduced rotation limits for specific connection types including welded unreinforced flange, bolted web moment connections, reduced beam section moment connections, and single-plate shear connections. The rotation limits specified for these connection types in the UFC 4-023-03 were reduced relative to ASCE 41-13 based on a series of tests on connections subjected to blast and/or column removal conducted by the U.S. Defense Threat Reduction Agency and analyses performed by Myers, Houghton & Partners (Karns et al. 2008). Fig. 1 shows a comparison between the applicable acceptance criteria and measured rotational capacities for single-plate shear connections under column loss from Weigand and Berman (2014). The uncertainty in the experimental data was estimated as ±1 % (Weigand and Berman, 2016). The acceptance criteria, which are shown as dashed lines, include rotation limits from ASCE/SEI 41-13 for both life safety (labeled ASCE 41-LS) and collapse prevention (labeled ASCE 41-CP), as well as rotation limits from UFC 4-023-03 for primary members (labeled UFC-Primary) and for secondary members (labeled UFC-Secondary). The UFC-Secondary line is the same as the ASCE 41-LS line. The equations used to calculate the rotation limits are shown in Table 1.

Fig. 1 shows that the ASCE 41 rotation limits would be unconservative if applied directly to consider column loss (i.e., they would predict larger rotational capacities than single-plate shear connections can actually sustain). The UFC-Primary rotation limits are conservative when compared to the measured rotational capacities, but the amount of conservativism (i.e., the amount that the measured rotational capacities lie above the UFC-Primary line) vary widely for the different connections, which had different geometries (span, plate thickness, thread-condition, etc.). The connections with the least conservativism had either the longest spans or threads included in the shear plane.

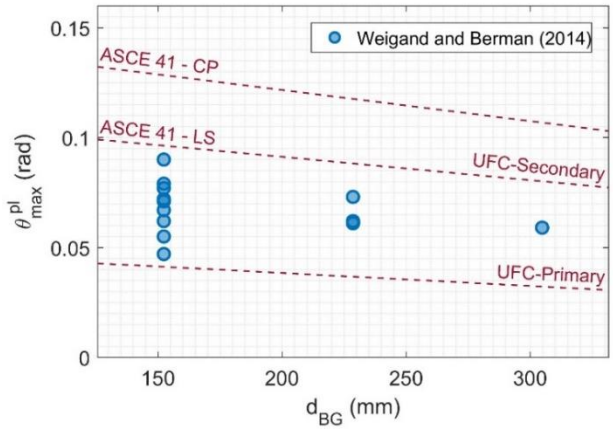

Figure 1: Comparison between rotation limits from ASCE/SEI 41 and UFC 4-023-03 and measured rotational capacities for connections subjected to column loss, as a function of the depth of the bolt group, d_{BG}.

Table 1: Specified Rotational Capacities for Single-Plate Shear Connections from ASCE 41-13 and UFC 4-023-03 (d_{BG} is the depth of the connection bolt group in mm).

Specification	Condition	Rotation Limit
ASCE 41-13	Life-Safety	$\theta_{\max}^{\mathrm{pl}} = 0.1125 - (0.0001063\ \mathrm{mm}^{-1})d_{BG}$
	Collapse Prevention	$\theta_{\max}^{\mathrm{pl}} = 0.1500 - (0.0001417\ \mathrm{mm}^{-1})d_{BG}$
UFC 4-023-03	Secondary Members	$\theta_{\max}^{\mathrm{pl}} = 0.1125 - (0.0001063\ \mathrm{mm}^{-1})d_{BG}$
	Primary Members	$\theta_{\max}^{\mathrm{pl}} = 0.0502 - (0.0000591\ \mathrm{mm}^{-1})d_{BG}$

A new standard, which is intended to specifically address disproportionate collapse, the *ASCE/SEI Standard for Mitigation of Disproportionate Collapse*, is currently under development. However, much of the existing guidance is still based on the ASCE/SEI 41-13 acceptance criteria. The new approach presented in this paper for calculating rotation limits for single-plate shear connections is based on the kinematics of connection response to column loss, and provides capabilities to overcome the deficiencies discussed above.

COMPONENT-BASED ANALYSIS OF FACTORS AFFECTING ROTATION LIMITS

Fig. 1 demonstrates that the amount of conservatism between the measured connection rotational capacities and the rotation limits specified in ASCE/SEI 41-13 and UFC 4-023-03 vary as a function of connection geometry. However, Fig. 1 only includes the specific connection geometries tested by Weigand and Berman (2014). Here, additional connection geometries are considered to answer two key questions:

1. What if the beam spans were longer?
2. What if the bolt threads were included in the shear plane?

Because experimental data are not available for these geometries, a component-based model for single-plate shear connections developed by Weigand (2016) is used to answer these two questions. In the component-based connection model, the connection is discretized into an arrangement of component springs that geometrically resembles the connection, where each component spring embodies a single bolt and characteristic-width segments of the shear plate and beam web (Fig. 2(a)). The component-based connection model was already validated against all 13 of the single-plate shear connection tests from Weigand and Berman (2014), and shown to predict their capacities within an average of 10 % (e.g., see Figs. 2(b) and 2(c)), using only the connection geometry, material properties, and applied loading (see Weigand (2014) for more details).

Fig. 3(a) shows the measured rotational capacities from Weigand and Berman (2014), with span length differentiated by marker color (all except one connection had threads excluded from the shear plane), Fig. 3(b) shows calculated rotational capacities for connections with 3.66 m (12 ft) longer spans (i.e., 12.8 m (42 ft) and 18.3 m (60 ft) spans) and all other connection geometry held constant, Fig. 3(c) shows calculated rotational capacities for connections with threads included in the shear plane, and Fig. 3(d) shows

calculated rotational capacities for connections with threads included and with the 3.66 m (12 ft) longer spans. Comparison of Figs. 3(a) and 3(b) shows that increasing the span would reduce the rotational capacities for all connections, and that one 3-bolt connection rotational capacity would actually fall below the UFC-Primary acceptance criteria. Comparison of Figs. 3(a) and 3(c) shows that including threads in the shear plane would also reduce the rotational capacities for all connections, and that four of the connection rotational capacities would fall below the UFC-Primary acceptance criteria. Including threads in the shear plane had a larger influence on the connection rotational capacities than did increasing the span (inferred by comparing Figs. 3(b) and 3(c)). Fig. 3(d) shows that connections having both threads included in the shear plane and long spans are particularly vulnerable to having rotational capacities that are non-conservative, relative to the UFC-Primary acceptance criteria (seven out of the total thirteen connection rotational capacities fall below the UFC-Primary acceptance criteria). This demonstrated potential for the rotational capacities of realistic connection geometries to be predicted non-conservatively by the most stringent current acceptance criteria (UFC-Primary) motivates the need for a better approach for calculating connection rotational capacities.

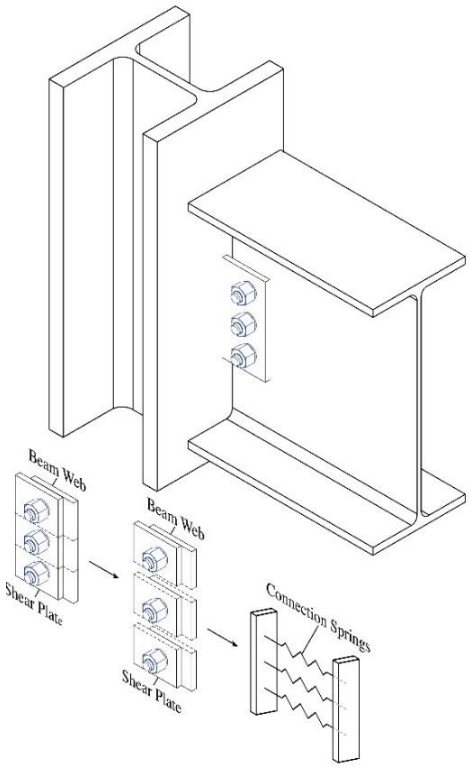

(a)

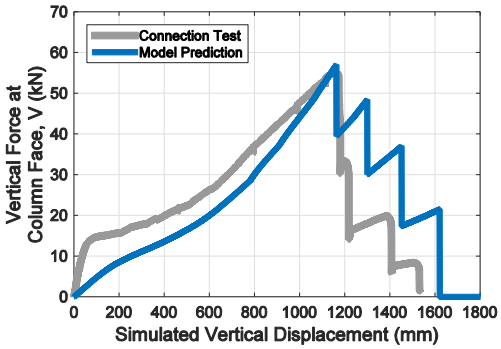

(b)

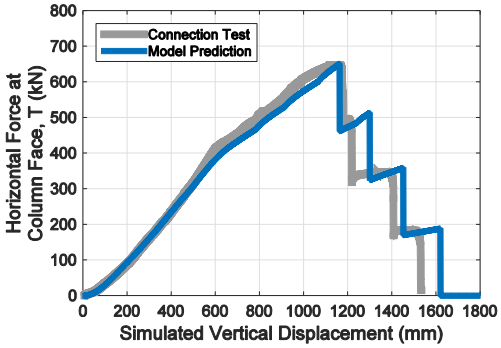

(c)

Figure 2: (a) discretization of single-plate shear connection into individual bolt-widths, (b) comparison of predicted vertical force-displacement response with connection data and (b) comparison of predicted horizontal force-displacement response from component-based model with connection data.

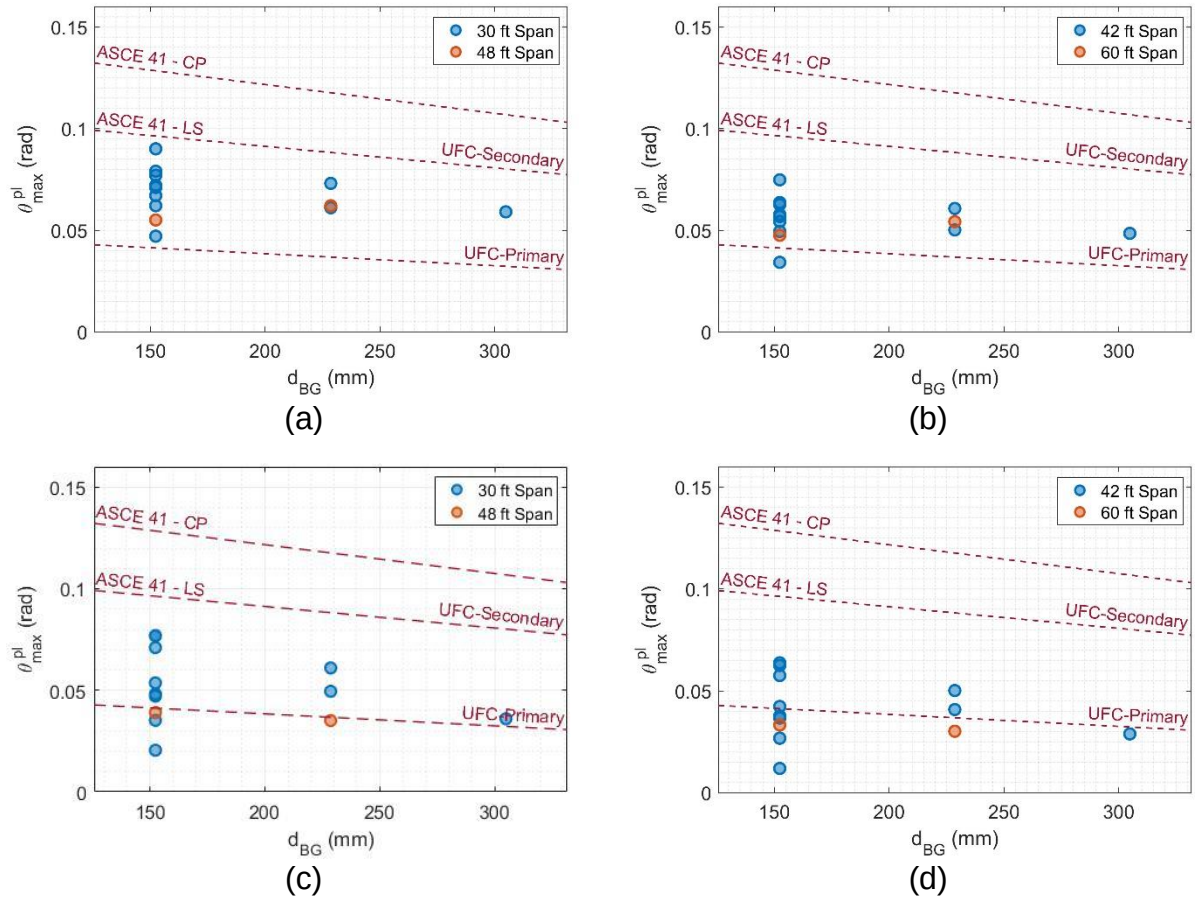

Figure 3: (a) Experimental data; calculated rotational capacities for, (b) increased span lengths and threads excluded from shear plane, (c) threads included in shear plane, and (d) increased span lengths and threads included in shear plane.

ANALYTICAL DERIVATION OF ROTATION LIMITS UNDER COLUMN LOSS

For frames designed to support gravity loads only, loss of a column results in large vertical deflections at the missing column that impose significant rotational demands on the connections. Significant axial demands can also be imposed, depending on the degree of restraint provided by the surrounding structure. Where the connections are discontinuous through the unsupported column (e.g., for a corner column loss scenario) minimal axial restraint is provided, and thus the axial demands are small. However, where the connections span continuously through the unsupported column (e.g., for an interior column loss scenario), the axial restraint provided by the surrounding structure can subject the connections to significant axial deformations in combination with large rotations. Fig. 4(a) illustrates the limiting case of no axial restraint, where the end columns are free to translate horizontally in-plane and the connections are subjected only to monotonically increasing rotation until failure. Fig. 4(b) illustrates the limiting case of perfect axial restraint, where translation of the column ends is prevented.

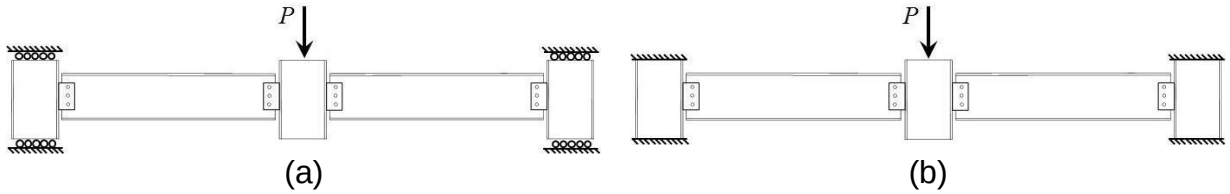

Figure 4: Column loss scenarios with (a) no axial restraint and (b) axial restraint.

The rotational demands imposed on the connections can be calculated in terms of the vertical deflection of the missing column, Δ, as

$$\theta = \tan^{-1}\left(\frac{\Delta}{L_{\mathrm{r}}}\right) , \tag{1}$$

where L_{r} is the distance between the centers of the bolt groups at the ends of the framing members in the undeformed configuration (Fig. 5). For the condition without axial restraint (Fig. 4(a)), no axial demands are imposed on the connections. For the condition with axial restraint (Fig. 4(b)), an axial deformation δ is imposed on each connection (see Fig. 5), which can be calculated as follows:

$$\delta = \frac{L_{\mathrm{r}}}{2}\left[\sqrt{1+\left(\frac{\Delta}{L_{\mathrm{r}}}\right)^2} - 1\right] . \tag{2}$$

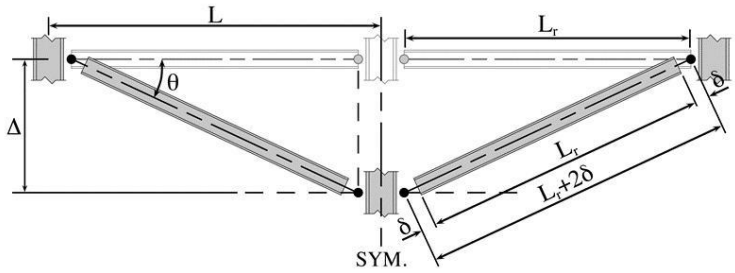

Figure 5: Connection demands based on vertical deflection of the missing column.

For both axial restraint conditions, the axial deformation of each connection spring (see Fig. 2(a)) can be calculated in terms of θ and δ as:

$$\delta_{\mathrm{j}} = \delta + y_{\mathrm{j}} \sin\theta \ , \tag{3}$$

where y_j denotes the vertical distance from the j^{th} connection spring to the center of the bolt group. Eqs. (1) - (3) are based on the assumption that the beams are rigid relative to the connections, so that the rotations and deformations localize in the connections. This rigid-body assumption is further discussed by Weigand and Berman (2014), including validation of the assumption through comparison with experimental measurements.

For the condition without axial restraint (i.e., $\delta = 0$), the connection spring deformations from Eq. (3) are essentially linear with increasing rotation (Fig. 6(a)). For the condition with axial restraint, δ is calculated from Eq. (2), and larger tensile deformations of the component springs are observed for a given level of rotation (Fig. 6(b)), relative to the case without axial restraint. Because of the dependence of Eq. (2) on the span length, larger span lengths result in increased tensile deformations of the component springs.

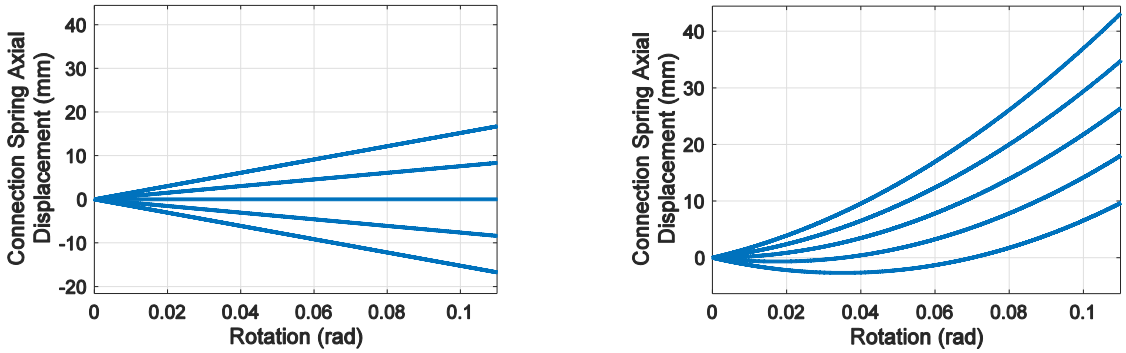

Figure 6: axial deformations of connection segments, δ_j, with (a) $\delta = 0$, and (b) $\delta \neq 0$.

If the limiting axial deformation for a single bolt row of a connection, δ_u, is known, either from experiments or from computational modeling, then the corresponding rotation limit for the connection, θ_u, can be calculated. The rotation limit, θ_u, corresponds to the configuration in which the axial deformation of an extreme bolt row (lowest or highest) reaches δ_u. Setting $y_j = d_{BG}/2$ in Eq. (3) for the extreme bolt row and introducing the small-angle approximation $\sin(\theta) \approx \theta$ allows Eq. (3) to be solved for θ_u, as

$$\theta_u = \frac{2(\delta_u - \delta)}{d_{BG}} \quad . \tag{4}$$

For the condition without axial restraint (i.e., $\delta = 0$), Eq. (4) reduces to $\theta_u = 2\delta_u/d_{BG}$. For the condition with axial restraint, substituting Eq. (2) into Eq. (4), introducing small-angle approximations, and neglecting higher-order terms (see Main and Sadek (2012) for more details), results in a quadratic equation for θ_u that yields the following positive root:

$$\theta_u = 2\sqrt{\left(\frac{d_{BG}}{2L}\right)^2 + \frac{\delta_u}{L}\left(1 + \frac{\delta_u}{L}\right)} - \frac{d_{BG}}{L} \quad . \tag{5}$$

Fig. 7 compares solution curves calculated from Eq. (5) against measured rotation limits for single-plate shear connections subjected to column loss from Weigand and Berman (2014), for 3-bolt and 4-bolt connections with 9.1 m (30 ft) and 14.6 m (48 ft) spans. Fig. 7 verifies that the rigid-body model provides a close approximation to the measured rotation at connection failure, as demonstrated by the close proximity of the connection data (circular markers) to the solution curves. The solution curves are also shown to be slightly conservative relative to the experimental data (i.e., the solution curves are consistently below the experimental data), which is expected based on the rigid-body model and the assumed perfect axial restraint.

By using Eq. (5), along with average measured values of the limiting axial deformation δ_u for different groups of connections tested by Weigand and Berman (2014), rotational capacities can be calculated and compared with the experimental data (Fig. 8). Compared with the wide scatter of the experimental data relative to current rotation limits (Fig. 1), Fig. 8 shows that Eq. (5) provides significantly improved consistency with the experimental data. The improved consistency is achieved by accounting for the influences of axial restraint, span length, and connection geometry, factors which current rotation

limits used in alternative load path analysis do not directly consider. Fig. 8 shows that Eq. (5) is conservative relative to the experimental data for all but one test, with the slight non-conservatism in that case resulting from the use of the average measured value for δ_u. Uncertainty in the deformation limit δ_u is the key factor affecting the uncertainty in the calculated rotational capacities. In selecting appropriate values of δ_u to use in design, uncertainty in the value of δ_u should be considered to ensure consistent reliability.

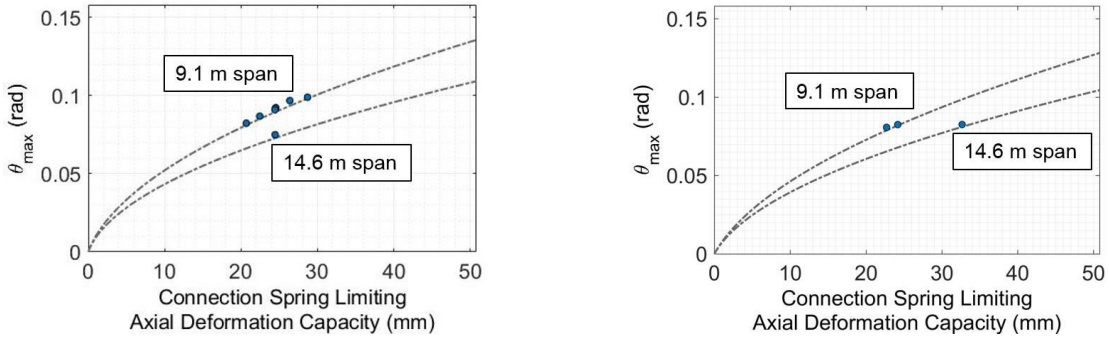

Figure 7: Comparison between Eq. (5) and measured rotational capacities for (a) 3-bolt single-plate shear connections and (b) 4-bolt single-plate shear connections.

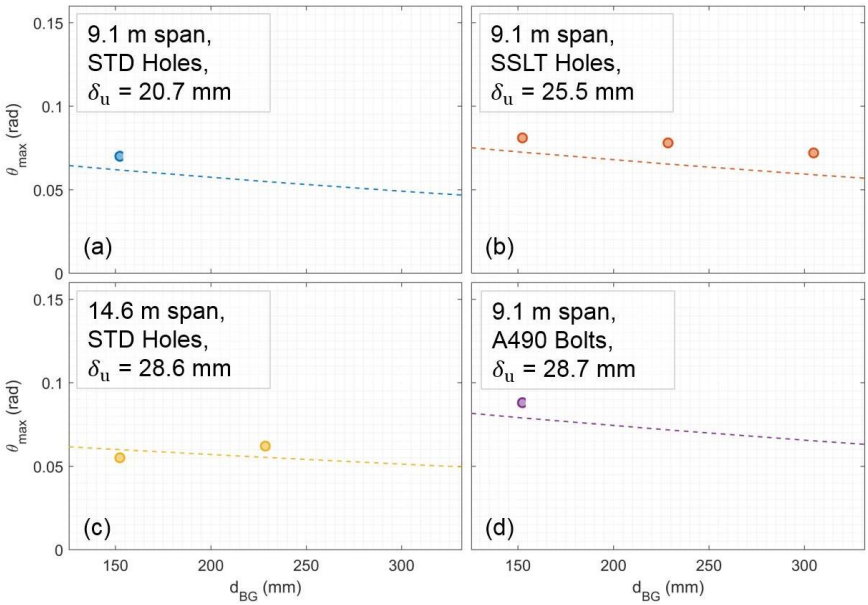

Figure 8: Comparison between Eq. (5) (dashed line) and measured rotational capacities for single-plate shear connections (circular markers).

SUMMARY AND CONCLUSIONS

When evaluating the performance of connections subjected to column loss, it is important to recognize that connections behave differently when subjected to seismic loads than when subjected to column loss. Acceptance criteria in existing specifications, which were developed based on results from seismic testing, may not be appropriate for column loss as they do not capture (1) differences in connection geometry (e.g., bolt diameter, plate

thickness, thread condition), (2) the influence of axial deformation demands on the connections, and (3) the influence of span length. As a result of these deficiencies, current acceptance criteria are not risk-consistent for connections with different geometries, or frames which have different spans.

Results from component-based models of single-plate shear connections showed that there exist connection geometries in which even the most stringent currently specified acceptance criteria (the UFC 4-023-03 rotation limits for primary members) would not be conservative for disproportionate collapse. However, a new approach in which the axial deformation capacities of component-width segments of the connection are used to calculate rotational capacities for the connections can overcome these deficiencies to provide results that are both risk-consistent and capture the influence of axial deformation demands on the connection, including those resulting from span length.

REFERENCES

ASCE (2013). *Seismic Evaluation and Retrofit of Existing Buildings, SEI/ASCE 41-13,* American Society of Civil Engineers, Reston, VA.

Karns, J.E., Houghton, D.L., Kim, J. and Hong, J. (2008). *GSA Steel Frame Bomb Blast & Progressive Collapse Test Program*, Contract No. GS-23F-0092P, January, 2008.

Johnson, E.S. Meissner, and Fahnestock, L.A. (2015). “Experimental Behavior of a Half-Scale Steel Concrete Composite Floor System Subjected to Column Removal Scenarios.” *J. Struct. Eng.,* 04015133.

Johnson, E.S., Weigand, J.M., Francisco, T., Fahnestock, L.A., Liu, J., and Berman, J.W. (2014). “Large-Scale Experimental Evaluation of the Structural Integrity of a Composite Steel and Concrete Building Floor System.” *Structures Congress,* Boston, MA.

Main, J.A. and Sadek, F. (2012). “Robustness of steel gravity frame systems with single-plate shear connections.” *NIST Technical Note 1749*, Gaithersburg, MD.

Weigand, J. M. and Berman, J. W. (2014). “Integrity of Steel Single Plate Shear Connections Subjected to Simulated Column Removal.” *J. Struct. Eng.*, 140 (5), 04013114, pp.1-12.

Weigand, J.M. (2014). “The Integrity of Steel Gravity Framing System Connections Subjected to Column Removal Loading.” Ph.D. Dissertation in Civil Engineering, University of Washington, Seattle, WA.

Weigand, J.M. (2016). “A Component-Based Model for Single-Plate Shear Connections with Pre-tension and Pinched Hysteresis.” *J. Struct. Eng.* Under review.

Weigand, J.M. and Berman J.W. (2016). “Steel Gravity Connections Subjected to Large Rotations and Axial Loads.” *Eighth International Workshop on Connections in Steel Structures (Connections VIII)*, Boston, Massachusetts, May, 2016.

DoD (2009). *Design of Buildings to Resist Progressive Collapse, UFC 4-023-03.* United States Department of Defense.

ENHANCED CONNECTIONS FOR IMPROVED ROBUSTNESS OF STEEL GRAVITY FRAMES

Jonathan M. Weigand
National Institute of Standards and Technology, Gaithersburg, MD 20899 USA
jonathan.weigand@nist.gov

Joseph A. Main
National Institute of Standards and Technology, Gaithersburg, MD 20899 USA
joseph.main@nist.gov

ABSTRACT

Potential vulnerability to collapse under column loss has been identified for steel gravity framing systems with simple shear connections. To address this potential vulnerability, an enhanced connection for steel gravity frames is proposed that incorporates U-shaped top and seat plates with long-slotted holes bolted to the beam flanges. Finite element analyses are used to evaluate the effectiveness of the enhanced connection under column loss scenarios. Addition of the U-shaped slotted plates is shown to increase the vertical resistance of a two-span beam assembly under center column loss to 2.5 times the resistance with conventional connections. Analysis of a composite floor system subject to interior column loss shows that incorporation of the enhanced connections achieves a 90 % increase in the ultimate vertical capacity, relative to the system with conventional connections, under uniform static loading. Under sudden column loss, the ultimate capacity of the floor system with enhanced connections is essentially equivalent to the applicable gravity load combination of 1.2*D* + 0.5*L*, while the system with conventional connections sustains only 56 % of the applicable gravity loading.

INTRODUCTION

Recent full-scale experiments (Lew et al. 2012) and computational analyses (Main and Liu 2013) have demonstrated the effectiveness of seismically designed steel moment frames in redistribution of gravity loads under column removal scenarios. In contrast, computational analyses (e.g., Main 2014) and experimental studies (Johnson et al. 2015) have indicated that steel gravity frames are potentially vulnerable to disproportionate collapse under column loss. Four column removal tests performed on a half-scale steel gravity framing system with composite slab on steel deck, by Johnson et al. (2015), showed that the floor system could only carry between 44 % and 62 % of the applicable gravity load combination of 1.2*D* + 0.5*L* for extraordinary events from American Society

Main, Joseph; Weigand, Jonathan.
"Enhanced connections for improved robustness of steel gravity frames."
Paper presented at Eighth International Workshop on Connections in Steel Structures (Connections VIII), Boston, MA. May 24, 2016 - May 26, 2016.

of Civil Engineers (ASCE) Standard 7-10 (ASCE 2010), where *D* = dead load and *L* = live load. To help address this potential vulnerability, researchers have begun to consider two primary approaches for enhancing the robustness of steel gravity frames: (1) enhancing the floor slab capacity through improved slab detailing, and (2) enhancing the connection capacity through improved connection detailing. While previous analyses have shown that the concrete slab on steel deck adds significant capacity under column removal, that capacity is sensitive to small variations in the slab thickness, slab continuity, detailing between deck sheets, and the attachment method to the perimeter framing (Main et al. 2015). Enhancements to the steel gravity connections are potentially more versatile and can be implemented both for new construction and for retrofit of existing structures.

In this study, high-fidelity numerical models of single-plate shear connections were first validated against experimental data from Weigand and Berman (2014) and then used to investigate steel gravity framing systems with enhanced connection detailing. The enhanced connections used U-shaped slotted steel plates, which were welded to the column flange and bolted to the beam flanges, to increase both the flexural capacity of the connection (at small rotations) and the tensile capacity of the connection (at large rotations). High-fidelity analyses were used to evaluate the component-level behavior of the U-shaped slotted plates under axial loading and to evaluate the behavior of the enhanced connections in a two-span beam assembly under center column loss. Reduced-order models were then used to evaluate the effectiveness of the enhanced connections in a two-bay by two-bay composite floor system under interior column loss.

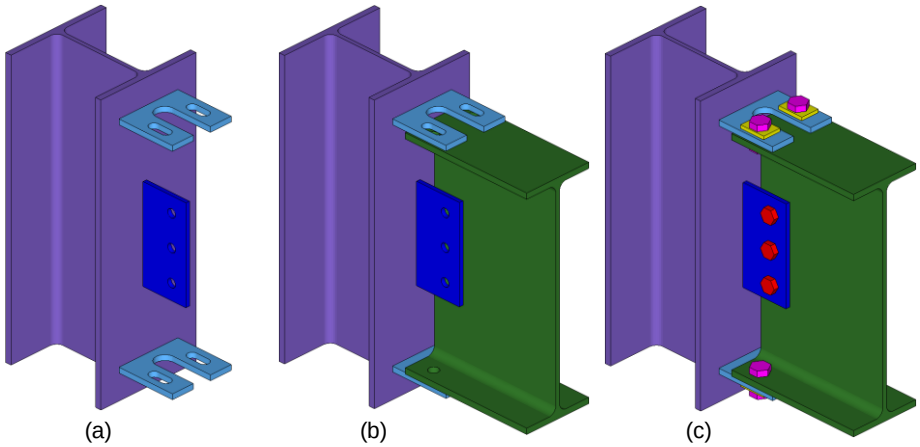

Figure 1: Enhanced single-plate shear connection: (a) U-shaped slotted top and seat plates welded to column; (b) beam in position; (c) bolted with rectangular plate washers.

ENHANCED CONNECTION DETAILS

The enhanced connection configuration includes top and seat plates, which are welded to the column and then bolted to the beam flanges (Figure 1). The top and seat plates have long-slotted holes to permit large slip displacements of the flange bolts prior to the initiation of bearing at the ends of the slots. Each top or seat plate has a U-shaped cutout that serves two purposes: (1) it allows the plate to be placed on either the interior or the

exterior face of the beam flange (exterior placement would be used in new construction while interior placement could be preferable for retrofit in some cases), and (2) it reduces the net section of the plate relative to the shear area of the bolts to ensure that tensile yielding develops in the plate sections adjacent to the slots, thus achieving significant plastic elongation of the slotted portion of the plate prior to tensile rupture (similar in concept to how a reduced beam section connection enhances ductility in flexure). Rectangular plate washers (Figure 1(c)) distribute the bearing stresses induced by pre-tension in the flange bolts. Standard holes are used in the beam flanges.

COMPUTATIONAL MODELING

High-fidelity finite-element modeling of the connections followed the approach described by Main and Sadek (2014) except that reduced-integration solid elements were used, rather than fully integrated elements, in order to better capture the localization of shear strain in the bolts. In the connection region, finely meshed hexahedral elements were used to represent the shear plate, top and seat plates, bolts, plate washers, and the beam (Figure 2). Outside of the connection region, the beam was modeled using shell elements, and nodal constraints were used to enforce compatibility of displacements and rotations at the solid/shell interface. Typical solid element sizes were 1.5 mm (0.06 in) for the bolts and 3 mm (0.12 in) for all other components. Contact was defined between all solid components to transfer forces through the bolted connection, and friction was included, with a static coefficient of friction of 0.34 for all interfaces, corresponding to an average value calculated from the extensive data compiled by Grondin et al. (2007).Piecewise-linear plasticity models were used to model the material behavior, with fracture simulated using element erosion, as described by Main and Sadek (2014). The stress-strain curve used to model the A325 bolts was based on tensile test data reported by Kulak et al. (1986). Stress-strain curves used to model the plates and wide-flange sections were obtained from tensile coupon testing of the actual materials used in single-plate shear connection tests by Weigand (2014), and data from one of these connection tests was used for model validation, as described in the following section.

Model Validation

The modeling approach was validated against results from a connection sub-assemblage test conducted by Weigand and Berman (2014), for a 3-bolt single-plate shear connection with a W12×72 column, W21×50 beam, 19.1 mm (¾ in) diameter ASTM A325 bolts, and a 9.5 mm (⅜ in) thick ASTM A36 shear plate (Specimen sps3b|STD|34|38|). Figure 2 illustrates the model used in the analysis, which consisted of two loading phases. In the initial phase, pre-tension was introduced in the bolts through thermal contraction, by artificially reducing the temperature of the bolts to achieve an average pre-tension of 185 kN (42 kip) per bolt. In the second phase, displacement-controlled axial and transverse loads were applied to the beam end, replicating the loading conditions used in the test (Weigand and Berman 2014), which imposed a combination of rotational and axial demands on the connection to represent a column loss scenario.

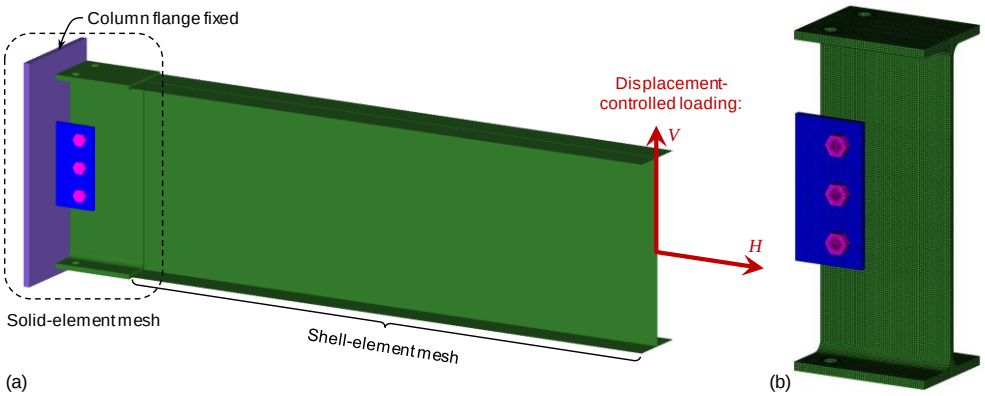

Figure 2: Computational model of specimen sps3b|STD|34|38| from Weigand and Berman (2014): (a) overview of model; (b) solid-element mesh.

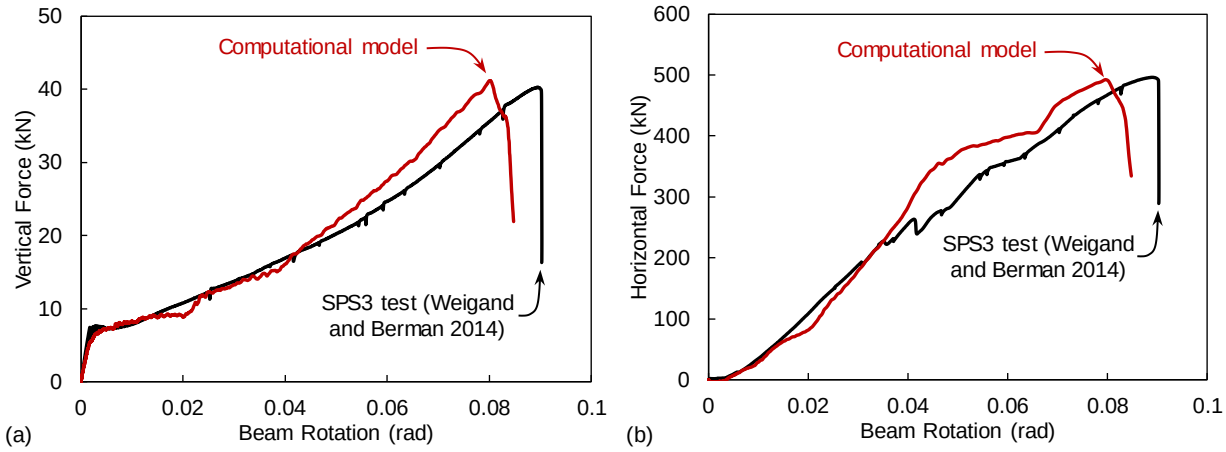

Figure 3: Comparison of computational and experimental results for (a) vertical force and (b) horizontal force vs. beam rotation. (Uncertainties in the experimental measurements are discussed by Weigand and Berman (2016).)

Figure 3 compares the computed vertical and horizontal forces with those obtained experimentally for Specimen sps3b|STD|34|38|. The peak vertical force from the computational model is 2 % greater than the experimental value and the peak horizontal force from the computational model is 1 % less than the experimental value. A somewhat larger discrepancy is observed for the rotation at peak load, for which the computational model underestimated the experimental value by 11 %. These discrepancies give an indication of the degree of uncertainty in the predictions of the computational model.

Component-Level Axial Behavior of U-Shaped Plate with Long-Slotted Holes

Prior to considering the behavior of enhanced connections under column loss, the model shown in Figure 4(a) was used to investigate the component-level behavior of a U-shaped plate with long-slotted holes under axial loading. A rectangular plate with standard holes was also modeled for comparison (Figure 4(b)). Plates made of ASTM A36 steel with a thickness of 12.7 mm (½ in) were considered, which were bolted to the flange of an ASTM

A992 W21×50 beam using two 22.2 mm (⅞ in) diameter ASTM A325 bolts. ASTM A36 plate washers with a thickness of 7.9 mm (5⁄16 in) were used for the U-shaped plate with long-slotted holes. One flange of the beam was modeled, including the flange-to-web-fillet, and nodes along the toe of the fillet were constrained to permit axial displacements only. Displacement-controlled axial loading was applied to one end of the beam flange, and the opposite ends of the A36 plates were fixed (Figure 4). Prior to axial loading, initial pre-tension of 234 kN (53 kip) was introduced in each bolt through thermal contraction.

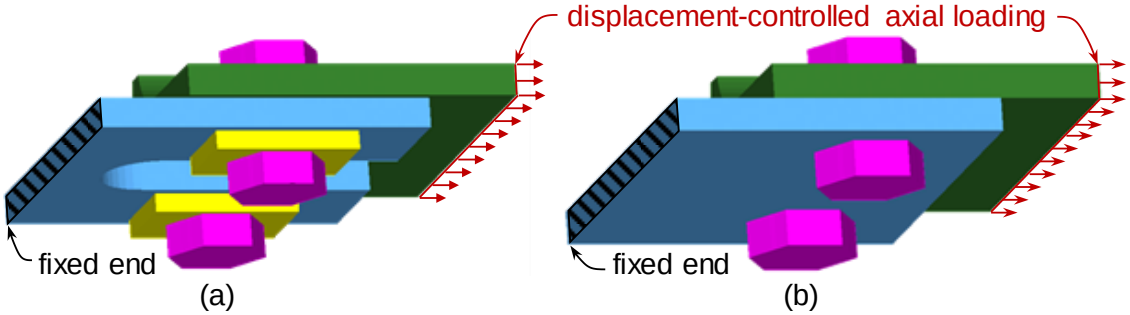

Figure 4: Component-level analysis models: (a) U-shaped plate with long-slotted holes; (b) rectangular plate with standard holes.

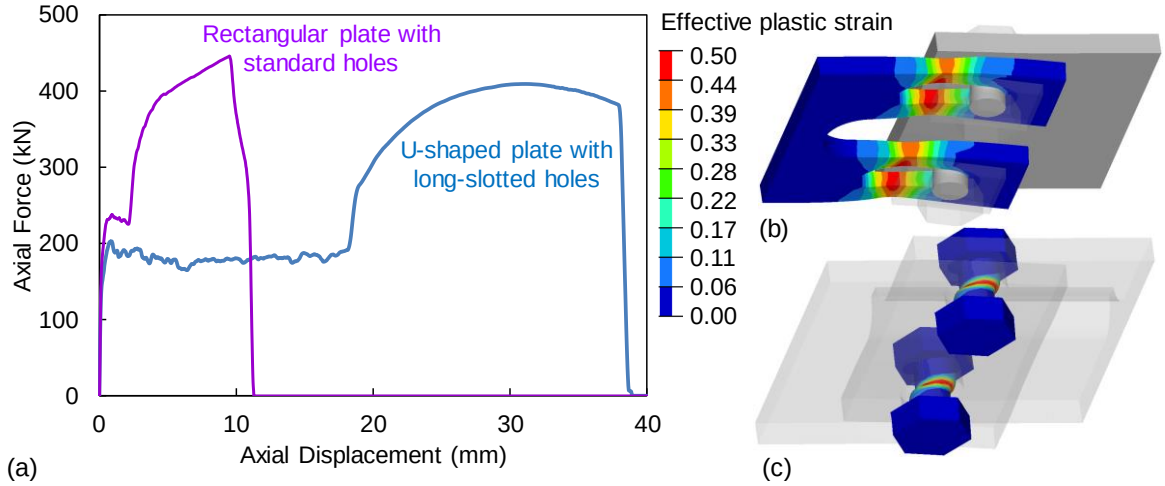

Figure 5: (a) Axial force-displacement results from component-level analyses, along with contours of effective plastic strain just prior to rupture for: (b) U-shaped plate with long-slotted holes; (c) flange bolts for rectangular plate with standard holes.

Figure 5(a) shows axial force-displacement curves obtained from the two models in Figure 4. For the model in Figure 4(a), Figure 5(b) shows contours of plastic strain just prior to tensile rupture of the U-shaped slotted plate, and for the model in Figure 4(b), Figure 5(c) shows contours of plastic strain just prior to shear rupture of the bolts. The peak axial force for the U-shaped slotted plate was slightly less (by 8 %) than that for the rectangular plate with standard holes, because of the intentional reduction in the net section of the U-shaped plate. However, the displacement at tensile rupture for the U-shaped slotted plate (38 mm (1.5 in)) was four times as large as the displacement at bolt

shear rupture for the rectangular plate with standard holes. The substantially larger displacements for the U-shaped slotted plate were developed initially through sliding of the bolts through the long slots (for displacements less than 18 mm (0.72 in), and subsequently through a combination of bearing deformations, bolt shear deformations, and elongation of the plate legs on each side of the long slots (see Figure 5(b)).

Two-Span Beam Assembly

A two-span beam assembly (Figure 6) was considered to evaluate the effectiveness of enhanced connections in bare steel framing (i.e., no floor slab) under column loss. A computational modeling approach similar to that illustrated in Figure 2 was used to analyze the response of the two-span beam assembly with different types of connections, including the two different types of top and seat plates illustrated in Figure 4. Figure 7(a) compares the results for these connections with those from a conventional single-plate shear connection. Figure 7(a) shows that the additional deformation capacity of the U-shaped plates with long-slotted holes results in a peak vertical capacity that is 46 % greater than that for rectangular top and seat plates with standard holes. Figure 7(a) also shows that the addition of U-shaped slotted top and seat plates results in a peak vertical capacity that is 2.5 times the vertical capacity for a conventional single-plate shear connection. Figure 7(b) shows that pre-tension in the flange bolts provides additional vertical resistance in the initial phase of the response, when the bolts are sliding in the slots, but has an insignificant effect after the onset of bearing deformations at a center column displacement of about 450 mm (18 in).

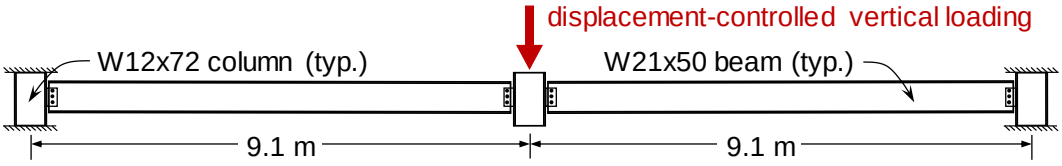

Figure 6: Two-span beam assembly.

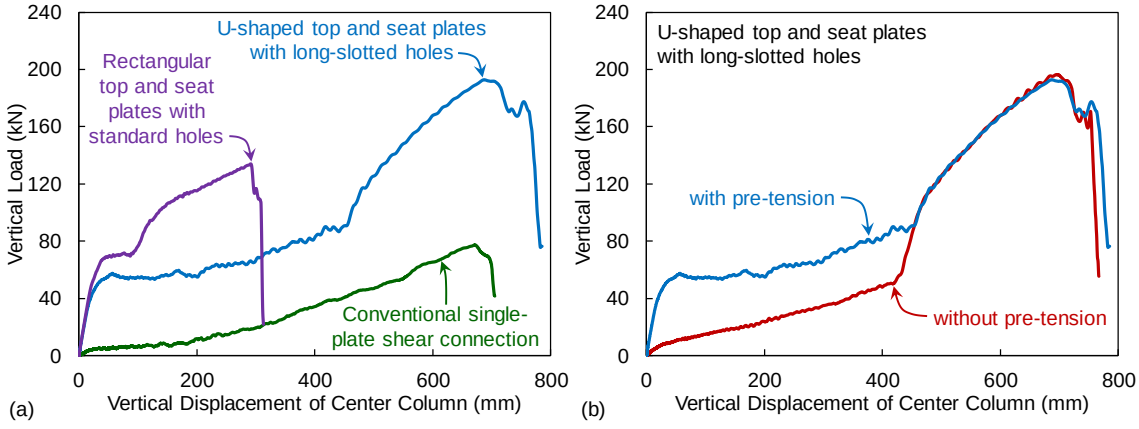

Figure 7: Vertical load-displacement analysis results for two-span beam assemblies: (a) comparison of results for different connection types; (b) influence of pre-tension.

Figure 8 shows that the behavior of the enhanced connections could be accurately represented using a reduced-order modeling approach in which the components of the connection were modeled as nonlinear springs interconnected by rigid links (Figure 9(a)). Such an approach has previously been successfully applied for moment connections (Sadek et al. 2013) and for single-plate shear connections (Main and Sadek 2014). Figure 8 shows that the reduced-order modeling approach captured the peak load from the high-fidelity model within 1 % and the corresponding displacement of the center column within 4 %. In this study, the force-deformation relationships for the nonlinear connection springs were defined using piecewise-linear approximations of results from high-fidelity finite element analysis of the connection components (Figure 9(b) and (c)). However, analytical models for the connection components could also be used, where available, such as the component-based model developed by Weigand (2016) for single-plate shear connections with pre-tension. The use of such a model facilitates parametric studies and optimization of connection configurations, which will be pursued in future studies.

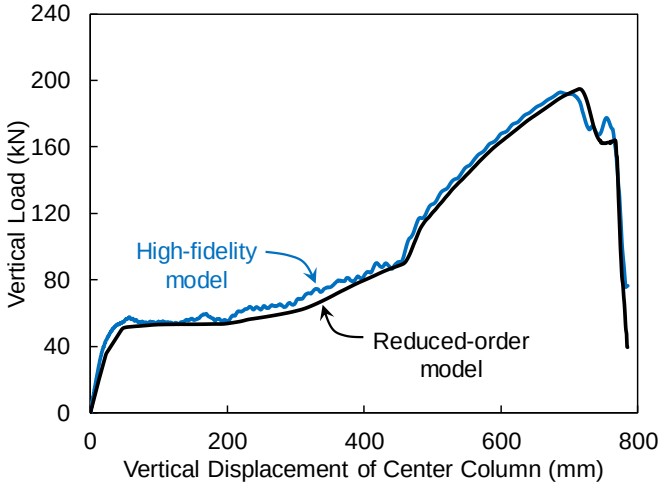

Figure 8: Reduced-order and high-fidelity model results for two-span beam assembly.

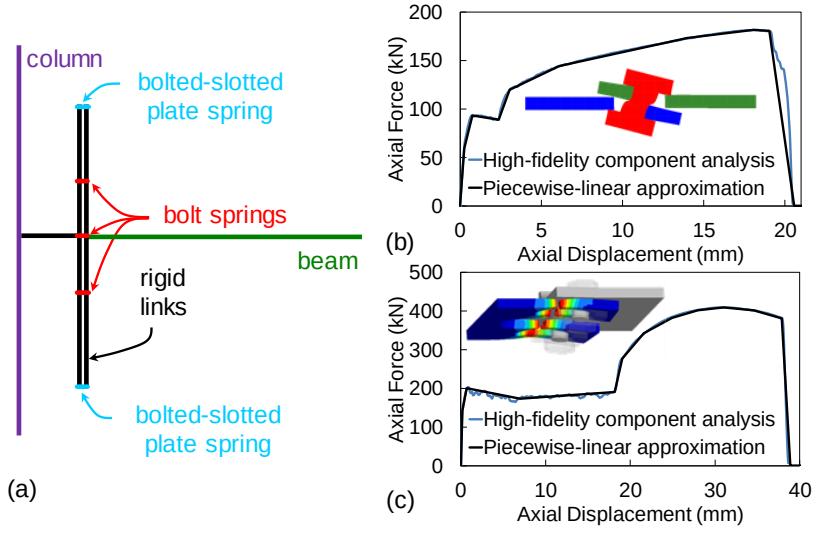

Figure 9: (a) Reduced-order connection model with force-displacement relationships for: (b) single-plate shear connection (one bolt row); (c) U-shaped slotted plate.

Composite Floor System

To evaluate the effectiveness of the enhanced connections in composite steel gravity framing, a prototype two-bay by two-bay composite floor system previously considered by Main (2014) was analyzed under center column loss, both with conventional single-plate shear connections and with enhanced beam-to-column and girder-to-column connections incorporating U-shaped slotted top and seat plates. The modeling approach for the composite floor system, illustrated in Figure 10, followed the approach proposed by Main (2014), in which the girders, beams, and columns were modeled with beam elements, and alternating strips of shell elements were used to represent the ribbed profile of the concrete slab on steel deck, with distinct integration points through the slab thickness for the steel deck, concrete, and welded wire reinforcement. Connections were modeled using a reduced-order approach as illustrated in Figure 9(a). Modeling of the conventional floor system in this study differed from Main (2014) in that a steeper softening modulus was used for the post-ultimate tensile resistance of concrete, as discussed by Main et al. (2015), and improved deformation limits were used for the single-plate shear connections, based on measurements from Weigand and Berman (2014), with a steep drop in resistance when those deformation limits were reached. The enhanced floor system was modeled using the piecewise-linear load-deformation relationship in Figure 9(c) to represent the U-shaped slotted plates.

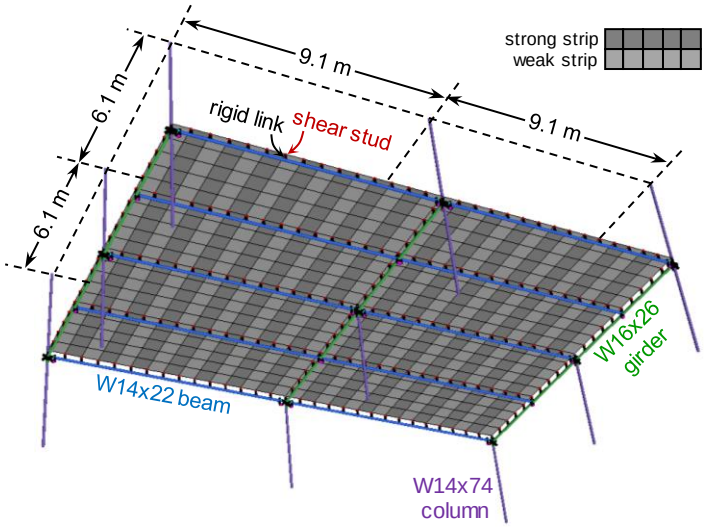

Figure 10: Reduced-order model of a 2-bay by 2-bay composite floor system.

Figure 11(a) shows computed curves of load intensity vs. center column displacement for floor systems with conventional and enhanced connections under uniform static loading with an unsupported center column. Figure 11(b) shows corresponding curves for sudden column loss, which were obtained from the curves in Figure 11(a) using the energy-based approach described by Main (2014). The floor system with conventional connections was unable to sustain the applicable gravity loading of $1.2D + 0.5L$, even under static loading. However, the enhanced connections increased the capacity of the floor system under

static loading by 90 %, resulting in a capacity that significantly exceeded the applicable gravity loading. As proposed by Bao (2014), a robustness index was calculated by normalizing the ultimate capacity under sudden column loss by the applicable gravity loading, whereby robustness indices of 0.56 and 0.99 were obtained for the systems with conventional and enhanced connections, respectively. The enhanced connections thus increased the robustness of the floor system by 76 %, resulting in an ultimate capacity under sudden column loss that was essentially equivalent to the applicable floor loading.

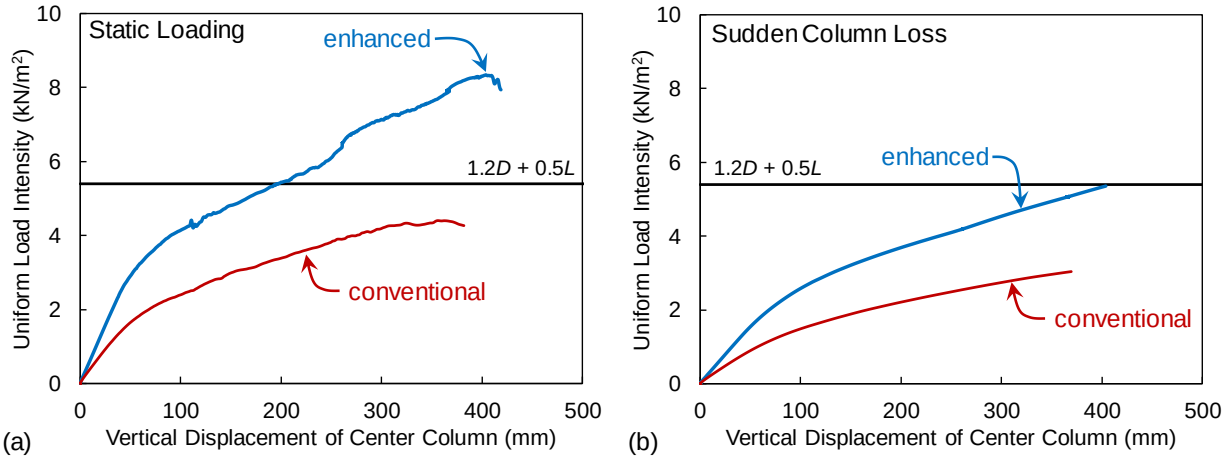

Figure 11: Uniform load intensity vs. center column displacement for floor systems with conventional and enhanced connections: (a) static loading; (b) sudden column loss.

SUMMARY AND CONCLUSIONS

This paper presented an enhanced steel gravity connection that used steel plates, bolted to the upper and lower flanges of the beam and welded to the column flange, to increase the flexural and tensile capacity of the connection. Analysis of the enhanced connection in a two-span beam assembly showed that it had a peak vertical resistance under column loss that was 2.5 times as large as that for a conventional single-plate shear connection. When implemented in system-level analyses of a two-bay by two-bay composite floor system, the enhanced steel gravity connections increased the vertical load-carrying capacity of the system under center column loss by 90 % under static loading. Robustness indices of 0.56 and 0.99 were calculated for the floor systems with conventional and enhanced connections, respectively, indicating that the enhanced connections increased the robustness of the floor system by 76 % and that the ultimate capacity of the enhanced floor system under sudden column loss is essentially equivalent to the applicable gravity loading. Future work will involve experimental evaluation of the performance of the enhanced connections under column loss scenarios and development of design procedures for the enhanced connections.

REFERENCES

ASCE (2010). *Minimum Design Loads for Buildings and Other Structures, SEI/ASCE 7-10,* American Society of Civil Engineers, Reston, VA.

Bao, Y, Main, J.A., Lew, H.S., and Sadek, F. (2014). "Robustness Assessment of RC Frame Buildings under Column Loss Scenarios." *Proc., Structures Congress*, Boston, MA, May, 2014.

Grondin, G., Jin, M. and Josi, G. (2007). "Slip-critical bolted connections – a reliability analysis for design at the ultimate limit state." *Structural Engineering Report No. 274,* University of Alberta.

Kulak, G.L., Fisher, J.W., and Struik, J.H.A., (1986). *Guide to Design Criteria for Bolts and Riveted Joints*, 2nd Edition, John Wiley & Sons, New York.

Lew, H.S., Main, J.A. Robert, S.D., Sadek, F., and Chiarito, V.P. (2012). "Performance of steel moment connections under a column removal scenario. I: Experiments," *Journal of Structural Engineering*, 139(1), 98-107.

Johnson, E.S. Meissner, and Fahnestock, L.A. (2015). "Experimental Behavior of a Half-Scale Steel Concrete Composite Floor System Subjected to Column Removal Scenarios." *Journal of Structural Engineering,* 04015133.

Main, J.A. (2014). "Composite Floor Systems Under Column Loss: Collapse Resistance and Tie Force Requirements." *Journal of Structural Engineering*, 140(8), A4014003.

Main, J.A. and Liu, J. (2013). "Robustness of Prototype Steel Frame Buildings against Column Loss: Assessment and Comparisons." *Proceedings of the ASCE/SEI Structures Congress*, Pittsburgh, PA, May, 2013.

Main, J.A. and Sadek, F. (2014). "Modeling and Analysis of Single-Plate Shear Connections under Column Loss." *J. Struct. Eng.*, 140(3), 04013070.

Main, J.A., Weigand, J.M., Johnson, E.S., Francisco, T.W., Liu, J., Berman, J.W., and Fahnestock, L.A. (2015). "Analysis of a Half-Scale Composite Floor System Test under Column Loss Scenarios." *Proceedings of the ASCE/SEI Structures Congress*, Portland, Oregon, April, 2015.

Sadek, F., Main, J.A., Lew, H.S., and El-Tawil, S. (2013). "Performance of Steel Moment Connections under a Column Removal Scenario. II: Analysis." 139(1), 108-119.

Weigand, J.M. (2016). "A Component-Based Model for Single-Plate Shear Connections with Pre-tension and Pinched Hysteresis." *J. Struct. Eng.* Under review.

Weigand, J. M. and Berman, J. W. (2014) "Integrity of Steel Single Plate Shear Connections Subjected to Column Removal Loading." *Journal of Structural Engineering.* 140(5), 04013114.

Weigand, J. M. and Berman, J. W. (2016) "Steel Gravity Connections Subjected to Large Rotations and Axial Loads." *Proc., Eighth International Workshop on Connections in Steel Structures (Connections VIII)*, Boston, Massachusetts, May, 2016.

Sensor Calibration and Registration for Mobile Manipulators

Steven Legowik
Robotic Research, LLC
Gaithersburg, MD , USA
email: legowik@roboticresearch.com

Roger Bostelman[1,2] and Tsai Hong[1]
[1]Intelligent Systems Division
National Institute of Standards and Technology
Gaithersburg, MD, USA
[2]IEM, Le2i, Université de Bourgogne,
Dijon, France
email: roger.bostelman@nist.gov and tsai.hong@nist.gov

Abstract—This paper describes the methods used to register a mobile manipulator to a workstation to perform assembly tasks. The nonlinear, least square model of the system is formulated and Ceres Solver is used to compute the position of the robot arm relative to the mobile base. The use of non-contact fiducials to test the accuracy and repeatability of the mobile manipulator positioning in the context of an assembly operation is also discussed. Using mathematical methods and indirect measurements it is possible to compute the offset between physical components of the system where direct measurement is not feasible.

Keywords- robot; AGV; mobile manipulator; collaborative robotics; registration; Ceres Solver; calibration.

I. INTRODUCTION

Industry is making increasing use of robotics for material transport and processing. These robotic systems make use of many innovative sensing technologies [2]-[5] and control techniques [6]-[9] to improve their versatility and agility. The traditional approach to flexible manufacturing is to use mobile robots to transport materials [10]-[11] between workstations containing stationary robotic manipulators [6]. Another approach is to move the robotic manipulators between the workstations [12] using an Automatic Ground Vehicle (AGV). This configuration is referred to as a mobile manipulator in this paper. The use of mobile manipulators can be advantageous in a number of situations. It can result in cost savings when a single mobile manipulator can be used to replace several stationary manipulators. The use of mobile manipulators is also useful in cases where the item being worked on is too large to be easily moved. Throughout this paper the term manipulator will refer to the robotic manipulator arm mounted on the mobile base, and the mobile base will be referred to as the AGV. The combination is referred to as a mobile manipulator.

The use of mobile manipulators in manufacturing presents new challenges [6]. The use of intelligent sensing systems such as computer vision or light detection and ranging (LADAR) sensors [13] can be used to measure a work-piece's location and orientation relative to the manipulator. To effectively act on sensor information, the systems need to know precisely where those sensors are located with respect to the other elements of the system. The calibration of a new sensor involves the determination of the position and orientation of the sensor relative to other sensors and manipulators. These parameters are difficult, or even impossible, to measure directly. Sometimes the only way of determining these unobservable system parameters is through the mathematical analysis of the sensor's own data. The calculation of arm-mounted camera offsets using images from the camera has been widely discussed in the literature [14]-[25]. In most of these methods, a key feature is the simultaneous solution of two sets of independent transformations. These transformations are typically the desired offset of the sensor and the pose of a calibration target. The solution of the calibration target pose is typically incidental to the solution of the desired offset. Similar methods can be applied to determining other system offsets.

The focus of this paper is on indirect methods for determining the mounting offset of a robot manipulator on a mobile base. Section II discusses the need to calibrate the offset between the manipulator base and the AGV's coordinate system. It also describes the equipment and methods used to collect the data and evaluate the results of the mounting offset calibration. Section III. discusses two methods of computing the mounting offset: the first using measurements taken at selected positions around a test artifact, and the second a method of computing the offset using Ceres Solver and a selection of measurements from a random set of positions around the test artifact. Section IV. discusses the effectiveness and accuracy of the two calibration methods discussed in Section III. Section V discusses the relative merits of using Ceres Solver for solving this type of calibration problem and the effects of measurement noise on the procedure.

II. WORKSTATION REGISTRATION

A. Description of the problem

The goal is to be able to use the AGV to move the manipulator to a workstation and be able to accurately assemble items in that workspace [26]. To perform this task, it is necessary to accurately determine the location of the manipulator relative to the workspace. Two crucial components of this are determining: (1) the actual (not just the commanded) position of the AGV and (2) the position of the manipulator relative to the AGV. For component one, we need to be able to get the position of the AGV from the navigation system in near real time. All our prior research to this point has involved off-line, AGV position data processing from log files. For the current task, we must be

Bostelman, Roger; Hong, Tsai; Legowik, Steven.
"Sensor Calibration and Registration for Mobile Manipulators."
Paper presented at The Fifth International Conference on Advances in Vehicular Systems, Technologies and Applications (VEHICULAR 2016),
Barcelona, Spain. November 13, 2016 - November 17, 2016.

able to pass the position information directly to the computer system that is controlling the manipulator.

The second requirement is to establish the offset between the AGV and the base of the manipulator. This will allow the AGV's position to be used to determine the global location of the manipulator when the AGV stops at a particular work station.

B. NIST Mobile Manipulator Testbed

The mobile manipulator used for the work described in this paper is a part of the National Institute of Standards and Technology (NIST), Robotic Systems for Smart Manufacturing Program. It was assembled as a platform for developing and testing performance standards [26]-[27] for mobile manipulators in industry.

The mobile manipulator consists of a six-axis manipulator mounted on top of an AGV. The AGV is an electrically-powered, all-wheel drive, automatic forklift designed for material transport in an industrial setting. The AGV navigates from location to location using a path network that is preprogrammed off-line. The AGV location is measured using a navigation system that uses a rotating laser range sensor to detect the locations of reflectors strategically mounted throughout the work area. The positions of the reflectors are surveyed during the initial setup of the system. During operation the position and orientation of the AGV is calculated based on the range and angle to reflectors within range of the navigation sensor.

In order to test the positioning accuracy and repeatability of the mobile manipulator, a laser retro-reflector sensor was mounted as the end-of-arm-tool (EOAT) of the manipulator. A digital signal is output from the sensor when the laser is emitted and reflected to the sensor. The signal is then read by the manipulator controller. Less intense reflections off of other objects in the workstation are ignored. The laser is used to interact with the Reconfigurable Mobile Manipulator Apparatus (RMMA) described in the next section.

C. Reconfigurable Mobile Manipulator Apparatus

The RMMA [26]-[28] is a test fixture developed at NIST to emulate the environment that would be encountered by a mobile manipulator. It was designed primarily to emulate the positioning requirements of an assembly task, specifically the peg-in-hole insertion task. It does this by providing a set of precisely positioned mount points for reflective targets. The targets are detected using a non-contact, laser retro-reflector sensor designed to detect the presence of retro-reflective targets in line with the laser beam. The sensor is mounted as the EOAT. The targets are designed to determine if the manipulator position is accurate enough for successful peg-in-hole insertion. The RMMA provides a way to test and verify the performance of mobile manipulator systems without the use of expensive 3D tracking systems [29].

The target fiducials are constructed using a piece of reflective material fixed behind a circular aperture. In some of the targets a fixed radius aperture is used, in others a variable aperture is used. A top down view of a target fiducial is shown in Fig. 1. The laser retro-reflector sensor is used to detect the alignment of the manipulator with the fiducial. A signal is returned by the sensor when the laser beam is reflected back by the fiducial. The position accuracy can be adjusted by varying the size of the aperture used to expose the reflector. In addition, a tubular collimator is added to the fiducial to restrict the detection angle of the fiducial. The position of a fiducial can be determined by performing a search starting somewhere near the fiducial's actual position. By performing a spiral grid search with a step size of half the aperture diameter, the position of the fiducial can be determined with an accuracy bounded by the

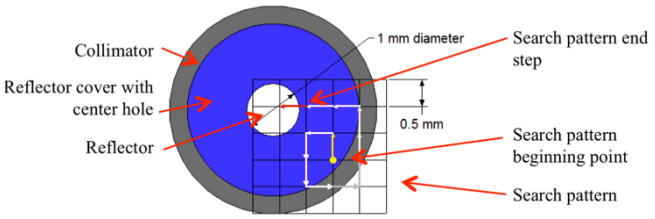

Figure 1. Top down view of an RMMA fiducial showing grid spiral search pattern.

aperture diameter. Fig. 1 illustrates the path followed during a spiral grid search.

Large circular reflectors can also be mounted on the RMMA to aid in mobile manipulator localization. The center of the large reflectors are measured by performing a bisecting search starting from a point within the radius of the reflector. The center is found by searching outward to find the reflector edges and bisecting that chord. After locating the center along one axis, a search for the reflector's edges is performed along an axis perpendicular to the first. After the endpoints of this second chord are determined, the center position of the reflector can be calculated. The bisection search is illustrated in Fig. 2(a). After the centers of two reflectors has been measured, the position and orientation of the pattern can be determined. Then the positions of all the other target reflectors in the pattern can be calculated based on their position relative to the registration reflectors.

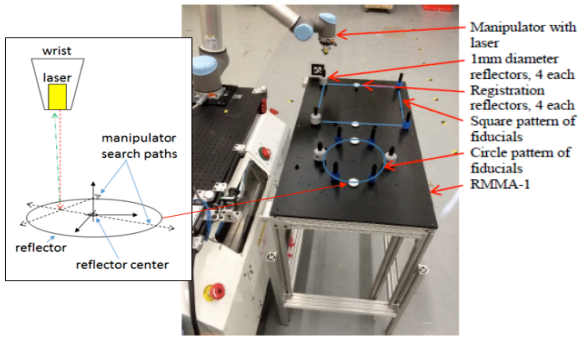

(a) (b)

Figure 2. (a) Bisection search concept, and (b) the mobile manipulator positioned next to the RMMA, the RMMA square and circle patterns, and the large reflectors within each pattern.

D. Registration to RMMA Patterns

The RMMA has a number of precisely-positioned, threaded holes into which the fiducials and reflectors can be mounted to exercise the system. There are two main target

configurations: a square target and a circular target as shown in Fig. 2(b). These are used to test the positioning accuracy and repeatability of the mobile manipulator after bisecting the large reflectors.

The two dimensional (2D) pose of the square and circle pattern of small reflectors can be determined by measuring the locations of two reflectors, large or small, on each pattern. The other small reflector locations in the pattern can be calculated based on their relative offsets when given the pattern pose. Either a pair of small reflectors using the search method or a pair of large reflectors using the bisect method can be used to register the mobile manipulator with the workspace represented by each pattern. For example, after moving to the calculated reflector positions, if the small reflector is not immediately detected, a search is performed. The distance between the initial position of the manipulator and the position at the end of the search can be used to provide information on the accuracy of the mobile manipulator's position and the accuracy of the registration.

III. MANIPULATOR CALIBRATION

A. *Manual calibration method*

We experimented with methods to allow strictly manual calibration of the manipulator mounting offset using a number of simple measurements. The idea was to select pairs of calibration data measurements that would lead to the simple calculation of a single value of the manipulator mounting offset. This was done by selecting pairs of positions around the target where the other parameters of the manipulator mounting offset would effectively cancel each other out.

The AGV positions were chosen to cancel out the effects of the other base offset parameters, or to minimize their effect on the computation. In testing, these values were good enough to come up with rough values of the offset, but not good enough for precise positioning of the manipulator. There were some interactions between the calibration variables that could not be completely eliminated using this method. However, the method works well as a sanity check for the other computation methods.

The equations below describe the manipulator offset calibration in a 2D plane. The value being determined is the 2D translational offset and rotation offset of the manipulator relative to the AGV. The reason for doing the calculations in 2D is that the method for taking the measurements using the laser sensor only constrains the position in 2D, and the AGV navigation solution is only 2D.

Fig. 3(a) illustrates a pair of mobile manipulator locations that isolates the x offset of the manipulator base.

$$A_{x1} + O_x - P_{x1} = A_{x2} - O_x + P_{x2}, \quad (1)$$

$$O_x = \tfrac{1}{2} (A_{x2} - A_{x1} + P_{x1} + P_{x2}), \quad (2)$$

where:

P is point in manipulator coordinates (P_x, P_y)

A is AGV coordinate (A_x, A_y, A_a=angle)

O is the manipulator mounting offset (O_x, O_y, O_a=angle)

Fig. 3(b) illustrates a pair of mobile manipulator locations that isolates the y offset of the manipulator base.

$$A_{y1} + O_y - P_{y1} = A_{y2} - O_y + P_{y2}, \quad (3)$$

$$O_y = \tfrac{1}{2} (A_{y2} - A_{y1} + P_{y1} + P_{y2}), \quad (4)$$

Fig. 3(c) illustrates a pair of mobile manipulator locations that isolates the angular offset of the manipulator base.

$$A_{x1} + O_x - P_{x1} + R_1 \sin O_a = A_{x2} + O_x - P_{x2} + R_2 \sin O_a, \quad (5)$$

where

$$R_n = (P_{xn}^2 + P_{yn}^2)^{1/2} \quad (6)$$

and

$$O_a = \sin^{-1}((A_{x1} - A_{x2} - P_{x1} + P_{x2}) / (R_2 - R_1)) . \quad (7)$$

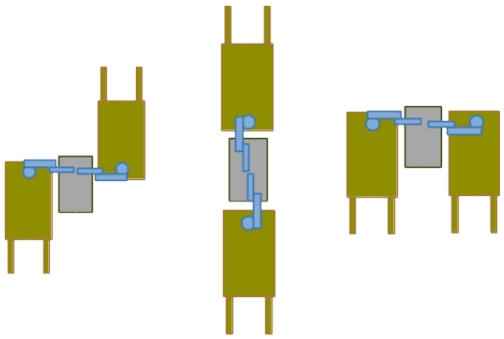

(a) (b) (c)

Figure 3. Mobile manipulator (green) positions relative to the RMMA (gray) selected for manual calibration of manipulator (blue) mounting offset.

These formulas assume the manipulator is mounted on the AGV with its positive y-axis pointing toward the rear (fork-end) of the AGV (in the direction of the AGV's negative x-axis).

There are a number of issues that limit the effectiveness of this approach for determining the manipulator base location. One issue is that despite the best efforts to position the AGV as described, there will be some errors in alignment. The result is that the other offset terms will not cancel out exactly, and there will be some interaction between the parameters that will affect the results of the calibration.

Another issue with this method is that it does not deal well with measurement error. Each parameter is calculated using a single pair of AGV positions. So any errors in the measurements are reflected directly in the calculated mounting parameters. The effects of measurement noise can be compensated for by averaging together a number of measurements at a given location.

B. *Calibration using Ceres Solver*

A better way to solve for the manipulator base offset is to express it in terms of a non-linear minimization problem. This allows all the interactions between the base offset parameters and the calibration measurements to be explicitly modeled. After the interactions between the calibration parameters and the calibration data have been modeled, the calibration parameters can be solved using iterative methods. The tool used to compute the iterative solution was the Ceres Solver library [1].

The calibration data consists of paired AGV and manipulator position data taken at various locations around the RMMA. The only constraint on the data is that it needs to be collected at a number of different AGV positions and angles in order for the solver to converge properly. Data from multiple target points can also be used as long as the association is maintained in the data model.

The mobile manipulator system model is formulated as:

$$wp(k) = agvPose(t) * robotPose * rp(k,t), \quad (8)$$

where:

- wp(k) is the estimated position of the *k*th target point in world coordinates;
- agvPose(t) is the measured pose of the AGV in world coordinates at time t;
- robotPose is the estimated pose of the manipulator in AGV vehicle coordinates;
- rp(k,t) is the measured location of the *k*th target point in manipulator coordinates at time t.

The agvPose(t) and robotPose are 2D transformations consisting of a translation and a rotation. The points wp and rp are 2D points. Individual calibration targets are enumerated by *k*, and individual calibration measurements are enumerated by *t*.

The program adjusts the values of wp(k) and robotPose to minimize the residual between the estimated world coordinates of the target points and the position value computed in (8) above using the calibration data. The estimate of the manipulator mounting offset is calculated using the data collected for the manual calibration augmented with additional samples not used in the manual calibration.

The relationship between the calibration data and the free variables is established in Ceres Solver by the creation of *residual blocks*. The residual is defined as the difference between the estimated value of wp and the value of wp calculated by (8). The Ceres Solver then iteratively solves for the values of wp and robotPose that minimize the sum of the squares of all the residuals defined by the residual blocks. Ceres can also make use of a loss function, which can be used to minimize the effect of outliers. When the loss function is $\rho(x) = x$, Ceres minimizes the mean squared error of the residuals. The encapsulation of the residual computation in the residual blocks also allows Ceres to automatically compute the partial derivatives of the modeling equations. This eliminates a potential source of user error.

This problem bears a close similarity to the three-dimensional (3D) simultaneous, robot-world, hand-eye calibration discussed in [14][15][16]. The camera calibration problem is typically expressed as $AX = ZB$, where X is the 3D pose representing the camera offset and Z is the 3D pose representing the location of the calibration target. It is easy to see that (8) can be manipulated into this form. Both X and Z are unknowns that have to be solved simultaneously. A number of closed-form solutions [25][14] have been proposed to solve for these values. The principle difference between the different solutions is how they resolve the weighting between the positional and rotational components [11] of the residual that defines the 'best' solution to the problem. Given the 2D nature of the current problem, it is probable that a closed-form solution to the problem can be formulated. However, since the calibration parameters do not need to be computed in real time, the iterative solution implemented with Ceres Solver is sufficient. The iterative solution method is also easily adapted to solve for other calibration constants, some of which may not be solvable with a closed-form solution.

More data is generally better data. Unlike the manual calibration approach, the iterative minimization approach can use additional data to minimize the effects of measurement noise. However, care must be taken to provide a suitably rich set of input data. For example, if all the samples were taken at different positions around the workspace, but with the same orientation, it is not possible to determine the orientation offset of the manipulator base. The iterative solution would either not converge, or would converge to an unstable value.

Care must also be taken in the construction of the system model used for iterative minimization. If two or more of the free variables are correlated, the model will be under constrained, and may not be able to converge to an answer. A high degree of correlation between variables can also lead to a high degree of sensitivity to the input data.

IV. RESULTS OF TESTING

The initial set of calibration data was collected manually. The AGV was moved manually to various locations around the RMMA and its position was recorded. Then the manipulator was moved manually to the positions of the first and second reflectors of the square target. The manipulator was moved until the retro-reflector sensor detected the reflectors. Then the position of the manipulator was manually recorded.

The reflectors used to collect the calibration data had a 3.2 mm (1/8 in) aperture. The positions of the AGV relative to the RMMA for the manual data collection are shown in Fig. 4. A subset of these measurements, shown in Fig. 3, was used to perform the manual calibration described in Section III.A. The orientation of the EOAT was maintained constant relative to the manipulator base so that any lateral offset of the sensor from the tool center could be ignored. Any offset at the tool becomes part of the base offset for the purposes of this calibration. A subsequent calibration of the base offset using all of the collected data was performed using Ceres Solver.

Testing of the manipulator base calibration was performed using an automated test program and the RMMA. A program was set up to drive the AGV to ten different positions around the RMMA as shown in Fig. 5. At each docking location, the position of the AGV, the world coordinate of the reflector, and the manipulator base offset were used to compute the robot coordinates of the reflectors using (8). After positioning the sensor, a search was performed to determine how far off the position calculation was.

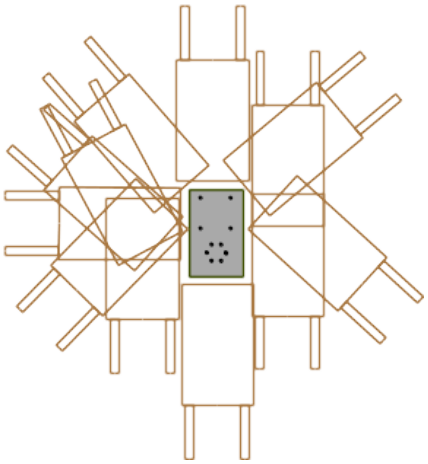

Figure 4. Position and orientation of AGV relative to the RMMA from manually collected calibration data.

Ideally, it should be possible to move the manipulator directly to the reflector based on the position of the AGV. Unfortunately, noise and systematic errors in the AGV position data prevent this. Fig. 6 shows a plot of consecutive samples of the AGV's *x*-axis position as the AGV sits motionless. The graph also shows a plot of the average value of samples 1 through n. This shows roughly how many samples need to average together to produce a reasonably stable position value. The *y* position and the orientation angle exhibit similar noise. The AGV position data is available at about 16 Hz, so it requires about 6.25 seconds to collect 100 samples. In this 2D case a simple average of the orientation angles is sufficient. In the general case of 3D orientations, greater care needs to be observed in averaging the orientation [32][33]. In addition to the random noise, tests also indicate that there are some systematic biases in the AGV position data depending on the location of the AGV.

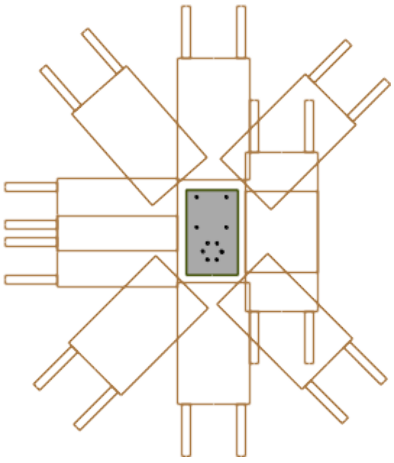

Figure 5. Docking locations used for automated data collection and system evaluation.

The goal is to be able to align the manipulator with the workspace in the minimum amount of time. The ideal situation is to be able to perform the insertion task immediately on arrival at the workstation. However, in this case it is necessary to compensate for the unavoidable measurement errors. It becomes a tradeoff between time spent averaging the position data to produce a stable value vs. time spent searching for registration points in the workspace.

The manual calibration method described in section III.A generated a base offset of (x = 831.5, y = - 7.5) mm and a rotation of 90.6°, yielding a mean square error of 1.25 mm and a maximum residual of 6.3 mm. The Ceres Solver came up with an offset of (x =833.637, y = -8.22223) mm and a rotation of 90.5314°, yielding a mean square error of 1.19 mm and a maximum residual of 10.7 mm. The Ceres Solver was seeded with a variety of initial conditions, including setting all the variable parameters to 0, and had no problems with convergence. The resulting offset positions agreed with each other within 0.1 mm

V. CONCLUSIONS

With care, Ceres Solver has proven to be a valuable tool in calibrating a variety of hard to measure constants in our robotic systems. It provides an easy to use framework for solving difficult non-linear problems iteratively. The main issues that have to be observed are that the model cannot be either over or under constrained if Ceres Solver is to converge properly.

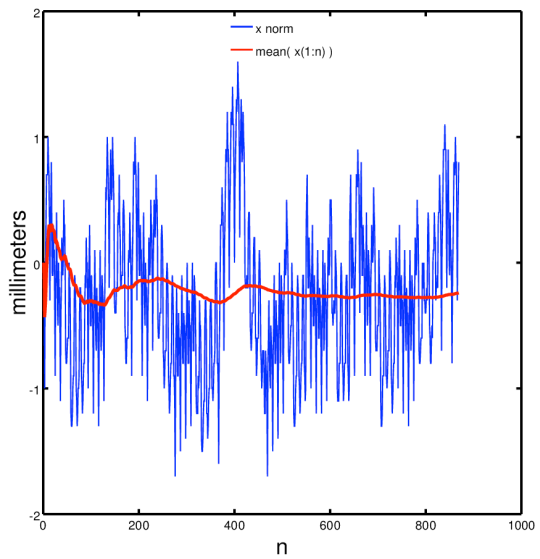

Figure 6. (blue)AGV position along x-axis, normalized to the first sample, x(1); (red) the mean of the normalized x value from x(1) to x(n).

Using Ceres Solver, we were able to compute the base offset of the manipulator mounted on a mobile platform despite the fact that the location of the AGV origin was not directly measureable. Using the computed offset and the location of the AGV, we were able to position the manipulator end effector within a few millimeters of the target regardless of the position and orientation of the AGV. While perfect initial positioning was not possible, the search

time required to achieve the desired alignment accuracy was greatly reduced by improving the initial positioning of the manipulator.

The limiting factors in being able to accurately position the end effector are the noise and systematic errors in the AGV navigation sensor. This affects both the final position calculation and the accuracy of the manipulator base transform. The AGV position errors in the measurement used to compute the base offset affect the quality of the solution derived. The quality of the solution can be assessed by examining the residuals left after the model has converged to a solution for the free parameters. Large residuals indicate corresponding errors in the calibration data, either random or systematic.

We plan on pursuing other methods to increase the speed of the workspace registration. The spiral grid search increases in time proportional to the square of the initial error. Performing a bisecting search on the large reflectors goes up approximately linearly with the size of the maximum expected error, since the size of the reflector needs to be scaled up to encompass the maximum initial positioning error. In the future, we are planning to investigate the use of camera-based position estimates to improve the alignment time.

DISCLAIMER

Commercial equipment, software, and materials are identified in order to adequately specify certain procedures. In no case does such identification imply recommendation or endorsement by the National Institute of Standards and Technology, nor does it imply that the materials, equipment, or software are necessarily the best available for the purpose.

REFERENCES

[1] S. Agarwal and K. Mierle, "Ceres solver," http://ceres-solver.org [retrieved August, 2016].

[2] B. Hamner, S. Koterba, J. Shi, R. Simmons, and S. Singh, "Mobile robotic dynamic tracking for assembly tasks," IEEE/RSJ International Conference on Intelligent Robots and Systems, pp. 2489-2495, 2009.

[3] R. Bostelman, T. Hong, and G. Cheok, "Navigation Performance Evaluation for Automated Guided Vehicle," 2015 IEEE International Conference on Technologies for Practical Robot Applications (TePRA), pp. 1-6 , 2015.

[4] R. E. Mandapat, "Development and evaluation of positioning systems for autonomous vehicle navigation," Florida University Gainesville Center for Intelligent Machines and Robotics, pp. 1-277, 2001.

[5] A. Kelly, B. Nagy, D. Stager, and R. Unnikrishnan, "Field and service applications an infrastructure free automated guided vehicle based on computer vision an effort to make an industrial robot vehicle that can operate without supporting infrastructure." IEEE Robotics & Automation Magazine, pp.24-34, 2007.

[6] B. Hamner, S. Koterba, J. Shi, R. Simmons, and S. Singh, "An autonomous mobile manipulator for assembly tasks," Autonomous Robot, pp.131-149 , 2010.

[7] J. Vannoy and J. Xiao, "Real-time Adaptive Motion Planning (RAMP) of mobile manipulators in dynamic environments with unforeseen changes," in IEEE Trans. on Robotics, pp.1199-1212 , 2008.

[8] H. Martínez-Barberá and D. Herrero-Pérez, "Autonomous navigation of an automated guided vehicle in industrial environments." Robotics and Computer-Integrated Manufacturing, pp.296-311, 2010.

[9] R. C. Arkin and R. Murphy, "Autonomous navigation in a manufacturing environment," IEEE Transactions on Robotics and Automation, pp.445-454 ,1990.

[10] H. F. Durrant-Whyte, "An autonomous guided vehicle for cargo handling applications." The International Journal of Robotics Research, pp.407-440, 1996.

[11] H. Martínez-Barberá and D. Herrero-Pérez, "Autonomous navigation of an automated guided vehicle in industrial environments." Robotics and Computer-Integrated Manufacturing, pp.407-440, 2010.

[12] S. Bøgh, M. Hvilshøj, M. Kristiansen, and O. Madsen, "Autonomous industrial mobile manipulation (AIMM): from research to industry." In 42nd International Symposium on Robotics. Pp. 1-9, 2011.

[13] M. Hvilshøj and S. Bøgh, "Little Helper-An autonomous industrial mobile manipulator concept," International Journal of Advanced Robotic Systems, pp.80-90, 2011.

[14] M. Shah, "Solving the Robot-World/Hand-Eye Calibration Problem Using the Kronecker Product," ASME Journal of Mechanisms and Robotics, Vol. 5, 031007, pp. 1-7, 2013.

[15] F. Dornaika and R. Horaud, "Simultaneous robot-world and hand-eye calibration, "IEEE Transactions on Robotics and Automation, pp.617-622 ,1998.

[16] H. Zhuang, Z. Roth, and R. Sudhakar, "Simultaneous robot/world and tool/flange calibration by solving homogeneous transformation of the form AX = YB," IEEE Trans. Robot. Automat, pp.549-554, 1994.

[17] A. Geiger, F. Moosmann, O. Car, and B. Schuster, "Automatic calibration of range and camera sensors using a single shot," ICRA, pp. 3936-3943 , 2012.

[18] H. S. Alismail, D. Baker, and B. Browning, "Automatic calibration of a range sensor and camera system," Second International Conference on 3D Imaging, Modeling, Processing, Visualization & Transmission. IEEE, pp. 286-292 ,2012.

[19] Z. Zhang, "A flexible new technique for camera calibration," IEEE Transactions on pattern analysis and machine intelligence, pp.1330-1334 , 2000.

[20] J-Y. Bouguet, "Camera calibration toolbox for matlab," < http://www.vision.caltech.edu/bouguetj/calib_doc/> [retrieved August, 2016].

[21] J. Weng, P. Cohen, and M. Herniou. "Camera calibration with distortion models and accuracy evaluation," IEEE Transactions on pattern analysis and machine intelligence 14.10, pp.965-980, 1992.

[22] O. D. Faugeras, Q.-T. Luong, and S. J. Maybank, "Camera self-calibration: Theory and experiments," European conference on computer vision, Springer Berlin Heidelberg, pp. 321-334, 1992.

[23] Y. Huang, X. Qian, and S. Chen, "Multi-sensor calibration through iterative registration and fusion, " Computer-Aided Design, pp.240-255, 2009.

[24] S. Spiess, V. Vincze, and M. Ayromlou, "On the calibration of a 6D laser tracking system for contactless, dynamic robot measurements," Instrumentation and Measurement Technology Conference, pp. 1203-1208 ,1997.

[25] M. Shah, R. D. Eastman, and T. Hong, "An overview of robot-sensor calibration methods for evaluation of perception systems," In Proceedings of the Workshop on Performance Metrics for Intelligent Systems, pp. 15-20, ACM, 2012.

[26] R. Bostelman, T. Hong, and J. Marvel, "Performance Measurement of Mobile Manipulators", SPIE 2015, Baltimore, MD, Vol. 9498, pp. 1-9, April 2015.

[27] R. Bostelman, T. Hong, and S. Legowik, “Mobile Robot and Mobile Manipulator Research Towards ASTM Standards Development”, SPIE 2016, Baltimore, MD, pp. 98720F-98720F , 2016.

[28] R. Bostelman, S. Foufou, S. Legowik, and T. Hong “Mobile Manipulator Performance Measurement Towards Manufacturing Assembly Tasks”, 13th IFIP International Conference on Product Lifecycle Management (PLM16), Columbia, SC, July 11-13, Vol. 9892, pp. F1-F10, 2016.

[29] R. Bostelman, J. Falco, M. Shah, and T. Hong, “Dynamic Metrology Performance Measurement of a Six Degree-of-Freedom Tracking System Used in Smart Manufacturing”, Autonomous Industrial Vehicles: From the Laboratory to the Factory Floor, ASTM Book chapter 7, 2016.

[30] R. Bostelman, R. Eastman, T. Hong, O. A. Enein, S. Legowik, and S. Foufou, “Comparison of Registration Methods for Mobile Manipulators,” CLAWAR, 2016.

[31] M. Shah, “Comparing Two Sets of Corresponding Six Degree of Freedom Data,” Computer Vision and Image Understanding, Volume 115, Issue 10, pp. 1355-1362. 2011.

[32] R. Hartley, J. Trumpf, Y. Dai, and H. Li, “Rotation averaging,” International journal of computer vision, 103(3), pp.267-305 , 2013.

[33] F. L. Markley, Y. Cheng, J. L. Crassidis, and Y. Oshman, “Averaging quaternions,” Journal of Guidance, Control, and Dynamics, pp.1193-1197, 2007.

Proceedings of the ASME 2016 International Mechanical Engineering Congress & Exposition
ASME IMECE 2016
November 11-17, 2016, Phoenix, Arizona, USA

IMECE2016-67220

A METHOD FOR CHARACTERIZING MODEL FIDELITY IN LASER POWDER BED FUSION ADDITIVE MANUFACTURING

Ibrahim Assouroko*
Université de Technologie de Compiègne
Compiègne, France
Email: ibrahim.assouroko@nist.gov

Felipe Lopez*
University of Texas at Austin
Austin, TX 78712
Email: felipelopez@utexas.edu

Paul Witherell
National Institute of Standards and Technology
Gaithersburg, MD 20899
Email: paul.witherell@nist.gov

ABSTRACT

As Additive Manufacturing (AM) matures as a technology, modeling methods have become increasingly sought after as a means for improving process planning, monitoring and control. For many, modeling offers the potential to complement, and in some cases perhaps ultimately supplant, tedious part qualification processes. Models are tailored for specific applications, focusing on specific predictions of interest. Such predictions are obtained with different degrees of fidelity. Limited knowledge of model fidelity hinders the user's ability to make informed decisions on the selection, use, and reuse of models. A detailed study of the assumptions and approximations adopted in the development of models could be used to identify their predictive capabilities. This could then be used to estimate the level of fidelity to be expected from the models. This paper conceptualizes the modeling process and proposes a method to characterize AM models and ease the identification and communication of their capabilities, as determined by assumptions and approximations. An ontology is leveraged to provide structure to the identified characteristics. The resulting ontological framework enables the sharing of knowledge about indicators of model fidelity, through semantic query and knowledge browsing capabilities.

Keywords: additive manufacturing, model fidelity, model characterization, ontology.

1 INTRODUCTION

Additive Manufacturing (AM) processes build objects layer-by-layer directly from three-dimensional models [1]. For years, AM was primarily used to make polymer prototypes. Now, however, AM processes are being employed in the production of end-use parts made of polymers, ceramics, and metals. AM-produced parts are rapidly capturing the attention of the aerospace and biomedical industries who see this technology as suitable for the production of small volumes of highly-complex components [2]. Many issues affect the broader adoption of AM in other industry sectors. Those issues can be traced to challenges with establishing repeatable non-burdening qualification of AM-produced components. Statistics-based quality control techniques, which are often used in the manufacturing industries, are not readily extendable to AM. Extensive testing is required to determine admissible deviations from optimal operating conditions, which are still not well defined in batch-size AM. As an alternative, researchers are trying to move beyond experiments and better incorporate computational models for faster and cheaper part qualification and process optimization in AM [3, 4].

A major challenge in modeling is accounting for and communicating the fidelity of the model. Here, we use the term fidelity as a measure of the extent to which the model faithfully captures and represents its real-world counterpart. Computational models have been developed at different levels of sophistication, resulting in predictions at different levels of fidelity. In the case of AM, for example, there are detailed models that include multiple highly-coupled physical processes, at the ex-

*This work was carried out while the authors were employed as Guest Researchers at the National Institute of Standards and Technology.

Assouroko, Ibrahim; Lopez, Felipe; Witherell, Paul.
"A method for characterizing model fidelity in laser powder bed fusion additive manufacturing."
Paper presented at ASME 2016 International Mechanical Engineering Congress & Exposition ASME IMECE 2016,
Phoenix, AZ. November 11, 2016 - November 17, 2016.

pense of requiring many hours of computation time [5–7]. At the other same time, there is an increasing interest in industry for low-cost models that also must make predictions in fractions of a second [8,9]. Understanding the predictive capabilities of such models requires identifying their characteristics, including their sources of uncertainty.

Good places to start the identification process are the assumptions and approximations that led to the development of the model. The physics of AM processes involve numerous and complex physical phenomena occurring at different length- and time scales. For simplicity, AM processes are often idealized by including only a subset of the phenomena. Even then, a number of simplifying assumptions are usually required to obtain a tractable mathematical model, often in the form of a set of differential equations. These differential equations are further approximated using numerical methods to produce a computational model that can be simulated on a computer. As such, the term assumption is used in the paper to refer to the set of modeling choices adopted by the modeler for the simplification of a physical system, in the course of the development of the mathematical model. Approximation, on the other hand is used to define the set of numerical methods employed to transform the mathematical model into a solvable form.

The development and selection of computational models often involves a balancing act between model fidelity and computational cost. Informed modeling choices should be supported by information on the fidelity of computational models, as determined by their characteristics. Model characteristics are defined as the unique traits of the model, which provide insight into its internal structure and properties. The method proposed in the paper captures such characteristics in an attempt to support the evaluation and communication of model fidelity. This paper builds on a previous study by Witherell *et al.* [10], who proposed an ontology-based characterization of AM models, following their physical domains and the input-output relationships

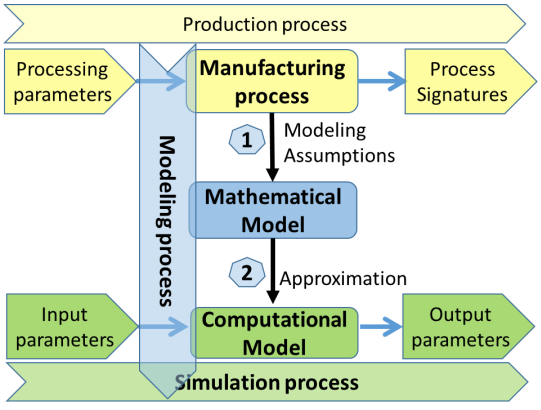

FIGURE 1: The modeling process connecting the worlds of production and simulation processes.

included in their development. We go beyond that classification by incorporating information on modeling assumptions and approximations, to be used as qualitative indicators of model fidelity in laser powder bed fusion (L-PBF) models. Specifically, the ontology provides a formal explicit representation of:

(a) modeling characteristics and their influence in model predictions,
(b) sets of axioms and mathematical rules that define and relate such modeling characteristics.

Qualitative knowledge on model fidelity can be extracted and shared to support informed assessment of L-PBF models.

The remainder of the paper is organized as follows. Section 2 presents the background for structuring and representing information in computational models, and gives insight into the approach proposed for model characterization and representation. Section 3 discusses details of the proposed conceptualization and characterization of L-PBF models. Section 4 presents the main elements of the resulting ontological framework, and discusses the support it provides in the identification and exchange of qualitative indicators of model fidelity. Finally, Section 5 presents some conclusive remarks, including the description of future work with focus on 1) the extension and validation of the proposed framework and 2) quantitative assessment of the influence of the identified modeling characteristics in model fidelity.

2 BACKGROUND

Some approaches have been proposed previously for the study of the information incorporated in computational models [11–13]. For instance, Bryden and Noble [11] discussed the requirements for the description of models and proposed a framework to describe the process of scientific modeling, which is similar to the one illustrated in Figure 1. Alternatively, Bedau [13] discussed the notion of "unrealistic" models and provided practical means to quantify potential discrepancies between models and the real world. Along similar lines, Di Paolo *et al.* [12] discussed 1) the need for a proper understanding of the internal operations of computational models and proposed 2) a methodology to reconcile potential discrepancies between computational models and experiments. Such a methodology would allow the modeler to determine where differences between models and the real world lie, and to assess the usefulness of such models.

The work of Di Paolo *et al.* suggests that a clear understanding of the internal operations of computational models could potentially help quantify levels of fidelity. As a result, methods that support clear and explicit representations of the internal operations of models are increasingly sought after as a means to determine the influence of those operations on model inadequacy. Such an explicit representation could be used to return qualitative indicators of the degree of model fidelity. Those indicators could be stored for future use in a knowledge-based system.

Assouroko, Ibrahim; Lopez, Felipe; Witherell, Paul.
"A method for characterizing model fidelity in laser powder bed fusion additive manufacturing."
Paper presented at ASME 2016 International Mechanical Engineering Congress & Exposition ASME IMECE 2016,
Phoenix, AZ. November 11, 2016 - November 17, 2016.
SP-357

Knowledge-based systems have been proposed in various domains to support design and analysis in engineering [14, 15]. Other types of knowledge-based frameworks have been proposed to represent physical systems at various levels of abstraction [16, 17]. Similar knowledge-based frameworks have been proposed across other engineering domains [18–21]. Ontologies provide popular foundation for creating many of these knowledge-based systems. Ontologies have been used to provide definitions of formal methods in modeling, while also addressing aspects of model fidelity [22–24]. In this paper we aim to use ontologies to represent the variety of information needed while addressing fidelity-related issues in computational models of L-PBF processes.

Fidelity problems in L-PBF models can originate from multiple sources, including certain internal characteristics of the model itself. In this article, we identify and map those sources to specific modeling elements, based on the assumptions and approximations adopted in the modeling process. Certain questions that help with these problems have been identified, and they are:

(a) what are the most appropriate mathematical models to represent a physical phenomenon?;
(b) what set of assumptions would be required to accurately define a given L-PBF model?;
(c) which physical law, initial and/or boundary conditions, material properties, etc. are usually employed in the definition of a given mathematical model?;
(d) which modeling characteristics are most likely to affect the fidelity of a given model in L-PBF?;
(e) how do these fidelity-related characteristics interoperate with other influential modeling elements?.

Answering these questions can help us identify the requirements and scope of L-PBF model abstractions. In creating such abstractions, we plan to use a descriptive ontology to form the basis of a knowledge-based framework. The ontology can be used to 1) browse and represent the sets of model characteristics available for the definition of a given L-PBF model and 2) provide insight into potential qualitative indicators of model fidelity. The framework can help classify the requirements for both model characteristics and model usages.

3 CHARACTERIZING PREDICTIVE CAPABILITIES OF POWDER BED FUSION MODELS

Assessment of the fidelity of an AM model unavoidably depends on the particular case being simulated (i.e., material properties, machine information, and process parameters), the adopted simulation parameters and the predictions of interest. Quantitative evaluation of model fidelity is possible with uncertainty quantification, which measures the individual contribution of various sources of uncertainty and their influence in the overall prediction uncertainty [25]. Without being specific to a particular case, the characteristics of such models can also be used to drive qualitative estimates of fidelity. In other words, knowing what capabilities a model has and lacks allows users to estimate how accurate model predictions may be if the right simulation inputs are provided.

Model characteristics in AM, as defined by assumptions and approximations, are determined during the modeling process (illustrated in Figure 1). Therefore, abstracting some common assumptions and approximations taken when modeling AM processes can help identify some of those characteristics. Examples of model characteristics can be found in the physical domain, physical laws, boundary and initial conditions, and the chosen numerical method, among others.

Model characterization can be performed for various types of models. For different types of models, the characterization methods may be similar, but the underlying physics and model form would differ. The phenomena presented in this paper are limited to irradiation absorption, heat transfer, and consolidation in L-PBF processes. In this section, the physics of each phenomenon and available model types are identified along with common modeling assumptions and approximation. Information on model characteristics is organized in the form of tables to aid visualization and facilitate their definition in the ontology introduced in section 4.

3.1 Irradiation absorption models

Irradiation absorption is related to how voids in a randomly-packed bed allow the laser beam to penetrate and reflect from the surface of powder particles. Computational models of irradiation absorption have been developed to predict the amount and distribution of the heat that is absorbed by the bed. Table 1 shows some common choices, found in the literature, for such models, including their characteristics as identified from assumptions and approximations. As seen in the table, each model depends on a governing physical law, which in turn depends on a combination of the following assumptions made by the modeler:

(a) Whether heat is assumed to penetrate the powder bed and adopt a volumetric distribution in the model or to be constrained on the surface.
(b) If the powder bed is idealized as a continuum or modeled as a distribution of interacting powder particles.

Common combinations of assumptions and the physical law of choice for such cases are presented in Table 1, along with numerical solution methods. For instance, in the simplest case, where absorption is assumed to be restricted to the surface, no mathematical model is required. This scenario can be found in the first line of the table. Other choices for absorption models (i.e., Beer-Lambert model, ray tracing models, or radiation transfer models) are available when absorbed energy is assumed to have a volumetric distribution. The type of distribution assumed for

Assouroko, Ibrahim; Lopez, Felipe; Witherell, Paul.
"A method for characterizing model fidelity in laser powder bed fusion additive manufacturing."
Paper presented at ASME 2016 International Mechanical Engineering Congress & Exposition ASME IMECE 2016,
Phoenix, AZ. November 11, 2016 - November 17, 2016.
SP-358

Dimensionality of absorbed energy	Distribution of material	Surface distribution of heat source	Law of Physics	Mathematical model	Numerical method	Model inputs	Output parameters	Ref.
Surface	Continuum	Gaussian, cylindrical, or point source				Absorptivity and surface irradiation	Surface distribution of absorbed heat	[26–31]
Volumetric	Continuum	Gaussian, cylindrical, or point source	Beer-Lambert law	Beer-Lambert model		Absorptivity, extinction coefficient, surface irradiation	Volumetric distribution of absorbed heat	[32, 33]
Volumetric	Particles	Gaussian	Specular reflection	Ray tracing model	Discrete element method	Surface irradiation, particle size and distribution, dimensions of powder bed, latent heat, absorptivity, and emissivity and reflectivity of particles	Volumetric distribution of absorbed heat	[34–36]
Volumetric	Particles	Gaussian	Radiation transfer	Radiation transfer model	Two-flux method	Surface irradiation, particle size, specular reflectivity, thermal conductivity, and melting temperature	Volumetric distribution of absorbed heat	[37–40]

TABLE 1: Modeling characteristics for irradiation absorption models.

the laser, which strongly influences the quality of the predictions, is shown as another characteristic of irradiation absorption models. Such information can guide experienced users to identify the amount of fidelity to be expected from each case. Additionally, the adoption of a larger set of input parameters increases the flexibility of the model, allowing it to adapt to more cases and increasing the fidelity that might be expected from it.

The fidelity to be expected from irradiation absorption models is strongly dependent on how close the simulation model is to the physical events it is meant to describe. For example, the Beer-Lambert law, which assumes an exponential decay for irradiation intensity as a function of depth, imposes a constraint on the simulation model that reduces fidelity. In the ray-tracing models, on the other hand, laser rays are assumed to bounce from powder surfaces based on the size and distribution of the powders. This bouncing seems to capture reality very well. As a result, a ray-tracing model, which does include laser-particle interactions, provides higher fidelity predictions than a Beer-Lambert model. Similar fidelity issues appear with simulation inputs that are accounted for or neglected (more inputs increase flexibility of the model and potentially improve its fidelity), the choice of numerical model, and other model characteristics.

3.2 Heat transfer models

Heat absorbed from the laser is dissipated through the powder bed, heating and consolidating the powder. Heat-transfer models attempt to predict 1) the distribution of the solid, liquid and mushy zones in the powder bed as well as 2) the temperature distribution in each zone. Given the complexity of the heat transfer phenomenon, which includes a large set of model characteristics, the modeler has to go through a series of modeling choices and simplification steps to fully determine whether thermal models are ready for simulation. The characteristics identified on models in the literature, as imposed by their underlying assumptions and approximations, are presented in Table 2.

At the macroscale level, all models are based on two laws: Fourier's law and conservation-of-energy law. The resulting mathematical model takes the form of a transport, partial-differential equation (PDE) for a chosen combination of transport property (thermal diffusivity or thermal conductivity) and a state variable (temperature or enthalpy). There is little difference in the fidelities of any of these combinations; but, it is still important for the user to know which combination has been adopted to determine the type of heat equation to be solved. For simplicity, the PDE is shown here for temperature as the state variable and thermal conductivity as the transport property[1]

$$\rho c_p \left(\underbrace{\frac{\partial T}{\partial t}}_{\text{time}} + \underbrace{\vec{v}\cdot\nabla T}_{\text{advection}} \right) = \underbrace{\nabla\cdot(k\nabla T)}_{\text{diffusion}} + \underbrace{f(x,y,z)}_{\text{source}}, \qquad (1)$$

where powder density is denoted by ρ, specific heat is c_p, thermal conductivity is k, volumetric heat generation is f, and $\vec{v}$ is the velocity in the fluid phase. In this equation, the advection term is often ignored if fluid flow is neglected[2]. It should also be noted that absorbed heat, as computed with the irradiation absorption model, can be accounted for either as a source or as a boundary condition (if assumed as a surface source).

[1] The structure of the heat transfer equation for other choices of state variable and transport property is similar. For a detailed discussion, refer to the classical book of Carslaw and Jaeger [45].

[2] The scope of this paper includes only models with no fluid flow.

Assouroko, Ibrahim; Lopez, Felipe; Witherell, Paul.
"A method for characterizing model fidelity in laser powder bed fusion additive manufacturing."
Paper presented at ASME 2016 International Mechanical Engineering Congress & Exposition ASME IMECE 2016,
Phoenix, AZ. November 11, 2016 - November 17, 2016.

Law of Physics	Transport property	State variable	Reference frame	Dimensionality of absorbed heat	Inclusion of absorbed heat	Phase change	Mathematical model
Conservation of energy and Fourier's law	Thermal conductivity	Temperature	Moving or fixed	Surface or volumetric	Source term	Implicit (included in specific heat) or explicit	Transport equation for temperature
Conservation of energy and Fourier's law	Thermal conductivity	Temperature	Moving or fixed	Surface or volumetric	Source term	Implicit (included in specific heat) or explicit	Transport equation for temperature
Conservation of energy and Fourier's law	Thermal conductivity	Enthalpy	Moving or fixed	Surface or volumetric	Source term	Implicit (included in specific heat) or explicit	Transport equation for enthalpy
Conservation of energy and Fourier's law	Thermal conductivity	Enthalpy	Moving or fixed	Surface or volumetric	Source term	Implicit (included in specific heat) or explicit	Transport equation for enthalpy
Conservation of energy and Fourier's law	Thermal diffusivity	Temperature	Moving or fixed	Surface or volumetric	Boundary condition	Implicit (included in specific heat) or explicit	Rosenthal-type equation

Model inputs	Boundary conditions	Initial conditions	Distribution of material	Numerical method	Prediction	Ref.
Powder density, specific heat, fluid velocity, absorbed heat	Semi-infinite, adiabatic, isothermal, or mixed	Initial distribution of temperature	Continuum	Finite element method, finite difference method	Time-history of temperature	[41]
Powder density, specific heat, fluid velocity, absorbed heat	Semi-infinite, adiabatic, isothermal, or mixed	Initial distribution of temperature	Particles	Discrete element method, Lattice Boltzmann method	Time-history of temperature	
Powder density, specific heat, fluid velocity, absorbed heat	Semi-infinite, adiabatic, isothermal, or mixed	Initial distribution of enthalpy	Continuum	Finite element method, finite difference method	Time-history of enthalpy	[27,28, 30,42]
Powder density, specific heat, fluid velocity, absorbed heat	Semi-infinite, adiabatic, isothermal, or mixed	Initial distribution of enthalpy	Particles	Discrete element method, Lattice Boltzmann method	Time-history of enthalpy	[43,44]
Powder density, specific heat, fluid velocity, absorbed heat	Semi-infinite	Initial distribution of temperature	Continuum	Analytical	Time-history of temperature	[31]

TABLE 2: Modeling characteristics for heat transfer models.

The terms included in the heat transfer equation can be used as indicators of the predictions that may be obtained from solving the model. For instance, transient thermal predictions (i.e., thermal history) may only be obtained if the time derivative is included in the equation. Additionally, the effect of melt pool dynamics in the thermal history can only be accounted for if the advection term is present in the heat transfer equation and it takes velocity predictions from a fluid mechanics model. The lack of any of these terms compromises the fidelity of the thermal predictions obtained from the model.

The mathematical problem is completed with adequate choices of models for phase change, and a set of boundary conditions. In the case of transient simulations, initial conditions are usually required as the starting point. Phase transformations may be ignored, modeled explicitly with a Stefan condition, or included in the form of a temperature-dependent specific heat. Most models use as boundary conditions a mix of convection, radiation and surface distribution of heat atop the powder bed; adiabatic boundary conditions on the side while the bottom is often semi-infinite, adiabatic, or in contact with a substrate.

If one assumes constant thermo-physical properties, neglects phase changes, and uses a reference frame attached to the heat source, a special type of thermal model can be created. This model is special because an analytical solution can be obtained for the temperature distribution as a function of thermal diffusivity [31]. Although simplistic, Rosenthal-type models provide 1) starting points in the development of more sophisticated models and 2) quick predictions of temperature and melt-pool geometry.

In general, simpler models, such as Rosenthal models, typically return predictions with less fidelity than more elaborate models such as lattice Boltzmann models and discrete-element models. Additionally, the adoption of a continuum to represent a bed of particles is expected to compromise the fidelity of the predictions making them similar to those reported in irradiation absorption models. Finally, the choice of boundary conditions is one of the most important characteristics that guide the user in

Assouroko, Ibrahim; Lopez, Felipe; Witherell, Paul.
"A method for characterizing model fidelity in laser powder bed fusion additive manufacturing."
Paper presented at ASME 2016 International Mechanical Engineering Congress & Exposition ASME IMECE 2016,
Phoenix, AZ. November 11, 2016 - November 17, 2016.

Material	Law of Physics	Consolidation mechanism	State variable	Mathematical model	Initial condition	Model inputs	Prediction	Ref.
Amorphous or crystalline	Atomic diffusion in crystal vacancies	Solid state sintering	Volume	Frenkel	Initial volume	Surface tension, diffusion coefficient, temperature, Boltzmann's constant, crystal lattice constant	Volume	[46]
Amorphous	Newtonian flow	Solid state sintering	Density or porosity	Mackenzie and Shutthelworth	Initial powder density	Surface tension, number of pores per unit volume, material viscosity	Density or porosity distribution	[47]
Crystalline	Non-Newtonian flow	Solid state sintering	Density or porosity	Mackenzie and Shutthelworth	Initial powder density	Surface tension, number of pores per unit volume, material viscosity, tuning parameter	Density or porosity distribution	[47]
Crystalline	Temperature-activated reaction	Solid state sintering	Density	Arrhenius-type equation	Initial powder density	Characteristic frequency, sintering activation energy, ideal gas constant, temperature, tuning coefficients	Density distribution	[48]
Crystalline or semi-crystalline	Temperature-dependent density	Melting	Density or porosity			Temperature, melting temperature	Temperature-dependent powder density	[27]

TABLE 3: Modeling characteristics for consolidation models.

the level of fidelity to be expected from heat transfer models. The incorporation of more accurate boundary conditions is expected to greatly improve the fidelity of a model.

3.3 Consolidation models

Thermally-activated consolidation is responsible for transforming selected regions of powdered material into fully-dense parts. Consolidation is of crucial importance in AM because most mechanical properties (e.g., tensile strength) have been found to decrease drastically whenever the porosity increases. In PBF processes, consolidation may occur by 1) solid state sintering, controlled by viscous diffusion; 2) partial melting, where part of the powder is melted while the rest remains solid; and 3) full melting, characterized by the rapid melting of all the heated powder into fully-dense material [49]. The physics of these mechanisms are substantially different and depend on the choice of material to be processed meaning that not all materials can be sintered or melted.

Table 3 provides information on the characteristics and modeling choices available for the definition of a consolidation model, which differ depending on whether the material is crystalline (ceramics, metal alloys, hard metals) or amorphous (amorphous and semi-crystalline thermoplastics).

In the case of sintering, a model is required to describe the variation in density as a function of temperature and time. A mathematical model, in this case, must be based on only one of these four physics principles: atomic diffusion in crystalline vacancies for Frenkels model [46], Newtonian or non-Newtonian flow for Mackenzie and Sutthelworths model [47], temperature-activated reaction for an Arrhenius-type equation [48]. Melting, on the other hand, is much faster and it is often assumed that density varies instantaneously when reaching melting conditions, thus not requiring any specific mathematical model.

For sintering, consolidation models are often governed by ordinary differential equations. For melting, consolidation models are governed by temperature-dependent properties. Both have simpler mathematical forms than heat transfer models. The definition of well-defined consolidation models requires only initial conditions (initial density), and coupling to thermal models that determine the numerical approach used to solve the system (numerical method, grid, solver, etc.).

The choices available in consolidation models are not driven by their expected fidelity. Rather, they are driven by the physical laws that govern the consolidation mechanism. Consequently, an incorrect choice of physical law could compromise the fidelity of the predictive model significantly. For example, using the physical laws governing solid state sintering when developing a model of the process used to fully melt metallic powder.

Tables 1 to 3, show that the prediction outputs of some models can be used as inputs to other models. As a result, more elaborate predictions can be built up from 1) the predictions obtained from simpler models and 2) a set of relationships that capture their inter-operation. For example, consolidation models determine density, which is an input in thermal models, which in turn determine temperature, which drives consolidation. Such rules are included in the ontology, to guide users along the modeling process and provide explicit knowledge about how model characteristics influence predictions that could be returned by models of other types.

Assouroko, Ibrahim; Lopez, Felipe; Witherell, Paul.
"A method for characterizing model fidelity in laser powder bed fusion additive manufacturing."
Paper presented at ASME 2016 International Mechanical Engineering Congress & Exposition ASME IMECE 2016,
Phoenix, AZ. November 11, 2016 - November 17, 2016.

4 AN ONTOLOGY TO LEVERAGE THE CHARACTERIZATION

We turn to OWL 2 Web Ontology Language [50] to formalize our proposed characteristics into an ontology and its associated knowledge-based framework that provides more means for reusability. The ontology was implemented using Protégé [51], a Java-based ontology development software tool developed by Stanford University. The ontological concepts described in this paper extend those discussed in [10]. Here we extend the categorical representation of those concepts by adding specific attributes to support the characterization of model fidelity. This enhanced ontology provides an explicit description of all the new concepts and their relationships. It connects the physics with the corresponding modeling concepts. In addition, the ontology should capture knowledge about the assumptions used in creating mathematical models, in choosing their input parameters, and in finding the solutions. The information in this ontology can be used to extract and navigate explicit knowledge about the specific characteristics affecting the fidelity of a given L-PBF process model. This knowledge then could serve as indicators to enhance the user's ability to 1) estimate the expected level of fidelity, and 2) make informed decision about the models reusability.

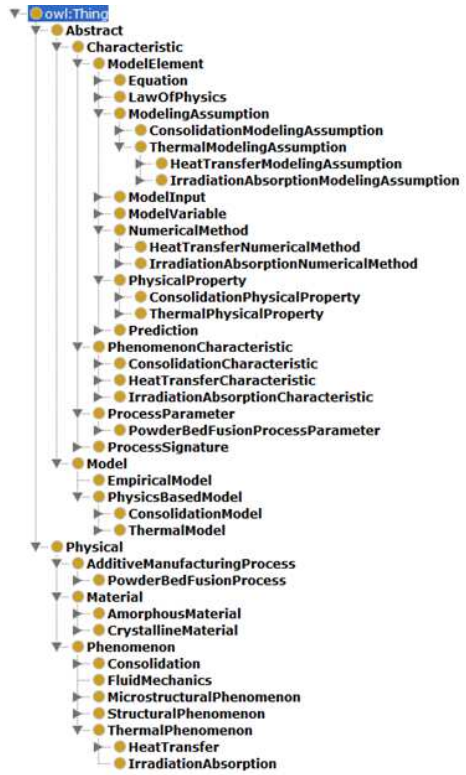

FIGURE 2: Taxonomy of top level entities in the AM ontology.

4.1 Hierarchy of the ontology

Figure 2 illustrates the hierarchical structure of most important high level entities in the AM ontology. This ontology is structured as two main AM concepts:

(a) the **Physical** concept that includes everything that has a position in the space-time domain and;
(b) the **Abstract** concept that includes everything else.

In essence, the separation between real and simulated is made at the highest level at the ontology.

Under **Physical**, we have the concepts of **AdditiveManufacturingProcess**, **Phenomenon**[3] and **Material**. **Phenomenon** is understood as an observable event, including input and output flows of matter and energy, which cannot be divided in smaller phenomena. **Material** briefly covers the different types of material families used in AM. **AdditiveManufacturingProcess** and **Phenomenon** are described as two different **Physical** entities; but, they are not completely disjoint, since a phenomenon (or a set of phenomena) can only occur during the course of a process.

Abstract entities are organized into two main concepts: **Model** and **Characteristic**. The notion of **Characteristic** is central to this ontology. There are two kinds of characteristics. The first are modeling characteristics, as defined in Section 3. The second are physical characteristics, which have a number of sources including machine vendors, material vendors, process engineers, and the dynamics of the process itself. Details of the modeling characteristics are presented in Tables 1 to 3.

The concept of **Model** is understood as a mathematical object that has the ability to represent a system or one of its components and to predict behavior of either. The mathematical object is valid for a set of defined conditions and simplified assumptions [52], which are likely to affect the fidelity of the model. A **Model** can be physics-based, empirical, or hybrid. In this paper, we focus only on physics-based models. A **PhysicsBasedModel** is referred to as a mathematical (or computational) model that describes some physical phenomenon based on first-principles and physical laws. Examples of physics-based model are:

(a) **HeatTransferModel** based on Fourier's law and energy conservation law, as characterized in Table 2;
(b) **IrradiationAbsorptionModel** based on, either Beer-Lambert law, radiation transfer law or physical reflection law, as provided by Table 1 and;
(c) **ConsolidationBySinteringModel** describing a Newtonian or non-Newtonian flow, or a temperature-activated reaction for a given material, under a certain processing conditions, as described in Table 3.

The concept of **Characteristic** subsumes four different types of abstract entities: **ModelElement**, **PhenomenonChar-**

[3] Although often similar to a phenomenon, in this article, the term "process" is reserved only for manufacturing processes and does not include the occurring phenomena pertaining to those processes.

Assouroko, Ibrahim; Lopez, Felipe; Witherell, Paul.
"A method for characterizing model fidelity in laser powder bed fusion additive manufacturing."
Paper presented at ASME 2016 International Mechanical Engineering Congress & Exposition ASME IMECE 2016,
Phoenix, AZ. November 11, 2016 - November 17, 2016.

acteristic, **ProcessParameter**, and **ProcessSignature**. **ModelElement** as proposed in the actual study, includes **ModelingAssumption**, **Equation**, **PhysicalProperty**, **ModelInput**, **ModelVariable**, **NumericalMethod** and **Prediction**. These entities are used, along with the modeling process, illustrated in Figure 1, to characterize a physics-based model. They can be assigned and coupled based on the step(s) in which they appear. These entities are important because they can impact model fidelity negatively. Such negative impacts result from the discrepancies introduced along the transition from a physical phenomenon to the mathematical model that represents it. These discrepancies can impact predictions obtained from solving the model.

A first level of discrepancy might involve an incorrect **ModelingAssumption**. For example, an incorrect physical law might be chosen to capture a simplification of a physical system, and the resulting predictions will be farther from what is believed to happen in reality. Another type of discrepancy can occur if the appropriate set of **Equation** entities are not chosen to describe a mathematical model. In this case, the predictions from the associated computational models will have less fidelity. Fidelity can also be lost or improved depending on whether the right set of **PhysicalProperty** and/or **ModelInput** entities are assigned for the simulation of a computational model.

In assessing fidelity-related issues, the preceding fidelity indicators are not enough. Consequently, the ontology should provide explicit, descriptive knowledge of these indicators sufficient to do a quantitative assessment of the predictive capabilities of the model in which they appear. This knowledge is provided in two forms, which are: knowledge about the defined AM modeling concepts and knowledge about the relationships among those concepts. These relationships are discussed in the following sections.

4.2 Taxonomy of relationships in the ontology

Relationships in the ontology have been created to define interconnections between any physical, abstract entity and its parent and child. Physical concepts, such as **Phenomenon**, interrelate with abstract concepts, e.g., **PhenomenonCharacteristic** through the role *hasCharacteristic*, and physics-based models interrelate the phenomenon(a) they describe through the role *represent*. The *partOf* relationship has been defined to accommodate the fact that two different concepts can exist at the same level of hierarchy with one still being part of the other, instead of defining a parent-child relationship between them. Example of this specificity in the current ontology is between **AdditiveManufacturingProcess** and **Phenomenon** where a phenomenon is not a subclass of an AM process but can only occur within the course of that process. The concept of **Characteristic** is defined along with the role *influences* (as inverse of *influencedBy*) that can exist between a characteristic, e.g. **HeatDissipationCharacteristic**, and one or several physical concepts, e.g., **Consolidation** and **FluidMechanics**. Some **ModelElement** concepts are semantically related to other abstract concepts they characterize (or are characterized by) through several relationships such as *definedBy*, *requires* and related sub-properties (*requiresAssumption*, *requiresInput*, *requiresApproximation*), *provides*, etc.

Illustrations of such interconnections are shown on Figure 3 to Figure 5, where several object properties are used to interrelate the different concepts playing roles in the characterization of irradiation absorption model, heat transfer for temperature model, and consolidation model.

4.3 Semantic queries allowed by the ontology

Ontologies support different levels of queries using query language such as SPARQL [53], and query tools such as SPARQL Query and DL Query tabs in Protégé [51]. At a first level are simple queries that can provide answers to a range of competency questions. Two examples of such queries (using DL Query tab) are given below:

(a) In the first example related to sintering model, the ontology is queried for the current equation used to predict density variations for crystalline materials in AM. The query returns ArrheniusTypeDensityVariation and CrystallineDensityVariation equations, which are the appropriate choices for that question.

(b) In the second example, one may be interested in knowing 1) which modeling parameter is influenced by variations in specific heat and 2) which phenomena this parameter influences the most. The query returns thermal diffusivity as the parameter; and heat transfer, consolidation and fluid mechanics as the phenomena.

More complex queries can be executed, as well. Typically, such queries attempt to retrieve information on the specific characteristics that determine and influence the quality of the predictions provided by a physics-based model, and their interconnections throughout the modeling transition, described in Figure 1. Figure 6 shows the possible transitions for the modeling and computation of a distribution of absorbed heat. These transitions result from the combination of complex sets of DL-queries on indicators and influencing characteristics including the nature of the heat source and the distribution of material, among others. Using this modeling transition graph, users can then retrieve additional knowledge about other specific concepts likely to affect the fidelity of the absorption model.

5 CONCLUSIVE REMARKS

Computational models in AM often face reusability challenges, partially driven by the limited understanding of a model's fidelity and the lack of knowledge that users have on the com-

Assouroko, Ibrahim; Lopez, Felipe; Witherell, Paul.
"A method for characterizing model fidelity in laser powder bed fusion additive manufacturing."
Paper presented at ASME 2016 International Mechanical Engineering Congress & Exposition ASME IMECE 2016,
Phoenix, AZ. November 11, 2016 - November 17, 2016.
SP-363

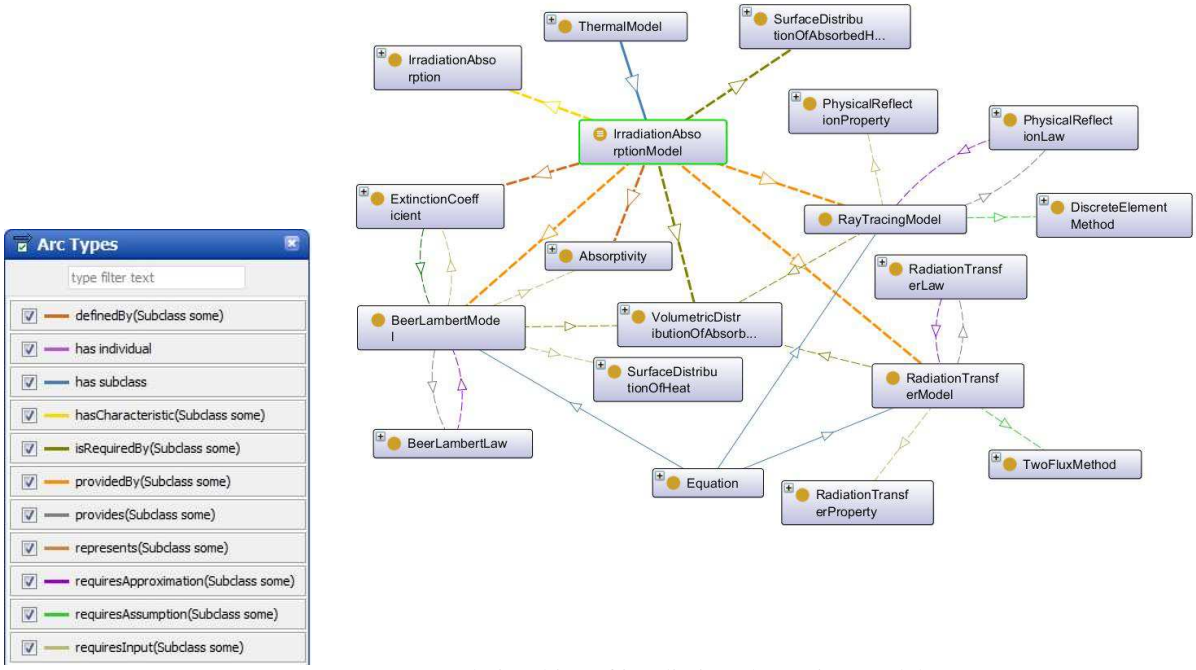

FIGURE 3: Relationships of irradiation absorption model.

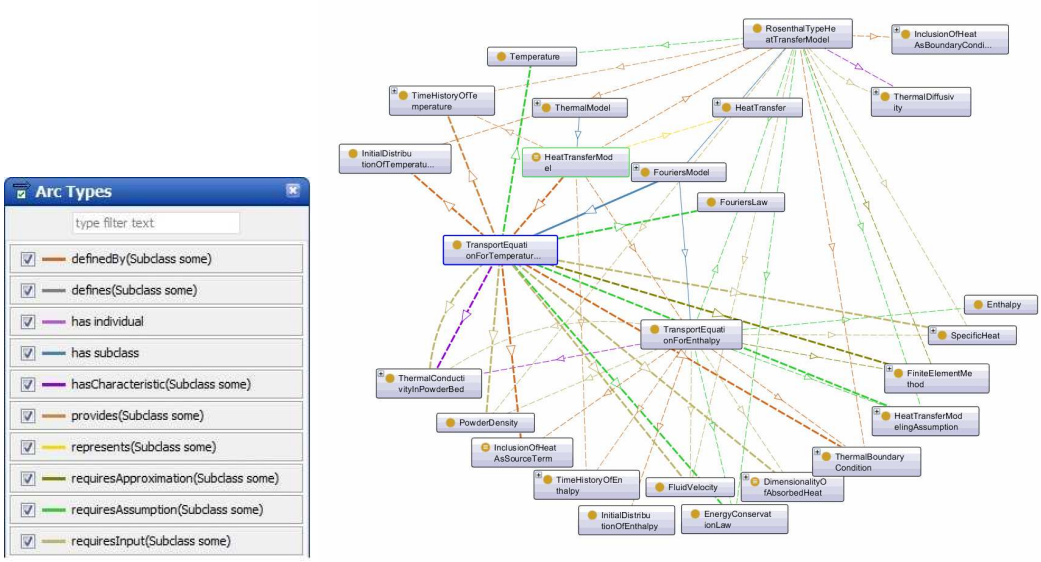

FIGURE 4: Relationships of heat transfer model.

petences and performance of the models. To better understand the unique characteristics that determine predictive capabilities of the models, a closer look has been given to the abstractions formed between physical processes and corresponding computational models.

This study sought a better understanding of the limitations in the predictive capabilities of physics-based models in AM. Our approach to achieve that understanding was based on explicit characterizations of the assumptions and approximations used to develop the corresponding computational models. We expressed these characterizations as sets of formal concepts in an ontology. The ontology provides the information needed to answer a wide

Assouroko, Ibrahim; Lopez, Felipe; Witherell, Paul.
"A method for characterizing model fidelity in laser powder bed fusion additive manufacturing."
Paper presented at ASME 2016 International Mechanical Engineering Congress & Exposition ASME IMECE 2016,
Phoenix, AZ. November 11, 2016 - November 17, 2016.

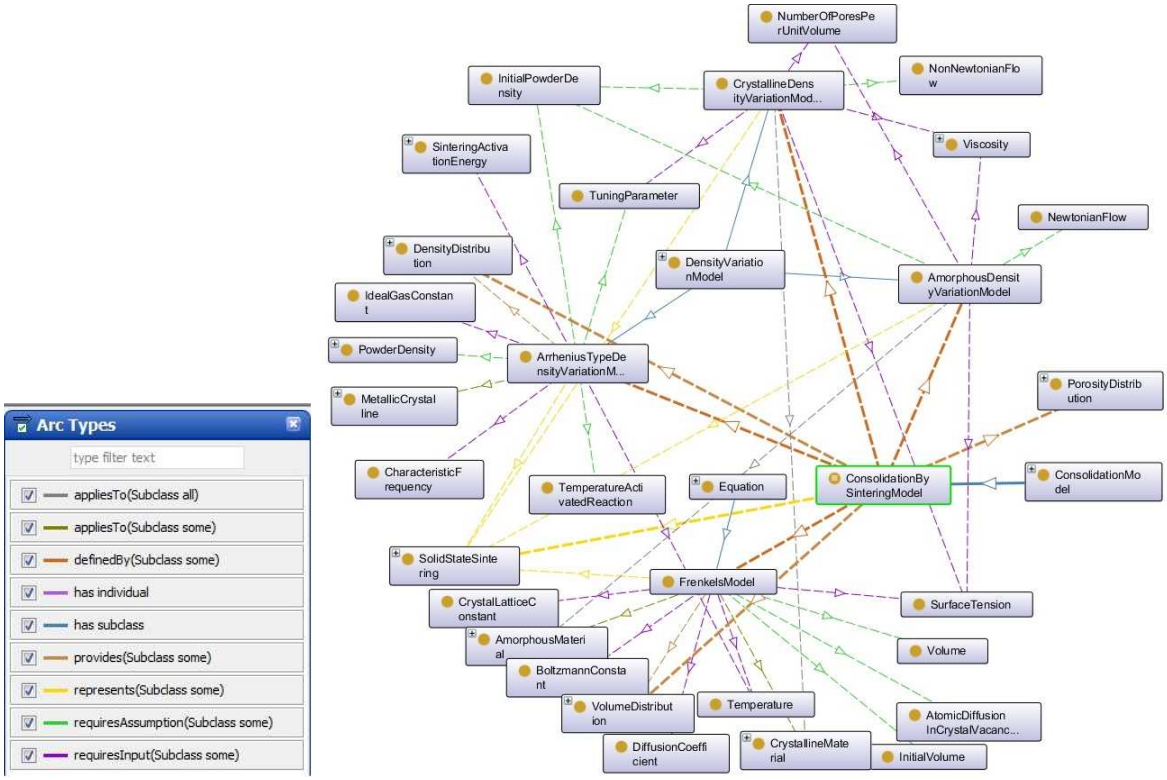

FIGURE 5: Relationships of consolidation model.

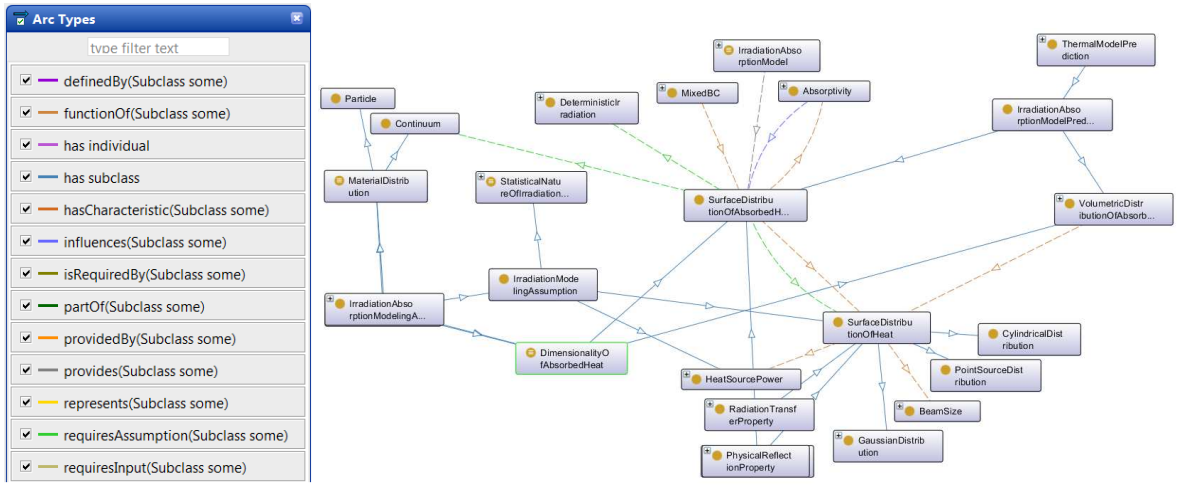

FIGURE 6: Modeling transition for absorbed heat.

range of competency-related and fidelity-related queries. Those queries are currently based on thermal and consolidation models only.

We intend to expand the ontology to address the impacts of assumptions and approximations on the predictive capabilities of fluid mechanics models, structural models, and microstructural models. Another ongoing work at NIST focuses on the origin and propagation of uncertainty sources in additive manufacturing models [25] and is expected to be incorporated into this work in future implementations.

SUPPLEMENTAL MATERIAL

The ontology described in this paper can be accessed at https://github.com/usnistgov/AMontology

Assouroko, Ibrahim; Lopez, Felipe; Witherell, Paul.
"A method for characterizing model fidelity in laser powder bed fusion additive manufacturing."
Paper presented at ASME 2016 International Mechanical Engineering Congress & Exposition ASME IMECE 2016,
Phoenix, AZ. November 11, 2016 - November 17, 2016.

DISCLAIMER

The full descriptions of the procedures used in this paper may require the identification of certain commercial products. The inclusion of such information should in no way be construed as indicating that such products are endorsed by NIST or are recommended by NIST or that they are necessarily the best materials, instruments, software or suppliers for described purposes.

ACKNOWLEDGMENT

The authors gratefully acknowledge the comments and suggestions provided by Peter Denno, from the National Institute of Standards and Technology, in the development of the ontology.

REFERENCES

[1] ASTM, 2012. F2792, Standard Terminology for Additive Manufacturing Technologies.

[2] Petrovic, V., Vicente Haro Gonzalez, J., Jorda Ferrando, O., Delgado Gordillo, J., Ramon Blasco Puchades, J., and Portoles Grinan, L., 2011. "Additive layered manufacturing: sectors of industrial application shown through case studies". *International Journal of Production Research,* ***49***(4), pp. 1061–1079.

[3] Beaman, J., and Lopez, F., 2014. "Emerging nexus of cyber, modeling, and estimation in advanced manufacturing: Vacuum arc remelting to 3D printing". *Mechanical Engineering,* ***136***(12), p. S8.

[4] Bourell, D. L., Leu, M. C., and Rosen, D. W., 2009. "Roadmap for additive manufacturing: identifying the future of freeform processing". *The University of Texas at Austin, Austin, TX*.

[5] Patil, N., Pal, D., Rafi, H. K., Zeng, K., Moreland, A., Hicks, A., Beeler, D., and Stucker, B., 2015. "A generalized feed forward dynamic adaptive mesh refinement and derefinement finite element framework for metal laser sinteringpart I: Formulation and algorithm development". *Journal of Manufacturing Science and Engineering,* ***137***(4), p. 041001.

[6] Pal, D., Patil, N., Kutty, K. H., Zeng, K., Moreland, A., Hicks, A., Beeler, D., and Stucker, B., 2016. "A generalized feed-forward dynamic adaptive mesh refinement and derefinement finite-element framework for metal laser sinteringpart II: Nonlinear thermal simulations and validations". *Journal of Manufacturing Science and Engineering,* ***138***(6), p. 061003.

[7] Khairallah, S. A., Anderson, A. T., Rubenchik, A., and King, W. E., 2016. "Laser powder-bed fusion additive manufacturing: physics of complex melt flow and formation mechanisms of pores, spatter, and denudation zones". *Acta Materialia,* ***108***, pp. 36–45.

[8] Kamath, C., 2016. "Data mining and statistical inference in selective laser melting". *The International Journal of Advanced Manufacturing Technology*, pp. 1–19.

[9] Yang, Z., Eddy, D., Krishnamurty, S., Grosse, I., Denno, P., and Lopez, F., 2016. "Investigating predictive metamodeling for additive manufacturing". In Proceedings of the ASME 2016 International Design Engineering Technical Conferences & Computers and Information in Engineering Conference.

[10] Witherell, P., Feng, S., Simpson, T. W., Saint John, D. B., Michaleris, P., Liu, Z.-K., Chen, L.-Q., and Martukanitz, R., 2014. "Toward metamodels for composable and reusable additive manufacturing process models". *Journal of Manufacturing Science and Engineering,* ***136***(6), p. 061025.

[11] Bryden, J., and Noble, J., 2006. *Computational modelling, explicit mathematical treatments, and scientific explanation*. MIT Press.

[12] Di Paolo, E. A., Noble, J., and Bullock, S., 2000. "Simulation models as opaque thought experiments". In Artificial Life VII: The Seventh International Conference on the Simulation and Synthesis of Living Systems, pp. 497–506.

[13] Bedau, M. A., 1999. "Can unrealistic computer models illuminate theoretical biology". In Proceedings of the 1999 Genetic and Evolutionary Computation Conference Workshop Program, pp. 20–23.

[14] Shephard, M. S., Baehmann, P. L., Georges, M. K., and Korngold, E. V., 1990. "Framework for the reliable generation and control of analysis idealizations". *Computer Methods in Applied Mechanics and Engineering,* ***82***(1-3), pp. 257–280.

[15] Turkiyyah, G. M., and Fenves, S. J., 1996. "Knowledge-based assistance for finite-element modeling". *IEEE Intelligent Systems*(3), pp. 23–32.

[16] Sheehy, M., and Grosse, I., 1997. "An object-oriented blackboard-based approach for automated finite element modeling and analysis of multichip modules". *Engineering with computers,* ***13***(4), pp. 197–210.

[17] Holzhauer, D., and Grosse, I., 1999. "Finite element analysis using component decomposition and knowledge-based control". *Engineering with Computers,* ***15***(4), pp. 315–325.

[18] Shen, W., and Norrie, D. H., 1999. "Agent-based systems for intelligent manufacturing: a state-of-the-art survey". *Knowledge and information systems,* ***1***(2), pp. 129–156.

[19] Szykman, S., Sriram, R. D., and Regli, W. C., 2001. "The role of knowledge in next-generation product development systems". *Journal of Computing and Information Science in Engineering,* ***1***(1), pp. 3–11.

[20] Navigli, R., and Velardi, P., 2005. "Structural semantic interconnections: a knowledge-based approach to word sense

Assouroko, Ibrahim; Lopez, Felipe; Witherell, Paul.
"A method for characterizing model fidelity in laser powder bed fusion additive manufacturing."
Paper presented at ASME 2016 International Mechanical Engineering Congress & Exposition ASME IMECE 2016,
Phoenix, AZ. November 11, 2016 - November 17, 2016.

disambiguation". *Pattern Analysis and Machine Intelligence, IEEE Transactions on,* ***27***(7), pp. 1075–1086.

[21] Szykman, S., Sriram, R. D., Bochenek, C., Racz, J. W., and Senfaute, J., 2000. "Design repositories: engineering design's new knowledge base". *IEEE Intelligent Systems*(3), pp. 48–55.

[22] Witherell, P., Krishnamurty, S., and Grosse, I. R., 2007. "Ontologies for supporting engineering design optimization". *Journal of Computing and Information Science in Engineering,* ***7***(2), pp. 141–150.

[23] Grosse, I. R., Milton-benoit, J. M., and Wileden, J. C., 2005. "Ontologies for supporting engineering analysis models". *AIE EDAM,* ***19***(01), pp. 1–18.

[24] Assouroko, I., Ducellier, G., Boutinaud, P., and Eynard, B., 2014. "Knowledge management and reuse in collaborative product development – A semantic relationship management-based approach". *International Journal of Product Lifecycle Management,* ***7***(1), pp. 54–74.

[25] Lopez, F., Witherell, P., and Lane, B., 2016. "Identifying uncertainty in laser powder bed fusion models". In Proceedings of the ASME 2016 Manufacturing Science and Engineering Conference.

[26] Zeng, K., Pal, D., and Stucker, B., 2012. "A review of thermal analysis methods in laser sintering and selective laser melting". In Proceedings of Solid Freeform Fabrication Symposium Austin, TX.

[27] Roberts, I., Wang, C., Esterlein, R., Stanford, M., and Mynors, D., 2009. "A three-dimensional finite element analysis of the temperature field during laser melting of metal powders in additive layer manufacturing". *International Journal of Machine Tools and Manufacture,* ***49***(12), pp. 916–923.

[28] Tolochko, N. K., Arshinov, M. K., Gusarov, A. V., Titov, V. I., Laoui, T., and Froyen, L., 2003. "Mechanisms of selective laser sintering and heat transfer in Ti powder". *Rapid Prototyping Journal,* ***9***(5), pp. 314–326.

[29] Dong, L., Makradi, A., Ahzi, S., and Remond, Y., 2009. "Three-dimensional transient finite element analysis of the selective laser sintering process". *Journal of Materials Processing Technology,* ***209***(2), pp. 700–706.

[30] Hussein, A., Hao, L., Yan, C., and Everson, R., 2013. "Finite element simulation of the temperature and stress fields in single layers built without-support in selective laser melting". *Materials & Design,* ***52***, pp. 638–647.

[31] Rosenthal, D., 1946. "The theory of moving sources of heat and its application to metal treatments". *Transactions of the ASME,* ***68***, pp. 849–866.

[32] Sun, M.-S. M., and Beaman, J. J., 1991. "A three dimensional model for selective laser sintering". In Proceedings of Solid Freeform Fabrication Symposium, Vol. 2, pp. 102–109.

[33] Moser, D., Fish, S., Beaman, J., and Murthy, J., 2014. "Multi-layer computational modeling of selective laser sintering processes". In ASME 2014 International Mechanical Engineering Congress and Exposition, American Society of Mechanical Engineers, pp. V02AT02A008–V02AT02A008.

[34] Moser, D., Pannala, S., and Murthy, J., 2015. "Computation of effective radiative properties of powders for selective laser sintering simulations". *JOM,* ***67***(5), pp. 1194–1202.

[35] Devesse, W., De Baere, D., and Guillaume, P., 2015. "Modeling of laser beam and powder flow interaction in laser cladding using ray-tracing". *Journal of Laser Applications,* ***27***(S2), p. S29208.

[36] Wang, X., and Kruth, J.-P., 2000. "A simulation model for direct selective laser sintering of metal powders". In International Conference on Engineering Computational Technology, pp. 57–71.

[37] Gusarov, A., and Kruth, J.-P., 2005. "Modelling of radiation transfer in metallic powders at laser treatment". *International Journal of Heat and Mass Transfer,* ***48***(16), pp. 3423–3434.

[38] Verhaeghe, F., Craeghs, T., Heulens, J., and Pandelaers, L., 2009. "A pragmatic model for selective laser melting with evaporation". *Acta Materialia,* ***57***(20), pp. 6006–6012.

[39] Hodge, N., Ferencz, R., and Solberg, J., 2014. "Implementation of a thermomechanical model for the simulation of selective laser melting". *Computational Mechanics,* ***54***(1), pp. 33–51.

[40] Khairallah, S. A., and Anderson, A., 2014. "Mesoscopic simulation model of selective laser melting of stainless steel powder". *Journal of Materials Processing Technology,* ***214***(11), pp. 2627–2636.

[41] Bugeda, G., Cervera, M., and Lombera, G., 1999. "Numerical prediction of temperature and density distributions in selective laser sintering processes". *Rapid Prototyping Journal,* ***5***(1), pp. 21–26.

[42] Kolossov, S., Boillat, E., Glardon, R., Fischer, P., and Locher, M., 2004. "3D FE simulation for temperature evolution in the selective laser sintering process". *International Journal of Machine Tools and Manufacture,* ***44***(2), pp. 117–123.

[43] Körner, C., Attar, E., and Heinl, P., 2011. "Mesoscopic simulation of selective beam melting processes". *Journal of Materials Processing Technology,* ***211***(6), pp. 978–987.

[44] Körner, C., Bauereiß, A., and Attar, E., 2013. "Fundamental consolidation mechanisms during selective beam melting of powders". *Modelling and Simulation in Materials Science and Engineering,* ***21***(8), p. 085011.

[45] Carslaw, H. S., and Jaeger, J. C., 1959. "Conduction of heat in solids". *Oxford: Clarendon Press, 1959, 2nd ed.*

[46] Frenkel, J., 1945. "Viscous flow of crystalline bodies under the action of surface tension". *Journal of Physics*

Assouroko, Ibrahim; Lopez, Felipe; Witherell, Paul.
"A method for characterizing model fidelity in laser powder bed fusion additive manufacturing."
Paper presented at ASME 2016 International Mechanical Engineering Congress & Exposition ASME IMECE 2016,
Phoenix, AZ. November 11, 2016 - November 17, 2016.

(Moscow), ***9***(5), pp. 385–391.
[47] Mackenzie, J., and Shuttleworth, R., 1949. “A phenomenological theory of sintering”. *Proceedings of the Physical Society. Section B,* ***62***(12), p. 833.
[48] Tontowi, A. E., and Childs, T., 2001. “Density prediction of crystalline polymer sintered parts at various powder bed temperatures”. *Rapid Prototyping Journal,* ***7***(3), pp. 180–184.
[49] Kruth, J.-P., Levy, G., Klocke, F., and Childs, T., 2007. “Consolidation phenomena in laser and powder-bed based layered manufacturing”. *CIRP Annals-Manufacturing Technology,* ***56***(2), pp. 730–759.
[50] W3C OWL Working Group, 2012. W3C OWL2 web ontology language. http://www.w3.org/TR/owl2-primer/. Accessed on: 08/01/2016.
[51] Stanford Center for Biomedical Informatics Research, 2012. Protégé ontology editor. http://protege.stanford.edu/. Accessed on: 08/01/2016.
[52] Oden, J. T., 2011. *An introduction to mathematical modeling: A course in mechanics*, 1st edition ed. Wiley.
[53] W3C, 2013. W3C SPARQL query language. https://www.w3.org/TR/sparql11-query/. Accessed on: 08/01/2016.

Assouroko, Ibrahim; Lopez, Felipe; Witherell, Paul.
“A method for characterizing model fidelity in laser powder bed fusion additive manufacturing."
Paper presented at ASME 2016 International Mechanical Engineering Congress & Exposition ASME IMECE 2016,
Phoenix, AZ. November 11, 2016 - November 17, 2016.

LASER PATH PLANNING AND POWER CONTROL STRATEGIES FOR POWDER BED FUSION SYSTEMS

H. Yeung[1], J. Neira[2], B. Lane[1], J. Fox[1], F. Lopez[1]

[1]Engineering Laboratory, [2]Physical Measurement Laboratory,
National Institute of Standards and Technology, Gaithersburg, MD 20899

Abstract

In laser powder bed fusion additive manufacturing (AM) process, laser scan path, velocity, and power are some of the most important parameters affecting the build quality. Control strategies for laser path and power are implemented and tested on a prototype testbed based on industrial standard G-code type programming language (referred to as AM G-code). The proposed AM G-code demonstrates different modes which define power-velocity-position profiles, and account for the laser and scanner dynamics. AM G-code is interpreted into *xy2-100* protocol and sent to the galvo scanners and laser using a custom transmitter. The actual scan path is compared with the commanded path during controlled tests. The proposed AM G-code interpreter modes are then evaluated considering the measured dynamic system response, and further discussed in contrast to commercial powder bed fusion systems.

Introduction

Laser powder bed fusion (LPBF) is an additive manufacturing (AM) process in which a focused, high power laser selectively melts geometric patterns into layers of metal powder, ultimately building a near fully dense freeform part. The LPBF fabrication process, and inherent resulting part quality, is determined by hundreds if not thousands of controlled and uncontrolled process parameters [1]. On a basic level, the laser control parameters (position, velocity, and power) and their respective synchronization, in conjunction with powder layer parameters (material, relative density, layer height, etc.) must be well-defined with certain combinations to adequately melt adjacent scan tracks and underlying substrate (or previously melted layers) to form fully dense solid parts. Many researchers have described various experimental approaches to determine appropriate parameter combinations, often termed ‘process mapping’ [2], which must be conducted for any new desired LPBF material.

Even when well-defined for near full density, varying the relative combination of these parameters can introduce known defects that plague LPBF parts. Pores, for example, have been attributed to various phenomena related to the power-velocity attributes or scan strategies (e.g., keyholing and collapse at high laser energy densities [3], or insufficient re-melting of adjacent scan vectors due to wide hatch spacing [4,5]. For example, Khairallah et al. noted that turning the laser off at the end of a scan vector can potentially cause pores to be trapped under the rapidly solidified melt pool, and recommended laser power decreased at these locations [6]. More adequately controlled velocity or power profiles along each scan vector can reduce probability of

Fox, Jason; Lane, Brandon; Lopez, Felipe; Neira, Jorge; Yeung, Ho.
“Laser Path Planning and Power Control Strategies for Powder Bed Fusion Systems."
Paper presented at Solid Freeform Fabrication Symposium, Austin, TX. August 8, 2016 - August 10, 2016.

pore formation, or provide a parametric space for other property optimization. Apart from solidification physics at the end of a single vector, the general size, shape, and timing of a laser scanning raster pattern are known to affect the melt pool thermal history of the part, thus the resulting local and global residual stress and microstructure [7–9]. Though commercial LPBF systems are rapidly improving and maturing, there is still wide potential fundamental research in melt pool, scan vector, and layer formation process physics.

To fully define scan strategies, a system must be able to control individual scan vectors, and to do that requires characterization of the galvo mirror and laser system dynamics, and subsequent synchronization. Commercial LPBF systems provide this calibration and synchronization; however, their controller software inherently imposes limits on scan strategy definition, since machines are primarily sold for part production rather than fundamental research. For this reason, the National Institute of Standards and Technology (NIST) is constructing an open architecture Additive Manufacturing Metrology Testbed (AMMT). The work described here describes the approach to achieve several objectives: 1) characterize the performance of the galvo scanner mirrors and laser for the AMMT, 2) develop initial building blocks for AMMT system control, including customized and fully defined scan vectors, and 3) demonstrate use of a potential standard open protocol for scan strategy definition.

Laser System

Galvo motors and mirrors

In LPBF AM process, a laser beam is directed by a pair of mirrors driven by galvo motors to achieve two-dimensional (x-y) scan, as shown in Figure 1. Galvo motors are limited rotation direct current (DC) torque motors optimized for high speed applications. The motors (mirrors) are rotated by the electromagnetic force proportional to the current flow in the motor coils. Closed-loop servo control is achieved through angular positon feedback from an internal encoder attached to the motor shaft. A proportional derivative (PD) control loop is usually implemented locally on the galvo driver board to quickly achieve target position without overshoot.

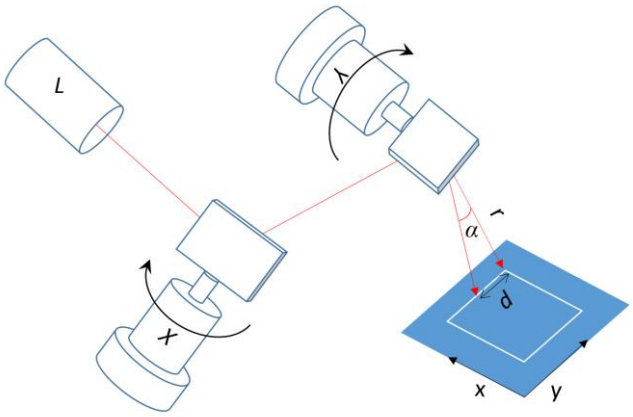

Figure 1: Typical scheme of a two-dimensional (x-y) optical scan system

Scan control system

For a small angle mirror rotation (angle α in Figure 1), the surface scan distance d can be approximated by $d = r \cdot \alpha$, where r is the traveling distance of the reflected laser beam and α is the rotation angle (Figure 1). If r is large, d is very sensitive to α. In galvo control α is the command signal and usually represented by a +/- 5 V voltage. A digital protocol called *xy2-100* is often adapted to transmit this command voltage from the system controller (computer) to the galvo driver. The command voltages are packaged into 20-bit 'words' and transmitted at frequency (f) up to 100 kHz per 'word', or 2 Mbps; hence the galvo position is updated every $1/f$ second.

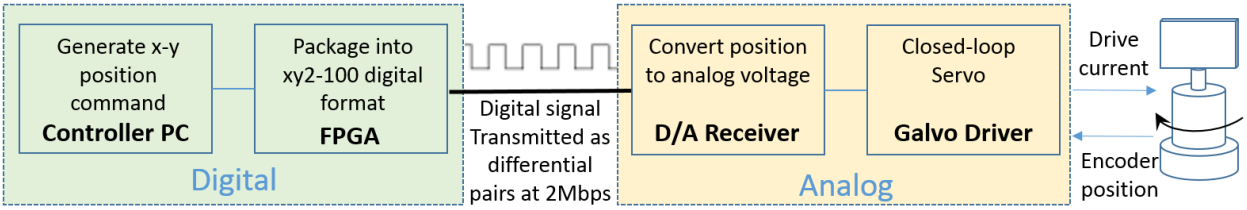

Figure 2: NIST AMMT laser control

Figure 2 shows the laser control implemented on the NIST AMMT. Scan lines/arcs are first converted into micro-steps (series of x-y positions) according to the predefined scan strategies on the Controller Personal Computer (PC). Each position is then packaged into *xy2-100* format on the Field Programmable Gate Array (FPGA) and transmitted through a differential signal transmitter. The digital positon signal is received by the Digital/Analog (D/A) Receiver and converted to analog voltage, and fed into the Galvo Driver as a command position to generate drive current to turn the mirror. The position detected by the galvo encoder is fed back to Galvo Driver to form a local closed servo loop. Most commercial LPBF AM systems have a similar design as Figure 2, except using proprietary software/hardware for path planning, x-y position generation, and *xy2-100* packaging.

To characterize the dynamic response of the galvo system, a high speed data acquisition system is set up to simultaneously capture the commanded position sent to the galvo driver (after D/A conversion) and the feedback (also referred to as measured) position from the galvo encoder (Figure 2).

Velocity Profile

A similar rectangular path was scanned with both an off-the-shelf commercial scanner system and with the NIST AMMT prototyping system, respectively. On the commercial system, only galvo positions and speed can be set. On the NIST AMMT, galvo acceleration can also be defined. The scan results are shown in Figure 3, where the lines labeled x_c,y_c and x_m,y_m represent the command and feedback x, y positions, respectively.

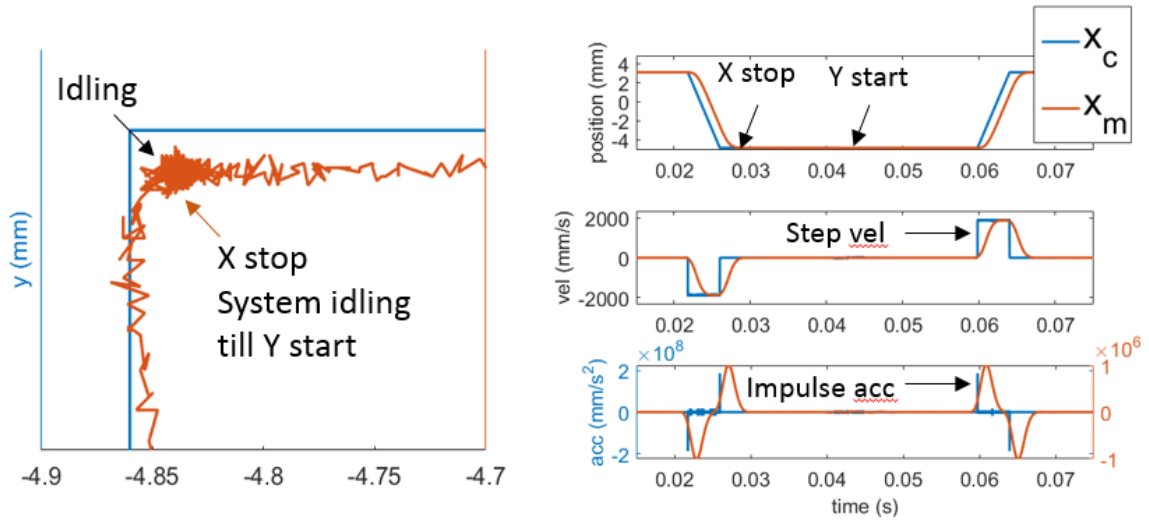

(a) Commercial scanner system

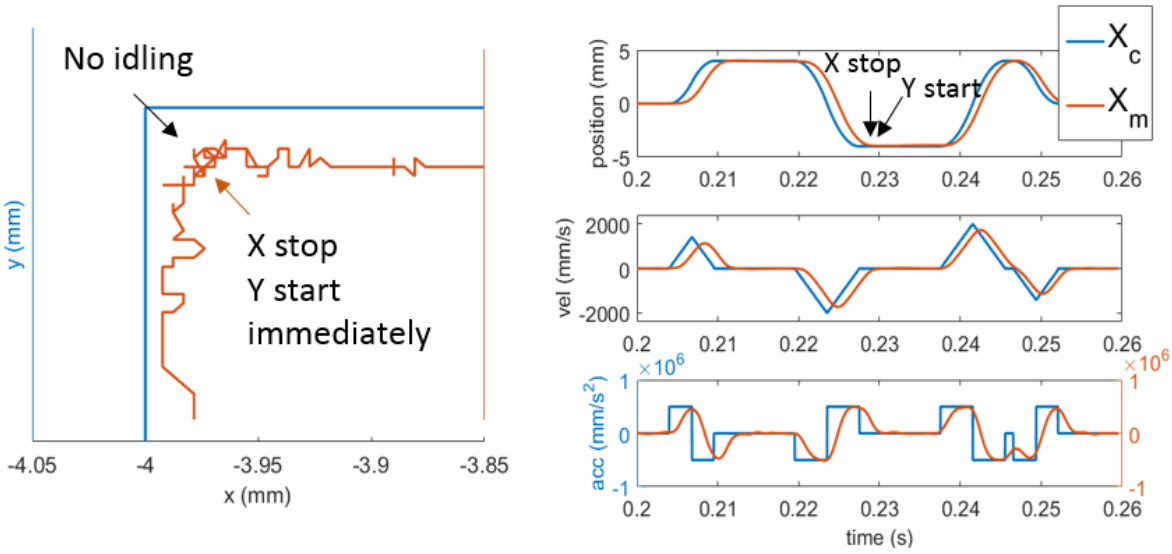

(b) NIST AMMT controller

Figure 3: A rectangle scanned by (a) commercial scanner system, (b) NIST AMMT controller. Blue color represents the command position; orange is the encoder feedback position. Left side shows the x-y plot of upper left rectangle corner. Right side shows the *X* axis position, velocity, and acceleration profile.

Figure 3a reveals that for this particular commercial system, to make the corner scan on the left, infinite (impulse) acceleration was assumed and enough time was left for the galvo *X* to settle before the subsequent galvo *Y* move (marked as '*Y* start'). However, the lack of velocity profile monitoring such as on the NIST AMMT (Figure 3b), and unknown idling period, result in uncertainty in galvo position and velocity at a particular time, making the laser power-position synchronization difficult, and prevents implementation of more sophisticated control algorithms presented in the following.

Frequency response

A frequency varying (0 Hz to 600 Hz) sinewave of amplitude 1 mm was fed into galvo *X* and *Y*, respectively. The feedback amplitude and phase delay were analyzed by Fast Fourier Transform (FFT) and plotted against frequency in Figure 4a.

For a sinusoidal motion $X(t) = A \cdot \sin(2\pi \cdot f \cdot t)$, where A is the amplitude, f is the frequency, and t is the time, acceleration $a = -A\,(2\pi \cdot f)^2 \sin(2\pi \cdot f \cdot t)$. Also, a phase delay ($d\theta$) can be converted to time delay (dt) by $dt = d\theta/(2\pi \cdot f)$. Figure 4b plots the amplitude of commanded acceleration, amplitude of measured acceleration, and delay time for galvo *X* and *Y*, respectively.

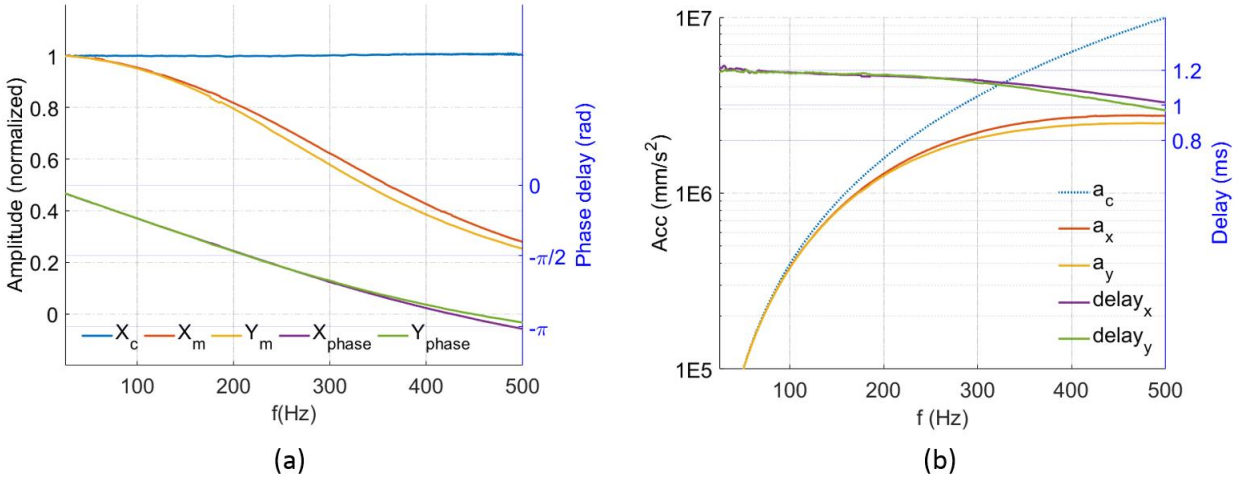

Figure 4: Frequency response analysis. (a) x_c is the input amplitude, x_m and x_{phase} are feedback amplitude and phase delay for galvo *X*, y_m and y_{phase} are for *Y*. (b) a_c is the input acceleration, a_x and delay_x are feedback acceleration and time delay for galvo *X*, a_y and delay_y are for *Y*.

Figure 4 shows galvo *Y* has a slightly slower response than galvo *X* at higher frequency. This could be caused by the larger mirror installed on galvo *Y*. At lower frequency (< 100 Hz), the response of Galvo *X* and *Y* are almost identical and follow closely (deviation < 5%) to the command. The delay times are also relatively constant of 1.20 ms. These parameters were further verified with the laser power switched on, and position measured from the burning marks (discussed in the *Experimental* section).

The laser source is a 500 W 1070 nm Ytterbium fiber laser unit. Relative laser power is monitored with a silicon photo diode. It shows laser power can be varied at its full amplitude within 100 µs. This makes it possible to modulate laser power at each position step.

AM G-code

Part of the rapid expansion and development of fused deposition modeling (FDM) plastic 3D printing is attributable to the RepRap and Maker communities [10]. Part of the utility of these systems, and contributor to the rapid adoption, is that they use a common control protocol so users of one system can quickly and rapidly program the toolpaths on different or new machines. G-code is the most commonly used numerical control (NC) programming language in motion control.

A G-code type programming language (referred to as AM G-code) is used to develop laser control on AMMT, with one additional keyword 'L' introduced to specify laser power. A detailed example of a G-code interpreter developed for 5-axis machining centers is given in [11]. Similar concepts, such as the G01 command for linearly interpolated motion, and G02/G03 command for clockwise / counter-clockwise circular interpolation, can be implemented for use in LPBF laser control, an example of which is shown in Figure 5. The arc window scan path in Figure 5a can be described by a 15 line AM G-code script in Figure 5b, compared to the 4476 line position commands of the *xy2-100* standard in Figure 5c.

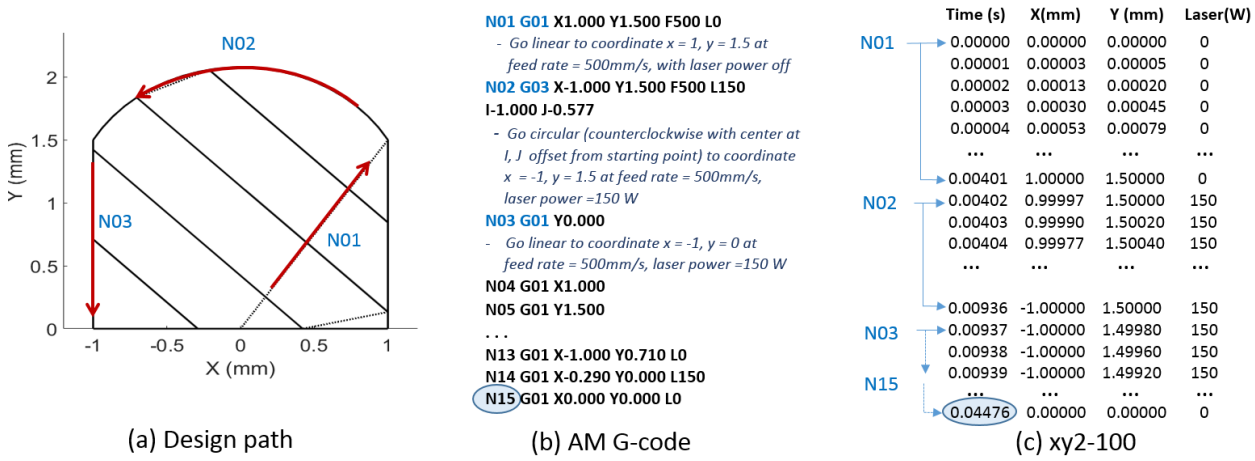

(a) Design path (b) AM G-code (c) xy2-100

Figure 5: AM G-Code example. The scan path in (a) can described by the AM G-code in (b) and *xy2-100* commands in (c).

An AM G-code interpreter is developed to convert the AM G-code into position commands of *xy2-100* standard. G-code motion commands (e.g., G01, G02, and G03), are composed of a set of more basic commands (e.g., start, accelerate, hold velocity, decelerate, stop). In contrast to machining G-code motion commands, which mostly consist of velocity and position control, LPBF systems require definition of velocity/position and laser power control. For this reason, three laser path control modes and three laser power control modes are defined, implemented, and demonstrated.

Laser path modes

The following three laser path interpreter modes were devised, and example position/velocity plots modeled as demonstration:

1. Exact stop mode - control stops motion exactly at the end of each move with maximum allowable deceleration. If there is a subsequent move, the motion will start immediately again with maximum allowable acceleration until it reaches the programmed speed, or until it needs to decelerate again.
2. Continuous mode - control tries to match the ending velocity of the line or vector with the starting velocity of the subsequent line. In order to do so, move is allowed to deviate (overshoot) from the designed path within the maximum tolerance.

3. Constant build speed mode - control keeps the speed constant during the build move. Build move is defined as a move with laser power on. If the preceding move does not end with velocity that exactly matches the current build move, extra moves (with laser power off) with maximum allowable acceleration are introduced to match it.

Figure 6 below illustrate the three laser path modes. The same design path / AM G-code in Figure 5 can be interpreted into different scan moves based on the laser path mode selected.

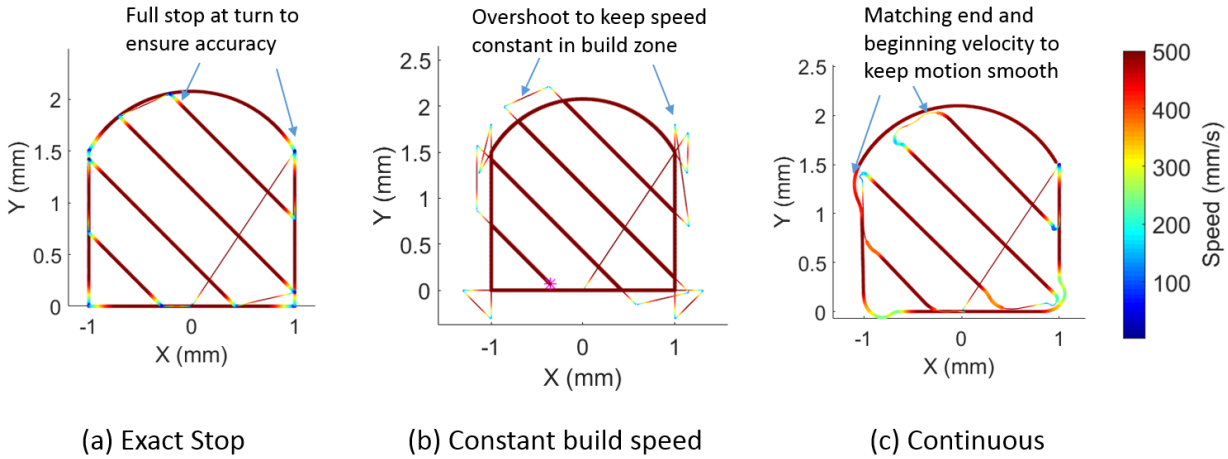

Figure 6: Laser path modes. (a) Exact stop. (b) Constant build speed. (c) Continuous. Speed variation is reprented by color

Laser power modes

Since laser power is an additional controllable parameter beyond position and velocity, new interpreter modes need to be devised. The following laser power interpreter modes were devised, with position/power plots modeled as demonstration.

1. Constant power mode - control keeps the power constant at the programmed level during each build move. If a subsequent move has a different power level, control sets the power to the new level.
2. Constant density mode - control keeps the power/speed ratio (power density) at a predefined constant during each move. This constant is not necessarily the same for all moves.
3. Thermal adjusted mode - control adjusts the power level according to the predefined thermal properties of the building process. For example, lower power at overhanging region, or raise power at initial stage while residual heat has not built up yet. It also provides a means for real time feedback control of power.

A simple thermal adjusted mode is implemented based on proximity. In Figure 7a, '*C*' marks the current laser position. Proximity of *C* is evaluated based on distance *d* between *C* and each scanned point in the semi-sphere centered at *C* and with predefined radius *r*. Sum of $(r - d)$ is used as a measurement for proximity. It is normalized and represented by color variation in

Figure 7a. If a metal plate is scanned, proximity can be used as an indicator of residual heat and laser power can be adjusted inversely proportional to it as shown in Figure 7b. More advanced thermal adjustment models can be developed in a similar way, and the time history factor of each scanned point can also be included.

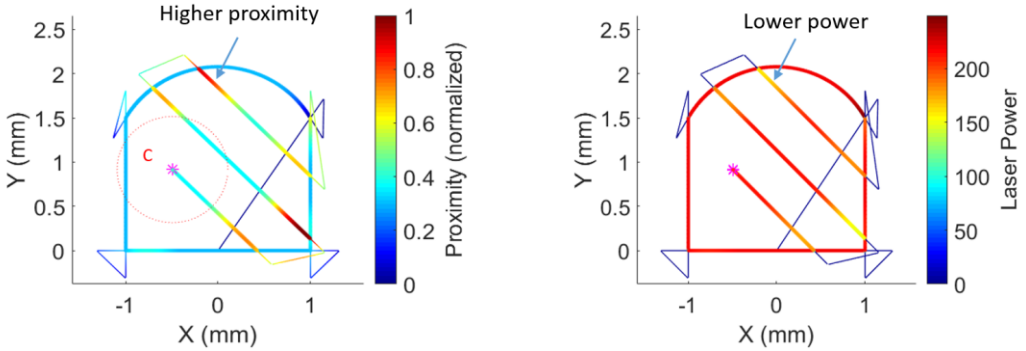

Figure 7: Demonstration of thermal adjusted laser power mode. (a) Proximity analysis based on distance of the evaluated point from its neighborhood. (b) Laser power adjustment based on proximity.

Experiemental

Four sets of scan experiements were conducted on the NIST AMMT. The workpiece was a circular stainless steel plate of 115 mm diameter and 5 mm thickness, placed inside a sealed box purged with Argon (except the first experiment which was in air).

Galvo-Laser synchronization

This experiment was to demonstrate a way to synchronize laser power to the galvo position. Two trapezoids with hatch lines spaced at 1 mm were scanned on an unsynchronized system. The scan path and result are shown in Figure 8. Speed was set at 1000 mm/s and constant build speed mode was used, so time is linear proportional to distance within the borders of the trapezoid. The red arrows indicate where the laser was supposed to turn off if the system was synchronized. The laser was actually turned off 1.2 mm earlier (blue arrows). Therefore, the galvo-laser delay was found to be 1.20 ms. This agrees quite well with the delay time found by frequency response analysis (Figure 4b) in the *Frequency response* section. More accurate calibration can be achieved with more finely spaced hatch lines. A 1.20 ms laser power-on delay was introduced to synchronize laser power to position for later experiments.

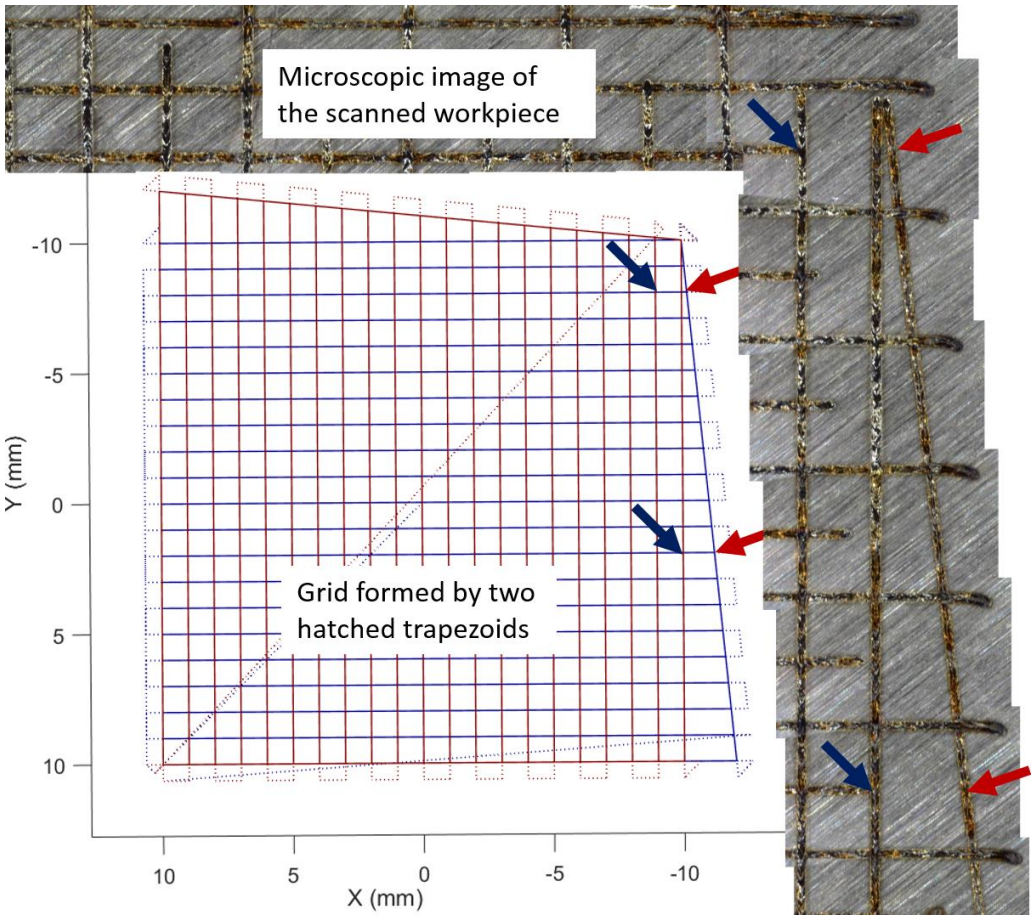

Figure 8: Calibration for galvo-laser delay. Two overlapped trapezoids with hatch lines (1 mm spacing) were scanned at 1000 mm/s. The red arrows indicate where the burnt lines were supposed to end, and blue arrows indicate where they actually ended. Therefore, laser power was turned off approximately1.20 mm (or 1.20 ms) earlier.

Power-speed process map

A power-speed process map is conducted to find out the feasible build range of AMMT, and also determine the effect of acceleration limitation on position accuracy. A crosshair pattern (Figure 10a) was scanned at 80 different speeds (200 mm/s to 2000 mm/s) and power (75 W to 250 W) combinations (Figure 9). The commanded line length and circle radius are 2 mm and 0.707 mm, respectively. The scans were done with constant build speed - constant power mode. Acceleration set for lines was 10^6 mm/s^2. Acceleration was not constrained for circles. The scanned line length and circle radius were measured from images (Figure 9) and plotted against the commanded speed (Figure 10b). The commanded circle radius is noted as r_c, commanded line length as l_c, measured radius as r_m, and measured line length as l_m.

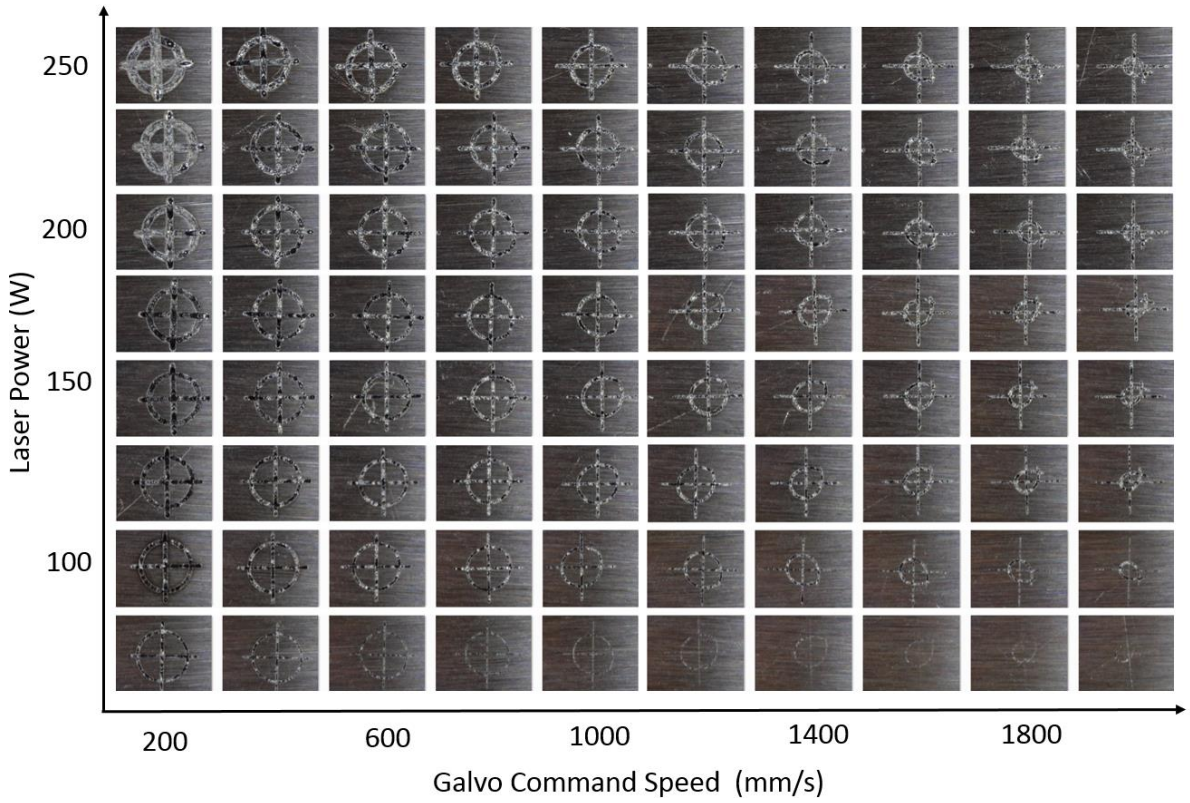

Figure 9: Power-speed process map. Power varies from 75 W to 250 W. Speed varies from 200 mm/s to 2000 mm/s. Same crosshair pattern was scanned at each power-speed setting.

As speed increases, l_m stays closely to l_c but r_m drops rapidly from r_c. At 2000 mm/s, $l_m = 1.96$ mm, $r_m = 0.2$ mm (Figure 10b). A circular motion of radius r and speed v can be represented in x-y coordinates by $x(t) = r \cdot \cos(\omega \cdot t)$ and $y(t) = r \cdot \sin(\omega \cdot t)$, where t is time, ω is angular velocity in rad/s and can be approximated by v/r. Acceleration $d^2x(t)/dt = -r \cdot \omega^2 \cdot \cos(\omega \cdot t)$ and $d^2y(t)/dt = -r \cdot \omega^2 \cdot \sin(\omega \cdot t)$. Therefore, to maintain a perfect circular motion, an acceleration with amplitude $a = r \cdot (v/r)^2$ is required for both x and y axis. As v increases, eventually the galvo motor could not meet the required acceleration, the circular motion is distorted and a smaller r_m results. $a_c = r_c \, (v/r_c)^2$ and $a_m = r_m \cdot (v/r_c)^2$ were defined as amplitude for commanded and measured acceleration and plotted in Figure 10b. Note, r_m is not very accurately defined for a distorted circle, nor is a_m; but the maximum error should be within 42 %. During the AM G-code interpretation, arc speed can be constrained based on the a_m value of the system to ensure accuracy.

It is interesting to compare the acceleration measurements from Figure 10b and Figure 4b. The points at which commanded acceleration $a_c = 5 \times 10^5$ were marked on both figures, and the corresponding measured acceleration was also noted (as 'actual'). For galvo Y the acceleration found from frequency response (Figure 4b) is 4.76×10^5 mm/s^2, from the circle scan (Figure 10b) is 4.95×10^5 mm/s^2. Considering the possible radius measurement error (Figure 10a), it is very consistent and also demonstrates this process map can be a possible method for system calibration.

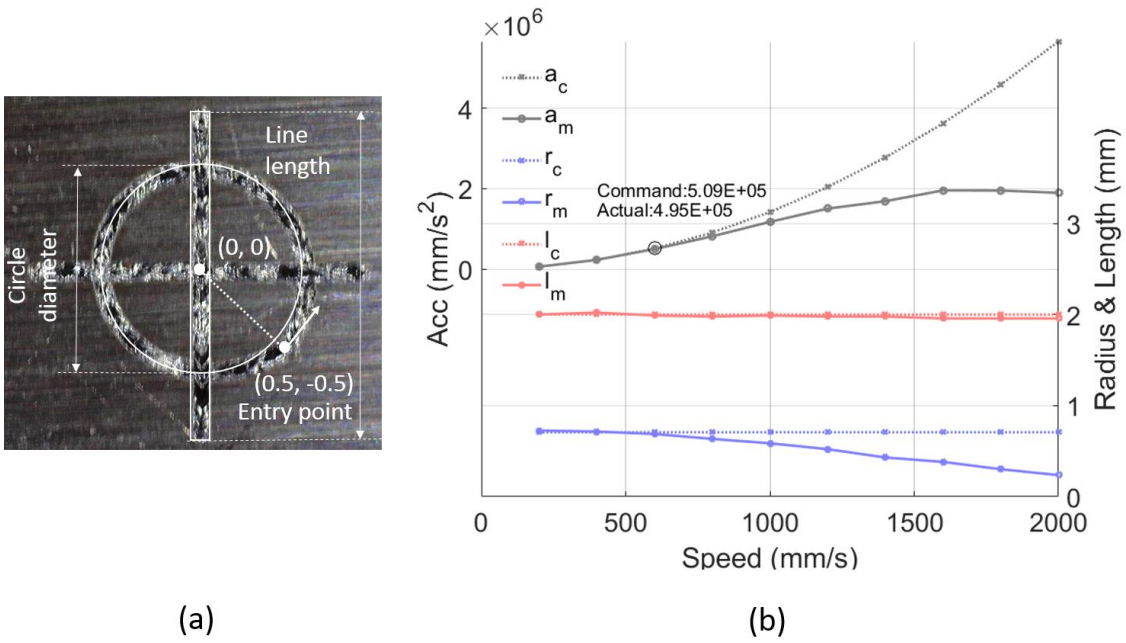

Figure 10: Effect of scanning speed on path accuracy. (a) Image shows a slightly distorted crosshair pattern scanned at power = 175 W and tangential speed = 800 mm/s. (b) l_c and l_m are the commanded and measured line length. r_c and r_m are the commanded and measured radius. a_c and a_m is the commanded and measured acceleration

AM modes

The arc window pattern in Figure 5 was scanned with the 3 x 3 combinations of scan path and laser power modes defined in the *AM G-code* section. Figure 11 shows the microscopic images for the bottom left corner of each scanned pattern. For each row the scan path is the same, only laser power varies; and vice versa for each column. The constant build speed path mode (first row) gives the most uniform bead, especially for the thermal adjusted power mode, since there is no swelling at the turn. However, a possible keyhole defect is observed at all three power modes (red arrows). This agrees with the prediction of [6], as in constant build speed mode the laser power is turned off immediately before the path overshoots. The gradually decreasing of laser power at the end of the scan is achieved in the exact stop path mode (third row). No keyhole is observed in any of these three power modes, but the corners are swollen (blue arrows), likely due to the excessive heat during slowing down. Further studies will be conducted to optimize the speed-power setting in exact stop - thermal adjusted mode to maintain the bead size as uniform as possible. It is not surprising to see the continuous path mode (middle row) actually gives the smoothest turn judged from the continuity of the bead (white arrows), although the price for this is accuracy, especially at higher velocity. Each mode has its pros and cons depending on the actual build requirements. The purpose here is to demonstrate the effect of different modes and the potential of incorporating them into a look-forward building strategy.

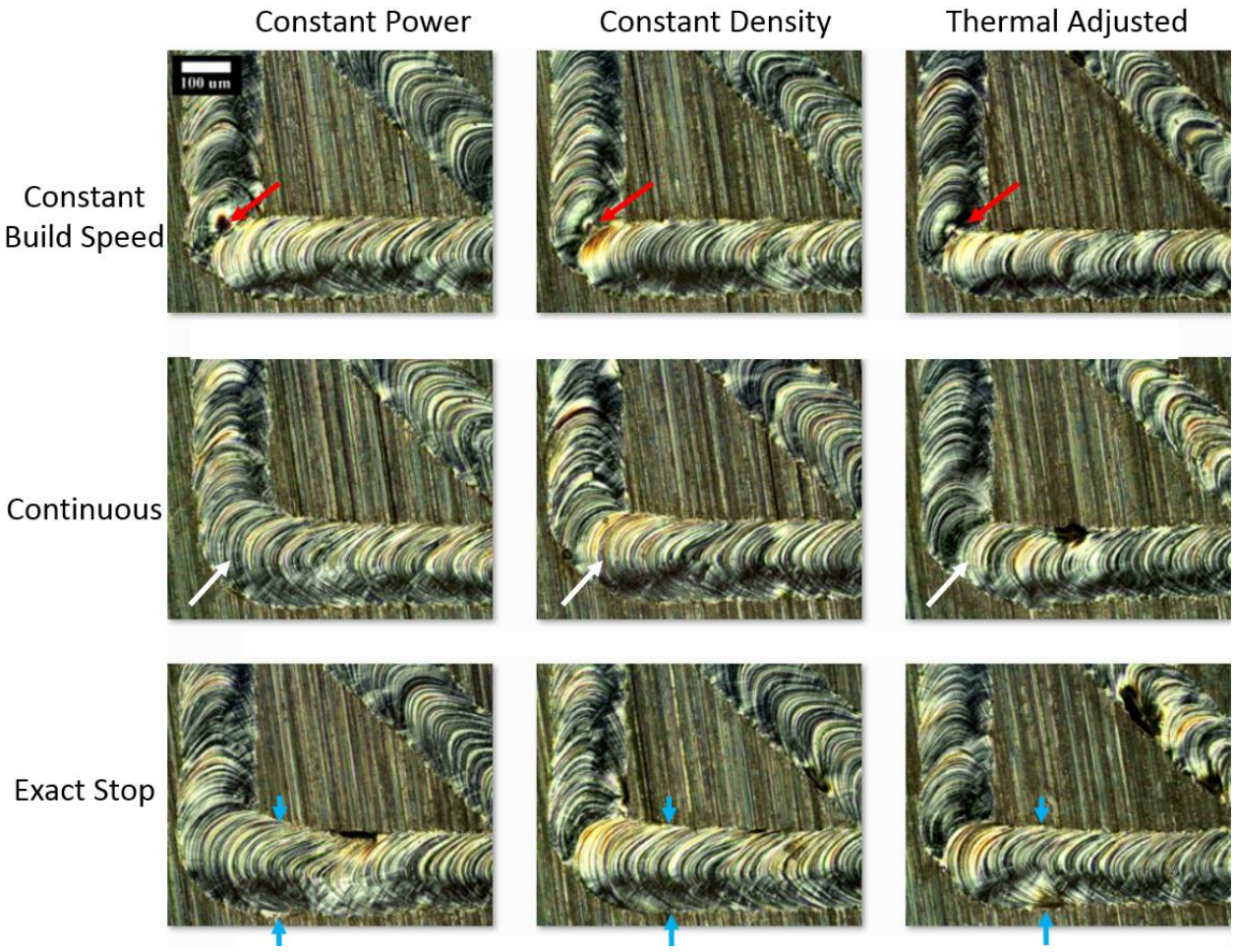

Figure 11: 3 x 3 combinations of scan path and laser power modes. The nominal scan speed is 500 mm/s, and maximum laser power is 250 W. The scale bar in the figure is 100 µm.

Scan with complicated strategies

Figure 12 shows a scan example on the AMMT with a combination of different modes. "NIST" was scanned with constant build speed - constant density mode, at 600 mm/s speed and 225 W maximum laser power. "AMMT/TEMPS" was scanned with continuous path - constant power mode, at 200 mm/s speed and 75 W laser power. G01, G02, and G03 were used to program linear and circular motions as illustrated in Figure 12b. 425 G-code lines were used to generate a 30 mm NIST logo and were interpreted into 218,507 *xy2-100* command lines. The G-code to *xy2-100* line ratio is approximately 1:500; and it will be 1:5000 if a 300 mm NIST logo is scanned. Comparing Figure 12b and Figure 12c, the bead size of "AMMT/TEMPS" was reduced to half simply through AM G-code parameter (speed/power) and interpretation mode settings. These are the programing efficiency and scan controllability that AM G-code can achieve.

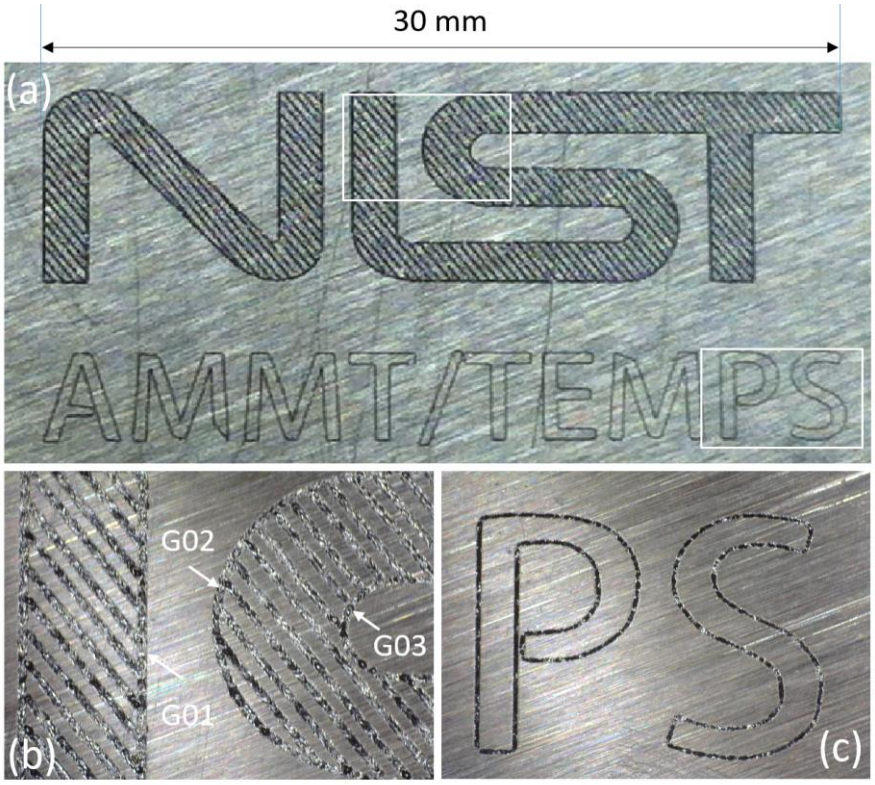

Figure 12: NIST logo was scanned at 600 mm/s, with constant build speed - constant density mode, at 225 W maximum laser power, with hatch size = 0.3 mm. AMMT/TEMPS was scanned at 200 mm/s, with continuous path - constant power mode, at 75 W laser power.

Discussion and Summary

As mentioned in the *Introduction*, there is an open field of potential research into laser path planning, scan strategy, and laser power control, with potential to reduce the likelihood of defects, control residual stress or microstructure, or improve the speed and efficiency of material consolidation. To provide this capability, the NIST AMMT requires highly controlled and defined laser power position and speed. To realize this capability, this paper describes how the scanner mirror and laser system are characterized, and how laser path planning and power control strategies are implemented. The laser control system is based on the *xy2-100* protocol, where scanner position (path) and laser power are updated at each 10 µs interval (100 kHz). Rather than require position commands at 100 kHz, we chose to package commands into a standard protocol based on G-code, which is extensible to larger and more complex scan strategies. The AM G-code interpreter is defined with three path and three power interpretation modes to enable high level path / power programming without losing the controllability. The AMMT laser system was first characterized with varying frequency sinewave input and galvo encoder feedback; experiments were then conducted with scans programmed by AM G-code and measurements were made from microscopic images. The results are highly consistent, and also demonstrate the full controllability of power-velocity-position profiles through different modes. Although similar scan strategies may have been studied previously, building them into AM G-code interpretation modes can greatly

improve the efficiency and consistency of their implementation, provide controllability for the NIST AMMT, and provide an example for promotion and potential standardization of an open source machine command protocol.

Future research on the AMMT will also test and evaluate potential real-time feedback control methodologies, based on knowledge gained from fundamental scan strategy, and process monitoring research to determine optimal control strategies. With careful design, an *xy2-100* package (Figure 2) can be completed within 1 clock cycle, or 25 ns on a typical 40 MHz FPGA system. It can be done at real time immediately before each positon/power command update. This provides an opportunity to adjust these commands in real time before each update. The work presented here to deconstruct and re-build the laser and scanner control will not only provide controllability of the AMMT, but will support development of a platform to research real time feedback control strategies and algorithms, with an ultimate goal of being able to adjust laser power based on the melt pool feedback at the same rate as the power update (100 kHz).

References

[1] Mani M, Lane B, Donmez M A, Feng S, Moylan S and Fesperman R 2015 *Measurement science needs for real-time control of additive manufacturing powder bed fusion processes* (Gaithersburg, MD: National Institute of Standards and Technology)

[2] Beuth J and Klingbeil N 2001 The role of process variables in laser-based direct metal solid freeform fabrication *JOM* **53** 36–9

[3] King W E, Barth H D, Castillo V M, Gallegos G F, Gibbs J W, Hahn D E, Kamath C and Rubenchik A M 2014 Observation of keyhole-mode laser melting in laser powder-bed fusion additive manufacturing *J. Mater. Process. Technol.* **214** 2915–25

[4] Thijs L, Verhaeghe F, Craeghs T, Humbeeck J V and Kruth J-P 2010 A study of the microstructural evolution during selective laser melting of Ti–6Al–4V *Acta Mater.* **58** 3303–12

[5] Yadroitsev I, Thivillon L, Bertrand P and Smurov I 2007 Strategy of manufacturing components with designed internal structure by selective laser melting of metallic powder *Appl. Surf. Sci.* **254** 980–3

[6] Khairallah S A, Anderson A T, Rubenchik A and King W E 2016 Laser powder-bed fusion additive manufacturing: Physics of complex melt flow and formation mechanisms of pores, spatter, and denudation zones *Acta Mater.* **108** 36–45

[7] Cheng B, Shrestha S and Chou K 2016 Stress and deformation evaluations of scanning strategy effect in selective laser melting *Addit. Manuf.* In Press, Corrected Proof

[8] Gockel J and Beuth J L 2013 Understanding Ti-6Al-4V microstructure control in additive manufacturing via process maps *Solid Freeform Fabrication Proceedings* Solid Freeform Fabrication Proceedings (Austin, TX) pp 666–74

[9] Mercelis P and Kruth J-P 2006 Residual stresses in selective laser sintering and selective laser melting *Rapid Prototyp. J.* **12** 254–65

[10] de Bruijn E 2010 On the viability of the Open Source Development model for the design of physical objects: Lessons learned from the RepRap project *Unpubl. DissMSc Thesis Tilburg Univ.*

[11] Kramer T R, Proctor F M and Messina E 2000 *The NIST RS274/NGC Interpreter-Version 3*

DESIGN, DEVELOPMENTS, AND RESULTS FROM THE NIST ADDITIVE MANUFACTURING METROLOGY TESTBED (AMMT)

B. Lane[1], S. Mekhontsev[2], S. Grantham[2], M. L. Vlasea[3], J. Whiting[1], H. Yeung[1], J. Fox[1], C. Zarobila[2], J. Neira[2], M. McGlauflin[1], L. Hanssen[2], S. Moylan[1], A. Donmez[1], J. Rice[2]

[1]Engineering Laboratory, [2] Physical Measurement Laboratory,
National Institute of Standards and Technology, Gaithersburg, MD 20899

[3]Mechanical and Mechatronics Engineering,
University of Waterloo, Waterloo, ON, Canada N2L 3GI

Abstract

The National Institute of Standards and Technology (NIST) is developing a facility titled the Additive Manufacturing Metrology Testbed that will enable advanced research into monitoring, controls, process development, and temperature measurement for laser powder bed fusion additive manufacturing and similar processes. This system provides an open control architecture as well as a plethora of sensor systems and calibration sources that are primarily radiance-based and aligned co-axially with the laser beam and focused on the laser interaction zone. This paper briefly reviews the system requirements, and details the current progress of the facility design and construction. Mechanical, optical, and control systems designs are detailed with select highlights that may be relevant to additive manufacturing researchers and system developers. Recent experimental results from the prototype laser control and in-situ monitoring system are also highlighted.

Introduction

Vlasea et. al. described the proposed construction of an additive manufacturing metrology testbed at the National Institute of Standards and Technology (NIST) that would provide a fully controlled research-oriented laser powder bed fusion (LPBF) system to enhance research capabilities in additive manufacturing (AM) and materials research [1]. This system is primarily designed to serve two different but supporting research endeavors by NIST's Engineering Laboratory (EL) and Physical Measurement Laboratory (PML), which require well-controlled and characterized high laser energy input applied to solid metals, metal powders, or other materials, and simultaneous measurement from a plethora of primarily optically-based metrological instruments. For EL's use, the system is given the moniker Additive Manufacturing Metrology Testbed (AMMT), and for PML's use, the system is named Temperature and Emittance of Melts, Powders, and Solids (TEMPS).

Donmez, M; Fox, Jason; Grantham, Steven; Hanssen, Leonard; Lane, Brandon; McGlauflin, Michael; Mekhontsev, Sergey; Moylan, Shawn; Neira, Jorge; Rice, Joseph; Vlasea, Mihaela; Whiting, Justin; Yeung, Ho; Zarobila, Clarence.
"Design, Developments, and Results from the NIST Additive Manufacturing Metrology Testbed (AMMT)."
Paper presented at Solid Freeform Fabrication Symposium, Austin, TX. August 8, 2016 - August 10, 2016.

Overarching goals for the system are as follows:

1. Build an open-platform LPBF testbed instrumented for fundamental process study and optimization, as well as optical metrology (AMMT).
2. Research the measurement science of various real time monitoring and control methods for measuring and improving AM build quality (AMMT).
3. Establish new emittance measurement capability for materials in various stages of aggregation over solid and liquid-phase temperatures (TEMPS).
4. Develop new NIST calibration services and standard reference data on polymers, ceramics, high temperature alloys, composites, and coatings (TEMPS).
5. Develop capacity to accurately measure temperature distribution across the melt pool under laboratory conditions (common goal).
6. Study methods for real-time process thermometry in the production environment (common goal).

Since the previous report [1], the concept has progressed from definition of goals and conceptual design, to near final mechanical and optical design, and initialization of the research facilities construction, system control architecture, and mechanical fabrication and assembly. In addition, initial controller programming and laser scanning tests on a prototyping system have been performed. The focus of this paper is to provide a general update on this progress. A comprehensive description of all design aspects would be too lengthy, so an 'overall' system design concept is provided here. Highlights are provided regarding ideas and results that may be pertinent to the additive manufacturing research community. While the TEMPS-based operations and design concepts will support additive manufacturing research, the focus of this paper is primarily on aspects pertaining to AMMT operation.

Design Functionality

Vlasea et al. described the general dual-functionality of AMMT/TEMPS system as operating in either build mode or radiance-based metrology mode [1]. In build mode, which is the primary mode for AMMT operation, the system is a fully controllable LPBF machine, with fully definable and controllable build parameters including but not limited to laser power, scan speed, layer thickness, and scan strategy. Primary focus of AMMT metrological research will be on radiometric measurements using optical instruments in a co-axial configuration, that is, aligned with the laser and monitoring dynamically changing radiant emission from the melt pool. Design flexibility also allows for staring configurations (as opposed to co-axial) for imaging or other radiometric sensors, which are either mounted within the vacuum chamber or externally mounted looking through viewports. These two configurations, allowing for melt pool monitoring or layer-wise imaging, are already being incorporated into commercial LPBF systems [2]. The advantage brought by the AMMT, apart from full process control, characterization, and reconfiguration flexibility, is that radiometric calibration sources will be located adjacent to the build bed, allowing for rapid in-situ calibration. In addition, processes and instrumentation composing the TEMPS systems will provide additional references and comparison.

In radiance based metrology mode, which is the mode for TEMPS-based operation, the system is reconfigured such that other optical beam lines and instrumentation are accessed. Similar to the co-axial configured instruments used in AMMT operation, the TEMPS-based operation will utilize emitted radiation from the heat affected zone transmitted to co-axially aligned optics and instruments. However, unlike in AMMT operation, which utilizes visible and near-infrared spectrum, TEMPS operation is broad band (visible to long-wave infrared), and thus requires special reflective or broadband optics [3].

This operation mode is intended to extend current capabilities at NIST for material optical property measurement [4], and allow measurement at higher temperatures, operation in vacuum or high purity inert environment, measurement at shorter wavelengths, and measurement of material phases other than solids. These extended phase measurements primarily focus on powders and liquids, but availability of high laser energy densities may allow for vapor and plasma characterization as well. One of the measurement procedures, titled the DYnamic Meltpool Emissometry (DYME) method, essentially replicates procedures used at NIST for spectral emissivity characterization of solid material samples [5]. However, the DYME method utilizes the moving melt pool (or non-liquid, laser heated spot) as a target, statically held in the field of view of the co-axial optical system, rather than a statically heated sample. This method, compared to previous methods using larger, isothermally heated samples, reduces oxidation, contamination, and/or evaporation due to the small area of the heat affected zone. These measurements have direct application to LPBF process monitoring and research, and details of the TEMPS-specific system design, operation, and measurement procedures will be provided in separate publications.

System Modules and Mechanical Design

Although complex, the overall system allows expanded flexibility for researchers to reconfigure subsystems individually by providing a modular and separable design. Figure 1 shows an external view of the computer aided design (CAD) assembly, in which the carriage is pulled out of the vacuum chamber onto the transfer dolly. The figure highlights the five main system modules. The removable carriage allows researchers to have better access to assemble, reconfigure, and clean subsystems on the carriage externally from the vacuum chamber.

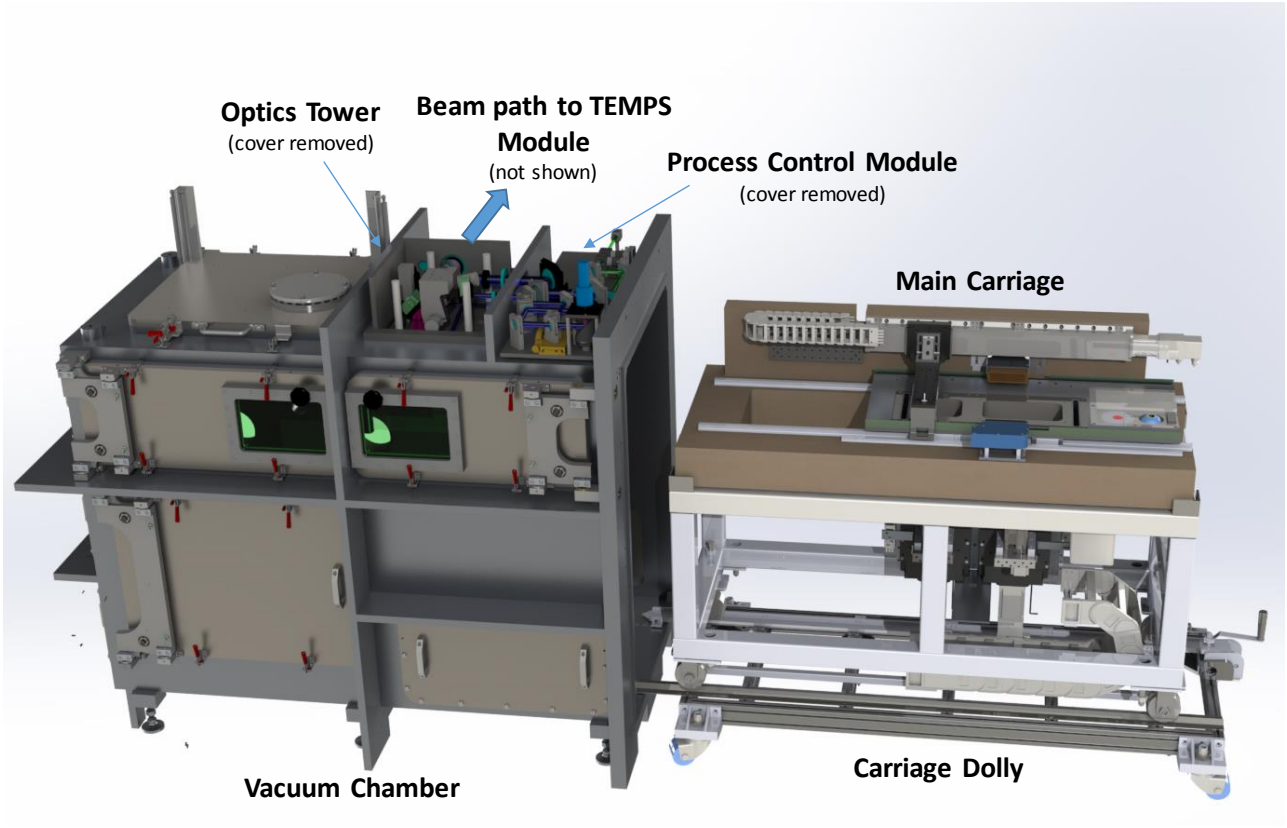

Figure 1: Solid model assembly of the AMMT/TEMPS system with the main carriage removed from the vacuum chamber. Not shown are the TEMPS module, which is positioned behind the vacuum chamber, and various cables and plumbing.

The *main carriage* is the main mechanical system built around a stainless steel frame and granite base, and houses the build bed, powder feed, recoating mechanisms, and most major mechanical and motion components. The carriage frame can be removed from the vacuum chamber by rolling along caster wheels on vee and flat tracks, and onto the external, mobile *carriage dolly*, which has similar tracks. The carriage dolly includes a winch and strap that connects to the main carriage to pull the carriage out of the vacuum chamber.

The *vacuum chamber*, designed for medium vacuum (0.1 Pa or 10^{-3} torr) operation, provides vacuum purging prior to backfilling with nitrogen or argon inert gas. This provides faster means to reduce oxygen levels compared to simply purging with inert gas. The vacuum chamber also provides access panels on all sides for cable and hose feedthroughs and user access to the build area and carriage underside. This also provides flexibility for incorporating future custom panels with ports or feedthroughs for newer or varying instrumentation or research projects.

The *optics tower* contains the main optical components to control and guide the heating laser, and divert back-emitted melt pool radiation to different modules. Pulling vacuum on the chamber will cause it to deflect, therefore the optics tower and fixed optical components are mechanically de-coupled from the chamber, and coupled to the granite by sitting on the optics tower bridge (not shown in Figure 1). The optics tower and internal components are vacuum compatible and can be purged, however a broadband window can be inserted between the optics

tower and main chamber to isolate the optics tower from vacuum. The optics tower contains the galvanometric (galvo) scanner mirrors, removable beamsplitter/reflector (RSR), mirrors etc. for the laser delivery path, the process monitoring path, or the metrology beam path. The back-emitted radiation from the melt pool is switched between the process control module or the TEMPS module by a manually swapped, kinematically mounted RSR accessed by opening the top lid of the tower. Either a broadband reflector, or laser-line reflector is exchanged in the RSR position to switch operation between the process control module, or the TEMPS module. The optics tower is kinematically mounted to the optics bridge, which is rigidly attached to the granite base, however it is mechanically isolated from the vacuum chamber through a sealed, vacuum gasket flange.

The *process control module* sits atop the chamber adjacent to the optics tower, and is the heart of the AMMT process monitoring for additive manufacturing research. This module is essentially an enclosed optical breadboard which contains the laser fiber, beam expander, negative lens, and other bending mirrors or windows for the laser injection beam path to the optics tower. When the broadband reflector (700 nm to 1100 nm) is installed in the RSR position within the optics tower, this module also receives the back-emitted radiation from the melt pool which is further filtered to the 700 nm to 900 nm range with another beamsplitter. This 700 nm to 900 nm bandwidth can then be further split to various optical sensors, including high speed imagers or photodetectors. The process monitoring module provides extra space for these different optical configurations and instruments to use the back-emitted light for researching various co-axial melt pool monitoring methods.

The *TEMPS module* (not shown in Figure 1) contains the toroidal mirror, folding mirrors, mirrored field stop, and other components to support spectral emissivity and reflectance measurements. The mirrored field stop allows back emitted radiation to pass through an aperture to various instruments, while reflecting the surrounding image to a high speed thermal imager. This allows the imager to 'see' the thermal field around the aperture, and help discern the relative location on or near the melt pool that is passed through the aperture to the sensors. TEMPS instruments include Fourier transform infrared (FTIR) spectrometer, visible array spectrograph, and filtered radiometers. Although not in the same physical location as the TEMPS module located behind the chamber but not shown in Figure 1, an in-situ hemispherical reflectometer (also not shown in Figure 1) used only for TEMPS operation will be incorporated within the build chamber, and be automatically placed on or removed from the build plane.

Structural/Metrology Loop

Ultimate positional and mechanical tolerance requirements of commercial LPBF systems may be dictated by the size of metal powder used (10 s of micrometers). However, as a metrological instrument, AMMT structural design aimed to not only reduce potential sources of geometric error in AM builds, but to ensure stability and repeatability of measurements. Rules and concepts from precision machine design are apt for incorporation into AM machine design. Analysis of a manufacturing system with respect to the structural/metrology loop(s) enables a systematic approach to error identification and tabulation. A guiding principle in precision machine design dictates that a smaller, less complex, and closed structural/metrology loop provides improved precision [6].

The structural loop, shown in Figure 2, consists of the mechanical coupling of rigid structures from the build layer to the scanner mirrors and laser beam path back to the build layer, with the granite base forming the central reference structure. As mentioned in the previous report

[1], the build bed, powder feed bed, and calibration sources are suspended in a gantry-type assembly from two rails on the granite base, and can be positioned along the X-direction with respect to the granite base using a ballscrew mechanism (not shown on the back side of the main carriage in Figure 1). This allows either the build bed or the calibration sources located within the carriage to be positioned directly under the optics tower, and accessed via the laser or co-axially aligned instruments. Using the CAD assembly, size and location of the carriage components were arranged to ensure the calculated center of mass is close to the mechanical center of the rails as possible. As previously mentioned, the optics tower is mechanically decoupled from the vacuum chamber, but rests upon kinematic mounts on the optics tower bridge, which is then coupled to the granite base.

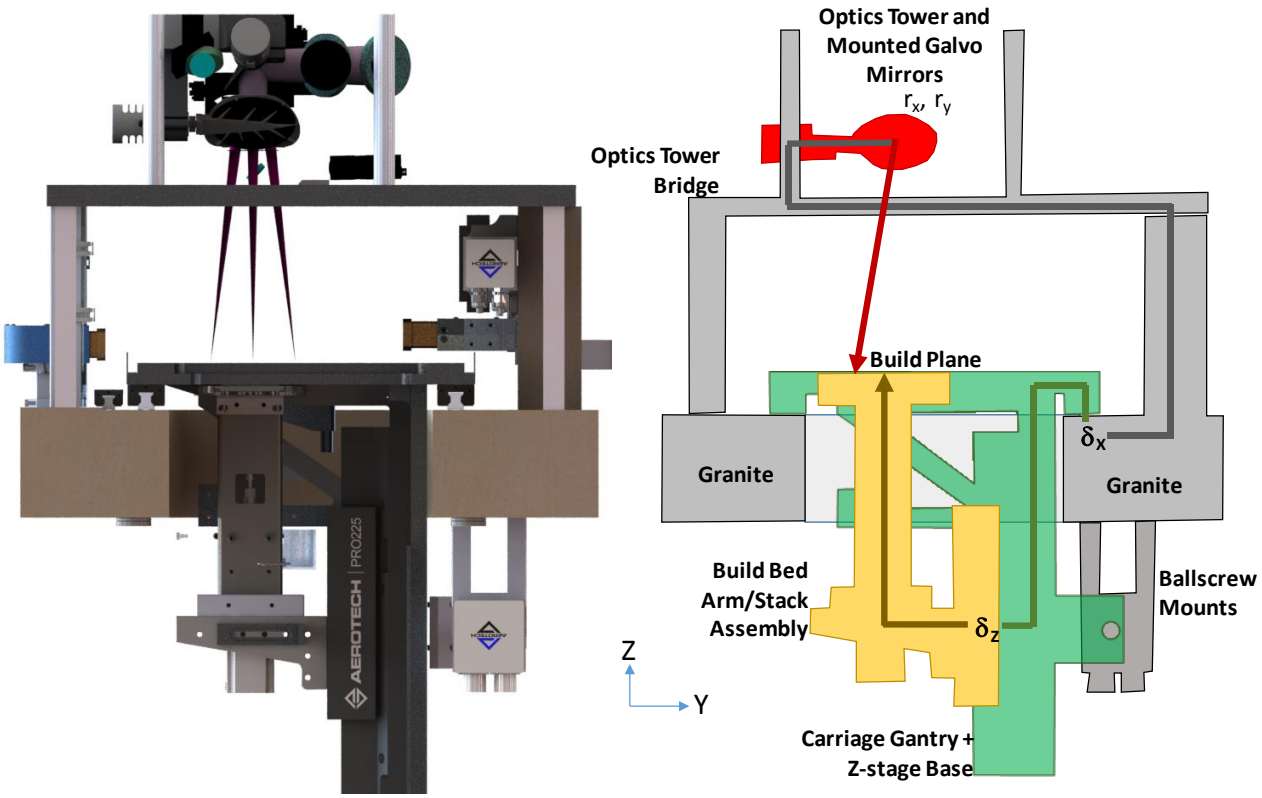

Figure 2: Mechanical linkage and metrology loop. Left: Solid model assembly view (multiple components hidden for clarity). Right: Schematic showing rigid structures, relative motion between rigid structures, and the metrology loop.

Though concepts from precision machine design were incorporated into the structural design of the AMMT system, many concepts were not directly transferable, and there is room for further research into the combination of machine tool metrology and optical system metrology for AM systems, especially when process monitoring instrumentation is considered. The AMMT, apart from the research objectives outlined above, will also act as a platform for researching the effects of machine components on part quality, and identify methods and requirements for error compensation and error budgeting.

Build Bed and Recoater Alignment

The designs of two subsystems on the carriage are detailed here, which differ from common commercial LPBF system configurations. Quality LPBF builds require consistent, smooth, and level powder layers, and thus require accurate alignment between the recoating plane and the build surface. The edge of the recoater blade forms a line in free space, and defines a plane when the recoater arm moves in the X-direction, shown in Figure 3 left. For uniform powder layer thickness, this recoater blade plane must be as parallel as possible to the build plate plane. Build layer thickness is then defined by the δz motion of the build arm motion stage. To parallelize two planes in free space requires two rotational adjustments with respect to one another. Many LPBF machines parallelize the build/recoater planes by implementing two rotational adjustments on the build plate, whereas we choose to separate the adjustment. Figure 3 left, demonstrates the relative motion and angular adjustments of the build plate and recoater blade. Not shown are the plate heating element, ceramic standoffs, or spring/felt seal assembly. The recoater blade is adjusted by a differential screw on one end, which rotates the blade about pivot bearings (angular flexures) on the other end. The recoater arm is positioned in δx by a motorized linear stage attached to the vertical wall on the granite, and held by an outrigger ball rail on the opposite side, also attached to the horizontal face of the granite.

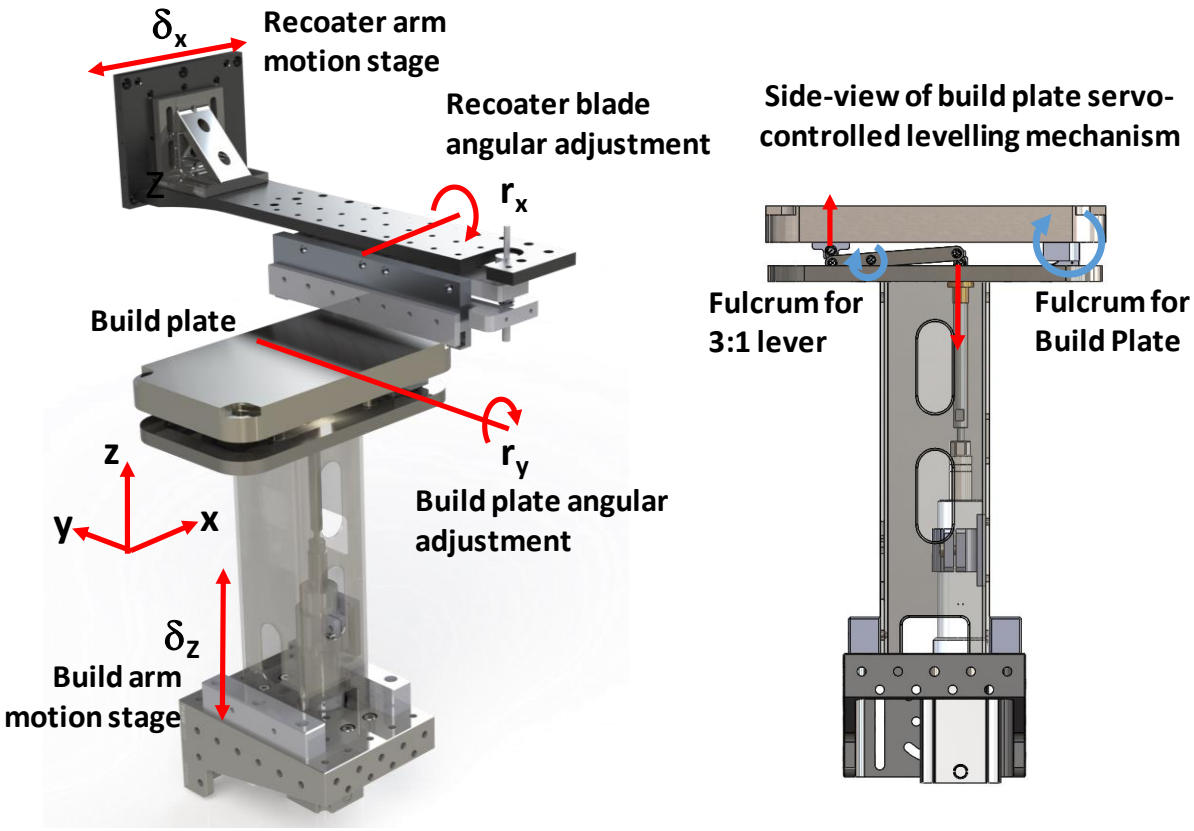

Figure 3: Left: Build plane and recoater plane parallelization adjustment coordinates. Note that some stiffening brackets and the outrigger ball rail connection are not shown. Right: Cutaway view of build arm showing internal linkage assembly for the automated build plate adjustment. An actuated pushrod rotates a 3:1 lever arm, which rotates the build plate's free edge about a pivot bearing fulcrum.

Provided the tight working space, an automated levelling mechanism was incorporated to align the build plate, shown in Figure 3 right. Again, certain elements such as the plate heater, standoffs, and spring/felt seal assembly are not shown. The five bar linkage mechanism transfers a linear displacement from a stepper motor with worm and rack gearbox, through a 3:1 lever arm (for mechanical advantage and improved positioning precision), to a pivoting build plate which rotates about the y-axis (r_y). Based on an estimated maximum distributed load, calculated design considerations included overall build plate stiffness, stiffness and strength of the pivot bearings, and detent torque of the motor.

Optical System Design

The driving design criteria for the process monitoring path is to create a 1:1 imaging system in the near infrared (NIR) which co-axially aligns an imager with the laser injection path, thus creating a stationary image of the melt pool. The 1:1 magnification was chosen so that a nominally 100 μm to 200 μm wide melt pool can be resolved between 10 pixels to 50 pixels, where typical Silicon (Si) based detector pixels are commonly between 4 μm to 10 μm. The near infrared spectrum was chosen for two reasons. Silicon based detectors, which are sensitive to visible and NIR, are less expensive and have a wider range of commercially available options. Another reason NIR was chosen, as opposed to visible spectrum, is so lower melt pool temperatures near the expected nickel or steel alloy melt pool solidus temperatures (around 1500 °C) can be better detected, since the maximum greybody radiant emission at this temperature is approximately 1.6 μm. However, choosing longer wavelengths is limited by the Si detector sensitivity cutoff at approximately 1200 nm, and the need to avoid the 1070 nm laser wavelength, which would potentially damage the detector. For the optical design, an imager sensitivity at 850 nm was chosen.

Multiple other sensor options and capabilities can be made possible within the process monitoring module. However, it was known early on that design requirements for the imager were most stringent and higher priority, and other sensors may be incorporated using various turning mirrors, beam splitters, and or hot/cold mirrors. Provided an imaging system with adequate spatial and spectral resolution is available, incorporation of other single-point detectors such as filtered photodetectors or pyrometers is trivial.

Optical Modeling and Optimization of the Process Monitoring Path

The optical system consists of laser injection and process monitoring paths co-located and sharing some components, shown in the Figure 4 schematic. The laser delivery fiber is terminated with a 60 mm focal length collimator producing collimated light at approximately 1070 nm. This light is reflected by the wavelength separator, whose coating is designed to reflect 1070 nm light in a narrow band, and transmit light in the NIR. The reflected laser light propagates through a Linear Translating lens (LTZ), through the window and Converging Lens Pair (CLP), and is then reflected by the mirrors in the scanner and converges to a focused spot onto the build plane. In the reverse direction, NIR light emitted from the build plane reflects off the mirrors in the scanner, through the CLP and window, through the LTZ, through the laser reflector, and is then directed through Custom Imaging Lenses (CIL) that forms an image for a camera to view. Fold mirrors and/or a custom relay lens can be used to direct the beam to be imaged to a more convenient location as needed.

The laser injection path is required to generate a focused spot having a full-width half-max (FWHM) of approximately 100 µm at an arbitrary location within a 100 mm x 100 mm square area below the scanner. It is the function of the LTZ to maintain the focus by compensating for the optical path length change resulting from the scanner mirrors' direction of the laser beam to the desired build plane locations. Commercial-off-the-shelf (COTS) parts for the LTZ and CLP are very good at maintaining this focus, but they were designed to work only over a very narrow wavelength band about 1070 nm. COTS parts are inadequate because of two requirements: 1) it is desired to monitor and image light from a 12 mm region at the build plane emitted in the NIR with the best possible image quality (the "diffraction limit") and 2) a focused, high power laser spot needs to be generated on the build plate at 1070 nm wavelength.

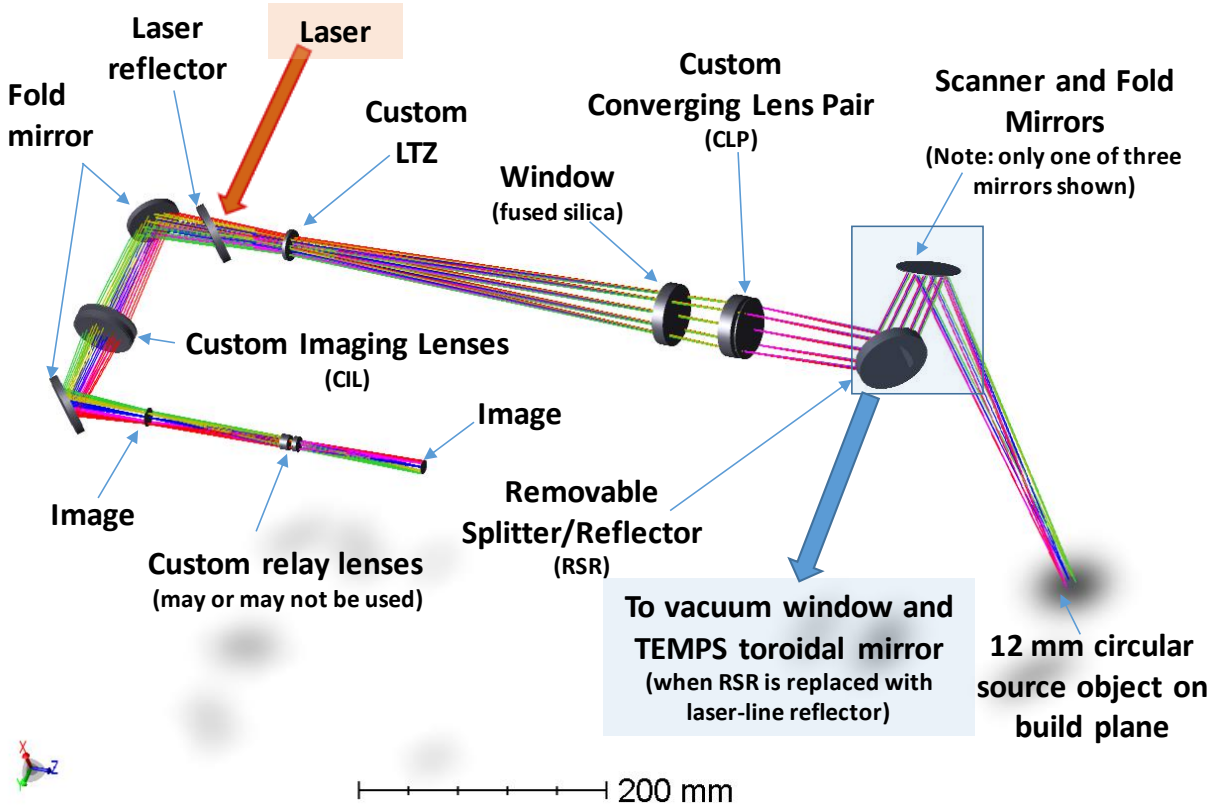

Figure 4: Schematic of ray tracing model used to optimize components for 1:1 imaging in process monitoring beam path. Current beam paths shown are for AMMT operation, where the laser-line reflector is in the RSR position.

To achieve diffraction-limited imaging performance in the NIR with 1:1 magnification in one direction as well as a focused laser beam at 1070 nm in the opposite direction, an "achromatic" solution is necessary, and custom LTZ, CLP, and CIL lenses are required. The lens surface curvatures and glass types were optimized using the ray-tracing optical design software based on a set of design criteria. The required operating wavelength bands, field-of-view, component temperature, and magnification all are included as constraints in the optimization routine. During the optimization process, the software automatically adjusts lens curvatures, glass types, and separation distances (the variables), and all within specified boundary constraints, resulting in simulated imaging performance characteristics (the objective functions).

The result of the optimization process yields a solution for the imaging having the performance shown in Figure 5. On the left-hand side, a laser beam directed to a point located on the build plane at (30,30) mm is shown. In the middle of Figure 5, spot diagrams for light at 850 +/- 25 nm emitted by a point at (30,30) and (30, 24) mm are shown. A spot diagram is an analog of the geometrical Point Spread Function (PSF) and diffraction effects are ignored. It illustrates the geometric image blur for a point source. Superimposed on each spot diagram is the "Airy disk", a contour whose radius represents the limit to the resolution when effects of diffraction are taken into account. Imaging can be no better than the diffraction limit. The radius of the Airy disk is a function of wavelength and system f-number (F/#) (Airy radius = $1.22 \cdot \lambda \cdot F/\#$) and is shown to be about 16 μm in Figure 5. The geometric spot diagram shows that the extent of the blur for a point source lays within the Airy disk and thus the performance of the imaging is diffraction-limited. Another way to express the performance of the imaging is in terms of the Modulation Transfer Function (MTF), shown at the right-hand side in Figure 5. MTF is a direct measure of how well details in the object are reproduced in the image. Since the imaging is 1:1, linear coordinates on the build plane are unscaled at the image plane and the MTF plot directly represents the spatial resolution at the build plane. MTF is widely accepted as the most important criterion for judging image quality and is typically specified in terms of spatial frequency as "line pairs per mm" or "cycles per mm". Diffraction effects limit the value of the MTF as the spatial frequency increases. As can be seen, the performance of the custom system results in an MTF that overlays the diffraction-limited MTF.

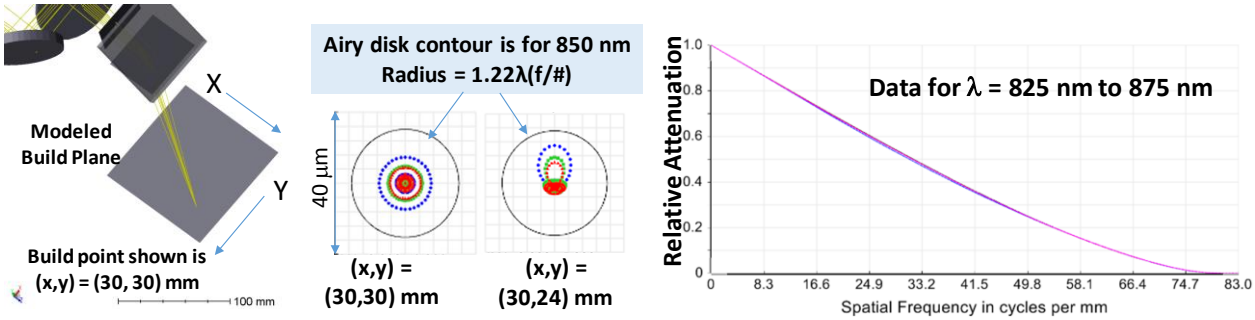

Figure 5: Optical modeling and optimization results for 1:1 imager resolution. Left: Schematic of physical model showing laser spot position coordinates. Center: Example spot diagrams showing point spread function (PSF) is encircled by Airy disk (thus diffraction limited performance) at center and 6 mm from center. Right: Modulation transfer function (MTF) showing spatial resolution.

Build Process and Environment Control

The AMMT control system design is process oriented and layer structured. The typical processes involved in AMMT can be divided into five major categories as shown in block diagram in Figure 6, and described as follows:

1. Laser control – laser power and gating, scan path (galvo position) and LTZ control.
2. High speed monitoring – in situ process monitoring, experiment data acquisition, and real time feedback.
3. Powder bed – build plate, powder feed, powder spread, and carriage motion and positioning.

4. Environment control – Build chamber preparation through vacuum purge, backfill, and inert gas circulation.
5. Environment monitoring – oxygen level, humidity, temperature, pressure, etc. monitoring.

Processes 1-3 are related to the building and build monitoring processes and realized using National Instrument (NI PXIe) and Aerotech systems, with main operations programmed in LabVIEW. Processes 4-5 are environment related and implemented by an Allen Bradley Programmable Logic Controller (PLC), programmed in Studio 5000 by ladder logic. The NI and PLC systems communicate to each other through an Open Platform Communications (OPC) server, where parameters in the PLC are published as global variables, read and written by Labview through the Datalogging and Supervisory Control (DSC) module.

The PLC is constantly monitoring and will shut down the system, in particular the laser, and trigger an alarm in cases such as abnormal high temperature, high O_2 level inside or low levels outside the chamber, chamber doors or panels open, etc. Since the PLC runs independently from building process control (NI controller), this provides a secondary guard against potential safety hazards.

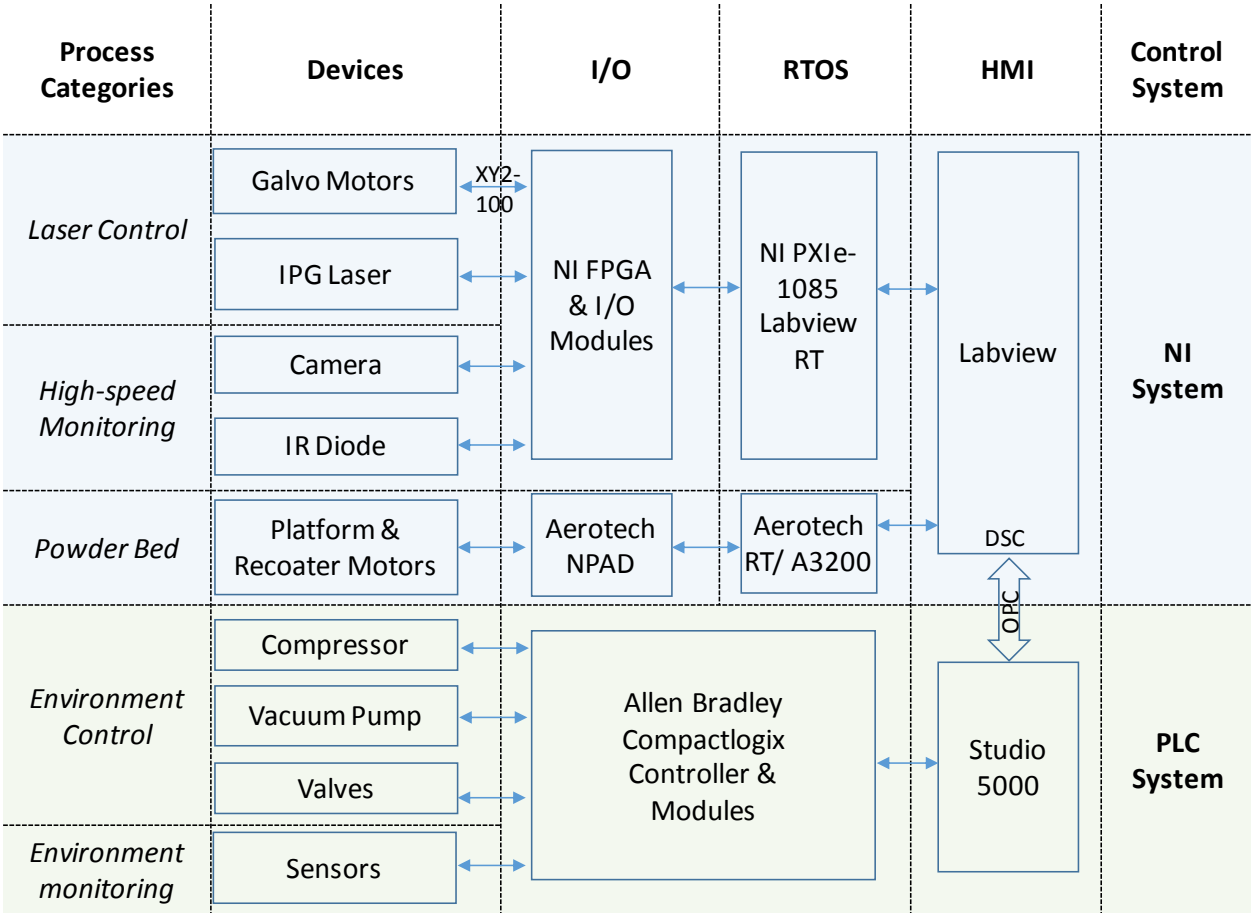

Figure 6: Overview of the NIST AMMT control architecture.

The block diagram is based on hardware, and much simplified and presented here to explain the architecture for AMMT control. Figure 6 can also be viewed as a layered structure from left to right.

1. Device – Individual hardware to perform the tasks listed in process categories.
2. I/O – Input / Output. This is a heterogeneous system and in general this layer refers to the interface between system controller and individual hardware device or driver.
3. RTOS – Real Time Operation System. NI PXIe-based system runs NI Linux Real-Time operating system, which also runs A3200 motion control Aerotech RTOS. On the RTOS, the PLC scans through all ladder logic in one clock cycle.
4. HMI – Human Machine Interface, which can also be referred to as the application layer. A Windows-based personal computer (PC) is used, with Labview and Studio 5000 installed. The user interface (UI), developed in Labview, also resides on this PC. All data, including process feedback and environment monitoring, are eventually logged here.

Environment Control Process

A build process starts with build chamber preparation. The chamber is first vacuumed to the preset level (0.1 Pa or 10^{-3} torr), then back filled by inert gas (argon or nitrogen). The experiment can also be conducted directly in vacuum if required. Refill is controlled by the PLC proportional-integral-derivative (PID) loop formed by proportional valves and pressure sensors. After the desired pressure is reached, the oxygen level is checked and if it is higher than the desired value, the vacuum-backfill (inert gas) process is repeated until the O_2 level is below the setpoint. The build cycle can then start.

The build cycle (powder feed, spread, and laser melting) can be started with vacuum purge, or inert gas recirculation. The circulation is powered by a 4 kW compressor, inert gas is pumped out of the chamber, filtered, cooled, and fed back into the chamber through three different ports into the chamber: 1) the air blanket, which is a custom-designed laminar flow nozzle directed right above the build plane, intended to uniformly remove vapor or melt pool ejecta, 2) the air knife, which is a high speed, thin flow layer located right below the scanner optics, intended to protect from contamination or deposition, and 3) the optics tower inlet, which maintains temperature of the mirrors and optics.

After the build process finishes, the inert gas is pumped out, and the chamber is back filled with dry air. The oxygen level warning sign will turn green only after the oxygen level reaches above 19.5%, to indicate it is safe to open the chamber door.

Laser Control

For LPBF AM, the laser beam is directed to the powder bed by a pair of mirrors driven by galvo motors. The galvos are limited rotational direct current (DC) motors with very fast response time, but are also very sensitive to noise. To eliminate transmission noise, an industrial standard digital communication protocol *xy2-100* is used to transfer control signal (position) from the field programmable gate array (FPGA) to the galvo driver. The *xy2-100* packages each position into a 20 bit 'word' and transmits it at 100 kHz per word (2 Mbps). Figure 7 shows the scheme for AMMT laser control. The scan path is generated on the controller PC together with laser power level according to the predefined scan strategies, and converted into *xy2-100* format on the FPGA. The digital signal is transmitted as differential pairs and converted back to analog voltage by the

digital to analog (D/A) receiver. It is then fed into the galvo driver as command signal, and form a closed-loop control with the position feedback from the galvo encoder.

The standard *xy2-100* protocol is only for positions (x, y, and z axis). The z-axis is typically relegated for controlling an LTZ lens. However, the AMMT utilizes this axis for laser power control to ensure high speed synchronization, as shown in Figure 7. The laser power level is also updated at 100 kHz, and is synchronized to each scanning step by introducing a constant, calibrated delay (laser response is much faster than galvo). Since the LTZ position strictly depends on galvo x-y position values, and not on commands from the controller PC, it is controlled through a lookup table programmed on the FPGA, which is based on angular measurements determined from optical ray tracing. This lays down the foundation for laser path planning and power control strategies.

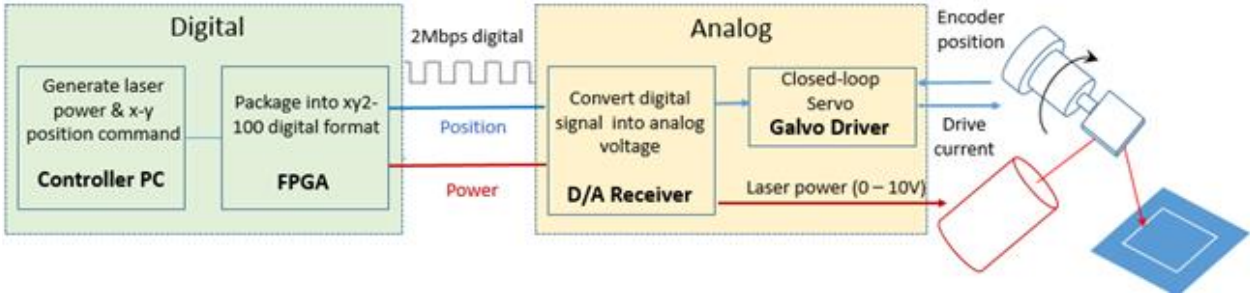

Figure 7: Laser path and power control.

Prototyping System

Certain design considerations for the AMMT/TEMPS required physical testing and evaluation of components, in particular to determine attributes that cannot be modeled using ray tracing software. In addition, the anticipated complexity of the monitoring and control system warranted attention prior to final system construction. In order to conduct these tests and initiate controller programming, the *prototyping system* was built which incorporates the laser, optics for the laser injection, galvo mirrors and driver system, and similar COTS components that will go into the process control module. Figure 8 shows a solid model schematic of the prototyping system with highlighted beam paths. Grantham et al. described several initial characterization tests, including laser spot size measurements, temporal laser control, and thermal load testing of various components to determine heating rates due to continual laser operation [3]. In the final AMMT/TEMPS facility, a prototyping system will exist along-side the full AMMT system with replicate components and similar capabilities to allow various testing and development before implementation on the AMMT.

Multiple other tests are currently being performed on the prototyping system, and are published elsewhere in this conference proceedings. These include system performance and control tests to evaluate the scan speed, acceleration, laser on/off timing, and positional accuracy of the laser spot. Results from these tests determined that the COTS galvo controller and command software were inadequate for our purposes, which initiated development of a custom design. Other tests include basic process mapping tests of single weld tracks, and simple scan patterns to provide qualitative comparison to commercial LPBF systems.

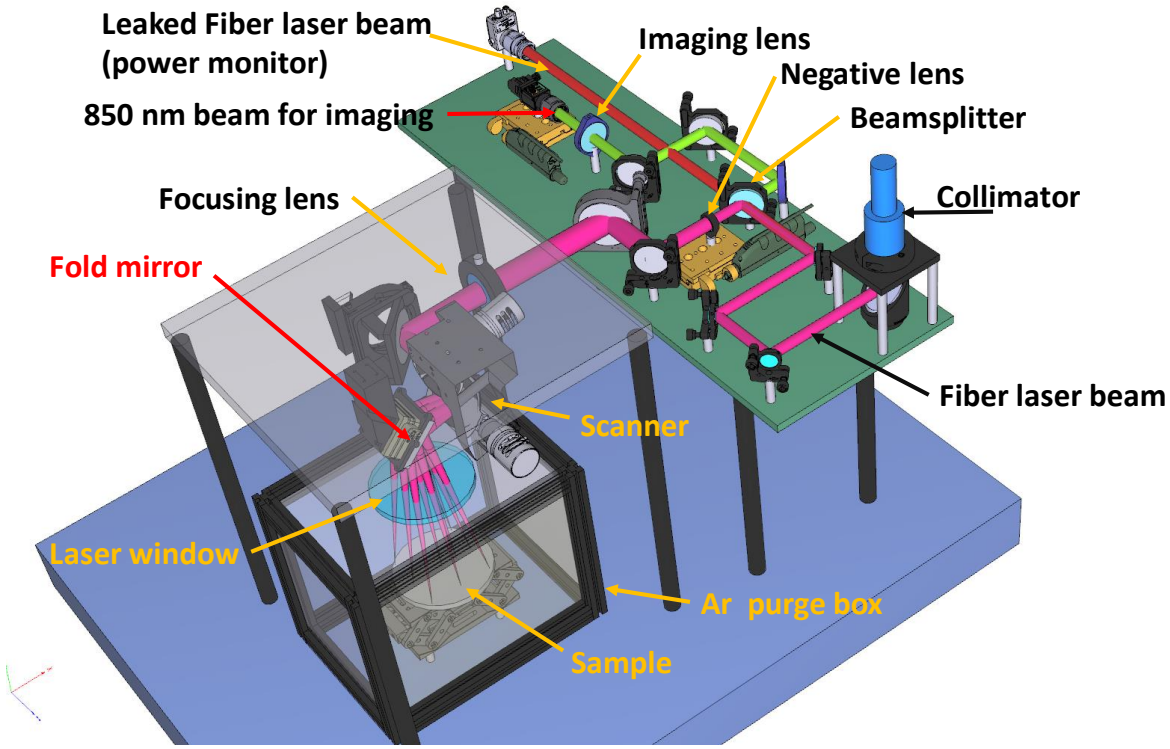

Figure 8: Schematic showing physical location of components within the prototyping system. The prototyping system is built on an optical table surrounded by a laser safety curtain.

One of the more important tests was to determine the level of optical throughput initiating from an incandescing melt pool and passing to the co-axially aligned sensors. Although one can calculate the expected optical throughput, adequate knowledge of the true melt pool temperature and emittance is very limited, therefore physical testing was necessary. Essentially, these tests were to determine at what integration time could the imager 'see' the melt pool. Though the custom optics for optimized resolution were not yet available, comparable signal from final optical design throughput is well approximated by the prototyping system.

The imager tested had 5.5 µm/pixel pitch, quantum efficiency of 63% (measured at 545 nm), and used the 850 +/- 25 nm bandpass filter. While scanning on bare 17-4 stainless steel (no powder) at 800 m/s scan speed and 200 W laser power, the center of the melt pool just saturated the imager (reached 4096 digital levels at 12-bit A/D) at an integration time of 100 µs, shown in Figure 9. During the 100 µs, the melt pool traveled 80 µm, or the approximate equivalent of 15 pixels. However, given the fact that the melt pool is stationary within the image, any motion blur will stem from perturbations in the melt pool size or intensity rather than its motion. Although the true melt pool size (defined by the liquidus/solidus boundary), approximated temperature, or other absolute measures cannot yet be determined, these tests indicate that there is adequate signal level to move forward.

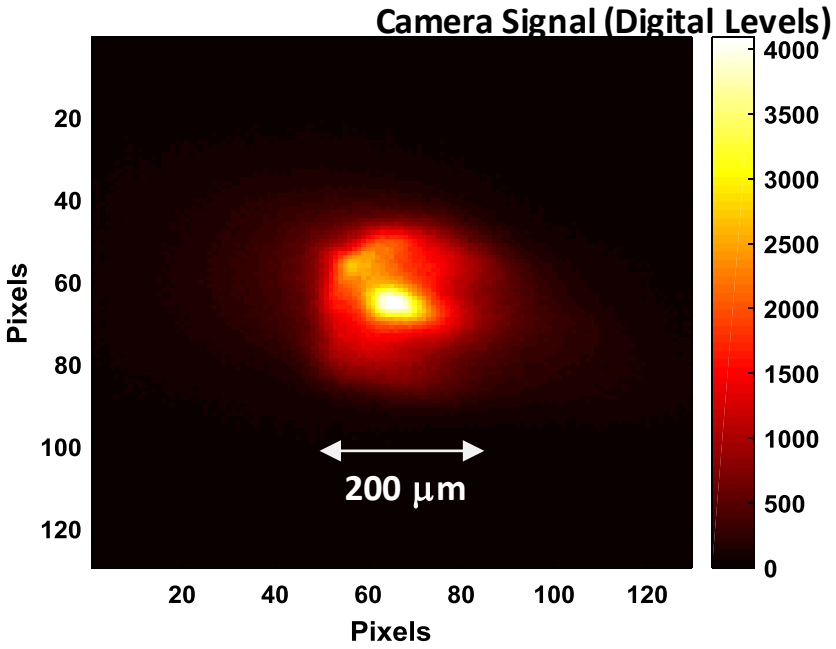

Figure 9: Melt pool image from co-axial imager in the prototyping system. Initial imaging tests were used to determine imager signal level vs. integration time.

Conclusions

This report reviewed the higher-level design of the AMMT/TEMPS system currently being constructed and tested at NIST. The system is essentially an LPBF additive manufacturing system, with a plethora of primarily optically-based sensor systems to enable high fidelity and well-characterized analysis of the melt pool and heat-affected zone. The two overarching purposes (additive manufacturing and materials optical property research) meet the combined interests of the NIST Engineering Laboratory (AMMT) and Physical Measurement Laboratory (TEMPS), respectively. The overall design applies concepts of modularization and accessibility to allow users to work to more easily on the instrument, and access and configure various modules separately from the main system. In addition, overall design flexibility and reconfigurability allow new experiment designs to be more easily incorporated, or various optical beam paths to be accessed for material property characterization, or AM monitoring and control. Foremost, full controllability and characterization enable users to fully define the LPBF process parameters to a high precision, and know how the system responds.

References

[1] Vlasea M, Lane B, Lopez F, Mekhontsev S E and Donmez M A 2015 Development of powder bed fusion additive manufacturing test bed for enhanced real time process control Proceedings of the Solid Freeform Fabrication Symposium (Austin, TX) p 527

[2] Dunsky C 2014 Process monitoring in laser additive manufacturing *Ind. Laser Solut.* **29**

[3] Grantham S, Lane B, Neira J, Mekhontsev S, Vlasea M and Hanssen L 2016 Optical design and initial results from NIST's AMMT/TEMPS facility vol 9738p 97380S–97380S–9

[4] Hanssen L, Kaplan S, Mekhontsev S, Khromchenko V, Burnett J and Zeng J 2015 Status Update of the NIST Infrared Optical Properties of Materials Program *Conf. Charact. Radiom. Calibration Remote Sens. CALCON*

[5] Hanssen L M, Mekhontsev S N and Khromchenko V B 2004 Infrared spectral emissivity characterization facility at NIST vol 5405pp 1–12

[6] Slocum A H 1992 *Precision Machine Design* (Englewood Cliffs, N.J.: Society of Manufacturing)

CHARACTERIZATION OF FEEDSTOCK IN THE POWDER BED FUSION PROCESS: SOURCES OF VARIATION IN PARTICLE SIZE DISTRIBUTION AND THE FACTORS THAT INFLUENCE THEM

J. Whiting, J. Fox

Engineering Laboratory
National Institute of Standards and Technology, Gaithersburg, MD 20899

Abstract

Substantial efforts have been placed on characterizing and modeling additive manufacturing processes. The wide scope of work already done has focused on the effects of process parameters such as laser power, hatch spacing, scan speed and strategy, and layer thickness on the final part's properties. However, the characteristics of the actual powder should also be considered. The particles' size, morphology, roughness, and chemical composition will affect the final part properties including surface texture, density, tensile strength, and hardness. This paper will share some of the measurement methods used at the National Institute of Standards and Technology (NIST) to better understand metal powder for additive manufacturing. These include the striation/separation in transportation and handling, sampling procedures, and the actual spreading of powder in the laser powder bed fusion process. Results are presented that illustrate variations in the particle size distribution as a function of location on the build platform, substrate/part surface condition, and vertical position.

Keywords: Powder bed fusion; particle size distribution; powder spreading

1 Introduction

The powder bed fusion (PBF) process allows complex geometries to be additively manufactured (AM) in various metals and alloys. The process consists of a focused laser (≈ 100 µm spot size) that melts specific regions of metal powder. Between laser scans, the build area is incrementally lowered allowing the recoating mechanism (usually a stiff blade or roller) to spread thin, 20 µm to 50 µm, layers of metal powder. While there has been increased industry use in recent years, the inability to ensure repeatable final part properties remains a primary factor preventing the widespread use of AM processes. These properties include tensile and fatigue strength, hardness, surface roughness, and density, all of which are highly dependent on the process parameters and conditions. The localized heating and cooling introduces residual stress that is often location dependent due to changes in geometry or scan strategy [1]. The environmental conditions as well as the part layout have been found to affect the final part properties [2-3]. Additionally, the final mechanical properties of a part depend on the orientation in which a part is built [4].

Though there has been substantial focus on documenting, modeling, and providing solutions for these known sources of variability in the PBF process, focus must also be placed on understanding the role played by the characteristics of the metal powder. Yadroitsev et al., using an analysis of variance, found the particle size distribution (PSD) to be a statistically significant

variable affecting the contact angle of a single track and the ratio of the remelted depth to the height of a single track [5]. Other groups have conducted similar research. Spierings et al. conducted an experiment using three stainless steel powders (316L), each of different size distributions to investigate the effect of the PSD of powder on the density, surface roughness, and mechanical properties of final parts. They found particle size to have significant effect on all three of the dependent variables measured. While it was possible to create 99% dense parts using each powder, the scan strategies needed to be individually optimized for each [6]. In a similar fashion, Gu et al. investigated the microstructural and mechanical properties of AM parts created using a titanium alloy powder (Ti6Al4V) procured from three separate suppliers. Again, using equivalent parameters, powders with different PSDs produced final parts with substantial differences in their tensile properties [7]. A similar comparison is made by Liu et al. using two powder types with similar mean sizes (< 2 μm difference), but dissimilar distributions. One of the 316L powders had a log-normal distribution and the other featured a skewing towards smaller particles. Although at low energy densities (created by either reducing the beam size or increasing the scan speed) the log-normally distributed powder created parts with significantly lower density and substantially rougher side surfaces, the same powder also produced parts with higher tensile properties [8].

All of the aforementioned findings share one thing in common: they serve as evidence that the PSD of the powder used in AM plays a significant role in determining the final part properties. Recognizing this, it becomes apparent that any sources of variability in the PSD of AM powders must be identified and documented. Slotwinski et al. have found PSD of the AM materials to vary depending on the location in the machine [9]. They found that particles larger than 60 μm were more likely to be spread past the build plate and consequently were not used in the build. The variability was attributed to the limited space (a layer height of 20 μm was used in the experiment) between the lower edge of the recoating mechanism and the prior layer of powder. It was theorized that the larger particles were unable to easily pass under the recoater, and were therefore spread over the powder bed and eventually into the collector. Besides this work, there has been very little published that characterizes spatial inconsistencies of the PSD of AM powders.

As it has been clearly shown that the PSD affects the repeatability of the PBF process and a variability in the PSD as a function of the location in the machine was documented [9], it is paramount that this spatial dependence of the PSD be investigated further. The work presented here investigates sources of variability in the PSD of metal AM powder in three situations: in a container in an as-received condition, in a loose powder bed, and in a powder bed with solidified parts.

2 Experimental Procedure

2.1 Sampling

While the situation in which powder is collected may differ, the basic tools remain the same. Firstly, the powder must be extracted in a controlled manner. As directed in ASTM B215 [10], a slot sampler should be used to extract powder in a loose, bulk condition. The conventional slot sampler, similar to a soil core sampler, is used to collect a continuous cylindrical volume of powder, making it nearly impossible to keep a free-flowing granular material from mixing during the sampling. In order to quantify any vertical segregation of particle sizes, discrete volumes must be sampled at incrementally deeper positions. The custom slot sampler, shown in Figure 1, features a conical tip to reduce the disturbance of the bulk powder as the device is plunged into the granular material as well as both a rotating collecting shaft that allows a controlled opening or

closing of the sampling volumes and a handle that provides ergonomic handling of the sampler. The volumes of the collection pockets are chosen to provide an optimal sample mass (≈0.3 g) for the later-described particle size analysis. While too little powder will decrease the accuracy of the PSD by measuring less powder, alternately, if too much powder is collected, the powder must be resampled, which often introduces biases depending on the sampling location. These biases can be minimized or possibly completely avoided with the use of a proper sampling technique like a riffler. Riffling is a technique that allows a bulk powder to be divided into smaller samples, each of which is a good representation of the original powder. The technique, suggested in ASTM B215 and illustrated in Figure 2, consists of the collection of powder from a stream of powder. The bulk powder is directed towards a chute by means of vibration. Upon exiting the chute, the powder is allowed to fall into a series of moving containers. If any segregation was present, it will be divided amongst each of the containers, assuming the riffler is operated correctly. With increasing numbers of rotations of the collection containers, the effectiveness of the operation increases, but the rule-of-thumb is that 100 rotations must be completed by the time all of the powder has flown through the chute.

The other situation in which powder must be collected is when it is sparsely spread on a solidified AM part. The part's upper surface is relatively rough (R_a from 9 µm to 19 µm [8]), which makes collection difficult. Mechanical removal, such as brushing or scraping, is ineffective in removing the powder. An apparatus was designed and fabricated allowing a vacuum to be used to collect powder in a controlled manner. This device will be described in detail in a later publication.

Figure 1: Custom slot sampler

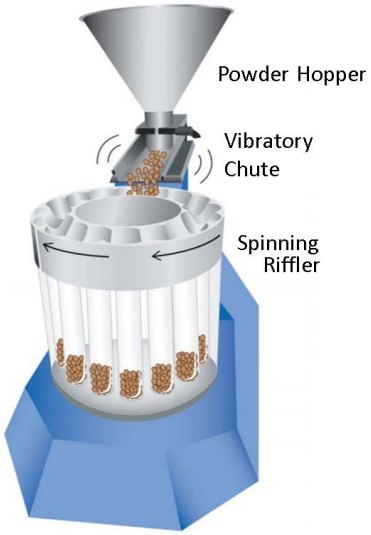

Figure 2: Schematic of a spinning riffler [10]

2.1.1 Powder As-received

Three 10 kg containers of stainless steel powder (17-4PH) are used to investigate any segregation of the powder's PSD. Most powder manufacturers ship metal powders in a plastic container that has been filled with argon prior to being sealed shut. The container often contains a silica gel desiccant to absorb any moisture. Each of the containers is opened and the desiccant

removed prior to being sampled with the slot sampler. All containers are sampled at their radial centers at three different heights. The lowermost sample has its vertical center at a height approximately 7 mm from the bottom, while the middle and top samples are approximately 44 mm and 88.5 mm from the bottom, respectively. Each of the samples taken is approximately three grams, which, being too large for the particle size analyzer, is riffled into eight samples prior to being measured.

2.1.2 Powder Bed

A loose powder bed is created by repeatedly spreading 20 µm layers of powder in a commercial PBF system without scanning the laser. The system uses a dispensing bed that moves incrementally up, providing powder to be spread across the build plate. The bed is built up to 2500 layers (50 mm total depth) prior to being sampled. The custom slot sampler, shown in Figure 1, is used to sample powder at nine locations in the build bed (see Figure 3) and one centrally located position in the dispenser.

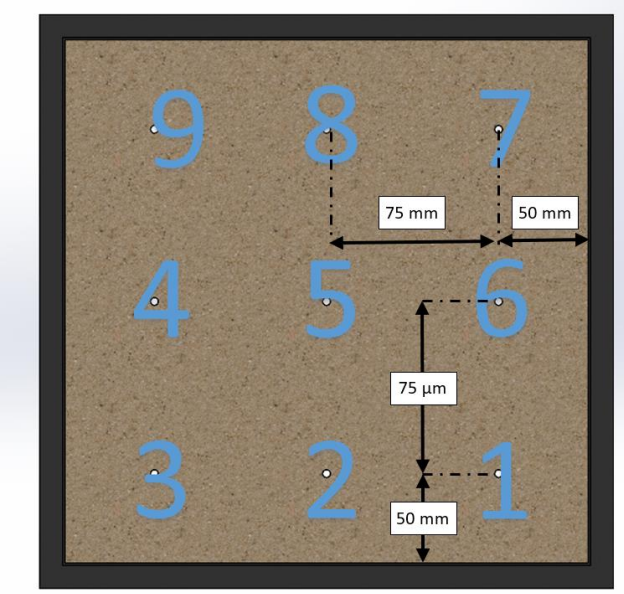

Figure 3: Sequence and locations of powder collection; the dark outlined perimeter refers to the outer edges of the build plate

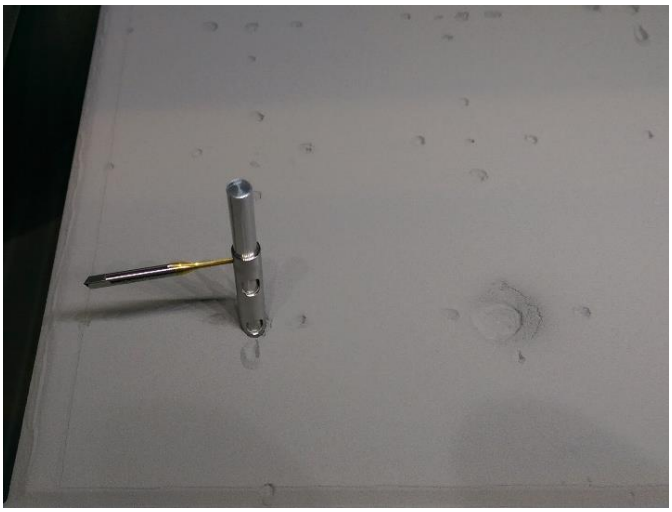

Figure 4: Custom slot sampler extracting powder in position #3

2.1.3 Powder on a Solidified Part

In order to be able to extract powder from the surface of a solidified part, the aforementioned vacuum apparatus is used. Filters with a pore size of less than 6 µm ensure that no particles pass through the filter. Powder is also extracted from before and after the part (where right refers to the side of the machine in which powder is dispensed) in order to allow the effect that the part's presence has on the spreading of powder to be better understood. The custom slot sampler (Figure 4) is used to extract powder from the part's vicinity. The sampler is pushed against the part's right side so that the outer edges of each are tangential. This is done to ensure that the sample extracted was from powder that was deposited onto the loose powder bed immediately prior to the recoater passing over the part. Powder is taken in a similar manner on the Collector

side to ensure the sample taken is from the powder that was pushed over the part and deposited in the region to the part's left (see Figure 5 & 6).

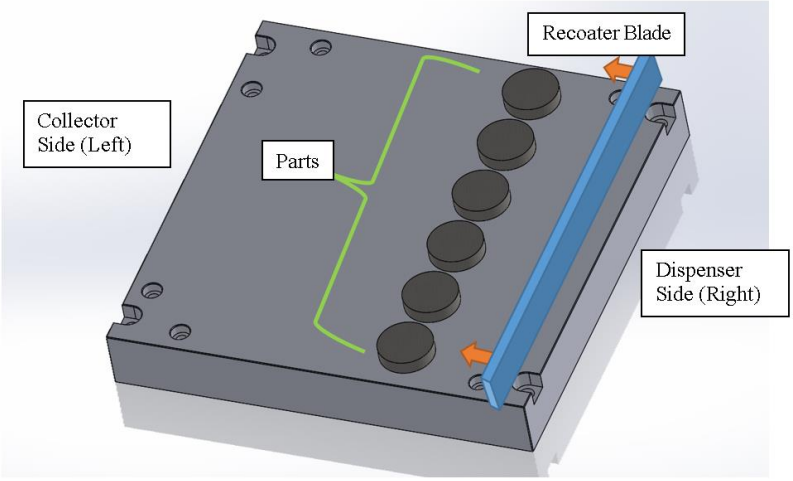

Figure 5: Build plate and part layout

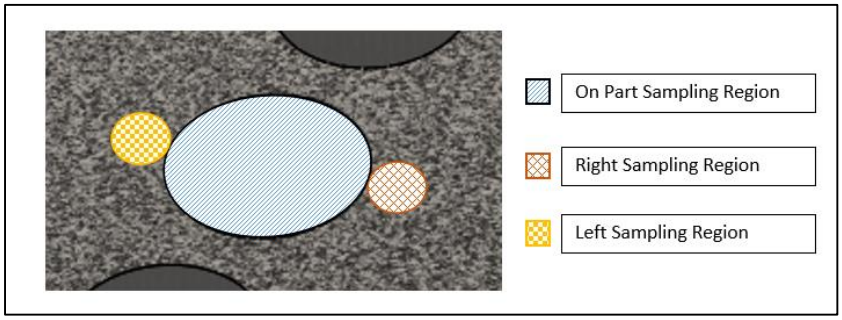

Figure 6: Sampling regions on, right, and left of solidified part

2.2 Measuring Size and PSD

An optically-based particle size analyzer is used to characterize the powder. The device uses two charge-coupled device cameras to conduct a dynamic image analysis method (ISO 13322-2). One of the cameras uses a higher magnification to resolve smaller particles and provide more accurate morphology measurements. The camera has a resolution of about 1 µm per pixel. There are numerous metrics that can be used to characterize the size of a particle, not to mention its morphology [11]. When measuring a particle that is not perfectly spherical, the methods used to characterize even something as simple as the diameter are not direct. Figure 7 illustrates a few of these methods. The Martin diameter uses the area bisector of the particle's profile, while the Feret or caliper diameter is the distance between two tangent lines that are perpendicular to the measurement direction. Another commonly used metric is the projected area diameter, which is the diameter of a circle having an equivalent area as the particle. Since nearly all of the particles in AM metal powders are nearly spherical and convex [9], the Feret or caliper diameter is reported in this paper. Additionally, the results from a size analysis can be reported in terms of the number, weight, or volume of the particles. Since the optically-based method measures the area of the particle's projection, and this area of a nearly spherical particle can easily be converted to volume, the results will be reported in terms of volume.

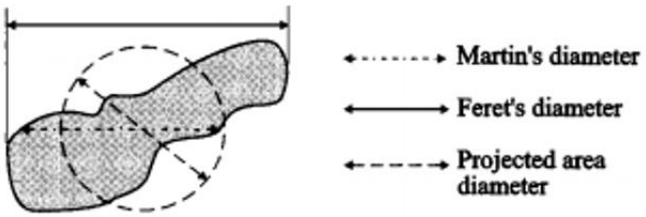

Figure 7: Methods of describing a non-spherical particle's diameter [12]

Results from particle size measurements are most often reported as either a cumulative or a frequency size distribution. A frequency size distribution plot is similar to a histogram with a series of size bins on the *x*-axis and the percentage of their respective populations (based on number, volume, or mass) on the *y*-axis. A cumulative size distribution also has the size of the particle on the *x*-axis, but the *y*-axis is displayed in terms of the accumulative percentage of the particles. As mentioned, the metric of "particle size" can be specified in many ways; this paper will report the particle size in terms of the Feret diameter. The cumulative and frequency distribution will always be reported in terms of particle volume. The D_{10}, D_{50}, and D_{90} of a sample's PSD refer to the maximum size corresponding to 10 %, 50 %, or 90 % of the particles. Unless otherwise noted, each powder sample is measured five times, and the plotted PSDs use the average of these five measurements for each size class with the standard deviation plotted as error bars.

3 Results and Discussion

3.1 Powder As-received

Table 1 and Figures 8-10 illustrate the PSDs at the three heights of the three containers sampled. It should be noted that the containers sampled were known to have dissimilar PSDs. To show this, the frequency distribution of the top location of each powder is plotted in Figure 11. Powder B has virtually no segregation of particle sizes, while Powder A and Powder C seem to have a slight variability with height. The sample taken from the middle height has the smallest particles of all three of the powders, though as shown in Figure 9, the change in the PSD of Powder B's samples is almost indiscernible. From this result, the difference in the initial PSDs seems to affect the segregation seen in the containers. However, the magnitude of the variation is on the same order as the 1 µm resolution of the particle size analyzer, and, considering the ranges of the PSD's standard deviations ($.04 < \sigma < .68$) shown in Table 1, this difference may be negligible.

Table 1: D_{10}, D_{50}, and D_{90} of the maximum Feret diameters and respective locations of powder collected from containers

	D_{10}		D_{50}		D_{90}	
Powder (location)	Average	σ	Average	σ	Average	σ
Powder A (top)	21.12	0.04	31.34	0.11	47.96	0.30
Powder A (middle)	20.28	0.15	30.04	0.30	45.84	0.50
Powder A (bottom)	20.82	0.22	30.74	0.26	46.80	0.51
Powder B (top)	26.12	0.08	37.86	0.21	55.98	0.68
Powder B (middle)	25.94	0.11	37.68	0.15	55.30	0.41
Powder B (bottom)	26.40	0.07	38.10	0.07	55.78	0.45
Powder C (top)	23.76	0.11	37.40	0.14	56.08	0.19
Powder C (middle)	22.78	0.08	35.46	0.13	54.48	0.26
Powder C (bottom)	23.88	0.08	37.04	0.17	55.58	0.24

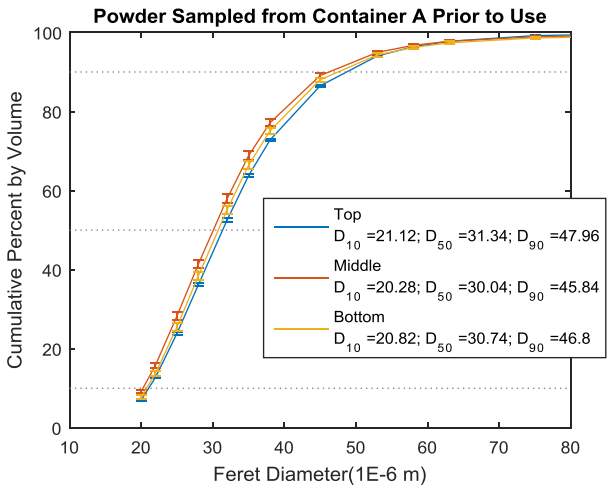

Figure 8: Cumulative size distribution of the maximum Feret diameter of the powder sampled from three heights in the Powder A container

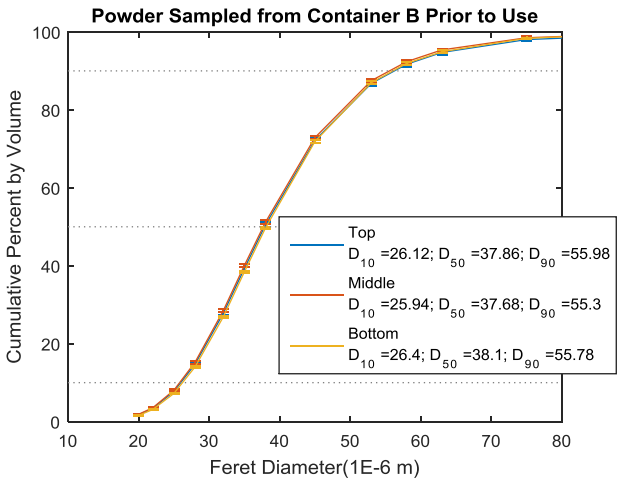

Figure 9: Cumulative size distribution of the maximum Feret diameter of the powder sampled from three heights in the Powder B container

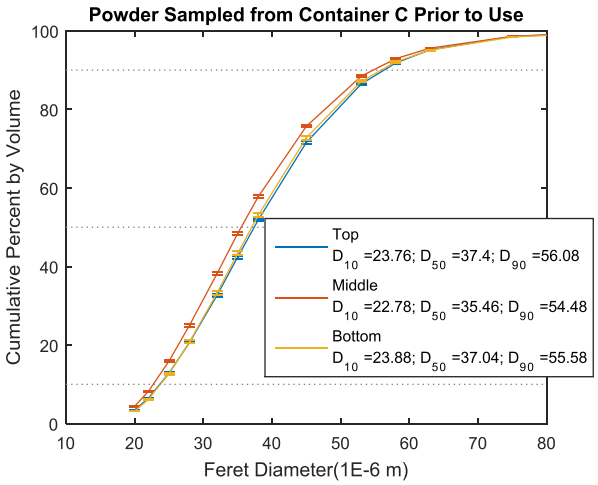

Figure 10: Cumulative size distribution of the maximum Feret diameter of the powder sampled from three heights in the Powder C container

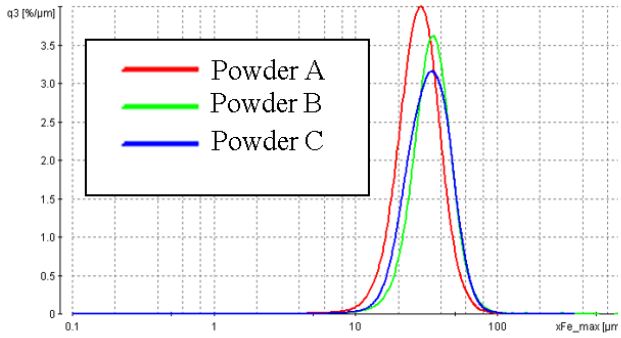

Figure 11: Frequency size distribution of the maximum Feret diameter of the powder sampled from the 'Top' location from each of the powder types

Box and whisker plots of the D_{10} are shown in Figure 12. The blue outline represents the 25th and 75th percentiles of the five measurements taken while the red line shows the median. The 'whiskers' (referring to the black lines) are the range of all values that are not considered outliers. A datum is considered an outlier if it is larger than q3 + 1.5(q3 – q1) or smaller than q1 – 1.5(q3 – q1), where q1 represents the 25th quartile and q3 the 75th. Figure 12, as well as Table 1, show the difference between the three locations. The powder sampled from the 'middle' location is smaller in all three powder types, but the difference is much more prevalent in Powder C and Powder A. A similar trend is seen in the D_{50} and D_{90} values. This vertically centered concentration of smaller

particles may be due to the manner in which the powder was loaded into the container or the disturbance from handling and transportation. Jenike theorized [13], Rémi and Meakin modeled [14], and Savage and Lun showed empirically [15] that finer particles often concentrate near the center of a pile of powder that has been poured. The smaller particles tend to cohere to one another, while the larger particles roll off to the side more easily. It is possible this same mechanism is driving the segregation seen here. As the container is rotated and jostled, the larger particles may move more easily to the extremities of the container. These small variations in the PSD as a function of height likely do not warrant the need for mixing prior to use. It is noted that more research is needed to verify these findings, as this is a narrow view of this segregation.

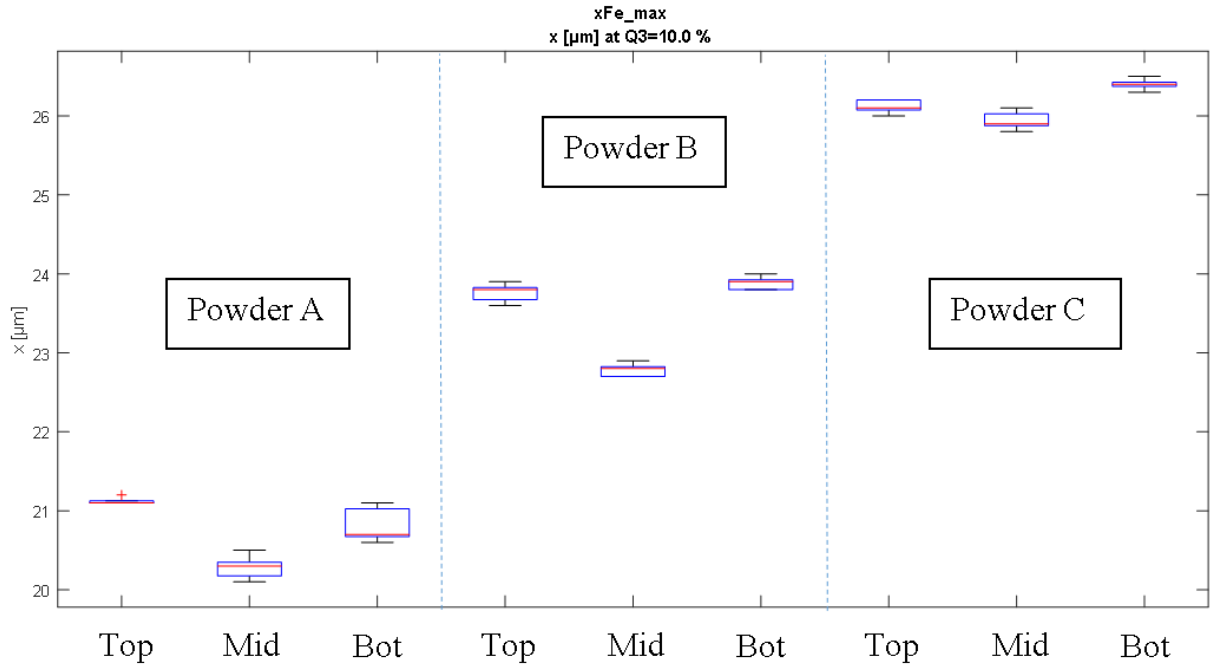

Figure 12: Box plots including 25th and 75th percentiles, median, range and outliers of D_{10} values of maximum Feret diameter; values are volume-based and data points are considered outliers if larger than q3 + 1.5(q3 – q1) or smaller than q1 –1.5(q3 – q1)

3.2 Powder Bed Sampling

Shown in Figure 13, there is very little difference in the powder sampled across the loose powder bed. The D_{50} of the powder sampled shows the largest range of size at 1.5 µm, which is very close to the 1 µm resolution of the optical particle size analyzer. As the variability of the PSDs approach this resolution, concerns regarding the uncertainty introduced throughout the experiment arise. Furthermore, the standard deviation from the five measurements used in calculating the PSDs ranges from 0.09 µm to 0.74 µm (Table 2) which is of a similar magnitude as the ranges documented. These trends are representative of what is seen in other samples.

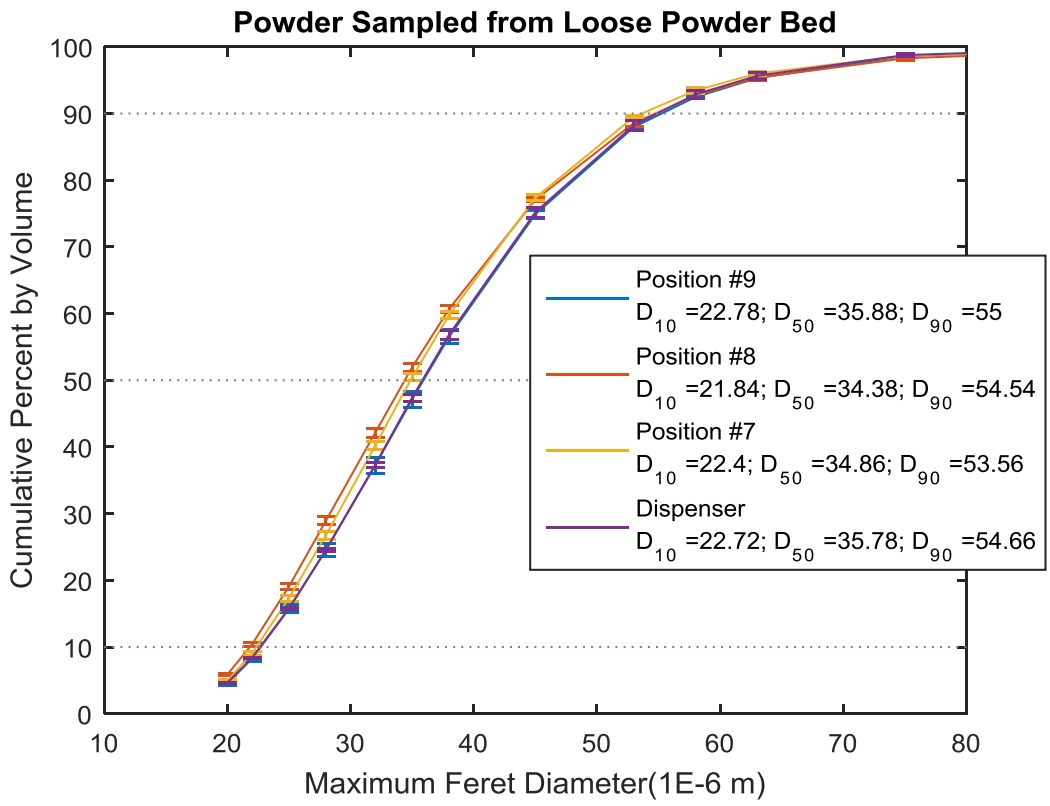

Figure 13: Cumulative size distribution (volume-based maximum Feret diameter) of powder sampled from a loosely spread powder bed using the custom slot sampler

Table 2 lists the standard deviations (σ) and D_{10}, D_{50}, and D_{90} of each of the powder samples from the '7'- '8'- '9' row (see Figure 3 for collection locations). The trends seen here are indicative of a spreading process that has little influence on the trends previously seen in the PSD of powder in the PBF process. This is potentially due to the loose, unpacked nature of the powder bed. While a limited gap between the recoating blade and the part surface or substrate limits the size of particles that can pass under, a loose powder bed may allow larger particles to embed themselves into the previously spread particles. The next section explores the influence of solidified parts on the PSD of the spread powder.

Table 2: D_{10}, D_{50}, D_{90} and standard deviations of the maximum Feret diameters and respective locations (diagram in Figure 3)

	D_{10}		**D_{50}**		**D_{90}**	
Powder Location	Average (μm)	σ (μm)	Average (μm)	σ (μm)	Average (μm)	σ (μm)
7	22.40	0.12	34.86	0.17	53.56	0.29
8	21.84	0.09	34.38	0.22	54.54	0.51
9	22.78	0.19	35.88	0.36	55.00	0.19
Dispenser (center)	22.72	0.08	35.78	0.16	54.66	0.74

3.3 On and Off Part Sampling

As seen in the previous two sections, there is minimal segregation of particle sizes in the as-received powder and in a spread powder bed, but there has been documented variability in the PSD of powder in the collector versus powder in the dispenser [9]. Therefore, the presence of solidified part surfaces must play a significant role in the segregation of various particle sizes. Figure 14 contains a cumulative size distribution of the powder sampled from the surface as well as from the right and left of a solidified part. As previously mentioned, the right side refers to the side of the part closer to the dispenser. An obvious skew of the size distribution is seen between the powder taken from the part and samples taken from its vicinity. The 'Part' powder is substantially smaller, while the 'Right' powder is only slightly (a range of D_{50} of 1.16 µm) smaller than the 'Left'. There is also a change in the distribution of the 'Part' powder, which is more easily visualized in a frequency distribution (shown in Figure 15). The distributions of the 'Left' and Right samples are similar with a slight skew towards smaller particles on the Left. The PSD of the Part powder has substantially smaller particles (D_{50} =31.54 µm compared to 35.08 µm and 36.24 µm for the 'Left' and 'Right' samples, respectively) and is narrower. The surface of the solidified part appears to act as a filter of the powder being spread. While the step in the layer height is only 20 µm, due to the densification of the loose powder during the melting and solidification, the actual vertical distance between the recoater blade's underside and the solidified part surface is substantially larger. Using a similar method as theorized in [16], the effective, steady-state layer height for a 20 µm build plate movement is approximately 33 µm, assuming a 99% dense final part. Since this is around the D_{50} (maximum Feret diameter) of the powder spread, a large portion of particles are unable to pass under the recoating blade. Though due to the relatively rough top surface of the solidified part, the actual effective layer thickness is highly variable and might allow larger particles to settle in the valleys between laser tracks.

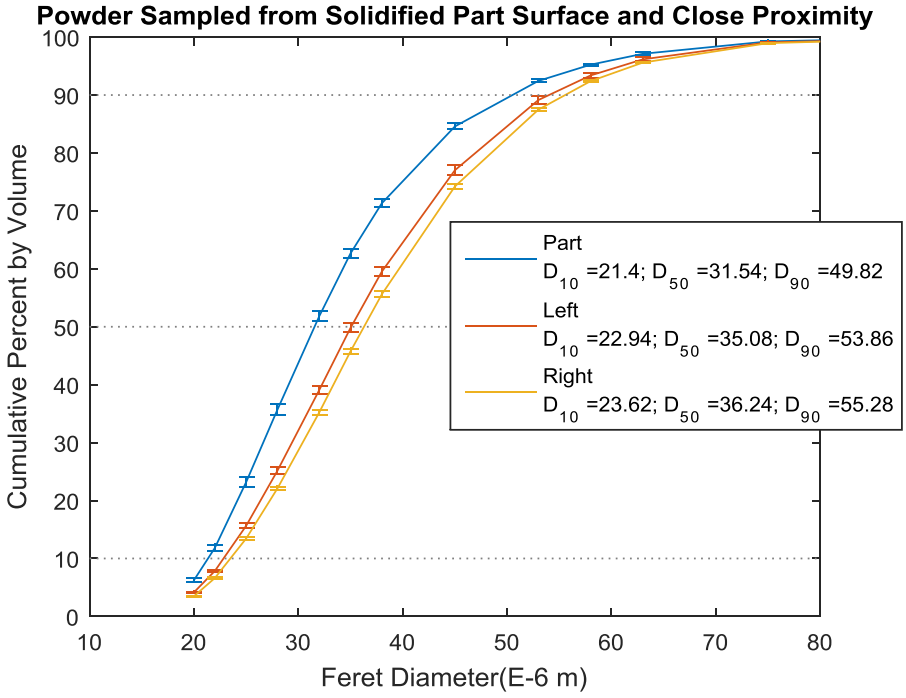

Figure 14: Cumulative size distribution (volume-based maximum Feret diameter) of powder sampled from the left, right, and surface of a solidified part

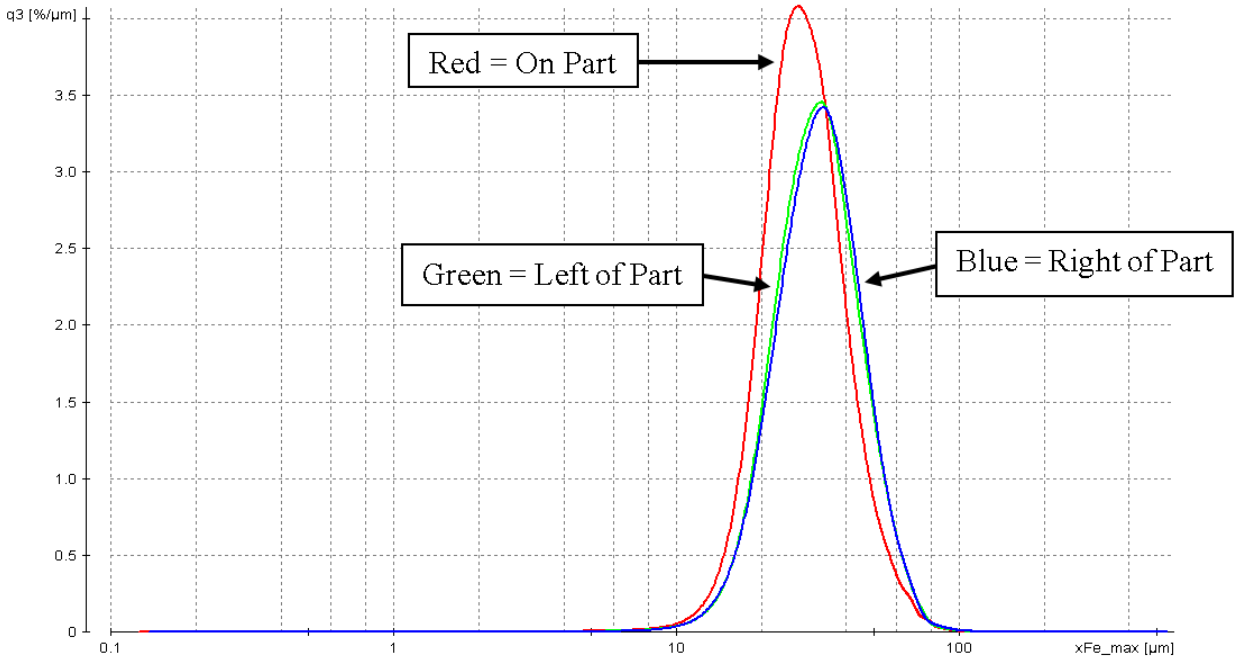

Figure 15: Frequency size distribution of powder sampled from the left, right, and surface of a solidified part; Red = on part, Blue = right of part, Green = left of part

4 Conclusions

The powder spreading in the PBF process is extremely complex. The fact that each powder particle is unique and that the cohesion forces between particles is dependent on the surfaces and geometries of these particles creates a very intricate process. Moreover, the intricate surfaces of solidified parts have been found to influence the spreading. While simplifications can and must be made in modeling efforts (e.g., perfectly spherical particles, smooth surfaces, finite size ranges), empirical analysis of the powder spreading must be conducted to ensure that the correct assumptions are made. The work presented here delineated the segregation of certain particle sizes in three situations. A minimal change in the PSD at different heights of the powder in its as-received condition was seen. There was also very little change in the size of the powder at different locations along the recoating direction of a loose powder bed. Significant differences in the particles collected from the top of a part versus the part's adjacent vicinity was seen, and potential reasons for this have been proposed. It is noted that the work shown here provides only a glimpse into the spatial dependence of the PSD of powder and should not be taken as concrete evidence but rather as a starting point for future research. Further research will focus on closely investigating the interaction between the powder and the recoating mechanism via empirical analysis as well as modeling. The rheological behavior of AM powders will be compared to the performance of the spreading in the PBF process.

References

[1] Mercelis, Peter, and Jean-Pierre Kruth. "Residual stresses in selective laser sintering and selective laser melting." *Rapid Prototyping Journal* 12, no. 5 (2006): 254-265.

[2] Simchi, A. "Direct laser sintering of metal powders: Mechanism, kinetics and microstructural features." *Materials Science and Engineering*: A 428, no. 1 (2006): 148-158.

[3] S. Dadbakhsh, L. Hao, and N. Sewell. "Effect of Selective Laser Melting Layout on the Quality of Stainless Steel Parts." *Rapid Prototyping Journal* 18, no. 3 (April 20, 2012): 241–49. doi:10.1108/13552541211218216.

[4] Paul, Ratnadeep, Sam Anand, and Frank Gerner. "Effect of thermal deformation on part errors in metal powder based additive manufacturing processes." *Journal of Manufacturing Science and Engineering* 136, no. 3 (2014): 031009.

[5] Yadroitsev, Igor, Ina Yadroitsava, Philippe Bertrand, and Igor Smurov. "Factor analysis of selective laser melting process parameters and geometrical characteristics of synthesized single tracks." *Rapid Prototyping Journal* 18, no. 3 (2012): 201-208

[6] Spierings, A.B., N. Herres, and G. Levy. "Influence of the Particle Size Distribution on Surface Quality and Mechanical Properties in Additive Manufactured Stainless Steel Parts." I*n 21st Annual International Solid Freeform Fabrication Symposium - An Additive Manufacturing Conference, SFF* 2010, 397–406. Austin, TX, United states, 2010.

[7] Gu, Hengfeng, Haijun Gong, J. J. S. Dilip, Deepankar Pal, Adam Hicks, Heather Doak, and Brent Stucker. "Effects of powder variation on the microstructure and tensile strength of Ti6Al4V parts fabricated by selective laser melting." *In Proceedings of the 25th Solid Freeform Fabrication Symposium*, Austin, Texas, USA, pp. 470-483. 2014.

[8] Liu, Bochuan, Ricky Wildman, Christopher Tuck, Ian Ashcroft, and Richard Hague. "Investigation the effect of particle size distribution on processing parameters optimisation in selective laser melting process." *In International solid freeform fabrication symposium: an additive manufacturing conference*. University of Texas at Austin, Austin, pp. 227-238. 2011.

[9] Slotwinski, J. A., E. J. Garboczi, P. E. Stutzman, C. F. Ferraris, S. S. Watson, and M. A. Peltz. "Characterization of Metal Powders Used for Additive Manufacturing." *Journal of Research of the National Institute of Standards and Technology* 119 (October 2014): 460. doi:10.6028/jres.119.018.

[10] ASTM Standard B215-15, 2015, "Standard Practices for Sampling Metal Powders." ASTM International, West Conshohocken, PA, 2003, http://dx.doi.org/10.1520/B0215-15.

[11] Cooke, April, and John Slotwinski. "Properties of metal powders for additive manufacturing: a review of the state of the art of metal powder property testing." US Department of Commerce, National Institute of Standards and Technology, 2012.

[12] Fan, Liang-Shih, and Chao Zhu. *Principles of gas-solid flows*. Cambridge University Press, 2005.

[13] Jenike, Andrew W. "Storage and flow of solids, bulletin no. 123." *Bulletin of the University of Utah* 53, no. 26 (1964).

[14] Jullien, Rémi, and Paul Meakin. "A mechanism for particle size segregation in three dimensions." *Nature* 344, no. 6265 (1990): 425-427.

[15] Savage, S. B., and C. K. K. Lun. "Particle size segregation in inclined chute flow of dry cohesionless granular solids." *Journal of Fluid Mechanics* 189 (1988): 311-335.

[16] Spierings, A. B., and G. Levy. "Comparison of density of stainless steel 316L parts produced with selective laser melting using different powder grades." *In Proceedings of the Annual International Solid Freeform Fabrication Symposium*, pp. 342-353. Austin, TX, 2009.

Towards a Road-Mapping Ontology for Open Innovation in Smart Manufacturing

Nenad Ivezic*, Miroslav Ljubicic
Systems Integration Division
Engineering Laboratory
NIST
Gaithersburg, MD, USA
{nenad.ivezic|miroslav.ljubicic}@nist.gov

***Abstract*— In nascent areas, such as Smart Manufacturing, new collaborative research and development programs (R&D) are frequently formed with the goal to ignite the innovation lifecycle. Yet, clearly formulating common goals and enabling shared understanding of key concepts, which are critical to achieving these goals, often involve long, drawn-out processes. These processes typically involve road-mapping that meet the need for informal, albeit imprecise and ambiguous, communications. We are starting to develop a road-mapping meta-model and an associated ontology to provide more precise and less ambiguous communications in a recently started R&D program on Smart Manufacturing. To that effect, in this paper, we analyze use cases to provide input into the meta-model and ontology development.**

Keywords - innovation; smart manufacturing; road-mapping; ontology; requirements; meta-model

I. INTRODUCTION

An essential task in R&D programs is to enable effective communication among the members of an emerging community, allowing efficient R&D program management, and open innovation processes. Traditionally, new R&D programs have been served well by developing road maps of planned activities. Such road maps often meet the need for informal, albeit imprecise and ambiguous, communications in emerging, cross-disciplinary communities. These communications issues can delay the completion of the road map considerably and inhibit the innovation process. For that reason, we explore Knowledge Technologies (KT) to enhance collaboration and communication in newly formed R&D programs by addressing the imprecision and ambiguity issues in road-mapping.

Our intention is to use KT to capture and represent the definitions of goals, issues, approaches, and other key concepts as information objects. We intend to share these concepts using new standards and available communication technologies. In doing so, we hope to achieve two goals. The first is to speed-up and improve the process of aligning different interpretations of these concepts. The second is to simultaneously reduce the number of interpretation conflicts that could impede that process.

In this paper, we lay a foundation for achieving those goals, and enabling collaboration, in a specific context: a new R&D program for Smart Manufacturing. That foundation will help in establishing an 'upper' ontology, which models key concepts in a 'generic' innovation process. That model helps to identify and enrich fundamental concepts and relationships that advance precision and remove ambiguities in communication within collaborating communities.

II. REQUIREMENTS

A recently started R&D program drives our exploration of KT for collaborative R&D program management. We adopt a traditional road-mapping framework as a base in addressing the need for shared concepts in the program management. We point to an opportunity to enrich the framework to address precision and ambiguity issues.

A. A New SM R&D Program – Enabling Composable Apps

National Institute of Standards and Technology (NIST) has initiated an R&D program to advance science of systems integration towards the vision of composable SM systems [1].

The new program explores the potential for provisioning of manufacturing services as unbundled "apps," which could be significantly more flexible and less expensive to use than the current monolithic manufacturing applications. However, integrating heterogeneous services is not a trivial job. In April 2016, NIST hosted a workshop, called *Drilling down on Smart Manufacturing -- Enabling Composable Apps*, to work with industry and academia on the technical and standards-based solutions that will be needed. A road-mapping effort is planned to enable effective collaboration in this growing community.

B. Road-mapping Concepts for Innovation Management

Road-mapping exercises are a common practice when initiating collaborative work in new, government-funded, R&D programs; cross-industry, technology-development efforts; and, company-specific innovation activities [2-5]. To help organize these exercises, a conceptual architecture for road-mapping has been previously proposed [6]. Figure 1 shows a view of the basic concerns addressed in the architecture. These concerns provide a base for understanding the kinds of communications needed in a collaborative, open, innovation setting. That setting requires consistent views of the (1) business/market context, which addresses the "why" questions, (2) system/product/service context, which addresses the "what" questions, and (3) technology/R&D capability contexts, which addresses the "how" questions.

Short Paper submission
* Corresponding author

Ivezic, Nenad; Ljubicic, Miroslav.
"Towards a Roadmapping Ontology for Open Innovation in Smart Manufacturing."
Paper presented at the 2016 International Conference on Collaboration Technologies and Systems,
Orlando, FL. October 31, 2016 - November 4, 2016.

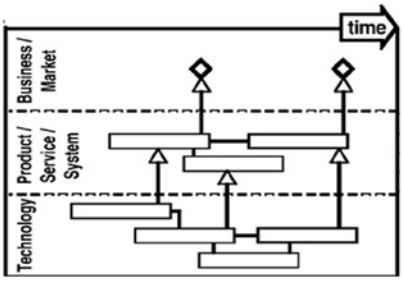

Figure 1. A Road-mapping Conceptual Architecture (after Phaal [6])

Using these road-mapping concepts, our requirements for shared conceptualization can be expressed with the following competency questions (CQs) [7]:

1) What Business Feature is of interest? A business feature is a specific characteristic of either a market driver or an enterprise driver of concern to the innovation effort.

2) What System Feature is of interest? A system feature is a characteristic of an implementable and usable artifact (such as a product, service, or system) that provides a desired effect with respect to a business feature of interest within the innovation effort.

3) What Technology (hereafter, Capability) Feature is of interest? A capability (technology or R&D resource) feature is an aspect of a capability that provides a desired effect with respect to a system feature within the innovation effort. It can be thought of as knowledge embedded in an artifact (either physical or informational) that provides some purposeful behavior with respect to an intended system function.

4) What System Feature enables a specific Business Feature? A system feature enables business features by way of some desired effect (often referred to as system function).

5) What Capability Feature enables a specific System Feature? A capability feature enables one or more system features by way of some purpuseful behavior, enabling the system function.

These questions are typically answered in an informal, imprecise, and ambiguous way when embarking on a traditional road-mapping effort. As an innovation effort matures, however, there is a need to make these answers more formal, more precise, and less ambiguous. This need can be met by a communication based on a richer set of concepts.

For example, in the NIST Smart Manufacturing R&D program, we have elaborated the three major concepts in Figure 1 as follows:

1) Business Feature: Efficient, usable messaging standards management processes.

2) System Feature: Messaging standards life cycle management (LCM) System.

3) Capability Feature: Business process model variability management method.

The following questions also arose from these elaborations.

1) What *key aspects* of efficient, usable messaging standards management processes describe desired business-level improvement for the intended innovation?

2) What are *key aspects* of messaging standards life cycle management (LCM) system for the intended innovation?

3) What are *key aspects* of the business process model variability management method for the intended innovation?

4) What is the *essential way* the messaging standards life cycle management (LCM) system impacts the efficient, usable messaging standards management processes?

5) What is the *essential way* the business process model variability management method aspects impact the messaging standards life cycle management (LCM) system aspects?

C. Enriching Road-mapping Concepts for Innovation

The following high-level CQs capture the general direction regarding requirements for enhanced shared conceptualization:

1) What properties effectively describe Business Features?
2) What properties effectively describe System Features?
3) What properties effectively describe Capabilities?
4) What properties effectively describe System Features enabling Business Features?
5) What properties effectively describe Capabilities enabling system Features?

III. DEVELOPMENT

In this section, we introduce new concept and relationship to support enriched communication in open innovation processes, leading to new competency question (CQ) types.

A. Developing Enriching Road-mapping Concepts

We saw how a traditional road-mapping framework provides a good basis to which enriching concepts can be added. We derived both general CQs and directions for specific CQs for communication about innovation processes.

We now propose an ontological structure to capturing and modeling those enriching concepts. We find inspiration for the enrichment from the research done in characterizing Behavior and Function concepts for product design and engineering [8]. The following properties are introduced in support of CQs:

1) What properties effectively describe Business Features?

a) Type: Is the business feature an external (market) or internal (enterprise) driver?

b) Performance: A measure of improvement of business utility due to the business feature; for example, time-efficiency, cost-efficiency.

2) What properties effectively describe System Features?

a) Function: A resource-processing ability, which takes material, energy, or information resources as input, and uses a processing method and a recipe to create a material, energy, or information resources as output.

b) Interface: Means and conditions to access a system function, including key non-functional aspects.

3) What properties effectively describe Capabilities?

a) Behavior: Specification of state changes of some capability resources as a result of interactions with the external world (aligned with the function interface).

4) What properties effectively describe System Features enabling Business Features?

a) Root Cause: An ability that prevents a drawback or problem, or that enables a capacity of relevance to the business feature.

5) What properties effectively describe Capabilties enabling System Features?

a) Mechanism: A transformation of behavior to function, which may be thought of as constraints imposed on behaviors (i.e., behavior properties we wish to be satisfied under certain conditions) to achieve a desired effect.

B. Using the Enriching Road-mapping Concepts

With the enriching conceptual properties, we are now in a position to state specific new CQs that support non-ambiguous interpretation and collaboration, such as the following:

1) What Performances, influenced by the Business Feature, are of interest?

2) What Function, enabled by the System Feature, allows the Performance of interest?

3) What Behavior, enabled by the Capability, allows the target Function?

4) What is the Root Cause that the Function impacts, causing the Performance of interest?

5) What is the Mechanism imposed on the Behavior, which enables the Function of interest?

In this way, we added (1) new road-mapping concepts and relationships to increase precision and decrease ambiguity in communication within open innovation processes; and (2) new CQs that may be answered once the enriched concepts and relationships are defined for the innovation area at hand.

IV. USE CASE ILLUSTRATIONS

In this section, we illustrate how new conceptual properties may support formulation of and responses to new, specific CQs. We take two use cases from the NIST Smart Manufacturing R&D Program on Composable Apps. For each use case, we provide values for the properties of the enriched conceptual road-mapping model that give answers to new CQs.

A. Use Case 1: Efficient, Usable Messaging Standards Management Processes

Table 1 shows new conceptual properties for the first use case, driven by *Efficient, Usable Messaging Standards Management Processes*, which provide responses to new CQs.

TABLE I. BUSINESS FEATURE: EFFICIENT, USABLE MESSAGING STANDARDS MANAGEMENT PROCESSES

CONCEPT/ PROPERTY	VALUE
Business Feature	**Efficient, usable messaging standards management processes**
- Type	External
- Performance	Time-Efficiency, Usability
- *Root Cause*	Identification, reuse, and construction of messaging standards based on well-defined business context, supporting consistent interpretation
System Feature	**Messaging Standards Life Cycle Management (LCM) System**
- Function	Creates and maintains, throughout life-cycle, consistent, business-context-specific messaging standards specification
- Interface	Messaging Standards LCM System User Interface (UI)
- *Mechanism*	Business Process and Message Exchange shared model definition
Capability	**Business Process Model Variability Management Method (Algorithm)**
- Behavior	Common patterns-based variability management of Business Process Model (BPMs) based on explicit Business Process and Message Exchange context conceptualization

B. Use Case 2: Consistent, Repeatable Integration Processes

Table 2 shows new conceptual properties for the second use case, driven by *Consistent, Repeatable Integration Processes*, which provide responses to new CQs.

TABLE II. BUSINESS FEATURE: CONSISTENT, REPEATABLE INTEGRATION PROCESSES

CONCEPT/ PROPERTY	VALUE
Business Feature	**Consistent, repeatable integration processes**
- Type	Internal
- Performance	Time-Efficiency
- *Root Cause*	Sharing of the aspects of the process (methods, terminology, guidelines) among the partners, preventing interpretation conflicts
System Feature	**Architecture/methodology for developing and maintaining standard-based, service-oriented integrations**
- Function	Creates and manages modularity-supporting, encapsulation-enabling, expandable, well-behaved systems integration/engineering approaches/specifications
- Interface	Design guidelines, tools
- *Mechanism*	Shared context definition model/ontology
Capability	**Evolvable/adaptable taxonomies and information models**
- Behavior	Terminology and conceptualization definition that can adopt to real world situations by iterative evolution of such terminologies and concepts for shared context definition of systems integration

V. Discussion

It is worthwhile to analyze the previous use cases in terms of value types assigned to conceptual properties. Next, we identify opportunities for development of KTs (i.e., road-mapping meta-model and ontology development) to support precise, unambiguous communication.

1) Business Feature (BF) refers to a process either including or following the System Function activities. This presents an opportunity to clarify and relate various Business Features, if they reference same value type, such as process.

2) Performance may take on numerous values that enable functional, utility-based, and non-functional reasoning. The property may also be used to prioritize desired performances.

3) Types may be only External, Internal, or External-Internal. This provides an easy way to clarify and discriminate between market, enterprise, or combined drivers.

4) Root Cause (RC) is either a characteristic (e.g., *"Sharing of the aspects of the process"*) or enumeration (e.g., *"Identification, reuse, and construction of messaging standards"*) of activities within and/or after the System Function activities. This presents an opportunity to clarify and relate various RCs. In addition, RC includes a statement of either enabling a capacity (e.g., *"supporting consistent interpretation"*) or preventing an issue (e.g., *"preventing interpretation conflicts"*). Enumerations of such capacities and issues of interest provides additional basis for clarification, comparison, and consistent interpretation.

5) System Feature (SF) is a description of a higher-level capability or a reference to an existing and, possibly, proven, capable higher-level approach (e.g., *"service-oriented integration"*) that relates to and informs the SF Function. References to shared codification of such higher-level approaches, architectures, or capabilities present an opportunity for disambiguation of an SF.

6) Function is a description of key transformations (e.g., *"creates and manages"*) and desired output and its qualities (e.g., *"encapsulation-enabling, expandable systems integration specification"*) that relates to and elaborates the System Feature description (e.g., What are implications of service-oriented integration?) Such specification of output qualities relates to the Root Cause (e.g., *"encapsulation-enabling, expandable systems integration specification"* positively affects *"sharing of the aspects of the processes"*).

7) Mechanism relates the external world to the Capability's Behavior, which references System Functions components (i.e., inputs, outputs, controls, and mechanism) within some form of a shared model that contains references to the outside world. Mechanism focuses on transformational aspect of the relationship between the Function and Behavior.

8) Behavior implies structure and content that relates to some specification of states and their changes, which constitute behavior. For example, in the second use case, the use of common patterns imply such states and changes, as the patterns are instantiated to create business process models. In other words, the state space and operators of change applied to that space are implicit in the set of the patterns and their parameterization used in business process modeling.

In addition, Behavior specification may be seen as making use of casual relations that govern that Behavior and imposes constraints on the relations, leading to desired System Functions. Behavior can be represented using ICOM (input, controls, outputs, mechanism) components of an IDEF0 model of system functions [9]. In that way, Behavior assigns properties to Function components and spells out intended meaning behind the Behavior concept.

VI. Conclusions

Our objective for this paper was to lay a foundation for knowledge-based methods in support of establishing and sharing definition of key concepts for innovation processes.

The primary contributions of the paper include (1) an extension of existing road-mapping architecture with concepts motivated from the Function-Behavior research; (2) a presentation of this conceptual foundation allowing greater precision and alignment in interpretations; and (3) illustration of application of such conceptual basis by answering competency questions for use cases from a new R&D program.

Our next steps include (1) adding temporal concepts to the model, addressing the strategic, innovative and operational activities, per road-mapping frameworks; (2) development of a formal metamodel and ontology, enabling a tool development based on the enriched model; and (3) evaluation of the enriched model for on-going road-mapping efforts in R&D programs.

Acknowledgment

Any mention of commercial products is for information only; it does not imply recommendation or endorsement by NIST.

References

[1] N. Ivezic, et al. (2015). "NIST Workshop on Open Cloud Architectures for Smart Manufacturing." [Online]. Available: http://dx.doi.org/10.6028/NIST.IR.8124.

[2] D. L. Bourell, D. W. Rosen and M. C. Leu. (2014). "The roadmap for additive manufacturing and its impact. *3D Printing and Additive Manufacturing*, vol. *1*, no. 1, pp.6-9.

[3] NIST. (2015). "Measurement Science Roadmap for Prognostics and Health Management for Smart Manufacturing Systems," [Online]. Available: http://www.nist.gov/el/isd/upload/Measurement-Science-Roadmapping-Workshop-Final-Report.pdf

[4] Semiconductor Industry Association. (1997). "*National technology roadmap for semiconductors*," SIA.

[5] J. M. Richey and M. Grinnell. (2004). "Evolution of roadmapping at Motorola.*Research," Technology Management*, vol. *47*, no. 2, pp.37-41.

[6] R. Phaal and G. Muller. (2009). "An architectural framework for roadmapping: Towards visual strategy," *Technological Forecasting and Social Change*, vol. *76*, no. 1, pp.39-49.

[7] M. Gruninger and M. Fox. (1994). "The role of competency questions in enterprise engineering," *Proceedings of the IFIP WG5*, *7*, pp. 212-221.

[8] B. Chandrasekaran and J. R. Josephson. (2000). "Function in device representation." *Engineering with computers*, vol. 16, no. 3-4, pp. 162-177.

[9] NIST, FIPS. (1993). "Publication 183: Integration Definition of Function Modeling (IDEF0)." National Institute of Standards and Technology,

Ivezic, Nenad; Ljubicic, Miroslav.
"Towards a Roadmapping Ontology for Open Innovation in Smart Manufacturing."
Paper presented at the 2016 International Conference on Collaboration Technologies and Systems,
Orlando, FL. October 31, 2016 - November 4, 2016.

Understanding Structure Ignition Vulnerabilities Using Reduced Size Sections of Building Components

MANZELLO, Samuel L.[1*], SUZUKI, Sayaka[2]

[1]*Fire Research Division, National Institute of Standards and Technology (NIST), Gaithersburg, MD USA*
[2]*Large Fire Laboratory, National Research Institute of Fire and Disaster (NRIFD), Chofu, Tokyo, JAPAN*

Abstract: The 2016 Fort McMurray, Canada, Wildland-Urban Interface (WUI) fire displaced more than 80,000 people, destroyed nearly 2,400 structures, and shut down nearly a quarter of Canada's oil production. Large outdoor fires in Japan mainly occur due to post-earthquake fires. Once structures are ignited in large outdoor fires, firebrand production from structures becomes a key factor in fire spread. Based on numerous post-fire disaster investigations, attached building components are known to be prone to ignition in WUI fires, and may provide pathways to structure ignition. The basis of this paper is to present ignition results for sections of full-scale building components using the recently developed experimental capability at the National Research Institute of Fire and Disaster (NRIFD). The building component sections were exposed to firebrand showers using a custom built continuous-feed firebrand generator with firebrand size and mass distributions similar to those measured from structure combustion. The results of this study are presented and discussed in this paper.

Keywords: Ignition, Firebrands, Large Outdoor Fires

1. Introduction

Recently, there have been significant number of wildfires that spread into communities, in Argentina, Australia, Brazil, Canada, Chile, France, Greece, Portugal, Spain, and the USA. Such fires are referred to as Wildland-Urban Interface (WUI) fires. Japan is another country that has been subject to large scale outdoor fires, but these fires have been initiated by earthquakes. A prominent mechanism of structure ignition in both WUI and urban fires is the production of firebrands, or embers [1].

Post-fire studies suggest that attached building components may provide a pathway for structures to ignite in WUI fires [see 2 for one example]. Examples of attached building components include decking and fencing assemblies. A recent study by the authors demonstrated that fencing assemblies may be ignited by firebrand showers, but the capability of the ignited fencing to transfer the fire to an adjacent structure, such as wall assembly, was not considered [3]. This was done intentionally, since the first step was to determine if firebrand showers could even ignite various wood fencing types.

As a result, this paper describes efforts to investigate the ability of firebrand showers to ignite fencing assemblies, and then observe the subsequent flame spread along the ignited assembly. Another significant difference with this work, from the prior study, is the fencing assemblies were exposed to firebrand showers similar to those produced from burning structures. As this is a very complex problem, sections of full-scale fencing/wall assemblies were experimented with using unique experimental capabilities developed by the authors at the National Research Institute of Fire and Disaster (NRIFD). These studies will provide guidance for further full-scale experimental campaigns focused on structure ignition by ignited fencing assemblies, such as those conducted at the Building Research Institute (Japan) [3], and recent studies conducted at NIST [4].

2. Experimental Description

Last year, the authors presented details of the recently developed reduced-scale experimental firebrand ignition facility at NRIFD at this conference [5]. The following experimental descriptions follows the facility closely. Yet, the details of firebrand generation differ significantly. The present focus was to generate firebrand showers similar to those produced from burning structures, not burning vegetation. This required using larger wood chips for firebrand generation than prior work. More details are provided below.

The reduced-scale continuous-feed firebrand generator consisted of two parts; the main body and continuous feeding component. The capability of a smaller-sized firebrand generator to develop continuous firebrand showers has been described [5].

For all experiments here, Japanese Cypress wood chips were used to produce firebrands. These were provided from a supplier and upon arrival, these chips were filtered using a 1 cm mesh to remove very fine wood pieces that settled during the shipping process. The chips were also oven dried, as they were shipped under wet conditions; moisture content was greater than 70 % on a dry basis. These size wood pieces were selected to produce firebrands with larger projected area at a specific mass than that used in our prior studies using continuous firebrand generation focused on vegetative firebrands. The wood feed rate used here was 80 g/min, which is near the upper limit for this reduced-scale firebrand generator [5].

As the base of the fan used to generate the wind in the NRIFD facility is located 1. 6 m from the floor, the conveyer was placed under a custom stage designed for experiments when using NRIFD's wind facility. The wind field exits from a 4.0 m diameter fan, and it is possible to generate wind speeds up to 10 m/s. The flow field was measured to be within ± 10 % over a cross-section of 2.0 m by 2.0 m.

When the blower was set to provide an average velocity below 4.0 m/s measured at the exit of the firebrand generator when no wood pieces were loaded, insufficient air was supplied for combustion and this resulted in a great deal of smoke being generated in addition to firebrands. Above 4.0 m/s, smoke production was mitigated but then many firebrands produced were in a state of flaming combustion as opposed to glowing combustion. In these experiments, glowing firebrands were desired [5]. It is important to note that these velocities are lower than those reported in [5], as different wood chips are used here as compared to Douglas-fir pieces used before.

Redwood lattice fencing assemblies were constructed for the experiments (see Figure 1). These were custom fabricated by using two, 0.61 m in height, 1.22 m in width, redwood lattice pieces, and held together using a 2 x 4 wood array.

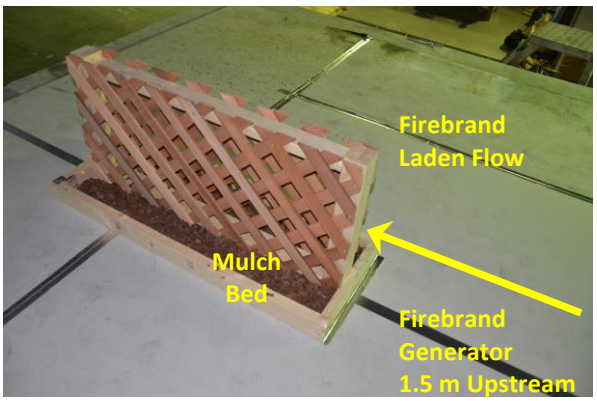

Figure 1 Picture of redwood lattice fencing assembly/mulch bed. These construction details were used for all experiments. All fencing assemblies (leading edge) were located 1.5 m from firebrand generator.

The redwood lattice pieces were purchased from a supplier in the USA. To simulate fine fuels that may be located near fencing assemblies, mini-pine bark mulch was used. Mini-pine bark nugget mulch was placed around the fencing assemblies at a depth of 51 mm (both sides). The mini-pine bark nuggets were oven dried and the density was 0.15 g/cm^3. Further details are shown in **Figure 1**.

3. Results and Discussion

Experiments were conducted for wind speeds of 4 m/s, 6 m/s, and 9 m/s. In all cases, the evolution of the ignition process was similar. Specifically, glowing firebrands ignited the mulch beds via smoldering combustion, and then the mulch transitioned to flaming combustion. These flaming mulch beds then ignited the redwood lattice fencing assemblies. **Figure 2** displays the temporal evolution of the ignition process for a wind speed of 9 m/s. At the highest wind speed considered, once the fencing assembly was fully involved in flaming combustion, significant firebrand production from fence combustion was observed (see **Figure 3**).

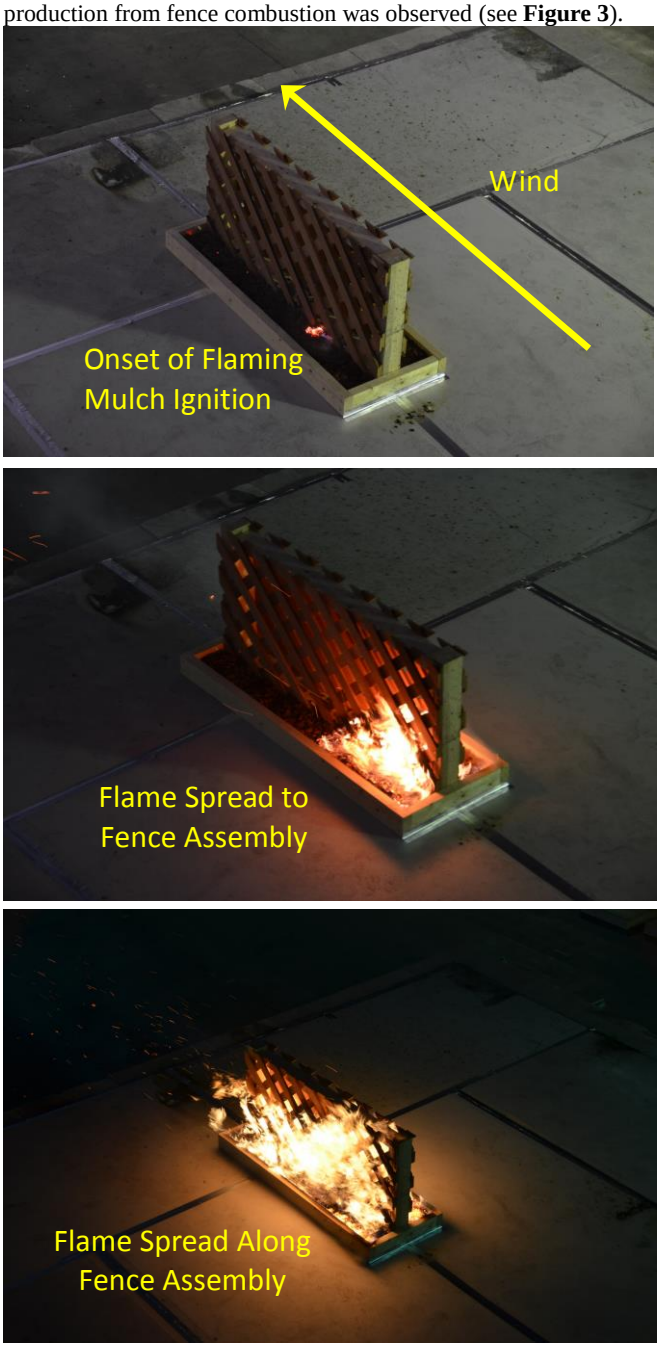

Figure 2 The temporal evolution of the redwood lattice fencing assembly/mulch bed for a wind speed of 9 m/s. The time from the top image to the bottom image is approximately 9 minutes.

Figure 3 Intense firebrand production was observed for the redwood lattice fencing assembly at 9 m/s.

The average number of firebrands arriving on the mulch beds was counted as a function of wind speed. To simplify the analysis, firebrands were counted on the left-hand side of the mulch bed, and these values were doubled for the entire assembly. Based on these analysis, the average total arrival number flux of firebrands was 6/m^{2}s, 5/m^{2}s, and 3/m^{2}s, for 4 m/s, 6 m/s. and 9 m/s, respectively. As the wind speed increased, less firebrands were able to deposit in the mulch beds. This result is qualitatively similar to past, full-scale experimental studies where the arrival number flux of firebrands decreased as the wind speed increased, for a given wall/mulch assembly [6].

The projected area of the firebrands directed at the fencing assembly/mulch bed was also quantified using a series of separate experiments where a water pan array was placed downstream of the firebrand generator. The firebrands were extracted, dried, and the mass (using balance) and projected area were determined using image analysis methods. Due to space limitations of this paper, these results will be presented at the conference.

4. Summary

This paper described results of experiments to investigate flame spread along fencing assemblies ignited by firebrand showers. As this is a very complex problem, sections of full-scale fencing/wall assemblies were experimented with using unique experimental capabilities developed by the authors at NRIFD. Firebrand showers resulted in ignition of the redwood lattice fencing assemblies with mulch beds present. For all wind speeds, flame spread was observed along the fencing assemblies. These studies will provide guidance for further full-scale experimental campaigns. The ability of a given burning fencing assembly to ignite adjacent wall assemblies will be considered in future experiments.

4. Acknowledgments

Mr. Marco G. Fernandez of NIST is appreciated for various assistance with this experimental campaign.

5. References

1. Manzello, S.L., *et al*., Workshop for Fire Structure Interaction and Urban and Wildland-Urban Interface (WUI) Fires – Operation Tomodachi Fire Research, *Fire Safety J*., 59:122-131, 2013.
2. Maranghides, A., *et al*., A Case Study of a Community Affected by the Waldo Fire – Event Timeline and Defensive Actions, NIST TN1910, 2015.
3. Suzuki, S., *et al*., Ignition of Wood Fencing Assemblies Exposed to Continuous-Wind Driven Firebrand Showers, *Fire Tech.*, 52: 1051-1067, 2016.
4. Johnsson, E., and Maranghides, A., Effects of Wind Speed and Angle on Fire Spread Along Privacy Fences, NIST TN 1894, 2016.
5. Suzuki, S., and Manzello, S.L., Reduced-Scale Experimental Facility to Characterize Firebrand Ignition, in Proceedings of the 53rd Japanese Combustion Symposium, Tsukuba, Japan, 2015.
6. Suzuki, S., *et al.*, Ignition of Mulch Beds Exposed to Continuous Wind-Driven Firebrand Showers, *Fire Tech*., 51:905-922, 2015.

The 24th CIRP Conference on Life Cycle Engineering

Using graph-based visualizations to explore key performance indicator relationships for manufacturing production systems

Michael P. Brundage[a]*, William Z. Bernstein[a], KC Morris[a], John A. Horst[a]

[a]*National Insitute of Standards and Technology, 100 Bureau Drive, Gaithersburg, MD, USA 20899-1070*
* Corresponding author. Tel.: +1-301-975-8798. *E-mail address:* michael.brundage@nist.gov

Abstract
Key Performance Indicators (KPIs) are crucial for measuring and improving the performance of a manufacturing process. An especially critical aspect of developing balanced process performance improvement strategies across all critical objectives is the need to discover the inherent relationships between all KPIs assigned to a targeted manufacturing process. This paper explores graph-based visual representations of the analytic relationships between KPIs and their underlying metrics to uncover and describe KPI relationships. Lessons learned are summarized as a list of requirements for the development of an interactive prototype that will allow users to dynamically explore KPI-related interdependencies through graph-based visualizations.

Peer-review under responsibility of the scientific committee of the 24th CIRP Conference on Life Cycle Engineering.

Keywords: Key Performance Indicators; Information Visualization; ISO 22400; Interdependencies; KPI Relationships; Manufacturing Process Improvement

1. Introduction

Manufacturers strive to monitor and improve the performance of production operations through the use of Key Performance Indicators (KPIs). KPIs indicate the level of performance a system is achieving through measurable attributes, such as the amount of material, energy, or time consumed in a process. With the advent of the Internet of Things (IoT) and the increasing availability of data in real time, manufacturers now have the opportunity to calculate a broad range of KPIs. KPIs are often interdependent; a common observation is that improving one KPI leads to a decrease in performance as indicated by another KPI, often inadvertently. Understanding these interdependencies can be a challenge due to their complexity. One would like to improve specific KPI performance without adversely affecting other KPIs. One of the challenges of IoT is navigating through an abundance of data but where the context for that data is often hard to ascertain. Often times, performance-related data is displayed on dashboards that do not provide sufficient details or the tools to properly explore KPIs and underlying metrics to drive improvement decisions.

While the relationships between various KPIs and their associated metrics are explored in literature [1], visualizations of these interrelationships are often an afterthought with basic tables providing a brief overview of pairwise metric/KPI relationships. Without a proper understanding of the complex relationships among KPIs, humans struggle to make the optimal improvement decisions. Furthermore, implementing KPI-related improvement strategies involves a wide range of organizational perspectives. A rich platform to explore KPI interdependencies will support multiple perspectives.

This paper proposes the use of graph-based visualization methods along with inputs from manufacturing process experts to address the above-mentioned challenges. The visualization techniques, both matrix- and network-based, are applied to select subsets of the 34 KPIs described in ISO 22400 [2] to highlight the interrelationships between various metrics and the associated KPIs. Best practices from the information visualization (InfoVis) community are evaluated for their suitability for KPI-related decision making. Lessons learned from the application of these practices will be used to develop a prototype interface for the exploration of KPI interdependencies.

The rest of the paper is structured as follows. Section 2 provides background on KPIs and visualization techniques. In Section 3, two graph-based visualization techniques—node-link diagrams and matrix-based layouts—are applied to illustrate the interrelationships of the KPIs. The different techniques are analyzed for their strengths and weaknesses, and lessons learned for visualizing KPI interdependencies are discussed. A prototype interface is presented that exploits advantages from both visualization techniques. Section 4 summarizes requirements for a hybrid visualization tool supporting dynamic exploration of KPI interdependencies and discusses requirements for KPI exploration where visualization may be effective.

Bernstein, William; Brundage, Michael; Horst, John; Morris, Katherine.
"Using graph-based visualizations to explore key performance indicator relationships for manufacturing production systems."
Paper presented at the 24th CIRP Conference on Life Cycle Engineering, Kanagawa, Japan. March 8, 2017 - March 10, 2017.

Table 1: KPIs and metrics used in this paper. Type includes KPIs (K), mid-level metrics (M), and low-level metrics (L). Shaded cells correlate to appearance in respective figure.

Abbr.	Name	Type	F1	F2	F3	F4	F5	F6
A	Availability	K	■	■	■	■	■	■
ADET	Actual Unit Delay Time	M	■			■		
ADOT	Actual Unit Down Time	L	■	■	■	■	■	■
AE	Allocation Efficiency	K	■	■	■	■	■	■
APT	Actual Production Time	L	■	■	■	■	■	■
AQT	Actual Queueing Time	M	■			■		
ATT	Actual Transportation Time	M	■			■		
AUBT	Actual Unit Busy Time	M	■			■		
AUOET	Actual Order Execution Time	M	■			■		
AUPT	Actual Unit Processing Time	M	■			■		
AUST	Actual Unit Setup Time	L	■	■	■	■	■	■
BL	Blockage Ratio	K	■	■	■	■	■	■
BLT	Blocking Time	L	■	■	■	■	■	■
CMR	Corrective Maintenance Ratio	K	■	■		■		
CMT	Corrective Maintenance Time	L	■	■		■		
E	Effectiveness	K	■	■		■		
FR	Fall of Ratio	K	■	■		■		
FTQ	First Time Quality	K	■	■		■		
GQ	Good Quantity	L	■	■		■		
NEE	Net Equipment Effectiveness	K	■	■		■		
OEE	Overall Equipment Effectiveness	K	■	■		■		
OTBF	Operating Time Between Failures	M	■			■		
PBT	Planned Busy Time	M	■			■		
PDOT	Planned Downtime	M	■			■		
PMT	Preventative Maintenance Time	L	■	■		■		
POT	Planned Operation Time	M	■			■		
PQ	Processed Quantity	M	■			■		
PQF	Produced Quantity in 1st Operation	M	■			■		
PRI	Planned Run time per Item	L	■	■		■		
PSQ	Planned Scrap Quantity	L	■	■		■		
PUOET	Planned Order Execution Time	M	■			■		
PUST	Planned Unit Setup Time	M	■			■		
QBR	Quality Buy Rate	K	■	■		■		
RR	Rework Ratio	K	■	■		■		
RQ	Rework Quantity	L	■	■		■		
SeR	Setup Ratio	K	■	■	■	■	■	■
SQ	Scrap Quantity	L	■	■		■		
SQR	Actual to planned Scrap Ratio	K	■	■		■		
SR	Scrap Ratio	K	■	■		■		
ST	Starvation Ratio	K	■	■	■	■	■	■
STT	Starvation Time	L	■	■	■	■	■	■
TE	Technical Efficiency	K	■	■	■	■	■	■
TTF	Time to Failure	M	■			■		
UE	Utilization Efficiency	K	■	■	■	■	■	■

2. Background

2.1. Understanding the Interdependencies of KPIs

KPIs are fundamental to addressing an organization's strategic goals [3] and to continuous improvement processes [4]. KPIs are based on measures of physical characteristics of a manufacturing system or process, such as the amount of resources consumed, the amount of output produced, and the time taken to execute a process. These measures, or metrics, are an index of an aspect of the system's performance, e.g. its efficiency or environmental impact. KPIs can exist at many levels of an organization, are debated within communities of interest, or may be tightly held as trade-secrets.

To illustrate this point, consider a set of KPIs related to equipment efficiency. These KPIs aggregate multiple goals into one indicator to measure performance of equipment or at the factory level. An example is the overall equipment effectiveness (OEE) indicator, which was created to measure equipment efficiency across three areas: availability, performance, and quality [3]. The OEE was extended further at the equipment level with the Production Equipment Efficiency (PEE) and Total Effective Equipment Performance (TEEP) indicators and at the factory-level with Overall Factory Effectiveness (OFE), Overall Throughput Effectiveness (OTE), Overall Production Efficiency (OPE), and Operational Asset Effectiveness (OAE) [5].

Other studies show similar relationships between metrics and sets of KPIs. Brundage et al. studied the interrelationship between production performance and energy consumption through cost explorations [6]. The interrelationships between various performance KPIs in the ISO 22400 standard were also explicitly studied in [1]. Further, IBM investigated correlations between various KPI networks and determined influential chains of metrics [7]. Chen and Zhou investigate the relationship between cycle time and throughput rates through quantile regression [8]. While these works examine different KPIs and their interrelationships within the manufacturing industry, they do not focus on visualizing KPI-related data in an understandable manner. This paper addresses that issue by exploring different visualization techniques and describing a prototype for understanding the KPI interdependencies that integrates the multiple visualization techniques. Table 1 lists the KPI and metrics studied in this paper. Each metric and KPI are classified based on which figures they appear as well as their type, including KPI (K), mid-level metric (M), and low-level metric (L).

2.2. Visualizations in Manufacturing

The fields of InfoVis and visual analytics provide evidence that presentation of and human-interaction with data simplifies decision-related scenarios for engineers. One of the earliest, most widely studied uses of InfoVis in the manufacturing domain is the process control chart, first proposed in 1932 by Shewhart as a statistical technique to make sense of individual process samples [9]. Production facilities around the world display process data, codified in color to represent different system states. Though such lean production tools have improved current engineering practice, other InfoVis-inspired techniques are not yet commonplace.

However, researchers are beginning to further explore the benefits of InfoVis for decision support in engineering practice. With respect to conceptual product design, Konigseder and Shea presented a visualization method for exploring a design space through grammar-based representations [10]. Ramanujan et al. developed a visualization prototype for exploring design characteristics of existing designs in the context of environmentally efficient decision making [11]. Others have implemented similar ideas

for visually assessing supply chain representations [12-13]. Within the manufacturing domain, InfoVis techniques have been mainly limited to performance dashboards. Mazumdar et al. proposed a knowledge-based visualization dashboard to allow users to quickly identify problems on the manufacturing floor [14]. Groger and Stach studied the feasibility of a mobile manufacturing dashboard, which allows both shop floor workers and production supervisors to understand performance in real-time [15]. In general, there is limited work in visually representing KPI-related data, and we have not found any directed work at visualizing KPI-related interdependencies.

3. Exploring KPI Visualization Methods

This paper explores the use of graph-based visualizations to enhance stakeholders' understanding of KPIs. The strengths and weaknesses of each technique are studied both in the context of (1) visualizing a large group of KPIs and their associated metrics and (2) a small, more focused subset of KPIs. The figures presented will not be the same for all sets of KPIs, however the weighting of the elements (nodes and links) are described in detail to reproduce the visualization method. Before discussing these techniques, we describe the data used in this work and related challenges.

3.1. Data Preparation and Challenges

The data used in this paper was derived from ISO 22400: Automation systems and integration - Key performance indicators (KPIs) for manufacturing operations management [2]. The relationships between the metrics and indicators defined in the above standard are investigated in the work presented by Kang et. al [1]. One challenge in visualizing the information is the discrepancy between units of KPIs and the metrics. For example, Actual Production Time (APT) is in units of time, while Good Quantity (GQ) is the number of good products produced and Overall Equipment Effectiveness (OEE) is represented as a percentage and, hence, unit-less. This becomes a barrier when performing what-if analysis to study the effect of changing a metric on different KPIs. We must understand how the value of change in one metric relates to the value of change of another metric (e.g. how does a change in unit time relate to a change in unit quantity?). This paper does not directly address this issue. Instead, subsets of KPIs with similar units are handled independently.

An important design consideration for developing visualizations is the appropriate mapping of visual variables to data. According to Jacque Bertin, visual variables include position, size, shape, value, color, orientation, and texture [16]. One guiding principle for visual variable selection is the resolution. A variable's resolution value is defined through experimentation and observation of human performance, i.e. perception and cognition. As an example, the possible combinations of color are theoretically infinite. However, humans can only distinctly perceive about 10 different colors in one visual field [17]. In this case, the functional resolution of color is equal to about 10. As a result, color should be assigned to denote no more than about 10 different data types. In the following examples, the assignment of visual variables was designed based on best practice.

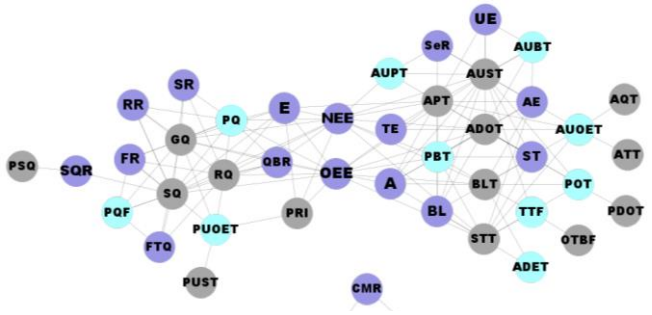

Figure 1: Undirected graph of relationships between all metrics and KPIs, generated using a force-directed layout algorithm. The purple nodes represent the KPIs, the blue nodes represent the mid-level metrics, which are dependent on the lower level metrics and are represented by the grey nodes. The labels on the graph nodes are the metrics and KPIs defined in [1].

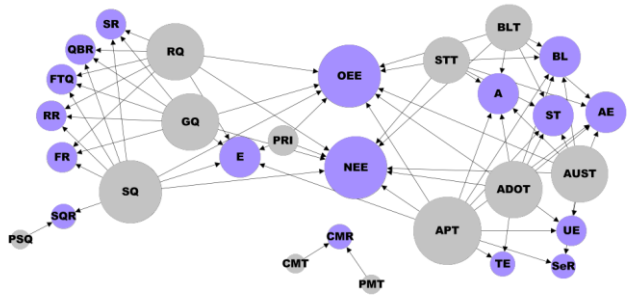

Figure 2: Graph of relationships between low level metrics and KPIs, produced through a force-layout algorithm. The size of the node is scaled based on the its degree (or the number of connections with other nodes). The purple nodes are KPIs, while the grey nodes are the low level metrics.

3.2 Node-Link Diagrams

Node-link diagrams illustrate the relationships, represented by lines, between different entities, represented by circles. Node-link diagrams are used to show the relationships between KPIs and the corresponding metrics. Figure 1 illustrates a network visualization representing an undirected graph, capturing all known functional relationships between low-level metrics, mid-level metrics, and KPIs. The mid-level metrics are dependent on low-level metrics and the KPIs can be dependent upon either mid-level or low-level metrics. Edges in this graph are defined as functional relationships between a metric and a KPI. The diagram shows two distinct node groups, a group that relates to time-based measurements and indicators (on the right side of the network) and the other that shows all elements related to quality-based measurements

Table 2: Summary of Lessons Learned for Node-Link and Matrix Based Visualizations

	Node-Link Diagram	**Matrix-Based**
Overview of KPI Relationships	Works well for sparse networks	Works well for dense networks
Presentation/Layout	Force-based layout	Clustering algorithm (e.g. Voor Hees)
What-if Analysis	Line thickness shows percent improvement	Colormap shows percent improvement
Degree of Connectivity	Quickly depicts connections	More difficult for human to decipher
Neighborhood Detection	Works for space networks with physics layout	Lots of flexibility, even with dense networks
Visual Variable Issues	Resolution of line thickness	Resolution of colors and alpha levels

(on the left side of the network). Overall equipment effectiveness (OEE) and net equipment effectiveness (NEE) fall in the middle as they measure both quality and time efficiency. This graph shows a general overview, but fails to illustrate the influence of any given metric on different KPIs.

In Figure 2, the mid-level metrics are removed and the relationships between the low-level metrics and the corresponding KPIs are shown. Here, node diameters are scaled based on node degree, or the number of connections. In other words, the more connections, the larger the node; the less connections, the smaller the node. As in Figure 1, Figure 2 groups both the quality metrics and KPIs (left) and the time based metrics and KPIs (right). In Figure 2, the metrics that have the highest influence on multiple KPIs and the KPIs that are dependent on the most metrics can easily be identified.

Lastly, improvement strategies through what-if scenarios with the node-link diagrams are shown. Figure 3 focuses on the time-based metrics and KPIs and can be used to study the effect of improving a metric (e.g., by a time unit of 10) on the KPIs. The node color represents whether a KPI meets a threshold as defined by system experts: orange means the KPI is not meeting the threshold; blue means the KPI is performing better than the threshold. The size of the nodes represents how far the KPI is from the threshold: the larger the node, the further the KPI is from the threshold. The edge color represents a positive (green) or negative (red) influence on the KPI and the edge weight is proportional to the change in the KPI when improving the metric. In this example, it can be seen that improving actual production time (APT) will lead to the biggest improvement across all KPIs since APT has the heaviest lines extending from it.

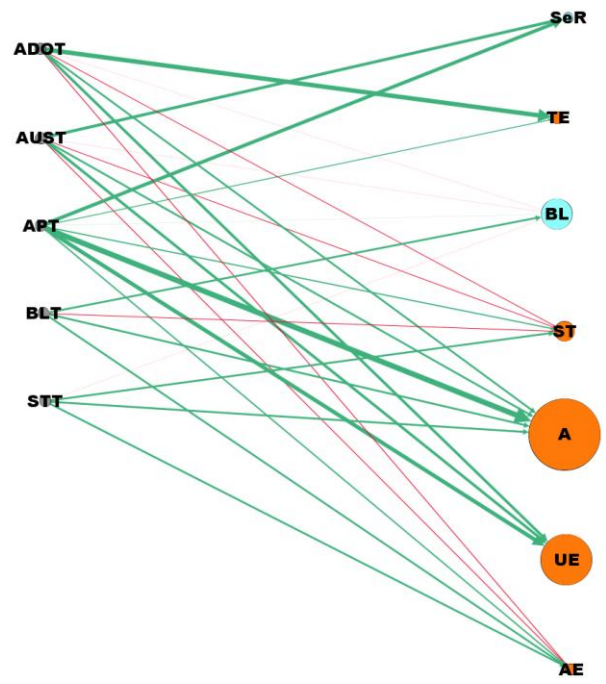

Figure 3: Node-link diagram of time-related KPIs and their metrics. The metrics are the nodes on the left, while the KPIs are the nodes on the right.

Lessons Learned

Node-link diagrams are useful for a quick general overview of the connections of metrics and KPIs, but can fail when trying to show the influence of a large set of metrics on their KPIs. Since node-link diagrams are better suited for sparse networks, it is necessary to narrow down the targeted data to best illustrate relationships using node-link diagrams. Additionally, the position of the nodes is dictated by the designer, and hence, the nodes are not fixed with respect to the field. This provides the designer with flexibility in visualizing the nodes based on their needs. In this case, position is used to depict communities of metrics and KPIs.

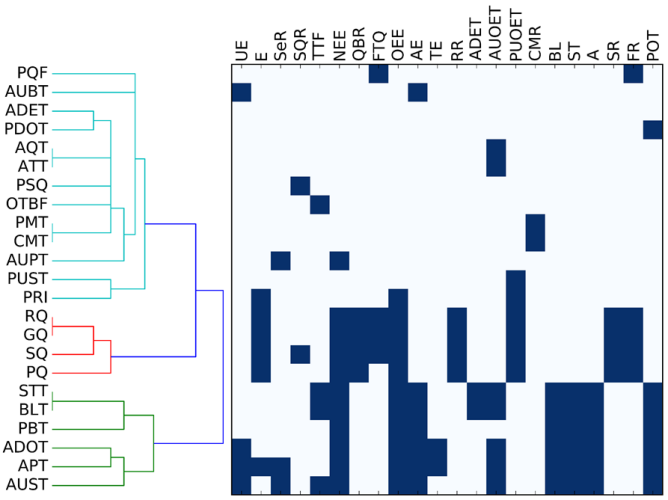

Figure 4: Matrix-based visualization of metrics relationships to KPIs. A functional relationship between a metric and a KPI is shown as a blue box on the right. The dendrogram (left) shows the similarity in functional interdependencies of the metrics to each other.

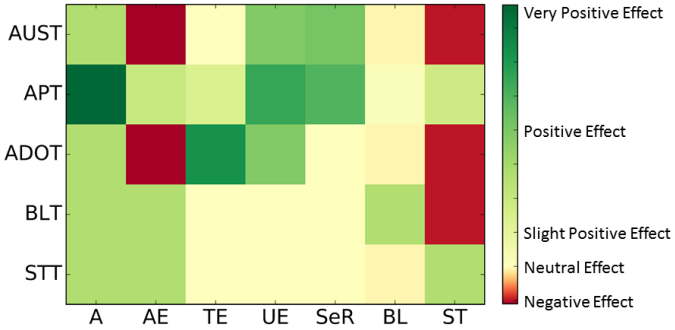

Figure 5: Heat map corresponding to the sensitivity of key performance indicator relative to a change in an underlying metric.

3.3 Matrix-Based Visualizations

The same adjacency matrices that were developed to generate the node-link diagrams were used to explore the efficacy of matrix-based visualization in the context of KPI interdependencies. Matrix-based visualizations are known to be effective for dense networks. Furthermore, another advantage lies in their ability to illustrate advanced analytics performed on the graph. For example, Figure 4 presents the results from a hierarchical clustering of the interdependencies between metrics and KPIs. Based on the Voor Hees Algorithm, groups of KPIs are defined and arranged based on the number of shared metrics [18]. The dendrogram to the left of the matrix is codified with the cluster distances represented by the length of the branches. For clarity, shorter branches in the dendrogram correspond to tighter clusters. This form of information visualization effectively reflects the relative difference in cluster distance. The matrix to the right of the diagram presents the adjacency matrix representing the KPI interdependencies. If a metric (represented as a row) has

a functional effect on a KPI (represented as a column), its corresponding cell in the matrix is highlighted blue.

Figure 5 illustrates another way of visualizing the same information as in Figure 3 but using a matrix-based layout. Instead of presenting the degree of change in a KPI by exploiting node diameter, in this diagram, sensitivity is codified by color (yellow as no effect on the KPI, red indicates a negative effect on the KPI, and green illustrates a positive effect on the KPI). This is similar to a heat map.

Lessons Learned:

A prominent advantage of using matrix-based representations compared with network visualization is the avoidance of occlusion issues. In other words, when interacting with the cells of a matrix, the rules that dictate the layout of information do not allow for entities to lie on top of one another. This characteristic also contributes to being a more appropriate option for dense networks as well as a better representation of clustering interdependencies (e.g. for large sets of KPIs and metrics). Also, the compactness of a matrix-based visualization lends itself to incorporating supporting diagrams, e.g. the dendrogram beside the matrix in Figure 4. On the contrary, matrices do not easily lend itself to human interaction. The tabular form imposes strict convention to data presentation and layout, which makes it difficult for a user to perform what-if analysis when determining which metrics to improve.

3.4 Coordinated Visualizations through Small Multiples

The observations summarized in Table 2 guided the development of a customized visualization interface to enable the exploration of metric-KPI independencies. One main goal was to align the advantages of node-link diagrams and matrix-based visualizations in order to enhance human understanding of KPI interdependencies. Small multiples are used, which use multiple graphs with similar scales to show the effect of changing metrics on the different KPIs. Figure 6 provides a screenshot of the prototype visualization tool. The prototype comprises of four primary elements:

Control Sliders (A): Sliders allow users to permute control variables (i.e. a chosen set of metrics) and dynamically view changes in the other mutually coordinated visualizations.

Dependent Metric Readout (B): Some KPIs in ISO 22400 are derived from lower level metrics. Here, these mid-level metrics are computed in accordance with the control sliders.

Sensitivity Matrix (C): Since one wants to understand the effect of individual control variables on each indicator value, a coordinated matrix visualization is provided that displays the effect of changing each individual metric on the indicators to which it is functionally related. An additional row is included below the matrix to summarize the overall change of the indicator with respect to the set of control variables.

Node-Link Diagram (D): Based on observation and common practice, sparse networks (or networks that exhibit low density) are readily visualized using a node-link diagram. Here, indicators and their low-level metrics are represented as nodes and any functional relationships as edges.

Nodes (E): Two different node types are defined corresponding to indicators and low-level metrics. Indicator nodes are represented as a small multiple, wherein its value is displayed on the outer margin of the box. At the center of the node, all low-level measures are displayed relating to the indicator with their normalized values.

Lessons Learned

The prototype is built on the concept of using independent elements combined with mutually coordinated small multiples as an intuitive interface. The prototype interface presented here is the first step to developing a fully functional interactive interface for decision makers to explore the interdependencies between KPIs and their underlying metrics. One lesson is that there is a danger that the system interface could suffer from scope creep. With each addition of a visualization feature, the interface becomes much more complex and less intuitive. For example, including the functions of the interrelationships between low-level and mid-level metrics in Figure 6 might make using the tool more complicated. However, the mutual coordination of multiple representations could provide more detailed and well-described exploration.

4. Discussion and Future Work

The purpose of this work is to identify methods to help guide decision makers in understanding the implications of varying manufacturing-related performance parameters, and visualizing their impact on multiple KPIs. For these relationships to be intuitively displayed, guiding principles from the fields of information visualization and visual analytics are used. Based on lessons learned from exploring node-link diagrams and matrix-based visualizations, we presented an initial prototype interface which emphasized mutually coordinated elements. As has been discussed, both graph-based visualizations, matrices and node-link diagrams, can provide an overview of all KPIs, metrics, and their relationships. These benefits will be further extended in the next prototype and it will become necessary to properly scale the system as a larger set of KPIs and metrics are integrated.

Several additional requirements for visualization to support

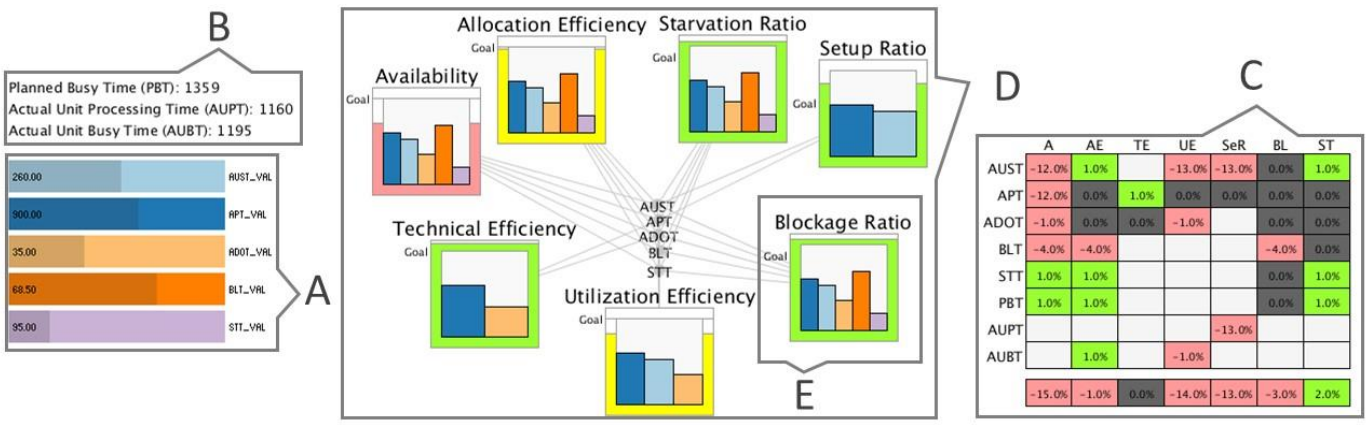

Figure 6: Mutually coordinated visualization enabling the exploration of the interdependencies between metrics and key performance indicators. Callouts to the primary elements denoted by their own character are described in the text.

Bernstein, William; Brundage, Michael; Horst, John; Morris, Katherine.
"Using graph-based visualizations to explore key performance indicator relationships for manufacturing production systems."
Paper presented at the 24th CIRP Conference on Life Cycle Engineering, Kanagawa, Japan. March 8, 2017 - March 10, 2017.

KPI exploration that have yet to be explored are identified here. First, the study of KPIs and their metrics lends itself to Shneiderman's visualization mantra, "overview first, zoom and filter, then details-on-demand" [19]. The current prototype does not address the functions of filtering or zooming. Filtering and zooming will be fundamental to KPI exploration as many organizations track very large sets of KPIs [4]. Filtering provides a method for emphasizing a particular set of metrics and/or KPIs. For example, in the current prototype, to narrow the scope, only time-based metrics were considered. In the next prototype, we will explore additional features, such as radio buttons or drop-down menus, and add the context of other communities of metrics and KPIs, e.g. quality-based metrics.

The second key requirement for KPI exploration will be the ability to perform what-if analysis on the effect of improving certain metrics on the various KPIs. This capability was initially illustrated in the prototype through the use of sliders to examine the effects of changing metrics. However, more sophisticated support for what-if analysis should be possible. Such capabilities may influence the way in which stakeholders prioritize the KPIs.

A third consideration for improving the prototype includes the use of visualization to represent non-functional relationships as well as environmental and human-related conditions (and their effect). For example, the range of certain metrics will vary based on the differences between human operators who inherently operate at different skill levels and as such may require different amounts of time for activities such as set-up, cleaning, unloading and loading time during machining. These variations greatly affect the bounds for certain control variables. For example, it might not be feasible to anticipate that an operator can decrease their set-up time by 5 mins. When non-functional relationships are quantified, the usefulness of the visualization tool will be enhanced, which can help managers better understand such abstract relationships. We also intend to address variations in human preference and its effect on human-based KPI prioritization. As of now, the importance of KPIs are prioritized based on the number and effective change of their interdependencies. We have yet to explore how interactive visualizations could help overcome differences of intuition.

Another consideration to which visualization may lend itself is in the reflection of trade-offs between different KPIs across multiple goals. For example, analyzing the relationships between throughput, quality, and energy consumption to find the interdependencies between these KPIs and relative contributions of associated metrics to competing goals should be explored. This is the essence of a multi-objective optimization for which intuition alone may be suboptimal or multi-objective optimization may not be feasible. Whether visualization can assist intuition to produce more optimal results should be explored. Our current prototype does not include any optimization problem formulation and we plan to explore this improvement.

Finally, we also plan incorporate multi-machine or multi-line scenarios. The interrelationships of KPIs at different machines or different production lines fundamentally change the underlying models, e.g. altering a metric at one machine might affect performance at another machine.

References

[1] Kang N, Zhao C, Li J, Horst JA. A Hierarchical structure of key performance indicators for operation management and continuous improvement in production systems. Int J Prod Res. 2016 Jan 29:1-8.

[2] ISO. ISO 22400: Key performance indicators (KPIs) for manufacturing operations management – Part 2: Definitions and descriptions. ISO Standard. 2014.

[3] Jung, K., Morris, K., Lyons, K., Leong, S., Cho, H. Mapping Strategic Goals and Operation Performance Metrics for Smart Manufacturing Systems. Procedia Computer Science. 2015; 44: 184-193.

[4] Kibiria, D., Morris, K., Kumaraguru, S. Methods and Tools for Performance Assurance of Smart Manufacturing Systems. Journal of Research at the National Institute of Standards and Technology. 2015 Dec; 121: 282-313.

[5] Muchiri P, Pintelon L. Performance measurement using overall equipment effectiveness (OEE): literature review and practical application discussion. Int J Prod Res. 2008;46(13):3517-35.

[6] Brundage M.P., Chang Q, Li Y, Arinez J, Xiao G. Implementing a Real-Time, Energy-Efficient Control Methodology to Maximize Manufacturing Profits. IEEE Trans. Syst., Man, Cybern., Syst. 2016 Jun;46(6):855-66.

[7] Fukuda M, Jeng JJ, Li Y, inventors; International Business Machines Corporation, assignee. Method and apparatus of constructing and exploring kpi networks. United States patent application US 12/115,913. 2009 Nov 12.

[8] Chen N, Zhou, S. Simulation-based estimation of cycle time using quantile regression. IIE Transactions. 2010 Jul 1;43(3):176-191.

[9] Woodall, W.H., Montgomery, D.C., Research Issues and Ideas in Statistical Process Control. Journal of Quality Technology. 1999 Oct 4;31(4): 376-387

[10] Königseder C, Shea K. Visualizing Relations Between Grammar Rules, Objectives and Search Space Exploration in Grammar-based Computational Design Synthesis. Journal of Mechanical Design. 2016.

[11] Ramanujan D, Bernstein WZ, Benjamin W, Ramani K, Elmqvist N, Kulkarni D, Tew J. A Framework for Visualization-Driven Eco-Conscious Design Exploration. J Comput Inf Sci Eng. 2015 Dec 1;15(4):041010.

[12] Bernstein WZ, Ramanujan D, Kulkarni DM, Tew J, Elmqvist N, Zhao F, Ramani K. Mutually coordinated visualization of product and supply chain metadata for sustainable design. Journal of Mechanical Design. 2015 Dec 1;137(12):121101.

[13] Bonanni L, Hockenberry M, Zwarg D, Csikszentmihalyi C, Ishii H. Small business applications of sourcemap: a web tool for sustainable design and supply chain transparency. In Proceedings of ACM CHI. 2010 Apr 10 (pp. 937-946).

[14] Mazumdar S, Varga A, Lanfranchi V, Petrelli D, Ciravegna F. A knowledge dashboard for manufacturing industries. InExtended Semantic Web Conference 2011 May 29 (pp. 112-124). Springer Berlin Heidelberg.

[15] Gröger C, Stach C. The mobile manufacturing dashboard. In Proceedings of IEEE Int Conf on Pervasive Computing and Communications Workshops on 2014 Mar 24 (pp. 138-140).

[16] Bertin J. Semiology of graphics: diagrams, networks, maps. 1983.

[17] Carpendale MS. Considering visual variables as a basis for information visualisation. 2003.

[18] Vorhees, E. Implementing agglomerative hierarchic clustering algorithms for use in document retrieval. Information Processing & Management. 1986; 22(6) 465-476.

[19] Scheiderman, B. The Eyes Have It: A Task by Data Type Taxonomy for Information Visualizations. IEEE Symposium on Visual Languages. 1996. 336-343.

Investigating Firebrand Accumulation over Various Scales

SUZUKI, Sayaka[1*], MANZELLO, Samuel, L.[2]

[1] *National Research Institute of Fire and Disaster, 4-35-3 Jindaiji-higashimachi, Chofu, Tokyo, 182-8508, Japan*
[2] *National Institute of Standards and Technology, 100 Breau Dr. Gaithersburg, MD, 20899, USA*

Abstract : As structures are exposed to wind, stagnation planes are produced around structures. Using full-scale experiments, the authors demonstrated that firebrands may accumulate in these stagnation planes. In a subsequent full-scale study performed by the authors that made use of firebrand showers of longer duration, experiments revealed that wind speed influences not only the spatial location and extent of the accumulated firebrands in the stagnation plane in front of the obstacle, but also the nature of the smoldering combustion intensity of the accumulated firebrands. All of the prior work was limited to firebrand distributions similar to burning vegetation conducted using full-scale experimental facilities. Here, the firebrand distributions were varied to simulate *both* burning structures and vegetation, and conducted using reduced-scale experimental facilities to determine if simpler experiments may provide insights into this complex problem.

Keywords : Firebrand, Accumulation, Large Outdoor Fires, WUI Fires

1. Introduction

Wildfires that spread into communities, referred to as Wildland-Urban Interface (WUI) fires, are a dilemma throughout the world. Japan has experienced large urban fires after strong earthquakes, such as 1997 Hanshin-Awaji Earthquake. When earthquakes hit densely-populated urban areas, the resulting urban fires are difficult to cope with.

A major factor in both WUI and urban fire spread, is firebrand production [1]. When structures burn in these fires, pieces of burning material, known as firebrands, are generated, become lofted, and are carried by the wind. This results in showers of wind-driven firebrands. These spot fires overwhelm firefighting resources after such earthquakes [1].

In Japan, several city fire spread models were developed for damage estimation. These models were based on the past city fire damages and use empirical formula under limited situations [2]. There is a lack of scientific and reliable data needed to advance such models further; especially for firebrand accumulation.

As structures are exposed to wind, stagnation planes are produced around structures. The authors demonstrated that firebrands may accumulate in these stagnation planes [3]. In a subsequent study performed by the authors [4], a series of full-scale experiments revealed that wind speed influences not only the spatial location and extent of the accumulated firebrands in the stagnation plane in front of the obstacle, but also the nature of the smoldering combustion intensity of the accumulated firebrands. This paper describes an in depth study of this phenomenon at reduced-scale to determine if useful insights may be obtained from simpler experiments. The firebrand distributions were varied to simulate *both* burning structures and vegetation, as prior studies were focused on vegetative firebrands [3-4].

2. Experimental Descriptions

A reduced-scale continuous firebrand generator was used to generate firebrand showers (Fig. 1) Details of this facility were presented in this conference last year [5]. The following experimental description follows the facility closely.

The reduced-scale continuous-feed firebrand generator consisted of two parts; the main body and continuous feeding component. The capability of a smaller-sized firebrand generator to develop continuous firebrand showers has been described [5]. Japanese Cypress wood chips and Douglas-fir wood pieces were used to produce firebrands. The Japanese Cypress wood chips had dimensions of 28 mm ±7.5 mm (L) by18 mm ± 6.3 mm (W) by 3 mm ± 0.8 mm (H) (average ± standard deviation), respectively, before combustion. These were provided from a supplier and filtered to remove really small wood chips by using a 1 cm mesh. Douglas-fir wood pieces were machined to dimensions of 7.9 mm (H) by 7.9 mm (W) by 12.7 mm (L).

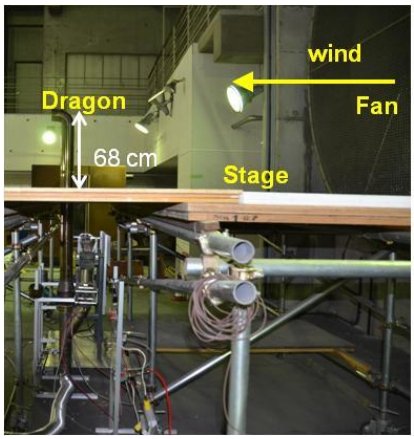

Figure 1 Experimental Setting in NRIFD's wind facility

The obstacle was placed downstream of the firebrand generator and the wind speed was varied at 4 m/s, 6 m/s, 8 m/s and 9 m/s. Specifically, the obstacle used in this study had the dimensions of 660 cm (H) by 1275 cm (W) and was located at a distance of 3 m from the device to visualize the transport process.

3. Results and Discussions

Figure 2 displays images of experiments with a 660 cm (H) x 1275 cm (W) obstacle with different wind speeds (4 m/s and 8 m/s) and feeding materials (Japanese Cypress chips and Douglas-fir wood pieces). Images shows that firebrands made from Japanese Cypress wood chips and from Douglas-fir wood pieces accumulated differently in front of the same obstacle.

Under a 4 m/s wind, it was observed that firebrands were unable to accumulate into one compact zone, rather scattered. As a wind speed increases, firebrands accumulated more in one zone. It was observed that firebrands made from Japanese Cypress wood chips managed to accumulate in front of the obstacle up to 10 m/s while those made from Douglas-fir wood pieces did not accumulate under 8 m/s and 10 m/s wind.

The accumulated area was measured using image processing software. Based on repeat measurements of different areas, the standard uncertainty in determining the projected area was ±10%. It is also important to mention that the obstacle was exposed to firebrand showers for the same duration.

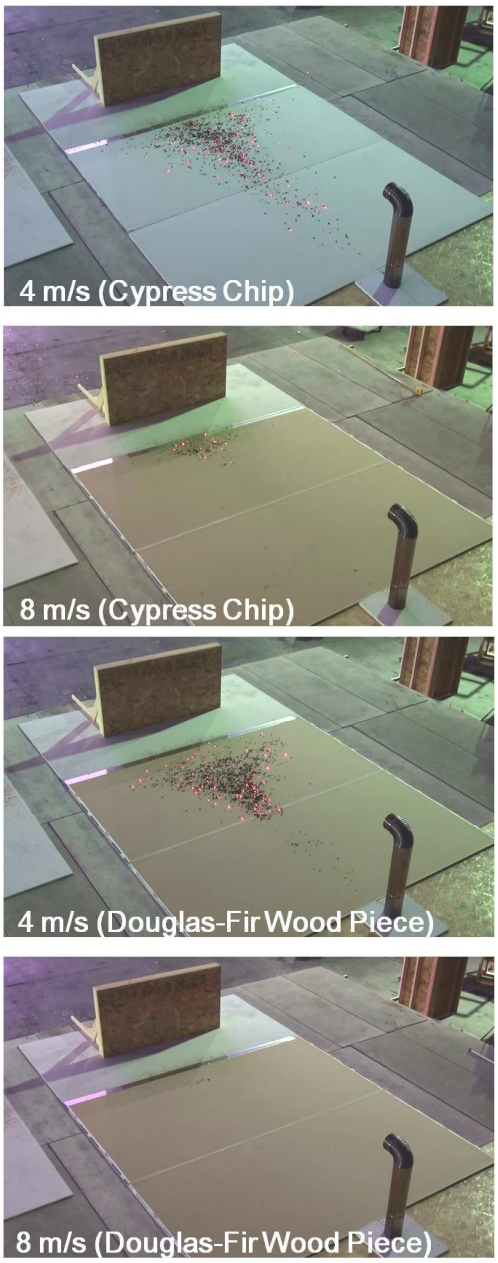

Figure 2 Images of experiments with a 660 cm (H) by 1275 cm (W) obstacle under different wind speeds -4 m/s and 8 m/s, with different feeding materials –Japanese Cypress wood chips and Douglas-fir wood pieces

Figure 3 displays the measured area of the accumulated firebrands as a function of wind speed. As the wind speed was increased, the area of accumulated firebrands was reduced significantly. It is obvious in Fig. 3 that firebrands from Douglas-fir wood pieces accumulated to smaller areas than those from Japanese Cypress wood chips.

Comparison was made in order to investigate the difference of accumulation behaviors of firebrands. Figure 4 displays the mass and size distributions of firebrands made from Japanese Cypress wood chips and Douglas-fir wood pieces under the same wind speed (6 m/s). Similar to the authors prior full-scale studies, firebrands made from Japanese Cypress wood chips have approximately double the projected areas at a certain mass, compared to firebrands generated from Douglas-fir wood pieces. It suggests that the difference of firebrand characteristics has effect on the accumulation behavior of firebrands in front of wall assemblies.

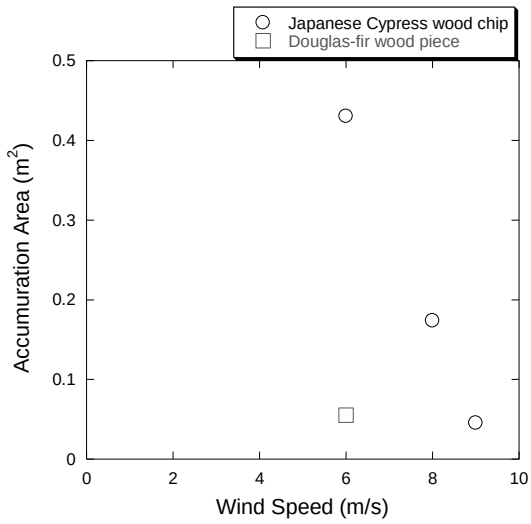

Figure 3 Measured accumulated area for various wind speeds.

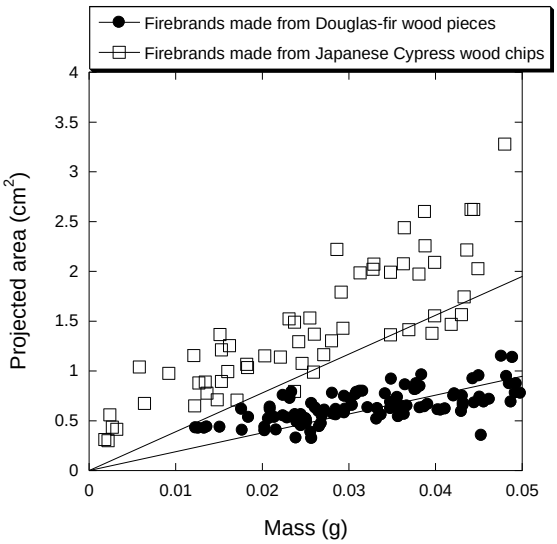

Figure 4 Mass and size distributions of firebrands made from Douglas-fir wood pieces and Japanese Cypress wood chips

4. Summary

A series of reduced-scale experiments were performed in order to investigate firebrand accumulation in front an obstacle using Japanese Cypress wood chips and Douglas-fir wood pieces. For a specified wind speed, it was found that the characteristics of firebrands has an effect of accumulation behavior of firebrands in front of an obstacle. An important qualitative similarity between the full-scale and reduced-scale vegetative firebrand studies is that increased wind speed resulted in decreased firebrand accumulation areas. Detailed investigation will be needed in the future for different obstacles placed downwind from the firebrand generator, as well as further full-scale experiments generating firebrands similar to structure production for comparison.

5. References

[1] Manzello, S.L., et al., Fire Saf. J. 59 (2013) 122-131.
[2] Iwami, T., et al., *Annual Meeting of Architectural Institute of Japan*, Tokyo, Japan, 2011. (in Japanese)
[3] Manzello, S.L., et al., Fire Saf J. 46 (2011) 568-578.
[4] Manzello, S.L, and Suzuki, S., *52nd Japanese Combustion Symposium*, Okayama, Japan, 2014.
[5] Suzuki, S., and Manzello, S.L., *53rd Japanese Combustion Symposium*, Tsukuba, Japan, 2015.

Quick Positional Health Assessment for Industrial Robot Prognostics and Health Management (PHM)

Guixiu Qiao, *Senior Member, IEEE,* Craig Schlenoff, *Senior Member, IEEE,* and Brian A. Weiss

***Abstract*— Robot calibration and performance will degrade if proper maintenance isn't performed. There have been challenges for manufacturers to optimize the maintenance strategy and minimize unexpected shutdowns. Prognostics and health management (PHM) can be applied to industrial robots through the development of performance metrics, test methods, reference datasets, and supporting tools. A subset of this research involves developing a quick health assessment methodology emphasizing the identification of the positional health (position and orientation accuracy) changes. This methodology enables manufacturers to quickly assess the static/dynamic position and orientation accuracies of their robot systems. In this paper, the National Institute of Standards and Technology's (NIST) effort to develop the measurement science to support this development is presented, including the modeling and algorithm development for the test method, the advanced sensor development to measure 7-D information (time, X, Y, Z, roll, pitch, and yaw), algorithms to analyze the data, and a use case to present the results.**

I. Introduction

As robotic technologies become more integrated with complex manufacturing environments, robot system reliability has become more critical. From the moment a robot system is put into service to enable a manufacturing process, the overall process, its constituent sub-systems, and components begin to degrade. Without maintenance, these degradations will lead to faults and/or failures impacting the process. These faults and/or failures ultimately lead to unexpected downtime and lost production if they are not remedied. Unexpected downtime and lost production are 'pain points' for manufacturers, especially in that they usually translate to financial losses. To minimize these pain points, manufacturers are developing new health monitoring, diagnostic, prognostic, and maintenance (collectively known as prognostics and health management (PHM)) techniques to advance the state-of-the-art in their maintenance strategies.

PHM is an approach to the system life-cycle support that seeks to reduce/eliminate time-based maintenance through accurate monitoring, incipient fault detection, and prediction of impending faults [1]. PHM can be applied in both the component level and system level. Component level PHM is typically focused on monitoring the health of individual components (e.g., gears, engines, and electronic devices) to determine if the health of the monitored component is degraded by taking into account environmental, operational, and performance-related parameters [2, 3]. System level PHM assesses the health of the overall system by taking into account the system architecture, system function, and process-related parameters [4]. System level PHM may delay the need to replace a component that would not immediately affect the operation of the system. In the case of monitoring the system where robot system reconfiguration and re-tasking is necessary (often driven by the market requirement for high design-variation and low-batch), efficient health monitoring should be addressed not only at component level, but also at higher system level since the decision making procedure may rely on the global industrial system state [4]. Many of the existing PHM strategies are adept at handling component PHM; fewer PHM techniques are capable of being integrated into the sometimes volatile nature of the manufacturing process (for example, system process changes and hardware reconfiguration) [5].

A robot system is complex. It contains robot arms, sensors, control systems, end-effectors, process tooling, power supplies, and software all working together to perform a task. To successfully perform a task, the robot system needs to deliver the position and orientation accuracy of the tool center position (TCP), the trajectory of the arm, the correct speed, force, and torque. The robot system's accuracy relies on the actual geometries of components in a robot cell. Tiny changes of the components, such as needed calibration of the robot arm, end-effectors, fixtures, and tooling in the robot cells, can cause inaccuracies of the robot TCP positions used in existing robot programs. In some systems where machine vision is applied to assist localizing the robot to the workpiece with high accuracy, the combined camera/robot system is critical since this drives the accuracy of the process. The degradation of a robot system's positional health (position and orientation accuracy) can lead to a decrease in manufacturing quality and production efficiency. The in-process system level health degradation is difficult to detect compared to a complete system break-down. Given the use of robot systems in many high precision industries (e.g., aerospace, automotive), it is important that robot system's positional health degradations be understood so that maintenance and control strategies can be optimized at the system level.

Enhancing positional health within manufacturing robotic operations would be greatly beneficial to the manufacturing community in terms of improving their efficiency and product quality while reducing scrap. Developing, advancing, and integrating monitoring, diagnostic, and prognostic capabilities will support these enhancements. However, there are numerous technological challenges that must be addressed to increase the capability of PHM, ultimately leading to improved accuracy.

Guixiu Qiao is with the National Institute of Standards and Technology, Gaithersburg, MD 20899 USA (phone: 301-975-2865; fax: 301-990-9688 e-mail: guixiu.qiao@nist.gov).

Craig Schlenoff is with the National Institute of Standards and Technology,Gaithersburg,MD20899USA(e-mail:craig.schlenoff@nist.gov).

Brian A. Weiss is with the National Institute of Standards and Technology, Gaithersburg, MD 20899 USA (e-mail: brian.weiss@nist.gov).

Qiao, Guixiu; Schlenoff, Craig; Weiss, Brian.
"Quick Positional Health Assessment for Industrial Robot Prognostics and Health Management (PHM)."
Paper presented at IEEE International Conference on Robotics and Automation 2017, Singapore. May 29, 2017 - June 3, 2017.

II. Challenges of the Quick Positional Health Assessment for Industrial Robots

Robot accuracy is defined as the measurement of the deviation between the commanded and attained robot position and orientation [6]. Accuracy can also represent the difference between commands and actual velocities, accelerations, forces, and torques. Robots are employed to accurately move, manipulate, and/or perform a process (e.g., welding) to certain specifications. The consideration of robot accuracy (static and dynamic) is one of the key elements when assessing the health state of an industrial robot used in the manufacturing process.

There are many challenges for the positional health assessment (position and orientation accuracy) of industrial robots. Challenges include: (1) lack of sensing technology to quickly acquire X, Y, Z, roll, pitch, and yaw information that describes the robot TCP accuracy. Existing 6-D measurement systems include laser tracker-based systems and optical tracking systems [7]. These systems are expensive. The laser tracker-based systems need to maintain line-of-sight between the laser tracker and the target. The optical tracking systems use reflective balls as markers and the near-infrared filter attached to lenses to obtain images which only contain the markers. The optical tracker's near-infrared cameras are "blind" to the environment. There is no redundancy when ambient light influences the reflected light from the targets [8]; (2) lack of test methods that can quickly and efficiently detect key performance metrics without interrupting production lines. For example, TCP accuracy needs to be assessed within a volumetric method because the error magnitudes and directions are different depending on the approach directions of joints. Efficient modeling and algorithms are needed for the test method to identify the health of the robot system; (3) lack of a PHM data taxonomy and architecture to support the interoperability between sensor/data formats and communication modes to capture, share, and analyze data across heterogeneous robot systems; (4) lack of PHM overall structure to enable various PHM technologies for robot systems, to be evaluated in an unbiased manner; and (5) lack of algorithms to analyze the results of the positional health assessment to detect the root cause of failures and the potential remedies to fix the problem.

To address the broad landscape of barriers and challenges, measurement science is needed which includes a collection of performance metrics, use case scenarios, test methods, reference datasets, and software tools to promote unbiased assessment to verify and validate (V&V) position and trajectory accuracy health assessment strategies. One specific area of NIST research is the Prognostics, Health Management, and Control (PHMC) project, which aims to develop the measurement science within several manufacturing domains to promote the advancement of monitoring, diagnostic, prognostic, and maintenance strategies [9]. This work is supported by the development of a robot system test bed.

The key building blocks of the test bed are shown in Fig. 1. The first key building block is the advanced sensing module for PHM (shown in the upper left of Fig. 1). Advanced sensing will be developed to measure and monitor the system's health status and will have three sensing layers: a system layer, a component layer, and an add-on layer. The system layer aims to support the overall system's health assessment, including

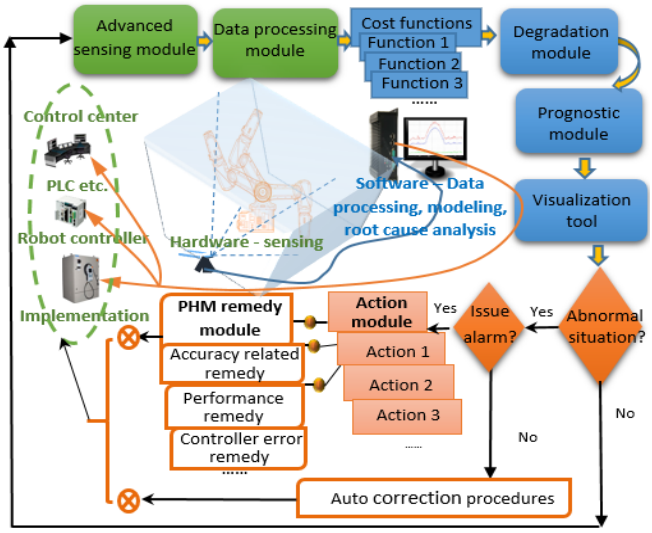

Figure 1. Key building blocks of the PHMC for Robotics structure

repeatability, accuracy, velocity, force, and torque; the component layer extracts data from the robots' controllers and/or embedded sensors to perform the on-line monitoring; the add-on layer promotes the inclusion of additional sensors to provide information that the component and system layers may be neglecting. The second key building block is the data processing module (shown as the data collection module in Fig. 1). This module will focus on the development of reference algorithms to fuse data captured from multiple sensors employed in the advanced sensing module. The data processing module will offer greater analysis capability through targeted data collection on top of complex and/or reconfigurable robotic applications. The third key building block is the development of algorithms for robot system health assessment and PHM V&V methods (collectively shown in the cost function module, degradation module, prognostic module, and visualization tools module in Fig. 1). As the fourth key building block, the closed-loop implementation (shown as the action module and the PHM remedy module in Fig. 1) of PHM solution within the control structure is reviewed. This structure serves as the back bone of use case development. The development and expansion of each module will further address elements of the measurement science. It also serves as the platform for reference dataset collection.

III. Quick Positional Health Assessment Methodology

Use cases are created within the overall test bed. The first use case is the development of a robot system quick positional health assessment methodology based on the increasing demand on industrial robot accuracy. This methodology contains the development of test methods, sensors used to take measurements, reference algorithms for data processing and health assessments, and V&V of PHM techniques. We will focus on the first three developments in this paper.

The robot system's positional health includes the robot arm's accuracy and the accuracy of any system interacting with the robot arm (e.g., a conveyor moving products within the range of the robot arm). By checking the position and orientation accuracy of the TCP and the part conveyors, users can get a quick health evaluation of the combined

conveyor/robot system since this drives the accuracy of the process. To assess the robot arm's positional health, a test method with a fixed loop motion is developed by extending the existing standard methods for robot performance, as described in [5]. This fixed loop motion of the robot arm is designed such that the test method can be executed periodically and in a relatively short amount of time. While the TCP is moving to these pre-determined positions, X, Y, Z, roll, pitch, yaw, and time (7-D information) data are being captured from a 7-D measurement system. All measurements will be taken under a global coordinate system which is defined on the 7-D measurement system. Analyzed position, time, and orientation data will provide a measure of the positional health of the robot system when compared to original specifications and prior measurements. Ideally, periodic data would be collected to track accuracy degradation with minimal disruptions to production. This accuracy degradation data would offer insight into the robot system's health.

A. Modeling and Algorithm Development for the Test Method

When developing the test method model for the robot positional health assessment, the model should reflect error sources of the robot system. Thus, after the positional health assessment, this model can be further used for the root cause analysis to find the problematic individual joints. Traditional modeling methods assume that joint motion is ideal, and the geometric relationships between the joints are constant. Yet there are also non-geometric errors, such as the non-ideal motion of joints, and deflections of the structure and joints due to external loading or gravity, backlash, etc. Those errors are position dependent. It means that the errors are not constant with respect to joint motion, but a model with parameters that depend on the pose of the robot. Furthermore, since each TCP pose (position and orientation) in the Cartesian space could have multiple inverse kinematic solutions, the error magnitude and direction changes by choosing different solutions. This makes the assessment of the TCP accuracy very difficult since it's hard to measure the accuracy from all directions. Given a measurement system that can capture the TCP's poses, a user can implement a simple strategy to run a working program and measure the robot's TCP movements. Deviations can be calculated from the measured positions to the nominal positions. The shortcoming of this strategy is that it cannot represent the overall positional health condition of the robot. The robot might be programmed to work in the "sweet zone" in the volume with the optimal approaching direction. If another program is called, this process would need to be performed again. There needs an efficient model/algorithm to support the test method that can calculate the robot's overall positional health results through its working volume using limited measurements. Moreover, there is challenge of how to decouple the measurement instruments' uncertainty from the actual robot errors. The presented modeling and algorithm development for the test method will solve these challenges.

In this use case development, the robot platform is the Universal Robot UR3 with CB3 controller. The UR3's serial kinematic structure with coordinate frames is shown in Fig. 2. Any error of the joint axes will be reflected in the TCP errors through the kinematic chain. Similar to machine tools, the errors of a joint axis (either a linear or a rotary axis) can be

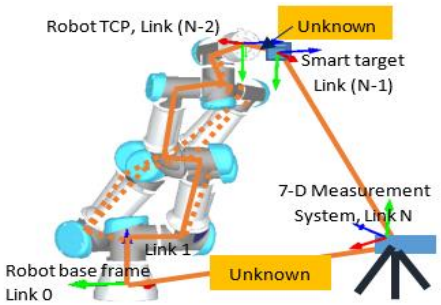

Figure 2. Robot system kinematic chain

described as geometric errors that are functions of joint positions. Each of the six robot joint axes contains six errors of the axis: three displacements of the axis (in x, y, and z direction) and three rotation errors of the axis (roll, pitch, and yaw errors). Fig. 3 shows a rotary axis (we refer to it as the

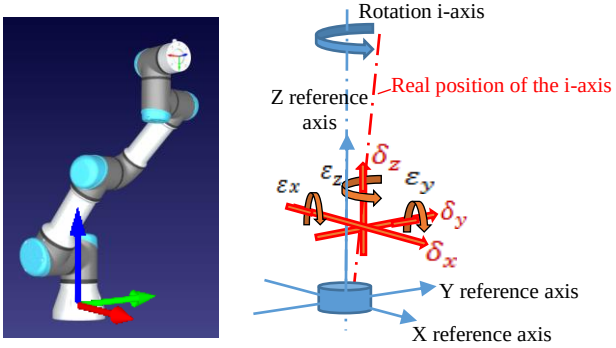

Figure 3. Six errors of a rotation axis

"i-axis" as the representation of a general situation), which represents the i^{th} joint of a robot. In Fig. 3, the real axis has deviated from its designed position. The reason for the deviation could be from the errors in robot geometry, axis motion, robot gear box degradation, backlash, thermal environment changes, or external loading/gravity. The errors of this axis are represented as: (1) δ_x - radial error motion of i-axis in X direction; (2) δ_y - radial error motion of i-axis in Y direction; (3) δ_z - axial error motion of i-axis in Z direction; (4) ε_x - tilt error motion around X of i-axis; (5) ε_y - tilt error motion around Y of i-axis; and (6) ε_z - angular positioning error (also called scale error of the rotation axis). The error model of the joint is described as:

$$E_{(i-1)i}(\theta) = \begin{bmatrix} 1 & -\varepsilon_z(\theta) & \varepsilon_y(\theta) & \delta_x(\theta) \\ \varepsilon_z(\theta) & 1 & -\varepsilon_x(\theta) & \delta_y(\theta) \\ -\varepsilon_y(\theta) & \varepsilon_x(\theta) & 1 & \delta_z(\theta) \\ 0 & 0 & 0 & 1 \end{bmatrix} \quad (1)$$

Where $E_{(i-1)i}$ is the transformation from frame i-1 to frame i and θ is the i^{th} joint angle variable.

Different from the traditional error model, the $\delta(\theta)$ and $\varepsilon(\theta)$ are not constant values, but are functions of axis locations which we refer to as a higher order model [10]. That means the error model can model not only the position-independent geometry errors, but also the position-dependent axis motion errors. Another challenge for the traditional error model is the lack of handling of the measurement noise. The uncertainties coming from measurements are usually treated as joint errors. In that case, the parameter estimates may be biased. In our model, an

implicit loop method is adapted to address this issue. In the implicit loop method, the mechanism is treated as having a closed loop from the first link out to the tool tip, and then back to the first link via a measuring device. The displacements around a closed loop sum to zero (or Identity matrix). With this convention, the measurement instrument is included in the loop. The measurement instrument's uncertainty is modeled inside the model equation using a weight. Joint and end-effector measurements are on equal footing, with weights assigned according to the accuracy of each joint. As shown in Fig. 2, the 7-D measurement system is included in the loop of the kinematic chain. The kinematic model of the robot is:

$$I = E_0 A_{01} E_{01} A_{12} E_{12} \dots A_{(N-1)N} E_{(N-1)N} A_{N0} E_{N0} \qquad (2)$$

Where A is the nominal axis motion, A_{01} is the nominal transformation from joint 0 to joint 1, E is the error of the joint, E_0 is the setup error of the robot base, and E_{01} is the transformation error from joint 0 to joint 1. Each E follows the definition shown in Equation (1). The δ(θ) and ε(θ) are high order Chebyshev polynomials with unknown polynomial coefficients to be solved by analysis algorithms.

B. *Method of Analysis*

Before calculating and deriving the error model from this kinematic model, there are two unknown transformations in the kinematic chain in Fig. 2. One is the $A_{(N-2)(N-1)}$ transformation that is from the TCP (link (N-2)) to the smart target (link (N-1)). The smart target is mounted on the robot end effector that is tasked by the measurement system to determine time, x, y, z, roll, pitch, and yaw information. Since, for different robots, it may need different adaptors, the transformation from the TCP to the smart target coordinate frame often requires calibration. The calibration needs to identify the six constant parameters of the $A_{(N-2)(N-1)}$ (three translations and three rotations). The other unknown transformation is the A_{N0} that is from the 7-D measurement system (link N) to the robot base frame (link 0). To avoid calibration processes as part of the setup overhead, these constant parameters are put in the error model to be identified together with the other high order parameters. This technology eliminates the time-consuming calibration and setup procedures, which are hurdles of new technologies' implementation in practical industrial applications.

Placing all measurements (joint and measuring device) in a single measurement vector x, Equation (2) becomes:

$$f(x, p) = 0 \qquad f : R^k \times R^n \rightarrow R^m \qquad (3)$$

$$x \in R^k,\ p \in R^n,\ f \in R^m$$

where x is a vector of motion variables and k is the number of measurements taken for each pose. The vector x may include joint and end-effector displacements being measured, as well as backlashes or other small unknown displacements. p is the vector of parameters in the error model to be estimated and n is the unknown number of parameters. m is the number of constraints or loops. We require $k \geq m$ and evaluate $(\partial f / \partial x) = m$ to guarantee that the loop can always be closed. The robot will be sent to various poses (a designed fixed loop motion), and a measurement of x for each pose will be obtained. For a particular pose i, let's assume the true value of the measurement vector is x_i, which we would record as measurement $\bar{x}_i$ with unknown measurement error $\hat{x}_i$, so that $x_i = \bar{x}_i + \hat{x}_i$. Throughout all of the sample poses, the parameters should be constant, but our initial estimates of $\bar{p}$ parameters may be in error by $\hat{p}$, that is $p = \bar{p} + \hat{p}$. For example, $\bar{p}$ might be the blueprint value of a link length and $\hat{p}$ would then be the error incurred in manufacturing the part.

$$f(x_i, p) = f(\bar{x}_i + \hat{x}_i, \bar{p} + \hat{p}) = 0, \qquad i=1, \dots, N \qquad (4)$$

where N is the number of sample positions.

The χ^2 error function is derived as:

$$\chi^2 = \sum_{i=1}^{N} \hat{x}_i^T \sum_x^{-1} \hat{x}_i + \hat{p}^T \sum_p^{-1} \hat{p} \qquad (5)$$

The implicit loop based maximum-likelihood estimation is used [10] to solve this error model and minimize the error by fitting the parameters in Equation (1). There are two outputs from this modeling method. The first one is the derived errors from the calculation of the position and orientation accuracy of the robot. The advantage of this method is that the uncertainties of the measurements are decoupled from the true errors and won't bias the analysis result. The second output is to find the maximum likelihood estimation of $\hat{p}$ to minimize the error function. Because $\hat{p}$ represents the unknown coefficients of the polynomials of the error terms in each of the E matrix, that result can be used to detect the root cause of axis errors. Moreover, compensation can be calculated to improve the accuracy of the kinematic model, which can be used in the future system remedy and prognostic algorithm development. To solve the implicit loop based maximum-likelihood estimation, one needs an innovative optimization algorithm because it's a combinatorial problem which has no concept of a derivative or gradient for algorithm converging. Traditional Quasi-Newton methods won't work on this problem. The optimization algorithms will be detailed in future publications.

C. *Fixed Loop Motion Design*

An important feature of the model (for the test method) is that it requires the measurements be evenly distributed in both joint space and Cartesian space. The even distribution in joint space prevents any errors from being missed or from being too heavily weighted. The even distribution of measurements in Cartesian space covers an entire workspace range of robot arm poses, including some that are near, far, high, and low, to evaluate arm accuracy and rigidity when the arm is both fully and minimally extended. A fixed loop motion needs to be designed to satisfy those requirements.

Fig. 4 shows the designed fixed loop motion of the UR3 robot created for the use case. The robot workspace is a spherical volume with a cylindrical dead zone in the center of the sphere. To generate this fixed loop motion, the following procedure is created: (1) in Cartesian space, a grid of poses is generated inside the robot workspace as the target poses (as shown in Fig.4 (a) and (b)); (2) inverse kinematic calculations are performed to check if the target positions are reachable by any configuration (if not, the target is skipped); (3) a linear motion path is planned between each pose. This means that each joint performs complicated motions to keep the TCP/tool on a straight line path; and (4) calculations are performed to check if the robot linear motion is possible. In the meantime, collision checking is also performed. If the linear motion is impossible, the algorithm will change the current joint configuration to a different configuration, then redo the check

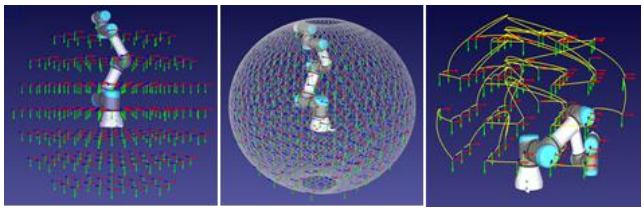

(a) (b) (c)

Figure 4. Robot fixed loop motion for test method

in step 4. For example, a pose of the UR3 robot in its workspace is represented by a 4×4 Linear Homogenous Transformations matrix (transforming from the robot base).

$$\begin{bmatrix} -1.000000 & -0.000227 & 0.000070 & 412.500000 \\ -0.000070 & -0.000000 & -1.000000 & 0.000000 \\ 0.000227 & -1.000000 & 0.000000 & 340.00000 \\ 0.000000 & 0.000000 & 0.000000 & 1.000000 \end{bmatrix}$$

Each pose in the space has multiple inverse kinematics solutions to convert it into joint angles. The number of solutions varies depending on the pose of the robot arm. In this example, this TCP has 20 possible options, as shown in Table 1 (using degree as the unit). J0 could vary from -182.9 to 176.1. J4 could vary from -176.1 to 333.5. In Step 4 of the procedure, when different configurations are needed, a search from all possible configurations is performed to select the satisfactory configuration for the even joint distribution requirement. If none of the configurations are possible, a curved motion path is attempted; if a curved motion path is not possible either (because there is a collision), this target pose is skipped. Otherwise, this pose is saved as one of the target positions in the fixed loop. This procedure is repeated until all of the poses in Fig. 4 (a) are evaluated. The final poses and paths are shown in Fig. 4 (c). In this particular example, because the robot is mounted on an optical table, only poses above the table surface clear the check procedures. After these initial procedures, a fixed loop of robot positions is saved that will be executed periodically. The reason for preferring linear motion paths is that extra analysis can be performed, such as errors from the best fit of the linear lines and square angles between the linear lines. While the TCP is moving to these pre-determined positions, the X, Y, Z, roll, pitch, yaw, and time data are being captured from a 7-D measurement system.

TABLE I. MUTLIPLE SOLUTIONS OF ROBOT INVERSE KINEMATICS

#	J0	J1	J2	J3	J4	J5	#	J0	J1	J2	J3	J4	J5
1	-183.9	-0.1	-40.2	-139.6	183.9	0	**11**	176.1	-0.1	-40.2	-139.6	183.9	0
2	176.1	-37.6	40.2	177.3	-176.1	0	**12**	176.1	-37.6	40.2	177.3	183.9	0
3	26.5	-142.4	-40.2	2.7	-26.5	0	**13**	26.5	-142.4	-40.2	2.7	333.5	0
4	26.5	-179.9	40.2	-40.4	-26.5	0	**14**	26.5	-179.9	40.2	-40.4	333.5	0
5	-183.9	-0.1	-40.2	-139.6	-176.1	0	**15**	-183.9	-37.6	40.2	177.3	183.9	0
6	-183.9	-37.6	40.2	177.3	-176.1	0	**16**	176.1	-0.1	-40.2	-139.6	-176.1	0
7	-333.5	-142.4	-40.2	2.7	-26.5	0	**17**	-333.5	-142.4	-40.2	2.7	333.5	0
8	-333.5	-179.9	40.2	-40.4	-26.5	0	**18**	-333.5	-179.9	40.2	-40.4	333.5	0
9	176.1	-37.6	40.2	-182.7	-176.1	0	**19**	176.1	-37.6	40.2	-182.7	183.9	0
10	-183.9	-37.6	40.2	-182.7	-176.1	0	**20**	-183.9	-37.6	40.2	-182.7	183.9	0

D. Advanced Sensing Development (a 7-D Measurement System)

Advanced sensing development is an important part of the PHMC for robotics structure to quickly acquire the 6D information (X, Y, Z, roll, pitch, and yaw) that describes the robot TCP accuracy. Existing 6D measurement systems include laser tracker-based systems and optical tracking systems [7]. These systems are expensive. The laser tracker-based system needs to maintain line-of-sight between the laser tracker and the target. The target mounting usually requires changing setups or work tools. The optical tracking system uses reflective balls as markers and the near-infrared filter attached to lenses to obtain images which only contain the markers. The optical tracker's near-infrared cameras are "blind" to the environment. There is no redundancy when ambient light influences the reflection light from the targets. The advanced sensor used to capture the 7-D information on the TCP needs to be a relatively low-cost solution for industrial implementation. The measurement system needs to be designed such that its integration and use does not interfere with the robot system's normal operations. Considering the measurement requirements for the positional health assessment test method, a 7-D measurement system is being developed by NIST to support this research effort. A vision-based design is selected because: (1) vision-based systems can obtain position and orientation information simultaneously; (2) camera technology can deliver sub-pixel accuracy. After optical triangulation, the sub-pixel accuracy provides the measurement system with a higher degree of accuracy than was previously available; and (3) vision systems are relatively easy to integrate [11]. Instead of using near-infrared cameras, high speed color cameras were selected. With new, advanced color image stereo technology, target detection can be more accurate by utilizing redundant information from color images. The 7-D measurement system consists of two high-speed color cameras, a high performance image processing control box (computer), special targets, and software tools.

Innovative target design is an important part of this work. Specific targets are designed as adaptors to mount on the robot arm's end-effector with known offsets from the TCP. The purpose of designing innovative target fixtures is to avoid tool changes during measurement which would require a brief interruption of the production. The specific target design is currently under consideration for a patent. Differing from and exceeding the performance of traditional stereo technology, the 7-D measurement system is designed and embedded with a time synchronization feature, which is important for analysis when fusing with other sensors for robot system health analysis. Also, a self-calibration method is created by utilizing the designed features on the specific target to avoid the condition where a camera-based measurement system needs to frequently self-calibrate. Moreover, the advanced color sensor processing technology is utilized which uses redundant information from the environment conditions for more accurate target detection. Design of the 7-D measurement system and the target will be detailed in future publications.

IV. USE CASE ANALYSIS, RESULTS, AND DISCUSSION

A use case analysis (under the existing robot platform) was performed using the simulated measurements with known robot joint errors and measurement uncertainty. In this use case, each axis's nominal forward kinematics ("A" matrix in Equation (2)) was constructed using the robot's Denavit-Hartenbert (DH) parameters. The robot's DH table is

omitted here for brevity. Simulated joint errors of J0 and J1 were added into the robot error model "E", following the definition in Equation (1). As shown in Fig. 5, the $\delta(\theta)$ and $\varepsilon(\theta)$ are not constant values but Chebyshev polynomials,

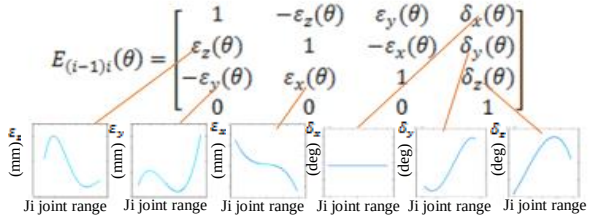

Figure 5. The joint Ji's simulated axis motion errors

which are used to represent the general position-dependent axis errors in industrial robots. The advantages of using Chebyshev polynomials are for the benefit of error model identification and scale invariance because of their two properties: (1) they are orthogonal over an interval; and (2) they have a similar scale over the same interval. Various measurement poses were generated as the fixed loop motion shown in Fig. 4 (c). Measurement noises with known uncertainty were added into simulated measurement results to simulate the environmental noise and instrument noise.

The error function χ^2 is derived in the form of Equation (5). Two outputs come out from the analysis. The first one is the derived errors from the calculation of the robot position and orientation accuracy. The second output is the maximum likelihood estimation of $\hat{p}$ to minimize the error function, which is not the main focus of this paper. For the calculation of the robot position and orientation accuracy, the analysis is not a simple deviation calculation from commanded poses to measured poses, but an identification of the error model to solve the χ^2 error function. The advantage of this method is that the uncertainties of the measurements are decoupled from the true errors and won't bias the analysis result. Also position-dependent errors are calculated more accurately because the advanced modeling method can model not only the motion error of all of the joints (both translation and rotation), but also the geometry error between the joints. Results of the position-dependent error distribution are shown in Fig. 6, with respect to X, Y, Z axis and 3D space under the

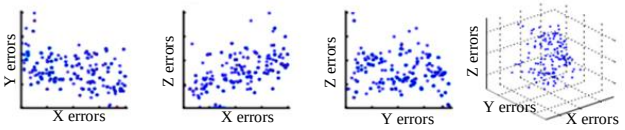

Figure 6. Error distribution on X, Y, Z, and 3D

world coordinates. The position-dependent error distribution can help to track the change of error distribution, provide a comparison of different robot systems' positional health, and establish a baseline of a robot system's positional health condition. Statistical results are also generated including average error, standard deviation of the error, and maximum error. The statistical results are more accurate because they are derived from the error model instead of directly calculating from the limited size of sample measurements.

In summary, this use case demonstrates the utilization of the quick health assessment methodology by using the advanced sensing system (a 7-D measurement system), the designed test method with the robot fixed loop motion, and the advanced error modeling and analysis technique. With this technology, users can assess the robot positional health faster, cheaper, and with higher accuracy. This can help to quickly detect and decrease the manufacturing quality degradation to reduce scrap. This methodology can be applied when environmental conditions change, after the work cell has been reconfigured, or whenever a manufacturer wants to determine if they have experienced a degradation.

V. Conclusion

NIST's development of measurement science to support the PHM for robotics technique is presented. A test bed is being constructed to provide a platform for the development. An advanced methodology of quick health assessment is developed to identify the health of the robot system, which can lead to reduce unexpected downtime, and ultimately improve a robot system's productivity, efficiency, and quality. NIST is seeking to develop additional industrial use cases for further applications. Future efforts are also under way to add more complexity to the environment, such as including conveyors, end-effectors, and tooling.

NIST Disclaimer

Certain commercial entities, equipment, or materials may be identified in this document in order to illustrate a point or concept. Such identification is not intended to imply recommendation or endorsement by NIST, nor is it intended to imply that the entities, materials, or equipment are necessarily the best available for the purpose.

References

[1] P. W. Kalgren, C. S. Byington, M. J. Roemer, and M. J. Watson, "Defining PHM, a lexical evolution of maintenance and logistics," 2006 IEEE Autotestcon, pp. 353-358, 18-21 Sept. 2006.

[2] N. M. Vichare and M. G. Pecht, "Prognostics and health management of electronics," IEEE Transactions on Components and Packaging Technologies, vol. 29, pp. 222-229, 2006.

[3] A. C. Bittencourt, "On modeling and diagnosis of friction and wear in industrial robots," Thesis, 2012.

[4] B. Abichou, A. Voisin, and B. Iung, "Bottom-up capacities inference for health indicator fusion within multi-level industrial systems," IEEE Conference on Prognostics and Health Management (PHM), pp. 1-7, 18-21 June 2012.

[5] G. Qiao and B. A. Weiss, "Advancing measurement science to assess monitoring, diagnostics, and prognostics for manufacturing robotics," International Journal of Prognostics and Health Management, vol. 013, 2016.

[6] B. Shirinzadeh, "Repeatability and accuracy - who cares and why?," Industrial Robot, vol. 27, pp. 250-251, 2000.

[7] B. Greenway, "Robot accuracy," Industrial Robot, vol. 27, pp. 257-265, 2000.

[8] G. Qiao and B. A. Weiss, "Accuracy degradation analysis for industrial robot systems " Accepted by the Proceedings of 2017 ASME International Manufacturing Science and Engineering Conference, vol. June 4-8, 2017, University of Southern California, SC, USA, 2017.

[9] B. A. Weiss, G. W. Vogl, M. Helu, G. Qiao, J. Pellegrino, M. Justiniano, et al., "Measurement science for prognostics and health management for smart manufacturing systems: key findings from a roadmapping workshop," in Annual Conference of the Prognostics and Health Management Society, Coronado, CA, 2015.

[10] C. W. Wampler, J. M. Hollerbach, and T. Arai, "An implicit loop method for kinematic calibration and its application to closed-chain mechanisms," IEEE Transactions on Robotics and Automation, vol. 11, pp. 710-724, Oct 1995.

[11] M. Švaco, B. Šekoranja, F. Šuligoj, and B. Jerbić, "Calibration of an Industrial Robot Using a Stereo Vision System," *Procedia Engineering*, vol. 69, pp. 459-463, 2014.

Acceptance Criteria for Nonlinear Alternative Load Path Analysis of Steel and Reinforced Concrete Frame Structures

J. M. Weigand[1], Y. Bao[2], and J. A. Main[3]

Engineering Laboratory, National Institute of Standards and Technology
100 Bureau Drive, Mail Stop 8611, Gaithersburg, MD 20899-8611

[1]Tel: (301) 975-3302; E-mail: jonathan.weigand@nist.gov
[2]Tel: (301) 975-2061; E-mail: yihai.bao@nist.gov
[3]Tel: (301) 975-5286; E-mail: joseph.main@nist.gov

ABSTRACT

Alternative load path analysis is the primary approach for evaluating the potential for disproportionate collapse in structural design. In this approach, individual load-bearing elements are notionally removed from a structure, and the remaining structure is required to sustain the applicable gravity loads without collapse. Column loss in steel and reinforced concrete frame structures can result in large vertical deflections that subject the beams and their connections to significant axial deformations in addition to large rotations. Failure of members and connections in alternative load path analysis is evaluated by comparing the plastic rotations of these components to acceptance criteria, defined as rotation limits, based largely on data from seismic tests. Axial demands on members and connections, which are important in column loss scenarios, were not relevant in this seismic testing, and thus the corresponding rotation limits may not be appropriate for column loss. This paper compares current acceptance criteria for alternative load path analysis with experimental data reported in the literature under column loss scenarios for steel gravity frames with single-plate shear connections and for reinforced concrete moment frames. Significant variability is observed in the level of conservatism of these acceptance criteria, and factors contributing to this variability are discussed. A new approach for defining acceptance criteria is summarized, which provides improved risk-consistency by directly accounting for the interaction of axial and rotational demands on the connections under column loss scenarios.

INTRODUCTION

Alternative load path analysis (ALPA) is the primary approach used to evaluate the potential for disproportionate collapse in structural design. In ALPA, various notional column loss scenarios are considered, and the capacity of the remaining structure to sustain the applicable gravity loads is evaluated. Failure in ALPA is evaluated by comparing the rotations developed in members and connections with acceptance criteria specified as rotation limits. Currently, the primary documents governing alternative load path analysis in the United States are the Unified Facilities Criteria (UFC) 4-023-03 *Design of Buildings to Resist Progressive Collapse* (DoD 2009), applicable to military buildings, and the General Services Administration (GSA) *Alternate Path Analysis & Design Guidelines for Progressive Collapse Resistance* (GSA 2013), applicable to civilian government buildings. The acceptance criteria in

Bao, Yihai; Main, Joseph; Weigand, Jonathan.
"Acceptance Criteria for Nonlinear Alternative Load Path Analysis of Steel and Reinforced Concrete Frame Structures."
Paper presented at 2017 Structures Congress, Denver, CO. April 6, 2017 - April 8, 2017.

UFC 4-023-03, which were subsequently adopted in the GSA Guidelines, were based primarily on seismic acceptance criteria specified in the American Society of Civil Engineers (ASCE/SEI) 41-13, *Seismic Evaluation and Retrofit of Existing Buildings* (ASCE 2013). Seismic acceptance criteria were adopted for use in ALPA because of the much more extensive experimental data and modeling guidance available for structural systems under seismic loading than under column loss.

While current acceptance criteria used in ALPA are based primarily on data from seismic testing, there are significant differences between the demands imposed on members and connections under seismic loading and under column loss. Low-cycle fatigue is an important issue in seismic loading that is not relevant to column loss. To account for this effect, seismic testing imposes rotation cycles of increasing magnitude on members and connections (e.g., Clark et al. 1997). As a result of this low-cycle fatigue, rotation limits based on seismic testing can be overly conservative for column loss. On the other hand, column loss can impose significant axial demands on beams and connections that are not relevant to seismic loading. The combination of axial and rotational demands can in some cases result in earlier failure than under purely flexural loading (e.g., for steel single-plate shear connections). In other cases, however, the development of catenary action can result in peak vertical loads that are achieved at much larger rotations than under purely flexural action (e.g., for reinforced concrete moment frames). In recognition of differences between seismic loading and column loss, some of the acceptance criteria in UFC 4-023-03 were modified relative to those in ASCE/SEI 41-13, in some cases based on additional experimental data or computational simulations specific to column loss. However, the modified acceptance criteria still consider only rotational demands and do not consider factors such as the span length and the axial restraint conditions, which can strongly influence the axial demands under column loss.

This paper presents a comparison of the acceptance criteria (rotation limits) specified in the UFC 4-023-03 with experimentally measured rotational capacities from structural assemblies tested under column loss. In the years since the development of the acceptance criteria in the UFC 4-023-03, numerous structural assemblies have been tested under column loss scenarios, providing an opportunity to evaluate the suitability of the current criteria. This paper focuses on steel gravity frames with single-plate shear ("shear tab") connections and on reinforced concrete moment frames. For single-plate shear connections and for reinforced concrete moment frames, the acceptance criteria in UFC 4-023-03 were modified relative to those in ASCE/SEI 41-13. Comparisons with the original acceptance criteria in ASCE/SEI 41-13 are also presented, with the recognition that these criteria are intended for analysis under seismic loading, not column loss. Significant variability is observed in the level of conservatism of the acceptance criteria in the UFC 4-012-03, largely because of the effect of axial demands, which are influenced by factors not considered in the current acceptance criteria, such as the span length. A new approach for defining acceptance criteria is summarized, which provides improved risk-consistency by directly accounting for the interaction of axial and rotational demands on the connections under column loss scenarios.

ACCEPTANCE CRITERIA IN CURRENT SPECIFICATIONS

Table 1 presents acceptance criteria from ASCE/SEI 41-13 and from UFC 4-023-03 for steel single-plate shear connections. The GSA Guidelines adopted the same acceptance criteria as in UFC 4-023-03, and therefore these are not listed separately. Equations for the limiting connection rotations are presented as functions of the depth of the connection bolt group, d_{BG}. Acceptance criteria from ASCE/SEI 41-13 are presented for two performance objectives: life safety (LS) and collapse prevention (CP). Acceptance criteria from UFC 4-023-03 are presented for both primary components (components whose contribution to structural resistance is included) and for secondary components (components whose contribution to structural resistance is neglected). In general, the UFC 4-023-03 adopts life safety acceptance criteria from ASCE/SEI 41-13 for both primary and secondary components, unless otherwise specified. However, Table 1 shows that the rotation limits for primary components in UFC 4-023-03 were reduced relative to the life safety criteria in ASCE/SEI 41-13. This reduction was based in part on numerical simulation of a single-plate shear connection subjected to column loss (Karns et al. 2008).

Table 1: Rotational capacities for single-plate shear connections from ASCE/SEI 41-13 and UFC 4-023-03.

Specification	Condition	Rotation Limit (rad)
ASCE/SEI 41-13 (ASCE 2013)	Life Safety	$\theta_{\max}^{\mathrm{pl}} = 0.1125 - (0.0001063\ \mathrm{mm}^{-1}) d_{\mathrm{BG}}$
	Collapse Prevention	$\theta_{\max}^{\mathrm{pl}} = 0.1500 - (0.0001417\ \mathrm{mm}^{-1}) d_{\mathrm{BG}}$
UFC 4-023-03 (DoD 2009; GSA 2013)	Primary Components	$\theta_{\max}^{\mathrm{pl}} = 0.0502 - (0.0000591\ \mathrm{mm}^{-1}) d_{\mathrm{BG}}$
	Secondary Components	$\theta_{\max}^{\mathrm{pl}} = 0.1125 - (0.0001063\ \mathrm{mm}^{-1}) d_{\mathrm{BG}}$

NOTE: The depth of the connection bolt group, d_{BG}, has units of mm.

Table 2 presents acceptance criteria from ASCE/SEI 41-13 and from UFC 4-023-03 for beams in reinforced concrete moment frames. The GSA Guidelines adopted the same acceptance criteria as in UFC 4-023-03, and therefore these are not listed separately. In Table 2, ρ is the reinforcement ratio, ρ' is the reinforcement ratio of the compression steel, ρ_{bal} is the balanced reinforcement ratio, V is the design shear force, b_w is the beam width, d is the distance from the extreme compression fiber to the centroid of the tension reinforcement, and f_c' is the compressive strength of concrete (see ASCE (2013) for further details on these definitions). Values between those listed in Table 2 are to be determined by linear interpolation.

Table 2 shows that for reinforced concrete beams, the rotation limits for primary components in UFC 4-023-03 were increased by a factor of approximately 2.5 relative to the LS acceptance criteria in ASCE/SEI 41-13. Similarly, the rotation limits for secondary components in UFC 4-023-03 were increased by a factor of 2.0 relative to the CP acceptance criteria in ASCE/SEI 41-13, or by a factor of 4.0 relative to the LS acceptance criteria. These increases indicate that reinforced concrete beams were considered to be capable of sustaining significantly larger rotations under column loss than under seismic loading.

Table 2: Rotational capacities for reinforced concrete beams from ASCE/SEI 41-13 and UFC 4-023-03.

Specification	Condition	$\frac{\rho - \rho'}{\rho_{\text{bal}}}$	$\frac{V}{b_w d\sqrt{f_c'}}$	Rotation Limit, $\theta_{\text{max}}^{\text{pl}}$ (rad)
ASCE/SEI 41-13 (ASCE 2013)	Life Safety	≤ 0.0	≤ 0.25	0.025
		≤ 0.0	≥ 0.50	0.020
		≥ 0.5	≤ 0.25	0.020
		≥ 0.5	≥ 0.50	0.015
	Collapse Prevention	≤ 0.0	≤ 0.25	0.050
		≤ 0.0	≥ 0.50	0.040
		≥ 0.5	≤ 0.25	0.030
		≥ 0.5	≥ 0.50	0.020
UFC 4-023-03 (DoD 2009; GSA 2013)	Primary Components	≤ 0.0	≤ 0.25	0.063
		≤ 0.0	≥ 0.50	0.050
		≥ 0.5	≤ 0.25	0.050
		≥ 0.5	≥ 0.50	0.038
	Secondary Components	≤ 0.0	≤ 0.25	0.100
		≤ 0.0	≥ 0.50	0.080
		≥ 0.5	≤ 0.25	0.060
		≥ 0.5	≥ 0.50	0.040

NOTE: V has units of N, b_w and d have units of mm, and f_c' has units of MPa.

COMPARISON WITH EXPERIMENTAL DATA

In this section, experimental data reported in the literature under column loss scenarios are compared with the acceptance criteria from UFC 4-023-03, with a focus on evaluating the level of conservatism provided by the acceptance criteria for column loss. Seismic acceptance criteria from ASCE/SEI 41-13, from which the UFC criteria were adapted, are also presented for comparison.

Steel Gravity Frames with Single-Plate Shear Connections

Figure 1(a) shows a comparison of measured rotational capacities from typical single-plate shear connections tested under column loss scenarios by Weigand and Berman (2014) with the acceptance criteria from UFC 4-023-03 and ASCE/SEI 41-13. The uncertainty in the experimental data was estimated as ±1 % (Weigand and Berman 2016). As illustrated in Figure 2 for a typical vertical load vs. beam chord rotation curve, the measured rotational capacities correspond to the rotation at the peak vertical load. Elastic rotations were deducted from the rotational capacities presented in Figure 1 for consistency with the acceptance criteria. Figure 1(a) shows that the acceptance criterion for primary components in UFC 4-023-03 was conservative for all 13 of the connections tested by Weigand and Berman (2014), although the level of conservativism varied widely, with measured rotational capacities in some cases of more than double the acceptance criterion. Figure 1(a) also shows that the LS acceptance criterion from ASCE/SEI 41-13 was non-conservative for all of the

connection geometries tested by Weigand and Berman (2014), confirming that the reduction of the rotation limits for primary components in UFC 4-023-03 relative to the seismic LS acceptance criterion is warranted (see Table 1).

A recent study by Weigand and Main (2016) further compared the acceptance criteria in UFC 4-023-03 to calculated rotational capacities for bare-steel single-plate shear connection configurations beyond those tested by Weigand and Berman (2014). Weigand and Main (2016) found that single-plate shear connections that used bolts with threads included in the shear plane, or those with longer-spans (between 12.1 m (40 ft) and 18.3 m (60 ft)), had sufficiently small rotational capacities that even the UFC 4-023-03 acceptance criteria for primary components would not be conservative. Main and Sadek (2012) identified the presence of a composite slab as another factor that is potentially detrimental to the rotational capacities of connections subjected to column loss, although the presence of the composite slab does provide increased capacity to sustain vertical loads. At the removed column, the slab response is very stiff in compression relative to the tensile stiffness of the connection bolt group, biasing the neutral axis of the connection toward the top of the beam flange and increasing the tensile deformations of the connection components for a given chord rotation. Figure 1(b) shows rotational capacities for single-plate shear connections, incorporating the effect of the composite slab on steel deck by locating the center-of-rotation of the connection at the top flange of the beam. These rotational capacities were calculated using the component-based model for single-plate shear connections formulated by Weigand (2016). A comparison between Figure 1(a) and Figure 1(b) shows that the effect of the composite slab would reduce the rotational capacities for all connection geometries, and Figure 1(b) demonstrates that the rotational capacities of three 3-bolt (152 mm-depth) connections would fall below the UFC 4-023-03 acceptance criteria for primary members. The demonstrated potential for the UFC 4-023-03 acceptance criteria to be non-conservative for single-plate shear connections motivates the need for a new approach for defining acceptance criteria such as that described by Weigand and Main (2016), summarized below.

Reinforced Concrete Moment Frames

Figure 3 presents measured rotational capacities from 23 reinforced concrete frame assemblies, tested under simulated column removal, and compares these with the rotation limits specified in UFC 4-023-03 and ASCE/SEI 41-13. As illustrated in Figure 4 for a measured vertical load vs. beam chord rotation curve, reinforced concrete moment frames typically exhibit an initial peak vertical load associated with flexural-arching action, followed by a drop in the vertical load associated with concrete crushing and plastic hinge formation at the beam-column joints, followed by a subsequent increase in load associated with the development of catenary action, with a final peak load that may or may not exceed the initial peak load. Red markers in Figure 3 represent rotational capacities associated with the initial flexural-arching-action stage of the response, as illustrated in Figure 4. Blue markers in Figure 3 represent rotational capacities associated with the catenary-action stage of the response, also illustrated in Figure 4. Blue markers are presented only when the peak vertical load associated with catenary action exceeded the peak vertical load associated with flexural-arching action.

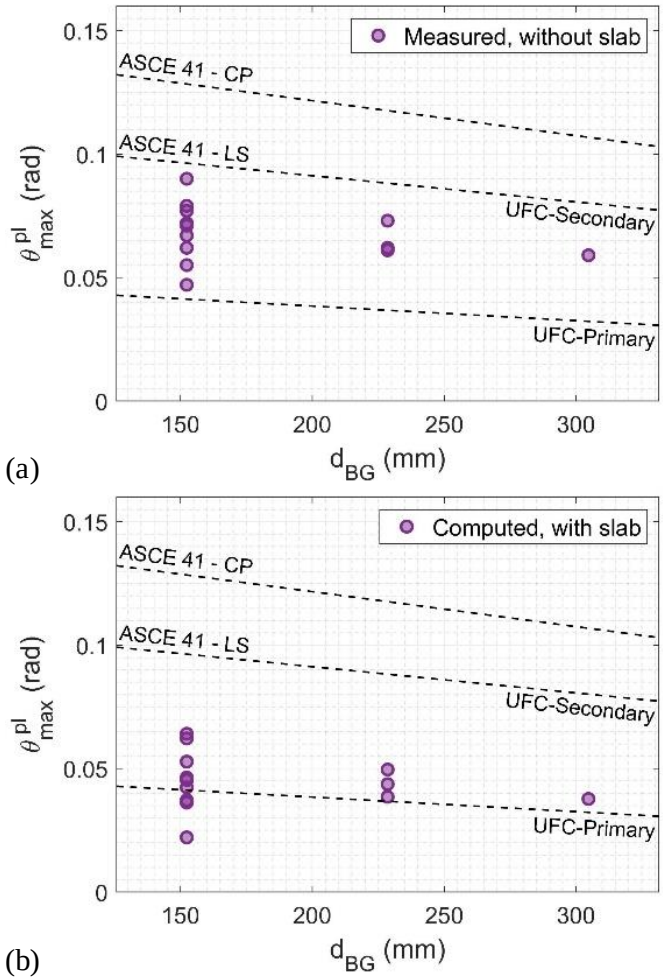

Figure 1: Comparison of acceptance criteria for single-plate shear connections from ASCE/SEI 41-13 and UFC 4-023-03 with rotations at peak load under column loss: (a) measured rotations for connections without slab (Weigand and Berman 2014) (b) computed rotations for connections with slab.

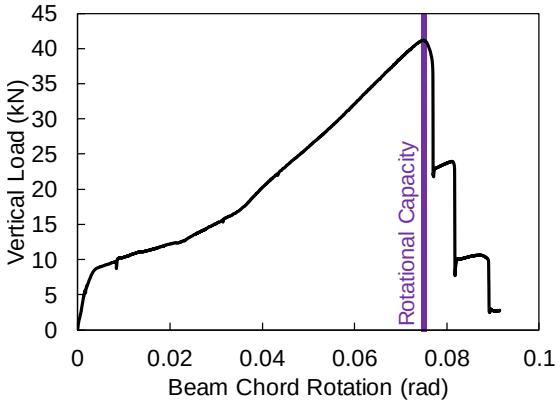

Figure 2: Vertical load vs. beam chord rotation for single-plate shear connection (specimen sps3b|STD|34|38|48L from Weigand and Berman 2014) with rotational capacity indicated.

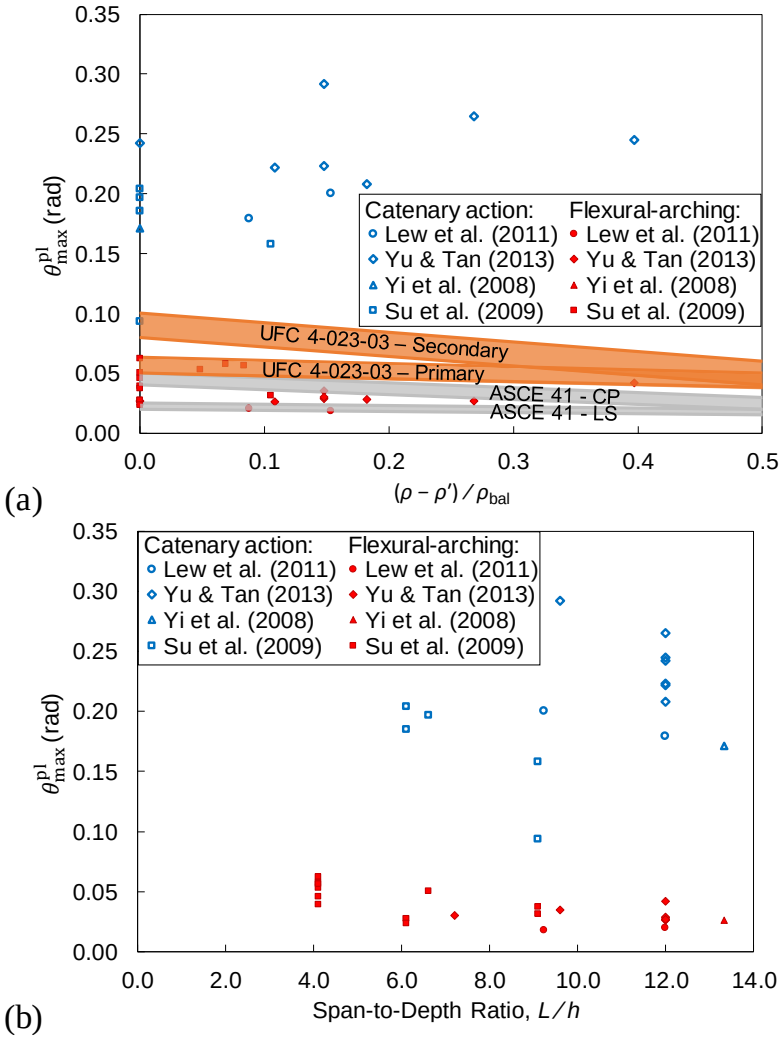

Figure 3: Plastic rotation limits for reinforced concrete beams as a function of (a) $(\rho - \rho')/\rho_{bal}$ and (b) span-to-depth ratio.

Figure 3(a) presents the measured rotational capacities as a function of the ratio $(\rho - \rho')/\rho_{bal}$. Because the rotation limits from ASCE/SEI 41-13 and UFC 4-023-03 depend on the normalized shear demand, $V/(b_w d\sqrt{f_c'})$, as well as on $(\rho - \rho')/\rho_{bal}$ (see Table 2), the rotation limits are plotted as shaded bands in Figure 3(a). The upper and lower bounds of each shaded band were obtained by linear interpolation from Table 2, with the lower bound corresponding to $V/(b_w d\sqrt{f_c'}) \geq 0.50$ and the upper bound corresponding to $V/(b_w d\sqrt{f_c'}) \leq 0.25$. The design shear demand for test specimens is generally not reported in the literature, so evaluating the effect of $V/(b_w d\sqrt{f_c'})$ was not possible. All of the rotational capacities associated with flexural-arching action were below the UFC 4-023-03 upper-bound rotation limit for primary components, which indicates that the UFC acceptance criteria are non-conservative for flexural-arching action. However, all except one of the rotational capacities associated with flexural-arching action were above the lower-bound ASCE/SEI 41-13 Life Safety (LS) rotation limit, which indicates that the LS acceptance criterion from ASCE/SEI 41-13 is generally conservative for flexural-arching action under column loss. All except one of

the rotational capacities associated with catenary action exceeded the UFC 4-023-03 upper-bound rotation limit for secondary components, which indicates that the UFC acceptance criteria generally are conservative for cases in which catenary action is developed. However, the level of conservatism varies widely, with measured rotational capacities in some cases of more than five times the acceptance criterion for primary components.

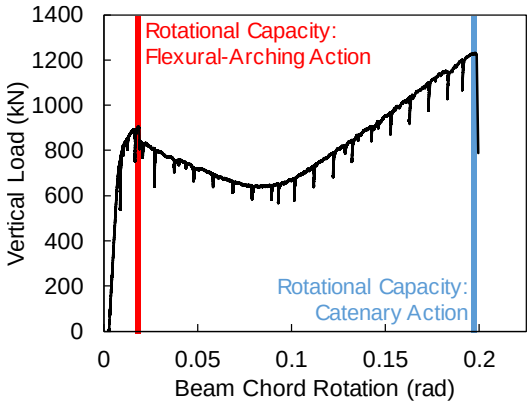

Figure 4: Vertical load vs. beam chord rotation for reinforced concrete special moment frame assembly from Lew et al. (2011) with rotational capacities associated with flexural-arching action and catenary action indicated.

Figure 3(b) shows data from the same 23 reinforced concrete frame assembly tests as in Figure 3(a), but presented as a function of the span-to-depth ratio, L/h. Figure 3(b) shows that reinforced concrete frames with span-to-depth ratios of less than 6 achieved their peak vertical capacity during the initial flexural-arching-action stage of the response and were unable to develop sufficient catenary action in the subsequent response to reach or exceed this initial peak. This implies that for reinforced concrete frames with span-to-depth ratios of less than 6, flexural-arching action may be the only response mechanism available for resisting disproportionate collapse. It is also important to recognize that development of catenary action requires axial restraint of the beams, which in some cases is not provided by the surrounding structural system (e.g., in a corner column loss scenario). When catenary action cannot be developed, much smaller rotations at peak load are attained, with the experimental data showing a maximum plastic rotation associated with flexural-arching action of 0.062 rad. As noted above, the UFC acceptance criterion for primary components is not conservative in such cases, but the LS acceptance criterion from ASCE/SEI 41-13 generally is conservative. As will be presented in future publications, improved risk consistency can be achieved by defining acceptance criteria for reinforced concrete moment frames using an approach like that of Weigand and Main (2016), which directly accounts for the combination of axial and rotational demands in a column loss scenario.

ROTATION LIMITS BASED ON DEFORMATION CAPACITIES

Weigand and Main (2016) demonstrated the effectiveness of a new approach for defining acceptance criteria for column loss that provides significantly improved risk

consistency, relative to ASCE/SEI 41-13 and UFC 4-023-03. In this approach, rotation limits for single-plate shear connections were calculated via the following equation:

$$\theta_{\mathrm{u}} = 2\sqrt{\left(\frac{d_{\mathrm{BG}}}{2L}\right)^2 + \frac{\delta_{\mathrm{u}}}{L}\left(1 + \frac{\delta_{\mathrm{u}}}{L}\right)} - \frac{d_{\mathrm{BG}}}{L} \ , \qquad (1)$$

where θ_{u} is the rotation limit, L is the span length, d_{BG} is the depth of the connection bolt group, and δ_{u} is the axial deformation capacity of a single bolt row of the connection, known either from experiments or from computational modeling. Eq. (1) assumes full axial restraint. For the condition with no axial restraint, Eq. (1) reduces to $\theta_{\mathrm{u}} = 2\delta_{\mathrm{u}}/d_{\mathrm{BG}}$.

The dependence of Eq. (1) on both the span length L and the depth of the bolt group allows these important aspects of the system to directly influence the calculated rotation limit under column loss. In addition, since Eq. (1) was derived by comparing the axial deformations imposed on the connection directly against the axial deformation capacity, δ_{u}, Eq. (1) allows for consideration of more aspects of the connection geometry, such as the shear plate thickness, bolt diameter, and bolt thread-condition (i.e., threads included or excluded from the shear plate) by selecting appropriate values of δ_{u} for each condition. Using rotation limits calculated from Eq. (1), Weigand and Main (2016) showed that improved consistency could be achieved for single-plate shear connections, relative to the ASCE/SEI 41-13 or the UFC 4-023-03 acceptance criteria, by accounting for the influences of axial restraint, span length, and connection configuration. A similar approach will be presented in future publications for steel moment frames and reinforced concrete moment frames.

SUMMARY AND CONCLUSIONS

This paper presented acceptance criteria for alternative load path analysis from UFC 4-023-03 (DoD 2009), which have also been adopted in the GSA Guidelines (GSA 2013) and are used in structural design of U.S. military and civilian government buildings to mitigate disproportionate collapse. The acceptance criteria were compared with measured rotational capacities under column loss scenarios for steel gravity frames with single-plate shear connections and for reinforced concrete moment frames. Comparisons with seismic acceptance criteria from ASCE/SEI 41-13, from which the UFC criteria were adapted, were also presented.

For steel gravity frames with single-plate shear connections, the UFC 4-023-03 adopted a rotation limit for primary components that was reduced relative to the life safety acceptance criterion in ASCE/SEI 41-13, in recognition of the increased axial demands imposed on the connections in a column loss scenario. Comparison with the experimental data confirmed that such a reduction was warranted, as the ASCE/SEI 41-13 life safety acceptance criterion was non-conservative for all 13 of the connection tested under column loss, while the UFC acceptance criterion for primary components was conservative for all of the connections. However, axial demands are not directly considered in the UFC rotation limits, and consequently, the level of conservatism of the acceptance criteria varied widely, with measured rotational capacities in some cases of more than double the acceptance criterion for primary components. Computational

analyses also indicated that the presence of a composite slab could cause the rotational capacities of some connections to fall below the UFC acceptance criterion for primary components. A new approach proposed by Weigand and Main (2016) for defining acceptance criteria would allow for improved risk-consistency by directly accounting for the combination of axial and rotational demands in a column loss scenario and enabling consideration of factors such as the influence of a composite slab.

For reinforced concrete moment frames, the UFC 4-023-03 adopted rotation limits for primary and secondary components that were increased relative to the life safety and collapse prevention acceptance criteria, respectively, in ASCE/SEI 41-13. For peak loads associated with flexural-arching action, comparison with the experimental data showed that this increase was not warranted. All of the rotational capacities associated with flexural-arching action fell below the UFC upper-bound rotation limit for primary components, whereas the ASCE/SEI 41-13 life safety acceptance criterion was generally conservative for flexural-arching action. The experimental data showed that the increased rotation limit was warranted for peak loads associated with catenary action, for which the UFC acceptance criterion for primary components was always conservative. However, the level of conservatism varied widely, with measured rotational capacities of more than five times the acceptance criterion in some cases. Importantly, it was noted that in some cases flexural-arching action may be the only response mechanism available for resisting disproportionate collapse. The experimental data showed that catenary action was not developed for span-to-depth ratios of less than six. Axial restraint of the beams is also required for the development of catenary action, which is not provided in cases such as a corner column loss scenario.

DISCLAIMER

REFERENCES

ASCE (2013). *Seismic Evaluation and Retrofit of Existing Buildings, ASCE/SEI 41-13,* American Society of Civil Engineers, Reston, VA.

Clark, P., Frank, K., Krawinkler, H., and Shaw, R. (1997). "Protocol for Fabrication, Inspection, Testing, and Documentation of Beam-Column Connection Tests and Other Experimental Specimens." SAC Steel Project Background Document. October, Report No. SAC/BD-97/02.

DoD (2009). *Design of Buildings to Resist Progressive Collapse, UFC 4-023-03.* United States Department of Defense.

GSA (2013). *Alternate Path Analysis & Design Guidelines for Progressive Collapse Resistance,* United States General Services Administration.

Karns, J.E., Houghton, D.L., Kim, J. and Hong, J. (2008). *GSA Steel Frame Bomb Blast & Progressive Collapse Test Program*, Contract No. GS-23F-0092P, January, 2008.

Lew, H.S., Bao, Y., Sadek, F., Main, J.A., Pujol, S., and Sozen, M.A. (2011). "An experimental and computational study of reinforced concrete assemblies under a column removal scenario." *NIST Technical Note 1720*, National Institute of Standards and Technology, Gaithersburg, MD.

Main, J.A. and Sadek, F. (2012). "Robustness of steel gravity frame systems with single-plate shear connections." *NIST Technical Note 1749*, Gaithersburg, MD.

Su, Y.P., Tian, Y., and Song, X.S. (2009). "Progressive collapse resistance of axially-restrained frame beams." ACI Structural Journal, 106(5), pp. 600-607.

Weigand, J.M. and Berman, J.W. (2014). "Integrity of Steel Single Plate Shear Connections Subjected to Simulated Column Removal." *Journal of Structural Engineering*, 140 (5), 04013114, pp.1-12.

Weigand, J.M. and Berman J.W. (2016). "Steel Gravity Connections Subjected to Large Rotations and Axial Loads." *Eighth International Workshop on Connections in Steel Structures (Connections VIII)*, Boston, Massachusetts, May, 2016.

Weigand, J.M. (2016). "Component-Based Model for Single-Plate Shear Connections with Pretension and Pinched Hysteresis." *Journal of Structural Engineering.* 04016178 (in press).

Weigand, J.M. and Main, J.A. (2016). "Deformation Limits and Rotational Capacities for Connections under Column Loss." *Proceedings of the Eighth International Workshop on Connections in Steel Structures*, Boston, MA, May, 2016

Yi, W.J., He, Q.F., Xiao, Y. and Kunnath, S.K. (2008). "Experimental study on progressive collapse-resistant behavior of reinforced concrete frame structures." *ACI Structural Journal*, 105(4), pp. 433-439.

Yu, J. and Tan, K. (2013). "Structural Behavior of RC Beam-Column Subassemblages under a Middle Column Removal Scenario." *Journal of Structural Engineering*, 139(2), pp. 233-250.

Proceedings of the 2016 Winter Simulation Conference
T. M. K. Roeder, P. I. Frazier, R. Szechtman, E. Zhou, T. Huschka, and S. E. Chick, eds.

STANDARDS SUPPORTING SIMULATIONS OF SMART MANUFACTURING SYSTEMS

Conrad Bock, Guodong Shao, Kevin Lyons,
Ronay Ak, KC Morris

Engineering Laboratory
National Institute of Standards and Technology
Gaithersburg, MD, USA

Bjorn Johansson

Product and Production Development
Chalmers University of Technology
SE-412 96 Gothenburg, Sweden

ABSTRACT

Manufacturing standards provide the means for industries to effectively and consistently deploy methodologies and technologies to assess their performance. These assessments set the stage for controlling manufacturing systems and processes and enabling continuous improvement within the enterprise. Several evolving manufacturing-related standards impact the manufacturing simulation community and software vendors. This panel explores standards that enable modeling and simulation to play a larger role in manufacturing enterprises through tighter integration of simulation with manufacturing operations.

1 INTRODUCTION

Standards and best practices provide a foundation for ensuring the health, safety, and prosperity of the United States and the world. These standards lay foundations for modeling and integrating manufacturing systems and related services. The panel discusses several standards that are important for manufacturing and supported by stakeholders and supportive communities. Standards that are highlighted through a panel discussion include SysML and BPMN from the Object Management Group (OMG), ISA-95 and ISO 15746 standards for manufacturing automation and integration, ASTM International standards for manufacturing process characterization and sustainable manufacturing, standards for data-driven modeling and simulations from the Data Mining Group (DMG) and work items on codes and standards on Computational Modeling and Simulation for Advanced Manufacturing from ASME's Verification and Validation (V&V) committee, and the Simulation Interoperability Standards Organization's (SISO) CMSD standard. Potential collaborations on standards development, testing, and implementations can be explored.

2 THE STANDARDS

OMG standards: System Modeling Language (SysML) is a general purpose graphical modeling language for specifying, analyzing, designing, and verifying complex systems. Business Process Model and Notation (BPMN) is a graphical modeling language for specifying processes that is accessible to subject matter experts. Both languages are widely known and have many commercial implementations providing simulation capabilities. On-going research is focused on integrating these models with simulation capabilities.

Manufacturing automation and integration standards: ISA-95 is an international standard developed to automate the interfaces to connect enterprise application systems with the control systems that operate a manufacturing plant's equipment. This standard can be applied in discrete, batch and continuous process industries. ISO 15746, *Automation systems and integration – Integration of advanced process control and optimization capabilities for manufacturing systems*, is a new standard that is based on the ISA 95 hierarchy. It is intended to facilitate the integration and interoperability of software tools that provide automation solutions to advanced process control and optimization (APC-O) problems.

ASTM E60.13 Sustainable Manufacturing: Develops standards that manufacturers can use to benchmark, assess, act on and communicate performance metrics, including standards to characterize, evaluate, improve, and measure gate-to-gate processes in the production of finished goods.

Ak, Ronay; Bock, Conrad; Johansson, Bjoern; Lyons, Kevin; Morris, Katherine; Shao, Guodong.
"Standards Supporting Simulations of Smart Manufacturing Systems."
Paper presented at 2016 Winter Simulation Conference, Arlington, VA. December 12, 2016 - December 14, 2016.

Standards for data driven modeling and simulation of manufacturing processes: Two standards focus on the use of manufacturing data as it relates to simulation. The DMG's Predictive Modeling Markup Language (PMML) provides a way for analytic applications to describe and exchange predictive models produced by data mining and machine learning algorithms. In addition, ASME has formed a new subcommittee on Verification and Validation (V&V) in Computational Modeling and Simulation for Advanced Manufacturing. This group defines procedures for V&V and Uncertainty Quantification (UQ) in modeling and simulation for advanced manufacturing.

SISO's Core Manufacturing Simulation Data (CMSD) standard specifies the information entities common to manufacturing simulations to facilitate simulation model construction and data exchange between simulation and other manufacturing applications within a shop floor. Cases for testing and implementing CMSD will be discussed and illustrated.

3 CURRENT STATE OF IMPLEMENTATION OF THE STANDARDS

Standards will reduce the costs of incorporating talent into organizations by providing a common understanding of concepts, procedures, and tools. The maturity and adoption of the different standards varies. The OMG's standardization process requires commercial implementations along with the issuance of the standard. In the case of SysML and BPMN, there are quite a few implementations and OMG has workgroups for interoperability testing of these tools. BPMN is used to drive workflow engines, some tools follow related Workflow Management Coalitions specifications. At least some of the tools include APIs, though OMG does not standardize these APIs currently.

The ISA 95 standard has been around for some time and is used as both a reference model for describing manufacturing and related software systems and as the basis for interface specifications. The ISO 15746 standard has three parts. Part 1 is an international standard that defines a reference interoperability framework based on the ISA 95 hierarchy. Part 2 is a draft international standard that defines an information model of APC-O to enable integration of different applications and systems. Part 3 is a working draft that defines procedures for verification and validation of a APC-O system. , Even though many companies' APC-O implementations conform with the concept of the standard, since the standard is relatively new, more applications still need to be implemented and demonstrated.

The ASTM standards for sustainable manufacturing provide a basis on which manufacturing processes can be characterized and subsequently included in simulations. This has been demonstrated through research projects; however, due to the newness of these standards adoption is not yet widespread. These standards form the basis for standard descriptions of manufacturing processes that can streamline the representation of those processes in a variety of simulations. Research is on-going to demonstrate these capabilities.

PMML is supported by many analytics platform such as R, ADAPA, SAS, Python, MATLAB. Recent improvements to PMML includes two new probabilistic models—Gaussian Process Regression and Bayesian Networks—provide two critical pieces of information for manufacturing applications: confidence bounds and distribution for the predictive estimations. Both are needed to provide the foundation for uncertainty quantification analysis. The new activities in ASME's V&V community will define best practices for how these features will be used. These technologies will allow for more rapid deployment of simulation results into manufacturing operations.

For CMSD, Connecticut Center for Advanced Technology (CCAT) created tools that enabled the translation of manufacturing information organized according to the CMSD standard to non-standard representations supported by commercial tools. The tool supports an interface that uses CMSD as a neutral intermediate representation to integrate different commercial simulation and other analysis tools.

Disclaimer

No approval or endorsement of any commercial product by the National Institute of Standards and Technology is intended or implied. Certain commercial software systems are identified in this paper to facilitate understanding. Such identification does not imply that these software systems are necessarily the best available for the purpose.

Alternative Load Path Analysis of a Prototype Reinforced Concrete Frame Building

Yihai Bao[1], Joseph A. Main[2], and H.S. Lew[3]

Engineering Laboratory, National Institute of Standards and Technology
100 Bureau Drive, Mail Stop 8611, Gaithersburg, MD 20899-8611

[1]Tel: (301) 975-2061; E-mail: yihai.bao@nist.gov
[2]Tel: (301) 975-5286; E-mail: joseph.main@nist.gov
[3]Tel: (301) 975-6060; E-mail: hai.lew@nist.gov

ABSTRACT

This paper presents alternative load path analysis of a 5-bay by 5-bay, 10-story prototype reinforced concrete moment frame building under column loss scenarios. This prototype building is used for example analysis problems in the *Alternative Load Path Analysis Guidelines*, which are being developed by the Disproportionate Collapse Technical Committee of the Structural Engineering Institute, and the analyses presented in this paper have been submitted for inclusion in these guidelines as part of the chapter on advanced numerical modeling. The prototype building was designed for seismic design category C, for a location in Atlanta, GA. Intermediate moment frames were selected as the lateral force-resisting system and were designed in accordance with the requirements of the American Concrete Institute 318 Building Code. A two-way concrete slab was used at each floor level, including the roof. Using a reduced-order finite-element modeling approach, full-building analyses are presented under three different first-story column loss scenarios, including a corner column, an edge column, and an interior column. Results from nonlinear dynamic analysis (i.e., sudden column removal) are compared with results from nonlinear static analysis (i.e., push-down analysis) using an energy-based procedure to account for the dynamic effects of sudden column loss. The robustness index for the building is also evaluated based on its ultimate capacity under the same set of sudden column loss scenarios.

INTRODUCTION

Alternative load paths in a structural system enable redistribution of loads after failure of a load-bearing member, thus preventing a progression of failures that could result in disproportionate collapse. Alternative load path analysis (ALPA) is a commonly accepted approach for evaluating the susceptibility of a structure to disproportionate collapse. A key first step in ALPA is the selection of appropriate initial damage scenarios. Multiple scenarios involving removal of load-bearing members must generally be considered to determine the most critical scenarios for design. Structural analysis is then performed to evaluate the adequacy of the structural members and connections to develop alternative load paths within specified strength and deformation limits. The Disproportionate Collapse Technical Committee of the Structural Engineering Institute is currently developing guidelines for performing ALPA. These

Bao, Yihai; Lew, Hai; Main, Joseph.
"Alternative Load Path Analysis of a Prototype Reinforced Concrete Frame Building."
Paper presented at 2017 Structures Congress, Denver, CO. April 6, 2017 - April 8, 2017.

guidelines present alternative modeling and analysis approaches that are categorized within three different levels of complexity: 1) simple mechanics-based hand- and spreadsheet- calculable methods, 2) analysis methods using structural analysis and design software, and 3) advanced numerical modeling and analysis methods. This paper presents ALPA approaches and examples for a reinforced concrete frame building that fall within the third category of advanced numerical modeling and analysis.

The modeling and analysis approaches presented in this paper are illustrated using example analysis problems from the *ALPA Guidelines* that correspond to a 10-story, 5-bay by 5-bay reinforced concrete moment frame building with a two-way concrete slab at each floor level. Three first-story column removal scenarios are analyzed, including removal of a corner column, an edge column, and an interior column. A reduced-order finite-element modeling approach is used, in which the beams and columns are modeled with beam elements, the slab is modeled using shell elements, and special interface beam elements are used to model bond slip and reinforcing bar fracture at critical beam sections. The reduced-order modeling approach captures important geometrically nonlinear response mechanisms such as arching action, catenary action, and slab membrane action. The material modeling considers nonlinear behavior and accounts for key effects such as concrete confinement, concrete damage and softening, bond slip of reinforcing bars, and reinforcing bar fracture. An approximate energy-based procedure is employed to demonstrate that the dynamic effects associated with sudden column loss can be evaluated from the results of a nonlinear static push-down analysis. Finally, the robustness index of the prototype building is calculated based on the ultimate capacities of the prototype building obtained from nonlinear static analysis under the set of column removal scenarios.

PROTOTYPE BUILDING

Fig. 1 shows elevation and plan views of the prototype reinforced concrete frame building. The building has a rectangular plan with five bays in each direction and a typical bay size of 9.1 m (30 ft) by 6.1 m (20 ft). There are no interior columns along gridlines 2 and 5, resulting in 12.2 m (40 ft) spans for the north-south interior girders that frame into the exterior columns. The first-story height is 4.6 m (15 ft), and the height of each upper story is 3.7 m (12 ft).

The building was designed for the combined effects of gravity and lateral loads as specified by the American Society of Civil Engineers (ASCE) Standard 7-02 (ASCE 2002). The gravity loads included self-weight, superimposed dead load, and live load, with values listed in Table 1 for typical floors and for the roof. For typical floors, live load reduction was considered based on Section 1607.9.1 of the International Building Code (ICC 2003). Wind and seismic loads were considered for a location in Atlanta, GA, for seismic design category C. The lateral loads are resisted by intermediate moment frames designed using the American Concrete Institute (ACI) 318-02 code (ACI 2002). A two-way normal-weight concrete slab with a thickness of 254 mm (10 in) was used for all floor levels, including the roof. Normal-weight concrete with a nominal compressive strength of 27.6 MPa (4000 psi) was used for all structural members. All reinforcing bars had a minimum specified yield strength of 414 MPa (60 ksi). Additional details on the design of the building are provided by Shen and Ghosh (2006).

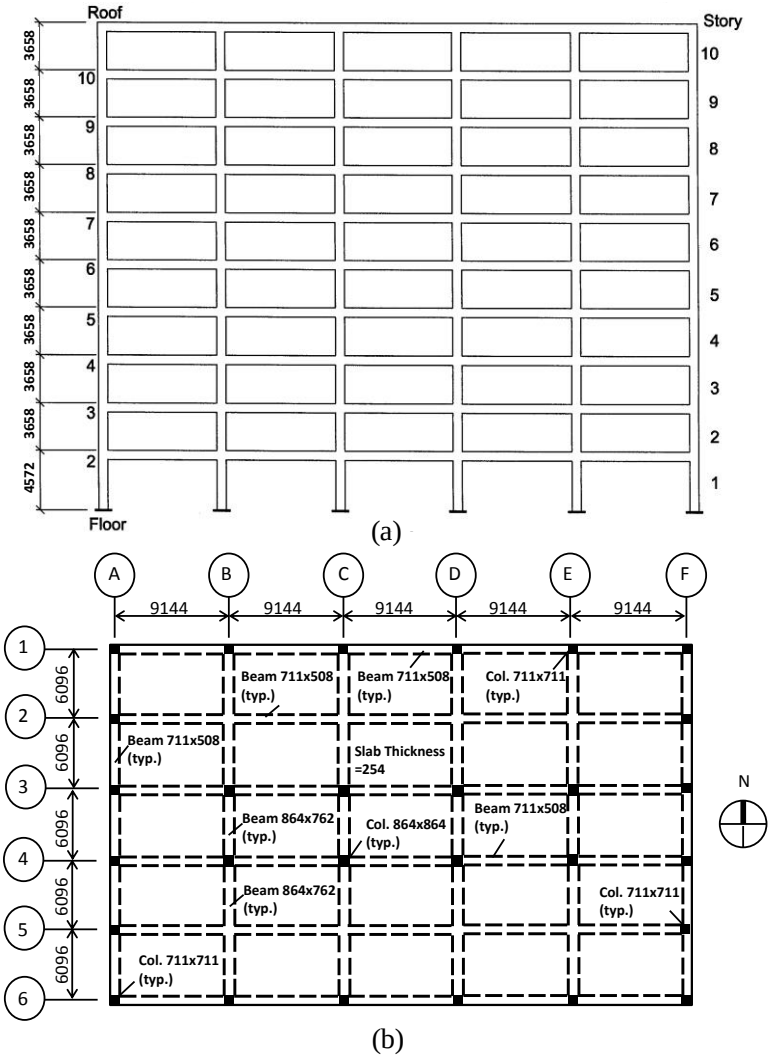

Fig. 1. Prototype concrete frame building: (a) elevation view and (b) plan view. (dimensions in mm)

Table 1. Gravity loads for prototype building.

	Load Intensity, kN/m^2 (lbf/ft^2)	
Gravity Load Type	Typical Floors	Roof
Self-weight	7.18 (150)	7.18 (150)
Superimposed dead load	1.44 (30)	0.48 (10)
Total dead load, *D*	8.62 (180)	7.66 (160)
Live load, *L*	4.79 (100)	1.20 (25)

MODELING APPROACH

As described in the following subsections, the prototype building was modeled using a reduced-order finite-element approach in which the beams and columns were modeled using beam elements and the slab was modeled using shell elements. Nonlinear material behavior was considered for the concrete and the steel reinforcement, and special interface beam elements were used to model bond slip and reinforcing bar fracture at critical beam sections. The LS-DYNA finite element software[1] (LSTC 2014) was used for the modeling and analysis in this study.

Reduced-order modeling of framing members and slabs. The reduced-order modeling approach used in this study, illustrated in Fig. 2, is a modified version of the approach presented previously by Bao et al. (2014b), with two notable simplifications:

(1) Joint shear deformations, which were considered by Bao et al. (2014b), were neglected in this study, since they were found to have an insignificant influence on the nonlinear response of the structure under column loss scenarios. The joints were modeled using rigid links with lengths corresponding to the dimensions of the joint region, as illustrated in Fig. 2.

(2) Nodes of the beam and shell elements, which were defined in different planes by Bao et al. (2014b), were defined in a common plane at the top surface of the slab in this study, thus simplifying the model development. Offsets were used to define the reference axes of the elements at their proper elevations, and nodal constraints were used to tie the beam elements to the shell elements, ensuring continuity of displacements and rotations at the interface between the beams and the floor slab (see Fig. 2).

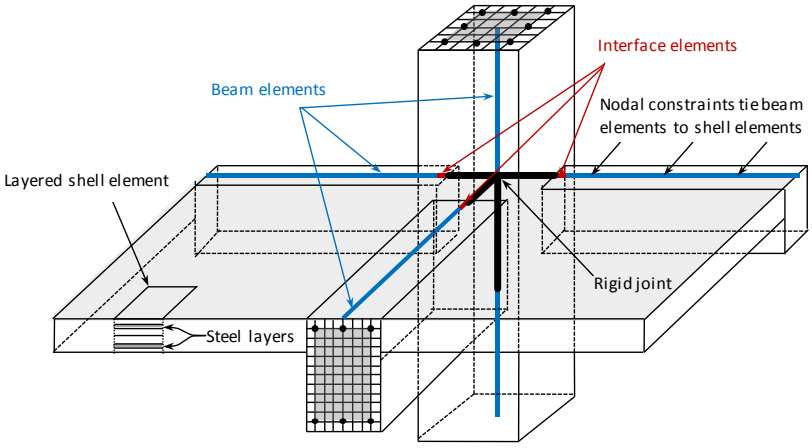

Fig. 2. Reduced-order model for RC frame building including floor slab

[1] Certain commercial entities or products are identified in this document in order to describe a procedure or concept adequately. Such identification is not intended to imply recommendation or endorsement by the National Institute of Standards and Technology, nor is it intended to imply that the entities or products are necessarily the best available for the purpose.

The floor slabs were modeled using layered shell elements with through-thickness integration, with distinct layers representing concrete and reinforcing steel. The beams and columns were modeled using Hughes-Liu beam elements with cross-section integration (Hallquist 2007), with distinct integration points for cover concrete, core concrete (for which confinement effects were considered as discussed in the following subsection), and reinforcing steel. Bond slip at critical cross sections, including the beam-to-column interfaces and the bar cut-off locations, was considered by using special interface elements (beam elements with cross-section integration) with a modified stress-strain relationship for the reinforcing bars that incorporated displacements due to bond slip, as discussed subsequently.

Material modeling. The material stress-strain relationships used in the analyses are illustrated in Fig. 3. Expected-strength material properties, rather than lower-bound material properties, were used in the analyses, as listed in Table 2. Expected strength factors from Table 10-1 of ASCE 41-13 (ASCE 2013) were used to translate lower-bound material properties to the expected-strength properties listed in Table 2, with an expected strength factor of 1.50 for the concrete compressive strength f_c' and a factor of 1.25 for the yield strength f_y and tensile strength f_u of reinforcing steel. The concrete tensile strength was calculated from the compressive strength according to the CEB-FIP model code (CEB 1991). The steel reinforcement was assumed to be ASTM A706, Grade 60, which has a minimum specified yield strength of 414 MPa (60 ksi) and a minimum specified tensile strength of 552 MPa (80 ksi).

For the reinforcing steel (Fig. 3(a)), the modulus of elasticity was assumed to be E_s = 200 GPa (29 000 ksi), the strain at the onset of hardening was assumed to be ε_{sh} = 0.01, the uniform strain at the onset of necking was assumed to be ε_u = 0.1, and the elongation at fracture was assumed to be ε_f = 0.2. Reinforcing steel was modeled using an isotropic piecewise-linear plasticity model. Fracture of reinforcing bars was considered in both the interface beam elements and in the shell elements representing the floor slabs by defining a critical plastic strain at which the stress would drop to zero.

For concrete, the modulus of elasticity was calculated as $E_c = 4700\sqrt{f_c'}$ MPa ($E_c = 57000\sqrt{f_c'}$ psi). For unconfined concrete, the stress-strain relationship proposed by Popovics (1973) was adopted, as shown in Fig. 3(b), where the strain ε_{c1} was assumed to be 0.0022 and the cutoff strain $n\varepsilon_{c1}$ is estimated according to the CEB-FIP model code (CEB 1991). To reduce spurious localization due to material softening, the appropriate value for the cutoff strain was calculated based on the element size to keep the compressive fracture energy $G_{f,c}$ constant. As a result of the confinement provided by the transverse reinforcement, the core concrete has enhanced strength and ductility (see Fig. 3(b)). The modified Kent-Park model proposed by Scott et al. (1982) was used to represent the effects of confinement. For concrete in tension (Fig. 3(c)), a linear stress-strain relationship is used up to the tensile strength f_t, beyond which the stress is reduced linearly with increasing strain. The post-ultimate softening modulus accounts for the tension-stiffening effect, in which reinforcement holds the concrete together after initial cracking, allowing the concrete to continue to carry some tension as cracks open. The ultimate strain associated with crack opening, ε_u^{cr}, which controls the softening modulus, is calculated based on the tensile fracture energy $G_{f,t}$ and the crack bandwidth h.

Table 2. Expected-strength material properties used in analysis.

Normal-weight concrete		ASTM A706 Grade 60 reinforcing bar	
Compressive strength, f_c'	Tensile strength, f_t	Yield strength, f_y	Tensile strength, f_u
41.4 MPa (6000 psi)	3.6 MPa (523 psi) *	517 MPa (75 ksi)	689 MPa (100 ksi)

* Calculated based on compressive strength (CEB 1991).

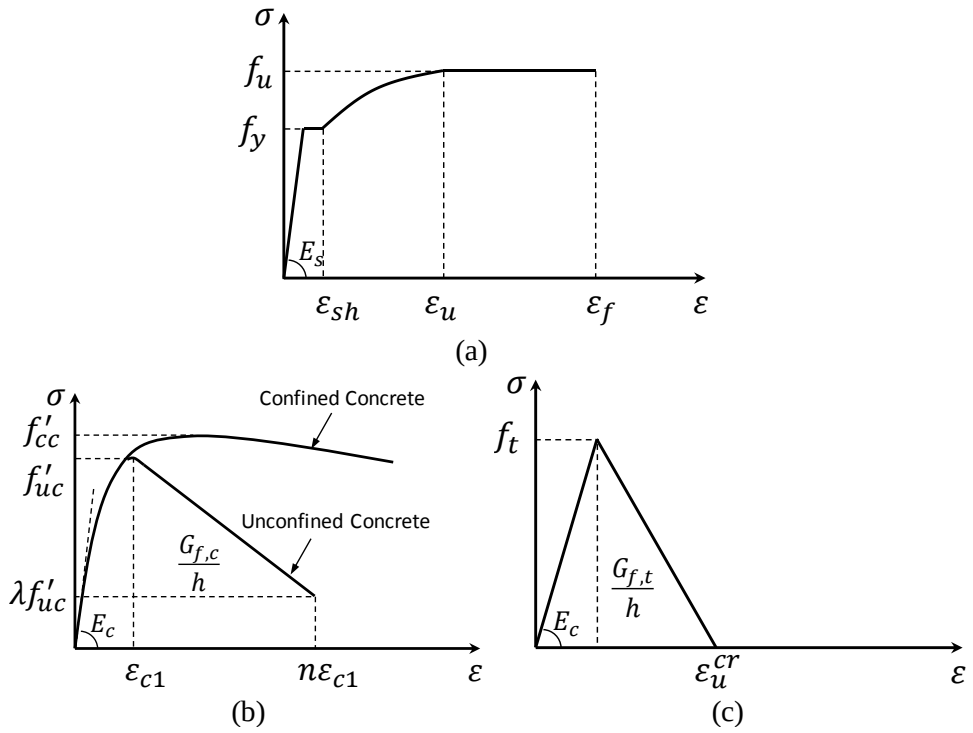

Fig. 3. Typical material stress-strain relationships: (a) reinforcing bar; (b) concrete in compression; and (c) concrete in tension

Bond-slip effects. Previous studies have indicated that the effects of bond-slip between concrete and reinforcing bars can be significant in computational simulations of reinforced concrete structures subject to column loss. If bond-slip is not considered, then bond-related failure modes cannot be captured, and the fully bonded assumption may result premature bar fracture due to strain localization at critical cross sections. In this study, bond-slip effects were considered in the interface elements at critical beam sections using the approach developed by Bao et al. (2014a), in which the stress-strain relationship of reinforcing bars is modified as follows:

$$\varepsilon' = \frac{L-L_0}{L_0} = \frac{s(\sigma)+\varepsilon L_0}{L_0} = s(\sigma) + f(\sigma) = f'(\sigma, L_0) \quad (1)$$

where s is the slip of the reinforcing bar at axial stress σ, L_0 is the original length of the reinforcing bar, and L is the deformed length of the reinforcing bar including slip. Further details on this approach for modeling bond slip were presented by Bao et al. (2014a).

The tension-stiffening effect is another important bond-related phenomenon in reinforced concrete members under tension. It is important to include the tension-stiffening effect for structural members subjected to tension throughout their cross-section, such as concrete slabs under membrane action. The tension-stiffening effect for concrete slabs is considered in this study through the post-ultimate softening modulus in the tensile response of concrete, as mentioned in the previous discussion of concrete material modeling.

ALTERNATIVE LOAD PATH ANALYSIS OF PROTOTYPE BUILDING

Two types of ALPA examples are presented in this paper: nonlinear dynamic analysis and nonlinear static analysis. The former involves direct dynamic analysis of the structural response to sudden column loss. The latter involves a static pushdown analysis, using an energy-based procedure to account for dynamic effects associated with sudden column loss.

Service-level gravity load. The service-level gravity loading selected for the example analysis problems in the *ALPA Guidelines* is based on the following load combination, as specified in GSA (2003):

$$G = 1.0D + 0.25L \tag{2}$$

where D is the dead load and L is the live load. It is noted that ASCE 7-10 (ASCE 2010) specifies a load combination of $1.2D + 0.5L$ for the residual capacity of structural systems following the notional removal of load-bearing elements. The load combination given by Eq. (2) is less conservative than that specified by ASCE 7-10, and it is noted the mean dead loads in modern construction typically correspond to a dead load factor of 1.05 or 1.10 (Ellingwood et al. 2007). Based on the gravity loads summarized in Table 1, Eq. (2) gives a combined gravity load of G = 9.82 kN/m^2 (205 lbf/ft^2) for typical floors and G = 7.96 kN/m^2 (166 lbf/ft^2) for the roof. These values of gravity loading were used in the analysis examples presented subsequently.

Nonlinear dynamic analysis of sudden column loss. Three individual column removal cases were considered in this study: the corner column A1, the edge column A3, and the interior column B3, all located at the first-story level. In the nonlinear dynamic analyses, the service-level gravity load G was first applied to the floor slabs, followed by sudden removal of the first-story column. In LS-DYNA, the sudden column removal was simulated by deleting the beam elements representing the corresponding column in a restart analysis of the building model loaded with the service-level gravity load G.

Fig. 4 shows contours of vertical displacement at the peak displacement after removal of the interior column B3 at the first-story level. Table 3 summarizes the structural responses of the prototype building under the three column loss scenarios. The prototype building remained stable for all column loss scenarios.

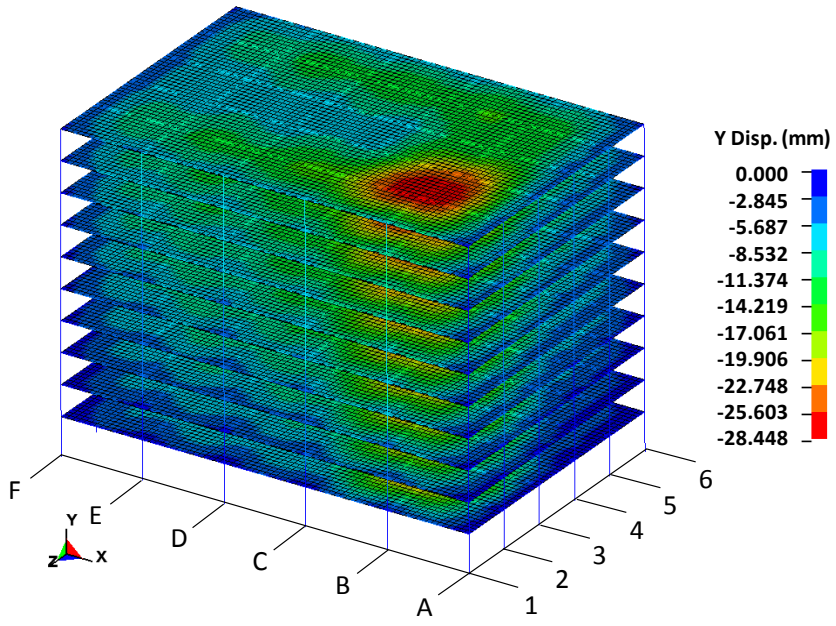

Fig. 4. Vertical displacement contours at peak displacement after sudden loss of column B3

Table 3. Results from nonlinear dynamic analysis of sudden column loss.

Column removal scenario	Final state of building	Peak displacement at removed column
Corner column A1	Stable	23 mm (0.90 in)
Edge column A3	Stable	19 mm (0.73 in)
Interior column B3	Stable	25 mm (0.96 in)

Nonlinear static push-down analysis. This section presents numerical procedures for structural robustness evaluation using nonlinear static push-down analysis. The loading scheme for a static push-down analysis is illustrated in Fig. 5, using the removal of column B3 as an example. The column is removed prior to application of gravity loading, and the service-level gravity loading G is first applied to the floor slab in bays unaffected by the column loss. Scaled gravity loading $\lambda_s G$ is then applied to the bays adjoining the removed column, and the push-down analysis is performed by increasing the dimensionless factor λ_s from zero up to the ultimate load intensity that can be sustained by the structural system under the specified column loss scenario.

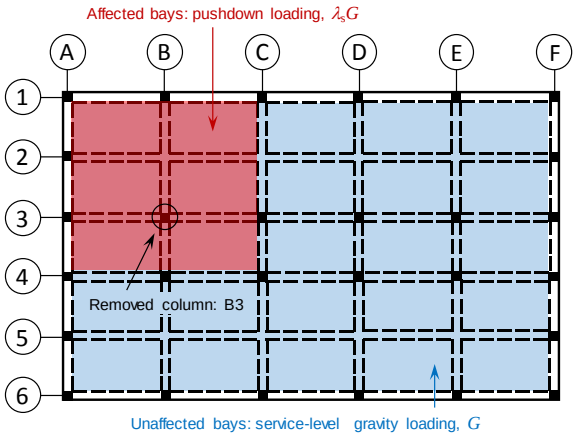

Fig. 5. Loading scheme for push-down analysis: removal of column B3

Fig. 6 shows the push-down curve obtained from nonlinear static analysis under removal of column B3, where the normalized load intensity λ_s is plotted against the vertical displacement at the removed column. As illustrated in Fig. 7, the collapse of the prototype building is initiated by failure of column B1 (circled in Fig. 7(a)), then progresses to the entire building (Fig. 7(b)). An approximate dynamic response curve, calculated from the static push-down curve based on the energy balance approach (Bao et al. 2014b, Main 2014, Izzuddin et al. 2008, Powell 2003), is also plotted along with the static response curve in Fig. 6. Each point on the approximate dynamic response curve relates the peak displacement at the removed column under sudden column loss with the corresponding load intensity applied to the affected bays. The normalized dynamic ultimate load intensity $\lambda_{d,u}$ is defined as the dynamic load intensity at the displacement corresponding to the peak static load intensity $\lambda_{s,u}$ (Main 2014; Bao et al. 2014b). A robustness index R is defined as the minimum value of the normalized ultimate capacity over all considered column removal scenarios:

$$R = \min_i\left(\lambda_{d,u}^i \middle| i \in \text{considered column removal scenarios}\right) \quad (3)$$

Table 4 lists the normalized static and dynamic ultimate load intensities for the three column removal scenarios along with the corresponding dynamic increase factors (DIFs), which are obtained as the ratio, $\lambda_{s,u}/\lambda_{d,u}$. The robustness index R of the prototype building under the considered column removal scenarios is 1.54, which is greater than 1.0, indicating that no collapse would occur under the three column removal cases that were considered. Nonlinear dynamic analysis of the prototype building under the removal of column B3 was also performed under different levels of gravity loading, to verify the approximate dynamic responses calculated from the nonlinear static push-down analysis results. In the dynamic analyses, higher-intensity loads were applied to the affected bays and the service-level gravity load G is applied to the rest bays. The results from direct dynamic analysis are plotted along with the approximate dynamic response curve in Fig. 6, showing a reasonably consistent trend. Although the results from direct dynamic analysis indicate that the prototype building may avoid collapse under a load intensity beyond $\lambda_{d,u}$, the value of $\lambda_{d,u}$ provides a conservative estimate for the largest normalized load intensity (1.80) that the prototype building can sustain without collapse under sudden column loss of column B3.

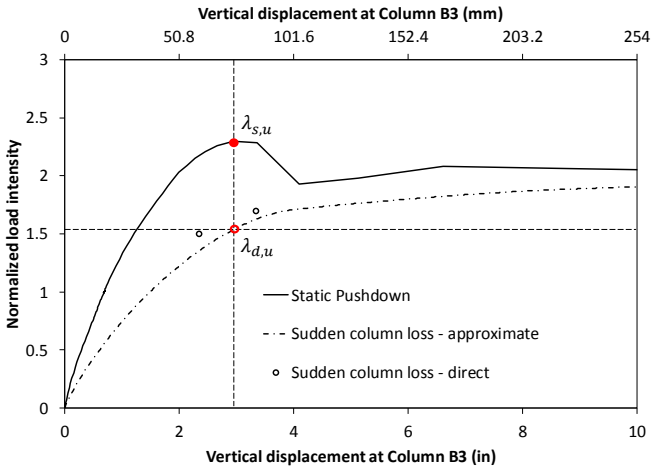

Fig. 6. Analysis results for prototype building under loss of column B3

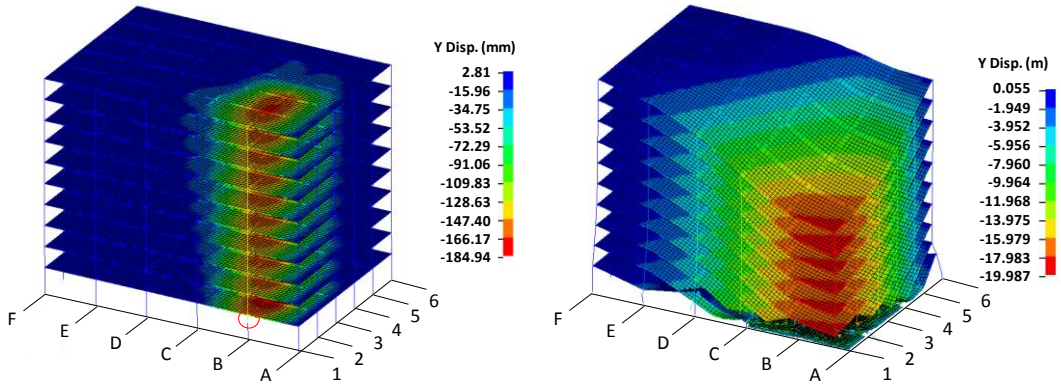

Fig. 7. Contours of vertical displacement from nonlinear static push-down analysis under removal of column B3: (a) initial collapse due to failure of column B1; (a) progressive collapse under continued pushdown-loading.

Table 4. Results from nonlinear static push-down analysis.

Column removal scenario	Static pushdown $\lambda_{s,u}$	Sudden column loss $\lambda_{d,u}$	Dynamic increase factor (DIF)
Corner column A1	5.06	4.24	1.19
Edge column A3	5.38	3.97	1.36
Interior column B3	2.30	1.54	1.49

CONCLUDING REMARKS

Alternative load path analysis (ALPA) was performed for a 5-bay by 5-bay, 10-story prototype reinforced concrete moment frame building under three column loss scenarios: a corner column, an edge column and an interior column, all at the first-story level. The three column loss scenarios were analyzed using two types of ALPA analysis: nonlinear dynamic analysis and nonlinear static push-down analysis. No collapse was observed for the three column loss scenarios considered using either type of analysis. From the results of the nonlinear dynamic analysis, the largest vertical displacement at the removed column was 25 mm (0.96 in), which corresponded to the loss of interior column B3. From the results of the nonlinear static push-down analyses, loss of interior column B3 was also the most critical, with the lowest normalized capacity under static push-down loading of $\lambda_{s,u}$ = 2.30 and the lowest normalized capacity from approximate dynamic analysis of $\lambda_{s,d}$ = 1.54. This latter value is the robustness index of the prototype building under the considered column removal scenarios. The approximate dynamic response calculated from push-down analysis using the energy-based approach was found to provide results that were reasonably consistent with nonlinear dynamic analysis. The predicted displacements from the approximate analysis tended to be larger than the displacements from nonlinear dynamic analysis under the same load intensity, and the approximate analysis gave conservative predictions of the ultimate capacity of the structural system under sudden column loss.

REFERENCES

American Society of Civil Engineers (ASCE). (2002). "Minimum design loads for buildings and other structures." *SEI/ASCE 7-02*, Reston, VA.

American Society of Civil Engineers (ASCE). (2010). "Minimum design loads for buildings and other structures." *SEI/ASCE 7-10*, Reston, VA.

American Society of Civil Engineers (ASCE). (2013). "Seismic evaluation and retrofit of existing buildings." *ASCE/SEI 41-13*, Reston, VA.

American Concrete Institute (ACI). (2002). "Building code requirements for structural concrete and commentary." *ACI 318-02 and ACI 318R-02*, Farmington Hills, MI.

Bao, Y., Lew, H.S., and Kunnath, S. (2014a). "Modeling of reinforced concrete assemblies under a column removal scenario," *J. Struct. Eng.*, 140(1), 04013026.

Bao, Y., Main, J.A., Lew, H.S., and Sadek, F. (2014b). "Robustness assessment of RC frame buildings under column loss scenarios." *Proc., ASCE/SEI Structures Congress 2014*, Boston, MA.

Comite Euro-International du Beton (CEB). (1991). *CEB-FIP Model Code 1990 Design Code*, Published by Thomas Telford, London, UK.

Ellingwood, B.R., Smilowitz, R., Dusenberry, D.O., Duthinh, D., Lew, H.S., and Carino, N.J. (2007). "Best practices for reducing the potential for progressive collapse in buildings." *NISTIR 7396*, National Institute of Standards and Technology, Gaithersburg, MD.

General Services Administration (GSA). (2003). "Progressive collapse analysis design guidelines for new federal office buildings and major modernization projects." Washington, DC.

Hallquist, J. (2007). "LS-DYNA keyword user's manual." Livermore Software Technology Corporation, Livermore, CA.

International Code Council (ICC). (2003). *International Building Code*, Falls Church, VA.

Izzuddin, B.A., Vlassis, A.G., Elghazouli, A.Y., and Nethercot. D.A. (2008). "Progressive collapse of multi-storey buildings due to sudden column loss – Part I: Simplified assessment framework." *Eng. Struct.*, 30, 1308-1318.

Livermore Software Technology Corporation (LSTC). (2014). *LS-DYNA, a program for nonlinear dynamic analysis of structures in three dimensions, Version R7.1.1*, Livermore, CA.

Main, J.A. (2014). "Composite floor systems under column loss: collapse resistance and tie force requirements." *J. Struct. Eng.*, 140, Special Issue: Computational Simulation in Structural Engineering, A4014003.

Popovics, S. (1973). "A numerical approach to the complete stress strain curve for concrete." *Cement and Concrete Research*, 3(5), 583-599.

Powell, G. (2003). "Collapse analysis made easy (more or less)." *Proc., Annual Meeting of the Los Angeles Tall Buildings Structural Design Council: Progressive collapse and blast resistant design of buildings*, Los Angeles, CA.

Scott, B.D., Park, R., and Priestley, M.J.N. (1982). "Stress-strain behavior of concrete confined by overlapping hoops at low and high strain rates." *ACI J.*, 79(1), 13-27.

Shen, Q. and Ghosh, S.K. (2006). "Assessing ability of seismic structural systems to withstand progressive collapse: Progressive collapse analysis of cast-in-place concrete frame buildings." *Report submitted to the Building and Fire Research Laboratory*, NIST, Gaithersburg, MD.

Eds.: Azad M. Madni, Barry Boehm
Daniel A. Erwin, Roger Ghanem; University of Southern California
Marilee J. Wheaton, The Aerospace Corporation
Redondo Beach, CA, March 23-25, 2017

Patterns for modeling operational control of discrete event logistics systems (DELS)

***Timothy Sprock*[a]**
[a] National Institute of Standards and Technology, timothy.sprock@nist.gov

Abstract

Designing smart operational control systems for Discrete Event Logistics Systems (DELS) requires a standard description of control behaviors executed at the operational management level of DELS control. In this paper, we propose a set of patterns for modeling the operational control mechanisms, organized by classes of control questions that all DELS must be able to answer. The pattern for each control question includes an analysis-agnostic functional definition of the control problem for that question, as well as a mapping of the decision variable in that problem to a particular function and execution mechanism in the base system.

Keywords: System Design Methods; Smart Manufacturing; Discrete Event Logistics Systems;

1. Introduction

Discrete Event Logistics Systems (DELS) are a class of dynamic systems that transform discrete flows through a network of interconnected subsystems [1]. These include systems such as supply chains, manufacturing systems, transportation networks, warehouses, and health care delivery systems. Traditionally, each specialized kind of DELS has been regarded as a distinct class of systems requiring its own dedicated research and development. However, these systems share a common abstraction, i.e. *products* flowing through *processes* being executed by *resources* configured in a *facility* (PPRF), and they appear together in integrated models of the enterprise. For example, production systems might integrate storage and fulfillment capabilities as well as material handling and transportation systems, and supply chains might integrate flows between warehouses, transportation systems, and manufacturing or health care facilities.

The increasing size, integration, and complexity of next-generation smart DELS requires more robust engineering design methods. Fundamental to more robust design methodologies are explicit system specifications and more powerful search and decision-support algorithms; see [2] for an example in the warehousing context. Next-generation smart control systems must integrate more information feedback from sensors in the plant and from global information systems, as well as accommodate greater automation. These systems are more software intensive than traditional plant designs, which have focused primarily on hardware selection and configuration. A standard description of operational control would enable

Sprock, Timothy.
"Patterns for modeling operational control of discrete event logistics systems (DELS)."
Paper presented at 15th Annual Conference on Systems Engineering Research (CSER),
Los Angeles, CA. March 23, 2017 - March 25, 2017.

development of a uniform interface to decision tools, supported by interoperable, or plug-and-play, analysis tools. However, despite progress on modeling the structure and behavior of DELS, a standard representation of operational control problems for DELS remains a challenge.

This paper presents a set of patterns for modeling the operational control mechanisms for DELS. These patterns include an analysis-agnostic description of each control problem that is used to connect the controller's decision problem to the corresponding actuator function and execution mechanism in the base system. The rest of the paper is organized as follows: Section 2 provides context for modeling operational control in DELS, Section 2.1 provides an informal introduction to the control problems, and Section 2.2 describes a simple form for defining control patterns. Then Section 2.3 uses the pattern form to capture each of the functional control mechanisms and provides a reference architecture for assembling control components. Then Section 2.4 describes a concrete application of the patterns to specifying a smart manufacturing system. Finally, Section 3 discusses future directions.

2. Modeling Operational Control in DELS

Operational control is the manipulation of flows of tasks and resources through a system in real-time, or near real-time. Each task requires or authorizes a DELS to use its resources to complete a portion of the process plan contained in that task. Operational control consists of multiple mechanisms, each including a function in the controller that prescribes actions to be taken and an actuator in the base system (or plant) that executes the prescribed action. A model of operational control is part of a broader approach to modeling DELS that includes a domain specific language, a reusable component library, and a reference architecture [3,4]. This broader model is organized into three layers: the structure layer that captures flow networks, process networks, and relationship networks; the behavior layer that describes each DELS using product, process, resource, and facility (PPRF) concepts; and finally, the control layer, which is the focus of this paper.

A standard analysis-agnostic representation of each control problem is necessary to bridge the gap between the system model and analysis models that support design methods and operational decision-making for the system, including statistical (description), discrete event simulation (prediction), and mathematical programming (optimization) models. This standard representation of operational control is a set of patterns in the DELS reference architecture [5]. These patterns for operational control can describe the control of existing systems, as well as guide design of control for new or modified systems.

2.1. The Operational Control Questions

The operational control layer of the DELS reference architecture is based on a set of control problems organized by questions posed by the base system to the controller and corresponding answers that prescribe control actions for the actuators in the base system to execute [4]. Each control question encapsulates a single function of a controller to manipulate the flows of tasks and resources (note that controllers may leverage several functions jointly, i.e. answer several questions together as is the case for scheduling). These control questions are:

1) “Should a task be served?” (*admission*);
2) If so, then “When should the task be serviced?” (*sequencing*); and,
3) “By which resource?” (*assignment*);
4) “Where (to which DELS for what process) should the task be sent after it completes the required processing at the current DELS?” (*routing*);
5) “When, and to which state, does the state of a resource need to be changed?” (*change in resource capacity or capability*).

Figure 1 illustrates the interaction between the base system and controller (control questions and answers), as well as the control execution mechanisms (actuator components in the base system). For more discussion on the functional requirements of the controller itself (how it answers the control questions), see [4,6].

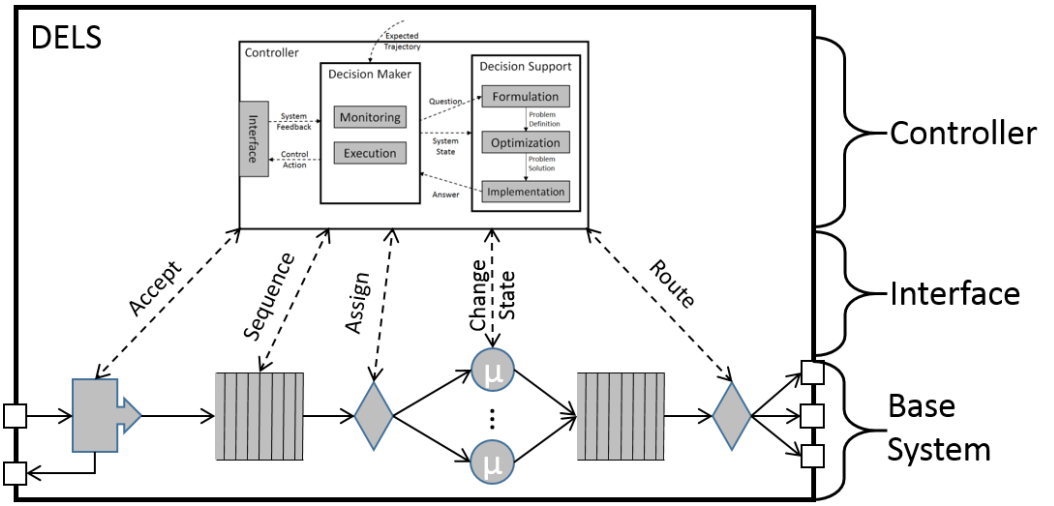

Figure 1. This illustrates the control execution mechanisms (the actuators in the base system), the functional architecture of the controller, and the interaction between the base system and controller (control questions and answers).

For example, production systems use manufacturing resources to service orders or jobs (a kind of task), leading to the following control problems:

1) Admission decides whether or not to accept an order from a customer. The decision may evaluate available production capacity, including raw material inventory on-hand, operator availability, and the current state of resources.
2) Sequencing orders includes decisions such as prioritization (of some customers' orders over others), coordination (of orders outbound to the same customer), batching (similar orders together for efficient processing or transport), delaying (service of an order until a future period or backordering), and splitting (an order into smaller lots to be processed over time).
3) Resource assignment refers to many interrelated problems including assigning scare resources to orders. Manufacturing resources may include labor, critical processing equipment, or material handling equipment. Orders may also require assignment of auxiliary resources such as tools, fixtures, and storage locations to enable process execution.
4) Routing physically or virtually directs orders to resource locations in a facility as required by product's process plan. The routing decision also accommodates unplanned auxiliary processing steps such as exception handling, quality inspection, or unexpected buffer storage, as well as routing optimization for automated guided vehicles (AGVs).
5) Changing the capability or capacity of resources includes replenishment of input material stocks, maintenance on automated systems, changing set-ups or tooling for machines, or anticipatory movement and pre-positioning of inventory or vehicles.

2.2. A form for defining operational control patterns

Operational control patterns bring together several representations of each control problem to describe the problem in a standard way. A simple form is used in this paper to define the patterns, derived from a function-behavior-structure representation [7,8]. The components of the form are:

- **Name**: Colloquial identifier of the control problem being addressed (the literature uses various names for the control problems).
- **Question**: Domain-independent, informal "what should I do?" kind of question that the base system poses to the controller (the answer to which is an appropriate control action).
- **Control Function**: Transformation, or mapping, of system objects and their state data to actionable control decisions. This transformation formalizes the control question and answer, where the question identifies an applicable control function, and the answers are the control decisions to be executed by the base system. The transformation specifies the functional interface, or signature, of conforming analysis models that answer this particular control question.
- **Decision Expression**: A formulation of the control function in terms of one or more binary decision variables (0/1) representing the decision, for use in an optimization analysis model. This part of the pattern describes the control action to be taken when the decision variable has 1 as a value.
- **Actuator Function**: Expected effect of the actuator in the base system, for use in simulation models. This is how the control function is carried out by the actuator.
- **Actuator**: Abstract actuator that is capable of carrying out the actuator function. The actuators in this paper are selected from common discrete event simulation modeling components.

The actuator function and actuator itself are used to specify the base system model and corresponding simulation models. The decision variable defines the intent of the optimization model (what question can it answer) that is used to provide decision support. Typically, the actuator and decision variable are developed independently without a shared representation of the control mechanism they are both expressing. The control function provides a common abstraction for these elements to follow, improving interoperability between simulation and optimization analysis models and between the decision support system and the base system it is guiding.

2.3. Patterns for modeling operational control of DELS

In Figure 2, the form described in section 2.2 is used to specify how to answer each operational control question from section 2.1:

1) Admission determines which tasks the controller should admit into the base system. The corresponding decision variable is a yes/no admission choice for each task. This decision is implemented by a function that adds an accepted task to the system's queue. This function is executed by a gate actuator, which is opened, or closed, according to the variable value.
2) Sequencing determines the order, or partial order, that admitted tasks will be serviced by the system. The corresponding decision variables determine the index (position) of each task in the queue. The ordering is implemented by a function that sorts the tasks by an index determined by the decision problem and is executed by the queue where tasks are waiting for service. The task at the head of queue is serviced next.
3) Assignment matches tasks to resources, or partitions the tasks into resource-specific subsets, based on resource capabilities. The decision variable matches tasks to resources, which is implemented by a function that places the task, either virtually or physically, into the assigned resource's queue. Depending on the modeling paradigm, the assignment can be executed by a switch that directs the flow of the task to the resource, which is common in resource-oriented

modeling, or it can be executed by seizing the resource from a pool.

4) To route a task for completion of its process plan, the current DELS (or the task itself) must determine where to send the task after the current DELS has completed the requested processes. Specifically, the routing decision identifies the next process required by the task's process plan (*nextProcess*) and selects a suitable DELS to perform that process (*targetDELS*). The actuator function is the composition of two functions: f is responsible for evaluating the task's process plan to determine the next required process (*nextProcess*), while g is responsible for finding a DELS (*targetDELS*) that is capable of executing the next required process for the task, via, e.g., by directory lookup or call for proposal. These two functions are not necessarily executed in any particular order; i.e. DELS can be solicited to perform each potential process before resolving alternative paths in the process plan or resolve the alternatives then find suitable DELS. This

	Admission	**Sequencing**
Question	"Should the task be served?"	"When (in what order) should the tasks be served?"
Control Function	$Admit$:Task $\rightarrow \mathbb{B}$	$Sequence$:Task $\rightarrow \mathbb{N}$
Decision Expression	$x_i = 1$, if task i is admitted to the system	$x_{ik} = 1$, if task i is serviced k^{th}
Actuator Function	Admit(Task) := {System. TaskSet} ∪ Task	Sequence(TaskSet) := sort(TaskSet, Index) = TaskSet′
Actuator	Abstract Gate	Abstract Queue

	Assignment	**Routing**
Question	"Which resource should serve the task?"	"Where (to which DELS for what process) should the task be sent after this DELS?"
Control Function	$Assign$: TaskSet × ResourceSet $\rightarrow \mathbb{B}^{\lvert T\rvert\times\lvert R\rvert}$	$Route$: Task.ProcessPlan $\rightarrow$ Process × DELS
Decision Expression	$x_{im} = 1$, if task i is assigned to resource m	$x_{OD} = 1$, if the task is output to DELS D for process O
Actuator Function	Assign(Task, Resource) := {Resource. TaskSet} ∪ Task	nextProcess $= f$(Task.processPlan) targetDELS $= g$(nextProcess) $Route$(Task) $= g \circ f \ \vee f \circ g$
Actuator	Abstract Switch or Resource Seize	Abstract Switch

	Change Capability State	**Change Capacity State**
Question	"Should the capability state of a resource be changed?"	"Should the capacity state of a resource be changed?"
Control Function	$ChangeState$: Resource.State $\rightarrow$ newState	$ChangeState$: Resource.State $\rightarrow$ newState
Decision Expression	$X_{ij}^{m} = 1$, if resource m is changed from state i to state j	$X_{ij}^{m} = 1$, if resource m is changed from state i to state j
Actuator Function	$changeService$(Process) := Resource.CurrentService $\rightarrow$ Process $changeLocation$(Location) := Resource.CurrentLocation $\rightarrow$ Location	$increaseCapacity$(Quantity) := Resource.CapacityMeasure + Quantity $decreaseCapacity$(Quantity) := Resource.CapacityMeasure − Quantity
Actuator	Abstract `Non-Preemptive Resource Setup' Task	Abstract `Change Resource Pool Size' Task

Figure 2. The patterns for operational control specification in DELS

function is executed by an abstract switch that outputs the task to a particular flow interface, which is connected to the selected target DELS.

5) Deciding to change the capability or capacity of a particular resource uses an abstraction of state to unify the models for answering this control question. The decision variable determines whether to transition resource *m* from state *i* to state *j,* where state is an abstraction for capability or capacity. The pattern for capability states describes the function, process, or service that a discrete state resource can execute at a particular time or a geographic location, i.e. serving tasks at a particular location. The pattern of capacity states describes the amount of work that can be assigned to a particular resource. The functions that change capability and capacity are abstractly modeled as set-up (*changeService*) and replenishment behaviors (*increaseCapacity*), respectively. Both behaviors are executed by generating an overhead task, which is accepted, scheduled, and executed by some other resource, such as an operator, maintenance resource, or procurement system.

The abstract actuators corresponding to control questions in Figure 2 are model library components for constructing system models. Figure 3 uses these components to formalize the process illustrated in Figure 1. Each component enables the DELS to control the flow of tasks and resources through the system. In Figure 3, a new task enters through the *inTask* port of the DELS and is handled by the *admissionGateway,* a gate type resource that decides whether to admit the task or not. The *admitTask* port (small rectangle on the border of the admissionGateway) interfaces with the controller, which provides the gate with a yes or no (Boolean) decision for each task. The admitted task then flows (filled triangle) into the queue containing the system's *taskSet*. The *sequenceIndex* port interfaces with the controller, which provides the queue with a sequence for the tasks stored in the queue. In this model, resources may be seized from a local *resourceSet* that is owned by the DELS, or may be requested and seized from outside the system through the *ioDELSResource* interface. The *resourceAssignment* port interfaces with the controller, which provides the set of resources that are assigned to serve the task. Once necessary resources have been acquired, the task and resource flow through the remaining internal control processes and actuators as follows:

- The task and resources flow to the *Process* node.
- After processing is complete, the reusable resources are released (*releaseResources)* back to the system's central *resourceSet* or out of the system through the *ioResource* port (flow not depicted).
- The task then enters an outbound queue (*completedTaskSet*) that stores completed tasks waiting to form move batches or the next DELS to be available.
- Finally, the task departs the completed task queue, is routed by the switch (*routing*) to its next DELS, and departs through the appropriate *outTask* port. The *nextNode* port interfaces with controller, which provides the target DELS (which output port) for the task to be routed.

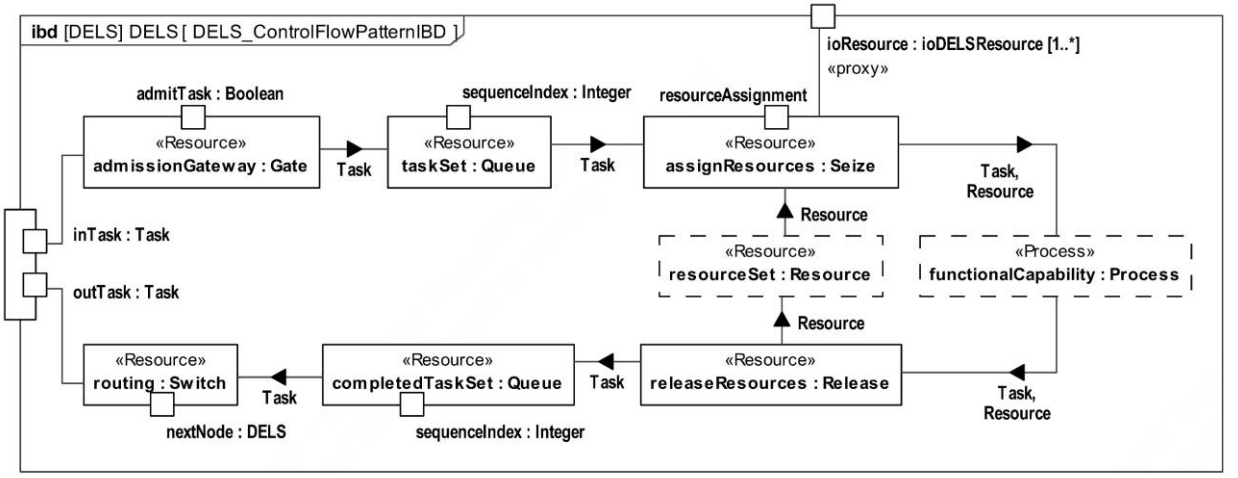

Figure 3. This shows how abstract actuators can be assembled to control the flow of a task through the system.

2.4. Applying the Patterns – Towards a Smart Manufacturing System Use Case

Designing operational control for DELS includes configuring operational control logic and selecting concrete actuators in the base system that execute the prescribed control actions. The patterns in section 2.3 describe operational control problems independently of DELS domains, enabling them to apply to all domains and improve interoperability of base system models with analysis models supporting control decisions, such as optimization. Analysis models are often constructed at a high-level of abstraction, but designing a system to execute control decisions requires selecting specific equipment to carry out the function of the abstract actuator (embodiment design). Some examples of concrete actuators for a smart manufacturing system are:

1) The admission gate might be a robotic arm that retrieves the physical workpiece, work in process, and other input resources associated with a task, from an AGV or pneumatic pusher that moves tasks from a centralized conveyor onto the system's local conveyor.
2) Sequencing, and its associated abstract queue for storing tasks waiting for service, might be done by a range of technologies with varying capabilities for executing complex control behaviors. For example, some non-automated storage solutions might only be capable of simple control behaviors; for example, a gravity-fed conveyor might only be capable of enforcing a First In First Out (FIFO) discipline. Some technologies may not be capable of enforcing any sequencing discipline at all; for example, a simple storage rack requires the operator, possibly with the aid of pick lights, to execute the desired sequencing discipline. Simple storage technologies might be augmented with an automated technology, such as a robotic arm capable of picking items from slots, to create a combined system that operates like an automated storage and retrieval systems (ASRS).
3) Assignment of concrete resources to each task depends on whether the task is being brought to the resource or if the resource is being seized and brought to the task. Many systems use both mechanisms. In the case of stationary equipment, such as in a work cell, the assignment mechanism might direct a task into the equipment's queue via pneumatic switch on a conveyor. For resources in a central pool of available discrete units, e.g., input materials, fixtures, or tools, the assignment actuator might be implemented as a robotic arm or AGV that removes the resource from a central buffer and transports it to the work station.

4) Routing tasks from the system often complements admission control and might rely on technologies similar to those that bring tasks into the system. However, in material handling systems where an AGV (or non-automated worker) deliver the task, the routing behavior must first summon an AGV to the system. Then a robotic arm, or similar mechanism to the admission actuator, can place the task onto the AGV.
5) Change state decisions generate an overhead task for the system, to perform set-up or maintenance, reposition a tool or vehicle, order additional inventory, etc. These overhead tasks are assigned, scheduled, and executed by their respective systems, e.g. maintenance, material handling, or procurement, which follow the same control pattern described in section 2.3.

3. Conclusions and Future Work

To facilitate design and analysis of dynamic, intelligent operational control methods for next-generation DELS, this research identifies a set of control problems, posed as questions to a controller, and patterns for defining the functional, behavioral, and structural aspects of these problems. The patterns use functional descriptions of operational control to connect the base system (plant) model with decision support models, such as optimization and simulation.

The standard description of operational control that is captured by the patterns in this paper supports the development of interoperable, or plug-and-play, analysis tools to answer the control questions. This unifying abstraction of operational control also enables a uniform architecture for each kind of controller, which is especially important for a flexible control architecture and transitioning from traditional centralized, hierarchical control to adaptive, decentralized or holonic architectures [9]. This vision contrasts with each DELS having a different controller architecture depending on its responsibilities, requirements, and the broader control hierarchy selected.

A future goal is formalizing the definitions of operational control for DELS that are documented here informally using patterns. The objective is to formalize the control questions into a canonical set that rigorously partitions the set of all DELS control problems into equivalence classes with a formal equivalence relation (~) based on the functional mapping and associated interface definition. Additional formalization is also required for the mapping between the functional definition and the analysis components.

Future extensions to the control patterns are expected to include concrete system modeling objects as a model library of components, an interface definition for optimization methods, and representative simulation modeling components. Additional reference implementation patterns will be developed that describe integration of simulation components with operational control methods (optimization). The goal is to verify and validate control in simulation and port the logic to a real system, as is common in other engineered systems.

Acknowledgements

The author thanks Conrad Bock for his helpful conversations and comments.

Commercial equipment and materials might be identified to adequately specify certain procedures. In no case does such identification imply recommendation or endorsement by the U.S. National Institute of Standards and Technology, nor does it imply that the materials or equipment identified are necessarily the best available for the purpose.

References

1. Mönch, L., Lendermann, P., McGinnis, L.F. and Schirrmann, A., 2011. A survey of challenges in modelling and decision-making for discrete event logistics systems. *Computers in Industry*, *62*(6), pp.557-567.

2. McGinnis, L. and Sprock, T., 2016. Toward an engineering discipline of warehouse design. *14th International Material Handling Research Colloquium.*
3. Thiers, G., 2014. A model-based systems engineering methodology to make engineering analysis of discrete-event logistics systems more cost-accessible. Ph.D thesis, Georgia Institute of Technology, Atlanta, GA. https://smartech.gatech.edu/handle/1853/52259
4. Sprock, T., 2016. A metamodel of operational control for discrete event logistics systems. Georgia Institute of Technology. Ph.D thesis, Georgia Institute of Technology, Atlanta, GA. https://smartech.gatech.edu/handle/1853/54946
5. Cloutier, R.J. and Verma, D., 2007. Applying the concept of patterns to systems architecture. *Systems engineering*, 10(2), pp.138-154.
6. Sprock, T. and McGinnis, L.F., 2015. A Conceptual Model for Operational Control in Smart Manufacturing Systems. *IFAC-PapersOnLine*, 48(3), pp.1865-1869.
7. Gero, J.S., 1990. Design prototypes: a knowledge representation schema for design. *AI magazine*, 11(4), p.26.
8. Umeda, Y., Takeda, H., Tomiyama, T. and Yoshikawa, H., 1990. Function, behaviour, and structure. *Applications of artificial intelligence in engineering V*,*1*, pp.177-194.
9. Dilts, D.M., Boyd, N.P. and Whorms, H.H., 1991. The evolution of control architectures for automated manufacturing systems. *Journal of manufacturing systems*, 10(1), pp.79-93.

Proceedings of the ASME 2017 12th International Manufacturing Science and Engineering Conference
MSEC2017
June 4-8, 2017, Los Angeles, CA, USA

DEVELOPING A CAPABILITY-BASED SIMILARITY METRIC FOR MANUFACTURING PROCESSES

Kevin Li
Department of Mechanical Engineering
University of Maryland
College Park, Maryland 20742

William Z. Bernstein*
Systems Integration Division
National Institute of Standards and Technology
Gaithersburg, Maryland 20899

KEYWORDS
Unit manufacturing process; process capability;
similarity metric; supplier discovery; database exploration

ABSTRACT
Manufacturing taxonomies and accompanying metadata of manufacturing processes have been catalogued in both reference books and databases on-line. However, such information remains in a form that is uninformative to the various stages of the product life cycle, including the design phase and manufacturing-related activities. This challenge lies in the varying nature in how the data is captured and represented. In this paper, we explore measures for comparing manufacturing data with the goal of developing a capability-based similarity metric for manufacturing processes. To judge the effectiveness of these metrics, we apply permutations of them to 26 manufacturing process models, such as blow molding, die casting, and milling, that were created based on the ASTM E3012-16 standard. Furthermore, we provide directions towards the development of an aggregate similarity metric considering multiple capability features. In the future, this work will contribute to a broad vision of a manufacturing process model repository by helping ease decision-making for engineering design and planning.

1 INTRODUCTION
Digital manufacturing has fundamentally changed the way in which organizations design, build, and assess products. The wealth of manufacturing-related data has been exploited in many ways, to date. According to a report by McKinsey Global Institute, "manufacturing stores more data than any other sector – close to 2 exabytes of new data stored in 2010" [1]. However, it is widely accepted that until now, the manufacturing world is far from meeting its true potential in the digital age [2]. This wealth of data unfortunately lacks sufficient context, which is negatively affecting its realized value. All in all, the manufacturing environment has become data rich yet information poor.

One challenge for (semi-)automating manufacturing decision making is properly representing tacit knowledge of manufacturing experts. Currently, manufacturing databases house general information and do not provide recommendations for complex decision scenarios. An example of such a decision scenario is finding a manufacturing supplier that meets specifications for a new design, or in short, supplier discovery. In this case, the decision maker must balance the capabilities of a single supplier across a variety of dimensions, e.g. produced shape, achievable tolerance and surface roughness. Narrowing down a particular manufacturing process based on capabilities is often left to the discretion of the human and their experience. Studies have shown that the coordination between machine-driven algorithms and human-based intuition improves decision making processes [3]. Similarly, one goal of this work is to enhance process discovery through human-machine coordination.

In this paper, we explore various techniques for defining the similarity of two manufacturing processes in the context of supplier discovery. The eventual goal of this research is to develop a general metric that enables faster and easier comparison of manufacturing process capabilities. We can envision that such a metric would complement existing efforts in ontology and linked

*Address all correspondence wzb@nist.gov

Bernstein, William; Li, Kevin.
"Developing a capability-based similarity metric for manufacturing processes."
Paper presented at The ASME 2016 Manufacturing Science and Engineering Conference (MSEC2016), Los Angeles, CA. June 4, 2017 - June 8, 2017.

data development to enhance design and manufacturing engineers' toolboxes to make better decisions. This paper proposes several metrics for different manufacturing attributes depending on the nature of the data. Furthermore, we present initial work towards a unified metric that takes into account multiple manufacturing capabilities in a weighted scheme.

The rest of the paper is organized as follows. Section 2 discusses relevant work from the perspective of standards, databases, and similarity metrics. Section 3 describes the script that was used to parse the data and the metrics that were adapted and developed to compare the processes. Section 4 presents results after computing the various metrics using a test dataset along with its interpretation. Section 5 addresses limitations of our approach, primarily focused on data-related issues. Section 6 looks at future work for the project and how it can be implemented into a larger initiative to facilitate the manufacturing design process. The vision of this work is to include the metric and the related algorithms within a structured database to enable better query mechanisms for human decision makers.

2 BACKGROUND & MOTIVATION

This section reviews related work with respect to (1) standardizing information models describing manufacturing systems, (2) storing information related to capabilities of manufacturing processes, and (3) developing similarity metrics for such information models. Here, we motivate our work for constructing an automated measure of similarity of manufacturing processes.

2.1 Standardizing manufacturing information models

Primary efforts in standardizing information models that formally characterize manufacturing processes include IS0 20140 [4] and ASTM E3012-16 [5], both of which focus on environmental considerations of manufacturing processes. Both standards address the need for improving environmental models to populate life cycle inventories (LCI). In fact, ISO 20140 specifically states that its proposed reference model directly aligns with the EcoSpold *de facto* standard that has been widely adopted for storing LCI and life cycle assessment (LCA) unit process models [6]. Though the focus of these two standards lies within environmental analysis, the reference models should be robust enough to include traditional performance attributes associated with manufacturing systems, e.g. cost, quality, and throughput.

One of the motivating factors for implementing a standard representation for manufacturing information is model storage and curation. In this light, we proposed an open web-based repository to promote data consistency and bridge the research gap between institutions and private sectors [7]. This repository adopts the ASTM E3012-16 standard and uses the Unit Manufacturing Process (UMP) as a formal model for capturing manufacturing data [5]. The UMP captures input and output information as well as various process parameters and can be modeled using data formatting languages such as eXtensible Markup Language (XML) or JavaScript Object Notation (JSON).

This paper focuses on the development of a metric to assess the similarity between such UMP models. We envision that this work will improve the navigability and usability of the proposed repository. Next, we review existing database incarnations for the manufacturing processes, specifically in the context of supplier discovery and process capability-based query.

2.2 Storing process capability information

Currently, there are several databases that store manufacturing information. The CES Selector from Granta Design[1], a commercial database designed for material selection, houses general information on manufacturing processes. Such information includes broad interval ranges of performance indicators, e.g. cost and CO_2 emissions per amount of material processed. Since the manufacturing capabilities of an organization are heavily dependent on their acquired manufacturing assets and resources, commercial databases, such as CES Selector, do not provide much specificity for manufacturing processes. From another perspective, there are a number of supplier discovery and service matching tools, e.g. Alibaba[2], in which it is possible to match process capability with available resources. However, in these tools' current form, such an effort would require significant costs in time to translate this information into a usable form. Also, it is possible that the posted capabilities of individual job shops and manufacturers could be over-claimed and not accurate [8].

In response to these challenges, there have been efforts in providing open and free access to manufacturing process capability information, such as CustomPart.Net[3]. Such databases provide a variety of estimation and manufacturing tools based on tabular information of material and manufacturing process, and supplier information. Examples of available tools include a milling speed and feed calculator, cost estimation for injection molding, and bend allowance calculator for sheet metal. These open sources claim widespread use in industry with thousands of reported estimations per month. In this paper, we use this type of information about manufacturing processes since the data is open, available, and seemingly trustworthy judging by its wide use as well as its use within similar research efforts [9].

2.3 Defining similarity between information models

Measuring the similarity between information models is nothing new. By definition, the similarity between two objects is a function of the commonality and the differences they share [10]. In this paper, we borrow concepts from similarity

[1] https://www.grantadesign.com/products/ces/
[2] https://www.alibaba.com/
[3] http://www.custompartnet.com/

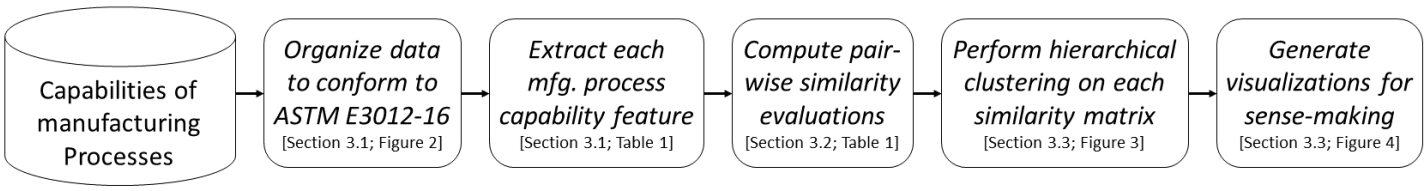

FIGURE 1. Flowchart specifying steps for the analysis performed. Here, we transform tabular data about manufacturing processes into a standard representation, abiding by ASTM 3012-16. We then compare each pair of manufacturing processes based on the computed similarity metrics, perform clustering on the resultant matrix, and generate visualizations as a reporting mechanism to aid in data sense-making.

measures from various applications areas, including biology, information science, and engineering.

In biomedical research, similarity measures have aided in the prediction of functions and interactions between different gene products such as proteins. These measures often utilize semantic similarity techniques due to an abundance of biomedical annotations such as the Gene Ontology [11]. In fact, now a fully adopted method, visual representations of microarray data, which represents this expression-based similarity, facilitates a deeper insight and understanding of the data to practitioners [12].

Likewise, incorporating ontologies is a key factor in building a successful model for representing manufacturing data. One attempt at creating a digital manufacturing ontology is the Manufacturing Service Description Language (MSDL) [13]. MSDL captures the abstract concepts and relationships between manufacturing services at a process, machine, shop, and supplier level. Other examples for assessing the similarity between manufacturing processes can be classified as edge-based counting methods. In these approaches, a taxonomic representation of the process universe, such as the Allen and Todd taxonomy [14], is used to determine distance between nodes in a network, e.g. in [15].

Similar approaches have also been used in the conceptual design phase, wherein only the function-component relationships are considered [16, 17], as well as in detailed design, wherein researchers have used similarity measures to uncover opportunities from existing designs [18, 19]. Others have focused specifically on cellular manufacturing, developing a metric for assessing the similarity of production lines [20]. Another approach used a graph-based metric to assess the similarity of manufacturing-based value chains [21].

Due to a lack of abundant annotations in the manufacturing industry, it can be argued that common ontology measures such as node-based approaches using information content (IC) and edge-based counting methods cannot be applied to current manufacturing data [22]. Edge-based methods using manufacturing process trees are also unreliable due to the uneven distribution of nodes and the inability to quantify the length between each parent and child node. In response, in this paper, we propose a hybrid approach wherein we combine both semantic and numerical information to develop a similarity metric to assess a manufacturing process's capabilities.

3 METHODOLOGY

In this paper, we present work towards a more comprehensive similarity metric for manufacturing processes based on their capabilities, such as achievable tolerance, surface roughness, and batch size. One of the primary challenges lies within the fact that manufacturing-related information housed in databases come in different forms, such as categorical and numerical expressions. As shown in Fig. 1, this section details the steps towards the development of this metric, including (1) data selection and processing, (2) the implementation of several different similarity calculations based on the data quality and nature of each selected capability, and (3) the visualization of the computed metrics to aid in decision making.

3.1 Pre-processing and organizing the data

Choosing the source of data was the first step as accessibility, representation, and uniformity of data were important factors to consider for an intuitive similarity measure. CustomPart.Net was chosen as it is an open-source database that can easily be accessed online and has an abundance of pre-formatted data. The database can also easily be expanded by collaborative use from institutions and private sectors. Access to larger, more specific amounts of data can enhance the existing similarity measures while also allowing for new measures to be introduced.

The standard format of a UMP model was used to capture the chosen dataset. In order to represent a UMP model, XML was chosen as the best format due to its simplicity to use and intuitive structure for human and machine reading.

A script was written using MATLAB that constructed individual XML files for each process from a conglomerate Excel spreadsheet. The raw data was captured in multiple formats and had to be properly sorted. The select features that were specified numerically occasionally came in ranges. These values were captured into upper and lower bounds as seen in the surface finish values in Fig. 2. Manufacturing data is also traditionally captured

```
<?xml version="1.0" encoding="utf-8"?>
<UMP name="Milling">
    <ProductProcessInformation name="Shapes_Typical"
        value="">
      <string-array name="Typical" value="">
        <item>Solid: Cubic</item>
        <item>Solid: Complex</item>
      </string-array>
    </ProductProcessInformation>
    <ProductProcessInformation name="Shapes_Feasible"
        value="">
      <string-array name="Feasible" value="">
        <item>Flat</item>
        <item>Thin-walled: Cylindrical</item>
        <item>Thin-walled: Cubic</item>
        <item>Thin-walled: Complex</item>
        <item>Solid: Cylindrical</item>
      </string-array>
    </ProductProcessInformation>
    <ProductProcessInformation name="Materials_Typical"
        value="">
    <ProductProcessInformation name="Materials_Feasible"
        value="">
    <ProductProcessInformation name="Lead_Time_Typical"
        unit="" value="Days"/>
    <ProductProcessInformation name="Lead_Time_Feasible"
        unit="" value="Hours"/>
    <ProductProcessInformation name="Tolerance_Typical"
        unit="in" value="0.001"/>
    <ProductProcessInformation name="Tolerance_Feasible"
        unit="in" value="0.0005"/>
    <ProductProcessInformation name="Max_Wall_Thickness
        _Typical_UB" unit="in" value="40"/>
    <ProductProcessInformation name="Max_Wall_Thickness
        _Typical_LB" unit="in" value="0.04"/>
    <ProductProcessInformation name="Max_Wall_Thickness
        _Feasible_UB" unit="in" value="72"/>
    <ProductProcessInformation name="Max_Wall_Thickness
        _Feasible_LB" unit="in" value="0.04"/>
    <ProductProcessInformation name="Surface_Finish_
        Typical_UB" unit="microinch" value="125"/>
    <ProductProcessInformation name="Surface_Finish_
        Typical_LB" unit="microinch" value="32"/>
    <ProductProcessInformation name="Surface_Finish_
        Feasible_UB" unit="microinch" value="500"/>
    <ProductProcessInformation name="Surface_Finish_
        Feasible_LB" unit="microinch" value="8"/>
    <ProductProcessInformation name="Batch_Size_
        Typical_UB" unit="" value="1000"/>
    <ProductProcessInformation name="Batch_Size_
        Typical_LB" unit="" value="1"/>
    <ProductProcessInformation name="Batch_Size_
        Feasible_UB" unit="" value="1000000"/>
    <ProductProcessInformation name="Batch_Size_
        Feasible_LB" unit="" value="1"/>
    <ProductProcessInformation name="Applications"
        value="">
      <string-array name="">
        <item>Machine Components</item>
        <item>Engine Components</item>
      </string-array>
    </ProductProcessInformation>
</UMP>
```

FIGURE 2. Example of a UMP generated wherein data from CustomPart.Net was organized via the ASTM E3012-16 standard.

in terms of typical and feasible data, where typical data reflects how a process is traditionally used, while feasible represents the physical limitations of the process. These limitations may be achieved at a sacrifice of efficiency in cost, energy, or production speed. Categorical data such as the materials were captured into string arrays for ease of processing later on.

In order to analyze the manufacturing data from any given database, the data can be entered into an Excel spreadsheet following a specific format, and similar UMP files will be generated. MATLAB was again chosen to run the remaining data processing and analysis. Using object-oriented programming methods, a simple "Process" class was created that reflected the format of the UMP by capturing each feature information into individual instance variables of the class.

3.2 Applying similarity metrics to process attributes

The information housed in the manufacturing database can be grouped into two classifications: numerical and categorical. Numerical data is expressed as nominal values or a range of values. Categorical data can be described as a list of attributes falling into a single classification. The treatments of each type of information are further explained below.

3.2.1 Numerical data For numerical information, wherein the values do not deviate by orders of magnitude, we used the Euclidean distance measure as seen in Eq. 1 and normalized it into a simple similarity function, as shown in Eq. 2.

$$D(x,y) = \sqrt{\sum_{i=0}^{n}(x_i - y_i)^2} \tag{1}$$

$$S(x,y) = \frac{\sqrt{x^2+y^2} - \sqrt{(x-y)^2}}{\sqrt{x^2+y^2}} = 1 - \frac{D(x,y)}{norm(x,y)} \tag{2}$$

where $D(x,y)$ denotes the Euclidean distance and $S(x,y)$ denotes the similarity of one entity, x, with respect to another entity, y. The element i refers to the number of elements or dimensions within a category, which was typically just one for this paper.

By applying the norm to Eq. 1, it can be rewritten to yield a result from 0 to 1, where a 1 signifies a perfect match. It is important that every metric is normalized onto the same scale in order to compare different features together in an aggregate equation. This concept will be explored later in the paper.

$$S(x,y) = exp[-\frac{\log(1+|x+y|)}{k}] \tag{3}$$

$$k = \sum_{i=0}^{n}\frac{\log(|x_i - y_i|)}{n} \tag{4}$$

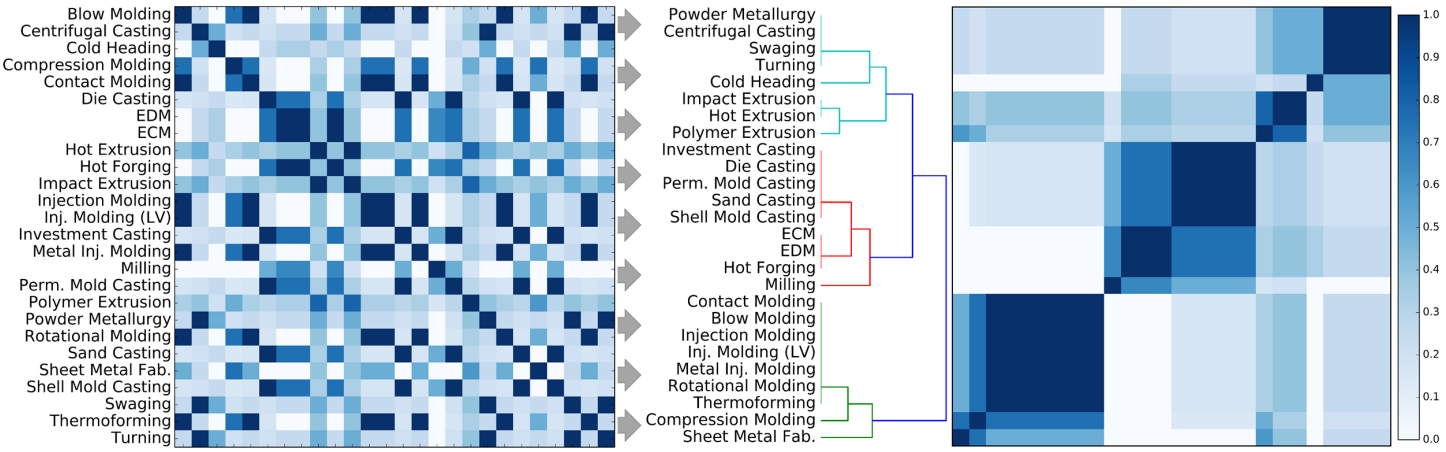

FIGURE 3. Left: example of a square similarity matrix generated. In this case, we are showing the results from a Jacquard index evaluation comparing categorical sets representing typical shapes that each process can produce. Here, we apply a colormap to indicate the level of similarity between two manufacturing processes, wherein the darker the blue denoting a higher similarity. Right: results of hierarchical clustering performed on this similarity matrix. The clusters are illustrated via a dendrogram, where its leaf labels correspond to the rows of the matrix on the right.

TABLE 1. Capability features extracted from CustomPart.Net

#	Feature	Type	Sim. Calc.
1	Shapes	Categorical	Eq. 5
2	Materials	Categorical	Eq. 5
3	Surface Finish	Numerical	Eq. 2
4	Tolerance	Numerical	Eq. 2
5	Max Wall Thickness	Numerical	Eq. 2
6	Applications	Categorical	Eq. 5
7	Batch Size	Numerical	Eq. 3
-	Aggregate Metric	Mixed	Eq. 7

Equation 3 was developed as a result of the batch size feature in the manufacturing data which differed on orders of magnitude. The data ranged from values of 10 to 1,000,000 which made ordinary distance measures such as Euclidean distance ineffective. One method that was attempted was to use the z-score technique to rescale each value based off of standard deviations. However, this method proved ineffective due to the the lack of spread in the data, as most values were captured in magnitudes of 10 rather than in specific quantities. An exponential function was picked as the metric of choice as it can scale values regardless of their magnitude. The exponential of the negative logarithm is a technique used to normalize the distance to a scale of 0 to 1. In order to achieve a similarity score of 0 for perfect similarity between two values, the value inside the logarithm needed to be scaled by 1. Finally, a weight, k, is used to alleviate the spread of the values, such that a large k value would yield a higher similarity score when comparing two values such as 10 and 1,000,000. After testing different k values, the mean of the log of every difference combination was chosen as seen in Eq. 4.

It should be noted that some attributes, such as batch size, were expressed as ranges. These intervals were separated into upper and lower bounds, denoted as UB_n and LB_n, respectively. Then, a similarity measure is applied to every combination of values such as UB_1 to UB_2, UB_1 to LB_2, etc. For simplicity, the largest similarity measure was taken out of the combinations.

3.2.2 Categorical data For categorical information, the Jaccard Index was adopted as a common measure for comparing two sets. As seen in Eq. 5, the similarity between two sets A and B can be taken as the intersection over the union of A and B. This is a simple but effective way to measure similarity for the materials and shapes where the data is evenly distributed among every process.

$$J(A,B) = \frac{|A \cap B|}{|A \cup B|} = \frac{|A \cap B|}{|A| + |B| - |A \cap B|} \tag{5}$$

Table 1 summarizes the manufacturing capabilities that were extracted from CustomPart.Net and the respective similarity metric applied to each. For each features, similarity matrices were computed to represent a total of 325 pairwise comparisons amongst 26 different processes. Next, we explore visualization options for presenting results from applying the various similarity measures.

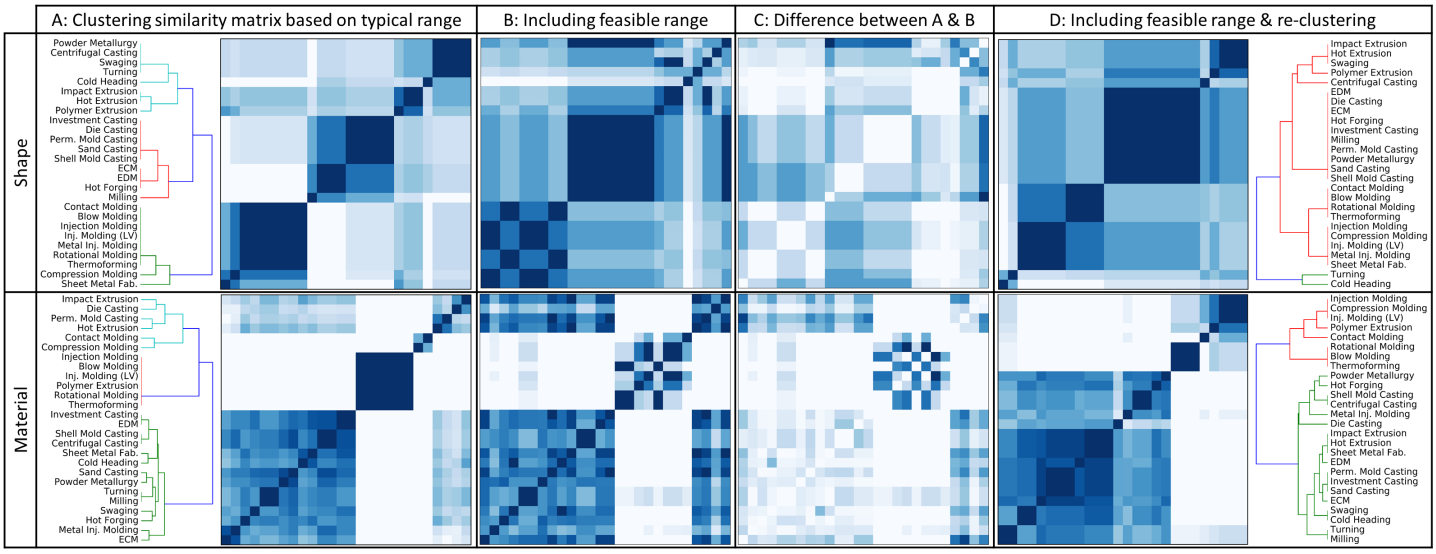

FIGURE 4. Analysis of the effect of expanding the set of typical features with feasible ranges. Here, we consider two of the studied capability features, shape (top) and material (bottom). Column A shows the results from the hierarchical clustering following the same procedure shown in Fig. 3. Column B illustrates the difference in similarity evaluation when including the feasible range. Note that we do not perform any re-clustering at this stage. Column C presents the difference between Columns B & A. Column D shows the shows the results from re-clustering based on Column B.

3.3 Visualizing the similarity matrices

Applying prudent visualization to scenarios with rich analytics allows human decision makers to quickly gain insight into data. This process of gaining insight through internal cognitive processes is commonly referred to as sense-making [3]. Here, we exploit accepted matrix-based visualization to gain deeper insight into the proposed similarity metrics. The primary visualization features are the clustered similarity matrix codified with a color scale, and its accompanying dendrogram.

First, we begin with each computed similarity matrix. An example of one matrix can be seen in Fig. 3 on the left. This matrix represents the values from the similarity evaluation depending on the metric used, wherein the darker the blue denotes the higher value of similarity. This is a square matrix, where the rows and columns represent the same set of processes.

Based on the values in the similarity matrix, we perform hierarchical clustering to identify communities of manufacturing processes based on sharing similar capabilities. To evaluate the distances between resultant clusters, we employ the Voor Hees Algorithm [23], seen in Eq. 6.

$$d(u,v) = max\{dist(u[i],v[j])\} \tag{6}$$

Based on the computed values from Eq. 6, we then build a dendrogram, to visualize the distances between the clusters, which can been seen in Fig. 3 on the right. A longer line translates to a larger distance between the clusters. If there is a vertical line adjacent to the leaf labels, this signifies that the processes are precisely the same based on that specific similarity evaluation. For example, in Fig. 3, *Powder Metallurgy*, *Centrifugal Casting*, *Swaging*, and *Turning* are exactly identical with respect to their capability of producing a typical set of shapes.

4 RESULTS

This section presents some insights drawn out by analyzing the similarity matrices representing various capability features. One of those insights is presented in Fig. 4. Here, we demonstrate some of the challenges associated with dealing with the data. The database provides two different ranges for each feature studied, one that describes the *typical* range of process capability and another broader set that characterizes the *feasible* range.

Figure 4 shows that including the feasible set of attributes affects the specific feature differently. In this case, we consider two capability features, shape and material, both of which are defined sets of strings. Column A presents both similarity matrices clustered solely based on the typical set of attributes (i.e. possible shapes and materials). We then append the sets with the additional attributes from each feasible set, as seen in Column B. Here, we re-calculate the similarity matrix based on the new sets of capabilities but do not re-order the rows. By investigating the difference of Column A and Column B, presented through a simple subtraction process in Column C, we show that, in these cases, the feasible range affects the process communities differ-

TABLE 2. Corpus of attributes for shape and material

Shapes–6 total	Materials–17 total
Flat; Thin-walled: Cubic; Thin-walled: Cylindrical; Thin-walled: Complex; Solid: Cylindrical; Solid: Cubic; Solid: Complex	Alloy Steel; Carbon Steel; Cast Iron; Stainless Steel; Aluminum; Copper; Lead; Magnesium; Nickel; Tin; Titanium; Zinc; Ceramics; Composites; Thermoplastics; Thermosets; Elastomers

ently. This is further enforced by re-clustering the similarity matrix based on the total set of attributes, including both typical and feasible ranges, seen in Column D.

To explain this difference in sensitivity, let us take Electrical Discharge Machining (*EDM*) and Electrochemical Machining (*ECM*) as an example. With respect to shape, as seen in Fig. 4A, *ECM* and *EDM* share identical sets of typical shapes with *Hot Forging*. After appending the original set of possible shapes with the feasible range, this cluster is expanded as seen in Fig. 4D. It now includes processes such as *Die Casting*, *Investment Casting*, and *Milling*. In summary, considering the complete range of feasible shapes, clusters become more inclusive.

If we consider the same processes, *EDM* and *ECM* for the material feature, we find key differences when compared to the shape feature. As seen in Fig. 4A, *EDM* is identical to *Investment Casting* and *ECM* is closest to *Metal Inj. Molding*. However, after appending with the feasible set and re-clustering (Fig. 4D), we see that clusters are less inclusive and often exhibit different characteristics. For example, *EDM* now represents a unique set of capabilities and is closest to *Sheet Metal Fab.*, *Hot Extrusion*, and *Impact Extrusion*.

This observation can be explained by investigating the nature of the data. Table 2 lists each corpus of terms for both the shape and material categories. The materials feature almost 3 times the amount of terms when compared with shapes, i.e. 17 compared to 6. This partly explains why the shape feature has much more inclusive clusters after including the feasible ranges. With fewer possible attributes, the shape feature can be expressed by a reasonable number of possible combinations. Once seeded with more possibilities, e.g. 17 concepts as in the materials feature, the clustering behaves differently.

Figure 5 shows other examples of clustered similarity matrices for selected features, only based on typical ranges of capabilities. Similar to above, the nature of the data drastically affects the "performance" of the hierarchical clustering. For Surface Finish, which is numerical data wherein similarity was computed based on Eq. 2, we see a large number of small clusters that exhibit considerable closeness. This is due to the variability in the data's numerical range but the metric still seems to successfully delineate communities within that range. For Batch Size, we see large clusters due to the the homogeneity of the database infor-

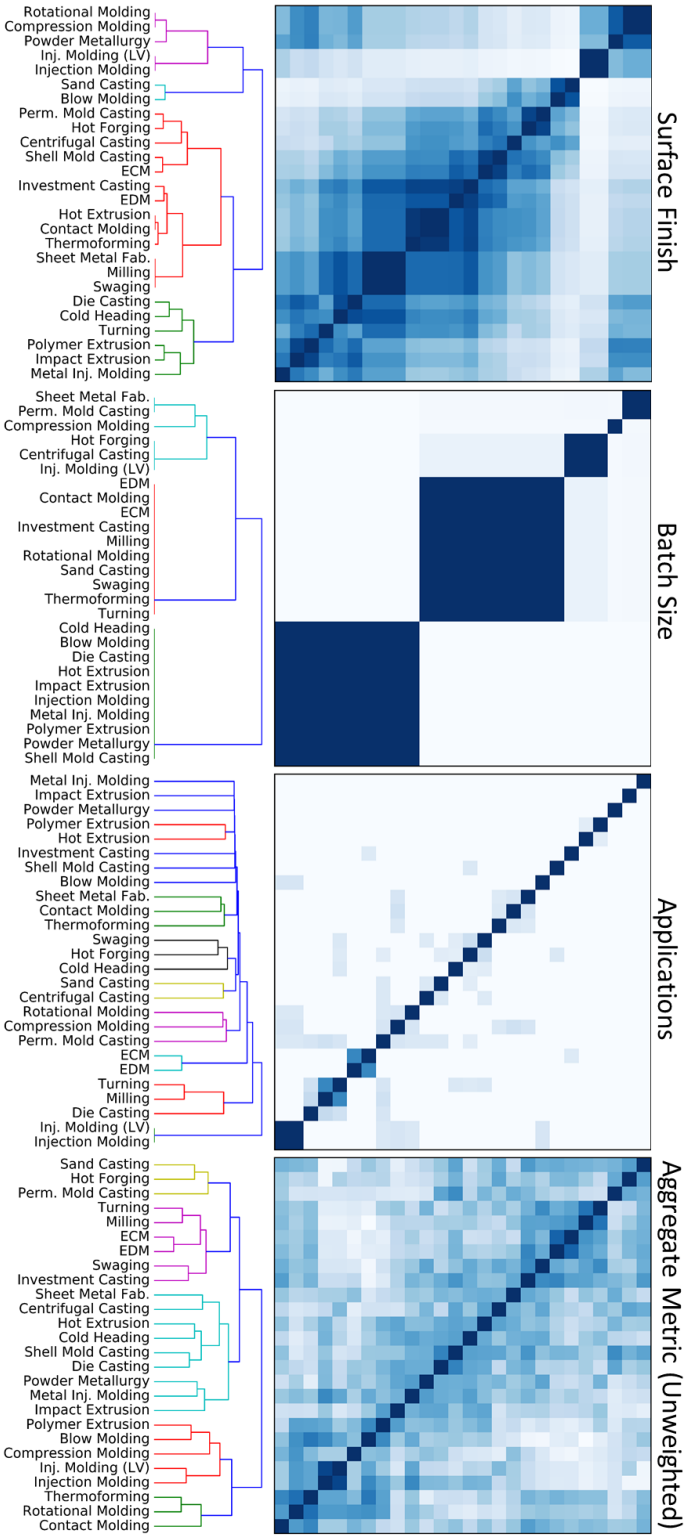

FIGURE 5. Clustering typical surface finish, batch size, applications, and an aggregate metric considering all features.

mation. In contrast, for Applications, which represent a corpus of 72 terms specifying engineering applications (e.g. gears, pipes, and aerospace components), we see few identifiable similar sets of processes due to the heterogeneity of terms.

The significant takeaway of our analysis is that the corpus of concepts for each capability feature has a seemingly large impact on the clustering. This becomes a challenge when developing an aggregate similarity metric that takes into account all capability features studied. The last matrix shown in Fig. 5, reflects the similarity calculations of every feature combined using an aggregate measure as seen in Eq. 7, where k is the weight of the feature i.

$$S(x,y) = \sqrt{\sum_{i=0}^{n} k_i (S_i)^2} \tag{7}$$

Without weighting the features within the overall distance measurement, we can see that the clustering algorithm does not identify distinct and tight clusters. Instead, we see a number of "loose" clusters, wherein it is difficult to discern similar processes based on the full set of capability features.

Based on these observations, we describe limitations of our work to motivate future work in the next section. This description will help account for these discrepancies within the data to specifically address the development of an aggregate similarity metric for manufacturing processes.

5 LIMITATIONS OF WORK

Limitations of our approach are tightly related to the nature of the data applied in this paper. Primary issues include (1) data granularity, (2) the heterogeneity of scales for the numerical data, (3) lack of understanding of the inter-relationships for various combinations of capability features, and (4) the scope and context of the data.

As shown in the previous section, the metrics that we applied to the data perform differently, sometimes poorly, based on the granularity of the data. When using semantic metrics such as the Jaccard Index, the distribution of terms and number of unique terms may lead to insubstantial measurements. The Application feature was a clear example of such a scenario. The dataset used 17 unique material types and 72 different application types. Although more data types may appear to benefit the similarity measure, with only 26 processes, the distribution of application types to processes was sparse, with many processes having unique applications. This also leads to issues in syntactic matching as similar words such as aviation and aerospace will not be matched even if they are semantically related. Currently, our method here does not address this issue. We do not treat the semantic similarity measures any differently based on the number of terms in a feature's corpus.

Another challenge is the significant difference in scale for numerical data, which could affect the aggregate similarity metric. For example, differences between batch size capability in the dataset differ on orders of magnitude, while differences in achievable tolerances are not as far apart, yet have critical importance (in real manufacturing scenarios) even with minor differences. In our approach, we use traditional feature scaling to curb these effects. However, this issue seems to pop up in the aggregation of multiple metrics with one another. A smarter approach to overcoming scale heterogeneity in the data is needed.

In addition, our method does not consider the interdependencies between various combinations of capability features. For example, material and shape characteristics of a product have significant interplay judging the feasibility of a real build. Down-selecting from a set of materials influences the feasible range of shapes, and vice versa, even before selecting a set of available processes. From initial experimentation, the interplay of correlated features also have an effect on the generated clusters of material for a weighted aggregated metric. The implications of assigning these weights have a seemingly significant impact on the clustering result. This limitation presents future research questions as to how to emphasize particular aspects of manufacturing capabilities to better inform process selection.

Lastly, the developed metrics are constrained based on the dataset that was used. The data does not model any specific design case, but rather general design parameters that are purely process specific. Empirical methods of data collection have been proven to accurately model and predict important aspects of manufacturing processes such as unit energy consumption [24]. The addition of such data can significantly enhance our current methods while also increasing their utility as energy is a major factor in calculating cost and environmental effect. Features from the dataset such as the shape also lack the depth to accurately classify specific products with complex designs. There have been assessments of shape signatures through spacial functions and histograms that could be applied to our metrics [25]. Analyzing the categorical and numerical comparisons of certain features will require more data that will require expanding beyond our current dataset.

6 CONCLUSION AND FUTURE DIRECTIONS

This paper highlights efforts towards the development of a similarity metric for manufacturing processes. The primary goal is to aid in decision-making in the context of supplier discovery, e.g. given a set of design requirements, and define the available set of processes and viable alternatives based on similar capability-based characteristics. Here, we review lessons learned from our experimentation and present future directions to address the limitations of our work.

A primary research direction is the inclusion of a weighting scheme for individual similarity evaluations of capabilities based on feature inter-dependencies or human preference. Inter-dependencies of capability features could also be heavily

domain-specific. For example, requirements for material selection and tolerance specification vary greatly between consumer products and aerospace applications.

Furthermore, in this work, we have not validated any of the identified clusters of manufacturing processes with human judgement and expert experience. Such tacit knowledge can be efficiently captured in description logic and then formally expressed in ontologies. We have yet to make the connection between our fully automated approach and some flexibility for human-operated tuning. One way of validating the clusters is to elicit expert advice for designing process plans on several simple assemblies. These assemblies would have characteristics similar to the features studied in the paper, including shape, material, and required tolerances. It remains unknown, however, if it would be possible to map these expert decisions to the clusters of processes in order to decide on a particular set of weights for the aggregate metric. Considering various efforts in storing such decisions within knowledge bases, there are some research opportunities for developing a more semi-automated technique for assessing similarity.

Finally, a data-driven metric to holistically evaluate the similarity of two manufacturing processes must be generalizable enough to work across different databases including differences in the granularity of information. Here, we explore the idea using very general tabular data from an on-line resource. However, if the manufacturing information was classified within different features or seeded with significantly more information, our similarity evaluation, in its current form, would not function properly. It is critical to develop a similarity measurement technique that is agnostic of a particular database and promotes flexibility in its tuning and eventual use.

DISCLAIMER

No approval or endorsement of any commercial product by NIST is intended or implied. Certain commercial equipment, instruments or materials are identified in this report to facilitate better understanding. Such identification does not imply recommendations or endorsement by NIST nor does it imply the materials or equipment identified are necessarily the best available for the purpose.

ACKNOWLEDGMENT

This work was partly funded by the Summer Undergraduate Research Fellowship (SURF) Program at NIST.

REFERENCES

[1] Manyika, Chui, B. B. D. R. B., 2011. Big data: The next frontier for innovation, competition, and productivity. Tech. rep., McKinsey Global Institute.

[2] Lee, J., Lapira, E., Bagheri, B., and Kao, H.-a., 2013. "Recent advances and trends in predictive manufacturing systems in big data environment". *Manufacturing Letters,* ***1***(1), pp. 38–41.

[3] Keim, D., Andrienko, G., Fekete, J.-D., Görg, C., Kohlhammer, J., and Melançon, G., 2008. "Visual analytics: Definition, process, and challenges". In *Information visualization*. Springer, pp. 154–175.

[4] ISO 20140-1, 2012. Automation systems and integration - environmental and energy efficiency evaluation method for manufacturing systems - part 1: Overview and general principles. Standard, International Organization for Standardization, Geneva, Switzerland.

[5] ASTM E3012-16, 2016. Standard guide for characterizing environmental aspects of manufacturing processes. Standard, ASTM International, West Conshohocken, PA, USA.

[6] Meinshausen, I., Müller-Beilschmidt, P., and Viere, T., 2014. "The ecospold 2 formatwhy a new format?". *The International Journal of Life Cycle Assessment*, pp. 1–5.

[7] Bernstein, W. Z., Mani, M., Lyons, K. W., Morris, K. C., and Johansson, B., 2016. "An open web-based repository for capturing manufacturing process information". In Proceedings of the ASME 2016 IDETC/CIE, American Society of Mechanical Engineers.

[8] Koh, T. K., Fichman, M., and Kraut, R. E., 2012. "Trust across borders: buyer-supplier trust in global business-to-business e-commerce". *Journal of the Association for Information Systems,* ***13***(11), pp. 886–922.

[9] Weissman, A., Petrov, M., and Gupta, S. K., 2011. "A computational framework for authoring and searching product design specifications". *Advanced Engineering Informatics,* ***25***(3), pp. 516–534.

[10] Lin, D., 1998. "An information-theoretic definition of similarity". In Proceedings of the 15th ICML, Vol. 98, International Conference on Machine Learning, pp. 296–304.

[11] Pesquita, C., Faria, D., Falcao, A. O., Lord, P., and Couto, F. M., 2009. "Semantic similarity in biomedical ontologies". *PLoS Computational Biology,* ***5***(7), p. e1000443.

[12] Saldanha, A. J., 2004. "Java treeviewextensible visualization of microarray data". *Bioinformatics,* ***20***(17), pp. 3246–3248.

[13] Ameri, F., and Patil, L., 2012. "Digital manufacturing market: a semantic web-based framework for agile supply chain deployment". *Journal of Intelligent Manufacturing,* ***23***(5), pp. 1817–1832.

[14] Todd, R. H., Allen, D. K., and Alting, L., 1994. *Manufacturing Processes Reference Guide*. Industrial Press Inc.

[15] Ramanujan, D., Bernstein, W. Z., Benjamin, W., Ramani, K., Elmqvist, N., Kulkarni, D., and Tew, J., 2015. "A framework for visualization-driven eco-conscious design exploration". *Journal of Computing and Information Science in Engineering,* ***15***(4), p. 041010.

[16] McAdams, D. A., and Wood, K. L., 2002. "A quantitative similarity metric for design-by-analogy". *Journal of Mechanical Design,* ***124***(2), pp. 173–182.

[17] Fernandes, R. P., Grosse, I. R., Krishnamurty, S., Witherell, P., and Wileden, J. C., 2011. "Semantic methods supporting engineering design innovation". *Advanced Engineering Informatics,* ***25***(2), pp. 185–192.

[18] Avramenko, Y., and Kraslawski, A., 2006. "Similarity concept for case-based design in process engineering". *Computers & Chemical Engineering,* ***30***(3), pp. 548–557.

[19] Witherell, P., Grosse, I. R., Krishnamurty, S., and Wileden, J. C., 2013. "Aiero: An algorithm for identifying engineering relationships in ontologies". *Advanced Engineering Informatics,* ***27***(4), pp. 555–565.

[20] Shafer, S., and Rogers, D., 1993. "Similarity and distance measures for cellular manufacturing. part ii. an extension and comparison". *The International Journal of Production Research,* ***31***(6), pp. 1315–1326.

[21] Zhu, Z., Morrison, G., Puliga, M., Chessa, A., and Riccaboni, M., 2015. "The similarity of global value chains: A network-based measure". *arXiv:1508.04392*.

[22] Resnik, P., et al., 1999. "Semantic similarity in a taxonomy: An information-based measure and its application to problems of ambiguity in natural language". *Journal of Artificial Intelligence Research,* ***11***, pp. 95–130.

[23] Müllner, D., 2011. "Modern hierarchical, agglomerative clustering algorithms". *arXiv:1109.2378*.

[24] Kara, S., and Li, W., 2011. "Unit process energy consumption models for material removal processes". *CIRP Annals-Manufacturing Technology,* ***60***(1), pp. 37–40.

[25] Cardone, A., Gupta, S. K., and Karnik, M., 2003. "A survey of shape similarity assessment algorithms for product design and manufacturing applications". *Journal of Computing and Information Science in Engineering,* ***3***(2), pp. 109–118.

Proceedings of the ASME 2017 12th International Manufacturing Science and Engineering Conference
MSEC 2017
June 4-8, 2017, Los Angeles, CA, USA

MSEC2017-2942

MEASUREMENT OF THE MELT POOL LENGTH DURING SINGLE SCAN TRACKS IN A COMMERCIAL LASER POWDER BED FUSION PROCESS

J.C. Heigel, B.M. Lane
National Institute of Standards and Technology
Gaithersburg, MD, U.S.A.

ABSTRACT

This work presents high speed thermographic measurements of the melt pool length during single track laser scans on nickel alloy 625 substrates. Scans are made using a commercial laser powder bed fusion machine while measurements of the radiation from the surface are made using a high speed (1800 frames per second) infrared camera. The melt pool length measurement is based on the detection of the liquidus-solidus transition that is evident in the temperature profile. Seven different combinations of programmed laser power (49 W to 195 W) and scan speed (200 mm/s to 800 mm/s) are investigated and numerous replications using a variety of scan lengths (4 mm to 12 mm) are performed. Results show that the melt pool length reaches steady state within 2 mm of the start of each scan. Melt pool length increases with laser power, but its relationship with scan speed is less obvious because there is no significant difference between cases performed at the highest laser power of 195 W. Although keyholing appears to affect the anticipated trends in melt pool length, further research is required.

INTRODUCTION

Metal additive manufacturing (AM) processes, such as powder bed fusion (PBF), can produce high-value parts with unique geometries and features that can significantly reduce weight or increase the performance of the fabricated part. However, these processes are extremely sensitive to thermal effects. For instance, the shape of the melt pool, which is created with a high intensity energy source such as a laser, is greatly affected by the part geometry due to its ability to conduct heat from the melt pool [1]. The resulting melt pool size, temperature gradients surrounding it, and thermal history during the entire process directly impact the microstructure and material properties of the final part [2] as well as its residual stress and distortion [3]. The significance of temperature and melt pool size on metal AM processes requires thorough investigation using measurement and simulation.

A variety of methods are capable of measuring the thermal history during AM processes. Thermocouples have been used to measure the temperature at select points on parts during a variety of AM processes and those measurements have been used to validate process models [4], [5] and to investigate different processing strategies [6]. However, thermocouples have limited application in AM research because they must be attached to the substrate before the process begins, and can only measure temperature near the melt pool if the process is paused to allow additional thermocouples to be attached [4]. Optical methods, such as pyrometers or cameras, are more appealing than thermocouples because the melt pool and the surrounding material can be directly observed. Unfortunately, these too have their challenges. Pyrometers, for instance, collect radiation from a finite area (large or small) and convert that into a single value, from which a true temperature may or may not be calculable [7]–[9].

Thermal cameras unfortunately do not directly measure temperature; they provide signals nominally proportional to the incident radiant flux on each pixel. In order to convert thermal camera signal to true thermodynamic temperature, the measured object's emissivity must be known. However, emissivity of metals may vary with temperature, wavelength, viewing angle, surface condition, material phase, surface chemistry, and more [10], and thus true temperature profiles on and near the melt

Contact author: jarred.heigel@nist.gov

Heigel, Jarred; Lane, Brandon.
"Measurement of the Melt Pool Length During Single Scan Tracks in a Commercial Laser Powder Bed Fusion Process."
Paper presented at American Society of Engineers International Manufacturing Science and Engineering Conference,
Los Angeles, CA. June 4, 2017 - June 8, 2017.

pool are very difficult to accurately measure. Fortunately, certain characteristics of the temperature profile can be attributed to known physical processes, namely, the solidification boundary of the melt pool. The exothermic reaction that occurs during the liquid to solid phase transformation causes the temperature to plateau during that transition, creating a discontinuity in the temperature profile. The camera signal corresponding to that discontinuity is then used to identify the melt pool boundary.

Several researchers have used the solidification boundary to measure melt pool geometry. For instance, Doubenskaia and colleagues used a mid-infrared camera to image the melt pool while laser cladding a titanium alloy (Ti-6Al-4V) using a laser to create a 2.5 mm wide spot into which powder was fed at a rate of 10.5 g/min [11]. They identified the liquidus-solidus transition in the temperature profile across the width of the melt pool. Other researchers have used the same approach to measure melt pool length during the PBF process, which has significantly smaller melt pool sizes compared to directed energy deposition processes, such as laser cladding. Price, Cheng, and their colleagues first demonstrated the capabilities of their infrared camera to measure the temperature and the liquidus-solidus transition during an electron beam PBF process [12], used those measurements to validate a finite element (FE) model [13], and then used the experimental method and model to investigate the impact of various processing conditions on the melt pool geometry [14]. Their measurement setup used a 60 Hz infrared camera that was mounted outside of the machine and tilted down 35° to observe a 31 mm by 23 mm area on the build surface. The melt pool length and width were shown to vary based on processing conditions. Instead of observing the melt pool from an angle outside of the build chamber, Yadroitsev and colleagues utilized a charge-coupled device (CCD) camera integrated into the optics of a laser PBF system to measure the melt pool while processing Ti-6Al-4V [15]. Once again the liquidus-solidus transition was prevalent and was used to identify the melt pool boundary.

Each of these studies that used the liquidus-solidus transition to identify the melt pool boundary was performed on titanium alloys, and used relatively slow camera speeds (frames per second) compared to the process scan speeds. High frame rates are required to measure the variability in the melt pool length over the distance it travels. Furthermore, there are no measurements of melt pool length on other materials relevant to AM processes, such as nickel alloys.

The objectives of this work are twofold: 1) to present the current capabilities at the National Institute of Standards and Technology (NIST) to measure process temperatures and melt pool lengths during powder bed fusion processes, and 2) to present melt pool length measurements for a variety of processing conditions on nickel alloy 625 (IN 625) substrates and to discuss their significance. An infrared camera is used to measure the emissions from single line laser scans on bare IN 625 substrates using a frame rate of 1800 frames per second. These measurements are performed on a commercial laser PBF system. The analysis of the measurement data is automated using an algorithm to detect the liquidus-solidus transition discontinuity and uses those results to measure the melt pool length. Results of this analysis are then compared to processing conditions and the results of other studies in the literature.

MEASUREMENT SETUP

Figure 1 shows the setup used in this study, which is an evolution of the one originally used by Lane and colleagues [16]. A custom door allows an infrared camera to be positioned as close and as perpendicular to the build surface as possible. The door is mounted to the same commercial laser PBF system, which uses a 200 W Yb-fiber laser to produce a 100 µm spot size on the surface of the substrate. This study also uses the same camera with a filter that only allows wavelengths between 1350 nm and 1600 nm to be detected. The integration time (shutter speed) of the camera is 40 µs and the frame rate is 1800 Hz. To achieve this frame rate, a limited window size is used (360 horizontal pixels, 128 vertical pixels). Considering the camera magnification of approximately 0.33x, a working distance of approximately 162 mm, and a relative angle between the camera and the target surface of 44°, the pixel resolution in the horizontal and vertical axes are 36 µm and 52 µm, respectively. This equates to a field of view (FOV) that is 12.96 mm wide and 6.82 mm tall.

A new calibration of the infrared camera is performed following the procedure outlined by Lane and Whitenton [17]. The following equation relates the camera signal (S, in digital levels, DL), to the temperature of a reference black body (T_{BB}):

$$T_{BB} = \frac{c_2}{A\, ln\left(C/S - 1\right)} - \frac{B}{A} \qquad 1$$

where c_2 is the second radiation constant (14338 µm/K) and the coefficients A, B, and C are determined by fitting the equation

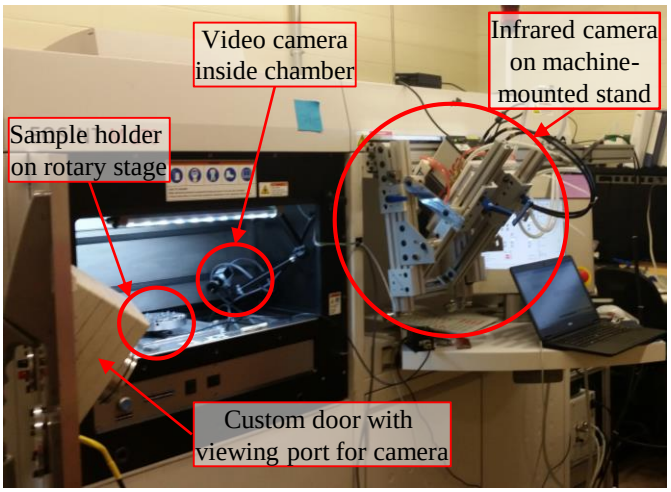

Figure 1 – Thermography setup on the commercial laser PBF system with the thermal camera set adjacent to the testing position and the custom door open, exposing the sample holder and video camera inside the chamber.

to the measurement. In this instance A=1.442, B=9.5×10^{-10}, and C=2.66×10^{7}. Figure 2 presents the black body measurements, the calibration curve, and the associated residuals. While this calibration can be used to measure the temperature of a black body to within a few degrees at high temperatures, it can only measure the radiant temperature of any object with an emissivity less than 1, as is the case in this study. Furthermore, the measurement uncertainty of this system is certainly higher than the reported residual since optical blur, motion blur, emissivity variation, and other potential components of measurement uncertainty must be measured individually, which is beyond the scope of this paper [16], [17].

In addition to the new camera calibration, several modifications are made to the setup to improve the quality and the quantity of measurements that can be made in a reasonable amount of time. First, the camera is attached to a new stand that is mounted directly to the machine, enabling the camera to be moved to allow the door to be opened and then repositioned so that it is focused on the same spot to within 1 mm. The second improvement is a sample holder mounted to a rotary stage that allows multiple samples to be loaded into the machine and indexed into the camera's field of view so that virgin sample surfaces can be scanned, as shown in Figure 3. This decreases the number of times the chamber door needs to be opened and closed, which requires time for the build chamber atmosphere to reach an environment with oxygen content less than 1 %.

In the current study, single line scans are made on square 3.2 mm thick IN 625 samples with a top surface area measuring 25.4 mm wide and 25.4 mm long. These samples are not pre-heated and have an initial temperature equal to the ambient temperature inside the build chamber (approximately 30 °C).

Table 1 presents the combinations and replications of laser scanning parameters investigated in this study. The laser power and scan speed are the programmed values. Combinations of these parameters are chosen based on the manufacturer recommended values for this material (Case 7) and the conditions investigated by Montgomery et al. in their study on the same machine [18]. The primary scan length for each case is 4 mm, though for some cases that length is increased to 8 mm and 12 mm to verify that steady state conditions are achieved.

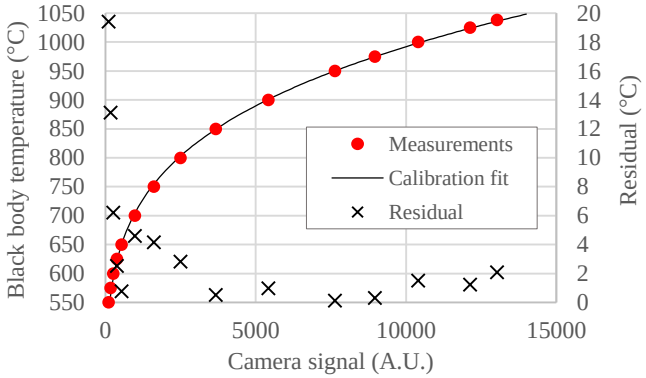

Figure 2 – Calibration results of the infrared camera.

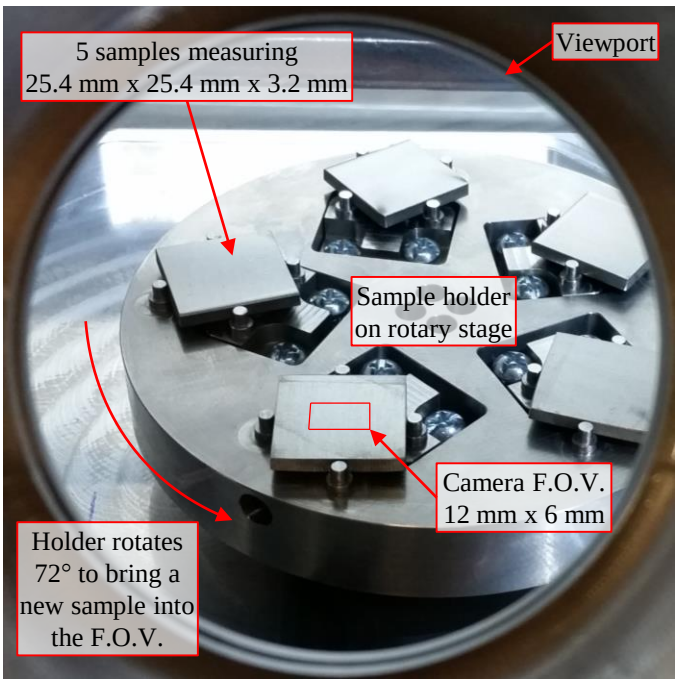

Figure 3 – The five samples held by the rotary stage as seen from the camera's perspective through the viewport on the custom door.

Table 1 – Test cases of varying laser power, scan speed, and scan length combinations.

Case	Power (W)	Speed (mm/s)	# of replications for scan lengths of: 4 mm	8 mm	12 mm
1	49	200	4	2	2
2	122	200	1	-	-
3	122	500	1	-	-
4	122	800	1	-	-
5	195	200	1	-	1
6	195	500	2	-	1
7	195	800	4	3	4

RESULTS

The infrared video by itself allows a qualitative analysis of the laser scan track; however, quantitative analysis is required to provide data and observations relevant to the research community. In the following sections, results from the infrared measurements are first shown, then the methodology used to analyze these results is developed, and finally the melt pool length measurements are presented.

The presentation of measurements in this study is limited to radiant temperature and the analysis of the data is focused on melt pool length because there is uncertainty surrounding the emissivity of the solidified material around the melt pool. The melt pool length can be measured without knowing true temperature using the liquidus-solidus transition, as demonstrated by other researchers [11]–[15].

Infrared Measurement Results

Figure 4 presents a typical infrared image from the steady state portion of each case. Steady state is defined in this work as the portion of a laser scan track during which the melt pool is fully developed and consistent. In most cases this is achieved after the laser has scanned over a distance between 1 mm and 2 mm, as will be shown later. In each image the laser scans from right to left and the leading edge of the 1038 °C radiant temperature isotherm (white), which is the highest measurable temperature of the camera using this calibration (Figure 2), is placed at the 0 mm mark on the horizontal axis to facilitate a quick, qualitative comparison between cases. A blue line indicates the center of the scan track. Each image shares the radiant temperature scale along the right side of the figure.

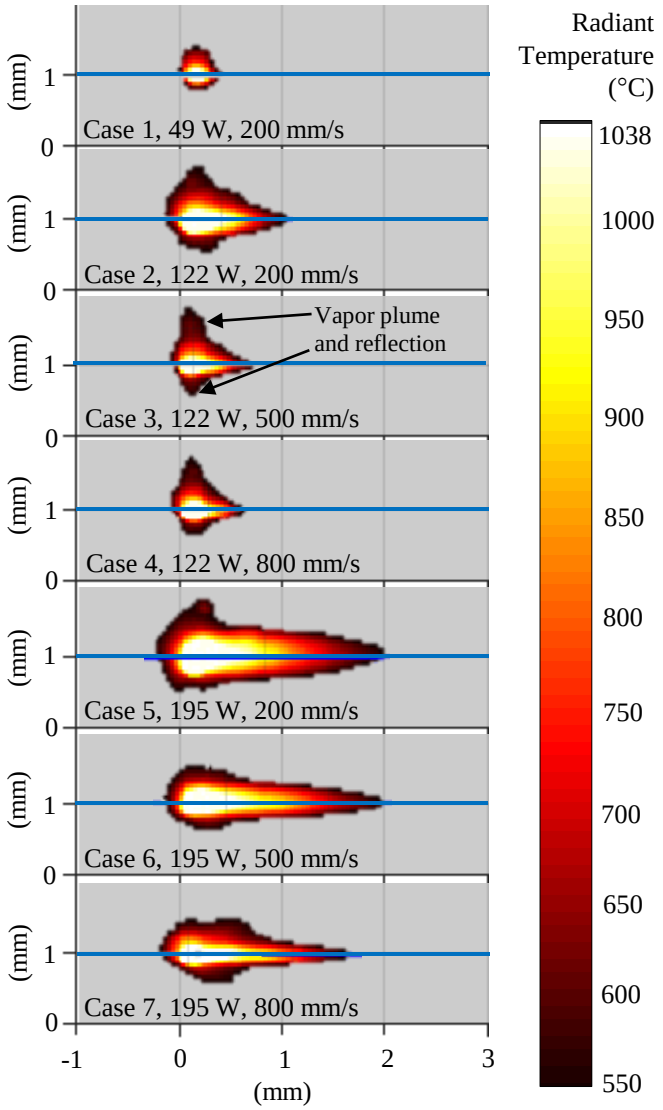

Figure 4 – A comparison of infrared images acquired from each case. Each image is representative of those acquired during steady state for each case. Temperatures below the detectable range of the camera (550 °C radiant) are gray.

The shape of these temperature gradients, especially those produced with higher laser powers, resembles those reported in other studies of laser scans using both experiment [9] and simulation [13], where it is wider in the front near the laser, and narrows behind the melt pool as the laser moves away and the material cools. Considering the similarity with these images and those in previous studies, caution must be exercised when interpreting these images due to the viewing angle of the camera and the vapor plume above the melt pool [19]. For instance, Case 3 in Figure 4 exhibits a plume above the melt pool that is reflected on the surface of the substrate (below the blue line). These plumes and their reflections, as well as the relatively large vertical scenel size (the area on the target that correlates to a single pixel), prevent any extraction of melt pool width from the data collected with this system.

Although no meaningful measurements can be made of the melt pool width, the melt pool length can be measured. Figure 5 presents the radiant temperature along the blue line for each infrared image shown in Figure 4. Once again, these plots are shifted along the horizontal axis so that the leading edges of the 1038 °C isotherm coincide, allowing easy comparisons.

The first observation that can be made from the curves in Figure 5 is that they are grouped by laser power. There is very little difference between Cases 5, 6, and 7, which all use a nominal laser power of 195 W. In each of those cases the 1038 °C radiant temperature isotherm is the same length (0.57 mm) and the cool down portions are similar, particularly Cases 5 and 6. Cases 3 and 4, which are created using the same nominal laser power of 122 W, are also very similar to each other (1038 °C isotherm length of 0.29 m and similar tails). However, Case 2 is longer even though it uses the same laser power of 122 W. The second observation pertains to the discontinuity in the cool-down portion of the temperature curves, particularly the ones generated with higher laser power. These discontinuities relate to the the liquidus-solidus transition observed by other researchers [11]–[15].

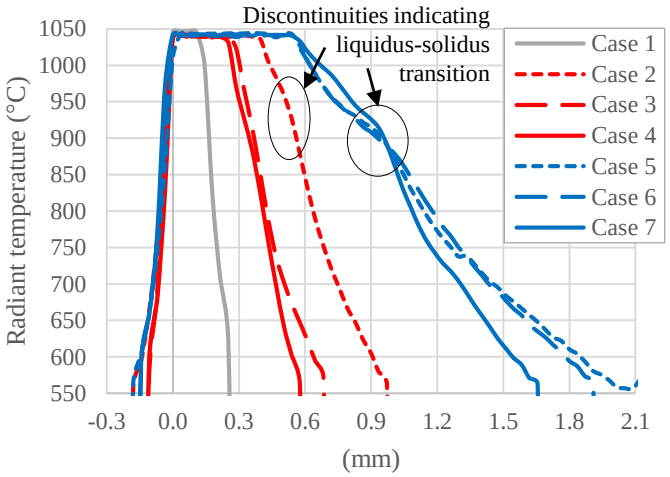

Figure 5 – Radiant temperature profile extracted along the blue lines in Figure 4.

Detection of the Liquidus-Solidus Transition

The presence of the discontinuity depends on the length of the temperature profile and the spatial resolution of the camera, as illustrated in Figure 6. This figure presents the temperature profiles to the right of (behind) the 1038 °C isotherms that were originally presented in Figure 5. For comparison's sake, the profiles have been shifted on the horizontal axis so their beginnings coincide. In addition, circles have been added to each plot to indicate every camera pixel used to measure the profile. As expected, the longer the distance over which the temperature decreases, the more pixels are able to measure it and the more evident the discontinuity becomes. For instance, if the transition is assumed (in this example) to occur at a radiant temperature of 900 °C for all cases, the numbers of pixels capturing data above and below that temperature (in Figure 6) are approximately 2 and 3 for Case 1, 4 and 10 for Cases 2 through 4, and 12 and 22 for Cases 5 through 7, respectively. Considering the subtle change in the temperature profile associated with the exothermic liquidus-solidus transition, it is impossible to detect when so few pixels are able to measure the gradient in Case 1, and is unreliable in Cases 2 through 4.

The average number of pixels (± 1 σ) above and below that hypothetical 900 °C radiant temperature threshold for every frame, during steady state of all replications, of each case, are presented in Table 2. The numbers in this table correspond well with the plots in Figure 6, indicating that those examples are representative of the steady state profiles of each case and further supporting the claim that the discontinuity cannot be adequately detected in Cases 1 through 4.

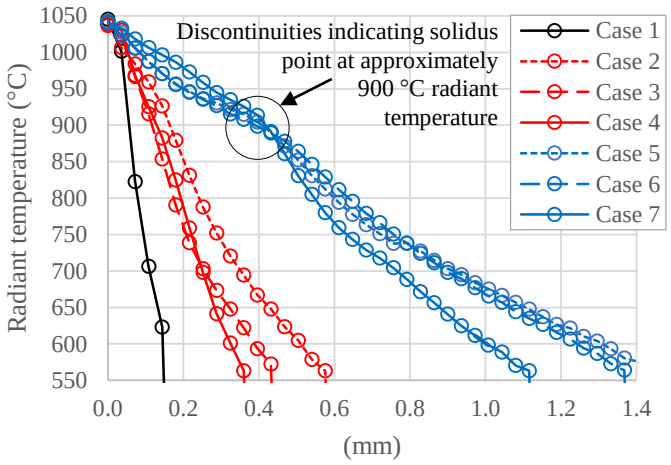

Figure 6 – The example temperature curves from Figure 5, isolated to the radiant temperature profile behind the 1038 °C isotherm.

Table 2 – Average number of frames and pixels available to use to detect the liquidus-solidus discontinuity.

Case	# of replications	Total # of frames	Average # of pixels between: 1038 °C to 900 °C	900 °C to 550 °C
1	8	503	0.8 ± 0.4	3.7 ± 0.5
2	1	15	3.7 ± 1.3	10.6 ± 4.1
3	1	10	3.0 ± 0.4	8.6 ± 1.6
4	1	6	2.8 ± 0.5	9.6 ± 3.5
5	2	144	10.2 ± 1.1	27.7 ± 4.6
6	3	54	10.7 ± 1.2	25.4 ± 2.3
7	11	151	10.1 ± 1.1	22.0 ± 2.6

Since there are a large number of frames to analyze (nearly 900), an algorithm is developed to identify the discontinuity. The minimum of the 2nd derivative of the temperature profile behind the 1038 °C radiant temperature isotherm is used to find the discontinuity, as shown in Figure 7. For each pixel the 1st and 2nd derivatives are calculated from a 3rd order polynomial that is fit to the measurement at that pixel and its 4 closest neighbors in that profile (5 total points).

Figure 8 shows the radiant temperatures of the discontinuity found in each frame of all Case 7 replications. These results are plotted against the approximate scan distance. In reality, the liquidus-solidus transition occurs over a constant (relatively narrow) temperature range that is dependent on the material and alloy [20]. However, the radiant temperature of this phenomena as measured by the infrared camera will be

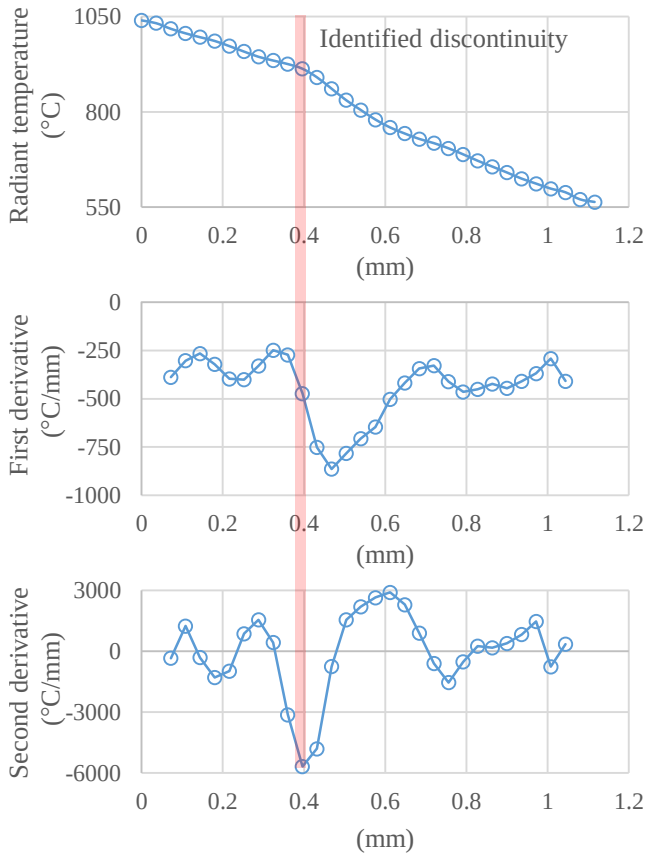

Figure 7 – An example of the algorithm used to detect the discontinuity at the liquidus-solidus transition. The radiant temperature profile is from the Case 7 profile presented in Figure 6. The minimum of the second derivative is used to identify the transition (vertical red line through each plot).

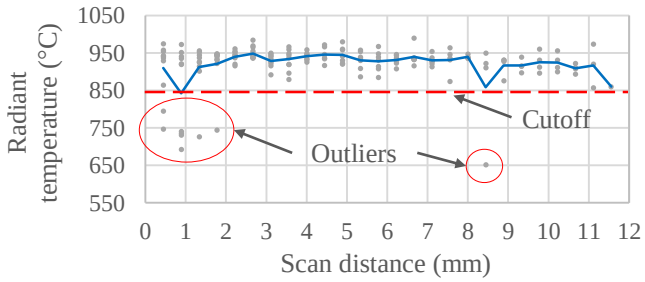

Figure 8 – The radiant temperature associated with the liquidus-solidus transition discontinuity in every frame for Case 7. Outliers are excluded from the analysis.

affected the emissivity, which is sensitive to the relative angle between the emitting surface and the camera [19]. Therefore, melt pool fluctuations could change this relative angle and make the discontinuity appear at different apparent temperatures. Interestingly, a greater number of outliers occur relatively close to the start of the scan, before a steady state melt pool can be achieved. Although worthy of investigation, an experimental investigation of these effects is currently not possible using the current setup due its magnification and frame rate.

Melt Pool Length Measurements

Once the radiant temperatures of all the discontinuities in every replication of a case are found, the outliers are rejected and the average is calculated. This average radiant temperature for each case is used to identify the leading and trailing edges of the melt pool for every replication of that case, enabling its length to be calculated. Since the temperature profiles in Cases 1 through 4 are too short to identify the discontinuity, an average radiant temperature is used which is calculated from Cases 5 through 7.

Table 3 presents the radiant temperatures used to identify the leading and trailing edges of the melt pool and the average melt pool length for each case. The variability of the radiant temperature is reported (± 1 σ), but is not considered when calculating the melt pool length. At this time, no analysis of the measurement uncertainty is performed, but will be a focus of future work. The melt pool data presented in Table 3 is the average length during steady state and its variability, ± 1 σ.

Figure 9 demonstrates the consistency in melt pool length measurements for all of the highest power cases (Case 5 through 7) and the distance traveled before reaching steady state. The average steady state length and the variability (± 1 σ) are represented by the solid and dashed black lines. Replications performed with different scan lengths are differentiated with markers of varying shapes and colors. These plots show that each replication within a certain case quickly converges to a steady state melt pool length after a short distance, making replications performed with different scan lengths indistinguishable. In the cases presented in Figure 9, steady state is achieved between 1 mm and 2 mm of travel, though there are a few exceptions that will be discussed shortly. The rapid increase in melt pool length to a steady state value, with no discernable difference between replications using different scan lengths, is observed in all other cases. Since the steady state melt pool length is unaffected by scan length (as long as the length is sufficiently long to achieve steady state), it is legitimate to average all steady state melt pool lengths, as they are reported in Table 3.

Table 3 – Results of the steady state melt pool analysis, average values and variabilities ± 1 σ.

Case	Power (W)	Speed (mm/s)	Radiant temperature used for detection (°C)	Melt pool length (µm)
1	49	200	942 ± 25	171 ± 16
2	122	200	942 ± 25	519 ± 29
3	122	500	942 ± 25	361 ± 27
4	122	800	942 ± 25	315 ± 27
5	195	200	961 ± 33	824 ± 109
6	195	500	949 ± 26	903 ± 102
7	195	800	936 ± 22	813 ± 79

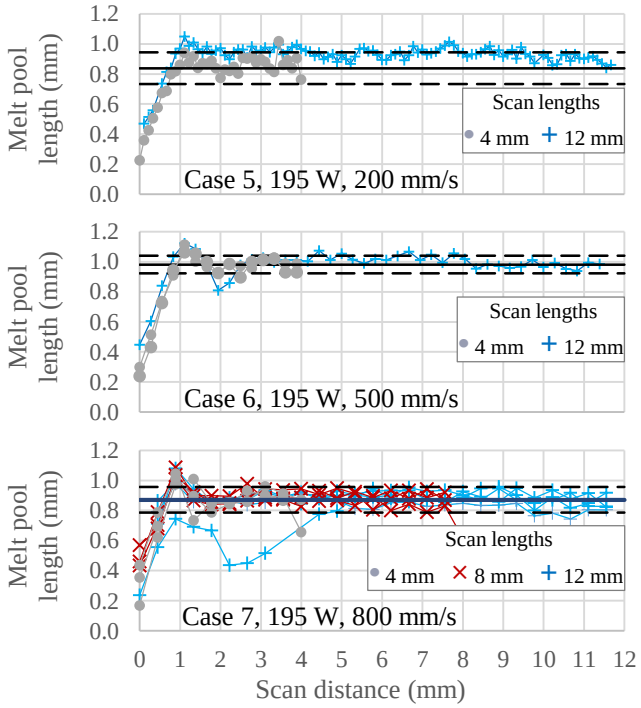

Figure 9 – Melt pool length as a function of laser scan distance for Cases 5, 6, and 7. The black solid line represents the average melt pool length during steady state while the black dashed lines are ± 1 σ.

There are a few outliers in the data presented in Figure 9. For instance, the final melt pool length measurement of some replications drops significantly below the steady state average. Analysis of these videos suggests that this is due to the final frame being captured after the laser is shut off and before the melt pool solidifies. The automated analysis algorithm used in this study cannot precisely determine the beginning and end of each scan because there is currently no signal from the machine to the data acquisition system indicating when the laser is on.

A few other replications do not follow the trend of the melt pool length rapidly increasing then becoming steady after a millimeter or two. For example, a few replications in Case 6 oscillate a bit before achieving steady sate. A more extreme instance occurs in Case 7, where one case nearly approaches steady state after 1 mm of travel, decreases in length over the next millimeter, and then increases and finally reaches steady state after another 3 mm of travel. Careful analysis of this video does not reveal any apparent cause for this behavior.

DISCUSSION

Figure 10 compares the average melt pool length for each case. Cases using the same nominal laser power are labeled to aid in the comparison of these measurements. This figure shows that melt pool length is closely related to the nominal laser power. Interestingly, the relationship with scan speed is less clear. According to the literature, the melt pool length is expected to decrease as the scan speed increases, though this relationship is expected to exponentially decay [9]. Cases 2 through 4 (122 W) exhibit this behavior; however, Cases 5 through 7 (195 W) do not. There is no significant difference between the three cases using the highest power.

The insensitivity of melt pool length to scan speed during the highest laser power cases (5 through 7) may be explained when considering the keyholing regime identified in an earlier study [18] and presented in Figure 11. This figure presents the power and velocity (P-V) map for IN 625 for the specific PBF machine used in the current study. The earlier study established lines of constant melt pool cross sectional area and the shaded region in which keyholing was observed [18]. The representative thermal images of each case from the current study are superimposed. Case 5 is well within the keyholing regime while Case 6 is near the transition into that regime. It is possible that the occurrence and extent of keyholing reduces the melt pool length, possibly due to the extra energy that is

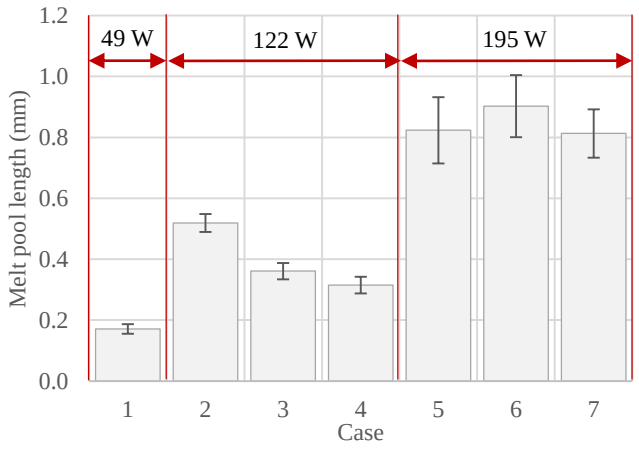

Figure 10 – Comparison of the melt pool lengths of each case. Cases with the same nominal laser power are grouped together to highlight the similarities in melt pool length. Error bars represent measurement variance of ± 1 σ.

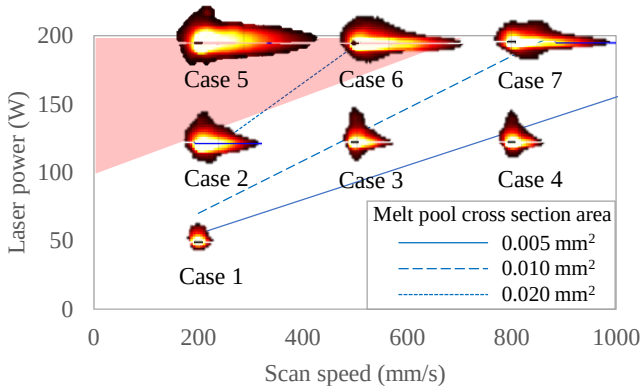

Figure 11 – The representative images and average melt pool length measurement mapped onto the P-V space. The shaded region in the upper left hand corner indicated where keyholing is expected according to Montgomery et al. [18].

expelled by the melt pool from ejected particles or from the deeper penetration of the melt pool, enabling the heat to be conducted deeper into the substrate compared to cases when keyholing does not occur.

The data shown in Figure 11 and Table 3 show that melt pool length increases along lines of constant melt pool cross section as the power and speed increase [18]. For instance, Cases 1 and 4 lie (nearly) on the same cross section line (0.005 mm^2) and the increase in power and speed from Case 1 to 4 increases the melt pool length from 171 µm to 315 µm (an increase of 84 %). Similarly, the melt pool length of Case 6 is 76 % greater than Case 2, while they both approximately fall on the 0.020 mm^2 line. More dramatically, along the 0.010 mm^2 cross section line, the melt pool length increases from Case 3 to Case 7 by 125 %. These results are consistent with the literature, since the length to depth ratio along those lines is expected to increase [18].

CONLCUSIONS

This work presents thermographic measurements of single track laser scans made using a commercial laser PBF machine on IN 625 plates. Infrared images acquired at a rate of 1800 frames per second are used to measure the temperature gradients in and around the melt pool. A variety of speed and power combinations are investigated using a number of replications performed at varying lengths. These power and speed combinations are based on earlier P-V mapping work on the same machine used in this study [18].

The melt pool length is measured from these gradients using the radiant temperature of the solidus transition. This transition manifests itself in the measured temperature gradients as a plateau in the curve which is caused by the release of energy during the solidification process and has been used by other researchers to identify the melt pool boundary. The true temperature gradient is not calculated in this study due to the unknown emittivity of the IN 625 surface at the observed temperatures and surface conditions.

Results from this study indicate that the melt pool length of single scan lines typically stabilizes within 1 mm to 2 mm of the start of the scan, reaching a steady state value that is strongly related to the nominal laser power. In contrast, the relationship with scan speed is less clear. Lower power cases (122 W) show a slight decrease in length with increasing scan speed, while the highest power cases (195 W) show no significant difference in length over the investigated scan speed range from 200 mm/s to 800 mm/s. Keyholing, which is expected to occur at the combination of high power and lower speed, possibly decreases the melt pool, negating the anticipated relationship between speed and melt pool length. Finally, the length of a melt pool does not correlate with its cross sectional area. Most of these observations are consistent with the literature.

Future work using this experimental setup and melt pool length measurement methodology will further investigate the effects in the keyholing region and the impact of the heat accumulated from successive scans on the melt pool length.

REFERENCES

[1] A. Vasinonta, J. L. Beuth, and R. Ong, "Melt pool size control in thin-walled and bulky parts via process maps," *Solid Freeform Fabrication Symposium Proceedings*, pp. 432–440, 2001.

[2] N. Hrabe and T. Quinn, "Effects of processing on microstructure and mechanical properties of a titanium alloy (Ti–6Al–4V) fabricated using electron beam melting (EBM), part 1: Distance from build plate and part size," *Materials Science and Engineering: A*, vol. 573, pp. 264–270, 2013.

[3] A. Dunbar *et al.*, "Experimental In Situ Distortion and Temperature Measurements During the Laser Powder Bed Fusion Additive Manufacturing Process. Part 1: Development of Experimental Method," *Additive Manufacturing*, 2016.

[4] J. C. Heigel, P. Michaleris, and E. W. Reutzel, "Thermo-mechanical model development and validation of directed energy deposition additive manufacturing of Ti–6Al–4V," *Additive Manufacturing*, vol. 5, pp. 9–19, 2015.

[5] A. J. Dunbar, E. R. Denlinger, M. F. Gouge, and P. Michaleris, "Experimental validation of finite element modeling for laser powder bed fusion deformation," *Additive Manufacturing*, vol. 12, pp. 108–120, 2016.

[6] E. R. Denlinger, J. C. Heigel, P. Michaleris, and T. A. Palmer, "Effect of inter-layer dwell time on distortion and residual stress in additive manufacturing of titanium and nickel alloys," *Journal of Materials Processing Technology*, vol. 215, pp. 123–131, Jan. 2015.

[7] M. Doubenskaia, M. Pavlov, S. Grigoriev, E. Tikhonova, and I. Smurov, "Comprehensive optical monitoring of selective laser melting," *Journal of Laser Micro Nanoengineering*, vol. 7, no. 3, pp. 236–243, 2012.

[8] C.-H. Cho, Y.-C. Hsieh, and H.-Y. Chen, "Welding pool measurement using thermal array sensor," 2015, vol. 9609, pp. 960912-960912–7.

[9] J.-P. Kruth, P. Mercelis, J. Van Vaerenbergh, and T. Craeghs, "Feedback control of selective laser melting," presented at the Proceedings of the 3rd International Conference on Advanced Research in Virtual and Rapid Prototyping, 2007, pp. 521–527.

[10] Y. S. Touloukian and D. P. DeWitt, "Thermophysical Properties of Matter - the TPRC Data Series. Volume 7. Thermal Radiative Properties - Metallic Elements and Alloys," 1970.

[11] M. Doubenskaia, M. Pavlov, S. Grigoriev, and I. Smurov, "Definition of brightness temperature and restoration of true temperature in laser cladding using infrared camera," *Surface and Coatings Technology*, vol. 220, pp. 244–247, 2013.

[12] S. Price, J. Lydon, K. Cooper, and K. Chou, "Experimental temperature analysis of powder-based electron beam additive manufacturing," *Solid Freeform Fabrication Symposium Proceedings*, pp. 162–173, 2013.

[13] B. Cheng, S. Price, J. Lydon, K. Cooper, and K. Chou, "On Process Temperature in Powder-Bed Electron Beam Additive Manufacturing: Model Development and Validation," *Journal of Manufacturing Science and Engineering*, vol. 136, no. 6, p. 61018, 2014.

[14] S. Price, B. Cheng, J. Lydon, K. Cooper, and K. Chou, "On Process Temperature in Powder-Bed Electron Beam Additive Manufacturing: Process Parameter Effects," *Journal of Manufacturing Science and Engineering*, vol. 136, no. 6, p. 61019, 2014.

[15] I. Yadroitsev, P. Krakhmalev, and I. Yadroitsava, "Selective laser melting of Ti6Al4V alloy for biomedical applications: Temperature monitoring and microstructural evolution," *Journal of Alloys and Compounds*, vol. 583, pp. 404–409, 2014.

[16] B. Lane, S. Moylan, E. Whitenton, and L. Ma, "Thermographic Measurements of the Commercial Laser Powder Bed Fusion Process at NIST," *Rapid Prototyping Journal*, vol. 22, no. 5, pp. 778-787, 2015.

[17] B. Lane and E. Whitenton, "Calibration and measurement procedures for a high magnification thermal camera," National Institute of Standards and Technology, Gaithersburg, MD, NISTIR 8098, Dec. 2015.

[18] C. Montgomery, J. Beuth, L. Sheridan, and N. Klinbeil, "Process mapping of Inconel 625 in laser powder bed additive manufacturing," *Solid Freeform Fabrication Symposium Proceedings*, pp. 1195–1204, 2015.

[19] S. A. Khairallah, A. T. Anderson, A. Rubenchik, and W. E. King, "Laser powder-bed fusion additive manufacturing: Physics of complex melt flow and formation mechanisms of pores, spatter, and denudation zones," *Acta Materialia*, vol. 108, pp. 36–45, 2016.

[20] L. del Campo *et al.*, "Emissivity measurements on aeronautical alloys," *Journal of Alloys and Compounds*, vol. 489, no. 2, pp. 482–487, Jan. 2010.

15th Annual Conference on Systems Engineering Research
Disciplinary Convergence: Implications for
Systems Engineering Research

Eds.: Azad M. Madni, Barry Boehm
Daniel A. Erwin, Roger Ghanem; University of Southern California
Marilee J. Wheaton, The Aerospace Corporation
Redondo Beach, CA, March 23-25, 2017

Toward a Diagnostic and Prognostic Method for Knowledge-Driven Decision Making in Smart Manufacturing Technologies

Thomas Hedberg, Jr.[a], *Allison Barnard Feeney*[a], *Jaime Camelio*[b]

[a] Systems Integration Division, National Institute of Standards and Technology, Gaithersburg Maryland 20899, {tdh1,abf}@nist.gov

[b] Grado Department of Industrial and Systems Engineering, Virginia Tech, Blacksburg Virginia 24061, jcamelio@vt.edu

Abstract

Making high-quality manufacturing decisions in real-time is difficult. Smart manufacturing requires sufficient knowledge be available to the decision maker to ensure the manufacturing system runs efficiently and effectively. This paper will present background information for managing and controlling decision making and technological innovation. We present a process definition for decision making that implements closed-loop diagnostic and prognostic control. Lastly, we discuss our emerging concept relative to smart manufacturing.

Keywords: decision making, smart manufacturing, technological innovation

1. Introduction

Smart manufacturing cannot be successful without proper management and technological innovation. The Oxford English Dictionary [1] defines *technology* as "the application of such knowledge for practical purposes." *Innovation [2]* is defined as "the alteration of what is established by the introduction of new elements or forms." And, *management [3]* is defined as "organization, supervision, or direction."

Using these definitions, we may define technological innovation as the *process for creating a new application of practical knowledge.* Thus, the management of technological innovation is the *organization, supervision, or direction of the process for creating a new application of practical knowledge.*

While, several "smart" technologies have existed in manufacturing since the 1980s, the integration of those technologies along with the convergence of information technology (IT) and operational technology (OT) has kicked off a period of an increased rate of innovation in manufacturing. In general, Tidd and Bessant [4] presented "key lessons learned about managing innovation." Tidd and Bessant [4] recommended that organizations be visible in promoting innovation across the whole business, build a project-based organization with a good portfolio management structure, utilize a stage-gate system, and institutionalize the use of tools. We must remember innovation requires the creation of something new. Therefore, creativity, development processes, and change management must be accounted for in decision making within the overall technological-innovation process.

Collaborative Product Development (CPD) [5], Concurrent Engineering [6], Designed for Manufacturing (DFM) [7], Design for Six Sigma (DFSS) [8], and Integrated Product and Process Development (IPPD) [9] are popular business strategies for managing new-development activities. Decision making is a common function in all of these strategies. Companies may combine these popular strategies with stage-gate processes to form their complete operating models. Further, industry desires to couple these methods with model-based systems engineering (MBSE), the "vee" diagram, and the larger-scoped model-based enterprise concept to enable effective decision making during development and manufacturing processes [10].

However, organizations often apply these methods without ever re-asking if the development and manufacturing activities are still the right pursuits -- that is, should the organization's overall goals change during and throughout the activities? This question and the desire to ensure the optimality, stability, effectiveness, and efficiency of technological-innovation process motivated this paper.

In this paper, we present our emerging and beginning work toward a diagnostic and prognostic method for knowledge-driven decision making in smart manufacturing technologies. We will show that decision-making, technological innovation, and the management/control of both are not mutually exclusive. First, we provide background knowledge discussing decision making, technological innovation and the management of both, while also comparing various types of control theories (e.g., controls engineering, management control, human factors). Then, we will present a process definition for decision making and discuss the relationship between technological innovation, its management, and smart manufacturing. We will use this information to describe the beginings of a concept for implementing closed-loop diagnostic control in technological-innovation and decision-making processes. Next, we will analyze and discuss our emerging concepts in relation to the “Digital Thread” in the manufacturing domain. Lastly, we will conclude with the utility of the concepts in supporting efficient and effective decision making.

2. Background

While developing our concept for controlling the manufacturing decision-making process, we had to collect cross-discipline understanding of technological innovation because the various roles (e.g., marketing, engineering, management, finance) that might affect manufacturing decisions. We focused our research on three areas of understanding. The first focus area was in defining the technological-innovation process. The next focus area was in managing decisions for creativity, development projects, and changes in organizations. The final focus area was on control theories in the context of engineering, manufacturing, and management interactions.

2.1. Defining the Technological-Innovation Process

Knight [11] proposed technological innovation means an organization has adopted a new concept beyond the generation stage of the concept. Porter [12] suggested technological innovation is a “new way of doing things that is commercialized.” Freeman and Soete [13] said, “an innovation in the economic sense is accomplished only with the first commercial transaction involving new product, process system, or device...” Tidd and Bessant [4] agreed innovation is the process of growing inventions into practical use. A diagram of the technological-innovation process based on Hollen [14] is shown in Fig. 1. The literature [14, 15], both recent and past, show technological innovation as a three-step process of discovery, development, and deployment.

The first phase in the technological-innovation process is discovery. We may consider this phase synonymous with invention. New knowledge is created during the discovery phase. The output from the discovery phase is typically a conceptual design from a Research and Development (R&D) activity.

The second technological-innovation phase is development. This phase is a transition activity. In product development, the conceptual-design task is transitioning towards detailed-design activities. Management of technological innovation is important during the development phase because successful commercialization depends on the maturity level of the technology. The output of the development phase is a complete definition for the technology.

The third phase is deployment. This phase is where a process is being deployed to production operations, or products are available for delivery to the marketplace. Development is complete or near completion when the deployment phase begins. The output of the last phase is a new and complete technology.

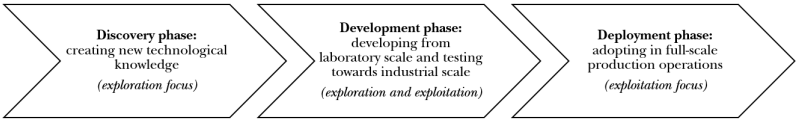

Fig. 1. Three-phase process definition for technological innovation (based on [14])

Management must remain a critical focus during the deployment phase because many scholars consider the commercialization of technology the least managed activity in the technological-innovation process [16]. The methods used to commercialize and market technology significantly influence the success or failure of products [17]. Products with newly-commercialized technology fail at a rate of 40% to 50% [16]. The demonstrated importance of management and decision-making is the motivation behind this paper.

2.2. Managing Decisions for Creativity, Development, and Change

"Creativity is the production of novel and useful ideas in any domain" [18]. Amabile [18] proposed a model of creativity that requires abilities in three major components, which are expertise, creative thinking, and intrinsic task motivation. The combined skills in each category enable creativity. The field of psychology teaches that anyone is capable of creativity, but the level of creativity is enhanced or limited by interactions with the social environment.

Lewin's Equation [19], $B = f(P, E)$, proposed behavior (B) is a function of interactions between people (P) and their environment (E). Following this idea, we argue innovation is a function of a person's creative ability and his/her interaction with the social environment. Further, Hoegl and Parboteeah [20] suggested that the quality of team collaboration influences the utilization of the teams' technical skills and directs those skills toward the critical-performance dimensions.

Considering, Hoegl and Parboteeah [20], we propose extending Lewin's Equation [19] to organizations by arguing that innovation is a function of the organization's overall creative ability and its social interactions within the environment. That is $I = f(\sum P_i, E \in O)$, where I represents innovation, i represents individuals in the organization, and O represents the organization. Therefore, managing and encouraging creativity at the personal level should support a positive environment for innovation at the organizational level.

Amabile [18] argued that individuals with basic capacities can develop moderately creative solutions to some problems some of the time. However, challenging problems of high importance require subject matter experts with extensive knowledge in the field of work. A baseline level of expertise in the engineering domain is needed to ensure the ideas produced by the creative process are "novel and useful" [18].

Amabile's [18] and Hoegl's and Parboteeah's [20] conclusions support Cooper's [21] recommendations for including all critical roles in a product-development process from the start of the process. Cooper further suggests there are two ways to succeed in innovation -- (1) doing projects right and (2) doing the right projects. Doing projects right requires a process to follow commonly accepted management guides. These guides should include using teams effectively, doing up-front research before starting development, analyzing the voice of the customer, and ensuring a stable product definition prior to deployment or launch. Doing the right projects requires the "right" expertise to know what the right portfolio of projects looks like. This relates to Amabile's [18] conclusion that a basic level of expertise is needed to determine if something is "novel and useful."

Cooper also developed a stage-gate process model that breaks the product-innovation process into five stages, each requiring the passage of a gate before proceeding to the next stage. The gates provide quality control to the process by incorporating go/no-go decisions at strategic points in the process. While Cooper's model provides a good foundation for managing product-development activities, it may fall susceptible to disruptive changes that could occur during the activities -- specifically changes due to the technological-innovation process. This opens up Cooper's model to the risk of pursuing decisions that are no longer the right decisions.

Manufacturing organizations operate in an environment of constant change. Organizations must be prepared to manage the changes through effective decision-making. Managing changes effectively is an important part of ensuring sustainable success within an organization. Organizational strategies, structures, skills, and cultures must evolve over time to reflect changes in markets and technology [22].

Specifically related to technology, change happens in cycles [22]. These cycles are best explained with an illustration presented in Fig. 2. Technology cycles begin with high rates of innovation until a dominant technology emerges. As technology matures, the rates of innovation slow. As competition continues in the market, eventually new technology needs to be developed to sustain success. This forces a rapid increase in the rate of innovation – leading to substitute technologies via the technological-innovation process.

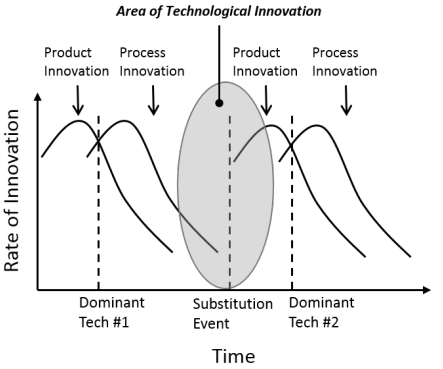

Fig. 2. Technology cycles and technological-innovation (based on [22])

In the manufacturing domain, data are being used in new ways that are beginning to enable near-real-time decision making. Data-driven decision making is at the core of Industrie 4.0, Industrial Internet of Things (IIoT), and Smart Manufacturing strategies. Significant innovations in data-driven techniques were achieved in the 1980s, but other technological innovations were dominant at that time. As the 2000s approached, the rate of manufacturing-related technical innovation decreased, causing manufacturing to look for new avenues to grow and increase productivity. Manufacturing is again in a time of increased innovation and the we believe the shaded area of technological innovation shown in Fig. 2 is imminent. New technologies and new integrations of technologies are revolutionizing the way manufacturing is conducted.

2.3. Control Theory Related to Manufacturing Decisions

Control means measuring a quantity or condition in a system and applying a determined quantity or condition to the system to correct or limit the deviation of the measured value from a desired value [23]. Using the word “system” in control problems refers typically to a representation of the actual thing that someone is trying to control.

In engineering, mathematical modeling is a common way of representing a system for controls analysis [23]. Modern control theory has become popular for analyzing complex systems, which often have multiple inputs and outputs as parts of the overall system [23]. A popular method for analyzing these types of complex systems is state-space analysis [24].

In our work, without pretension of being exhaustive, we were less interested in the formulation of representative models. Our interest was in developing a foundational structure to describe the behavior of the system completely at any point in time. That is important for being able to accurately assess the decision-making process. This is why we were interested in control theory – specifically state-space analysis.

While modern control theories provide great values to the engineering domain, they tend to lack complete diagnostics to facilitate controlling the decision-making process. We must also review control in the contexts of management and human-factors. Management-control systems include human-resource tools. Organizations might employ management-control techniques in budgets, rules, operating procedures, and performance-appraisal systems to help gain control over employee behaviors [25].

Performance-appraisal systems may include goal setting, which is important to achieving organizational objectives [26]. Organizations implement goal setting with employees because studies show goal setting supports positive motivation and contributes to improved employee performance [27]. Goal setting has also been shown to create competition amongst employees and teams, which increases motivation throughout an organization [28] and improves decision-making processes [27].

Since the 1960’s, organizations have used Drucker's [29] work, “Management by Objectives,” to control behaviors. Drucker's work has five steps: (1) define organizational objectives, (2) set worker objectives, (3) monitor progress, (4) evaluate performance, and (5) reward results. In the first step, management describes the organization's vision and objectives to the employees. In the second step, each employee meets with management to set specific goals for the employee. The third and fourth steps relate to monitoring and

measuring the progress of each employee's goals and providing an evaluation at the end of the performance period. In the last step, the organization rewards each employee based on his/her results.

In Drucker's theory, goal setting is an integral part in all levels of an organization. Ceresia [27] suggested robust management control is supported by both taking into account Drucker's guidance and ensuring positive employee motivation. However, Drucker's theory and Ceresia's recommendations also lack guidance in continuously assessing organization objectives and goals.

Simon [30] published directly on the topic of using control systems to drive strategic renewal. He defines management control systems as “formal, information-based routines and procedures managers use to maintain or alter patterns in organizational activities.” Simon also outlines a business strategy with four variables that require assessment. He called these variables “levers of control,” which he defined as belief systems, boundary systems, diagnostic-control systems, and interactive-control systems.

We are most interested in the diagnostic-control-systems lever, which provides controls in an optimal spot of the organization because input controls and process standardization do not provide diagnostic management. Input controls maximize creativity but increase risks to cost controls, while organizational goals and standardization minimize creativity and innovation. Diagnostic control systems monitor organizational outcomes, which get compared against important performance dimensions of a strategy. Simon called these “critical performance variables.”

In manufacturing industries, critical performance variables are called key performance indicators (KPIs). Simon suggested using KPIs to track the probability of meeting goals or the largest potential for gain over time. These categories of KPIs are considered effectiveness criterion and efficiency criterion, respectively.

The standard ANSI/ISA 95 [31] provides guidance to integrating control systems into enterprise hierarchies. The standard describes a pyramid hierarchy starting with an enterprise level at the top, then moving down to an operations-management level, then a sensing and control level, and finally a devices level. The standard, itself, focuses on the operations-management level.

In Fig. 3 we combine the work of Ogata [23], Drucker [29], Simons [30], and ANSI/ISA 95 [31] to form a model for strategy diagnosis in a manufacturing-enterprise-control-system integration. This model demonstrates how organizational strategies, structures, skills, and cultures could evolve according to Tushman [22]. The model depicted in Fig. 3 provides a good foundation for controlling the strategies of organizations implementing smart manufacturing, but, like Cooper's [21] model and Drucker's [29] theory, our model for strategy diagnosis may be susceptible to the various types of change -- resulting in organizations pursuing strategies that are no longer ideal.

Argyris' [32] developed the concept of double-looping learning. We can represent the concept as a control system. Examples of single-loop-learning and double-loop-learning as control systems are shown in Fig. 4. In the double-loop example, there are two “sensors.” The first sensor measures the system output in context to the local goal. The second sensor measures the system output in context to the overall goal.

In double-loop learning, the system inputs are modified based on the system output compared to the local goal, but the local goal may also be modified in light of the system output not trending toward the overall goal. The system could also be controlled by modifying the overall goal instead of the local goal.

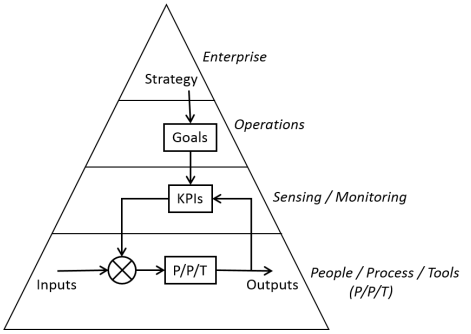

Fig. 3. Strategy diagnosis in an enterprise-control system integration (based on [23, 30, 31])

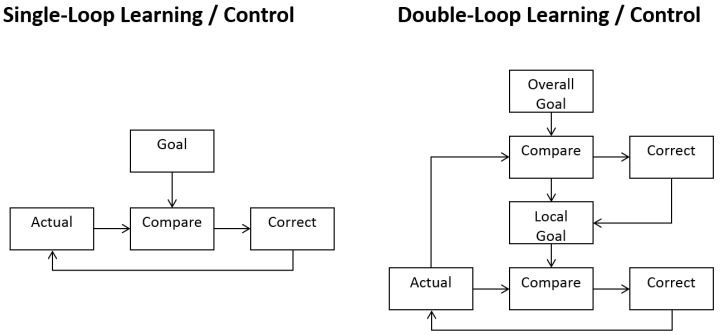

Fig. 4. The single-loop learning process compared to the double-loop-learning process (based on [33])

3. Process Definition for Knowledge-Driven Decision Making in Smart Manufacturing Technology

Informed by literature cited in Section 2, we developed a concept for controlling decision making through the technological-innovation process to close the gaps we identified in previous works, specifically continuous assessment of goals and why an organization pursues the technological innovations that they do.

Double-loop learning is a control technique for managing change [32-34]. Double-loop learning may be used by an organization to decide when to increase the rate the of innovation. Double-loop learning is a way for organizations to break the single-loop learning pattern of, "this is the way we have always done it." Strategically-driven organizations typically define governance goals to influence actions that lead to results and consequences. The goals define why organizations do what they do. The actions are what the organizations do. The results and consequences are what organizations obtain.

In single-loop learning, organizations only modify what they do (actions) based on what the organizations obtain (results). This is a process of repeated attempts at the same problem with no variation of method and without ever questioning the goal. With double-loop learning, organizations modify what they do (actions) and reevaluate why they do what they do (goals) basing both on what the organizations obtain (results). This is a process of modifying goals in light of experience or possibly rejecting goals all together after multiple failed attempted [34].

Double-loop learning is important to the technological-innovation process because of the 40% to 50% failure rate of new-commercialized technology as estimated by Chiesa [16]. While single-loop learning may assist organizations in developing the smart manufacturing technology, double-loop learning would ensure the technology is the right technology the organization should be pursuing.

Double-loop learning, knowledge bases, and popular management-control techniques are integrated into the decision-making process to form our knowledge-driven decisions concept shown in Fig. 5. Our concept represents the decision-making process based on generated knowledge and experience. In the decision-making process, our knowledge represents a group of "answers" to previous, and even future, questions. Our decision represents our recognition of a question. We use our knowledge to make decisions. Unfortunately, that is often where the process stops. Due to our interactions and pressures with the work environment, a secondary question of, "how good was the decision?" is not often addressed.

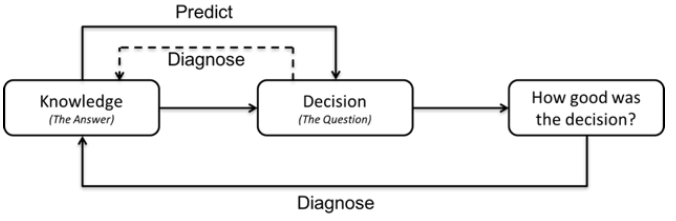

Fig. 5. The knowledge-decision cycle for knowledge-driven decision making

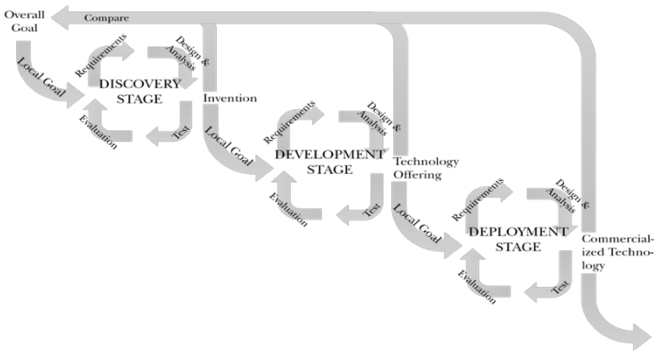

Fig. 6. Phase-gate process definition for the management of technological innovation with integrated double-loop control

For smart manufacturing to be successful, we must analyze each decision outcome against the expected results. This analysis enables the decision maker to diagnose if the knowledge used to make the decision was sufficient or if new knowledge is required to improve the decision in the future. This is a feed-back control loop. But just knowledge supports making decisions, we can also use the knowledge to predict the type of decisions we can make in the future. That prediction (i.e., prognosis) activity is a feed-forward control loop that enables secondary diagnosis of the knowledge to determine if new knowledge is needed.

For example, double-loop learning may be integrated with a stage-gate process as shown in Fig. 6 by setting an overall goal at the start of the process, defining local goals for each stage of a design or manufacturing process, and then comparing the output of each stage with the overall goal. Requirements are managed within each stage to ensure design, analysis, test, and evaluation meet the local goals.

in developing our concept, we assume the activities of the discovery, development, and deployment stages are out of scope. We represent each stage as a system, enabling us to integrate each stage using system-of-systems methods. Stage-internal processes and methods are irrelevant; we focus on the inputs and outputs of each stage and the interactions required between each stage.

We also recognize that feedbacks could come from many different disciplines (e.g., marketing, finance, supply chain). We assume those feedbacks are made directly to the stage that has a need to know. Therefore, those feedbacks are out of scope for this work.

The first step in employing our concept is to determine the overall goal(s) of the decision cycle – in this case, deploying a new technology. Goal development should follow commonly-used processes. We are not proposing a change to existing goal setting practices; our concept is concerned with making goal assessments a continuous process throughout the decision-making process.

Next, the overall goal(s) are broken down to appropriate localized goals for each stage of the technological-innovation process. This process is similar to developing a work breakdown structure in project management. Local goals should be determined for each stage based on the expected outcome of each stage. In addition, the outputs of each stage become a part of the inputs for the next stage.

When a stage is near completion, an evaluation of the stage's requirements and localized goals is conducted. The results of the evaluation would determine if the technology is ready to move to the next stage. If the technology passes the stage evaluation, that stage is complete. But the technology doesn't move to the next stage yet. The technology needs to be assessed against the overall goal(s). For example, in the discovery stage potential questions that should be asked are:

- Does the technology align with the overall goals of the organization or vice-versa?
- Would the technology provide continuous value or provide a competitive advantage?
- Are there any other overall goals to which the technology could align?

We adapted Cooper's [21] purpose for gates to our concept. The purpose of each gate is to provide an assessment of the quality of the technology while ensuring the right technologies and overall goals are pursued. Gates are meant to deal with three quality issues in the technological-innovation process [21]: (1) quality of execution in the process, (2) business rationale for the technology and overall goals, (3) and quality of the action plan for controlling the process.

4. Discussion

Our example for technology deployment using our decision-making concept could be applied to the concept of the “Digital Thread” and model-based enterprise (MBE). The digital thread is concerned with how data flows between engineering, manufacturing, business processes, and across supply chains. A MBE approach uses these models, rather than documents, as the data source for all engineering activities throughout the product lifecycle. The core MBE tenets are models are used to drive all aspects of the product lifecycle and data is created once and reused by all downstream data consumers.

Hedberg et al. [35] proposed a conceptual lifecycle information framework and technology (LIFT) for digitally integrating all phases of the product lifecycle. digital thread is key to a successful deployment of the framework and requires an accurate definition of the product (system). The product definition includes the shape, context, and behavior of the system. For example, the shape defines geometry and associated parameter configuration requirements. The context provides information for the various viewpoints across the product lifecycle; such that information is available for each function / role in the lifecycle at the time when the information is needed. Lastly, the behavior describes how the system is required to interact in a given context (e.g., how the system should interact with a cutting tool in manufacturing or how the system should interact with the product end-user).

The LIFT concept is described in three layers: (1) linked-product-lifecycle data, (2) data certification and traceability layer, and (3) data-driven applications. Data is linked together across the entire product lifecycle using agent-based methods. A certification and traceability layer would ensure trust in the linked data by adding meta-data denoting who had done what to the data and when it was done. Lastly, data-driven applications leverage data for knowledge-bases, decision support, requirements management, and control.

Combining our decision-making concept with the LIFT concept supports a new paradigm that treats the product lifecycle as a cyber-physical-social system. In this context, computer-aided technologies (CAx), machines, products, and people are combined, analyzed, and measured for performance outputs and decision outcomes. Decisions are made under uncertainty throughout the entire lifecycle. How do we reduce the uncertainty and variation? Further, how do we define and understand stakeholder needs, convert those needs into system requirements, and ensure the system attributes comply with the requirements? Answering those questions relates to the feed-back and feed-forward loops in our decision-making concept. Machine learning techniques may be applied to the linked data layer of the LIFT concept. This enables knowledge to be built by diagnosing decisions in the lifecycle. That knowledge is then used to predict the types of decisions that could be made, so before any decision is made, it is possible to determine whether sufficient knowledge exists.

We invested heavily in double-loop feedback during the development of our decision-making concept. Single-loop control has many uses, but our literature review identified several gaps with single-loop control in decision-making activitis. The primary gap is the overall goal in development and manufacturing projects is not being reassessed. We believe the integration of double-loop control in our concept results in better decisions through reducing the risk of bullwhip or oscillatory effects.

While bullwhip effects traditionally apply to distribution channels, the decision-making process can experience oscillatory swings when not controlled properly. Our concept ensures the inputs, outputs, and requirements of decision are carefully assessed at the appropriate point in time against the overall goals of the organization. This ensures a stable and steady flow through the technological-innovation process. Without our concept, deploying smart-manufacturing technologies could potentially experience performance swings above and below optimal states as technology is aligned to the goals of the various process stages in a manufacturing enterprise, the eventual development of new processes, and the overall goals of the organization.

5. Conclusion

The successful maturing of a new concept through commercialization requires nurturing and oversight, which only proper management controls would provide, in our case, with the use of double-loop learning. The process of technological innovation and its management must coexist and complement each other through the decision-making process. Cooper [21] outlined eight key factors of success in product development from which we extracted the following technology development insight:

- Quality of executing the technological-innovation process is key to an eventual product's success.
- Quality of executing (e.g., market research, technical assessments, business analysis) the discovery stage of the technological-innovation process is pivotal to the success of an eventual product.
- Quality of executing marketing activities, including building the voice of the customer, potentially increases the success rate of technology by over 100%.

Our concept for controlling the decision-making process supports Cooper's [21] eight key factors of success. Furthermore, the key factors could be the foundation for assessment criteria throughout the concept. This would enable the application of quality-assurance-like methods to decision making.

We've begun to show that proper management and technological innovation are critical for successful deployment of smart manufacturing. We've also proposed literature-supported process definitions for technological innovation and a concept for controlling it. We believe organizations would benefit from understanding the relationship of the proposed concept and activities of each phase in technological-innovation process. Additional research is needed in quantifying measures throughout the technological-innovation process.

We recognize that evaluation-based decision outcomes are subjective. Additional research in evaluation criteria and methods for implementing stage-gates into our concept is needed to make outcomes objective. For example, we are interested in how decision trees, heuristics, Markov chain, and Bayesian networks could assist in evaluating the outcome of decisions and how knowledge building could be automated.

Also, additional research is needed to develop measures related to output-input relationships in decision making. The goal of these measures would be to provide the user of our concept with an efficient way to determine the effectiveness and performance efficiency of each decision against an overall goal. This would help the user determine if an overall goal needs to be revised in light of the work determined by the local goals or vice-versa.

In closing, we believe our concept supports effective and efficient management of the technological-innovation process. Our concept for data-driven decision making could enable a harmony between the technological-innovation process and its management that would support

Disclaimer and Acknowledgements

The work presented in this paper is an official contribution of the National Institute of Standards and Technology (NIST) and not subject to copyright in the United States. Certain commercial systems are identified in this paper. Such identification does not imply recommendation or endorsement by NIST. Nor does it imply that the products identified are necessarily the best available for the purpose.

We wish to thank Mark Carlisle (NIST), Vijay Srinivasan (NIST), and the conference peer-reviewers for their reviews and comments.

References

[1] Technology, "Entry 4b," in *The oxford english dictionary*, Online ed Oxford: Oxford University Press, 2015.

[2] Innovation, "Entry 1a," in *The oxford english dictionary*, Online ed Oxford: Oxford University Press, 2015.

[3] Management, "Entry 1a," in *The oxford english dictionary*, Online ed Oxford: Oxford University Press, 2015.

[4] J. Tidd and J. R. Bessant, *Managing innovation : Integrating technological, market, and organizational change*, 4th ed. Hoboken, NJ: Wiley, 2009.

[5] M. Li, S. Gao, and C. C. Wang, "Real-time collaborative design with heterogeneous {cad} systems based on neutral modeling commands," *Journal of Computing and Information Science in Engineering,* vol. 7, pp. 113-125, 2006. DOI: 10.1115/1.2720880

[6] A. Kusiak, *Concurrent engineering : Automation, tools, and techniques*. New York: Wiley, 1993.
[7] C. E. S. da Silva, E. G. Salgado, C. H. P. Mello, E. da Silva Oliveira, and F. Leal, "Integration of computer simulation in design for manufacturing and assembly," *International Journal of Production Research,* vol. 52, pp. 2851-2866, 2014/05/19 2014. DOI: 10.1080/00207543.2013.853887
[8] K. Yang and B. El-Haik, *Design for six sigma : A roadmap for product development*, 2nd ed. New York: McGraw-Hill, 2009.
[9] J. M. Usher, U. Roy, and H. R. Parsaei, *Integrated product and process development : Methods, tools, and technologies*. New York: Wiley, 1998.
[10] T. D. Hedberg Jr, N. W. Hartman, P. Rosche, and K. Fischer, "Identified research directions for using manufacturing knowledge earlier in the product life cycle," *International Journal of Production Research,* vol. 55, pp. 819-827, 2017. DOI: 10.1080/00207543.2016.1213453
[11] K. E. Knight, "A descriptive model of the intra-firm innovation process," *The Journal of Business,* vol. 40, pp. 478-496, 1967. DOI: 10.2307/2351630
[12] M. E. Porter, *The competitive advantage of nations*. New York: Free Press, 1990.
[13] C. Freeman and L. Soete, *The economics of industrial innovation*, 3rd ed. Cambridge, Mass.: MIT Press, 1997.
[14] R. M. A. Hollen, F. A. J. Van Den Bosch, and H. W. Volberda, "The role of management innovation in enabling technological process innovation: An inter-organizational perspective," *European Management Review,* vol. 10, pp. 35-50, 2013. DOI: 10.1111/emre.12003
[15] T. W. Malnight, "Emerging structural patterns within multinational corporations: Toward process-based structures," *The Academy of Management Journal,* vol. 44, pp. 1187-1210, 2001. DOI: 10.2307/3069396
[16] V. Chiesa and F. Frattini, "Commercializing technological innovation: Learning from failures in high-tech markets*," *Journal of Product Innovation Management,* vol. 28, pp. 437-454, 2011. DOI: 10.1111/j.1540-5885.2011.00818.x
[17] M. A. Schilling, *Strategic management of technological innovation*. New York: McGraw-Hill/Irwin, 2005.
[18] T. M. Amabile, "Creativity and innovation in organizations," *Harvard Business Review,* 1/5/1996 1996.
[19] K. Lewin, F. Heider, and G. M. Heider, *Principles of topological psychology*, 1st ed. New York, London,: McGraw-Hill book company, inc., 1936.
[20] M. Hoegl and K. P. Parboteeah, "Creativity in innovative projects: How teamwork matters," *Journal of Engineering and Technology Management,* vol. 24, pp. 148-166, 3// 2007. DOI: 10.1016/j.jengtecman.2007.01.008
[21] R. G. Cooper, *Winning at new products : Accelerating the process from idea to launch*, 3rd ed. Cambridge, Mass.: Perseus Pub., 2001.
[22] M. L. Tushman and C. A. O Reilly, III, "Ambidextrous organizations: Managing evolutionary and revolutionary change," *California Management Review,* vol. 38, pp. 8-30, 1996.
[23] K. Ogata, *Modern control engineering*, 4th ed. Upper Saddle River, NJ: Prentice Hall, 2002.
[24] K. Ogata, *State space analysis of control systems*. Englewood Cliffs, N.J.,: Prentice-Hall, 1967.
[25] E. Flamholtz, "Effective organizational control: A framework, applications, and implications," *European Management Journal,* vol. 14, pp. 596-611, 12// 1996. DOI: 10.1016/S0263-2373(96)00056-4
[26] K. Warren, *Strategic management dynamics*. Chichester, West Sussex, England ; Hoboken, NJ: J. Wiley & Sons, 2008.
[27] F. Ceresia, "A model of goal dynamics in technology-based organizations," *Journal of Engineering and Technology Management,* vol. 28, pp. 49-76, 3// 2011. DOI: 10.1016/j.jengtecman.2010.12.004
[28] E. Flamholtz, *Effective management control : Theory and practice*. Boston: Kluwer Academic Publishers, 1996.
[29] P. F. Drucker, *The practice of management*, 1st ed. New York,: Harper, 1954.
[30] R. Simons, *Levers of control: How managers use innovative control systems to drive strategic renewal*: Harvard Business Press, 2013.
[31] The International Society of Automation, "Enterprise-control system integration − part 3: Activity models of manufacturing operations management," ed. North Carolina: ISA, 2013.
[32] C. Argyris and D. A. Schön, *Organizational learning*. Reading, Mass.: Addison-Wesley Pub. Co., 1978.
[33] D. G. Reinertsen, *Managing the design factory : A product developer's toolkit*. New York: Free Press, 1997.
[34] C. Argyris, *Teaching smart people how to learn*. Boston, Mass.: Harvard Business Press, 2008.
[35] T. Hedberg Jr, A. Barnard Feeney, M. Helu, and J. A. Camelio, "Towards a lifecycle information framework and technology in manufacturing," *Journal of Computing and Information Science in Engineering,* 2016. DOI: 10.1115/1.4034132

EXPOSING FENCING ASSEMBLIES TO FIREBRAND SHOWERS CHARACTERISTIC OF BURNING STRUCTURES

Samuel L. Manzello
Fire Research Division
National Institute of Standards and Technology (NIST)
Gaithersburg, MD USA 20899
samuelm@nist.gov

Sayaka Suzuki
Large Fire Laboratory
National Research Institute of Fire and Disaster (NRIFD)
Chofu, Tokyo, JAPAN

Ichiro Hagiwara
Department of Fire Engineering
Building Research Institute (BRI)
Tsukuba, Ibaraki, JAPAN

ABSTRACT

Wildland-Urban Interface (WUI) fires have devastated communities on multiple continents. Large outdoor fires in Japan mainly occur due to post-earthquake fires, which may result in severe urban fire spread. Once structures are ignited in these fires, firebrand production from structures becomes a key factor in fire spread. The authors are constructing a database of firebrand production from burning structures, as there is a little quantifiable data available in the literature. Based on post-fire disaster investigations, fencing assemblies are known to be prone to ignition in WUI fires, and may provide pathways to structure ignition. In this work, a comparison of ignition results from full-scale fencing assembly experiments conducted using the Building Research Institute's (BRI) full-scale wind tunnel facility, to mock-ups of full-scale fencing assemblies using the recently developed experimental capability at the National Research Institute of Fire and Disaster (NRIFD) are discussed. In both experimental facilities, the fencing assemblies were exposed to firebrand showers using custom built continuous-feed firebrand generators with size and mass distributions similar to the structure firebrand database mentioned above. The purpose was to determine if similar fencing ignition vulnerabilities were observed for reduced sized experiments. These results are required to guide the necessary configurations of fencing assembly mock-ups that can potentially be used in standard laboratory test methods. The results of this study will be presented.

INTRODUCTION

Recently, there have been significant number of wildfires that spread into communities, in Argentina, Australia, Brazil, Canada, Chile, France, Greece, Portugal, Spain, and the USA. Such fires are referred to as Wildland-Urban Interface (WUI) fires. Japan is another country that has been subject to large scale outdoor fires, but these fires have been initiated by earthquakes. A prominent mechanism of structure ignition in both WUI and urban fires is the production of firebrands, also referred to as embers[1].

Hagiwara, Ichiro; Manzello, Samuel; Suzuki, Sayaka.
"Exposing Fencing Assemblies to Firebrand Showers Characteristic of Burning Structures."
Paper presented at 2017 Fire and Materials Conference, San Francisco, CA. February 6, 2017 - February 8, 2017.

Post-fire studies suggest that attached building components may provide a pathway for structures to ignite in WUI fires[2]. Examples of attached building components include decking and fencing assemblies. A recent study by the authors demonstrated that fencing assemblies may be ignited by firebrand showers, but the capability of the ignited fencing to transfer the fire to an adjacent structure, such as wall assembly, was not considered[3]. This was done intentionally, since the *first step* was to determine if firebrand showers could even ignite various wood fencing types.

The focus of this paper is to present a comparison of ignition results from full-scale fencing assembly experiments conducted using the Building Research Institute's (BRI) full scale wind tunnel facility, to mock-ups of full-scale fencing assemblies using the recently developed experimental capability at the National Research Institute of Fire and Disaster (NRIFD). In both experimental facilities, the fencing assemblies were exposed to firebrand showers using custom built continuous-feed firebrand generators with size and mass distributions similar to the structure firebrand database developed by the authors.

It is of interest to determine if similar fencing assembly ignition vulnerabilities were observed for reduced sized experiments. Such data are required to guide the necessary configurations of fencing assembly mock-ups that can potentially be used in standard laboratory test methods. Furthermore, obtaining insights into ignition behaviour from reduced sized experiments is a desirable tool. It is hoped that these studies will also provide guidance for further full-scale experimental campaigns focused on structure ignition by ignited fencing assemblies, such as those conducted at the Building Research Institute (Japan), and recent studies conducted at NIST[4] to investigate fire spread along fencing assemblies using a burner (without firebrand attack).

EXPERIMENTAL DESCRIPTION

Full-Scale Experiments at the Building Research Institute (BRI)

The interested reader is referred elsewhere for a comprehensive description of the redesigned full-scale continuous feed firebrand generator system used here[5]. Namely, the feeding system was redesigned to be able to generate firebrand size and mass distributions using larger wood chips in an effort to produce a wider range of exposure conditions, as compared to prior studies[3]. Recent experiments have evaluated the performance of full-scale roofing components exposed to structure firebrand showers using this redesigned firebrand generator[6]. For completeness, a terse overview is provided presently.

The device consisted of the main body and continuous feeding component. The main body of the generator was the same as prior investigations (Dragon component); the feeding system was rebuilt. The feeding system was connected to the main body and was equipped with two gates to prevent fire spread. A blower was connected to the main body and the purpose of the blower is to loft and control the combustion state of the firebrands. A difficulty when constructing this device was designing a completely contained feeding system shielded from the wind tunnel flow.

The feeding system consisted of a pneumatic cylinder coupled to a cylindrical container where wood chips were stored (see **Figure 1**). Below the wood chip storage area, a plate was installed that allowed variation in the volume of wood chips to fall from the storage area to the first gate. This plate was set precisely to allow a specific mass of wood chips to fall into this volume. When the air pressure was applied, the sliding rod of the pneumatic cylinder moved forward and separated the wood chips from the storage area to the first gate, where they were then dropped into the second gate that leads to the Dragon where they are ignited (see **Figure 1**). The gate system was required to contain the fire from spreading from the Dragon to the feed system and each gate was driven by pneumatic cylinders as well.

For all experiments, Japanese Cypress wood chips were used to produce firebrands. These were provided from a supplier and upon arrival, these chips were filtered using a 10 mm mesh to remove very fine wood pieces. The chips were also oven dried, as they were shipped under wet conditions. The sizes of wood pieces were selected to produce firebrands with larger projected area at a specific mass than our prior studies using continuous firebrand generation[3]. As structure firebrand production is an important factor in WUI and urban fire spread, the authors have begun to develop a database of firebrand production from burning structures/structure components, and have demonstrated the ability to generate firebrands similar to structure firebrands from this database[5]. The fencing assemblies, described below, were exposed to these structure firebrand showers.

As in prior experiments using the NIST Dragon, the new experimental device was installed inside the test section of BRI's Fire Research Wind Tunnel Facility (FRWTF). The facility was equipped with a 4 m diameter fan to produce the wind field. The cross section of the FRWTF is 5 m wide by 4 m high. The maximum wind speed available using the FRWTF is 10 m/s. The leading edge fencing assemblies were placed at a distance of 3.25 m downstream of the full-scale Continuous Feed Firebrand Generator.

Redwood lattice fencing assemblies were constructed for the experiments (see **Figure 2**). These were custom fabricated by using two 1.22 m in height, 2.44 m in width, redwood lattice pieces, and held together using a 2 x 4 wood array (2 x 4 boards are 38 mm by 89 mm). While two-sided Redwood lattice fencing assemblies were used in this study, this type of fencing assembly may also be used in a one-sided configuration. Experiments are also underway to investigate these differences between one-sided and two-sided configurations, both at NIST and BRI/NRIFD. To simulate fine fuels that may be located near fencing assemblies, mini-pine bark mulch was used. Mini-pine bark nugget mulch was placed around the fencing assemblies at a depth of 51 mm (both sides). The mini-pine bark nuggets were oven dried and the density was 0.15 g/cm^3. Pine bark nugget mulch is known to be harder to ignite than other types of mulch, so this mulch type was selected to be able to clearly see the dynamic ignition process. These redwood lattice fencing assembly/mulch beds were exposed to firebrand showers. Further details are shown in **Figure 2.**

Figure 1 Picture of full-scale continuous feed firebrand generator installed at BRI's FRWTF. Japanese Cypress wood chips are feed into the device to produce firebrand showers similar to burning structures.

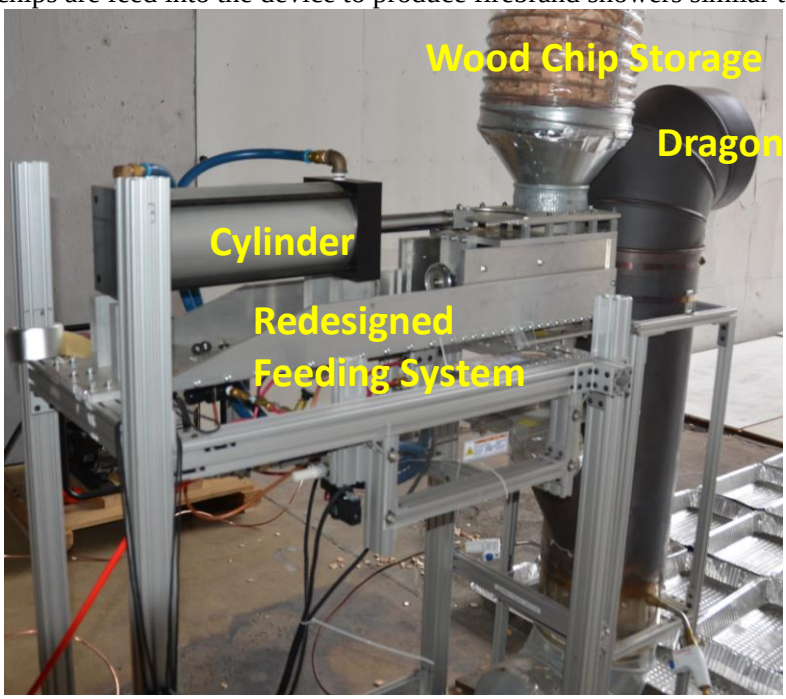

Figure 2 Picture of full-scale Redwood lattice fencing assembly with mulch bed.

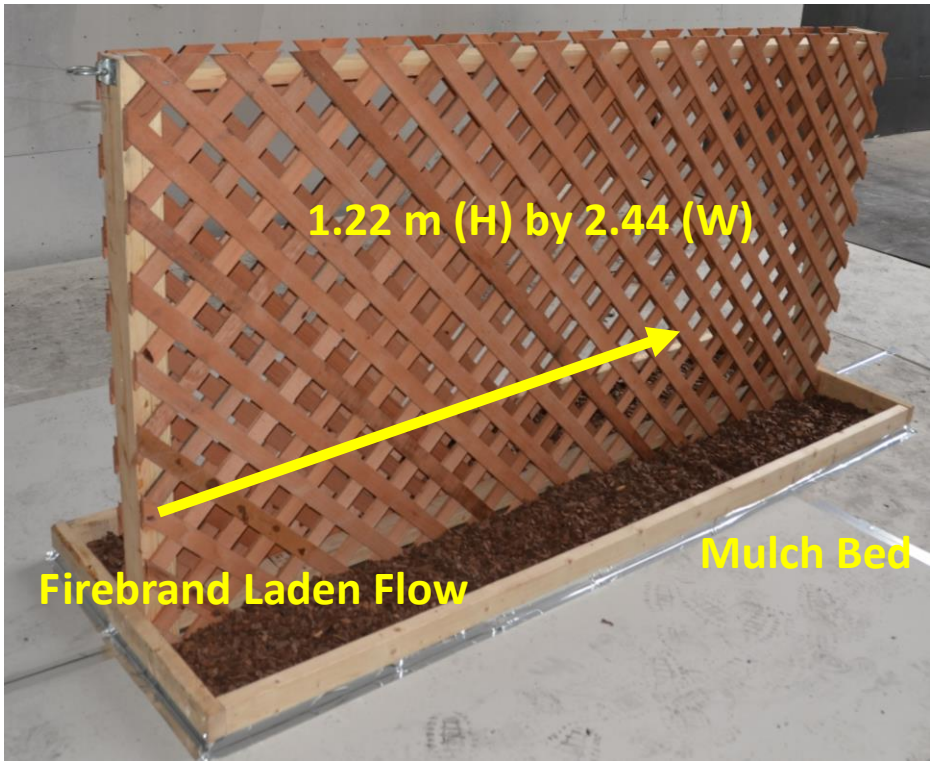

Reduced-Scale Experimental Facility at National Research Institute of Fire and Disaster (NRIFD)

A reduced-scale continuous-feed firebrand generator was used to generate firebrand showers (see **Figure 3**). A conveyor was used to feed wood pieces continuously into the device. For all tests, Japanese Cypress wood chips were used to produce firebrands. These same size wood pieces were used in the full-scale fencing assembly studies (above) and have been shown to be within projected area/mass of burning structures. Specifics of the wood feeding rate are provided below. Recently, this facility has been used to expose mock-ups of full-scale roofing assemblies to firebrand showers and the interested reader is referred elsewhere for a more comprehensive description of the National Research Institute of Fire and Disaster's facility (NRIFD)[7].

Since the base of the fan used to generate the wind field is located 1.6 m from the floor, the conveyor was placed under a custom stage designed for experiments when using the NRIFD wind facility (see **Figure 3**). The flow field was measured to be within ± 10 % over a cross-section of 2.0 m by 2.0 m.

Mock-ups of full-scale Redwood lattice fencing assemblies were constructed for the experiments. The fencing assemblies were custom fabricated by using two, 0.61 m in height, 1.22 m in width, redwood lattice pieces, and held together using a 2 x 4 wood array (see **Figure 4**). To simulate fine fuels that may be located near fencing assemblies, mini-pine bark mulch was used. Mini-pine bark nugget mulch was placed around the fencing assemblies at a depth of 51 mm (both sides). The mini-pine bark nuggets were oven dried and the density was 0.15 g/cm^3. The leading edge fencing assemblies were placed at a distance of 1.5 m downstream of the reduced-scale Continuous Feed Firebrand Generator in an effort to have the arrival number flux of firebrands similar to the full-scale experiments.

Figure 3 Schematic of reduced-scale continuous feed firebrand generator installed at NRIFD (side view). The diameter where the firebrands exit the firebrand generator (Dragon) was 10 cm. The stage dimensions were 5.5 m wide, 6.4 m long, with a height of 1.6 m.

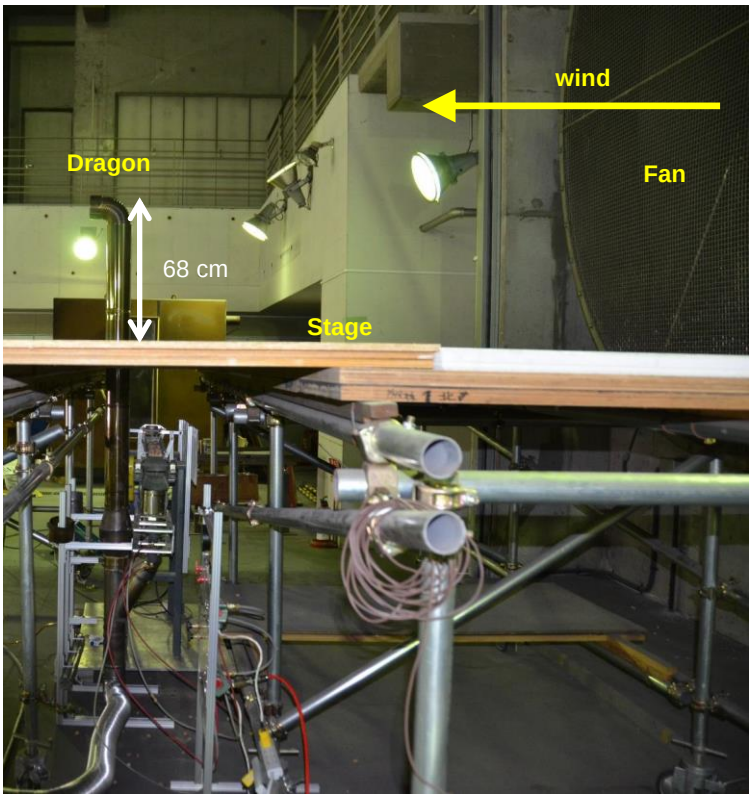

Figure 4 Picture of mockup of full-scale Redwood lattice fencing assembly with mulch bed. The dimensions were 0.61 m (H) and 1.22 m (W).

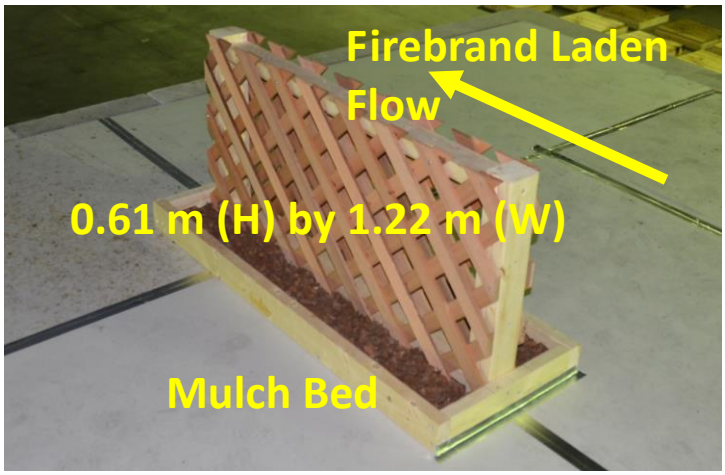

RESULTS AND DISCUSSION

Full-Scale Fencing Assemblies

It was found that 170 g ± 30 g, fed into the Dragon every 15 s, provided an adequate firebrand generation rate to ignite fencing assemblies. A supply of 170 g corresponded to approximately 560 wood

pieces deposited every 15 s. The number flux (number of firebrands generated/m^{2}s), at the exit of the device, was measured at a feeding rate of 170 g every 15 s (680 g/min). To determine the number flux, the number of firebrands was counted at every frame of the video recording, and summed every second. Based on the analysis, the number flux reached a steady value of 530/m^{2}s 150 s after feeding began. Mass flux data (mass of firebrands generated/m^{2}s) were calculated by multiplying the number flux and the average mass of each firebrand at a feed rate of 170g every 15 s.

The projected area of the firebrands directed at the fencing assembly/mulch bed was also quantified using a series of separate experiments where a water pan array was placed downstream of the firebrand generator. The firebrands were extracted, dried, and the mass (using balance) and projected area were determined using image analysis methods. **Figure 5** displays the projected area of the generated firebrands for various wind speeds. In **Figure 5**, data are presented for *both* the full-scale and reduced-scale firebrand generators. The reduced-scale firebrand generator data, however, is described below. Image analysis software was used to determine the projected area of a firebrand by converting the pixel area using an appropriate scale factor. More details on the methodology used are available elsewhere[6]. The standard uncertainty in determining the projected area was ± 10 %. The mass of each firebrand was measured by a precision balance. The standard uncertainty in the firebrand mass was approximately ± 1 %. The mean mass and standard deviation of each firebrand were obtained and observed to be 0.03 g ± 0.02 g. Therefore, the mass flux of generated firebrands was calculated to be 16 g/m^{2}s for the full-scale firebrand generator.

Figure 5 Size and mass distribution of generated firebrands for full-scale and reduced-scale firebrand generators (comparison at 6 m/s, and 9 m/s).

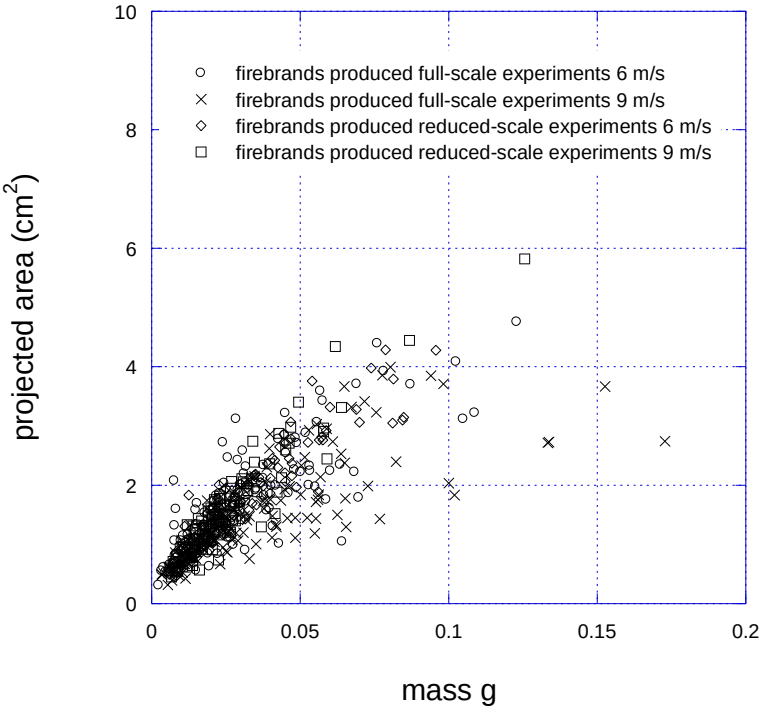

Experiments were conducted for wind speeds of 4 m/s, 6 m/s, and 9 m/s. In all cases, the evolution of the ignition process was similar. Specifically, glowing firebrands ignited the mulch beds via smoldering combustion, and then the mulch transitioned to flaming combustion. These flaming mulch beds then ignited the redwood lattice fencing assemblies. **Figure 6** displays the temporal evolution of the ignition process for a wind speed of 4 m/s. At the highest wind speed considered (9 m/s), once the fencing assembly was fully involved in flaming combustion, significant firebrand production from fence combustion was observed (see **Figure 7**; firebrands were observed to be transported outside the wind tunnel).

Figure 6 Temporal evolution of Redwood lattice fencing assembly/mulch bed ignition for wind speed of 4 m/s. The top panel displays smoldering ignition in the mulch bed from firebrand attack. The smoldering mulch bed has transitioned to flaming ignition, and the Redwood lattice fencing assembly is ignited (middle panel). In the bottom panel, the ignition has spread to the entire Redwood lattice fencing assembly.

Figure 7 Redwood lattice fencing assembly/mulch bed combustion with a wind speed of 9 m/s. Significant firebrand production may be observed.

Not all the firebrands that are generated by the Dragon arrive at the fencing assembly/mulch bed. The average number of firebrands arriving on the mulch beds was counted as a function of wind speed. To simplify the analysis, firebrands were counted on the left-hand side of the mulch bed, and these values were doubled for the entire assembly. Based on these analysis, the average total arrival number flux of firebrands was $4/m^2s$ (average total arrival number flux based on results for 4 m/s and 9 m/s wind speeds). As described below, efforts were made to try to have a similar firebrand arrival number flux for the mock-up experiments.

Mock-Ups of Full-Scale Fencing Assemblies

To expose the mockups of full-scale fencing assemblies to firebrand showers, a reduced-scale continuous-feed firebrand generator was used. A conveyor was used to feed wood chips continuously into the reduced-scale firebrand generator. The conveyor belt was operated at 1.0 cm/s, and wood chips were put on the conveyor belt at 12.5 cm intervals. The wood feed rate was fixed at 80 g/min, near the upper limit of reduced-scale firebrand generator. These same size wood chips were used in the full-scale roofing assembly study. The sizes of Japanese Cypress wood chips used for firebrand generation (before combustion) were 28 ±8 mm (length), 18 ±6 mm (width), and 3 ±1.0 mm (thickness) (average ±standard deviation), respectively. **Figure 5** displays the projected area of the generated firebrands at 6 m/s, and 9/s using the same analysis methods described for the full-scale continuous feed firebrand generator (see above).

Similar to the full-scale experiments, the wind speed was varied from 4 m/s to 9 m/s. In all cases, the evolution of the ignition process was similar to the full-scale fencing assembly experiments. Specifically, glowing firebrands ignited the mulch beds via smoldering combustion, and then the mulch transitioned to flaming combustion. These flaming mulch beds then ignited the redwood lattice fencing assemblies.

Figure 8 displays the temporal evolution of the ignition process for a wind speed of 4 m/s. At the highest wind speed considered (9 m/s), once the fencing assembly was fully involved in flaming combustion, significant firebrand production from fence combustion was also observed (see **Figure 9**).

Figure 8 Redwood lattice fencing assembly/mulch bed combustion with a wind speed of 4 m/s. The dynamics of the ignition process were similar to the full-scale experiments. The top panel displays smoldering ignition in the mulch bed from firebrand attack. The smoldering mulch bed has transitioned to flaming ignition, and the Redwood lattice fencing assembly is ignited (middle panel). In the bottom panel, the ignition has spread to the entire Redwood lattice fencing assembly.

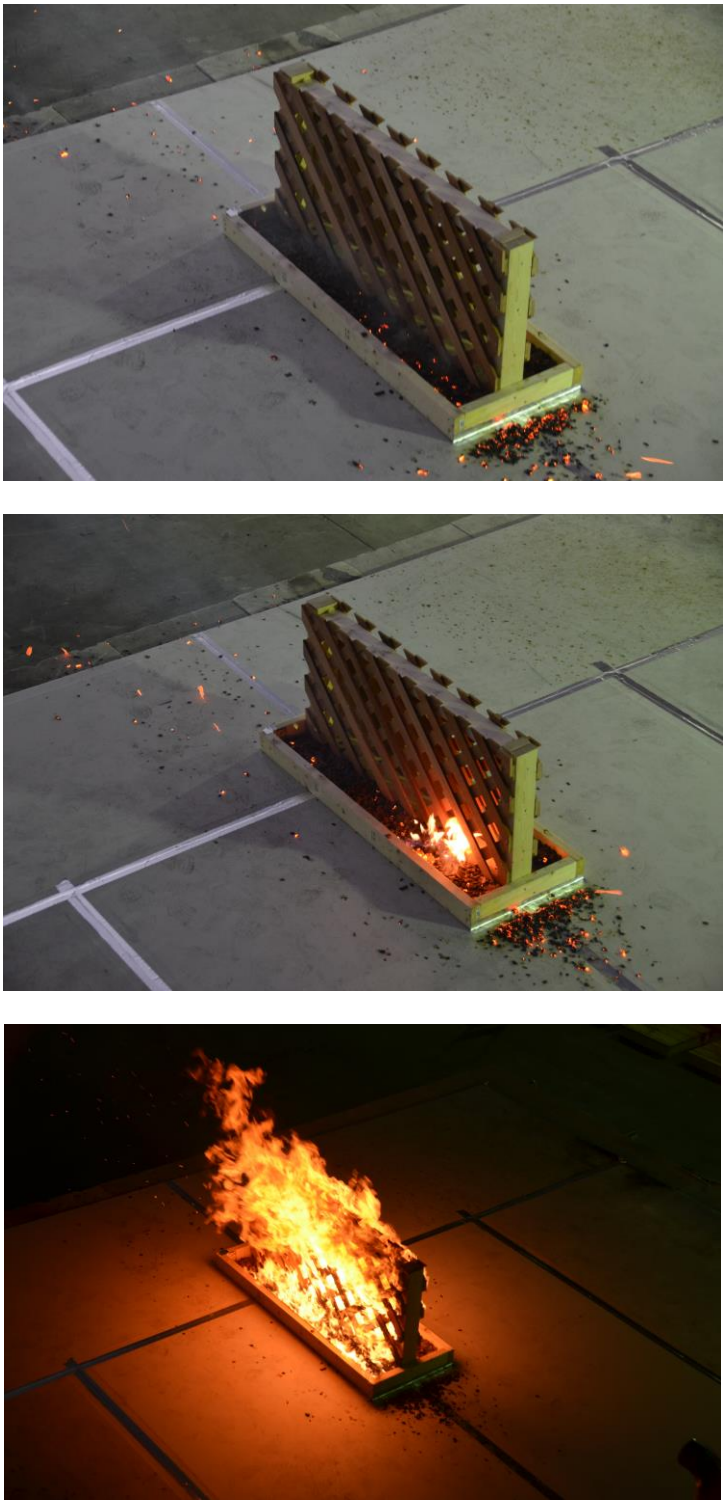

Figure 9 Mockup of full-scale Redwood lattice fencing assembly/mulch bed combustion with a wind speed of 9 m/s. Significant firebrand production may be observed.

The average number of firebrands arriving on the mulch beds was counted as a function of wind speed. To simplify the analysis, firebrands were counted on the left-hand side of the mulch bed, and these values were doubled for the entire assembly. Based on these analysis, the average total arrival number flux of firebrands was 4.5/m^{2}s (average total arrival number flux based on results for 4 m/s and 9 m/s wind speeds).

It is important to note that similar ignition behaviors were observed between the full-scale fencing assemblies and the mock-up of full-scale fencing assemblies. It is believed that this was observed since the following parameters were matched: size and mass of firebrands that are generated, the arrival number flux of firebrands, wind speeds, and same ignitable materials. Additional experiments are required for other fencing assembly types to further verify these important findings.

SUMMARY

The authors are constructing a database of firebrand production from burning structures, as there is a little quantifiable data available in the literature. Fencing assemblies are known to be prone to ignition in WUI fires, and may provide pathways to structure ignition. In this work, a comparison of ignition results from full-scale fencing assembly experiments conducted using the Building Research Institute's (BRI) full scale wind tunnel facility, to sections of full-scale fencing assemblies using the recently developed experimental capability at the National Research Institute of Fire and Disaster (NRIFD) was presented. In both experimental facilities, the fencing assemblies were exposed to firebrand showers using custom built continuous-feed firebrand generators with size and mass distributions similar to the structure firebrand database mentioned above.

Firebrand showers resulted in ignition of the full-scale redwood lattice fencing assemblies with mulch beds present. In all cases, the evolution of the ignition process was similar to the full-scale fencing assembly experiments. Specifically, glowing firebrands ignited the mulch beds via smoldering combustion, and then the mulch transitioned to flaming combustion. These flaming mulch beds then ignited the redwood lattice fencing assemblies.

It is believed that ignition similarities were observed since the following parameters were matched: size and mass of firebrands that are generated, the arrival number flux of firebrands, wind speeds, and same ignitable

materials.

Naturally, further analyses of these interesting findings are in progress. In particular, a well-defined approach to quantify the flame spread along the fencing is required. In the case of firebrand showers, ignition may be observed at multiple points along the fencing assembly/mulch bed due to the dynamic firebrand attack, in contrast to recent NIST experiments[4], where the fencing assembly/mulch bed was always ignited at the leading edge using a burner. Experiments are also required for other fencing assembly types to further verify these important findings.

These results will provide guidance for further full-scale experimental campaigns focused on structure ignition by ignited fencing assemblies, such as those ongoing at the Building Research Institute (Japan), and those also currently in progress at NIST using burners for ignition, as compared to firebrand showers.

The ability of a given burning fencing assembly to ignite adjacent wall assemblies will be considered in future experiments. Furthermore, obtaining insights into ignition behaviour from reduced sized experiments is a desirable tool, as understanding firebrand attack on buildings is a complex and difficult task.

ACKNOWLEDGEMENTS

Mr. Marco Fernandez of NIST's Engineering Laboratory (EL) is acknowledged for shipping materials for the experiments.

REFERENCES

1. Manzello, S. L., Yamada, T., Jeffers, A., Ohmiya, Y., Himoto, K., and Fernandez-Pello, A.C., Workshop for Fire Structure Interaction and Urban and Wildland-Urban Interface (WUI) Fires – Operation Tomodachi Fire Research, *Fire Safety Journal*, 59 (2013) 122-131.

2. Maranghides, A., McNamara, D., Vihnanek, R, Restaino, J., and Leland, C., A Case Study of a Community Affected by the Waldo Fire – Event Timeline and Defensive Actions NIST TN1910, 2015.

3. Suzuki, S., Johnsson, E., Maranghides, A., and Manzello, S.L., Ignition of Wood Fencing Assemblies Exposed to Continuous-Wind Driven Firebrand Showers, *Fire Technology*, 52 (2016) 1051-1067.

4. Johnsson, E., and Maranghides, A., Effects of Wind Speed and Angle on Fire Spread along Privacy Fences NIST TN 1894, 2016.

5. Manzello, S.L., and Suzuki, S., Generating Firebrand Showers Characteristic of Burning Structures, *Proceedings of the Combustion Institute*, 36 (2016), published online.

6. Suzuki, S., Nii, D., and Manzello, S.L., The Performance of Wood and Tile Roofing Assemblies Exposed to Continuous Firebrand Assault, *Fire and Materials* (2016), published on-line.

7. Suzuki, S., and Manzello, S.L., *Fire Safety Science* 12 (2017), in review.

Procedure for Selecting Key Performance Indicators for Sustainable Manufacturing

Deogratias Kibira
Morgan State University
Baltimore, MD, USA
deogratias.kibira@nist.gov

Michael P. Brundage
National Institute of Standards and Technology
Gaithersburg, MD, USA
Michael.brundage@nist.gov
ASME Member

Shaw Feng[1]
National Institute of Standards and Technology
Gaithersburg, MD, USA
Shaw.feng@nist.gov

KC Morris
National Institute of Standards and Technology
Gaithersburg, MD, USA
kcm@nist.gov

ABSTRACT

The need for an open, inclusive, and neutral procedure in selecting key performance indicators (KPIs) for sustainable manufacturing has been increasing. The reason is that manufacturers seek to determine what to measure to improve environmental sustainability of their products and manufacturing processes. A difficulty arises in understanding and selecting specific indicators from many stand-alone indicator sets available. This paper presents a procedure for individual manufacturers to select KPIs for measuring, monitoring and improving environmental aspects of manufacturing processes. The procedure is the basis for a guideline, being proposed for standardization within ASTM International. That guide can be used for (1) identifying candidate KPIs from existing sources, (2) defining new candidate KPIs, (3) selecting

[1] Corresponding author: shaw.feng@nist.gov

Brundage, Michael; Feng, Shaw; Kibira, Deogratias; Morris, Katherine.
"Procedure for Developing Key Performance Indicators for Sustainable Manufacturing."
Paper presented at ASME 2017 International Manufacturing Science and Engineering Conference, Los Angeles, CA. June 5, 2017 - June 8, 2017.

appropriate KPIs based on KPI criteria, and (4) composing the selected KPIs with assigned weights into a set. The paper explains how the developed procedure complements existing indicator sets and sustainability-measurement approaches at the manufacturing process level.

Key Words: KPI Criteria, Value Function, KPI Selection, Sustainable Manufacturing

INTRODUCTION

Manufacturing companies face increasing pressure to improve the sustainability of their operations [1, 2, 3]; however, beyond reduce, reuse, recycle programs, little guidance is available to help manufacturers minimize their environmental impacts [4]. In response to the increasing pressures and as a forum for establishing responsible practices, ASTM initiated a subcommittee on Sustainable Manufacturing (ASTM E60.13).

A literature review shows that major sustainability indicators are defined for specific, individual businesses [5]. Indicators that are uniformly defined and harmonized, therefore, are largely missing. A few major indicator sets have been developed for analyzing sustainability and scoring manufacturing organizations. For example, the Organization for Economic Cooperation and Development (OECD) [6] Core Environmental Indicators (CEI) includes 46 indicators to measure the impact of industrial activities on the environment in industrialized countries. The United Nations (UN) Commission on Sustainable Development [7] identifies 96 indicators to address environmental deterioration due to human activities. The indicators are created for businesses, companies, and factories; however, few publicly-available indicator sets exist at the operational level for individual processes. Standard procedures for identifying, defining, selecting, and composing a required set of Key Performance Indicators (KPIs) for manufacturing are lacking.

This paper addresses the question of what to measure to assess environmental sustainability at the manufacturing process level. The scope includes identification, definition, selection, and composition of environmental KPIs for individual processes. It complements guidelines specified in standards such as ASTM 2986-15 [8], ASTM 3012-16 [9], ISO 22400 [10], and ISO 20140 [11]. The purpose is to provide a guide for industry to identify candidate KPIs from existing sources, define new candidate KPIs, select the most effective KPIs based on KPI criteria, and compose a final KPI set. The approach relies on both human judgment and quantitative methods. The humans are stakeholders and subject matter experts, who are aware of the activities that are important to the success of the organization.

In section 2, we review the state of the art as well as challenges for sustainable manufacturing KPI ranking. This is followed by a description of value-focused concepts and the value function approach for KPI selection. Section 3 describes the proposed procedure for defining. Section 4 shows a demonstration of the procedure with a case study. Section 5 presents a discussion and conclusion of the paper.

2 BACKGROUND AND RELATED WORK

In the past decade, there has been considerable research in sustainable manufacturing and related measurement methodologies. Haapala et al. thoroughly review concepts, tools, and methods for sustainable manufacturing [12]. Duflou et al. provide a systematic overview of energy and resource efficiency methods and techniques for discrete part manufacturing [13]. These and similar publications review and analyze methodologies for developing sustainable manufacturing practices from the

enterprise level to the process level. However, assessing sustainability performance requires the availability of appropriate key performance indicators (KPIs).

2.1 Sources for sustainable manufacturing indicators

Efforts to select indicators for sustainable manufacturing have led to the establishment of best practices at the organizational level as well as lifecycle-impact-assessment methods. A best practice example is the Global Reporting Initiative, which consists of indicators to assess sustainability along three dimensions: economy, environment, and society [14]. A lifecycle assessment method example is IMPACT 2002+, which contains 14 midpoint categories mapped to four damage categories [15].

Recently, however, efforts have been made to develop other sources of indicators, indices, and frameworks for the lower control levels in manufacturing. The Lowell Center for Sustainable Production, proposed an indicator framework for shifting towards more sustainable manufacturing practice [16]. The research proposed twenty-two indicators and a guide to their application. In 2009, the National Institute of Standards and Technology (NIST) created a public repository of sustainability indicators to consolidate work of several organizations in the sustainable manufacturing area [17]. Joung et al. [2] categorized indicators for sustainable manufacturing and Park and Kremer [18] further categorized fifty-five environmental sustainability indicators using text mining-based objective information. However, Sikdar [19] claimed that no consensus exists on a reasonable taxonomy of sustainability-related metrics. Thus, indicators are defined inconsistently since every company, and indeed every opportunity for measured performance, has its own set of indicators.

2.2 Key performance indicator selection for sustainable manufacturing

Carlucci [20] noted that the selection of KPIs is necessary to assess the performance of a production management system. However, selecting a small set of KPIs from the large number of those available for a manufacturing process is often not straightforward. Secondly, selecting appropriate indicators to monitor the sustainability of processes and products is challenging due to the variety and complexity of those processes.

Efforts towards indicator selection include a methodology for establishing and improving performance measures that focus on overall equipment effectiveness [21]. Two related patents in the field exist. The first describes a method of selecting performance indicators so that they are relevant to an organization's business strategies [22]. The second describes KPI scorecard editor to rate different indicators against each other [23]. These patents, however, are proprietary and do not provide an open framework for KPI selection.

Garetti and Taisch noted the need for a structured framework to support selection of a suitable set of indictors [24]. To this end, a general KPI scheme for on-line process monitoring was developed in [25]. But, it does not provide a methodology to define new KPIs.

In summary, major problems for developing KPIs are (1) inconsistent definitions of KPIs, (2) a lack of an effective selection method for environmental KPIs for the manufacturing process, (3) a lack of KPI effectiveness evaluation methods, and (4) a lack of a KPI set composition method. This paper represents an initial step to addressing

these problems. It proposes an approach that uses a common set of selection criteria rather than evaluating KPIs against each other.

2.3 Decision making under multiple criteria

Decision-making is the process of selecting a course of action from among alternative choices. The KPI selection methodology presented in this paper uses concepts of decision theory and multi criteria decision-making (MCDM), and is based on value-focused and value-function approaches. It includes both human judgment and quantitative methods.

Dieter and Schmidt [26] describe several steps for making choices to obtain the best outcome of a situation. The steps include establishing objectives, developing alternatives, evaluating alternatives against objectives, and choosing what holds the best promise for achieving the objectives. Evaluating alternatives is one of the most difficult steps because it requires overcoming, among others, making decisions under conflicting requirements, setting priorities, and establishing objectives

Each objective is a statement of what the decision maker wants to achieve in the decision context. The criteria represent objectives that KPIs should satisfy as they are evaluated. MCDM methods include the weighted sum method, weighted product method, and analytic hierarchy process, elimination and choice translating reality, and technique for order preference by similarity [27].

Another common approach is for stakeholders to rank alternatives from the best to the worst depending on their preference. Collins et al. proposed a selection and improvement methodology for KPIs based on the weighted sum of values determined

by value functions [28, 29]. This paper further explores the use of value functions for selection criteria and use it for ranking candidate KPIs for selection of a final KPI set.

2.4 Value Functions for decision-making

Value-focused thinking is a way of using values to evaluate, rank, and choose the best among a set of alternatives [30]. Concepts of utility and value-focused thinking are more often used in economic analysis to understand preferences for products or investments. Value is a perceived benefit from acquiring and using a product or service, and upon which the motivation for making one choice over others is based. Values are obtained from value functions that are constructed by subject matter experts. But logical and systematic concepts are needed to qualitatively identify and structure the values that are appropriate to a situation while simultaneously constructing a value function [31]. Values are used to rank KPIs against the criteria.

Ezell [32] views the importance level assigned as a form of 'investment' on part of the stakeholder, and value as the benefit of doing so. Ranking candidate KPIs using value functions begins with identifying selection criteria followed by developing value functions for each criterion. Finally, a multiple objective decision making process using a value function for each criterion as proposed by Keeney [31] can be adopted to make criteria quantifiable. The process is described in the next section.

3 PROPOSED APPROACH FOR DEVELOPING KPI SETS

This section describes an approach to systematically rank candidate KPIs in order of effectiveness for sustainability assessment of a manufacturing process. It involves identifying candidate KPIs, selecting, ranking, and composing a final KPI set. These activities are illustrated in Figure 1. The first step is to establish organizational goals.

FIGURE 1 GOES HERE

3.1 Establishing KPI objectives

A KPI objective is a target of achievement to improve environmental sustainability of a manufacturing process. Individual KPI goals are obtained from organizational sustainability goals. KPI objectives represent activities to achieve identified KPI goals. Goals can be set as a normative standard for the organization or industry and should be applicable to all stakeholders.

3.2 KPI Identification

With sustainability goals established, the next step is to search literature and websites for candidate KPIs. KPI developers can first analyze KPIs currently in use and identify gaps in the KPIs necessary for the defined sustainability goals. If gaps exist and no KPIs can be found in literature, new KPIs should be defined. Candidate KPIs should be expressed using the format in ISO 22400-1 for ease of communication among stakeholders [10].

KPIs are often expressed in terms of associated metrics. Examples of metrics are energy consumption, water use, and material use. These metrics can either be measured directly (e.g. energy consumption measured with power meters) or estimated through physics-based equations (e.g. energy consumption estimated based on machine settings and material properties). Manufacturers should determine additional metrics not currently measured but necessary to address KPI objectives. When a new metric is needed, a manufacturer should consider the measurement methods (such as sensors or human input), the measurement costs, and the time needed to measure.

3.3 KPI Definition

There are two approaches to defining a new KPI: bottom-up and top-down. The bottom-up approach starts with identifying current and necessary metrics and then assembling them into a new KPI. For example, if the objective is to reduce energy waste at a process, then measuring both total energy and energy needed for a task (necessary energy) will be required. Example KPIs could be "total energy waste = total energy – necessary energy" or "energy waste efficiency = necessary energy/total energy." The bottom-up approach is more useful when addressing the improvement of a single process.

The top-down approach focuses on defining a new KPI from the goals and identifying the necessary metrics to calculate that KPI. The method chosen is based on the manufacturer's situation. The top-down approach is driven by organizational goals and may include several manufacturing processes relevant to the goal. Table 1 is an example of a KPI formatted using the ISO 22400-1 template [10].

TABLE 1 GOES HERE

3.4 KPI Selection

Once candidate KPIs are identified, experts and stakeholders are enlisted to rank the KPIs based on their effectiveness of sustainability assessment. The criteria for this ranking are determined independently from the KPIs themselves. The list of potential criteria can be extensive [33, 34, 35]. Therefore, a systematic approach involving multiple stakeholders is used to identify a set of selection criteria. Stakeholders include line managers, supervisors, and shop floor workers who make their proposals for selection criteria. This information is then aggregated. A final set of criteria is obtained

after additional review by the stakeholders. Further, previous experience in similar situations can also be used to determine the number and type of criteria needed.

FIGURE 2 GOES HERE

Typically, criteria are not of equal weight during KPI selection. As such, experts develop a value function for each criterion, as mentioned in the previous section. Value functions capture experts' assessments of the value of a criterion. Developing a value function starts with the definition of importance levels to be assigned to the criterion. Figure 2 is an example of a value function for the "actionable" criterion. It has six defined levels of importance and values in the range 0 to 100. The (horizontal) X-axis of the function has ordinal scores correlating to possible importance levels. Subject matter experts identify the value they associate with each importance level and these are shown on the (vertical) Y-axis. In this case, the experts give some value to a criterion that the work group can directly act on what is being measured by a KPI, i.e., whether a KPI is actionable. The experts in this example consider this information to have some value to enable other actions. But stakeholders would have to assign the maximum importance level for the most value that the work group can take action. Each importance level has a description that shows emphasis of the criterion during KPI ranking and a corresponding value or "benefit". Numerical values associated with both the importance level and the experts' evaluation of the criterions' value are represented on a graph. The shapes of value functions can differ depending on subject matter experts' expression of variation of importance of a given criterion with increasing assigned emphasis.

In the next step, stakeholders independently assign the levels of importance for all the criteria for each candidate KPI. A value is obtained from the value function for each importance level assigned. An average is calculated for the values obtained from all stakeholders for each criterion for each KPI. The final value of the importance of a KPI depends on values obtained for all the criteria. Many algorithms exist for calculating this final value. One simplified method is to calculate the total sum of values obtained from all the criteria. Ranking of KPIs is based on the final aggregated value of a KPI relative to that of other candidate KPIs.

The average value function for criteria i from all stakeholders can be represented as . If n is the number of criteria, m is the number of stakeholders, then the final value (or aggregated value) of a KPI's importance is:

Aggregated value $= \sum_{i=1}^{n} v_i(x_i)$

3.5 KPI Composition

Different sustainability objectives often result in different KPIs as seen in Figure 3. To compose different KPIs, they must be on the same scale of measurement. Secondly, the KPIs should be assigned relative importance based on their perceived contribution to the sustainability goal. These two activities are referred to as normalization and weighting respectively. There are different methods used for normalization. Typically, the more important the KPI, the more weight it is assigned. Weights are dimensionless values.

KPI organization is a layered structure of KPI objectives, sub-goals, and sustainability goals. KPI objectives are at the bottom while sustainability goals are at the top. Sub-goals lie in between the sustainability goals and KPI objectives. The relationship between KPI objectives, sustainability sub-goals, and sustainability goals are expressed in the goal-objective structure. Using this structure, measurements based on KPIs can be properly aggregated to evaluate whether manufacturing processes meet the sustainability objective.

FIGURE 3 GOES HERE

4 DEMONSTRATION WITH A CASE STUDY

This section illustrates the procedure described above for selecting effective KPIs. We use a case of a powdered metal product manufacturing. The processes involved are compacting, sintering, and machining, as shown in Figure 4. This study focusses on the machining process.

FIGURE 4 GOES HERE

Three stakeholders (design manager, plant manager, and manufacturing engineer) are tasked to select appropriate KPIs that would assess the achievement of sustainability goals to make the following reductions within one year:

1) solid waste by 10 %
2) CO2 emissions by 20 %
3) energy consumption by 15 %

In the next step stakeholders search the literature for candidate KPIs that help achieve the above specified goals. Six candidate KPIs are identified. They are 1) material efficiency, 2) virgin material efficiency, 3) CO2 emissions, 4) N2O emissions, 5) energy

per part, and 6) energy efficiency. These KPIs are deemed sufficient for the KPI goals and, therefore, no new KPIs are defined. The stakeholders next select the following criteria for ranking the KPIs:

1) Cost effectiveness: The degree of perceived cost benefit of implementing the KPI.

2) Quantifiable: The degree to which a KPI can be stated numerically and precisely.

3) Calculable: The degree of correctness and completeness of the calculation required to compute the value of the KPI.

4) Management support: The willingness of plant management to support the choice of appropriate KPIs, achievement of KPI targets, and performance of the tasks necessary to improve target KPI values.

5) Comparable: The degree to which historic data is maintained and available for comparison to current values.

6) Understandable: The degree to which the meaning of the KPI is comprehensible by team members, particularly with respect to corporate goals.

The value functions are then created by subject matter experts for each criterion. The stakeholders assign an importance level to the criterion for each KPI. For each importance level assigned, a value is obtained using the value functions. Table 2 shows the importance level on a scale 0-6 for each KPI assigned by one stakeholder. The values (obtained from the value function) vary in range 0-100. All three stakeholders perform the same process and their results averaged. The averages for all stakeholders

per criterion, as well as the aggregated averages for all criteria (rating), are shown in Table 3.

TABLE 2 GOES HERE

TABLE 3 GOES HERE

The stakeholders scores show that the KPIs rank as follows: 1) Energy per Part, 2) Material Efficiency, 3) CO2 Emissions, 4) Virgin Material Efficiency, 5) Energy Efficiency, and 6) N2O Emissions. The stakeholders decide on a cutoff point of 475 and select Material Efficiency, Energy Intensity, and CO2 emissions to measure the sustainability objectives.

5 DISCUSSION AND CONCLUSION

Currently, standard procedures to select effective KPIs for manufacturing process sustainability do not exist. The paper has developed a method using selection criteria and value functions to rank candidate KPIs so that a final set is selected. The method combines both human input and quantitative analysis. The procedure will enable manufacturers to consistently select effective environmental KPIs across facilities to be shared among different manufacturers.

The approach is a step towards a standard guide for developing KPI sets for assessing environmental aspects of manufacturing processes. It complements existing standards for (1) KPI identification at operational level (ISO 22400-1), (2) for unit manufacturing process characterization (ASTM E3012-16), and (3) gate-to-gate environmental sustainability evaluation of manufacturing processes (ASTM E2986-15). This paper is a basis for a guide that has been proposed to the ASTM standard for members, consisting primarily of industrial practitioners, to review and comment.

However, membership is open to any interested party. A standard is expected to be completed soon.

The KPI selection process will better support researchers and practitioners in making informed use of KPIs if it is encoded into software. Procedures for selecting the stakeholders and subject matter experts can also be formalized and documented. Choices for criteria definition, value function development, final value aggregation methods as well as normalization and weighting methods can be made available. This paper contributes to a wider field of using KPIs for performance measurement of manufacturing systems. Work on describing relationships between manufacturing KPIs has been initiated to enable understanding of which KPIs have the greatest impact on others as well as the type and form of impact. We anticipate that the results will include formal methods for developing and representing such relationships. The methods developed will be applied to environmental KPIs, which will further enhance the process of developing a final KPI set.

One of the major issues in KPI selection and application is that emphasizing one KPI may result in deterioration of another. By analyzing the interrelationships of various KPIs and their underlying metrics, it may be possible to calculate a similarity score, which could aid in the selection of the effective KPIs. For example, if multiple KPIs are based on the same metrics for computation, it might be possible to only use one KPI to measure towards the sustainability goal. On top of this, if one KPI that is already measured directly influences another KPI that is not measured, then it may be possible

to calculate both KPIs without the need for additional data collection devices or measurements.

Repositories of KPIs for manufacturing processes will be helpful to provide pre-defined KPIs for selection of those suitable to the different specific processes being studied. Repositories should be easily accessible and extensible to organize KPIs as more are included. Advanced search capabilities should support accuracy and speed in finding appropriate KPIs and will be a topic of future research.

ACKNOWLEDGMENT

This effort has been sponsored in part under the cooperative agreement No. 70NANB13H153 between NIST and Morgan State University. This material is declared a work of the U.S. Government and is not subject to copyright protection in the United States of America.

DISCLAIMER

Certain commercial software products or services may be identified in this paper. These products or services were used only for demonstration purposes. This use does not imply approval or endorsement by NIST, nor does it imply that these products are necessarily the best for the purpose. This material is declared a work of the U.S. Government and is not subject to copyright protection in the United States of America.

NOMENCLATURE

V	variables should appear in first column with the description in second column, m
I	all variables should appear in italics
tl	two-letter abbreviations should appear in italics
tla	three-letter abbreviations should not appear in italics
Re	Reynolds number and similar abbreviations do not use italics
T	use the “Tab” key to add more rows to this table

REFERENCES

[1] MIT Sloan Management Review and Boston Consulting Group (2011). "Sustainability: The 'Embracers' Seize Advantage," MIT Sloan Management Review Research Report, Winter 2011.

[2] Joung, C., Carrell, J., Sarkara, P., Feng, S. (2013). "Categorization of Indicators for sustainable manufacturing," Ecological Indicators, 24, pp. 148–157.

[3] Moldan, B., Janouskova, S., and Hak, T. (2012) "How to understand and measure environmental sustainability: Indicators and targets," Journal of Ecological Indicators, 17, pp. 4 – 13.

[4] Kang, N., Zhao, C., Li, J., and Horst, J. (2016). "A hierarchical structure of key performance indicators for operation management and continuous improvement in production systems," International Journal of Production Research, 54(21), pp. 6333 - 6350.

[5] Gaurav, A., Rachuri, S., Fiorentini, X., Mani, M., Fenves, S., Lyons, K., and Sriram, R. (2008). "Extending the Notion of Quality from Physical Metrology to Information and Sustainability," Journal of Intelligent Manufacturing, 22, 737-750. doi:10.1007/s10845-009-0333-3.

[6] OECD Toolkit (2011). OECD Sustainable Manufacturing Toolkit, http:// www.oecd.org/innovation/green/toolkit, OECD Publishing, Paris, France.

[7] UN-CSD (the United Nations Committee on Sustainable Development). (2007) "Indicators of Sustainable Development: Guidelines and Methodologies," (3rd Eds.), the United Nations, New York, New York, 2007, http://www.un.org/esa/sustdev/natlinfo/indicators/guidelines.pdf.

[8] ASTM E2986-15 (2015). "Standard Guide for Evaluation of Environmental Aspects of Sustainability of Manufacturing Processes," ASTM International.

[9] ASTM E3012-16 (2016). "Standard Guide for Characterizing Environmental Aspects of Manufacturing Processes," ASTM International.

[10] ISO 22400-1:2014, (2014). "Automation systems and integration— Key Performance Indicators (KPIs) for manufacturing operations management; Part 1: Overview, concepts, and terminology," International Organization for Standardization.

[11] ISO 20140-1:2013 (2013). "Automation systems and integration -- Evaluating energy efficiency and other factors of manufacturing systems that influence the environment -- Part 1: Overview and general principles.", International Organization for Standardization.

[12] Haapala, K.R., Zhao, F., Camelio, J., Sutherland, J.W., Skerlos, S.J., Dornfeld, D., Jawahir, I.S., Clarens, A.F., Rickli, J.L. (2013). "A Review of Engineering Research in Sustainable Manufacturing," Journal of Manufacturing Science and Engineering, 135 (4), 041013-011013-16.

[13] Duflou, J. R., Sutherland, J.W., Dornfeld, D., Herrmann, C., Jeswiet, J., Kara, S., Hauschild, M., Kellens, K. (2012). "Towards energy and resource efficiency manufacturing: A processes and systems approach" CIRP Annals – Manufacturing Technology, 61 (2), pp. 587-609.

[14] GRI (Global Reporting Initiative) (2006). "Sustainability reporting Guidelines," Version 3.0, 200-2006 GRI, http://www.globalreporting.org.
[15] EPFL (Swiss Federal Institute of Technology), "IMPACT 2002+," http://www.quantis-intl.com/en/impact-2002, visited June 15, 2016.
[16] Veleva, V., and Ellenbecker, M. (2001). "Indicators of sustainable production: Framework and methodology", Journal of Cleaner Production, (9), pp. 529-549.
[17] NIST Engineering Laboratory 2009, "Sustainable Manufacturing Indicator Depository," Available online at: http://www.mel.nist.gov/msid/SMIR/index.html, 2009 accessed on 10/5/2016).
[18] Park, K., Kremer, G.E.O, (2017). "Text mining-based categorization and user perspective analysis of environmental sustainability indicators for manufacturing and service systems," Journal of Ecological Indicators, 72, pp. 803-820
[19] Sikdar, S., (2003) "Sustainable development and sustainability metrics," AIChE Journal, 49, (8), pp. 1928–1932.
[20] Carlucci, D. (2010). "Evaluating and selecting key performance indicators: an ANP-based model." Measuring Business Excellence, 14, (2), pp. 66–76.
[21] Ahmad, M.M. and Dhafr, N. (2002). "Establishing and improving manufacturing performance measures," Robotics and Computer Integrated Manufacturing,18, 171-176
[22] Patent 2005. (2005). Razvi, N., Deppe, M., Oswald, W., Guenther, M., Performance Indicator Selection https://www.google.com/patents/US20060235778
[23] Patent 2007, (2007). Van de Walker Handy, S., Birkedal Peterson, P., Wilson, B., Hulen, C.J. Key Performance Indicator Scorecard Editor https://www.google.com/patents/US8095417
[24] Garetti, M. and Taisch, M., (2012). "Sustainable manufacturing: trends and research challenges," Production Planning & Control, 23 (2-3), pp. 83-104.
[25] Rakar, A., Zorzut, S., Jovan, V., (2004). "Assessment of Production Performance by Means of KPI" Proceedings of the Control, pp. 6-9.
[26] Dieter, G. E., and Schmidt L. C., (2013). "Engineering Design," Fifth Edition, McGraw-Hill.
[27] Triantaphyllou, E., (2013). "Multi-Criteria Decision Making Methods: A Comparative Study," Kluwer Academic Publishers.
[28] Collins, A., Hester, P. T., Ezell, B., and Horst, J., (2016). "An improvement selection methodology for Key Performance Indicators." Environment, Systems and Decisions, 36 (2), pp. 196-208.
[29] Clemen, R. and Reilly, T., (2001). "Making Hard Decisions," South-Wester Cengage Learning, Mason, OH.
[30] Keeney, R. (1992). "Value focused thinking: A Path to Creative Decision-making," Harvard University Press.
[31] Keeney, R. L. and Raiffa, H. (1993). "Decisions with Multiple Objectives: Preferences and Value Tradeoffs." Cambridge University Press.
[32] Ezell, B. C. (2004). "Quantifying vulnerability to critical infrastructure systems." PhD Dissertation, Department of Engineering Management, Old Dominion University, Norfolk, VA.

[33] Martins, A.A., Mata, T.M., Costa, C.A.V. and Sikdar, S.K., (2007). "Framework for Sustainability Metrics," Industrial & Engineering Chemistry Research, 46, pp. 2962-2973.
[34] Tanzil, D., and Beloff, B.R. (2006). "Assessing Impacts: Overview on Sustainability Indicators and Metrics," Wiley Periodicals, Inc.
[35] ISO 22400-2: 2011, (2011). "Automation systems and integration – Key performance indicators (KPIs) for manufacturing operations management – Part 2: Definitions and descriptions of KPIs," International Organization for Standardization.

Figure Captions List

Table Caption List

Figure 1: Illustration of the effective KPI identification and selection process

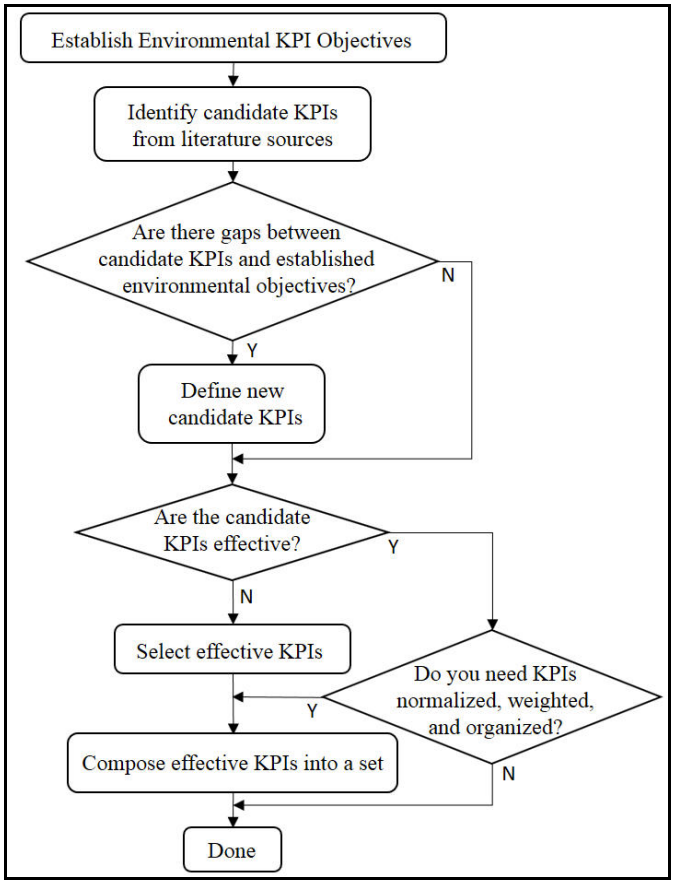

Figure 2: Example of a value function for the criterion "actionable"

Importance Level	Level	Experts' Value Assessment
Not important	0	0
Somewhat important	1	2
Fairly important	2	5
Important	3	12
Very important	4	35
Extremely important	5	100

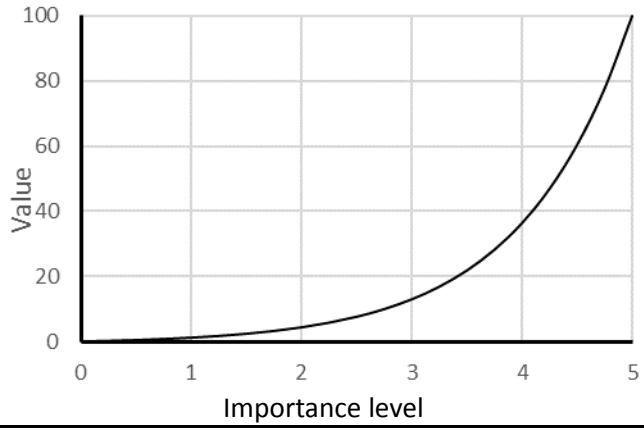

Figure 3: KPI Composition for material efficiency

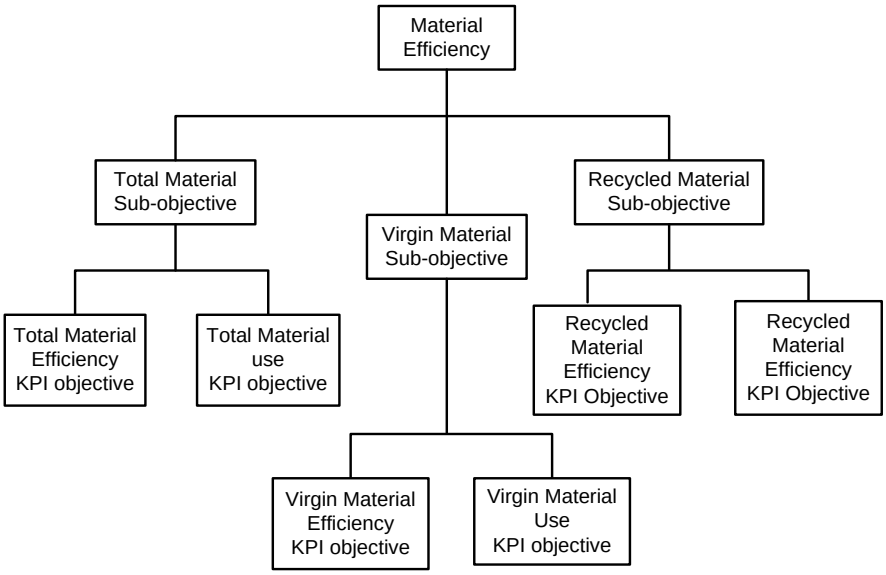

Figure 4: Manufacturing process for powdered metal products – focus on machining

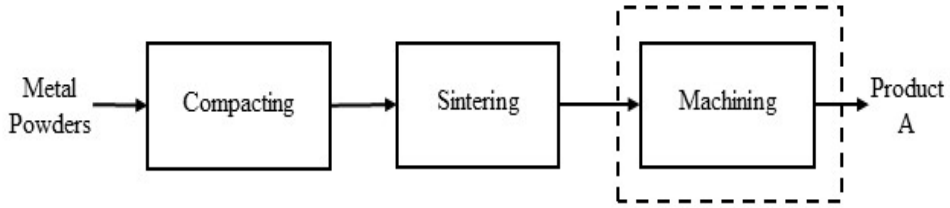

Table 1: Example KPI – Total Energy Waste

KPI description	
Content:	
Name	Total Energy Waste
ID	
Description	The total energy waste measures the difference between theoretical energy and the actual energy consumed by the process.
Scope	Process Level
Formula	Total Energy Waste = EC – NE, where EC = energy consumed by the process in kWh where NE = necessary energy in kWh
Unit of Measure	kWh
Range	Min: 0 Max: process dependent
Trend	The lower, the better
Context:	
Timing	Periodically
Audience	Operator, supervisor, management
Production methodology	Discrete, Batch
Notes	The total energy waste provides insight into energy waste at a process by comparing the energy needed at a process to the actual energy consumed.

Table 2: Design Manager Rankings

Stakeholder 1 (Design Manager)												
Legend: *L – Level* *V – Value*	Material Efficiency		Virgin Material Efficiency		CO_2 Emission		N_2O Emission		Energy per Part		Energy Efficiency	
	L	*V*	*L*	*V*	*L*	*V*	*L*	*V*	*L*	*V*	*L*	*V*
Cost Effectiveness	2	40	3	53	5	100	5	100	5	100	5	100
Quantifiable	6	100	6	100	5	36	5	36	6	100	6	100
Calculable	4	100	4	100	4	100	4	100	4	100	4	100
Management Support	5	100	4	72	4	72	4	72	3	47	3	47
Comparable	4	100	4	100	3	78	3	78	4	100	4	100
Understandable	5	100	5	100	5	100	5	100	5	100	5	100

Table 3: Average stakeholder values and final aggregate

	Material Efficiency	Virgin Material Efficiency	CO_2 Emission	N_2O Emission	Energy per Part	Energy Efficiency
Cost Effectiveness	49	49	100	64	90	64
Quantifiable	100	50	36	21	79	79
Calculable	93	93	100	93	100	85
Management Support	82	72	72	64	64	41
Comparable	85	85	85	61	84	76
Understandable	100	99	100	98	100	100
Aggregate value	**509**	448	**493**	402	**517**	444

Proceedings of 2017 ASME International Manufacturing Science and Engineering Conference
MSEC17
June 4-8, 2017, University of Southern California, SC, USA

MSEC2017-2782

ACCURACY DEGRADATION ANALYSIS FOR INDUSTRIAL ROBOT SYSTEMS

Guixiu Qiao
National Institute of Standards and Technology
Gaithersburg, MD, USA

Brian A. Weiss
National Institute of Standards and Technology
Gaithersburg, MD, USA

KEY WORDS

Robot Systems, Accuracy Degradation, Degradation Analysis, Robot System Prognostics and Health Management (PHM), Condition Monitoring

ABSTRACT

As robot systems become increasingly prevalent in manufacturing environments, the need for improved accuracy continues to grow. Recent accuracy improvements have greatly enhanced automotive and aerospace manufacturing capabilities, including high-precision assembly, two-sided drilling and fastening, material removal, automated fiber placement, and in-process inspection. The accuracy requirement of those applications is primarily a function of two main criteria: (1) The pose accuracy (position and orientation accuracy) of a robot system's tool center position (TCP), and (2) the ability of a robot system's TCP to remain in position or on-path when loads are applied. The degradation of a robot system's tool center accuracy can lead to a decrease in manufacturing quality and production efficiency. Given the high output rate of production lines, it is critical to develop technologies to verify and validate robot systems' health assessment techniques, particularly the accuracy degradation. In this paper, the National Institute of Standards and Technology's (NIST) effort to develop the measurement science to support the monitoring, diagnostics, and prognostics (collectively known as prognostics and health management (PHM)) of robot accuracy degradation is presented. This discussion includes the modeling and algorithm development for the test method, the advanced sensor development to measure 7-D information (time, X, Y, Z, roll, pitch, and yaw), and algorithms to analyze the data.

INTRODUCTION

In recent years there is a growing demand within the automotive and aerospace industry for greater robot accuracy [1, 2]. With the accuracy improvement in both position and orientation, the articulated robot arm can be applied to a much broader range of applications that were once limited to custom machines, including high precision assembly, two-sided drilling and fastening, material removal, automated fiber placement, and in-process inspection. Compared to custom machines, the robot's articulated arm can span a relatively large working envelope capable of navigating along highly curved surfaces and into tight spaces. Since the robot's mass is relatively low, the foundation (e.g., supporting structure) requirements of robots are minimal. Robot applications bring manufacturers benefits in both improving flexibility and reducing costs with these noted advantages.

Robot accuracy is defined as the measurement of the deviation between the commanded and attained robot 6-D (six degree-of-freedom) position and orientation [3]. Accuracy can also represent the difference between commanded and actual velocities, accelerations, forces, and torques. Improving accuracy (i.e., lessening the difference between commanded and actual values) allows rapid deployments of industrial robot applications by rapidly transferring or downloading robot programs between two "identical" robot cells. It enables the quick replacement of a robot in a manufacturing system by reducing or eliminating re-teaching processes. High robot accuracy during manufacturing ensures that parts are precisely manufactured with predictable results even after changes are made to the process. High accuracy is also critical in data-driven applications, such as those applications developed using off-line programming methods [4]. High accuracy enables the use of offline programs to minimize the robot downtime (e.g., the time-consuming task to train a robot to drill thousands of holes on an airplane's fuselage). The market requirement for high design-variations and low-batch production has driven users and integrators to look more towards "off-line programming". Using robots for in-process inspection or gauging is another application that calls for high accuracy of a robot's pose because the robot is an influential part of the measurement operations [5, 6]. There are a large number of automotive and aerospace applications that currently utilize and could benefit from the flexibility of robotics with high accuracy to perform metrology on manufactured parts.

Qiao, Guixiu; Weiss, Brian.
"Accuracy Degradation Analysis for Industrial Robot Systems."
Paper presented at ASME International Manufacturing Science and Engineering Conference, Los Angeles, CA. June 4, 2017 - June 8, 2017.

High accuracy robots are becoming valuable tools for many of the afore-mentioned processes that lead to substantial cost savings for the manufacturing industry [7].

The degradation of a robot system's pose accuracy can lead to a decrease in manufacturing quality and production efficiency. Robots are used to accurately move, manipulate, and/or perform a process (e.g., welding, drilling, assembling) to certain specifications. The robot system's pose accuracy relies on the actual geometries and positions of components in a robot cell. Tiny changes of link length, tools, and objects (geometric errors) in the workspace can cause inaccuracies of the TCP pose used in existing robot programs. There are also non-geometric errors, such as the non-ideal motion of joints, and deflections of the structure and joints due to external loading or gravity. The sag from the link masses and payload can create significant errors at the TCP if there is no compensation. Another aspect unique to robotics is the general use of harmonic gear drives or strain wave gears. These gears use flexible membranes, which can result in a loss of accuracy, particularly with wear over time. The flexible element in these joints can also generate significant backlash error. The backlash error can vary significantly over the range of motion of the joint [8].

It is important that robot system degradations be understood so that maintenance and control strategies can be ideally optimized. Degradation analysis of the TCP accuracy is one of the key elements when assessing the health state of an industrial robot within the manufacturing industry. Health monitoring, diagnostics, prognostics, and maintenance (collectively known as Prognostics and Health Management (PHM)) have gained considerable attention within the robot system domain with respect to the design, implementation, operations (including control), and maintenance phases. Accuracy degradation is difficult to detect when the system is still operational as compared to detecting a complete system break-down. There are many challenges for the TCP health assessment of industrial robots.

- **Lack of sensor technology to quickly acquire 6-D information (X, Y, Z, roll, pitch, and yaw) that describes the robot's TCP accuracy.** Existing 6-D measurement systems include laser tracker-based systems and optical tracking systems [9]. These systems are expensive. The laser tracker-based systems need to maintain line-of-sight between the laser tracker and the target. The optical tracking systems use reflective balls as markers and the near-infrared filter attached to lenses to obtain images which only contain the markers. The optical tracker's near-infrared cameras are "blind" to the environment. There is no redundancy when ambient light influences the reflected light from the targets[10]. Development is needed for advanced sensing to enable the quickly acquirement of 6-D information. NIST research begins to address this challenge; this effort is presented in the Advanced Sensor Development for System Level Sensing section of this paper.

- **Lack of test methods that can quickly and efficiently capture key TCP accuracy metrics without interrupting production line.** For example, TCP accuracy needs to be assessed within a volumetric method because the error magnitudes and directions are different depending on the approach directions of joints. Efficient modeling and algorithms are needed for the test method to identify the health of the robot system.

- **Lack of a PHM data taxonomy and architecture**. There is a lack of interoperability between sensor/data formats and communication modes to capture, share, and analyze data across heterogeneous robot systems. This challenge can be remedied through the creation of 1) a data taxonomy for PHM that covers data formats, storage, semantics, and other pertinent elements and 2) standard data interfaces and communication protocols. Communication protocol standards are already in use by numerous machine tools and a range of relevant sensors yet it would be advantageous to expand this capability to robot systems [11].

- **Lack of PHM overall structure to enable various PHM technologies, as applied to robot systems, to be evaluated in an unbiased manner.** This challenge can be solved through the development of an overarching architecture framework for PHM with standards and key performance indicators (KPIs). This framework would include benchmarking current states, determining key performance indicators, and defining a standard architecture aimed at performance assessment and traceability.

- **Lack of algorithms to analyze the results of the TCP pose health assessment to detect the root cause of failures and the potential remedies to fix the problem.** Solutions are needed to apply remedies to controllers (i.e., improved programmable logic controller (PLC) control strategies, or maintenance recommendations, such as re-calibration or gearbox changes).

To address the broad landscape of barriers and challenges, measurement science is needed which includes a collection of performance metrics, use case scenarios [12], test methods, reference datasets, and software tools to promote unbiased assessment to verify and validate position and trajectory accuracy health assessment strategies. One specific area of NIST research is the Prognostics, Health Management, and Control (PHMC) project, which aims to develop the measurement science within several manufacturing domains to promote the advancement of monitoring, diagnostic, prognostic, and maintenance strategies [13]. The PHMC for robotics, as a research thrust, is actively developing measurement science to promote the design, test, verification, and validation (V&V) of PHM technology for industrial robot systems. In this paper, the development of the quick assessment of the robot TCP accuracy degradation is presented as a subset of the robot health performance metrics.

DEGRADATION ANALYSIS LEVELS FOR INDUSTRIAL ROBOT SYSTEMS

A PHMC for Robotics Test Bed is being constructed at NIST to provide a platform for the development, testing, verification, and validation of the planned *Health and Control Management*

of Robot Systems measurement science output. The test bed will serve as the home to several industrial robot arms and promote the generation of operationally-relevant test methods and datasets [13]. The test bed will support research to address the challenge of the lack of a PHM overall structure to enable various PHM technologies, as applied to robot systems. One of the use cases developed using the test bed is the quick health assessment methodology to identify the health of the robot system, with an emphasis on the subset of the robot health performance metrics – TCP pose accuracy (6-D accuracy of position and orientation, including when loads are applied) and dynamic accuracy (TCP pose accuracy while the arm is in motion). The output of this effort will provide manufacturers with a methodology that will enable them to quickly assess the TCP pose health of their robot systems when environmental conditions change or after the work cell has been reconfigured. This methodology can also allow manufacturers and technology developers to verify and validate their own PHM techniques that monitor robot health in terms of TCP pose accuracy.

Advanced sensing provides important input for this research to monitor, diagnose, and predict the system's health status to avoid the condition where a robot would malfunction (with degraded accuracy) or unexpectedly halt/shutdown. For the industrial robot TCP pose accuracy degradation, there are four levels of degradation analysis. These levels are shown in Fig. 1: the controller level sensing and analysis, the environmental level sensing and analysis, the add-on level sensing and analysis, and the system level sensing and analysis. From the system level to the controller level, information is becoming more granular by sensing information in more focused ways on specific elements of the system.

System level sensing and analysis aims to actively assess the health of the overall system by taking into account the system architecture, system function, and process-related parameters [14]. For system level accuracy degradation analysis, integrated sensors are needed to efficiently assess the TCP's pose accuracy degradation. The reason to avoid using multiple 1-D (one dimensional) or 2-D (two dimensional) sensors is that the setup is complex and introduces error stacking. To resolve the challenges described in the previous section where there has been a lack of sensor technology that can quickly acquire the 6-D information of TCP accuracy, a 7-D (seven dimensional) measurement system (time, X, Y, Z, roll, pitch, and yaw) is developing at NIST to directly measure and assess the TCP pose

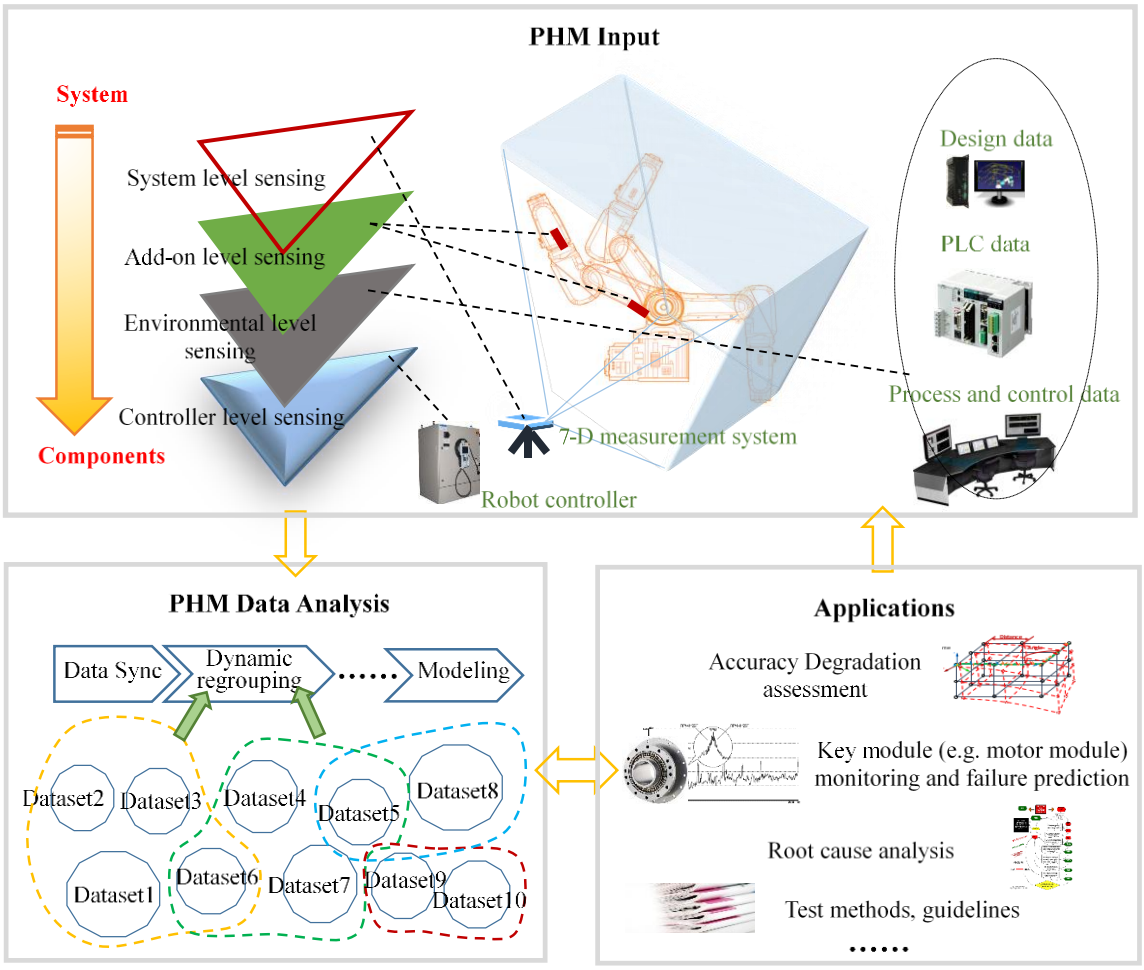

Figure 1. Four levels of degradation analysis for industrial robot accuracy degradation

accuracy degradation of the robot's TCP. A test method is also developed to analyze the TCP accuracy degradation in a volumetric way (evaluate TCP errors from different direction in 3D space) because the error magnitudes and directions are different depending on the approach of joints. The 7-D information is captured with a time synchronization feature. Data synchronization is important for fusion of this data with data from other levels to support root cause analysis [15-17]. NIST's work at this level emphasizes the development of advanced sensing (the 7-D measurement system) and the test method (including model and analysis algorithm) that can quickly and efficiently assess the TCP accuracy degradation.

The add-on level sensing and analysis are developed to collect pre-designed features from the targeted sub-systems. The add-on sensing promotes the inclusion of additional sensors to provide information that the controller and system layers may be neglecting. NIST's research at this level emphasizes the key subsystem/module (e.g., motor module) identification and suitable sensing methodology selection. The design of the add-on system needs to be easily integrated in the system's controller(s) without complex interface and wiring.

The environmental level sensing and analysis are developed to collect information about environmental conditions and settings while a robot is performing a task. Information includes design data (e.g., the program that a robot is running), process data, system integration control data, and PLC data. The environmental level sensing and analysis can help to clarify the operational settings of the robot (e.g., speed of the robot, temperature changes, or payload changes) when an anomaly is detected (by the system level sensing and analysis), or the parameters of an on-going robot operation when a dataset is collected from a controller. There are still challenges of how to integrate and align the environmental level data with the controller level data and the add-on level data for deeper data analysis.

Controller level sensing and analysis extracts data from the robot controllers and/or embedded sensors. Collected information includes actual joint position, commanded joint position, actual joint speed, joint current, joint voltage, motor temperature, etc. The controller level sensing is not the direct measurement of the TCP's accuracy degradation, but can highlight issues in the system through data analysis. Robot original equipment manufacturers (OEMs) and integrators have started the effort of extracting data from controllers. So far, most of the data collection tools are built based on the OEMs' own proprietary controller system. Standard data interfaces and communication protocols that can be applied among different robots are still missing. NIST's work at this level is to address the challenge of the lack of a PHM data taxonomy and architecture for robot applications, and moreover, develop methods and algorithms to analyze the data, including root cause analysis.

Using the four levels of degradation analysis, the robot system's TCP accuracy degradation can be quickly assessed by the system level sensing and analysis. Once accuracy degradations are detected from the system level sensing, data from other levels are added to the data analysis (as shown in the PHM data analysis module in Fig. 1). Datasets can be dynamically regrouped for different focuses. The controller level sensing and analysis provides detailed component information about abnormal issues that may influence the robot's TCP accuracy. The environmental level sensing and analysis provides the operational settings when an issue occurs. Combining data (from different sensing levels) supports deep data analysis, including root cause analysis. Dedicated applications can be developed to monitor the key modules, constantly update the key modules' health status, and link the key modules' health status with the system health status, ultimately helping to optimize the maintenance strategy.

As the first step of the accuracy degradation analysis, the 7-D sensor development and the test method development for the system level sensing and analysis are discussed in the next two sections. This discussion will include the algorithm that will calculate the robot's TCP pose health results through its working volume using limited measurements.

ADVANCED SENSOR DEVELOPMENT FOR SYSTEM LEVEL SENSING

The robot system's TCP accuracy includes the robot arm's accuracy and the accuracy of any system interacting with the robot arm (e.g., a conveyor moving products within the range of the robot arm). By checking the position and orientation accuracy of the TCP and the part conveyors, users can get a health evaluation of the combined conveyor/robot system since this drives the accuracy of the process. Advanced sensing development is an important part of the PHMC for robotics structure to quickly acquire the 6-D information (X, Y, Z, roll, pitch, and yaw) that describes the robot TCP accuracy.

Existing measurement systems that can measure 3-D or 6-D information are shown in Fig. 2. The measurement systems 1-3 are laser trackers from different manufacturers. Laser trackers

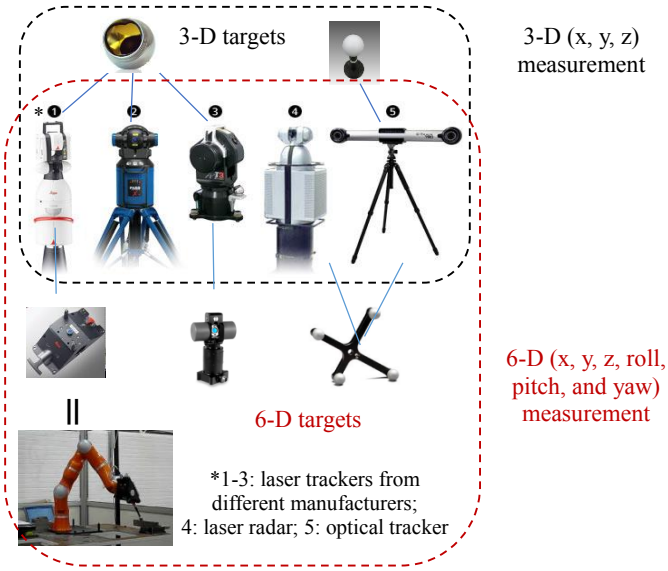

Figure 2. Existing 3-D and 6-D measurement systems

are instruments that can measure 3-D coordinates by tracking a laser beam to a retro-reflective target held in contact with the object of interest [18]. Light reflected off the target retraces its path, re-entering the tracker at the same position it originated. This provides distance information. A laser tracker also contains two angular encoders. Encoders measure the angular orientation of the tracker's two mechanical axes: the azimuth axis and the elevation axis. The angles from the encoders and the distance from the laser are sufficient to precisely calculate the center (x, y, z) of the retro-reflective targets. Retro-reflective targets are considered 3-D targets since only x, y, and z information are measured from target types. 6-D targets are designed to capture the extra orientation information. For laser trackers, a 6-D target has retro-reflector(s) mounted on the target to track the laser beam and get the x, y, and z position information. The extra orientation information is measured by embedding other sensors in the target, or adding a camera system on the tracking head to capture the features that define the coordinate frame on the 6-D target (e.g., multiple light-emitting diodes (LEDs) on the target that define a coordinate frame). Tracker systems are expensive. These measurement systems required line-of-sight to be maintained between the laser tracker and the target. This means that the tracker will ultimately lose its view of the target when observing the target on a robot rotating to an angle. In this case, the robot's TCP rotation has to be limited. The 6-D target should be mounted on the robot's TCP. Mounting the target typically requires the production line to be stopped to change the setup or work tools.

The fourth measurement system is the laser radar which is also shown in Fig. 2 [18]. Laser radar scans the workspace and outputs measurement data as 3-D point clouds. Laser radar can measure a 6-D target (e.g., with multiple reflective spheres that define a coordinate frame as shown in Fig. 2). Getting the 6-D information may take multiple steps of software operations (e.g., segmentation of the 6-D target point cloud is needed from the surrounding objects; removing outliers; best-fit of spherical centers). The best-fit accuracy varies depending on the quality of the point cloud and the quality of segmentation. Laser radar is expensive and not an efficient measurement system for the robot 6-D information acquirement.

The fifth measurement system shown in Fig. 2 is the optical tracker. The optical tracker is a 3-D localization technology based on monitoring a defined measurement space using two or more cameras. Each camera is equipped with an infrared (IR) pass filter in front of the lens, and a ring of IR LEDs around the lens to periodically illuminate the measurement space with IR light. Objects that need to be tracked are equipped with retro-reflective markers (e.g., reflective spheres). The 3-D position can be measured by using a single marker in the measurement space. Multiple markers are placed on each object to measure the orientation of an object or to track multiple objects simultaneously. There are limitations of this measurement system. It is difficult to ensure multiple markers can be seen from each angle. Also, the images of the near-infrared cameras only contain the markers. They are "blind" to the environment. There is no redundancy when ambient light influences the reflected light from the targets [9].

Besides the need to avoid the limitations of the existing measurement systems, several features are required by the robot TCP pose accuracy measurement:

- The measurement system should be relatively low-cost solution for industrial implementation.
- The measurement system needs to be designed such that its integration and use does not interfere with the robot system's normal operations. This includes avoiding the scenario where a robot system's end-effector needs to be removed or adjusted to accommodate a target sensor.
- The measurement system needs to be robust for industrial environments. For example, target(s) should be resistant to industrial dust, oil, etc.
- The measurement system should provide robust measurements also in ambient light conditions.

To address the challenges of advanced sensing, a 7-D measurement system is being developed by NIST to support this research effort. A vision-based design is selected because: (1) vision-based systems can obtain position and orientation information simultaneously; (2) camera technology can deliver sub-pixel accuracy in feature calculation (after optical triangulation, the sub-pixel accuracy provides the measurement system with a higher degree of accuracy than was previously available); (3) vision systems are becoming relatively low-cost and easy to integrate given their recent advancement and maturation [19].

The 7-D measurement system is designed as shown in Fig. 3. It consists of two high-speed color cameras, a high

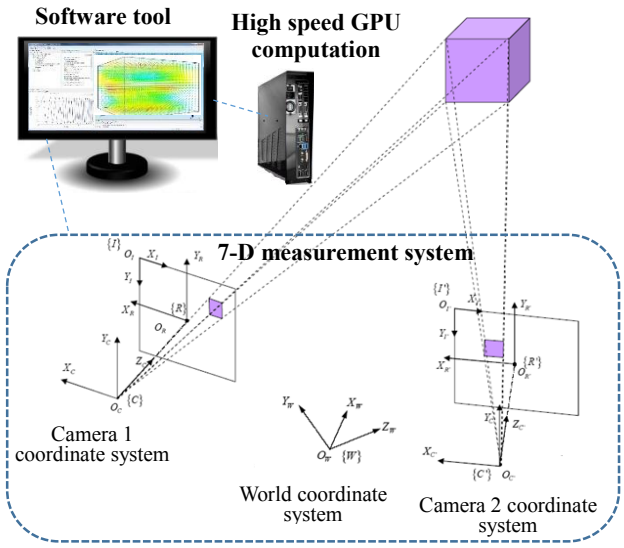

Figure 3. 7-D measurement system

performance image processing control box (operating on a personal computer), special targets, and software tools. Instead of using near-infrared cameras, high speed color cameras were selected to address the negative influence of the ambient light.

New, advanced color image stereo technology promotes more accurate target detection by utilizing redundant information from color images. An advanced image-distortion-correction algorithm is applied. High density differential technologies are developed to help with the removal of the background noises. Parallel calculation and hardware acceleration are used for fast image processing. The graphics processing unit (GPU) programming is utilized to enable the implementation of complex image processing algorithms. Differing from and exceeding the performance of traditional stereo technology, the 7-D measurement system is designed and embedded with a time synchronization feature. Time synchronization is important for the analysis when fusing this data with other sensor data for deep robot system health analysis. Additionally, a self-calibration method is created to avoid the condition where a camera-based measurement system needs to frequently self-calibrate.

Innovative target design is an important part of this work. The customized target is designed to address three specific challenges: (1) Maintaining line-of-sight between the 7-D measurement system and the target; (2) Maintaining the same measurement uncertainty when the target rotates at different angles; and (3) Low-cost and easy to mount on the robot arm's tool with known offsets from the TCP. This target design supports avoiding tool changes during measurement which would require some interruption of the production. Specific target design is not discussed in this publication; this design is currently under consideration for a patent.

The 7-D measurement system will be mounted on the floor or table to measure TCP positions. No alignment is needed from the 7-D system to the robot, so the 7-D system can be moved to other stations without the need for time-consuming set up procedures. Outputs from the 7-D measurement system are points (time, X, Y, Z, pitch, yaw, and roll) under the fixed instrument coordinate system.

TEST METHOD AND ALOGRITHM DEVELOPMENT FOR SYSTEM LEVEL DEGRADATION ANALYSIS

Given a measurement system (e.g., the 7-D measurement system) that can capture TCP pose (position and orientation), a user can implement a simple strategy to run a working program and measure the robot's TCP movements. Deviations can be calculated from the measured positions to the nominal positions. The shortcoming of this strategy is that it cannot represent the overall TCP pose health condition of the robot. Since each TCP pose in the Cartesian space could have multiple inverse kinematic solutions, as a result, the error magnitude and direction changes by choosing different solutions. This makes the assessment of the TCP accuracy degradation very difficult since it is hard to measure the accuracy from all directions. The robot might be programmed to work in the "sweet spot" in the volume with the optimal approaching direction(s). If another program is called, this testing process would need to be performed again. Similar to the existing robot standards (e.g., ISO 9283), most standard methods are designed more to assess repeatability, but not for accuracy [9]. Moreover, the practical application of the test method requires it to be performed in industrial environments with minimal setup. System setup increases the overhead because of the cost of shutting down a production line, especially when a system contains hundreds of robots working together. There needs to be an efficient model and algorithm to support the test method that can calculate the robot's overall TCP pose health results through its working volume using limited measurements.

When developing the model for the test method, the model should reflect error sources of the robot system. Thus, after the TCP pose health assessment, this model can be further used for the root cause analysis to find the problematic individual joints. An example of a robot's serial kinematic structure with coordinate frames is shown in Fig. 4. Any error of the joint axes will be reflected in the TCP errors through the kinematic chain. Similar to machine tools, the errors of a joint axis (either a linear or a rotary axis) can be described as geometric errors that are

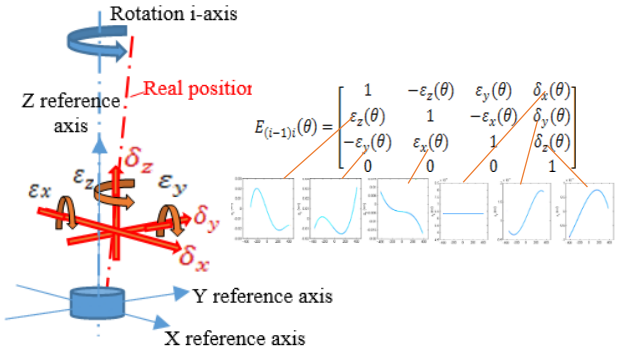

Figure 4. Six errors of a rotation axis

functions of joint positions. Each of the six robot joint axes contains six errors of the axis: three displacements of the axis (in x, y, and z direction) and three rotation errors of the axis (roll, pitch, and yaw errors). Fig. 4 shows a rotary axis (we refer to it as the "i-axis" as the representation of a general situation), which represents the i^{th} joint of a robot. In Fig. 4, the real axis has deviated from its designed position. The reason for the deviation could be from the errors in robot geometry, axis motion, robot gear box degradation, backlash, thermal environment changes, or external loading/gravity. The errors of this axis are represented as: (1) δ_x - radial error motion of i-axis in X direction; (2) δ_y - radial error motion of i-axis in Y direction; (3) δ_z - axial error motion of i-axis in Z direction; (4) ε_x - tilt error motion around X of i-axis; (5) ε_y - tilt error motion around Y of i-axis; and (6) ε_z - angular positioning error (also called scale error of the rotation axis). The error model of the joint is described in Equation (1):

$$E_{(i-1)i}(\theta) = \begin{bmatrix} 1 & -\varepsilon_z(\theta) & \varepsilon_y(\theta) & \delta_x(\theta) \\ \varepsilon_z(\theta) & 1 & -\varepsilon_x(\theta) & \delta_y(\theta) \\ -\varepsilon_y(\theta) & \varepsilon_x(\theta) & 1 & \delta_z(\theta) \\ 0 & 0 & 0 & 1 \end{bmatrix} \quad (1)$$

Where $E_{(i-1)i}$ is the transformation from frame *i-1* to frame *i* and θ is the i^{th} joint angle variable.

$$T_0(x) = 1$$
$$T_1(x) = x$$
$$T_{n+1}(x) = 2xT_n(x) - T_{n-1}(x)$$

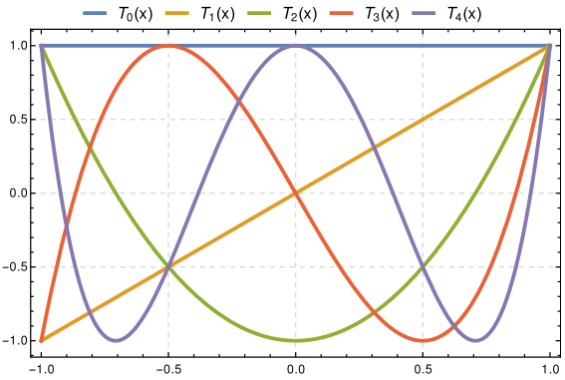

Figure 5. Plot of the first five Chebyshev polynomials

Different from the traditional error model, the δ(θ) and ε(θ) are not constant values. They are functions of axis locations which we refer to as a higher order model (compared to the zero order model) [20], which means the model can handle non-geometric errors, such as the non-ideal motion of joints, deflections of the structure and joints due to external loading or gravity, backlash, etc. As shown in Fig. 4, the error model of the "i-axis" contains six errors ($\varepsilon_x(\theta)$,$\varepsilon_y(\theta)$,$\varepsilon_z(\theta)$,$\delta_x(\theta)$,$\delta_y(\theta)$,$\delta_z(\theta)$). Each is represented as a high order Chebyshev polynomial with unknown polynomial coefficients to be solved [20]. In this way the error model can represent not only the position-independent geometry errors, but also the position-dependent axis motion errors. The reasons to use Chebyshev polynomials are that (1) they are orthogonal to each other over an interval; and (2) they all have a similar scale over the same interval. The first five Chebyshev polynomials are plotted in Fig. 5. Chebyshev polynomials are orthogonal from [-1, 1], and have all n roots and n+1 extremum in [-1, 1]. These properties make them particularly useful as approximating basis polynomials. A simple linear mapping function is used to map the negative axis travel limit to -1 and the positive travel limit to 1.

Another challenge for the traditional error model is the lack of handling measurement noises. The uncertainties coming from measurements are usually treated as joint errors. In that case, the parameter estimates may be biased. In our model, an implicit loop method is adapted to address this issue. In the implicit loop method, the mechanism is treated as having a closed loop from the first link out to the tool tip, and then back to the first link via a measuring device. The displacements around a closed loop sum to zero (or Identity matrix). With this convention, the measurement instrument is included in the loop. The measurement instrument's uncertainty is modeled inside the model equation using a weight. Joint and end-effector measurements are equally weighted, with weights assigned according to the accuracy of each joint. As shown in Fig. 3, the 7-D measurement system is included in the loop of the kinematic chain. The kinematic model of the robot is represented in Equation (2):

$$I = E_0 A_{01} E_{01} A_{12} E_{12} \dots A_{(N-1)N} E_{(N-1)N} A_{N0} E_{N0} \qquad (2)$$

Where A is the nominal axis motion, A_{01} is the nominal transformation from joint 0 to joint 1, E is the error of the joint, E_0 is the setup error of the robot base, and E_{01} is the transformation error from joint 0 to joint 1. Each E follows the definition shown in Equation (1). The δ(θ) and ε(θ) are high order Chebyshev polynomials with unknown polynomial coefficients to be solved by analysis algorithms. Our complete parameter list is the unknown coefficients of the polynomials of the error terms in each of the E matrices. The order of polynomial should be large enough (e.g., 6-8 for most of the robotic systems) to capture all of the dominant error characteristics, but not too large as to over fit the data. Now it remains to identify the constant coefficients describing the Chebyshev polynomials that describe the joint dependent errors.

After the test method model is developed, a test method with a fixed loop motion is developed by extending the existing standard methods for robot performance, as described in [21]. This fixed loop motion of the robot arm is designed such that the test method can be executed periodically and in a relatively short amount of time. While the TCP is moving to these pre-determined positions, the X, Y, Z, roll, pitch, yaw, and time data (7-D information) are being captured from a 7-D measurement system. All measurements will be taken under a global coordinate system which is defined on the 7-D measurement system. Analyzed position, time, and orientation data will provide a measure of the TCP pose accuracy of the robot system when compared to original specifications and prior measurements. Ideally, periodic data would be collected to track accuracy degradation with minimal disruptions to production. This accuracy degradation data would offer insight into the robot system's health.

An important feature of the model (for the test method) is that it requires the measurements be evenly distributed in both joint space and Cartesian space. The even distribution in joint space prevents any errors from being missed or from being too heavily weighted. The even distribution of measurements in Cartesian space covers an entire workspace range of robot arm poses, including some that are near, far, high, and low, to evaluate arm accuracy and rigidity when the arm is both fully and minimally extended. A fixed loop motion needs to be designed to satisfy those requirements.

Fig. 6 shows the designed fixed loop motion created at NIST for a demo robot. The robot workspace is a spherical volume with a cylindrical dead zone in the center of the sphere. To generate this fixed loop motion, the following procedure is performed: (1) in Cartesian space, a grid of poses is generated inside the robot workspace as the target poses (as shown in Fig.6 (a)); (2) inverse kinematic calculations are performed to check if the target positions are reachable by any configuration (if not, the target is skipped); (3) a linear motion path is planned between each pose (this means that each joint performs complicated motions to keep the TCP/tool on a straight line path); and (4)

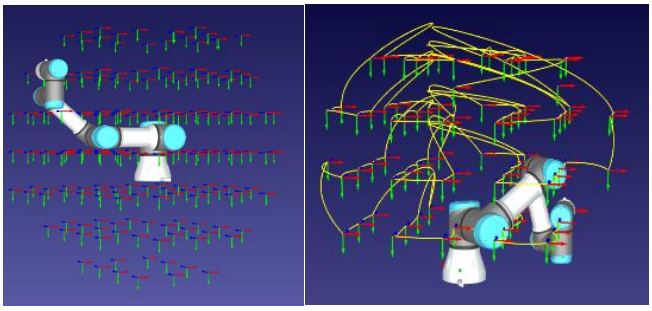

(a) (b)

Figure 6. Robot fixed loop motion for test method

calculations are performed to check if the robot linear motion is possible. In the meantime, collision avoidance is also performed. If the linear motion is impossible, the algorithm will change the current joint configuration to a different configuration, then redo the check in step 4. If none of the configurations are possible, a curved motion path is attempted; if a curved motion path is not possible either (because there is a collision), this target pose is skipped. Otherwise, this pose is saved as one of the target positions in the fixed loop. This procedure is repeated until all of the poses in Fig. 6 (a) are evaluated. The final poses and paths are shown in Fig. 6 (b). In this particular example, because the robot is mounted on an optical table, only poses above the table surface clear the check procedures. After these initial procedures, a fixed loop of robot positions is saved that will be executed periodically. The reason for preferring linear motion paths is that extra analysis can be performed, such as errors from the best-fit of the linear lines and square angles between the linear lines. While the TCP is moving to these pre-determined positions, the X, Y, Z, roll, pitch, yaw, and time data are being captured from a 7-D measurement system.

Placing all measurements (joint and measuring device) in a single measurement vector x, Equation (2) becomes:

$$f(x, p) = 0 \qquad f: R^k \times R^n \rightarrow R^m \tag{3}$$

$$x \in R^k,\ p \in R^n,\ f \in R^m$$

where x is a vector of motion variables and k is the number of measurements taken for each pose. The vector x may include joint and end-effector displacements being measured, as well as backlashes or other small unknown displacements. p is the vector of parameters in the error model to be estimated and n is the unknown number of parameters. m is the number of constraints or loops. We require $k \geq m$ and evaluate $(\partial f/\partial x) = m$ to guarantee that the loop can always be closed. The robot will be sent to various poses (a designed fixed loop motion), and a measurement of x for each pose will be obtained. For a particular pose i, let's assume the true value of the measurement vector is x_i, which we would record as measurement $\bar{x}_i$ with unknown measurement error $\hat{x}_i$, so that $x_i = \bar{x}_i + \hat{x}_i$. Throughout all of the sample poses, the parameters should be constant, but our initial estimates of $\bar{p}$ parameters may be in error by $\hat{p}$, that is $p = \bar{p} + \hat{p}$. For example, $\bar{p}$ might be the blueprint value of a link length and $\hat{p}$ would then be the error incurred in manufacturing the part.

$$f(x_i, p) = f(\bar{x}_i + \hat{x}_i, \bar{p} + \hat{p}) = 0, \quad i=1, \ldots, N \tag{4}$$

where N is the number of sample positions.

The χ^2 error function is derived as:

$$\chi^2 = \sum_{i=1}^{N} \hat{x}_i^T \sum_x^{-1} \hat{x}_i + \hat{p}^T \sum_p^{-1} \hat{p} \tag{5}$$

The implicit loop based maximum-likelihood estimation [20] is used to solve this error model and minimize the error by fitting the parameters in Equation (1). To solve the implicit loop based maximum-likelihood estimation, one needs an innovative optimization algorithm because it's a combinatorial problem which has no concept of a derivative or gradient for algorithm converging. Traditional Quasi-Newton methods won't work on this problem [22]. The optimization algorithms will be detailed in future publications. There are two outputs from this modeling method. The first one is the derived errors from the calculation of the TCP pose accuracy of the robot. The advantage of this method is that the uncertainties of the measurements are decoupled from the true errors and won't bias the analysis result. The second output is to find the maximum likelihood estimation of $\hat{p}$ to minimize the error function. Because $\hat{p}$ represents the unknown coefficients of the polynomials of the error terms in each of the E matrix, that result can be used to detect the root cause of axis errors. Moreover, compensation can be calculated to improve the accuracy of the kinematic model, which can be used in the future system remedy and prognostic algorithm development.

CONCLUSION

This paper presents the NIST's development of the robot TCP pose health assessment methodology by using the advanced sensing system (a 7-D measurement system), the designed test method with the robot fixed loop motion, and the advanced error modeling and analysis technique. With this technology, users can assess the robot TCP pose health faster, cheaper, and with higher accuracy. This can help to quickly detect and decrease the manufacturing quality degradation to reduce scrap, and ultimately improve a robot system's productivity, efficiency, and quality. This methodology can be applied when environmental conditions change, after the work cell has been reconfigured, or whenever a manufacturer wants to determine if they have experienced a degradation. Since the methodology has been successfully developed, NIST personnel are constructing use cases within the NIST robotic system test bed. NIST is also seeking to develop additional industrial use cases for further applications.

NIST DISCLAIMER

Certain commercial entities, equipment, or materials may be identified in this document in order to illustrate a point or concept. Such identification is not intended to imply recommendation or endorsement by NIST, nor is it intended to imply that the entities, materials, or equipment are necessarily

the best available for the purpose.

REFERENCES

[1] Young, K., and Pickin, C. G., 2000, "Accuracy assessment of the modern industrial robot," Industrial Robot-an International Journal, 27(6), pp. 427-436.

[2] Buschhaus, A., Blank, A., Ziegler, C., and Franke, J., 2014, "Highly Efficient Control System Enabling Robot Accuracy Improvement," Procedia CIRP, 23, pp. 200-205.

[3] Shirinzadeh, B., 2000, "Repeatability and accuracy - who cares and why?," Industrial Robot, 27(4), pp. 250-251.

[4] Pan, Z., Polden, J., Larkin, N., Van Duin, S., and Norrish, J., 2012, "Recent progress on programming methods for industrial robots," Robotics and Computer-Integrated Manufacturing, 28(2), pp. 87-94.

[5] Edinbarough, I., Balderas, R., and Bose, S., 2005, "A vision and robot based on-line inspection monitoring system for electronic manufacturing," Computers in Industry, 56(8–9), pp. 986-996.

[6] Ngan, C., and Tam, H., 2004, "A non-contact technique for the on-site inspection of molds and dies polishing," Journal of Materials Processing Technology, 155–156, pp. 1184-1188.

[7] DeVlieg, R., 2010, "Expanding the use of robotics in airframe assembly via accurate robot technology," SAE Int. J. Aerospace, 3(1), pp. 198-203.

[8] Sammons, P. M., Ma, L., Embry, K., Armstrong, L. H., Bristow, D. A., Landers, R. G., and Asme, 2014, "Modeling and compensation of backlash and harmonic drive-induced errors in robotic manipulators," Proceedings of the ASME 9th International Manufacturing Science and Engineering Conference, 2.

[9] Greenway, B., 2000, "Robot accuracy," Industrial Robot, 27(4), pp. 257-265.

[10] 2017, "Optical Tracking Explained," Retrived from http://www.ps-tech.com/3d-technology/optical-tracking?.

[11] Vijayaraghavan, A., Sobel, W., Fox, A., Dornfeld, D., and Warndorf, P., 2008, "Improving machine tool interoperability using standardized interface protocols: MT Connect," Proceedings of 2008 International Symposium on Flexible Automation.

[12] Brian A. Weiss, M. M. H., Gregory W. Vogl, Guixiu Qiao December 5-7, 2016 "Use Case Development to Advance Monitoring, Diagnostics, and Prognostics in Manufacturing Operations " Intelligent Manufacturing Systems, Austin, TX.

[13] Weiss, B. A., Vogl, G. W., Helu, M., Qiao, G., Pellegrino, J., Justiniano, M., and Raghunathan, A., 2015, "Measurement Science for Prognostics and Health Management for Smart Manufacturing Systems: Key Findings from a Roadmapping Workshop," Annual Conference of the Prognostics and Health Management Society 2015, P. Society, ed., PHM Society, Coronado, CA, p. 11.

[14] Abichou, B., Voisin, A., and Iung, B., 2012, "Bottom-up capacities inference for health indicator fusion within multi-level industrial systems," IEEE Conference on Prognostics and Health Management (PHM), pp. 1-7.

[15] Mahto, D., and Kumar, A., 2008, "Application of root cause analysis in improvement of product quality and productivity," Journal of Industrial Engineering and Management, 1(2), pp. 16-53.

[16] De, S., Das, A., and Sureka, A., 2010, "Product failure root cause analysis during warranty analysis for integrated product design and quality improvement for early results in downturn economy," International Journal of Product Development, 12(3-4), pp. 235-253.

[17] Li, M.-H. C., Al-Refaie, A., and Yang, C.-Y., 2008, "DMAIC approach to improve the capability of SMT solder printing process," IEEE Transactions on Electronics Packaging Manufacturing, 31(2), pp. 126-133.

[18] Mautz, R., 2009, "Overview of current indoor positioning systems," Geodesy and Cartography, 35(1), pp. 18-22.

[19] Švaco, M., Šekoranja, B., Šuligoj, F., and Jerbić, B., 2014, "Calibration of an Industrial Robot Using a Stereo Vision System," Procedia Engineering, 69, pp. 459-463.

[20] Wampler, C. W., Hollerbach, J. M., and Arai, T., 1995, "An implicit loop method for kinematic calibration and its application to closed-chain mechanisms," IEEE Transactions on Robotics and Automation, 11(5), pp. 710-724.

[21] Qiao, G., and Weiss, B. A., 2016, "Advancing Measurement Science to Assess Monitoring, Diagnostics, and Prognostics for Manufacturing Robotics " International Journal of Prognostics and Health Management, 7(13).

[22] Phillips, F., 2006, "A Novel Means of Software Compensation for Robots and Machine Tools," SAE Technical Paper 2006-01-3167.

Proceedings of the ASME 2017 12th International Manufacturing Science and Engineering Conference
MSEC2017
June 4-8, 2017, Los Angeles, CA, USA

MSEC2017-2787

HIERARCHICAL DECOMPOSITION OF A MANUFACTURING WORK CELL TO PROMOTE MONITORING, DIAGNOSTICS, AND PROGNOSTICS

Brian A. Weiss
National Institute of Standards and Technology
Gaithersburg, Maryland, USA

Guixiu Qiao
National Institute of Standards and Technology
Gaithersburg, Maryland, USA

KEY WORDS

Condition Monitoring, Diagnostics, Maintenance, Manufacturing Processes, Manufacturing Systems, Prognostics, Robot Systems, Use Cases

ABSTRACT

Manufacturing work cell operations are typically complex, especially when considering machine tools or industrial robot systems. The execution of these manufacturing operations requires the integration of layers of hardware and software. The integration of monitoring, diagnostic, and prognostic technologies (collectively known as prognostics and health management (PHM)) can aid manufacturers in maintaining the performance of machine tools and robot systems by providing intelligence to enhance maintenance and control strategies. PHM can improve asset availability, product quality, and overall productivity. It is unlikely that a manufacturer has the capability to implement PHM in every element of their system. This limitation makes it imperative that the manufacturer understand the complexity of their system. For example, a typical robot system includes a robot, end-effector(s), and any equipment, devices, or sensors required for the robot to perform its task. Each of these elements is bound, both physically and functionally, to one another and thereby holds a measure of influence. This paper focuses on research to decompose a work cell into a hierarchical structure to understand the physical and functional relationships among the system's critical elements. These relationships will be leveraged to identify areas of risk, which would drive a manufacturer to implement PHM within specific areas.

INTRODUCTION

Advanced technology continues to emerge at a rapid pace as manufacturers, technology developers, and technology integrators further integrate operations technology with information technology to produce their own iterations of Smart Manufacturing. Smart Manufacturing is focused on bridging and connecting hardware, software, and data to increase operational efficiency, asset availability, and quality while decreasing unscheduled downtime and scrap [1-4]. The successful implementation of these paradigms will lead to greater efficiency within manufacturing operations enabling manufacturers to be more responsive to changing consumer demand and more resilient in the face of increased competition.

Robot systems play a role in many manufacturing environments including automotive [5-7], electronics [8, 9], consumer packaged goods [10], and aerospace [11-13] manufacturing. Smart Manufacturing is having a positive impact on robotic operations occurring on the factory floor. More diverse systems, sub-systems, and components are being connected together which is leading to an increase in robot work cell capabilities. The American National Standards Institute, Inc. (ANSI) defines an industrial robot system to include a robot, end-effector(s), and any equipment, devices, or sensors required for the robot to perform its task [14]. Examples of additional equipment, devices, and sensors include vision and proximity sensors (e.g., camera, laser), safety elements (e.g., light curtain), supervisory controller (e.g., Programmable Logic Controller (PLC)), and other supporting automation (e.g., conveyor belt). Figure 1 presents an example of a robot work cell including some of its key elements.

The integration of these elements and the increase of 'moving parts' generate greater complexity, especially when considering robot-robot and human-robot operations. More complexity leads to more sources of error which can compromise the efficiency and quality of the process. Inclusion of condition monitoring, diagnostics, and/or prognostics (collectively known as prognostics and health management (PHM)) can provide greater intelligence of equipment and process health which can minimize unscheduled downtime, increase efficiency, and improve overall productivity.

Qiao, Guixiu; Weiss, Brian.
"Hierarchical Decomposition of a Manufacturing Work Cell to Promote Monitoring, Diagnostics, And Prognostics."
Paper presented at ASME 2017 12th International Manufacturing Science and Engineering Conference (MSEC2017),
Los Angeles, CA. June 4, 2017 - June 8, 2017.

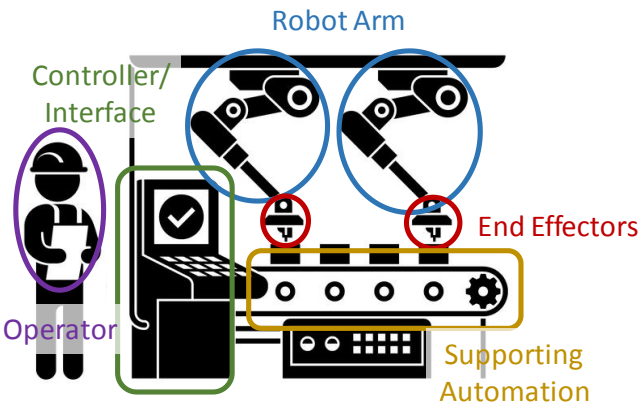

Figure 1. Example Robot Work Cell (MicroOne/Fotolia)

The United States (U.S.) Federal Government has a research focus to advance the means of assessing, verifying, and validating PHM technologies operating within manufacturing environments [15, 16]. This effort is being conducted at the National Institute of Standards and Technology (NIST) and includes a focus on machine tool and robot work cell manufacturing operations. NIST researchers are actively developing use cases, performance metrics, test protocols, and reference data sets to enable the verification and validation (V&V) of PHM technologies. This paper focuses on decomposing an example robot work cell into an appropriate hierarchical structure through organizing the physical and functional elements such that manufacturers can determine appropriate boundaries with which to overlay condition monitoring, diagnostic, and prognostic technologies. The research is aimed at addressing the question – *How can appropriate physical and functional boundaries be determined within a manufacturing work cell to effectively monitor, maintain, and control the work cell?* To that end, this paper is organized as follows: the Manufacturing Robot Work Cell section discusses typical robot work cells within manufacturing environments and how their complexities, and faults and failures, are evolving with the emergence of new technologies; the PHM section presents background on PHM techniques and technologies that provide monitoring, diagnostic, and prognostic intelligence; the Research Approach section discusses how NIST is organizing its efforts to develop the necessary use cases, test methods, performance metrics, and reference data sets to promote V&V; the Robot Work Cell Hierarchy section presents a proposed method to structure, organize, and delineate physical and functional boundaries to identify areas for PHM inclusion; and the Conclusion section wraps up the paper and presents next steps in the research.

MANUFACTURING ROBOT WORK CELLS

Robot work cells, with industrial robot arms, have operated in manufacturing environments to perform numerous operations including welding, painting, drilling, and material handling [17, 18]. Across the range of robot systems, industrial robotics continues to be a substantial investment by the manufacturing community to improve product quality, increase productivity, and lower costs. The evolution of various technologies, including more intelligent and affordable sensors, displays, end-effector technologies, and control systems has enabled industrial arm-based robot work cells to become more viable options for a larger portion of the manufacturing community [19]. Many of these robot work cells operate for extended periods of time across multiple work shifts. Maintenance strategies for these work cells are either:

- Reactive (fix it when it breaks),
- Preventative (maintenance is performed at specified intervals),
- Predictive (maintenance is performed based upon measured performance and/or health),

…or a combination thereof [20, 21]. Even with regular maintenance, robot system operations will degrade, increasing the potential for faults or failures. Faults and failures can 'naturally' occur through degradation from expected operations, yet the appearance of faults and failures can also be accelerated through a variety of errors. Faults and failures can be related to hazards; faults and failures can produce hazards and the presence of hazards can lead to faults and failures. The Occupational Safety and Health Administration (OSHA) has identified seven potential robotic work cell hazards [22]. A subset of these hazards are due to faults or failures:

- Human Errors – Includes erroneous commands entered into the teach pendant by the operator, ignoring/misinterpreting data presented by the system, and failure to follow all safety protocols
- Control Errors – Includes errant controller code and degradation of controller hardware
- Mechanical Failures – Includes degradation of motors and gears of the robot arm and actuators, motors of the end-effector, and faulty sensors providing inaccurate data to the controller
- Environmental Sources – Includes pronounced changes in temperature, humidity, and sunlight (which can impact certain sensor readings)
- Power Systems – Includes power surges and power loss

There is no single way that these faults and failures can be classified. Some faults and failures are the root causes (a sensor has a loose wire and is therefore reporting erroneous data to the controller) while other faults and failures emerge once the root cause has occurred (a robot arm is hitting a box because the controller is telling the arm that nothing is in front of it because the proximity sensor has a loose wire and is reporting that the area is clear of obstacles). Three principle categories have been developed to classify faults and failures [19] [23-25]. These categories are designated:

- Faults – Typically design defects, inaccurate signals, or incorrect decisions that impact the system's ability to function properly. Some faults may accelerate the degradation of a component or sub-system (e.g., a robot arm returns a fault when it is over-loaded. Excessive over-loading of the robot arm can result in increased wear and tear on gears and motors).

- Soft Failures – Degradation or wear and tear that has resulted in decreased process efficiency, productivity, and/or product quality. Soft failures, if left unaddressed, can lead to hard failures. An example of a soft failure would be a degraded motor in a robot arm that is now limited in the speed at which it can move. The robot may still be capable of completing its required task, yet it may take more time than specified.
- Hard Failures – Degradation or wear and tear that has resulted in breakage that has compromised the productivity and/or quality of the process. Hard failures are typically indicated with the system being in a frozen/shutdown state or in a state of performing egregious behaviors. Examples of hard failures include a complete motor failure where a joint has gone limp or a controller error where the robot no longer moves.

The different types of faults and failures presented above highlight the complexity of robot work cells operating within manufacturing environments. Additional complexity is continually being added to work cells with the inclusion of more collaborative robotic systems – robots working with other robots and robots working in closer proximity to humans [26]. It becomes much more important to accurately monitor, diagnose, and predict faults and failures in work cells when humans are operating in relatively close proximities.

Further complexity in a robot work cell stems from any reconfiguration(s) that occur throughout the life of the work cell and its key components. Different types of faults presented above highlight the complexity of robot work cells operating within manufacturing environments. Consider a robot work cell that is tasked with material handling operations (e.g., a robot that manipulates boxes off of a conveyor belt). Over time, components and sub-components will have to undergo a range of maintenance activities to maintain productivity and quality targets. At some point, it's likely that it will be more cost effective to replace one of the key components or sub-components with a new one as compared to repairing this component. Suppose that the 20-year-old robot is now replaced with a new robot. It's likely that the new robot will have greater capabilities than the old robot (unless you find a new iteration of the same robot). After integrating the new robot into the work cell, it's discovered that the work cell is operating at its expected performance as compared to when the old robot was in place and operating to specification. However, it is possible that the new robot is faster, more accurate, capable of lifting heavier loads, etc. With that being the case, the operator has the potential to increase the productivity of the work cell and/or quality of the work cell's output. If/when the operator takes advantage of the new robot's capabilities, the robot, which may have been the 'weak-link' in the prior iteration of the work cell, may now be the strongest link in the work cell. In this situation where the robot work cell was reconfigured to accommodate a new robot arm, all of the relationships between the robot arm and other key components (e.g., end-effector, controller, sensors, safety systems) have changed [since the old arm was replaced with a new arm]. Not only does baseline performance of the robot work cell need to be reestablished with the new arm, the relationships between any component interfacing with the robot need to be understood so the degradation and wear and tear on these elements can be similarly understood. An analogous situation occurs when the work cell must be reconfigured to produce a different part. The work cell is likely to undergo some type of hardware and/or software reconfiguration which thereby alters the relationships among key physical and functional elements. Changing relationships will change how the various elements degrade over time.

Given the robot work cell's complexity, PHM can offer monitoring, diagnostic, and prognostic capabilities to track key performance metrics to examine the impact of the many relationships present in the work cell with respect to the relationship influence on overall system, process, and equipment health.

PROGNOSTICS AND HEALTH MANAGEMENT

Advancing PHM in the manufacturing environment can lead to substantial savings for an organization. PHM may ultimately enable a machine or system to self-diagnose and self-heal with enough intelligence to be both aware of its current health and make an appropriate decision given both its state and goals. This is known as the proactive/intelligent maintenance strategy and is the topic of substantial research [27-29]. Current PHM technologies are enabling the three afore-mentioned maintenance strategies (reactive, preventative, and predictive) within a range of manufacturing environments [30-34] .

PHM research has led to studies and reviews that compare existing PHM methods along with highlighting their strengths and limitations [35-38]. More specifically, reviews of PHM-based standards have also been conducted [39-41].

Collectively, PHM methods can be summarized below in Fig. 2. Each of these methods can be applied in vastly unique ways given the uniqueness of each manufacturing facility, subsequent work cells, etc.

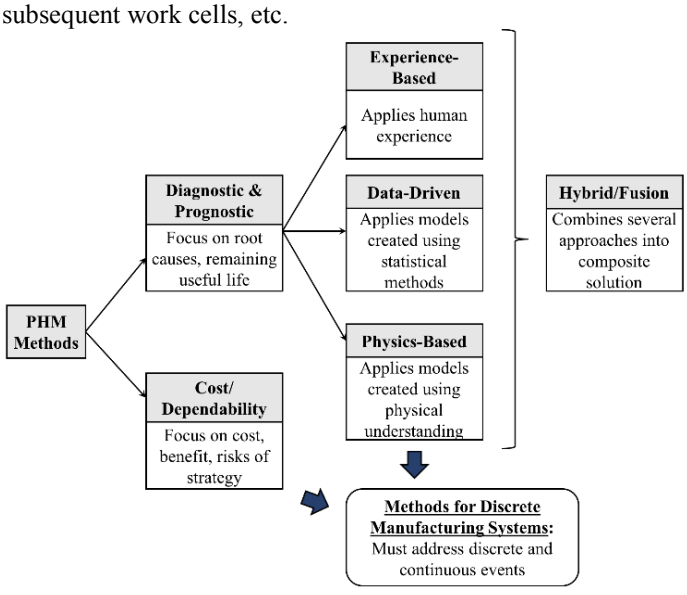

Figure 2. Description of general PHM methods [38]

Literature reviews and direct discussions with the PHM community (e.g., PHM technology developers, PHM technology integrators, and manufacturers as the end-users of PHM) have highlighted a need to improve the existing maintenance strategies that are currently used within a factory. Most manufacturers employ a mix of reactive and preventative maintenance strategies to ensure sufficient operations. Relatively few manufacturers have implemented predictive maintenance strategies to enhance their monitoring, diagnostic, and prognostic capabilities. Minimizing reactive maintenance while enhancing (ideally, optimizing) preventative and predictive maintenance requires a greater understanding of where and how PHM can be implemented in the manufacturing environment. As PHM becomes more important to the manufacturing community, more people have recognized the importance of developing and improving various PHM implementations. One challenge is that the PHM community is largely void of methods to verify and validate the capabilities of these emerging PHM techniques.

RESEARCH APPROACH

The NIST research team is taking a methodical approach to develop the necessary use cases, performance metrics, test methods, reference datasets, and software tools to provide a means of verifying and validating PHM within manufacturing robot work cells [16, 39]. Given the complexity of a typical robot work cell, it is important to initiate the research in a basic manner where variables, especially those that influence system, process, and equipment health, are minimized. This breeds the development of a basic robot work cell. For NIST's research efforts, this takes the form of a robot arm and its controller where the robot is hard-coded in its operations as opposed to being influenced by external sensing, safety, or human inputs. This basic work cell is being used by NIST as the foundation for the development of a quick health assessment methodology that will allow manufacturers to verify the health of their robot in terms of its positional accuracy [19]. Besides simplifying the robot work cell, it's also important to limit the research focus to a specific area(s) of PHM to avoid too much complexity too soon. While the complexity of the work cell can be considered the first axis of influence, the second axis that influences complexity and difficulty of the problem is that of the specific PHM and decision-making focus (see Fig. 3). NIST's research efforts will increase in complexity by adding additional, manufacturing-relevant components to the work cell and employing diagnostic and prognostic techniques at different levels of the work cell. Further using the NIST research example, the quick health assessment methodology is aimed at monitoring the health of the robot arm (in terms of its positional accuracy), offering some diagnostic information (with respect to the health of specific joints), and providing intelligence to update the robot's control strategy accordingly (i.e., compensating for performance errors due to health degradation).

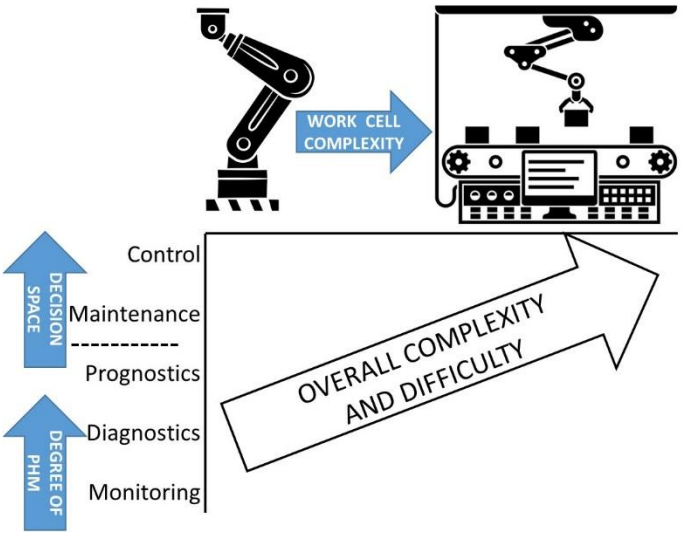

Figure 3. NIST Research Approach (Funway5400, MicroOne/Fotolia)

As NIST's research efforts expand, so too will the complexity of the robot work cell and the degree to which PHM and the decision space are included. This will lead to greater complexity and more challenging research. Embracing greater complexity and difficulty requires a thoughtful way of organizing and structuring the complexity of the robot work cell. A single robot arm and its controller, without any other elements, are still somewhat complex. Adding external sensors, end-effectors, safety systems, supporting automation, etc. makes it more complex. A hierarchical model is proposed to promote the structuring and organization of the overall work cell, its constituent physical components, and sub-components. Likewise, this physical hierarchy has a mirror that maps the system's overall capabilities and building-block functions. The development of this hierarchy will make it easier to identify boundaries within the work cell for the inclusion and advancement of PHM.

ROBOT WORK CELL PHM ANALYSIS HIERARCHY

A robot work cell can be viewed as a hierarchy of systems and components. This type of physical decomposition is both critical in the design of a new system and also understanding the relationships and interactions of an existing system as defined in the National Aeronautics and Space Administration's (NASA's) Systems Engineering Handbook [42]. Building upon this systems engineering approach, Multi-Relationship Evaluation Design (MRED) was developed as a means of decomposing a complex system into its key physical components and functional capabilities for the purpose of strategically evaluating the performance of specific sub-systems, components, and capabilities at differing levels of the system [43-47]. Although MRED is focused on performance evaluation, it can be leveraged to hierarchically decompose the physical components and sub-components, in concert with the system's capabilities to delineate boundaries for PHM. Figure 4 presents an abstract hierarchical decomposition of a physical system based upon the MRED effort. Note that the physical makeup of the system is

typically more complex than the three levels (*System*, *Component,* and *Sub-Component*) where there could be sub-system levels before reaching the component level. Adapting the MRED definitions of the below key terms for this effort becomes:

- *Component* – An essential part or feature of a *System* that contributes to the *System's* ability to accomplish a goal(s).
- *Sub-Component* – An element, part, or feature of a *Component* that can be isolated for the purpose of maintenance or replacement.
- *System* – A group of cooperative or interdependent *Components* forming an integrated whole to accomplish a specific goal(s).

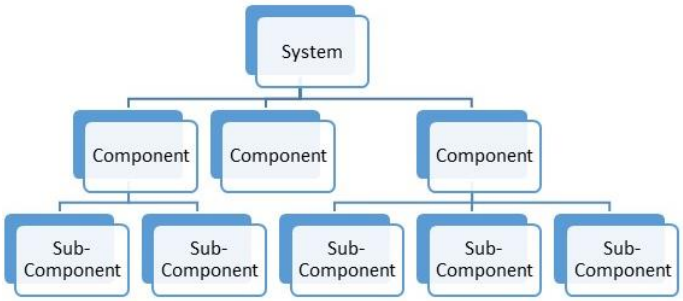

Figure 4. Hierarchical Physical Decomposition

Distinctions between what is a *System, Component,* and *Sub-Component* are based upon several key factors including: 1) what elements are physically separate allowing them to be independently maintainable or replaceable and 2) the logical/functional connections between multiple elements. The process of distinguishing elements from one another will be clarified later in this section through the discussion of the two-arm robot work cell example.

From the MRED effort, each of these physical levels are defined as *Technology Test Levels*. Considering the focus of this NIST-led effort, it would be more appropriate to define these levels as *Monitoring, Maintenance, and Control Levels* (*MMCLs*).

Figure 5 leverages additional terms from MRED that are applied to this research effort and would be *MMCLs*.

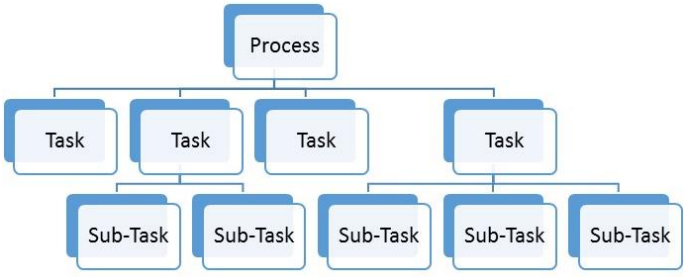

Figure 5. Hierarchical Functional Decomposition

- *Process* – The overall activity that the *System* is configured to perform.
- *Task* – A specific activity within the overall *Process*. A *System* performs a single *Process* that is made up of one or more *Tasks*. A *Task* is enabled by either a single *Component* or multiple *Components* working together.
- *Sub-Task* – A building block function of a *Task*.

Coupling in the functional concept of a *Task*, the relationship between physical and functional elements is presented in Figure 6. Considering that *Sub-Components* and *Sub-Tasks* are building block elements of *Components* and *Tasks*, respectively, Fig. 6 could be substantially expanded to include these *Sub-* level elements.

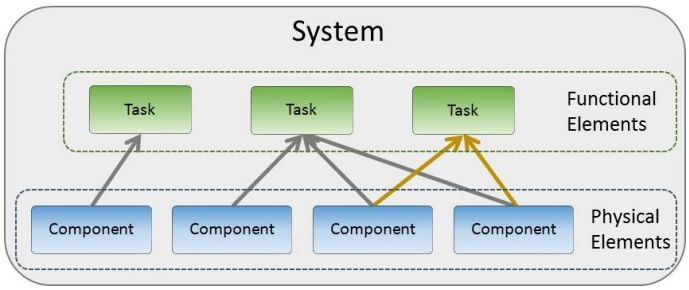

Figure 6. Component and Capability Mapping Diagram

MMCLs highlight user-defined areas that 1) designate specific physical elements (i.e., *System, Component, Sub-Component*) and/or functions (i.e., *Task, Sub-Task*) that should be monitored to track current and predict future health states; 2) identify physical elements for maintenance to be performed pending the results of monitoring efforts; and functions whose control strategies need to be updated given current and predicted health. Each *MMCL* has one or more metrics that are monitored and reviewed for maintenance and control decisions. Likewise, metrics monitored at one level may be leveraged for maintenance or control decisions at another level. Given the uniqueness of every system, metrics are also user-defined.

The hierarchical decomposition is applied to a two-arm robot work cell. Figure 7 identifies the key *Components* within the *System.* This figure will also be referenced to highlight the key *Tasks* that produce the overall *Process*. The following steps are prescribed to decompose an existing *System* to determine the *MMCLs*.

1. Identify the objective/goal of the *System*.
2. Identify the *Process* that the *System* is to perform.
3. Identify the physical boundaries of the *System* necessary for decomposition. The boundaries are based upon what is necessary to physically accomplish the objective/goal. This step may be performed simultaneously with Step 2.
4. Break-down the *System* into *Components*. Physical boundaries of *Components* can be discretionary based upon what can reasonably be physically separated for the purposes of repair and replacement.
5. Breakdown the *Components* into *Sub-Components*.
6. Break-down the *Process* into constituent *Tasks*.

7. Break-down the constituent *Tasks* into *Sub-Tasks*. *Process* and *Task* decomposition is influenced by what can be functionally separated from a control perspective.
8. Determine the performance metrics that are necessary to determine if the objective/goal is accomplished. These metrics would be similar to NASA's *Measures of Effectiveness* [42]. *"Measures of Effectiveness* are the operational measures of success that are closely related to the achievement of mission or operational objectives in the intended operational environment" [42].
9. Determine any performance metrics that are necessary to assess whether the *Process* is successfully completed as specified. It's possible that some of the metrics identified in Step 4 also assess the overall *Process* which would present metrics that can assess both the objective and the *Process*. These metrics would be similar to NASA's *Measures of Performance* which "characterize physical or functional attributes relating to the *System"* [42].
10. Determine the metrics that are necessary to assess the success of *Tasks* and *Sub-Tasks*. Likewise, determine any additional metrics necessary to assess the health of *Components* and *Sub-Components* that make-up the overall *System* and influence the *Process*. These metrics would be most comparable to NASA's *Technical Performance Measures* which are considered critical and measurable performance attributes that can be monitored [42].

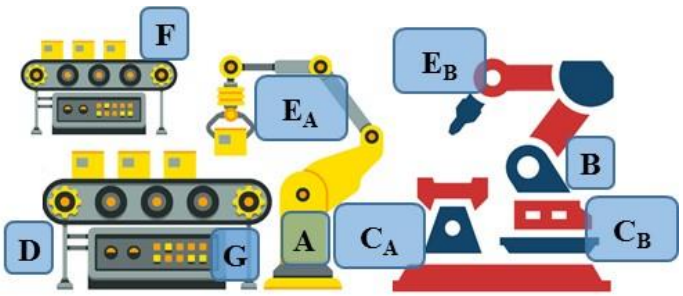

Figure 7. Two-arm Robot Work Cell – Key *Components* (MicroOne, Motorama/Fotolia)

Steps 1 through 9 present the hierarchical decomposition of a pre-existing *System* and *Process*. It is important to note that some of the steps may be done simultaneously given that the *System* is already known. Likewise, some of these steps are presented in brief due to space limitations. The importance of going through these steps is to capture and organize the structure of the *System* and the *Process* to identify the most ideal areas, within the structure, to incorporate PHM. The remainder of this section decomposes the example two-arm robot work cell according to these steps. The following section begins the discussion of how PHM can be integrated into a decomposed *System*.

Step 1: The objective of the *System* presented in Fig. 7 is for parts to be marked in a specific location and sent to the next station in a specified amount of time. Since the example work cell is designed as an industrially-relevant use case, the marking of a part is representative of a robot moving to a precise location with respect to the part and altering the part to support the finished product. Specifically, having a robot perform this type of activity is similar to having a robot drill a hole or perform a spot weld.

Step 2: The *Process* that the *System* performs is for two robots to work together to manipulate parts off of an incoming conveyor system, apply a mark to a precise location on the incoming parts, and return the parts to an outgoing conveyor system.

Step 3: The physical boundaries of the *System* begin with the part entering the work cell and end with the part leaving the work cell. The physical boundaries do not include the room/building that the work cell resides. Specifically, the boundaries of the *System* are defined by its key *Components*.

Step 4: The key *Components* of the work cell, presented in Fig. 7, are the two robot arms (A and B), their respective controllers (C_A and C_B), their respective end-effectors (E_A and E_B), the inbound conveyor (D), the outbound conveyor (F), and the supervisory PLC (G). Other key *Components* not shown in Fig. 7 include a vision sensor that detects the position and orientation of parts on the inbound conveyor, D, any safety elements as deemed necessary based upon the expected proximity of human operators/supervisors, and the fixtures that hold parts while they are being marked.

Step 5: Each of the two robots can be broken down into their six constituent joints – the base, shoulder, elbow, wrist 1, wrist 2, and wrist 3, and the robot controller. Each of the six joints could be further broken down into their constituent motors and encoders. The conveyor is decomposed into its physical structure, motor, and encoder. Depending upon the safety system configuration (e.g., safety mat(s), light curtain(s)), these can be decomposed further.

Step 6: The key *Tasks*, shown in Fig. 9, underscore the *Process* flow of the *System*. The *Process* begins with *Task 1* – parts move on the inbound conveyor, D, until they arrive at a pre-determined location within the reach of robot arm A. *Task 2* involves robot arm A grasping the nearest part with its gripper, E_A, and placing it on the fixture next to robot arm B. *Task 3* calls for robot arm B to 'mark' the fixture part with its tool tip, E_B. After the fixture part is marked, *Task 4* calls for robot arm A to remove the part from the fixture and place it on the outbound conveyor, F. *Task 5* calls for Conveyor F to move the 'marked' part to its next destination. It is important to note that this robot work cell (i.e., the *System*) is being designed to be inclusive of numerous *Components* and *Tasks* commonly found in manufacturing environments according to case studies and site visits [20, 21, 48].

Step 7: Each of the afore-mentioned *Tasks* presented in Step 6 can be broken down into *Sub-Tasks*. For brevity, only *Task 1* will be broken down into *Sub-Tasks*. These *Sub-Tasks* are:

- *Task 1, Sub-Task 1* – A part on the incoming conveyor moves until it comes into the field of view of an

overhead vision sensor (which is above the end of the conveyor closest to Robot A)

- *Task 1, Sub-Task 2* – When a part is detected in the field of view of the overhead vision sensor, the sensor indicates to the Programmable Logic Controller (PLC) that a part is present [in the vision sensor's field of view].
- *Task 1, Sub-Task 3* – The PLC sends a signal to the conveyor telling it to stop.
- *Task 1, Sub-Task 4* – The PLC sends the vision sensor data to Robot A's controller that includes the position and orientation of the part in view.

Step 8: The performance metrics that are defined to indicate whether the overall objective has been accomplished include:

- *Takt Time* – This metric is measured in seconds and represents the frequency a completed part exits the work cell.
- *Mark Accuracy* – This metric is measured in millimeters and represents how far from the part's center the mark is made

Step 9: The performance metrics that are defined to indicate the successful completion of the *Process* include:

- *Cycle Time* – This metric is measured in seconds and represents the total amount of time a part spends in the work cell (i.e., the total time it takes a part to complete *Tasks 1* through 5).
- *Quality Degradation* – This metric represents the change in quality that a part experiences as it runs through the work cell. For example, parts could be accurately marked and run through the work cell rather quickly, yet Robot A could be damaging parts while it is manipulating them or Robot B is making erroneous marks in addition to accurately marking the top of parts.

It is reasonable that *Takt Time* and *Mark Accuracy* could also be considered *Process*-level performance metrics. Overall Equipment Effectiveness (OEE) could also be another metric used at the objective level and/or the *Process* level [49]. However, the effectiveness and value of this metric has been a recent topic of debate [50]. The value of OEE for this specific work cell is being discussed in comparison to simply using its aggregate metrics: asset availability, productivity, and quality.

Step 10: The performance metrics that are defined to assess the *Tasks* and *Sub-Tasks* are too numerous to be presented. They include a range of time measurements with respect to robot, part, and conveyor movements. Additional metrics include accuracy of the vision system and the robot movement.

The robot work cell presented in Fig. 7 can be characterized in the hierarchical physical decomposition presented in Fig. 8. This decomposition presents key physical *MMCLs* that seem reasonable to monitor during the afore-mentioned manufacturing process based upon the critical contributions of each *Component* to the *System*. The organization of this figure could be challenged. For example, it would be plausible for the Supervisory PLC, G, to be placed at the top of the hierarchy (situated where 'Robot Work Cell' appears) given that the PLC will be the 'brains' of the manufacturing process and coordinate all activities. From a control perspective, this would be a reasonable structure. Given that this decomposition is purely physical, the PLC is placed on the same level as other key *Components* since, physically, none of the other *Components* is located inside of the boundaries of the PLC. To further extend the physical decomposition, it was noted earlier that each robot could be broken down further into individual joints. Each of these joints could be broken down further into their respective gears, motors, and wiring, and then down further into shafts, nuts, bolts, etc. Physically decomposing this robot work cell down to the nuts and bolts level is not practical from the perspective of monitoring, maintenance, and control. It may be useful to stop the physical decomposition at the level of the robot arm or it may be useful to go down to the next level that identifies specific joints; this decision is directly influenced by historical knowledge of what can practically be monitored, where problems occur, and how maintenance is performed. In this specific work cell, it is beneficial to decompose the work cell down to specific joints. Further, each joint would be further decomposed into its constituent motor, encoder, current sensor and gearing. Again, the full decomposition is not visualized in this paper.

Performing a *Component* and *Task* mapping adds clarity with respect to the relationships of the *MMCLs*. Figure 9 presents this initial mapping. Only *Task 1* and *Task 4* are mapped out between the *Component* and *Task* levels. *Tasks 2, 3,* and *5* are not shown due to space limitations. Several key *Sub-Components* are added for each robot, yet a majority of *Sub-Components* and all of the *Sub-Tasks* are not shown for brevity. It is evident that there are many relationships between the physical and functional levels. Likewise, some physical elements contribute to multiple *Tasks*. Now that Steps 1 through 10 are complete for the robot work cell, *System* and *Process* have been sufficiently decomposed to more easily identify the *MMCLs* based upon fault and failure knowledge of the individual elements and historical data of the work cell, if the work cell has been in service and data has been captured prior to this decomposition.

INFLUENCE OF RISK ON THE HIERARCHY

As discussed in the earlier section, the hierarchies can be challenged. It is possible that the hierarchies will evolve as the risk of potential faults and failures is understood. These hierarchies could also impact the *MMCLs.* If a *System, Component, Sub-Component, Task,* or *Sub-Task* is considered low risk (i.e., very unlikely to fail, and if it does fail, the failure will have negligible impact and/or be very easy to remedy) in the overall manufacturing process, then it is unlikely that this *MMCL* will be independently bounded. Conversely, if a *MMCL* is considered high risk (i.e., very likely to fail or if it does fail, the failure would have a severe impact on the manufacturing process), then it is very likely that the *MMCL* will be clearly specified so it can be monitored, maintained, and/or controlled.

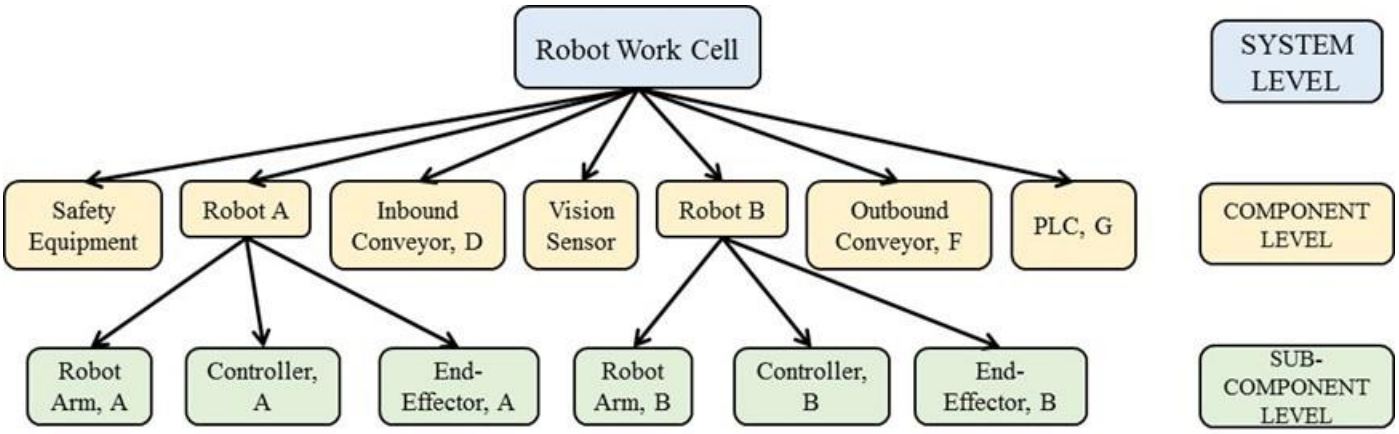

Figure 8. Physical Hierarchical Decomposition of Robot Work Cell

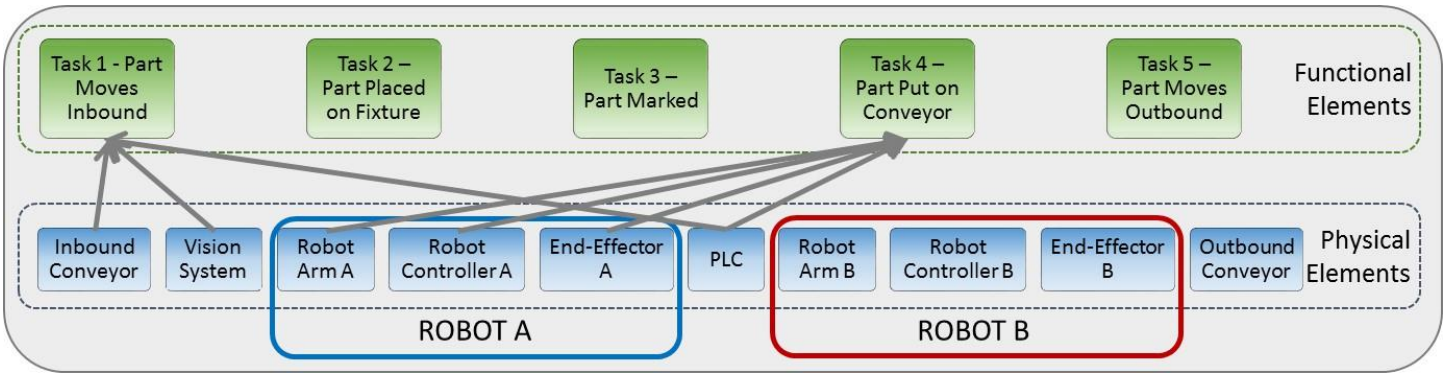

Figure 9. Component and Task Mapping

Figure 10 presents an example risk matrix. This matrix presents risk (low, low medium, medium, medium-high, and high) in

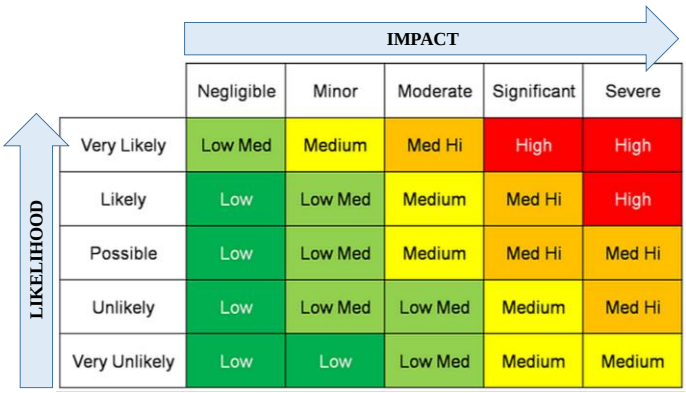

Figure 10. Risk Matrix [51]

terms of likelihood (very unlikely, unlikely, possible, likely, very likely) and impact (negligible, minor, moderate, significant, severe). Organizations use this matrix to evaluate levels of risk so they can clearly differentiate the various types of risk present. This type of risk matrix can be paired with the *System* and *Process* decompositions to indicate the varying levels of risk that a *Component, Sub-Component, Task,* and *Sub-Task* will fail during its designated manufacturing process. In practice, it would be expected that an organization would not tolerate any high risk, or even medium high risk, where the potential, for such faults and failures would be designed out of the system and therefore eliminated. Different organizations apply the risk matrix in terms of quantifying likelihood and impact values. The following guidelines are presented:

- Likelihood – corresponds to a percentage or frequency that the *MMCL* will experience a fault or failure. Values can be quantified as percentages (e.g., Very Likely – greater than 50 % chance of fault/failure occurrence, Likely – between 25 % to 50 % chance of fault/failure, Possible – between 10 % to 25 % chance of fault/failure, Unlikely – between 1 % to 10 % chance of fault/failure, Very Unlikely – less than 1 % chance of failure) or as frequencies (e.g., Very Likely – fault/failure may occur once/day of operations, Likely – fault/failure may occur once/week, Possible – fault/failure may occur once/month, Unlikely – fault/failure may occur once/year, Very Unlikely – fault/failure may occur once/lifetime)
- Impact – corresponds to the significance that a fault/failure of an *MMCL* will have on the operations. Impacts can be quantified in terms of loss of quality or

productivity, which can both be turned into loss of dollars. Example quantifications of impact could be Severe – *Process* is offline for greater than a week, Significant – *Process* is offline between one day to a week, Moderate – *Process* is offline between an hour to a day, Minor – *Process* is offline between 10 minutes to an hour, and Negligible – *Process* is offline for less than 10 minutes. Some risk matrices that are actively used quantify impact in terms of personnel injury. This effort is focused on fault/failure impact to the manufacturing process and not impact on personnel.

The hierarchical *System* and *Process* decompositions provide a technology developer, technology integrator, or manufacturer the means of delineating the boundaries of *MMCLs* of importance. Establishing these boundaries must be coupled with an understanding of how much risk each *MMCL* carries with them so that the appropriate PHM technique(s) can be applied. This paper lays the foundation for this research effort where future work has begun to add greater clarity to this process.

FUTURE WORK

Building upon this effort, the next step in this research is to further link *MMCLs* across the physical and functional hierarchies. Further understanding these linkages will enable technology developers, technology integrators, and manufacturers to identify key relationships between *MMCLs*. This will enable additional guidelines to be provided to support strategic inclusion of PHM through the *System* and *Process*.

Next, common robot work cell faults and failures will be mapped back to the physical and functional hierarchies. This will include highlighting which faults and failures are the root cause vs. the faults and failures that result from a connected *MMCL* failing. In parallel with linking common faults and failures, metrics will also be identified and integrated that enable monitoring, diagnostics, and prognostics to occur.

CONCLUSION

Technology developers, technology integrators, and manufacturers must be strategic in their implementation of monitoring, diagnostic, and prognostic techniques within their manufacturing processes. Insufficient PHM can lead to costly faults and failures that compromise the manufacturing process, and, ultimately, the organization's health. Too much PHM can be expensive in terms of the materials (e.g., sensors, computers) and labor (e.g., personnel to design the PHM system, develop new algorithms, monitor the PHM system). This builds the foundation for a process that will aid in the strategic placement of PHM throughout a manufacturing process by promoting the delineation of clear boundaries across *MMCLs* and defining PHM priorities through risk assessment. PHM techniques are implemented largely because there is a risk of a fault or a failure. If the risk cannot be eliminated, then the organization must weigh the value of PHM vs. the value of realizing the fault or failure. No PHM technique is 100 % accurate or perfect, yet PHM's implementation within a range of manufacturing environments has been documented in terms of having positive impacts. The process presented in this paper would add greater rigor to the integration, and extent of, PHM across a manufacturing process.

NIST DISCLAIMER

The views and opinions expressed herein do not necessarily state or reflect those of NIST. Certain commercial entities, equipment, or materials may be identified in this document to illustrate a point or concept. Such identification is not intended to imply recommendation or endorsement by NIST, nor is it intended to imply that the entities, materials, or equipment are necessarily the best available for the purpose.

REFERENCES

[1] McKinsey, G. I., 2012, "Manufacturing the future: The next era of global growth and innovation," McKinsey Global Institute.

[2] PCAST, 2014, "Report to the President: Accelerating U.S. Advanced Manufacturing," Executive Office of the President - President's Council of Advisors on Science and Technology.

[3] PCAST, 2012, "Report to the President: Capturing Domestic Competitive Advantage in Advanced Manufacturing," Executive Office of the President - President's Council of Advisors on Science and Technology.

[4] Kagermann, H., Helbig, J., Hellinger, A., and Wahlster, W., 2013, Recommendations for implementing the strategic initiative INDUSTRIE 4.0: Securing the future of German manufacturing industry; final report of the Industrie 4.0 Working Group, Forschungsunion.

[5] Kahan, T., Bukchin, Y., Menassa, R., and Ben-Gal, I., 2009, "Backup strategy for robots' failures in an automotive assembly system," International Journal of Production Economics, 120(2), pp. 315-326.

[6] Kusuda, Y., 1999, "Robotization in the Japanese automotive industry," Industrial Robot, 26(5), pp. 358-360.

[7] Wilson, M., 1999, "Vision systems in the automotive industry," Industrial Robot, 26(5), pp. 354-357.

[8] Edinbarough, I., Balderas, R., and Bose, S., 2005, "A vision and robot based on-line inspection monitoring system for electronic manufacturing," Computers in Industry, 56(8–9), pp. 986-996.

[9] Malheiros, P., Costa, P., Moreira, A. P., Ferreira, M., and Ieee, 2009, "Robust and Real-time Teaching of Industrial Robots for Mass Customisation Manufacturing Using Stereoscopic Vision," Iecon: 2009 35th Annual Conference of Ieee Industrial Electronics, Vols 1-6, pp. 2205-2210.

[10] Zwicker, C., and Reinhart, G., 2014, "Human-robot-collaboration system for a universal packaging cell for heavy electronic consumer goods," Enabling Manufacturing Competitiveness and Economic Sustainability, Springer, pp. 195-199.

[11] DeVlieg, R., 2010, "Expanding the use of robotics in airframe assembly via accurate robot technology," SAE Int. J. Aerospace, 3(1), pp. 198-203.
[12] Jeffries, K. A., 2013, "Enhanced Robotic Automated Fiber Placement with Accurate Robot Technology and Modular Fiber Placement Head," SAE International Journal of Aerospace, 6(2), pp. 774-779.
[13] Summers, M., 2005, "Robot capability test and development of industrial robot positioning system for the aerospace industry," SAE transactions, 114(1), pp. 1108-1118.
[14] American National Standards Institute, I., 2007, "Robots for Industrial Environment - Safety requirements - Part 1 - Robot," Terms and definitions, Robotic Industries Association, Ann Arbor, Michigan, p. 44.
[15] Pellegrino, J., Justiniano, M., Raghunathan, A., and Weiss, B. A., 2016, "Measurement Science Roadmap for Prognostics and Health Management for Smart Manufacturing Systems," NIST Advanced Manufacturing Seriess (AMS).
[16] Weiss, B. A., Vogl, G. W., Helu, M., Qiao, G., Pellegrino, J., Justiniano, M., and Raghunathan, A., 2015, "Measurement Science for Prognostics and Health Management for Smart Manufacturing Systems: Key Findings from a Roadmapping Workshop," Annual Conference of the Prognostics and Health Management Society 2015, P. Society, ed., PHM Society, Coronado, CA, p. 11.
[17] Smith, C. B., "Robotic friction stir welding using a standard industrial robot," Proc. 2nd International Friction Stir Welding Symposium, Gothenburg, Sweden, TWI, Published on CD, Citeseer.
[18] Engelberger, J. F., 2012, Robotics in practice: management and applications of industrial robots, Springer Science & Business Media.
[19] Qiao, G., and Weiss, B. A., "Advancing Measurement Science to Assess Monitoring, Diagnostics, and Prognostics for Manufacturing Robotics," International Journal of Prognostics and Health Management, 7, p. 13.
[20] Jin, X., Siegel, D., Weiss, B. A., Gamel, E., Wang, W., Lee, J., and Ni, J., 2016, "The present status and future growth of maintenance in US manufacturing: results from a pilot survey," Manufacturing Rev., 3, p. 10.
[21] Jin, X., Weiss, B. A., Siegel, D., and Lee, J., 2016, "Present Status and Future Growth of Advanced Maintenance Technology and Strategy in US Manufacturing," International Journal of Prognostics and Health Management, 7 (Special Issue on Smart Manufacturing PHM)(Sp5), p. 18.
[22] Occupational Safety and Health Administration, 2016, "Industrial Robots and Robot System Safety," https://www.osha.gov/dts/osta/otm/otm_iv/otm_iv_4.html#6.
[23] Caccavale, F., Marino, A., and Pierri, F., "Sensor fault diagnosis for manipulators performing interaction tasks," Proc. Industrial Electronics (ISIE), 2010 IEEE International Symposium on, IEEE, pp. 2121-2126.
[24] Bittencourt, A. C., 2012, "On Modeling and Diagnosis of Friction and Wear in Industrial Robots," Thesis.
[25] Wang, R., Liu, L., and Xu, F., 2008, "Research on prognostics technology of robot system," Machine Tool and Hydraulics, 30(11), pp. 15-19.
[26] Marvel, J. A., Falco, J., and Marstio, I., 2015, "Characterizing Task-Based Human–Robot Collaboration Safety in Manufacturing," Systems, Man, and Cybernetics: Systems, IEEE Transactions on, 45(2), pp. 260-275.
[27] Barajas, L. G., and Srinivasa, N., "Real-time diagnostics, prognostics health management for large-scale manufacturing maintenance systems," Proc. ASME International Manufacturing Science and Engineering Conference, MSEC2008, ASME Foundation, pp. 85-94.
[28] Lee, J., Ghaffari, M., and Elmeligy, S., 2011, "Self-maintenance and engineering immune systems: Towards smarter machines and manufacturing systems," Annual Reviews in Control, 35(1), pp. 111-122.
[29] Lee, J., Ni, J., Djurdjanovic, D., Qiu, H., and Liao, H., 2006, "Intelligent prognostics tools and e-maintenance," Computers in industry, 57(6), pp. 476-489.
[30] Ahmad, R., and Kamaruddin, S., 2012, "An overview of time-based and condition-based maintenance in industrial application," Computers & Industrial Engineering, 63(1), pp. 135-149.
[31] Coats, D., Hassan, M. A., Goodman, N., Blechertas, V., Shin, Y.-J., and Bayoumi, A., "Design of advanced time-frequency mutual information measures for aerospace diagnostics and prognostics," Proc. 2011 IEEE Aerospace Conference, AERO 2011, IEEE Computer Society.
[32] Butcher, S. W., 2000, "Assessment of Condition-Based Maintenance in the Department of Defense," Logistics Management Institute, McLean, Virginia.
[33] Montgomery, N., Banjevic, D., and Jardine, A. K. S., 2012, "Minor maintenance actions and their impact on diagnostic and prognostic CBM models," Journal of Intelligent Manufacturing, 23(2), pp. 303-311.
[34] Tian, Z., Lin, D., and Wu, B., 2012, "Condition based maintenance optimization considering multiple objectives," Journal of Intelligent Manufacturing, 23(2), pp. 333-340.
[35] Kothamasu, R., Huang, S. H., and VerDuin, W. H., 2006, "System health monitoring and prognostics - a review of current paradigms and practices," The International Journal of Advanced Manufacturing Technology, 28, pp. 1012-1024.
[36] Muller, A., Crespo Marquez, A., and Iung, B., 2008, "On the concept of e-maintenance: review and current research," Reliability Engineering & System Safety, 93(8), pp. 1165-1187.
[37] Peng, Y., Dong, M., and Zuo, M. J., 2010, "Current status of machine prognostics in condition-based maintenance: a review," The International Journal of Advanced Manufacturing Technology, 50(1-4), pp. 297-313.
[38] Vogl, G. W., Weiss, B. A., and Helu, M., 2016, "A review of diagnostic and prognostic capabilities and best practices for manufacturing," Journal of Intelligent Manufacturing.
[39] Vogl, G. W., Weiss, B. A., and Donmez, M. A., 2014, "Standards Related to Prognostics and Health Management (PHM) for Manufacturing," No. NISTIR 8012, National Institute

of Standards and Technology (NIST), Gaithersburg, Maryland, USA.
[40] Vogl, G. W., Weiss, B. A., and Donmez, M. A., "Standards for prognostics and health management (PHM) techniques within manufacturing operations," Proc. Annual Conference of the Prognostics and Health Management Society 2014.
[41] Zhou, Y., Bo, J., and Wei, T., 2013, "A review of current prognostics and health management system related standards," Chemical Engineering Transactions, 33, pp. 277-282.
[42] Kapurch, S. J., 2010, NASA Systems Engineering Handbook, DIANE Publishing.
[43] Weiss, B. A., and Schmidt, L. C., 2013, "Multi-relationship evaluation design: Formalization of an automatic test plan generator," Expert Systems with Applications, 40(9), pp. 3764-3774.
[44] Weiss, B. A., 2012, "Multi-Relationship Evaluation Design (MRED): An Interactive Test Plan Designer for Advanced and Emerging Technologies," Doctoral Dissertation, University of Maryland, College Park, Maryland, USA.
[45] Weiss, B. A., and Schmidt, L. C., "Multi-Relationship Evaluation Design: Formalizing Test Plan Input and Output Elements for Evaluating Developing Intelligent Systems," Proc. ASME 2011 International Design Engineering Technical Conferences and Computers and Information in Engineering Conference, American Society of Mechanical Engineers, pp. 365-374.
[46] Weiss, B. A., and Schmidt, L. C., "The multi-relationship evaluation design framework: creating evaluation blueprints to assess advanced and intelligent technologies," Proc. Proceedings of the 10th Performance Metrics for Intelligent Systems Workshop, ACM, pp. 136-145.
[47] Weiss, B. A., Schmidt, L. C., Scott, H. A., and Schlenoff, C. I., "The Multi-Relationship Evaluation Design framework: Designing testing plans to comprehensively assess advanced and intelligent technologies," Proc. ASME 2010 International Design Engineering Technical Conferences and Computers and Information in Engineering Conference, American Society of Mechanical Engineers, pp. 603-616.
[48] Helu, M., and Weiss, B. A., "The current state of sensing, health management, and control for small-to-medium-szed manufacturers," Proc. ASME 2016 Manufacturing Science and Engineering Conference, MSEC2016.
[49] Edrington, B., Zhao, B., Hansel, A., Mori, M., and Fujishima, M., "Machine monitoring system based on MTConnect technology," Proc. 3rd International Conference on Through-Life Engineering Services, TESConf 2014, Elsevier, pp. 92-97.
[50] Liker, J. K., 2014, "Is OEE a Useful Key Performance Indicator?," Industry Week.
[51] Davies, M., 2015, "Making a Risk Matrix Useful," http://causalcapital.blogspot.com/2015/08/making-risk-matrix-useful.html.

Proceedings of the ASME 2017 12th International Manufacturing Science and Engineering Conference
MSEC2017
June 4-8, 2017, Los Angeles, CA, USA

MSEC2017-2979

TOWARDS IDENTIFYING THE ELEMENTS OF A MINIMUM INFORMATION MODEL FOR USE IN A MODEL-BASED DEFINITION

Alexander McDermott Miller
Purdue University
West Lafayette, Indiana, USA

Nathan W Hartman
Purdue University
West Lafayette, Indiana, USA

Thomas Hedberg
National Institute of Standards Technology
Gaithersburg, Maryland, USA

Allison Barnard Feeney
National Institute of Standards Technology
Gaithersburg, Maryland, USA

Jesse Zahner
Purdue University
West Lafayette, Indiana, USA

ABSTRACT

The Model-Based Enterprise (MBE) paradigm is being adopted by manufacturing companies in a variety of industries. Companies benefit from enhanced visualization, documentation, and communication capabilities when 3D annotated product definitions, or Model-Based Definitions (MBD) replace two-dimensional drawings throughout an enterprise. It is critical that product information, much of which is defined implicitly in drawings, is not lost in this transition. This presents a challenge to authors and translators of 3D models used through the product lifecycle. They must understand the semantics of the product information typically presented by a drawing then explicitly include this information, in a computer-interpretable form, in the MBD.

The research study described in this paper seeks to discover what is the minimum set of required information to carry out all the tasks in a given workflow of a model-based enterprise. A survey was conducted across various industry sectors to identify the foundational elements of this Minimum Information Model (MIM) in selected workflows. This study identified the information used within the specific workflows, the capabilities of 3D CAD models to carry this information, and the implications for doing so.

KEYWORDS.

Minimum Information Model (MIM)
Model-Based Definition (MBD)
Model-Based Enterprise (MBE)

INTRODUCTION

Model-based definition (MBD) is a digital artifact (representation) of an object or system. It is representative of the physical object or system and all of its attributes, and is used to communicate information within various MBx activities in a model-based enterprise. The model-based definition should be rich in information – shape, behavior, and context – and it travels the information architecture within an enterprise (including its extended supply chain and customers), providing input to the various authors and consumers who need it. However, in today's industrial environment the MBD is often thought of as a replacement for a 2D drawing. A model-based definition's effectiveness in communicating, visualizing and documenting information has led to widespread adoption. [1] Although MBD practices are of significant value, there are still concerns about the transition from drawings to models. One issue is that critical information stored in an MBD can be lost in machine to machine communication due to translation errors. Therefore, there is a need to understand the minimum amount of information required at each phase of a product's lifecycle to ensure critical information is not lost. A second issue is a lack of common understanding regarding the information to be included in an MBD that were historically included in a drawing. This research proposes the identification of the *minimum information model* (MIM). The minimum information model is the set of information which is required for the completion of tasks within specific phases of the product lifecycle.

MOTIVATION

The manufacturing environment historically used drawings in the engineering design and production process for

Barnard Feeney, Allison; Hartman, Nathan; Hedberg, Thomas; Miller, Alexandar; Zahner, Jesse.
"Towards Identifying the Elements of a Minimum Information Model for Use in a Model-Based Definition."
Paper presented at ASME 2017 International Manufacturing Science and Engineering Conference, Los Angeles, CA. June 4, 2017 - June 8, 2017.

communicating information, visualization, and documentation of design intent [1]. Put simply, drawings were the most effective method to communicate product definition because of the tools used in design; triangles and t-squares eventually gave way to 2D computer aided design (CAD) systems, however the primary output was still a paper-based artifact [2]. Even though CAD tools facilitated the design process, and enabled engineering drawings to be generated faster and more accurately, 2D CAD was still nothing more than an electronic drafting board [3]. As computer-aided design software matured, more complex shape definitions for increasingly complex products were able to be captured. However, the 3D model, while able to capture complex shape, typically did not effectively capture behavioral and contextual information as well. The variety of information historically found on a drawing is often missing from 3D CAD models due to the software's inability to completely capture behavioral and contextual information.

Since a three-dimensional model *can* contain significantly more information than a drawing, many companies are choosing to make annotated 3D models a key component for communication within their enterprise. However there is much debate about which information elements to include to support the extended enterprise outside of the engineering function. This has led to the concept of the *model-based entreprise* (MBE). A model-based enterprise is an environment. It is an organization that has transformed itself to leverage model-based information in its various activities and decision-making processes. In this environment, the model serves as a dynamic artifact that used by various authors and consumers of information for their respective tasks. The MBE embraces feedback from the various lifecycle stages to improve the model representation for the creation of subsequent products and product iterations. People working within the enterprise have an enlightened view of digital product information that can be leveraged in their daily work.

Just as people used drawings in their job functions throughout the product lifecycle, today people are beginning to use a model-based definition in their job functions inside engineering, manufacturing, supplier management and other areas of the organization. Model-based engineering, model-based manufacturing (MBm), model-based sustainment (MBs), and any other model-based [activity] (MBx) are categories of activities within the model-based enterprise. Any of these activities (and the people in them) use digital product data to represent shape, behavioral, and contextual information carried by the model-based definition to execute their functional role. Model-based activities are conducted by relying on the predictive and archival capabilities of the model, by replying on its high levels of fidelity to physical object or system.

A model-based entreprise presents a challenge to authors and consumers of 3D models used throughout the product lifecycle. Because not all authors and consumers need the same information to perform their job, the model must often be translated to a different form containing different amounts of information. This issue did not typically exist when using drawings because the medium of communication (paper) could seamlessly pass from one person to another. However due to proprietary data formats and incomplete implementation of data exchange standards in modern CAD tools, the types of information historically found in those drawings is often lost in translation. As such, the standards development community has differentiated between the *presentation* (graphical display) of information, and *representation* (contextual understanding) of information. This difference in the level of sophistication of information embedded in the CAD model is a fundamental tenet of a model-based definition. To successfully leverage the power of a model-based definition, it is important to understand the behavioral and contextual semantics of the product information typically presented by a drawing, and then explicitly include this information in a computer-interpretable form in the model-based definition. It is critical that product information, much of which is defined implicitly in drawings and not at risk of loss due to a change in the communications medium, be protected during the transition to MBD in practice.

Model-based definition standards, such as ASME Y14.41 and ISO 16792, attempt to prescribe rules for how to define specific model-based product definition information. Although these standards potentially provide a foundation for MBD that specifies *how* to express certain types of information in a model, they do not specify *which* information types should be included in a model for a given workflow. [4, 5] In this context, a workflow is a sequence of tasks which, when completed, accomplish a specified objective. The minimum information model specifies the set of required information that workflow participants utilize to complete their tasks. Accurately identifying this information will help a company transition to the use of MBD by providing a general framework for capturing necessary information.

The research described in this paper is the foundation for defining the minimum information model. This research was scoped to answer two questions: (1) from a predetermined list of information, what information does each specified workflow utilize? and (2) how do the humans involved in the specified workflows understand the capabilities of CAD tools to carry product information currently communicated to them?

As stated previously, the evolution of MBD towards the replacement of two-dimensional drawings has created a need to understand the minimum amount of information required in certain workflows so as not to inadvertently expose intellectual property or to unintentionally increase model complexity. The use of models; however, poses challenges to authors and consumers of information in the enterprise due to issues with software compatibility and information complexity. This research attempts to identify the MIM in order to ensure that the information required for specific common workflows promotes effective communication.

BACKGROUND

Information in Engineering Drawings

Historically, drawings were used to communicate information. In an engineering setting, they represented the most

effective way to communicate how to produce something based on the design tools available at the time. Over time, drawings became more sophisticated in their information content and their representation of the object being documented. Modern technical drawings often contain more information related to the product definition than actual geometry views of the object [2]. While the orthographics views of the geometry explicitly define shape, the other non-geometric data contained on drawings is often defined implicitly, requiring contextual understanding on the part of the reader to make sense of the information. The level of contextual understanding needed is typically dependent upon the drawings reader's tasks in their given workflow [6]. This contextual information is not "called out" like a dimension or tolerance, rather it is interpreted by the reader of the drawing.

The implicit information is a critical component in engineering drawings; without it, production efforts would be hindered, inspection processes would often be incomplete, and assembly methods would tend to lack needed information to define the proper fit. As drawing creation evolved to meet the communication and validation needs within specific corporate production environments and their supply chains, the result was a variety of ways to apply the well-defined body of national and international drawing standards, with each application being unique to individual companies.

This individualized application of drawing standards within a specific company began to cause challenges within the various manufacturing sectors and their supply chains. Since any given company often has their own way of executing specific processes and interpreting specific sets of information, the resulting intepretations of information from drawings across industry sectors often meant a diferent interpretation of the same drawing from one company to another. Participants of different workflows would receive the same drawings, but each participant's interpretation of the information presented in the drawings will differ [7]. Even the definition of MBD standards for using 3D CAD models in place of 2D drawings [8, 9] has not stopped the occurrence of individualized interpretation.

As the evolution of product definition and documentation has prompted the transition from 2D, paper-based drawings to digit, 3D annotated models, the differences in contextual interpretation of those artifacts has remained. A related issue in this discussion of contextual interpretation of artifacts is spatial proximity. In the past, engineering employees often worked in the same location as the production personnel making the product, which allowed for quick, informal communication. This helped prevent the loss of implicit information and promoted behavioral and contextual understanding of the design and production of the product, because if a person was unable to understand an aspect of the drawing, they could easily find the answer. Now, global supply networks, and "design anywhere, make anywhere" business models have made it necessary that the semantic interpretations of digital artifacts (i.e., 3D model-based definitions) be explicitly defined [10,11].

While the transition to digital MBD representations has arguably made dissemination of product information easier, the disparate nature of information authoring tools has raised a vexing dilemma. Most companies do not store all of their product definition or production data in a common database, which makes aggregating that data difficult. While this was still true when people primarily used paper-based drawings, the challenge was slightly less in that the paper medium was the common denominator. Even when the transition was made to 2D CAD systems, the output that was shared was often paper-based. And since neither paper drawings nor 2D CAD drawings were associated parametrically to a 3D model, information could be readily changed without the overhead of affecting a 3D model or having to edit a 3D model to initiate a change in a 2D drawing. Moreover, materials data, work instructions, process specifications, and other information, which could easily be included on a 2D drawing and that might conceptually be stored in a model-based definition, are not easily aggregated today into a 3D model. The discontinuity among product data authoring systems must change in order for the MBD methodology to succeed in the long term as something more than a simple remaster of a drawing definition by including implicit information. While the method of product definition or interpretation is important, the method for information dissemination is just as critical [12].

Model-Based Definition

The digital, model-based definition is rapidly becoming the artifact of choice to document and communicate product definition information within many large companies, as well as their extended supply networks. The use of MBD allows companies to leverage the resources invested in the definition and creation of the product model, as well as the visualization and communication capacity that a 3D digital medium provides. In doing so, companies are beginning to eliminate the use of 2D drawings, or at least relegate the 2D drawing to being used as a reference document rather than the document of record [13]. Moreover, the efficiencies gained when a company transitions to being a model-based enterprise require the use of the model-based definition [14, 15]. Furthermore, industry has found success using MBD for workflows such as manufacturing, planning, product-services procurement, and marketing [4, 16].

Yet even in companies making the transition to the use of MBD in lieu of 2D drawings, the transition has not been without challenges. While the aerospace and automotive industries have led the 2D-to-3D transition [4], their extended supply networks have been slow to adopt the change in technology and methodology. Employee training costs, increased costs in software licenses, and the inherent complexity of 3D-based processes are often listed as reasons that small and medium manufacturers (i.e., automotive and aerospace suppliers) do not adopt or implement MBD technologies and processes. While the three-dimensional model as a geometry definition within the design and engineering functions has become ubiquitous across industry sectors, a redundancy has occurred as companies or certain functions within companies have not wanted to give up their use of 3D drawings [14, 17].

By using the three-dimensional model and adopting an model-based enterprise approach, a company potentially

eliminates redundant product definitions. The advantage of the 3D CAD model is contains enough geometric information to consolidatedefinitions; however, by default, it will still lack the behavioral and contextual definitions withough a conscious effort on the part of the definition author to include them. So while the CAD model is likely to be used to define final product geometry, it may not necessarily be thought of as the master product definition today given the disparate locations of the data necessary to complete such a definition. However, the 3D CAD model is an opportunistic choice to embed and transfer product information [18] due to its communicative capacity and ubiquitous adoption when human consumers of product information are in the loop.

The consolidation of product definition data into a model-based definition provides numerous benefits across the lifecycle. For every user of 3D CAD models in design, engineering, or manufacturing, there are thirty potential users of data in marketing, product documentation, sales, support, customer service, and beyond [19]. Boeing demonstrated the power of successful MBD implementations. Boeing engaged in a Virtual Product Development technique where the product design, tooling, and manufacturing processes, prior to fabrication were verified virtually. This approach achieved a 62% reduction in product development time and 42% reduction in the cost of development [14, 20]. MBD has proven to be a more effective method of communication than engineering drawings. Due to this, 3D CAD Model usage will continue to grow. To maintain the benefits and maximize the utility of the 3D CAD Model, it can be used to consolidate product definition information.

Although models can carry the same explicit information defined in drawings, the next step in their development is the creation of a 3D CAD model that contains all information required for the specific individual who would use the model. The minimum information model would benefit multiple actors within the lifecycle by delivering the information neded in a specific workflow in a specific lifecycle stage. The use of MBD (and by extension, the minimum information model) within manufacturing companies is an appropriate approach due to the benefits offered by leeraging the 3D model [13].

Minimum Information Model

As stated previously, companies have begun the transition to model-based definition. Some of those companies already have successfully replaced the 2D drawing with the 3D CAD model, while others remain in the process of doing so. The capture of explicit drawing information was the first step of a longe process to the successful adoption of MBD. It is now necessary to develop understanding of the minimum information set necessary for employees within specific workflows of a product-producing company. The marriage of shape, behavioral, an contextual information within MBD processes has the potential to enhance productivity by capturing both the implicit and explicit information historically contained within 2D drawings. There is little documentation about how to develop MBD artifacts and methods past the level of definition of a drawing replacement. The current industry trajectory is to simply move the annotations from a 2D drawing into similar locations within the three-dimensional models as annotations visible to the user [13].

There is a growing body of literature and industrial interest in the identification of requirements for proper MBD implementation. One research team analyzed different levels of MBD implementation and analyzed their effectiveness. This research was process oriented and sought to identify what improvements need to be made for MBD implementation. Their research identified that the use of MBD as the master definition needed improvements in data standardization and process visualization [21]. The need to structure the process information in a useful and effective method has driven research to standardize the data representation. Information is contextual across the lifecycle and different departments and/or processes in the lifecycle may require different types of MBD datasets [22]. Researchers also have begun constructing design MBD (dMBD) and process MBD (pMBD) models and concluded that further identification of non-geometrical information still needs to be perfected [23].

Expanding MBD beyond drawing definition will also require improvements to CAD authoring software tools currently in use, as weill as improvements to the database and data model structures currently used by commercial CAD software and product data management software tools. While distributed product development systems, and innovations in communication technologies, are closing information gaps between engineering and the remainder of the lifecycle [24], enhanced data security, network architecture, and compression technologies will be needed to disseminate more well-developed MBD data files. Once these technologies reach adequate levels of performance, a complete understanding and definition of the model-based product information required will be needed.

This research study in the first stage of a two-part study, establishing the preliminary definition and context of the minimum information model, with the second stage expanding and validating that definition through the use of a future Delphi study. Once completed, the MIM would be the set of information that the workflow participants require for completing their tasks. This means that if an element of the MIM is missing, the workflows processes will be hindered. This research looks to build upon the MBD definition by providing guidelines for the information that will be created and passed to and from each workflow to streamline production. Therefore, one must understand the definition of an *element* in the context of the minimum information model.

The MIM is comprised of a set of elements. The elements exist in current workflows. The following statement must be true to classify information as a MIM element: the information is consulted in completing the tasks of the workflow the MIM represents. The MIM elements can be split into two subsets. These subsets are *primary information* and a*uxiliary information*. The primary information is the set of information that most work tasks in this workflow utilize. Dimensions are primary information for manufacturing. The auxiliary information is the set of information that is unique to specific

workflow participants. To be an element of the auxiliary information set an element must be consulted by at least one participant of the workflow in completing the task. An example of an auxiliary information element is the atypical use of an analysis model by design, or manufacturing. A key aspect to consider for auxiliary information is that it has high variance. The MIM is the union of these two sets, and furthermore, an element of the primary information set cannot be a member of the auxiliary information set and vice versa. Understanding the components of the MIM set is critical to successful implementation of the MIM.

Both subsets of the MIM are valuable, but the primary information set affects a much larger population of the workflow, potentially all of it. The primary information must be communicated clearly and logically because improper communication may negatively affect the population.

The auxiliary information set has two aspects that confound identification of the information. The auxiliary information set contains low use information as well as industry, or company specific information. Handling of industry or company specific information will likely only be possible by further categorizing the MIM workflows. Second, it is possible that the auxiliary information set will be in a flux state, and therefore, difficult to maintain. It is possible that consistent evaluation of the information in use within the workflow can be done to maintain the auxiliary information, but how to best handle the Auxiliary information may not be clear, and may require a more interventionist approach, instead of presupposing the information required.

These two aspects of the auxiliary information set led to the pursuit of the primary information set elements in the minimum information model. For the remainder of this paper, when we discuss being considered part of the MIM, we are referring to being a member of the primary information set.

SURVEY DESIGN

We designed a survey in the pursuit to identify the elements of the minimum information model. This survey was distributed via a web service, Qualtrics, and was promoted via email blasts and social-media advertising. The questions in the survey targeted our two research questions: (1) what is the minimum amount of data that is necessary to communicate to the next consumer in the lifecycle and (2) what are the capabilities of CAD tools to carry the minimum information level?

Our goal was to ensure comprehensive responses from as many participants as possible. The will contain a standardized information base. For that to be possible, a large response group was required to confidently represent the population of participants' respective workflows. We recognize that the quality of the survey outcome is dependent on the quality of the survey questions posed and the responses received. Therefore, we worked with subject matter experts to validate the questions and provided multiple choice responses to minimize the uncertainty of the survey results and manage the overall quality of the survey.

The first portion of the survey collected demographic information. Questions one and two were geared towards the company with which the participant currently worked. The participants identified their own industry such as defense, automotive, medical, etc. Participants also indicated the size of their company. Company size was indicated in ranges of fifty employees, and capped at 500 or more.

Next, participants identified information about their company's geographic location and their own job area within the company. The locations were preliminarily divided into inside U.S. and outside U.S., and then further subdivided. If they were in the U.S., they were asked what region of the U.S. If they were outside the U.S., they were asked what continent. The participants then indicated their current job area within the company. A list of job areas was provided and participants had the option to enter their own job description if it was not represented by the job areas listed. This question identified positions such as design engineer, analyst, manufacturing engineer, or quality engineer.

Following demographics, two more questions about how engineering information was communicated were asked these two questions were: (1) how do you currently receive engineering related information? and (2) in which workflow do you most actively participate? The first question looked at industry's current level of model adoption. Participants indicated the method by which most engineering related information was communicated. The second question separated participants into one of the four workflows that were identified for the minimum information model. The four workflows were (1) concept-to-prototype, (2) prototype-to-detailed product definition, (3) detailed product definition-to-manufacturing, and (4) manufacturing-to-inspection. The participants also had the option to indicate they did not actively participate in these workflows. If participants indicated that they did not actively participate in one of the identified workflows, the survey concluded.

From here, the survey segmented into four distinct workflows, but with similar structure. The first question in each section was, "What type of information is created or used in the workflow?" Participants were presented with a series of check boxes that referenced specific information pertinent to their workflow and could select all that applied. An option to add free text was also provided.

Following this question, the participants indicated if drawings were used to communicate the information. If the participants indicated that drawings were not being used to communicate this information, then they would be queried on what other documents were used to communicate the information. Next, participants were asked, "In your company, could the items in Question 8 (What type of information is created or used in the workflow?) be communicated via a 3D model of the product instead of a drawing?" If their answer was no, then the participants were asked, "What prevents models from being used to communicate this information in this workflow?" However, if they selected yes, then the participants skipped that question. Each workflow was structured in this manner with the information indicated in the first question varying.

The final question was a qualitative question, which allowed participants to provide any comments on the topic of using model-based definition in place of drawings. This concluded the survey for identifying the minimum information model. In the following sections, the results are presented in detail.

RESULTS

The minimum information model survey had 89 respondents. Of these 89 responses, 76 completed the demographics portion. Eighty-five percent of the respondents were from the U.S. with 63 percent from the Midwest and approximately 10 percent respectively for the Northeast, Northwest, Southeast, and Southwest.

Of the 15 percent outside the U.S., 36 percent were from Asia and 64 percent were from Europe. These respondents indicated that they worked in a wide variety of industries, with relatively even distribution within each industry. The respondents answered a question to determine the size of the company for which they were currently working. The data reflects that this survey captures the opinions of both small and large companies with a slight skew towards larger companies, which could simply be due to larger companies having proportionally greater numbers of engineers.

Going forward with this survey, narrowing the MIM to an industry sector and company size would be better suited to address the specific needs of specific areas. There are potentially different variables in each field that affect the use of 3D CAD models and creating the MIM, capturing the differences between fields is an important aspect of the minimum information model. The survey collected information regarding the respondents' current job area, with this distribution highly skewed toward design engineer. Sixty-eight participants submitted an answer to this question, and 33 participants indicated they were design engineers. To improve the survey, it would be important to try and capture more positions at the companies outside the categories of *design engineer* and *management*.

Regardless of the highly skewed current job title, the distribution of their current workflows was excellent. Therfore, meaningful data was collected from each of the workflows and contributes to the use of the minimum information model. Maintaining a proper distribution of workflow participants should be kept in mind in follow on research efforts.

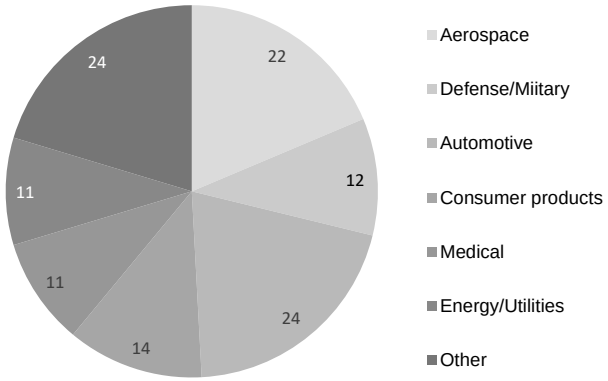

Figure 1 Distribution of Participants Industry

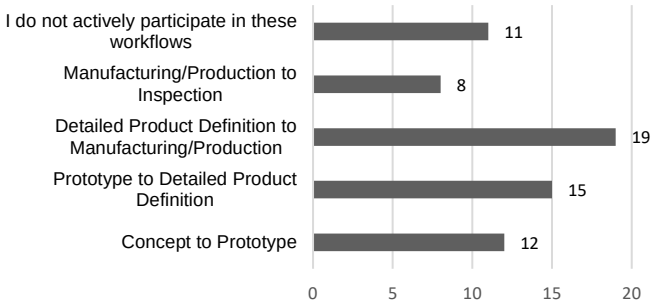

Figure 2 Participants workflow distribution

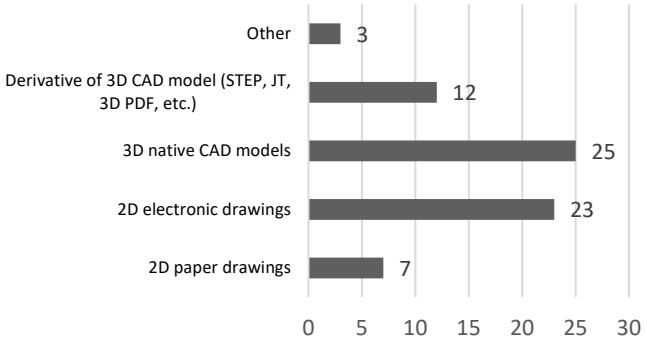

Figure 3 Response for how participants receive information

After respondents indicated the workflow in which they most actively participated, the survey placed the participants into groupings to determine the requirements and capabilities of each individual workflow with respect to model-based definition and minimum information model. The four workflows were *concept-to-prototype*, *prototype-to-detailed product definition*, *detailed product definition-to-manufacturing*, and *manufacturing-to-inspection*.

Each of these had very similar questions. In the cases where the questions were the same, they were aggregated. The remainder of this section summarizes the results of the aggregated data of identical questions.

The data displayed and discussed in this section reflects the responses of all participants in each of the workflows. Identical

questions separated by workflow were aggregated. The aggregate data provided insight into industry's readiness to adopt model-based definition. These questions intended to identify industry's level of readiness to convert to a model-based enterprise. These questions targeted the methods in which data was consumed, created, and then transferred and whether 3D CAD models could perform these tasks in place of two-dimensional drawings. All participants in the survey could indicate the medium in which they receive product information for consumption. In Figure 3, 58 percent use a CAD model or a derivative of a CAD model and 36 percent use a 2D-electronic drawing. Only 11 percent still use 2D-paper drawings as the medium for data exchange. The distribution of 3D CAD models already compromises over 50 percent product information exchange. In addition, when including 2D-electronic drawings nearly 90 percent of the product information medium is considered.

It is apparent that the 3D CAD model is the primary source of data transfer for most employees at these companies and the use of the 3D CAD model as the master definition would be beneficial to industry. Even though the primary medium for data exchange is through CAD models or their tools, most information being consumed is through drawings. Ninety-six percent of respondents indicated that they only use drawings or drawings in addition to other auxiliary documents for use or creation within their respective workflows.

Utilizing a CAD or derivative model to carry information is the most common product definition format utilized in this survey. The replacement of drawings with three-dimensional models could provide numerous benefits, but the three-dimensional model first needs to replace two-dimensional drawings and capture all information they contain. Respondents were asked if models can deliver the data created or used within their respective workflows. Overwhelmingly, respondents indicated that the 3D CAD model can deliver this information.

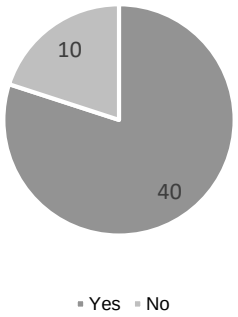

Figure 4 Could models be used in place of drawings in your workflow?

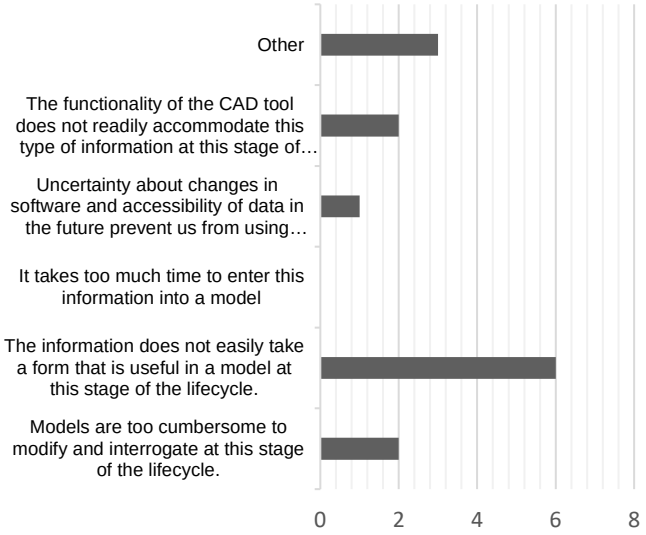

Figure 5 Issues adoption of MBD faces

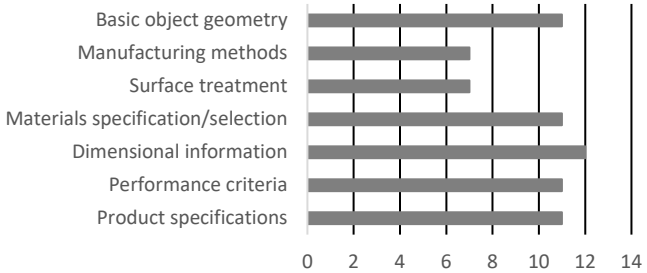

Figure 6 Participants responses for what information was created or used in the the product information for concept-to-prototype

The model is now at a point where it can replace the drawing, but to effectively make the transition, all information and issues must have discrete answers. Respondents who indicated that models could not replace drawings within their company were prompted to determine the inhibitors of 3D CAD model usage that ultimately inhibited the development of model-based definition.

In Figure 5, the main inhibitor of the use of 3D CAD models was that the information did not easily take a form that is useful in a model at this stage of the lifecycle. Each of the listed issues was indicated at least one time except for the issue that it took too much time to input this data into a three-dimensional model. There are concerns for the use of MBD, but most respondents believe model-based definition can carry the information that they are consuming or creating. In the follow paragraphs, each individual workflow is broken down. Regarding the information to be contained in the MIM, any information selected should be considered and further researched. This discussion only pertains to information that was selected by five or more participants. The purpose behind reporting only on information which had a selection of five or greater was to ensure that the information was necessary to that workflow. Individual respondent's processes

will vary and may utilize different information, but there is a subset of information which is necessary to complete a workflow. The MIM is intended to identify this necessary information subset. The lists that were developed to help identify information used or created in each workflow were populated through discussion with companies. They are not intended to be a complete list of information to be standardized in the MIM, but they do formulate a foundation on which to start understanding and building the minimum information model. A low response rate does not signify exclusion from the MIM, but rather states that further research is required.

The concept-to-prototype workflow had twelve respondents (see Figure 2). concept-to-prototype respondents indicated the information that was created or used within this workflow (see Figure 6). Eleven concept-to-prototype respondents indicated that product specifications, performance criteria, materials specification or selection, and basic object geometry were created or used in this workflow. All respondents in this workflow selected dimensional information. Seven indicated that surface treatments and manufacturing methods were also created or used in the concept-to-prototype workflow. Respondents were then queried if this information was communicated via drawings. Eleven indicated yes, but with accompanying documents. One indicated no.

When drawings were not used to communicate information, then corporate standards, test documents and contracts were used to communicate the information being created or used. Participants were asked if they thought models could communicate this information. Seven indicated yes and four indicated no. The four whom indicated that models could not be used were polled to determine what inhibited the use of models. This group did not converge on one primary cause of the problem. Instead, the data shows that there are many concerns that could prevent the use of models to communicate this information. Three participants indicated that information did not take a useful form in the 3D CAD model and two participants indicated that models do not take a form that is conducive to work on the manufacturing floor in the other comments section of the survey. It was also stated in the other response that stakeholders do not have a method for 3D CAD model manipulation.

The prototype-to-detailed product definition had 14 respondents. Results for the material created or used within the workflow are listed in Figure 7. All fields within this section had at least one selection that the information was used or created.

Dimensional information (13) and materials specification or selection (12) were the most selected choices. Two other choices that also had 10 selections were refined object geometry and tolerance information. Revision or version history obtained nine. Performance characteristics, surface treatment and manufacturing methods has six, seven, and eight respectively. Refer to Figure 7 for all distributions. Most of this information was communicated via drawings with three indicating drawings only, nine indicating drawings and accompanying documents, and two selecting no. The two respondents who indicated that drawings were not used stated that corporate standards and specification drawings were used to communicate this information. Respondents indicated that the information created or used within their workflow was capable of being communicated by three-dimensional models. The respondents who indicated that models could not be used only indicated that internal processes prevented the use of 3D CAD models to replace drawings.

Nineteen respondents were part of the detailed product definition-to-manufacturing workflow. Results for what information is created or used in the detailed product definition-to-manufacturing workflow were highly varied with response ranging from four to 16. More than 10 participants in this workflow indicated detailed product geometry, final dimension information, tolerance information or geometric dimensioning and tolerancing (GD&T), materials specifications and finished surface characteristics. These respondents indicated that this information was communicated to them via drawings and other accompanying documents. Drawings were always involved in the communication of information between detailed product definition and manufacturing. Three respondents indicated that models could not be used to replace drawings in detailed product definition-to-manufacturing. Even with all respondents relying on drawings in this workflow, most respondents indicated that models can replace drawings.

Eight respondents indicated that they were part of the manufacturing-to-inspection workflow. The indication of information used or created is shown in Figure 9. Notable figures include, six respondents indicating that detailed product geometry, final dimensions, and manufacturing methods were used in this workflow. Seven indicated that finished surface characteristics were created or used.

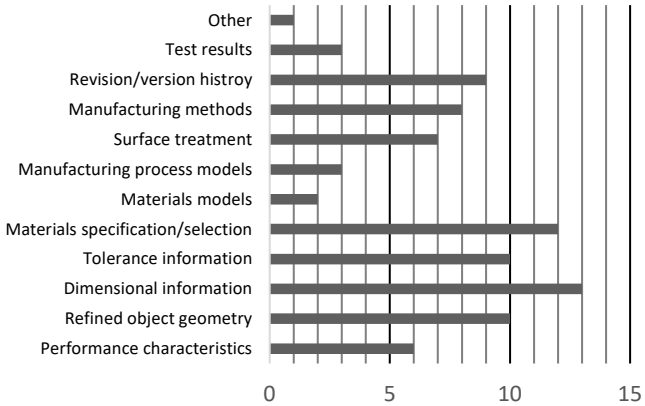

Figure 7 Participants responses for what information was created or used in the prototype-to-detailed product definition workflow

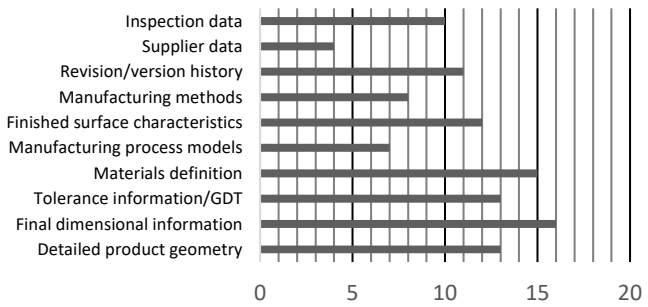

Figure 8 Participants responses for what information was created or used in the detailed product definition-to-manufacturing workflow

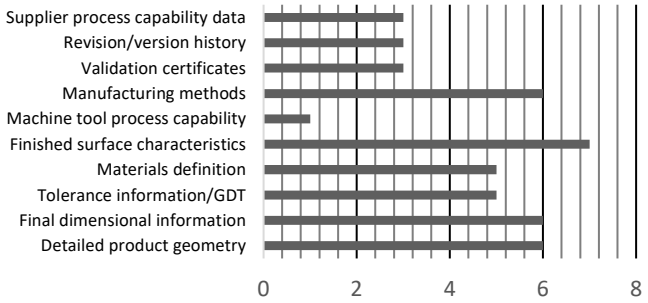

Figure 9 Participants responses for what information was created or used in the manufacturing-to-inspection workflow

The respondents indicated that drawings were always used to communicate information in this workflow and six indicated other accompanying documents were also required. Materials selection and tolerance information or GD&T were selected by five respondents. The options other than those discussed had fewer than five respondents. All subjects in this workflow indicated that the method for communication was either drawings or drawings and their accompanying documents. Overwhelmingly, this workflow indicated that models could replace drawings within the manufacturing-to-inspection workflow.

The only inhibitor indicated in this workflow is uncertainties concerning long term archival and retrieval (LOTAR). This workflow had one of the highest selections of the capabilities of CAD tools to communicate the information that was stored within drawings.

DISCUSSION

MBD has begun to infiltrate manufacturing companies in a variety of industries. Companies are using MBD to generate competitive advantage, enhanced time to market, and improved costs. Initial MBD was limited to the use of the model as a method of design, but the definition of the product was still captured with drawings. This leads to redundancy in the documentation of the product and possible confusion as to what is the master data.. A desire to replace the use of drawings with models was born from this problem. When addressing this conversion to MBD, it is crucial that no product information is lost. Creating a model-based enterprise requires an understanding of what information is needed in a model for an individual to complete all their required tasks. A survey of manufacturing companies was done to shed light on the information required within model-based definition. This level of information represents the minimum information model.

By minimum, it refers to the set of information needed to complete a task in a workflow. It is the amount of information for a specific domain to complete most tasks within that domain. A minimum information model cannot yet be fully defined from this survey, but critical information has been identified and insight into building the minimum information model. This survey also measured the capability of industry's readiness to use models as the master definition and the potential inhibitors of model use.

The minimum information model within the concept-to-prototype workflow has begun to take shape. The information (product specifications, performance criteria, dimensional information, materials specification or selection, surface treatment, manufacturing methods, and basic object geometry) that was indicated as used or created within the concept-to-prototype workflows were all indicated by more than five participants in the workflow. This data forms the foundation for the MIM within this workflow.

In addition to the information created or used in this workflow, participants indicated whether models could communicate this information. Only seven participants indicated that models could communicate this information. This was the lowest of all four workflows, and considering the sample size of 11, it was close to 50 percent. More research is required to address whether this workflow can use models as the master definition.

The majority response for why models could not be used was that the information does not easily take a form that is useful in a model at that stage. The inhibitors to using the three-dimensional model appear primarily related to the use of the CAD tool and not the abilities of the tool itself. The data suggests the inherent ease of use of drawings is not overcome by the effectiveness of the CAD tool, and that the use of the CAD tool to communicate this information would impede the communication of this information. In the other category, one of the respondents indicated that there is difficulty using the information on a manufacturing floor because it would require the setup of a terminal where floor workers could interrogate the model. This would also require the workers on the shop floor to train on use of the 3D CAD model. This workflow had the largest indication that CAD tools were incapable of replacing drawings, but the result may be tied to the comfort level of the respondents.

There was no indication that the model could not hold the information, instead only that it was difficult to use the information that was held by the model. This workflow needs to be analyzed further to ensure that using a model in place of drawings during the creation of a product is possible.

In summary, all options for information within this workflow appear to be contained within the minimum

information model. Additional research is needed to understand how models could effectively allow information to be created and used.

For the prototype-to-detailed product definition workflow, 85 percent of respondents indicated that models could communicate the information used or created within their process. The choices selected by more than five respondents were refined object geometry, dimensional information, tolerance information, revision or version history, manufacturing methods, surface treatment, performance characteristics and materials specification or selection. Drawings communicated this information to 11 of 13 respondents.

Workflow participants had significant support for models can communicate the information used from drawings. Eleven out of 13 respondents indicated models could be used for this information. The respondents who indicated models could not be used stated that it was internal processes that prevented the use of models. One respondent did not indicate why. This suggests models can replace the information being used or created in this workflow, but the business process for the company will need to change to implement model-based definition. Adapting business processes to the use of models will be a challenging next step in MBD implementation.

detailed product definition-to-manufacturing workflow indicated that 3D CAD models could replace drawings for the communication of information use or created. This field had 18 respondents and they formed some consensus on the information required for this workflow. The information being used or created by more than 5 respondents were detailed product geometry, final dimensional information, tolerance information or GD&T, materials definition, manufacturing process models, manufacturing methods, revision or version history, inspection data and finished surface characteristics.

Regarding the workflows' readiness to adopt MBD, the workflow had an overwhelmingly positive response to the use of 3D CAD models. 83 percent indicated models can replace drawings for communication. On top of this figure, all participants in this workflow were using drawings to communicate the information. The respondents who indicated that models could not be used were primarily concerned that the CAD tool was not easily used for the communication of this information. One respondent indicated LOTAR as a barrier to replacing drawings.

Manufacturing-to-inspection had only eight respondents but they also provided a consensus on the type of information used or created within the workflow. More than 5 participants in this workflow indicated each of detailed product geometry, final dimensional information, finished surface characteristics, tolerance information or GD&T, materials definition, and manufacturing methods.

All but one workflow participant indicated that this information could be communicated via models. The one who did not believe models were capable, indicated that LOTAR held back the use of models, not the capability of the models. All respondents within this workflow also utilize drawings and some utilize models already. Although all workflow participants are using drawings, they all supported that models can deliver information at the same level as drawings.

Although the MIM is workflow specific, there is useful information to be considered across the workflows. This information's level of detail or completion varied, but the type of data was similar. This data was dimensional information, object geometry and material's definition. There are also interesting trends between the workflows. These three attributes may form the foundation for the "lifecycle" minimum information model. It was also indicated in a follow-up note that MBD requires each workflow to have its defined data levels to ensure that they are not overburdened with excess information. The minimum information model need within the MBE is already being felt.

Most respondents indicated models could be used to communicate the information within their workflows. It is likely the tools do not prevent the use of the 3D CAD model. There are some instances where a three-dimensional model may not be the correct method of communication. For example, one such case was indicated in the other category – on a shop floor it would be difficult to work with 3D CAD model instead of a drawing. There are many challenges with implementing three-dimensional model usage on a shop floor, such as the hardware to interrogate a 3D CAD model. However, the same hardware also provides many benefits such as the visualization tools, which come with a 3D CAD model medium. A related opinion was that it would be difficult for stakeholders who do not have a method to interrogate 3D CAD models. Both cases have a variety of solutions and are capable of efficient management.

Based on the results of this survey, industry is ready to adopt a MBD approach to data distribution. Most respondents indicated that models are currently capable of replacing drawings. Most responses indicating that models could not be used were related to use of the data when stored within a CAD tool. Specifically, the information does not easily take a form that is useful in a CAD tool. This implies that the data can be stored in a CAD tool and that it can deliver the information, but that a drawing is better at delivering this information. It is possible that this is more related to the CAD operator and less related to the capabilities of the CAD tool. The user of the information will affect the usefulness of the information.

This research has set the foundation for an important concept needed within MBD, the minimum information model. This research began moving towards the MIM definition, but did not identify the specifics of the MIM set within each workflow. Further research will need to be done to support this. This research did address the views of workflows participants on the model's ability to carry the information that they utilize regularly. The 3D CAD model is ready to begin replacing drawings in multiple workflows, and more research will need to be done to address the concerns raised by the research participants as to hindrances into implementing a more sophisticated model-based definition.

CONCLUSION

Moving towards an MBE presents many challenges and obstacles. One of these is having a complete understanding of the information flowing within the organization. This is difficult to capture, because of the nature of an organization, but there is significant value in it. The minimum information model is a formalized model meant to capture a specific subset of information communicated within an organization that will assist in communicating and presenting information within an organization. The following section presents on notable concepts developed from this research.

An interesting trend seems to be developing for data creation and use. When the previous workflow highly selected an information type, the following workflow would also select it highly. This indicates that the subsequent workflows would commonly use data created at the previous step in the lifecycle. An example of this is that tolerance information was highly selected in prototype and then dropped slightly in the subsequent workflows. There needs to be more data and a statistical analysis to confirm this. As of now, this is merely speculative. A follow-up survey could visualize the flow of information through the workflows and whether information loses or gains value to end-users as it passes through a lifecycle. Defining the minimum information flow through a company would assist in building the minimum information model. To build this information flow, an ontology of engineering information would need to be created. This would identify the equivalent information as it passes through the lifecycle. However, first one must identify the information used and created within each workflow.

Applying information science to discovery of requirements has long been needed. The key discovery is that it will remain difficult to use 3D models on the factory floor in the near future. Oftenly, the only computers at machine tools and additive manufacturing equipment on the factory floor are those used as operator interfaces and those will not be used to interrogate models. There are exceptions to this, but this is a concern for those who have not transitioned.

In addition to the shop floor difficulties, LOTAR provides a challenge to implementing MBD. A plan for LOTAR is imperative for MBD because LOTAR was indicated in two of the four workflows as an inhibitor of use of the 3D CAD model as the master definition. LOTAR is a concern when products can be used for extended periods (e.g., 70 or more years in aerospace) and software continues to upgrade. LOTAR was the only indicated inhibitor of 3D CAD models that addresses the CAD tool as not equally capable of delivering the same level of capabilities as a drawing. Developing a business plan for LOTAR before the implementation of a CAD tool must be done to begin model-based definition.

The data collected supports the use of MBD, and minimizing drawing creation to when required and as supplemental material to describe the product definition. The clear majority for data exchange within industry is either a 3D CAD model, a derivative, or a 2D-electronic drawing generated from a three-dimensional model. Industry is at a level where the 3D CAD model becoming the master model would streamline processes and reduce redundancy of product definition. To adequately make this change, industry will need to determine all information used or created in drawings.

Our survey represents a baseline level of information being consumed by the different workflows, but it may not reflect all information that is consumed within each of these workflows. For a company to make the jump from drawings to 3D CAD models, as the master definition, a company should survey its employees to determine the required information used or created within two-dimensional drawings.

Capture of implicit information is a critical first step to convert from the use of two-dimensional drawings. Loss of information during the transition would be detrimental to the production process. Many participants had positive feedback to using models in place of drawings in the other section of the survey, which indicates that it would be beneficial to upgrade to a MBD environment. Some concerns were listed as well, which were grounded in some real issues with the CAD tools, such as data fidelity and compatibility. One respondent indicated that each workflow needs its own defined data requirements to eliminate an information overload.

Industry's evolution from the use of two-dimensional drawings to MBD has begun to take shape. Specific information is emerging as the minimum required data the employee needs to complete his or her tasks. It is imperative that all workflow information is considered when building the minimum information model. Our survey represents a foundation for the requirements of the MIM and supports the hypothesis that 3D CAD models can replace drawings in a production environment. While the common MIM information elements identified by the survey seem clear, it is less certain the impact of the domain-specific influences on the ability of the user to consume the information. Targeting samples from user populations inside specific companies to build the MIM would be more beneficial than the broad scope of the current survey. Capturing all information within specific workflows is difficult when the respondents are not distributed across all positions in the workflows.

A follow-up survey should be undertaken to derive the information elements of the minimum information model. The follow-up survey should focus on narrowing the minimum information model requirements. Each workflow is to be given an abundance of options, possibly even options where the same information is being referenced, but with different terminology, to ensure that they are selecting only information they are using or creating. Inputting control information would also be beneficial to ensure that individuals are thoughtfully selecting data being used and not responding haphazardly. This will shed light onto what the MIM consists of for each workflow. In addition to creating control information, it would be beneficial to force respondents to indicate the information's level of value to them and the necessity of the information to create their data.

This survey would have alternative uses for identifying movement of data through the workflows. One such use would be defining the equivalent or derivatives of data types to identify how data is moving through workflows, as well as where it starts

and stops. This visualization would help create a checklist for defining the medium to carry this information in each lifecycle. The following paragraph details research conducted along this thread.

A follow-on study exploring the minimum information model based on the research conducted in this paper is currently being pursued. A Delphi study was chosen as the most effective approach to detailing the minimum information model. A Delphi study format will allow the consultation of multiple established industry leaders and experts in different fields. This method has provided a connection of information that, while common in nature, differs depending on work sector or job role. The study was done to allow experts to collaborate on the idea of a minimum information model and to help us observe what specific information is required when passing information from one workflow to another

This research helps begin defining the MIM for use in model-based definition practice. More research is required to define the MIM within specific workflows, and follow on research will be necessary to complete the definition of the minimum information model. In addition, this research supports the notion that MBD adoption has begun and models are fully capable of replacing drawings in engineering processes.

ACKNOWLEDGMENTS

We would like to thank Purdue University, the PLM Center of Excellence, and the National Institute of Standards and Technology (NIST) for their support in conducting this research.

The Engineering Laboratory of the National Institute of Standards and Technology (NIST) supported research reported in this paper under the following grants and/or cooperative agreements:

- 70NANB15H311, Purdue University, "Extending and Evaluating the Model-Based product definition"

The contents of this report do not necessarily reflect the views of NIST. NIST and the authors do not make any warranty, expressed or implied, nor assume any legal liability or responsibility for the accuracy, completeness, or usefulness of any information, product, or process included in the reports.

This paper may identify certain commercial systems. Such identification does not imply recommendation or endorsement by NIST. Nor does it imply that the products identified are necessarily the best available for the purpose.

REFERENCES

[1] Bertoline, G. R., Wiebe, E. N., Miller, C. L., & Nasman, L. O. 2005, "Fundamentals of graphics communication." McGraw-Hill.

[2] French, T.E., Svenson, C.L., Helsel, J.D., Urbanick, B., 1990, "Mechanical Drawing: CAD Communications", 11th ed., McGraw-Hill, New York, NY, pp. 26.

[3] Chen, K.-Z., Feng, X.-A. Ding, L., 2002, "Intelligent approaches for generating assembly drawings from 3-D computer models of mechanical products", Computer Aided Design **34** (5), pp. 347–355.

[4] ASME, American Society of Mechanical Engineers, 2003 "Digital Product Definition Data Practices", vol. ASME Y14.41-2003, American Society of Mechanical Engineers, **91** New York, pp. viii.

[5] Camba, J. D., & Contero, M., 2015, "Assessing the Impact of Geometric Design Intent Annotations on Parametric Model Alteration Activities," Computers in Industry, **71**, pp. 35-45.

[6] Dori, D., & Tombre, K., 1995, "From engineering drawings to 3D CAD models: are we ready now?" Computer-Aided Design, **27**(4), 243-254.

[7] Bechky, B. A., 2003, "Object Lessons: Workplace Artifacts as Representations of Occupational Jurisdiction1", American Journal of Sociology, **109**(3), pp. 720-752.

[8] Haight, B., 2003, "New ASME standard for CAD", Automotive Industries AI **183** (10).

[9] Conover, J. S., Zeid, I., 2006, "Development of a prototype for transfer of drawing annotations into the ASME Y14.41 standard", International Mechanical Engineering Congress and Exposition, IMECE2006—Computers and Information in Engineering, American Society of Mechanical Engineers, Chicago, IL, United States, pp. 8.

[10] Morey, B. 2014, "Interpreting the Language of GD&T in Metrology", Manufacturing Engineering, **153**(3), pp. 105-+.

[11] Louhichi, B., & Rivest, L. 2014, "Maintaining consistency between CAD elements in collaborative design using association management and propagation." Computers in Industry, 65(1), 124-135.

[12] Dong, A., & Agogino, A. M. (1998). "Managing design information in enterprise-wide CAD usingsmart drawings", Computer-Aided Design, **30**(6), pp. 425-435.

[13] Adamski, W., 2010, "Adjustment and Implementation of CAD/CAM Systems Being Used in Polish Aviation Industry," Journal of Machine Engineering, **10**(3), pp. 37-47.

[14] Quintana, V., Rivest, L., Pellerin, R., Venne, F., & Kheddouci, F., 2010, "Will Model-based Definition Replace Engineering Drawings throughout the Product Lifecycle? A Global Perspective from Aerospace Industry," Computers in Industry, **61**(5), pp. 497-508.

[15] Hedberg, T., Lubell, J., Fischer, L., Maggiano, L., and Barnard Feeney, A., 2015, "Testing the Digital Thread in Support of Model-Based Manufacturing and Inspection," ASME. Journal of Computing and Information Science in Engineering, 16(2):021001-021001-10.

[16] Versprille K., 2008 “Model-based Definition for the Masses”, Collaborative Product Development Associates, http://store.connectpress.com/product42.html.

[17] SASIG, Strategic Automotive Product Data Standards Industry Group, 2008 “3D Annotated Model Standard”, vol. JAMAEIC042, Japan, pp. 53, http://www.aiag.org/.

[18] Boeing, 2007, “Quality Assurance Standard for Digital Product Definition at Boeing Suppliers”, http://www.boeingsuppliers.com/supplier/D6-51991.pdf (visited on December 12, 2015).

[19] E. Subrahmanian, S. Rachuri, S.J. Fenves, S. Foufou, R.D. Sriram, Product lifecycle management support: a challenge in supporting product design and manufacturing in a networked economy, International Journal of Product Lifecycle Management 1 (1) (2005) 4–25.

[20] A.M. Price, Virtual Product Development Case Study of the T-45 Horizontal Stabilator, vol. 4, AIAA, Reston, VA, USA/Long Beach, CA, USA, 1998, pp. 3041– 3051.

[21] Alemanni, M., F. Destefanis, and E. Vezzetti. "Model-based definition design in the product lifecycle management scenario." *The International Journal of Advanced Manufacturing Technology* 52.1-4 (2011): 1-14.

[22] Liu, F., & Qiao, L. H. (2012, April). Product Information Modeling and Organization with MBD. In *Applied Mechanics and Materials* (Vol. 163, pp. 221-225). Trans Tech Publications.

[23] J. Han, F. P. Zhang, B. Gao, J. Zhang, Y. He, "Unified Product Information Modeling Using Model-Based Definition Technology", Advanced Materials Research, Vols. 591-593, pp. 837-840, 2012.

[24] Camba, J., Contero, M., & Salvador-Herranz, G. (2014). Implementation Challenges of Annotated 3D Models in Collaborative Design Environments. In *Cooperative Design, Visualization, and Engineering* (pp. 222-229). Springer International Publishing.

Identifying High Resource Consumption Supply Chain Points: A Case Study in Automobile Production

Douglas Thomas, Anand Kandaswamy, and Joshua Kneifel

Abstract: The Pareto principle posits that roughly 80 % of a problem is due to 20 % of the causes, allowing for the targeting of specific efficiency solutions. This paper examines whether the resources used in production are consistent with this principle and then seeks to develop a method to identify those supply chain entities that account for a disproportionally high level of resource consumption compared to other supply chain entities. A novel multi-factor approach is used where resources examined include time, cost, labor, environmental impact, and depreciable assets. The method utilizes data from the BEA 2007 Benchmark make and use tables, Annual Survey of Manufactures, Survey of Plant Capacity Utilization, Manufacturing Energy Consumption Survey, RS Means construction cost data, and an environmentally extended Input-Output database for Life Cycle Assessment (LCA). The approach facilitates the identification of economy-wide opportunities for efficiency improvement in manufacturing, a topic that has limited research devoted to it. Those production activities that consume high levels of resources provide a strong opportunity for efficiency improvement, affecting multiple stakeholders. This method is illustrated by examining automobile manufacturing as a case study. The results suggest that the cost distribution is consistent with the Pareto principle where 20 % of supply chain entities account for 89 %, 89 %, and 91 % of value added, labor hours, and environmental impacts from automobile manufacturing, respectively. Additionally, sixteen supply chain entities were above the 90th percentile in value added, environmental impact, and labor hours for automobile manufacturing, implying efficiency improvements could be obtained across multiple resources simultaneously. For those supply chain entities that would, traditionally, be considered a supplier (i.e., those that manufacture intermediate parts, components, and materials as opposed to those that provide services), the environmental impact, flow time, labor hours, and depreciable assets were above the 90th percentile for one supply chain entity and an additional two are above the 80th percentile.

1. Introduction

To achieve economy-wide efficiency improvements, researchers have suggested that "the supply chain must become the focus of policy management, in contrast to the traditional emphasis on single technologies/industries." [1] System-level inefficiencies can result from companies working independently from one another, such as through the "bullwhip effect" where variations in demand are magnified through a supply chain.[2, 3] Another issue lies in the location of supply chain entities. Manufacturers individually decide on the location of production, but individual decisions may not result in an efficient national supply chain arrangement. Firm level analyses of data can also be a source of inefficiencies, as this can hide economy-wide impacts. For example, a firm might conclude that their transportation cost represents a small portion of their total; however, it is reasonable to expect that they would not consider their suppliers' transportation costs included in material purchases. The result is that the true cost of transportation through the manufacturing life-cycle may not be examined at the firm level.

One of the economic benefits of efficiency and productivity improvements in production is long term economic growth and increases in per capita income.[4] The US is among the highest per capita GDP

[1] Tassey, Gregory. "Rationales and Mechanisms for Revitalizing US Manufacturing R&D Strategies." *Journal of Technology Transfer*. 35(2010). 283-333.

[2] Lee, H. L., P. Padmanabhan, and S. Whang. The Bullwhip Effect in Supply Chains. Sloan Management Review. 38 (1997): 93-102.

[3] Bray, Robert L. and Haim Mendelson. Management Science. "Information Transmission and the Bullwhip Effect: An Empirical Investigation." (March 2012): 860-875. http://dx.doi.org/10.1287/mnsc.1110.1467

[4] Weil, David N. Economic Growth. United States: Pearson Education Inc., 2005. 181

countries in the world[5] and to maintain this high level of income, the US must continue to advance efficiency and productivity in its economy. However, as factory level and individual supply chain level efficiency improvements are exhausted, it will become necessary to further examine production issues that span across establishments, industries, and supply chains. As a whole, the US has experienced a slowdown in productivity since 2004, resulting in GDP being $2.7 trillion less than it might be otherwise.[6] With a multitude of products, processes, and activities, a holistic approach will require a systematic method to examine production across these factors. The standard categorization of labor and industry activity combined with Input-output analysis, which was originally developed by economist Wassily Leontief,[7] provides a foundation for such an approach. Input-output models are typically used to estimate the impact of a shift in demand for a good or service, but they also provide information on inter-industry activity, making such models an invaluable resource for industry-by-industry resource use within the US economy.

A frequently invoked axiom posits that roughly 80 % of a problem can be traced to 20 % of the cause(s), a phenomenon referred to as the Pareto principle. [8] This paper examines whether the costs and resources used in production are consistent with Pareto's principle, with a small fraction of the supply chain accounting for most of the resource consumption. It then seeks to advance the identification of those supply chain entities that account for a disproportionally high level of resource consumption. A method is developed and used to examine automobile manufacturing as a case study. Automobile manufacturing represents a large industry with many intermediate parts and components, making it a favorable case study for examining the supply chain. A multi-factor approach is used where five measures of resource consumption are examined: material flow time, cost measured in value added, labor cost, environmental impact, and gross depreciable assets. The statistical dispersion of value added, labor hours by industry, labor hours by occupation, and environmental impacts is measured using the Gini coefficient. The purpose of this approach is to facilitate the identification of economy-wide opportunities for efficiency improvement in manufacturing. Those production activities that consume high levels of resources provide a strong opportunity for efficiency improvement affecting multiple stakeholders. Public entities, trade organizations, and other change agents that seek to maximize efficiency improvement through innovative solutions must prioritize their efforts to get the largest reduction per expenditure dollar. It is important to note that there are a number of factors that are relevant to choosing the most economical investments to improve efficiency. The approach in this paper is a tool for examining one of those factors.

2. Methods

This paper uses input-output data and analysis to examine various aspects of the supply chain for manufacturing. Figure 1 illustrates the supply chain analysis being conducted. Industries are categories of establishments (i.e., physical locations of economic activity) based on the product being produced and the processes being used. Commodities (i.e., products and services) are exchanged between industries and are also delivered to the final consumer. For a particular finished commodity, in this case automobiles, a number of values are estimated: the amount of value added from each industry, the total cost of labor by

[5] World Bank. GDP Per Capita, PPP. 2011-2015. Accessed September 2016. http://data.worldbank.org/indicator/NY.GDP.PCAP.PP.CD?order=wbapi_data_value_2014+wbapi_data_value+wbapi_data_value-last&sort=desc.

[6] Syverson, Chad. "Challenges to Mismeasurement Explanations for the US Productivity Slowdown." National Bureau of Economic Research. Working Paper 21974. Accessed September 2016. http://www.nber.org/papers/w21974

[7] Miller, Ronald E. and Peter D. Blair. Input-Output Analysis: Foundations and Extensions. Second Edition. New York: Cambridge University Press, 2009.

[8] Hopp, Wallace J. and Mark L. Spearman. Factory Physics. Third Edition. Long Grove, IL: Waveland Press, 2008. 674.

occupation, the environmental impact from each industry, the value of associated gross depreciable assets from each industry, and the time it takes for a material to move through an industry (note that this flow time measure is only applicable to industries that handle materials). Flow time and the gross value of depreciable assets relate to the use of capital such as machinery and buildings. These two measures are only available for supply chain entities that are within the manufacturing industry. Thus, industries such as transportation and mining will be examined using value added, labor hours, and environmental impact. Labor is analyzed as the sum of a particular labor category needed from all industries to produce a commodity, in this case automobiles (e.g., the sum of the red labor category from Industry A, B, and C to produce the finished commodity shown in Figure 1). The five measures together identify supply chain entities where multiple types of resources are being consumed at high levels. Below is a description of how the estimates are calculated. The methods in this paper build on those in Thomas and Kandaswamy (2016)[9], Thomas and Kandaswamy (2016)[10], and Thomas and Kneifel (2016).[11]

2.1. Industry Flow Time

Time is an important metric for measuring the use of capital because an increase in the time needed for production increases the necessary capital. This paper does not track the flow of physical goods *directly*, but rather tracks the flow of costs, which parallels the flow of physical goods. [12] This paper uses the term flow time, which might also be referred to as throughput time: the time that elapses between buying raw materials for the production process and selling the finished product.[13]

The calculation for flow time can be thought of as water flowing through a hose into a bucket. The cost of goods sold, $COGS$, is the total amount of water that runs into the bucket over a period of time. The inventory values are the amount of water in the hose at any given time. Since we know the total amount of water that flowed out of the hose (i.e., the amount in the bucket or $COGS$), we can estimate how many times the hose was filled and emptied over that period of time (inventory turns) by dividing the amount in the bucket by the volume of the hose. This method makes the assumption of first-in first-out (FIFO), where the oldest goods on hand are sold first.[14] The proposed method for estimating the sum of the flow time for materials and supplies inventories, work-in-process inventories, and finished goods inventories for a particular NAICS code is:

Equation 1

$$FT_{IND,Total} = \sum_{i=1}^{N} IRR_{IND} \times \frac{\left(INV_{IND,i,BOY} + INV_{IND,i,EOY}\right)/2}{\left(INV_{IND,Total,BOY} + INV_{IND,Total,EOY}\right)/2} \times \frac{365}{TRN_{IND,Total}}$$

[9] Thomas, Douglas and Anand Kandaswamy. "Identifying High Resource Consumption Areas of Assembly-Centric manufacturing in the United States." National Institute of Standards and Technology. White paper. 2016.
[10] Thomas, Douglas and Anand Kandaswamy. "Improving Manufacturing Efficiency through Supply-Chain Flow Time." National Institute of Standards and Technology. White paper. 2016.
[11] Thomas, Douglas and Joshua Kneifel. "Identifying Environmental Impact Hotspots of Assembly-Centric Manufacturing in the US." National Institute of Standards and Technology. White paper. 2016.
[12] Meigs, Robert F. and Walter B. Meigs. Accounting: The Basis for Business Decisions. 9th edition. New York, NY: McGraw-Hill Inc., 1993. 991.
[13] Horngren, Charles T, Walter T. Harrison Jr., Linda Smith Bamber. Accounting. 5th edition. Upper Saddle River, NJ: Prentice Hall, 2002. 773.
[14] Meigs and Meigs, 409.

Where

$FT_{IND,Total}$ = Total estimated flow time for industry IND

i = Inventory item where i is materials and supplies (MS), work-in-process (WIP), or finished goods (FG) inventories.

$INV_{IND,Total,BOY}$ = Total inventory (i.e., materials and supplies, work-in-process, and finished goods inventories) for industry IND at the beginning of the year

$INV_{IND,Total,EOY}$ = Total inventory (i.e., materials and supplies, work-in-process, and finished goods inventories) for industry IND at the end of the year

$TRN_{IND,Total}$ = Inventory turns for industry IND (defined below)

IRR_{IND} = Industry reiteration rate for industry IND (defined below)

The days that a dollar spends in each of the inventory categories is being calculated by taking the total number of days in a year and dividing it by the number of inventory turns TRN, which is the number of times inventory is sold or used in a time period such as a year (see below). This is then multiplied by average inventory of type N divided by the total inventory. The product in the equation is adjusted by an industry reiteration rate IRR, which is an estimate of the number of times a material is processed in one industry (see below). Finally, the summation of all types of inventory is calculated for industry IND. Work-in-process inventories can be broken into two categories: 1) work-in-process and 2) work-in-process downtime when the factory is closed. The analysis of time flow will focus on work-in-process, as this is the time spent on production. This calculation is discussed below.

Inventory Turns: Inventory turns, TRN_{Total}, is the number of times inventory is sold or used in a time period such as a year.[15, 16, 17] It is calculated as the cost of goods sold (COGS), which is the cost of the inventory that businesses sell to customers,[18] divided by the average inventory:

Equation 2

$$TRN_{Total} = \frac{COGS}{\left(\frac{INV_{Total,BOY} + INV_{Total,EOY}}{2}\right)}$$

Where

$COGS = AP + FB + MAT + DEP + RP + OTH + \left(INV_{Total,BOY} - INV_{Total,EOY}\right)$

AP = Annual payroll

FB = Fringe benefits

[15] Horngren, Harrison, Smith, and Bamber, 186.
[16] Stickney, Clyde P. and Paul R. Brown. Financial Reporting and Statement Analysis. Mason, OH: Southwestern, 1999. 136-137.
[17] Hopp and Spearman. 230.
[18] Horngren, Harrison, Smith, and Bamber, 168.

MAT = Total cost of materials

DEP = Depreciation

RP = Rental payments

OTH = Total other expenses

Inventory turns is usually stated in yearly terms and is used to study a number of fields, such as distributive trade, particularly with respect to wholesaling.[19] The data for calculating $COGS$ is from the Annual Survey of Manufactures. In the previous two equations, inventories are calculated using the average of the beginning of year inventories and end of year inventories, which is standard practice.[20]

Industry Reiteration Rate: The reiteration rate is an estimate of the number of times a material is processed in one industry. A material may go through more than one establishment in an industry. For example, a chemical plant could produce chemical A while another plant produces chemical B from chemical A. Both establishments are in the same industry because they both make chemicals, which would mean that the materials were in inventory approximately twice as long as would be calculated using only the inventory data from the Annual Survey of Manufactures (ASM). One can calculate the number of establishments a material goes through before it is diminished below a certain threshold using a logarithmic function with base P, which is the industry reiteration rate:

Equation 3

$$IRR = log_p T$$

Where

IRR = Industry reiteration rate

P = Proportion of materials, parts, containers, packaging, and resales that are purchased

from an establishment in the same industry (defined below).

T = The selected threshold, which is between 0 and 1. The threshold represents the level of P at which it is believed materials would only go through one establishment in that industry; therefore, for values of P that are less than T the industry reiteration rate is 1. A threshold can be selected by examining P values from industries where a product only goes through one establishment in that industry. The threshold would then either be equal to one of those P values or based on them (e.g., average or maximum value). For those industries that are below the threshold, the reiteration rate is simply 1. The result is that the IRR is greater than or equal to one.

Two datasets are used to estimate P: the BEA Benchmark Input-Output Use data and the Annual Survey of Manufactures. The Benchmark Use table provides inter-industry purchases, including the purchases an industry makes from itself. The Annual Survey of Manufactures provides the total cost of materials, parts, containers, and packaging used as well as the cost of resales, which are items purchased and resold without being altered. The inter-industry purchases are divided by the sum of the cost of materials, parts, containers, and packaging used and the cost of resales.[21] This provides P, a proportion of material purchases from the same industry:

[19] Hopp and Spearman. 230.

[20] Horngren, Harrison, and Bamber. 725, 186.

[21] Resales include items bought and sold in the same condition.

Equation 4

$$P = \frac{Purchases\ an\ Industry\ Makes\ from\ Itself}{Materials, Parts, Containers, and\ Packaging + Resales}$$

This is an average proportion of materials purchased from another establishment within the same industry; thus, if P equals 0.3 for industry X, then, on average, an establishment in industry X purchases 30 % of its materials from other establishments in that industry.

The industry reiteration rate makes the basic assumption that establishments in an industry have similar P values because they compete against each other in producing similar products. As a material moves from one establishment to another, a proportion P of the material moves on to an establishment in the same industry. A proportion of that proportion then moves on to another establishment within the same industry. The log function estimates how many of these proportions a material goes through before it is diminished below the selected threshold by estimating to what power P must be raised to equal T. For example, let's say that industry X has a proportion P of 0.50 and one selects a threshold of 0.125. The industry reiteration rate would be:

$$IRR = log_{0.5}0.125 = 3$$

This suggests that, given this threshold, a material is likely to go through around three establishments in industry X, on average.

It must be noted that this is a proxy measure. In order to know the average number of establishments a material travels through, it would be necessary to map the interactions of the hundreds, thousands, and even tens of thousands of establishments in each industry. Such an effort would be technically infeasible; therefore, we must rely on a proxy. Although the industry reiteration rate is not a precise measurement, it creates a multiplier that increases as an industry purchases more goods from itself relative to its purchases from other industries. It also provides a rate that can be compared between industries.

For the analysis, a threshold of 0.03 was selected. Industries that would be expected to go through only 1 establishment tended to have a P value of 0.03 or less. For example, printing is likely to go through only one establishment and had a P value of 0.028. Another example with a value of 0.002 is automobile manufacturing (i.e., assembly), which is an industry that is separate from auto parts production and, therefore, would likely only go through one establishment. The selected threshold should be appropriate for all industries, as it is applied to all the manufacturing industries in the supply chain. As the threshold is lowered the reiteration rate increases; therefore, a higher threshold moves toward assuming that a material moves through fewer establishments while a lower threshold moves toward assuming it moves through more establishments.

Work-in-Process Downtime: Flow time for work-in-process inventories (FT_{WIP}) consists of two components: the time that a good is in work-in-process while the factory is open and the time that a good is in work-in-process while the factory is closed. Separating the two out is useful for understanding where the flow time occurs. The time when the factory is closed can be estimated by multiplying the total flow time for work in process by the ratio of total hours that the plant is open:

Equation 5

$$FT_{WIPD} = \left(1 - \frac{Hr_{Plnt}}{168}\right) \times FT_{WIP}$$

Where:

FT_{WIPD} = Flow time for work-in-process downtime when the factory is closed

Hr_{Plnt} = Average plant hours per week in operation from the quarterly Survey of Plant Capacity Utilization

FT_{WIP} = Flow time for work-in-process

Breaking the flow time for work-in-process into time when the factory is open and closed aids in understanding the activities that are occurring during flow time.

The calculations for tracking flow time, FT, can be made for any individual NAICS code category. Materials flow from establishments in one NAICS code to establishments in another NAICS code. These movements can be traced using Input-Output data from the BEA. The Use table from the BEA Benchmark Input-Output tables provides the items each industry purchases from other industries, which was used to create a supply chain map. This data, however, includes not only the materials, but also the energy, machinery, services, and other items that are not part of the final product. To track the flow time and inventory time from NAICS code to NAICS code, it is necessary to identify only those activities that process materials that are physically part of the final product. To identify these activities, the data from the Use table that applies to manufacturing was extracted by examining the NAICS code descriptions and activities.

2.2. Environmental Impact

The measure of environmental impact is calculated using input-output analysis combined with TRACI 2 impact categories and the Analytical Hierarchy Process to weight the categories. A description of the calculations is below.

Input-Output Analysis: The Make-Use tables are used for Input-Output analysis.[22] The model operates under constant returns to scale and thus ignores potential economies of scale. [23] The model also assumes that a sector uses inputs in fixed proportions. These issues are, typically, relevant to analyses that examine the impact of a change in demand.[24] This paper is not seeking to predict the impact of a change in demand, but rather seeks to track the total resources used for the production of particular goods; therefore, ignoring economies of scale and assuming sectors use inputs in fixed proportions has minimal impact on this analysis. This paper also uses an industry-by-commodity Input-Output format as outlined in Horowitz and Planting (2006), which accounts for the fact that an industry may produce more than one commodity or product, such as secondary products and by-products.[25, 26, 27]

[22] Miller. 135-138.
[23] Ibid., 16.
[24] Horowitz, Karen J. and Mark A. Planting. Concepts and Methods of the US Input-Output Accounts. Bureau of Economic Analysis. September 2006. <http://www.bea.gov/papers/pdf/IOmanual_092906.pdf>
[25] Ibid.
[26] Miller. 184.
[27] European Commission. Eurostat Manual of Supply, Use, and Input-Output Tables. 2008 Edition. 2008. Accessed September 2016. http://ec.europa.eu/eurostat/documents/3859598/5902113/KS-RA-07-013-EN.PDF/b0b3d71e-3930-4442-94be-70b36cea9b39?version=1.0.

An input-output analysis develops a total requirements matrix that when multiplied by the vector of final demands equals the output needed for production. The total requirements matrix is developed using the methods outlined in Horowitz and Planting (2006):

Equation 6

$$X = W(I - BW)^{-1} * Y$$

Where:

$X =$ Vector of output required to produce final demand

$Y =$ Vector of final demand

$W = (I - \hat{p})D$

$B = U\hat{g}^{-1}$

$I =$ Identity matrix

$D = V\hat{q}^{-1}$

$p =$ A column vector in which each entry shows the ratio of the value of scrap produced in each industry to the industry's total output.

$U =$ Intermediate portion of the use matrix in which the column shows for a given industry the amount of each commodity it uses—including noncomparable imports, scrap, and used and secondhand goods. This is a commodity-by-industry matrix.

$V =$ Make matrix, in which the column shows for a given commodity the amount produced in each industry. This is an industry-by-commodity matrix. V has columns showing only zero entries for noncomparable imports and for scrap.

$g =$ A column vector in which each entry shows the total amount of each industry's output, including its production of scrap. It is an industry-by-one vector.

$q =$ A column vector in which each entry shows the total amount of the output of a commodity. It is a commodity-by-one vector.

$\widehat{\ }$ A symbol that when placed over a vector indicates a square matrix in which the elements of the vector appear on the main diagonal and zeros elsewhere.

In Equation 6, a total requirements matrix $W(I-BW)^{-1}$ is multiplied by a vector of final demand for commodities Y to estimate the total output X. All variables in Equation 6 have known values in the input output data. The output X required to produce an alternate level of final demand can be calculated by altering the final demand vector from the actual final demand Y in the input output data to Y'. For this analysis, Y' has the actual final demand for assembly-centric commodities and zero for other commodities. This alteration reveals the output needed to produce only assembly-centric commodities.

Environmental Impact Categories: The TRACI 2 impact categories are each an aggregation of multiple emissions converted to a common physical unit. For example, the global warming impact category includes impacts of many pollutants, such as carbon dioxide (CO_2), methane (CH_4), nitrous oxide (NO_X), and fluorinated gases, which are converted to their carbon dioxide equivalent (CO_2e) impact and aggregated to estimate the total impact for that impact category. The environmental impacts are measured in terms of the common physical unit per dollar of output. The impact can be calculated by multiplying the output in the Input-Output analysis by the impact categories.

Impact Category Weights: Having 12 environmental impact categories makes it difficult to rank industry environmental activity; therefore, the 12 impact categories have been combined into a single environmental metric using the Analytical Hierarchy Process (AHP). AHP is a mathematical method for developing weights using normalized eigenvalues. It involves making pairwise comparisons of competing items based on a multilevel hierarchy developed by the user. The weights used in this paper were developed for the BEES software and can be seen in Table 1.[28] This paper uses 12 of the 13 impact categories for which weights were developed. Indoor Air Quality (IAQ) is excluded because it is more applicable to the design of buildings and ventilation systems rather than to manufacturing activities. The weight of IAQ is proportionally allocated to the other 12 impact categories. The final metric for each industry or industry/commodity combination is the proportion of the total impact from assembly-centric products. The percent of environmental impacts, based on the weights, are calculated using the following equation:

Equation 7

$$
\begin{aligned}
Env_{z,Y'} = {} & \frac{x_{z,Y'} * GWP_z}{\sum_{i=1}^{n} x_{i,Y'} * GWP_i} * 0.30 + \frac{x_{z,Y'} * Acid_z}{\sum_{i=1}^{n} x_{i,Y'} * Acid_i} * 0.03 + \frac{x_{z,Y'} * HHA_z}{\sum_{i=1}^{n} x_{i,Y'} * HHA_i} * 0.09 \\
& + \frac{x_{z,Y'} * Eut_z}{\sum_{i=1}^{n} x_{i,Y'} * Eut_i} * 0.06 + \frac{x_{z,Y'} * OD_z}{\sum_{i=1}^{n} x_{i,Y'} * OD_i} * 0.02 + \frac{x_{z,Y'} * Sm_z}{\sum_{i=1}^{n} x_{i,Y'} * Sm_i} * 0.04 \\
& + \frac{x_{z,Y'} * Eco_z}{\sum_{i=1}^{n} x_{i,Y'} * Eco_i} * 0.07 + \frac{x_{z,Y'} * HHC_z}{\sum_{i=1}^{n} x_{i,Y'} * HHC_i} * 0.08 + \frac{x_{z,Y'} * HHNC_z}{\sum_{i=1}^{n} x_{i,Y'} * HHNC_i} * 0.05 \\
& + \frac{x_{z,Y'} * PE_z}{\sum_{i=1}^{n} x_{i,Y'} * PE_i} * 0.10 + \frac{x_{z,Y'} * LU_z}{\sum_{i=1}^{n} x_{i,Y'} * LU_i} * 0.06 + \frac{x_{z,Y'} * WC_z}{\sum_{i=1}^{n} x_{i,Y'} * WC_i} * 0.08
\end{aligned}
$$

Where

$Env_{z,Y'} =$ Environmental impact from industry z for final demand Y'

$GWP_z =$ Global warming potential per dollar of output for industry z

[28] Lippiatt, Barbara, Anne Landfield Greig, and Priya Lavappa. Building for Environmental and Economic Sustainability. National Institute of Standards and Technology. 2010. Accessed September 2016. http://www.nist.gov/el/economics/BEESSoftware.cfm.

$Acid_z =$ Acidification per dollar of output for industry z

$HHA_z =$ Human health –criteria air pollutants – per dollar of output for industry z

$Eut_z =$ Eutrophication per dollar of output for industry z

$OD_z =$ Ozone depletion per dollar of output for industry z

$Sm_z =$ Smog per dollar of output for industry z

$Eco_z =$ Ecotoxicity per dollar of output for industry z

$HHC_z =$ Human health – carcinogens – per dollar of output for industry z

$HHNC_z =$ Human health – non-carcinogen – per dollar of output for industry z

$PE_z =$ Primary energy consumption per dollar of output for industry z

$LU_z =$ Land use per dollar of output for industry z

$WC_z =$ Water consumption per dollar of output for industry z

$x_{z,Y'} =$ Output for industry z with final demand Y'

Energy: One challenge with examining the impacts of manufacturing by industry is that energy impacts become disaggregated into multiple industries such as mining, transportation, and electricity generation. However, an efficiency improvement in energy use within a factory has immediate implications for the impact associated with energy and its supply chain; therefore, energy should be treated as a single unit rather than disaggregated entities. To address this issue, an estimate of the aggregated impacts of energy is examined by altering the final demand vector Y in Equation 6 to the final demand vector Y'' where the final demand for "*electric power generation, transmission, and distribution"* is equal to 1 and demand for all other commodities in the final demand vector Y'' is set to zero. This allows us to calculate the environmental impacts from each industry to produce a unit of impact from assembly-centric manufacturing:

Equation 8

$$Env_{z,Y''} = \frac{x_{z,Y''} * GWP_z}{\sum_{i=1}^{n} x_{i,Y'} * GWP_i} * 0.30 + \frac{x_{z,Y''} * Acid_z}{\sum_{i=1}^{n} x_{i,Y'} * Acid_i} * 0.03 + \frac{x_{z,Y''} * HHA_z}{\sum_{i=1}^{n} x_{i,Y'} * HHA_i} * 0.09$$
$$+ \frac{x_{z,Y''} * Eut_z}{\sum_{i=1}^{n} x_{i,Y'} * Eut_i} * 0.06 + \frac{x_{z,Y''} * OD_z}{\sum_{i=1}^{n} x_{i,Y'} * OD_i} * 0.02 + \frac{x_{z,Y''} * Sm_z}{\sum_{i=1}^{n} x_{i,Y'} * Sm_i} * 0.04$$
$$+ \frac{x_{z,Y''} * Eco_z}{\sum_{i=1}^{n} x_{i,Y'} * Eco_i} * 0.07 + \frac{x_{z,Y''} * HHC_z}{\sum_{i=1}^{n} x_{i,Y'} * HHC_i} * 0.08 + \frac{x_{z,Y''} * HHNC_z}{\sum_{i=1}^{n} x_{i,Y'} * HHNC_i} * 0.05$$
$$+ \frac{x_{z,Y''} * PE_z}{\sum_{i=1}^{n} x_{i,Y'} * PE_i} * 0.10 + \frac{x_{z,Y''} * LU_z}{\sum_{i=1}^{n} x_{i,Y'} * LU_i} * 0.06 + \frac{x_{z,Y''} * WC_z}{\sum_{i=1}^{n} x_{i,Y'} * WC_i} * 0.08$$

From Equation 8, the indirect impact of electricity (i.e., the impact from other industries such as mining and transportation associated with electricity production) per percentage point of direct impact can be estimated:

Equation 9

$$IIPP_E = \frac{\left[\sum_{i=1}^{n} Env_{z,Y''}\right] - Env_{E,Y''} - Env_{Nat,Y''}}{Env_{E,Y''}}$$

Where

$IIPP_E =$ Indirect Impact per percentage point of direct impact from "*electric power generation, transmission, and distribution"*

$Env_{E,Y''} =$ Environmental impact from the "*electric power generation, transmission, and distribution"* for final demand Y''

$Env_{Nat,Y''} =$ Environmental impact from the "*natural gas distribution*" for final demand Y''

A similar calculation can be made for natural gas where final demand for Y'' is set to 1 for "*natural gas distribution*" and zero for all other commodities:

Equation 10

$$IIPP_{Nat} = \frac{\left[\sum_{i=1}^{n} Env_{z,Y''}\right] - Env_{E,Y''} - Env_{Nat,Y''}}{Env_{Nat,Y''}}$$

Where

$IIPP_{Nat} =$ Indirect Impact per percentage point of direct impact from natural gas

Equation 9 and Equation 10 calculate and parse out the indirect impacts of the energy consumed from the production of assembly-centric manufacturing while incorporating the weights previously discussed.

An additional issue with energy is that it is associated with completely different types of processes and purposes. Some energy is used for heating and cooling of buildings while other energy is used for operating machinery. Grouping these together masks the source of energy consumption. The BEA Input-Output data provides estimates of energy use; however, it does not provide the detail in how the energy is used, which would allow for a more targeted approach to addressing energy efficiency improvements. In order to better understand energy use, the Manufacturing Energy Consumption Survey (MECS) was used to separate the BEA energy data into use categories to show both the quantity of energy consumption as well as the purpose for which the consumption occurs. The energy use categories provided include: *indirect uses-boiler fuel*, *process heating*, *process cooling and refrigeration*, *machine drive*, *electro-chemical processes*, *other process use, facility HVAC, facility lighting*, *facility support*, *onsite transportation*, *other non-process use*, and *end use not reported*. Electric power generation, transmission, and distribution from the BEA data is broken into these categories by portioning out coal mining, electricity generation, and natural gas distribution by proportions calculated from the Energy Information Administration (EIA). The MECS data and BEA data both have varying levels of NAICS code aggregation. The MECS data can be aggregated up when it is more detailed than the BEA data. When the BEA data is more detailed it is assumed that the proportions remain the same for the detailed NAICS codes. This issue illustrates the need for advanced coordination between data collection entities.

2.3. Value Added

The total requirements matrix $W(I - BW)^{-1}$ from Equation 6, which shows the total output required to meet a given level of final demand, is multiplied by final demand in the input-output data to estimate the

total output. The output required to produce a particular level of final demand can be calculated by altering final demand to Y'. For this analysis, Y' equals final demand for those NAICS codes representing assembly-centric products and zero for those that do not, making this an examination of assembly-centric products and their supply chains.

Value added is calculated by assuming the proportion of output needed to produce a commodity is the same proportion of value added, which is consistent with methods proposed by Miller (2009). The proportions calculated using the input-output analysis are then multiplied by the value added and scaled to 2014 dollars using the estimate of gross output for that year:

Equation 11

$$VA_{z,Y',2014} = \frac{x_{z,Y',2007}}{x_{z,2007}} * VA_{z,2007} * \left(\frac{x_{z,2014}}{x_{z,2007}}\right)$$

Where

$VA_{z,Y',2014}$ = Value added from industry z with final demand Y' in 2014

$x_{z,2007}$ = Total output for industry z in 2007

$x_{z,2014}$ = Total output for industry z in 2014

$x_{z,Y',2007}$ = Output for industry z with final demand Y' in 2007

$VA_{z,2007}$ = Total value added from industry z in 2007

Imports are calculated in a similar fashion, where the proportion of total output used from a particular industry is the same for imports.

Energy Analysis: Similar to the environmental analysis, value added was broken into energy use categories including: *indirect uses-boiler fuel*, *process heating*, *process cooling and refrigeration*, *machine drive*, *electro-chemical processes*, *other process use*, *facility HVAC*, *facility lighting*, *facility support*, *onsite transportation*, *other non-process use*, and *end use not reported*.

2.4. Labor

In order to examine labor activity, Bureau of Labor Statistics employment data from the Occupational Employment Statistics is matched with the BEA IO NAICS categories. For this analysis, the Bureau of Labor Statistics employment data has been mapped to the detail level found in the 2007 Benchmark Input-Output data. In instances where the NAICS codes for the occupation data did not match that of the input-output data, the values were estimated. When the BEA data had a NAICS code at a lower level of detail than the occupation data, the occupation data was aggregated up to the BEA level of detail. If the occupation data was at a lower level of detail, then the BEA levels were estimated by assuming the proportion of the cost of compensation in the BEA was the same as that for employment. This provides an estimate of occupational employment by industry at the NAICS level of detail. To estimate the hours of labor, these estimates are multiplied by the average hours per week for each occupation and by the total weeks per year. These hours are then multiplied by wages per hour and adjusted to match the BEA estimates of compensation assuming the BEA proportions of labor are the same as that calculated using BLS data. When examining a specific product commodity such as automotive manufacturing, the input-

output calculations are used to estimate the output from each industry required to produce the given product. The proportion of the total output needed from each industry is multiplied by the occupational employment for each industry to estimate the amount of labor, which is consistent with methods proposed in Miller (2009). The result is a matrix of the amount of labor needed, categorized by NAICS by occupation, to produce the relevant commodity.

Equation 12

$$C_{z,s,Y'} = \frac{x_{z,Y'}}{x_z} * C_{z,s,} * \left(\frac{E_{z,s} * LH_s * W_{z,s}}{\sum_{i=1}^{n} E_{z,i} * LH_s * W_{z,i}} \right) * \left(\frac{x_{z,2014}}{x_{z,2007}} \right)$$

Where

$C_{z,s,Y'} =$ Compensation for occupation s in industry z with final demand Y'

$C_{z,s,} =$ Total compensation for occupation s in industry z

$x_z =$ Total output for industry z

$x_{z,Y'} =$ Output for industry z with final demand Y'

$E_{z,s} =$ Employment for industry z and occupation s

$LH_s =$ Labor hours per employee for occupation s

$W_{z,s} =$ Hourly wages per employee for industry z and occupation s

2.5. Gross Value of Depreciable Assets

Depreciable assets are measured in a similar fashion to labor. The proportion of output estimated from the input-output calculations is multiplied by the total depreciable assets for that industry, resulting in an estimate of depreciable assets utilized for the production of the commodity being examined. An estimate for buildings and machinery/equipment is made by utilizing RS Means data. The total square footage of manufacturing space from the Manufacturing Energy Consumption survey is multiplied by the average construction cost per square foot from RS Means. This is assumed to be the buildings share of depreciable assets with the remaining amount assumed to be machinery/equipment:

Equation 13

$$DB_{z,Y'} = \frac{x_{z,Y',2007}}{x_{z,T,2007}} * (SF_z * RM)$$

Equation 14

$$DM_{z,Y'} = \left[\frac{x_{z,Y',2007}}{x_{z,T,2007}} * DA_z \right] - DB_{z,Y'}$$

Where

$DB_{z,Y',MB} =$ Depreciable building assets from industry z associated with final demand Y' in 2014

$DM_{z,Y'}$ = Depreciable machinery assets from industry z associated with final demand Y' in 2014

$x_{z,T,2007}$ = Total output for industry z in 2007

$x_{z,Y',2007}$ = Output for industry z with final demand Y' in 2007

SF_z = Estimated square feet of manufacturing floor space for industry z

RM = RS Means estimated construction cost per square foot of manufacturing floor space

DA_z = Gross value of depreciable assets (end of year) from the annual survey of manufactures

A similar calculation is made for the purchase of new and used capital assets, where the proportion of output estimated from the input-output calculations is multiplied by the value of new and used capital assets purchased.

Equation 15

$$CE_{z,Y',MB} = \frac{x_{z,Y',2007}}{x_{z,T,2007}} * CE_{MB}$$

Where

$CE_{z,Y',MB}$ = Capital expenditures by industry z with final demand Y' on MB, where MB is either machinery or buildings

$x_{z,T,2007}$ = Total output for industry z in 2007

$x_{z,Y',2007}$ = Output for industry z with final demand Y' in 2007

$CE_{z,MB}$ = Total capital expenditures by industry z on MB, where MB is either machinery or buildings

3. Data

There are a number of datasets needed to examine costs, environmental impacts, time flow, and capital. These datasets include the Annual Survey of Manufactures from the US Census Bureau, the Economic Census from the US Census Bureau, the Bureau of Economic Analysis (BEA) Benchmark Input-Output data, environmentally extended input-output data, Occupational Employment Statistics from the Bureau of Labor Statistics, Energy Consumption Survey from the Energy Information Administration, and RS Means cost data. These datasets are described below.

Input-Output Data: Every five years the BEA computes benchmark input-output tables, which tends to have over 350 industries.[29] The data is provided in the form of make and use tables, with their corresponding matrices replacing the Leontief method. [30] In the US, industries are categorized by NAICS codes. There are two types of make and use tables: "standard" and "supplementary." Standard tables closely follow NAICS and are consistent with other economic accounts and industry statistics, which classify data based on establishment. Note that in this context an "establishment" is a single physical

[29] Bureau of Economic Analysis. Input-Output Accounts Data. November 2014. Accessed September 2016. http://www.bea.gov/industry/io_annual.htm.

[30] A System of National Accounts, Studies in Methods, Series F/No. 2/Rev. 3, New York, United Nations, 1968.

location where business is conducted. This should not be confused with an "enterprise" such as a company, corporation, or institution. Establishments are classified into industries based on the primary activity within the NAICS code definitions; however, establishments often have multiple activities. An establishment is classified based on its primary activity. Data for an industry reflects all the products made by the establishments within that industry; therefore, secondary products are included. Supplementary make-use tables reassign secondary products to the industry in which they are primary products. The data in this report utilizes the standard make-use tables.

Manufacturing Data: The Annual Survey of Manufactures (ASM) is conducted every year except for when the Economic Census is conducted (i.e., years ending in 2 or 7). The ASM provides statistics on employment, payroll, supplemental labor costs, cost of materials consumed, operating expenses, value of shipments, value added, fuels and energy used, and inventories. The Economic Census, used for years ending in 2 or 7, is a survey of all employer establishments in the US that has been taken as an integrated program at 5-year intervals since 1967. Both the ASM and the Economic Census use NAICS classifications. The inventory data from the Economic Census and Annual Survey of Manufactures is broken into materials inventory, work-in-process inventory, and finished goods inventory. It is important to note that a finished product for an establishment in one industry might be reported as a raw material by an establishment in a different industry. For example, the finished product inventories of a steel mill might be included in the material inventories of a stamping plant. The inventory data does not have a breakout for transport time or down time; therefore, other data must be used for these purposes.

Data on Plant Hours: In order to estimate the work-in-process downtime (i.e., the time that materials are in work-in-process, but the plant is closed) one can employ data from the Survey of Plant Capacity Utilization. This data provides quarterly statistics on the rates of capacity utilization for the US manufacturing industry by NAICS code. In addition to providing capacity utilization, it also provides data on the average plant hours per week in operation for an industry.[31]

Environmental Data: For environmental data, this paper applies a suite of environmentally extended Input-Output databases for Life Cycle Assessments (LCA) developed under contract for NIST by Dr. Sangwon Suh of the Bren School of Environmental Science and Management at the University of California, Santa Barbara.[32] This data has been utilized in a number of environmental efforts, including NIST's Building for Environmental and Economic Sustainability (BEES)[33] and Building Industry Reporting and Design for Sustainability (BIRDS)[34] software and related publications. This data utilizes the 12 TRACI 2 impact categories: global warming potential, primary energy consumption, human health – criteria air pollutants, human health – carcinogens, water consumption, ecological toxicity[35], eutrophication[36], land use, human health – non-carcinogens, smog formation, acidification, and ozone depletion. The units of measurement are provided in Table 1. This environmental data is organized by 2002 BEA codes for the Benchmark Input-Output tables, and matched and adjusted to the 2007 BEA Input-Output tables. The environmental data was adjusted from being in impact units per 2002 dollars to impact units per 2007 dollars using the consumer price index from the Bureau of Labor Statistics.

[31] US Census Bureau. Survey of Plant Capacity Utilization: How the Data are Collected. Accessed September 2016. http://www.census.gov/manufacturing/capacity/how_the_data_are_collected/.

[32] This work is based on Suh, S. Developing a sectoral environmental database for input-output analysis: the comprehensive environmental data archive of the US, Economic Systems Research. 17: 4(2005): 449-469.

[33] National Institute of Standards and Technology. Building for Environmental and Economic Sustainability. Accessed September 2016. http://www.nist.gov/el/economics/BEESSoftware.cfm.

[34] National Institute of Standards and Technology. Building Industry Reporting and Design for Sustainability. Accessed September 2016. https://birdscom.nist.gov/.

[35] The potential of a chemical released into the environment to harm terrestrial and aquatic ecosystems.

[36] The addition of mineral nutrients to the soil or water, which in large quantities can result in generally undesirable shifts in the number of species in ecosystems and a reduction in ecological diversity

Labor Data: The Bureau of Labor Statistics maintains an Occupational Employment Statistics (OES) program, which produces employment and wage estimates using the Standard Occupational Classification System and NAICS. The OES categorizations includes over 800 occupations and over 450 industries; however, archived data covers fewer industries (Bureau of Labor Statistics). The data is gathered through surveys and covers full-time and part-time wage and salary workers in nonfarm industries. The self-employed, owners and partners in unincorporated firms, household workers, or unpaid family workers are not covered in the survey. The data is available for the nation as a whole as well as by state, metropolitan area, and nonmetropolitan area. The OES surveys approximately 200 000 establishments every six months on a three-year survey cycle that results in 1.2 million establishments being surveyed. The data is provided by NAICS codes and by the Standard Occupational Classification System. Two industry categories of labor data were not available to be broken out: construction and agriculture. However, the costs of this labor are included in the capital purchases and industry purchases categories.

Energy Data: The Energy Information Administration collects energy data through the Manufacturing Energy Consumption Survey (Energy Information Administration). It is conducted on a quadrennial basis and samples approximately 15 500 establishments drawn from a nationally representative sample frame that includes 97 % to 98 % of the manufacturing payroll. Energy data is categorized by the NAICS codes and end use. For this analysis it is used to break the input-output data into more specific categories. This survey also provides the square footage of manufacturing floor space by NAICS code. This value is used to estimate the construction value of the buildings that house manufactured goods.

Depreciable Assets Data: In years ending in 2 or 7 the Economic Census is conducted, which is a survey of all employer establishments in the US where the response is required by law. It has been taken as an integrated program at 5-year intervals since 1967. Both the ASM and the Economic Census use NAICS classification; however, prior to NAICS the Standard Industrial Classification system was used. The Economic Census sent out nearly 4 million forms to businesses representing all US locations and industries. Four items from this data is used in this paper: gross depreciable assets, retirements, capital expenditures on buildings, and capital expenditures on machinery.

Building Data: RS Means provides data on construction costs for a range of building types and components. The cost per square foot of factory construction was used to estimate the value of constructed buildings housing manufacturing activity (RS Means 2005).

4. Results and Discussion

This paper develops a methodology using input-output data and analysis combined with other industry data to examine whether resources are disproportionally consumed in the production of a particular finished commodity, in this case automobiles, and if so, what activities account for this higher consumption. This case study provides a proof of concept in examining national level production for advancing efficiency in other manufacturing industries. The approach considers five measures of resource consumption: the amount of value added from each industry, the total cost of labor by occupation, the environmental impact from each industry, the value of associated gross depreciable assets, and the time it takes for a material to move through an industry (note that this flow time measure is only applicable to industries that handle materials). Flow time and the gross value of depreciable assets relate to the use of capital such as machinery and buildings. These two measures are only available for supply chain entities that are within the manufacturing industry; therefore, industries such as transportation and mining were examined using value added, labor hours, and environmental impact. Since this paper focuses on the distribution of resource consumption, the results are presented in terms of the percent of the total consumption of a particular resource and also in terms of percentile where the largest categories of consumption are among the highest percentile.

As seen in Figure 2, the results show that the consumption of resources is consistent with Pareto's principle where 20 % of the cause represents greater than 80 % of the resource consumption. That is, a

subset of supply chain entities represents a disproportional amount of the resource consumption. The results show that 20 % of supply chain entities account for 89 %, 89 %, and 91 % of value added, labor hours, and environmental impacts from automobile manufacturing, respectively. Improving the efficiency in these areas of the supply chain would lead to disproportional reductions in the resources needed for production. The distribution of value added, labor hours by industry, labor hours by occupation, and environmental impacts are such that they have a Gini coefficient of 0.87, 0.86, 0.86, and 0.87, respectively. The Gini coefficient is a measure of statistical dispersion where 0 represents equal distribution (i.e., each cost category represents the same proportion of total cost) and 1 represents total unequal distribution.

The results by industry for value added, labor hours, and environmental impact are shown in Table 2, Table 3, and Table 4, respectively. Each are categorized by industry NAICS code, which are categories of establishments, as illustrated in Figure 1. Table 2 shows that the final assembly of the automobile (NAICS 336111) is approximately 17 % of the total cost measured in value added, which means that nearly 83 % of the costs occur throughout establishments in the supply chain. "Wholesale trade" is the next highest (7.7 %) with sales people from this industry being a significant contributor (not shown). The 3rd, 4th, and 5th ranked supply chain entities are automobile parts industries (engine parts (336310), transmission and power train parts (336350), and other automotive parts (336390)). The "management of companies and enterprises" (e.g., company headquarters) is ranked 6th, which emphasizes the cost of operating large automobile manufacturing companies. These top 6 industries account for 45.6 % of the value added.

Labor hours in Table 3, Figure 3, and Table 6 are categorized by industry NAICS code; thus, it is the total labor occurring at categories of establishments. Labor is also categorized by occupation, as seen in Table 5. In terms of labor hours by industry, the final assembly (NAICS336111) (18.0 %), "wholesale trade" (9.5 %), and the "management of companies and enterprises" (5.6 %) activities are the largest consumers of labor. Moreover, these categories of establishments account for a larger proportion of labor hours than other categories of establishments in the supply chain. In terms of labor hours by occupation, "team assemblers" (14.5 %), "laborers and freight, stock, and material movers" (2.7 %), and "machinists" (2.5 %) are the largest contributors while five additional occupations account for 2.0 % to 2.5 % each and 16 account for 1.0 % to 2.0 %. These are the sum of labor hours throughout the supply chain for each occupation. If we recall the supply chain illustration in Figure 1, our approach is similar to summing the total labor hours in each industry for a particular occupation required to produce the finished commodity. Using either approach to categorize labor hours, labor is more broadly distributed across the supply chain than the value added.

Environmental impacts are categorized by industry NAICS codes. In terms of environmental impacts (Table 4), "automobile manufacturing" (22.0 %), "iron and steel mills and ferroalloy manufacturing" (6.3 %), "electricity and natural gas" (4.9 %), and "glass and glass product manufacturing (4.8 %) are the four largest contributors. Moreover, these categories of establishments account for a larger proportion of environmental impacts than other categories in the supply chain for automobile manufacturing.

Many of the same industries account for large fractions of value added, labor, and environmental impacts. Figure 3 and Table 6 identify those items that are above the 80th percentile for labor hours, environmental impact, and value added (i.e., those items that appear in Table 2, Table 3, and Table 4). There are 6 items that appear above the 95th percentile for all categories and 16 total items above the 90th percentile. "Electricity and natural gas" for all purposes (NAICS 2121, 2211, 2212) along with "glass and glass product manufacturing" (NAICS 327200), "iron and steel mills and ferroalloy manufacturing" (NAICS 331110), "automobile manufacturing" (NAICS 336111), "wholesale trade" (NAICS 420000), and "truck transportation" (NAICS 484000) were above the 95th percentile for all three measures. These establishment categories (i.e., NAICS codes), consume a disproportional amount of resources compared to other establishments in the automobile supply chain.

In addition to "Iron and steel mills and ferroalloy manufacturing" (NAICS 331110) being above the 95th percentile, a number of other metal and steel categories appear above the 90th percentile in all three measures, including "steel product manufacturing from purchased steel" (NAICS 331200), "ferrous metal foundries" (NAICS 331510), and "nonferrous metal foundries" (NAICS 331520). The high ranking of these metal and steel oriented categories emphasizes that the efficient use of steel can have a high impact on multiple resource measures relating to multiple stakeholders. There may also be opportunities for efficiency improvement in the use of metal and steel, as it is estimated that more than a quarter of steel is scrapped in the production process.[37] A number of entities have made this deduction and are focusing their research efforts on these efficiency improvements. For example, the National Institute of Standards and Technology has an automotive lightweighting group that examines these issues. The US Geological Survey estimates that 15 % of steel is scrapped when steel is cut, drawn, extruded, or machined.[38]

"Truck transportation" (NAICS 484000) appeared above the 95th percentile and "rail transportation" (NAICS 482000) appeared above the 90th percentile for all three measures. Additionally, "laborers and freight, stock, and material movers, hand" (SOC 537062) was the second largest labor occupation category in Table 5 and "heavy and tractor-trailer truck drivers" (SOC 533032) was 7th. The appearance of these items emphasizes that efficiency improvements in transportation throughout the supply chain can have a high impact on multiple resource categories relating to multiple stakeholders. There might be opportunities for efficiency improvement in this area, as approximately 20 % of truck miles are driven with no product being transported,[39]. Reducing these empty miles would decrease labor, capital expenditures, and traffic. Several methods are being considered across the global economy to reduce these excess miles. In Germany, a new auction platform aims to improve truck space utilization.[40] Other efforts to co-load or ride-share have also received some attention. Innovative solutions like these might reduce the resources consumed in the transport of goods.

As previously mentioned, "wholesale trade" (NAICS 420000) appears above the 95th percentile for all three categories. Wholesalers sell or arrange the purchase/sale of goods to other businesses from a warehouse or office. Customers are, generally, reached through in-person communication, which might explain why "sales representatives" (SOC 414012) and "sales representatives, wholesale/manufacturing, technical/scientific products" (SOC 414011) are ranked 5th and 45th in labor hours in Table 5.[41] Advancing the dissemination of information on intermediate products might reduce the sales burden needed for distributing intermediate parts and components to producers. In addition to sales activity, wholesalers function as a warehouse to store inventory. Additional warehousing costs are categorized as "warehousing and storage" (NAICS 493000), which is above the 80th percentile in cost (Table 2), and labor hours (Table 3). Warehouses are needed to buffer for unpredictable fluctuations in demand. Improved forecasting in demand might lessen the need for inventory/warehousing and in turn reduce wholesale trade costs.

Figure 4 and Table 7 show manufacturing industries above the 70th percentile for environmental impact, flow time, labor hours, value added, and depreciable assets for automobile manufacturing. Figure 4 and Table 7 select supply chain entities only from establishments categorized as manufacturing entities that

[37] Allwood, Julian M and Jonathan M Cullen. Sustainable Materials with Both Eyes Open. UIT Cambridge Ltd. 2012. Accessed January 2017. http://www.withbotheyesopen.com/index.html.
[38] Fenton, Michael D. "Iron and Steel Recycling in the United States in 1998." US Geological Survey. 3. Accessed January 2017. https://pubs.usgs.gov/of/2001/of01-224/.
[39] Bureau of Transportation Statistics, US Department of Transportation. Freight Facts and Figures 2015. Table 3-11 page 41. Accessed January 2017. https://www.rita.dot.gov/bts/sites/rita.dot.gov.bts/files/FFF_complete.pdf.
[40] Science Daily. "Ride-Sharing for Road Freight." Accessed January 2017. https://www.sciencedaily.com/releases/2011/04/110406132022.htm.
[41] US Census Bureau. North American Industry Classification System. Accessed January 2017. http://www.census.gov/eos/www/naics/.

handle intermediate components. These are the establishments that would, typically, be considered by a manufacturer to be a supplier. Other establishments categorized as non-manufacturing (e.g., management of companies and enterprises) are, therefore, not included. The 70th percentile is used, as there are very few industries where all five measures are above the 80th percentile. "Iron and steel mills and ferroalloy manufacturing" (NAICS 331110) is the only manufacturing supply chain entity that is above the 90th percentile for all five factors shown in Table 7. Only two additional items are at or above the 80th percentile: "other electronic component manufacturing" (NAICS 33441A) and "copper rolling, drawing, extruding and alloying" (NAICS 331420). These are the high resource consumption entities among those that would, typically, be considered a supplier.

5. Summary

This paper examines whether the resources used in the production of a specific commodity are consistent with the Pareto principle, and advances the identification of those supply chain entities that account for a disproportionally high level of resource consumption by examining automobile manufacturing as a case study. A multi-factor approach is used where the time, cost, labor, environmental impact, and depreciable assets are examined to facilitate the identification of economy-wide opportunities for efficiency improvement in manufacturing. Those production activities that consume high levels of resources across the different measures provide a strong opportunity for efficiency improvements affecting multiple stakeholders. The results suggest that the cost distribution is consistent with the Pareto principle where 20 % of the industries in the supply chain represent greater than 80 % of the total resource consumption. The data show that 20 % of supply chain entities account for 89 %, 89 %, and 91 % of value added, labor hours, and environmental impacts from automobile manufacturing, respectively. Six industries were above the 95th percentile in value added, environmental impact, and labor hours for automobile manufacturing while an additional 10 are above the 90th percentile. "Electricity and natural gas" for all purposes (NAICS 2121, 2211, 2212) along with "glass and glass product manufacturing" (NAICS 327200), "iron and steel mills and ferroalloy manufacturing" (NAICS 331110), "automobile manufacturing" (NAICS 336111), "wholesale trade" (NAICS 420000), and "truck transportation" (NAICS 484000) were above the 95th percentile for all three measures. Transportation, steel, sales, and warehousing appear in multiple ways (i.e., labor categories, industry categories, and different resource types) and there might be opportunities for efficiency improvement in these areas. For instance, for 20 % of the miles driven for truck transportation the truck is empty and more than a quarter of steel ends up as scrap, resulting in even more transportation.

For those supply chain entities that handle intermediate parts and components (i.e., the entities that would, traditionally, be considered suppliers), the environmental impact, time, labor hours, and depreciable assets were examined. One item is above the 90th percentile in all five categories, "Iron and steel mills and ferroalloy manufacturing" (NAICS 331110). This category also appeared in Figure 3, which is consistent with steel having a disproportional impact on multiple resource types. An additional two items are above the 80th percentile: "other electronic component manufacturing" (NAICS 33441A) and "copper rolling, drawing, extruding and alloying" (NAICS 331420). The areas identified in this paper as being above the 80th percentile in the consumption of multiple resource types provide strong opportunities for efficiency improvements that impact multiple stakeholders. Reducing resource consumption in these select areas will have a disproportional impact on total resource consumption, including costs and natural resources consistent with Pareto's Principle.

Bibliography

A System of National Accounts, Studies in Methods, Series F/No. 2/Rev. 3, New York, United Nations, 1968.

Allwood, Julian M. and Jonathan M Cullen. Sustainable Materials with Both Eyes Open. UIT Cambridge Ltd. 2012. Accessed January 2017. http://www.withbotheyesopen.com/index.html.

Block, Fred L. and Matthew R. Keller. State of Innovation: The US Government's Role in Technology Development. New York, NY: Taylor & Francis, 2016.

Bray, Robert L. and Haim Mendelson. Management Science. "Information Transmission and the Bullwhip Effect: An Empirical Investigation." (March 2012): 860-875. http://dx.doi.org/10.1287/mnsc.1110.1467

Bureau of Economic Analysis. Input-Output Accounts Data. November 2014. Accessed September 2016. http://www.bea.gov/industry/io_annual.htm.

Bureau of Transportation Statistics, US Department of Transportation. Freight Facts and Figures 2015. Table 3-11 page 41. Accessed January 2017. https://www.rita.dot.gov/bts/sites/rita.dot.gov.bts/files/FFF_complete.pdf.

Chhajed, Dilip and Timothy J. Lowe, Building Intuition: Insights From Basic Operations Management Models and Principles, Chapter 5, p. 82 (2008)

Energy Information Administration. Manufacturing Energy Consumption Survey. Accessed September 2016. http://www.eia.gov/consumption/manufacturing/

European Commission. Eurostat Manual of Supply, Use, and Input-Output Tables. 2008 Edition. 2008. Accessed September 2016. http://ec.europa.eu/eurostat/documents/3859598/5902113/KS-RA-07-013-EN.PDF/b0b3d71e-3930-4442-94be-70b36cea9b39?version=1.0.

Fenton, Michael D. "Iron and Steel Recycling in the United States in 1998." US Geological Survey. 3. Accessed January 2017. https://pubs.usgs.gov/of/2001/of01-224/.

Hopp, Wallace J. and Mark L. Spearman. Factory Physics. Third Edition. Long Grove, IL: Waveland Press, 2008. 674.

Horngren, Charles T., Walter T. Harrison Jr., Linda Smith Bamber. Accounting. 5th edition. Upper Saddle River, NJ: Prentice Hall, 2002. 773.

Horowitz, Karen J. and Mark A. Planting. Concepts and Methods of the US Input-Output Accounts. Bureau of Economic Analysis. September 2006. <http://www.bea.gov/papers/pdf/IOmanual_092906.pdf>

Lee, Hau L., V. Padmanabhan, and SSeungjin Whang. The Bullwhip Effect in Supply Chains. Sloan Management Review. 38 (1997): 93-102.

Lee, Yung-Tsun Tina, Frank H. Riddick, and Björn Johan Ingemar Hohansson. "Core Manufacturing Simulation Data – A Manufacturing Simulation Integration Standard: Overview and Case Studies." International Journal of Computer Integrated Manufacturing. vol 24 issue 8 (2011): 689-709.

Lippiatt, Barbara, Anne Landfield Greig, and Priya Lavappa. Building for Environmental and Economic Sustainability. National Institute of Standards and Technology. 2010. Accessed September 2016. http://www.nist.gov/el/economics/BEESSoftware.cfm.

Meigs, Robert F. and Walter B. Meigs. Accounting: The Basis for Business Decisions. 9th edition. New York, NY: McGraw-Hill Inc., 1993. 991.

Miller, Ronald E. and Peter D. Blair. Input-Output Analysis: Foundations and Extensions. Second Edition. New York: Cambridge University Press, 2009.

National Institute of Standards and Technology. "NIST General Information." Accessed September 2016. http://www.nist.gov/public_affairs/general_information.cfm.

National Institute of Standards and Technology. Building for Environmental and Economic Sustainability. Accessed September 2016. http://www.nist.gov/el/economics/BEESSoftware.cfm.

National Institute of Standards and Technology. Building Industry Reporting and Design for Sustainability. Accessed September 2016. https://birdscom.nist.gov/.

National Science Foundation. "On the Origins of Google." Accessed September 2016. https://www.nsf.gov/discoveries/disc_summ.jsp?cntn_id=100660.

National Science Foundation. NSF Sensational 60. 2010. 11. https://www.nsf.gov/about/history/sensational60.pdf.

Robert D. Niehaus, Inc. Reassessing the Economic Impacts of the International Standard for the Exchange of Product Model Data (STEP) on the US Transportation Equipment Manufacturing Industry. November 26, 2014. Contract SB1341-12-CN-0084.

Science Daily. "Ride-Sharing for Road Freight." Accessed January 2017. https://www.sciencedaily.com/releases/2011/04/110406132022.htm.

Stickney, Clyde P. and Paul R. Brown. Financial Reporting and Statement Analysis. Mason, OH: Southwestern, 1999. 136-137.

Suh, Sangwon Developing a sectoral environmental database for input-output analysis: the comprehensive environmental data archive of the US. Economic Systems Research. 17: 4(2005): 449-469.

Syverson, Chad. "Challenges to Mismeasurement Explanations for the US Productivity Slowdown." National Bureau of Economic Research. Working Paper 21974. Accessed September 2016. http://www.nber.org/papers/w21974

Tassey, Gregory. "Rationales and Mechanisms for Revitalizing US Manufacturing R&D Strategies." Journal of Technology Transfer. 35(2010). 283-333.

Thomas, Douglas and Anand Kandaswamy. "Identifying High Resource Consumption Areas of Assembly-Centric manufacturing in the United States." National Institute of Standards and Technology. White paper. 2016.

Thomas, Douglas and Anand Kandaswamy. “Improving Manufacturing Efficiency through Supply-Chain Flow Time.” National Institute of Standards and Technology. White paper. 2016.

Thomas, Douglas and Joshua Kneifel. “Identifying Environmental Impact Hotspots of Assembly-Centric Manufacturing in the US.” National Institute of Standards and Technology. White paper. 2016.

US Census Bureau. North American Industry Classification System. Accessed January 2017. http://www.census.gov/eos/www/naics/.

US Census Bureau. Survey of Plant Capacity Utilization: How the Data are Collected. Accessed September 2016. http://www.census.gov/manufacturing/capacity/how_the_data_are_collected/.

Weil, David N. Economic Growth. United States: Pearson Education Inc., 2005. 181

Wessner, C. W. and A. W. Wolff. Rising to the Challenge: US Innovation Policy for the Global Economy. National Research Council (US) Committee on Comparative National Innovation Policies: Best Practice for the 21st Century. Washington (DC): National Academies Press (US). 2012. Accessed September 2016. http://www.ncbi.nlm.nih.gov/books/NBK100307/.

World Bank. GDP Per Capita, PPP. 2011-2015. Accessed September 2016. http://data.worldbank.org/indicator/NY.GDP.PCAP.PP.CD?order=wbapi_data_value_2014+wbapi_data_value+wbapi_data_value-last&sort=desc.

Figure 1: Supply Chain Illustration

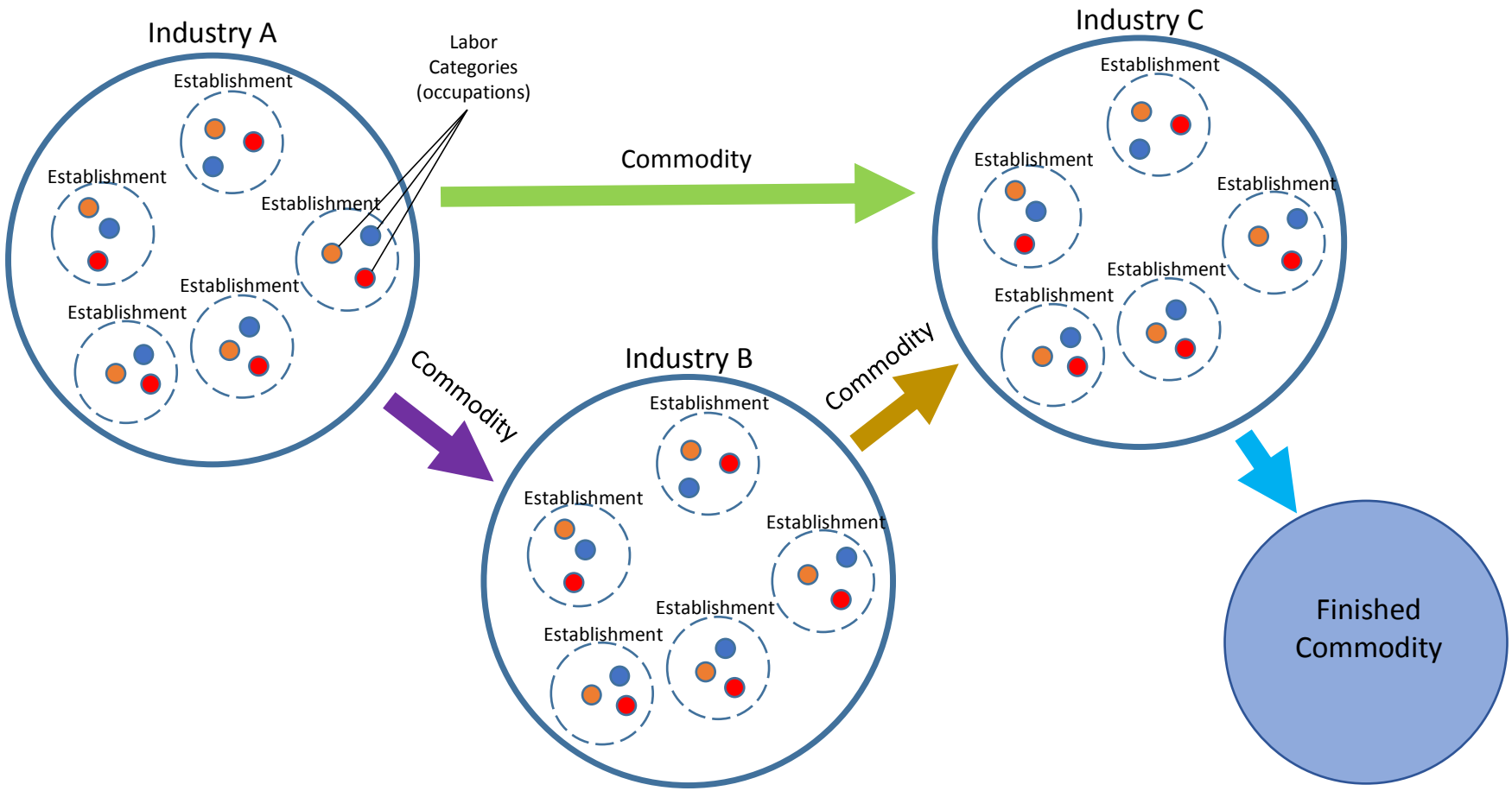

Kandaswamy, Anand; Kneifel, Joshua; Thomas, Douglas.
"Identifying High Resource Consumption Supply Chain Points: A Case Study in Automobile Production."
Paper presented at 25th International Input-Output Conference, Atlantic City, NJ. June 19, 2017 - June 23, 2017.

Table 1: Environmental Impact Categories and Weights for Assessing Impact

Items to be measured	**Units**	**Weights**
Global Warming Potential	kg CO_2 eq	0.30
Acidification	H^+ moles eq	0.03
Human Health- Criteria Air Pollutants	kg PM_{10} eq	0.09
Eutrophication	kg N eq	0.06
Ozone Depletion	kg CFC-11 eq	0.02
Smog	kg O_3 eq	0.04
Ecotoxicity	CTUe	0.07
Human Health - Carcinogens	CTUHcan	0.08
Human Health – Non- Carcinogens	CTUHnoncan	0.05
Primary Energy Consumption	thousand BTU	0.10
Land Use	acre	0.06
Water Consumption	kg	0.08

Figure 2: Cumulative Percent of Value Added/Labor/Environmental Impact by Percentile

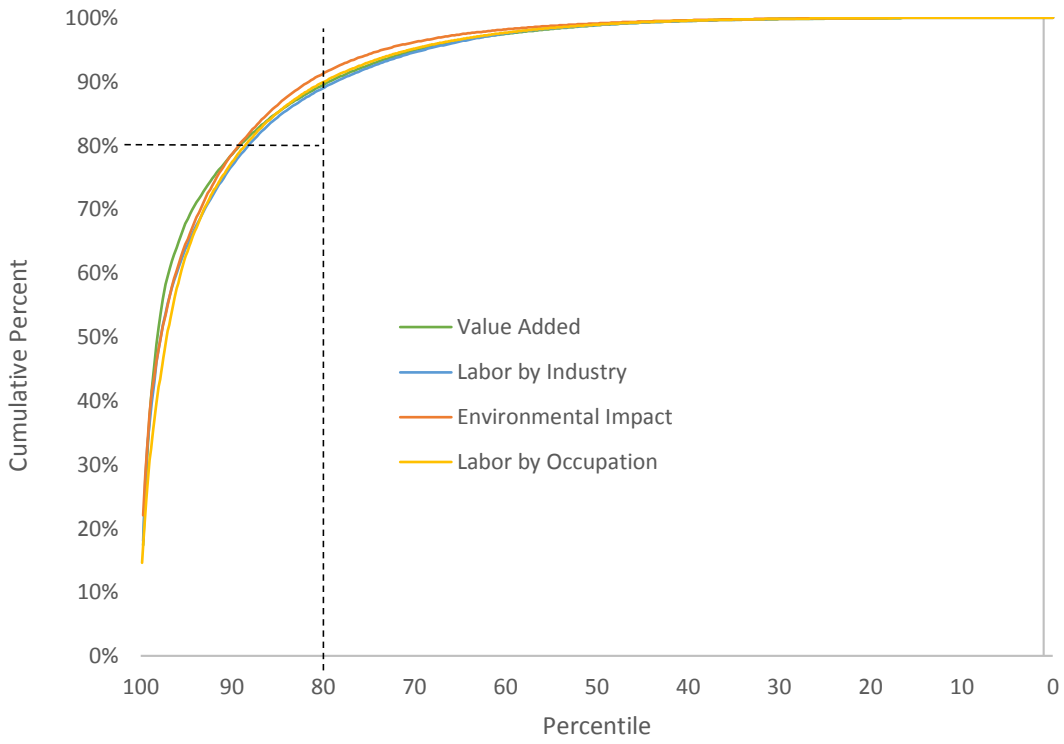

Table 2: Automobile Manufacturing Costs (Measured in Value Added), Top 20 %

Code	NAICS Description	% of Total
336111	Automobile manufacturing	17.32%
420000	Wholesale trade	7.71%
336310	Motor vehicle gasoline engine and engine parts	6.81%
336390	Other motor vehicle parts manufacturing	5.56%
336350	Motor vehicle transmission and power train parts	4.17%
550000	Management of companies and enterprises	4.02%
211000	Oil and gas extraction	3.26%
331110	Iron and steel mills and ferroalloy manufacturing	2.59%
3363A0	Motor vehicle steering/suspension/brake systems	2.31%
336360	Motor vehicle seating and interior trim manufacturing	2.22%
336370	Motor vehicle metal stamping	2.20%
333618	Other engine equipment manufacturing	1.33%
336320	Motor vehicle electrical and electronic equipment	1.21%
212/221	Electricity and Natural Gas	1.14%
334300	Audio and video equipment manufacturing	1.06%
316000	Leather and allied product manufacturing	1.06%
331419	Primary smelting and refining of nonferrous metal	1.01%
327200	Glass and glass product manufacturing	0.94%
332720	Turned product and screw, nut, and bolt manufacturing	0.90%
484000	Truck transportation	0.88%
326190	Other plastics product manufacturing	0.81%
324110	Petroleum refineries	0.74%
334413	Semiconductor and related device manufacturing	0.63%
332710	Machine shops	0.61%
33441A	Other electronic component manufacturing	0.59%
541100	Legal services	0.55%
52A000	Monetary authorities and depository credit	0.55%
326210	Tire manufacturing	0.55%
331510	Ferrous metal foundries	0.53%
331520	Nonferrous metal foundries	0.53%
531ORE	Other real estate	0.52%
541610	Management consulting services	0.49%
33291A	Valve and fittings other than plumbing	0.47%
482000	Rail transportation	0.45%
561300	Employment services	0.45%
331200	Steel product manufacturing from purchased steel	0.43%
331411	Primary smelting and refining of copper	0.42%
325211	Plastics material and resin manufacturing	0.42%
524100	Insurance carriers	0.41%
333612	Speed changer/industrial high-speed drive/gears	0.41%
533000	Lessors of nonfinancial intangible assets	0.40%
33131A	Alumina refining and primary aluminum production	0.40%
541200	Accounting/tax preparation/bookkeeping/payroll services	0.39%
336112	Light truck and utility vehicle manufacturing	0.39%
33399B	Fluid power process machinery	0.39%
325190	Other basic organic chemical manufacturing	0.34%
33411A	Computer terminals and other computer peripheral equipment	0.34%
541800	Advertising, public relations, and related services	0.34%
212100	Coal mining	0.33%
332500	Hardware manufacturing	0.33%
561700	Services to buildings and dwellings	0.33%
541300	Architectural, engineering, and related services	0.32%
332991	Ball and roller bearing manufacturing	0.32%
331490	Nonferrous metal rolling/drawing/extruding/alloying	0.31%
332800	Coating, engraving, heat treating and allied activities	0.30%
230301	Nonresidential maintenance and repair	0.29%
2122A0	Iron, gold, silver, and other metal ore mining	0.29%
33299B	Other fabricated metal manufacturing	0.28%
325110	Petrochemical manufacturing	0.28%
326110	Plastics packaging materials and unlaminated film/sheets	0.27%
334514	Totalizing fluid meter and counting device manufacturing	0.26%
517110	Wired telecommunications carriers	0.26%
336211	Motor vehicle body manufacturing	0.25%
5419A0	Marketing/professional/scientific/technical services	0.25%
333613	Mechanical power transmission equipment manufacturing	0.24%
332310	Plate work and fabricated structural product manufacturing	0.23%
33211B	Crown and closure manufacturing and metal stamping	0.22%
493000	Warehousing and storage	0.22%
331420	Copper rolling, drawing, extruding and alloying	0.22%
322210	Paperboard container manufacturing	0.22%
326290	Other rubber product manufacturing	0.21%
333415	Air conditioning, refrigeration, and warm air heating equipment	0.21%
523A00	Securities and commodity contracts intermediation/brokerage	0.20%
522A00	Nondepository credit intermediation and related activities	0.20%
326220	Rubber and plastics hoses and belting manufacturing	0.20%
325510	Paint and coating manufacturing	0.20%
339990	All other miscellaneous manufacturing	0.19%
335920	Communication and energy wire and cable manufacturing	0.19%
221100	Electric power generation, transmission, and distribution	0.19%
541512	Computer systems design services	0.19%

Table 3: Automobile Manufacturing Labor Hours, Top 20 %

Code	NAICS Description	% of Total
336111	Automobile manufacturing	17.97%
420000	Wholesale trade	9.49%
550000	Management of companies and enterprises	5.57%
336350	Motor vehicle transmission/power train parts manufacturing	3.29%
336310	Motor vehicle gasoline engine/engine parts manufacturing	3.29%
336390	Other motor vehicle parts manufacturing	3.25%
336370	Motor vehicle metal stamping	3.17%
332710	Machine shops	2.01%
484000	Truck transportation	1.94%
336360	Motor vehicle seating and interior trim manufacturing	1.92%
561300	Employment services	1.72%
3363A0	Motor vehicle steering/suspension/brake manufacturing	1.56%
326190	Other plastics product manufacturing	1.32%
561700	Services to buildings and dwellings	1.18%
327200	Glass and glass product manufacturing	1.16%
331510	Ferrous metal foundries	1.10%
331520	Nonferrous metal foundries	1.07%
331110	Iron and steel mills and ferroalloy manufacturing	0.93%
332720	Turned product and screw, nut, and bolt manufacturing	0.91%
336320	Motor vehicle electrical/electronic equipment	0.87%
336211	Motor vehicle body manufacturing	0.81%
332800	Coating, engraving, heat treating and allied activities	0.78%
541610	Management consulting services	0.77%
333618	Other engine equipment manufacturing	0.74%
561400	Business support services	0.72%
52A000	Monetary authorities and depository credit intermediation	0.71%
493000	Warehousing and storage	0.67%
722110	Full-service restaurants	0.67%
212/221	Electricity and Natural Gas	0.65%
541300	Architectural, engineering, and related services	0.64%
334300	Audio and video equipment manufacturing	0.61%
316000	Leather and allied product manufacturing	0.60%
541200	Accounting, tax preparation, bookkeeping, and payroll services	0.59%
326210	Tire manufacturing	0.58%
541100	Legal services	0.58%
331200	Steel product manufacturing from purchased steel	0.54%
332310	Plate work and fabricated structural product manufacturing	0.53%
334413	Semiconductor and related device manufacturing	0.52%
482000	Rail transportation	0.52%
722211	Limited-service restaurants	0.51%

Code	NAICS Description	% of Total
33211B	Crown and closure manufacturing and metal stamping	0.49%
561600	Investigation and security services	0.46%
332991	Ball and roller bearing manufacturing	0.45%
33441A	Other electronic component manufacturing	0.43%
322210	Paperboard container manufacturing	0.42%
4A0000	Other retail	0.42%
531ORE	Other real estate	0.41%
522A00	Nondepository credit intermediation and related activities	0.41%
48A000	Scenic/sightseeing transportation and support activities	0.41%
492000	Couriers and messengers	0.40%
33291A	Valve and fittings other than plumbing	0.38%
33399B	Fluid power process machinery	0.37%
332320	Ornamental and architectural metal products manufacturing	0.36%
441000	Motor vehicle and parts dealers	0.35%
33211A	All other forging, stamping, and sintering	0.35%
339990	All other miscellaneous manufacturing	0.33%
541800	Advertising, public relations, and related services	0.33%
541512	Computer systems design services	0.33%
326110	Plastics packaging materials/unlaminated film/sheet manufacturing	0.31%
5419A0	Marketing/professional/scientific/technical services	0.30%
524200	Insurance agencies, brokerages, and related activities	0.29%
524100	Insurance carriers	0.28%
211000	Oil and gas extraction	0.26%
326290	Other rubber product manufacturing	0.25%
721000	Accommodation	0.25%
562000	Waste management and remediation services	0.24%
33299B	Other fabricated metal manufacturing	0.24%
333415	Air conditioning/refrigeration/warm air heating equipment	0.24%
332600	Spring and wire product manufacturing	0.24%
323110	Printing	0.24%
523A00	Securities and commodity contracts intermediation and brokerage	0.23%
54151A	Other computer related services, including facilities management	0.22%
326220	Rubber and plastics hoses and belting manufacturing	0.21%
561900	Other support services	0.21%
212100	Coal mining	0.21%
325211	Plastics material and resin manufacturing	0.21%
481000	Air transportation	0.20%
811300	Commercial/industrial machinery/equipment repair/maintenance	0.20%
314900	Other textile product mills	0.19%
325510	Paint and coating manufacturing	0.19%

Note: Electricity/natural gas can appear twice. One as the total (NAICS 212/221) and the uses of energy (e.g., NAICS 221100-B)

Table 4: Environmental Impact of Automobile Manufacturing, Top 20 %

Code	NAICS Description	% of Total
336111	Automobile manufacturing	22.00%
331110	Iron and steel mills and ferroalloy manufacturing	6.25%
212/221	Electricity and Natural Gas	4.86%
327200	Glass and glass product manufacturing	4.79%
111900	Other crop farming	3.33%
316000	Leather and allied product manufacturing	2.56%
2122A0	Iron, gold, silver, and other metal ore mining	2.40%
324110	Petroleum refineries	1.87%
484000	Truck transportation	1.83%
325180	Other basic inorganic chemical manufacturing	1.78%
113000	Forestry and logging	1.71%
325190	Other basic organic chemical manufacturing	1.59%
211000	Oil and gas extraction	1.51%
325211	Plastics material and resin manufacturing	1.39%
321200	Veneer/plywood/engineered wood product	1.26%
221100	Electric power generation/transmission/distribution	1.23%
313200	Fabric mills	1.11%
3252A0	Synthetic rubber/artificial and synthetic fibers and filaments	1.07%
420000	Wholesale trade	1.02%
325110	Petrochemical manufacturing	0.91%
482000	Rail transportation	0.89%
331520	Nonferrous metal foundries	0.88%
326190	Other plastics product manufacturing	0.83%
212100	Coal mining	0.83%
221100-D	Machine Drive	0.82%
33131A	Alumina refining and primary aluminum production	0.79%
331200	Steel product manufacturing from purchased steel	0.78%
33441A	Other electronic component manufacturing	0.76%
331510	Ferrous metal foundries	0.75%
336112	Light truck and utility vehicle manufacturing	0.68%
313100	Fiber, yarn, and thread mills	0.66%
336390	Other motor vehicle parts manufacturing	0.63%
333618	Other engine equipment manufacturing	0.61%
339990	All other miscellaneous manufacturing	0.61%
326210	Tire manufacturing	0.59%
331490	Nonferrous metal rolling/drawing/extruding/alloying	0.58%
322210	Paperboard container manufacturing	0.56%
1121A0	Beef/cattle ranching/farming/feedlots	0.54%
550000	Management of companies and enterprises	0.53%
1111B0	Grain farming	0.49%

Code	NAICS Description	% of Total
321100	Sawmills and wood preservation	0.46%
322130	Paperboard mills	0.46%
332720	Turned product and screw, nut, and bolt manufacturing	0.45%
31161A	Animal (except poultry) slaughtering, rendering, and processing	0.42%
336350	Motor vehicle transmission and power train parts manufacturing	0.42%
324190	Other petroleum and coal products manufacturing	0.42%
336310	Motor vehicle gasoline engine and engine parts manufacturing	0.41%
331419	Primary smelting/refining of nonferrous metal	0.40%
313300	Textile and fabric finishing and fabric coating mills	0.40%
3219A0	All other wood product manufacturing	0.40%
562000	Waste management and remediation services	0.39%
326110	Plastics packaging material/unlaminated film/sheet manufacturing	0.39%
331411	Primary smelting and refining of copper	0.38%
332800	Coating, engraving, heat treating and allied activities	0.37%
336370	Motor vehicle metal stamping	0.35%
33131B	Aluminum product manufacturing from purchased aluminum	0.33%
212230	Copper, nickel, lead, and zinc mining	0.33%
221100-B	Process Heating	0.33%
331420	Copper rolling, drawing, extruding and alloying	0.32%
332114	Custom roll forming	0.32%
325510	Paint and coating manufacturing	0.32%
332710	Machine shops	0.31%
33211A	All other forging, stamping, and sintering	0.31%
33299B	Other fabricated metal manufacturing	0.30%
314110	Carpet and rug mills	0.29%
221200-B	Process Heating	0.27%
336211	Motor vehicle body manufacturing	0.27%
221100-G	Facility HVAC (g)	0.25%
327100	Clay product and refractory manufacturing	0.25%
481000	Air transportation	0.24%
33211B	Crown and closure manufacturing and metal stamping	0.24%
326290	Other rubber product manufacturing	0.23%
332310	Plate work and fabricated structural product manufacturing	0.23%
336360	Motor vehicle seating and interior trim manufacturing	0.23%
1111A0	Oilseed farming	0.23%
322120	Paper mills	0.22%
315000	Apparel manufacturing	0.21%
561700	Services to buildings and dwellings	0.20%
334413	Semiconductor and related device manufacturing	0.20%
314900	Other textile product mills	0.20%

Note: Electricity/natural gas can appear twice. One as the total (NAICS 212/221) and the uses of energy (e.g., NAICS 221100-B)

Table 5: Labor Hours for Automobile Manufacturing by Occupation, Top 20 %

Code	NAICS Description	% of Total
512092	Team Assemblers	14.54%
537062	Laborers and Freight, Stock, and Material Movers, Hand	2.73%
514041	Machinists	2.49%
511011	First-Line Supervisors of Production and Operating Workers	2.43%
414012	Sales Representatives (Wholesale and Manufacturing)	2.32%
512099	Assemblers and Fabricators, All Other	2.06%
533032	Heavy and Tractor-Trailer Truck Drivers	2.04%
519061	Inspectors, Testers, Sorters, Samplers, and Weighers	2.03%
111021	General and Operations Managers	1.78%
434051	Customer Service Representatives	1.65%
439061	Office Clerks, General	1.46%
499071	Maintenance and Repair Workers, General	1.39%
172112	Industrial Engineers	1.38%
499041	Industrial Machinery Mechanics	1.34%
537051	Industrial Truck and Tractor Operators	1.26%
514031	Cutting/Punching/Press Machine Setters/Operators/Tenders, Metal/Plastic	1.26%
435071	Shipping, Receiving, and Traffic Clerks	1.21%
514121	Welders, Cutters, Solderers, and Brazers	1.14%
132011	Accountants and Auditors	1.12%
514011	Computer-Controlled Machine Tool Operators, Metal and Plastic	1.11%
433031	Bookkeeping, Accounting, and Auditing Clerks	1.07%
519198	Helpers--Production Workers	1.07%
514111	Tool and Die Makers	1.04%
519199	Production Workers, All Other	1.00%
436014	Secretaries/Administrative Assistants, Except Legal/Medical/Executive	0.96%
172141	Mechanical Engineers	0.91%
113051	Industrial Production Managers	0.85%
435081	Stock Clerks and Order Fillers	0.84%
514072	Molding/Coremaking/Casting Setters/Operators/Tenders, Metal/Plastic	0.83%
372011	Janitors and Cleaners, Except Maids and Housekeeping Cleaners	0.82%
514081	Multiple Machine Tool Setters, Operators, and Tenders, Metal and Plastic	0.77%
472111	Electricians	0.77%
537064	Packers and Packagers, Hand	0.75%
431011	First-Line Supervisors of Office and Administrative Support Workers	0.71%
533033	Light Truck or Delivery Services Drivers	0.70%
512022	Electrical and Electronic Equipment Assemblers	0.66%
514122	Welding, Soldering, and Brazing Machine Setters, Operators, and Tenders	0.61%
131199	Business Operations Specialists, All Other	0.58%
512031	Engine and Other Machine Assemblers	0.57%
435061	Production, Planning, and Expediting Clerks	0.53%

Code	NAICS Description	% of Total
131023	Purchasing Agents, Except Wholesale, Retail, and Farm Products	0.52%
113031	Financial Managers	0.50%
514033	Grinding/Lapping/Polishing/Buffing Tool Setters/Operators/Tenders, Metal/Plastic	0.49%
491011	First-Line Supervisors of Mechanics, Installers, and Repairers	0.49%
414011	Sales Representatives, Wholesale/Manufacturing, Technical/Scientific Products	0.48%
131161	Market Research Analysts and Marketing Specialists	0.45%
339032	Security Guards	0.45%
131111	Management Analysts	0.45%
412031	Retail Salespersons	0.44%
112022	Sales Managers	0.44%
151121	Computer Systems Analysts	0.43%
131071	Human Resources Specialists	0.43%
151132	Software Developers, Applications	0.42%
436011	Executive Secretaries and Executive Administrative Assistants	0.41%
119041	Architectural and Engineering Managers	0.40%
519111	Packaging and Filling Machine Operators and Tenders	0.40%
514021	Extruding and Drawing Machine Setters, Operators, and Tenders, Metal and Plastic	0.39%
413099	Sales Representatives, Services, All Other	0.37%
519121	Coating, Painting, and Spraying Machine Setters, Operators, and Tenders	0.37%
151151	Computer User Support Specialists	0.35%
499043	Maintenance Workers, Machinery	0.35%
373011	Landscaping and Groundskeeping Workers	0.34%
353021	Combined Food Preparation and Serving Workers, Including Fast Food	0.33%
516031	Sewing Machine Operators	0.32%
493031	Bus and Truck Mechanics and Diesel Engine Specialists	0.30%
353031	Waiters and Waitresses	0.30%
173026	Industrial Engineering Technicians	0.29%
519041	Extruding, Forming, Pressing, and Compacting Machine Setters, Operators, and Tenders	0.29%
151133	Software Developers, Systems Software	0.29%
514034	Lathe and Turning Machine Tool Setters, Operators, and Tenders, Metal and Plastic	0.29%
151142	Network and Computer Systems Administrators	0.28%
533031	Driver/Sales Workers	0.28%
519122	Painters, Transportation Equipment	0.27%
113021	Computer and Information Systems Managers	0.27%
131081	Logisticians	0.27%
499044	Millwrights	0.27%
411012	First-Line Supervisors of Non-Retail Sales Workers	0.27%
434171	Receptionists and Information Clerks	0.27%
231011	Lawyers	0.26%
433021	Billing and Posting Clerks	0.25%

Figure 3: Automobile Manufacturing Supply Chain Entities Above the 70th Percentile for Labor Hours, Environmental Impact, and Value Added

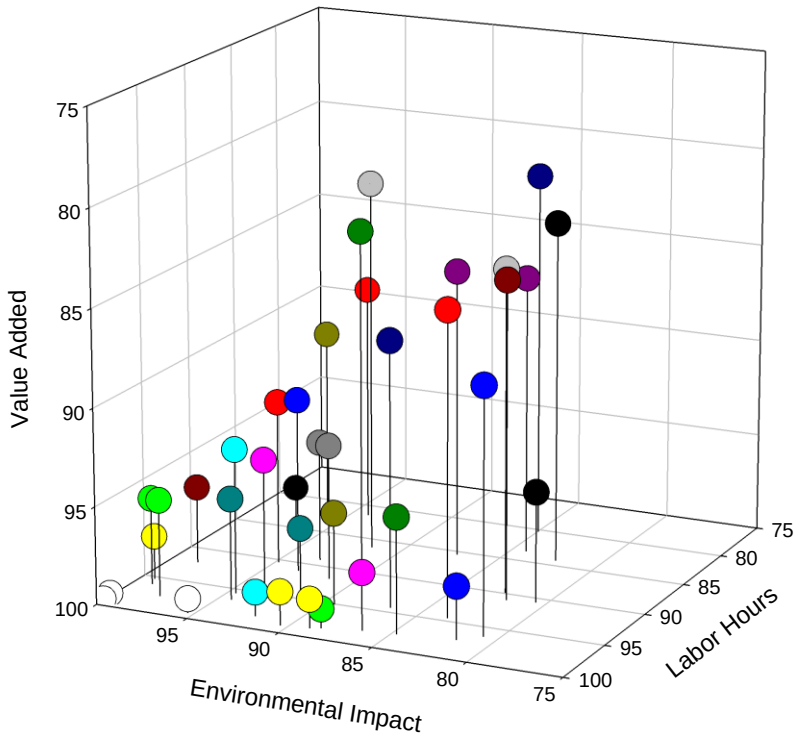

Note: Table 6 is the Key to the colors in this figure

Table 6: Automobile Manufacturing Supply Chain Entities Above the 80th Percentile for Labor Hours, Environmental Impact, and Value Added

	Color	Code	NAICS Description	Percentile		
				Labor	Envir. Impact	Value Added
**		2121, 2211, 2212	Electricity and Natural Gas	100	100	100
**		336111	Automobile manufacturing	100	100	100
**		420000	Wholesale trade	99	95	99
**		331110	Iron and steel mills and ferroalloy manufacturing	95	99	98
**		327200	Glass and glass product manufacturing	96	99	96
**		484000	Truck transportation	98	98	95
*		336390	Other motor vehicle parts manufacturing	98	92	99
*		550000	Management of companies and enterprises	99	90	98
*		316000	Leather and allied product manufacturing	92	99	96
*		326190	Other plastics product manufacturing	97	94	95
*		331520	Nonferrous metal foundries	96	95	93
*		333618	Other engine equipment manufacturing	94	92	97
*		331510	Ferrous metal foundries	96	93	93
*		482000	Rail transportation	90	95	92
*		326210	Tire manufacturing	92	91	93
*		331200	Steel product manufacturing from purchased steel	91	93	91
		336350	Motor vehicle transmission and power train parts manufacturing	99	89	99
		336310	Motor vehicle gasoline engine and engine parts manufacturing	99	88	99
		336370	Motor vehicle metal stamping	98	86	97
		332720	Turned product and screw, nut, and bolt manufacturing	95	89	95
		211000	Oil and gas extraction	84	97	98
		332710	Machine shops	98	85	94
		336360	Motor vehicle seating and interior trim manufacturing	97	82	97
		33441A	Other electronic component manufacturing	89	93	94
		325211	Plastics material and resin manufacturing	81	97	91
		332800	Coating, engraving, heat treating and allied activities	94	87	86
		334413	Semiconductor and related device manufacturing	91	81	94
		561700	Services to buildings and dwellings	96	81	87
		212100	Coal mining	82	94	88
		336211	Motor vehicle body manufacturing	95	83	84
		322210	Paperboard container manufacturing	89	91	83
		339990	All other miscellaneous manufacturing	86	92	81
		326110	Plastics packaging materials/unlaminated film/sheet manufacturing	85	87	85
		332310	Plate work and fabricated structural product manufacturing	91	82	84
		33211B	Crown and closure manufacturing and metal stamping	90	83	83
		33299B	Other fabricated metal manufacturing	83	84	86
		326290	Other rubber product manufacturing	84	82	83
		325510	Paint and coating manufacturing	80	85	81

** All above 95th percentile

* All above 90th percentile

Figure 4: Automobile Manufacturing Supply Chain Entities Above the 70th Percentile for Time, Labor, Environmental Impact, Value Added, and Depreciable Assets (Only Manufacturing Supply-Chain Entities)

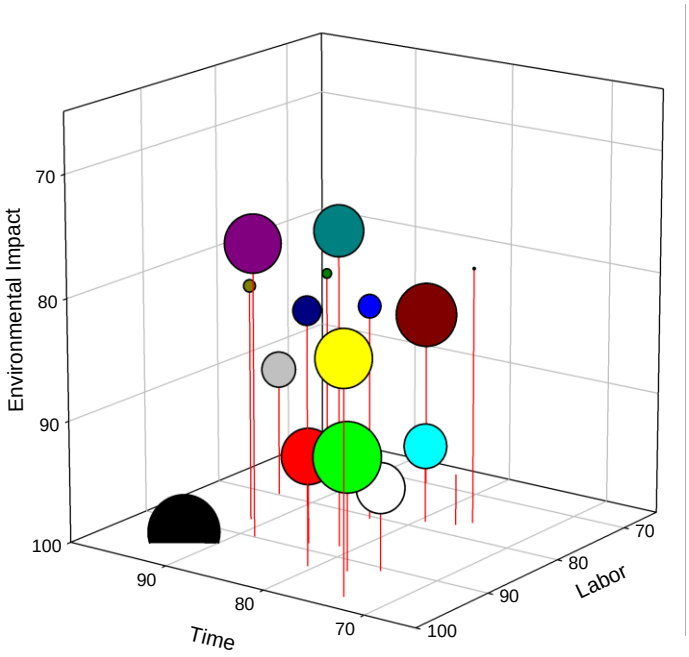

Note: The size of the bubbles represent the percentile of value added (80th percentile to the 100th). Table 7 is the key to the colors in this figure.

Table 7: Automobile Manufacturing Supply Chain Entities Above the 70th Percentile for Time, Labor, Environmental Impact, Value Added, and Depreciable Assets (Only Manufacturing Supply-Chain Entities)

			Percentile				
Color	BEA NAICS	Description	Labor Hours	WIP Time	Environmental Impact	Value Added	Depreciable Assets
	331110	Iron and steel mills and ferroalloy manufacturing	95	92	99	98	98
	333618	Other engine equipment manufacturing	92	77	91	96	93
	334413	Semiconductor and related device manufacturing	90	89	76	92	95
	33441A	Other electronic component manufacturing	89	84	93	92	84
	331200	Steel product manufacturing from purchased steel	91	75	93	89	92
	332710	Machine shops	97	74	81	92	93
	331490	Nonferrous metal (except copper and aluminum) rolling, drawing, extruding and alloying	80	94	89	85	86
	331419	Primary smelting and refining of nonferrous metal (except copper and aluminum)	70	85	86	95	87
	33211A	All other forging, stamping, and sintering	86	92	81	77	86
	33291A	Valve and fittings other than plumbing	88	81	74	90	84
	336211	Motor vehicle body manufacturing	93	81	79	82	81
	33131A	Alumina refining and primary aluminum production	78	79	94	88	78
	331420	Copper rolling, drawing, extruding and alloying	81	84	82	81	81
	33131B	Aluminum product manufacturing from purchased aluminum	73	93	83	76	82
	313200	Fabric mills	78	77	96	73	77
	327100	Clay product and refractory manufacturing	76	76	79	73	76

Development and Evaluation of Two New Droplet Evaporation Schemes for Fire Dynamics Simulations

JASON FLOYD[1], RANDALL MCDERMOTT[2]
[1]JENSEN HUGHES, Rockville, Maryland, USA
[2]National Institute of Standards and Technology, Gaithersburg, Maryland, USA

ABSTRACT

The evaporation of sprinkler droplets is an important phenomena in fire simulations both for heat removal from the gas and for heat removal from surfaces. The Fire Dynamics Simulator (FDS) has seen a number of different evaporation models over its history where each subsequent model has attempted to address limitations and issues with the previous model. In this paper, we address the problems of potential numerical instability and super-saturation that may occur in explicit time integration of the droplet equations. Two novel numerical approaches are developed and evaluated. The first is based on an analytical solution that relaxes the cell composition and temperature toward the equilibrium values. The second method is an implicit solution to the droplet equations. The two approaches are verified and validated using both single droplet and practical sprinkler calculations. Ultimately, the implicit approach is demed the most cost effective for practical fire simulations.

KEYWORDS: FDS, large-eddy simulation, evaporation, sprinklers

NOMENCLATURE

A	surface area (m^2), computational time (s)
B, C	computational time per droplet (s/droplet)
c	heat capacity (J/kg/K)
F, G	droplet temperature solution components
H	enthalpy (J)
h	heat transfer coefficient ($W/m^2/K$)
h_l	liquid enthalpy (J/kg)
h_m	mass transfer coefficient (m/s)
h_v	heat of vaporization (J/kg)
M	total normalized vaporization rate (1/s)
N	number of particles per cell
m	droplet mass (kg)
$\dot{q}_r$	droplet radiation absorption (W)
t	time (s)
T	droplet temperature (K)
T_g	gas temperature (K)
T_w	wall temperature (K)
Y	vapor mass fraction (kg/kg)
V	cell volume (m^3)

Greek

β	analytical solution parameter ($kg^{1/3}/s$)
$\delta\hat{t}$	small time step (s)
Δt	time step size (s)
ρ	gas density (kg/m^3)
χ	area per mass factor ($m^2/kg^{2/3}$)
ω	relaxation time constant (1/s)

superscripts

n	time step

subscripts

eq	cell equilibrium condition
f	film
g	gas
i	droplet index
l	liquid at equilibrium
m	mass transfer
v	vapor, vaporization
w	wall

INTRODUCTION

The evaporation of sprinkler droplets is an important phenomena to consider when modeling the thermal environment due to a fire. For standard large drop sprinklers (e.g. not a watermist system), efficacy of droplets have been estimated analytically [1] and confirmed experimentally [2] to remove between 11 % and 26 % of the heat produced by a fire. Watermist systems can remove 100 % of the heat produced by a fire either by extinguishment or by providing sufficient evaporation to maintain compartment temperatures at or below the boiling point of water [3].

A successful model of droplet evaporation in fire dynamics simulations should

(1) accurately represent droplet dynamics

(2) conserve mass and energy

(3) be computationally efficient

(4) be numerically stable

(5) obtain the correct equilibrium state

(6) be independent of the order in which the droplets are processed

Typical computational fluid dynamics (CFD) codes use either stiff explicit or segregated implicit ODE time integrators to solve the droplet dynamics equations. These solvers, in general, satisfactorily address the issues of accuracy and conservation (Items 1 and 2).

To address computational efficiency (Item 3) CFD codes do not track every droplet from a sprinkler—the cost would be too high. Instead, a smaller number of "superdroplets", where each superdroplet represents multiple individual droplets. This approach, while cost effective, can lead to extremely high rates of heat and mass transfer when very fine droplets require a large superdroplet weighting factor. These high heat and mass transfer rates present significant numerical challenges for computational efficiency and numerical stability (Item 4). The methods presented in this paper are aimed at addressing these two critical, practical issues in droplet evaporation for fire modeling applications.

The methods discussed in this work also address equilibrium (Item 5) and droplet order (Item 6) more directly than in the past. These are subtle issues that are discussed in more detail later in the paper.

The NIST Fire Dynamics Simulator (FDS) [4, 5] has seen a number of approaches to droplet evaporation in an attempt to achieve the desirable model attributes listed above. A brief history is summarized below:

FDS 1-4 used an explicit solver for the heating and evaporation of droplets. During this time period, development of routines for droplet transport and evaporation focused on applications like the sprinkler suppression of commodity using a simple exponential decay of the heat release rate based on the delivered quantity of water [6].

FDS 5 came with a significant overhaul to the droplet model. This in large part resulted from efforts to model water mist systems where the approach taken in FDS 1-4 resulted in numerical instabilities. In a water mist system, especially upon initial discharge, very large changes in droplet temperature and gas temperature can occur. The explicit approach being used could result in large, non-physical swings in gas and droplet temperature leading to numerical instabilities. The droplet model was changed to a semi-implicit method where the droplet mass and temperature were solved implicitly and the gas temperature (and wall temperature for a droplet on a solid surface) was solved explicitly. This approach resolved many of the issues with numerical instabilities. As more rigorous verification and validation practices became used in FDS development, this semi implicit approach underwent further modifications to ensure the conservation of energy.

FDS 6 introduced some additional changes to the droplet model. Most notably, a self-consistent set of thermophysical properties was introduced for common species using NIST-JANAF data [7]. This effort ensured the correct equilibrium state was being reached. Users of FDS continued trying to expand its application space with applications including very fine water mist (fog) and sprinkler suppression of pyrolyzing materials. The new routine had difficulties with these two classes of problems: droplets impacting hot surfaces with low conductivity and low thermal inertia (for example foams) and simulations with very fine water mist. The root cause in both cases was that the explicit solver being used for the gas and wall temperatures was resulting in large overshoots or undershoots in temperature prediction. This resulted in anomalous temperatures in the simulation or runtime failures when bad temperature values were used in other subroutines.

DEVELOPMENT OF NEW EVAPORATION SCHEMES

In this work, two new schemes are developed and evaluated to address the shortcomings of other methods discussed above. The first is a relaxation method based on an analytical solution to an alternate set of droplet equations. The second is an implicit, drop-wise approach (which we ultimately determine to be superior in terms of computational cost and ease of implementation). Below we present the governing equations followed by an overview of the new schemes. Details are provided in Appendices A and B.

Governing Equations

The governing equations for droplet evaporation are given below and may be found in Ref. [8]. Summations are over all droplets in a computational cell. Again, note that each individual droplet represents a superdroplet with a mass weighting factor (omitted here to avoid complicating the equations). Details may be found in [4].

$$\frac{\mathrm{d}m_i}{\mathrm{d}t} = A_i h_{m,i} \rho \left(Y_v - Y_{l,i}\right) \tag{1}$$

$$\rho V \frac{\mathrm{d}Y_v}{\mathrm{d}t} = -\sum_i \frac{\mathrm{d}m_i}{\mathrm{d}t} \tag{2}$$

$$m_i c_i \frac{\mathrm{d}T_i}{\mathrm{d}t} = A_g h_g \left(T_g - T_i\right) + A_w h_w \left(T_w - T_i\right) + \frac{\mathrm{d}m_i}{\mathrm{d}t} h_v + \dot{q}_r \tag{3}$$

$$m_g c_g \frac{\mathrm{d}T_g}{\mathrm{d}t} = -\sum_i \left(A_g h_g \left(T_g - T_i\right) + \frac{\mathrm{d}m_i}{\mathrm{d}t} \left(h_v + h_l\right) \right) \tag{4}$$

$$m_w c_w \frac{\mathrm{d}T_w}{\mathrm{d}t} = -\sum_i A_w h_w \left(T_w - T_i\right) \tag{5}$$

Equation (1) defines the droplet evaporation as a function of the droplet surface area, A_i and a mass transfer coefficient, $h_{m,i}$, times the difference in the gas vapor fraction, Y_v, and the droplet surface vapor fraction, $Y_{l,i}$, evaluated using the Clausius-Clapeyron equation.

Equation (2) defines the rate of change in vapor mass in a gas cell as the sum of the evaporation rates of the droplets in the cell.

Equation (3) defines the rate of change in the droplet temperature, T_i. This consists of two convective terms, an evaporation term, and a radiation absorption term. The first convective term is for heat transfer to the gas based on the droplet area exposed to the gas, A_g, and a gas heat transfer coefficient, h_g. The second convective term is for heat transfer to the wall based on the droplet area exposed to the wall, A_w, and a wall heat transfer coefficient, h_w. The third term accounts for energy lost due to the heat of vaporization, h_v. The fourth term, $\dot{q}_r$, represents the radiative energy absorbed by the droplet.

Equation (4) defines the rate of change in the gas temperature, T_g. It sums the heat transfer from the droplet plus the enthalpy of evaporated mass over all droplets in the cell.

Equation (5) defines the rate of change in the wall temperature, T_w. It sums the heat transfer from the droplet over all droplets on the wall cell.

Note that fluid properties used for determination of the heat and mass transfer coefficients (conductivity, diffusivity, viscosity) are evaluated at the droplet film temperature, $T_{f,i}$, using the one-third rule, as discussed in [9]:

$$T_{f,i} = T_i + \left(T_g - T_i\right)/3 \tag{6}$$

Heat of vaporization is evaluated at the droplet surface temperature, which is the same as the droplet temperature in the thermally thin limit considered here.

Relaxation-to-Equilibrium Method

The relaxation-to-equilibrium method (hereafter "relaxation" method) presented in this paper is a novel numerical approach to a class of transient problems where an equilibrium state can be readily established but where an equilibrium solution may not be desirable. Such problems include drag, chemical kinetics, and evaporation. In general, one does not know *a priori* whether the time step dictated by other physics in the

problem will require a time accurate solution or an equilibrium solution. In the case where the correct solution is equilibrium, it does not make sense to waste time marching toward the solution with an explicit integration technique. The alternative of using a fully implicit, nonlinear solution method can also be complex and expensive. The method we present here has some of the advantages of a fully explicit approach and some advantages of the implicit approach. We are able to obtain a time accurate solution for small time steps and a stable equilibrium solution in one large quasi-explicit time step. The details of the scheme are provided in Appendix A.

As we discuss below, evaluation of the exponentials and logarithms inherent in the analytical solution significantly hinder its performance compared to the other method we will discuss in this paper, a novel semi-implicit formulation. We stress that this conclusion is problem dependent. But for the practical engineering problems considered here, the relaxation method is more expensive than the semi-implicit scheme. Therefore, ultimately, the semi-implicit approach will become the default in future versions of FDS. The development and results of the relaxation method are still retained in this paper, however, since the method is novel and may be useful in other fire science problems.

Implicit Method

It was postulated that the numerical issues in the droplet routine could be due to inconsistencies between the explicit update of the gas and wall temperatures and the implicit determination of the droplet evaporation rate. To remedy this problem, we developed and implemented a method where the dependent variables are treated implicitly, while other quantities are linearized using their initial values. Implicit solutions for Y_v, T_i, and T_g (and the wall temperature T_w, if necessary) are developed in Appendix B.

The equations are solved on a droplet-by-droplet basis. Thus, if the number of droplets in a cell is greater than one the initial conditions for Y_v, T_g, and T_i for a given droplet are taken from the result of the integration from the previous droplet. The order in which the droplets are processed is not set explicitly. Rather, in a typical fire application the chaotic path of the droplets combined with their initial numerical ordering (during the droplet injection step) lead to a quasi-random droplet order for a given cell during the evaporation time integration. In a typical engineering calculation, it would be rare for more than one droplet to be in a cell.

RESULTS AND DISCUSSION

Verification and Validation

This section presents the results of a series of verification and validation cases. Verification is the process of demonstrating that a model implementation accurately represents its conceptual framework (are the equations being solved correctly) and validation is the process of demonstrating that a model, based on its intended use, makes reasonable predictions of the real world [10]. The cases are from the FDS verification suite [11]. The FDS verification suite contains eight cases testing droplet evaporation. Five of the eight cases are shown below to highlight the performance (in terms of the model properties listed above) of the current version (FDS 6.5.3 at the time of the writing), which will be referred to as the "explicit" approach, compared against the relaxation and implicit approaches. The cases that follow test mass and energy conservation, the end equilibrium state, and the prediction of the evaporation rate.

Case 1: Complete Evaporation of Monodisperse Droplets

The geometry for this case (*water_evaporation_1* in the FDS verification suite), is a 1 m^3 box with adiabatic walls uniformly gridded with 10 cm cells. The initial conditions in the box are 200 °C air at 0 % humidity. The box is uniformly seeded (10 droplets per cell) with 0.01 kg of static droplets at 20 °C and a uniform diameter of 200 μm. Since the droplets are cooler than the air and the air has no water vapor, a non-equilibrium condition exists. Equilibrium will be achieved at a point where the droplet temperature equals the gas temperature and vapor mass fraction in the gas equals the droplet equilibrium vapor fraction. The equilibrium condition can be determined analytically using the thermophysical properties of air and water. The approach is to first determine the initial total enthalpy present (i.e., the sum of the droplet and gas enthalpies). Then a new temperature is selected, the equilibrium vapor fraction for that temperature computed, liquid evaporated to meet the equilibrium vapor condition, and the total enthalpy computed (accounting for pressure work

in a sealed domain) and compared to the initial enthalpy. This process is repeated until the final enthalpy equals the initial enthalpy. For Case 1, the equilibrium condition results in all the water evaporating. Table 1 shows the expected results and the results computed by the explicit, equilibrium, and implicit methods. All evaporation methods predict the expected values with only minor errors.

Table 1. Results of Verification Case 1: Complete Evaporation of Monodisperse Droplets

Variable	Expected Value	Explicit	Relaxation	Implicit
Relative Humidity (%)	2.1	2.1	2.1	2.1
Change in gas enthalpy (kJ)	-167	-166	-166	-166
Change in water enthalpy (kJ)	159	159	159	159
Change in pressure (Pa)	7810	7800	7790	7801
Final temperature (°C)	154	154	154	154

Case 2: Steady State Evaporation in Hot Channel Flow

The geometry for this case (FDS *water_evaporation_4*), is a 3 m $\times$ 1 m $\times$ 1 m tunnel. One end of the tunnel is open, the other end has an inlet condition of 500 °C air at 1 m/s and 0 % humidity, and the remaining walls are adiabatic. After a brief period to allow the flow field to develop, static droplets are injected into the tunnel at a rate of 0.05 kg/s and a temperature of 20 °C with a uniform diameter of 20 μm. There is sufficient excess energy over the boiling point of water in the inflowing air to fully evaporate the mass of droplets being injected. Using the thermophysical properties of air, one can compute the enthalpy flow of the incoming air and the enthalpy flow of the outgoing air, which now contains water vapor. Table 2 shows the expected results and the results computed by the explicit and the implicit methods (note, based on timing results shown later in the paper, the equilibrium method was not developed to the point of being able to run this case). Both the explicit and the implicit methods predict the expected values with only minor errors.

Table 2. Results of Verification Case 2: Steady State Evaporation in Hot Channel Flow

Variable	Expected Value	Explicit	Implicit
Heat flow prior to droplets (kW)	230	229	229
Heat flow after droplets (kW)	107	107	107

Cases 3: Single Droplet Rate of Evaporation (Verification)

Case 3 (FDS *water_evaporation_8*) compares the FDS time accurate solution against the evaporation model of [9]. The simulation consists of an injection of a 100 μm droplet at 10 °C into 60 °C air with an initial water vapor mass fraction of 10 %. Results are shown below in Fig. 1(left). With a sufficiently small time step, here $\Delta t = 0.001$ s, all three numerical methods produce the same results, which is to be expected for convergent schemes. Minor differences between FDS and the Li & Chow numerical solution are attributable to small differences in fluid properties, drag formulations, and the fact that the Li & Chow solution is effectively zero dimensional (solution of ODEs), whereas the FDS solution is, of course, integrated in a CFD solver.

Cases 4: Single Droplet Rate of Evaporation (Validation)

Case 4 (FDS *water_evaporation_5*) evaporates a single 1 mm droplet initially at 9 °C in 25 °C air. The expected results are from experimental test data [12] where a single droplet was suspended on a glass fiber. Results are shown in Fig. 1(right). Again, the numerical methods all produce the same result for the same problem. Note that here care has been taken to ensure that fluid properties for the explicit results have been evaluated in exactly the same manner as for the relaxation and implicit methods.

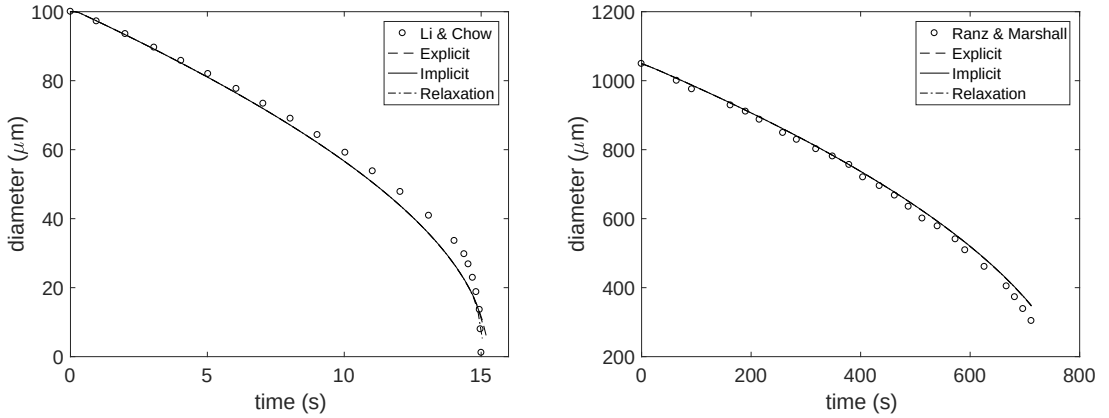

Fig. 1. (Left) Case 3: Single droplet verification with drag. Comparison with numerical solution of Li and Chow [9]. (Right) Case 4: Single droplet validation in quiescent air. Comparison with experimental data of Ranz and Marshall [12].

Case 5: Energy Conservation in Droplet-Wall Interaction

This case (FDS *water_evaporation_6*) extends the complete evaporation case to include heat transfer to walls. The geometry for the case is a 1 m^3 box with adiabatic walls and an adiabatic ceiling. The floor is a plate with an insulated back that is 1 mm thick with a density of 1000 kg/m^3, a heat capacity of 1 kJ/(kg·K), and an initial temperature of 250 °C. The initial condition in the box is 100 °C air and 0.1 kg of water droplets with an initial temperature of 20 °C and an initial diameter of 2 mm. The droplets are defined as a liquid with a heat capacity of 2 kJ/(kg·K), a boiling point of 100 °C, a density of 1000 kg/m^3, and a heat of vaporization at the boiling point of 173.15 kJ/kg. Following the procedure outlined in Case 1, the final state can be computed using the solid, liquid, and gas thermophysical properties. Table 3 shows the expected results and the results computed by the explicit and the implicit evaporation methods (note, based on timing results shown later in the paper, the equilibrium method was not developed to the point of being able to run this case). Both methods predict the expected values with only minor errors.

Table 3. Results of Verification Case 4: Energy Conservation in Droplet-Wall Interaction

Variable	Expected Value	Explicit	Implicit
Change in pressure (Pa)	34600	34500	34500
Final gas temperature (°C)	172	172	172
Final wall temperature (°C)	172	172	172

Algorithm Cost

Given the suitable and comparable results of the two schemes, computational cost becomes the criterion for acceptance of the method. Below we discuss the computational complexity.

Execution time t for the relaxation and the implicit methods, respectively, can be characterized as

$$t = A + B \times N \tag{7}$$

$$t = C \times N \tag{8}$$

where N is number of droplets per cell and A, B, and C are constants. A is the time to find the equilibrium solution once droplet masses and enthalpies have been determined in the gas cell. Initially, it was thought that this cost might limit the performance of the relaxation method. B is the cost in the relaxation method to sum the mass and enthalpy of a single droplet in a gas cell plus the time to update the droplet mass and temperature once the equilibrium condition is known. C is the cost to update one droplet with the semi-implicit method.

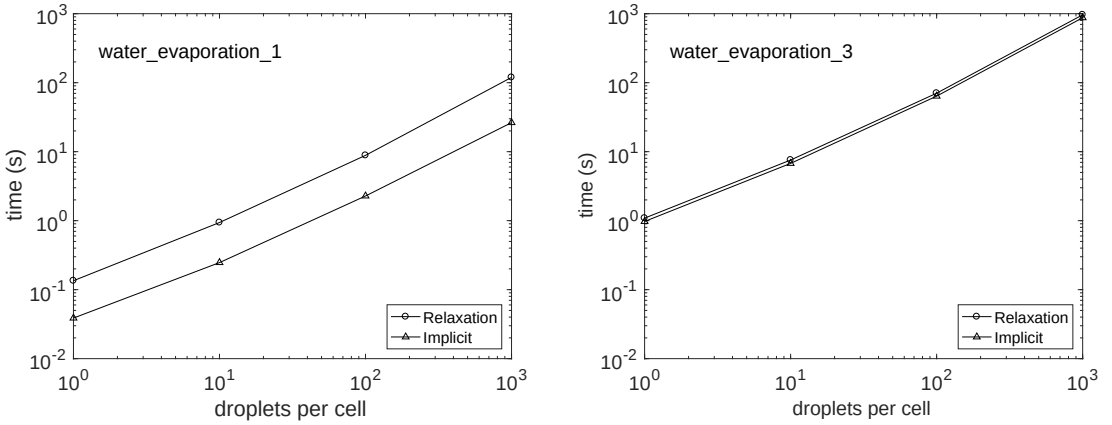

Fig. 2. Results of the algorithm cost for various numbers of particles per cell for complete evaporation (left, Evaporation 1) and partial evaporation (right, Evaporation 3) of monodisperse droplets.

The assumption underlying the development of the relaxation model was that $C > B$ and that for some small number of droplets per cell the analytical solution would be cheaper than the implicit approach. Note that for $C > B$ the cost of relaxation is less than implicit when

$$N > A/(C-B) \tag{9}$$

However, if $C < B$ then, by definition, implicit is always cheaper.

The relative costs, C and B, are determined using two sets of simulations. The first uses Case 1 from above. The second uses a similar case which increases the initial gas temperature to 500 °C and increases the initial droplet diameter to 200 μm. In this second case the droplets do not fully evaporate. Each case is run with a varying number of droplets per cell. The results are shown in Fig. 2. As seen, the relaxation model is always more costly, even for a large number of droplets per cell. In the complete evaporation case (left, Evaporation 1) relaxation is significantly more expensive. It must be concluded, therefore, that $C < B$ for the current implementation. We attribute this result to the significant number of exponential and logarithmic operations needed to evaluate the analytical solution for the relaxation scheme. Contrary to our original assumptions, it appears that evaluation of the equilibrium state is reasonably efficient. Therefore, the relaxation scheme may yet be useful. The present results, however, have led to the adoption of the implicit method going forward.

Test of Expanded Application Space

The prior section demonstrates that the proposed implicit method conserves mass and energy, makes reasonable predictions of the evaporation rate, obtains the correct equilibrium end state, and avoids significant computational cost. The explicit method performed similarly for these simple tests. This section of the paper demonstrates that the new, implicit method overcomes limitations of the explicit method routine and expands the application space of the evaporation model.

As previously discussed, the explicit evaporation model does not directly couple the gas and wall temperature to the droplet temperature solution. This can result in non-physical changes in gas and wall temperature under some conditions. For example, consider a cold superdroplet (representing many real droplets) hitting a hot wall with a very low thermal inertia. Without an implicit wall temperature update in the evaporation model, the heat transfer to the wall will be significantly over predicted for typical FDS time steps. In the wall heat transfer routine, that heat transfer imposed as a boundary condition could result in a very large drop in surface temperature. Similarly for the gas temperature, consider very small droplets not at thermal equilibrium with the gas. The high surface area to volume ratio of small drops can lead to over predictions of heat transfer with the gas when the gas temperature is not treated implicitly. The result can be non-physical changes in the cell gas temperature.

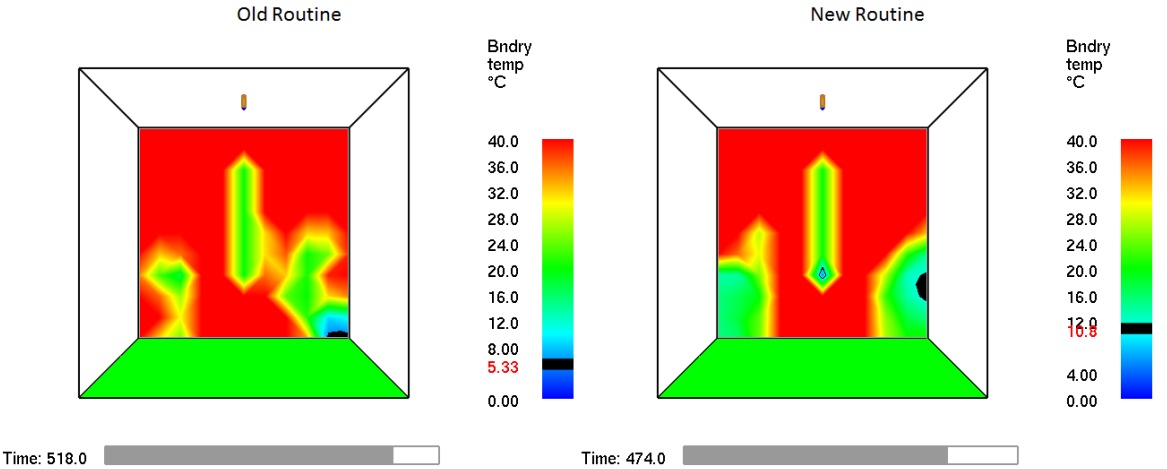

Fig. 3. Wall temperatures resulting from droplets on a burning, low density, low thermal conductivity surface (Left - Explicit, Right - Implicit). Black highlighted contour is lowest temperature.

Cold Spray on Hot Insulated Walls

In this example, a geometry is defined that consists of a burner against a wall made of a combustible, low density, low thermal conductivity material. The burner is allowed to ignite the material, and after a brief period of fire spread, a sprinkler is operated. With the explicit method, this test case is unsuccessful. The low density and low thermal conductivity of the material results in a very small amount of mass in the first wall cell node. Shortly after sprinkler operation, overshoots in the prediction of the wall temperature result in excessive heat removal that eventually leads to a wall cell reaching a 0 K surface temperature, and FDS aborting its calculation.

The new implicit routine couples the wall cell surface temperature to the droplet temperature computation. This limits the amount of heat transfered from the hot wall to the cold droplets on its surface. The result is that very large temperature decreases are avoided and the simulation is stable. Note that presently the implicit method is not fully coupled with the 1D solid phase heat transfer solver (which would be costly), so lower than expected temperatures do occur but not at the magnitude seen with the explicit method. While the exact moment of the failure is not captured in the output files, Fig. 3 shows the output interval for each simulation that had the lowest observed temperatures. The figure shows the wall temperatures for the explicit method on the left and for the implicit method on the right. For each simulation the contour highlighting the lowest temperature at that time is displayed as a black contour with the value in the color bar in red text. As seen the implicit method does not show the very low temperatures seen with the explicit method. The new routine also avoids the numerical error and allows the simulation to complete successfully.

Injection of Very Fine Mist

This example demonstrates an application where very fine water mist is injected. The simulation consists of a 5 m $\times$ 5 m $\times$ 10 m box at 30 °C with a water mist nozzle at mid-height. The nozzle injects a very fine mist of 50 μm at 10 °C. In the explicit method, with the droplet temperature decoupled from the gas temperature, there is an overshoot in heat transfer from the gas to the droplets near the nozzle, resulting in droplet temperatures in excess of 75 °C. Investigation of this scenario determined that the very small droplets had a very high evaporation rate and heat transfer rate. Since the gas temperature was not being solved implicitly together with the droplet temperature, some droplets initially overshot the gas temperature. Those (now hot) droplets then convected the heat back to the gas resulting in elevated gas temperatures in some regions. In the implicit method, the simultaneous solution of the gas and droplet temperature prevents the droplets from overshooting the gas temperature as they heat up. The result is no droplets see temperatures over the initial gas temperature. This is shown below in Fig. 4 which shows droplets colored by temperature shortly after the spray injection starts. With the old routine some droplets were heating to over 80 °C and

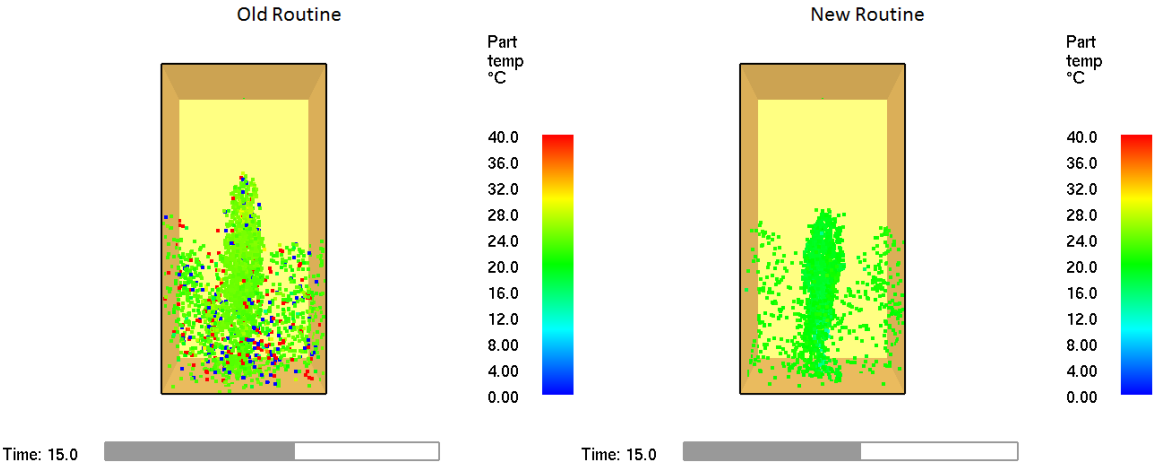

Fig. 4. Injection of very fine, cold water mist into air (left - Explicit, right - Implicit).

some were cooling to freezing (0 °C). In the new routine droplets do not exceed 22 °C, a more reasonable value given an initial gas temperature of 30 °C.

CONCLUSIONS

Droplet evaporation capabilities have seen a continuous evolution since the release of FDS 1 in response to user desires to expand the application space of FDS. This paper continues that evolution by deriving two new approaches for solving the droplet heat and mass transfer equations since explicit approaches for evaporation do not perform well under conditions of very small droplets or cold droplets on hot surfaces with low thermal inertia. The first approach is a novel relaxation-to-equilibrium method, which is applicable to a range of problems requiring time accuracy and stability, such as drag, chemical kinetics, and evaporation. While successful in correctly predicting equilibrium conditions and droplet evaporation rates, the relaxation method proved to be costly for the engineering applications chosen for this study. This led to the development of the second approach, a semi-implicit solution to the governing equations for a single droplet.

The implicit approach has been implemented in FDS and tested against a range of verification and validation problems. The approach was also tested against problems where the explicit method did not perform well. Results demonstrate that the implicit approach conserves mass and energy, and correctly predicts equilibrium without a significant change in computational cost.

REFERENCES

[1] W.K. Chow. On the evaporation effect of sprinkler water spray. *Fire Technology*, 25:364–372, 1989. doi: http://dx.doi.org/10.1007/BF01040382.

[2] S.C. Li, D. Yang, L.H. Huo, Y.Z Li, and H.B. Wang. Studies of cooling effects of sprinkler spray on smoke layer. In *Fire Safety Science – Proceedings of the Ninth International Symposium*, pages 861–872. International Association of Fire Safety Science, 2008. doi: http://dx.doi.org/10.3801/IAFSS.FSS.9-861.

[3] G.G Back, C.L. Beyler, P.J. DiNenno, R. Hansen, and R. Zalosh. Full-scale testing of water mist fire suppression systems in machinery spaces. CG-D-26-98, United States Coast Guard, Washington, DC, 1998.

[4] K. McGrattan, S. Hostikka, R. McDermott, J. Floyd, C. Weinschenk, and K. Overholt. Fire Dynamics Simulator Technical Reference Guide Volume 1: Mathematical Model. NIST SP 1018-1, National Institute of Standards and Technology, Gaithersburg, MD, 2016.

[5] K. McGrattan, S. Hostikka, R. McDermott, J. Floyd, C. Weinschenk, and K. Overholt. Fire Dynamics Simulator User's Guide. NIST SP 1019, National Institute of Standards and Technology, Gaithersburg, MD, 2016.

[6] A. Hamins and K. McGrattan. Reduced-scale experiments to characterize the suppression of rack storage commodity fires. NISTIR 6439, National Institute of Standards and Technology, Gaithersburg, MD, 1999.

[7] M.W. Chase, C.A. Davies, and et al. NIST JANAF Thermochemical Tables 1985 Version 1. NIST SRD 13, National Institute of Standards and Technology, Gaithersburg, MD, 1986.

[8] N. Cheremisinoff. *Encyclopedia of Fluid Mechanics, Volume 3: Gas-Liquid Flows*. Gulf Publishing Company, Houston, TX, 1986.

[9] Y.F. Li. and W.K. Chow. Study of water droplet behavior in hot air layer in fire extinguishment. *Fire Technology*, 44:351–381, 2008. doi: http://dx.doi.org/10.1007/s10694-007-0036-2.

[10] A.B. Carter. DoD Modeling and Simulation (M&S) Verification, Validation, and Accreditation (VV&A). DOD 5000.61, United States Department of Defense, Washington, DC, December .

[11] K. McGrattan, S. Hostikka, R. McDermott, J. Floyd, C. Weinschenk, and K. Overholt. Fire Dynamics Simulator Technical Reference Guide Volume 2: Verification. NIST SP 1019, National Institute of Standards and Technology, Gaithersburg, MD, 2016.

[12] W.E. Ranz and R. Marshall. Evaporation from droplets. *Chemical Engineering Progress*, 48:141–146, 1952.

A Development of a Stable Relaxation Solution

In this appendix, we present a solution method based on relaxation to the "equilibrium state" of a given computational cell. The scheme uses a forward Euler solution at extremely small time steps for the initial relaxation rate, ensuring convergence. Stability is guaranteed for large time steps because we solve the governing equations analytically. As a result, the scheme is first-order accurate and never over-shoots the saturation condition.

Our goal is to design a single step scheme which does not over-shoot the saturation condition. The equilibrium state of the droplet mass and temperature are determined by the cell pressure, composition, and the enthalpy. Then, as if we were looking up the result in a steam table, we establish the equilibrium droplet temperature and droplet mass, the values which would be obtained if the rate equations were integrated to time equals infinity.

The enthalpy of the cell is given by

$$H = \sum_i m_i c_{p,l}(T_i) T_i + m_g \bar{c}_{p,g}(\mathbf{Y}, T_g) T_g \tag{10}$$

$$= \sum_i (m_i - \delta m_i) c_{p,l}(T_{eq}) T_{eq} + (m_g + \delta m) \bar{c}_{p,g}(\mathbf{Y}, T_{eq}) T_{eq} - \dot{q}_r \tag{11}$$

where $\delta m = \sum_i \delta m_i$ is the total mass evaporated at equilibrium conditions. The specific heat of the gas, $\bar{c}_{p,g}$, is tabulated as a function of temperature and composition and includes the heat of vaporization.

Note that *equilibrium* does not imply *saturation*. The cell equilibrium is the resulting state of gas phase composition, temperature, and quality (vapor fraction) under adiabatic conditions. There are two situations

to consider at equilibirum: (1) all water evaporates (under-saturated) and (2) only a fraction of the water evaporates (saturated). Details of the algorithm to determine this state are omitted here for brevity.

The method we have developed to integrate the evaporation model is called a *relaxation scheme*. It takes advantage of two known facts:

(1) An explicit update to Eqs. (1) through (5) is stable and accurate for some small time step.

(2) The equilibrium solution should be obtained for large time steps.

The strategy is to recast the ODEs into a form with a simple analytical solution that is consistent with the facts just stated.

The ODE for the gas phase vapor fraction from Eq. (2) is

$$\rho V \frac{\mathrm{d}Y_v}{\mathrm{d}t} = -\sum_i \frac{\mathrm{d}m_i}{\mathrm{d}t} = -\rho \sum_i A_i h_{m,i}(Y_v - Y_{l,i}) \tag{12}$$

This equation is recast into the form

$$\frac{\mathrm{d}Y_v}{\mathrm{d}t} = -\omega (Y_v - Y_{eq}) \tag{13}$$

which has the simple solution

$$Y_v(t) = Y_{eq} + (Y_{v,0} - Y_{eq}) \exp(-\omega t) \tag{14}$$

It remains that we find a value for the time constant ω such that the solution (14) closely approximates the solution to (12) for small time steps. It is guaranteed that $Y_v = Y_{eq}$ for large time steps. The error for anything in between is impossible to access given the myriad of assumptions underlying the model, and we should be happy with a smooth transition between the two extremes.

The time constant ω is obtained by equating the solutions to a forward Euler update of the model (12) with the relaxation solution (14) at some arbitrarily small (but numerically reasonable) time step. Define $\delta\hat{t} \equiv (1 \times 10^{-3})\Delta t$. We may then write

$$Y_v(\delta\hat{t}) = Y_{v,0} - \delta\hat{t} \underbrace{\frac{1}{V} \sum_i A_i h_{m,i}(Y_{v,0} - Y_{l,i})}_{M} = Y_{eq} + (Y_{v,0} - Y_{eq}) \exp(-\omega \delta\hat{t}) \tag{15}$$

Solving for the time constant yields

$$\omega = -\frac{1}{\delta\hat{t}} \ln\left(1 - \frac{\delta\hat{t} M}{Y_{v,0} - Y_{eq}}\right) \tag{16}$$

which, with $\delta\hat{t}$ sufficiently small, is a positive number with units of s^{-1}.

With a closed form solution for the gas phase vapor fraction we can obtain an analytical solution to Eq. (1). The droplet mass as a function of time is

$$m(t) = \left(m_0^{1/3} + \frac{\beta}{3\omega}\left[1 - \exp(-\omega t)\right]\right)^3 \quad ; \quad \beta = \rho \chi h_m (Y_{v,0} - Y_{l,0}) \quad ; \quad \chi = 4\pi \left(\frac{3}{4\pi\rho_w}\right)^{2/3} \tag{17}$$

Note that χ comes from expressing the area of a drop with mass m as $A = \chi m^{2/3}$. The factor β may be thought of as the rate of mass transfer independent of the droplet mass.

The solution (17) is a cubic (see Fig. 5) and the mass becomes zero when t is

$$t_{m=0} = -\frac{1}{\omega} \ln\left(1 + \frac{3\omega m_0^{1/3}}{\beta}\right) \tag{18}$$

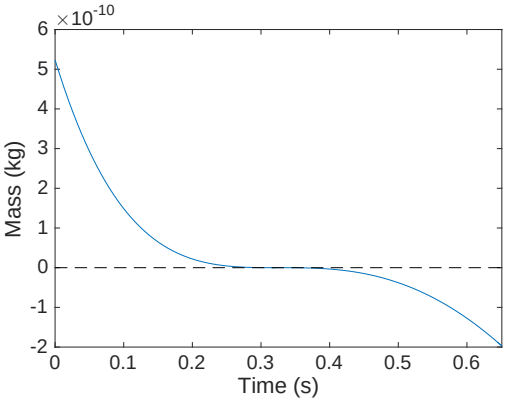

Fig. 5. Droplet mass solution for arbitrary parameter values ($m_0 = 5.3 \times 10^{-10}$, $\omega = 1$, $\beta = -0.0087$). For these parameters, the time to zero mass is $t_{m=0} = 0.3254$.

If the natural log argument is ≤ 0, this means the droplet does not fully evaporate.

Assume the gas phase temperature decays to equilibrium at the same rate as the mass.

$$T_g(t) = T_{eq} + (T_{g,0} - T_{eq})\exp(-\omega t) \tag{19}$$

The most difficult part of this integration is the droplet temperature. Based on the assumed solution (predictor) for the gas phase temperature, Eq. (19), the droplet temperature ODE may be rewritten as

$$\frac{\mathrm{d}T}{\mathrm{d}t} = m^{-1/3}\frac{\chi h}{c_{p,l}}([T_{g,0} - T_{eq}]\exp(-\omega t) + [T_{eq} - T]) + m^{-1}\frac{\dot{q}_r}{c_{p,l}} + m^{-1/3}\frac{\beta h_v}{c_{p,l}}\exp(-\omega t)$$

$$= F(t)T + G(t) \tag{20}$$

where

$$F(t) = -m^{-1/3}\frac{\chi h}{c_{p,l}} = \frac{-\chi h/c_{p,l}}{(m_0^{1/3} + \frac{\beta}{3\omega}[1 - \exp(-\omega t)])} \tag{21}$$

$$G(t) = \frac{\left(\frac{\chi h}{c_{p,l}}[T_{g,0} - T_{eq}] + \frac{\beta h_v}{c_{p,l}}\right)\exp(-\omega t) + \frac{\chi h}{c_{p,l}}T_{eq}}{(m_0^{1/3} + \frac{\beta}{3\omega}[1 - \exp(-\omega t)])} + \frac{\frac{\dot{q}_r}{c_{p,l}}}{(m_0^{1/3} + \frac{\beta}{3\omega}[1 - \exp(-\omega t)])^3} \tag{22}$$

A Crank-Nicolson scheme can be used to solve for the droplet temperature. This scheme is stable. However, it does not respect the equilibrium temperature. Overshoots and undershoots are avoided by setting the temperature to the equilibrium temperature when necessary.

The Crank-Nicolson scheme is

$$\frac{T^{n+1} - T^n}{\Delta t} = F(t^{n+\frac{1}{2}})\left(\frac{T^{n+1} + T^n}{2}\right) + G(t^{n+\frac{1}{2}}) \tag{23}$$

which leads to

$$T^{n+1} = \frac{T^n\left[1 + \frac{\Delta t F(t^{n+\frac{1}{2}})}{2}\right] + \Delta t\, G(t^{n+\frac{1}{2}})}{\left[1 - \frac{\Delta t F(t^{n+\frac{1}{2}})}{2}\right]} \tag{24}$$

where $t^{n+\frac{1}{2}} \equiv \frac{1}{2}(t^{n+1} - t^n)$. This scheme is stable because $F < 0$.

With the gas phase water vapor mass fraction determined as $Y_v(\Delta t)$, via Eq. (14), and individual droplet temperatures determined by Eq. (24), the gas phase temperature may be obtained from a simple energy balance. In practice, the appropriate source terms are accumulated and passed to the gas phase energy equation, which in FDS forms the velocity divergence constraint [4].

B Development of the Implicit Solution

In this appendix, we consider evaporation of a single drop in a computational cell away from the wall. Hence, our goal is to develop a solution for (a) the cell water vapor mass fraction Y_v, (b) the cell gas phase temperature T_g, and (c) the temperature of the ith droplet T_i. The inclusion of convective heat transfer to a wall surface cell is straight-forward. Details are provided in the FDS Technical Reference Guide [4].

The ODEs to be integrated are, respectively, the change in cell water vapor mass fraction, the change in the droplet temperature, and the change in the cell gas phase temperature:

$$\rho V \frac{\mathrm{d}Y_v}{\mathrm{d}t} = -\frac{\mathrm{d}m_i}{\mathrm{d}t} \tag{25}$$

$$m_i c_i \frac{\mathrm{d}T_i}{\mathrm{d}t} = A_g h_g (T_g - T_i) + \frac{\mathrm{d}m_i}{\mathrm{d}t} h_v + \dot{q}_r \tag{26}$$

$$m_g c_g \frac{\mathrm{d}T_g}{\mathrm{d}t} = -A_g h_g (T_g - T_i) + \frac{\mathrm{d}m_i}{\mathrm{d}t} (h_v + h_l) \tag{27}$$

Below we will consider the time integration for a single substep in the evaporation routine, which updates the local computational cell from time t^n to $t^n + \Delta t^n$. Usually, $\Delta t^n = \Delta t_{\mathrm{LES}}$. However, it is possible that subtimesteps may be required to prevent spurious mass and temperature overshoots. In what follows, unless otherwise specified RHS quantities are evaluated at the beginning of the substep, t^n (hence the designation "semi-implicit" method). This limits the stability range of the method (since the method is not fully implicit it is not unconditionally stable), but it greatly simplifies the solution procedure.

To begin the development, we expanded Eq. (25) with the mass loss rate (to be determined) evaluated at the midpoint of the time interval:

$$Y_v^{n+1} = Y_v^n - \frac{\Delta t^n}{\rho V} \left(\frac{\mathrm{d}m_i}{\mathrm{d}t} \right)^{n+\frac{1}{2}} \tag{28}$$

Substituting Eq. 28 into a Crank-Nicolson expansion of Eq. (1) we have

$$\begin{aligned} \left(\frac{\mathrm{d}m_i}{\mathrm{d}t} \right)^{n+1/2} &= -\frac{A_g h_{m,i} \rho}{2} \left(Y_{l,i}^{n+1} + Y_{l,i}^n - Y_v^{n+1} - Y_v^n \right) \\ &= -\frac{A_g h_{m,i} \rho}{2} \left(Y_{l,i}^{n+1} + Y_{l,i}^n - Y_v^n + \frac{\Delta t^n}{\rho V} \frac{\mathrm{d}m_i}{\mathrm{d}t} - Y_v^n \right) \\ &= -\frac{A_g h_{m,i} \rho}{2} \left[\frac{Y_{l,i}^{n+1} + Y_{l,i}^n - 2Y_v^n}{1 + \frac{\Delta t^n A_g h_{m,i}}{2V}} \right] \end{aligned} \tag{29}$$

Next, we find an approximation for the droplet surface equilibrium mass fraction $Y_{l,i}^{n+1}$ via the expansion

$$Y_{l,i}^{n+1} = Y_{l,i}^n + \left(\frac{\mathrm{d}Y_l}{\mathrm{d}T} \right)_i (T_i^{n+1} - T_i^n) \tag{30}$$

The derivative is determined from a chain rule expansion:

$$\left(\frac{\mathrm{d}Y_l}{\mathrm{d}T}\right)_i = \left(\frac{\mathrm{d}Y_l}{\mathrm{d}X_l}\right)\left(\frac{\mathrm{d}X_l}{\mathrm{d}T}\right)_i \tag{31}$$

The water vapor mole fraction on the surface of the droplet is determined from the Clausius-Clapeyron equation:

$$X_{v,l} = \exp\left[\frac{h_v W_v}{R}\left(\frac{1}{T_b} - \frac{1}{T_i}\right)\right] \tag{32}$$

For a binary mixture in air, the relationship between the vapor mass and mole fractions is given by

$$Y_{v,l} = \frac{X_{v,l}}{X_{v,l}(1 - W_a/W_v) + W_a/W_v} \tag{33}$$

Differentiating Eqs. (32) and (33) and substituting into (31) yields

$$\left(\frac{\mathrm{d}Y_l}{\mathrm{d}T}\right)_i = \frac{W_a/W_v}{\left(X_{l,i}(1 - W_a/W_v) + (W_a/W_v)\right)^2}\,\frac{h_v W_v}{R T_i^2}\exp\left[\frac{h_v W_v}{R}\left(\frac{1}{T_b} - \frac{1}{T_i}\right)\right] \tag{34}$$

Using (34) in (30), subsequently (30) in (29), and then (29) in (26) and (27), leaves two equations with two unknowns, T_i^{n+1} and T_g^{n+1}, to be solved simultaneously. As previously noted, unless otherwise indicated, all RHS quantities are evaluated at the beginning of the substep, t^n.

$$T_i^{n+1} = T_i^n + \frac{\Delta t^n}{m_i c_i}\left[A_g h_g\left(\frac{T_g^{n+1} + T_g^n}{2} - \frac{T_i^{n+1} + T_i^n}{2}\right) - \frac{A_g h_{m,i}\rho\left(Y_{l,i}^n + \frac{1}{2}\left(\frac{\mathrm{d}Y_l}{\mathrm{d}T}\right)_i\left(T_i^{n+1} - T_i^n\right) - Y_v^n\right)}{1 + \frac{\Delta t^n A_g h_{m,i}}{2V}} h_v + \dot{q}_r\right] \tag{35}$$

$$T_g^{n+1} = T_g^n + \frac{\Delta t^n A_g}{m_g c_g}\left[-h_g\left(\frac{T_g^{n+1} + T_g^n}{2} - \frac{T_i^{n+1} + T_i^n}{2}\right) + \frac{h_{m,i}\rho\left(Y_{l,i}^n + \frac{1}{2}\left(\frac{\mathrm{d}Y_l}{\mathrm{d}T}\right)_i\left(T_i^{n+1} - T_i^n\right) - Y_v^n\right)}{1 + \frac{\Delta t^n A_g h_{m,i}}{2V}}(h_v + h_l)\right] \tag{36}$$

Finally, the updated cell water vapor mass fraction, Y_v^{n+1}, may be found using (30) in (29), and then (29) in (28).

$$Y_v^{n+1} = Y_v^n + \frac{\Delta t^n}{\rho V}\frac{A_g h_{m,i}\rho}{2}\left[\frac{2Y_{l,i}^n + \left(\frac{\mathrm{d}Y_l}{\mathrm{d}T}\right)_i\left(T_i^{n+1} - T_i^n\right) - 2Y_v^n}{1 + \frac{\Delta t^n A_g h_{m,i}}{2V}}\right] \tag{37}$$

Special Cases

There are several special situations to consider. If the cell is on a surface and the droplets have impacted the surface then an additional heat transfer term with a wall temperature T_w is needed. The system of equations becomes 3×3, which complicates the algebra but the solution is nevertheless straightforward.

When the droplet completely evaporates, T_i^{n+1} is obviously undefined. In this case, a check is performed to ensure that the net heat transfer from the gas (and wall if present) does not exceed the energy required to evaporate the drop.

If the droplet temperature has increased over the boiling point (there is no inherent process in the method that prevents this), additional mass is evaporated to lower the temperature to the boiling point.

If the end state is supersaturated or if there is an unusually large change in droplet or gas temperature, then the timestep is subdivided and the droplet solution is repeated.

Proceedings of the ASME 2017 Power and Energy Conference
PowerEnergy2017
June 26-30, 2017, Charlotte, North Carolina, USA

PowerEnergy2017-3589

CYBER-PHYSICAL SYSTEM DEVELOPMENT ENVIRONMENT FOR ENERGY APPLICATIONS

Thomas Roth
Eugene Song
Martin Burns
Smart Grid & Cyber-Physical Systems Program Office
Engineering Laboratory
National Institute of Standards and Technology
Gaithersburg, MD 20899-8200 USA
{thomas.roth,eugene.song,martin.burns}@nist.gov

Himanshu Neema
William Emfinger
Janos Sztipanovits
Institute for Software-Integrated Systems
Vanderbilt University
Nashville, TN 37212 USA
{himanshu,emfinger,sztipaj}@isis.vanderbilt.edu

ABSTRACT

Cyber-physical systems (CPS) are smart systems that include engineered interacting networks of physical and computational components. The tight integration of a wide range of heterogeneous components enables new functionality and quality of life improvements in critical infrastructures such as smart cities, intelligent buildings, and smart energy systems. One approach to study CPS uses both simulations and hardware-in-the-loop (HIL) to test the physical dynamics of hardware in a controlled environment. However, because CPS experiment design may involve domain experts from multiple disciplines who use different simulation tool suites, it can be a challenge to integrate the heterogeneous simulation languages and hardware interfaces into a single experiment. The National Institute of Standards and Technology (NIST) is working on the development of a universal CPS environment for federation (UCEF) that can be used to design and run experiments that incorporate heterogeneous physical and computational resources over a wide geographic area. This development environment uses the High Level Architecture (HLA), which the Department of Defense has advocated for co-simulation in the field of distributed simulations, to enable communication between hardware and different simulation languages such as Simulink and LabVIEW. This paper provides an overview of UCEF and motivates how the environment could be used to develop energy experiments using an illustrative example of an emulated heat pump system.

Introduction

A cyber-physical system (CPS) consists of a set of interacting cyber-physical devices where each device contains some cyber computation that can sense events from and actuate changes on a physical infrastructure. Examples of CPS include smart cities, intelligent buildings, and the smart grid. One method to validate a CPS design uses hardware-in-the-loop (HIL) in conjunction with simulations to test the runtime dynamics of a cyber-physical device in a virtual test environment. A challenge of experiments that incorporate both HIL and simulations is that they often require a testbed that integrates hardware components with multiple, heterogeneous simulation environments.

A large number of HIL testbeds which offer unique experimental opportunities cannot be replicated due to limitations in both hardware cost and development time [1–5]. These testbeds often have different architectures and utilize different simulation languages because of their independent development histories, and an experiment tailored for one testbed might not be compat-

Burns, Martin; Emfinger, William; Neema, Himanshu; Roth, Thomas; Song, Yuyin; Sztipanovits, Janos.
"Cyber-Physical System Development Environment for Energy Applications."
Paper presented at 2017 11th International Conference on Energy Sustainability (ES2017), Charlotte, NC. June 26, 2017 - June 30, 2017.
SP-612

ible with another architecture. The inability to exploit the full range of available resources in the CPS landscape leads to segregated groups of researchers who are experts in a single testbed environment but face challenges in the adoption of external research advances. In addition, integrated experiments for CPS require access to resources pooled from multiple domains to produce faithful models of the deployed system. For example, experiments on smart cities may involve collaboration across domains such as transportation, energy, and emergency response. An experiment should integrate models developed in those domains, which may involve domain-specific tools (e.g. a traffic simulator written in C++), to achieve the most realistic result.

NIST envisions a universal CPS environment for federation (UCEF) which enables experiments to exploit multiple testbed architectures using a common interface. The United States Department of Defense mandated a common integration platform in the field of distributed simulators called the High Level Architecture (HLA) [6]. This paper demonstrates the use of HLA in the design and implementation of cyber-physical devices using an integration architecture that supports collaboration between physical hardware and simulations. The approach is highlighted using an example CPS implementation of an HVAC system controlled by a thermostat with a remote temperature sensor, which is a straightforward and well understood application that does not require deep domain expertise to comprehend.

The rest of the paper is organized as follows. Section II provides an overview of HLA and the design process to implement an HLA federation. Section III demonstrates this design process in an example CPS through implementation of a distributed HVAC system. Section IV outlines other work on the integration of HLA with hardware, and the paper concludes with Section V.

High Level Architecture

HLA is an IEEE standard for distributed simulation in which individual simulations called federates join together to form a cooperative federation [6]. All federates in a federation interact using a Run-Time Infrastructure (RTI) software implementation of a set of HLA services such as publish-subscribe messaging, logical time management, and distributed object management. Data exchanges between the federates must adhere to a federation object model (FOM) which defines the set of messages understood by the federation. Although the original intent of HLA was to allow federated co-simulation of simulation platforms such as MATLAB and Modelica, a CPS federate could represent a cyber-physical device. This section provides a brief overview of this paper's approach to designing an HLA federation with hardware-in-the-loop. The overview is based on a model-based simulation integration environment developed and maintained by Vanderbilt University called the Command and Control Wind Tunnel (C2WT) [7], but has been sufficiently generalized to be applicable to alternative HLA development environments.

Federation Stack Architecture

HLA does not mandate a specific RTI implementation, which can consist of two different types of components. A Local RTI Component (LRC) provides an Application Program Interface (API) to interface federates with the RTI, and a Central RTI Component (CRC) coordinates the other run-time components. A specific RTI implementation may provide a centralized CRC, multiple hierarchical CRCs, or no CRC. The results in this paper use an open-source RTI implementation called Portico which implements the LRC at each federate and requires no CRC [8]. Fig. 1 shows a federation stack architecture for this implementation that illustrates the necessary components for a federate. This figure contains three example federate types: a simulation, a cyber-physical device, and a federation manager that drives an experiment.

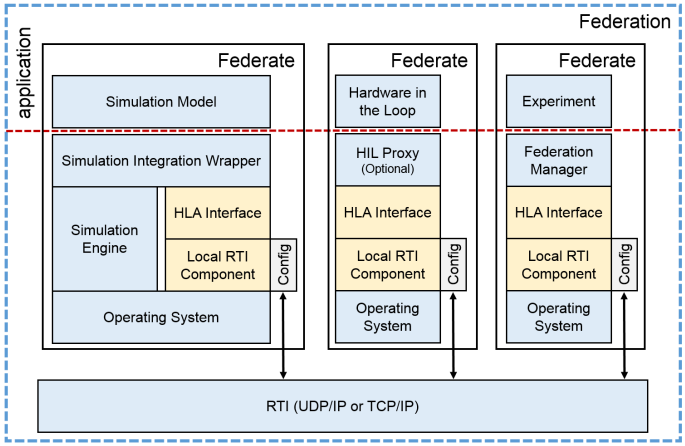

FIGURE 1. Federation Stack Architecture

Each federate has a *Local RTI Component* implementation which enables it to communicate with the federation, and all federates must use the same LRC implementation to ensure coherent communication between the federation members. The Portico LRC implementation uses either TCP/IP or UDP/IP sockets for its intra-federation communication. On top of this communication infrastructure, an *HLA Interface* exposes the set of standardized services available for federates. For the C2WT integration environment, the HLA interface is a Java abstract class which exposes the various HLA services as Java functions. The implementation of the LRC and its HLA interface are uniform across all of the federate types.

For simulation platforms such as MATLAB, the federate must also contain a *Simulation Engine* that runs the simulation models. The simulation engine may not have a native RTI interface. In order to make these platforms compatible with HLA, an adapter labeled the *Simulation Integration Wrapper* must be

Burns, Martin; Emfinger, William; Neema, Himanshu; Roth, Thomas; Song, Yuyin; Sztipanovits, Janos.
"Cyber-Physical System Development Environment for Energy Applications."
Paper presented at 2017 11th International Conference on Energy Sustainability (ES2017), Charlotte, NC. June 26, 2017 - June 30, 2017.
SP-613

developed to translate the HLA interface into the language of the simulation engine. These wrappers are reusable and all of the models for the same simulation engine use the same wrapper implementation to join an HLA federation.

For hardware-in-the-loop, there is no simulation engine and the ease of HLA integration depends on whether the hardware controller can run the RTI implementation and its dependencies. The Portico LRC, for example, is written in Java and might not be able to run on all embedded systems. For the cases that do not support Java, an *HIL proxy* for the hardware must be deployed on a separate, compatible processor. This proxy federate serves as an adapter between the hardware and the HLA interface and can use any protocol to connect to the hardware while using the LRC's communication stack to expose the hardware interface to the federation.

Each federation has an additional *Federation Manager* that coordinates the other federates and runs the experiment. The federation manager's responsibilities include creation of the federation and management of synchronization points such as simulation start. The federation manager can also affect the operational flow of an experiment based on its intermediate results, providing a powerful and flexible experiment design capability. This federation manager is not part of the HLA standard, but is a natural way to provide the ability to affect the runtime behavior of a federation execution for an experiment. It is important to note that the federation manager is a normal HLA federate and has the same access to the HLA services as all other federates in the federation.

Federate Development Workflow

The NIST vision of a UCEF testbed consists of an open database of simulation and hardware federates as described in the prior section that can be composed into complex cyber-physical experiments. One requirement for this vision is an integration environment where the various pieces of the stack architecture can be developed and assembled. Fig. 2 shows the development workflow to create the necessary parts for this architecture.

The Web Generic Modeling Environment (WebGME), developed by Vanderbilt University, provides tools and methods for creating meta-models for rich Domain-Specific Modeling Languages (DSMLs) which can then be used to design domain models and generatively synthesize programs [9]. WebGME has been leveraged to create a DSML for modeling HLA federations. In practice, WebGME could be replaced with an alternative tool in the development workflow as long as the new tool maintained the same interfaces shown in the figure. One function of WebGME is to model *Federate Interfaces*, which in the language of HLA would be the Simulation Object Model (SOM) which describes the publish-subscribe model for a federate. A second function of WebGME is to use code generation to transform the modeled federate interfaces into basic federate implementations,

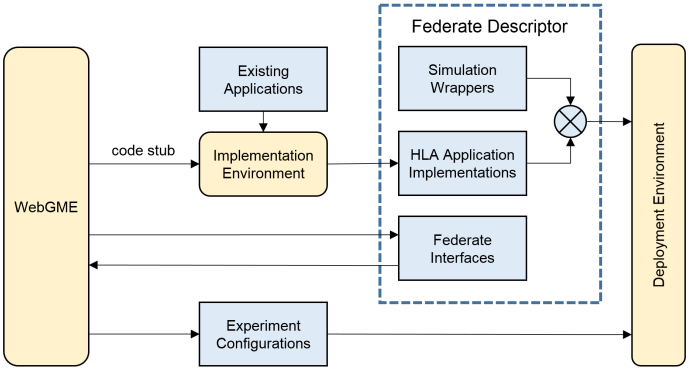

FIGURE 2. Federation Development Workflow

or *code stubs*. This generated code stub contains the HLA interface block shown in Fig. 1, which must then be extended into either a simulation or hardware application. An *Implementation Environment* (such as MATLAB or Java) must be used to either extend this code stub or integrate it with an *Existing Application* to produce an *HLA Application*. If the HLA application uses a simulation platform that requires custom wrapper code to integrate with HLA, then the application code must be combined with the *Simulation Integration Wrapper* prior to deployment. A federate descriptor combines the federate interface, its implementation in either simulation or hardware, and any simulation wrapper necessary to integrate the federate with HLA.

After a database of federate descriptors has been developed, a subset of the descriptors must be combined together to form a federation that performs some useful experiment. Another function of WebGME is the ability to produce *Experiment Configurations* which includes programming the federation manager's runtime behavior using a graphical language such as courses of action [10] or colored Petri nets [11]. The experiment configuration defines which federate descriptors will participate in the federation, where each federate descriptor will be deployed, and what script the federation manager will use for the experiment.

Example HVAC System

This section introduces a simple heating, ventilating, and air conditioning (HVAC) system that will be used to demonstrate the implementation of a hardware federate in HLA. An HVAC system was selected as the example implementation because it is a well understood application.

Fig. 3 shows the federation design for a thermostat that controls the HVAC system using a remote temperature sensor. The federation consists of three federates excluding the federation manager. The HVAC federate controls a relay board connected to two fans and a Peltier heat pump to change the temperature of a pair of heatsinks. The remote temperature sensor federate reads the temperature measurement of a sensor placed inside one

Burns, Martin; Emfinger, William; Neema, Himanshu; Roth, Thomas; Song, Yuyin; Sztipanovits, Janos.
"Cyber-Physical System Development Environment for Energy Applications."
Paper presented at 2017 11th International Conference on Energy Sustainability (ES2017), Charlotte, NC. June 26, 2017 - June 30, 2017.
SP-614

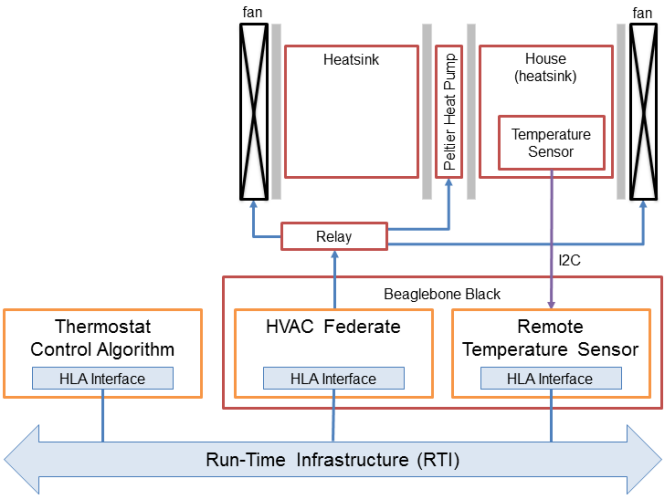

FIGURE 3. Federated HVAC System Design

heatsink that represents a house. Both of these federates run on a BeagleBone Black (BBB) and communicate with a thermostat federate over the RTI. The thermostat can remotely pull the house temperature from the temperature sensor via the BBB, compare it to some internal set point, and then remotely issue commands to the heat pump to maintain the set point.

Hardware Implementation

The thermostat issues heating and cooling commands to the heat pump to control the temperature of the heatsink that represents a house. A Peltier heat pump can transfer heat from one side of the device to the other based on the direction of the electric current. This enables the heat pump to provide both of the required heating and cooling functions. Fig. 4 shows the hardware implementation of the federated HVAC system. At the top of the figure, a 12 V, 5 A Peltier Thermo-Electric Cooler Module and Heatsink Assembly is mounted onto an additional heatsink and fan assembly with thermal paste and an aluminum clamp. A Microchip MCP9808 temperature sensor is inserted into the right heatsink to measure the temperature of the house. The temperature sensor communicates using a 2-wire inter-integrated circuit (I2C) bus that allows for serial communication between a master device (e.g. BBB) and its slave devices (e.g. temperature sensor).

The BBB is an embedded computer with an AM335x 1 GHz ARM Cortex-A8 processor that is compatible with Debian, Android, Ubuntu, and Cloud9 [12]. The libbulldog Java library for the BBB provides low-level IO capabilities for embedded linux systems which includes the ability to access the general purpose IO pins and communicate to slave devices using I2C [13]. Fig. 5 shows how the BBB was integrated with the hardware in the HVAC system. A 4-channel relay board was inserted between the BBB and the heatsinks and fans, with one pin allocated for

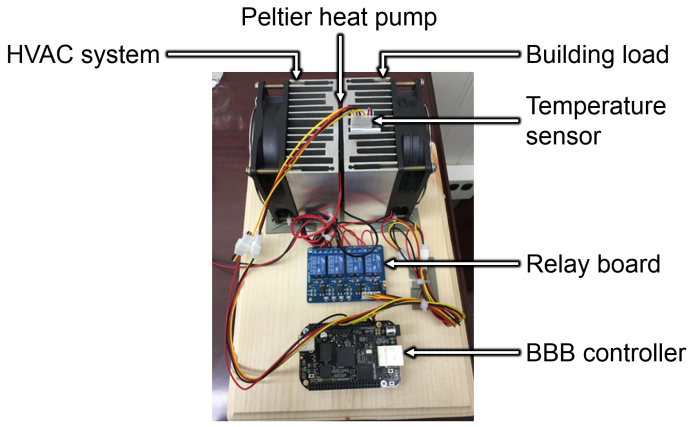

FIGURE 4. HVAC System Hardware Implementation

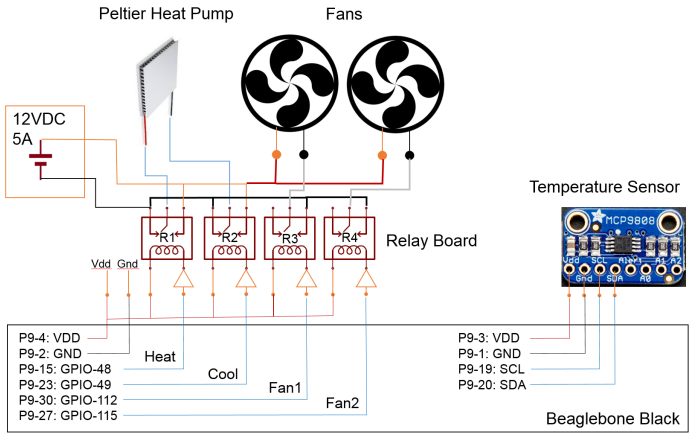

FIGURE 5. BeagleBone Black Pin Connections

each fan and two pins for the heat pump. The fan signal represents its on/off state, while the two heat pump signals determine whether the unit is off, heating, or cooling. The BBB is also connected to the temperature sensor using its I2C serial communication ports. These connections allow the federates running on the BBB to read the temperature measurement and control the heat pump and associated fans.

Federate Implementation

The hardware implementation discussed so far falls into the *Existing Applications* box in Fig. 2. This section will describe how to create the three required federate descriptors to turn the hardware into an HLA application.

The first step is to design the various federate interfaces in WebGME. Fig. 6 shows the federation design for the HVAC system in this environment. The federation consists of three federates: a hardware HVAC federate which controls the relay board, a HIL proxy federate for the temperature sensor, and a soft-

Burns, Martin; Emfinger, William; Neema, Himanshu; Roth, Thomas; Song, Yuyin; Sztipanovits, Janos.
"Cyber-Physical System Development Environment for Energy Applications."
Paper presented at 2017 11th International Conference on Energy Sustainability (ES2017), Charlotte, NC. June 26, 2017 - June 30, 2017.
SP-615

ware thermostat federate for the control algorithm that uses the temperature measurement to generate heating and cooling commands. The temperature sensor federate publishes a single interaction called SensorMessage which contains the temperature measurement from the sensor located in the house heatsink. The thermostat federate subscribes to this interaction, with the expectation that the temperature measurement will be used to perform some amount of internal computation. The result of this computation is published to the HVAC federate through the ControlMessage interaction which contains four bit values for the relay board in the hardware implementation.

The code generation capability of WebGME can generate code stubs from these federate interfaces which contain boilerplate HLA code for connecting to the Portico LRC implementation. For the thermostat control algorithm, this code stub was extended into a simple Java program that extracts the temperature measurement from the SensorMessage, compares the measurement to an internal set point, and generates heating or cooling commands to maintain that set point. The HVAC federate was also extended into a Java program that turns the generated heating and cooling commands into electronic actuation. Its implementation leverages the libbulldog library which provides a Java interface to the BBB general I/O pins connected to the relay board. The temperature sensor required an HIL proxy federate to translate between the communication infrastructure provided by the Portico LRC implementation and its I2C serial bus. This proxy federate uses I2C to read the measurement produced by the temperature sensor, package the measurement in an HLA message format, and broadcast the measurement to the federation. The temperature sensor proxy federate was also developed in Java and used the same libbulldog library to create an I2C connection between the BBB and the temperature sensor device. Fig. 7 shows a sequence diagram of one round of message exchanges between the three federates during the federation execution.

The complete federate descriptor for each federate consists of its Java implementation and the WebGME project that defines its interface. Because the HVAC system did not require a simulator, none of the federate descriptors include a simulation integration wrapper. Now an experiment must be designed that describes the configuration in which the federate descriptors will be used in a larger federation.

Experimental Federate Design and Results

The experiment was configured to run both the HVAC and temperature sensor federates on the BBB and the thermostat federate on an Ubuntu desktop machine. The Ubuntu machine was connected to the BBB using a USB cable, and all communication used a USB network interface. The thermostat federate was configured to maintain a temperature set point of 38°C with a tolerance of 1°C. As mentioned before, an additional federation manager federate was used to create the federation and coordinate the progression of the experiment. The federation manager was deployed on the Ubuntu machine using the experimental configuration generated by WebGME to inform it of the other federates expected to participate in the federation. Once all of the federates had joined the federation execution, the federation manager began a simulation that was configured to run for 180 seconds. Fig. 8 shows the temperature measurement read by the BBB during the federation execution. The BBB federate that controls the heatsink temperature was implemented using a simple control algorithm that did not model the physical system dynamics. Using the tools described in this paper, this control federate could be replaced with a federate using a different control algorithm that includes a prediction model to keep the temperature within the 1°C tolerance. The HLA implementation of the HVAC system with a remote temperature sensor functions as intended, and the federates coordinate over HLA to maintain the desired temperature set point.

Related Work

The original intent of HLA was to enable co-simulation between simulators with no notion of the hardware-in-the-loop described in this paper. There are pure simulation environments that integrate multiple tools using HLA federation to model more complex systems appropriate for the CPS domain. EPOCHS is one example which uses HLA to combine power simulation software with a network simulator to enable more accurate simulation of smart grids [14]. These simulation environments are useful experimental tools, but are not readily applicable to HIL testbeds. There have been several efforts which have extended HLA to support hardware for specific experiments in the domains of mechatronic systems [15], power systems [16], and embedded devices [17]. These efforts were focused on domain specific experimental outcomes rather than documentation of the development process for hardware federate interfaces, and their approaches are consistent with the architecture detailed in this paper.

In addition to efforts to develop HLA interfaces for specific simulations or hardware, several development environments to design these interfaces have emerged in recent literature. The authors in [18] extend the SysML modeling language to support HLA federation design and add a code generation capability to transform SysML models into code stubs for federate implementation. The authors in [19] introduce the architecture and workflow required to integrate new simulators with HLA using a similar SysML approach. Both of these environments are consistent with the figures and discussion in Section II with the exception of modeling using SysML instead of the model integration language for WebGME.

Burns, Martin; Emfinger, William; Neema, Himanshu; Roth, Thomas; Song, Yuyin; Sztipanovits, Janos.
"Cyber-Physical System Development Environment for Energy Applications."
Paper presented at 2017 11th International Conference on Energy Sustainability (ES2017), Charlotte, NC. June 26, 2017 - June 30, 2017.
SP-616

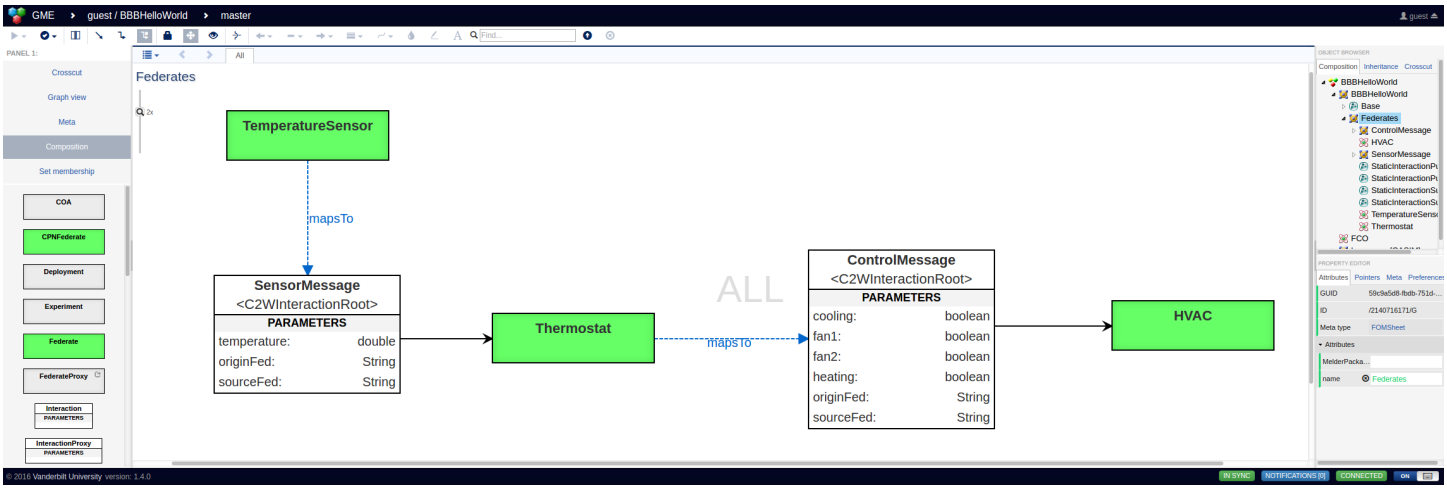

FIGURE 6. Federation Design of the HVAC System in WebGME

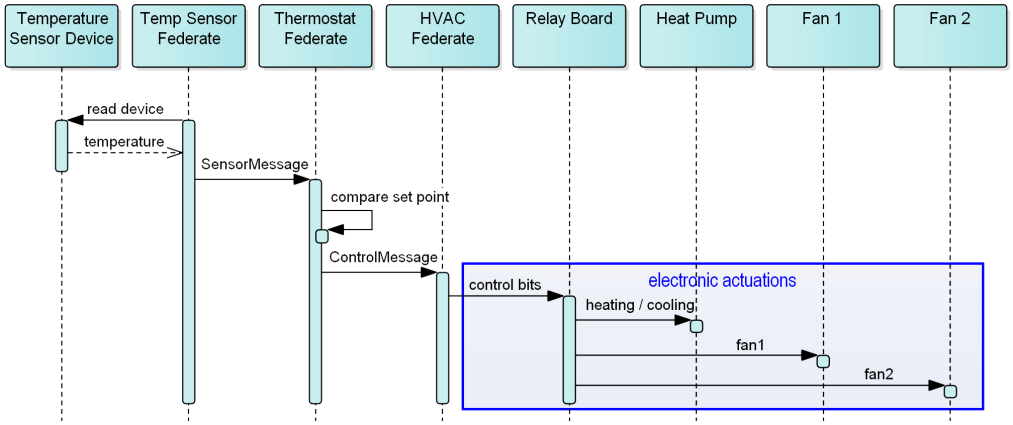

FIGURE 7. Sequence Diagram of the Federation Execution

Conclusion

This paper demonstrated how to design and implement HLA federates for cyber-physical devices using an example HVAC application. The original intent of HLA was to enable co-simulation of discrete simulation platforms, but the design and implementation of simple hardware federates can easily conform to the standard. The tools and design process described in this paper can be used to integrate more complex hardware implementations with HLA, leading to the development of federates that encapsulate entire testbed architectures.

Further efforts to integrate complex hardware with HLA could potentially enable a public database of federate descriptors which includes both simulation and hardware from which an experiment could be assembled to test sophisticated energy applications. However, adherence to the HLA standard does not require documentation of a federate's functionality beyond the simulation object model that describes data exchanges in terms of publications and subscriptions. For a CPS, the data exchange model is insufficient to capture the complexities of a physical system which might have instability concerns related to the timing and values of the messages it receives from different sources. One aspect missing from the presented architecture is a means to document these interoperability constraints which would enable a domain expert to determine when a set of federate descriptors were composable. Future work will begin to enumerate the interoperability constraints that must be documented for each federate.

The goal of this research is to realize federate descriptors for testbeds and refine the federation development workflow to support multiple testbed architectures. The end result will be the design of a universal CPS environment for federation (UCEF) that is flexible enough to run experiments across multiple domains using resources from multiple HIL testbeds. NIST is working with Vanderbilt University and others to develop the components

Burns, Martin; Emfinger, William; Neema, Himanshu; Roth, Thomas; Song, Yuyin; Sztipanovits, Janos.
"Cyber-Physical System Development Environment for Energy Applications."
Paper presented at 2017 11th International Conference on Energy Sustainability (ES2017), Charlotte, NC. June 26, 2017 - June 30, 2017.
SP-617

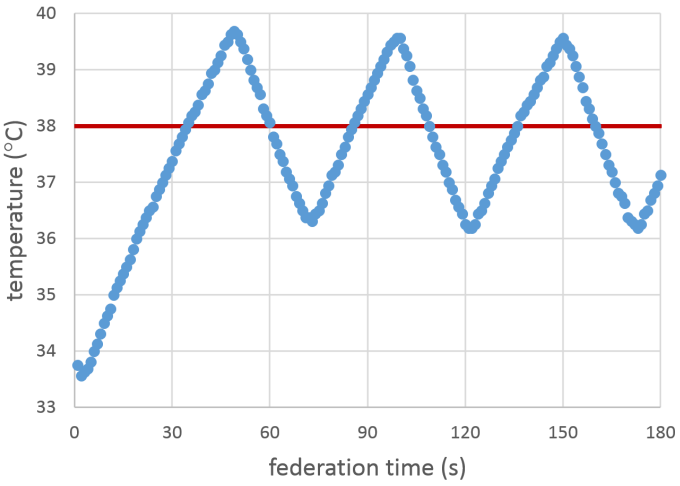

FIGURE 8. Temperature during Federation Execution

of this design and package them into a development environment to readily model, implement, and deploy CPS experiments.

REFERENCES

[1] Chen, X., and Sun, J., 2011. "Characterization of inverter-grid interactions using a hardware-in-the-loop system testbed". In 2011 8th International Conference on Power Electronics and ECCE Asia (ICPE & ECCE), IEEE, pp. 2180–2187.

[2] Prokhorov, A. V., Gusev, A. S., and Borovikov, Y. S., 2013. "Hardware-in-the-loop testbed based on hybrid real time simulator". In Innovative Smart Grid Technologies Europe (ISGT EUROPE), 2013 4th IEEE/PES, IEEE, pp. 1–5.

[3] Stanovich, M. J., Leonard, I., Sanjeev, K., Steurer, M., Roth, T. P., Jackson, S., and Bruce, M., 2013. "Development of a smart-grid cyber-physical systems testbed". In Innovative Smart Grid Technologies (ISGT), 2013 IEEE PES, IEEE, pp. 1–6.

[4] Pang, X., Wetter, M., Bhattacharya, P., and Haves, P., 2012. "A framework for simulation-based real-time whole building performance assessment". *Building and Environment,* ***54***, pp. 100–108.

[5] Haves, P., and Xu, P., 2007. "The building controls virtual test bed a simulation environment for developing and testing control algorithms, strategies and systems". In Proc. of the 10-th IBPSA Conference, pp. 1440–1446.

[6] , 2010. "IEEE standard for modeling and simulation (M&S) high level architecture (HLA)– framework and rules". *IEEE Std 1516-2010 (Revision of IEEE Std 1516-2000)*, Aug, pp. 1–38.

[7] Hemingway, G., Neema, H., Nine, H., Sztipanovits, J., and Karsai, G., 2012. "Rapid synthesis of high-level architecture-based heterogeneous simulation: a model-based integration approach". *Simulation,* ***88***(2), pp. 217–232.

[8] Portico. https://github.com/openlvc/portico. [accessed 11-March-2016].

[9] Maróti, M., Kecskés, T., Kereskényi, R., Broll, B., Völgyesi, P., Jurácz, L., Levendovszky, T., and Lédeczi, Á., 2014. "Next generation (meta) modeling: Web-and cloud-based collaborative tool infrastructure.". In MPM@ MoDELS, pp. 41–60.

[10] Neema, H., Karsai, G., and Levis, A., 2015. "Next-generation command and control wind tunnel for courses of action simulation". *Technical Report ISIS-15-119*, May, p. 119.

[11] Jensen, K., 1987. "Coloured petri nets". In *Petri nets: central models and their properties*. Springer, pp. 248–299.

[12] Beaglebone black. https://beagleboard.org/black. [accessed 8-April-2016].

[13] libbulldog. http://beagleboard.org/project/libbulldog. [accessed 02-June-2016].

[14] Hopkinson, K., Wang, X., Giovanini, R., Thorp, J., Birman, K., and Coury, D., 2006. "EPOCHS: a platform for agent-based electric power and communication simulation built from commercial off-the-shelf components". *IEEE Transactions on Power Systems,* ***21***(2), pp. 548–558.

[15] Kanai, S., Miyashita, T., and Tada, T., 2007. "A multi-disciplinary distributed simulation environment for mechatronic system design enabling hardware-in-the-loop simulation based on HLA". *International Journal on Interactive Design and Manufacturing (IJIDeM),* ***1***(3), pp. 175–179.

[16] Jablkowski, B., Spinczyk, O., Kuech, M., and Rehtanz, C., 2014. "A hardware-in-the-loop co-simulation architecture for power system applications in virtual execution environments". In 2014 Workshop on Modeling and Simulation of Cyber-Physical Energy Systems (MSCPES), IEEE, pp. 1–6.

[17] Brito, A. V., and Nascimento, T. P., 2015. "Verification of embedded system designs through hardware-software co-simulation". *International Journal of Information and Electronics Engineering,* ***5***(1), p. 68.

[18] Bocciarelli, P., D'Ambrogio, A., Giglio, A., and Gianni, D., 2013. "A SaaS-based automated framework to build and execute distributed simulations from SysML models". In 2013 Winter Simulation Conference (WSC), IEEE, pp. 1371–1382.

[19] Jain, A., Fujimoto, R., Crittenden, J., Liu, M., Kim, J., and Lu, Z., 2015. "Towards automating the development of federated distributed simulations for modeling sustainable urban infrastructures". In 2015 Winter Simulation Conference (WSC), IEEE, pp. 2668–2679.

Burns, Martin; Emfinger, William; Neema, Himanshu; Roth, Thomas; Song, Yuyin; Sztipanovits, Janos.
"Cyber-Physical System Development Environment for Energy Applications."
Paper presented at 2017 11th International Conference on Energy Sustainability (ES2017), Charlotte, NC. June 26, 2017 - June 30, 2017.
SP-618

A GENERALIZED METHOD FOR FEATURIZATION OF MANUFACTURING SIGNALS, WITH APPLICATION TO TOOL CONDITION MONITORING

Max Ferguson
Stanford University
Stanford, CA, USA

Kincho H. Law
Stanford University
Stanford, CA, USA

Raunak Bhinge
Infinite Uptime, Inc.
Berkeley, CA, USA

Yung-Tsun Tina Lee
National Institute of Standards and Technology (NIST)
Gaithersburg, MD, USA

ABSTRACT

The application of machine learning techniques in the manufacturing sector provides opportunities for increased production efficiency and product quality. In this paper, we describe how audio and vibration data from a sensor unit can be combined with machine controller data to predict the condition of a milling tool. Emphasis is placed on the generalizability of the method to a range of prediction tasks in a manufacturing setting. Time series, audio, and acceleration signals are collected from a Computer Numeric Control (CNC) milling machine and discretized into blocks. Fourier transformation is employed to create generic power spectrum feature vectors. A Gaussian Process Regression model is then trained to predict the condition of the milling tool from the feature vectors. We highlight that this multi-step procedure could be useful for a range of manufacturing applications where the frequency content of a signal is related to a value of interest.

INTRODUCTION

The application of modern machine learning techniques to manufacturing processes provides an opportunity to increase productivity and improve overall product quality in traditional manufacturing lines [1]. The adoption of predictive models within the industrial value chain is part of a larger transition often referred to as the industrial internet, which promises to bring substantially increased operational effectiveness as well as the development of entirely new business models, services, and products [2].

In order to increase manufacturing productivity while reducing maintenance costs, it is crucial to develop more intelligent maintenance strategies, that can predict when maintenance should be performed [3]. Reliable tool-condition monitoring is likely to play an important role in the reactive maintenance strategies of future manufacturing facilities.

Bhinge, Raunak; Ferguson, Max; Law, Kincho; Lee, Yung-Tsun.
"A Generalized Method for Featurization of Manufacturing Signals, With Application to Tool Condition Monitoring."
Paper presented at the 37th Computers and Information in Engineering Conference IDETC2017, Cleveland, OH. August 6, 2017 - August 9, 2017.

Numerous machine learning models have been proposed to optimize a range of tasks, from robotic control to machine failure detection [4,5]. One of the hurdles preventing adoption on a broader scale is that preprocessing raw data into relevant features is a subjective and difficult process [6]. In developing most machine learning models, a domain expert is given the task of carefully selecting a set of inputs, normally referred to as features, that yield optimum performance for the given prediction task. While such a technique has been considered the status quo for some time, recent progress in deep learning has demonstrated that automatic feature selection often yields superior performance than manual feature selection [7]. The recent popularization of Deep Recurrent Neural Networks provides a promising method of analyzing time series data [8]. However, the development of deep neural networks requires a large training dataset and tremendous computational power [9].

Researchers have previously demonstrated that the condition of a machine tool can be inferred from features of the vibration and audio signals [10,11]. A number of researchers have attempted to use the skew and kurtosis coefficients of the audio and acceleration time-series to predict the condition of the tool, but with mixed results [11–13]. Bukkapatnam et al. developed a tool wear prediction technique using an artificial neural network (ANN) with features inspired by the principles of nonlinear dynamics [14]. Sanjay et al. developed a model for predicting tool flank wear using ANNs [15]. The feed rates, spindle speeds, torques, machining times, and thrust forces were used to train the ANN model. Wu et al. reviewed these methods and demonstrated an alternative approach using random forests with a set of manually selected features [3]. A wide range of tool monitoring techniques have been reviewed by Dimla et al [16]. They concluded that existing techniques perform well on carefully selected experimental data, but there is a need for a multi-level system capable of handling unprocessed data.

While the application of machine learning to continuous time series data brings about its own difficulties, there are several characteristics of manufacturing that make it a perfect match for machine learning. First, manufacturing tends to be a repetitive process, and hence the time series signals from manufacturing often tend to be repetitive. Second, faults in the manufacturing process are likely to produce a different signal, and can be identified by comparing the time series signal against that from an operational product line.

In this paper, we outline a methodology for extracting information from a time series data source, with emphasis on generalizability. In this method, the time series signals are aggregated, transformed, and then classified. In the first step, we break the time series into a series of blocks, using instructions from the machine controller. In the tool wear example, each block corresponds to a single cutting action of the milling machine. However, the method only requires that the blocks represent a signal from some repeated part of the process. In the second step, we calculate the power spectral density (PSD) of each time series block using Fast Fourier Transform (FFT). Finally, we train a Gaussian Process Regression (GPR) model to predict tool condition based on the PSD vectors.

The remainder of the paper is organized as follows: In the first section, we review how time series audio and vibration data are collected from a Computer Numeric Control (CNC) machine, namely a Mori Seiki NVD1500DCG. In the next section, we describe how the time series data is divided into blocks using information from the machine controller. We then discuss how feature vectors are developed to represent the frequency content of the audio and acceleration sensors. We conclude by demonstrating that the frequency vectors contain information about the tool condition, and subsequently show that they can be used to predict tool condition using a GPR algorithm.

TIME SERIES DATA COLLECTION

In this section, we describe how time series acceleration and acoustic data were collected from a CNC milling machine, namely a Mori Seiki NVD1500DCG. As shown in Figure 1, a waterproof sensor unit from Infinite Uptime was attached to the vise of the milling machine.

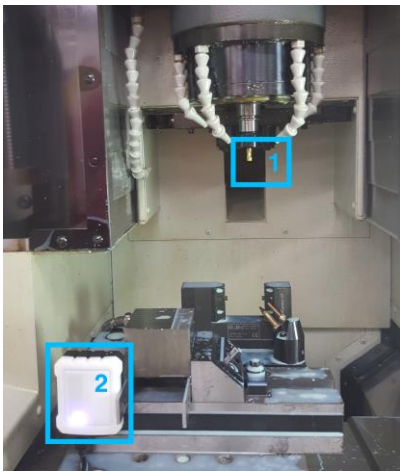

FIGURE 1. A MORI SEIKI NVD1500DCG MILLING MACHINE WITH CUTTING TOOL (1) AND SENSOR UNIT FROM INFINITE UPTIME (2)

The sensor unit was capable of measuring both the audio and triaxial acceleration signals inside the milling machine. The acceleration signal was recorded in the x-, y- and z-directions at 1000 Hz. The audio signal was recorded at 8000 Hz. Data is streamed from the sensor to a laptop computer using a Universal Serial Bus (USB) connection.

The milling machine was programmed to produce a number of simple 'parts' by removing material from a solid steel block. Each part consisted of 20 separate cutting actions performed by the milling machine. Figure 2 shows a section of acceleration time series data recorded using the sensor unit.

The machining data, such as tool position and rotation speed, were recorded from the FANUC controller. An MTConnect agent was used to synchronize the data from the milling machine and stream it to a laptop computer, along with a timestamp. A post-processing step was used to convert the machining data into a set of operations performed by the machine. The post-processing involved a simulation step, which is previously described in an earlier paper [17].

GENERIC FEATURE VECTORS

In machine learning, the process of featurization involves converting raw data into a vector form that is suitable for the chosen machine learning model. The featurization process often reduces the dimensionality of the data, which in turn reduces the computational burden of training the predictive model. In this section, we describe how the time series data is split into blocks using the controller data, and then converted into feature vectors.

In a more traditional application of machine learning, we would attempt to identify a range of different measures that correlate strongly with the target value of interest, which, in this study, is tool condition. A number of researchers have attempted to use the skew and kurtosis coefficients of the audio and acceleration time series to predict the condition of the tool with mixed results [11–13]. While this approach is valuable, it can also limit the application of the model to a very specific scenario. Instead, we create relatively large feature vectors, and use an optimization algorithm to assign a weight to each feature.

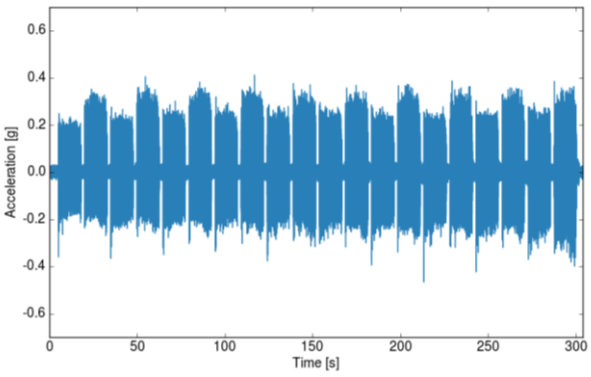

FIGURE 2. MEASURED ACCELERATION SIGNAL IN THE X-DIRECTION WHILE PRODUCING A SINGLE PART

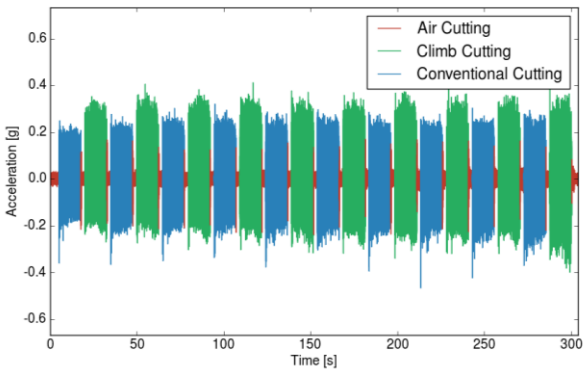

FIGURE 3. ACCELERATION SIGNAL IN THE X-DIRECTION, AFTER BEING AUTOMATICALLY LABELED USING THE CONTROLLER DATA.

Discretizing Time Series Data

The first step of preprocessing a time series data is to divide the data into blocks, according to the type of operation performed by the machine. The data from the milling machine controller is used to automatically label the time series data. Labelling the time series makes the dataset more structured, and thus makes the dataset more suitable for use with machine learning algorithms. The milling machine performs a number of different operations to produce a part. Figure 3 shows the time series data in the production of a part that involves 10 climb-cutting operations and 10 conventional-cutting operations. Each cutting operation is separated by a brief "air cutting" operation, in which the machine pauses briefly between cuts. We use the terms "climb cutting" and "conventional cutting" refer to the relationship between the rotation direction to the feed direction. A detailed description of these operations has been discussed earlier [17].

The audio and vibration signals produced are dependent on the type of cutting operation being performed by the milling machine, as illustrated in Figure 3.

Estimating the Power Spectral Density

Next, we estimate the power spectral density (PSD) of each time series block. As the audio and acceleration signals are periodic, the PSD provides an elegant way to summarize the information about the signals. In many cases, comparing the PSD of different blocks can reveal information about the underlying physical process.

FFT is used to estimate the PSD of each time series block. For each acceleration or audio signal, $s \in \mathbb{R}^N$, the PSD is given by:

$$\hat{s}(\omega) = \frac{1}{N}\left|\sum_{n=0}^{N-1} s(n)e^{-i\omega n}\right|^2, \qquad (1)$$

where $\hat{s}(\omega)$ is the PSD of the signal at angular frequency ω. The PSD is computed at a discrete set of frequencies $\omega = 2\pi k/T$ for $k \in \{1 \dots N\}$, where T is the sampling period of the signal.

When the PSD is estimated in this manner the PSD vector $\hat{s} \in \mathbb{R}^N$, has the same length as the input time series signal $s \in \mathbb{R}^N$. Because inconsistencies exist in manufacturing processes, the length of each time series block varies slightly. This variation is typical of most manufacturing processes, where small variations tend to occur in each iteration of a repetitive process [18]. On the other hand, in machine learning it is expected that the length of the feature vectors is the same. Therefore, we calculate the PSD over sequential windows of constant length, and average the results. Specifically, the time series is broken into *M* consecutive segments, where each segment has a length of 256 points. The PSD is calculated for each of the *M* segments. The PSD for the entire block is obtained by averaging the PSDs for each segment. There are several benefits of computing the PSD in this manner. First, the length of the frequency coefficient vector is now the same across all time series blocks. Second, the averaging process helps to reduce noise in the PSD, while still providing a consistent estimate of the PSD [19].

To create a generic feature vector, the PSD vectors of each signal are combined. Let $\hat{\boldsymbol{a}}$ be the audio PSD and $\hat{\boldsymbol{v}}_x$, $\hat{\boldsymbol{v}}_y$ and $\hat{\boldsymbol{v}}_z$ be the vibration PSD. We denote the generic feature vector as:

$$\boldsymbol{x}^i = \begin{bmatrix} \hat{\boldsymbol{a}} \\ \hat{\boldsymbol{v}}_x + \hat{\boldsymbol{v}}_y + \hat{\boldsymbol{v}}_z \end{bmatrix}, \qquad (2)$$

where the generic feature vector $\boldsymbol{x}^i$ contains the PSD from the audio and vibration signals. The PSD vector for the vibration data in each direction are added. By Parseval's theorem the result will always have the same signal energy as the sum of energies of the components [20]. In this way, the vibration component of the generic feature vector is largely invariant to the rotation of the accelerometer.

To demonstrate that the generic feature vector contains relevant information about the physical process, several feature vectors are compared. Figure 4 compares the feature vectors from operations with different cutting strategies. Figure 5 compares the coefficients from a new tool and a worn tool.

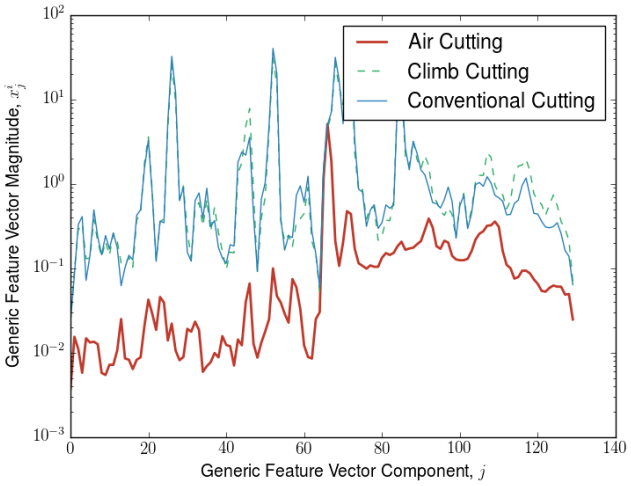

FIGURE 4. COMPARISON OF FEATURE VECTORS WHILE THE MACHINE WAS PERFORMING DIFFERENT CUTTING OPERATIONS.

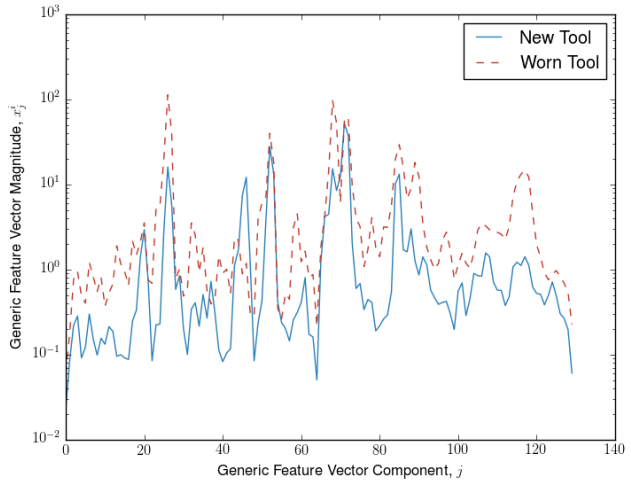

FIGURE 5. COMPARISON OF FEATURE VECTORS FOR A NEW TOOL AND A WORN TOOL, WHILE A CLIMB CUTTING OPERATION WAS BEING COMPLETED

TOOL CONDITION PREDICTION MODEL

In this section, we develop a GPR model to predict tool condition using the generic frequency feature vectors. A number of alternative techniques such as k-Nearest Neighbors and Support Vector Regression were considered. GPR is chosen as it performs particularly well with noisy data. An additional benefit of GPR is that it provides a distribution on the target value, as opposed to a scalar estimate.

GPR has been used to develop models for a range of manufacturing problems. In [21], GPR was used to predict the energy consumption of a CNC milling machine using features such as spindle speed and cutting type. A variant of GPR called Local Gaussian Process Regression (LGPR) was used in [4] to develop a model for real-time robot control. The Predictive Model Markup Language (PMML) was recently extended to offer GPR support, as described in [22] and [23], providing a standardized format to save and transport GPR models.

Data Collection

The Mori Seiki milling machine was used to produce parts until the cutting tool became severely damaged, or the cutting tool broke. A total of 14 tools were used to produce 56 parts. The audio and vibration time series were recorded as described earlier.

In a typical manufacturing environment, machine tools tend to last several days. To accelerate the testing process, the operating parameters of the machine were adjusted to increase the rate of tool-wear by increasing the feed rate and reducing the rotation speed. With the adjusted operating parameters, the operating lifetime of a cutting tool was reduced to about 30 minutes in this experiment.

Defining Tool Condition

A number of different methods have been proposed to measure the condition of a machine tool. While quantitative measurements such as the wear depth have been proposed as tool condition measures, these measures often fail to accurately capture wear when the blade becomes chipped.

In this study, we define the condition of the milling machine tool $y_c \in [0,1]$, based on the remaining lifetime of the tool, as estimated after manually examining the tool with a microscope. The scale is defined such that 100 % indicates a new tool in perfect condition, and 50 % indicates the condition at which the tool would be replaced in a commercial manufacturing operation. Figure 6 illustrates four different states of the machine tool flute.

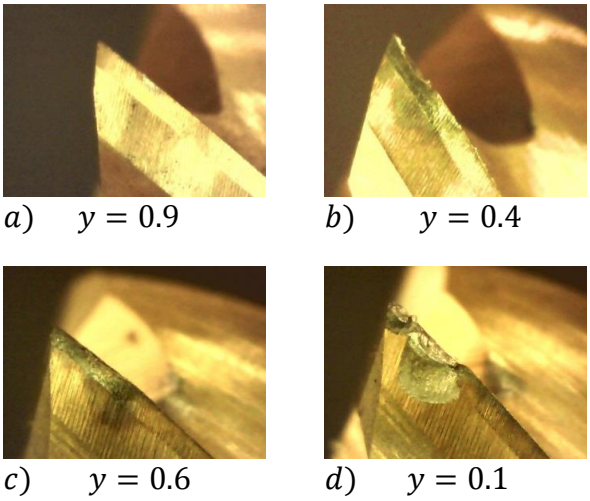

FIGURE 6. TOOL FLUTE IN DIFFERENT STATES OF CONDITION. A LOWER VALUE OF y INDICATES MORE WEAR

Gaussian Process Model

In GPR, a Gaussian process (GP) is used as a prior to describe the distribution on the target function $y = f(x)$. A GP is a generalization of the Gaussian probability distribution for which any finite linear combination of samples has a joint Gaussian distribution [24].

A GP can be fully specified by its mean function m(·) and covariance kernel function k(·,·).

$$p(f^{1:n}) = GP\big(m(\cdot), k(\cdot,\cdot)\big). \tag{3}$$

The mean function $m(\cdot)$ captures the overall trend in the target function value and the kernel function $k(\cdot,\cdot)$ is used to approximate the covariance by representing the similarity between the data points [24]. For the tool condition model, we choose to use the zero function as the mean function.

In general, we denote the input as $\boldsymbol{x}^i \in \mathbb{R}^{\boldsymbol{n}}$ and the target value as $y \in \mathbb{R}$. In the proposed data processing method, the input $\boldsymbol{x}^i$ is the generic feature vector. A GP is used as a prior to describe the distribution on the target function $y^i = f(\boldsymbol{x}^i)$. We attempt to learn the target function by incorporating prior knowledge captured in historical data. Suppose the current data set is denoted by $\boldsymbol{D} = \{(\boldsymbol{x}^i, y^i) | i = 1, \dots n\}$. With GPR, the measured output $y^{new} = f(\boldsymbol{x}^{new})$ corresponding to the new feature vector x^{new} and the historical outputs $y^{1:n}$ in the training data set follow a multivariate Gaussian distribution:

$$\begin{bmatrix} \boldsymbol{y}^{1:n} \\ f^{new} \end{bmatrix} \sim N\left(\boldsymbol{0}, \begin{bmatrix} \mathbf{K} & \boldsymbol{k} \\ \boldsymbol{k}^T & k(\boldsymbol{x}^{new}, \boldsymbol{x}^{new}) \end{bmatrix}\right), \tag{4}$$

where the entries in the vector $\boldsymbol{k}$, and the covariance kernel matrix $\mathbf{K}$, are defined respectively as:

$$\boldsymbol{k}_i = k\big(\boldsymbol{x}^i, \boldsymbol{x}^{new}\big), \tag{5}$$

$$\mathbf{K}_{ij} = k\big(\boldsymbol{x}^i, \boldsymbol{x}^j\big). \tag{6}$$

The covariance kernel matrix $\mathbf{K}$ is often precomputed on the training data, allowing new predictions to be computed efficiently.

Selecting a Kernel Function

The covariance kernel function provides an efficient method to compute the similarity between two generic feature vectors. In GPR, the kernel function is used to estimate the covariance between two input vectors, $\boldsymbol{x}^{\mathrm{i}}$ and $\boldsymbol{x}^j$.

The Automatic Relevance Determination (ARD) squared exponential kernel is often used with GPR, as it automates the selection of feature weights. The ARD squared exponential function can be expressed as:

$$k(\boldsymbol{x}^i, \boldsymbol{x}^j) = \gamma \exp\left(-\frac{1}{2}(\boldsymbol{x}^i - \boldsymbol{x}^j)^T \mathrm{diag}(\boldsymbol{\lambda})^{-2}(\boldsymbol{x}^i - \boldsymbol{x}^j)\right), \tag{7}$$

where the kernel function is described by the hyper-parameters, γ and $\boldsymbol{\lambda}$. The signal variance hyper-parameter γ quantifies the overall magnitude of the covariance value. The hyper-parameter λ_k where $k \in \{1 \dots |\boldsymbol{\lambda}|\}$ is used to quantify the relevancy of the input feature x_k^i when predicting the response y. During the training process, an optimization problem is constructed to maximize the likelihood of the training data, relative to the hyper-parameters γ and $\boldsymbol{\lambda}$ [24].

Noise Model

Each tool condition label y, is likely to contain random noise due to the complex nature of tool wear and the manual labelling method. To account for this random noise we assume that each

observed value contains some random noise ϵ, such that $y = f(\boldsymbol{x}) + \epsilon$. We assume that this noise follows an independent, identically distributed Gaussian distribution with zero mean and variance σ_ϵ^2:

$$\epsilon \sim \mathcal{N}(0, \sigma_\epsilon^2). \tag{8}$$

It follows from the independence assumption that the noise model can be represented by adding a noise term to the kernel function [24]:

$$k(\boldsymbol{x}^i, \boldsymbol{x}^j) = \gamma \exp\left(-\frac{1}{2}(\boldsymbol{x}^i - \boldsymbol{x}^j)^T \mathrm{diag}(\boldsymbol{\lambda})^{-2}(\boldsymbol{x}^i - \boldsymbol{x}^j)\right) + \sigma_\epsilon^2 \delta_{ij}, \tag{9}$$

where δ_{ij} represents Kronecker delta function which serves to selectively add the noise variance σ_ϵ^2 to the covariance value.

Model Regularization

The size of the hyperparameter vector is dependent on the choice of kernel and the length of the input vector $\boldsymbol{x}^i$. With the ARD squared exponential kernel, the number of hyperparameters can become reasonably large:

$$|\boldsymbol{\theta}| = |\gamma| + |\boldsymbol{\lambda}| = 1 + |\boldsymbol{x^i}|. \tag{10}$$

The large number of hyperparameters increases the flexibility of the model, allowing it to represent high-dimensional relationships. The increased model complexity also makes it prone to overfitting. In machine learning, regularization is commonly used to limit the parameter space of the model. Bayesian model selection is an alternative approach to regularization, used to constrain the model complexity, as described in [25]. We start by defining a prior $p(\boldsymbol{\theta})$ on the hyperparameters $\boldsymbol{\theta}$, to restrict the hyperparameter space. Hereafter we will refer to $p(\boldsymbol{\theta})$ as the hyperprior, as is common in existing literature [24]. In the proposed methodology, we choose the hyperprior to minimize the weights in $\boldsymbol{\theta}$.

$$p(\boldsymbol{\theta}) \sim \mathcal{N}(0, \alpha^2 \boldsymbol{I}), \tag{11}$$

where α is a regularization parameter which controls the flexibility of the model. For a large α, the model will tend to fit to the training data well, but is unlikely to generalize well to the unseen test data. As the value of α is decreased the model will become more constrained, and the generalization error will tend to decrease. The optimum value of α is found through cross-validation.

Training Procedure

In the training procedure a GP is fitted to the training data set. Suppose we denote the dataset $\boldsymbol{D} = \{(\boldsymbol{x}^i, y^i) | i = 1, \ldots n\}$ for time series block i. The GPR training procedure involves selecting a set of hyperparameters to maximize the marginal likelihood of the training data. The marginal distribution of the observations can be expressed as:

$$p(\boldsymbol{y}^{1:n}|\boldsymbol{\theta}) = \int p(\boldsymbol{y}^{1:n}|\boldsymbol{f}^{1:n})\, p(\boldsymbol{\theta}) p(\boldsymbol{f}^{1:n}|\boldsymbol{\theta})\, d\boldsymbol{f}^{1:n}. \tag{12}$$

The unknown function $\boldsymbol{f}$ can be marginalized out of (12) to obtain the marginal likelihood of the training observations. The hyperparameters $\boldsymbol{\theta}$ are chosen to maximize the marginal likelihood of observations in a given training data set $\boldsymbol{D}$. An optimization equation is formed to maximize the marginal likelihood, and obtain to the optimum hyperparameters $\boldsymbol{\theta}^*$:

$$\boldsymbol{\theta}^* = \arg\max_{\theta} \log p\,(\mathbf{y}^{1:n}|\boldsymbol{\theta}\,). \tag{13}$$

Finding the optimum hyperparameters using (13) requires an iterative approach as the value of the kernel matrix **K** is inherently dependent on the hyperparameters. The process for obtaining the optimum hyperparameters is well documented in the literature [24]. The MATLAB library GPML [25] is chosen to optimize the hyperparameters.

Scoring Procedure

In GPR, the aim of the scoring procedure is to obtain a posterior distribution f^{new} on the output value, based on the previously unseen observation $\boldsymbol{x}^{new}$. In the case where the mean function is zero, the posterior distribution on the response f^{new} for the newly observed input $\boldsymbol{x}^{new}$ can be expressed as a Gaussian distribution:

$$f^{new} \sim \mathcal{N}\left(\mu(\boldsymbol{x}^{new}|\boldsymbol{D}^n), \sigma^2(\boldsymbol{x}^{new}|\boldsymbol{D}^n)\right). \quad (14)$$

The posterior mean $\mu(\boldsymbol{x}^{new}|\boldsymbol{D}^n)$, and associated variance $\sigma^2(\boldsymbol{x}^{new}|\boldsymbol{D}^n)$, can be calculated directly. As the posterior distribution is 1D Gaussian, the posterior mean and variance are sufficient to fully describe the posterior distribution. That is, the posterior distribution can be expressed as [24]:

$$\mu(\boldsymbol{x}^{new}|\boldsymbol{D}^n) = \boldsymbol{k}^T(\mathbf{K} + \sigma_\epsilon^2\mathbf{I})^{-1}\boldsymbol{y}^{1:n}, \quad (15)$$

$$\sigma^2(\boldsymbol{x}^{new}|\boldsymbol{D}^n) = k(\boldsymbol{x}^{new}, \boldsymbol{x}^{new}) - \boldsymbol{k}^T(\mathbf{K} + \sigma_\epsilon^2\mathbf{I})^{-1}\boldsymbol{k}. \quad (16)$$

MODEL PERFORMANCE

When evaluating machine learning models, it is common practice to divide the data set into a training set and testing set. The model is trained on the training set and then tested on the previous unseen data in the testing set. Data points from three cutting tools were randomly selected for the testing set. Two GP models are trained to predict tool condition; the first is trained with the generic feature vectors from the climb-cutting blocks, and the second is trained with the feature vectors from the conventional-cutting blocks.

The two models are used together to predict the condition of the tool, for each point in the testing set. Figure 7 and Figure 8 provide a comparison of the model predictions with the human labels. In the ideal case, the model would predict the same values as the human labels, and the plotted points would align with the dotted diagonal line. It can be observed that the trained model predicts the tool conditions comparable to the human labeled results.

The tool condition predicted by the model closely aligns with the human labelled tool condition for relatively new tools, especially for tool condition in the 90-100 % range. This is most likely because the new tools provide a very consistent audio and vibration signal. Once the tool condition drops below 40 % there is a larger variation in the audio and vibration signals, making tool condition prediction more difficult. For example, a cutting tool at 40 % condition may have sustained heat damage and worn smooth, or it may have undergone brittle failure and chipped. Both failure modes would provide different audio and vibration signals, but the model is expected to label both cases as 40 % wear. The confidence interval increases as the condition decreases, indicating that it is harder to predict more heavily worn tools, as shown in Figure 7 and Figure 8.

It is likely that the accuracy of the model could be improved by increasing the amount of data in the training data set. The training data set does not contain many time series segments for worn tools, as a number of tests had to be stopped before the tool condition dropped below 20 %. Increasing the number of training data points collected with worn tools could reduce the confidence intervals in the predictions.

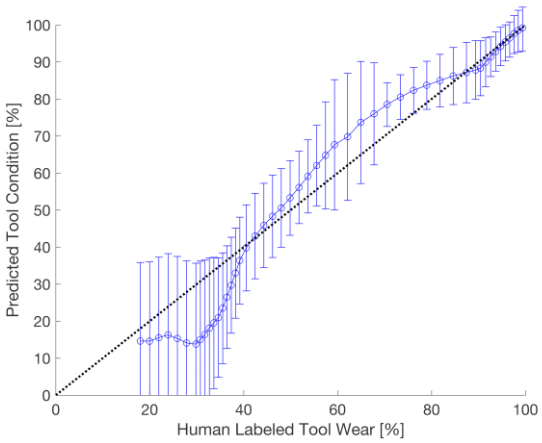

FIGURE 7. TOOL CONDITION PREDICTION FOR THE CLIMB CUTTING ACTIONS IN ONE OF THE THREE TEST DATASETS. THE ERROR BARS INDICATE ONE STANDARD DEVIATION IN THE TARGET DISTRIBUTION.

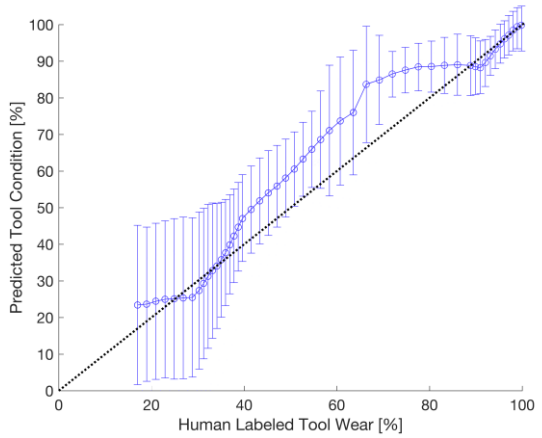

FIGURE 8. TOOL CONDITION PREDICTION FOR THE CONVENTIONAL CUTTING ACTIONS IN ONE OF THE THREE TEST DATASETS. THE ERROR BARS INDICATE ONE STANDARD DEVIATION IN THE TARGET DISTRIBUTION.

However, in an industrial application the cutting tool will be replaced before it reaches 50 % wear, so the accuracy of the model is less critical for heavily worn tools.

DISCUSSION

This study demonstrates how information from a milling machine controller can be combined with sensor data to predict the condition of the milling machine tool. Information from the milling machine controller was used to aggregate the time series data over a set of finite intervals. The frequency content in each time series block were summarized using a PSD. The PSD from the audio and vibration signals were combined to create a generic feature vector, containing information about each time series block.

The use of a non-parametric regression model, namely GPR, allowed the complex relationship between the generic feature vector and the target value to be modelled. The ARD squared exponential kernel was used to automate the feature selection process. The combination of the generic feature vectors and automated weighting procedure make this technique applicable to a range of different modelling tasks in the manufacturing domain. However, the cross-validation training procedure increases the training time by an order of magnitude.

The GP model provides confidence bounds for the predictive estimations, which are useful when interpreting the reliability of a prediction at some arbitrary time. The confidence bounds would likely prove useful in a practical application where the tool-condition predictions were used to determine when to change machine tools.

FUTURE WORK

For this method to have practical applications, it must generalize well to a range of different machines and machine operations. A similar technique could be applied to predict tool condition on a range of different manufacturing machines. The same technique could also be applied to correlate time series signals with surface quality or bearing failure.

ACKNOWLEDGMENT

The authors acknowledge the support by the Smart Manufacturing Systems Design and Analysis Program at the National Institute of Standards and Technology (NIST), US Department of Commerce. This work was performed under the financial assistance award (NIST Cooperative Agreement 70NANB17H031) to Stanford University. The authors would like to acknowledge the collaboration with the late Professor David Dornfeld of University of California Berkeley, who was instrumental in making the experiments possible.

DISCLAIMER

Certain commercial systems are identified in this paper. Such identification does not imply recommendation or endorsement by NIST; nor does it imply that the products identified are necessarily the best available for the purpose. Further, any opinions, findings, conclusions, or recommendations expressed in this material are those of the authors and do not necessarily reflect the views of NIST or any other supporting U.S. government or corporate organizations.

REFERENCES

[1] Monostori, L., 2003, "AI and Machine Learning Techniques for Managing Complexity, Changes and Uncertainties in Manufacturing," Engineering Applications of Artificial Intelligence, **16**(4), pp. 277–291.

[2] Hermann, M., Pentek, T., and Otto, B., 2016, "Design Principles for Industrie 4.0 Scenarios," *49th Hawaii International Conference on Hawaii International Conference on System Sciences (HICSS)*, IEEE, pp. 3928–3937.

[3] Wu, D., Jennings, C., Terpenny, J., Gao, R. X., and Kumara, S., 2017, "A Comparative Study on Machine Learning Algorithms for Smart Manufacturing: Tool Wear Prediction Using Random Forests," Journal of Manufacturing Science and Engineering, **139**(7), p. 71018.

[4] Nguyen-Tuong, D., and Peters, J., 2008, "Local Gaussian Process Regression for Real-Time Model-Based Robot Control," *2008 IEEE/RSJ International Conference on Intelligent Robots and Systems*, IEEE, pp. 380–385.

[5] Tai, A. H., Ching, W.-K., and Chan, L.-Y., 2009, "Detection of Machine Failure: Hidden Markov Model Approach," Computers & Industrial Engineering, **57**(2), pp. 608–619.

[6] Du, K.-L., and Swamy, M., 2013, *Neural Networks and Statistical Learning*, Springer Science & Business Media.

[7] Wollsen, M. G., Hallam, J., and Jørgensen, B. N., 2016, "Novel Automatic Filter-Class Feature Selection for Machine Learning Regression," *INNS Conference on Big Data*, Springer, pp. 71–80.

[8] Zhao, R., Yan, R., Chen, Z., Mao, K., Wang, P., and Gao, R. X., 2016, "Deep Learning and Its Applications to Machine Health Monitoring: A Survey," submitted to IEEE Transactions on Neural Networks and Learning Systems.

[9] Aggarwal, C. C., 2014, *Data Classification: Algorithms and Applications*, Chapman & Hall/CRC.

[10] Kannatey-Asibu, E., and Dornfeld, D. A., 1982, "A Study of Tool Wear Using Statistical Analysis of Metal-Cutting Acoustic Emission," Wear, **76**(2), pp. 247–261.

[11] Silva, R., Reuben, R., Baker, K., and Wilcox, S., 1998, "Tool Wear Monitoring of Turning Operations by Neural Network and Expert System Classification of a Feature Set Generated from Multiple Sensors," Mechanical Systems and Signal Processing, **12**(2), pp. 319–332.

[12] Diniz, A., Liu, J., and Dornfeld, D., 1992, "Correlating Tool Life, Tool Wear and Surface Roughness by Monitoring Acoustic Emission in Finish Turning," Wear, **152**(2), pp. 395–407.

[13] Dimla, D. E., 2000, "Sensor Signals for Tool-Wear Monitoring in Metal Cutting Operations—a Review of Methods," International Journal of Machine Tools and Manufacture, **40**(8), pp. 1073–1098.

[14] Moon, F. C., and Kalmár-Nagy, T., 2001, "Nonlinear Models for Complex Dynamics in Cutting Materials," Philosophical Transactions of the Royal Society of London A: Mathematical, Physical and Engineering Sciences, **359**(1781), pp. 695–711.

[15] Sanjay, C., Neema, M., and Chin, C., 2005, "Modeling of Tool Wear in Drilling by Statistical Analysis and Artificial Neural Network," Journal of Materials Processing Technology, **170**(3), pp. 494–500.

[16] Dimla, D., Lister, P., and Leighton, N., 1997, "Neural Network Solutions to the Tool Condition Monitoring Problem in Metal Cutting—a Critical Review of Methods," International Journal of Machine Tools and Manufacture, **37**(9), pp. 1219–1241.

[17] Bhinge, R., Biswas, N., Dornfeld, D., Park, J., Law, K. H., Helu, M., and Rachuri, S., 2014, "An Intelligent Machine Monitoring System for Energy Prediction Using a Gaussian Process Regression," *2014 IEEE International Conference on Big Data*, pp. 978–986.

[18] Braha, D., 2013, *Data Mining for Design and Manufacturing: Methods and Applications*, Springer Science & Business Media.

[19] Hayes, M. H., 2009, *Statistical Digital Signal Processing and Modeling*, Wiley India Limited.

[20] Landin, N., Romano, J. M., McMahan, W., and Kuchenbecker, K. J., 2010, "Dimensional Reduction of High-Frequency Accelerations for Haptic Rendering," *International Conference on Human Haptic Sensing and Touch Enabled Computer Applications*, Springer, pp. 79–86.

[21] Park, J., Law, K. H., Bhinge, R., Biswas, N., Srinivasan, A., Dornfeld, D. A., Helu, M., and Rachuri, S., 2015, "A Generalized Data-Driven Energy Prediction Model with Uncertainty for a Milling Machine Tool Using Gaussian Process," *ASME 2015 International Manufacturing Science and Engineering Conference*, American Society of Mechanical Engineers.

[22] Ferguson, M., Law, K. H., Park, J., Bhinge, R., Dornfeld, D. A., and Lee, Y.-T. T., 2016, "Evaluation of a PMML-Based GPR Scoring Engine on a Cloud Platform and Microcomputer Board for Smart Manufacturing," *2016 IEEE International Conference on Big Data*.

[23] Park, J., Lechevalier, D., Ak, R., Ferguson, M., Law, K. H., Lee, Y.-T. T., and Rachuri, S., 2017, "Gaussian Process Regression (GPR) Representation Using Predictive Model Markup Language (PMML)," Smart and Sustainable Manufacturing Systems. Manuscript submitted for publication.

[24] Rasmussen, C. E., and Williams, C. K., 2006, *Gaussian Processes for Machine Learning*.

[25] "Documentation for GPML Matlab Code" [Online].Available: http://www.gaussianprocess.org/ gpml/code/matlab/doc/

Healthy Buildings 2017 Europe
July 2-5, 2017, Lublin, Poland

Paper ID 0242 ISBN: 978-83-7947-232-1

Carbon Dioxide Generation Rates from Building Occupants

Andrew Persily[1,*], Lilian de Jonge[2]

[1] National Institute of Standards and Technology (NIST), Gaithersburg Maryland, USA
[2] George Mason University, Fairfax Virginia, USA

[*]*Corresponding email: andyp@nist.gov*

SUMMARY
Indoor carbon dioxide (CO_2) concentrations have been used in the fields of building ventilation and indoor air quality (IAQ) for decades to estimate ventilation rates, to control outdoor air ventilation rates, and to assess IAQ. These applications employ CO_2 generation rates for the building occupants, which historically and currently are based on approaches and data from the literature that are many decades old. CO_2 generation rates depend on an individual's level of physical activity, as well as their sex, age and body size. These dependencies have been studied for decades within the fields of human metabolism and exercise physiology, but that knowledge has not been incorporated by the IAQ community. This paper describes a more robust and up-to-date method for estimating CO_2 generation rates for use in ventilation and IAQ analyses.

KEYWORDS
Carbon dioxide; human metabolism; physical activity

1 INTRODUCTION
Indoor CO_2 concentrations have been prominent in discussions of building ventilation and indoor air quality (IAQ) since the 18th century. More recent discussions have focused on the impacts of CO_2 on building occupants and the use of indoor CO_2 to estimate ventilation rates and to control outdoor air ventilation rates (Persily, 2015). While the rates at which building occupants generate CO_2 are key to these applications, the generation rates currently in use are not based on recent references or a thorough consideration of the impacts of occupant characteristics.

The fields of human metabolism and exercise physiology have studied human activity for many decades, focusing on rates of energy expenditures, oxygen consumption and CO_2 generation, as well as the individual factors that affect these rates. These factors include sex, age, height, weight and body composition, with fitness level and diet composition also affecting energy expenditure and the ratio of O_2 consumed to CO_2 produced.

This paper summarizes current approaches to estimating CO_2 generation rates and outlines an updated approach described in detail in Persily and de Jonge (2017).

2 CURRENT APPROACH TO ESTIMATE CO_2 GENERATION RATES

The ventilation and IAQ fields use the following equation to estimate CO_2 generation rates from building occupants (ASHRAE, 2013b):

$$V_{CO2} = \frac{0.00276\, A_D\, M\, RQ}{(0.23\, RQ + 0.77)} \tag{1}$$

where V_{CO2} is the CO_2 generation rate per person (L/s); A_D is the DuBois surface area of the individual (m^2); M is the level of physical activity, sometimes referred to as the metabolic rate (met); and RQ is the respiratory quotient. A_D is calculated from height H in m and the body mass W in kg as follows:

$$A_D = 0.203 H^{0.725} W^{0.425} \tag{2}$$

The respiratory quotient, RQ, is the ratio of the volumetric rate at which CO_2 is produced to the rate at which oxygen is consumed, and its value depends primarily on diet (Black et al., 1986). Based on data on human nutrition in the U.S, specifically the ratios of fat, protein and carbohydrate intake (Wright and Wang, 2010), RQ equals about 0.85.

Equation 1 first appeared in the Thermal Comfort chapter of the ASHRAE Fundamentals Handbook in 1989. That discussion, as well as the current discussion in the handbook, references Nishi (1981), which presents that equation as a means of measuring the metabolic rate of an individual. Nishi does not discuss the basis of this equation nor provide references. The ASHRAE Fundamentals Handbook also contains a table of metabolic rates for various activities, which has remained unchanged since the 1977 edition (ASHRAE, 2013b). These values are based on references predominantly from the 1960s, though some are even older. The same metabolic rate values are contained in the ASHRAE thermal comfort standard (ASHRAE, 2013a), with similar data contained in ISO standard 8996 (ISO, 2004). As noted later in this paper, there are more recent and comprehensive sources of metabolic rate data.

The above equations and data are currently being used to estimate CO_2 generation rates. For example, ASTM D6245 notes that for an average-sized adult (A_D = 1.8 m^3) engaged in office work at 1.2 met, the corresponding CO_2 generation rate is 0.0052 L/s (ASTM, 2012). For a child (A_D = 1 m^2) at the same level of physical activity, the corresponding CO_2 generation rate is 0.0029 L/s. Note that discussions of the application of Equation 1 to ventilation and IAQ do not generally consider effects of air density on CO_2 generation rates, simply presenting these rates in volumetric units without specifying the air temperature or pressure.

3 ESTMATION OF CO_2 GENERATION RATES

This section describes a new approach to estimating CO_2 generation rates from building occupants based on the information from the fields of human metabolism and exercise physiology, as described in much more detail in Persily and de Jonge (2017). This approach uses the basal metabolic rate (BMR) of the individual(s) of interest combined with their level of physical activity. This contrasts with Equation 1, which only considers their body surface area and level of physical activity.

The first step in estimating the CO_2 generation rate is to determine the *BMR* of the individuals of interest. Equations for estimating *BMR* values as a function of sex, age and body mass are presented in Schofield (1985) and are shown in Table 1. For example, the *BMR* of an 85 kg male between 30 y and 60 y old is 7.73 MJ/day and 6.09 MJ/day for a 75 kg female in this same age range. The next step is to estimate their level of physical activity in terms of the value of *M* that corresponds to the activities in which they are involved.

Table 1. *BMR* values (Schofield, 1985). (m is body mass in units of kg)

	BMR (MJ/day)	
Age (y)	Males	Females
< 3	0.249 m – 0.127	0.244 m – 0.130
3 to 10	0.095 m + 2.110	0.085 m + 2.033
10 to 18	0.074 m + 2.754	0.056 m + 2.898
18 to 30	0.063 m + 2.896	0.062 m + 2.036
30 to 60	0.048 m + 3.653	0.034 m + 3.538
>= 60	0.049 m + 2.459	0.038 m + 2.755

There are two primary references for obtaining information on energy requirements for different physical activities. The first is a report prepared by the Food and Agriculture Organization of the United Nations (FAO), the World Health Organization (WHO) and the United Nations University (UNU), which discusses human energy requirements as a function of age and other individual characteristics (FAO, 2001). The second is a web-based compendium of physical activities (Ainsworth et al., 2011b; Ainsworth et al., 2011a). The rate of energy use of an individual, or group of individuals, engaged in a specific activity is estimated by multiplying the *BMR* value for that individual or group by a factor that characterizes the specific activity. The FAO report refers to this factor as the physical activity ratio (*PAR*), while the web-based compendium refers it as the metabolic equivalent using the term *MET*. In this paper, the variable *M* (in dimensionless units of met) is used to describe the ratio of the human energy use associated with a particular physical activity to the BMR of that individual. Persily and de Jonge (2017) contains tables of values of *M* for various activities from the FAO report and from the web-based compendium.

Once the *BMR* value and the value of *M* for the relevant activity have been determined, their product in units of MJ/day is converted to L of oxygen consumed per unit time. This conversion is based on the conversion of 1 kcal (0.0042 MJ) of energy use to 0.206 L of oxygen consumption (Lusk, 1924). The exact conversion depends on the relative oxidation of carbohydrates and fat, but given the variation in the factors used in calculating CO_2 generation rates, a value of 0.206 L is a reasonable approximation. This conversion results in 1 MJ/day of energy use corresponding to 0.00057 L/s of oxygen consumption, which based on a respiratory quotient *RQ* of 0.85 (discussed above), corresponds to 0.00048 L/s of CO_2 production. A *BMR* value of 7.73 MJ/day, mentioned above for an 85 kg male between 30 y and 60 y of age, therefore corresponds to 0.0037 L/s of CO_2 production. Using the physical activity level of 1.5 met for sitting tasks, light effort (e.g. office work) results in a CO_2 generation rate of 0.0056 L/s, which is close to the value of 0.0052 L/s cited in ASHRAE Standard 62.1 and ASTM D6245 for an adult.

Based on the approach just described, the CO_2 generation rate is expressed in L/s at an air pressure of 101 kPa and a temperature of 273 K, with *BMR* in units of MJ/day and *M* in met, using Equations (3) and (4). Adjustments to other values of air pressure and temperature are described in Persily and de Jonge (2017).

$$V_{CO2} = RQ\ BMR\ M\ 0.000569 \quad (3)$$

Assuming RQ equals 0.85, Equation 3 can be expressed as:

$$V_{CO2} = BMR\ M\ 0.000484 \quad (4)$$

In order to facilitate use of these calculations, Table 2 contains CO_2 generation rates for a number of *M* values over a range of ages for both males and females. The mean body mass values are based on data in the EPA Exposure Factors Handbook, specifically the values in Tables 8-4 for males and 8-5 for females (EPA, 2011). These values are most accurate, but still inherently approximate, when applied to a group of individuals and will not generally be accurate for a single individual.

Table 2. CO_2 generation rates for ranges of ages and level of physical activity

			CO_2 generation rate (L/s)						
Age (y)	**Mean mass (kg)**	***BMR* (MJ/day)**	Level of physical activity (met)						
			1.0	1.2	1.4	1.6	2.0	3.0	4.0
Males									
< 1	8.0	1.86	0.0009	0.0011	0.0013	0.0014	0.0018	0.0027	0.0036
1 to <3	12.8	3.05	0.0015	0.0018	0.0021	0.0024	0.0030	0.0044	0.0059
3 to < 6	18.8	3.90	0.0019	0.0023	0.0026	0.0030	0.0038	0.0057	0.0075
6 to < 11	31.9	5.14	0.0025	0.0030	0.0035	0.0040	0.0050	0.0075	0.0100
11 to < 16	57.6	7.02	0.0034	0.0041	0.0048	0.0054	0.0068	0.0102	0.0136
16 to < 21	77.3	7.77	0.0037	0.0045	0.0053	0.0060	0.0075	0.0113	0.0150
21 to < 30	84.9	8.24	0.0039	0.0048	0.0056	0.0064	0.0080	0.0120	0.0160
30 to < 40	87.0	7.83	0.0037	0.0046	0.0053	0.0061	0.0076	0.0114	0.0152
40 to < 50	90.5	8.00	0.0038	0.0046	0.0054	0.0062	0.0077	0.0116	0.0155
50 to < 60	89.5	7.95	0.0038	0.0046	0.0054	0.0062	0.0077	0.0116	0.0154
60 to < 70	89.5	6.84	0.0033	0.0040	0.0046	0.0053	0.0066	0.0099	0.0133
70 to < 80	83.9	6.57	0.0031	0.0038	0.0045	0.0051	0.0064	0.0095	0.0127
>= 80	76.1	6.19	0.0030	0.0036	0.0042	0.0048	0.0060	0.0090	0.0120
Females									
< 1	7.7	1.75	0.0008	0.0010	0.0012	0.0014	0.0017	0.0025	0.0034
1 to <3	12.3	2.88	0.0014	0.0017	0.0020	0.0022	0.0028	0.0042	0.0056
3 to < 6	18.3	3.59	0.0017	0.0021	0.0024	0.0028	0.0035	0.0052	0.0070
6 to < 11	31.7	4.73	0.0023	0.0027	0.0032	0.0037	0.0046	0.0069	0.0092
11 to < 16	55.9	6.03	0.0029	0.0035	0.0041	0.0047	0.0058	0.0088	0.0117
16 to < 21	65.9	6.12	0.0029	0.0036	0.0042	0.0047	0.0059	0.0089	0.0119
21 to < 30	71.9	6.49	0.0031	0.0038	0.0044	0.0050	0.0063	0.0094	0.0126
30 to < 40	74.8	6.08	0.0029	0.0035	0.0041	0.0047	0.0059	0.0088	0.0118
40 to < 50	77.1	6.16	0.0029	0.0036	0.0042	0.0048	0.0060	0.0090	0.0119
50 to < 60	77.5	6.17	0.0030	0.0036	0.0042	0.0048	0.0060	0.0090	0.0120
60 to < 70	76.8	5.67	0.0027	0.0033	0.0038	0.0044	0.0055	0.0082	0.0110
70 to < 80	70.8	5.45	0.0026	0.0032	0.0037	0.0042	0.0053	0.0079	0.0106
>= 80	64.1	5.19	0.0025	0.0030	0.0035	0.0040	0.0050	0.0075	0.0101

4 DISCUSSION

The approach described in this paper for estimating CO_2 generation rates from individuals is based on concepts from the fields of human metabolism and exercise physiology, as well as more recent data than those currently used in the fields of ventilation and IAQ. It is intended to replace the equation that has been used for decades within the ventilation and IAQ communities (Equation 1 in this paper) and offers important advantages. First, it is worth noting that the previous equation is based on a 1981 reference that provides no explanation of its basis, while the new approach is derived using principles of human metabolism and energy expenditure. Also, the new approach characterizes body size using mass rather than surface area, which in practice is estimated not measured. Body mass is easily measured and data on body mass distributions are readily available. The new approach also explicitly accounts for the sex and age of the individuals being considered, which is not the case with Equation 1. As new data on body mass become available, these data can be used to adjust CO_2 generation rates accordingly. Similarly, new research results on *BMR* values and new approaches to their estimation can also be easily applied to these calculations.

The CO_2 generation rate estimation method described here is applicable to groups of individuals, as the theory behind the method and the data are based on groups, not single individuals. If the rate of energy consumption or CO_2 generation of a specific individual is needed, it must be measured for that individual to account for differences that can exist due to that person's body composition, diet, genetics and other factors. When considering a population of individuals in a building or space, the average values derived using the described approach will be more reliable than for a single individual. However, that reliability should be increased by characterizing the specific population of interest in terms of sex, age, body mass and activity level. Methods for performing such characterizations in a standardized fashion are not described in this paper. The increased accuracy of CO_2 generation estimates that may be achieved by doing so have not been studied, but additional research would be useful to demonstrate their value.

5 CONCLUSIONS

This paper presents an approach to estimating CO_2 generation rates from building occupants for use in the fields of IAQ and ventilation. The approach and data are based on concepts from the fields of human metabolism and exercise physiology. They constitute a significant advance in the analysis of IAQ and ventilation and should be considered in future applications of CO_2 in ventilation and IAQ studies and standards. In addition, the sources of physical activity data identified should be incorporated into the references that currently use older and much more limited data sources, i.e., ASHRAE Standard 55, the ASHRAE Fundamentals Handbook, ISO Standard 8996, and ASTM D6245 (ASHRAE, 2013b; ISO, 2004; ASTM, 2012; ASHRAE, 2013a).

6 REFERENCES

Ainsworth, B., Haskell, W., Herrmann, S., Meckes, N., Bassett Jr, D., Tudor-Locke, C., Greer, J., Vezina, J., Whitt-Glover, M. and Leon , A. (2011a) The Compendium of Physical Activities Tracking Guide, Healthy Lifestyles Research Center, College of Nursing & Health Innovation, Arizona State University, Available from: https://sites.google.com/site/compendiumofphysicalactivities/.

Ainsworth, B., Haskell, W., Herrmann, S., Meckes, N., Bassett Jr, D., Tudor-Locke, C., Greer, J., Vezina, J., Whitt-Glover, M. and Leon , A. 2011b. Compendium of Physical Activities: a second update of codes and MET values. *Medicine and Science in Sports and Exercise*, 43(8), 1575-1581.

ASHRAE. 2013a. *ANSI/ASHRAE Standard 55-2013, Thermal Environmental Conditions for Human Occupancy*, American Society of Heating, Refrigerating, and Air-Conditioning Engineers, Inc., Atlanta, GA.

ASHRAE. 2013b. *Fundamentals Handbook,* Atlanta, GA, American Society of Heating, Refrigerating and Air-Conditioning Engineers, Inc.

ASTM. 2012. *Standard Guide for Using Indoor Carbon Dioxide Concentrations to Evaluate Indoor Air Quality and Ventilation*, West Conshohocken, PA, American Society for Testing and Materials, (D6245-12).

Black, A.E., Prentice, A.M. and Coward, W.A. 1986. Use of Food Quotients to Predict Respiratory Quotients for the Double-Labelled Water Method of Measuring Energy Expenditure. *Human Nutrition: Clinical Nutrition*, 40C, 381-391.

EPA. 2011. *Exposure Factors Handbook*, Washington DC, U.S. Environmental Protection Agency, EPA/600/R-09/052F.

FAO. 2001. *Human Energy Requirements. Report of a Joint FAO/WHO/UNU Expert Consultation*, Geneva, Food and Agriculture Organization of the United Nations, Food and Nutrition Technical Report Series 1.

ISO. 2004. *Ergonomics of the thermal environment — Determination of Metabolic Rate*, Brussels, International Organization for Standardization, (EN ISO 8996).

Lusk, G. 1924. Analysis of the Oxidation of Mixtures of Carbohydrate and Fat. *Journal of Biological Chemistry*, 59, 41-42.

Nishi, Y. (1981) Measurement of the Thermal Balance of Man, In: Cena, K. and Clark, J. A. (eds) *Bioengineering Thermal Physiology and Comfort*, New York, Elsevier, 29-39.

Persily, A. 2015. Challenges in developing ventilation and indoor air quality standards: The story of ASHRAE Standard 62. *Building and Environment*, 91, 61-69. 10.1016/j.buildenv.2015.02.026.

Persily, A.K. and de Jonge, L. 2017. Carbon Dioxide Generation Rates of Building Occupants. *Indoor Air*, Accepted: 14 March 2017. 10.1111/ina.12383.

Schofield, W.N. 1985. Predicing Basal Metabolic Rate, New Standards and Review of Previous Work. *Human Nutrition: Clinical Nutrition*, 39C (Supplement 1), 5-41.

Wright, J.D. and Wang, C.-Y. 2010. *Trends in Intake of Energy and Macronutrients in Adults From 1999-2000 Through 2007-2008*, Hyattsville MD, Centers for Disease Control and Prevention, National Center for Health Statistics.

BUILDING COMPONENT PERFORMANCE EXPOSED TO FIREBRAND SHOWERS CHARACTERISTIC OF BURNING STRUCTURES

Samuel L. Manzello[1] and Sayaka Suzuki[2]
[1]National Institute of Standards and Technology (NIST), USA
[2]National Research Institute of Fire and Disaster (NRIFD), Japan

1. INTRODUCTION

There been numerous wildfires that spread into communities, in Argentina, Australia, Brazil, Canada, Chile, France, Greece, Portugal, Spain, and the USA. Such large outdoor fires are referred to as Wildland-Urban Interface (WUI) fires. Japan is another country that has been subject to large scale outdoor fires, such as the recent Itoigawa City Fire that occurred in Niigata, Japan. A prominent mechanism of structure ignition in both WUI and urban fires is the production of firebrands, or embers [1].

Attached building components may provide a pathway for structures to ignite in large outdoor fires. Examples of attached building components may include fencing assemblies. A recent study by the authors demonstrated that fencing assemblies may be ignited by firebrand showers, but the capability of the ignited fencing to transfer the fire to an adjacent structure, such as wall assembly, was not considered [2].

As a result, this paper describes efforts to investigate the ability of firebrand showers to ignite fencing assemblies, and then observe the subsequent flame spread along the ignited assembly to an *adjacent wall*. The fencing assemblies were exposed to firebrand showers similar to those produced from burning structures. As this is a very complex problem, mock-up sections of full-scale fencing/wall assemblies were experimented with using unique experimental capabilities developed by the authors at the National Research Institute of Fire and Disaster (NRIFD).

2. EXPERIMENTAL DESCRIPTION

The reduced-scale firebrand ignition experimental facility was described in a prior JAFSE proceedings [3]. As a result, only a brief description is provided here. The reduced-scale continuous-feed firebrand generator consisted of two parts; the main body and continuous feeding component. For all experiments here, Japanese Cypress wood chips were used to produce firebrands. These were provided from a supplier and upon arrival, these chips were filtered using a 10 mm screen to remove very fine wood pieces. The chips were also oven dried, as they were shipped under wet conditions. These size wood pieces (average length, width, and thickness are 28, 18, and 3 mm, respectively) were selected to produce firebrands with larger projected area at a specific mass than that used in our prior studies using continuous firebrand generation focused on vegetative firebrands. The wood feed rate used here was 80 g/min, which is near the upper limit for this reduced-scale firebrand generator.

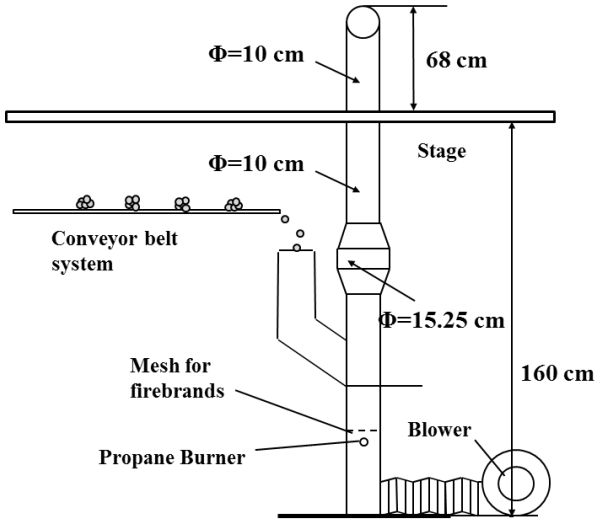

Figure 1 Drawing of reduced-scale continuous firebrand generator.

Since the base of the fan used to generate the wind in the NRIFD facility is located 1.6 m from the floor, the conveyer was placed under a custom stage designed for experiments when using NRIFD's wind facility. The wind field exits from a 4.0 m diameter fan, and it is possible to generate wind speeds up to 10 m/s. The flow field was measured to be within ± 10 % over a cross-section of 2.0 m by 2.0 m.

The blower was set to provide an average velocity of 4.0 m/s measured at the exit of the firebrand generator when no wood pieces were loaded. In these experiments, glowing firebrands were desired; flaming firebrands were produced if the blower wind speeds were higher.

Redwood lattice fencing assemblies were constructed for the experiments. These were custom fabricated by using two, 0.61 m in height, 1.2 m in width, redwood lattice pieces, and held together using a 2 x 4 wood array. While two-sided redwood lattice fencing assemblies were used in this study, this type of fencing assembly may also be used in a one-sided configuration. Experiments are also underway to investigate the differences between one-sided and two-sided configurations, as well as entirely different fencing types such as Western Red Cedar privacy fencing.

3. RESULTS AND DISCUSSIONS

A total of 10 experiments were conducted for wind speeds of 4 m/s, 6 m/s, and 9 m/s. In all cases, the evolution of the ignition process was similar. Specifically, glowing firebrands ignited the mulch beds (mini-pine bark mulch) via smoldering combustion, and then the mulch transitioned to flaming combustion. These flaming mulch beds then ignited the redwood lattice fencing assemblies. The ignited fencing assemblies then transferred the fire to adjacent walls. **Figure 2-3** displays the temporal evolution of the ignition process for a wind speed of 6 m/s, and 9 m/s, respectively.

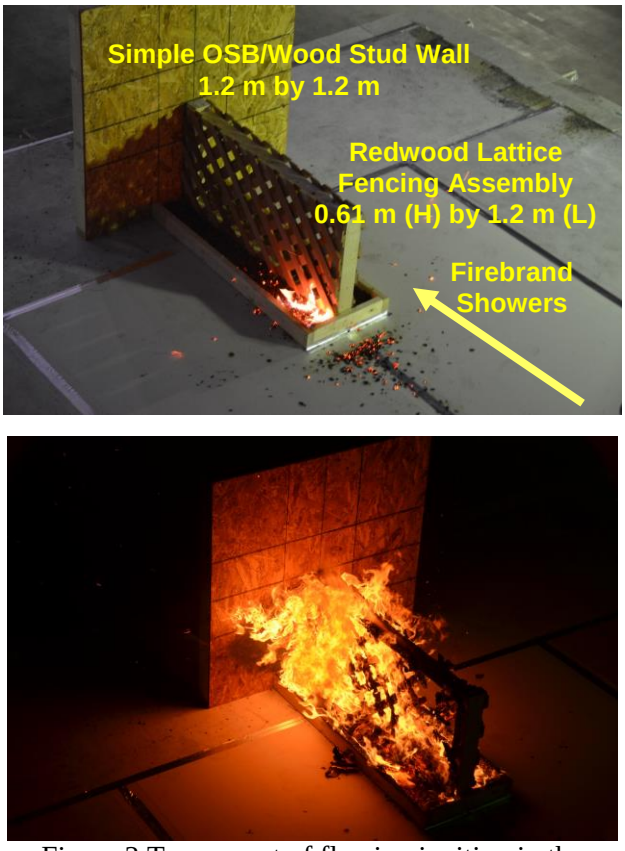

Figure 2 Top - onset of flaming ignition in the mulch bed; bottom - flame spread from the ignited fencing assembly to wall (6 m/s).

In all experiments, the wall was eventually ignited by fire from the redwood lattice fencing assemblies. Under higher wind speeds (9 m/s), significant firebrands were generated from the redwood lattice fencing as well.

4. SUMMARY

This paper describes efforts to investigate the ability of firebrand showers to ignite fencing assemblies, and then observe the subsequent flame spread along the ignited assembly to an adjacent wall.

Figure 3 Flame spread from the ignited fencing assembly to wall for 9 m/s wind speed.

In particular, recent work compared ignition results from full-scale redwood lattice fencing assembly experiments conducted using the Building Research Institute's (BRI) full-scale wind tunnel facility, to mock-up to sections of full-scale fencing assemblies using the experimental capability at the National Research Institute of Fire and Disaster (NRIFD). As a first step, the fencing assemblies *were not attached* to an adjacent wall. In all cases, the evolution of the ignition process was similar to the full-scale fencing assembly experiments [4].

The results in the present conference paper set the stage to conduct a similar comparison across varying sized experiments regarding the evolution of flame spread from ignited fencing assemblies to *adjacent walls*.

5. ACKNOWELDGEMENTS

Mr. Marco Fernandez of NIST is acknowledged for shipping materials for experiments.

6. REFERENCES

[1] Manzello, S.L., *et al.*, Fire Saf. J., 59:122-131, 2013.
[2] Suzuki, S., *et al.*, Fire Tech., 52: 1051-1067, 2016.
[3] Suzuki, S., and Manzello, S.L, 27th Annual JAFSE Symposium, 2015.
[4] Manzello, S.L., *et al.*, Fire and Materials Conference Proceedings, 2017.

ANALYSIS ON THE EFFECT OF WIND ON FIREBRAND ACCUMULATION IN FRONT OF OBSTACLES

Sayaka Suzuki[1] and Samuel L. Manzello[2]
[1]National Research Institute of Fire and Disaster, Japan
[2]National Institute of Standards and Technology, USA

1. INTRODUCTION

Wildfires that spread into communities, referred to as Wildland-Urban Interface (WUI) fires, have destroyed communities throughout the world. Japan does not have an issue of fires spreading from the wildlands to communities [1]. Rather, Japan experiences urban fires. Since most Japanese cities are densely populated, severe fire spread occurs within these urban areas [1].

An interesting similarity, that is a major factor in both WUI and urban fire spread, is firebrand production. When vegetation and structures burn in these fires, pieces of burning material, known as firebrands, are generated, become lofted, and are carried by the wind. This results in showers of wind-driven firebrands.

As structures are exposed to wind, stagnation planes are produced around structures. In a prior scoping study, the authors demonstrated that firebrands may accumulate in these stagnation planes [2]. This paper describes a more in depth analysis of this phenomenon. Specifically, new insights have been made possible by an improved experimental design to generate continuous wind-driven firebrand showers. While these experiments have been presented before [3], no analysis was offered to the observed results until now.

2. EXPERIMENTS

Experiments were performed by using the full-scale Continuous-Feed Firebrand Generator. The full-scale wall with varied size was placed downstream of the device and the wind speed was varied in increments of 2 m/s up to 10 m/s. Specifically, two walls with dimensions of 1.32 m (H) by 2.44 m (W), and 2.44 m (H) by 2.44 m (W) were used. Different dimensions were intentionally selected to determine the influence of the obstacle profile on potential firebrand accumulation zones. These were located at a distance of 7.5 m from the Continuous-Feed Firebrand Generator to visualize the transport process. The experiments were conducted in the Building Research Institute's Fire Research Wind Tunnel Facility (FRWTF).

For all experiments, Douglas-fir wood pieces, shown in **Fig. 2**, machined to dimensions of 7.9 mm (H) by 7.9 mm (W) by 12.7 mm (L) were used to produce firebrands. Firebrands generated from these sized wood pieces have been shown to be commensurate to firebrand sizes measured from burning vegetation, as opposed to those quantified from burning structures (see authors second paper in these JAFSE proceedings for more information).

In all experiments, the same amount of wood pieces was fed into Dragon so that all the walls were attacked by firebrand showers for the same duration. In total, 10 minutes of feeding, which corresponds to 8 kg of wood pieces, was provided.

3. RESULTS & DISUSSIONS

Experimental results were compared with a simple analysis on the wind effect on firebrand accumulation. In total, 8 conditions (2 configurations for 4 different wind speeds) were considered for this experimental series.

3.1. Experimental Results

Figure 1 (Left) displays images of the experiments conducted with 2.44 m (H) by 2.44 m (W) obstacle placed downstream of firebrand showers (6 m/s and 10 m/s are shown). At a wind speed of 4 m/s (not shown), the firebrands were unable to accumulate into compact zones. At 6 m/s, the most significant accumulation was observed. Little accumulation was observed at the highest wind speed used (10 m/s).

Figure 1 (Right) displays images of the experiments conducted with 1.32 m (H) by 2.44 m (W) obstacle placed downstream of firebrand showers (6 m/s and 10 m/s are shown). Similar to the experiments with the 2.44 m by 2.44 m wall, at a wind speed of 4 m/s (not shown), the firebrands were unable to accumulate into compact zones. At 6 m/s, the most significant accumulation was observed. No accumulation was observed at the highest wind speed used (10 m/s). For both obstacles, it is believed that at the highest wind speed of 10 m/s, little or no firebrand accumulation was observed due to the enhanced flow recirculation present afforded by the higher wind speeds.

3.2. Analysis

A simple analysis was performed in order

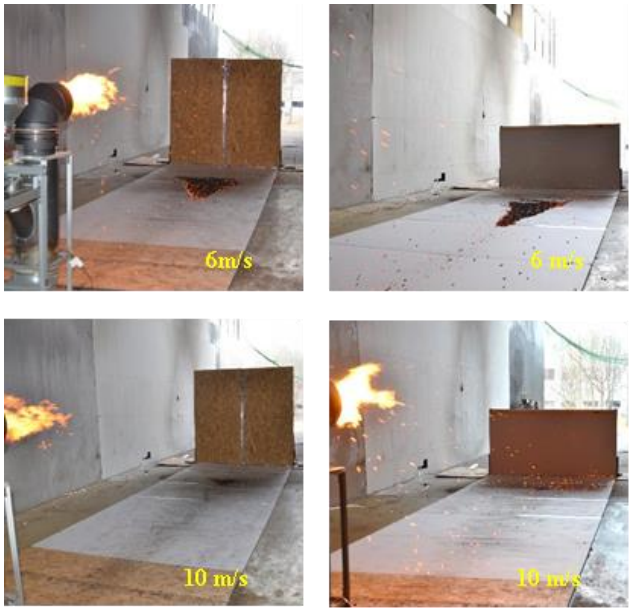

Figure 1 Firebrand accumulations. Left: 2.44 m (H) by 2.44 m (W) obstacle and Right: 1.32 m (H) by 2.44 m (W) obstacle. Top: 6 m/s and Bottom: 10 m/s

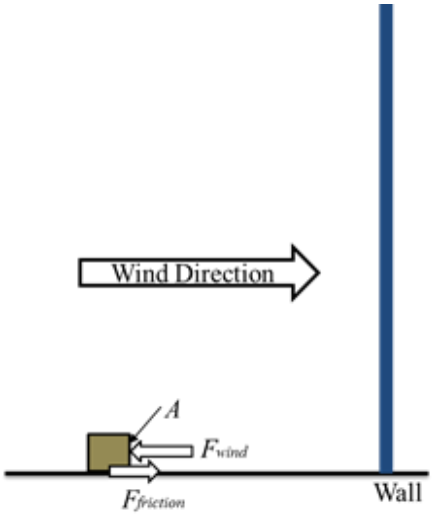

Figure 2 Schematic of force balance on a firebrand

to investigate the effect of wind on firebrand accumulation. The force by wind on a firebrand (F_{wind}) should be balanced with the friction force between the firebrand and the floor (gypsum board). ($F_{friction}$) (see **Figure 2**).

$$F_{friction} = F_{wind} \quad (1)$$

Here,

$$F_{friction} = \mu m_{firebrand} g \quad (2)$$

$$F_{wind} = \frac{1}{2}\rho_{air} v^2 \times A \quad (3)$$

Therefore, μ is the friction coefficient between gypsum board and smoldering firebrands, $m_{firebrand}$ is mass of a firebrand, ρ_{air} is the air density, g is gravitation acceleration, v is wind speed on a firebrand, and A is an area of firebrand facing a wind.

$$\mu m_{firebrand} g = \frac{1}{2}\rho_{air} v^2 \times A \quad (4)$$

There is no study on friction coefficient between gypsum board and smoldering firebrands (or any burning wood) so we assume μ = 0.5 based on the friction coefficient data between wood [3]. Also, we measured A = 0. 78 cm^2 and $m_{firebrand}$ = 0.05 g as the average projected area, and average mass of firebrands, respectively. Eventually v is calculated to be 2.3 m/s. A wind speed of 2.3 m/s may be considered a critical value for a firebrand to remain in front of an obstacle. As shown, for 10 m/s wind, with 1.32 m wall (H), and 2.44 m wall (H), different behaviors of firebrand accumulation were observed. The possibility of flow near the critical wind speed, for 10 m/s applied wind to these obstacles, was investigated by simulating BRI's FRWTF using FDS with a grid size of 10 cm [5].

FDS simulations (10 m/s) confirmed the experimental findings: no accumulation was observed in front of a wall of 1.32 m (H), since velocities there were higher than the critical wind speed (2.3 m/s). Accumulation was possible for 2.44 m (H) wall, since simulations showed the critical wind speed was not exceeded.

4. SUMMARY

A simple analysis was performed to investigate critical wind speed for firebrands to accumulate in the stagnation zone and the same behavior was confirmed by wind profile using FDS simulation.

5. ACKNOLEDGEMENT

Dr. Ichiro Hagiwara is appreciated for allowing us to use BRI's wind tunnel.

6. REFERENCES

[1] Manzello, S.L., Fire Saf. J., 59 (2013) 122-131.
[2] Manzello, S.L., et al., Fire Saf J. 46(2011) 568 578.
[3] Manzello, S.L., and Suzuki, S., Fire and Materials Conference, San Francisco, CA, 2015.
[4] Japanese Society of Mechanical Engineers, JSME Mechanical Engineers' Handbook, Alpha2, (2004), Maruzen (in Japanese).
[5] McGrattan K, et al., (2013) Fire dynamics simulator 6, Technical Note.

Measurement of process dynamics through coaxially aligned high speed near-infrared imaging in laser powder bed fusion additive manufacturing

Jason C. Fox*[a], Brandon M. Lane[a], Ho Yeung[a]
[a]National Institute of Standards and Technology, 100 Bureau Drive, Gaithersburg, MD, USA 20899

ABSTRACT

For process stability in laser powder bed fusion (LPBF) additive manufacturing (AM), control of melt pool dimensions is imperative. In order to control melt pool dimensions in real time, sampling frequencies in excess of 10 kHz may be required, which presents a challenge for many thermal and optical monitoring systems. The National Institute of Standards and Technology (NIST) is currently developing the Additive Manufacturing Metrology Testbed (AMMT), which replicates a metal based laser powder bed fusion AM process while providing open architecture for control, sensing, and calibration sources. The system is outfitted with a coaxially aligned, near-infrared (NIR) high speed melt pool monitoring (MPM) system. Similar monitoring systems are incorporated into LPBF research testbeds, and appearing on commercial machines, but at lower available frame rates, which may limit observation of higher frequency events such as spatter or size fluctuations. This paper presents an investigation of the coaxial imaging systems of the AMMT to capture the process dynamics, and quantify the effects of dynamic fluctuations on melt pool size measurements. Analysis is carried out on a baseline experiment with no powder material added, melt pool size measurements collected in-situ are compared to ex-situ measurements, and results are discussed in terms of temporal bandwidth. Findings will show that, even at the frame rate and resolution presented, challenges in relating in-situ video signals to the ex-situ measurement analysis remain.

Keywords: Additive Manufacturing, Laser Powder Bed Fusion, Melt Pool Monitoring, Control

1. INTRODUCTION

Laser powder bed fusion (LPBF) is an additive manufacturing (AM) technique which utilizes a high power, focused laser to selectively melt layers of metal powder, which ultimately form a near fully-dense, three-dimensional structure. Multiple deficiencies plague this process, such as defects (porosity, residual stress, anisotropic microstructure, etc.) and overall part-to-part variability which inhibits part qualification and certification for aerospace or medical applications [1]. In-situ process monitoring is a suite of tools with high potential to address the problem of qualification and certification. Process monitoring enables a 'certify as you build' concept [2], in which data collected from sensors and instruments during the build process can provide sufficient part quality information so that the need for post-process destructive or non-destructive evaluation (NDE) is significantly reduced [3].

Process monitoring for LPBF is still largely in a research and development phase; however, several monitoring technologies are being implemented by LPBF machine manufacturers or third party developers [4,5]. Many of these techniques focus on process signatures stemming from the laser-induced melt pool. One melt pool monitoring (MPM) technique, now appearing on multiple commercial LPBF systems, utilizes a high-speed camera placed in the optical path co-axially aligned with the laser. This co-axial MPM method utilizes either a beam-splitter or spectrally selective mirror to separate out the laser wavelength from radiation stemming from the incandescing melt pool source. This creates a nominally stationary image of the melt pool on the imaging detector. Berumen et al. provided one of the first analyses of the spatial and temporal requirements of a co-axial MPM system as a function of melt pool size and scanning speed [6]. In their example, they surmised that 15 pixels were sufficient magnification (e.g., 10 μm/pixel to observe a 150 μm melt pool) and one frame per melt pool width was sufficient speed (e.g., 6 666 frames/s to capture a 150 μm wide melt pool scanning at 1 m/s) to capture melt pool signatures in a co-axial MPM system.

Certain commercial entities, equipment, or materials may be identified in this document in order to describe an experimental procedure or concept adequately. Such identification is not intended to imply recommendation or endorsement by the National Institute of Standards and Technology, nor is it intended to imply that the entities, materials, or equipment are necessarily the best available for the purpose.

*Jason.Fox@NIST.gov; 1 (301) 975-2171

Ultimately, signatures captured from a co-axial MPM system are intended to correlate to some physical qualities of the melted scan tracks, and ultimately the quality of the final part composed of millions of these tracks. Conversely, high resolution ex-situ measurements of scan tracks and their surface morphology may be used to qualify observations made with a co-axial MPM system and provide physical context for the captured images. In the work presented here, we compare directly ex-situ scan track measurements (width and height variation) with high speed co-axial MPM. Temporal resolution (defined by the camera frame rate and integration time) is set nearly an order of magnitude higher than the requirements outlined by Berumen at al. (30 000 frames/s). This allows melt pool size fluctuations, or other phenomena such as particle ejecta, to be better captured, which otherwise may affect MPM spatial (size) signatures. Optical magnification of the system utilized in this work provides 15 μm/pixel imaging, which is on par with the aforementioned requirements. However, it should be noted that the projected pixel size (μm/pixel) is not the definition of the spatial resolution, which is affected by optical blur.

With these aspects in mind, the purpose of this paper is to understand the relationship between signatures captured from a co-axial MPM and the resultant scan track. To accomplish this goal, a methodology for the analysis of co-axial high speed NIR MPM video is presented along with detailed ex-situ measurement of the solidified scan track. Analysis is performed on a single scan track as a baseline experiment to maintain focus on the development of the methodology. While analysis techniques of the MPM signal are purposefully kept to simple mathematical operations, they are shown to be capable of highlighting variations due to key events, such as material ejecta. Finally, the relationship between the MPM signal and resultant scan track is discussed.

2. METHODOLOGY

Experiments were performed in the Additive Manufacturing Metrology Testbed (AMMT) prototyping system [7,8], shown in Figure 1. The system uses a 500 W multimode Yb fiber laser at 1070 nm wavelength, which is delivered through two XY galvanometer scan mirrors, and focused onto a horizontal build platform within an inert gas chamber. This creates a nominally 100 μm full width at half maximum (FWHM) spot at the laser focus. Light emitted from the laser-heated region is passed back co-axially with the laser beam path, but transmitted through a beam splitter which reflects off the 1070 nm laser wavelength, and transmits wavelengths from 950 nm to 400 nm. This transmitted light is then focused with an imaging lens and passed through an 850 nm filter (40 nm bandpass) directly onto the Silicon-based complementary metal oxide semiconductor (CMOS) detector of a vertically-mounted high speed camera, shown in Figure 2. Pixel pitch on the detector is 20 μm/pixel, and magnification of the imaging lens equates this to approximately 12 μm/pixel on the image plane (≈ 1.3x). The high-speed camera is capable of 6400 frames/s at full 1024 pixel x 1024 pixel window, however a sub-window of 256 pixel x 256 pixel was set to achieve higher frame rate of 30 000 frames/s. The camera was also set with a 31.62 μs exposure time; which is close to one full frame period (inverse of the frame rate).

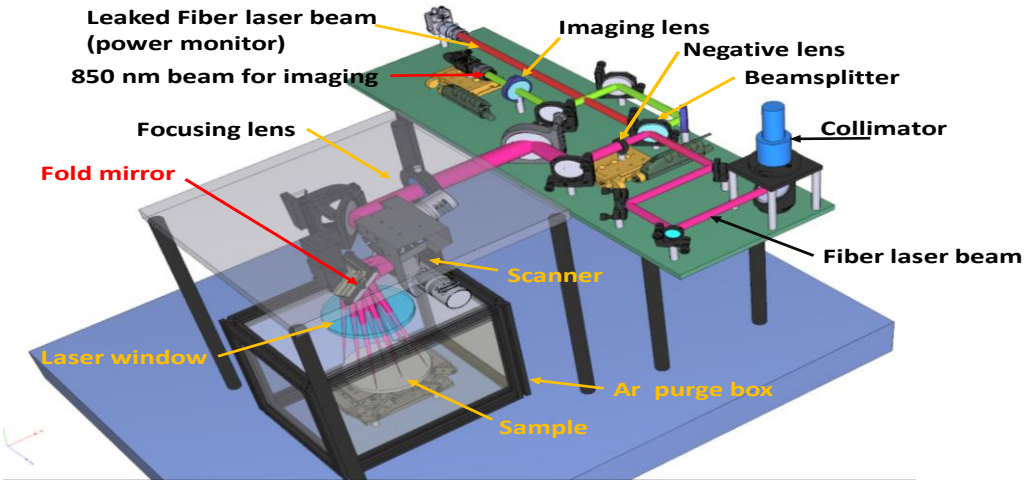

Figure 1. Schematic of the AMMT prototype system [8].

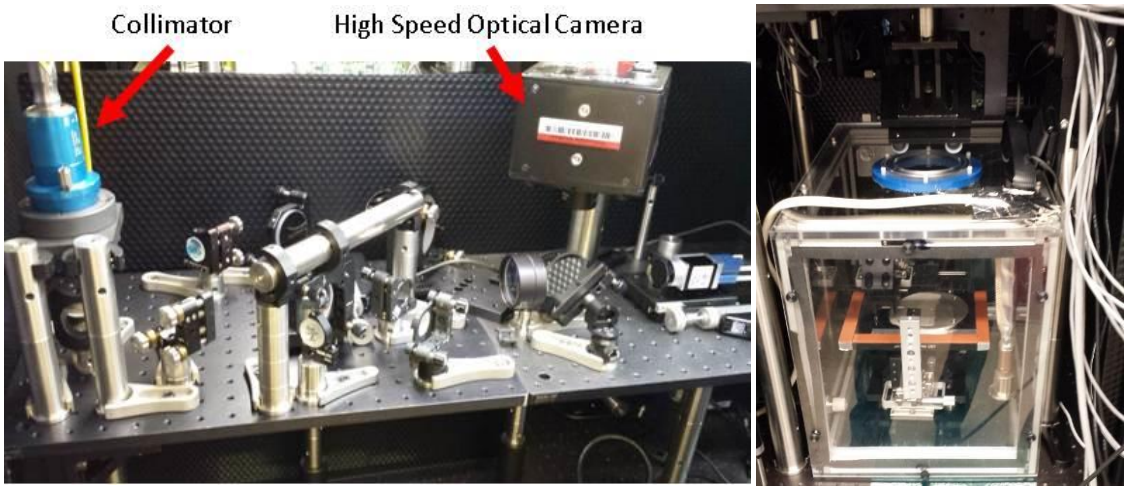

Figure 2. Laser collimator, optical components, and high speed optical system (left). Fold mirror, purge box, and sample positioning system (right).

The data taken from the camera is converted to an 8-bit digital signal, with dynamic range from 0 to 255 digital levels. An example frame from the high-speed camera can be seen in Figure 3, which was taken during a scan on a 17-4 stainless steel plate. In this image, much of the center portion of the melt pool is saturated, and areas far from the melt pool are at the noise floor of the camera. This is a result of the exceedingly high temperatures and temperature gradients on the melt pool surface. The exposure time of the camera was adjusted until the approximated melt pool width (≈ 100 μm) was achieved in the camera image when masked with a digital level threshold of 128, or roughly the center of the dynamic range. From these images, further analysis can be performed to develop more exact relationships to ex-situ scan track measurements.

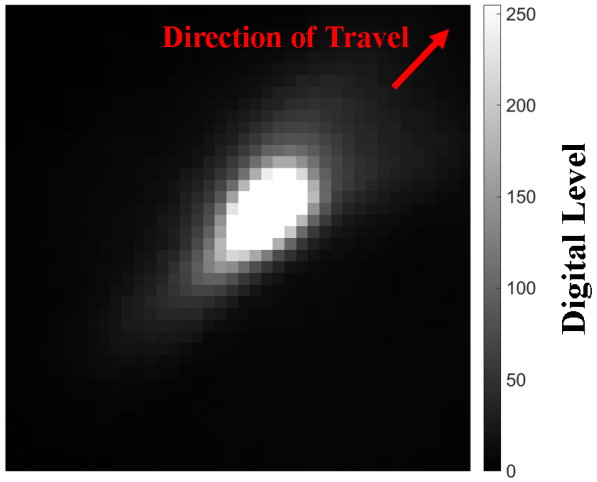

Figure 3. Single frame from the coaxially aligned high-speed imaging system.

While more advanced techniques for analysis of the video data exist, the number of computations required for those methods may be prohibitive for digital processing and real-time feedback control. As such, the focus of the data analysis will be on simple mathematical operations that can be performed very quickly. One method for analysis of the videos is to perform a conversion to binary using a pre-defined threshold. Area measurements can then be made by counting the number of pixels above the threshold. Width measurements can also be performed on the binary video by counting the maximum number of registered pixels in a line perpendicular to the direction of travel. Examples of how different thresholds change the image from Figure 3, as well as area and width measurements on the resulting binary image, can

be seen in Figure 4. Note that these threshold levels are chosen less for a calibrated measurement and more for the identification of features and anomalies, which is discussed later in the paper.

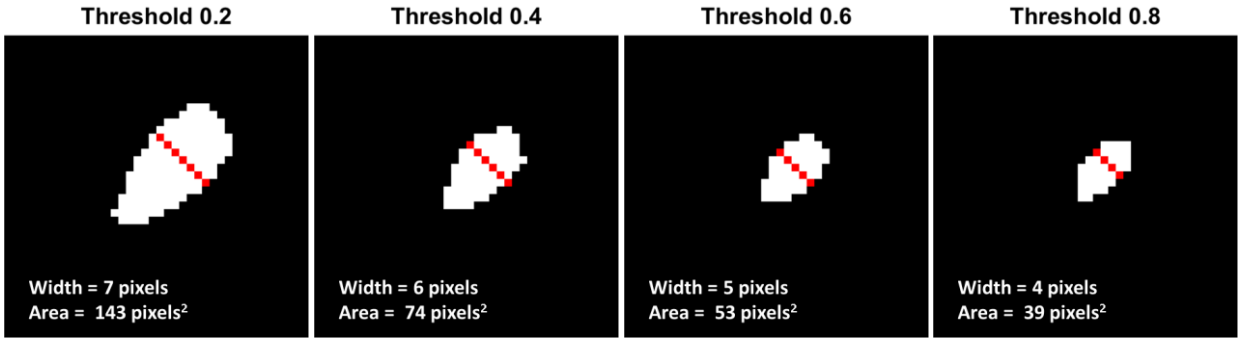

Figure 4. Examples of conversion to binary using different threshold levels. Values for the threshold are from 0 to 1, where 0 would include any pixel with a value greater than 0 in the binary image and 1 would not include any pixels. Area is calculated as the sum of red and white pixels. Width is calculated as the sum of red pixels.

Ex-situ analysis of the laser scan tracks from the experiment was performed via optical microscope for measurement of the scan track width and laser confocal microscope with a 405 nm source for measurement of the scan track height. The optical images were taken using a 50x objective and stitched using the microscope manufacturer's built-in stitching algorithm. Topographic measurements were taken using 20x enhanced contrast (EC) Epiplan-Apochromatic objective with a 0.6 numerical aperture and 0.5x tube lens, resulting in 0.62 µm per pixel. Topographic data was only corrected for tilt and piston (i.e., adjusted so that the average height of the surface is set to zero) and no other filtering was applied.

Width measurement can also be performed using the optical images. Often in literature, width measurements are reported as a single measurement or average with little or no information as to the variability of the width provided. To correlate the MPM signal to features in the resultant scan track, however, a detailed record of the width along the full length of the scan track is required. As such, width measurements were performed by manually tracing the edges of the scan track in the optical images and using commercially available analysis software to determine the distance between the traces. An example of this measurement can be seen in Figure 5.

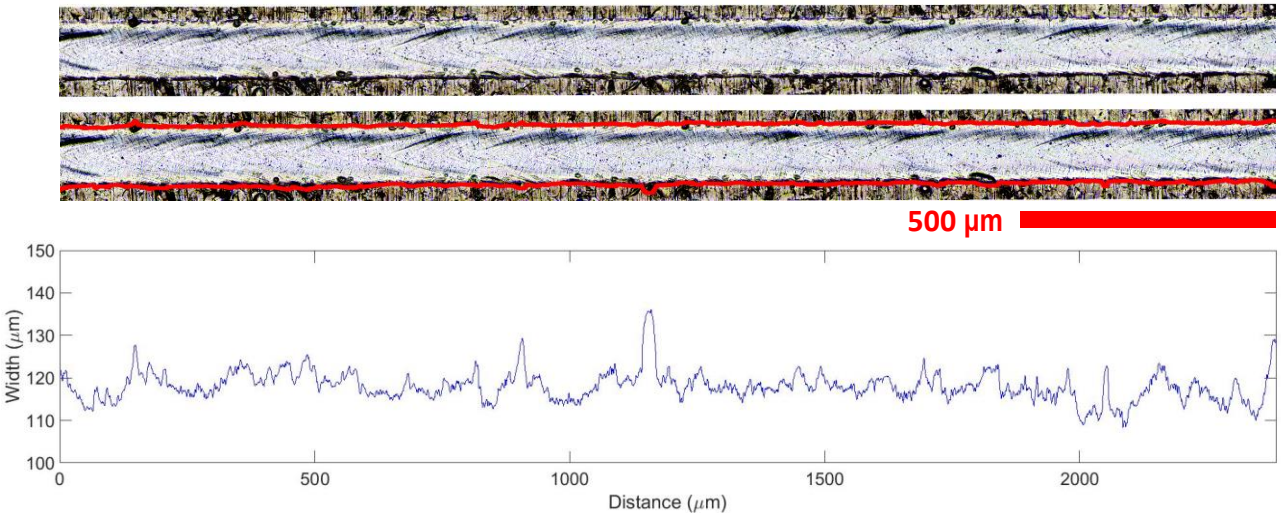

Figure 5. Center image of the track (top), trace of the track highlighted in red (center), and measured width (bottom). The traces in this figure have been widened for visibility and may not represent the true position used in the analysis. Measurement error is estimated to be ±2 µm based the ability to accurately determine the edge of the track accounting for the focus of the image at the edge of the track and size of pixels.

3. EXPERIMENTAL RESULTS

For this analysis, a single scan track using a source power of 195 W and velocity of 800 mm/s on 17-4 stainless steel was deposited with no powder material added (i.e., beam on plate only). This experiment will serve as a baseline measurement for development of appropriate methodologies. Prior work by NIST has found that higher variance in melt pool size and greater dynamics in MPM systems can be expected when scanning over powder material and that stronger understanding of the process and analysis methodologies can be achieved through preliminary experiments without the added layer of powder material [9,10]. Therefore, while additional scan tracks at this and other power and velocity combinations were performed with and without the layer of powder material, analysis of those results will be reserved for future publication and this paper will focus only on the development of the methodology using data from the scan track without any added powder material at the aforementioned power and velocity.

3.1 In-Situ Melt Pool Monitoring Results

The pixel count from various thresholds, previously described in Figure 4, for each frame of the video can be seen in Figure 6. This method, in theory, should provide a qualitative understanding as to changes in melt pool (i.e., increases and decreases in size). However, it should be noted that this is only indicative of the apparent melt pool size. True melt pool size based on MPM imaging requires calibration of the camera, which has not yet been performed. Additionally, the apparent melt pool size in the image stems from the incandescent light generated by the hot surface, which depends on the temperature and emissivity of the surface, both of which vary spatially. In addition, gain, gamma, exposure time, etc. affect the apparent melt pool size in the image [11].

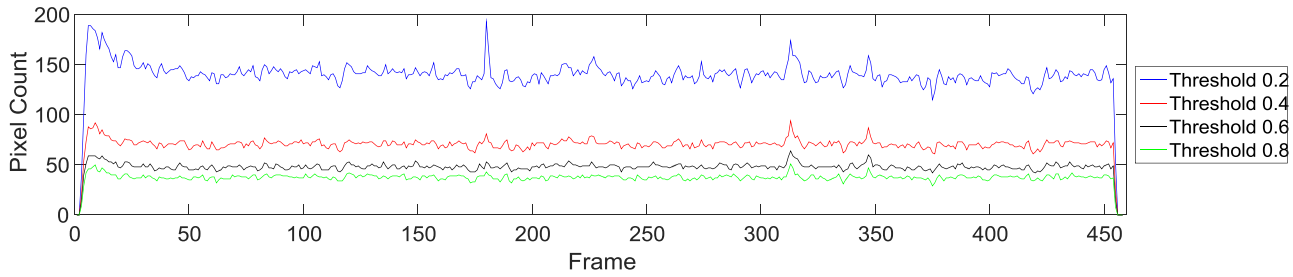

Figure 6. Example pixel count of melt pool size after conversion to binary using different threshold levels. Values for the threshold are from 0 to 1, where 0 would include any pixel with a value greater than 0 in the binary image, 0.5 would only include pixels with a value in the top 50 %, and 1 would not include any pixels.

A threshold level of 0.3 leads to approximately 6 pixels in the width of the melt pool and a threshold level of 0.2 leads to approximately 7 pixels in the width of the melt pool. With a 15 µm pixel size and using a center to center distance across the pixels, this corresponds to 106 µm to 127 µm, respectively, which is in accordance with the expected scan track width. The maximum width of the melt pool using a threshold level of 0.2 for the entire video can be seen in Figure 7.

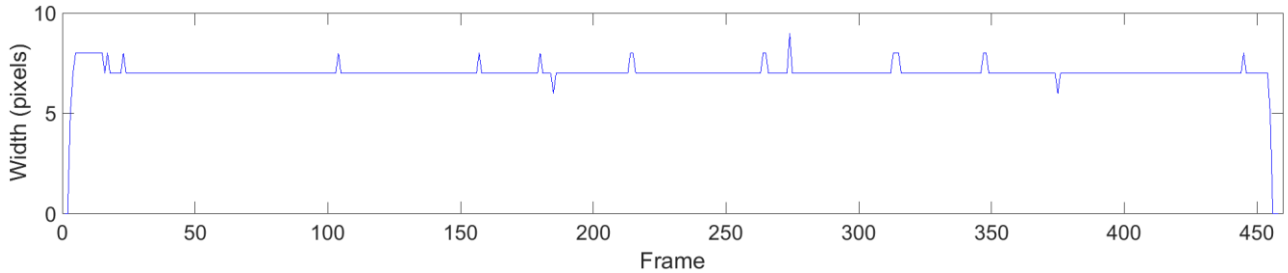

Figure 7. Maximum width of the melt pool for a threshold level of 0.2.

3.2 Ex-Situ Measurement Results

Images of the resultant scan track, taken via optical microscope, are shown in Figure 8.

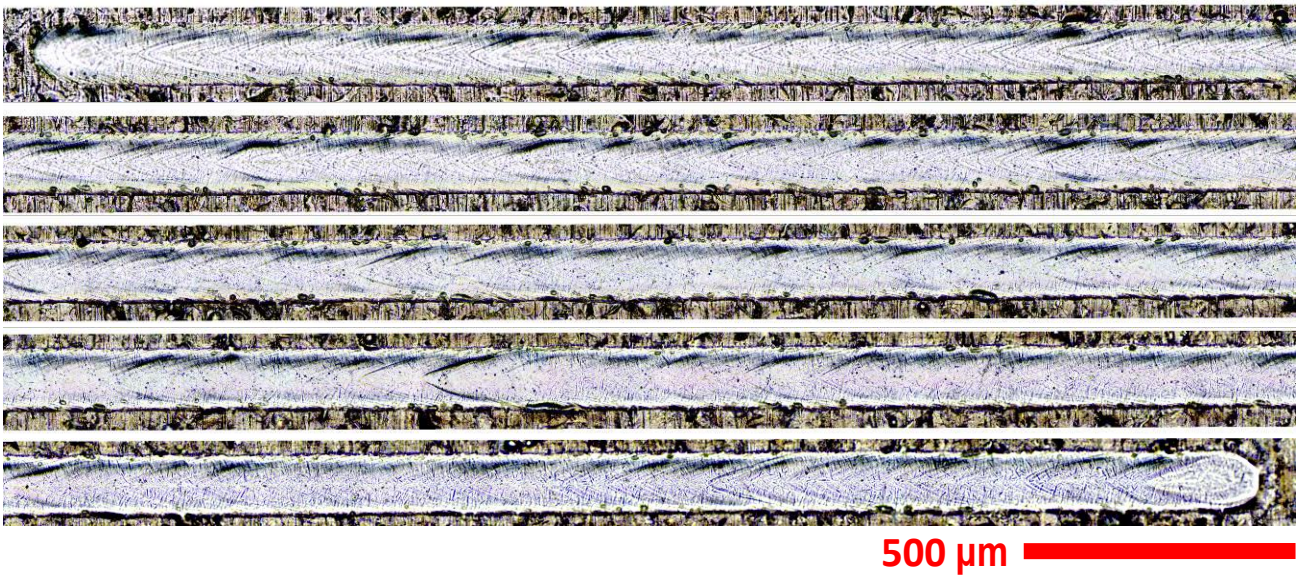

Figure 8. Optical images of the scan track. Direction of scan is from left to right. For better visibility, the image has been split into five sections, with the top being the start of the track and the bottom being the end.

Measurement of the scan track width using the method previously described in the Methodology section can be seen in Figure 9. The average can be calculated from this measurement after removing the first and last millimeter to minimize end effects from the laser turning on and off at the start and end of the scan track. The result is an average width of (117.9 ± 4.3) µm, where the number following the ± is one standard deviation, which is on par with expectations and the width measurements from the high-speed video, detailed in the previous section. Note that the length of the track is shorter than the expected 12 mm, which may be a result of errors incurred by the stitching algorithm of the microscope.

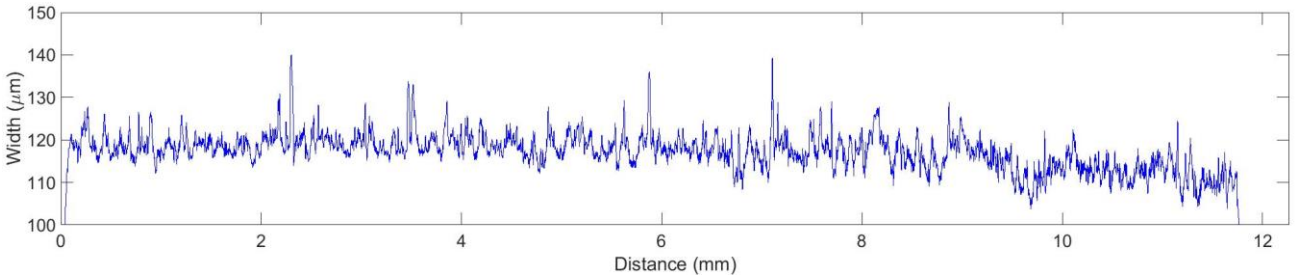

Figure 9. Measured width of the full scan track using the optical images shown in Figure 8.

Height data was also acquired using the laser confocal microscope described in the Methodology section to determine if evidence can be found relating the in-situ camera data to the solidified melt track. A height profile, which was taken down the center of the scan track and will be used in later comparisons, can be seen in Figure 10.

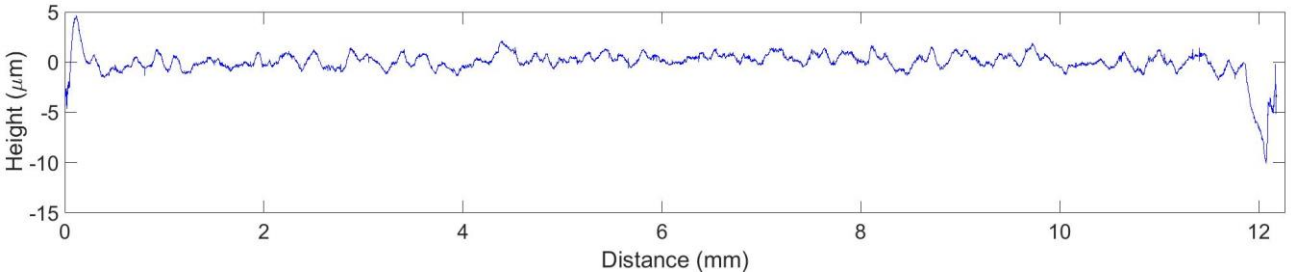

Figure 10. Surface topography measurement of the scan track. Profile was taken down the center of the scan track via laser confocal microscope.

4. COMPARISON OF MEASUREMENT TECHINQUES

With the different methodologies for analyzing the scan track defined, a comparison of these methods can be made to determine if variations in the data from one method translate to variations in the data in another method. The data from in-situ high speed video is time based (i.e., frames/s) and the data from ex-situ measurements is spatially based (i.e., distance from the start of the scan track). However, since the frame rate of the camera and travel velocity of the experiment are known, an approximate distance down the track can be calculated using the following equation:

$$x = \frac{N \times F}{V}, \tag{1}$$

where x is the distance from the start of the scan track, N is the number of frames since the start of the track, F is the frame rate (30 000 frames/s in this experiment), and V is the travel velocity (800 mm/s in this experiment). A comparison of the different data sources and a highlight of features that will be investigated can be seen in Figure 11.

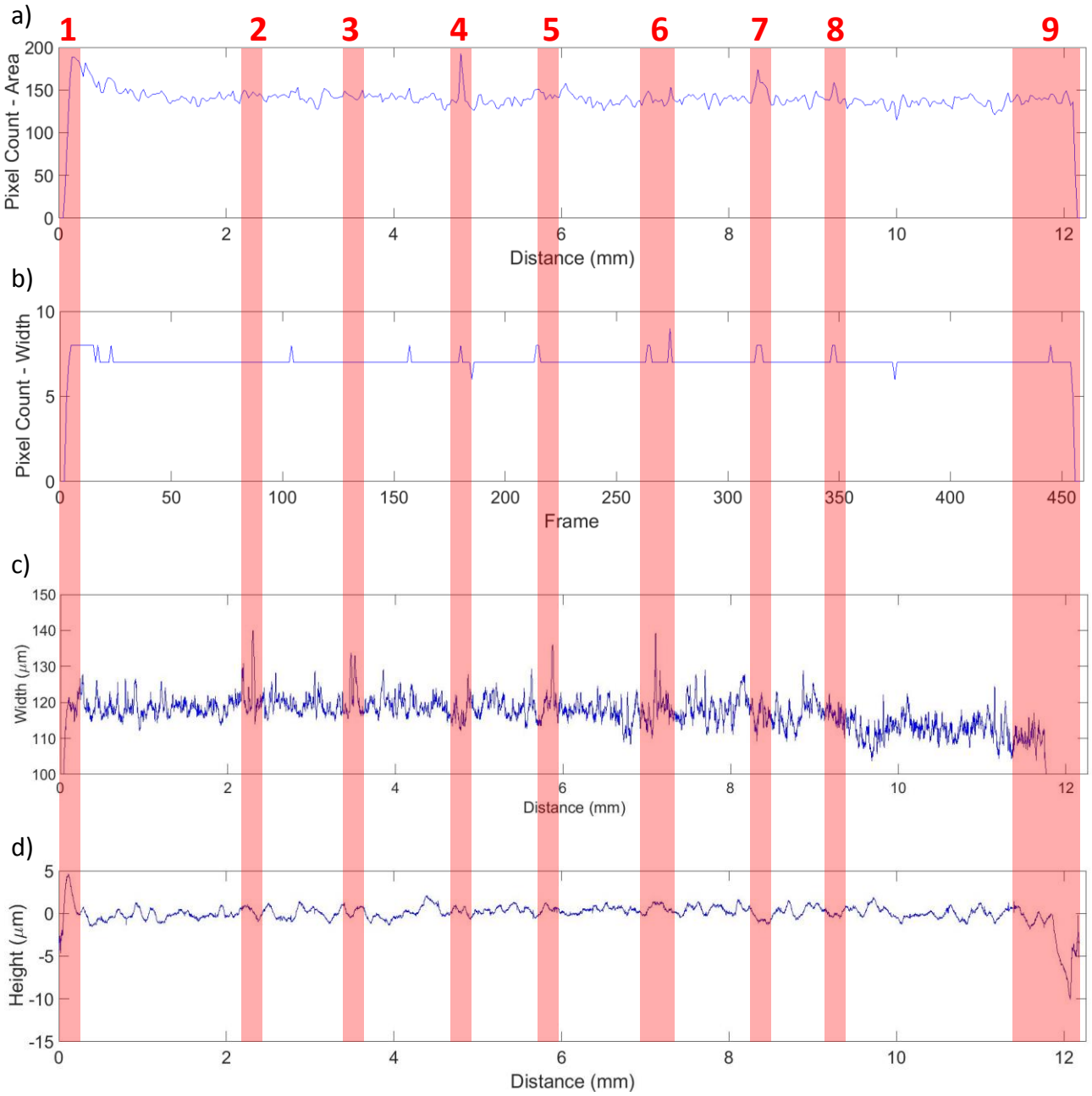

Figure 11. A comparison of the data from the in-situ high speed video with a 0.2 threshold applied depicting a) the total pixel count and b) the melt pool width pixel count, as well as ex-situ measurement of the scan track c) width and d) height. Key features in the data are denoted in red and numbered from 1 to 9.

4.1 Analysis of Feature 1

Still frames from the high-speed video, the binary conversion using a threshold level of 0.2, and measurement of area and width from the binary image can be seen in Figure 12. The data from this portion of the video shows an increase in the area and width measurements. Note that the average area for the 0.2 threshold is (139.1 ± 18.6) pixel^2.

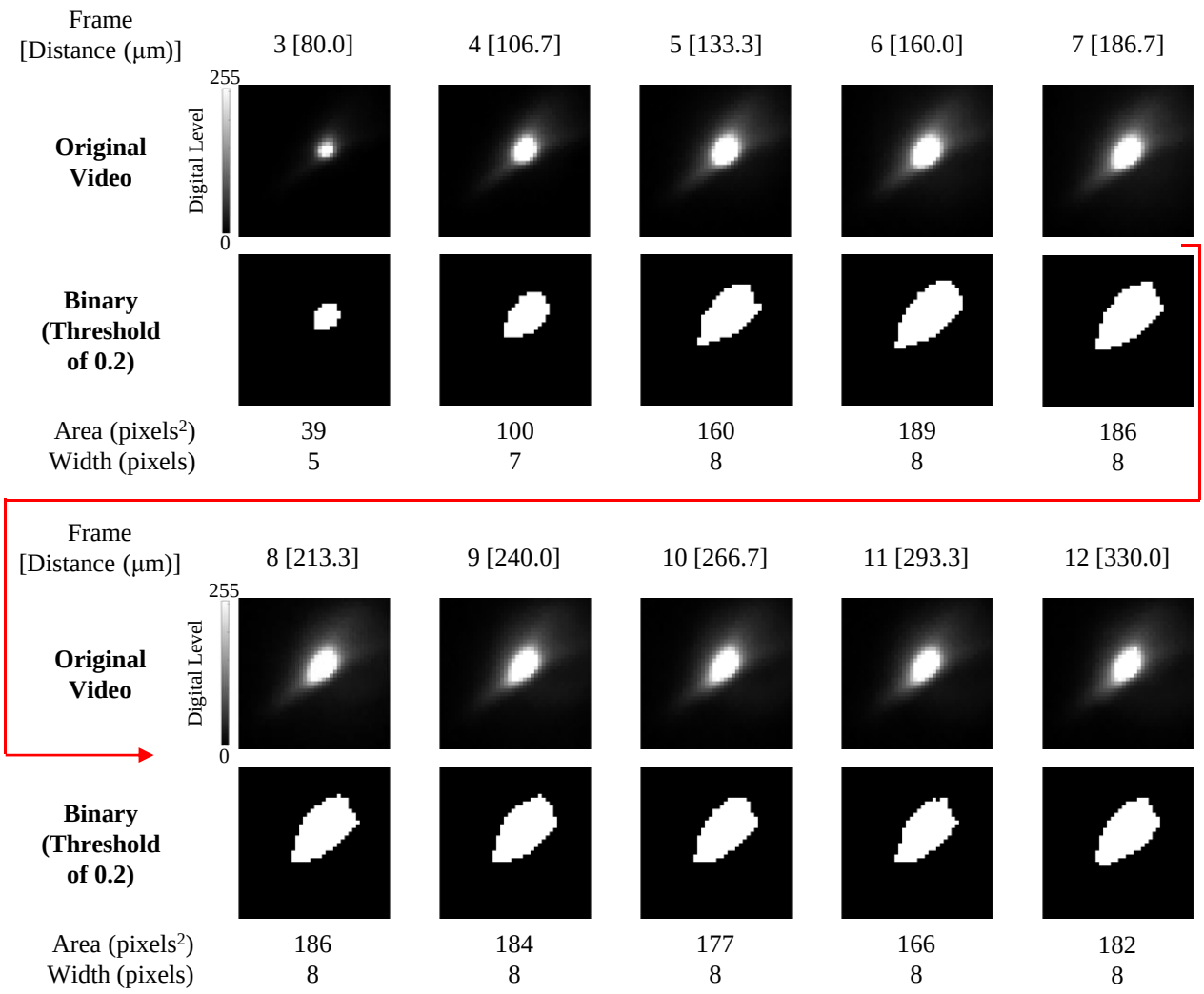

Figure 12. Still frames from the high-speed video representing data artifact 1, as presented in Figure 11. The size of the images presented are 40 pixels by 40 pixels. Direction of travel is previously defined in Figure 3.

Height data from start of the track, which is the location corresponding to video frames seen in Figure 12, can be seen in Figure 13. While a consolidation of material can be seen at the start of the scan track, it is not clear that this is related to the increased pixel count from the start of the video (i.e., measurements in Figure 12). This type of feature is likely due to fluid and surface tension effects in the molten metal. Prior work from Lawrence Livermore National Laboratory has shown that this type of feature is created well behind the point where the heat source is positioned on the surface [11]. Therefore, despite an apparent 'peak' at feature 1 in the camera data and surface height measurements, the physical bump and the apparent peak in brightness likely stem from two different physical phenomena.

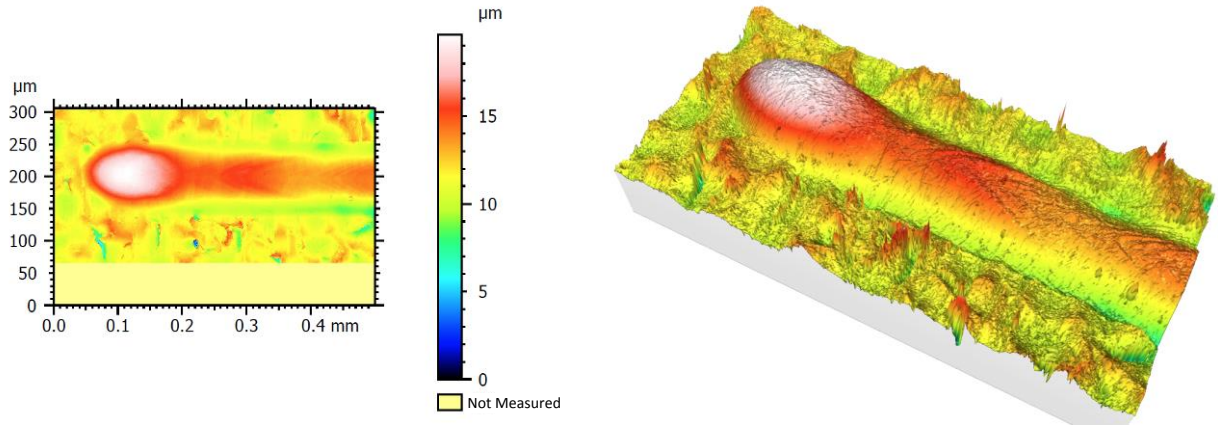

Figure 13. Height data from the scan track at a position corresponding to feature 1, which was previously described in Figure 11.

4.2 Analysis of Feature 2

An optical image of the scan track and height data near the location corresponding to feature 2 in Figure 11, can be seen in Figure 14 and matching features from the optical and topographic data have been highlighted. Interestingly, what appears to be a solidified melt droplet in the optical image shows up as a recess in the height measurement, leading to questions on the ability of optical images alone to correctly identify features. For this feature, no video stills are included as no noticeable variation in the video data was seen.

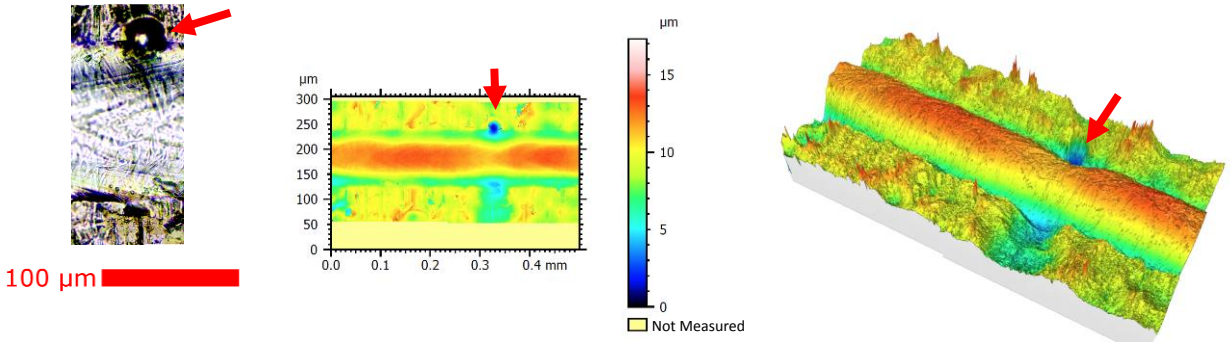

Figure 14. Optical image of the scan track and height data at a position corresponding to feature 2 described in Figure 11. Travel direction is to the right.

4.3 Analysis of Feature 3

An optical image of the scan track and height data near the location corresponding to feature 3 in Figure 11, can be seen in Figure 15 and matching features from the optical and topographic data have been highlighted. For this feature, no noticeable variation in the video data can be seen and so video stills are not included.

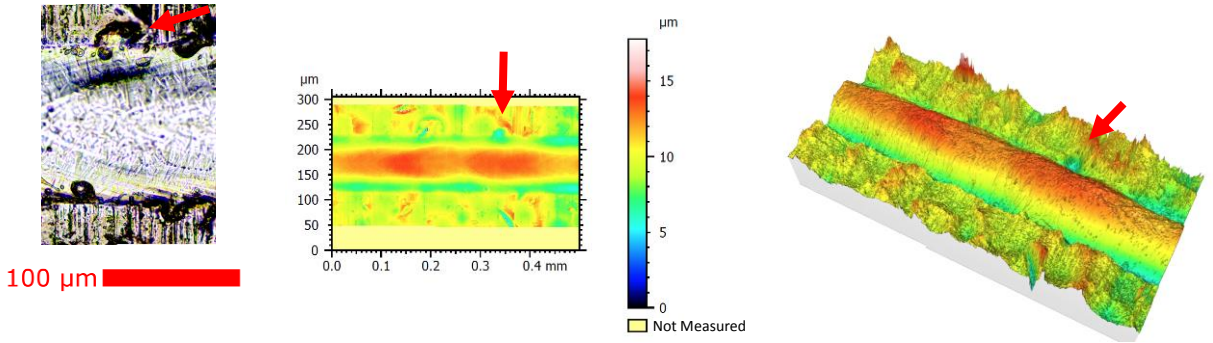

Figure 15. Optical image of the scan track and height data at a position corresponding to feature 3 described in Figure 11. Travel direction is to the right.

4.4 Analysis of Feature 4

Still frames from the high-speed video, the binary conversion using a threshold level of 0.2, and measurement of area and width from the binary image can be seen in Figure 16. The data from this portion of the video shows material being ejected from the melt pool, which is also represented as a spike in the pixel area of the binary image.

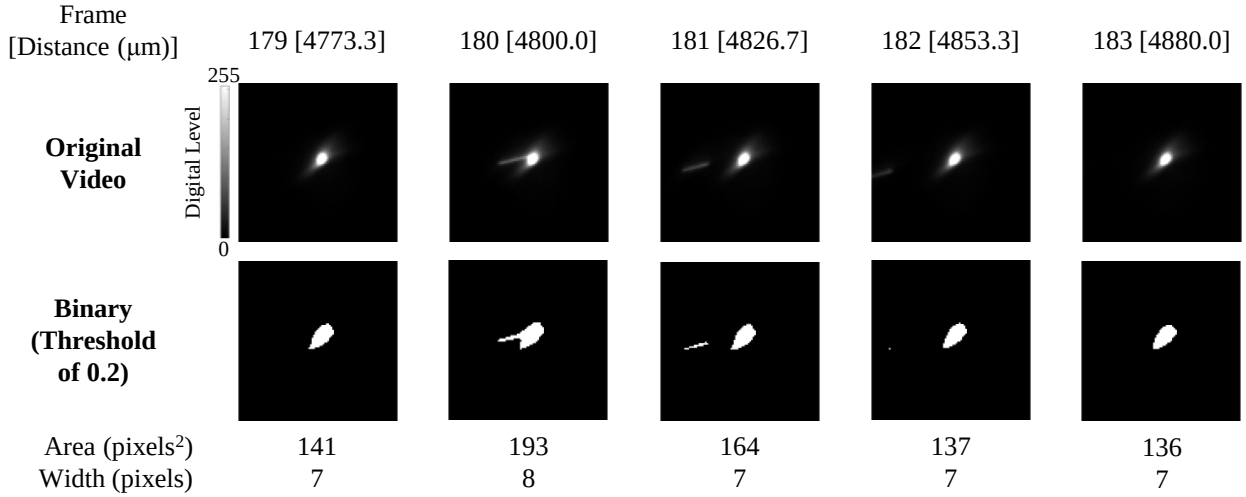

Figure 16. Still frames from the high-speed video representing feature 4, as presented in Figure 11. The size of the images presented are 100 pixels by 100 pixels. Direction of travel is previously defined in Figure 3.

An optical image of the scan track and height data near the location corresponding to feature 4 in Figure 11, can be seen in Figure 17. From these images, little variation in the surface can be seen near points of material ejecta.

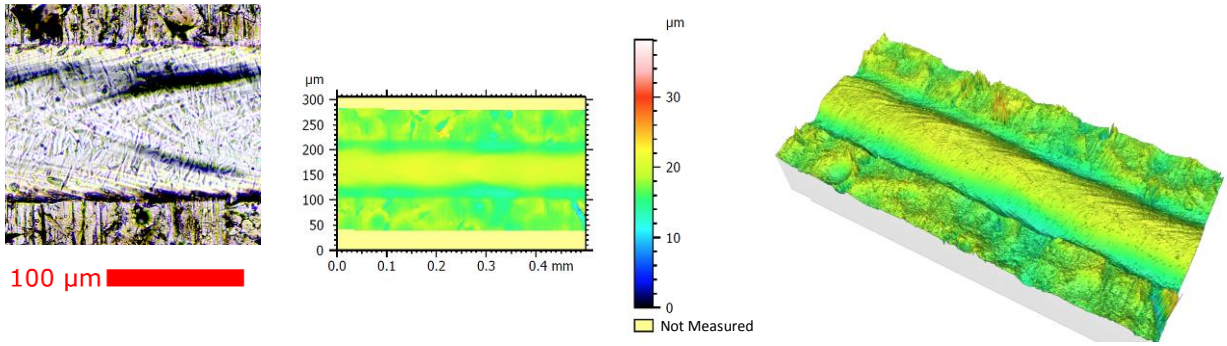

Figure 17. Optical image of the scan track and height data at a position corresponding to feature 4 described in Figure 11. Travel direction is to the right.

4.5 Analysis of Feature 5

An optical image of the scan track and height data near the location corresponding to feature 5 in Figure 11, can be seen in Figure 18. For this feature, it is difficult to match the optical image to a corresponding position in the height data as the microscope used does not provide a true color overlay onto the height data (a commercially available feature of some systems). Additionally, no noticeable variation in the video data can be seen and so video stills are not included.

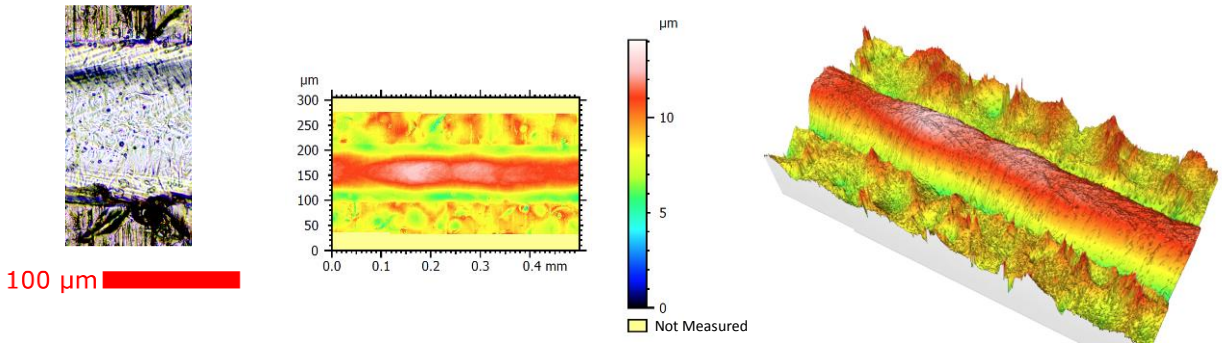

Figure 18. Optical image of the scan track and height data at a position corresponding to feature 5 described in Figure 11. Travel direction is to the right.

4.6 Analysis of Feature 6

Still frames from the high-speed video, the binary conversion using a threshold level of 0.2, and measurement of area and width from the binary image can be seen in Figure 19 and the corresponding optical image and height data can be seen in Figure 20. Video frames near this position show a glowing piece of material to the right of the melt pool in frame 274. This feature likely corresponds to the feature highlighted in the optical and topographic data in Figure 20.

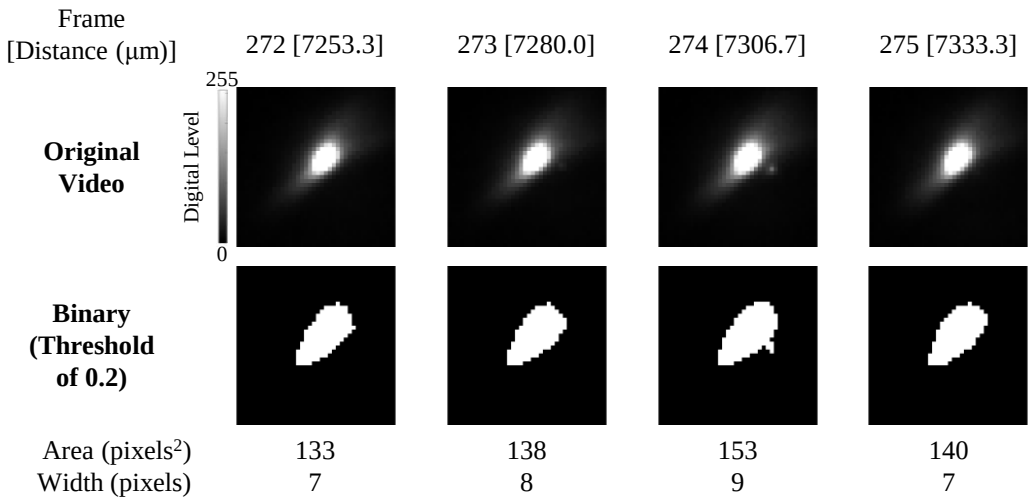

Figure 19. Still frames from the high-speed video representing feature 6, as presented in Figure 11. The size of the images presented are 40 pixels by 40 pixels. Direction of travel is previously defined in Figure 3.

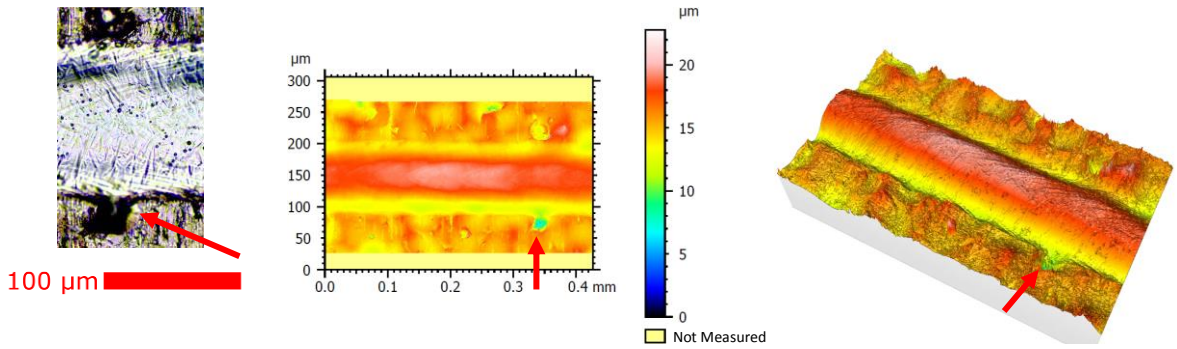

Figure 20. Optical image of the scan track and height data at a position corresponding to feature 6 described in Figure 11. Travel direction is to the right.

4.7 Analysis of Feature 7

Still frames from the high-speed video, the binary conversion using a threshold level of 0.2, and measurement of area and width from the binary image can be seen in Figure 21. The data from this portion of the video shows an increase in the size of the melt pool, which is also seen in the measured area of the binary image.

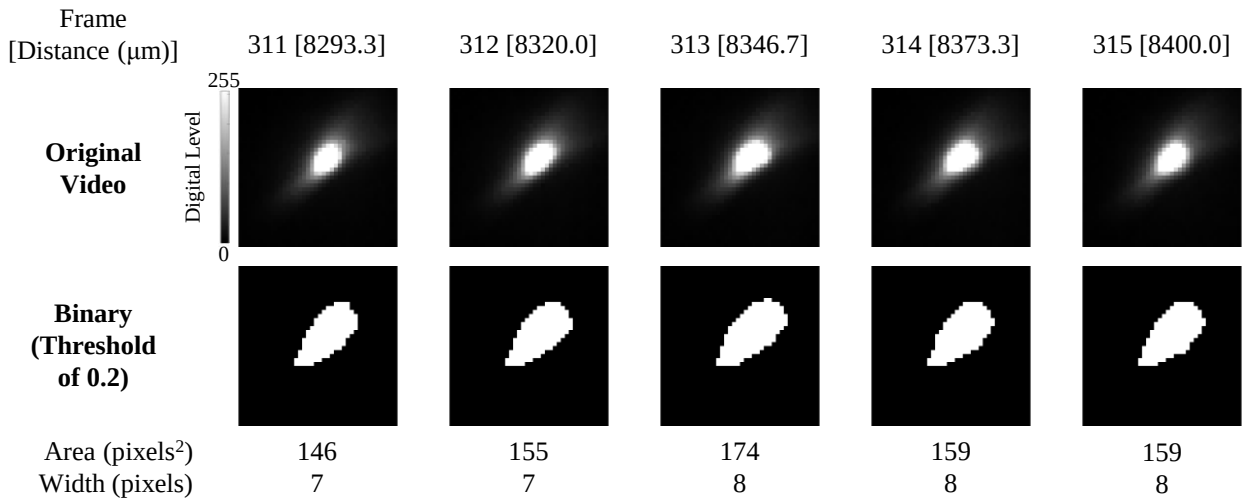

Figure 21. Still frames from the high-speed video representing feature 7, as presented in Figure 11. The size of the images presented are 40 pixels by 40 pixels. Direction of travel is previously defined in Figure 3.

An optical image of the scan track and height data near the location corresponding to feature 7 in Figure 11, can be seen in Figure 22. From these images, little variation in the surface can be seen to relate back to the video data in Figure 21.

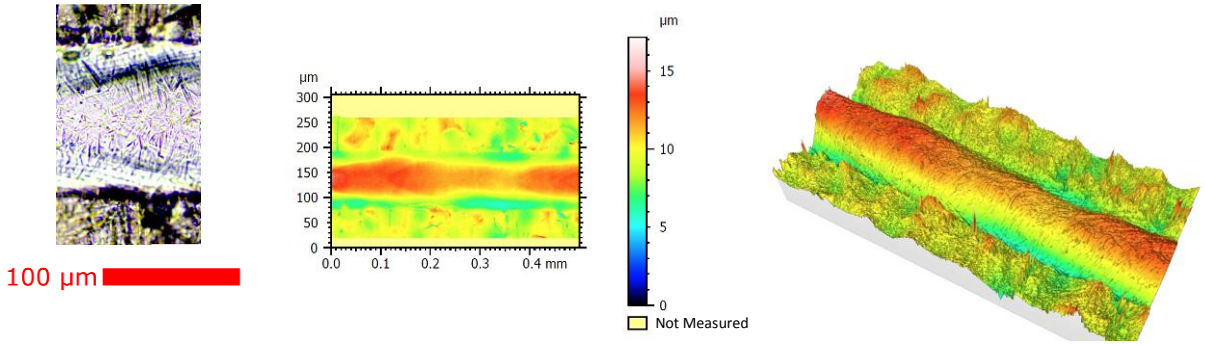

Figure 22. Optical image of the scan track and height data at a position corresponding to feature 7 described in Figure 11. Travel direction is to the right.

4.8 Analysis of Feature 8

Still frames from the high-speed video, the binary conversion using a threshold level of 0.2, and measurement of area and width from the binary image can be seen in Figure 23 and the optical image and height data from the location corresponding to video frames can be seen in Figure 24. Video frames near this position show a glowing piece of material to the right of the melt pool in frames 347 and 348. Unlike the data seen from feature 6, this feature did not have any distinct relation to the optical or height data in Figure 24.

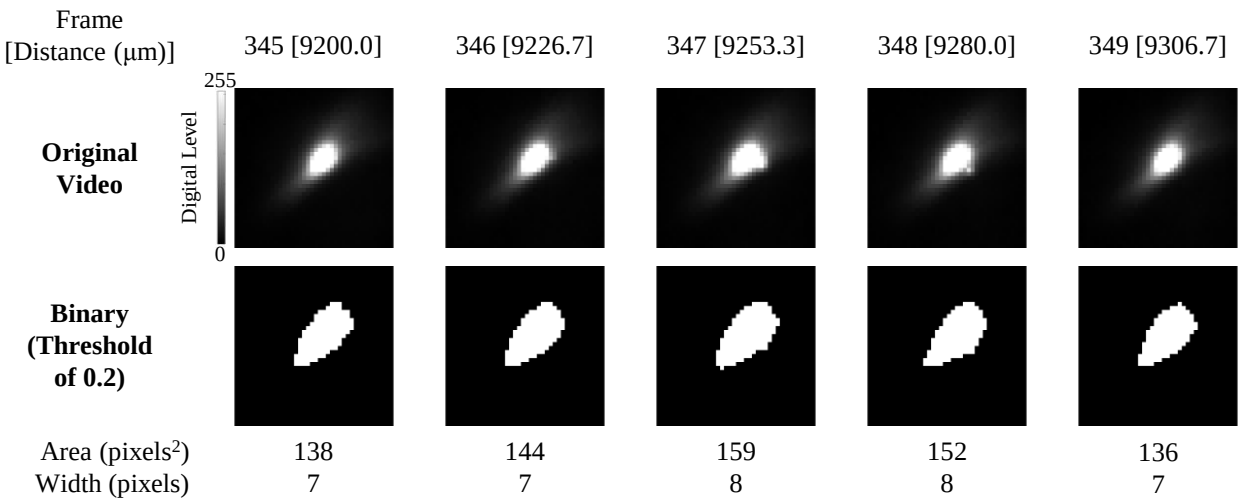

Figure 23. Still frames from the high-speed video representing feature 8, as presented in Figure 11. The size of the images presented are 40 pixels by 40 pixels. Direction of travel is previously defined in Figure 3.

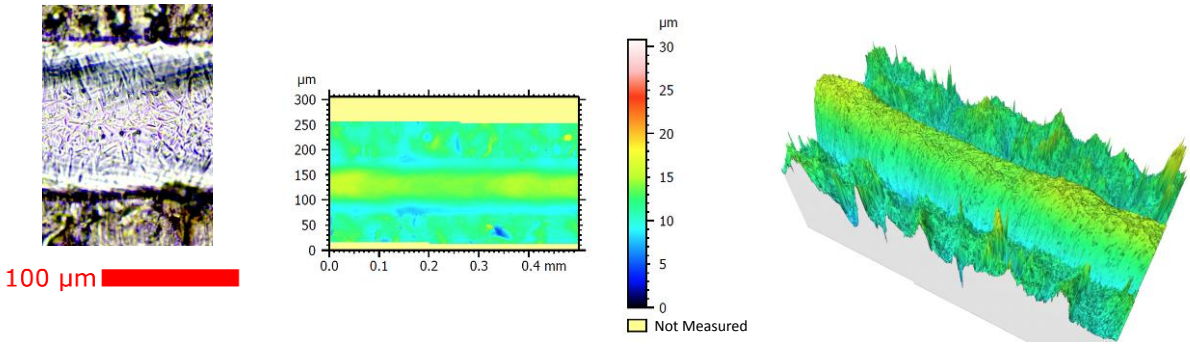

Figure 24. Optical image of the scan track and height data at a position corresponding to feature 8 described in Figure 11. Travel direction is to the right.

4.9 Analysis of Feature 9

Height data near the end of the track, corresponding to feature 9 in Figure 11, can be seen in Figure 25. At the end of the scan track, a recess can be seen showing the rapid freezing of the melt pool. There is, however, no evidence of this change from the in-situ video nor the optical width measurement, providing additional support to the conclusion that the corresponding camera data and topographic data for feature 1 do not correspond to the same physical phenomena.

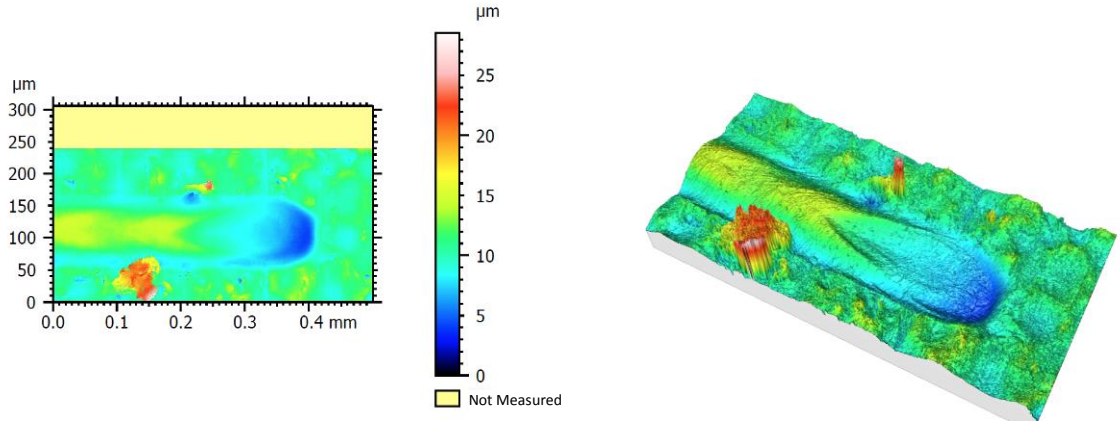

Figure 25. Height data from the scan track at a position corresponding to feature 9 described in Figure 11. Travel direction is to the right.

5. DISCUSSION

Analysis of the still frames has allowed for better characterization of the variation seen in the pixel counts, but it is clear from the data presented and analysis methods described in this paper that the signatures from in-situ and ex-situ measurements lack consistency and prevalence to determine specific correlations using the analysis methods described for this specific test case. Video data from features 1 and 7 show an increase in the overall size of the melt pool, with no clear relation to the ex-situ analysis (e.g., optical images, width measurements, or height measurements). Ex-situ measurements from features 2, 3, 5, and 9 show significant variation in the width measurement with no corresponding variation in the video data. Finally, while video data from features 6 and 8 show glowing material to the side of the melt pool, only feature 6 had corresponding variations in the ex-situ analysis.

This, however, does not prohibit additional features of interest or more advanced data analysis methods from aiding the development of these correlations. Recall that the standard deviation of the optical width measurement is only 4.3 µm, whereas the scale on the high-speed camera is 15 µm/pixel, not including effects of image blur. Thus, it is difficult to assume that any variation on this size scale can be captured through the described techniques. In addition to exploration of more advanced analysis techniques, future work will expand the experiments to include additional power and velocity combinations, the addition of powder material, and the influence of heat build-up from adjacent scan tracks. These scenarios are more indicative of a true LPBF build and are expected to create additional features typical of the process. Such features are expected to include larger variations in melt pool width and height or keyhole formation, and therefore more evidence to align the in-situ sensor signals to ex-situ scan track measurements.

6. CONCLUSIONS

A methodology for analyzing a coaxially aligned high speed NIR camera signal, monitoring a LPBF process has been presented. The analysis has been applied to an initial test case, which was performed on the AMMT prototype system at NIST, using 17-4 stainless steel. The result of the analysis has shown that, while the system can capture real-time events of the process, such as material ejecta, significant correlation between events captured by the in-situ monitoring system and features of the resultant scan track width and topography was not able to be obtained due to a limited type and frequency of observed events. As such, further analysis and experimentation is required to determine temporal and spatial locations for features of interest in the in-situ monitoring equipment and ex-situ measurement analysis.

7. ACKNOWLEDGEMENTS

The authors would like to acknowledge Brian Fisher of Carnegie Mellon University for his assistance in developing the optical camera setup and determination of the true magnification of the video images. Brian performed this work while serving as a NIST Pathways Graduate Research Assistant.

REFERENCES

[1] Energetics Inc. for National Institute of Standards and Technology. "Measurement science roadmap for metal-based additive manufacturing" (2013). http://www.nist.gov/el/isd/upload/NISTAdd_Mfg_Report_FINAL-2.pdf (accessed December 15, 2014).

[2] Mazumder, J., Song, L. "Advances in Direct Metal Deposition," Proceedings of the International Mechanical Engineering Congress and Exposition (2013). doi:10.1115/IMECE2013-65042.

[3] Huang, Y., Leu, M. C., Mazumder, J., Donmez, A., "Additive Manufacturing: Current State, Future Potential, Gaps and Needs, and Recommendations," Journal of Manufacturing Science and Engineering, 137, 014001-01-014001-10 (2015). doi:10.1115/1.4028725.

[4] Spears T. G., Gold S. A., "In-process sensing in selective laser melting (SLM) additive manufacturing," Integrating Materials and Manufacturing Innovation 5, 1–25 (2016). doi:10.1186/s40192-016-0045-4.

[5] Grasso, M., Colosimo, B. M. "Process defects and in situ monitoring methods in metal powder bed fusion: a review," Meas Sci Technol (2017), 28:044005. doi:10.1088/1361-6501/aa5c4f.

[6] Berumen, S., Bechmann, F., Lindner, S., Kruth, J. P., Craeghs, T., "Quality control of laser- and powder bed-based Additive Manufacturing (AM) technologies," Phys Proc 5, Part B,617–22 (2010). doi:10.1016/j.phpro.2010.08.089.

[7] Grantham, S., Lane, B., Neira, J., Mekhontsev, S., Vlasea, M., Hanssen, L., "Optical design and initial results from NIST's AMMT/TEMPS facility," Proc. SPIE 9738, p. 97380S–97380S–9 (2016). doi:10.1117/12.2214246.

[8] Lane, B., Mekhontsev, S., Grantham, S., Vlasea, M.L., Whiting, J., Yeung, H., Fox, J. C., et al., "Design, Developments, and Results from the NIST Additive Manufacturing Metrology Testbed (AMMT)," Proceedings of the 26th Annual International Solid Freeform Fabrication Symposium – An Additive Manufacturing Conference, Austin, TX, p. 1145–60 (2016).

[9] Heigel, J. C., Lane, B. M., "Measurement of the Melt Pool Length During Single Scan Tracks in a Commercial Laser Powder Bed Fusion Process," Proceedings of the ASME 2017 12th International Manufacturing Science and Engineering Conference, Los Angeles, CA, USA (2017).

[10] Lane, B., Moylan, S., Whitenton, E. P., Ma, L., "Thermographic measurements of the commercial laser powder bed fusion process at NIST," Rapid Prototyping Journal 22,778–87 (2016). doi:10.1108/RPJ-11-2015-0161.

[11] Fox, J. C., Lopez, F. F., Lane, B. M., "On the Requirements for Model-Based Thermal Control of Melt Pool Geometry in Laser Powder Bed Fusion Additive Manufacturing," Proceedings of the 2016 Material Science & Technology Conference, Salt Lake City, UT (2016).

[12] Khairallah, S. A., Anderson, A. T., Rubenchik, A., King, W. E., "Laser powder-bed fusion additive manufacturing: Physics of complex melt flow and formation mechanisms of pores, spatter, and denudation zones," Acta Materialia 108,36–45 (2016). doi:10.1016/j.actamat.2016.02.014.

Identification of machine tool geometric performance using on-machine inertial measurements

G.W. Vogl[1], R. Pavel[2], A. Archenti[3], T.J. Winnard[4], M.M. Mennu[5], B.A Weiss[1], and M.A. Donmez[1]

[1]National Institute of Standards and Technology (NIST), Gaithersburg, MD, USA
[2]TechSolve, Cincinnati, OH, USA
[3]KTH Royal Institute of Technology, Brinellvägen 68, 10044, Stockholm, Sweden
[4]Andrews University, Berrien Springs, MI, USA
[5]University of South Florida, Tampa, FL, USA
gvogl@nist.gov, pavel@TechSolve.org, archenti@kth.se, winnard@andrews.edu, mmennu@mail.usf.edu, brian.weiss@nist.gov, alkan.donmez@nist.gov

Abstract
Machine tools degrade during operations, yet accurately detecting degradation of machine components such as linear axes is typically a manual and time-consuming process. Thus, manufacturers need automated and efficient methods to diagnose the condition of their machine tool linear axes with minimal disruptions to production. Towards this goal, a method was developed to use accelerometer and rate gyroscope data from an inertial measurement unit (IMU) for identification of changes in the translational and angular errors due to axis degradation. An IMU was created for application of the method on a machine tool. As a proof of concept for detection of translational error motions, IMU data was collected on a machine tool with experimentally simulated degradation; as the worktable moved along its nominal path, a cross-axis moved along a swept sinusoidal pattern with micrometer-level amplitudes. In another experiment, data was collected at three different locations on a worktable for the same axis motion. These experiments showed that the IMU detected micrometer-level and microradian-level degradation of linear axes, revealing that the IMU-based method is plausible for use in smart machine tools.

Keywords
Machine tool, Linear Axis, Error, Degradation, Diagnostics

1. Introduction

Over a machine tool's lifetime, various faults lead to performance degradation, lowering accuracy and repeatability [1]. Typical sources of errors within linear axes are due to pitting, wear, corrosion, and cracks of the system components such as guideways and recirculating balls [2]. A typical machine tool has multiple linear axes, and their accuracies directly impact the quality of manufactured parts. As degradation increases, tool-to-workpiece errors increase that eventually may result in a loss of production quality and/or a failure [3]. Yet knowledge of degradation is elusive; proper assessment of axis degradation is often a manual, time-consuming, and potentially cost-prohibitive process.

While direct methods for machine tool performance evaluation are well-established [4] and reliable for position-dependent error quantification, such measurements typically interrupt production [5]. An online condition monitoring system for linear axes is needed to help reduce machine downtime, increase productivity and product quality, and improve knowledge about manufacturing processes [6]. Previous attempts at condition monitoring of linear axes had limited success, partly because of the lack of robustness and defined relationships of signals to axis

Archenti, Andreas; Donmez, M; Mennu, Matlock; Pavel, Radu; Vogl, Gregory; Weiss, Brian; Winnard, Thomas.
"Identification of machine tool geometric performance using on-machine inertial measurements."
Paper presented at 6th International Conference on Virtual Machining Process Technology (VMPT 2017),
Montreal, Canada. May 28, 2017 - June 2, 2017.

degradation composed of a wide range of spatial frequencies. Consequently, efficient quantitative measures are needed to monitor the degradation of linear axes.

2. IMU for Industrial Application

One potential solution for online monitoring of linear axis degradation is the use of an inertial measurement unit (IMU) [7, 8] that processes accelerometer and rate gyroscope data to detect changes in the translational and angular error motions due to axis degradation [8]. For industrial application, the IMU should be physically small and economical while satisfying measurement needs. As seen in Figure 1, an industrial IMU was created that is about 9 cm long and contains a triaxial accelerometer and a triaxial rate gyroscope. The bandwidths and noise properties of these sensors are shown in Table 1. A custom IMU was needed to satisfy design constraints such as cost, size, and accuracy.

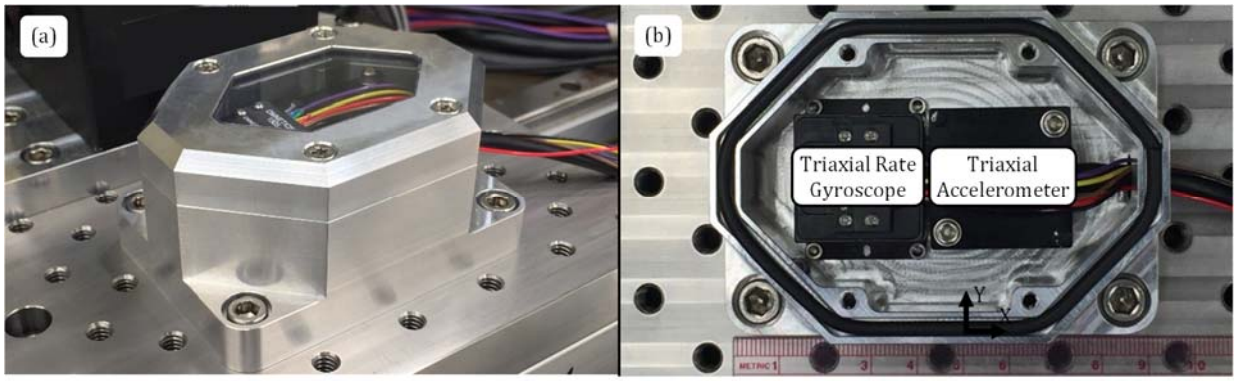

Figure 1 (a) Isometric view of industrial IMU and (b) top view of industrial IMU without its lid.

Table 1 Properties of sensors in industrial IMU.

Sensor	Bandwidth[a]	Noise
Accelerometer	0 Hz to 500 Hz	20 (μm/s^2)/√Hz
Rate Gyroscope	0 Hz to 200 Hz	35 (μrad/s)/√Hz

[a] frequencies correspond to half-power points, also known as 3 dB points

3. Detection of Translational Degradation

Repeated testing of the IMU on a machine tool is required for acceptance testing. Figure 2 shows an experimental setup of the IMU on a horizontal milling machine at TechSolve, Inc. The IMU is attached to the worktable, which can translate in two directions since the X-axis is stacked on the Z-axis. Of course, unwanted translational errors exist and can worsen due to degradation as the machine tool produces parts. For example, the error motion E_{ZX} is the translational error, as a function of X, in the Z-direction for X-axis motion. Because the X- and Z-axes are stacked for the machine tool, we can simulate E_{ZX} via two-axis commanded motion. The boxed inset of Figure 2 shows the points used for machine path generation. As the X-axis moves from 0 mm to 1250 mm, the Z-axis experiences a swept-sine-like form of degradation with magnitude A. The path is independent of feed rate, which can be as large as 10 m/min (0.1667 m/s). Hence, data was collected for 50 runs for each of three speeds for use within the method [8]: 0.1667 m/s (Fast speed), 0.1 m/s (Moderate speed), and 0.02 m/s (Slow speed). The fast speed of 0.1667 m/s was the machine limit, but preferably a speed of 0.5 m/s would have been used otherwise. Furthermore,

the magnitude A was changed to represent different levels of degradation. Data was collected for five values of A: 0 µm (representing no degradation), 5 µm, 10 µm, 15 µm, and 20 µm (representing significant degradation). Consequently, the swept-sine-like motion is a "mechanically-simulated degradation" that will test the ability of the industrial IMU to measure micrometer-level degradation for various spatial frequencies.

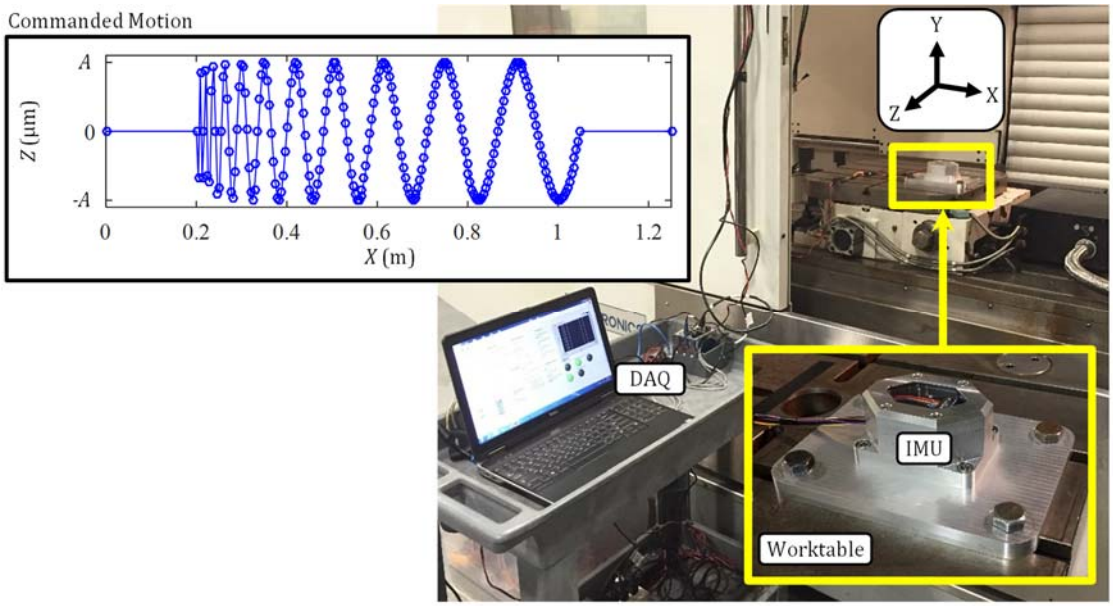

Figure 2 Experimental setup of IMU on machine tool at TechSolve. Commanded machine tool motion (Z versus X) shown in boxed inset.

IMU data was collected and processed for each of the five values of A, the parameter representing translational error motion in the Z-direction due to 'degradation'. The results of each set of 50 runs were averaged to yield the estimated straightness error motion E_{ZX} for each value of A. Figure 3(a) and Figure 3(b) compare the commanded and estimated values for $\mathrm{hp}(E_{ZX})$, the high-pass filtered values of E_{ZX}. The error motions are high-pass filtered because the specific accelerometer was determined *post facto* to have noise during testing that exceeded the noise specification listed in Table 1. Hence, convergence of E_{ZX} did not occur to sufficient levels for spatial frequencies below 1.25 m^{-1}, so those terms were filtered out via the use of zero-phase forward and reverse digital infinite impulse response (IIR) Butterworth filters.

Figure 3(b) shows how the mechanically-simulated degradation is detected by the IMU-based method. As the commanded degradation amplitude A increases to 20 µm, as seen in Figure 3(a), the estimated degradation amplitude also increases, as shown in Figure 3(b). Error motions due to the sensor noise and mechanical elements of the machine tool are present in the curves of Figure 3(b), but the degradation terms are still clearly visible. The estimated degradation amplitudes seen in Figure 3(b) are roughly similar to the commanded ones seen in Figure 3(a), but the estimated amplitudes increase as the spatial frequency of the swept-sine decreases. When the spatial frequency is at its highest around $X = 0.2$ m, the required accelerations for the commanded motions within Figure 3(a) for $A = 20$ µm are as high as 1.75 m/s^2 for the fast speed (0.1667 m/s), which is far greater than the maximum allowable acceleration for the machine tool during feed motion. Hence, the high-frequency motions for $A = 20$ µm near $X = 0.2$ m are not detectable

because they did not occur with amplitudes near 20 µm, but rather with much smaller amplitudes. Unfortunately, a laser-based device, such as a laser tracker, was not available to measure the actual amplitudes during motion for verification and validation of the acceleration-limiting motion.

The high-passed motions, shown in Figure 3 for various amplitudes A, can be processed with a single metric value for comparison and tracking of 'degradation'. Figure 3(c) shows the scaled root mean square (rms) of each of the curves seen in Figure 3(a) and Figure 3(b). The metric for the commanded motion increases linearly from 0 µm (the smallest value for A) to 20 µm (the largest value for A) as A increases, while the metric for the estimated motion increases fairly linearly from about 5 µm to about 16 µm. The estimated-motion metric value reaches 5 µm, instead of 0 µm, at $A = 0$ µm because even with no commanded cross-axis motion ($A = 0$ µm), the Z-axis still exhibits an error motion as the X-axis moves. At the other end, the estimated-motion metric value reaches 16 µm, instead of 20 µm, at $A = 20$ µm because of the machine tool's acceleration limit that inhibits the Z-axis motion, as evidenced in Figure 3(b). Nonetheless, Figure 3(c) reveals how even a simple metric, based on results from the IMU-based method, can track linear axis degradation in a quantitative manner.

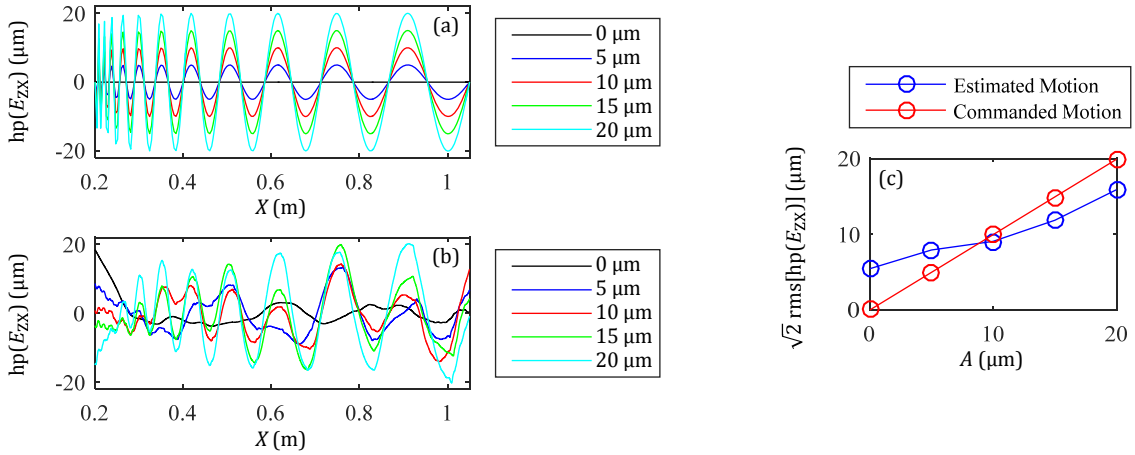

Figure 3 Comparison of (a) commanded and (b) estimated high-pass filtered error motions with their (c) metric values as a function of 'degradation' amplitude.

4. Detection of Angular Error Motion

Another experiment was conducted to test the capability of the IMU for on-machine detection of error motions. However, before experimentation, the IMU was improved via replacement of the triaxial accelerometer with a different model that had relatively stable low-frequency noise, but higher overall noise (69 (µm/s^2)/√Hz) compared to the accelerometer used in the first experiment (see Table 1).

Figure 4(a-d) shows an experimental setup of the IMU on a vertical milling machine at the National Institute of Standards and Technology (NIST). For each dataset, the IMU is attached to the worktable at one of three different locations (A, B, or C) and the Y-axis travels between Y = 0 m and Y = 0.5 m. Hence, IMU data was collected for 50 runs sequentially at each location with motion back and forth along the Y axis for use within the method [8]. The three speeds for data collection are 0.5 m/s (fast speed), 0.1 m/s (moderate speed), and 0.02 m/s (slow speed). The IMU data was then used to estimate the three angular error motions at each of the three worktable locations (A, B, and C). The accelerometer and rate gyroscope data were processed to estimate

two angular error motions (E_{AY} and E_{BY}) according to Fig. 3(b) in Ref. [8], while the rate gyroscope data only was used to estimate the third angular error motion (E_{CY}) according to Fig. 3(a) in Ref. [8]. If the worktable is rigid, then the estimated angular error motions should be identical among each location.

Figure 4(e-g) shows the estimated angular errors based on the IMU data. Error motion data was also collected at each location with a laser-based commercial reference system (with standard uncertainties of 0.7 µm and 3.0 µrad), and the data from the reference system is shown in the figures (as thinner lines) for comparison purposes. At each worktable location, reference data was collected for five runs, which were averaged to produce the curves seen in Figure 4(e-g). The standard deviations of each set of five runs was also used to produce the shaded 95%-confidence zones in Figure 4(e-g). Thus, the shaded zones represent a contribution towards, but not the total of, the measurement uncertainty. As seen in Figure 4(e-g), the estimated angular errors from the IMU data match each other respectively to within about 5 µrad for the three worktable locations (A, B, and C). Also, the estimated error motions from the IMU match those from the reference system to within about 8 µrad. The differences may be due to differences in error type (inertial for IMU, while relative for the reference system) as well as to sources of uncertainty.

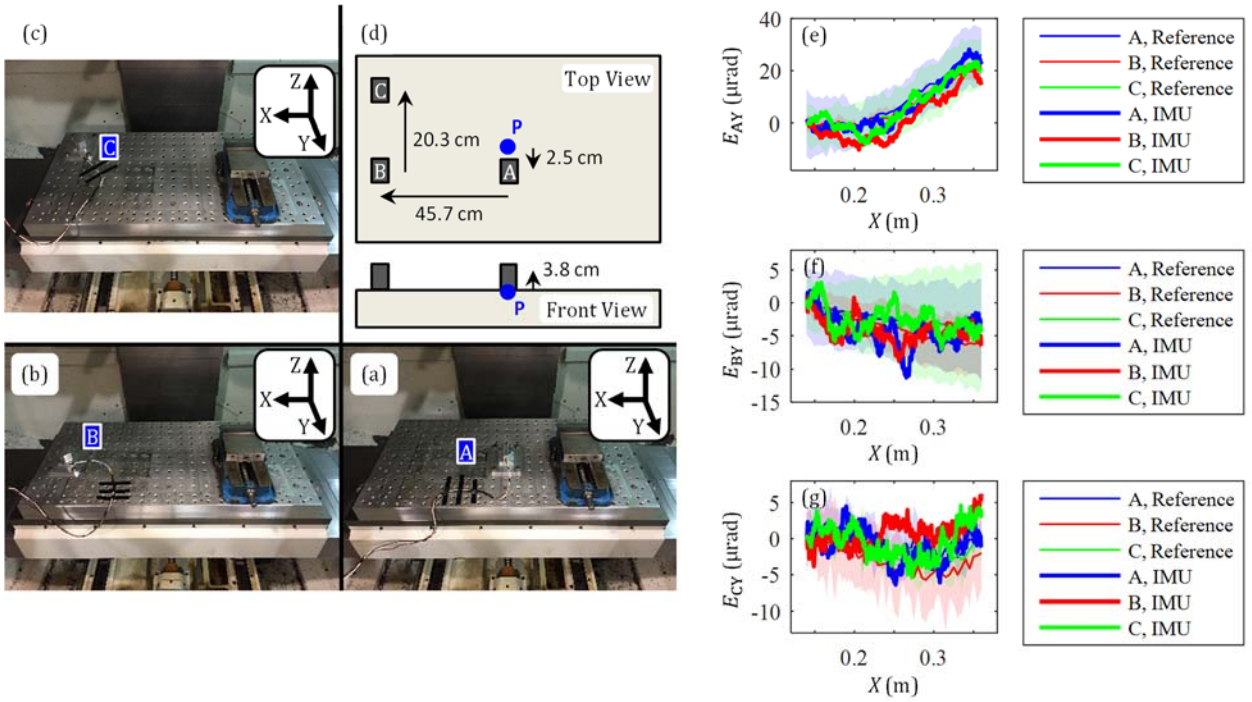

Figure 4 Experimental setup of IMU on machine tool worktable: Pictures of IMU at (a) Location A, (b) Location B, and (c) Location C and (d) schematic of three IMU locations relative to center point P of worktable. Angular errors (e) E_{AY}, (f) E_{BY}, and (g) E_{CY} based on data collected at the three locations (Locations A, B, and C) with the IMU and a commercial reference system. The reference data has shaded areas representing measurement expanded uncertainties (k = 2) at 95% confidence based on five runs.

5. Conclusions

An 'industrial IMU' was developed to test the effectiveness of a new IMU-based method for on-machine application. The industrial IMU includes a triaxial accelerometer and a triaxial rate gyroscope, both with noise levels shown to be sufficiently low for convergence via averaging. One

experiment was conducted in which two stacked axes were moved simultaneously to simulate translational degradation up to 20 μm in amplitude. The IMU data showed that the mechanically-simulated degradation is detected by the IMU-based method. However, the error motions needed to be high-pass filtered because the specific accelerometer had noise levels that exceeded its specification, revealing how the industrial IMU must be improved for future applications. In a second experiment, data was collected from an improved IMU at three different locations on a worktable for the same axis motion. The IMU results were within about 8 μrad of those from a laser-based reference system. Both experiments show that the IMU-based method is capable of detecting micrometer-level and microradian-level degradation of linear axes.

When coupled with existing data exchange and formatting standards, verified and validated data from an 'industrial IMU' could provide manufacturers and machine tool operators with near-real-time equipment health, diagnostic, and prognostic intelligence to significantly enhance asset availability and minimize unscheduled maintenance. This information can be coupled with equipment performance metrics and quality data (resultant from part inspection) to enable the prediction of future machine performance and part quality based upon current and projected equipment health.

Acknowledgements

The authors thank Brian Pries, Travis Shatzley, Dan Falvey, and Jay Brandenburg of the Fabrication Technology Group (NIST), and Dennis Dill (TechSolve) for their outstanding contributions with the experimental setup.

References

[1] Li Y, Wang X, Lin J, Shi S (2014) A Wavelet Bicoherence-Based Quadratic Nonlinearity Feature for Translational Axis Condition Monitoring. *Sensors* 14(2):2071-2088.

[2] Zhou Y, Mei X, Zhang Y, Jiang G, Sun N (2009) Current-Based Feed Axis Condition Monitoring and Fault Diagnosis. *4th IEEE Conference on Industrial Electronics and Applications, ICIEA 2009*, 1191-1195.

[3] Uhlmann E, Geisert C, Hohwieler E (2008) Monitoring of Slowly Progressing Deterioration of Computer Numerical Control Machine Axes. *Proceedings of the Institution of Mechanical Engineers, Part B: Journal of Engineering Manufacture* 222(10):1213-1219.

[4] International Organization for Standardization (2012) ISO 230-1 - Test Code for Machine Tools − Part 1: Geometric Accuracy of Machines Operating under No-Load or Quasi-Static Conditions.

[5] Khan AW, Chen W (2009) Calibration of CNC Milling Machine by Direct Method. *2008 International Conference on Optical Instruments and Technology: Optoelectronic Measurement Technology and Applications*, 7160:716010.

[6] Teti R, Jemielniak K, O'Donnell G, Dornfeld D (2010) Advanced Monitoring of Machining Operations. *CIRP Annals - Manufacturing Technology* 59(2):717-739.

[7] Vogl GW, Weiss BA, Donmez MA, 2015, A Sensor-Based Method for Diagnostics of Machine Tool Linear Axes, Annual Conference of the Prognostics and Health Management Society 2015. Coronado, CA: PHM Society, p. 10.

[8] Vogl GW, Donmez MA, Archenti A (2016) Diagnostics for Geometric Performance of Machine Tool Linear Axes. *CIRP Annals - Manufacturing Technology*

Industrial Wireless: Problem Space, Success Considerations, Technologies, and Future Direction

Richard Candell, *Senior Member, IEEE* and Mohamed Kashef, *Member, IEEE*

***Abstract*—The use of wireless technologies within factories demands a comprehensive understanding of the problems and potential solutions associated with the rigors of the manufacturing environment. A clearly defined problem space would significantly ease the selection and deployment of appropriate wireless solutions to connected factory systems. A mapping of potential technologies to classes of use cases within the problem space will be useful to factory operators, system integrators, and wireless systems manufacturers. Identification of use cases, not addressed by existing technologies, may be used to spur targeted innovation where reliability, resilience, latency, and scalability are joint concerns. Motivated by the industry need for independent practical guidelines and solutions to difficult wireless control problems, this paper provides a classification of the problem categories where networking technologies may be deployed. It then maps specific technologies that may serve as interim or terminal solutions for those use cases identified within the problem space taxonomy.**

***Index Terms*—industrial wireless, industrial communication, industrial control, networked control, manufacturing, cyber-physical systems, taxonomy**

I. Introduction

A. Purpose

Industrial wireless is a key enabling technology for the Industrial Internet of Things (IIoT). The IIoT promises lower costs of deployment, increased mobility of factory assets, massive interconnectivity, improved situational awareness, increased efficiency of the operation, and improved operations analytics. IIoT and advanced manufacturing technology seek to improve competitiveness, productivity, and responsiveness to customer needs. However, it is often stated that where wireless is deployed, factory enhancements fail to meet expectations typically in areas of reliability, resilience, and scalability. Moreover, transmission security is often cited as an area of concern. Risk averse organizations will establish policies that preclude wireless to be deployed for specific types of applications such as feedback control or safety. Yet, factory operators are increasingly demanding that wireless be deployed for critical and sometimes perceivably dangerous applications. For this reason, the National Institute of Standards and Technology (NIST) is developing best practice guidelines to help factory operators select appropriate wireless systems for their particular use case and then deploy that solution effectively. Such a mission requires participation by factory operators, system integrators, and device manufacturers. A comprehensive taxonomy of the existing problem space within industry and a survey of existing and missing technologies are necessary to the success of such a mission. This paper provides our classification of industrial wireless cases and links current technologies to those use cases if applicable.

R. Candell is with Intelligent Systems Division, Engineering Laboratory, National Institute of Standards and Technology, Gaithersburg, MD, USA 20899 (e-mail: richard.candell@nist.gov).

M. Kashef is an associate researcher with Advanced Networking Division, Information Technology Laboratory, National Institute of Standards and Technology, Gaithersburg, MD, USA 20899 (e-mail: mohamed.hany@nist.gov).

B. Related Work

The use of industrial wireless networks has been studied in many works in the literature. However, no comprehensive survey of the whole problem space of industrial communications has been performed.

In [1], the authors have introduced a comparison between the commercial and industrial communications networks where an industrial network has been divided to five different levels. These levels include field equipment, controller level, application, supervisory, and external networks. The differences in requirements between different levels are discussed. Moreover, three types of information are considered which are control, diagnostic, and safety information as described in [2]. However all these levels of industrial networks are mentioned in [1], the article focuses only on the manufacturing and instrumentation communications and does not consider other types of communications networks that exist in industrial environments. Also, in [3], three levels of communications are considered which are device, control, and information levels. Moreover, the current wired industrial technologies for these levels are discussed briefly.

More works focused on the communications at the field devices level where sensing and control information is transfered. In [4], the communication between field devices has

Candell, Richard; Hany, Mohamed.
"Industrial Wireless: Problem Space, Success Considerations, Technologies, and Future Direction."
Paper presented at Resilience Week: International Symposium on Resilient Communications Systems,
Wilmington, DE. September 18, 2017 - September 22, 2017.

been studied where the requirements for a large number of nodes may not be achieved. The use of fieldbus solutions limit the scalability and resilience and hence industrial Ethernet capabilities are introduced in this article. Moreover, in [5], the communication for monitoring and control operations is discussed. A comparison between fieldbus technologies, industrial Ethernet, and wireless solutions is performed. The author has discussed the use of Wi-Fi, Bluetooth, ZigBee, and WirelessHART technologies in industrial applications. Similarly, the authors of [6] considered the industrial communications networks requirements in process automation specifically at field devices level. Finally, in [7], many case-studies are discussed for communication networks in industrial scenarios. Moreover, the design steps for these solutions are briefly discussed.

C. Paper Organization

The rest of the paper is organized as follows. The problem space for employing wireless networks is presented in Section II. Then, the technical considerations while designing industrial wireless networks are discussed briefly in Section III. In Section IV, a mapping between the problem space and the current technology space is provided. Finally in Section V, future directions and conclusions are presented.

II. Problem Space

A. Introduction and Success Considerations

Implementing a factory enhancement program requires economic and technical planning, and justification. Wireless technologies by themselves are interesting and can provide value; however, it is incumbent upon plant leadership to fully assess the potential risks and benefits of the enhancement before proceeding with deployment. Wireless technologies are often deployed as a means to monitor or control factory process. They have the potential to unlock improved observability and control. By understanding the problem space and the risks and benefits of potential wireless solutions, factory operators can assess if the rewards outweigh the risks. In navigating the risk/reward question, we assert that any wireless program must address one or more of the following success criteria before embarking on an enhancement involving wireless communications.

a) Reliability: Wireless systems can be deployed to add redundancy or replace faulty wired solutions with a more reliable wireless solution for particularly harsh industrial environments where temperature, pressure, vibration, radiation, and chemistry may make wired communication unreliable.

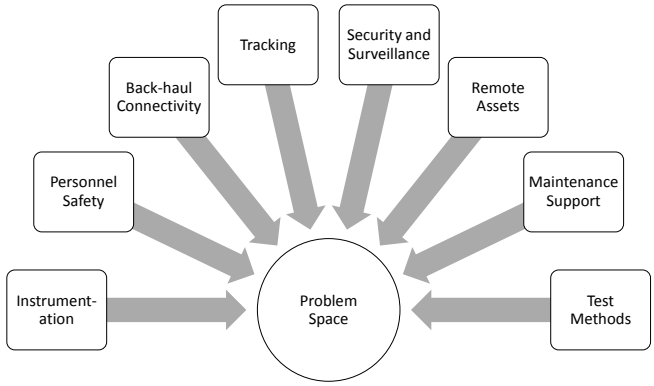

Fig. 1. Industrial wireless technologies are applicable across most aspects of an industrial operation.

b) Safety: Wireless systems may be used to detect or prevent injury to humans. They may be used as backup to wired systems or serve as the primary communication system.

c) Production Cost: Wireless systems can increase observability and the resulting data may be used for precise optimization of the factory operations, machine scheduling, and maintenance.

d) Quality: Various measurements are possible to improve quality of the factory output. Using wireless solutions may make deployment of sensors and inspection equipment more practical.

e) Environment: Wireless sensors and control mechanisms may be used to detect toxic conditions and prevent environmental accidents from occurring. Wireless actuation devices may serve to improve reliability and address environmental mitigation control.

f) Regulations: In some scenarios, government regulations may require specific sensor instrumentation to be deployed for certain scenarios. Wireless solutions could make regulatory compliance practical or cost effective in some cases.

B. Use Cases

Once a plant upgrade enhancement program is initiated, and some type of wireless technology is anticipated, the first step in realizing the program is defining and understanding the problem space where wireless technologies will be used. To support this assessment, we provide a taxonomy of industrial use cases to which wireless communication may be employed. The industrial wireless landscape is diverse, and a classification of those technologies can be helpful in mapping particular technologies to an application. Our classification is shown in Fig. 1 and includes instrumentation, safety, and backhaul connectivity, among others. Each class of the problem space is explained in the following subsections.

Candell, Richard; Hany, Mohamed.
"Industrial Wireless: Problem Space, Success Considerations, Technologies, and Future Direction."
Paper presented at Resilience Week: International Symposium on Resilient Communications Systems,
Wilmington, DE. September 18, 2017 - September 22, 2017.

1) Manufacturing Instrumentation: Manufacturing instrumentation includes devices commonly known as sensors and actuators. Sensors transmit measured variables from the physical process. Actuators receive manipulation variables from a controller and apply changes to the physical process. This class of application demands typically a very low latency and high reliability communication channel.

2) Personnel Safety: Industrial settings can be hazardous to both humans and machines. For humans, conditions may arise that pose a substantial risk for injury or death. For machines, conditions may develop that cause substantial damage requiring extensive repair or replacement. Prevention of industrial accidents is therefore of paramount importance within factories [8]. Slips, trips, and falls on the same level are commonly cited as lead causes of injury [9]. Falls from higher levels are of great concern to the aerospace industry [10] as inspection teams must work on elevated levels where falls prove fatal. Within the oil and gas industry, safety concerns include air toxicity and combustibility in both open and confined spaces where reliable monitoring and reporting save lives. Wireless gas leak detection and leak localization provide important and effective safety enhancements to such systems [11]. Within smart manufacturing systems where humans and robots work closely and even within traditional robot environments, safety systems provide an added layer of protection to prevent human injury [12], [13]. Within these human-robot environments, it is clear that reliable, low-latency communication is an important aspect of safety implementation, and, as mobility of robots within the factory increases, reliable low-latency wireless networks will become increasingly important to safety implementation.

3) Back-haul Connectivity: The back-haul is generally defined as the network that connects a lower level network to a higher level network [14]. Back-haul connectivity is usually characterized by large amounts of transfered data. In industrial environments, various types of back-haul scenarios are needed to be deployed for the operation of industrial communication networks. We can divide the back-haul problem space into three partitions which are i) nearby or indoor back-hauls, ii) distant back-hauls, and iii) geographically remote back-hauls. This categorization is based on the distance over which data is transfered.

First, the indoor back-haul networks are used in factory floors or process plants for data transfer between the control level networks to data centers, and higher level application layer networks. Second, the distant back-hauls are used for information transfer between various buildings in a plant where the two ends may have a line of sight (LOS) or need a non-LOS (NLOS) technology [15]. Finally, the geographically remote back-hauls are used for information transfer between sites in different cities or even countries such as data transfer to headquarters. Various technologies which are currently used for back-haul networks are discussed in [15].

4) Tracking: Tracking in industrial environments is employed to follow the states of inventory, personnel, and tools which help in process control and factory management [16]. The focus of this class of the problem space is the set of transmissions related to the tracking process itself and not the recovered data transmissions back to higher levels. We categorize the tracking wireless systems to the following divisions based on various requirements: i) materials tracking, ii) personnel tracking, iii) tools tracking, iv) inventory management, v) localization, and vi) identification.

Materials, personnel, and tools tracking is focused on following the state and the location of the tracked item. The selection of the used technology will depend on the tracked item characteristics including its speed, required accuracy level, and scalability [17]. Inventory management includes the decisions related to the change of inventory status over time. Identification and localization are required for the determination of the position and identity of a person or an item at a specific situation or time. It can be important in safety and security related applications.

The characteristics and applications of various tracking, localization, and identification technologies are discussed in [16]. These technologies include the use of specific wireless communications technologies like the global positioning system (GPS), and the radio-frequency identification (RFID) or deploying the general-purpose technologies like Wi-Fi, Bluetooth, and the cellular-based technologies. Moreover, examples of the existing products for assets tracking and their performance are compared in [17].

5) Security and Surveillance: Industrial installations require protection of the physical grounds, the operation, and the data produced from the installation. This protection requires surveillance of the property and implementation of network security controls. Guidance on selecting which controls are applicable to a specific risk level may be found in [18]. Assessment of the security robustness of specific wireless technologies is outside the scope of this paper; however, the implementation of physical security controls such as personnel authorization and grounds protection requires transmission of varying amounts of data. Transmission of such data includes voice traffic, video, and status information. In some installations, security and surveillance transmissions will coexist with factory instrumentation. This is sometimes the case with IEEE 802.11 mesh networks carrying voice, video, and

instrumentation traffic.

6) Remote Assets: Remote monitoring and control extend the range of the management to remote sites, especially in the process industry. Industrial remote communications provide access to widely distributed assets such as well head and pipeline monitoring [19]. The main goals of employing remote monitoring and control are minimizing labor cost, improved operations of remote sites, and prevention of unplanned failures [20].

The use of wireless networks in remote monitoring and control reduces the installation and maintenance cost significantly. However, the main challenge for industrial wireless remote monitoring and control is security and hence encryption and authentication protocols are deployed. Examples of remote assets communications are discussed in [19].

7) Maintenance Support: Factories require maintenance teams to keep machinery operating efficiently. Machines may be instrumented with sensors that measure machine health data such as vibration levels or current calibration values. Using this information, machines can be scheduled for maintenance prior to failure thereby allowing the factory to operate without unexpected interruption. Maintenance of the factory may also include automation of the building and infrastructure for climate control. Heating, ventilation, and air conditioning (HVAC) systems can be automated such that the ambient conditions are controlled. Augmented reality is an emerging technology that promises to bring knowledge to the factory floor allowing maintenance personnel to gain access to information during uncertain situations [21]. Augmented reality is a high-bandwidth application that requires high-reliability, high-throughput wireless connectivity within the factory.

8) Test Methods: Industrial control systems are often intolerant of communication faults and network latency, and often require very high transmission reliability [22]. Depending on the purpose of the wireless network (monitoring, supervisory control, feedback control, or safety monitoring), understanding the system performance of the network may be critical. For feedback control and safety monitoring systems, understanding the performance of the network from the perspective of the industrial controller or safety alarm system is essential. Factory operators, system integrators, and control systems designers are rarely experts in wireless communications systems. Considerations such as electromagnetic propagation, antenna efficiency, path loss exponents, packet error rates, and medium access are often foreign concepts to factory engineers. If factory engineers are expert in wireless theory and design practice, the information that they need to make educated decisions are usually unavailable. When available, link quality metrics such as packet loss ratios are informative but can be difficult to understand with complex mesh architectures and routing algorithms.

Moreover, it is generally difficult to measure these quantities for operational networks. The control system designer will only need to know the statistical distribution of latency and reliability of information through the network to design a controller that is robust. Therefore, practical methods for characterizing the performance of the wireless network that do not require an in-depth understanding of wireless communications or electromagnetic wave propagation are needed.

III. Technical Considerations

A. Radio Frequency (RF) Environment

Using wireless communications in industrial environments requires the knowledge of the RF environment characteristics and their behavior under the added wireless networks. The first step is obtaining and modeling field data in industrial environments. In [23], the RF environments of multiple examples of industrial scenarios were studied where models and characterization parameters have been derived. Moreover, theoretical models are proposed to model the RF channel such as the IEEE802.15.4a model including its channel impulse response [24]. In characterizing the RF environments, various parameters should be included, such as the multi-path, the interference sources, the mobility, and shadowing effects. Moreover, the operating frequency band can play an important role based on the required performance and the nature of RF activity in a certain environment.

B. Device Characteristics

Another important aspect while deploying wireless networks in industrial environments is the used devices characteristics. Typically, the harsh industrial environments in many applications require higher ratings of the used devices. The considered device characteristics include size, weight, power, cost, safety, and ingress protection (IP) ratings. Based on the application requirements and the physical environments, these device requirements are determined.

C. Network Characteristics

Table I lists requirements typically expected of a network based on its intended purpose and problem domain. Industrial networks will have three basic characteristics: reliability, latency, and scale. These characteristics are described in the following subsections. The numbers listed in the table are based on existing applications. It is difficult to provide a standard metric for all use cases as each will impose different requirements on the network. In some cases, the control algorithm can be designed to adapt to information loss and

Candell, Richard; Hany, Mohamed.
"Industrial Wireless: Problem Space, Success Considerations, Technologies, and Future Direction."
Paper presented at Resilience Week: International Symposium on Resilient Communications Systems,
Wilmington, DE. September 18, 2017 - September 22, 2017.

delay, thereby improving the performance of the physical system.

1) Latency: is a measure of the delay that information takes to arrive at its destination. We define latency, l, as the measured delay from the time of an event to the time in which knowledge of that event is made available to an application. Using the Open Systems Interconnection (OSI) model as a guide, latency would be measured at the application layer. In a packaging system, an example of measured latency would be the time between a proximity event and the time knowledge of that event is received by a programmable logic controller.

2) Reliability: is a measure of the likelihood of data loss within the industrial network. We define reliability, r, as the probability that a block of transmitted data is delayed long enough to become obsolete or lost due to noise. Similar to latency, we measure reliability at the application layer thereby ignoring technology-specific issues such as data segmentation and retries similar to the approach taken in the developing 5G cellular networks for machine-to-machine communications [25].

3) Scale: is a measure of the number of devices that may be deployed within a network without sacrificing reliability or latency. The network size will often dictate the maximum bandwidth allotted to any one node. The larger the network, the less bandwidth is alloted for transmissions between nodes. The complexity of a fully interconnect mesh will theoretically exhibit factorial growth in network interconnections. In practice, signal-to-noise ratios between nodes, programming within the governing network controller, and provisioned constraints will limit the number of interconnections. Most wireless sensor network specifications such as WirelessHART, ISA100.11a, and Zigbee provide support for large scale deployments; however, in such deployments, the network infrastructure must support the throughput load of the network and the scan rate requirements of the factory application [26]. The ISA100.11a standard provides support for distributed access points, prescribed routing, and a partitioned architecture to allow for large-scale deployments.

4) Interoperability: In a factory application, easy integration of devices is essential to the flow of data through a network. While many wireless standards exist, making physical layer integration of devices within the wireless domain easier, most industrial networks fail to address the application layer well. WirelessHART describes an application layer interface, while ISA100.11a provides the constructs for such an interface. ZigBee and Wi-Fi provide neither the interface nor the constructs for an application layer protocol. On the back-haul side of wireless networks which usually begins at a wireless gateway and ends at an automation server, many protocols such as Open Platform Communications (OPC) and Modbus make integration easier; however, again, they fail to specify the interface but instead provide the constructs. The authors assert that a standardization of the automation interface (gateway to automation server) is needed to provide such interoperability.

TABLE I
INDUSTRIAL CONTROL LATENCY, ERROR RATE, AND SCALABILITY CONSIDERATIONS FOR WIRELESS DEPLOYMENTS.

	Latency, l ms	Pr. Loss, r	Scale, s
Monitoring	$l < 1000$	$r < 10^{-5}$	$s < 10,000$
Supervisory Control			
Flow-based	$l < 1000$	$r < 10^{-6}$	$s < 30$
Job-based	$l < 100$	$r < 10^{-7}$	$s < 10$
Feedback Control			
Flow-based	$l < 1000$	$r < 10^{-6}$	$s < 100$
Job-based	$l < 10$	$r < 10^{-7}$	$s < 10$
Safety	$l < 10$	$r < 10^{-7}$	$s < 10$

5) Security: Prescribing security controls within an automation system requires understanding of the risk of not implementing these controls and the impacts of them on the physical process. Work is being undertaken to measure the impacts of cybersecurity controls on the physical process as explained in [27] and [28]. In addition, the work is being undertaken to assess the impacts of stealthy attacks as described in [29]. NIST Special Publication 800-82 and IEC-62443 provide best practice guidelines for the implementation of a cybersecurity program in an automation system.

IV. WIRELESS TECHNOLOGY APPLICABILITY

Many existing wireless technologies could be applied to the use cases in Section II. Others may be applicable with limitations, and others are not applicable entirely. Table II captures mapping of technologies to applicable use cases. This table represents assertions by the authors of applicability of wireless technologies to industrial control systems problem domains based on industry practice and original intent of the technology. The authors assert that the problem domains and wireless technologies included within this table represent the majority of problems found within industry and the existing technologies that may be applied. Technologies were evaluated based on original design intent, latency, reliability, energy, and practicality. Modifications may be made to the listed technologies resulting in applicability to a specified problem; however, possible modifications were not considered. Very low bit rate (VLBR) wide area networks (WAN) are assumed to have an infrastructure-based topology and support a bit rate of under 600bps.

Candell, Richard; Hany, Mohamed.
"Industrial Wireless: Problem Space, Success Considerations, Technologies, and Future Direction."
Paper presented at Resilience Week: International Symposium on Resilient Communications Systems,
Wilmington, DE. September 18, 2017 - September 22, 2017.

TABLE II
ASSERTED APPLICABILITY OF WIRELESS TECHNOLOGIES.

		Flow-based					Job-based						Safety				Back-haul				Tracking					Security							Remote			Maint.		
		Process Monitoring	Supervisory Control	Feedback Control	Alarm Conditions	In-situ Inspection	Factory Monitoring	Assembly: Sensing	Assembly: Actuation	Robots: Supervision	Robots: Feedback Control	Quality Inspection	Fall Prevention	Confined Spaces	Critical Event Detection	Human-Machine Colocation	Nearby or Indoor	Distant: LOS	Distant: BLOS	Geographically Remote	Indoor Machine Localization	Materials in Storage	Materials in Production	Tools	Personnel	Voice and Video Communication	Video Surveillience	Drone-based Surveillance	Grounds Control	Spectrum Monitoring Data	Personnel Authorization	Well-head Monitoring	Pipeline Monitoring	Tank Level Monitoring	Machine Health Monitoring	Building Automation	Augmented Reality
Home/Office	IEEE 802.11	●	●	◐	◐	-	●	◐	◐	◐	◐	◐	○	○	◐	○	●	●	●	-	◐	ϟ	ϟ	ϟ	ϟ	●	●	●	●	●	●	◐	○	◐	◐	●	●
	IEEE 802.15.1	○	○	○	○	○	○	◐	◐	◐	○	●	○	◐	○	○	○	○	○	○	○	○	ϟ	●	◐	▼	▼	▼	○	○	◐	○	○	○	◐	○	▼
Industrial	IEEE 802.15.4 TDMA	●	●	◐	◐	-	●	◷	◷	◷	◷	◐	◷	◐	◐	○	▼	▼	▼	▼	◐	ϟ	ϟ	ϟ	◐	▼	▼	▼	◐	▼	○	●	●	●	●	●	▼
	IEEE 802.15.4 CSMA	◐	◐	○	○	-	●	◷	◷	◷	◷	◐	◷	◐	◐	○	▼	▼	▼	▼	◐	ϟ	ϟ	ϟ	◐	▼	▼	▼	◐	○	○	◐	◐	◐	●	●	▼
	IEEE 802.11 TDMA	⚹	⚹	⚹	⚹	-	⚹	⚹	⚹	⚹	⚹	⚹	⚹	⚹	⚹	⚹	-	-	-	-	⚹	-	-	-	-	-	-	-	⚹	-	-	⚹	⚹	⚹	⚹	⚹	-
	VLBR WAN	●	●	○	◐	-	●	◷	◷	◷	◷	◷	◷	○	○	○	▼	▼	▼	▼	◐	◐	◐	◐	◐	▼	▼	▼	◷	○	○	○	○	○	◐	◐	○
Satellite	Geostationary	◐	◐	○	○	○	○	○	○	○	○	○	○	○	○	○	○	○	○	◐	○	○	○	○	○	◐	◐	○	◐	◐	◐	◐	◐	◐	○	○	◐
	Low-earth Orbit	◐	◐	○	○	○	○	○	○	○	○	○	○	○	○	○	○	○	◐	◐	○	○	○	○	○	◐	◐	◐	◐	◐	◐	◐	◐	◐	◐	○	◐
	VLBR WAN	◐	◐	○	◐	○	◷	◷	◷	◷	◷	◷	◷	○	○	○	▼	▼	▼	▼	○	○	○	○	◐	▼	▼	▼	◐	○	○	○	○	○	◐	○	▼
Tracking	RFID	-	-	-	-	-	-	-	-	-	-	-	-	-	-	-	-	-	-	-	○	●	●	●	●	-	-	-	-	-	-	-	-	-	-	-	-
Optical	Indoor Dispersive	⚹	⚹	⚹	⚹	○	⚹	⚹	⚹	⚹	⚹	⚹	⚹	⚹	⚹	⚹	⚹	○	○	○	⚹	ϟ	ϟ	ϟ	ϟ	⚹	⚹	○	○	⚹	○	○	○	○	⚹	○	○
	Free-space	◐	◐	◐	◐	○	○	○	○	○	○	○	○	○	○	○	●	●	●	○	◐	○	○	○	○	●	●	○	○	○	○	○	●	○	●	○	○	●
Cellular	Legacy	◐	◐	○	○	-	○	○	○	○	○	○	◷	◷	◷	◷	◐	◐	◐	◐	○	○	○	○	○	○	○	○	○	⚹	◐	◐	◐	◐	◐	▼	▼
	4G	◐	◐	○	◷	-	○	○	○	○	○	○	◷	◷	◷	◷	◐	◐	◐	◐	○	○	○	○	○	●	●	◐	●	●	●	◐	◐	◐	○	○	○
	5G	⚹	⚹	⚹	⚹	-	⚹	⚹	⚹	⚹	⚹	⚹	⚹	⚹	⚹	⚹	●	●	●	○	⚹	⚹	⚹	⚹	⚹	⚹	⚹	⚹	⚹	⚹	⚹	⚹	⚹	⚹	⚹	⚹	⚹
Land-mobile	All types	○	○	○	○	○	○	○	○	○	○	○	○	○	○	○	▼	▼	○	○	○	○	○	○	○	◐	○	○	●	○	◐	○	○	○	○	○	○
Specialty	Leaky Coax	◐	◐	-	◐	◐	◐	-	-	○	○	-	○	◐	◐	-	◐	○	○	○	◐	●	●	○	○	○	○	○	●	○	●	○	○	○	◐	◐	○

Legend: ●: Technology fully supports problem domain, ◐: Supports problem domain with practicality, throughput, latency, reliability, or energy limitations, ϟ: Energy requirements of assumed battery-powered devices prevent applicability, ◷: Latency prevent applicability, ▼: Throughput prevents applicability, ⚹: Emerging technology or evolution may support problem domain, ○: Not recommended, -: Not considered by authors.

V. CONCLUSIONS

This work represents a step toward employing wireless technologies in industrial environments where all classes of problems which wireless technologies can be used to solve have been comprehensively and collectively discussed. The success criteria and the technical aspects for employing wireless technologies in various scenarios have been considered briefly. More work is needed where success criteria are to be quantified and prioritized for various industrial scenarios. More detailed discussion is needed regarding technical considerations while employing wireless networking, including the physical environmental aspects such as the factory floor parameters, obstructions, data models, and interaction between various items within the factory floor. Finally, we have introduced a mapping between technologies and the discussed problem classes to highlight various industrial problems which can be solved or need more work while employing wireless technologies. Multiple comparisons between the current technologies exist in the literature. However, this work initiates consideration of the problem space where wireless technologies are employed. NIST has introduced this work while continuing to develop its capabilities as described in [28] to explore applicability of wireless technologies to specific industrial scenarios capable of replication within a laboratory space. An RF channel emulator is used to simulate the RF environment to include fading and multipath. A technical working group was created to directly address the needs of the wireless users employing wireless within their factories.

DISCLAIMER

Certain commercial equipment, instruments, or materials are identified in this paper in order to specify the experimental procedure adequately. Such identification is not intended to

Candell, Richard; Hany, Mohamed.
"Industrial Wireless: Problem Space, Success Considerations, Technologies, and Future Direction."
Paper presented at Resilience Week: International Symposium on Resilient Communications Systems,
Wilmington, DE. September 18, 2017 - September 22, 2017.

imply recommendation or endorsement by the National Institute of Standards and Technology, nor is it intended to imply that the materials or equipment identified are necessarily the best available for the purpose.

ACKNOWLEDGMENT

The authors would like to thank the participants of the 2017 IEEE Applications Systems Symposium Industrial Wireless Workshop for valuable inputs and discussions regarding the topics covered in this article.

REFERENCES

[1] B. Galloway and G. P. Hancke, "Introduction to industrial control networks," *IEEE Communications Surveys Tutorials*, vol. 15, no. 2, pp. 860–880, Second 2013.

[2] J. R. Moyne and D. M. Tilbury, "The emergence of industrial control networks for manufacturing control, diagnostics, and safety data," *Proceedings of the IEEE*, vol. 95, no. 1, pp. 29–47, January 2007.

[3] "What are industrial communication networks? an overview," http://www.electricaltechnology.org/2016/12/industrial-communication-networks-systems.html, accessed: 2017-04-20.

[4] P. Danielis, J. Skodzik, V. Altmann, E. B. Schweissguth, F. Golatowski, D. Timmermann, and J. Schacht, "Survey on real-time communication via ethernet in industrial automation environments," in *Proceedings of the 2014 IEEE Emerging Technology and Factory Automation (ETFA)*, Sept 2014, pp. 1–8.

[5] "Connectivity provides the lifeline of industrial control," http://electronicdesign.com/industrial/connectivity-provides-lifeline-industrial-control, accessed: 2017-04-20.

[6] W. Ikram and N. F. Thornhill, "Wireless communication in process automation: A survey of opportunities, requirements, concerns and challenges," in *UKACC International Conference on Control 2010*, Sept 2010, pp. 1–6.

[7] "Industrial communications professional services: Delivering high-performing communication network systems for industrial applications," https://www.gegridsolutions.com/Communications/Professional Services_GEA-12702B-E_160418_R001.pdf, accessed: 2017-04-20.

[8] D. Smith, B. Veitch, F. Khan, and R. Taylor, "Understanding industrial safety: Comparing fault tree, bayesian network, and {FRAM} approaches," *Journal of Loss Prevention in the Process Industries*, vol. 45, pp. 88 – 101, 2017. [Online]. Available: http://www.sciencedirect.com/science/article/pii/S0950423016304260

[9] W.-R. Chang, S. Leclercq, T. E. Lockhart, and R. Haslam, "State of science: occupational slips, trips and falls on the same level," *Ergonomics*, vol. 59, no. 7, pp. 861–883, 2016, pMID: 26903401. [Online]. Available: http://dx.doi.org/10.1080/00140139.2016.1157214

[10] R. Candell, "NIST-IR Report on Industrial Wireless Systems Workshop," 2017, to appear.

[11] F. Chraim, Y. B. Erol, and K. Pister, "Wireless gas leak detection and localization," *IEEE Transactions on Industrial Informatics*, vol. 12, no. 2, pp. 768–779, April 2016.

[12] A. Huber and A. Weiss, "Developing human-robot interaction for an industry 4.0 robot: How industry workers helped to improve remote-hri to physical-hri," in *Proceedings of the Companion of the 2017 ACM/IEEE International Conference on Human-Robot Interaction*, ser. HRI '17. New York, NY, USA: ACM, 2017, pp. 137–138. [Online]. Available: http://doi.acm.org/10.1145/3029798.3038346

[13] A. M. Zanchettin, N. M. Ceriani, P. Rocco, H. Ding, and B. Matthias, "Safety in human-robot collaborative manufacturing environments: Metrics and control," *IEEE Transactions on Automation Science and Engineering*, vol. 13, no. 2, pp. 882–893, April 2016.

[14] M. Jaber, M. A. Imran, R. Tafazolli, and A. Tukmanov, "5g backhaul challenges and emerging research directions: A survey," *IEEE Access*, vol. 4, pp. 1743–1766, 2016.

[15] "Wireless backhaul spectrum policy recommendations and analysis," http://www.gsma.com/spectrum/wp-content/uploads/2014/12/Wireless-Backhaul-Spectrum-Policy-Recommendations-and-Analysis-Report.-Nov14.pdf, accessed: 2017-04-20.

[16] A. Khudhair, S. Jabbar, M. Sulttan, and D. Wang, "Wireless indoor localization systems and techniques: Survey and comparative study," *Indonesian Journal of Electrical Engineering and Computer Science*, vol. 3, no. 2, pp. 392–409, August 2016.

[17] "Asset tracking and inventory systems market survey report," https://www.dhs.gov/sites/default/files/publications/Asset Tracking and Inventory Systems Market Survey Report December 2016.pdf, accessed: 2017-04-20.

[18] K. Stouffer, V. Pillitteri, S. Lightman, M. Abrams, and A. Hahn, "Guide to Industrial Control Systems (ICS) Security," National Institute of Standards and Technology, Gaithersburg, MD, Tech. Rep., jun 2015. [Online]. Available: http://nvlpubs.nist.gov/nistpubs/SpecialPublications/NIST.SP.800-82r2.pdf

[19] "Industrial remote communication: Efficient remote access to plants, machines and mobile applications," https://www.industry.usa.siemens.com/automation/us/en/industrial-communications/remote/Documents/E20001-A660-P820-X-7600_WS_Remote_Communication_web.pdf, accessed: 2017-04-20.

[20] G. Philbrook, "Remote monitoring technologies lower costs, improve operations," http://www.plantengineering.com/single-article/remote-monitoring-technologies-lower-costs-improve-operations/8242e6952a7fd3ded0e608602cef4f3d.html, accessed: 2017-04-20.

[21] V. Paelke, "Augmented reality in the smart factory: Supporting workers in an industry 4.0. environment," in *19th IEEE International Conference on Emerging Technologies and Factory Automation, ETFA 2014*, 2014.

[22] L. Zhang, H. Gao, and O. Kaynak, "Network-Induced Constraints in Networked Control Systems: A Survey," *IEEE Transactions on Industrial Informatics*, vol. 9, no. 1, pp. 403–416, 2013.

[23] R. Candell, C. Remley, J. Quimby, D. Novotny, A. Curtin, P. Papazian, G. Koepke, J. Diener, and M. Kashef, "Industrial wireless systems: Radio propagation measurements," National Institute of Standards and Technology, Gaithersburg, MD, Tech. Rep., 2017. [Online]. Available: http://nvlpubs.nist.gov/nistpubs/TechnicalNotes/NIST.TN.1951.pdf

[24] A. F. Molisch, "IEEE 802.15.4a channel model-final report IEEE P802 15.04," Tech. Rep., 2004.

[25] B. Holfeld, D. Wieruch, T. Wirth, L. Thiele, S. A. Ashraf, J. Huschke, I. Aktas, and J. Ansari, "Wireless communication for factory automation: an opportunity for lte and 5g systems," *IEEE Communications Magazine*, vol. 54, no. 6, pp. 36–43, June 2016.

[26] Q. Wang and J. Jiang, "Comparative examination on architecture and protocol of industrial wireless sensor network standards," *IEEE Communications Surveys Tutorials*, vol. 18, no. 3, pp. 2197–2219, thirdquarter 2016.

[27] R. Candell, T. Zimmerman, and K. Stouffer, "An industrial control system cybersecurity performance testbed," *National Institute of Standards and Technology. NISTIR*, vol. 8089, 2015.

[28] R. Candell and K. Lee, "Measuring the effect of wireless sensor network communications on industrial process performance," in *2015 ISA process control and safety symposium, Houston, TX*, 2015.

[29] D. I. Urbina, J. A. Giraldo, A. A. Cardenas, N. O. Tippenhauer, J. Valente, M. Faisal, J. Ruths, R. Candell, and H. Sandberg, "Limiting the impact of stealthy attacks on industrial control systems," in *Proceedings of the 2016 ACM SIGSAC Conference on Computer and Communications Security*. ACM, 2016, pp. 1092–1105.

Combinatorial Testing of Full Text Search in Web Applications

M S Raunak[1] D. Richard Kuhn[2] Raghu Kacker[2]
raunak@loyola.edu kuhn@nist.gov raghu.kacker@nist.gov
[1]Loyola University of Maryland [2]National Institute of Standards and Technology

Abstract: **Database driven web applications are some of the most widely developed systems today. In this paper, we demonstrate use of combinatorial testing for testing database supported web applications, especially where full-text search is provided or many combinations of search options are utilized. We develop test-case selection techniques, where test strings are synthesized using characters or string fragments that may lead to system failure. We have applied our approach to the National Vulnerability Database (NVD) application and have discovered a number of "corner-cases" that had not been identified previously. We also present simple heuristics for isolating the fault causing factors that can lead to such system failures. The test method and input model described in this paper have immediate application to other systems that provide complex full text search.**

I. INTRODUCTION

Web-based applications, especially ones driven by a back-end database, continue to be some of the most common custom software being developed in today's world. Many applications store their data in an SQL database or in a no-SQL data store at the back-end servers and query and update them to provide information searched by the users and other transaction-oriented service. The architecture of these applications is usually layered, utilizing many different, often loosely connected components. Testing these applications effectively remains a challenge for the software engineering community. High profile web application failures have resulted in cases where testing was insufficient [2][3]. A wide variety of general-purpose strategies and techniques for systematically testing applications are well established and widely practiced [1].

In this paper we focus on a highly specific test procedure for full-text search in the National Vulnerability Database (NVD), a large, heavily used public internet database. Text search is one of the fundamental components of web applications used in every industry. Thus, strong testing of this component is essential for high assurance, but it is often handled as simply one aspect of overall system testing. The test procedure documented in this paper seeks to provide stronger testing for this fundamental component.

After implementing a new feature in the NVD, developers discovered that certain special characters resulted in "Server Error" responses. However it was not clear which specific combinations of special characters triggered this response, or how many such problematic cases existed. Some of these were corrected, but it was decided to apply combinatorial methods to attempt to identify all inputs that caused the server error response.

Decision makers in industry and government rely on testing to determine readiness of systems for deployment, so defensible measures of test completeness are essential. Testing any reasonable application exhaustively is nearly always impractical. The two crucial questions testing researchers aim to study are how to select the test cases, and how many to select; i.e., when to stop testing. These questions become especially challenging for integration and system testing of any large application. The goal is to select test cases at the integration and system testing level such that the fault finding probability is maximized. One can try to achieve this goal by systematically covering a large section of the input space including many corner cases or unexpected values that may potentially cause failures.

Combinatorial Testing [4] has been shown to be an effective approach. In this paper, we demonstrate use of combinatorial approaches to develop test cases that systematically test important components of database-backed web applications. Our case study reveals that such systematic exploration of input space using covering arrays can be a very useful way of identifying failure scenarios that are otherwise not discovered.

Web applications are typically developed in a multi-tiered fashion. Fig. 1 shows a high level generic architecture of most of these applications. The outermost layer is the presentation layer, which provides the interface for client interaction. Application developers use HTML, CSS, and client side scripting languages to make the user interface intuitive and useful. The Middle layer is often served by an Application Server framework such as JBoss, WebSphere or Netweaver. These application servers are often built around common web servers such as Apache and IIS. Programmers develop their business logic and run their programs on these Application Server environments. At the innermost layer sits a DBMS such as mySQL, MS SQL, Oracle, DB2 etc. The application servers provide support for interacting with the DBMS through standard protocols like Java Database Connectivity (JDBC), Common Object Request Broker Architecture (CORBA) etc.

While developing a web application, there are programming modules that are developed at each level. Programmers often write stored procedures, which are

Feng, Shaw; Kibira, Deogratias.
"Environmental KPI Selection Using Criteria Value and Demonstration."
Paper presented at APMS 2017 International Conference Advances in Production Management Systems (APMS 2017),
Hamburg, Germany. September 3, 2017 - September 7, 2017.

groups of SQL statements stored and executed in the RDBMS, i.e., at the innermost layer, to reduce server-client

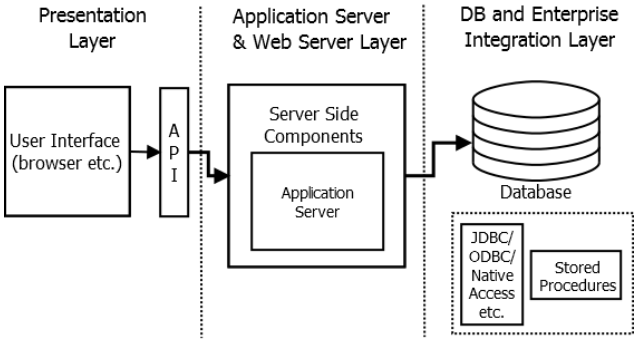

Fig. 1. A Typical Multi-Layered Web Application

network traffic, and to make the system more secure by hiding many of database-level details. The middle layer, where most of the business logic is implemented, often includes integration of other already developed modules or service calls to independent web services. Similarly, for receiving and reacting to user interaction and presenting the output of the application to the client, program modules are developed and deployed to interact with the middle layer directly. All these component interactions, both at the same layer and across layers, require systematic and thorough testing. Programmers and managers are usually good at making sure that unit tests are developed and run regularly while different programming units are being developed. However, testing unit interactions during integration, and testing the overall system systematically once it has been developed, often receive relatively little attention. Anecdotal evidence suggests that the primary reason for this relative lack of integration and system testing is often deadline pressure and not allowing enough time for testing during project estimation and planning phase. A second factor that makes this scenario more challenging is the fact that a systematic process of testing these types of application is not yet well established. A third challenge comes from the often dynamic nature of the underlying data, which makes it more difficult to develop test oracles to support test cases that can be automated.

In this study, we explore a systematic way of testing certain system level testing of database backed web applications and report the effectiveness of our approach.

II. Related Work

Because of their practical importance, database applications have been the subject of a variety of investigations of combinatorial test methods. In particular, combinatorial testing is especially appropriate because database systems must parse and interpret complex queries structured as regular expressions or predicates [15]. In addition to the complexity of the inputs, database applications are also characterized by the need to test both the database functions and the database system interaction with the application that accesses the database [20]. The test problem is further complicated by dependence on the initial database state, which may influence structural coverage metrics, i.e., the degree to which the code can be exercised [8] The complexity of database queries has led to the need for specialized coverage metrics that include the evaluation of conditions in search predicates [7].

Some research has shown that the distribution of *t*-way faults in MySQL database applications is similar to many other application domains, following the interaction rule that most faults are caused by a single factor or two factors interacting, with progressively fewer by 3-way or higher strength interactions [19]. The empirical data showed that a significant proportion of SQL faults involved 3-way or higher strength interactions, suggesting the need for combinatorial methods. Pairwise testing was shown to be effective [15] for discovering many bugs not detected by conventional test methods. It was shown that CT detected a wide range of previously undiscovered faults in a web based database using 2-way through 4-way testing [16]. These methods were also shown to be effective for testing security of database applications [17][18].

Also relevant to our work are investigations comparing the effectiveness of covering arrays with random test generation. This question has been studied in a variety of contexts. In many cases the comparison between combinatorial and random methods has considered only pairwise test arrays, with an equal number of randomly generated tests. Schroeder et al.[22] compared randomly generated tests with *t*-way arrays for $t = 2, 3, 4$. Covering arrays were generated using a tool called TVG, and applications tested had input model configurations of $2^{16}5^{1}8^{1}$ and $2^{7}3^{10}4^{2}$. Because the covering arrays were large, random test sets of the same size covered 95% to 99.99% of the *t*-way combinations, and there was no significant difference between *t*-way testing and random testing. This example illustrates the point that coverage of combinations is a key consideration, whether this is achieved by covering arrays or other test generation methods. Another study [23] found than manually constructed tests could be more effective than 2-way test arrays, but at higher strengths there was no difference, and results from randomly generated tests were not consistent. A number of studies have consistently found covering arrays to be more effective than random tests, including [24][25][26], which investigated the testing of logical expressions.

Others showing significantly better results for *t*-way testing include [27][28][29]. Two key considerations must be evaluated in comparing the two approaches to testing: combinatorial coverage of test sets, and input model design. It is easy to show that a large enough randomly generated

test set will cover a high proportion of *t*-way combinations, so the comparison between covering arrays and random test generation is largely a question of efficiency, at least at lower interaction strengths. For *t*-way testing of 4-way and above, a random test set covering the same proportion of combinations may be prohibitively large. The importance of the input model can be seen in research that demonstrates significant differences in structural coverage and fault-detection effectiveness as the input model is changed. Examples include [30], where branch coverage was increased from roughly 70% to 100% only through input model changes, and [31], which demonstrated improved fault detection results for both covering arrays and random tests depending on the input model used.

III. Approach

Our approach is to search for failure scenarios through systematic coverage of the input space and user interactions at the system testing level. For database backed web applications, especially the ones that primarily render some subset of data for information purposes, one of the major components is some sort of query functionality. Users are provided an interface to query the underlying information in many different ways. Consider the case of searching the catalogs of any library or the flight search in a travel application on the web. An important testing aspect in these scenarios is to verify that the search functionality behaves as expected under all circumstances.

In addition to testing for expected functional behavior, any application, especially the ones available over the web, also needs to be tested for potential failure scenarios against unexpected input. If there are unintentionally mistyped or maliciously created inputs that can cause system failure or unexpected behavior, then it also becomes a security issue, which demands attention. Developers and testers often test only the most common expected interaction from users, which is also commonly known as `Happy Path Testing'. This testing practice leaves out the necessary aspect of searching for system failures under unexpected user inputs or interactions.

We use a combinatorial approach and come up with covering array of a wide range of input combinations. We utilize these covering arrays to create test cases. For this particular study, we focus on primarily two types of test-scenarios: a) user inputted strings that may cause failures, and b) user selected options in a web form.

IV. Case Study

To apply our approach of developing effective test cases using combinatorial coverage for systematically testing database-backed web application, we selected the National Vulnerability Database or NVD [12] project. NVD is a project under the Computer Security Division of the National Institute of Standards and Technology (NIST). It maintains a repository of publicly known hardware and software vulnerabilities in a standardized fashion. Every vulnerability is uniquely identified by a CVE-ID (Common Vulnerability and Exposure Id), which is primarily assigned by the MITRE corporation and, to a limited degree, by some other CVE Numbering Authorities (CNAs) [13]. Once a reported vulnerability has been assigned a CVE-ID, it finds its way to the NVD group at NIST. Here the submitted CVE is thoroughly analyzed for standardization and is placed under one or more CWE (Common Weakness Enumeration) categories. Additionally, NVD analysts checks all the references, standardizes different aspects of the vulnerability description, and assign a severity score to the vulnerability following Common Vulnerability Scoring System or CVSS [14]. Once a new vulnerability has been standardized, categorized, and reference-checked, they are made available for public use through the NVD web site. This NVD data provides support for many valuable services such as enabling automation of vulnerability management, security measurement, and compliance (e.g. FISMA).

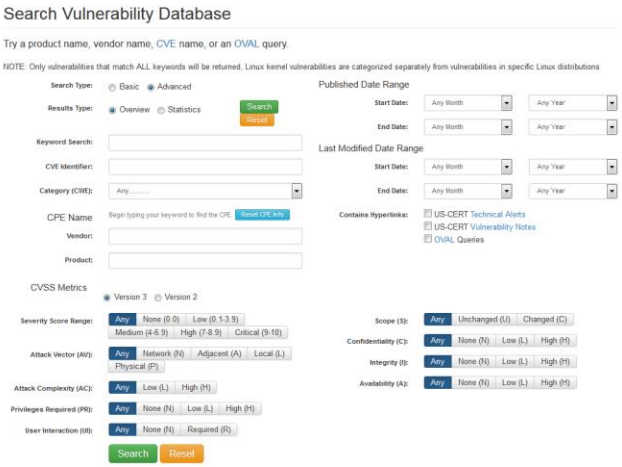

Fig. 2. Advanced Search Option of NVD Data

The NVD website provides a user interface for looking up information about all the CVEs and their corresponding information stored in its data set. In the base search form, there is only an option to perform keyword search. The NVD application looks for whatever the user has inputted in its database and shows results for entries with the search string in them. NVD also provides an advanced search option. In this web form, it allows users to search for any keyword, CWE category, CVE-Id as well as a large number of different options such as date-range (month and year) and CVSS scores. Fig. 2 shows an image of the web form for the advanced search page. In both the basic and advanced search options, there is an option for keyword search in this search function. The user can type in search phrases like “buffer overflow”, “X 509”, “Android”, or “2.3”, to look up vulnerabilities that match these keywords. In the advanced search page, a user can choose a CWE category from a

drop-down list and search for all the CVEs that have been categorized under that CWE. There are also a number of fine grained search options related to the different fields of a CVSS 2.0 or 3.0. When the user chooses these additional search criteria, the search functionality queries its database and returns the number of CVEs that met the criteria. If there are hits, the CVEs are listed as shown in Fig. 3.

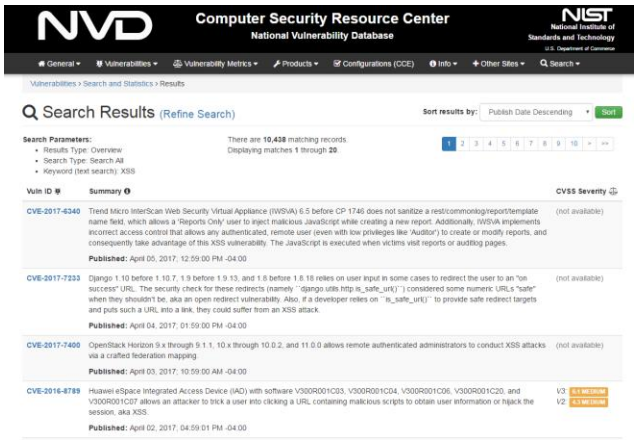

Fig. 3. Search Result Page of NVD

A. Combinatorial Input Model for Search Strings

One of our objectives for this study has been to systematically discover if there are search strings that may result in unexpected behavior from the NVD system. For any web application, coming up with an effective set of search strings to test the search functionality (e.g., keywords search) of the system is one of the common challenges for any test designer.

Instead of focusing only on likely keywords that users may use in a search, we approached the problem with a goal of creating keywords that are a combination of expected inputs such as simple strings and potentially unexpected symbols. Our hypothesis is that how the system responds to such rarely used search strings may not have thoroughly been tested for many web applications.

Parameter Name	Parameter Type	Parameter Value
First	Enum	[(,{,[,quote,sp,NUL,~,!,`,2]
Second	Enum	[sp,string,NUL,.]
Third	Enum	[and,or,amp,pipe,sp,NUL,-,/,backslash,3]
Fourth	Enum	[sp,string,NUL,.]
Fifth	Enum	),},],quote,sp,NUL,~,%,',4]

Fig. 4. Input Model for Generating Test Search Strings

We have taken the combinatorial approach to synthesize the search strings. Fig. 4 shows the five parameters, whose values are combined to create the test strings. Each parameter is comprised of a set of strings or special characters. There are 10, 4, 10, 4, and 10 enumerated values in the respective five parameters. All possible combinations of these values create 16,000 possible test strings. In addition to the generic term "string" to represent any string, there are two special strings: "and" and "or". The term "sp" represents space and "NUL" represents an empty string. The use of "NUL" allows us to synthesize strings that can have different special characters at different positions of the synthesized strings including at the beginning and at the end of the strings. Other special characters include different types of left (*(,{,[*) and right (*),},]*) brackets, single (`, ') and double (") quotes, dot (.), ampersand (&), pipe (|), exclamation sign (*!*), hyphen (-), percent sign (*%*), slash (*/*), backslash (\), and tilde (~). These special characters are not chosen completely randomly. Since NVD allows searching for any string in CVE descriptions and other associated information within the vulnerability database (full-text search), it is conceivable that some users may construct search strings with special characters that they are looking for within the descriptions.

B. Test Set Generation

Using the input model described above, 2-way, 3-way, and 4-way covering arrays were constructed using the ACTS tool. Test set sizes and failures are shown in Table I.

TABLE I. *t*-WAY TESTS AND RESULTS, *t*=2,3,4

t	Number of tests	Number of failed tests	% of failures
2	100	12	12.0
3	999	129	12.9
4	3125	473	15.1

TABLE II. RANDOM TESTS AND RESULTS

Test set	Number of Tests	Number of failed tests	% of failures
random 1	100	13	13.0
random 2	100	17	17 .0
random 3	100	13	13 .0
random 4	100	12	12 .0
random 5	100	7	07 .0
random 6	100	7	07 .0
random 7	100	7	07 .0
random 8	100	11	11 .0
random 9	100	12	12 .0
random 10	100	12	12.0

Because random or "fuzz" testing is often used in database testing, we generated random test sets of the same size as each of the *t*-way test sets, with results as shown in Table II for $t = 2$. Tests were generated by randomly selecting a value from each of the five factors detailed above. Results varied significantly and in three cases of the 10 runs, more failures were found in the random tests than with 2-way covering arrays. This occurred because with random generation, multiple occurrences of a fault-triggering combination would appear in some test sets more than others. Following the test runs, we used the fault location tool described in [34] to locate combinations that occurred

in failing tests that were not also in passing tests, as described in the next section.

V. Results and Discussions

The NVD is a heavily used database, averaging approximately 7.3 million accesses per month. It was tested extensively in development, and has been in continuous use, in some form, since 1998. Its usage profile is not unlike many other large, widely used information systems. While faults have been discovered occasionally, the system continues to perform adequately for the users who rely on it. Whenever faults have been found, they have been repaired quickly and have not disrupted service. The NVD group implemented a new version of full-text search in Spring 2016 and became aware of some new issues. They fixed some of the problems with special characters. Faced with the classic SE constraints of inadequate time and resources as well as tools and techniques to easily identify all failure scenarios with the new implementation, they approached us for a systematic and thorough testing of their search functionality.

The faults identified in this paper show that even long-term operation does not guarantee eventual discovery of *all* failures. Moreover, any new feature implementation may cause a number of new failures, which is unlikely to be discovered by a traditionally designed test suite. The failure-triggering combinations found in this study are clearly "corner cases", very unusual combinations of character strings that are unlikely to occur in practical use. From a $4^2 10^3$ input configuration, we identified 49 input string combinations that result in non-timeout related failures, or roughly 0.3% of the 16,000 possible combinations in the input space as modeled. It is notable that all of these are 2-way combinations containing at least one special character.

Fault-triggering combinations can be determined using simple heuristics described in [34]. More sophisticated methods exist for fault location, e.g. [32][33], but the simple heuristics below are quick and easy to apply for this test problem. For a deterministic system, in which a given set of input values always produces the same result independent of the order of variable values, let P = {combinations in passing tests} and F = {combinations in failing tests}. The following rules were applied:

- *Elimination*: For a deterministic system, $F \setminus P$ must contain the fault-triggering combinations because if any of those in were in P, then the test would have failed.
- *Interaction level lower bound*: If all t-way tests pass, then clearly a t-way or lower strength combination did not cause the failure.
- *Interaction continuity*: For each level of t, we compute $S_t = F_t \setminus P_t$, the suspicious t-way combinations that may have triggered a failure. Because t-way tests cover all combinations of t-way or lower strength, a combination that triggered the failure in F_t must also occur in F_{t+1}, F_{t+2}, etc. So we remove any combination in S_t from S_k for any $k > t$.

Initially, $F \setminus P$, combinations in failed tests not also in passed tests, were as shown in Table III. These sets were reduced by testing each individually, resulting in 49 2-way combinations, 144 3-way combinations, and 373 4-way combinations that all triggered failures. However, a lower strength combination that triggers a failure would also produce a failure if it is contained in any higher strength combination. For example, if the 2-way combination &% triggers a failure, it will also do so in a 3-way combination &%{. Therefore, suspect 3-way combinations were removed from the 4-way suspect set and suspect 2-way combinations were removed from the 3-way and 4-way sets. As shown in Table 1, it was then possible to conclude that only 2-way combinations were responsible for all failures discovered. The complete set of failure-triggering combinations is shown in Table IV.

Table III. Interaction identification

	2-way	3-way	4-way
Initial	49	144	373
removing (t-1)-way		0	124
removing (t-2)-way			0

It is important to note that if the test goal is strong assurance that all faults have been discovered, then 3-way and 4-way testing are necessary, even though they do not discover any additional failing combinations. Without running these stronger interaction tests, we would not have been able to conclude that the 2-way combinations likely represented the complete set of faults for this input model. Any reasonable testing scheme will require that we continue testing as long as errors are being discovered. High strength covering arrays provide a stopping criterion. If no new failures are discovered after increasing t-way coverage to (t+2)-way, it is unlikely that any new faults will be found.

Table IV. Failure triggering combinations

&%	.~	or~	|4	~3
&'	/~	str&	|str	~4
&.	2&	str|	|}	~\
&4	2|	str~	|~	~and
&str	2~	{&	~%	~or
&}	3~	{|	~&	~str
&~	\~	{~	~'	~|
-~	`&	|%	~-	~}
.&	`|	|'	~.	~~
.|	`~	|.	~/	

Text searches are among the most common tasks in information systems. Although the test procedure described in this paper addresses only this narrow problem, it is designed to be usable across the broad range of systems that require text search.

Covering arrays vs. random tests: Because *fuzz testing* is commonly used in many test situations, we compared the combinations covered by *t*-way arrays with coverage for an equal number of randomly generated tests. Fig. 5 shows a representative example for a random test set of the same size as a 3-way test set developed for the input model described in Sect. IV. The area under a curve represents the total combination coverage [35] for a given level of *t*, and the right-hand Y intercept represents the minimal coverage. For example, if variables are binary and there are one or more 2-way combinations where only 00 and 10 are covered (out of 00, 01, 10, 11), then the minimal coverage is 50%. The example test set in Fig. 5 shows approximately 95% 2-way, 84% 3-way, and 42% 4-way coverage. All 2-way combinations have at least 90% of settings covered, 3-way at least 65%, and 4-way at least 30% coverage.

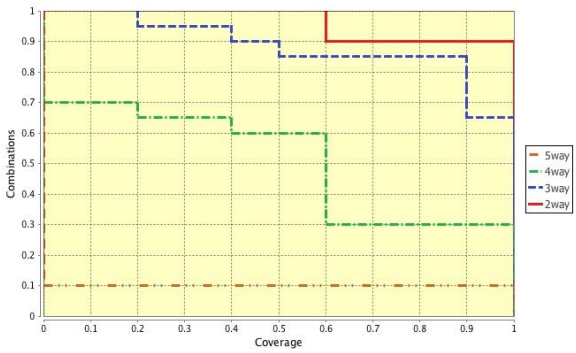

Fig. 5. Combinatorial coverage of random tests

Now consider what these coverage levels mean for assurance. With roughly 95% of 2-way combinations covered, we could expect to detect 46 or 47 of the 49 faults. So the fault detection capability of random tests, in this case, compares relatively well with covering arrays - *if we are not seeking high assurance*. Random testing falls short in two aspects for high assurance: 1) inadequate combination coverage for fault detection; and 2) inadequate coverage for a stopping criterion. For safety or mission-critical systems, finding only 95% of faults is unacceptable. Moreover, we would have no way of estimating the degree to which faults have been discovered without extending testing until the relevant input space has been covered.

Fuzz testing or other random test generation can be an efficient and appropriate means of fault discovery, but sound engineering requires a defensible method for measuring test thoroughness. Structural coverage metrics provide one set of reasonable measures - full branch or condition coverage indicates a degree to which executable code has been exercised. Measuring combinatorial coverage of tests can provide a complementary measure to structural coverage, because it shows what proportion of the input space has been included in tests. Any combination not covered by the test set is to some degree unknown territory - even with full structural coverage we do not know what the code will do with a particular combination of inputs. Similarly, extended use of a system does not guarantee that some inputs will not produce a failure, as shown by the NVD testing described in this paper. Using covering arrays makes it easy to check system response to rare inputs, to a degree that is unlikely and difficult to achieve with conventional test methods or through continuous use for many years.

VI. Future Work

Database-backed web applications usually also allow users to select advanced search options to select a subset of entries from the database that match multiple criteria. Our case study, NVD, is no exception. There is an advanced search option users can choose to narrow down their search results using many different criteria. Fig. 2. Shows an image of the NVD advanced search page. In addition to providing support for the keyword search, users can search for a specific CVE-Identifier such as CVE-2016-1234. There is option to select for a particular CWE category (e.g., CWE-94: Code Injection). Users can also choose a specific vendor or product to search for vulnerabilities associated with that vendor or product. There are two sets of date-ranges: published-date and last-modified-date that users can use to narrow their search. Additionally, there is a way to select options for different factors that define the CVSS scores of the known vulnerabilities stored in the database.

Like the keywords search, *CVE-Identifier*, *vendor*, and *product* search option allows the use of any string in the search fields. The other options are drop-down lists that users will have to choose an option from. There are 106 different CWE categories to select from in the NVD advanced search page. Similarly for CVSS version 2, users can choose from multiple options for *Severity Score Range* (SSR) of *Any*, *Low* (0-3), *Medium* (4-6), *High and Medium (4-10), and High (7-10)*. For *Attack Vector* of CVSS 2, there are options of *Any*, *Network* (N), *Adjacent* (A), and *Local* (L). There are other options available for selection for each of the other components of CVSS, which is comprised of *Access Complexity* (AC), *Authentication* (Au), *Confidentiality* (C), *Integrity* (I) and *Availability* (A). Even if we leave out the free-string search options for keywords, CVE Identifier, vendor, and product names, there are 1.45×10^{16} combinations of values for exhaustively testing the advanced search page of NVD application.

Since our goal is to look for search values and options that may lead to unexpected behavior or system failure, we

designed another input model with a selected subset of the parameter values for each of the search options. Fig. 6 shows the model we used to synthesize search strings to query the NVD database. In addition to utilizing the expected values for each of the advanced search options, we added an unexpected value such as "off" or "X".

Parameter Name	Parameter Type	Parameter Value
results_type	Enum	[overview,statistics,off]
cwe_id	Enum	[CWE-20,CWE-119,CWE-89,CWE-off]
pub_date_start_month	Enum	[-1,0,5,off]
pub_date_start_year	Enum	[1990,2000,2004,off]
publish_date_end_month	Enum	[6,11,12,off]
pub_date_end_year	Enum	[2007,2016,2020,off]
cvss_version2_severity	Enum	[LOW,MEDIUM,HIGH,OFF]
AV	Enum	[N,A,L,X]
AC	Enum	[L,M,H,X]
Au	Enum	[N,S,M,X]
C	Enum	[N,P,C,X]
I	Enum	[N,P,C,X]
A	Enum	[N,P,C,X]

Fig. 6. Input Model for Advanced Search Options

NVD allows direct querying of their database through the construction of search URLs. The designers left this option open for allowing programmatic search of different aspects of the information stored in the database. We utilized this feature to synthesize web search URLs combining parameter values shown in Fig. 6 and tested the NVD search engine responses. In our preliminary results, a large fraction of test cases resulted in a "Server Error" response. For example, 30 out of 33 test cases from 2-way and 767 out of 820 test cases from 4-way covering array produced an error response. The NVD developers indicate that these server errors are not necessarily bugs; rather a non-descriptive response to the end-user while processing invalid input.

It does appear that most of the unexpected parameter values result in server error response. However, not all unexpected values resulted in the error response. For example, a "-1" for *starting month* parameter results in a regular response from the application. Clearly there are some anomalies in how unexpected or invalid inputs are treated by the application. As future work, we plan to more deeply investigate the resiliency of NVD system against unexpected parameter values for advanced search options. We also plan to research the coverage we can gain from applying combinatorial testing approach over the 'Advanced Search's parameter input space. It would be interesting and useful to determine the combination factors that can cause 'Advanced Search' to fail. Initial test results have already revealed that certain valid CWE-category search can also cause failures while combined with other valid parameter values, which is something the application developers did not anticipate.

VII. Conclusions

We investigated the application of combinatorial testing to string text searches in the US National Vulnerability Database, a system that is accessed more than 70 million times a year. The current software build is operational 24 hours a day. Our testing and analysis revealed 49 inputs that produced server errors in the current build. These inputs were 2-way combinations of special characters and strings, and test cases built from 2-way through 4-way covering arrays demonstrated that no other combinations beyond these 49 resulted in the server error response. This result demonstrates the effectiveness of combinatorial methods for detecting and determining the full extent of rare faults.

The test procedure described in this paper addresses a specific test problem. It can be applied with little or no change to many systems that incorporate text searches. Text search is an essential component in systems within nearly all industries, and some are safety or mission-critical. Applying test methods such as those described in this paper can help to remove rare faults that could result in significant failures in operation.

Equally important, the methods described here provide a defensible criterion for test completion. Because covering arrays include all *t*-way factor combinations, we can show that the entire input space has been covered up to whatever *t*-way combinations are used. In contrast, "fuzz testing" or other conventional methods do not include measures of the input space that has been tested, and often rely on a "more is better" heuristic without an ability to measure completeness. Using covering arrays, or measuring combinatorial coverage of random tests, provides a sound test engineering method with defensible, quantitative measures of test completeness.

Acknowledgements

The authors would like to thank the NIST NVD group at for their assistance with this work. This study was supported by NIST ITL Grant 70NANB17H035.

Disclaimer: *Products may be identified in this document, but identification does not imply recommendation or endorsement by NIST, nor that the products identified are necessarily the best available for the purpose*

References

[1] H. Zhu, P. A. V. Hall, and J. H. R. May, "Software unit test coverage and adequacy," ACM Computing Surveys, vol. 29, no. 4, pp. 366–427, 1997.

[2] M. Heusser, "6 software development lessons from healthcare.gov's failed launch," CIO, November 2013.

[3] D. Doherty, "Team obama never finished testing healthcare.gov before launching it," CBS News, November 2013.

[4] R. Kuhn, R. Kacker, Y. Lei, and J. Hunter, "Combinatorial software testing," Computer, vol. 42, no. 8, pp. 94–96, Aug 2009.

[5] L. S. Ghandehari, J. Czerwonka, Y. Lei, S. Shafiee, R. Kacker, and R. Kuhn, "An empirical comparison of combinatorial and random testing," 2014 IEEE Seventh

Intl Conf on Software Testing, Verification and Validation Workshops, March 2014, pp. 68–77.

[6] K. Haller, "The test data challenge for database-driven applications," Third Intl Workshop on Testing Database Systems, ACM, 2010, pp. 6:1– 6:6.

[7] M. J. Su´arez-Cabal and J. Tuya, "Using an sql coverage measurement for testing database applica-tions," SIGSOFT Softw. Eng. Notes, vol. 29, no. 6, pp. 253–262,2004.http://doi.acm.org/10.1145/1041685.1029929

[8] M. Emmi, R. Majumdar, and K. Sen, "Dynamic test input generation for database applications," in Proceedings of the 2007 Intl Symp on Software Testing and Analysis, ser. ISSTA '07. New York, NY, USA: ACM, 2007, pp. 151–162.

[9] K. Taneja, Y. Zhang, and T. Xie, "Moda: Automated test generation for database applications via mock objects," IEEE/ACM Intl Conf on Automated Software Eng., New York, NY, USA: ACM, 2010, pp. 289–292.

[10] A. Bertolino, "Software testing research: Achievements, challenges, dreams," in Proc. of ICSE Future of Software Engineering (FOSE), 2007, pp. 85–103.

[11] D. Willmor and S. M. Embury, "An intensional approach to the specification of test cases for database applications," 28th Intl Conf on Software Engineering, New York, NY, USA: ACM, 2006, pp. 102–111

[12] NIST. (2007) National vulnerability database (nvd). [Online]. Available: https://nvd.nist.gov/

[13] MITRE/CVE. (2003) https://cve.mitre.org

[14] NIST/ CVSS. (2012) https://nvd.nist.gov/cvss.cfm

[15] Tsumura, K., et al., April. Pairwise coverage-based testing with selected elements in a query for database applications. *Software Testing, Verification and Validation Workshops (ICSTW), 2016 IEEE Ninth Intl Conf on* (pp. 92-101). IEEE.

[16] Bozic, J., Simos, D.E. and Wotawa, F., 2014, May. Attack pattern-based combinatorial testing. *9th Intl Wrkshp on Automation of Software Test* (pp. 1-7). ACM.

[17] Garn, B., Kapsalis, I., Simos, D.E. and Winkler, S., On the applicability of combinatorial testing to web application security testing: a case study. *2014 Workshp Joining AcadeMiA and Industry Contributions to Test Automation and Model-Based Testing* (pp. 16-21).

[18] Bozic, J., Garn, B., Simos, D.E. and Wotawa, F., April. Evaluation of the IPO-family algorithms for test case generation in web security testing. In *Software Testing, Verification and Validation Workshops (ICSTW), 2015 IEEE Eighth Intl Conf on* (pp. 1-10). IEEE.

[19] Ratliff, Z.B., Kuhn, D.R., Kacker, R.N., Lei, Y. and Trivedi, K.S., The Relationship between Software Bug Type and Number of Factors Involved in Failures. In *Software Reliability Engineering Workshops (ISSREW), 2016 IEEE Intl Symp on* (pp. 119-124). IEEE.

[20] K. Haller, "The test data challenge for database-driven applications," Third Intl Workshop on Testing DatabaseSystems, ser. DBTest '10. New York, NY, USA: ACM, 2010, pp. 6:1– 6:6.

[21] Ghandehari, L.S., Czerwonka, J., Lei, Y., Shafiee, S., Kacker, R. and Kuhn, R., 2014, March. An empirical comparison of combinatorial and random testing. In *Software Testing, Verification and Validation Workshops (ICSTW), 2014 IEEE Seventh Intl Conf on* (pp. 68-77). IEEE.

[22] Schroeder, P. J., Bolaki, P., & Gopu, V. (2004, August). Comparing the fault detection effectiveness of n-way and random test suites. In *Empirical Software Engineering, 2004. ISESE'04. Proceedings. 2004 Intl Symp on* (pp. 49-59). IEEE.

[23] Ellims, M., Ince, D. and Petre, M., 2008, September. The effectiveness of t-way test data generation. In *Intl Conf on Computer Safety, Reliability, and Security* (pp. 16-29). Springer Berlin Heidelberg.

[24] Vilkomir, S., Starov, O. and Bhambroo, R., 2013, March. Evaluation of t-wise approach for testing logical expressions in software. In *Software Testing, Verification and Validation Workshops (ICSTW), 2013 IEEE Sixth Intl Conf on* (pp. 249-256). IEEE.

[25] Ballance, W.A., Vilkomir, S. and Jenkins, W., April. Effectiveness of pair-wise testing for software with boolean inputs. *Software Testing, Verification and Validation, 2012 IEEE Fifth Intl Conf* (pp. 580-586)

[26] Kobayashi, N., Tsuchiya, T. and Kikuno, T., 2001, July. Applicability of non-specification-based approaches to logic testing for software. In *Dependable Systems and Networks, 2001. DSN 2001.* (pp. 337-346). IEEE.

[27] Bell, K.Z. and Vouk, M.A., 2005, December. On effectiveness of pairwise methodology for testing network-centric software. In *Information and Communications Technology, 2005. Enabling Technologies for the New Knowledge Society: ITI 3rd Intl Conf on* (pp. 221-235). IEEE.

[28] Bryce, R.C. and Colbourn, C.J., 2006. Prioritized interaction testing for pair-wise coverage with seeding and constraints *Inf.Software Tech.*, *48*(10), pp.960-970.

[29] Ghandehari, L.S., Czerwonka, J., Lei, Y., Shafiee, S., Kacker, R. and Kuhn, R., An empirical comparison of combinatorial and random testing. *Software Testing, Verification and Validation Workshops (ICSTW), 2014 IEEE Seventh Intl Conf on* (pp. 68-77). IEEE.

[30] Bartholomew, R. (2013, May). An industry proof-of-concept demonstration of automated combinatorial test. In *Automation of Software Test (AST), 2013 8th Intl Workshop on* (pp. 118-124). IEEE.

[31] Borazjany, Mehra N., et al. "An input space modeling methodology for combinatorial testing." *Software Testing, Verification and Validation Workshops (ICSTW), 2013 IEEE Sixth Intl Conf on*. IEEE, 2013.

[32] Colbourn, C. J., & McClary, D. W. (2008). Locating and detecting arrays for interaction faults. *Journal of combinatorial optimization*, *15*(1), 17-48.

[33] Wang, Z., Xu, B., Chen, L., & Xu, L. (2010, July). Adaptive interaction fault location based on combinatorial testing. In *Quality Software (QSIC), 2010 10th Intl Conf on* (pp. 495-502). IEEE.

[34] Kuhn, D. R., Kacker, R. N., & Lei, Y. (2010). SP 800-142. Practical Combinatorial Testing.

[35] Kuhn, D. R., Kacker, R. N., & Lei, Y. (2016). Measuring and specifying combinatorial coverage of test input configurations. *Innovations in Systems and Software Engineering*, *12*(4), 249-261.

Balisage: The Markup Conference

Using DITA to Create Security Configuration Checklists

A Case Study

Joshua Lubell
Computer Scientist
National Institute of Standards and Technology
<lubell@nist.gov>

Abstract

Many software tools use security configuration checklists expressed in the Extensible Configuration Checklist Description Format (XCCDF) to monitor computers and other information technology products for compliance with security policies. But XCCDF syntax is checklist author-unfriendly. And complex relationships and dependencies between and among checklist rules, checking instructions, and software platforms make it difficult to reuse or repurpose existing XCCDF content in new checklists. The Darwin Information Typing Architecture (DITA) can tame XCCDF syntax and facilitate content management and reuse. A case study comparing the use of specialization and other DITA features with a currently-deployed ad hoc XCCDF authoring system demonstrates the advantages of the DITA approach.

Table of Contents

1. Introduction

The Extensible Configuration Checklist Description Format (XCCDF [1]) Waltermire represents structured collections of security configuration rules for target systems. XCCDF is part of the Security Content Automation Protocol (SCAP — pronounced ess-cap) Quinn Radack: an ecosystem of interoperable Extensible Markup Language (XML) W3C-XML vocabularies, reference data, and software tools. SCAP serves as a "digital thread" Hedberg for cybersecurity Lubell2015. System administrators rely on SCAP to secure their servers, workstations, and networks. XCCDF saves

checklist developers the pain of having to learn multiple proprietary formats and lowers deployment barriers for automated configuration checking. XCCDF-expressed checklists can be used with any SCAP-conforming software product.

XCCDF is a powerful and versatile language, but it is not checklist author-friendly. Although XCCDF enables automation of security configuration scans and generation of human-readable documentation, it is of limited use in helping authors reuse existing content when developing a new checklist. XCCDF is designed in a modular manner to facilitate reuse of sub-elements across different checklists. However, as checklist target types proliferate, efficient management of such content becomes increasingly challenging. Also, XCCDF's syntax is verbose and cluttered with namespaces, making checklist authoring labor-intensive and error-prone.

These shortcomings were of less concern in the recent past when most computing occurred on commodity hardware running one of a small number of popular operating systems. But today the mobile computing revolution and the “Internet of Things” are spawning a greater variety of devices, operating systems, and applications that need protection from cyber-threats. Creating XCCDF content for this multitude of platforms is becoming untenable. Checklist authors need better tools to cope with this new diversity — and with the ever-increasing need to prevent security incidents.

This paper explores how the Darwin Information Typing Architecture (DITA) OASIS-DITA can improve life for XCCDF checklist authors. Section 2 provides an overview of XCCDF and introduces a sample checklist to be used as a case study. Section 3 describes the ad hoc approach the SCAP Security Guide (SSG) OpenSCAP-SSG project uses to address XCCDF and SCAP authoring and reuse challenges. Section 4 illustrates how DITA “topic” and “map” element type specializations can be used to improve the XCCDF authoring experience. Section 5 discusses how DITA can meet reuse challenges in a more robust and maintainable manner than the SSG approach described. Section 6 summarizes the case study results and offers some concluding remarks.

2. XCCDF Overview and Example

The XCCDF specification Waltermire defines XCCDF's data model and processing semantics. The current version of XCCDF is 1.2. The specification references a schema XCCDF as XCCDF's normative XML representation. This schema's `<Benchmark>` element is the root element of a checklist, or “benchmark document” using XCCDF terminology. A `<Benchmark>` element contains a collection of `<Rule>`, `<Value>`, and `<Group>` elements. A `<Rule>` specifies a single item to check, such as a firewall's default setting. A `<Rule>` also specifies how the checking should be done, such as with an implementation-specific scripting language or with the Open Vulnerability Assessment Language (OVAL) OVAL, an SCAP standard for representing system configuration information, assessing machine state, and reporting assessment results. A `<Value>` represents a named parameter that can be used within rules and tailored for a particular configuration scenario. A `<Group>`

collects <Rule>, <Value>, and other <Group> elements into an aggregation that is meaningful to a checklist user, for example, a collection of firewall configuration settings.

A <Benchmark> element also contains one or more <Profile> elements. A <Profile> is a named collection of references to <Group>, <Rule>, and <Value> elements. Profiles allow different combinations of groups and rules to be enabled so that they are included in a series of tests, or disabled so that they are not. Profiles can also tailor the value of the named parameters in <Value> elements. Profiles allow a single benchmark to support different test scenarios by enabling different combinations of tests and parameter values. XCCDF's <Profile> element increases a benchmark document's versatility, but also increases the document's complexity by adding many cross references.

This paper uses as an ongoing example a simple XCCDF checklist consisting of four ungrouped rules for version 7 of Red Hat Enterprise Linux (RHEL7) [2], none of which use any <Value> parameters. The example was extracted from a more complex XCCDF checklist developed by the Center for Internet Security CIS. Two of the rules pertain to SELinux StPierre, a Linux kernel module for Mandatory Access Control (MAC). MAC is the security principle of limiting the ability of a user or running application to access system resources Hu. The other two rules apply to firewall configuration. The checklist defines two profiles:

- “Firewall with MAC” referencing all four rules,
- “Firewall” referencing only the two firewall-related rules.

Figure 1

```
<Benchmark xmlns="http://checklists.nist.gov/xccdf/1.2"
id="xccdf_gov.nist_benchmark_Red_Hat_Enterprise_Linux_7_Benchmark"
style="SCAP_1.2">
   <status date="2016-06-02">interim</status>
   <title>Red Hat Enterprise Linux 7 Benchmark</title>
   <description>…</description>
   <version>2.1.0</version>
   <metadata>…</metadata>
   <Profile id="xccdf_gov.nist_profile_Firewall">…</Profile>
   <Profile id="xccdf_gov.nist_profile_Firewall_with_MAC">…</Profile>
   <Rule id="xccdf_gov.nist_rule_Ensure_SELinux_not_disabled_in_
bootloader_configuration" selected="false"…>…</Rule>
   <Rule id="xccdf_gov.nist_rule_Ensure_SELinux_is_installed"
selected="false"…>…</Rule>
   <Rule id="xccdf_gov.nist_rule_Ensure_iptables_is_installed"
selected="false"…>…</Rule>
   <Rule id="xccdf_gov.nist_rule_Ensure_firewall_rules_exist_for_all_
open_ports" selected="false"…>…</Rule>
</Benchmark>
```

XCCDF checklist representing RHEL7 example.

Figure 1 shows the high-level XCCDF representation of this checklist. Ellipsis symbols indicate lower-level details omitted for brevity. In this checklist, all rules have a `@selected` attribute set to "false". Thus, no rules in the benchmark document are processed by default. Instead, each profile must explicitly select the rules it wishes to include in its test scenario (as shown later in Figure 3).

Figure 2 shows the checklist loaded as input into SCAP Workbench OpenSCAP-Workbench, a security configuration scanner user interface. The user has selected the "Firewall with MAC" profile. The "Rules" pane displays the title and description of each rule in the profile. If the user were to click on the "Scan" button, the software would scan a remote machine to determine compliance with the four profile rules and report the results back to the user.

Figure 3 shows the XCCDF representation of the "Firewall with MAC" profile. The `<select>` elements reference the rules comprising the profile. Each `<select>` element has an `@idref` attribute identifying a rule and a `@selected` attribute set to "true" to explicitly include the referenced rule for use in the profile's test scenario.

Figure 2

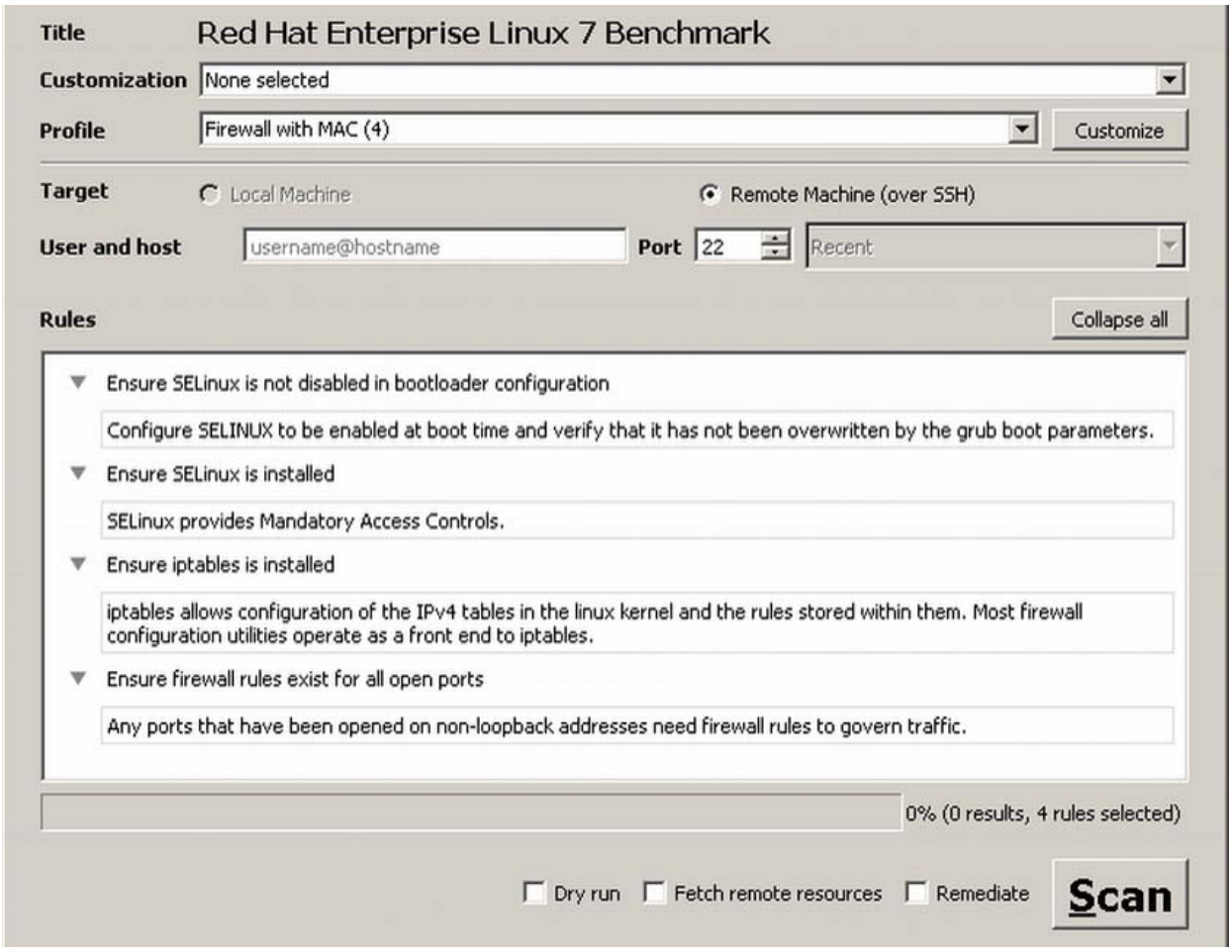

Firewall with MAC profile loaded into SCAP configuration scanner software.

The XCCDF markup shown in Figure 1 and Figure 3 exhibits the following characteristics:

- Identifiers are long. XCCDF requires that identifiers be both unique and descriptive, and that they contain a reverse-Domain Name System (DNS) style string associated with the content author. The profile identifier and four rule identifiers all meet these requirements.
- Rule identifiers are repetitive. They all start with `"xccdf_gov.nist_rule_"`.

These characteristics promote interoperability and completeness, but at the expense of author-friendliness and maintainability.

Now consider Figure 4, the XCCDF representation of the first of the four rules referenced by the "Firewall with MAC" profile. This rule checks whether SELinux is enabled. The `<description>` and `<rationale>` elements document the rule and its justification. The `<complex-check>` element represents a Boolean expression of `<check>` elements, which in turn reference the code for determining whether the system being scanned complies with the rule. In this example, checking is done using OVAL. Each `<check-content-ref>` element's `@href` attribute references an external file containing OVAL definitions, and the `@name` attribute identifies the particular OVAL definition used to perform the check. Like XCCDF, OVAL requires identifiers to be descriptive and use reverse-DNS syntax.

Figure 3

```
<Profile xmlns="http://checklists.nist.gov/xccdf/1.2"
id="xccdf_gov.nist_profile_Firewall_with_MAC">
  <title>Firewall with MAC</title>
  <description>This profile extends the "Firewall" profile to check
configuration of Mandatory Access Control(MAC).</description>
  <select idref=
"xccdf_gov.nist_rule_SELinux_not_disabled_in_bootloader_configuration"
selected="true"/>
  <select idref=
"xccdf_gov.nist_rule_SELinux_is_installed" selected="true"/>
  <select idref=
"xccdf_gov.nist_rule_iptables_is_installed" selected="true"/>
  <select idref=
"xccdf_gov.nist_rule_firewall_rules_exist_for_all_open_ports"
selected="true"/>
</Profile>
```

Profile in XCCDF.

The XML in Figure 4 exhibits the same XCCDF characteristics as the profile XML shown in Figure 3. Additionally:

- There are multiple Uniform Resource Identifiers (URIs): the XCCDF default namespace `http://checklists.nist.gov/xccdf/1.2` and the OVAL URI `http://oval.mitre.org/XMLSchema/oval-definitions-5`.
- The markup representing the checking of the rule is verbose and complex.

The rule's `<complex-check>` markup complexity is partly because the check requires a Boolean expression referencing three OVAL definitions, but the `<check-content-ref>` syntax and

repetitive `@system` attributes further exacerbate matters. This added verbosity is perhaps necessary to allow for possibilities such as check systems other than OVAL, and embedded code for performing a check. However, given that SCAP-conforming tools are required to support OVAL as a checking language in XCCDF, and most XCCDF benchmarks use OVAL, this extra verbosity is generally not needed in practice.

Figure 4

```
<Rule xmlns="http://checklists.nist.gov/xccdf/1.2" id="xccdf_gov.nist_
rule_SELinux_not_disabled_in_bootloader_configuration" selected="false">
  <title>Ensure SELinux is not disabled in bootloader
configuration</title>
  <description>Configure SELINUX to be enabled at boot time and verify
that it has not been overwritten by the grub boot parameters.
</description>
  <rationale>SELinux must be enabled at boot time in your grub
configuration to ensure that the controls it provides are not overridden.
</rationale>
  <complex-check operator="OR">
    <complex-check operator="AND">
       <check system="http://oval.mitre.org/XMLSchema/oval-definitions-5">
         <check-content-ref
href="CIS_Red_Hat_Enterprise_Linux_7_Benchmark_v2.1.0-oval.xml"
name="oval:gov.nist.redhat_redhat_enterprise_linux_7:def:1058"/>
       </check>
       <check system="http://oval.mitre.org/XMLSchema/oval-definitions-5">
         <check-content-ref
href="CIS_Red_Hat_Enterprise_Linux_7_Benchmark_v2.1.0-oval.xml"
name="oval:gov.nist.redhat_redhat_enterprise_linux_7:def:1059"/>
       </check>
     </complex-check>
     <check system="http://oval.mitre.org/XMLSchema/oval-definitions-5">
        <check-content-ref
href="CIS_Red_Hat_Enterprise_Linux_7_Benchmark_v2.1.0-oval.xml"
name="oval:gov.nist.redhat_redhat_enterprise_linux_7:def:1060"/>
     </check>
   </complex-check>
</Rule>
```

Rule in XCCDF.

The discussion so far has focused on XCCDF characteristics that impede authoring such as verbosity and redundancy. An additional concern is that XCCDF and other SCAP languages do not facilitate reuse of content applicable to multiple platforms Lubell2017. To see why, consider as an example the third rule shown in Figure 2, “Ensure iptables is installed.” Iptables, an application for configuring the Linux kernel firewall, is available in all Linux distributions. Therefore, this rule is potentially applicable to all Linux systems.

A reasonable way to check for compliance with this rule would be for the rule's OVAL definition to invoke RHEL's package manager, rpm, to verify that iptables is installed. But unlike iptables, not all Linux distributions come with rpm. Fedora, an open source Linux distribution closely related to

RHEL, has rpm. On the other hand, Debian and Ubuntu (a Debian derivative) both use dpkg for package management. Figure 5 shows the relationships between the Debian, Ubuntu, RHEL, and Fedora Linux distributions in terms of their shared kernel and package manager components.

Figure 5

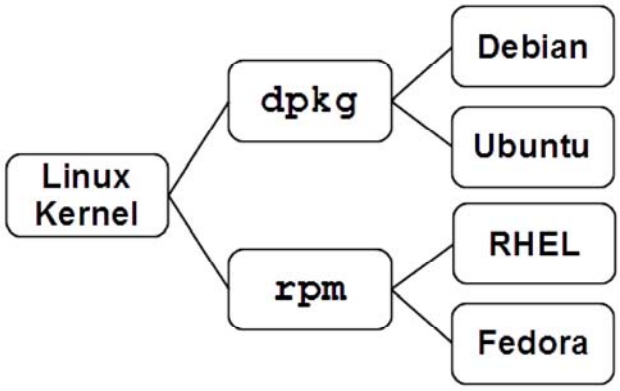

Linux distribution shared components.

This example illustrates the problem of platform fragmentation. Platform fragmentation occurs when the same operating system, software application, or hardware component is bundled by multiple entities — with each "bundler" providing different customizations Vecchiato. Although XCCDF and other SCAP languages allow for associations between rules or collections of rules and platforms, the SCAP ecosystem currently does not provide the kind of guidance shown in Figure 5 to checklist authors. Therefore, checklist authors need other methods and tools outside the scope of SCAP to help them leverage taxonomic and other relationships to maximize reuse when creating new checklists. The next section discusses how this is done in the SSG project.

3. The SCAP Security Guide Approach

The SSG OpenSCAP-SSG is an open source project whose output is a growing collection of SCAP-expressed content (security guides) for Linux distributions and software applications. This SSG-generated SCAP content is widely used in government and industry. Current and recent users include cloud computing providers, national defense agencies, and the financial services and airline industries [3]. The SSG "source code" consists of:

- Scripts and Extensible Style Language Transformations (XSLT) W3C-XSLT for generating SCAP content,
- XML files that serve as input to the scripts and XSLT.

To deal with platform fragmentation and to facilitate source code management, the source code is modularized. Shareable module files applicable to two or more security guides reside in a single "shared" directory tree. Platform-specific module files applicable only to an individual security guide reside in platform-specific directory trees. The XML input files are further modularized into logically-related checklist components such as profiles, groups, and OVAL definitions. Building SCAP security guides from the source requires running scripts that perform XML transformations, macro substitutions, and merging of the XML input modules into bigger SCAP-conforming files.

SSG contributors create rules, profiles, and other XML input modules using a shorthand XML vocabulary. The shorthand is less verbose and namespace-heavy than the XCCDF markup shown in Section 2. The SSG build process converts the shorthand to XCCDF and OVAL. This build process is complicated and requires SSG contributors to understand not only SCAP, but also the one-off way the SSG source files are organized and structured Preisler.

Figure 6 shows a high-level view of the SSG source code directory structure. The `shared` directory subtree shown in the left-hand column contains content, XSLT, and scripts applicable to more than one Linux distribution. Platform-specific subtrees contain content, transforms, and scripts applicable only to a single distribution or application. The right-hand column shows the subtree for RHEL7. Each distribution-specific directory tree has a Makefile with targets needed for building SCAP content for that distribution. A master Makefile in the source code root directory has targets for building all the SCAP content.

Figure 6

Shared Content and Transforms

```
shared
├── images
├── misc
├── modules
├── oval
├── references
├── remediations
├── templates
├── transforms
├── utils
└── xccdf
```

RHEL7-specific Content and Transforms

```
RHEL
└──7
    ├── input
    │   ├── auxiliary
    │   ├── oval
    │   └── profiles
    ├── kickstart
    ├── templates
    ├── transforms
    └── utils
```

SSG source code shared and RHEL7-specific directory subtrees.

All rules and profiles in the source code are defined using the SSG shorthand XML. Rules that are common across multiple Linux distributions, such as the rule for determining whether SELinux is enabled, reside in `shared/xccdf`. Rules specific to a particular Linux distribution are in the distribution's `input` directory subtree. Since all rules for RHEL7 come from `shared/xccdf`, the RHEL7 `input` directory has no `xccdf` subdirectory. Profiles are distribution-specific and reside in the distribution's `input/profiles` directory.

XSLT stylesheets in a platform-specific `transforms` directory generate SCAP-conforming XML, such as the RHEL7 benchmark shown in Figure 1. These stylesheets use `<xsl:include>` elements to incorporate stylesheets from `../../../shared/transforms`. The stylesheets first combine the individual shorthand XML files (both shared and distribution-specific) into a single shorthand benchmark file. They then transform the combined shorthand benchmark into an XCCDF-conforming benchmark document.

The SSG XSLT stylesheets support reuse not only of structural checklist components such as rules, but also of inline fragments. The stylesheets automatically insert frequently-occurring fragments when feasible to do so. For example, the value of the `@system` attribute in all XCCDF rules using OVAL is the same URI: `http://oval.mitre.org/XMLSchema/oval-definitions-5` . Therefore, the shorthand XML syntax omits `@system` and its value, saving authors the trouble of having to repeatedly specify it.

For reusable fragments where the author determines placement, the SSG shorthand employs "-macro" elements. For example, a RHEL7 checklist author might want to use the full name of the product to which the checklist applies — "Red Hat Enterprise Linux 7" — in multiple places within elements where mixed content is allowed. To save authors the trouble of having to specify a full product name for every occurrence, the RHEL-specific XSLT in `RHEL/7/transforms` contains the following variable declaration:

```
<xsl:variable
name="product_long_name">Red Hat Enterprise Linux 7</xsl:variable>
```

The stylesheet in `shared/transforms` for converting the combined shorthand XML components into an XCCDF benchmark contains the following template rule:

```
<xsl:template match="product-name-macro">
  <xsl:value-of select="$product_long_name"/>
</xsl:template>
```

The template rule and variable declaration enable an SSG author to specify a product name inline as `<product-name-macro/>`. Doing so not only minimizes the opportunity for undetected typos, but also maximizes the reusability of the `<rule>` or other structural element containing the product name.

Figure 7

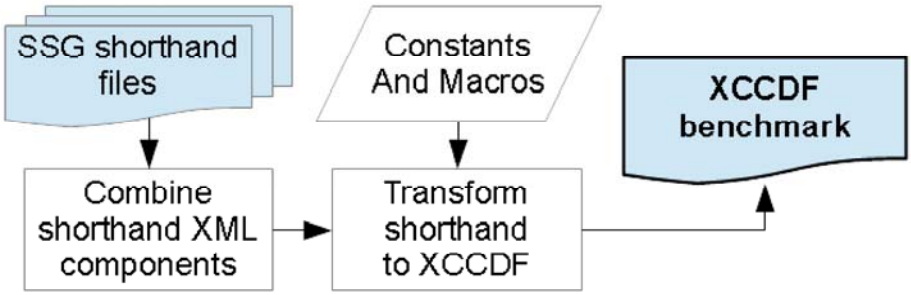

SCAP Security Guide transformation from shorthand to XCCDF.

Figure 7 summarizes the overall SSG transformation process discussed in the preceding paragraphs. The stylesheets first combine individual shorthand XML files and then, using constants defined as variable declarations and macros defined as template rules, produce an XCCDF-conforming benchmark document.

4. Specialized DITA Element Types for XCCDF

The DITA standard OASIS-DITA is an XML-based architecture for creating, managing, reusing, and delivering technical content. A variety of authoring applications and processors — commercial as well as free and open source — conform to DITA OASIS-DITA-xml.org. DITA has two basic building blocks: the “topic” and “map” element types. A “topic” is a reusable chunk of information. A “map” is an aggregation of topics or other maps. DITA supports reuse not only of topics and maps, but also of inline XML elements and fragments.

DITA information types are specializable. Specialization is an information modeling technique that helps avoid inconsistency and facilitate interoperability Krima. A specialized information type is a refinement of an existing base type and therefore must be at least as constrained. Specialization imposes some discipline on designers of new DITA information types, with the upside that implementations can easily leverage other DITA-conforming implementations Kimber. DITA includes built-in specialized element types based on the “topic” base type, such as “concept”, “task”, “reference”, and “glossary group”. DITA also allows for definition of new specialized element types based on “topic”, “map”, or other specialized types.

In this section, I define new DITA specialized element types to support the authoring of XCCDF rules and profiles. I also provide examples of other XCCDF elements for which DITA specializations could be defined. These types have the same advantages as the XCCDF shorthand vocabulary, but with the added benefits of validation and more author-friendliness when using DITA-aware XML editing software. The specialization approach follows guidance from the DITA standard OASIS-DITA and from Eliot Kimber's DITA Configuration and Specialization Tutorials Kimber.

Rule Element Type

To develop a specialized DITA information type for XCCDF rule authoring, let us begin by revisiting the “Ensure SELinux is not disabled in bootloader configuration” rule shown in Figure 4. A DITA “rule” element type should mitigate the three XCCDF authoring barriers highlighted in Section 2:

1. Repetitive and overly long identifiers,
2. Namespace proliferation,
3. Overly verbose check expressions.

I choose to define the new “rule” element type as a specialization of the DITA “concept” topic type. A “concept” has the loosest content model of DITA's built-in topic-based types, making it easy to specialize. `<concept>`, the “concept” topic type's root element, contains a `<title>` followed by `<conbody>`, the main body element. `<conbody>` may contain DITA `<section>` elements, which subdivide content within a topic and are not allowed to be nested. DITA `<sectiondiv>` elements subdivide content within a `<section>` and may be nested inside one

another. <section> and <sectiondiv> may contain mixed content including <xref>, a DITA linking element. <xref> has an @href attribute, which may reference another topic, map, or non-DITA resource.

The next step is to create a “rule” document type shell based on the “concept” document type shell. A DITA document type shell defines which elements and attributes are allowed in a DITA document, and is usually specified using Document Type Definition (DTD) syntax. The DITA standard provides a modular architecture for document type shells to facilitate creation of new shells. A recommended practice is to make a copy of an existing shell (the “concept” shell in our case) and modify the modules as needed for the new document type.

Figure 8 shows the “Ensure SELinux is not disabled in bootloader configuration” rule represented in a manner similar in spirit to the SSG shorthand syntax, which mitigates the XCCDF rule authoring barriers. The new “rule” document type shell will specify a grammar for authoring rules such as the rule in Figure 8.

Figure 8

```
<rule id="SELinux_not_disabled_in_bootloader_configuration">
  <title>Ensure SELinux is not disabled in bootloader configuration
</title>
  <rulebody>
    <description>Configure SELINUX to be enabled at boot time and
verify that it has not been overwritten by the grub boot parameters.
</description>
    <rationale>SELinux must be enabled at boot time in your grub
configuration to ensure that the controls it provides are not
overridden.</rationale>
    <check>
      <OR>
        <AND>
          <oval href="oval/1058.dita"/>
          <oval href="oval/1059.dita"/>
        </AND>
        <oval href="oval/1060.dita"/>
      </OR>
    </check>
  </rulebody>
</rule>
```

Rule represented using specialization of concept DITA topic [4].

Looking at Figure 8 in the context of the DITA “concept” element type, one observes the following:

- The <oval> element can be specialized from DITA's <xref> element, without additional constraints.
- <OR> and <AND> can be specialized from DITA's <sectiondiv> element, constrained to allow one or more <oval> elements or Boolean expressions as content.
- <check> can be specialized from DITA's <section> element, constrained to allow either a single <oval> element or Boolean expression of <oval> elements as content.

- <description> and <rationale> can be specializations of <section> without additional constraints.
- <rulebody> can be specialized from <conbody>, but constrained to allow only a <description>, <rationale>, and <check> as content.
- <rule> can be specialized from <concept>, but constrained to allow only a <title> and <rulebody> as content.
- The DITA <title> element can be used as is.

After creating a "rule" document type shell reflecting these observations, I add DITA @class attributes with default values to each specialized element: <rule>, <rulebody>, <description>, <rationale>, <rationale>, <check>, <AND>, <OR>, and <oval>. Default values are used to hide the DITA specialization machinery from authors, who have no need to see it when editing content. The @class attribute specifies the element's specialization hierarchy — a mapping from the element name to its more generalized DITA concept and topic element equivalents. For example, the <rule> element's @class attribute has the value "- topic/topic concept/concept rule/rule ", which specialization-aware DITA processors interpret to mean

> The <rule> element in the "rule" element type specializes <concept> from the "concept" element type, which in turn specializes <topic> from the "topic" element type.

Table I

Specialization hierarchies and document type shell constraints for each "rule" element.

Element	Specialization Hierarchy (@class value)	Document Type Shell Constraints
<rule>	"- topic/topic concept/concept rule/rule "	(title, rulebody)
<rulebody>	"- topic/body concept/conbody rule/rulebody "	(description, rationale, check)
<description>	"- topic/section concept/section rule/description "	none
<rationale>	"- topic/section concept/section rule/rationale "	none
<check>	"- topic/section concept/section rule/check "	(OR | AND | oval)
<OR>	"- topic/sectiondiv concept/sectiondiv rule/OR "	(OR | AND | oval)+
<AND>	"- topic/sectiondiv concept/sectiondiv rule/AND "	(OR | AND | oval)+
<oval>	"- topic/xref concept/xref rule/oval "	none

Table I shows the specialization hierarchy and document type shell constraint for each new element in the "rule" element type. The specialization hierarchy effectively specifies the default specialization-aware DITA processing behavior. DITA specialization hierarchies maximize reuse

of existing markup and transformation code Priestley. The document type shell constraints specify requirements for valid XML.

Suppose an XCCDF rule author were to use a DITA specialization-aware XML application such as Oxygen XML Editor. Figure 9 shows the “Ensure SELinux is not disabled in bootloader configuration” rule as presented in Oxygen's user interface. The screen capture occurred when the user was about to insert a new element following the `<oval>` element whose `@href` value is `oval/1059.dita`. A simple Cascading Style Sheet (CSS) W3C-CSS augments Oxygen's CSS styling for the “concept” element type by adding “Rule:”, “Description:”, “Rationale:”, and “Check:” labels, as well as the parentheses and “OR” and “AND” in the check expression. This is *all* the CSS code does. Other presentation aspects such as the fonts used and the clickable `@href` links are derived using the specialization hierarchies shown in Table I.

Figure 9

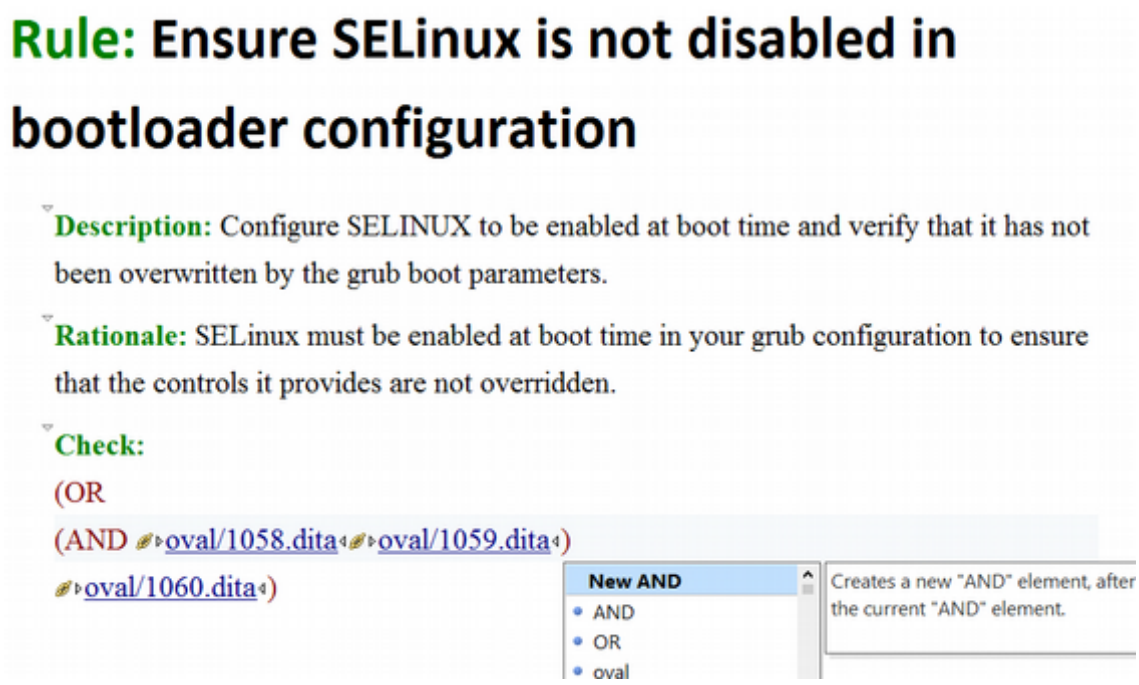

Rule in DITA specialization-aware authoring environment.

Analogous to the CSS augmentation of the default DITA presentation, the rule document type shell constraints shown in Table I augment the default DITA visual editing and validation capabilities. The drop-down list of elements shown in Figure 9 limits the user's choices to inserting an `<AND>`, `<OR>`, or `<oval>` element, or adding a new `<AND>` after the current `<AND>` element. Any DITA “concept” topic document type shell constraints not overridden by the “rule” document type shell remain. For example, the user can add any content inside the `<description>` or `<rationale>` elements permitted by the “concept” document type shell's content model for `<section>`.

Profile Element Type

I choose to define the new “profile” element type as a simple specialization of the DITA “map” element type. <map>, the “map” type's root element, may contain a <title>, followed by a <topicmeta> element, followed by a sequence of <topicref> elements. <topicmeta>, in this context, specifies metadata applicable to all topics in the map, and may contain a brief description of the map in a <shortdesc> element. The <topicref> element uses @href to reference a map resource.

I first create a “profile” document type shell based on the “map” document type shell. Figure 10 shows the “Firewall with MAC” profile represented in a manner similar in spirit to the SSG shorthand syntax, and that mitigates the XCCDF authoring barriers discussed in Section 2.

Figure 10

```
<profile id="Firewall_with_MAC">
  <title>Firewall with MAC</title>
  <profilemeta>
    <shortdesc>This profile extends the "Firewall" profile to check
configuration of Mandatory Access Control (MAC).</shortdesc>
  </profilemeta>
  <rule href=
"rules/SELinux_not_disabled_in_bootloader_configuration"/>
  <rule href="rules/SELinux_is_installed"/>
  <rule href="rules/iptables_is_installed"/>
  <rule href="rules/firewall_rules_exist_for_all_open_ports"/>
</profile>
```

Profile represented using specialization of DITA <map> [5].

Table II

Specialization hierarchies and document type shell constraints for each “profile” element.

Element	Specialization Hierarchy (@class value)	Document Type Shell Constraints
<profile>	"- map/map profile/profile "	(title, profilemeta, rule+)
<profilemeta>	"- map/topicmeta profile/profilemeta "	none
<rule>	"- map/topicref profile/rule "	none

Looking at Figure 10 in the context of the DITA “map” document type, one observes the following:

- <rule> can be specialized from DITA's <topicref> element, without additional constraints.
- <profilemeta> can be specialized from DITA's <topicmeta> element, without additional constraints.
- <profile> can be specialized from DITA's <map> element, but constrained to allow only a <title>, <profilemeta>, and one or more <rule> elements as content.
- The DITA <title> and <shortdesc> elements can be used as is.

Table II shows the specialization hierarchy and document type shell constraint for each new element in the “profile” type. Figure 11 shows the Oxygen presentation with clickable `@href` links. Minimal CSS styling adds the “Profile:” label. All other presentation characteristics are inherited from the “map” element type's CSS styling.

Figure 11

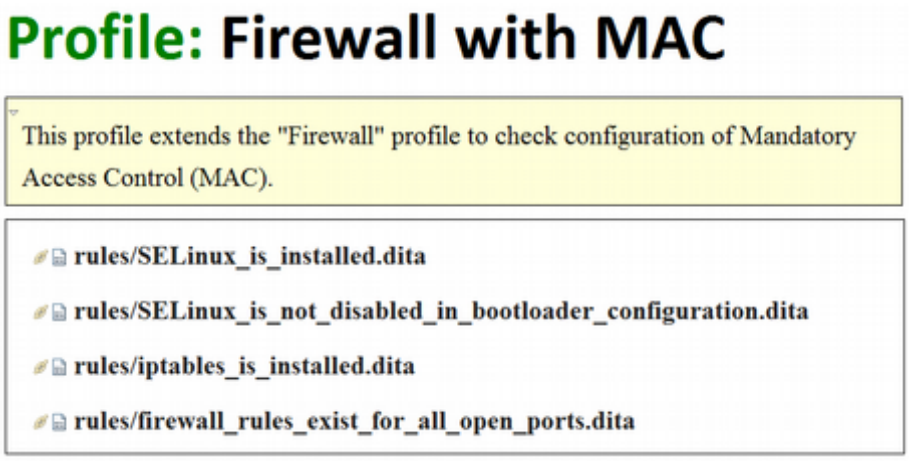

Profile in DITA specialization-aware authoring environment.

Other Element Types

The previous subsections demonstrated how shorthand XML vocabularies for XCCDF rules and profiles can be implemented as specializations of the DITA “concept” and “map” element types respectively. Specialization can also be used to create DITA element types for XCCDF groups and values as well. A “group” type could be specialized from the DITA “map” element type, and “value” can be specialized from the base “topic” type or one of the DITA built-in types specialized from “topic”.

An XCCDF benchmark document as a whole could be represented using a “benchmark” element type specializing “map”. Doing so would explicitly represent the high-level checklist structure, which the SSG build system represents implicitly in Makefiles and in the XSLT implementing the “Transform shorthand to XCCDF” box in the Figure 7 flowchart. DITA maps have additional benefits besides making the transformation process more explicit and self-documenting for XCCDF authors. As the next section will discuss, maps enable reuse of XCCDF content and can reduce the coding needed to implement the shorthand-to-XCCDF transformation.

5. Reuse and Implementation Considerations

This section revisits the SSG approach covered in Section 3 from a reuse perspective. The first subsection describes how maps and other DITA features can improve upon SSG solutions for reusing XCCDF content. The second subsection discusses how the use of DITA can simplify implementation of the conversion from shorthand XML to XCCDF.

Block and Inline Content Reuse

DITA maps can improve upon the SSG "`shared/xccdf`" reuse mechanism. Relying on directory subtrees imposes a rigid hierarchy on reuse relationships, and is insufficient to account for all the varieties of platform fragmentation. There are a lot ways to categorize platforms. The package manager-based classification shown in Figure 5 is just one of many. Lineage is another way to characterize a platform. For example, Ubuntu Linux is derived from Debian, while RHEL is a commercial sibling of the open source Fedora. Linux distributions can also be classified according to graphical desktop environment. For example, some Linux distributions come bundled with GNOME , while others come with Enlightenment. And GNOME and Enlightenment each have variants. Linux distributions optimized for specialized hardware, increasingly common as the "Internet of Things" continues to grow, add yet another wrinkle to platform fragmentation. Raspbian Raspbian, a Debian derivative tailored for Raspberry Pi hardware, is an example of a hardware-optimized Linux distribution.

Multiple DITA maps can be used to slice and dice a repository of DITA resources for creating XCCDF benchmarks covering a wide variety of Linux-based platforms. Each map can represent a different platform class. And maps can overlap with one another, or a map can reference another map. Maps can capture parent-child relationships as well as sibling relationships. Also, DITA supports conditional profiling OASIS-DITA, which allows the same content to be associated with multiple organization schemes as defined using DITA's filtering attributes. The classification possibilities are endless. Unlike the SSG `shared` directory subtree, a DITA map-based approach is flexible enough to keep pace with growing platform fragmentation.

Figure 12

```
<benchmark class="- map/map benchmark/benchmark ">
  <title>Benchmark for <ph keyref="product_name"/></title>
  <keydef keys="product_name"><topicmeta><keywords>
        <keyword>Red Hat Enterprise Linux 7</keyword>
  </keywords></topicmeta></keydef>
  <intro href="introduction.dita" class=
"- map/topicref benchmark/intro "/>
  …
</benchmark>
```

Key defined in benchmark's root map and referenced in `<title>` element.

The discussion of DITA so far has focused on topics and maps, with an emphasis on reusability of topic-based information such as XCCDF rules. In addition to facilitating reuse of structural block content, DITA provides mechanisms for reusing inline content. These mechanisms can be applied to frequently repeated fragments in an XCCDF benchmark document such as the product name ("Red Hat Enterprise Linux 7" in our scenario). One such DITA capability is content key references, a method for indirectly addressing inline content locations Oxygen.

A content key and key reference can implement the same functionality as the “product-name-macro” SSG's XSLT template rule. One way to do this is to use DITA's `<keydef>` element to define a “product_name” key in a benchmark's root map as shown in the DITA benchmark document (specializing on the base “map” element type) in Figure 12. The “product_name” key can then be referenced from anywhere within the root map using the `@keyref` attribute of the DITA `<ph>` (phrase) element.

The “product_name” key can also be referenced from within any resource the root map references. For example, the referenced topic `introduction.dita` could contain the following paragraph:

```
<p>This document provides prescriptive guidance for establishing a
secure configuration for <ph keyref="product_name"/> systems.</p>
```

Code Reuse

A major benefit of DITA is that it can reduce the amount of coding needed to transform a collection of resources to a desired output format. The savings result from the DITA standard's requirements for output-producing processors. A conforming DITA processor must be able to merge topics in a map as well as resolve content references, eliminating the need for custom transformation code to perform these functions. A specialization-aware DITA processor can do all the above for specialized DITA documents through inheritance of processing behavior from base types via the `@class` attribute. The DITA Open Toolkit DITA-OT, an output-producing and specialization-aware DITA processor used in Oxygen and other XML software applications, illustrates the potential benefits of DITA for transformation of shorthand XML to XCCDF.

The DITA Open Toolkit is not part of the DITA standard — they are separately managed. However, both originated from the same research and development effort at IBM Priestley S-R. The Toolkit does not support XCCDF out of the box, but has an extensible plug-in mechanism for implementing custom output formats or adding additional functionality to existing output formats. The plug-in architecture allows for developers to reuse built-in transformation code, as well as code from other plug-ins, by integrating new XSLT via “extension points.” The DITA Open Toolkit's built-in transformation code includes a preprocessing module that implements map operations and content references. The preprocessing is used in all transformations by default.

A Toolkit XCCDF plug-in would require XSLT template rules matching against `@class` attribute values to convert elements from the specialized types from Section 4 into XCCDF equivalents. For example, the template rule below transforms the “rule” element type's `<rule>` element into an `<xccdf:Rule>` element. The value of `$rule-prefix` could be passed as a parameter to the plug-in. For the RHEL7 example from Section 2, the parameter value would be “xccdf_gov.nist_rule_”. `fn:rule-id` is a stylesheet-defined function that constructs a reverse-DNS syntax XCCDF identifier from `$rule-prefix` and the `<rule>` element's `@id` attribute value.

```
<xsl:template match="*[contains(@class, ' rule/rule ')]">
  <xccdf:Rule id="{fn:rule-id($rule-prefix,@id)}" …>
    <xsl:apply-templates/>
  </xccdf:Rule>
</xsl:template>
```

The template rule below transforms the “rule” element type's `<oval>` element into an `<xccdf:check>` element with a nested `<xccdf:check-content-ref>`. `fn:oval-def` constructs the OVAL definition's reverse-DNS name from the `$oval-def-prefix` parameter value (“oval:gov.nist.redhat_redhat_enterprise_linux_7:def:” for the RHEL7 example) and the `<oval>` element's `@href` attribute value. `$oval-uri` provides the value of `<xccdf:check>`'s `@href` attribute (“http://oval.mitre.org/XMLSchema/oval-definitions-5”). `<xccdf:check-content-ref>`'s `@href` attribute is assigned the value of `$oval-location` (“CIS_Red_Hat_Enterprise_Linux_7_Benchmark_v2.1.0-oval.xml”).

```
<xsl:template match="*[contains(@class, ' rule/oval ')]">
  <xccdf:check system="{$oval-uri}">
    <xccdf:check-content-ref
      href="{$oval-location}"
      name="{fn:oval-def($oval-def-prefix,@href)}"/>
  </xccdf:check>
</xsl:template>
```

6. Conclusion

The case study described in this paper investigated the feasibility of DITA for creating XCCDF security configuration checklists, and whether DITA could improve upon the SCAP Security Guide project's ad hoc approach to authoring and reuse. Proof-of-concept implementations of DITA element types for rules and profiles showed that DITA specialization is both feasible and offers tangible benefits beyond the SSG shorthand XML, such as validation and an improved authoring experience. Additional analysis and examples showed how DITA topic maps can improve reuse of structural XCCDF elements, and how DITA features such as key referencing can facilitate reuse of inline fragments.

This case study has a significant limitation. Analysis was limited to a single XCCDF checklist with only four rules, two profiles, and no `<Group>` or `<Value>` XCCDF elements. The rule and profile DITA element types do not provide the full range of XCCDF's flexibility [6]. For example, “rule” and “profile” do not consider XCCDF checklist capabilities such as automated remediation of misconfigurations. Similarly, the case study also assumed checklist authors would use OVAL for rule checking and would adopt a specific convention for using the `@selected` attribute. While these simplifying assumptions align with a large amount of the XCCDF content published thus far, some authors might find these assumptions limiting. Until more sophisticated checklists from a cross section of Linux platforms are studied, it would be premature to conclude definitively that DITA will revolutionize the development of XCCDF and other SCAP content. The SSG authoring

approach may have its shortcomings, but it has been successful in producing an impressive collection of widely-deployed SCAP content. Further implementation and testing are needed to determine whether the promising results presented in this paper can scale up to a collection of larger and more diverse checklists.

An open question is to what extent adoption of DITA as an alternative to the SSG's ad hoc authoring approach would simplify the SSG transformation shown in Figure 7. At the very least, assembly relationships, platform commonalities, and reusable structures and fragments would be more maintainable explicitly represented in DITA than implicitly represented in XSLT and Makefiles. Additionally, DITA's default processing of maps and key references should simplify implementation of the “Combine shorthand XML components” and “Transform shorthand to XCCDF” steps. Implementing an XCCDF plug-in would be a good way to learn how much the DITA Open Toolkit further simplifies implementation.

Author's Note

I am grateful to Eliot Kimber for his DITA Configuration and Specialization Tutorials, which were immensely helpful when writing this paper and creating the implementation examples. I also wish to thank Charles Schmidt, co-author of the XCCDF specification, for his thoughtful and helpful review of an earlier draft.

Appendix. List of Acronyms

CSS	Cascading Style Sheet
DITA	Darwin Information Typing Architecture
DTD	Document Type Definition
MAC	Mandatory Access Control
NIST	National Institute of Standards and Technology
OVAL	Open Vulnerability Assessment Language
RHEL	Red Hat Enterprise Linux
SELinux	Security-Enhanced Linux
SCAP	Security Content Automation Protocol
SSG	SCAP Security Guide
URI	Uniform Resource Identifier
XCCDF	Extensible Configuration Checklist Description Format
XSLT	Extensible Stylesheet Language Transformation

References

[CIS] Center for Internet Security. “CIS Red Hat Enterprise Linux 7 Benchmark v2.1.0” (2016). https://benchmarks.cisecurity.org [Prose documentation, XCCDF, and OVAL available to CIS members]

[DITA-OT] DITA Open Toolkit. http://www.dita-ot.org

[Hedberg] T. Hedberg, J. Lubell, L. Fischer, L. Maggiano, and A. Barnard Feeney. “Testing the Digital Thread in Support of Model-Based Manufacturing and Inspection.” *Journal of Computing and Information Science in Engineering.* 16 (2) (2016). 10.1115/1.4032697

[Hu] V.C. Hu, D.R. Kuhn, T. Xie, and J. Hwang. “Model Checking for Verification of Mandatory Access Control Models and Properties.” *International Journal of Software Engineering and Knowledge Engineering.* 21 (1). pp. 103–27 (2011). 10.1142/S021819401100513X.

[Kimber] E. Kimber. *DITA for Practitioners Volume 1: Architecture and Technology*. XMLPress (2012). [Configuration and Specialization tutorials online at http://www.xiruss.org/tutorials/dita-specialization]

[Krima] S. Krima and J. Lubell. “Flat Versus Hierarchical Information Models in PLM Standardization Frameworks.” In *Product Lifecycle Management for Digital Transformation of Industries: 13th IFIP WG 5.1 International Conference, PLM 2016, Columbia, SC, USA, July 11-13, 2016, Revised Selected Papers.* R. Harik, L. Rivest, A. Bernard, B. Eynard, and A. Bouras, Eds. Cham: Springer International Publishing. pp. 121–133 (2016). 10.1007/978-3-319-54660-5_12

[Lubell2015] J. Lubell. “Extending the Cybersecurity Digital Thread with XForms.” In *Proceedings of Balisage: The Markup Conference 2015.* Balisage Series on Markup Technologies, vol. 15 (2015). 10.4242/BalisageVol15.Lubell01

[Lubell2017] J. Lubell and T. Zimmerman. “The Challenge of Automating Security Configuration Checklists in Manufacturing Environments.” In *Critical Infrastructure Protection XI.* M. Rice and S. Shenoi, Eds. Springer Berlin Heidelberg (2017). [To appear]

[OASIS-DITA] Organization for the Advancement of Structured Information Standards. “Darwin Information Typing Architecture (DITA) Version 1.3 Part 2: Technical Content Edition.” OASIS Standard (2016).http://docs.oasis-open.org/dita/dita/v1.3/dita-v1.3-part2-tech-content.html

[OASIS-DITA-xml.org] Organization for the Advancement of Structured Information Standards. “DITA XML.org.” http://dita.xml.org

[OpenSCAP-SSG] OpenSCAP Portal. “SCAP Security Guide.” http://www.open-scap.org/security-policies/scap-security-guide

[OpenSCAP-Workbench] OpenSCAP Portal. “SCAP Workbench.” https://www.open-scap.org/tools/scap-workbench

[OVAL] OVAL Documentation. http://ovalproject.github.io

[Oxygen] Oxygen XML Editor Blog. “DITA Reuse Strategies (Short Tutorial describing all DITA Reuse possibilities).” http://blog.oxygenxml.com/2015/11/dita-reuse-strategies-short-tutorial.html

[Priestley] M. Priestley and D. A. Schell. “Specialization in DITA: Technology, Process, & Policy.” In *Proceedings of the 20th Annual International Conference on Computer Documentation.* pp. 164–176 (2002). 10.1145/584955.584980

[Preisler] M. Preisler. “Contributing to SCAP Security Guide — Part 1.” https://martin.preisler.me/2016/10/contributing-to-scap-security-guide-part-1

[Raspbian] Raspbian. https://www.raspbian.org

[StPierre] P. St. Pierre. “Securing Linux with Mandatory Access Controls.” *Linux.com* (2005). https://www.linux.com/news/securing-linux-mandatory-access-controls

[Quinn] S. Quinn, K. Scarfone, and D. Waltermire.“ Guide to Adopting and Using the Security Content Automation Protocol (SCAP) Version 1.2 (Draft).” NIST Special Publication 800-117. Revision 1 (2012). http://csrc.nist.gov/publications/PubsDrafts.html#SP-800-117-Rev.%201

[Radack] S. Radack and R. Kuhn. “Managing Security: The Security Content Automation Protocol.” *IT Professional.* vol. 13(1). pp. 9–11 (2011). 10.1109/MITP.2011.11

[S-R] K. Schengili-Roberts. “Don Day and Michael Priestley on the Beginnings of DITA: Part 1.” http://www.ditawriter.com/don-day-and-michael-priestley-on-the-beginnings-of-dita-part-1

[Vecchiato] D. Vecchiato, M. Vieira, and E. Martins. “The Perils of Android Security Configuration.” *Computer.* vol. 49(6). pp. 15-21 (2016). 10.1109/MC.2016.184

[Waltermire] D. Waltermire, C. Schmidt, K. Scarfone, and N. Ziring. “Specification for the Extensible Configuration Checklist Description Format (XCCDF) Version 1.2.” NIST Interagency Report 7275 Revision 4 (2012). https://scap.nist.gov/specifications/xccdf

[W3C-CSS] World Wide Web Consortium. “Cascading Style Sheets Level 2 Revision 1 (CSS 2.1).” W3C Recommendation (2011). https://www.w3.org/TR/CSS2

[W3C-XML] World Wide Web Consortium. “Extensible Markup Language (XML) 1.0 (Fifth Edition).” W3C Recommendation (2008). https://www.w3.org/TR/xml

[W3C-XSLT] World Wide Web Consortium. “XSL Transformations (XSLT) Version 2.0.” W3C Recommendation (2007). https://www.w3.org/TR/xslt20

[XCCDF] XCCDF — The Extensible Configuration Checklist Description Format. https://scap.nist.gov/specifications/xccdf

---

[1] An Appendix lists all acronyms and their expansions.

[2] Certain commercial and third-party products and services are identified in this paper to foster understanding. Such identification does not imply recommendation or endorsement by the National Institute of Standards and Technology, nor does it imply that the materials or equipment identified are necessarily the best available for the purpose.

[3] https://www.open-scap.org/security-policies/scap-security-guide/#references

[4] This “rule” element type assumes that an XCCDF rule is disabled by default. Thus, an XCCDF `<Rule>` element generated from a DITA “rule” should have `@selected="false"`. Although more restrictive than the XCCDF specification, this assumption allows for a more simplified “rule” syntax.

[5] This shorthand syntax assumes that rules in the benchmark are disabled by default. Identifying a rule in a profile thus implies that it should be changed to a selected status (with `@selected="true"`).

[6] This lack of flexibility is a limitation of the case study and not of DITA. The rule and profile element types described in this paper only scratch the surface of what is possible with DITA's specialization mechanism.

***Balisage:** The Markup Conference*

THE EFFECT OF POWDER ON COOLING RATE AND MELT POOL LENGTH MEASUREMENTS USING IN SITU THERMOGRAPHIC TECNIQUES

J. C. Heigel* and B. M. Lane*

*National Institute of Standards and Technology[1], Gaithersburg, MD 20899

Abstract

High-speed thermal cameras enable in situ measurement of the temperatures in and around melt pools generated during powder bed fusion processes. These measurements can be used to validate models, to monitor the process, and to understand the microstructure formed during the process. Unfortunately, pre-placed powder layers complicate the measurement due to spatter and irregular surfaces that impact emissivity. The objective of this work is to present high speed thermographic measurements of single and multiple scan tracks on substrates with and without pre-placed powder and to analyze and compare the impacts of powder on melt pool length and cooling rate measurements.

Introduction

Thermographic measurements of powder bed fusion (PBF) provide valuable insight into the process. The measurements can be used to study the process [1–3], to validate models [4], to better understand the material transformations that occur during the process [5–6], or to develop real-time monitoring and control techniques [7 - 11]. However, optical measurement of the surface temperature is challenging for a variety of reasons, such as the variable emissivity of the surface [12–13] and spatter that regularly occurs during the process [14]. While many studies have implemented thermographic techniques to measure the melt pool length and cooling rates during PBF processes, the impact of the process on the measurement and its error have not been well characterized.

Many of the challenges involved with thermography of PBF can be alleviated by removing the powder and studying the process while scanning on bare metal surfaces. Although this strategy removes the experiment from the actual process that consolidates layers of powder, it has two advantages. First, scans on bare surfaces are easier to measure, enabling the measurement itself to be studied. The second advantage is that the simplified process is easier to simulate and allows the modeler to validate the physics and material model without the powder, decreasing the number of variables in the model.

For instance, similar to other studies [1, 3, 4, 6, 7, 9–11], the earliest PBF thermography studies performed by the National Institute of Standards and Technology (NIST) were performed during the build of a small part [14–15]. Although informative, the chaotic nature of the spatter and the rough solidified surface made the process of quantifying the measurements difficult. Consequently, the experiments have been simplified by removing the powder so that better quality data could be acquired during single line

[1] Certain commercial equipment, instruments, or materials are identified in this paper in order to specify the experimental procedure adequately. Such identification is not intended to imply recommendation or endorsement by the National Institute of Standards and Technology, nor is it intended to imply that the materials or equipment identified are necessarily the best available for the purpose. This publication was prepared by United States Government employees as part of their official duties and is, therefore, a work of the U.S. Government and not subject to copyright.

Heigel, Jarred; Lane, Brandon.
"The effect of powder on cooling rate and melt pool length measurements using in situ thermographic techniques."
Paper presented at Solid Freeform Fabrication Symposium, Austin, TX. August 7, 2017 - August 9, 2017.

scans, enabling the melt pool length to be measured over the processing space [2] and to provide model validation data [5]. Now that the measurement process and thermal behavior of the material are better understood, powder can be re-introduced into the experiment so that its effect on the measurement and the process can be investigated.

This objective of this work is to present a preliminary investigation into the impact that powder has on thermographic measurements of melt pool length and cooling rate. Several cases are studied, two single line scans and two multiple scan tracks, half on a bare surface and the other half on a single layer of hand-spread powder. The acquired thermal images are qualitatively compared to understand spatter and the approximate length of the hot region as a function of line count. Radiant temperature profiles are extracted from these images and the cooling rate is calculated. Observations are made from these comparisons and their impact on the current work and on the future direction of the thermographic effort at NIST is discussed.

Experimental Method

The experiments consist of scanning single tracks and small areas using a commercial laser PBF machine and measuring the radiant temperature of the process using a high-speed thermal camera. The camera observes a 12 mm by 6 mm area in the build chamber through a custom fabricated door [2, 14]. The camera operates at a frame rate of 1800 Hz and an integration time of 40 µs, and the system is sensitive to wavelengths between 1350 nm and 1600 nm and can measure radiant temperature between 550 °C and 1038 °C. Although the camera does not directly measure the true temperature of the surface, the camera signal and surface temperature are related according to [16]:

$$S_{\text{meas}} = F(T_{\text{radiant}}) = \varepsilon \cdot F(T_{\text{true}}) + (1 - \varepsilon) \cdot F(T_{\text{environment}}) \quad (1)$$

where S_{meas} is the signal measured by the camera, $F(T_{\text{radiant}})$ is a calibration function to convert the signal measured by the camera to a black-body temperature, T_{true} is the actual temperature of the target surface, $T_{\text{environment}}$ is the temperature of the environment, and ε is the emissivity of the surface. When the emissivity of the surface is unknown, as in this study, the radiant temperature of the surface is reported.

Figure 1 presents the setup inside the build chamber. Figure 1A is a view through the viewport on the custom door of the rotary sample holder and five 25 mm square substrates (3 mm thick). Figure 1B shows a close-up of one of the samples after an area has been scanned.

Table 1 presents the four different cases studied in this work. Cases 1 and 2 produce single line scan tracks while Cases 3 and 4 scan a 5 mm x 4 mm area using multiple consecutive scans (39 in total, alternating direction). The scans are offset by 0.1 mm (hatch distance). Cases 1 and 3 are executed on bare substrates whereas Cases 2 and 4 are performed on a single hand-spread layer of powder (approximately 36 µm thick). In each case the nominal laser power is 195 W and the scan speed is 800 mm/s. In all cases, each scan track is 5 mm long.

Table 1 - The test cases investigated in the current work.

	Case 1	Case2	Case 3	Case 4
Number of scan tracks	1	1	39	39
Layer of powder?	No	Yes	No	Yes

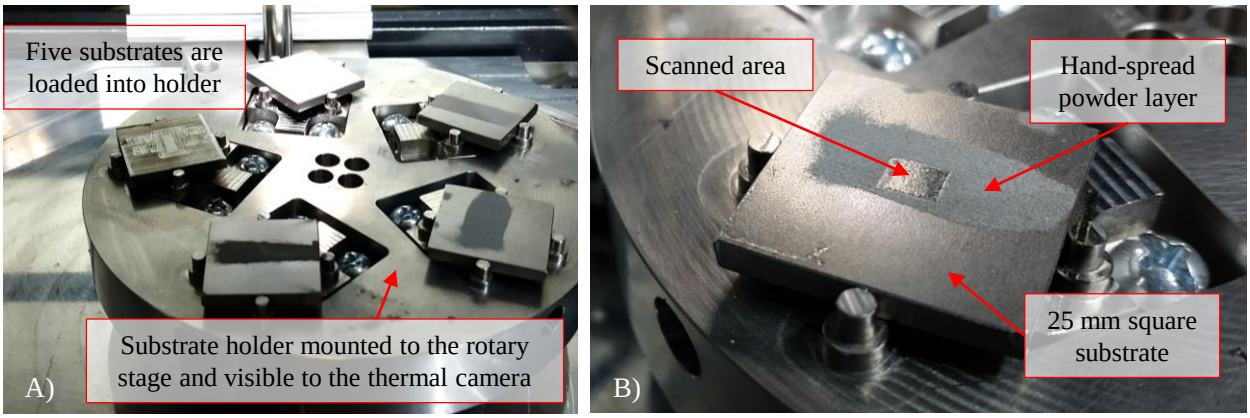

Figure 1 - Experiment setup inside the PBF build chamber. A) Image acquired through the viewport on the custom door showing the sample holder and small substrates. B) Close up of a substrate with a hand-spread powder layer after scanning an area (Case 4).

Results

Figure 2 presents select frames acquired during steady-state in Cases 1 and 2. As found in the prior study by the authors, steady-state occurs after the laser has traveled approximately 1.5 mm [2]. Case 1 appears to be more consistent and shorter than Case 2. The plume is visible following above the scan track, with a slight reflection of it below the track. In contrast, the Case 2 is far less consistent. A significant amount of spatter can be seen above and behind the track, making the images look far more

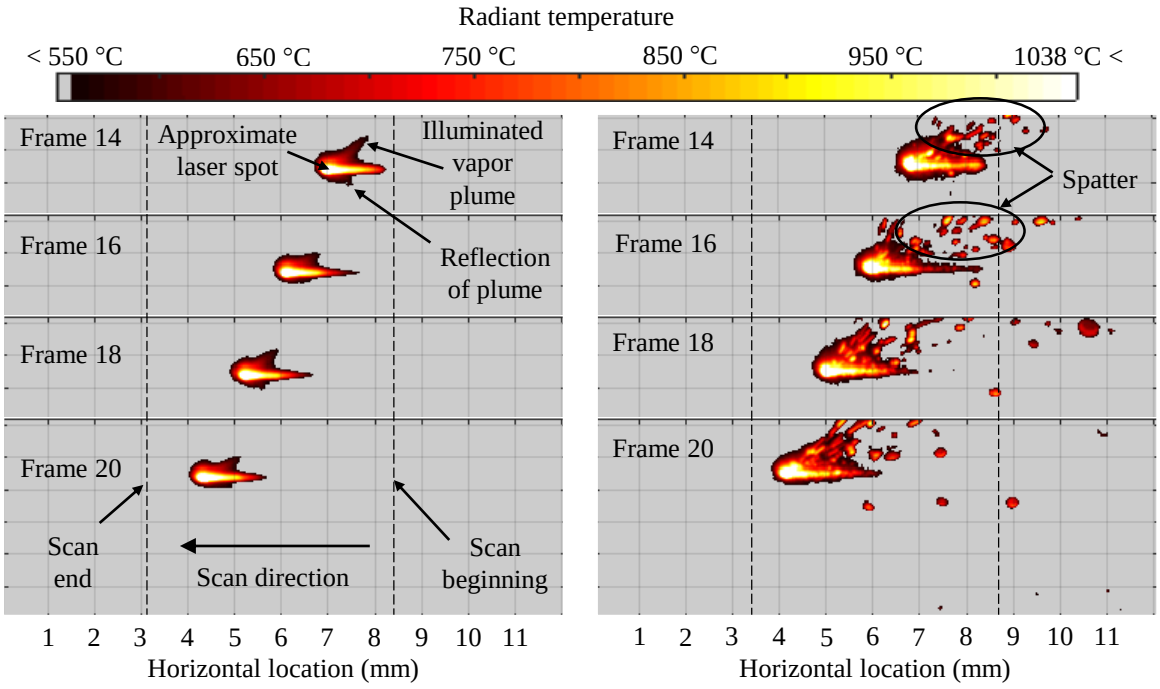

A) Case 1, single scan track on a bare plate

B) Case 2, single scan track on a layer of powder

Figure 2 - Select frames acquired using the thermal camera during steady state of the single scan tracks.

chaotic than the bare surface scans.

Select frames during the deposition of Cases 3 and 4 are shown in Figure 3. These frames are acquired immediately before the conclusions of their respective scan tracks. The length appears to increase as more lines are scanned and it seems that steady state is achieved shortly after the 7th scan track. In Case 4, which has a layer of powder, the amount of spatter is greater during the first scan track than in subsequent tracks.

Figure 4A presents the temperature profiles extracted along the scan track from each frame acquired during steady state in Cases 1 and 2. The melt pool length and the solidus-to-liquidus radiant temperature

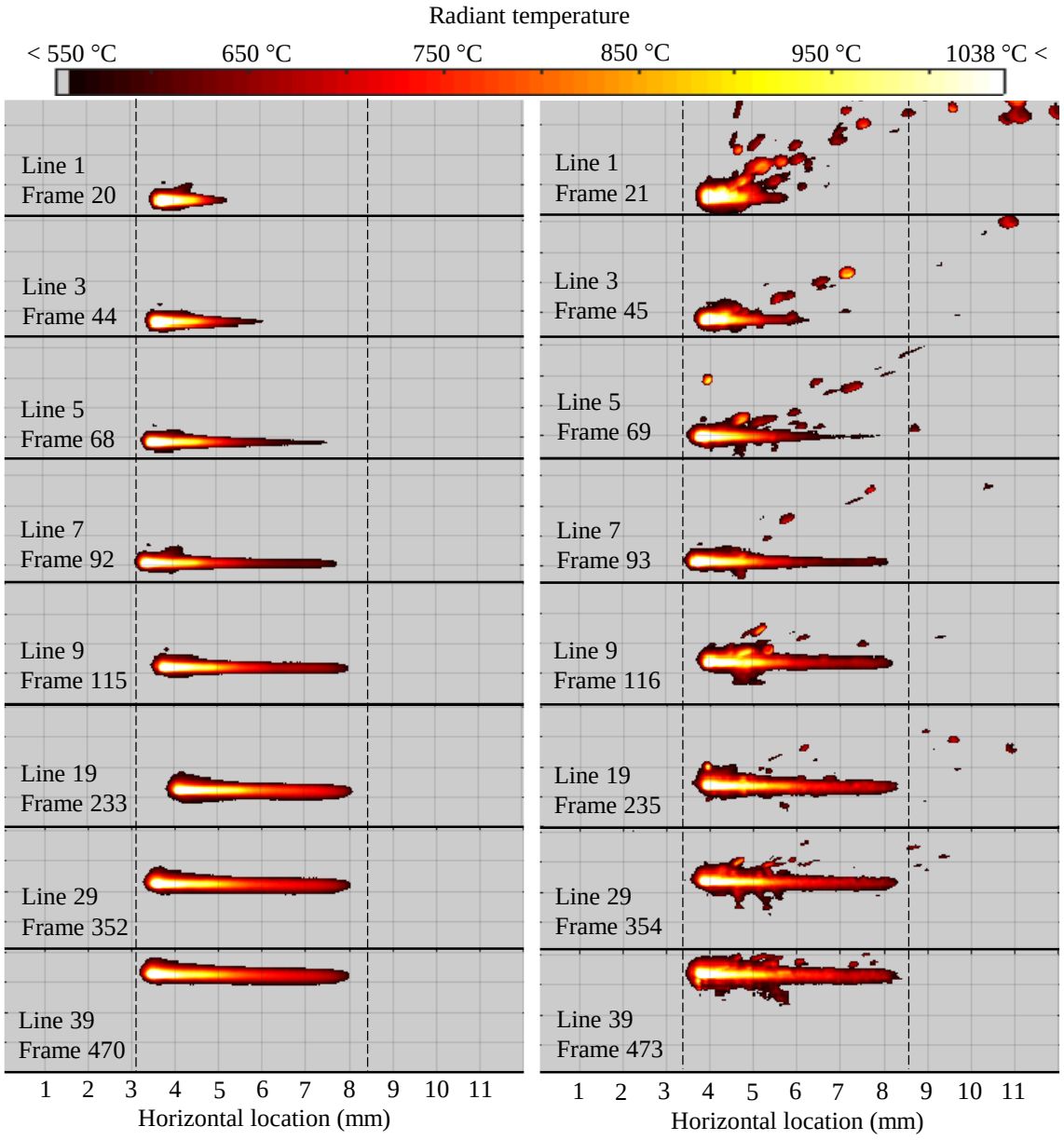

A) Case 3, multiple line scans on a bare plate

B) Case 4, multiple line scans on a layer of powder

Figure 3 - Frames acquired immediately before the completion of select scan tracks during Cases 3 and 4.

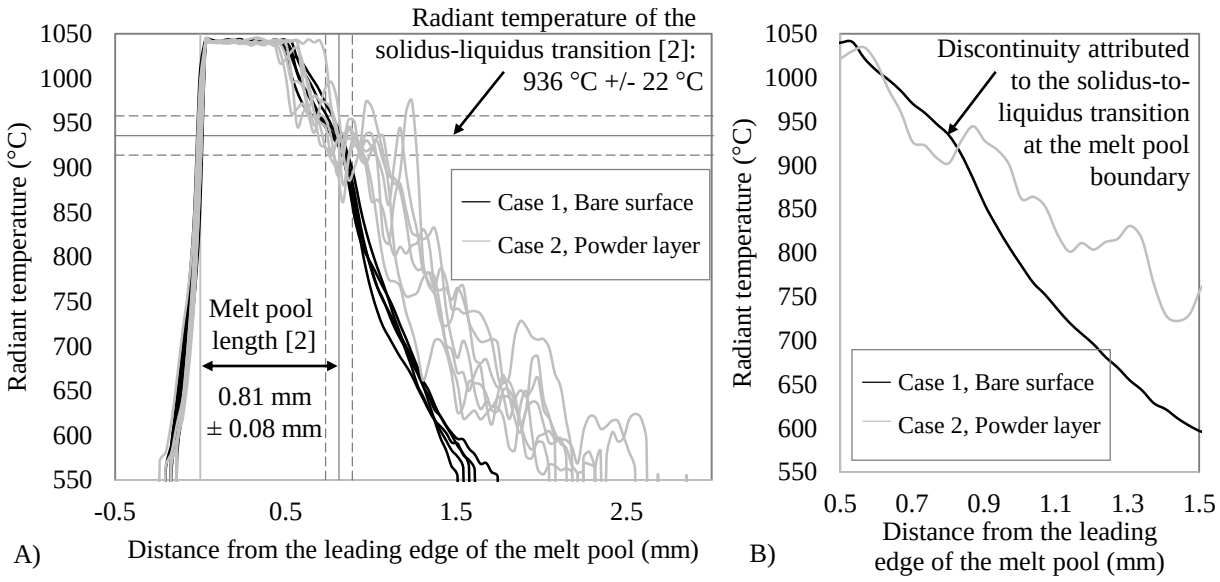

Figure 4 – The steady state radiant temperature profiles in Cases 1 and 2 (A). The vertical and horizontal lines indicate the melt pool length measurement and the solidus-to-liquidus radiant temperature [2]. For those values, one standard deviation is reported. B) an individual profile from each case to illustrate the discontinuity attributed to the solidus-to-liquidus transition.

found in the earlier study are included for comparison [2]. The gray horizontal lines indicate the radiant temperature of the solidus-to-liquidus transition while the vertical gray lines indicate the front and back of the melt pool, based on the length measured in the earlier study. These plots support the observations made of Figure 2. The bare surface scan in Case 1 produces consistent temperature profiles, whereas the Case 2 scan on a layer of powder produces profiles that have a significant amount of variation and have a greater radiant temperature. A closer investigation of these profiles suggests that, although the discontinuity associated with the solidus-to-liquidus transition cannot be detected in the powder case, it appears that the melt pool length is similar between the two cases, as illustrated with an example in Figure 4B.

Figure 5 presents temperature profiles of select scan tracks first shown in Figure 3. Once again, the profiles of the bare surface scan are smooth, whereas those of the powder layer scan have a significant amount of variation, though the variation is less as the scan line number increases. Although the discontinuity associated with the solidus-to-liquidus transition is imperceptible in the powder layer radiant temperature profiles due to this variability, the melt pool length can be measured by assuming the bare surface measurements in the previous study can be applied to the powder layer. If this assumption is valid, then in both cases the melt pool length nearly doubles in each case from the first line (approximate length of 0.76 mm) to the end of the 39th line (approximate length of 1.5 mm).

The rate at which the scan track cools from 900 °C to 700 °C (radiant temperature) is calculated using the following equation and the results are presented in Figure 5:

$$CR = \frac{200\ °C}{(p_{700\ °C} - p_{900\ °C})\,{}^{r}/_{v}} \tag{2}$$

where *CR* is the cooling rate in radiant temperature, *v* is the scan velocity (800 mm/s), *r* is the horizontal camera instantaneous field of view (0.036 mm per pixel), and *p* is the location (pixel) in the frame of interest where the radiant temperature profile equals 900 °C and 700 °C. The markers for Cases 1 and 2

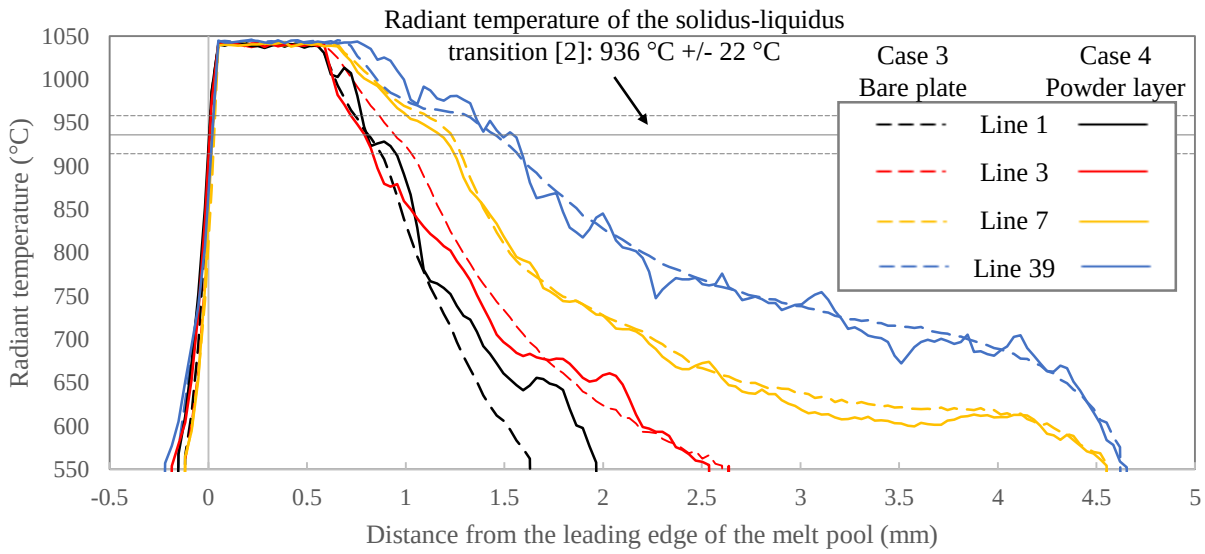

Figure 5 - The radiant temperature profile near the end of select scan track that were initially presented in Figure 3. The solid horizontal line indicates the mean solidus-to-liquidus transition temperature, while the dashed horizontal lines represent one standard deviation [2].

present the mean of calculations performed on all frames acquired during steady state. The standard deviation of those calculations (1σ) is reported in the text on the plot. The markers indicating Cases 3 and 4 represent the calculation from a single frame acquired at the end of each odd-numbered scan track. For each of the multiple scan track cases, the cooling rate decreases as the line count increases, reaching an apparent steady state value around the 20th line. The average and standard deviation (1σ) is calculated for the odd numbered scan tracks, from 21 to 39, and is reported on the figure. In both multi-line cases, the cooling rate decreases to values that are approximately 15 % to 20 % of the values measured in the single scan track cases. The standard deviation of the measured values also decreases by an order of magnitude or more from the single scan tracks to the steady state multiple track scans.

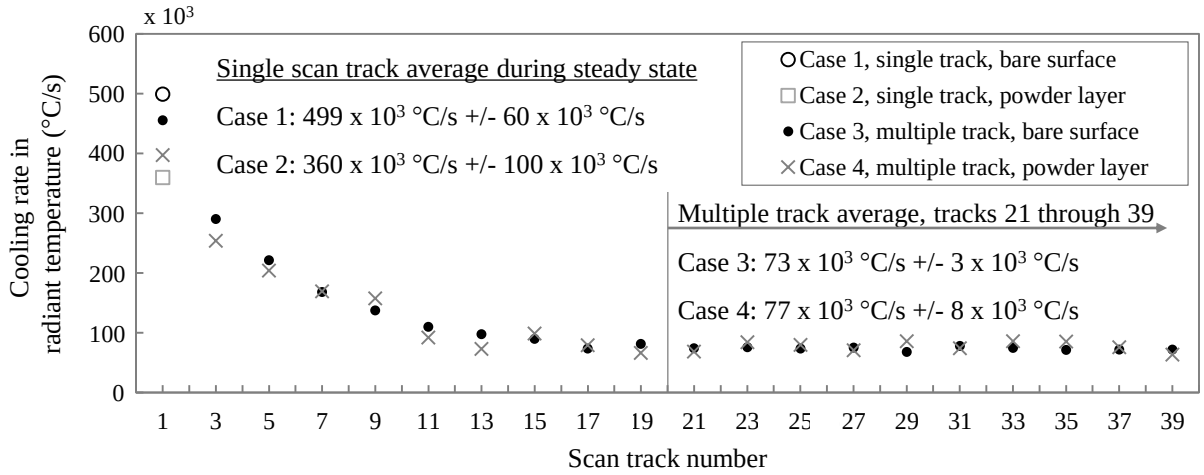

Figure 6 - The rate the material cools from 900 °C to 700 °C for each odd numbered scan track.

Discussion

The results presented in this work confirm that thermographic measurements of scan tracks on layers of powder are more complex than when the same scans are performed on bare surfaces. Scans on powder result in greater fluctuations along the temperature profile of the scan track behind the melt pool. Considering the camera system used in this study and its resolution, these fluctuations mask the discontinuity that is associated with the solidus-to-liquidus transition and could be detected in the bare surface scans. Since the discontinuity is regularly used to identify the melt pool boundary and measure the melt pool length, the melt pool length could not be measured without assuming the radiant temperature of the transition is similar in the bare surface and powder layer scans. Further work is required to confirm if this assumption is valid. In addition, the single scan tracks on a powder layer appear to be hotter than on bare surfaces, as demonstrated in Figure 4, and the cooling rate in radiant temperature is slower, as indicated in Figure 6. The hotter appearance and slower cooling rate in the radiant temperature scale could be attributed to two factors that require a more detailed analysis.

1) The powder layer effectively increases the absorption efficiency of the laser, leading to a greater amount of energy entering the part [17] and increasing the melt pool length and the residual temperature in the track.
2) The effective emissivity of the track is greater when created on a powder layer than on a bare surface, leading to an apparent hotter temperature in the radiant temperature scale even though the true temperature is equal to the bare surface scan. The effective emissivity could be elevated in the powder layer cases by:
    a. The rougher surface of the scan track [18].
    b. The elevated scan track (due to the solidified powder layer) changing the relative viewing angle, which has been shown to affect emissivity [12], [13].
    c. Reflections from the spatter on the scan track, increasing the signal measured by the camera according to Equation (1).

A more detailed investigation is required to understand the impact of each of these possible factors to understand whether powder does impact the melt pool length and the temperature in single track scans, or if it only appears to have an effect.

Analysis of the multiple scan track cases suggest that the temperature between the bare surface and powder layer scans are not as different as they appear in the single line cases. As the scan lines count increases, the temperature profiles of the two cases have better agreement, as shown in Figure 5. Furthermore, the variability appears to decrease, as does the spatter, after the first few lines, as indicated in Figure 5 and Figure 6. These observations suggest the following:

1) Spatter can have a significant impact on both the magnitude of the temperature profile and its variability.
2) The deposition of successive tracks, that are deposited moving away from the camera, has a different impact on effective emissivity than that of a single scan track.
3) The difference in energy absorption between scans on bare surface and single layers of powder is only significant for the first layer, since denudation draws powder into the track, exposing the bare surface for each successive track [19], [20].

Once again, a more detailed experiment must be designed to investigate these and other possibilities.

Conclusions

This work presented thermographic measurements acquired during the powder bed fusion process. Single and multiple scan tracks were executed on both bare surfaces and hand-spread powder layers. The results were compared to gain insight into the effect of powder on both the process and the measurement. Results indicate that the presence of powder increases the variability in the radiant temperature profiles behind the melt pool that that while the single scan tracks appear to be hotter in radiant temperature, it is unclear if the increase is due to differences in true temperature or the effective emissivity of the surface. The multiple scan track results indicate that the bare surface and powder layer scans are more similar as the number of scan lines increase. Future work will improve upon the experimental method and analysis to answer questions that could not be answered in this preliminary study.

References

[1] M. Doubenskaia, A. Domashenkov, and I. Smurov, "Study of the laser melting of pre-deposited intermetallic TiAl powder by comprehensive optical diagnostics," *Surface and Coatings Technology*, vol. 321, pp. 118–127, 2017.

[2] J. C. Heigel and B. Lane, "Measurement of the Melt Pool Length During Single Scan Tracks in a Commercial Laser Powder Bed Fusion Process," in *Proceedings of the ASME 2017 12th International Manufacturing Science and Engineering Conference (MSEC 2017)*, Los Angeles, CA, 2017, vol. 12.

[3] E. Rodriguez, J. Mireles, C. A. Terrazas, D. Espalin, M. A. Perez, and R. B. Wicker, "Approximation of absolute surface temperature measurements of powder bed fusion additive manufacturing technology using in situ infrared thermography," *Additive Manufacturing*, vol. 5, pp. 31–39, 2015.

[4] S. Price, B. Cheng, J. Lydon, K. Cooper, and K. Chou, "On Process Temperature in Powder-Bed Electron Beam Additive Manufacturing: Process Parameter Effects," *Journal of Manufacturing Science and Engineering*, vol. 136, no. 6, p. 061019, 2014.

[5] T. Keller *et al.*, "Application of finite element, phase-field, and calphad-based methods to additive manufacturing of Ni-based superalloys," *Acta Materialia*, 2017.

[6] I. Yadroitsev, P. Krakhmalev, and I. Yadroitsava, "Selective laser melting of Ti6Al4V alloy for biomedical applications: Temperature monitoring and microstructural evolution," *Journal of Alloys and Compounds*, vol. 583, pp. 404–409, 2014.

[7] J.-P. Kruth, P. Mercelis, J. Van Vaerenbergh, and T. Craeghs, "Feedback control of selective laser melting," in *Proceedings of the 3rd International Conference on Advanced Research in Virtual and Rapid Prototyping*, 2007, pp. 521–527.

[8] P. Lott, H. Schleifenbaum, W. Meiners, K. Wissenbach, C. Hinke, and J. Bültmann, "Design of an optical system for the in situ process monitoring of selective laser melting (SLM)," *Physics Procedia*, vol. 12, pp. 683–690, 2011.

[9] M. Doubenskaia, M. Pavlov, S. Grigoriev, E. Tikhonova, and I. Smurov, "Comprehensive optical monitoring of selective laser melting," *Journal of Laser Micro Nanoengineering*, vol. 7, no. 3, pp. 236–243, 2012.

[10] H. Krauss, C. Eschey, and M. Zaeh, "Thermography for monitoring the selective laser melting process," presented at the Proceedings of the Solid Freeform Fabrication Symposium, 2012.

[11] J. Raplee *et al.*, "Thermographic Microstructure Monitoring in Electron Beam Additive Manufacturing," *Scientific Reports*, vol. 7, p. 43554, 2017.

[12] J. Heigel, B. Lane, and S. Moylan, "Variation of Emittivity with Powder Bed Fusion Build Parameters," presented at the Proceedings of the 2016 Annual International SFF Symposium, 2016.

[13] L. del Campo *et al.*, "Emissivity measurements on aeronautical alloys," *Journal of Alloys and Compounds*, vol. 489, no. 2, pp. 482–487, Jan. 2010.

[14] B. Lane *et al.*, "Thermographic measurements of the commercial laser powder bed fusion process at NIST," *Rapid prototyping journal*, vol. 22, no. 5, pp. 778–787, 2016.
[15] B. Lane, E. Whitenton, and S. Moylan, "Multiple sensor detection of process phenomena in laser powder bed fusion," presented at the SPIE Commercial+ Scientific Sensing and Imaging, 2016, pp. 986104–986104.
[16] B. Lane, E. Whitenton, V. Madhavan, and A. Donmez, "Uncertainty of temperature measurements by infrared thermography for metal cutting applications," *Metrologia*, vol. 50, no. 6, p. 637, 2013.
[17] R. W. McVey, R. M. Melnychuk, J. A. Todd, and R. P. Martukanitz, "Absorption of laser irradiation in a porous powder layer," *Journal of Laser Applications*, vol. 19, no. 4, pp. 214–224, Nov. 2007.
[18] G. Strano, L. Hao, R. M. Everson, and K. E. Evans, "Surface roughness analysis, modelling and prediction in selective laser melting," *Journal of Materials Processing Technology*, vol. 213, no. 4, pp. 589–597, 2013.
[19] I. Yadroitsev, P. Bertrand, and I. Smurov, "Parametric analysis of the selective laser melting process," *Applied surface science*, vol. 253, no. 19, pp. 8064–8069, 2007.
[20] M. J. Matthews, G. Guss, S. A. Khairallah, A. M. Rubenchik, P. J. Depond, and W. E. King, "Denudation of metal powder layers in laser powder bed fusion processes," *Acta Materialia*, vol. 114, pp. 33–42, 2016.